Proceeding of the
International Conference on Electrical, Computer and Telecommunication Engineering
01- 02 December 2012 (ICECTE2012), RUET, Rajshahi-6204, Bangladesh

ICECTE2012: PI-0001

An Innovative Design of an optimized Grid Tied Solar Photovoltaic (PV) System

M.M. Farhad[1], M.M. Ali[2], M.M. Hossain[3]
Department of Electrical and Electronic Engineering, Ahsanullah University of Science and Technology
Tejgaon Industrial Area, Dhaka, Bangladesh
E-mail: mehedi.farhad99@gmail.com, marfiraj@yahoo.com, marufeeebuet@yahoo.com

ABSTRACT
Due to the increasing concern about the global demand for energy, it is important to reduce the installation cost of the whole solar photovoltaic system. In this paper we have shown that the grid tied solar photovoltaic (PV) system can be developed by omitting the energy storage device which is very much suitable as it requires less installment cost. This paper proposed a new design of a photovoltaic system which can be operated by feeding the solar power to the utility power grid. As a whole a significant reduction in the system cost and efficient system performance is shown in this paper.

KEY WORDS: Smart control, Grid connected PV system, PV system without storage, Net metering, Grid-tie inverter**.**

1. INTRODUCTION

The global demand of power is increasing day by day. As well as the demand of fossil fuel is increasing with that power demand. Bangladesh relies heavily on fossil fuels especially Natural Gas resources for its power generation. To meet this increasing power demand with a small use of fossil fuel, we need to install more solar PV system with the most effective manner. According to the data up to September 2011, more than 1 million off-grid solar PV systems have been installed in the rural area throughout Bangladesh having capacity 50MW. But still the growth rate of PV system and its contribution to the national energy is not sufficient due to the technical inconvenience and installation cost of the PV system. This paper presents an improved and cost efficient way to synchronize the PV array output with the utility grid using a special control scheme. So that, an individual solar PV system owner can acts as an electricity provider to the national power grid.

2. CONVENTIONAL OFF GRID AND GRID-TIED SYSTEM

PV systems can be installed without being connected with the conventional grid lines are off grid system. Moreover there is a very little use of on grid system.

2.1 Conventional Off Grid System

Typical configuration of an off-grid PV system is depicted below in Fig 1. This system is consists of a PV array with a charge controller, battery and DC load. This can be operated to drive an AC load by using an Inverter.

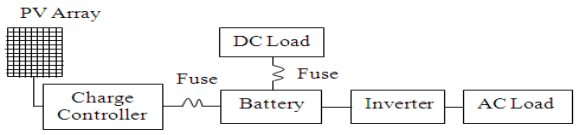

Fig. 1, Schematic diagram of a off-grid PV system with AC and DC loads.

2.2 Conventional Grid Tied PV System

Still grid tied PV system is not a popular PV installation system in the world. Some of the grid tied system has been designed earlier which was not so efficient at all. Configuration of a typical grid-tied PV system is given below in Fig2.

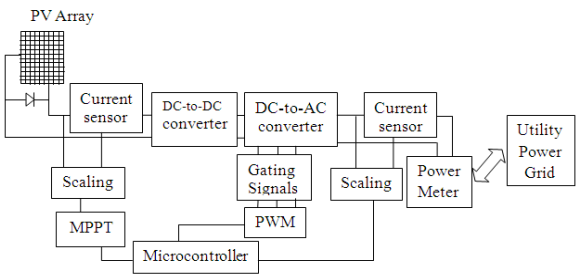

Fig. 2, Block diagram of a grid-tied PV system

3. PROPOSED GRID-TIED PV SYSTEM

In this paper we have proposed a newly designed grid tied PV system, whose depiction is given below.

3.1 System Layout

A newly designed grid-tied PV system is shown in Fig.3. Here the grid-tied PV system is consists of an internal processing junction box with its three end point. These are solar power, utility power grid and Residential load. Here this system always tries to feed the solar power to the utility power grid. At the same time the residential load will consume the power from the utility power grid. But if the grid

power is unavailable then the residential load demand will be supplied by the solar power.

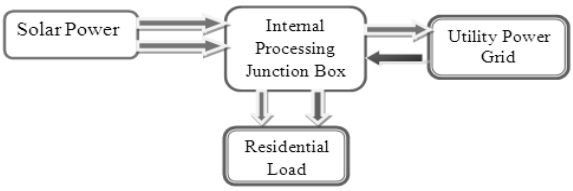

Fig.3, Layout diagram of the planned grid-tied PV system

3.2 Schematic Diagram and the Relay Position

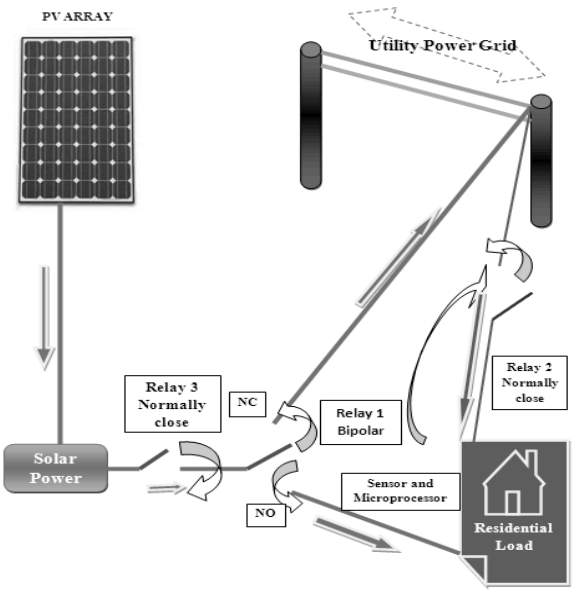

Fig. 4, Diagram of the planed grid-tied PV system

As the illustration in Fig.4, the power flow from the PV array and the utility power grid is controlled by three relay. The positions of the relays are also shown in Fig.4. During normal operation relay 3 always at Normally Close (NC) position. At day time when sunlight and grid power is available relay 1 and relay 2 both will be at NC position. So that the solar power will feed to the grid through relay 1 and at the same time residential load will consume power from utility power grid through relay 2. But if grid power is unavailable relay 2 will be off and relay 3 will be at Normally Open (NO) position. So that, the solar power can flows to the residential load. Again if there is any overloading situation due to the residential load the relay 3 will operate to disconnect the connection and ensure the safety of the system. At the same time it will generate a signal to the consumer for reducing the load. This is how the system will operate with a most efficient manner.

3.3 Grid-Tied PV System Block Diagram

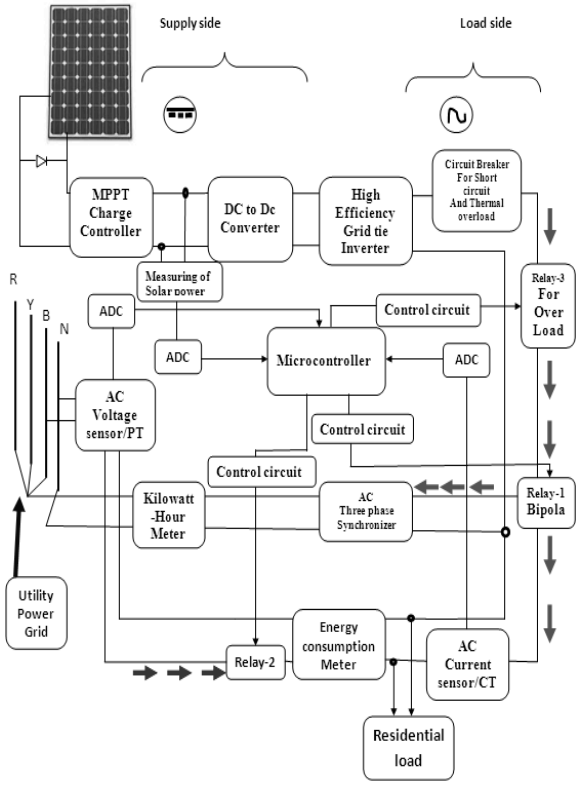

Fig. 5, Grid-Tied PV system block diagram

Fig.5 demonstrates the block diagram of the control scheme. The system block diagram consists of solar PV array, MPPT charge controller, DC to DC converter, High efficient Grid Tie inverter, AC three phase synchronizer, Microcontroller, DC power measuring device, CT, PT, ADC (Analogue to Digital converter), Relays and Metering device. We can describe all those elements in three parts:

3.3.1 Voltage Control of Solar PV Array

The power output of a PV array depends on the voltage level where it operates under a given condition of irradiance and cell-surface temperature. For efficient operation, a PV array should operate near at the peak point of the V-I curve [1]. Various Maximum Power Tracking (MPPT) techniques have been proposed in [2] and [3]. The MPPT device of the block diagram in Fig.6 always tries to stable the PV output voltage and also ensure the maximum power output of the PV system.

3.3.2 Grid Tie Inverter

The inverter is the heart of the PV system and is the focus of all utility-interconnection. An inverter is a device that converts direct current to alternating current. The PV inverters are classified into two categories, Stand Alone Type and Synchronous Grid Tie Type. Synchronous inverter is a special type of inverter which is specially designed for solar panel [4]. This type of inverter always collect the data of

voltage and frequency of utility power grid by a AC synchronizer and synchronize the inverter output with the utility power grid. So that, it is possible to install a medium to large-size PV array and remain hooked up to the utility power grid [4].

3.3.3 Control Section

The power measuring block measures the solar power with respect to time. The AC current sensor senses the residential load current which can be converted in power by multiply with the system voltage. The output of the measured solar power and the load demand goes to the microcontroller through two ADC (Analogue to Digital converter). The availability of the grid power can be detected by a PT. The output of the PT goes to the microcontroller through another ADC. With the help of these data microcontroller will send signal to the relay control circuit. Then the relays will operate according to the decision of the microcontroller. The relay control circuit consists of a 1kΩ resistance and a NPN Transistor (BD135). Fig.6 shows the relay control circuit. Here pic16F88, 28 pin microcontroller with 16MHZ clock pulse generator and IC7805 voltage regulator can be used to obtain best performance of the system.

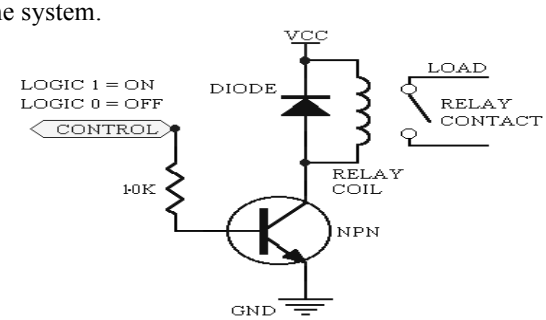

Fig. 6, Relay control circuit

4. CONTROL SCHEME FLOW CHART

Fig. 7 shows the flow chart of the control scheme. According to the flow chart we develop a programme in mikroC and also in assembly code to check the system performance. Here, after initialization of the system parameter the microcontroller always check the availability of grid power and solar power and take decision to control the relay 1 and relay 2. The microcontroller also compares the solar power with the residential load to control the relay1 and relay 3. According to the technical requirement in IEEE 1547, to prevent islanding situation the microcontroller always monitor the voltage and frequency of the grid and disconnect the grid tie inverter from the grid for any worse situation by controlling relay 1.

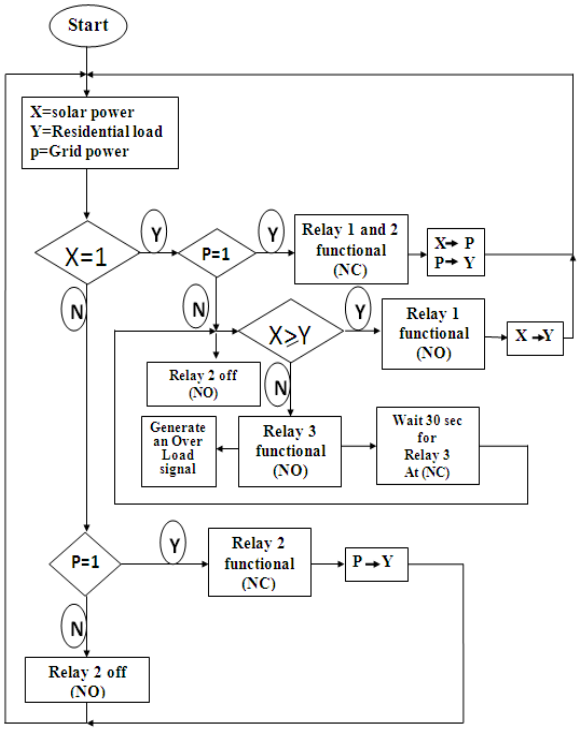

Fig. 7, Flow chart of the control scheme

5. NET METERING SYSTEM

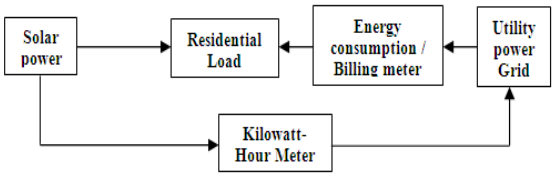

Fig. 8, Net metering system

In our system a solar photovoltaic (PV) plant owners can also enjoy the opportunity of net metering by selling energy to the National grid when the consumed energy is less than the Delivered energy. Here we use two meter for metering the consumed and delivered power.The energy consumption/billing meter will record how much energy is consumed by the costumer from the utility power grid. When the kilowatt-hour meter will record the amount of energy is delivered from the solar system to utility power grid. Fig.8 shows the net metering system.

6. ADVANTAGES OF THE DESIGNED SYSTEM

A typical solar system would require a large battery bank to storage the solar energy. By removing this expensive storage device the system installation cost can be maintained within an acceptable limit. Grid tied system is more power efficient than a conventional solar system. It ensures full utilization of solar energy whereas battery discharge rate is 60% to 65% in conventional off-

grid solar system in Bangladesh. As energy storage capacity of these batteries degrade with time and need replacement which required extra cost for the system owner. This grid-tied system also represents the consumer as an energy provider to the utility power grid. Net metering allows system owners to get credit for any electricity the system sends to the grid. If the grid power is unavailable, still the system will continue to supply critical on-site loads.

7. COST ANALYSIS OF THE PV SYSTEM

Fig. 9 shows the graph of installation cost vs PV array Wp of a PV system with and without storage device. Here for a typical system we assume the relative cost of the components as: PV array Tk/- 100 per Wp, Battery Tk/- 100 per AH, Inverter Tk/-50 per Watt, Charge controller Tk/- 100 per Amp. This graph shows that the system cost will be cheap for a same Wp PV array installation without storage device.

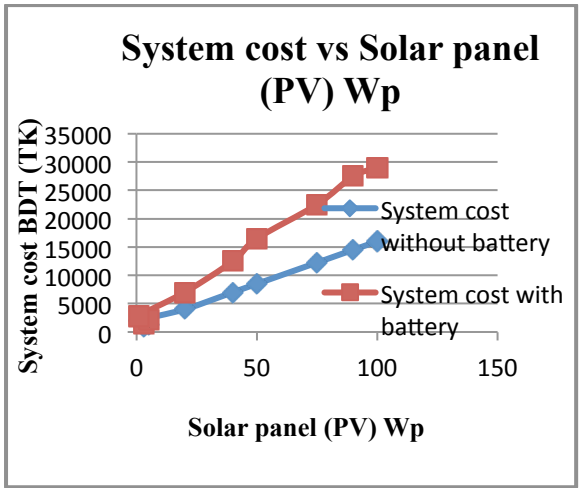

Fig. 9 System cost vs solar panel (PV) Wp.

8. LIMITATION OF THE DESIGNED SYSTEM

In this paper we have come within the reach of a new PV system design. But in our design we have also some limitations. This grid-tied system without storage can't supply power during night or rainy day when sunlight is not sufficient. Again power output from certain renewable energy sources, like wind and solar, can be intermittent. Fluctuation in output can negatively affect power grid frequency, voltage, component performance, causing instability in the power generation system and interrupted service to the customers.

9. CONCLUSIONS

This system has been designed with a concept of micro photovoltaic power station. Still the solar PV system installation cost is not within an acceptable limit. Proper step should be taken to reduce the solar PV system cost. So that, the general electricity consumer can concentrates their attention in grid-tied PV system. We hope there will be occur a lot of activity regarding grid-tied PV system and then our work may help to decide an optimized way.

So, in this paper we have shown an advanced grid-tied PV system which is suitable for Bangladesh as well as for other countries to produce more energy from renewable energy sources. Thus every photovoltaic system which is installed in any where can be treated as a micro PV power station, no matter what ever the generation capacity of the plant.

10. ACKNOWLEDGMENT

This study was made possible with the help of the installed PV system at Ahsanullah University of Science and Technology. Special thanks to Professor Dr. Shahidul Islam Khan and Assistant Professor Md. Maruf Hossain for their useful discussion.

REFERENCES

[1] M. R. Mojumder, A. M. Bhuiyan, H. Kadir, M. N. Shakil, A. Rahman, "Design & analysis of an optimized Grid-Tied PV system: Perspective Bangladesh" *IACSIT international journal of engineering and technology*, Vol.3, No. 4, August 2011.

[2] T. Noguchi et al., "Short-current pulse-based maximum-power-point tracking method for multiple photovoltaic-and-converter module system," *IEEE Trans. Ind. Electron.*, vol. 49, no. 1, pp. 217–223, Feb. 2002.

[3] K. H. Hussein, "Maximum photovoltaic power tracking: An algorithm for rapidly changing atmospheric conditions," *Proc. Inst. Electr. Eng.—Generation, Transmission, Distribution*, vol. 142, no. 1, pp. 59–64, Jan. 1995.

[4] M. Gohul, T. Jayach, A. M. Ali, T. G. Raju, N.Santhosh Kumar, M.R. Saravanan, "Anew design of grid tie inverter for a grid interactive solar photovoltaic power generation-An alternative option for energy conservation & security" *IJECT* Vol. ,2, Issue 3, Sept.2011.

Proceeding of the
International Conference on Electrical, Computer and Telecommunication Engineering
01- 02 December 2012 (ICECTE2012), RUET, Rajshahi-6204, Bangladesh

ICECTE2012: PI-0002

Current-Voltage Characteristics of Hydrogenated a: Si Thin Film Solar Cells: An Analytical Approach

M. M. Rahman[1], M. M. Haque[2], Md. Iqbal Bahar Chowdhury[3]
[1, 2,,3] Department of EEE, United International University
E-mail: milton_uiu@yahoo.com, haque082@gmail.com,ibchy@eee.uiu.ac.bd

ABSTRACT
An analytical model has been developed for J-V characteristics of a-Si-H p-i-n solar cells. The model is based on the perturbation theory. The developed model provides more computational efficiency as well as better physical insight.

KEYWORDS: a-Si-H thin flim Solar cell, Analytical current-voltage characteristics, Photo-generated Current Density, Dark Saturation Current Density, Exponential photon absorption.

1. INTRODUCTION

The second generation thin film solar cells draws increasing interest of the researchers because of their lower production cost and improved efficiency. Hydrogenated amorphous Si (a-Si:H) absorber based cells are one of the most potential photoconductors for thin film solar cells because of their excellent efficiency [1]. These solar cells use p-i-n type structure where the p and n-layers are few nm and the i-layer is $:1\ \mu m$ thick. The incident photons are mainly absorbed in the i-layer and the photo-generated carriers are collected by the built-in electric field in this layer. The voltage-dependent charge collection in the intrinsic absorber layer is the dominant charge collection mechanism in thin film solar cells [4].

Till to date a few theoretical models [4, 5] have been proposed in the literature to describe the current-voltage characteristics of a-Si:H-based thin film solar cells. Hegedus *et. al.* [3] have shown in their work that the most successful model calculates the photocurrent by considering carrier drift and utilizing Hecht collection efficiency formula in the nearly intrinsic absorber layer. But their model [4] is based on an unrealistic assumption that all the carriers are generated at the top interface of the absorber layer for all incident photons. This model also used a number of fitting parameters which includes maximum photocurrent with complete charge collection, reverse saturation current, effective attenuation constant, series resistance and carrier ranges and hence, limited the applicability of the model. Mannan *et. al.* [5] developed an analytical expression for the external voltage dependent photocurrent by considering exponential photon absorption, exponential electron-hole pair generation throughout the absorber layer, carrier trapping and carrier drift in the absorber layer. Although they derived an analytical expression for photocurrent in the absorber layer, they used numerical approaches to derive the J-V characteristics and used carrier ranges and series resistance as fitting parameters.

This work aims to analytically derive the J-V characteristics. In doing so the concept of the perturbation theory has been utilized. The model considered the absorber layer as lightly doped i-layer and hence, uniform electric field can be assumed to exist throughout the absorber layer. The voltage drop across the series resistance is calculated using the doping levels. Therefore, the proposed approach needs no fitting parameters.

2. ANALYSIS

The net current density of a solar cell can be expressed as

$$J(V) = J_d(V) - J_{ph}(V) \tag{1}$$

where $J_d(V)$ is the the dark saturation current density and $J_{ph}(V)$ is the photo-generated current density. Since the heavily-doped n and p-layers are very thin and the intrinsic base (a-Si:H) region is relatively wider, J_{ph} can be approximated as the photo-generated current component in the i-layer only. The voltage-dependent electric field throughout this region can be assumed as constant and can be expressed as

$$E(V) = \frac{V_{bi} - (V - JR_s)}{W_d} \tag{2}$$

where W_d is the width of the intrinsic layer. Unlike the work [5], this work uses V_{bi} instead of the fitting parameter V_0. In Ref. [5], the voltage drop across the intrinsic layer JR_s is calculated from a measured

value of R_s. In this work, JR_s is calculated using the following expression

$$J(V)R_s = J(V)\int_0^{W_d} \frac{1}{q\mu_n n(x) + q\mu_p N_a} dx \quad (3)$$

where symbols have their usual meanings.

2.1. Derivation of Photo-Generated Current Density

The photogeneration current in the i-layer is the sum of the photogenerated electron current (J_n) and hole current(J_p). Since electric field is the dominant mechanism for current conduction in the i-layer, diffusion component of these currents are negligible. The basic equations required to deduce these drift-dominated currents are:

$$J_n = -qn\mu_n E \quad (4)$$

$$J_p = -qp\mu_p E \quad (5)$$

$$\frac{dJ_n}{dx} = \frac{qn}{\tau_n} - qG \quad (6)$$

$$\frac{dJ_p}{dx} = -\frac{qp}{\tau_p} + qG \quad (7)$$

where μ_n (μ_p) is the electron (hole) mobility, τ_n (τ_p) is the electron (hole) lifetime, the negative signs in Eqns. (4, 5) are due to the negative direction of the electric field E given by Eqn. (2) and G is the wavelength-dependent optical generation rate given by

$$G = \alpha(\lambda)\frac{I(\lambda)\lambda}{hc} e^{-\alpha_1(\lambda)W_B} e^{-\alpha(\lambda)x}$$
$$= \alpha(\lambda)G_0 e^{-\alpha(\lambda)x} \quad (8)$$

where α_1 is the absorption coefficient of silicon emitter leyer. Combining the above equations [Eqns. (4) and (6) and Eqns. (5) and (7)] results in first order differential equations of electrons and holes as

$$\frac{dn}{dx} + M_n n = G_n \quad (9)$$

$$\frac{dp}{dx} - M_p p = -G_p \quad (10)$$

where $M_n = \frac{1}{\mu_n \tau_n E}$, $G_n = \frac{G}{\mu_n E}$ and $M_p = \frac{1}{\mu_p \tau_p E}$, $G_p = \frac{G}{\mu_p E}$. Since the hole and electron start drifting immediately after generation i.e. $n(W_B) \approx 0$ and $p(W_B + W_d) \approx 0$, the solutions of the electron and holes are obtained as

$$n(x) = n_0(e^{-\alpha x} - e^{-M_n x}) \quad (11)$$

$$p(x) = p_0(e^{-\alpha x} - e^{M_p(x-W_d)-\alpha W_d}) \quad (12)$$

where

$$n_0 = \frac{\alpha G_0 e^{-\alpha W_B}}{(M_n - \alpha)\mu_p E}$$

$$p_0 = \frac{\alpha G_0 e^{-\alpha W_B}}{(M_p + \alpha)\mu_p E}$$

According to [5], the electron and hole current densities in the i-layer can be expressed as

$$J_n(V,\lambda) = \frac{q\mu_n E}{W_d}\int_{W_B}^{W_B+W_d} n(x)dx$$
$$= \frac{\alpha q G_0 e^{-\alpha W_B}}{(\alpha - M_n)W_d}(J_0 + J_{n1}) \quad (13)$$

$$J_p(V,\lambda) = \frac{q\mu_p E}{W_d}\int_{W_B}^{W_B+W_d} p(x)dx$$
$$= -\frac{\alpha q G_0 e^{-\alpha W_B}}{W_d(M_p + \alpha)}(J_0 - J_{p1}) \quad (14)$$

where

$$J_0 = \frac{1}{\alpha} e^{-\alpha W_B}(1 - e^{-\alpha W_d})$$

$$J_{n1} = \frac{1}{M_n} e^{-M_n W_B}(e^{-M_n W_d} - 1)$$

$$J_{p1} = \frac{1}{M_p} e^{M_p(W_B - W_d)-\alpha W_d}(e^{M_p W_d} - 1)$$

The total photogenerated current J_{ph0} at a particular wavelength λ then can be expressed as

$$J_{ph0}(V,\lambda) = J_n(V,\lambda) + J_p(V,\lambda) \quad (15)$$

The total photogenerated current density is obtained by integrating over all incident photon wavelengths of the solar spectra, i.e.

$$J_{ph}(V) = \int_0^{\infty} J_{ph0}(V,\lambda)d\lambda \qquad (16)$$

2.2. Derivation of Dark Current Density

Since the recombination current dominates over the diffusion current, the dark current density J_d can be approximated as the forward biased recombination current density in the i-layer and can be expressed as [5]

$$J_d(V) = \frac{qn_iW_d}{2\sqrt{\tau_n\tau_p}} e^{\frac{q(V-JR_s)}{AKT}} \qquad (17)$$

where A is the diode ideality factor. In Ref. [5], A is used as a fitting parameter. In this work, the actual value of $A = 2$ is used. Therefore, this work does not need to use any fitting parameters.

2.3. Analytical Derivation of Total Current Density

From Eqns. (2) and (17), it is evident that determination of the total current density, J for a given load voltage, V is analytically intractable. However, using the concept of perturbation theory this intractability problem can be resolved. Since J_{ph} can be solved and $J_d \rightarrow 0$ under short circuit condition (i.e. V=0), the total current density J can be approximated as J_{ph} when $V = 0$. This is not the case for $V \neq 0$, where J_d is required and hence, in turn, the knowledge of J is required to determine the voltage drop across the series resistance R_s [Eqns. (2) and (17)]. Using the concept of perturbation theory, the JR_s at $V = 0$ can be used to determine at $V = \delta V$.

This is justifiable, since the change in n(x) and p(x) compared to N_a is negligible [Eqn. (3)] and hence, the change in current densities can also be negligible, provided that the change in the voltage is very little i.e $\delta V \rightarrow 0$.

Therefore, the n(x), p(x) and JR_s at $V = 0$ can be applied to readily determine the J_d and E and hence, the total current density J at $V = \delta V$ using Eqns. (2) and (17). The same process can be repeated at the $V = 2\delta V, 3\delta V, 4\delta V.....$ where the values of n, p and J at $V = \delta V, 2\delta V, 3\delta V.....$ respectively are used. Therefore, for each δV increment of voltage, J can be analytically determined.

Since the proposed approach needs no fitting parameters, it is more advantageous than the conventional numerical models. Therefore, the approach can provide better physical insight in the J-V characteristics. Although apparently similar to the numerical modeling approaches, the proposed approach is quite different. In the proposed approach, the total current density at any voltage level (V) can be determined only when the same at $V - \delta V$ is known. The number of iteration in the proposed approach, therefore, is limted to the size of δV. Therefore, the approach is expected to be computationally more efficient.

3. RESULTS

Following the analytical procedure outlined in the previous section and using the air mass (AM) 1.5 global spectrum from the ASTM G-173-03 standard [6] as the incident photon flux $I_0(\lambda)$, the J-V characteristics of a-Si:H p-i-n solar cells is plotted and analyzed in this work. The absorption coefficient for amorphous silicon is obtained from the absorption curves in Ref. [7]. The i-layer thickness is $2\ \mu m$.

Fig. 1 shows the J-V characteristics for different sun intensities (100%, 32% and 10% of 1.5 AM global spectrum). J-V curves in this plot improve when intensity level is higher, since increase in the intensity level increases the photo-generated current and hence the short-circuit current I_{SC}.

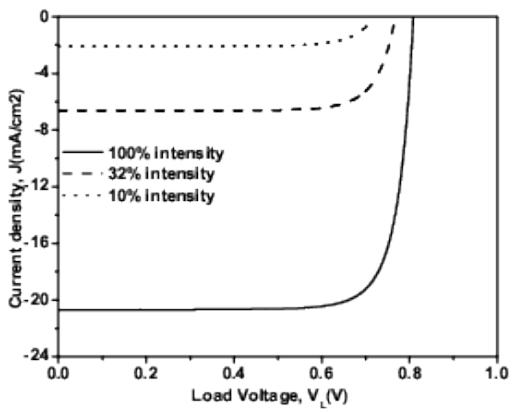

Fig. 1: Net current density versus voltage at three sun intensities.

Fig. 2 shows that increase in the width of the intrinsic layer increases I_{SC} whereas the same decreases the open circuit voltage V_{OC}. When the width increases the optical absorption increases. This results in

increased photo-generation and hence the short-circuit current. Again, increase in width increases the series bulk resistance which results in a corresponding reduction in the open-circuit voltage.

Fig. 3 shows that increase in the hole lifetime-mobility product increases I_{SC} keeping V_{OC} almost constant, whereas Fig. 4 shows that the increase in the electron lifetime-mobility product increases V_{OC} keeping I_{SC} almost constant. This indicates that the former has an effect similar to that of the series resistance and the later has the effect similar to the shunt resistance. Moreover, a comparison between these plots reveal that the J-V characteristics is more sensitive to the hole transport than to the electron transport.

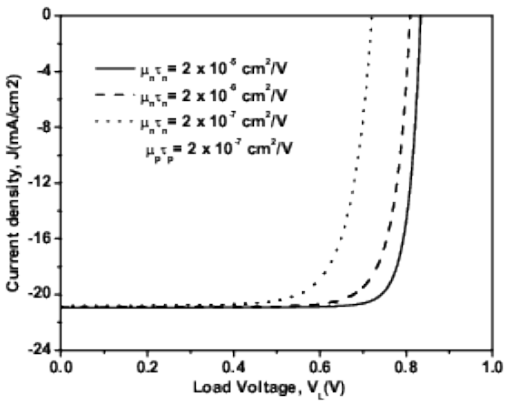

Fig. 2: Theoretical net current density versus voltage for various level of $\mu_n\tau_n$ product of electron in a-Si solar cells.

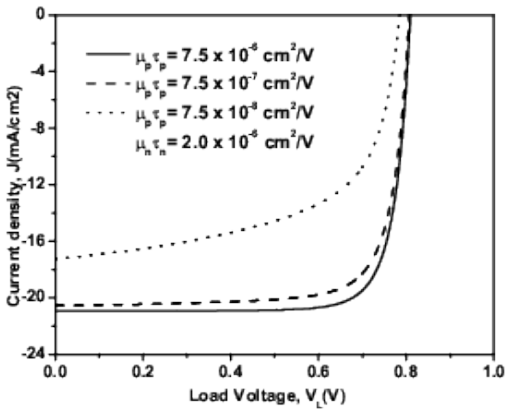

Fig. 3: Theoretical net current density versus voltage for various level of $\mu_p\tau_p$ product of hole in a-Si solar cells.

4. CONCLUSION

An analytical approach has been developed to deduce the J-V characteristics of a-Si:H thin film solar cells having intrinsic absorber layer. It is expected that the proposed approach is computationally more efficient and offers better physical insight than the conventional numerical approaches available in the literature.

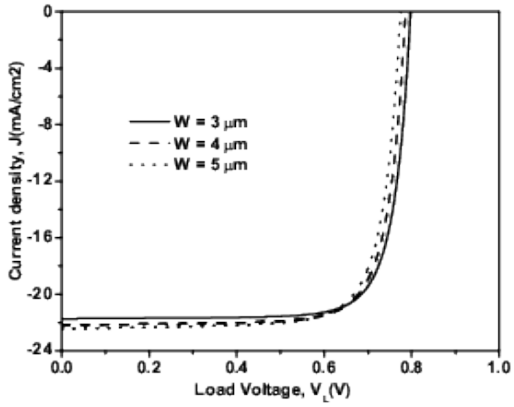

Fig. 4: Theoretical net current density versusvoltage for various width in a-Si solar cells.

REFERENCES

[1] M. A. Green, K. Emery, Y. Hishikawa and W. Warta,``Solar cell efficiency tables (version 35)", *Prog. Photovolt. Res. App*l., vol. 18, pp. 144 –150, 2010.

[2]. J. Nelson, The Physics of Solar Cells, Imperial College Press, Chap. 8, 2003.

[3]. C.Thompson, D. Desai, and S. Hegedus, ``Voltage Dependent Photocurrent Collection in CdTe/CdS Solar Cells", *Prog. Photovolt. Res. Appl*., vol. 15, pp. 587–602, 2007.

[4]. S. S. Hegedus,``Current Voltage Analysis of a-Si and a-SiGe Solar Cells Including Voltage-dependent Photocurrent Collection", *Prog. Photovolt.Res.,* vol. 5, pp.151–168, 1997.

[5]. M. A. Mannan, M. S. Anjan and M. Z. Kabir, ``Modeling of Current-Volatge Characteristics of Thin Film Solar Cells", *Solid-State Electron.*, vol. 63, pp.49–54, 2011.

[6]. S. M. Sze, Semiconductor Devices: Physics and Technology, John Willey & Sons., Chap. 9, 2002.

[7]. http://rredc.nrel.gov/solarspectram/am1.5

Analytical Modeling of Internal Quantum Efficiency of CIGS Solar Cell

Mahiuddin Mahmud Romel[1], Habibur Rahman Khan[2], Nasim Saba Shommo[3], Md. Iqbal Bahar Chowdhury[4]
[1,2,3,4]EEE department, United International University
E-mail: mmromel@gmail.com, habib.eee077@gmail.com, nsshommo@gmail.com, ibchy@eee.uiu.ac.bd

ABSTRACT
In this paper an analytical model for the internal quantum efficiency is developed for the CIGS based Solar Cell. In doing so a uniform electric field has been assumed in the depletion region. The developed model shows that this proposed model can provide a better physical insight for Internal Quantum Efficiency for CIGS solar cells.

KEY WORDS**:** Thin film Solar Cell, Heterojunction Cells, CIGS, Internal Quantum Efficiency, Absorption Coefficient.

1. INTRODUCTION

The second-generation thin film solar cells are increasingly promising for their cheaper production and better efficiency. $CuIn_{1-x}Ga_xSe_2$ (CIGS) based cell is one of the most potential photoconductors for thin film solar cells because of its excellent efficiency [1]. The subscript x represents the mole fraction. The CIGS based solar cells have a substrate device structure of grid /ZnO /CdS /CIGS/Mo/glass [2][3]. The CIGS based cells are p-n heterojunction cells, where a very thin layer (50 μ m) of CdS acts as a highly doped n-layer and CIGS layer acts as lightly doped p-type absorber layer [4]. The thickness of the p-layer is 3000 μm. The voltage dependent charge collection in the depleted absorber layer is the dominant charge collection mechanisms in thin film solar cells [3][5].

Internal Quantum Efficiency η is one of the most important factors of a solar cell because the efficiency of the solar cells is still limited; for example, commercial panels and terrestrial energy conversion, the efficiency is approximately 10% and up to 24% respectively [6]. The physics can be described by modeling the η accurately. So, various researchers have been working on the accurate modeling of η considering various effects. For CIGS based solar cells, Gloeckler [7] describes the device physics. Johansson [8] developed a numerical model of CIGS cell based on one diode model, whereas Gloeckler [9] derived a numerical model using AMPS Modeling. But these works did not develop an analytical model of η for CIGS solar cells.

In this work, an analytical model of η is developed for CIGS based solar cells and also observed the change of η with changing in lifetime and doping concentration.

2. ANALYSIS

2.1 Basic Equations

The hole current density, J_p within the depletion region is given as:

$$J_p = qp(x)\mu_p(x)E_p(x) - qD_p(x)\frac{dp(x)}{dx} \quad (1)$$

where μ_p and D_p are hole mobility and hole diffusivity respectively.The Current continuity equation is given by :

$$\frac{dJ_p}{dx} = -q(R-G) \quad (2)$$

The electron current density, J_n within the depletion region is given as:

$$J_n = qn(x)\mu_n(x)E_n(x) + qD_n(x)\frac{dn(x)}{dx} \quad (3)$$

where μ_n and D_n are electron mobility and electron diffusivity respectively.The Current continuity equation is given by :

$$\frac{dJ_n}{dx} = q(R-G) \quad (4)$$

R-G is the net recombination rate.

2.2 Physical Models

2.2.1 Recombination-Generation

As we consider low doping, only SRH recombination will be present in our model. Therefore, from current continuity equation we get

$$\frac{dJ_P}{dx} = -q\frac{P}{\tau_p} + q\alpha G_0 e^{-\alpha x} \quad (5)$$

$$\frac{dJ_n}{dx} = q\frac{n}{\tau_n} - q\alpha G_0 e^{-\alpha x} \quad (6)$$

2.3 Boundary Conditions

Boundary condition for depletion region are given as below:

1. for electrons at $x = W_E + W_d$;

$$n(W_E + W_d) = \frac{n_i^2}{N_A} \quad (7)$$

2. for holes at $x = W_E$;

$$P(W_E) = \frac{n_i^2}{N_D} \quad (8)$$

2.4 Model Derivation

1. The hole current equation (1) can be rearranged as

$$\frac{dJ_p}{dx} = q\mu_p E_p \frac{dp}{dx} \quad (9)$$

Using equation (9) and equation (5) we will get a first order differential equation of p(x) as follows:

$$\frac{dp}{dx} + \frac{p}{\tau_p \mu_p E_p} = \frac{-\alpha G_0 e^{-\alpha x}}{\mu_p E_p} \quad (10)$$

Now solving this first order differential equation we get

$$P(x) = C_p e^{\frac{-x}{\tau_p \mu_p E_p}} - \frac{G_0}{\mu_p E_p} e^{-\alpha x} \quad (11)$$

Here, C_p is constant.

Now using boundary condition from equation (7) we get the value of C_p and this is:

$$C_p = \left(\frac{n_i^2}{N_d} + \frac{F_0}{\mu_p E_p} e^{-\alpha W_E}\right) e^{\frac{W_E}{\tau_p \mu_p E_p}} \quad (12)$$

Now, substituting this value of C_p in equation (11) we get the value of $p(x)$ and then from equation (1) we get the value of $J_p(x)$.

2. The electron current equation (3) can be rearranged as

$$\frac{dJ_n}{dx} = q\mu_n E_n \frac{dn}{dx} \quad (13)$$

Using equation (13) and equation (6) we will get a first order differential equation of n(x) as follows:

$$\frac{dn}{dx} - \frac{n}{\tau_n \mu_n E_n} = \frac{-\alpha G_0 e^{-\alpha x}}{\mu_n E_n} \quad (14)$$

Now solving this first order differential equation we get

$$n(x) = C_n e^{\frac{x}{\tau_n \mu_n E_n}} + \frac{G_0}{\mu_n E_n} e^{-\alpha x}$$

(15)

Here, C_n is constant.

Now using boundary condition from equation (8) we get the value of C_n and this is:

$$C_n = \left(\frac{n_i^2}{N_A} - \frac{G_0}{\mu_n E_n} e^{-\alpha(W_E + W_d)}\right) e^{\frac{-(W_E + W_d)}{\tau_n \mu_n E_n}} \quad (16)$$

(8)

Now, substituting this value of C_n in equation (15) we get the value of n(x) and then from equation (3) we get value of $J_n(x)$.

3. Now the total current is:

$$J_{tot}(x) = J_p(x) + J_n(x) \quad (17)$$

Now internal quantum efficiency is given by,

$$\eta = \frac{J_{tot}}{J_G} \quad (18)$$

where

$$J_G = q\int G_0 \left(1 - e^{-\alpha(W_E + W_d + W_b)}\right) \quad (19)$$

3. RESULTS

The results for the proposed model are presented and analyzed in this section. The base width of the CIGS cell is chosen as 3000 μm. Fig. (1) shows that left side of the figure is the base region while right side is the emitter and the middle region is the depletion region. This figure shows that η is the highest in the depletion region where η in the base side is low because of the low absorption and the emitter side is for the surface recombination. Fig. (2) and Fig. (3) show the variations on η with the variation of lifetimes. From Fig. (2), it is seen that η slightly changes when the lifetime of electrons changes because of the increase in carrier generation. The effect of variation of lifetime of holes on the internal quantum efficiency is plotted in Fig. (3). Keeping τ_n constant and increasing τ_p, the Internal Quantum Efficiency increases because carrier generation increases with the increasing τ_p. Comparing this two figures (2) and (3), hole transport is dominant. Fig. (4) showing the effect of changing the doping concentration, N_a on the Internal Quantum Efficiency. If we increase the doping concentration, N_a while keeping N_d constant, then the Internal Quantum Efficiency deceases because with the increasing N_a, the width of the depletion region decreases. For this, the generation in the depletion region also decreases. So, η decreases.

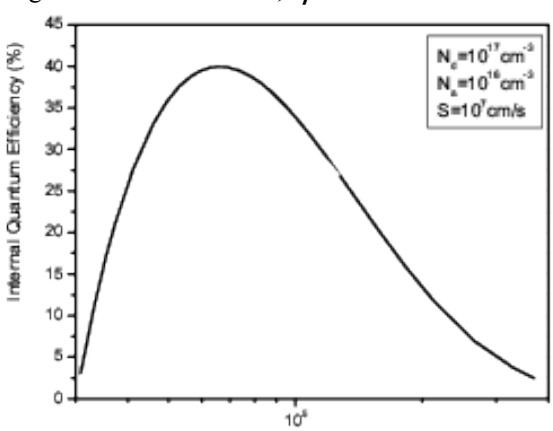

Figure 1: The change of internal quantum efficiency with respect to absorption coefficient in the depletion region and $N_d = 10^{17} cm^{-3}$, $N_a = 2\times10^{16} cm^{-3}$, $S = 10^7 cms^{-1}$.

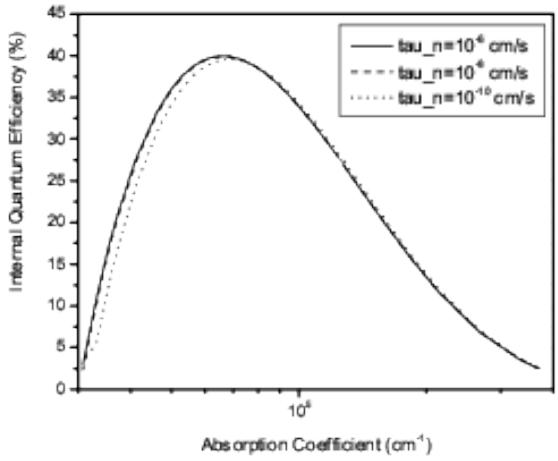

Figure 2: The change of internal quantum efficiency with respect to absorption coefficient in the depletion region with change in the life time of electron, where, $\tau_p = 10^{-10} s$, $S = 10^7 cms^{-1}$, $N_a = 2\times10^{16} cm^{-3}$, $N_d = 10^{17} cm^{-3}$.

4. Conclusion

In this work, an analytical model of Internal Quantum Efficiency for Cigs based solar cells has been derived considering uniform field in the depletion region. The results of the developed model points out that hole transport is dominant and if doping concentration (N_a) increase, then internal quantum efficiency decreases.

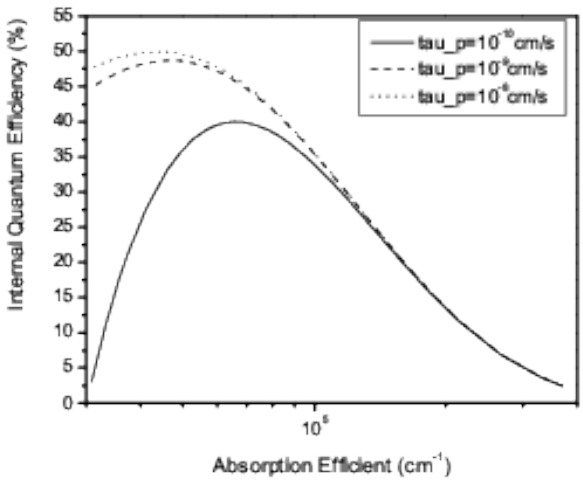

Figure 3: The change of internal quantum efficiency with respect to absorption coefficient in the depletion region with change in the life time of hole, where, $\tau_n = 10^{-6} s$, $S = 10^7 cms^{-1}$, $N_a = 2\times10^{16} cm^{-3}$, $N_d = 10^{17} cm^{-3}$.

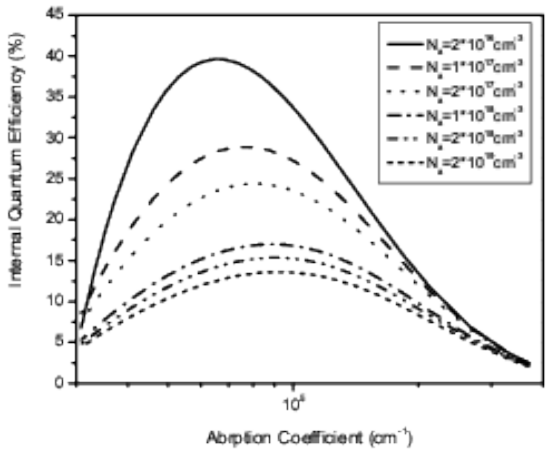

Figure 4: The change of internal quantum efficiency with respect to absorption coefficient in the depletion region with change in the doping concentration (N_a), where, $\tau_p = 10^{-10} s$, $\tau_n = 10^{-6} s$, $S = 10^7 cms^{-1}$, $N_d = 10^{17} cm^{-3}$.

REFERENCES

[1] M. A. Green, K. Emery, Y. Hishikawa, and W. Warta, "Solar Cell Efficiency Tables (version 35)", *Prog. Photovolt: Res. Appl.,* vol. 18, pp. 144-150, 2010.

[2] J. Nelson, "The physics of solar cells", Imperial College Press, Chapter 8, 2003.

[3] S. S. Hegedus and W. N. Shafarman, "Thin-film Solar Cells: Device Measurements and Analysis", *Prog. Photovolt: Res. Appl.,* vol. 12, pp. 155-176, 2004.

[4] M. A. Mannan, M. S. Anjan, M. Z. Kabir, "Modeling of Current-Voltage Characteristics of Thin Film Solar Cells", *Solid-State Electron.*, vol. 63, pp. 49-54, 2011.

[5] S. S. Hegedus, "Current Voltage Analysis of a-Si and a-SiGe Solar Cells Including Voltage -Dependent Photocurrent Colection", *Prog. Photovolt: Res. Appl.,* 1997;vol. 5, pp. 151-168, 1997.

[6] D. Cheyns, J. Poortmans, P. Heremans, C. Deibel, S. Verlaak, B. P. Rand, and J. Genoe, *Phys. Rev. B*, vol. 77, 165332, 2008.

[7] M. Gloeckler, A. L. Fahrenbruch, and J. R. Sites, “Numerical Modeling of CIGS and CdTe Solar Cells: Setting the Baseline”, Proceedings Of *3rd World Conference on Photovoltaic Energy Conversion*, pp. 491-494, 2003.

[8] J. Johansson, "Modelling and Optimization of CIGS Solar Cell Modules", Master's Thesis, Lund University, 2007

[9] M. Gloeckler, "Numerical Modeling of CIGS Solar Cells: Definition of the Baseline and Explanation of Superposition Failure", Master’s Thesis, Colorado State University, 2003.

Empirical Investigation of Powering a Campus with Non-Conventional Energy Resources

F. M. T. Enam[1], Sharjil Rahman[2], Parvez M. Rafi[3], Md. S. U. Osmani[4], Bishwajit B. Pathik[5]
American International University-Bangladesh (AIUB), Banani, Dhaka.
E-mail: [1]tenam_13@yahoo.com,[2]qwrafa@gmail.com, [3]rafi.13534@gmail.com,
[4]osmani_osan@yahoo.com, [5]bishwajit.b.pathik@gmail.com

ABSTRACT
This paper is about the hypothetical study on designing the future permanent campus of American International University–Bangladesh (AIUB), a leading private university in Bangladesh, by means of combining renewable energy resources. In this study first the arbitrary load of AIUB future campus has been calculated. Then all available renewable energy resources have been studied and three major sources namely, solar, wind and biogas have been selected due to their applicability and availability in the campus location. Again, all the possible types of solar panels as well as wind turbines and biogas reactors have been studied for maximum electric power generation with highest efficiency and minimum cost. The maximum power generated by biogas has been measured considering the contribution from 15% of total number of human in the university. By considering the free space, efficiency, annual average wind speed, average sunlight, etc. possible solar and wind power contribution have been calculated. The study compares the yearly running, repair and maintenance cost of combo-renewable energy, diesel generator and PDB power. It is interesting that supply with combo-renewable resources will cost the least, which represents a great hope for solving the power crisis of our country as well as can bring Green revolution throughout the world.

KEY WORDS: Combo-renewable campus, renewable energy, smart grid.

1. INTRODUCTION

Currently Bangladesh is facing a major problem in generating enough electrical power with conventional way like natural gas, coal, petroleum or hydroelectric power plants to fulfill the demand of the nation. To cope up this situation, it is very necessary to use non-conventional energy sources such as solar, wind, biogas, tidal, geo-thermal energy etc. as the alternative sources of producing electricity in sufficient amount. Combining all non-conventional resources can be possible for getting better production of electricity. This study opens a new pathway for other Bangladeshi universities as well as private and public institutions to design and develop their organizations using this concept i.e. using combination of renewable energy sources for meet up the demand of electricity. In case of excess production, it is also possible that organizations could supply to the grid after fulfilling their requirements.

2. RELATED STUDY

2.1 Photovoltaic Power

The photovoltaic (PV) power technology uses semiconductor cells (wafers), generally several square centimeters in size. From the solid-state physics point of view, the cell is basically a large area p-n diode with the junction positioned close to the top surface. The cell converts the sunlight into direct current electricity. Numerous cells are assembled in a module to generate required power.

There are three main types of solar panel in commercial production based on silicon semiconductors - the difference being the form that the silicon is in.

(a) Monocrystalline Modules: [6] Thesemodules are composed of cells cut from a piece of continuous crystal. The material forms a cylinder which is sliced into thin circular wafers. These modules are most efficient as well as most popular technology on market. These modules take up small area on roof.

(a) **(b)** **(c)**

Fig. 1: High efficiency **(a)**Monocrystalline [5] **(b)** Polycrystalline [6], **(c)** Amorphous Module [4]

(b) Polycrystalline Modules: Polycrystalline cells are made from similar silicon material except that instead of being grown into a single crystal, it is melted and poured into a mold. This forms a square block that can be cut into square wafers with less waste of space or material than round single-crystal or monocrystalline wafers.

(c) Amorphous Modules: Although crystalline silicon PV is the dominant technology choice today, amorphous silicon technology is very cost competitive. The three contributing factors for higher performance – low temperature coefficient, blue light absorption, and thermal annealing – help a-Sioutperform other technologies under a variety of climates. [3]

2.2 Wind Power

Wind is a form of solar energy and is caused by the uneven heating of the atmosphere by the Sun, the irregularities of the Earth's surface, and rotation of

the Earth. The amount and speed of wind depends on the Earth's terrain and other factors. The wind turbines use the kinetic energy of the wind and convert that energy into mechanical energy, which in turn can be converted into electricity by means of a generator.

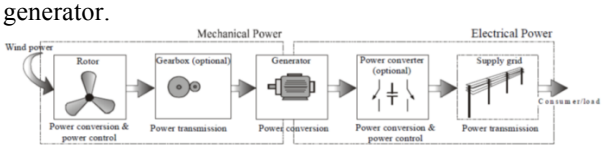

Fig. 3: Converting wind power to electrical power in a wind turbine

There are two types of turbines. The turbines are-

(a) Horizontal Axis Wind Turbines (HAWT): A HAWT has a similar design to a windmill; it has blades that look like a propeller that spin on the horizontal axis. Horizontal axis wind turbines have the main rotor shaft and electrical generator at the top of a tower. Small turbines are pointed by a simple wind vane placed square with the rotor (blades), while large turbines generally use a wind sensor coupled with a servo motor.

(a) **(b)**

Fig. 4: (a) A Horizontal Axis Wind Turbine, and **(b)** A Vertical Axis Wind Turbine

(b) Vertical Axis Wind Turbines (VAWT): These turbines have the main rotor shaft arranged vertically. The main advantage of this arrangement is that the wind turbine does not need to be pointed into the wind. This is an advantage on sites where the wind direction is highly variable or has turbulent winds. With a vertical axis, the generator and other primary components can be placed near the ground, so the tower does not need to support it, also makes maintenance easier. The main drawback of a VAWT generally creates drag when rotating into the wind.

2.2.1 Wind Tunnel

Many wind turbines can only work in high wind condition, while they cannot work in a normal (micro) wind condition. SZNE "Wind Tunnel" High Efficiency Micro wind Generator can work well in a normal (micro) wind condition. The conversion efficiency is 47%, in the same wind condition, it converts more wind energy into electricity which generates more power output than others. It can install on roof of building, on land, on sea.

(a) Single Fan (b) Double Fan (c) Three Fan

Fig. 5: Types of SZNE wind tunnels.

2.3 Biogas Energy

Biogas originates from bacteria in the process of bio-degradation of organic material under anaerobic (without air) conditions. The natural generation of biogas is an important part of the biochemical carbon cycle. Methanogens (methane producing bacteria) are the last link in a chain of micro-organisms which degrade organic material and return the decomposition products of the environment.

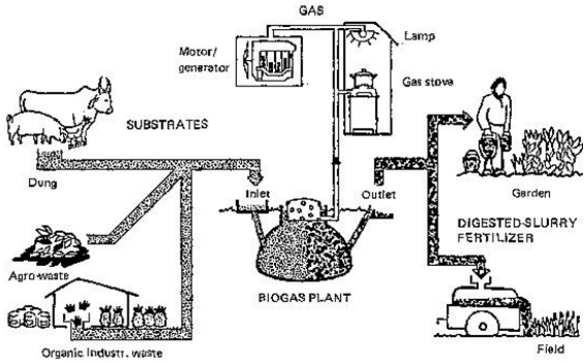

Fig. 6: A typical biogas-system configuration

In principle, all organic materials can ferment or be digested. However, only homogenous and liquid substrates can be considered for simple biogas plants: faces and urine from cattle, pigs, possible from poultry and wastewater from toilets. When the plant is filled, the excrement has to be diluted with about the same quantity of liquid; if possible, the urine should be used. Waste and wastewater from food processing industries are only suitable for simple plants if they are homogenous and in liquid form. The maximum of gas-production from a given amount of raw material depends on the type of substrate.

2.4 Future Permanent Campus of AIUB

Due to the rapid expansion of faculties, disciplines, curriculums and students; the administrative body ofAmerican International University-Bangladesh(AIUB) has decided to build its own campus befitting its present and future requirements. A unique campus has planned for with all modern facilities coupled with echo friendly technology suiting the futuristic environmental challenges.

Fig. 7: Future AIUB Campus

3. STUDY FINDINGS

The approximate basic loadlike fan (80W), tube-light (40W), computer (200W), and projector (240W)for the permanent campus of American International University-Bangladesh (AIUB) has been calculated using secondary data. The total consumption of AIUB campus has been considered as 621KW.

Table 1: Load Calculation of AIUB Permanent Campus

Energy Consumption Places	Number of Places	Number of Equipment (per place)				Consumption (kW)
		Fan	Tube-Light	Computer	Projector	
Class Room	87	8	16	1	1	149.64
Laboratories	50	8	16	1	1	86
Computer Lab	15	8	16	40	1	142.8
Office	60	8	16	8	0	172.8
Auditorium	2	50	200	0	1	24.96
Library	1	50	200	0	0	12
Recreation Building	1	50	200	0	0	12
Rest Room	50	0	2	0	0	4
Parking area	1	10	200	0	0	8.8
Corridor & Stair ways	1	0	200	0	0	8
Total Consumption						**621**

Four major types of solar panel (Ballasted Mount, Hybrid Mount, Pitched Roof and Ground Mount) have been found to be considered. From table 2 it can be said that by installing Hybrid Mount Solar Panel the cost can be minimized with required output using less area.

Vertical axis wind turbine has preferred instead of horizontal axis wind turbine because it is less noisy,highly efficient, blades are light weighted and can cover all air directions. As in Bangladesh air velocityis low, SZNE wind tunnel is used to increase efficiency 45% and air speed from 2m/s to 12 m/s.

Table 2: Calculation of Power Using Solar Energy

Installation Types	Cost Per Unit (Thousand Tk.)	Power Rating(kW)	Area(m^2)	Required output(kW)	Required Panels	Required Area(m^2)	Cost (Tk in Lac)
Ballasted Mount	22.7	0.24	1.25	318	1,325	1,656.25	301.33
Hybrid Mount	13.1	0.24	1.25	318	1,325	1,656.25	***172.66***
Pitched Roof	14.4	0.24	1.6	318	1,382	2,212.17	199.68
Ground Mount	23.2	0.24	1.6	318	1,200	1,920.00	277.88

Table 3: Power Calculation by Wind Energy

Installation Types	Cost Per Unit (Thousand Tk.)	Power Rating (kW)	Area (m^2)	Required output (kW)	Required Turbines	Required area (m^2)	Cost (Tk in Lac)
VAWT (20kW)	1,660,000	20	410	198.7	6	3,514.29	***93.91***
VAWT (50kW)	7,849,476	50	1130	198.7	3	4,237.50	111.01
VAWT (100kW)	8,656,817	100	1630	198.7	2	3,492.86	214.26

Bio-Gas energy can be produced with five types of digestor reactors, i.e.Floating Cover, Fixed Dome, Plastic Bag, Prefabricated Steel and Horizontal/Vertical. The initial cost of all digester with gas holder is US $ 50-60 per m^3 of digester volume and also repair and maintenance cost is 2% of capital cost.

Students on AIUB = 10,000
Percentage of total people = 15
Total number of people = 1500
Excreta per person = 0.4 kg
Total amount of excreta = 600kg
Per kg excreta to biogas = $0.037m^3$
Total amount of biogas = $22.2m^3$
Biogas per m^3 to electricity = 4.698kWh
Total amount of electricity = 104.2956kWh
Cost of Digester= Tk 20 Lac
Repair & maintenance (5%) = Tk 5 Lac

Minimum cost of panels, turbines, wind tunnel and reactors are included in cost calculation. So, total

cost = Tk 172.66 Lac + Tk 93.91 Lac + Tk 25Lac +Tk 2 Lac = Tk 331.75 Lac By adding yearly 10 % repairing and maintenance cost, total yearly cost becomes = **Tk 331.75 Lac**

Through 775kVA Diesel Generator, 621kW load can be generated. Cost of MITW 775kVA Diesel Generator = Tk 48.83 Lac [15]
Fuel consumption (100% load) = 168.1 l/h [15]
Fuel consumption for 14 hours = 2353.4 l
Running cost (61tk per liter) = Tk 1.44 Lac
Repairing cost (5%) = Tk 2.44 Lac
So, yearly cost of running, repair and maintenance of diesel generator is **Tk 528.04 Lac**

Again, Yearly total cost of PDB power = 14*621*365*12 = **Tk 380.79 Lac**

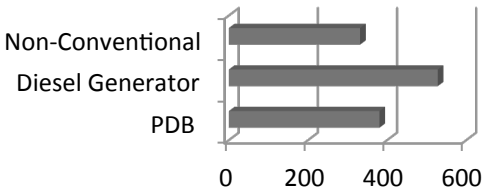

Fig. 8: Comparison of annual cost of different source

It is a surprising fact that although the initial cost is higher but the lowest annual cost can be obtained using non-conventional energy sources.

4. FUTURE WORK

Powering a campuswith non-conventional energy sources is completely a new concept for generating energy in a university.If the demand of AIUB permanent campus is fulfilled then one day it would be possible to fulfill the basic demand of Dhaka city through our concept.

5. CONCLUSIONS & RECOMMENDATIONS

It appears that in the future, energy mix rather than a single renewable energy technology will be dominant. [11] As the cost is lowest the combination of different non-conventional sources is one way of providing energy requirement in environmentally sustainable way. The aim of this analysis was to quantify in which way renewable energy can be used for designing university campuses as well as set out to evaluate a range of renewable energy technologies and their suitability for the permanent campus of AIUB as well as Bangladesh.

REFERENCES

[1] Y. V. Makarov, "Incorporating Wind Generation and Load Forecast Uncertainties into Power Grid Operations", *Wind Energy Management System EMS Integration Project*, USA, January 2010.
[2] A. Keyhani, M. N. Marwali, M. Dai, "Integration of Green and Renewable Energy in Electric Power systems", A. John Wiley and Sons, USA, 2010.
[3] E. F. Fuchs, M. A.S. Masoum, "Power Conversion of Renewable Energy Systems", Springer – Verlag London Limited, UK, 2011.
[4] Dr. M. M. Qurashi, Engr. T. Hussain, "Renewable Energy Technologies for Developing Countries Now and to 2023", Islamic Educational, Scientific and Cultural Organization, 2005.
[5] R. Foster, M. Ghassemi, A. Cota, "Solar Energy Renewable Energy and the Environment", CRC Press Tylor& Francis Group, 2010.
[6] R. Pode, B. Diouf, "Solar Lighting", Springer – Verlag London Limited, UK, 2011.
[7] V. Nelson, "Wind Energy Renewable Energy and the Environment", CRC Press Tylor& Francis Group, 2009.
[8] M. R. Patel, "Wind and Solar Power Systems", CRC Press, USA, 2000.
[9] A. M. Gorlov, Tidal Power, Northeastern University, Boston, Massachusetts, USA, 2011.
[10] Z. Fan, "Tidal Power Energy", University of Gavle, Department of technology and Built environment
[11] M. Islam, "Utilization of Renewable Energies in Bangladesh", 2002.
[12] M. C. Percival, P. S. Leung, P. K. Datta, "The Development of a Vertical Turbine for Domestic Electricity Generation", Tyne and Wear, UK.
[13]Mitsubishi Heavy Industries Ltd, "Diesel Generator Sets", available at http://mittronik.com/en/power-systems.php.
[14] Astralux Ltd, "Vertical Axis Wind Turbine 100KW", available at http://newwindturbine.com/wind-turbines/vertical-axis-wind-turbine-vawt-100-kw/
[15] Alibaba.com, "775kva Diesel Generator", available at http://www.alibaba.com/showroom.html.
[16] Shenzen New Energy Development Co. Ltd, "Wind Tunnel Technology", available at http://www.szne.com.cn/en_products_10.htm
[17] Alibaba.com, "Vawt 50kw Horizontal Axis Wind Turbine", available at http://www.alibaba.com /showroom/vawt-turbines-50kw.html
[19] Alok Jha.(2008) "Second Generation Tidal Turbines Promise Cheaper Power", available at http://www.guardian.co.uk/environment/2008/sep/04 /waveandtidalpower.renewableenergy
[20] Ceramatec, Inc. "Advance Energy Storage", available at http://www.ceramatec.com
[22] U.S. Department of Energy, "Hydropower technology", available at http://www.eere.energy.gov /basics/renewable_energy/hydropower.html

Effect of Ge-Content on the Internal Quantum Efficiency of a SiGe Solar Cell

Md.Rashedul Huqe[1], Khalid Mahfuz Kollince[2] , Dr.Md.Iqbal Bahar Chowdhury[3]
[1,2,3]EEE department, United International University
E-mail: rashedul_uiu@yahoo.com, km.kolince@gmail.com, ibchy@eee.uiu.ac.bd

ABSTRACT
In this work an analytical model for the internal quantum efficiency of the emitter region of a nonuniformly and heavily doped SiGe solar cell has been developed. The doping dependency of carrier mobility and carrier lifetime, the band-gap narrowing effect and SRH and Auger recombination mechanisms are considered for this model. In order to observe the effects of dosing level of Ge, three dosing profiles are considered e.g. uniform, triangular and trapezoidal profile. An elegant exponential approximation technique has been employed to simplify the complicated nature of variable coefficients of the working differential equation. The model results show that the increased Ge-content results in significant improvement in the internal quantum efficiency.

KEY WORDS**:** Internal Quantum Efficiency, Doping-dependent Mobility, Triangular Ge-dosing Profile, Exponential Doping Profile.

1. INTRODUCTION

Internal quantum efficiency (η_e) is one of the most important performance parameters of the solar cells. An accurate model of η_e that can describe its physics satisfactorily, therefore, always draws the attention of the solar cell researchers. This η_e can be increased by introducing non-uniform doping profile in the emitter region, or in the base region or in both. This is the concept of a drift field solar cell [1]. However, the non-uniformity of the doping profile introduces various non-ideal effects i.e. doping dependence of carrier mobility and carrier lifetime, bandgap narrowing effects etc. Till to date various researchers have been working on the accurate modeling of η_e considering these effects. Alemo *et. el.* [2] have studied the physics of heavily doped emitter and developed a model for η_e. Bassore *et. el.* [3] developed a numerical model whereas Park *et. el.* [4] deduce an analytical solution for η_e. Bisschop *et. el.* [5] derived an analytical solution for collection efficiency using integral series. Later, Misumi *et. el.* [6] experimented the effect of compositional distribution of SiGe solar cells on the conversion efficiency. Chang *et. el.* [7] investigated the optimized design for SiGe Solar cells and made a theoretical analysis. These works did not develop an analytical model of η_e for SiGe solar cells.

The first analytical model that considered all the non-ideal effects mentioned above has been developed by Sujoy *et. el.* [8]. But their model is based on Si-solar cells. Later Huqe *et. el.* [9] deduced an analytical solution for the base region of SiGe Solar cell. In this work an attempt has been made to develop an analytical model of η_e for the emitter region of a SiGe solar cell.

2. ANALYSIS

2.1 Basic Equations

The governing differential equations required in the emitter region are

$$J_p = qp(x)\mu_p(x)E(x) - qD_p(x)\frac{dp(x)}{dx} \quad (1)$$

$$\frac{dJ_p}{dx} = -q(R-G) \quad (2)$$

where symbols have their usual meanings. Considering band-gap narrowing effect due to heavy doping, the electric field $\frac{E}{V_T}$ under low-injection can be expressed as

$$\frac{E}{V_T} = -\frac{d}{dx}lnN_d(x) + \frac{d}{dx}lnn_{ie,SiGe}^2(x) \quad (3)$$

The doping profile and the trapezoidal Ge-dosing profile in the emitter can be expressed as [8, 9]

$$N_d(x) = N_d(0)u(x) = N_d(0)e^{\frac{\eta x}{W}} \quad (4)$$

$$y(x) = m_{Ge}x + y_E \quad (5)$$

where,$m_{Ge} = \frac{(y_C - y_E)}{W_E}$,y_C and y_E are Ge content at the edge of $B-E$ junction and the emitter surface respectively. When $y_E = 0$, the dosing profile of triangular and $y_C = y_E$ the profile is box-shaped.

2.2 Physical Models

The effective intrinsic carrier concentration in SiGe is [14]

$$n_{ie,SiGe}^2(x) = \gamma_r n_{i0,Si}^2 e^{\frac{\Delta E_{gHD}(x) + \Delta E_{gGe}(x)}{KT}} \quad (6)$$

where $n_{i0,Si} = 1.4\times10^{10}\ cm^{-2}$. γ_r is the ratio of the effective density of states in SiGe to the effective density of states in silicon, ΔE_{gHD} is the bandgap narrowing (BGN) due to heavy doping and ΔE_{gGe} is the BGN due to the presence of Ge-content and are given by

$$\gamma_r = exp\left(-\sqrt{5\times y_{av}}\right) \quad [10][11] \quad (7)$$

$$\Delta E_{gGe}(x) = qV_{gGe}y(x) \quad [11][12] \quad (8)$$

$$\Delta E_{gHD}(x) = qV_{gHD} ln\left(\frac{N_d(x)}{N_{ref}}\right) \quad [13] \tag{9}$$

According to [9], Eqn. (6) can be organized as

$$n_{ie,SiGe}^2(x) = n_{i0,SiGe} u^{\gamma_{2n}} \tag{10}$$

where

$$n_{i0,SiGe} = \gamma_r n_{i0,Si}^2 \left(\frac{N_d(0)}{N_{ref}}\right) e^{\frac{V_{gGe}}{V_T}} \tag{11}$$

$$\gamma_{2n} = \gamma_2 + \frac{V_{gGe}}{V_T}\frac{W_B m_{Ge}}{\eta} \quad , \quad \gamma_2 = \frac{E_{BGN}}{V_T}$$

In the presence of Ge content,the hole diffusivity should be changed as [14]

$$D_p(x) = bD_{p,si}(x) \tag{12}$$

Where $b = 1 + 3\times\frac{(y_C+y_E)}{2}$.

According to [8, 9], the hole current continuity equation can be reorganized as

$$\frac{dJ_p}{dx} = -\frac{qp}{\tau_p} + G_L e^{+\alpha x} \tag{13}$$

where the sign of exponent for 'G' is taken as positive to incorporate the negative direction of x in the emitter region and

$$\frac{1}{\tau_p} = \frac{\tau_{p0}}{1+\frac{N_d}{N_{ref}}} + C_{An}N_d^2 \tag{14}$$

$$G_L = \frac{q\alpha(\lambda)I(\lambda))\lambda}{hc} \tag{15}$$

where the first term of Eqn (14) represents SRH recombination and the second term represents Auger recombination.

2.3 Model Derivation

Differentiating Eqn. (1) with respect to x, combining with Eqn. (2) and then rearranging, results in a second order nonhomogeneous differential equation of p(x) as

$$\frac{d^2p}{dx^2} + G_1(x)\frac{dp}{dx} + G_2(x)p(x) = G_3(x) \tag{16}$$

where

$$G_1(x) = -\left[\frac{E}{V_T} + \frac{dln}{dx}\left(\frac{1}{qD_p}\right)\right] \tag{17}$$

$$G_1(x) = -\left[\frac{d}{dx}\left(\frac{E}{V_T}\right) - \frac{E}{V_T}\frac{dln}{dx}\left(\frac{1}{qD_p}\right) + \frac{1}{\tau_p D_p}\right] \tag{18}$$

$$G_1(x) = -\frac{G_L}{D_p}e^{\alpha x} \tag{19}$$

$$\frac{E}{V_T} = -\frac{\eta}{W_E}(1-\gamma_{2n}) \tag{20}$$

Since D_p, τ_p is of complicated form instead of a simple exponential, the above differential equation becomes analytically intractable. Using exponential approximation technique [8, 9], the term $\frac{1}{qD_p\tau_p}$ can be approximated as R_0u^k. Therefore, the coefficients of Eqn. (15) can be rearranged as

$$G_1(x) = \left[(1-\gamma_{2n}-\gamma_3)\frac{\eta}{W}\right] \tag{21}$$

$$G_2(x) = -\left[qR_0u^{k+\gamma_3} + \frac{\eta^2}{W^2}\gamma_3(1-\gamma_{2n})\right] \tag{22}$$

$$G_3(x) = -qFG_Lu^{\left[\frac{W}{\eta}\alpha+\gamma_3\right]} \tag{23}$$

Solving the differential equation gives the minority hole density p(x) and the hole current density $J_p(x)$ as (see: Appendix) (9)

$$p(x) = C_1I_0u^{\alpha_1} + C_2K_0u^{\alpha_2} + V_0u^{\alpha_3} \tag{24}$$

$$J_p(x) = J_0\exp^{\frac{v_{BE}}{V_T}} - J_{ph} \tag{25}$$

Finally, the internal quantum efficiency can be expressed as

$$\eta_e = \frac{J_{ph}}{q\int_0^W G_L e^{\alpha x}dx} \tag{26}$$

3. RESULTS

Three different dosing profiles of Germanium (Ge) content (box, triangular and trapezoidal) and exponential profile of base doping are used in this work. All these dosing profiles aid the electric field depending on their gradient. The higher is the gradient, the higher are the electric field and the subsequent internal quantum efficiency (η_e). All of the Figs. (2), (1) and (3), therefore, displays the higher η_e for SiGe-solar cells compared to that of Si-only solar cells.

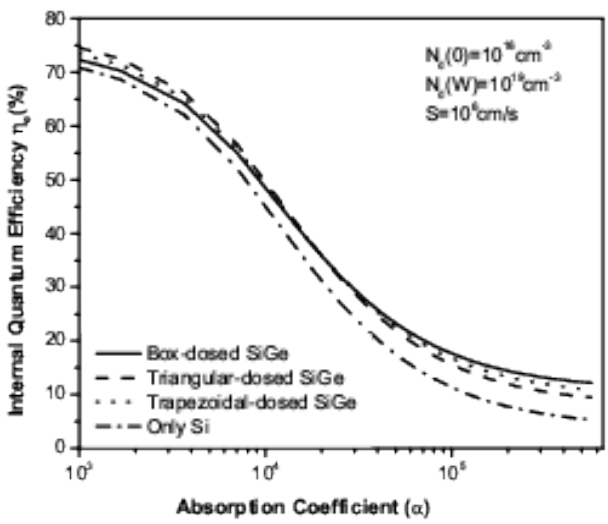

Figure 1: Effect of different profile of Ge content on internal quantum efficiency against the variation of absorption coefficient. Here SRH and Auger both recombination are considered and $N_d(W) = 1\times10^{19}cm^{-3}$, $N_d(0) = 1\times10^{16}cm^{-3}$, $S = 10^6cm/s$.

Increase of the emitter width increases the volume recombination rate and hence, decreases the internal quantum efficiency. This fact is observed in the Fig. (2). The effect of variation of peak emitter doping $[N_d(W)]$ on the internal quantum efficiency is plotted in Fig. (3). This plot shows that η_e decreases as $N_d(W)$ increases. This can be explained as follows. Since $N_d(0)$ and emitter width are kept constant, the increase of $N_d(W)$ results in increase in the slope of the doping profile (η) and hence the

corresponding increase in the electric field. However, the increase in $N_d(W)$ also increases the collision of carriers which reduces the carrier mobility. The carrier mobility is further reduced by the increased electric field. Indeed, the reduction of carrier mobility increasingly dominates over the increase of the electric field as $N_d(W)$ increases. Hence, η_e is found decreasing as $N_d(W)$ increases.

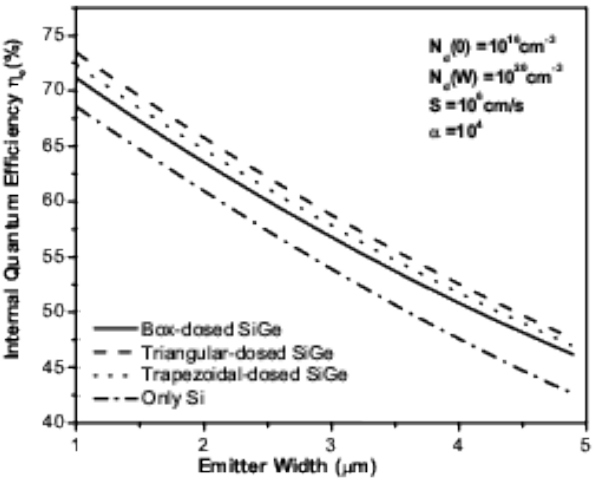

Figure 2: Effect of different profile of Ge content on internal quantum efficiency against the variation of Emitter Width. Here both SRH and Auger recombination are considered and $N_d(W) = 1\times10^{20}cm^{-3}$, $N_d(0) = 1\times10^{16}cm^{-3}$, $\alpha = 5\times10^4$, $S = 1\times10^6 cm/s$.

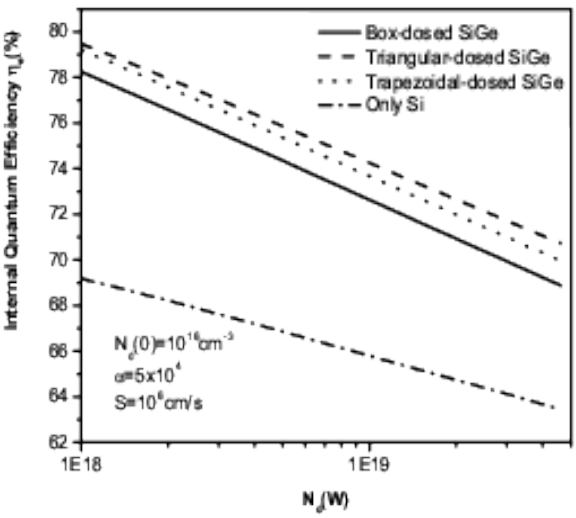

Figure 3: Effect of different profile of Ge content on internal quantum efficiency against the variation of peak emitter doping $N_d(W)$. Here SRH and Auger both recombination are considered and $N_d(0)$ is fixed at $1\times10^{16}cm^{-3}$, $S = 1\times10^6 cm/s$, $\alpha = 5\times10^4$.

Fig. (4) showing the effect of Trapezoidal-dosing slope M_{ge} on the internal quantum efficiency. Here Y_e and emitter width are kept constant. With the increase of M_{ge}, the slope of dosing increases, which causes the electric field to increase and hence, the internal quantum efficiency to increases.

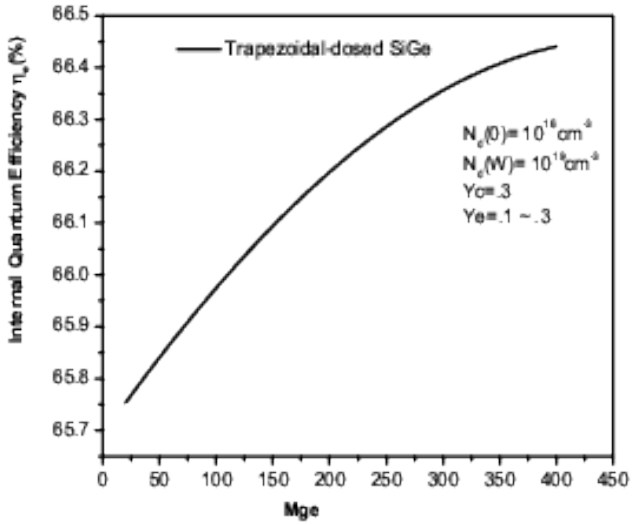

Figure 4: Effect of Trapezoidal-dosed slope(Mge) on SiGe in the internal quantum efficiency. Here SRH and Auger both recombination are considered and $N_d(W) = 1\times10^{19}cm^{-3}$, $N_d(0) = 1\times10^{16}cm^{-3}$, $\alpha = 5\times10^4$, $S = 1\times10^5 cm/s$,$Y_c = .3$,$Y_e = .1.3$.

4. CONCLUSION

An analytical model of internal quantum efficiency has been developed in this work by considering doping-dependency of the carrier mobility as well as both SRH and Auger recombination mechanisms in the emitter region. The results of the developed model points out that Ge-dosing profile has significant effects on the internal quantum efficiency. Of the three dosing profiles, the triangular profile shows the highest internal quantum efficiency. Instead of using box-dosing profile, it is better to use trapezoidal profile for which increase in dosing profile gradient m_{ge} can significantly increase the internal quantum efficiency.

5. APPENDIX

Letting $u^{k+\gamma_3} = z^2$ converts the second order differential equation (16) into a nonhomogeneous modified Bessel equation of order β as

$$\frac{d^2p}{dz^2} + \frac{1}{z}(1+a)\frac{dp}{dz} - \frac{1}{z^2}[(bz)^2 + C]p = A_1 z^{m_1-2} \quad (27)$$

where $b = \sqrt{qCF_h}\frac{2W_E}{\eta(k+\gamma_3)}$, $C = 4\frac{(1-\gamma_{2n})\gamma_3}{(k+\gamma_3)^2}$,

$a = \frac{2(1-\gamma_{2n}-\gamma_3)}{k+\gamma_3}$, $m_1 = \frac{2\left(\frac{W_E}{\eta}\alpha+\gamma_3\right)}{k+\gamma_3}$, $A_1 = -\frac{4F_h G_L W_E^2 q}{\eta^2(k+\gamma_3)^2}$,

$\beta = \frac{1-\gamma_{2n}+\gamma_3}{k+\gamma_3}$. The solution of this DE gives,

$$V(x) = (C_1+V_1)I_\beta(bz) + (C_1+V_2)K_\beta(bz) \quad (28)$$

where, $V_1 = -\frac{(K+\gamma_3)A_1K_0}{(K+\gamma_3)m_1+2\beta_0}u^{\frac{(K+\gamma_3)m_1+2\beta_0}{2}}$, $V_2 = \frac{(K+\gamma_3)A_1I_0}{(K+\gamma_3)m_1+2\alpha_0}u^{\frac{(K+\gamma_3)m_1+2\alpha_0}{2}}$. Using exponential

approximation technique, $I_\beta(bz) = I_0 u^{\alpha_0}$ and $K_\beta(bz) = K_0 u^{\beta_0}$. Then, Eqn. (28) results in

$$V(x) = C_1 I_0 u^{\alpha_0} + C_2 K_0 u^{\beta_0} + u^{F_0} V_0 \quad (29)$$

where $F_0 = \gamma_3 + \frac{\alpha w}{\eta} + \alpha_0 + \beta_0$, $V_0 = \frac{A_1 K_0 I_0 (K+\gamma_3)}{2(\gamma_3 + \frac{\alpha w}{\eta} + \alpha_0)} - \frac{A_1 K_0 I_0 (K+\gamma_3)}{2(\gamma_3 + \frac{\alpha w}{\eta} + \beta_0)}$, $\alpha_1 = \alpha_0 - \frac{be}{2}$, $\alpha_2 = \beta_0 - \frac{be}{2}$, $\alpha_3 = F_0 - \frac{be}{2}$, $be = \frac{1-\gamma_{2,Ge}-\gamma_3}{2}$. Now applying Boundary condition and putting $x = 0$ gives

$$J_0 = \frac{q D_p(0) n_{ie,SiGe}^2}{N_d(0)} \left[B_{10} \left(\frac{E_p}{V_T} - \frac{\eta \alpha_3}{w} \right) - B_{20} \left(\frac{E_p}{V_T} - \frac{\eta \alpha_2}{w} \right) \right] \quad (30)$$

$$J_{ph} = q D_p(0) \left[\left(\frac{E_p}{V_T} - \frac{\eta \alpha_3}{w} \right) - B_{21} \left(\frac{E_p}{V_T} - \frac{\eta \alpha_2}{w} \right) - B_{11} \frac{E_p}{V_T} - \frac{\eta \alpha_3}{w}) \right] V_0 \quad (31)$$

where,

$$B_{10} = \frac{A_{2w}}{A_{2w} - A_{1w}}, \quad B_{11} = \frac{A_{2w} - A_{3w}}{A_{2w} - A_{1w}}$$

$$B_{21} = \frac{A_{1w} - A_{3w}}{A_{2w} - A_{1w}}, \quad B_{20} = \frac{A_{1w}}{A_{2w} - A_{1w}}$$

$$A_{1w} = \left\{ \frac{E_p}{V_T} - \frac{\eta \alpha_1}{w} - \frac{S}{D_p(w)} \right\} \exp^{\eta \alpha_1}$$

$$A_{2w} = \left\{ \frac{E_p}{V_T} - \frac{\eta \alpha_2}{w} - \frac{S}{D_p(w)} \right\} \exp^{\eta \alpha_2}$$

$$A_{3w} = \left\{ \frac{E_p}{V_T} - \frac{\eta \alpha_3}{w} - \frac{S}{D_p(w)} \right\} \exp^{\eta \alpha_3}$$

REFERENCES

[1]. M. Wolf *IRE*, vol. 51, pp. 674, 1963.

[2] . Jesus A. Del Alemo and Richard M. Swason, "The Physics and Modeling of Heavily Doped Emitters", *IEEE Trans. Electron Devices*, vol. 31, no. 12, pp. 1878-1888, December 1984.

[3]. P. A. Basore, D. T. Rover and A. W. Smith, "PC-1D version 2: Enhanced numerical solar cell modeling", in conf. Ref. *20th IEEE Photovolt. Special*, pp. 389, December 1988.

[4]. J. S. Park, A. Neugroschel, and W. C. Sinke, "Systematic Analytical Solutions for minority carrier transport in Semiconductors with position-dependent composition, with application to heavily doped silicon", *IEEE Trans. Electron Devices*, vol. 33, no. 2, pp. 240, December 1986.

[5]. FREERK J. Bisschop, Leendert A. Verhoef, and W. C. Sinke, "An Analytical Solution for the collection efficiency of solar-cell Emitters with arbitary doping profile", *IEEE Trans. Electron Devices*, vol. 37, no. 2, pp. 358-364, December 1990.

[6]. M. Tayanagi, N. Misami, W. Pan, K. Ohdaira, K. Fujiwara, Y. Nose and K. Nakajima "Improvement in the conversion efficiency of single-junction SiGe solar cells by intentional introduction of the compositional distribution ". *Journal of App. Phys.*, vol. 101, no. 5, pp. 054504-054506, Mar. 2007.

[7]. S. T. Chang, M. H. Liao, and W.-K. Lin "Si/SiGe Hetero-junction Solar Cell with the Optimization Design and Theoretical Analysis", *Thin Solid Films*, Vol.519, pp.5022-5025, 2011.

[8]. S. K. Saha, S.yeda Israt Ferdaus, Iqbal Chowdhury, "Effect of Field Dependent Mobility and Simultaneous Consideration of Both SRH and Auger Recombination on the Analytical Modeling of Internal Quantum Efficiency of a Si-Solar Cell" *Tencom 2011 IEEE conference*, 21-24 Nov. 2011, pp.662-666.

[9]. M. R. Huqe, H. M. Aziz, K. M. Kolince, M. S. Uddin, M. I. B. Chowdhury, "Effect of Ge-dosing Profile of Exponentially-doped Base on the Internal Quantum Efficiency of a SiGe Solar Cell", *International Conference on Devices, Circuits and Systems (ICDCS),2012* , 15-16 March 2012,Coimbatore, India,PP 119-123.

[10]. A. Zareba, L. Lukasiak, and A. Jakubowski, "Modeling of SiGe-base heterojunction bipolar transistor with gaussian doping distribution," *Solid-State Electron."*, vol. 45, pp. 2029-2032, 2001.

[11]. V. S. Patri and M. J. Kumar, "Profile Design Considerations for minimizing base transit time in SiGe HBT's", *IEEE Tran. on Electron Devices*, vol. 45, pp. 1725-1731, Aug 1998.

[12]. H. Kroemer, "Two integral relations pertaining to electron transport through a bipolar transistor with a nonuniform energy gap in the base region", *Solid-State Electron*, vol. 28, pp. 1101-1103, 1985.

[13]. J. W. Slotboom and H. C. d. Graaff, "Measurement of bandgap narrowing in Si bipolar transistors", *Solid-State Electron.*, vol. 19, pp. 857- 862, 1976

[14]. S. Basu, "Analytical modelling of base transit time of SiGe HBTs including effect of temperature", *International Semiconductor Conference, CAS'08*, vol. 2, pp. 339-342, Oct 2008.

(27)

Feasibility Study on Generation of Electricity Using Concentrated Solar Power Technology in Bangladesh

Md. Nasmus Sakib Khan Shabbir[1], Md. Samiul Zahid[2], Md. Forhad Zaman[3]

Department of Electrical & Electronic Engineering, Rajshahi University of Engineering & Technology

E-mail: [1]eng.sakib@gmail.com, [2]samiulzahid@gmail.com, [3]m.fzaman@yahoo.com

ABSTRACT

By using Concentrated Solar Power (CSP) technology about 2135.55MW power is generated around the world and more 2526.9 MW will be generated within 2014. Bangladesh has a very suitable solar irradiation for CSP technology. This paper presents the overall comparison between photovoltaic and concentrating solar power technology at the same rated power output and atmosphere and the feasibility of establishing CSP plants in Bangladesh on the basis of solar irradiation. Among all available CSP power generation technology, parabolic trough has been chosen as a feasible one.

.

KEY WORDS: Renewable energy, solar irradiation, concentrated solar power, PV, Bangladesh.

1. INTRODUCTION

Now a days in our country scarcity of power is one of the major concern of the authority and generation of power, is typically depends on fossil fuel, natural gas, coal etc which have hazardous effect on environment and their availability is rapidly decreasing. Nowadays the source of clean renewable energy is a burning question in the world. Under such a circumstance solar energy can achieve the place as the replacement of conventional sources of energy. Solar energy is a natural, permanent, continuous, renewable source of energy.

Roughly 35% of solar radiation is reflected back into space, another 18% is absorbed by the atmosphere and about 47% reaches the earth [1].

Solar energy is very large and inexhaustible source of energy. The power from the sun intercepted by the earth is approximately 1.8×10^{11} MW, which is many thousands of time larger than the present consumption rate on the earth of all commercial energy sources [1]. In many regions of the world, every square kilo-meter of land can produce 200-300 GWh/year of solar electricity. This is equivalent to the annual production of a conventional coal or gas fired 50 MW power plants or over the total life cycle of a solar power generation system to the energy contained in 16 million barrels of oil. Thus solar energy could supply all the present and future energy needs of the world on a continuing basis. This makes it one of the most promising unconventional energy sources.

Concentrating solar thermal (CSP) and photovoltaic (PV) are the two available technology for power generation using solar energy. Solar thermal energy plants have been investigated since about 20 years in three different variants: parabolic trough power plants, solar dishes and central receiver power plants. In solar thermal the heat radiated from the sun is used to generate power. The reflective surface of a parabolic trough concentrates sunlight onto a receiver tube located along the trough's focal line, heating the fluid in the tube, which is then transported through pipes to a steam turbine coupled to the generator to produce electricity. The troughs are normally designed to track the sun along one axis, predominantly north-south.

Bangladesh is situated between 20.30 - 26.38 degrees north latitude and 88.04 - 92.44 degrees east which is an ideal location for solar energy utilization. Daily average solar radiation varies between 4 to 6.5 kWh per square meter or about 2.7MWH/year on the total surface area of the country enough to meet the total demand of the country. Maximum amount of radiation is available on the month of March-April and minimum on December-January.

Here we will study the feasibility of generation of electricity using solar thermal technology in Bangladesh

2. STATUS OF NEW PLANTS

Around the world about 2135.55MW power is generated by CSP technology among them 809MW is generated in USA, 1532.3MW in Spain, 25MW in Algeria.

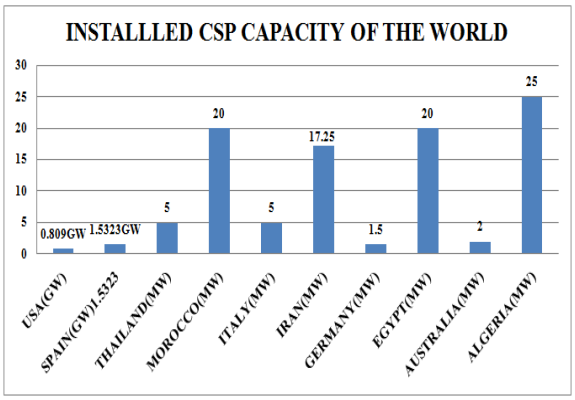

Fig. 1 Installed CSP Capacity of The World [6].

Within 2014 another 2526.9 MW power will be generated around the world. Among them 1260MW in USA, 776MW in Spain, 250MW in Israel, 100MW in UAE & India and 27.5MW in China [6].

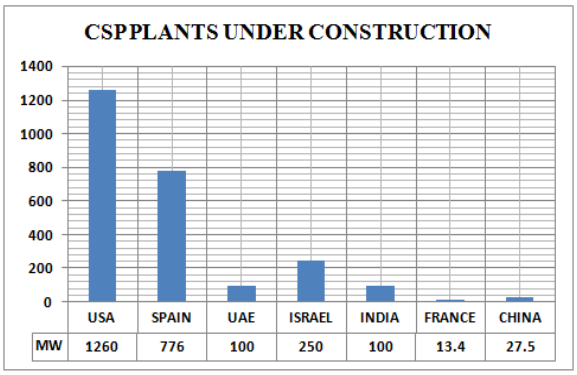

Fig. 2 CSP Plants Upcoming Within 2014 [6].

Recently USA has announced that they will build another 6510MW power by CSP technology. Even Spain, China, Morocco, Australia, Israel, Iran has declared to build another 1080.08MW, 2000MW, 2000MW, 250MW, 180MW, 72MW CSP power plants respectively. On a total it has been announced that about 2526.9 MW CSP power plants will be build within 2014 and another 14246.08MW within four or five years[6].

3. COMPARISON BETWEEN CSP AND PV

A solar-thermal power plant could cost 18 cents per kilowatt-hour whether solar-PV system costs about 40 cents per kilowatt-hour over the power plant's lifetime. Solar thermal power plants can generate power 24 hours by preserving the heat to a medium and then use it during night but PV can generate only at daytime. Within 20 to 25 years PV plants will lost a considerable amount of its efficiency.

Table 1 Overall Comparison between CSP & PV Power Plants [2]

OVERALL COMPARISON BETWEEN CSP AND PV POWER PLANTS		
	PV	CSP
Rated power (MW)	40.000	40.000
Number of the collectors	160	816
Total area(m^2)	60 x 104 x 2	45 x 104 x 2
Number of 500-kWp inverters	80	None
Equivalent yearly operation hours (h)	1,400	4,200(3 times)
Yearly produced Energy (MWh)	56.000	168.000 (3 times)
Maintenance costs per year(initial investment)	2%,	1%,
Efficiency in Standard Test Conditions	0.17	0.67
Setup coast/unit capacity(€)	1.89915	3.45231

Table 1 shows that, CSP plants produces more energy than PV plant. So, economic return of CSP is greater. Moreover, the area occupied by CSP plant is 25 percent smaller than that occupied by PV plant. Nevertheless, the initial investment to install the CSP plant is very higher than the PV.

4. ENVIRONMENTAL DATA

CSP power generation vastly depends on solar irradiation. Rainy days, foggy days, daily average of bright sunshine hours must be taken into consideration.

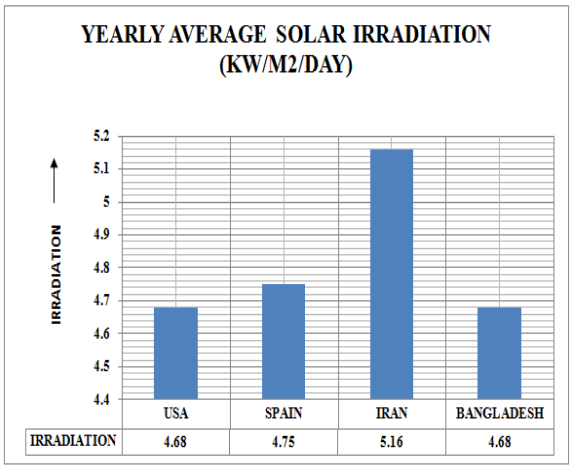

Fig 3 Yearly Average Solar Irradiation of Different Countries [7].

Bangladesh and USA has same 4.68 kw/m^2/day irradiation and USA is about to generate 2069MW

power by CSP technology within 2014 but nothing in Bangladesh [6][7].

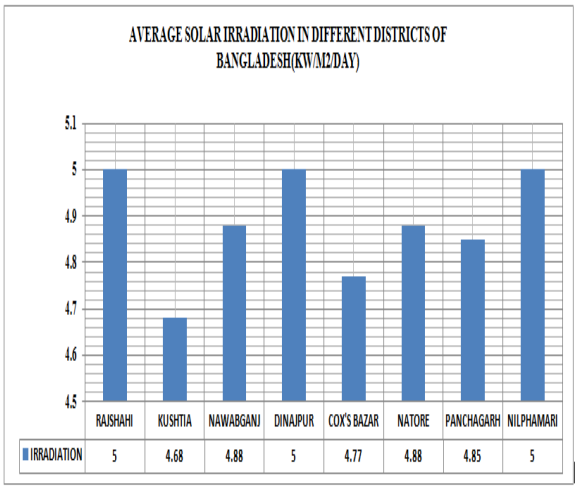

Fig 4 Yearly Average Solar Irradiation in Different Districts of Bangladesh [7].

.

Table 2 Monthly average daily Solar Radiation (kW h/m^2 day) [7]

Month	Rajshahi	Nilphamari	Nawabganj	Dinajpur
January	4.32	4.32	4.32	4.32
February	5.25	5.30	5.25	5.3
March	5.95	6.22	5.95	6.22
April	6.33	6.47	6.33	6.47
May	6.17	6.12	5.74	6.12
June	5.25	5.12	5.04	5.12
July	4.79	4.31	4.41	4.31
August	5.16	4.41	4.36	4.41
September	4.96	3.99	4.03	3.99
October	4.88	4.78	4.42	4.78
November	4.42	4.68	4.46	4.68
December	3.82	4.24	4.21	4.24

From the figure 4 & table 2, it is observed that north side of the country is suitable for CSP plant establishment.

Table 3 Monthly Solar Irradiation of Cities Having at Least 100MW CSP Plant [7].

Month	Mojave desert USA	Gaudix Spain	Indiana town USA	San joe de valle, Spain
January	2.9	2.5	3.41	2.54
February	3.77	3.38	4.12	3.43
March	5.25	4.57	5.02	4.6
April	6.65	5.45	5.91	5.72
May	7.68	6.32	6.14	6.51
June	8.1	7.33	5.44	7.41
July	7.49	7.61	5.54	7.59
August	6.7	6.55	5.16	6.79
September	5.68	5.07	4.6	5.28
October	4.38	3.52	4.25	3.73
November	3.28	2.54	3.62	2.67
December	2.7	2.1	3.91	2.18

From the table 3, it is observed that, USA and Spain are not suitable for CSP power generation in winter season due to very low solar irradiations.

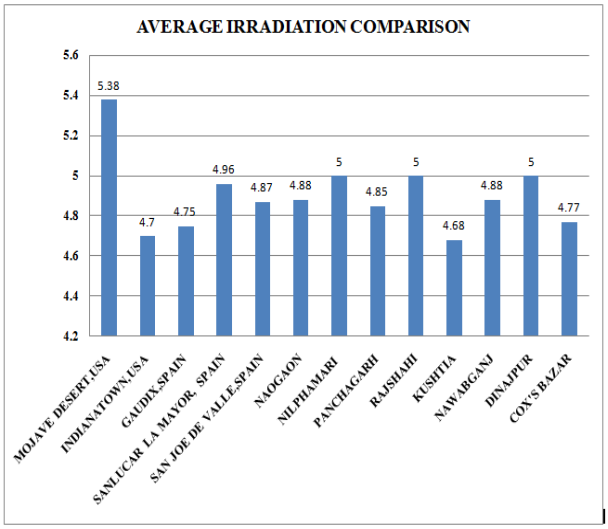

Fig. 5 Average Solar Irradiation Comparison [7].

From the figure 5, it is clear that, in Bangladesh Rajshahi, Dinajpur, Nilphamari, Nawabganj and Natore districts are suitable for CSP plants implementation.

5. HEAT AND ENERGY

The important equations are given below:

Heat removal factor, F_R is given by the following equation,

$$F_R = \frac{mC_P}{ArU}\left[1 - e^{-\frac{ArU}{mC_P}}\right] \text{[3]} \quad (1)$$

From **Eq. 1**we get, F_R= 0.85

The absorbed solar energy,

$$S = HR\rho\gamma(\tau\alpha)_e \text{[3]} \quad (2)$$

From **Eq. 2** we get, S= 112.54 W/m^2

Useful gain,

$$Q_u = F_R A_a\left[S - \frac{ArU}{Au}\left(t_{fi} - t_a\right)\right] \text{[3]} \quad (3)$$

From **Eq. 3** we get, Q_u= 7873 Watts

The exit fluid temperature,

$$t_{fo} = t_{fi} + \frac{Qu}{mC_P} \quad \text{[3]} \quad (4)$$

From **Eq. 4** we get, t_{fo}= 38.3 ^{0}C

The equation parameters and constants:
m=Flow rate of HTF
C_p=Specific Heat[4]
A_r=Area Of The Receiver Pipe
U=Heat Transfer Coefficient
F_R=Heat Removal Factor
HR=Incident Beam Radiation
ρ =Specular Reflectance [5]
γ =The Intercept Factor [5]
$(\tau\alpha)_e$=Transmittance Absorbance Product [5]
t_{fi}=Fluid Inlet Temperature At 30°C
t_a=Ambient Temperature In 30°C
t_{fo}=Exit Fluid Temperature
m_s=Flow Rate Of Steam

6. RESULT

According to the data, if we use 720 troughs in total we can generate 16.5861 MW of power. To establish the power plant approximately 120096 m^2 space required which is almost equal to 20 football playing grounds.

7. CONCLUSION

Concentrated solar power technology is suitable for large scale power generation. The advantage of this technology is, no extra apparatus such as inverter is used here. Heat can be stored for unfavorable weather and night. This technology is clean and it emits no harmful gasses. The world is switching into renewable energy from conventional energy as the amount of conventional fuel is decreasing day by day. So it is high time to start using solar energy like the developed countries In Bangladesh, Dinajpur, Nilphamari, Nawabgonj, Natore districts are suitable places for establishing Concentrated Solar Power (CSP) plant to solve our power scarcity.

REFERENCES

[1] Rahaman, LA.[et.al.], ”Design Construction and Installation of Cylindrical Parabolic Solar Concentrator”, A 4th B.Sc Engg. Project, I.I.T. Dhaka, Bangladesh.

[2] Silvano Verguraa, “Revista Eletrônica Sistenas & Gestão” Volume 6, 2011, pp. 210-220.

[3] G. D. Rai “Solar Energy Utilization”, Khanna Publishers, Fifth Edition, 2005, pp. 226, 229.

[4] Therminol VP-1 Heat Transfer Fluid by SOLUTIA Chemical Co. Ltd.

[5] SkyTrough Brochure 2011, SkyFuel Inc, USA

[6] Online references: last accessing date: 20 September, 2012
List of Solar Thermal Power Plants http://en.wikipedia.org/wiki/List_of_solar_thermal_power_stations

[7] Online references: last accessing date: 20 September, 2012
Surface meteorology and Solar Energy - A renewable energy resource web site (release 6.0) sponsored by NASA's Earth Science Enterprise Program http://eosweb.larc.nasa.gov/sse/RETScreen/

Proceeding of the
International Conference on Electrical, Computer and Telecommunication Engineering
01- 02 December 2012 (ICECTE2012), RUET, Rajshahi-6204, Bangladesh

ICECTE2012: PI-0009

Biomass to Electricity-Global Scenario and the Prospects in Bangladesh

M. A. Kader, B. K. Das, Amit Roy, N. N. Mustafi and M. Rokunuzzaman*
Department of Mechanical Engineering
Rajshahi University of Engineering & Technology, Rajshahi-6204, Bangladesh
Phone & Fax: + 880721-750319
Email: kader_042017@yahoo.com*, barun_ruet@yahoo.com,
amit.me39@gmail.com, nnmustafi@yahoo.com, rzaman_mctr@yahoo.com

ABSTRACT
Renewable energy encompasses a broad range of energy resources. To meet the increasing demand of electricity alternative sources of electricity production are given more importance. The huge amount of waste biomass generates in the world as well as in Bangladesh due the rapid growth of population can be a potential source of electricity production. Biomass energy sources are major source of renewable energy and it contributes 14% of the world energy consumption but in some developing country it supplies around 90% of the total energy consumption. This paper presents the potential of biomass energy resources in the whole world and especially in Bangladesh. It also discuss about the possible method of power generation in Bangladesh from the viewpoint of different promising available technologies.

KEY WORDS: Biomass, electricity, renewable energy, sustainability, Bangladesh.

1. INTRODUCTION

The supply of sustainable energy is one of the main challenges that mankind will face over the coming decades. Biomass can make a substantial contribution to supplying future energy demand in a sustainable way. It is presently the largest global contributor of renewable energy, and has significant potential to expand in the production of heat, electricity, and fuels for transport. The third largest renewable energy resource for electrical generation is biomass. While biofuels production, to power cars, has generated a lot of attention, many studies suggest that a far more efficient use of plant material in the energy system is to produce electricity, and then to use that electricity for a variety of purposes, including transportation. Like hydro power, biomass can be stored, making it a dispatchable source of power. Power generation can also be combined with heat/cooling production in CHP plants, which utilize a much higher share of the energy content than stand alone power plants. Global production of biomass and biofuel is growing rapidly due to the increasing price of fossil fuels, growing environmental concerns, and considerations regarding the security and diversification of energy supply. There are many scenarios that predict a high potential for biomass in the future. There have also been many studies performed in recent decades to estimate the future demand and supply of bioenergy. Overall, the world's bioenergy potential is large enough to meet the global energy demand in 2050.

Bangladesh is experiencing a severe electric power capacity crisis that is only likely to worsen over the next 15 years. There are a number of underlying reasons for the crisis, but ultimately the country lacks the fossil fuel resources required to conduct a large scale grid expansion program. The installed capacity in Bangladesh as increased by roughly 2,000MW between 2009-2011 and is now about 6,900MW (August 2011). According to reports, Bangladesh at present generates 5000 MW power. Peak hour demand of 6,000 MW everyday and increases on hot summer days. Bangladesh electricity supply strongly relies on gas: More than 80% of the power plants are fired by gas. The acute gas shortage causes a loss in production of around 600MW [1]. Alternative approaches to electrifying the country must be found. Biomass energy can be a potential source of electricity generation of Bangladesh.

2. BIOMASS RESOURCES

Biomass is any organic matter—wood, crops, seaweed, animal wastes—that can be used as an energy source [2]. Biomass is probably our oldest source of energy after the sun. For thousands of years, people have burned wood to heat their homes and cook their food. Some biomass sources of energy are: Agricultural residue, energy from refuse, energy crops, municipal solid waste, and animal waste

3. BIOMASS TO ENERGY

3.1 Energy Conversion Technology

There are many bioenergy routes which can be used to convert raw biomass feedstock into a final energy product. Several conversion technologies have been developed that are adapted to the different physical

nature and chemical composition of the feedstock. Some conversion technology is listed below.

- Direct combustion
- Co-firing
- Gasification
- Anaerobic digestion
- Land filling
- Pyrolysis

3.2 Global Scenario of Electricity Production from Biomass

Biomass currently provides about 10% of the world's primary energy supplies most being used in developing countries as fuel wood or charcoal for heating and cooking [3]. Biomass use for power and CHP generation is steadily expanding in Europe, mainly in Austria, Germany, the United Kingdom, Denmark, Finland and Sweden, where bioelectricity is mostly produced from wood residues and MGW in cogeneration plants. According to REN21 Global Status Report 2006, global biomass power capacity added in 2005 amounted to 2–3 GW, bringing total capacity to about 44 GW. In 2004 Germany, Hungary, the Netherlands, Poland, and Spain registered annual capacity increases of 50%– 100% or more. In Australia, Austria, Belgium, Denmark, Italy, South Korea, New Zealand and Sweden, growth was in the range of 10%–30% [4]. The biomass power industry is also active in the United States where some 85% of total wood process wastes (excluding forest residues) are used for power generation. Countries that are major producers of sugar cane are often major producers of (or are developing) bio-electricity from biogases power plants. A proliferation of small projects, including power plants and biogas digesters, is recorded in both IEA and emerging economies. Progress with rural use of biomass energy is difficult to track. It is especially hard to distinguish between modern and traditional biomass use, which still dominates in rural areas of developing countries (REN 21). China, Brazil, Latin American, Thailand, Cambodia and India are turning increasingly to biomass power plants and gasifiers alongside solar PV, small hydro and wind power. Some 70 MW of small-scale biomass gasification systems for off-grid power generation and 3.8 million household-scale biogas plants are installed in India. China reported 17 million existing biogas users in 2005. India is very rich in biomass. It has a potential of 19,500 MW (3,500 MW from bagasse based cogeneration and 16,000 MW from surplus biomass). Currently, India has 537 MW commissioned and 536 MW under construction. The facts reinforce the idea of a commitment by India to develop these resources of power production [5]

Use of biomass stoves is growing in Africa (Morocco, Uganda, Malawi, Ethiopia). Heat and power generation from biomass accounted for 7% of some $38 billion invested in new renewable energy capacity worldwide in 2005 (excluding large hydro) [5]. Around the world, a growing number of nations have recognized the economic, social, and environmental benefits of renewable energy and are enacting tax incentives and other policy measures favorable to renewable technologies. In Germany, Japan, Spain, and a handful of other countries, clear government commitments to renewable energy and strong, effective policies have overcome barriers and created demand for these technologies, leading to dramatic growth in renewable industries and driving down costs.

3.3Country data of Electricity Generation form Biomass

Global Biomass power capacity increased from about 66GW in 2010 to almost 72 GW at the end of 2011. The United States leads the world in biomass-based power generation, with other significant producers in the EU in addition to Brazil, China, India, and Japan. Most sugar producing countries in Africa generate power and heat with bagasse-based combined heat and power (CHP) plants. Improvements in the logistics of biomass collection, transport, and storage over the past decade, and growing international trade (particularly in pellets), have helped to remove constraints on plant size, and the size of facilities in some countries is increasing as a result. Almost 72 GW of biomass power generation capacity was in place worldwide by the end of 2011, up from an estimated 66 GW in 2010.30 Electricity is generated from biomass through direct firing or co-firing (with coal or natural gas) of solid biomass, renewable MSW, biogas, and liquid biofuels in electricity-only and CHP plants. About 88.3% of biomass power is generated with solid biomass fuels. The United States continues to lead the world in terms of total solid biomass-based power generation, with other significant bioenergy power producers in the EU (led by Germany, Sweden, and theU.K.), Brazil, China, India, and Japan.At the end of 2011, total installed capacity of Bioenergy power plants in the United States, including renewable MSW, was nearly 13.7 GW, up about 3% over 2010 (13.3 GW).32 U.S. net generation of electricity from solid biomass increased from 56.1 TWh in 2010 to 56.7 TWh in 2011[6]. The Country Notes on Bioenergy reflect the data and comments provided by WEC Member Committees in 2009/10, supplemented where necessary by information provided for previous editions of the WEC Survey of Energy Resources. Unless otherwise specified, the data relate to the year 2008[7].

Table 1: Country Notes on Bioenergy

Country name	Biomass type	Biomass production (million tonnes	Electricity generating capacity(MW)
Australia	MSW	6.9	103.7
	Sugar cane bagasse	11.4	368. 6
Brazil	MSW	40	41.87
	Sugar cane bagasse	140.89	3608
	Wood	92.61	148.481
France	MSW	2.394	772.8
	Wood	6.379	
Germany	MSW	0.94	852
	Wood		142
Japan	MSW	0.601	230
	Sugar cane bagasse	0.08	
	Wood	0.438	
USA	MSW	101	16,099 MWh
	Agriculture residue	165	38,762 MWh
China	MSW	152	2000
	Agriculture residue	700	

3.4 Biomass Energy in Bangladesh

Bangladesh is one of the most densely populated countries with 80% of the population living in rural areas [8].The country's electricity demand has been growing by 7.5% annually since 1990. Around 40% of its population has access to electricity-one of the lowest in the world according to the statistics of the power division. Renewable energy sources contribute less than 1.0 % of the total electricity generation [1]. But the government has targeted to augmented contribution of the renewable energy sources to 5.0% by 2015 to generate around 450MWe from renewable sources. Bangladesh is now poised to depend on renewable sources –solar, wind, biomass and biogas due to amid growing concerns over a steady decline of non renewable resources such as fossil fuel which has prompted many countries to seek alternative sources of energy to meet the future needs. The total annual generation and recoverable amounts of biomass in Bangladesh are about 165 and 90MT/year respectively. Agricultural residues represent 48% of the total recoverable biomass followed by 23.9% from animal wastes and poultry droppings. In 2006, the biomass consumption for energy in Bangladesh was about 350 pico-Joules (PJ). At an average annual growth rate of 1.3%, the consumption in 2010 will be about 370 PJ. The total recoverable biomass energy of the country in 2006 was about 1250 PJ from which about 820 PJ of biomass energy was available for electricity generation. On the other hand, the total biomass energy consumption in 2006 was about 473 PJ. Assuming the same average annual growth rate of 1.3%, the biomass consumption in 2010 will be about 286 PJ. Therefore, the amount of biomass energy available in 2006 was 777 PJ, which is equivalent to 216 terawatt-hours (TWh). According to these two estimates and considering that the consumption of biomass for non-energy purposes is negligible, the annual available biomass energy potential for electricity generation in Bangladesh is in the range of 216- 250 TWh[9]A large amount of biomass can be saved annually in Bangladesh by employing improved (i.e. more efficient) cooking stoves, furnaces, boilers and other devices consuming biomass fuels. Overall efficiencies of the traditional mud cooking stoves used in Bangladesh vary from 5% to 10%. A number of improved stoves have been developed by the Bangladesh Council of Scientific and Industrial Research (BCSIR).

The Institute for Fuel Research and Development (IFRD) has been engaged in a pilot-scale dissemination of improved model biomass-fired stoves, capable of saving 50-70% of fuel compared with traditional stoves, all over the country. These improved stoves are gradually gaining popularity. Biomass briquettes have the advantages of easy transportation, better handling, cleaner and more efficient combustion and higher volumetric calorific value of the fuel. It also produces a fuel that is suitable for a variety of applications. Briquetting of sawdust and other agro residues has been practiced for many years in several countries. Briquettes can be produced with a density of 1200~1400 kg/m3 whereas the corresponding value for common wood is 500-700 kg/m3. Accordingly, savings of diesel fuel during the transportation of residues or wood are substantial: a 10 ton truck can transport 34 times more weight of briquette than loose biomass fuel. There are two types of machines used for briquetting the biomass: piston presses (also known as die and punch machines) and screw extruders. The screw extruder technology has proved successful in briquetting rice husk and saw dust in Europe, Japan, Malaysia, Taiwan and Thailand. The machines operating in Bangladesh are of heated-die type and there are currently 906 of these machines in operation.

The Power Cell in a study paper has said that around 2,200 MW of power could be generated by using alternative energy sources. MSW is generated at a rate of 0.325 to 0.485 kg/cap/day obtained from different sources as 75 to 85% residential, 11-22% commercial, 1 to 1.5% institutional, 0.5 to 1.25% There is an insignificant variation of composition in MSW at six major cities of Bangladesh. The rapidly

biodegradable portion is normally very high compared to other portions, essentially due to the use of fresh vegetables and in municipal services and 0.4 to 2.5% others. The compositions are 68 to 81% food & vegetables, 7 to 11% paper & paper products, 3 to 5% polythene & plastics and 9 to 16% others [10]. As per ADB mission, landfill technology is suitable for electricity generation from MSW in Dhaka city for it's high moisture content [11]. Dhaka city alone has a capacity higher than 5000 tons/day, and the potential power generation is about 20MW [11]. Some study shows the potential of electricity generation from MSW in Rajshahi city is around 5-10MWe considering the quality of MSW by mass burn incineration [12]. The calculation shows that by adopting active biogas collection procedure in the major landfills of the main cities can produce 190MWh of electricity [13].

In the year, 2011 the rice production is around 32.88 million tonnes which is 3.4% higher than the previous year. Husk is the waste biomass produce during the rice processing on average it accounts for 20% of the paddy produced, on weight basis. The husk production per annum is about 6.57 million tonnes which is used to produce producer gas through gasification process with heating value of 4~6 MJ/Nm^3 for application in internal combustion engines. If considering half of the total husk is used for parboiling of rice and domestic purposes; the rest of the husk could be produced 200MWe electric power [14].

4. CONCLUSION

Biomass can be potential sources of Electricity generation. It reduces the dependency on fossil fuel and also environmental friendly. Bangladesh is facing a severe crisis in electricity generation due to the supply and reserve of natural gas that is reducing day by day. About 90% of our electricity generation depends on natural gas. In Bangladesh, the contribution of Renewable source in electricity generation is very negligible. But it has potential sources for electricity generation such as biomass and solar power system. Bangladesh is an agricultural country and has enormous biomass resource such as agricultural residue, municipal solid waste, poultry droppings etc. Government support could significantly encourage biomass-fueled electricity and other low-carbon energy technologies.

REFERENCES

[1] BPDB- Bangladesh Power Development Board, "Key Statistics", June, 2011

[2]Renewable Energy-Power for a sustainable future" edited by Godfrey Boyle.

[3]International Energy Agency, 2006. World Energy Outlook 2006, Paris.

[4] REN21 Global Status Report 2006

[5]Rport on "Overview of Renewable Energy Potential of India" by Peter Meisen, October 2006

[6]EIA,—Electricity Net Generation From Renewable Energy by Energy Use Sector and Energy Source, 2004 – 2008, 'from Renewable Energy Consumption and Electricity Preliminary Statistics, 2008, released July 2009.

[7] World Energy Council, 2010 survey of Energy resources/ Bioenergy.

[8] BBS, Statistical Year Book of Bangladesh, 2011. Bangladesh Bureau of Statistics, Dhaka

[9] http://www.thedailystar.net/forum/2010/January /biogas.htm

[10]Alamgir M, Ahsan A. "*Municipal solid waste and recovery potential: Bangladesh perspective*", Iranian Journal of Environmental Health Science and Engineering, Vol 4, pp.67–76, 2007.

[11]PREGA. Promotion of renewable energy, energy efficiency and greenhouse gas abatement (PREGA) Bangladesh. Dhaka city solid waste to electricity energy project. A pre-feasibility report. Bangladesh Centre for Advanced Studies, Dhaka; 2005

[12] Rouf, Md. Abdur. Prospect of Electric Energy from Solid Wastes of Rajshahi City Corporation: A Metropolitan City in Bangladesh. 2011 2nd International Conference on Environmental Engineering and Applications IPCBEE vol.17 (2011) © (2011) IACSIT Press, Singapore.

[13]Md Mosleh Uddin, Md Sadman Sakib Mojumder, Biogas Production From Municipal Waste: Prospect in Bangladesh ,Cyber Journals: Multidisciplinary Journals in Science and Technology, Journal of Selected Areas in Renewable and Sustainable Energy (JRSE), October Edition, 2011

[14]M. Ahiduzzaman. "Rice Husk Energy Technologies in Bangladesh" *Agricultural Engineering International: the CIGR Ejournal*. Invited Overview No. 1. Vol. IX. January, 2007.

Proceeding of the
International Conference on Electrical, Computer and Telecommunication Engineering
01- 02 December 2012 (ICECTE2012), RUET, Rajshahi-6204, Bangladesh

ICECTE2012: PI-0010

Technical Evaluation of Photo Voltaic Micro Utility Systems Installed by Grameen Shakti for Rural Electrification in Bangladesh

S.M. Najmul Hoque[1], Sivanappan Kumar[2], Barun Kumar Das[1], Mohammad Roqibul Islam[3],
[1] Department of Mechanical Engineering, Rasjshahi University of Engineering and Technology, Bangladesh.
[2]Energy Field of Study, Asian Institute of Technology, Thailand
[3] Manager (Project Development and CDM), Grameen Shakti, Bangladesh
E-mail: shumon99234@gmail.com, kumar@ait.ac.th, barun_ruet@yahoo.com and mrislam.gs@msn.com

ABSTRACT
Around 1.2 million SHSs have already installed by December 2011 in rural Bangladesh. But at the beginning in 1996, it was very difficult to sale SHSs because of its high cost and low awareness. To solve this problem in 1999, CMES introduced PV micro utility packages in the rural market places of Bangladesh in co-operation with Asian Institute of Technology, Thailand and Grameen Shakti, Bangladesh under the finance of SIDA. This paper presents the technical analysis of PV MU systems installed by Grameen Shakti, in Bangladesh. Result shows that the average overall efficiency of PV MU systems was 5.42% in Bangladesh and individual component of PV systems also have shown good performance. The degradation of panel performances was not significant with age. The performance of batteries, charge controllers, lamps and lamp circuits were also investigated and found to be good.

KEY WORDS: Rural electrification, Bangladesh, PV Micro utility, Grameen Shakti, Technical evaluation

1. INTRODUCTION

Electricity is the most convenient form of energy that is needed for basic household appliances and cannot be replaced by other forms of energy. At present, 1.441 billion people or 20% of the world's population do not have access of electricity in the world and most of these people live in rural areas of Asia and Africa [1]. In Bangladesh, only about 47% of the populations have access to electricity [2]. The present installed electricity generation capacity is about 6837.50 MW. The per capita electricity consumption in Bangladesh is 182 kWh p.a. that is still among the lowest in the world [2].

Solar Photovoltaic technology is one of the most suitable among all renewable energy sources in Bangladesh to produce low carbon electricity as the potential of other renewable sources are not sufficient enough to produce electricity in large scale. Bangladesh is situated between $20^0\ 34^/$–$26^0\ 38^/$ degrees north latitude and $88^0\ 01^/$–$92^0\ 41^/$ degrees east, which is ideal for solar energy utilization. The daily average solar radiation varies between 4 and 6.5 kWh/m^2[3]. Rural electrification through solar PV technology is popular in Bangladesh. The concept of solar home systems started in 1996-97, and the rate of installation was very low initially because of high initial cost. This increased significantly from 2004 to 2010 because of the soft credit through installment, reduction of price and the favorable policy of Bangladesh government[4].Though installment system for payment exists in Bangladesh, still at present solar home systems are not affordable for many poor in the villages. In order to help such consumers, Grameen Shakti (GS) and Center of Mass Education and Science (CMES) in coordination with Asian Institute of Technology, Thailand introduced the first PV micro utility (PV MU) in Bangladesh in October 1999[5]. Under this model, an entrepreneur installs the system at his own premise and shares the electricity generated with his neighbors. The owner of the system is responsible for making installment payments to GS and the users will pay monthly or daily rent to the owner. This micro-utility model has become very popular in the rural market places and more than 10,000 micro-utility systems are now in use the rural market places of Bangladesh [6].

2. METHODOLOGY

Information of 150 PV micro utility systems at 11 different locations in Bangladesh was collected. Dinajpur, Mymensingh, Gazipur, Manikgong, Dhaka, Khulna, Barishal, Bhola, Chandpur and Rangamati were the districts from where the data were collected. Thirty five systems from nine places among those 150 systems were selected to monitor by field visit. Survey was done during October, 2011 to January, 2012 to study the technical feasibility. The specifications of individual components of the PV MU systems, their performance and the systems' overall performance are analyzed. The existing design of PV MU systems were compared with the

design procedure using Renewable Energy Technology Screening (RETScreen) software. Besides, compliance of PV MU equipments with IDCOL (Infrastructure Development Company Ltd) standards was also conducted.

3. TECHNICAL ANALYSIS

3.1 Capacity

There are around 10,000 micro utility systems installed by Grameen Shakti in rural market places [6]. The owners choice of system W_p with percentage of micro utility system found in Bangladesh are shown in figure 1. It was found that the preferred micro utility was 50 W_p system as this allows 3/4 CFL lamps and most of the shops in the rural villages do not need more than one or two lamps.

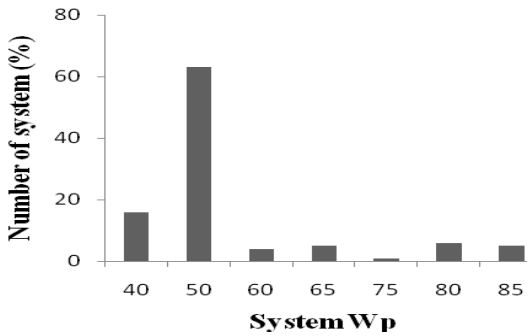

Figure 1: Owner choice of PV MU system

3.2 Performance of PV Panel

Performance of PV panel is evaluated to know whether the panel is producing desired amount of current and voltage. The open circuit voltage and short circuit current were measured to see the panel output. All the measurements were done on clear and shiny day and near solar noon. Additional measurements were also done on another shiny day whether a panel gave lower value than the expectation. Though all these precautions were taken, values varied as the radiation was not the same thought the monitoring period. Dust accumulation on panel and improper panel orientation for some panel were the another reasons of deviating. The mean and standard deviation of measured open circuit voltage (V_{oc}) and short circuit current (I_{sc}) of panels are shown in table 1. Measurements of open circuit voltage and short circuit current indicated that Kyocera, Japan brands were shown better performance than other brands. The mean and standard deviation values suggest that all the panels used for the PV micro utility packages were found good.

3.3 Drop of V_{oc} and I_{sc} compared to new panel

The output of panel (V_{oc} and I_{sc}) found from the field were compared with the output of the new panel in the field condition. This was then used to calculate the drop of V_{oc} and I_{sc} with panel age.

Table: 1: Mean and standard deviation of measured V_{oc} and Isc of panel

System Wp	Open Circuit Voltage (V_{oc})		Short circuit current (I_{sc})	
	Mean (V)	Standard deviation (V)	Mean (amp)	Standard deviation (amp)
40	19.09	0.917	1.84	0.172
50-65	19.05	0.602	2.59	0.309
80-85	19.43	0.568	4.25	0.185

The results are shown in figure 2. The average voltage drop was 3.66% from the maximum amount found for new panel. It was also observed that the degradation was increased with age. The average voltage drop for five years old panel was 3.39%, and after 5 years it was 4.45%.

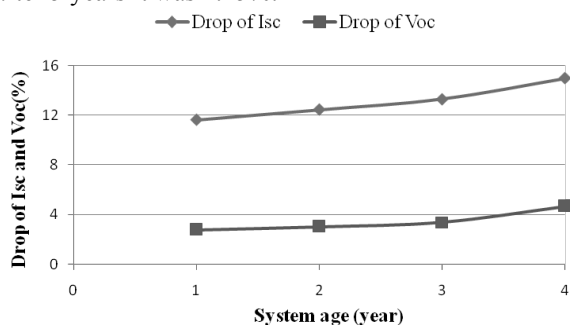

Figure 2: Degradation of short circuit current and open circuit voltage compare to new panel

The minimum and maximum drop of I_{sc} was 2.7% and 20.33% respectively and the average drop was 13.46%. The average drop of I_{sc} for the panel age below 5 years was 12.39% and this was 16.56% after 5 years. The degradation of panel should not be more than 10% within 10 years according to panel manufacturer and IDCOL standard. Though the current drop was little bit higher than the expected, this was mainly due to the dust accumulation on panel and variation of radiation as current varies significantly with solar radiation [7].

3.4 Performance of Battery

GS design of battery (Ah), Battery capacities (Ah) found during data collection were compared with the battery Ah calculated according to battery sizing formula and shown in table 2. The batteries especially smaller W_p system batteries seen to be over sized. Both installers and manufacturers of batteries should put some effort to produce proper Ah batteries for a particular W_p system because oversize battery can increase the system cost and is also not good for battery life.

Table 2: Comparison of GS (battery) design with the data collection from field and with standard battery design formula.

System Wp	GS Design (Battery Ah)	Observation from field (Battery Ah)	Calculation by using battery sizing formula (Ah)
40	56,60	56,60 and 71	42
50	80	80 and 100	55
60	80	80 and 100	69
65	100	100	69
75	100	100	83
80	100	100 and 130	97
85	130	130	109

Besides, out of 35 batteries, 29 batteries (83%), were found in the half charge region and showed the value between 1200 to 1250 gm/lit. The values should be more than 1200 as measurement was done near the solar noon (11am-2pm). 11.43% batteries showed specific gravity higher than 1250gm/lit. This could be could be mainly because of less use of battery the night before the evaluation. On the other hand, two seven years old batteries were also found within 1150-1250 gm/lit regions. Besides, 61% batteries were found to have same specific gravity in all cells and the remaining 39% were showed difference but not more than 20 gm/lit. The mean and the standard deviation of the specific gravity of the batteries were 1230 gm/lit and 22.96 gm/lit.

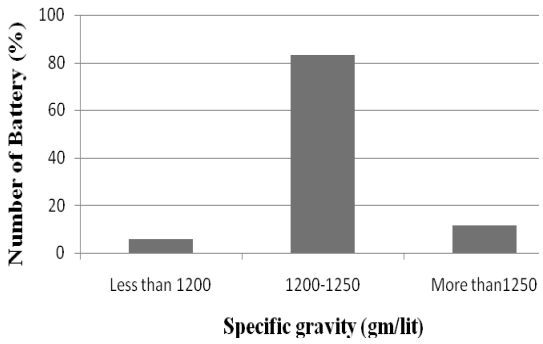

Figure 3: Specific gravity of batteries of monitored PV system

All the batteries were found to be working during the monitoring period. Terminal voltages, level of electrolyte and operation environment of batteries were observed and found satisfactory. The lowest value of terminal voltage was 12.18 V and the highest was 13.33 V.

3.5 Performance of charge controller

GS were found to make their own charge controller by fourty six (46) Grameen Technology Center (GTC) situated throughout the Bangladesh. Fuse burn of a charge controller was a common phenomenon and around 50% owners reported that they experienced this problem in their charge controller. But GS technician and owner could easily change the fuse on the spot. Out of 35 monitored systems, two owners changed their charge controller twice and another 03 owners changed it three times. High voltage disconnect (HVD) and Low voltage disconnect (LVD) of charge controllers were measured to find whether charge controller were working according to the IDCOL standard [HVD= 14.3±0.2 and LVD= 11.6±0.1 (IDCOL, 2005)]. As shown in figure 4, only 12 (34%) charge controllers out of 35 were found within the standard HVD range and the remaining 25 charge controllers (71%) deviated from the original value of 14.5V but, almost all of them were within 15 V. Mean of HVD was 14.66. This higher value can charge the battery more and can provide longer duration of service at night but is not preferable for the battery for long run. Over charge can create gassing effect in the battery also.

On the other hand, according to figure 5, most of the LVD values were within the range. Out of 35 monitored systems, 19 (55%) were within the range and the deviation was not significant for the remaining 46%. The mean for the LVD was 11.65V which was quite good. Six charge controllers had LVD of 11.4V and only one had 11.3V. Low LVD can increase the depth of discharge of battery and can increase the duration service at night but not well for battery in long run.

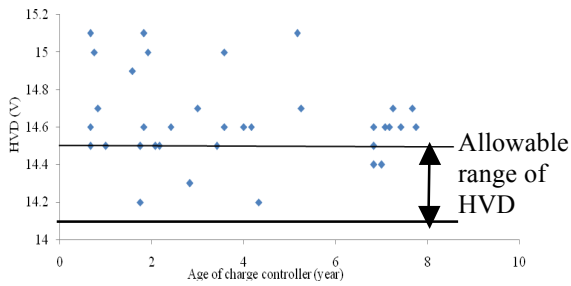

Figure 4: HVD of charge controller with their age

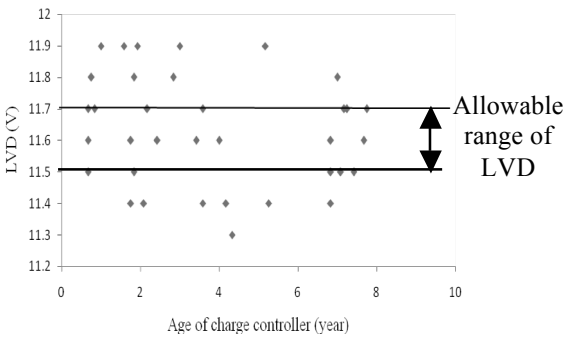

Figure 5: LVD of charge controller with their age

3.6 Overall efficiency of micro utility systems

The average overall operating efficiency of micro utility systems installed by GS in rural Bangladesh was 5.42%. Efficiencies were mostly depended on the loads used by the user rather than age. The system satisfying full load had higher efficiency. Panel efficiencies were found to be 12-16% from manufactures guideline and other losses within the systems were battery efficiency 85%, Charge controller efficiency 98% and allowable cable loss 2%. Overall efficiency of higher W_p systems were higher as more number of loads were used with the higher W_p system. Studies on the performance of solar home system in the rural areas are few. Reinders et al (1999) evaluated the performance of solar home system in a village of Indonesia and found the average overall design efficiency was around 5% [8]. The main losses were within the module, battery charging and battery storage. On the other hand, the average overall efficiencies were around 4.7% for the solar home system in Argentina [9]. The PV MU systems in Bangladesh have comparable efficiency with other countries and were very near the design efficiency.

4. CONCLUSION

The important findings from the study are summarized below:

i) 40 to 85 W_p system were used as PV MU in rural Bangladesh and the most preferred capacity was 50 W_p by the users.

ii) Performance of PV panels was found good. Average value of open circuit voltage and short circuit current were 19.19 Volt and 2.90 amps.

iii) It was found that panel performance was good though some panel age was more than 6 years. Degradation of panel performance with age was not significant. The average voltage drop was 3.66% and current drop was 13.46%. Around 89% panels were correctly tilted at 23^0 and 94% were facing exactly south.

iv) Out of 35 systems, only 03 owners reported that they had changed their first battery. The remaining 32 owners were still using their first battery though some the battery age was more than 07 years.

v) LVD and HVD of charge controllers were measured. Mean and standard deviation of LVD were 11.6 V and 0.188V which were within the acceptable range whereas the mean and standard deviation for HVD were 14.66 V and 0.23 V.

vi) The design energy output of 40, 50, 60-65, 80 and 85 W_p systems were 84, 112,140,196 and 224 Wh/day respectively. These designs were compared with RETScreen design and found very close. Actual energy used by the user was also near the design values.

REFERENCES

[1] World Energy Outlook.The Electricity Access Database. www.iea.org, 2010.

[2] Power Cell Bangladesh , Present Power Situation, official website of Power Cell, Bangladesh. www.powercell.gov.bd, 2011.

[3] Islam MR, Islam and M.R.A. Beg "*Renewable energy resources and technologies Practice in Bangladesh*". Renewable and Sustainable Energy Review,12(2), 299-343, 2008.

[4] Renewable Energy policy Bangladesh, Power division, Ministry of Power, Energy and Mineral Resources, Government of the People Republic Bangladesh, 2008.

[5] Ibrahim, M., Anisuzzaman, M., Kumar, S. and Bhattacharya, S.C "*Demonstration of PV micro-utility system for rural electrification*". Solar Energy, 72(6), 521-530, 2002.

[6] GS Solar Home System Program, Grameen Shakti, Bangladesh. www.gshakti.org, 2011.

[7] Wenham S. R., Green . M. A., Watt M. E. and Corkish R. Applied Photovoltaics. UK and USA. Earthsean, 2007.

[8] Reinders A.H.M.E., Pramusito, Sudradjat A., Dijk V.A.P. V., Mulyadi R. Turkenburg W.C. *Sukatani revisited: on the performance of nine-year-old solar home systems and street lighting systems in Indonesia*. Renewable and Sustainable Energy Reviews, 3(1), 1-47, 1999.

[9] Pontoriero D., Blasco I., Hoese A. "*Efficiency analysis on solar home PV-systems in rural areas*". Renewable energy, 15(1-4), 602-605, 1998.

Proceeding of the
International Conference on Electrical, Computer and Telecommunication Engineering
01- 02 December 2012 (ICECTE2012), RUET, Rajshahi-6204, Bangladesh

ICECTE2012: PI-0011

Installation of PV Solar System on the Rooftop of Multistoried Buildings: A Cogeneration Concept

Yeasir Arafat[1], Purnata Roy[1], M.B. Upama[1] and Ayed Al Sayem[1]
[1]Department of EEE, BUET, Dhaka 1000, Bangladesh
E-mail: *arafat@eee.buet.ac.bd

ABSTRACT
PV solar modules directly convert solar radiation into electricity at efficiency (η)around the range of 9-20%. If surface temperature of a solar panel can be reduced by 10^0C, η will increase by 2.3%, as found in the work of R. Subarkah and Belyamin. So we have designed a cooling system for large scale use of solar modules using the concept of cogeneration.During the hottest hours of the day, cooling water will be supplied through copper coils built within the panels.As water circulates through these pipes, hot solar panels exchange heat with the water which can be re-used.

KEY WORDS: PV solar system, conversion efficiency, efficiency optimization, heat re-use, cogeneration.

1. INTRODUCTION

One of the determining factors, on which the amount of energy a solar panel can produce depends, is its conversion efficiency. The efficiency is determined by comparing how much electrical energy a solar cell produces to the amount of optical energy that irradiates on it. The output power produced depends on the short circuit current (J_{sc}) and open circuit voltage (V_{oc})[1]. When the solar cell is heated, the current, J_{sc} will increase, but the voltage, V_{oc} will decrease. Since the voltage decreases faster than the current increases, the result is an overall decrease in the output power. So with an increase in surrounding temperature, the efficiency of a solar cell goes down. Performance of a solar panel deteriorates from its optimum condition at standard test condition temperature (25°C) with increasing temperature. In Bangladesh, temperature variation is significant in a full day. Also, temperature varies in winter and in summer. The average temperature of our country is 27°C. But on a clear sunny day, during midday, it can be as high as 38°C [2] or more. So power output from a large solar system will be much less than the specified output.

To solve this problem, we have implemented a thermal management methodology of the PV solar panels that is based on 'Forced Water Flow Cooling System [3].Experiments show that, in case of monocrystalline silicon solar panel, if the surface temperature can be reduced by 10^0C, the cell efficiency will increase by 2.3% [3].For a large number of panels, the amount of heat absorbed by the circulated water from the solar panels is huge. The concept of cogeneration helps us to recycle the hot water for useful purposes.

2. THEORY

Therelation between output power of solar PV array and temperature can be given by the following equation [4]-

$$P_{PV} = Y_{PV} \times f_{PV} \left(\frac{\bar{G}_T}{\bar{G}_{T,STC}}\right) \times [1 + a_P(T_C - T_{C,STC})] \quad (1)$$

where,
Y_{PV}= the rated capacity of the PV array (kW)
f_{PV}= the PV derating factor (%)
$\bar{G}_T$= the solar radiation incident on the PV array in the current time step (kW/m^2)
$\bar{G}_{T,STC}$=incident radiation at standard test conditions (1 kW/m^2)
a_P= the temperature coefficient of power (%/°C)
T_C= Cell temperature in the current time step (°C)
$T_{C,STC}$= PV cell temperature under standard test conditions (25 °C)

The temperature coefficient of power indicates how strongly the PV array power output depends on the cell temperature, meaning the surface temperature of the PV array. It is a negative number because power output decreases with increasing cell temperature. The following table contains the average values of the temperature coefficient of power for various types of PV modules.

Table 1: Values of the temperature coefficient of power (%/°C) for different types of PV modules [4]

PV module type	Modules a_P	Average value of a_P(%/°C)
Polycrystalline Si	7	-0.48
Monocrystalline Si	4	-0.46
Mono/amorphous Si-hybrid	1	-0.30
Thin film amorphous Si	4	-0.20
Thin film CIS	1	-0.60

Some product brochures do not specify the temperature coefficient of power, but do specify thetemperature coefficient of the open-circuit

voltage. In that case, the temperature coefficient of power can be calculated using the approximation suggested by Duffie and Beckman [4]:

$$\alpha_p \approx \frac{\mu_{V_{OC}}}{V_{mp}} \quad (2)$$

where,

$\mu_{V_{OC}}$= the temperature coefficient of the open-circuit voltage (V/°C)

V_{mp}= the voltage at the maximum power point under standard test conditions (V)

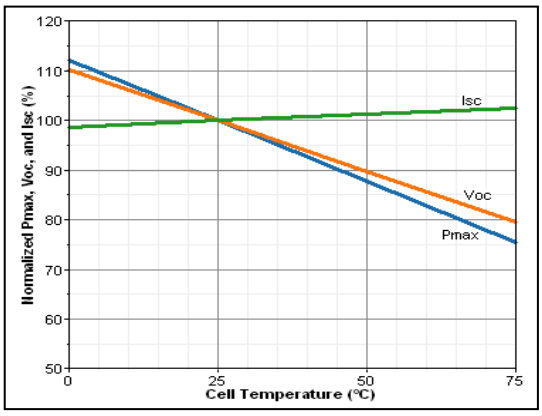

Figure 1: Relationship of Normalized Power, V_{OC} and I_{SC} with respect to the Cell Temperature [4]

3. PV SOLAR OUTPUT POWER VARIATION WITH TEMPERATURE

A moderately large system with 200 monocrystalline solar panels on the rooftop of a six storied building has been designed. The average output power of such a module at the annual average temperature (27 °C) using Eq. 1 and Table 1 is 30.2544 W (putting Y_{PV}= 200W, f_{PV}=0.8, $\bar{G}_T$=4.591kwh/m^2/day=0.191 kw/m^2)and the total average output drawn from the system is 6.0509 kW.

3.1 Increasing Temperature

Duringsummer, the temperature in our countrybecomes very high and it reaches about 35^{0}C-40^{0}C at midday. High temperature has an adverse effect on the system output. For example, if the temperature increases above 10^{0}C than the average temperature, the average output power of a single module becomes28.268W (1.9864Wreduced) and the total power reduction due to high temperature is 397W.

3.2 Decreasing Temperature

In winter, the temperature falls down far below the STC temperature (near about 15^{0}C). Though, output reduces due to lack of radiating power (input), this cold situation can be capitalized for the improvement of the panel efficiency.

The above phenomena indicate that if the module temperature can be maintained approximately around STC temperature during the hot summer days, the efficiency will be improved significantly.

4. HEAT ABSORBING METHODOLOGY

4.1 Describing the Method

Coldwater is supplied from the building's overhead water tank through a pipe towards the solar panels. There are copper pipes inscribed at the backside of the solar panel in spiral form. Water circulates through these pipes and heat is conducted from the hot solar panels through the copper pipes into the water. The temperature of the water is increased. Forced flowing water causes the replacement of hot water with the cooler one. Forced flow created due to gravity by the placement of the water tank at a position higher than the solar cell module. The hot water is then drained into another pipe. The hot water pump is connected to another reserve tank placed at the ground floor. Excess hot water is collected at this tank and processed for re-use. Study shows that the cooling water flow rate of 400ml/min can reduce the solar cell surface temperature by 10.9°C [3]. This requires14.4 m^3 ofwater flow per day(3 hours each day) for 200 solar panels.

4.2 Cooling System Arrangement

4.2.1 Calculation of the diameter of the pipes:The diameter of the pipe required is calculated as follows:0.4 m m^3/min = 0.4/3.786 gpm = 0.11 gpm [5]. If we select uPVC pipe for the system, the lowest diameter pipe for supplying water available in market is 12.7 mm, which allows water flow up to 0.03636 m^3/min. To control the 0.4 m m^3/min water flow through the 12.7 mm pipe, we have use control valve.To reduce the total no of pipes we have grouped 200 no of solar modules into **7** sections (Section 1 to Section7). The required diameter for input pipe in a section is calculated as follows:

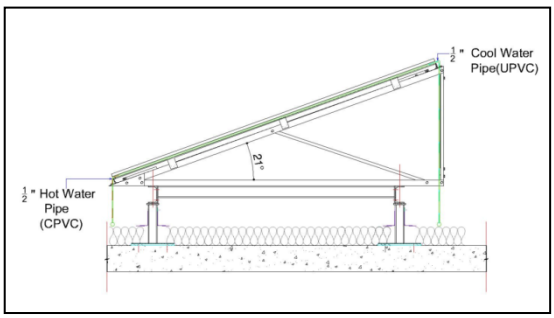

Figure 2: Cooling Water Flow Path within a Solar Module

For Section 1: No of modules in this group are 72. Flow of water required for each module is 400mL/min for sufficient cooling. So water flow through the input pipe in this section should be 72x0.4 m m^3/min

Table 2: Input Pipe Capacities of Different Sections:

Section no.	No of modules	Required water flow (m^3/min)	Input pipe diameter (mm)
Section 1	72.000	0.0288	12.700
Section 2	24.000	0.0096	12.700
Section 3	18.000	0.0072	12.700
Section 4	24.000	0.0096	12.700
Section 5	24.000	0.0096	12.700
Section 6	22.000	0.0088	12.700
Section 7	16.000	0.0064	12.700

In similar way, flow of water in main pipe which supply water from overhead water tank is found to be 0.080 m^3/min and its diameter will be 19.1 mm.

4.2.2 Cold and hot water supply system: In the following 2 figures, the cold and hot water supply system has been depicted**.**

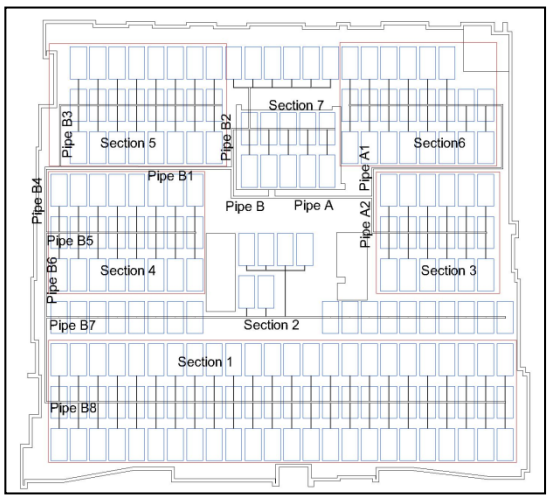

Figure 3: Cold Water Supply System on the Roof

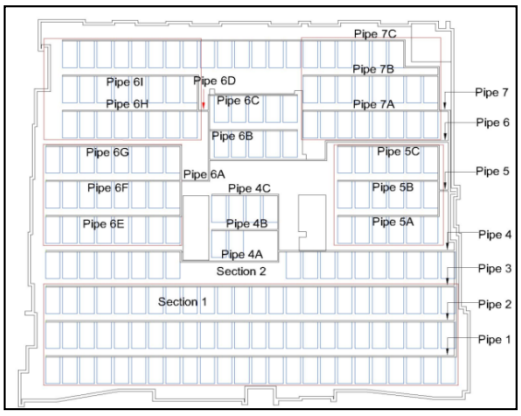

Figure 4: Hot Water Collecting System on the Roof

Hot water from solar modules should be collected usingCPVC pipe**,** the capacity of which is similar to the uPVC pipe.So, 12.7 mm and 19.1 mm CPVC pipes will be used for designing hot water flow.

4.2.3 Calculation of the size overhead water tank, and hot water reservoir: For 25 apartments in a 6-storied building, the required water reservation will be 25x6x225 L= 33.750 m^3 [6].If water should be pumped 2 times in a single day, the volume of the water tank will be 16.875 m^3.So the overhead water tank size may be 5.5 m × 3.0 m × 1.4 m [6].For solar system cooling,14.4 m^3 water has to be added in the overhead water tank.To accommodate this, the overhead water tank size may be 5.5m × 3.0m × 3 m, a 1.6 m increase in tank height is required.The hot water should be collected by CPVC pipes and stored in a hot water reservoir. The volume of it may be 14.4 m^3 and size 3.05 m ×3.05 m× 1.8 m.

4.2.4 Time-dependent Cooling System along with Cogeneration: Now a days, many high rise buildings in Bangladesh use pre-heaters and heaters to supply hot water to the flats. We can supply this hot water from copper coils to the hot water reservoir built in the floor immediately below the rooftop. Then it would go to the flats through hot water supply pipe and be used for bath and cooking purposes. The rest of the hot water from the solar system is stored in the hot water tank built in the ground floor. From there, it would be mixed with the water stored in the underground water tank.The whole amount of hot water from the panels is not mixed into the underground tank at a time because mixing hot water increases the main tank's water temperature and it can exceed the comfortable limit if the mixing is not controlled. So, we have introduced time-dependent cooling system. In this method, the mixing of water is intentionally delayed. Small volume of water is mixed at certain time intervals so that the increase in temperature of water in the main tank is limited within 1^0C only.

4.3Thermodynamic Analysis

4.3.1 Amount of heat transferred from solar panels to the water:Water is heated and its temperature is increased by 10.9°C. The total heat energy stored in the hot water per day due to temperature rise= m.s.Δθ Joule.

Density of water= 1000 Kg/m^3

Volume of water flown per day= 14.4 m^3

The mass of the water, m = density of water ×volume of water flown per day = 1000×14.4 Kg = 14400 Kg

Specific Heat Capacity of water, s= 4200 J/Kg.°C

Difference between initial and final temperature of water, Δθ=10.9°C Total Heat Energy=14400Kg ×4200J/Kg°C×10.9°C= 6.5923×10^8 Joule.

4.3.2 Thermodynamic Analysis of Time-dependent Cooling System**:** Hot water from the solar cooling system exhaust is collected by CPVC pipes and a part of it is stored in a reservoir which is thermally

insulated. From this reservoir hot water will be supplied to the flats for bathing and cooking purposes. In this way we can cogenerate hot water from the cooling arrangement.If the amount of hot water supplied to the flats is 2.5 m^3, the heat absorbed by this portion of water =2.5*1000*4200*10.9J=1.14×10^8Joule.Sothe amount of hot water required to be cooled will be reduced by an amount of 2.5 m^3.Rest of the hot water will go to the hot water reservoir placed in ground floor. As this reservoir is not thermally insulated, thermal radiation will reduce the water temperature gradually.Quantity of water stored in the hot water reservoir =11.9 m^3. If this hot water will be kept in it for 3 hours, the heat radiation will be=5050Js^{-1}*3600*3s=5.454×10^7Joule.

So, the amount of heat energy present in the hot water reservoir will be (6.5923×10^8-1.14×10^8-5.454×10^7) = 4.907×10^8 Joule. After keeping the hot water idly for 3 hours in the reservoir, this water will be mixed with water in the underground water tank in two steps.In the underground water tank, water is reserved for two days. So capacity of this tank will be 33.750*2 m^3 = 67.50 m^3.We want to mix 11.9 m^3 of hot water with 55.6 m^3 of normal temperature water in two steps to keep the increase in water temperature within 1°C.Heat required to 1°C increase in underground reservoir's water temperature=$55.6\times1000\times4200\times1$Joule= 2.335×10^8 Joule. As a result, first we have to mix only that quantity of hot water which contains2.335×10^8Joules heat energy. The quantity of hot water containing 2.335×10^8 Joule heat energy={$2.335\times10^{8/}(4200\times10)$}kg= 5000, kg =5 m^3 of hot water. So 5 m^3 of hot water from the hot water reservoir will go to the underground reservoir through the connecting pipes using the gravitational force.If we use CPVC pipe of 12.7 mm it will flow 0.03 m^3/min of water. So the time required to flow 5 m^3 of water = (5 m^3/ 0.03 m^3/min) = 167 min = about 3 hours.We will mix the rest of the water after waiting for more 3 hours.During this 6 hours (3 hours to mix the water in the first step+3 hours waiting period) period heat will be radiated from the hot water reservoir.So the amount of heat energy radiated from the hot reservoir in 6 hours=5050 Js^{-1} * 3600 *6s = 1.091×10^8 Joule. As a result, the amount of heat energy present in the hot-water reservoir=(4.907×10^8-2.335×10^8-1.091×10^8)Joule=1.481×10^7 Joule. So, we will mix (11.9-5) m^3 =6.9 m^3 water which contain 1.481×10^7 Joule of heat energy with 55.6 m^3 of water in the underground reservoir.The resulting increase in the underground water temperature={1.481×10^7/ ($4200\times6.9\times1000$)}^{o}C=0.51 ^{o}C.

***4.3.3 Cost involved and benefits*:** A total structural cost of Tk. 1,15,000, cooling and hot water pipe of Tk. 30,000 and annual operational cost of Tk. 19,000 is required, whereas Tk. 1,50,000 may be saved annually by increasing the panel efficiency due to cooling and saving electricity bill expenses for water heating purpose in residences. So, we see, the cogeneration method can add up to Tk. 1,35,000 (assuming 10% depreciation) to its revenue from solar electricity production. The cogeneration also has environmental benefits.

5. CONCLUSIONS

The output power of PV solar system varies significantly with temperature variation. In order to cool down the surface temperature of the solar panels the methodology of forced water flow through pipes is used and significant improvement in system efficiency is achieved. For a large scale use of solar panels, huge water is required. Natural cooling would take a long time to cool down this large volume of hot water. So we have supplied a portion of this hot water to the flats for domestic use and recycle the rest of the hot water using time dependent cooling methodology. This method is economically beneficial because this hot water cooling method use the gravitational force and the operation and maintenance cost of using a geyser is eliminated.

6. ACKNOWLEDGEMENTS

The authors would like to thank the Dept. of EEE, BUET, Dhaka,Bangladesh, for various supports.

REFERENCES

[1].Nelson, Jenny,The Physics of Solar Cells, London: Imperial College, 2003. Print

[2].N. C. Bhowmik,Bangladesh Renewable Energy Report,APCTT-UNESCAP, 2012

[3].R. Subarkah, Belyamin, Improved Efficiency Solar Cells with Forced Cooling Water, retrieved on 16/10/2011.

[4].HOMER, Software for Micro Power Optimization Modeling, retrieved on 16/10/2011

[5]. www.bpdb.gov.bd, The Electricity Tariff in Bangladesh, retrieved on 21/9/2011

[6]. http://www.ergon.com.au/your-home/accounts--and--billing/electricity-prices#content-id-58257, retrieved on 16/10/2011

Proceeding of the
International Conference on Electrical, Computer and Telecommunication Engineering
01- 02 December 2012 (ICECTE2012), RUET, Rajshahi-6204, Bangladesh

ICECTE2012: PI-0012

High Efficient Three-Junction Tandem Cell Based on Cadmium Alloys

Sayeda Anika Amin[1], Sartaz Tabinna Salim[2] and K.M.A. Salam[3]
Department of Electrical Engineering and Computer Science, North South University, Bashundhara R/A, Dhaka, Bangladesh
E-mail: anika.amin.30@gmail.com, sartaz05@hotmail.com,asalam@northsouth.edu

ABSTRACT
The efficiency of the present day triple junction solar cell can be improved by design optimization of each subcell and by introducing new materials. In this paper we introduce a new three-junction cell based on alloys of Cadmium and analyze the performance of this cell by comparing it with other 3-junction cells. The CdSe/CdTe/$Hg_{0.71}Cd_{0.29}Te$ 3-junction cell has shown significant photon absorption in the entire solar spectral range and a theoretical efficiency of 45.4% in terrestrial AM 1.5 condition.

KEY WORDS: Photovoltaic, Multijunction, Cadmium Selenide, Cadmium Telluride, Mercury Cadmium Telluride.

1. INTRODUCTION

One of the primary goal of solar cell design is to improve efficiency. Solar cell efficiencies have improved over time by increasing number of junctions. Each junction is capable of extracting energy from a portion of the solar spectrum. A new path to improve efficiency is to use new photovoltaic materials which possess a bandgap range that can extract energy from a large portion of the solar spectrum.

The most efficient present day multijunction cell photovoltaic cells are made of GaInP, GaInAs and Ge layers on Ge substrate [1, 2]. The researchers in Spectrolab have claimed to achieve a record efficiency of 41.6% for concentrator cells [2]. Alloys of group III and V of the periodic table have been used to fabricate these multijunction cells. One of the limitations of group III-V materials is that all the junctions in the cell need to be lattice matched i.e. all layers must have similar crystal structure. Mismatches in lattice constant of different layers create dislocations in the lattice of the cell layers and significantly deteriorates the overall efficiency of the solar cell [3]. To overcome these limitation alloys of other groups which have high optical absorption co-efficient and are less affected by lattice mismatches can be used. Recently alloys of group II-VI have been used and experimented in the photovoltaic research arena because of their direct bandgap and high optical absorption co-efficient [4]. Another important reason of using II-VI materials is that lattice mismatches over 15% and dislocation densities above $10^6 cm^{-2}$ have very little effect on the device properties [3]. The reason that dislocations have a smaller deleterious effect on the electronic properties of II-VI materials may lie in the more ionic, less covalent nature of II-VI materials. In this paper, we have designed a 3 junction cell based on group II-VI cadmium alloys and made a comparsion of the photon absorptance of this cell with other 3-junction cells. Further we calculated the theoretical efficiency of the proposed cell under terrestrial AM1.5 condition.

2. CdSe/CdTe/$Hg_{0.71}Cd_{0.29}Te$ 3-JUNCTION TANDEM CELL

Photons incident on the surface of a semiconductor will be either reflected from the top surface or will be absorbed in the material or will be transmitted through the material. Absorbed photons will raise electron from the valence band to the conduction band and thus generate power. So power generation of photovoltaic devices depend on photon absorptance. Transmittance and reflectance are considered as loss mechanisms in PV devices as photons which are not absorbed do not generate power.

In our work, we proposed a 3-junction cell based on group II-VI materials. The top layer of our cell comprises of Cadmium Selenide (CdSe) which has a direct bandgap of 1.74 eV. The middle layer or the absorber layer is Cadmium Telluride (CdTe) which has a bandgap of 1.44 eV. In the bottom layer we have used Mercury Cadmium Telluride (($Hg_{0.71}Cd_{0.29}Te$) with a bandgap ranges from 0.3-0.5eV. Mercury Cadmium Telluride (HgCdTe) is an alloy of CdTe and HgTe. It is claimed to be the third semiconductor of technological importance after Silicon and Gallium Arsenide. Depending on the Cadmium composition HgCdTe can be tuned to any bandgap between 0-1.5 eV. Our simulation results have shown that $Hg_{0.71}Cd_{0.29}Te$ is a good candidate to be used as a bottom layer in a multijunction cell.

3. SIMULATION AND RESULTS

3.1 Top layer

The top layer of a multijunction cell captures the high energy photons and passes the rest of the photons on to be absorbed by lower bandgap layers. In order to achieve a high performance the bandgap of the top layer of a multijunction cell should be 1.6-1.8 eV [5]. The bandgap of Cadmium Selenide used in this cell is 1.74 eV which is nearly perfect for the use in top layer. Some of the materials which have been commonly used as the top layer are GaP (2.2eV), GaInP (1.8eV), AlGaAs (1.98eV). We have made a comparison of the photon absorptance of these materials with Cadmium Selenide (CdSe) using the Photonics RT simulator [6] and obtained the following results:

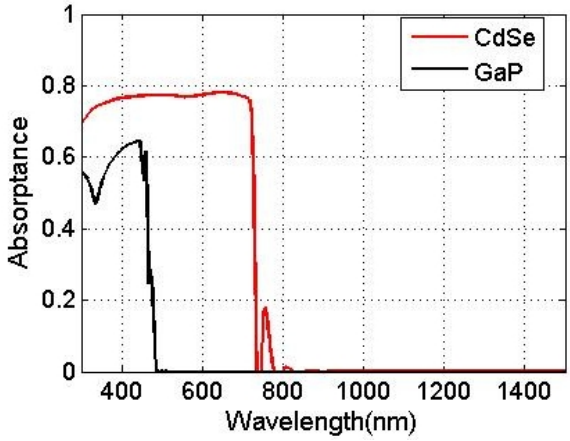

Fig.1 Comparison of photon absorptance of CdSe and GaP.

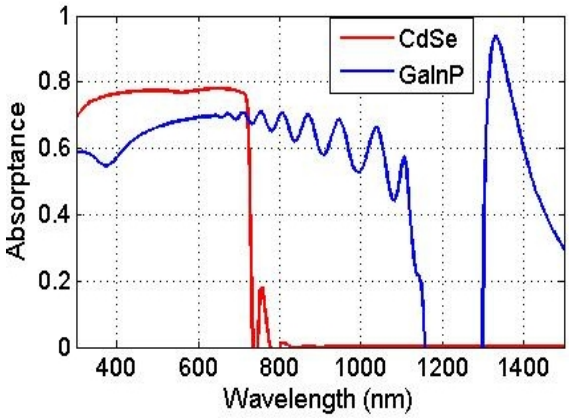

Fig.2 Comparison of photon absorptance of CdSe and GaInP.

The simulation results in Fig.1, 2 and 3 clearly indicate that the photon absorptance of CdSe is higher than GaP, GaInP and AlGaAs. The CdSe material helped to increase the photon absorption in the range of 300nm-712 nm contributing in the overall absorption of the cell.

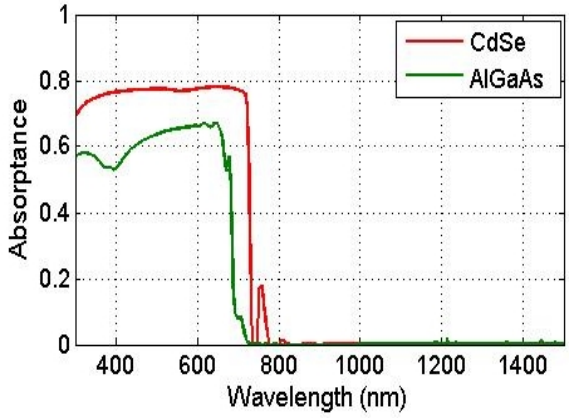

Fig.3 Comparison of photon absorptance of CdSe and AlGaAs.

3.2 Absorber layer

The most commonly used absorber layers are GaAs and InGaAs. In our triple junction cell CdTe has been used as the absorber layer. In the middle or absorber layer the photons of incident radiation are efficiently absorbed resulting in the creation of electron-hole pairs.

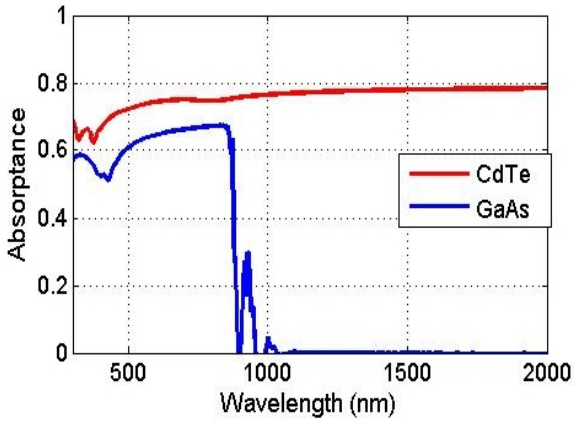

Fig.4 Comparison of absorptance of CdTe and GaAs.

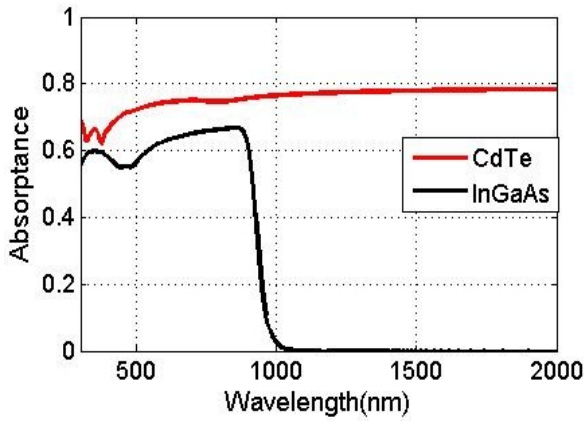

Fig.5 Comparison of photon absorptance of CdTe and InGaAs.

The high absorptance of CdTe in fig.4 and 5 proves that CdTe could possibly be a better absorber than InGaAs and GaAs.

3.3 Bottom layer

Mercury Cadmium Telluride ($Hg_{0.71}Cd_{0.29}Te$) has been used as the bottom layer. The electron mobility and refractive index of HgCdTe with a large Hg content is very high [7]. Highly pure and crystalline HgCdTe can be fabricated by epitaxy on either CdTe or CdZnTe substrates.

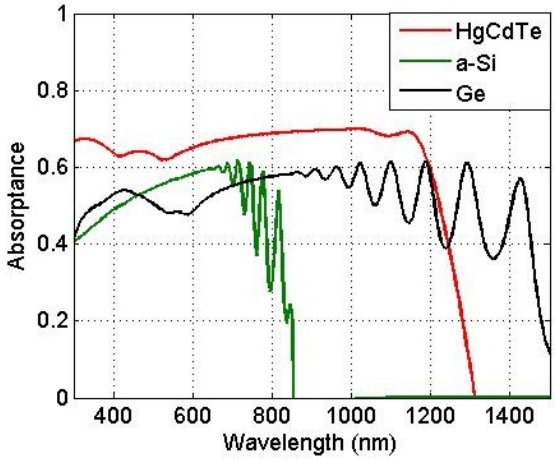

Fig.6 Comparison of photon absorptance of amorphous Silicon, Germanium and Mercury Cadmium Telluride (HgCdTe).

$Hg_{0.71}Cd_{0.29}Te$ has shown high photon absorption in the range of 300nm to 1250nm. The absorption is much higher than Germanium and amorphous silicon which are commonly used as the bottom layer in MJ cells.

3.4 Comparison with GaInP/GaInAs/Ge

Fig.7 depicts the overall absorptance, reflectance and transmittance of CdSe/CdTe/$Hg_{0.71}Cd_{0.29}Te$. Our goal is to increase the absorptance and reduce the transmittance and reflectance so that the maximum solar energy is utilized and more number of mobile holes and electrons are created.

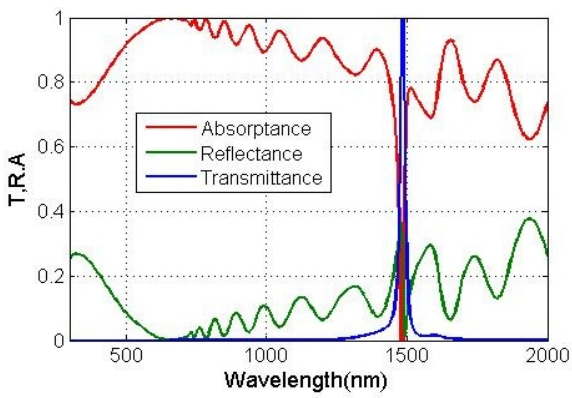

Fig.7 Absorptance, Reflectance and Transmittance of CdSe/CdTe/$Hg_{0.71}Cd_{0.29}Te$ cell.

Spectrolab has measured an efficiency of 41.6% and independently confirmed a metamorphic three-junction GaInP/GaInAs/Ge cell under the standard spectrum for terrestrial concentrator solar cells at 240 suns (24.0W/cm^2, AM1.5D, low AOD, 25°C) [2]. This is so far the highest efficiency achieved by any multi-junction cell. We have simulated this cell in order to observe the photon absorption and achieved the following result:

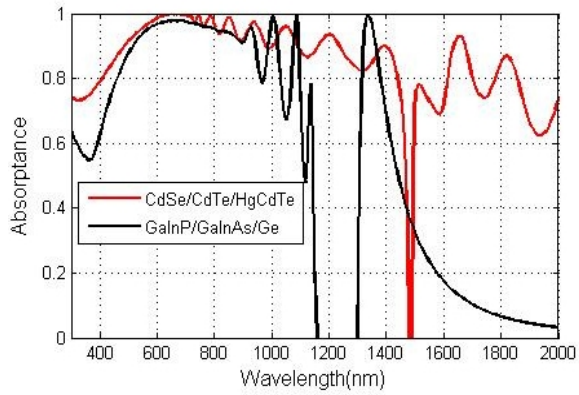

Fig.8 Photon absorptance of GaInP/GaInAs/Ge cell and CdSe/CdTe/$Hg_{0.71}Cd_{0.29}Te$ cell.

From the above fig we see that the absorptance of photons at some wavelengths is higher in our CdSe/CdTe/$Hg_{0.71}Cd_{0.29}Te$ cell than GaInP/GaInAs/Ge cell. This high absorptance indicates that CdSe/CdTe/$Hg_{0.71}Cd_{0.29}Te$ cell has a great potential for further multijunction applications.

4. EFFICIENCY

The conversion efficiency, η, of solar cells is calculated as the ratio between the generated maximum power, P_m, generated by a solar cell and the incident power P_{in}.

$$P_{in} = \int_0^\infty I(\lambda)d\lambda \tag{1}$$

$I(\lambda)$ is the solar illumination of the ASTM AM1.5 [8]. It is known that only photons with energy higher than the bandgap energy of the absorber generate electron-hole pairs. The fraction of the incident power, P_{abs} that is absorbed by a solar cell is expressed as:

$$P_{use} = \frac{E_g \int_0^{\lambda_g} I(\lambda) \frac{\lambda}{hc} d\lambda}{\int_0^{\lambda_g} I(\lambda) d\lambda} \quad (2)$$

Eg is the bandgap, h is planck's constant and c is the velocity of light. λ_g is the cutoff wavelength of the cell.The fraction of the absorbed energy that the cell can deliver as a useful energy, P_{use} is described as:

$$P_{use} = \frac{E_g \int_0^{\lambda_g} I(\lambda) \frac{\lambda}{hc} d\lambda}{\int_0^{\lambda_g} I(\lambda) d\lambda} \quad (3)$$

The overall efficiency is given by,

$$\eta = P_{abs} . P_{use}$$

$$= \frac{\int_0^{\lambda_g} I(\lambda) d\lambda E_g \int_0^{\lambda_g} I(\lambda) \frac{\lambda}{hc} d\lambda}{\int_0^{\infty} I(\lambda) d\lambda \int_0^{\lambda_g} I(\lambda) d\lambda} \quad (4)$$

We calculated the theoretical efficiency of the record breaking cell GaInP/GaInAs/Ge and compared with our 3-junction cell. Table 1 shows that the calculated efficiency of our 3-junction cell is 2.3% higher than the calculated efficiency of Spectrolab's GaInP/GaInAs/Ge cell.

Cell	**AM1.5, 1 sun Efficiency**
GaInP/GaInAs/Ge	43.1%
CdSe/CdTe/$Hg_{0.71}Cd_{0.29}Te$	45.4%

Table 1. Calculated theoretical efficiencies of GaInP/GaInAs/Ge and CdSe/CdTe/$Hg_{0.71}Cd_{0.29}Te$.

5. CONCLUSIONS

In this work, we have shown that cadmium alloys have a great potential for multijunction cell applications. We compared the photon absorptance of the different individual layers of this cell with other photovoltaic materials. Further we calculated the absorptance and overall efficiency of the entire cell and compared the result with Spectrolab's highest efficient 3-junction GaInP/GaInAs/Ge cell.The high photon absorption and the theoretical efficiency of 45.4% indicate that CdSe/CdTe/$Hg_{0.71}Cd_{0.29}Te$ cell has a great potential to be used in multijunction cell applications.

REFERENCES

[1]. R. R. King, D.C. Law, K. M. Edmondson, C.M. Fetzer, G. S. Kinsey, H.Yoon, R. A. Sherif and NN.H.Karam, "40% efficient metamorphic GaInP/GaInAs/Ge multijunction solar cells", *Applied Physics Letters,* Vol.90, May, 2007.

[2]. R. R. King, "Raising the Efficiency Ceiling in Multijunction Solar Cells", *Proc. Of Stanford Photonics Research Center Symposium,*Sep. 14-16, 2009.

[3]. J. W. Garland, T. Biegala, M. Carmody, C. Gilmore, and S. Sivananthan, "Next-generation multijunction solar cells: The promise of II-VI materials", *Journal of Applied Physiscs,* Vol.109, May 2011.

[4]. M. Afzaal and P. O. Brien, "Recent Developments in II-VI and III-VI semiconductors and their applications in solar cells", *Journal of Materials Chemistry,* Vol.16, pp. 1597-1602, 2005.

[5]. T. J. Coutts, J. S. Ward, D. L. Young, K. A. Emery, T. A. Gessert and R. Noufi, *Progress in Photovoltaics*, Vol.11, pp.359-375, Sept 2003.

[6]. Photonics RT: Wave propagation in Multilayer Structures. Available at: www.nanohub.org.

[7]. E. Finkman and S. E. Schacham, "The exponential optical absorption bandtail of $Hg_{1-x}Cd_xTe$", Journal of Applied Physics, Vol.56 (10), 1984.

[8]. ASTM, "Reference Solar Spectral Irradiance: Air Mass 1.5 Spectra. Available at : http://rredc.nrel.gov/solar/spectra/am1.5/

Proceeding of the
International Conference on Electrical, Computer and Telecommunication Engineering
01- 02 December 2012 (ICECTE2012), RUET, Rajshahi-6204, Bangladesh

ICECTE2012: PI-0013

Effect of Composition Grading on the Efficiencyof Heterojunction Thin Film CIGS Solar Cell

*Yeasir Arafat[1],Ayed Al Sayem[1]and M.M.S. Hassan[1]
[1]Department of EEE, BUET, Dhaka 1000, Bangladesh
E-mail: *arafat@eee.buet.ac.bd, ayedalsayem143@gmail.com

ABSTRACT
Because of its low material consumption and relatively high efficiency, thin film solar cell is a technology of great potential.Simulations have been performed to optimize the gradingeffect of Gallium composition in $CuIn_{1-x}Ga_xSe_2$ *which can greatly influence the efficiency of this device. Effect of change on open circuit voltage, short circuit current density, fill factor and efficiency has been studied. Device Simulator SILVACO ATLAS has been used for this purpose. It has been found that thin film CIGSsolar cells can have a better efficiency for graded Gallium profile and can be very effective for gaining higher efficiency.*

KEYWORDS:Thin film solar cell, efficiency improvement,composition grading,SILVACO ATLAS,CIGS.

1. INTRODUCTION

A solar cellis usually made of semiconducting materials, which converts radiant optical energy into electrical energy and this phenomenon is known as the photovoltaic effect. Solar devices manufactured from wafers of monocrystalline or polycrystalline silicon are the dominant technology in the commercial market at present situation. Solar cells based on the thin film of semiconducting materials are the emerging technologies with great potential in harvesting green energy. One such thin film technology is based on a compound of Copper, Indium, Gallium and Selenium abbreviated as $Cu(In,Ga)Se_2$ or CIGS [1]-[2]. Main advantages of this thin film technology are the low material consumption and high efficiency which both make this technology economically competitive.

Gallium is a very important material in CIGS solar cell. Here in this paper,the effect of Galliumcomposition grading has been demonstrated to get higher efficiency.Few works have been done on this topic [3]-[4]. In some works, front grading has been considered [3] and in some works back grading has been considered [4]. In the present work, only back grading has been considered for a very thin CIGS Solar cell.

2. SOLAR CELL PARAMETERS

The purpose of this study was to find the effect of Gallium composition grading for achieving higher efficiency. The whole cell thickness was 1.68 micro meter long, base width was 10 micro meters. The ZnO thickness was 1 micro meter, Cds thickness was 0.02 micro meter, CIGS absorber thickness was 0.36 micro meter and Molybdenum thickness was 0.3 micro meter. Doping in Cds (emitter) was 10^{18}per $cm^3$and doping in CIGS was $2x10^{16}$ per cm^3.

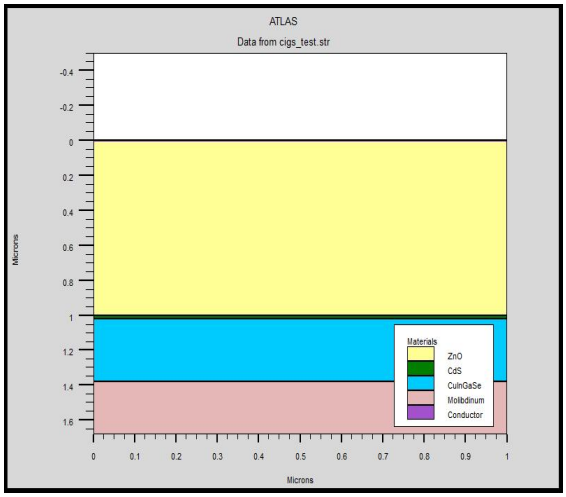

Figure1: Structure of CIGS solar cell as shown in SILVACO ATLAS

3. SIMULATION AND RESULTS

The simulation has been done under AM0 spectrum.

3.1 Open Circuit Voltage:

Open Circuit Voltage is a key factor in efficiency gain in CIGS solar cell for higher Gallium composition. The diode characteristics get better for higher Gallium content because of high band gap. Open circuit voltage increased as we gradually increase the composition of Gallium. At first we just used pure CIS then we include Gallium composition from 0.1 to 0.7. For both box shape and graded (peak) composition, the open circuit voltage increased as we expected but open circuit

voltage was lower in graded than box shape for all level of composition.

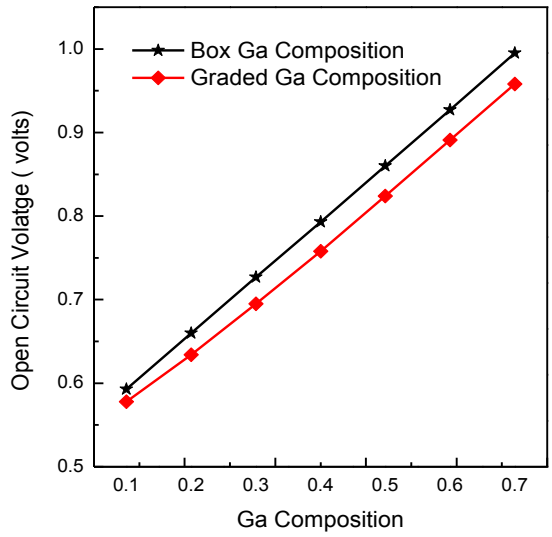

Figure2: Change in open circuit voltage for Gallium composition variation

3.2 Short Circuit Current:

As we know as the band gap increases it gets difficult for generating photo current.

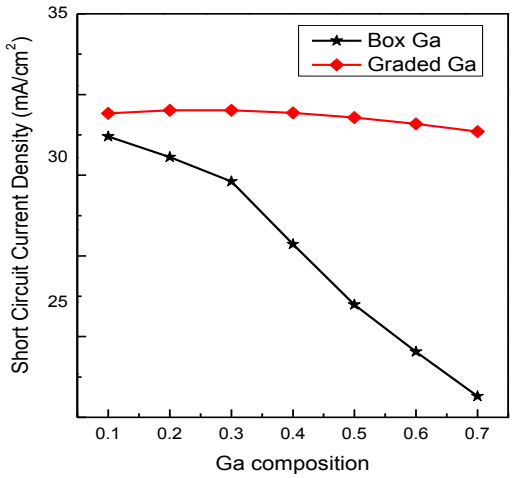

Figure3: Change in short circuit current density forGallium compositionvariation

As we introduce more and more Gallium, the band gap increases. As a result, short circuit current density gets reduced as the composition is increased for box shaped gallium profile. But for graded profile, short circuit current density didn't reduce that much as it did for box shape profile. This is a key advantage in obtaining higher efficiency for graded Gallium composition. Short circuit current decreased from 31.34 mA/cm^2 to 21.73 mA/cm^2 for box shaped profile but for graded profile, short circuit current density decreased from 31.56 mA/cm^2 to 30.91 mA/cm^2. This is one of the most effective impactsof composition grading on solar cell efficiency.

3.3 Fill Factor:

Fill factor is defined as the ratio of the actual maximum obtainable power to the product of the open circuit voltage and short circuit current. This is a very important parameter in evaluating the performance and electrical efficiency of solar cells.

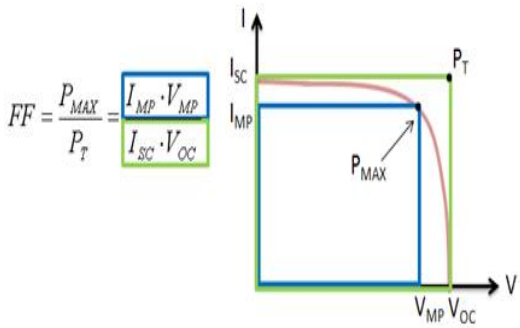

Figure4: Fill Factor of a solar cell

$$\text{Fill Factor} = \frac{V_{mp} \times I_{mp}}{V_{OC} \times I_{SC}}$$

where,

V_{OC}= Open circuit voltage

I_{SC} = Short circuit current

I_{mp} = Maximum obtainable current

V_{mp} = Maximum obtainable voltage

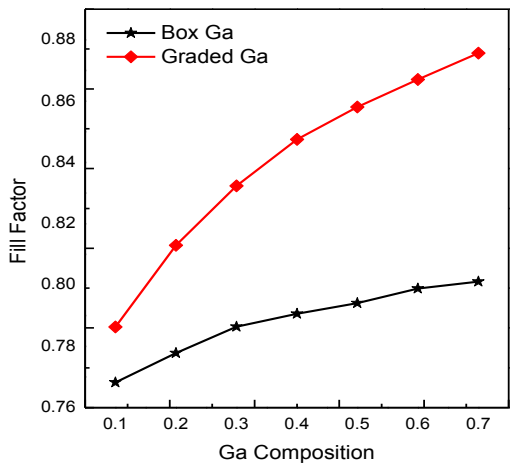

Figure5: Change in fill factor for Gallium compositionvariation

For both box and graded gallium profile,fill factor increased. But for box profile, it increased slightly from0.768 to 0.801 where for graded profile it increased from 0.786 to 0.876. 11.45 % increase in fill factor for graded profile but only 4.3% increase box profile.

3.4 Efficiency

As the purpose of the study was to know the effect of Gallium composition grading on CIGS solar cell, we didn't optimize other parameters and they remained constant for the whole simulation process. Here we found the lowest efficiency for 0 composition or pure CIS solar cell. Taking it as a standard we find the efficiency gain in percentage for gradual composition in both cases: box profile and graded profile.

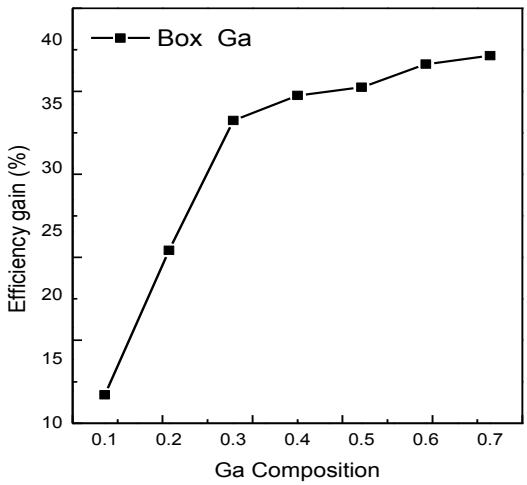

Figure 6: Efficiency gain for Gallium composition

We found that efficiency increased for both box and graded shape profile for higher Gallium amount but in case of box, after 0.3 composition, efficiency doesn't increased that much (Fig. 6).But in case of graded Gallium composition with peak of Gallium composition changing from 0 to 0.7, efficiency increased almost linearly (Fig. 7). The comparative efficiency gain from pure CIS to graded Gallium composition of CIGS is shown in Fig. 8.

While using the same amount of Gallium, the graded shape profile gives a lot of efficiency gain than the box shape so for material cost this is a very important factor that introducing same amount of Gallium in graded shape gives a huge advantage over box shape. Both the efficiency gain curves (for box and graded shape) are given in Fig. 8.

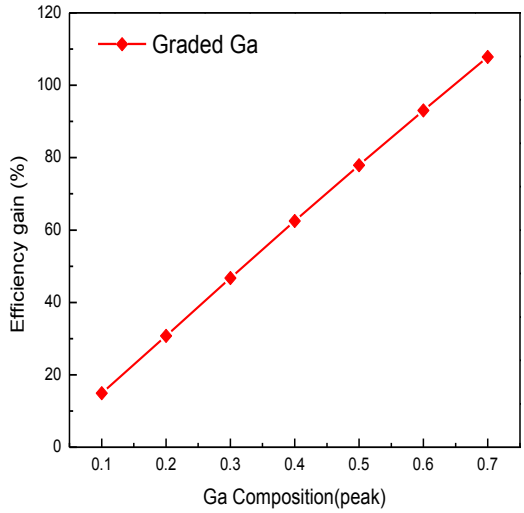

Figure 7:Efficiency gain for Gallium composition (Graded)

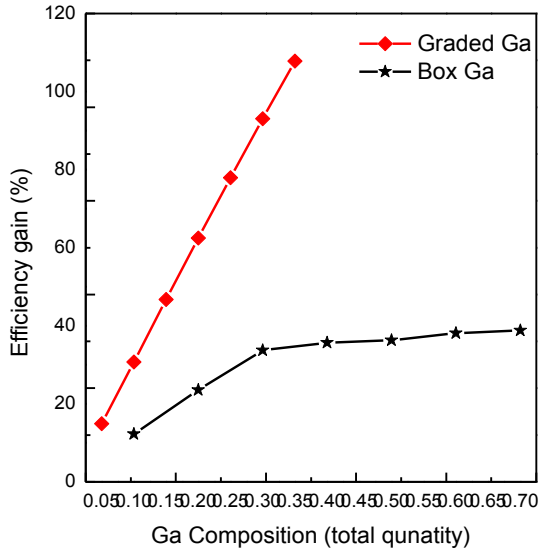

Figure8: Efficiency gain for both box and gradedGallium

4. CONCLUSION

In this paper, a unique technique has been taken into consideration which can improve the efficiency of heterojunction CIGS thin film solar cell. Here, we have demonstrated the effect of composition grading in heterojunction thin film CIGS solar cell by TCAD simulation. Grading in CIGS solar cells can be very effective for achieving high efficiency. With more composition of Gallium, open circuit voltage increases but it also decreases the short circuit current. But if grading is done in Gallium composition short circuit current doesn't reduce much as it does in box shape Gallium profile though open circuit voltage is little

lower in graded than in box shape. Fill factor doesn't gets benefited in box shape Gallium composition in case of high composition but in graded case, fill factor increases almost linearly with Gallium composition. With the same amount of Gallium in graded shape can give much higher efficiency than box shape. By introducing more Gallium in CIGS heterojunction thin film solar cell can give high efficiency but it will be costly too. So by grading the Gallium content can give high efficiency even at low composition of Gallium.

5. ACKNOWLEDGMENT

The authors of this article would like to thank the Department of EEE, BUET, Dhaka, Bangladesh, for its various supports especially for providing internet, online library and computing facilities.

REFERENCES

[1]. Joar Johansson, "Modelling and Optimization of CIGS Solar Cell Module," Master's Thesis, LundsUniversitet, December, 2007.

[2]. M.A. Contreras, B. Egaas, K. Ramanathan, J. Hiltner, A.Swartzlander, F. Hasoon, R. Noufi, "Towards 20% efficiency in Cu(In,Ga)Se_2polycrystalline solar cells",*Proc. Photovoltaic Res*. pp. 311–316, Appl. 7, 1999

[3]. J. L. Gray , Y. J. Lee, "Numerical modeling of graded band gap CIGS solar cells", *Proc. 1st World Conf. Photovoltaic Energy Conversion*, pp. 123-126,1994

[4]. M. Bodegard, O. Lundberg, J. Malmstrom, L. Stolt, "High voltage Cu(In,Ga)Se2 devices with Ga-profiling fabricated using co-evaporation", *Proc. 28thIEEE Photovoltaic Specialist Conf.*, pp. 450-453,2000.

Proceeding of the
International Conference on Electrical, Computer and Telecommunication Engineering
01- 02 December 2012 (ICECTE2012), RUET, Rajshahi-6204, Bangladesh

ICECTE2012: PI-0014

Cost Effective and Energy Efficient Modelling of Solar Wind Hybrid Power System

M. A. Motin[1], Md. Forhad Zaman[2], Niloy Biswas[3], M.R.I. Sheikh[4]*
[1,2,3,&4]*Department of Electrical and Electronic Engineering, Rajshahi University of Engineering & Technology*
[1]motin_eee_06@yahoo.com, [2]m.fzaman@yahoo.com, [4] ris_ruet@yahoo.com

ABSTRACT
Demand for energy is increasing day by day because of population increase and industrialization but we have very limited resources. In this critical stage of energy crisis, renewable energy is one of the most important alternative energy sources. Wind and solar power is the cheapest energy source at this stage. In this paper energy efficient renewable energy based Base System for an isolated location, such as Saint Martin's Island, has been proposed. Saint Martin's is one of the most beautiful tourist islands in Bangladesh where grid connected electric system for the residents and for the telecommunication system will not be possible to launch even in future. The residential consumers use diesel, kerosene and wood for fulfilling their energy demand. Solar and Wind resources are the hybrid options for the Island. HOMER, a software for optimization of renewable based hybrid systems, has been used to find out the finest technically, economically and environmentally viable renewable based energy efficient system.

KEY WORDS: Solar system, wind turbine, hybrid system, photo voltaic solar cell, converter.

1. INTRODUCTION

Bangladesh has a large unsatisfied demand for energy, which is growing by 10 percent annually [1]. Currently, it has the lowest per capita consumption of commercial energy in South Asia. Presently total generation capacity is 6727 MW. Of this capacity 3534 MW is from public sector and 3193 MW is from the private sector, which is 53% and 47% respectively of the total generation capacity [2]. To meet the cumulative demand of electricity coal, gas, diesels are being used to produce electricity. But it is also insufficient. In order to lessen the pressure of power demand on our conventional power plant, renewable energy like wind and solar power can be used. In Bangladesh, the country receives an average daily solar radiation of 4 – 6.5 kWh/m^2. So solar energy can be a potential source of power to produce electricity. Despite large potential, in most cases the utilization of solar energy has been limited to traditional uses such as crop and fish drying in the open sun. Solar photovoltaic (PV) are gaining acceptance for providing electricity to households and small businesses in rural areas. Moreover in Bangladesh, winds are available mainly during the Monsoons and around one to two months before and after the Monsoons. During the months starting from late October to the middle of February, winds either remain calm or are too low to be of any use by a traditional windmill. Except for the above mentioned period of four months, a windmill if properly designed and located, can supply enough energy to be marketable. So wind power can be used to produce electricity.

2. SOLAR DATA ANALYSIS

Bangladesh receives an average daily solar radiation of 4 – 6.5 kWh/m^2. Maximum amount of radiation is available on the month of March-April and minimum on December - January. Renewable Energy Research Centre (RERC), Dhaka University (DU) is the only source which has got long-term measured data of Dhaka city in Bangladesh [UNESCAP 2000]. The published data are average of results of hourly measurement of over three years global (G) and diffuse (D) radiation with Eppley Precision Pyrometer. Bangladesh Meteorological Department has 34 sunshine recording stations situated generally in towns and cities. Department of Mechanical Engineering, Bangladesh University of Engineering and Technology, (BUET) has also got time series data of Dhaka city.

TABLE I
ANNUAL AVERAGE GLOBAL HORIZONTAL IRRADIANCE(GHI) FOR COASTAL AREA OF BANGLADESH

Month	Saint Martin	Kuakata	Teknaf	Kutubdia	Mongla
January	4.84	4.67	4.59	4.62	4.66
February	5.54	5.01	5.02	5.01	4.99
March	6.41	5.65	5.58	5.52	5.59
April	6.48	6.03	6.57	6.2	5.78
May	5.96	5.47	4.91	5.13	5.29
June	3.6	3.72	3.37	3.65	3.40
July	3.62	3.94	3.32	3.38	3.87
August	3.69	4.00	3.84	3.82	3.97
September	4.34	4.27	3.92	3.91	3.58
October	4.72	4.35	4.15	4.33	4.06
November	4.42	4.54	4.54	4.59	4.49
December	4.54	4.19	4.11	4.14	4.22
Average	4.85	4.65	4.49	4.53	4.49

3. WIND DATA ANALYSIS

Bangladesh has a 724km long coastal line along the Bay of Bengal. There are also many islands in the Bay where wind speed is high enough to provide Electricity commercially. The strong south/south-western monsoon wind come from the Indian Ocean travelling a long distance over the Bay of Bengal, through the coastal area of Bangladesh. This wind blows over Bangladesh from March to September with a monthly average speed of 3m/s to 9m/s at different height [4]. According to studies of Meteorological Department, BACS, LGED, BUET winds are available in Bangladesh mainly during the monsoon. (7 months March to September).

TABLE II
MONTHLY AVERAGE WIND SPEED IN THE SAINT MARTIN AT 25M HEIGHT

Month	V_{av}(m/s)	V_{max}(m/s)
January	5.08	23.32
February	4.71	19.78
March	4.29	18.94
April	3.58	20.03
May	5.75	26.30
June	5.96	29.80
July	5.33	24.20
August	5.96	20.40
September	**4.79**	**17.70**
October	4.17	15.90
November	3.79	14.50
December	4.08	15.20

TABLE III
WIND SPEED Vs AVAILABLE POWER

Rest of months (October to February) wind speed remains either calm or too low. The peak wind speed occurs during the month of June and July. Wind velocity at the coastal area and isolated island is quite higher than rest of the locations [5].

Wind power classes	10m		50m	
	Wind power density (w/m^2)	Average wind speed m/s(mph)	Wind power density (w/m^2)	Average wind speed m/s(mph)
1	0-100	0-4.4 (0-9.8)	0-200	0-5.6 (0-12.5)
2	100-150	4.4-5.1 (9.8-11.5)	200-300	5.6-6.4 (12.5-14.3)
3	150-200	5.1-5.6 (11.512.5)	300-400	6.4-7.0 (14.3-15.7)
4	200-250	5.6-6.0 (12.5-3.4)	400-500	7.0-7.5 (15.7-16.8)
5	250-300	6.0-6.4 (13.414.3)	500-600	7.5-8.0 (6.8-17.9)
6	300-400	6.4-7.0 (14.315.7)	600-700	8.0-8.8 (17.9-19.7)
7	400-1000	7.0-9.4 (15.721.1)	700-800	8.8-11.9 (19.7-26.6)

4. DESIGN OF HYBRID SYSTEM

The total energy production in case of stand-alone system using only PV modules or wind turbine is an expensive technical solution [6]. This requires a large surface, and in winter period when the solar potential is low the consumers can be supplied with energy through a large storage capacity. The above disadvantages suggest that the design procedure of the stand-alone system is necessary to analyse the possibility to use other green energy production equipments. In effective operation, mixing the produced energy by this green source the designed stand-alone system can operate economically. I n the case of hybrid energy system several types of generators are used, shows the switching mod of this green energy sources type. As shown along a PV generator into this stand-alone system a wind turbine is incorporated into this energy production unit. In practice, in case of standalone hybrid systems it is important to use that kind wind turbine, which cut in wind speed is low. The produced energy is stored in batteries and the consumer is supplying with good quality energy (constant voltage and frequency) through an inverter. In our thesis work we considered St Martin's island where we want to apply this hybrid power system. We are interested about St Martin's because it is one of the most beautiful Tourist Islands in Bangladesh where grid connected electric system for the inhabitants will not be possible to establish even in future. Diesel, Kerosene and wood are the main fuels for fulfilling the energy demand. Solar and Wind resources are the hybrid options for the Island [7].

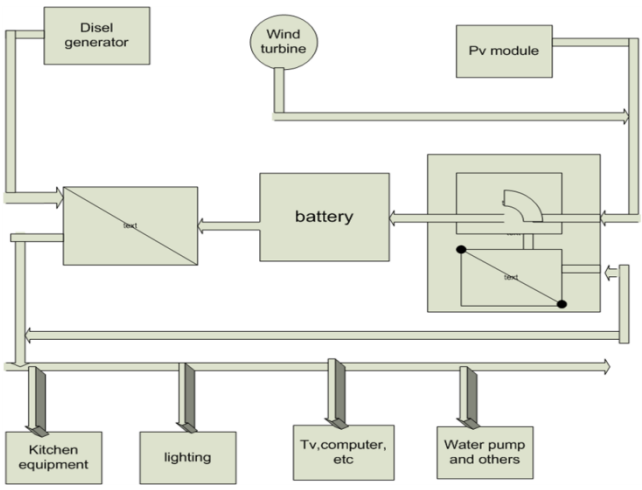

Fig. 1 Block diagram of solar-wind hybrid system

In this Solar-Wind Hybrid System, as proven technology, using inverters is proposed to supply 220 V. A.C. (grid-quality) electricity, which can be combined with the wind turbine generated electricity, the wind turbines being designed to directly produce 220 Volt alternating current electricity.

4.1 Photovoltaic Module

The cost of PV module including installation has been considered as 300 BDT / W for Bangladesh. Life time of the modules has been taken as 25 years and these are tilted at 21 degree with no tracking mode. Fig shows the scatter plot of

PV power and incident solar radiation for the selected solar panel.

4.2 Wind Generator

The load demand is very low for a single home system and the price per KW turbine cost is very high for low capacity wind turbine compare to that of high capacity ones. Also low capacity wind turbine is not much available. Now a day, research and development are going on to improve the technology and designing low capacity turbine with low cut-in speed at around 2.5 m/s. For this analysis, a ENERCON E33 has been considered. It's rated power is 330 KW AC. The cost of the turbine with tower and installation has been considered as 500000 $ / turbine. Figure shows the power curve of the selected turbine.
Wind turbine : Enercon E33
Rated Power: 330 KW AC
Diameter: 33.4m

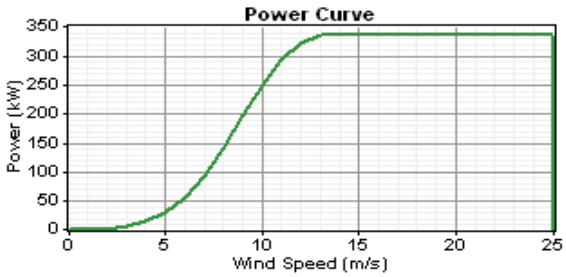

Fig. 2 Wind Speed V_s Output Power

4.3 Converter

Converter is used to store ac current to the battery bank and supply the power back to the system when it is needed. It converts ac current into dc and dc current into ac. We assumed, inverter has 92% efficiency and rectifier has 94% efficiency. The converter has life time of 20 years. We consider the converter price 100 USD per 1KW.

5. ELECTRICAL LOAD DEMAND

A typical electrical load system for a single home in St Martin's has been considered for load analysis. For a particular house we consider a light, fan, TV and other small loads. In HOMER we made a 24 hours load profile for a single home. There are 778 families in the island. If we consider an average load demand of all the houses is same then we can find the total electrical load demand for the island is 3.1MW/d [8].

TABLE IV
APPLIANCES FOR SINGLE HOME USER

Appliances	Number	Capacity(w)
Florescence light	2	20
Fan	1	80
TV(color)	1	100
Others	2	50
Total capacity		250

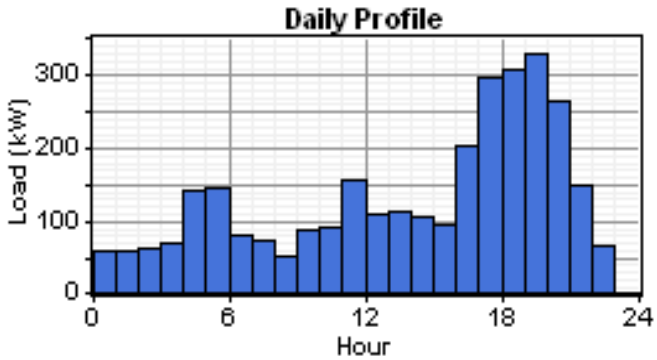

Fig. 3 Average load for total houses of St Martin's(monthly)

6. RESOURCES

We used solar and PV to generate power. They are shown as graphically.

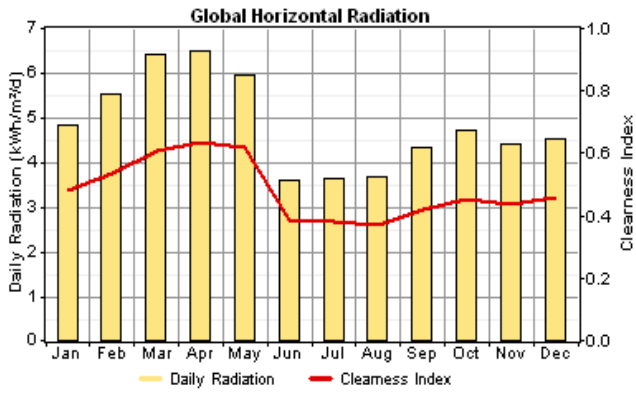

Fig. 4 Monthly Solar Radiation in Saint Martin Island KWh/m^2

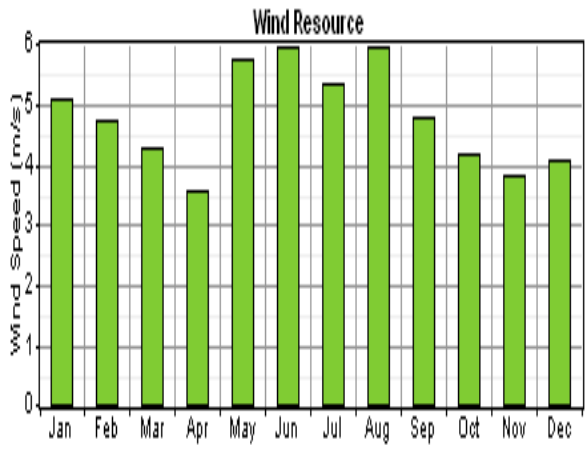

Fig. 5 Monthly Average Wind Velocity (ms^{-1}) Variation in Saint Martin Island

7. RESULT AND ANALYSIS

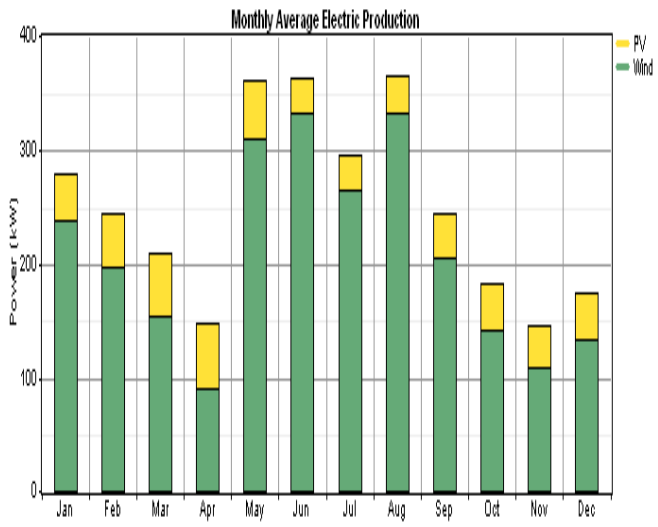

Fig. 6 Monthly Average Electric Production from Solar Module and Wind Turbine

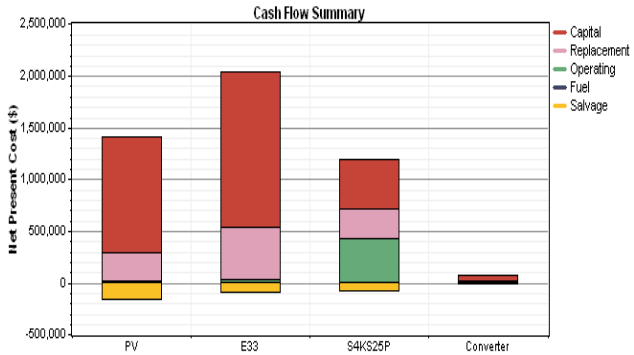

Fig.7 Cash Flow Summary (Capital, Replacement, Operating, Fuel, Salvage)

TABLE V
COMPARISON OF PER UNIT COST WITH OTHER POWER SYSTEM

Energy Technology	Fuel Cost KWh(TK)	Initial Investment KWh(TK)	Transmission and Distribution Cost KWh(TK)	Total Cost Per KWh(TK)
Coal	7	1.25	1.25	8.5
Oil	21.85	1.5	1.25	24.6
Gas	1.11	1.10	0.85	3.06
PV + Wind	0.00	20.78	0.5	21.28

8. CONCLUSION

By comparing with other power system we have seen that, the per unit cost is lower than oil base power station. It has no maintenance cost and no running cost. So it's per unit cost is decreasing day by day. As we standing in the 21st century, our life is directly depending on Electricity. But the energy crisis is becoming a huge threat for economical development of our country. In the coastal area and the isolated islands where grid connections is not feasible ,alternative electric sources like solar-wind system can be very cost effective. So hybrid system like solar-wind system is more appropriate for this kind of situation.

REFERENCES

[1] http://en.wikipedia.org/wiki/Bangladesh

[2] http://www.powerdivision.gov.bd/index.php?page_id=26

[3] http://www.energymatters.com.au/renewable-energy/solar-power/solar- panels.php

[4] http://en.wikipedia.org/wiki/Wind_power

[5] A.N.M. Mominul Islam Mukut, M.Sc., Md. Quamrul Islam, Ph.D., and Muhammad Mahbubul Alam, Ph.D., ''Prospect of Wind Energy in the Coastal Belt of Bangladesh'', Msc thesis, Department of Mechanical Engineering, Dhaka University of Engineering and Technology.

[6] Mohammad Golam Kibria Khan, Talha Rahman and M.M. Alam, ''Wind energy in bangladesh: prospects and utilization initiatives'', Msc thesis, Department of Mechanical Engineering, BUET.

[7] M. Shamim Kaiser, S K Khadem, H R Ghosh, S Kaiser, S K Aditya, ''Energy efficient system for st martin's island of bangladesh'', Bsc thesis, Department of Electronics and Telecommunication Engineering, Daffodil International University.

[8] A Pre-Feasibility Study Report, ''Solar-Wind-Diesel Hybrid For Power Generation in Small Towns and Villages'' Prepared by the PREGA National Technical Experts from Bangladesh Centre for Advanced studies, Tech Rep. 2010

Proceeding of the
International Conference on Electrical, Computer and Telecommunication Engineering
01- 02 December 2012 (ICECTE2012), RUET, Rajshahi-6204, Bangladesh
ICECTE2012: PI-0015

Future of Electricity and Smart power generation

Mst. Tajmera Sultana[1], Nilroton Sarkar[2], Liton chandra paul[3]
[1,2]Department of Electrical & Electronic Engineering
[1,2]University of Information Technology & Sciences
[3]Department of Electronics & Telecommunication Engineering
[3]Rajshahi University of Engineering & Technology
E-mail: tajmera_13@ymail.com, niilroton75@gmail.com, litonpaulete@gmail.com

ABSTRACT
The electric energy has become part and parcel of the modern society and the demand of it is increasing day by day. Most of the electric energy is generated from fossil fuel. Our current rate of fossil fuel usage will lead to an energy crisis this century. In order to tackle these issues, there is a growing concern over our reliance on conventional electricity sources and their long-term environmental , climate change , and security of supply implications and much hope is vested in the ability of future technological progress. In this paper, we present future condition of electricity and new way of reaching the goal of smart power generation.

KEY WORDS: Electricity generation, Challenges of the future, Renewable power, Smart power, Availability and Reliability of smart power generation.

1. INTRODUCTION

The greatest scientific achievement of the nineteenth century is the discovery of electricity. The twentieth century is making use of electricity so extensively that it has almost changed the face of the earth. It does everything for our comfort and convenience with the utmost efficiency at all hours. Today it would be difficult, if not impossible, to imagine a world without electricity. The Electricity can be generated in many ways. Electricity generation is the process of generating electric energy from other forms of energy. The fundamental principles of electricity generation were discovered during the 1820s and early 1830s by the British scientist Michael Faraday. His basic method is still used today: electricity is generated by the movement of a loop of wire, or disc of copper between the poles of a magnet [1].

The electrical energy can be generated in different methods including: Static electricity (from the physical separation and transport of charge, examples: lightning), Electromagnetic induction (where an electrical generator, dynamo or alternator, examples: copper wire), Electrochemistry (the direct transformation of chemical energy into electricity, examples: fuel cell), Photoelectric effect (the transformation of light into electrical energy, Examples: solar cells), Thermoelectric effect (the direct conversion of temperature differences to electricity, examples: thermocouples), Piezoelectric effect (from the mechanical strain of electrically anisotropic molecules or crystals, examples: Liquid Crystal Display), Nuclear transformation (the creation and acceleration of charged particles, examples: alpha particle emission).

Electrochemical electricity generation is also important in portable and mobile applications. Currently, most electrochemical power comes from closed electrochemical cells ("batteries") [2], which are arguably utilized more as storage systems than generation systems; but open electrochemical systems, known as fuel cell. Fuel cells can be used to extract power either from natural fuels or from synthesized fuels (mainly electrolytic hydrogen) and so can be viewed as either generation systems or storage systems depending on their use.

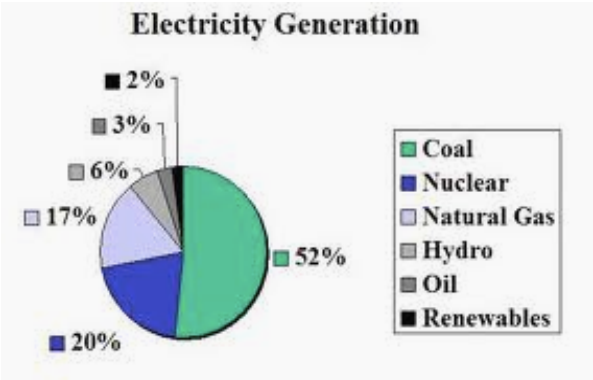

Figure:-1 Electricity generation by fuel sources.

From this fig:-1, it is seen that coal is mainly used to generate the electricity. Renewable are also used, but it is very rare. That is, generation of electricity is mainly depends on the fossil fuel.

2. METHODOLOGY

2.1 Introduction to fossil fuel

Fossil fuels are fuels formed by natural processes such as anaerobic decomposition of buried dead organisms. The age of the organisms and their

resulting fossil fuels is typically millions of years, and sometimes exceeds 650 million years [3]. Fossil fuels contain high percentages of carbon and include coal, petroleum, and natural gas [4].
It was estimated by the Energy Information Administration that in 2007 primary sources of energy consisted of petroleum 36.0%, coal 27.4%, and natural gas 23.0%, amounting to an 86.4% share for fossil fuels in primary energy consumption in the world [5].

Years of production left in the ground with the current proved reserves and flows above

- Coal: 148 years
- Oil: 43 years
- Natural gas: 61 years

Years of production left in the ground with the most optimistic proved reserve estimates (Oil & Gas Journal, World Oil)

- Coal: 417 years
- Oil: 43 years
- Natural gas: 167 years

World energy consumption was growing about 2.3% per year. Nowadays, discussion emphasizes worldwide energy balance. It is also valuable to understand the ratio of reserves to annual consumption (R/C) by region or country. Alternatives to fossil fuels are a subject of intense debate worldwide.

2.2 The present condition of electricity generation

At a present, most of the electricity is generated by using the fossil fuels like natural gas, coal, oil etc.

Natural gas is a naturally occurring hydrocarbon gas mixture consisting primarily of methane, with other hydrocarbons, carbon dioxide, nitrogen and hydrogen sulfide [6].
This natural gas is used to generate the electricity. Natural gas combustion plant results in CO_2 emissions.

Coal plays a vital role in electricity generation worldwide. Coal-fired power plants currently fuel 41% of global electricity. In some countries, coal fuels a higher percentage of electricity [7]. Efficiency gains in electricity generation from coal-fired power stations will play a crucial part in reducing CO_2 emissions at a global level [7].

Oil is still used as fuel for electricity generating plants. Like other fossil fuels, this liquid is the end-product of millions of years of decomposition of organic materials.
Three technologies are used to convert oil into electricity:

- *Conventional steam* - Oil is burned to heat water to create steam to generate electricity.
- *Combustion turbine* - Oil is burned under pressure to produce hot exhaust gases which spin a turbine to generate electricity.
- *Combined-cycle technology* - Oil is first combusted in a combustion turbine, using the heated exhaust gases to generate electricity. After these exhaust gases are recovered, they heat water in a boiler, creating steam to drive a second turbine.

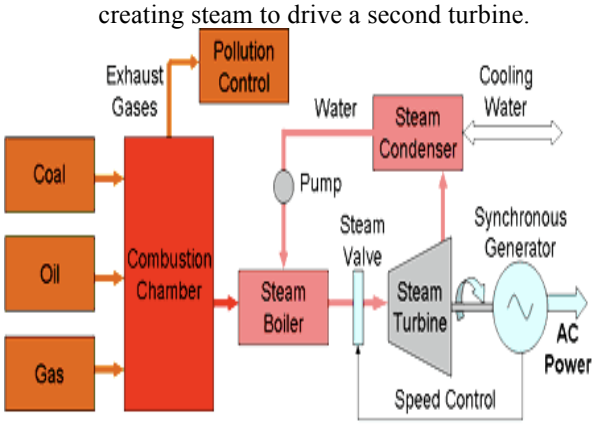

Fossil Fuel Powered Steam Turbine Electricity Generation

Figure:-2 Electricity generation from the fossil fuels.

Fossil fuelled plants use coal (60%), oil (10%) or gas (30%) in purpose designed combustion chambers to raise steam. The steam is used as a prime over of generator and the generator produces the electricity.

2.3 Challenges of the future

The future has always had a strong appeal to the human mind, both individually and collectively. Electricity is the very basis of our civilization. After the first fumbling experiments it began to permeate society. Currently we are facing a future of ever-increasing demand for electricity. One side the amount of the fossil fuel is limited, other hand, the combustion process is notorious for its potential to release unpleasant gases and solids into the atmosphere. Naturally occurring fuels are not pure by any standards and contain uncontrolled amounts of other elements and compounds which may be left as residues when the fuel is burned. The combustion process itself can create noxious gases from the fuel or from impurities in the fuel if not properly controlled [8]. Another unavoidable consequence of burning any fossil fuel is that the process generates

greenhouse gases, mostly Carbon dioxide (CO_2) but also Sulphur dioxide (SO_2) and Methane (CH_4), all of which contribute to global warming [8]. On the other hand, Carbon dioxide (CO_2) is also responsible to damage the ozone level, which level protects us from the dangerous rays.

There is no Philosopher's Stone to solve the problems we are facing in the future. And there is no single, simple solution. Despite all the globalization the conditions in different societies, countries, and Continents are very different from each other. This has to be taken into account in trying to find the best solution for each case. We have to figure out What kind of a future we are aiming at, and then make the right choices.

3: Increasing demand of Electricity

Electric energy is a crucial ingredient for creating wealth and comfort with the increasing the standard of living. Demand for electric power will therefore drastically increase in the world during the next decades. To fulfill this demand, we can use renewable sources to generate electrical energy and we also can use the smart power generation process to make comfortable and healthy world.

3.1 Renewable Power

Renewable energy is energy which comes from natural resources such as sunlight, wind, rain, tides, waves and geothermal heat, which are renewable (naturally replenished). About 16% of global final energy consumption comes from renewable, with 10% coming from traditional biomass, which is mainly used for heating, and 3.4% from hydroelectricity. New renewable (small hydro, modern biomass, wind, solar, geothermal, and befouls) accounted for another 3% and are growing very rapidly [9]. The share of renewable in electricity generation is around 19%, with 16% of global electricity coming from hydroelectricity and 3% from new renewable [9].

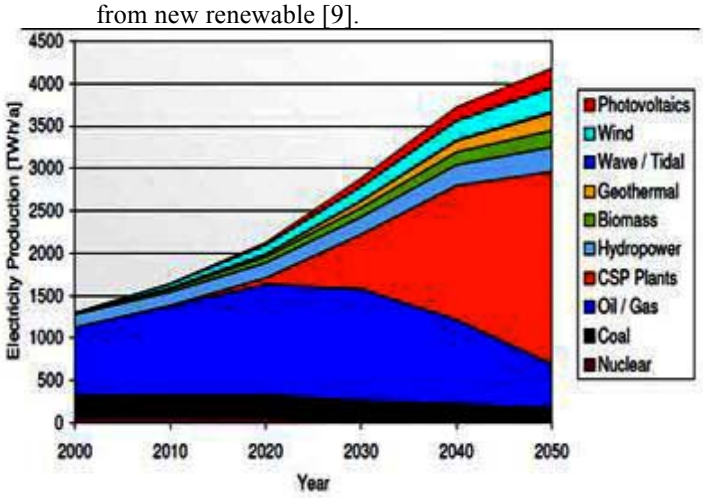

Figure:-3 Relative shares of energy sources of for power generation.

In this figure, it is seen that the generation of electricity from the fossil fuels will be decreased day by day and it will be increased from the renewable sources.

Renewable electricity production, from sources such as wind power and solar power, is sometimes criticized for being variable or intermittent. However, the International Energy Agency has stated that deployment of renewable technologies usually increases the diversity of electricity sources and, through local generation, contributes to the flexibility of the system and its resistance to central shocks [10].

3.2 Smart power generation

Smart power generation is a concept of matching electricity production with demand using multiple identical generators which can start, stop and operate efficiently at chosen load, independently of the others, making them suitable for base load and peaking power generation [11].

Renewable sources of electricity substantially Complicate the task of transmission system operators. This is because of the large variations in their power output over time. Further challenges arise from a possible large-scale introduction of electric vehicles. Although such vehicles might help by filling up valleys in electricity demand during the night, the big question is if such an idealistic scheme fits with real-life needs. Therefore, most of the challenges have to be solved by a kind of smart

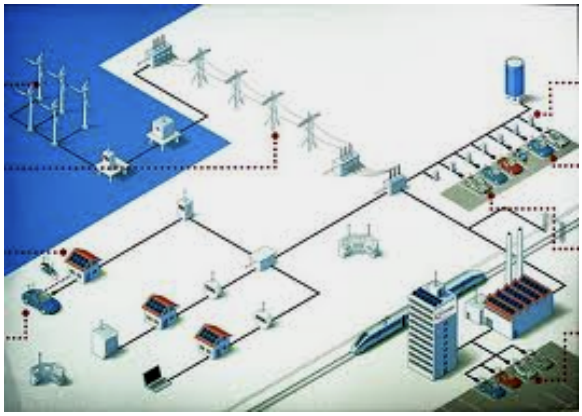

power generation.

Figure:-4 the outlines of the smart power supply from power generation to the consumers.

Properties of smart power generation:

- Fast starting
- Fast ramping up and down of load.
- Fuel flexibility.
- Minimum maintenance outage time.
- Remote control of output.

- Short building time.
- Easy adaptable capacity.
- Low capital expenditure.

The smart grid represents the full suite of current and proposed responses to the challenges of electricity supply. A smart grid precisely limits electrical power down to the residential level, network small-scale distributed energy generation and storage devices, communicate information on operating status and needs, collect information on prices and grid conditions, and move the grid beyond central control to a collaborative network [12].

3.3 Availability and Reliability of smart power generation

The smart power generation goals can best be met with a number of high-performance generating units in parallel. Each individual generating unit must be able to run independently, so that e.g. failure of a

Single unit will not hamper the other units in carrying out their task. The generating units in parallel should preferably be of an identical design. So, Power plants in a competitive environment should preferably be able to run whenever required. The reliability of individual electricity generating units, whatever the size or the type, can never reach a figure as high as 99.9%. The reason is that such machines consist of many interacting components, each with a finite life and with sensitivities to breaking down. Costs and technology prohibit the production of components of an infinitely high quality. Clearly, smart power generation provides maximum reliability and flexibility.

4. Result

The demand of electricity is increasing day by day and also many problems are increasing. Renewable energy also is not proper to give the required output without any new technology. In this situation, Smart power generation with fast reacting cascading generating units in parallel lowers fuel consumption, increases reliability and reduce the maintenance costs and also help to face these problems. Smart electric appliances can help balance electricity production and demand only on a short time basis. Smart power generation as one of the enablers of renewable energy sources is an interesting result of that creativity and skill.

5. Future work

In future, we can use the smart power generation system with the renewable sources. This system can be improved by using the digital equipments, wireless system and other improved technologies and the more electricity can be generated with low cost and easily. As a result we can be able create a developed, comfortable, healthy and digital world.

6. Conclusion

In this paper, we have tried to show that we are facing what types of problem to generate the electricity and how we are facing the different problems like climate changes. We have also tried to show that we can use the renewable sources to generate the electricity in stead of fossil fuel. But there is also another problem to generate energy from renewable sources. That is, the electricity generated from the renewable sources can be used only the local used, it can not be transmitted over long distances. Renewable fuels such as liquid bio fuels and gas from biomass and waste will add to the benefits of back-up power plants. To provide the broad range of electricity from the renewable sources we can use the smart technology. The ideal power plant of the future is therefore a smart generator with inherently high fuel efficiency over a wide load range. So, we can say that if we use the smart power generation method, we will be able to tackle these issues and also will be able to provide the demandable electricity to the world.

REFERENCES

[1] 'The Institution of Engineering & Technology: Michael Faraday'

[2] World's Largest Utility Battery System Installed in Alaska (press release, 2003-09-24), U.S. Department of Energy.

"13,670 nickel-cadmium battery cells to generate up to 40 megawatts of power for about 7 minutes, or 27 megawatts of power for 15 minutes."

[3] Paul Mann, Lisa Gahagan, and Mark B. Gordon, "Tectonic setting of the world's giant oil and gas fields," in Michel T. Halbouty (ed.) *Giant Oil and Gas Fields of the Decade, 1990–1999*, Tulsa, Okla.: American Association of Petroleum Geologists, p.50, accessed 22 June 2009

[4] "Fossil fuel", www.sciencedaily.com

[5] "U.S. EIA International Energy Statistics". Retrieved 2010-01-12

[6] "Composition of natural gas". Naturalgas.org. Retrieved 2012-07-14

[7] www.worldcoal.org

[8] www.mpoweruk.com

[9] World Energy Assessment (2001). Renewable energy technologies, p. 221

[10] International Energy Agency (2007). Contribution of Renewables to Energy Security IEA Information Paper, p. 5

[11] Klimstra, Jakob; Hotakainen, Markus (2011). *Smart Power Generation*. Helsinki: Avain Publishers. ISBN [[Special: BookSources/789516928466|789516928466

[12] Patrick Mazza (2005-04-27) (doc). *Powering Up the Smart Grid: A Northwest Initiative for Job Creation, Energy Security, and Clean, Affordable Electricity.* Climate Solutions. p. 7. Retrieved 2008-12-01.

Proceeding of the
International Conference on Electrical, Computer and Telecommunication Engineering
01- 02 December 2012 (ICECTE2012), RUET, Rajshahi-6204, Bangladesh

ICECTE2012: PI-0016

Economic Evaluation of the PV Micro Utilities Installed by Grameen Shakti for Rural Electrification in Bangladesh

S.M. Najmul Hoque [1,], Barun Kumar Das[1], S. Kumar [2], and M Mahmud Roni[1]*
[1] Department of Mechanical Engineering, Rajshahi University of Engineering & Technology, Bangladesh
[2] Energy Field of Study, Asian Institute of technology, Thailand
shumon99234@gmail.com, barun_ruet@yahoo.com, kumar@ait.ac.th and roni_93_me@yahoo.com

ABSTRACT
Sharing expensive technology can serve many users, even poor users. Grameen Shakti has developed a special program named PV micro utility (PV MU)to make it easier for those who cannot afford SHSs individually. Under this program, Grameen Shakti allows people to share the cost and the subsequent benefit of using a SHS. In this study, operation and financial mechanism, analysis of cost of systems, tariff system, simple payback period, NPV and IRR of the micro utility systems have been analyzed to show the financial viability of PV Micro utilities from the PV MU owner's perspective. Results suggest that these systems have simple payback period of around 4-6 years. The NPV of systems varied from 27,000 BDT to 144,000 BDT. The levelized electricity cost of PV MU systems is 70 BDT (~0.86 $)/kWh in Bangladesh. The owner has to spend only 7.50 BDT/day but can earn at least 30-40 BDT per day, and up to 130-200 BDT/day.

KEY WORDS: Rural Electrification, Solar PV, Grameen Shakti, Bangladesh, Economic Evaluation

1. INTRODUCTION

There cannot be any economical development without electricity. Only 47% of Bangladeshi people have access to grid electricity [1] and only 8% are connected with the governmental natural gas supply system and, most of them live in cities [2]. As a result, rural communities suffer from an under-utilized economy and depressed business activities. This lack of energy and power reduces business hours and does not enable people to access modern technology and equipment which are required for development. Mobility of the people is also hampered after dusk due to security problems. Grameen Shakti solar program has addressed many of these issues by extending business hours and increasing business turnover. However, many people cannot afford Solar Home Systems individually. This is one of the barriers to the scaling up of the Grameen Shakti Solar Program and the revitalization of the rural economy, through the use of Solar PV technology. This paper presents the economic analysis of solar PV micro utility installed by Grameen Shakti in Bangladesh.

2. METHODOLOGY

Information about 150 PV micro utility systems at 11 different locations in Bangladesh was collected. The places of data collections are shown in figure 1. Dinajpur, Mymensingh, Gazipur, Manikgong, Dhaka, Khulna, Barishal, Bhola, Chandpur and Rangamati were the districts from where the data were collected. Thirty five systems from nine places among those 150 systems were selected to monitor by field visit. Survey was done during October, 2011 to January, 2012 to study the technical feasibility, financial and social impact of PV MU system.

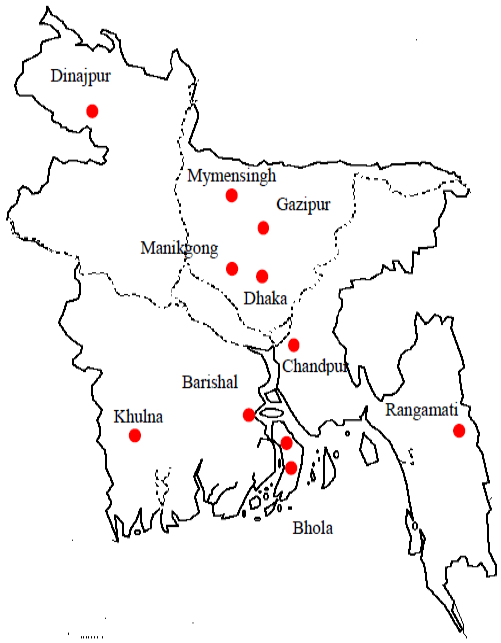

Figure 1: Data collection at different places in Bangladesh

Operational and financial mechanism, analysis of cost of systems, tariff system, simple payback period, NPV and IRR of the micro utility systems have been analyzed to show the financial viability of PV MU from the PV MU owner's perspective under financial analysis. All the cost and benefit are converted in to monetary values and project life is considered as 20 years. However, the benefits like environmental impacts, long term benefits of children education due

to having good quality of light at home, social benefits of having trained technicians in rural areas or creation of new business opportunities due to SHS is excluded. To calculate the financial analysis following equations are used [3]:

Payback period= I/(R-E)

NPV= CO+ PV

Present value= Σ Cn/$(1+r)^n$

IRR= i1-NPV1 * ((i 2 - i 1) / (NPV2-NPV1))

Where I: Investment, R:Return, E: Expenses, CO: Initial Investment at period 0 which is a negative figure, Cn: total cash flow, r: discounting rate, NPV1and NPV2 for two different interest rates and NPV1 is positive and NPV2 is negative.

3. FINANCIAL ANALYSIS

The viability of any project or business can be determined from financial analysis. In this study, operation and financial mechanism, analysis of cost of systems, tariff system, simple payback period, NPV and IRR of the micro utility systems have been analyzed to show the financial viability of PV MU from the PV MU owner's perspective.

3.1 Financial Scheme of PV MU in Bangladesh

The operational and financial mechanism of PV micro utility program in Bangladesh is shown in Figure 2. It is somewhat similar to the SHS program. The main difference is that this is designed for rural market places and under this program the owner has to rent electricity to his neighbor (shop). The PV micro utility concept was started to provide electricity to the extremely poor people of the country. The owner pays only 10% down payment, and the rest (90%) is payable in 42 monthly installments with no service charge [4]. For other packages of individual SHS, installment period is 36 months; down payment was not less than 15% and the service charge per year is 5% to 8%. GS is responsible for providing (free) maintenance during the installment period. GS also replaces the parts if needed in this period. After the installment period, the owner of the system can agree with GS for one year free maintenance by paying 300 BDT.

There is no meter for electricity bill measurement for this system. The users of this kind of system pay on a daily or monthly basis. GS normally does not fix the amount charged by the owner to the user. The payment varied from 5-10 BDT/day/CFL for daily system. For monthly system, payment for electricity was found to vary between 200-300 BDT/ month/CFL.

In most of the cases, owners have a main switch and turn it on just after sunset. Duration of service varied according to the contract between owner and user but it was found that this duration was about 3 to 5 hours/day. According to the contract, owner will have no responsibility for CFL used by the user. The users have to maintain and replace their CFL as per their needs and use.

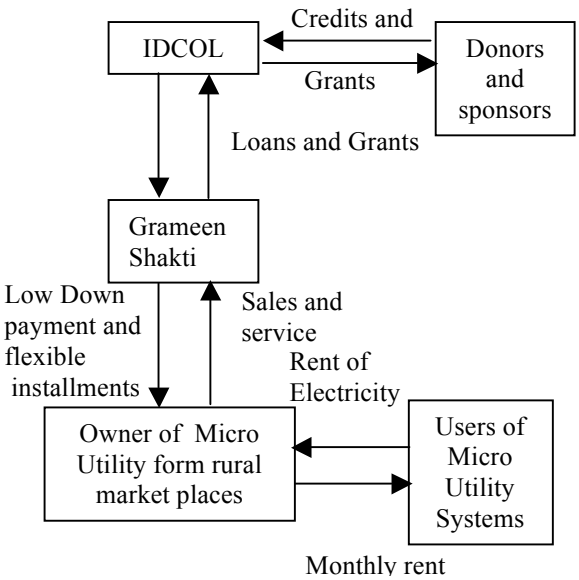

Figure 2: Operational and financial procedure

3.2 Cost of PV micro utility system

Under the Grameen Shakti micro utility program, 40 to 85 W_p systems are used as micro utility in the rural market places in Bangladesh. The cost of a 40 W_p system was 23,600 BDT, whereas for a 85 W_p system, the cost was 44,800 BDT.

Battery, PV panel and charge controller are the three main components of the PV system. GS also provides structure for panel and battery, lamps and ballast, switch, switch board and necessary wires during the installation period. But, the owner or user had to buy other equipments if they need, such as, adapter, DC-DC converter for radio, cassette and mobile charger, etc.

The breakdown of total cost of a 50 W_p system is shown in table 1. Battery and solar panel were the main two reasons of the high cost of the PV system. Solar panel contributed to 28%, whereas battery cost was around 30% of the total cost though most of the batteries were produced in Bangladesh. The cost of charge controller was only 3% of total cost as GS was producing charge controller locally within the country. Three years after sale service and installation cost 13.50%, overhead cost 10%, cable, switches and others 7.50% and lamp shade 5% were the significant others costs.

Except these, tube lights and steel structure for panel contributed 2% and 1% of total cost respectively. This break down of cost was also similar for 40 and 60 W_p system as price variation was not much. On the other hand, percentage of battery and panel cost was little bit higher for 80 and 85 W_p system. It was found that for 80 and 85 W_p battery and panel cost were 33% and 30% of the total cost respectively.

Table 1: Break down of cost of PV MU in rural Bangladesh

Components	Price (%)
Battery	30%
Solar panel	28%
3 Years after sales service and installment collection	13.50%
Overhead cost	10%
Others (cable, switch etc)	7.50%
4 Lampshades	5%
Charge controller	3%
4 tube lights	2%
Structure	1%
Total	100%

3.3 Levilised cost of PV MU electricity

The total expense of a PV MU system in its entire life is calculated in terms of the levilised cost of PV MU electricity. The calculation was done for a 50 W_p system as most of the owners used 50 W_p system. During field visit, it was found that many 07 years aged batteries were still operating. So, 02 batteries were assumed to be replaced during the entire 20 years project life. Salvage value of battery was considered (subtracted) from the new battery cost as it was around 23% of initial cost of the battery, and was given to the owner if the owner sells his old battery to GS.The panel life is assumed to be 20 years [3,5,6]. Minimum life and average cost of CFL was assumed to be 02 years and 120 BDT (Source: Field visit, 2011). By considering no price escalation and zero salvage value of panel after 20 years, it is found that cost of PV MU electricity is around 70 BDT (~0.86 $)/kWh. Price escalation is assumed to be zero because increasing trend of battery cost can be levilised by decreasing trend of panel and charge controller. Costs are assumed at present market price. This calculation was done for worst case scenario. At, worst case, if 03 batteries are needed are replaced then the electricity cost of PV MU is 80 BDT (~.96$) /kWh. Chaurey and Kandpa calculated the cost of PV electricity for SHS and micro grid in India was 38.80 and 38.76 Rs/kWh respectively [6]. In China, it was 0.67-0.73 USD/kWh [7].

It is also seen that the owner of the system has to expend only 7.47 BDT/day according to the actual scenario and even in worst case this cost is 8.58 BDT/day.

A PV MU owner can earn at least 30-40 BDT/day by renting three lights and saving from kerosene. The earning can be 130 BDT-200 BDT/ day or more if owner start any new business activity. Increase of equipment cost is not considered for this calculation because increasing trend of kerosene and diesel cost can also increase the saving of owner.

The cost of PV MU in Bangladesh can be reduced by producing all the equipments within the country. During field visit, it was found that there was lack of quality PV accessories in the market. Bangladesh government should help to produce Si and solar panels within the country. Though the panel cost is reducing in the international market, the panel price depends on dollar exchange rate- it is increased to 80 BDT from 70 BDT within the last two years (2009-2011). The government also should think about policy and direct subsidy for solar PV electricity production to popularize the PV MU.

3.4 Payback period, NPV and IRR

Payback period, NPV and IRR of the monitored PV MU systems were calculated and presented in table 2. Payback of PV MU varied mainly because of income from renting electricity, saving from kerosene, extra business activity by the owner after installing the PV system and amount of profit increase after installing the PV systems. For this analysis, extra business activity and amount of profit increase after installing the PV MU system are not considered as these variables were very much unstable, difficult to estimate and depend on many factors. Environmental benefit also not considered for this analysis as the owner of the system cannot claim environmental benefit according to the contract. Simple payback is an indicator that shows the time frame of the return of an investment. On the other hand, NPV is calculated by bringing all the cost and revenue to the year zero with the average deposit and lending interest (8.6% and 14.9%) of last five years [8]. Sample calculation for simple payback, NPV and IRR are shown as appendix-A. IRR is the discount rate that makes present value zero. For a project, shorter payback period and higher NPV and IRR are desirable to risk free investment.

Table 2: Simple Payback, NPV and IRR of PV MU systems

Parameter	Systems W_p			
	40	50	60-65	80-85
Simple Payback period (year)	6.28	5.70	5.30	4.20
NPV (8.6%)	40919	58358	77412	136302
NPV (14.9%)	24528	35145	47020	84943
IRR (%)	95	107	127	213

Results show that PV MU systems operating at rural market places of Bangladesh provide reasonable payback, higher positive NPV and good IRR. Higher W_p system shows lower payback period and more positive NPV and IRR. Because, most of the 80-85 W_p system owner had multiple business in the market and so they used mantle lamp hazzak before installing PV MU that consumes at least half a liter kerosene per day for 04 hours. Income from rent was also higher for higher W_p systems. The projects will be much more attractive if owners do some extra business activity. During field visit, very few owners were found to do extra business like mobile charging business or mobile phone booth. Both government and PV installer should train users about the new business opportunity as well as maintenance training.

Financial evaluation of SHS in Bangladesh was done by Mondal 2010. According to his study, payback period varied 2 to 6.34 years and NPV varied -8422 BDT to 162,181 BDT with a discount rate of 12% [3]. Higher (positive) value of NPV and IRR are found in this study because of the increase of kerosene price as compared to Mondal's 2010 study.

4. CONCLUSION

The following conclusions can be made based on financial analysis:

i) Cost of PV MU systems varied from 23,600 BDT to 44,800 for a capacity from 40 to 80 W_p systems. Solar panel and battery were the two main components for the high cost. Battery comprises 30% of total cost whereas panel cost was 28% of total cost.

ii) Cost of electricity of PV MU systems were around 70.50 BDT (~0.86 USD)/kWh. Owner of the PV MU system has to expend only around 8 BDT/day but he can earn 30-40 BDT/day by renting three lights and saving from kerosene. Earning can be 130 BDT-200 BDT/ day or more if owner start any new business activity.

iii) PV MU systems are financially attractive too. Simple payback period of PV MU varied from 4.30 years to 06 years, and NPV varied 27,404 BDT to 88,408 BDT with a discount rate of 14.9%.

iv) Users of this kind are glad to pay 5-10 BDT/day/CFL as they are getting good quality non interruptible light at a cost lower than that for kerosene.

v) Bangladesh government should think about the local production of all the accessories within the country to control the cost. As of now 10,000 PV MU systems have been installed in the country without any direct subsidy from the government. To popularize PV MU systems, the government should promote policies on direct subsidy through the Rural Electrification Board.

REFERENCE:

[1].Power Cell Bnagladesh , Present Power Situation, official website of Power Cell,.Bangladesh. www.powercell.gov.bd, 2011

[2].Petrobangla, Official website of Bangladesh Oil, Gas and Mineral Corporation www.petrobangla.org.bd ,2012.

[3]. Mondal A.H., *Economic viability of solar home systems: Case study of Bangladesh*. Renewable Energy 35 (2010) 1125–1129

[4]. GS, Solar Home System Program, Grameen Shakti, Bangladesh ". www.gshakti.org, 2011.

[5]. Chakrabarty S., Islam T., *Financial viability and eco-efficiency of the solar home systems (SHS) in Bangladesh.* Energy 36 (8), 2011, 4821-4827

[6]. Chaurey A. and Kandpal T.C., Assessment and evaluation of PV based decentralized rural electrification: An overview. *Renewable and Sustainable. Energy Reviews*14 (8), 2010, 2266–2278.

[7]. Byrne J, Shen B, Wallace W, The economics of sustainable energy for rural development: a study of renewable energy in rural China. *Energy Policy*. 26(1), 1998, 45–54.

[8] World Bank. Bangladesh: Bolstering Economic Growth to Reduce Poverty, http://www.worldbank.org.bd, 2011

Proceeding of the
International Conference on Electrical, Computer and Telecommunication Engineering
01- 02 December 2012 (ICECTE2012), RUET, Rajshahi-6204, Bangladesh

ICECTE2012: PI-0017

Introduction to Dye Sensitized Solar Cells in Bangladesh

M.F. Hossain
[1] Nanotechnology and Photovoltaic's Laboratory, Department of Electrical & Electronic Engineering, Rajshahi University of Engineering & Technlogy (RUET)
E-mail:faruk94_ruet@yahoo.com

ABSTRACT
During the last decades the energy problem on the planet has been growing steadily. To overcome those problems it is necessary to change the energy infrastructure within this century. Dye-sensitized nanocrystalline solar cells (DSCs) are of great interest as a cost-effective alternative to conventional silicon photovoltaics. The photoanode in DSCs is a mesoporous anatase TiO_2 film consisting of interconnected spherical nanoparticles, sensitized by a monolayer of dye molecules. Upon visible light absorption, excited sensitizer molecules inject an electron into the conduction band of TiO_2. These carriers are subsequently transported toward and collected by a back-contact electrode. This paper describes the DSCs technology compared to the conventional cells and its prospects in Bangladesh.

KEY WORDS: Fossil fuel, PV technology, Dye-sensitized solar cell, Nanocrystalline cell.

1. INTRODUCTION

The dye-sensitized solar cells (DSC) provide a technically and economically credible alternative concept to present day p–n junction photovoltaic devices [1]. In contrast to the conventional systems where the semiconductor assume both the task of light absorption and charge carrier transport the two functions are separated here. Light is absorbed by a sensitizer, which is anchored to the surface of a wide band semiconductor. Charge separation takes place at the interface via photo-induced electron injection from the dye into the conduction band of the solid. Carriers are transported in the conduction band of the semiconductor to the charge collector [2]. The use of sensitizers having a broad absorption band in conjunction with oxide films of nanocrystalline morphology permits to harvest a large fraction of sunlight. Nearly quantitative conversion of incident photon into electric current is achieved over a large spectral range extending from the UV to the near IR region. Overall solar (standard AM 1.5) to current conversion efficiencies (IPCE) over 80% have been reached. There are good prospects to produce these cells at lower cost than conventional devices. Here we present the current state of the field, discuss new concepts of the dye-sensitized nanocrystalline solar cell (DSCs) including heterojunction variants and analyze the perspectives for the future development in Bangladesh.

2. MATERIALS USED IN DSCs

The architecture of a dye solar cell (DSC) is shown in Figure 1. The DSC consists of a dye-coated nanoporous metal-oxide (TiO_2, ZnO) semiconductor electrode and a counter electrode, and between these electrodes there is an electrolyte containing redox mediator (I^-/I_3^-). The glass substrates are coated with a transparent conducting oxide (TCO). Fluorine doped tin oxide (SnO_2:F), FTO is most commonly used. The nanoporous metal-oxide semiconductor electrode prepared on FTO glass substrate, called working electrode (WE). The thickness of the metal-oxide semiconductor layer is about 10 μm; the resulting effective surface is about 1000 times larger as compared to a dense, compact metal oxide layer [2]. The FTO at the counter electrode is coated with few atomic layers of platinum (Pt), in order to catalyze the redox reaction with the electrolyte.

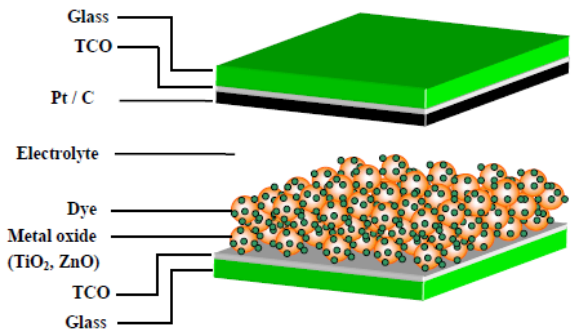

Fig.1: Architecture of DSCs.

On the surface of the metal oxide electrode, a monolayer of dye molecules is adsorbed [3]. The huge nanoporous surface of metal-oxide electrode allows for adsorbing sufficiently large number of dye molecules for efficient light harvesting. The employed dye molecule is usually a ruthenium (Ru)

metal-organic complex. The spectral absorption of the dye lies between 300 nm and 800 nm.

Between the inter-electrode space, a liquid redox electrolyte is encapsulated. In particular, the liquid electrolyte is able to penetrate the nanopores of the metal-oxide. The redox couple iodide/triiodide (I^-/I_3^-) is commonly used. The ionic iodide liquid acts as a solvent for iodine (I_2), which reacts with iodide to form triiodide (I_3^-):

$$I_2 + I^- \rightarrow I_3^- \quad (1)$$

During cell operation the following redox reaction takes place:

$$I_3 + 2e^- \leftrightarrow 3I^- \quad (2)$$

In general, best efficiencies are obtained upon illumination from the metal-oxide side. However, the DSC is usually semi-transparent and may be illuminated from the platinum side also.

3. OPERATING PRINCIPLES OF DSCs

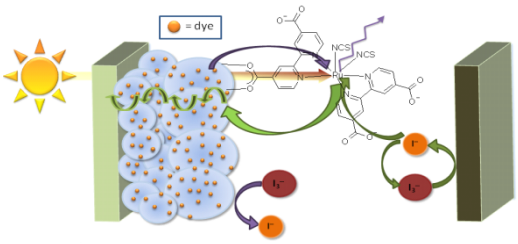

Fig. 3. Principles and configuration of DSCs

Dye-sensitized solar cells effectively separate the two functions provided by silicon in a traditional cell design (as shown in Fig. 3). Normally the silicon acts as both the source of photoelectrons, as well as providing the potential barrier to separate the charges and create a current. In DSCs, the semiconductor is used solely for charge separation, the photoelectrons are provided form a separate photosensitive dye. Additionally the charge separation is not provided solely by the semiconductor, but works in concert with a third element of the cell, an electrolyte in contact with both. The regenerative working cycle of the dye-sensitized solar cell is depicted in Fig.4, showing schematically the relative energy levels of a working DSCs [1-4].

(1) The incoming photon is absorbed by the dye (D) molecule adsorbed on the surface on the semiconductor and an electron from a molecular ground state D^0 is excited to a higher lying excited state D*.
(2) The excited electron is then injected into the conduction band (CB) of the semiconductor, leaving the dye molecule to an oxidized state D^+.
(3) The injected electron percolates through the porous semiconductor to the TCO layer of the glass substrate (negative electrode, anode) and finally through an external load to the counter electrode (positive electrode, cathode).
(4) At the counter-electrode the electron is transferred to the triiodide in the electrolyte to yield iodine, and the cycle is closed by the reduction of the oxidized dye by the iodine in the electrolyte
(5) The operation of the cell is regenerative in nature, since no chemical substances are neither consumed nor produced during the working cycle, as visualized in the cell reaction.

The operating cycle can be summarized in chemical reaction technology as (Mathews et. al. 1996)

Anode: $S + h\upsilon \rightarrow S^*$ Absorption (3)

$S^* \rightarrow S^+ + e^-(TiO_2)$ Electron injection (4)

$2S^+ + 3I^- \rightarrow 2S + I_3^-$ Regeneration (5)

Cathode: $I_3^- + 2e^-(Catalyst) \rightarrow 3I^-$ (6)

Cell: $e^-(catalyst) + h\nu \rightarrow e^-(TiO_2)$ (7)

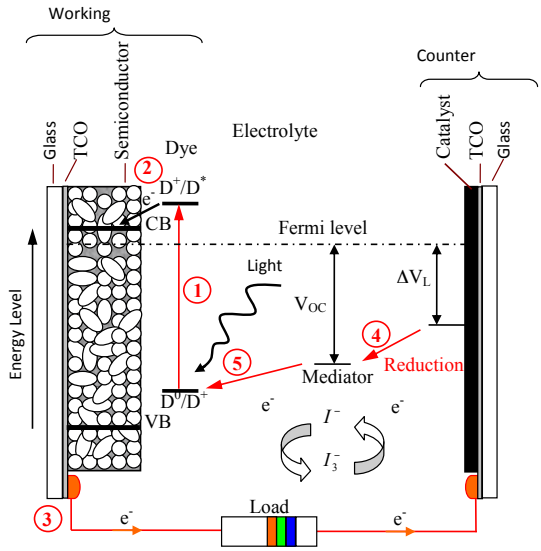

Fig. 4: The working principle of the dye-sensitized nanostructured solar cells.

4. DSCs VS. OTHER SOLAR CELLS

The important features that distinguish DSC from conventional photovoltaics are as follows:

i) It is photoelectrochemical cell: charge separation occurs on interface between a wide band gape semiconductor and an electrolyte.
ii) It is a nanoparticulate cell: it is not a dense film as is amorphous silicon, but a 'light sponge'.
iii) It is a dye-sensitized solar cell: a dye monolayer chemically absorbed on the semiconductor is primary absorber of sunlight; free charge carriers are generated by electron injections from a dye molecule, excited by visible radiation.

4.1. Advantages of DSCs over other solar cells

Compared to other solar cells, the dye-sensitized solar cell has the following advantages:

i) Much less sensitive to angle of incidence of radiation good in refracted and reflected light.
ii) Performs over much wider range of light conditions due to the high internal surface of semiconductor ("light sponge") – can be designed for operation at very low light.
iii) Can be designed to operate optimally over a wide range of temperatures.
iv) Much less sensitive to a partial shadowing
v) Option for transparent modules – so can be used for day-lighting, roof lighting, displays
vi) DSCs production needs only commonly available non vacuum processing equipment making it vastly cheaper to set up facilities
vii) DSCs have significantly lower embodied energy than all other forms of solar cells
viii) Lower production costs and Cheaper material bill

5. FABRICATION OF DSCs

The prepared TiO_2 films were dye-sensitized by soaking the films in a dye solution (Ruthenium Complexes) for 24 h – 48 h at room temperature [4]. The opposing glass plates are offset so that all of the TiO_2 is covered by the counter electrode, and the 5 mm strip of the glass not coated by the TiO_2 is exposed (as shown in Fig. 5). The exposed sides of the device will serve as the contact points for the negative and positive electrodes so that electricity can be extracted to test the cell. Two binder clips are used to gently hold the plates together at the other edges (as shown in Figure 5). The iodide electrolyte solution is 0.5 M potassium iodide mixed with 0.05 M iodine in water free ethylene glycol. One or two drops of the iodide/ iodine electrolyte solution can then be placed at the edges of the plates and the two binder clips are alternately opened and closed while in place. The liquid is drawn into the space between the electrodes by capillary action, and can be seen to "wet" the stained TiO_2 film. The active cell area was 0.25 cm^2.

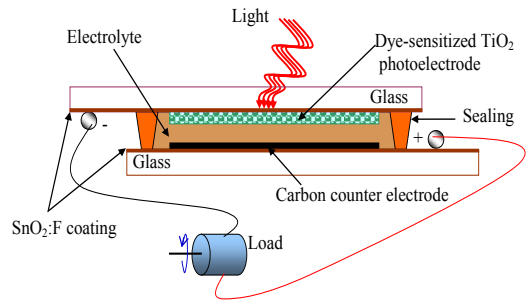

Fig. 5: A schematic diagram of the construction of DSCs.

5.1. Measurement setups of dye-sensitized solar cells

The complete solar cell/light detector can be taken outside and measured under illumination by sunlight. Light should be entering the glass "sandwich" through the TiO_2-coated glass plate. Maximum current and voltage output can easily be determined by attaching volt-ohm meter directly to the two sides of the cell using wires with alligator clips attached to their ends. The negative electrode is the TiO_2-coated glass, and should be attached to the black (-) wire of the meter, and the positive electrode (+) is connected to the counter electrode. Use a ruler to measure the dimensions of the active (stained) area of the solar cell and divide the output current by this area. Record the electrical output values and compare the various types of dye extraction procedures used.

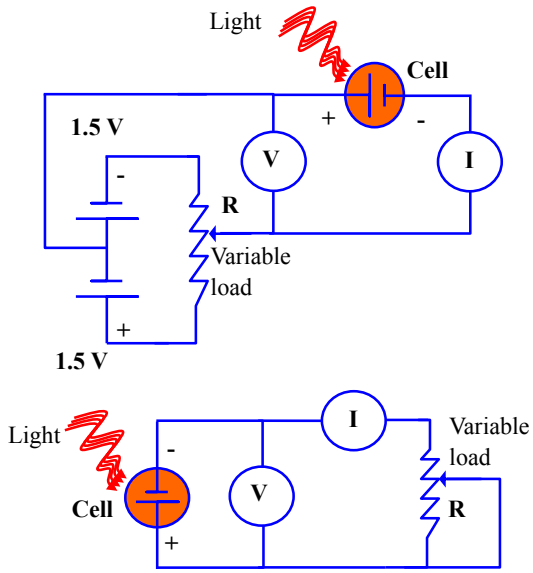

Fig. 6: Two possible light detector or solar cell current-voltage characteristics measurement set-ups. The solar cell is represented as diode or battery.

For indoor measurements, the cell was irradiated with an artificial sunlight simulator, consisting of a SOLAX lamp (model: SET-140F, SERIC Ltd.) equipped with integral parabolic reflector and ultraviolet and an infrared-blocking filter. Only the visible spectrum (400 nm – 900 nm) of light was used for our measurement. The current voltage (I-V) curves are then measured using a 1kΩ potentiometer as variable load (shown in Fig. 6). Point by point current and voltage data can be gathered at each incremental resistance value and plotted on the graph paper. If a cell dries out, another drop of electrolyte can be added to the edges of the plates to revive it. The cell may also be heat sealed, using gasket made from a low melting point polymer film used in food packaging, such as Dupont Surlyn 1702.

5.2. Basic Solar Cell parameters:

The current depends on voltage, and a plot of current versus voltage is called I-V curve of the cell. The characteristics of an I-V curve depend e.g. on illumination and on temperature. A typical I-V curve is shown in Fig. 7.

If the voltage is zero, i.e. the cell is short circuited, short circuit current I_{SC} is generated. If, on

the other hand there is no current in the cell, the voltage over the cell is the opern circuit voltage V_{OC}. The generated power equals current times voltage, and the power voltage dependence corresponding to the I-V curve in Fig. 4.1 is also shown. The maximum of the power voltage curve is called the maximum power point (MPP). The voltage, current and power at MPP are V_{mpp}, I_{mpp}, P_{max} respectively.

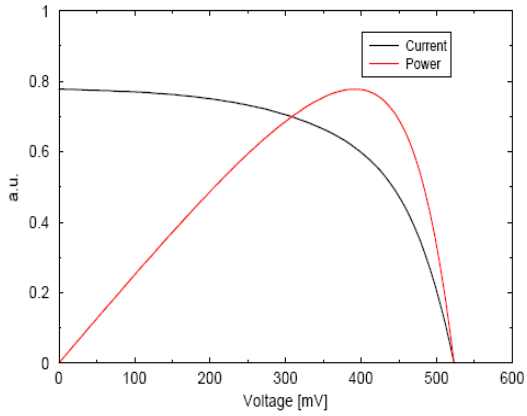

Figure 7: A typical I-V and power curves of a Solar cell

The current conversion efficiency, η_{eff} of a solar cell is defined as the ratio of the output power of the cell and incident irradiance.

$$\eta_{eff} = \frac{P_{out}}{Pin} = \frac{V_{mpp} I_{mpp}}{P_{in}} = \frac{V_{oc} I_{sc} \times FF}{P_{in}} \quad (8)$$

where FF, the fill factor, is defined as the ratio

$$\eta_{eff} = \frac{V_{mpp} I_{mpp}}{V_{oc} I_{sc}} \quad (9)$$

The fill factor is a important part of the efficiency of the cell. High open circuit voltage and short circuit current are essential in achieving high efficiencies, but paired with a low fill factor, the overall efficiency of the cell will remain low.

Incident photon to current conversion efficiency (IPCE) is another important parameter when determining the performance of a solar cell. IPCE is the number of electrons flowing through the external circuit divided by the number of photon incident on the solar cell surface at a particular wavelength, λ [1]. In the case of dye-sensitized solar cell, it is defined as the ratio of the observed photocurrent (short circuit current) divided by the incident photon to current flux, uncorrected for reflective losses during optical excitation through the conducting glass electrode. It can be also be considered as a product of three components as follows

$$IPCE(\lambda) = LHE(\lambda)\phi_{inj}\eta_{el} = 1240\frac{I_{sc}(\lambda)}{\lambda\phi_{h\nu}(\lambda)} \quad (10)$$

where the light harvesting efficiency (LHE) depends on the spectral properties of the dye, charge injection yield (ϕ_{inj}) depends on the excited state redox potential and lifetime, and charge collection efficiency (η_{el}) depends on the structure and morphology of the TiO_2 layer. The right part of the equation (10) is the general definition of IPCE, which can be applied to all solar cells (λ is the wavelength and $\phi_{h\nu}(\lambda)$ is the photon flux). Futher explanation of different factors of the equation (10) can be found in [2]. IPCE is often referred to as photocurrent action spectrum, spectral response or (external) quantum efficiency.

6. DSCs PROPECTS IN BANGLADESH

Solar Energy is inexhaustible and pollution free. It is available everywhere; but the greatest amount is available between two broad band's encircling the earth between 15" and 35" latitude north and south. Fortunately, Bangladesh is situated between 20"43' north and 26"38' north latitude and as such Bangladesh is in a very favorable position in respect of the utilization of solar energy. Annual amount of radiation varies from 1840 to 1575 kwh/m^2 which is 50-100% higher than in Europe. Taking an average solar radiation of 1900 kwh per square meter, total annual solar radiation in Bangladesh is equivalent to 1010 X 10^{18} J. Present total yearly consumption of energy is about 700 X 10^{18} J [9]. These shows even if 0.07% of the incident radiation can be utilized, total requirement of energy in the country can be met. At present energy utilization in Bangladesh is about 0.15 watt/sq. meter land area, whereas the availability is above 208 watt/sq. meter. This shows the enormity of the potentiality of this source in this country (Eusuf, 1997). Due to its initial large cost mainly the rooftop photovoltaic cells yet not become so popular. As a low cost PV cell the DSSC can be considered as an alternative to that for mitigating country's crisis of energy through the use of solar energy.

Conclusion:

Although DSCs posses some disadvantages but it is more efficient in many respects in comparison with conventional rooftop photovoltaic cells. Moreover lots of research works has brought the technology ease of use commercially. Bangladesh: expecting to produce a huge amount of energy from solar power can think of using DSCs as an alternative to the existing PV cell in considering its cost mainly and the other shortcomings over DSCs.

References

[1] B. O'Regan and M. Grätzel, "A Low-Cost, High-Efficiency Solar Cell Based on Dye-Sensitized Colloidal TiO_2 Films," Nature **353**, 737 (1991).

[2] M. Grätzel, "Dye-Sensitized Solar Cells," J Photochem. Photobiol.C - Photochem. Rev. **4**, 145 (2003).

[3] M. Grätzel, "The Advent of Mesoscopic Injection Solar Cells," Prog. Photovoltaics **14**, 429 (2006).

[4] M.F. Hossain, Study of dye-sensitized solar cells fabricated with nanostructured materials, PhD dissertation, University of Toyama, Japan.

Proceeding of the
International Conference on Electrical, Computer and Telecommunication Engineering
01- 02 December 2012 (ICECTE2012), RUET, Rajshahi-6204, Bangladesh

ICECTE2012: PI-0018

Design of a Cost Effective Off-Grid Wind-Diesel Hybrid Power System in Kutubdia Island of Bangladesh

Feroz Ahmmed Bhuyan[1], Abdul Khaleque[2], G. K. M. Hasanuzzaman[3], Md. Monjur Ellahi Rafi[4]
[1, 2, 3&4] Department of Electrical and Electronic Engineering,
Rajshahi University of Engineering & Technology, Rajshahi-6204, Bangladesh.
E-mail: ferozeee@gmail.com, khaleque_eee@yahoo.com, rafiruet@yahoo.com

ABSTRACT
This paper proposes a cost effective design of off-grid wind-diesel hybrid power system in a grid isolated island, Kutubdia, Bangladesh. Wind power is integrated into traditionally diesel only remote area power supply (RAPS) systems to reduce the harmful emissions and life cycle costs significantly. HOMER simulation software is used for this purpose. Local wind speed and estimated electric loads are used which makes the simulation simple. Finally, the environmental effects are also analyzed.

KEY WORDS: Renewable energy, Off-grid, Wind-Diesel hybrid system, Wind Turbine.

1. INTRODUCTION

Bangladesh is a developing country having large population. The coastal area in the southern part of Bangladesh has a huge potential of wind power generation. On the other hand islands like Sandwip, Kutubdia, Maheshkhali, St. Martin are not suitable for grid-connected system. WIND-DIESEL hybrid power system considerably reduces the fuel consumption cost, and carbon emission in the environment as opposed to their conventional diesel only counterpart [1~3]. Introduction of wind generators in wind-diesel hybrid power systems, system stability is becoming an important factor to the power companies. Due to the changing characteristics of wind speed the most crucial issue is to assess the capacity adequacy of the hybrid system in addressing the electricity demand of the consumers. Wind-Diesel Hybrid power systems with long term energy storage can optimally use RE resource [4]. A suitable mathematical model can be developed for wind-diesel hybrid power system [5] to study frequency disturbance on an island electric system. Improved sizing method of storage units is reported in [6] and [7]. This paper presents a cost effective design of off-grid wind-diesel hybrid power system in the island Kutubdia of Bangladesh.Utilization of Renewable Energy sources is growing in grid-connected mode as well as in remote isolated communities.

2. METHODS AND SIMULATION MODELS

Kutubdia of Bangladesh is chosen as a simulation region and it has an area of 36 square miles (93 km^2), 18 miles (29 km) in length and 2 miles (3.2 km) in breadth. The wind blows over Bangladesh from March to September with a monthly average speed of 3 m/s to 9 m/s at different heights. Wind speed data is chosen according to the studies of Bangladesh Meteorological Department (BMD) shown in Table 1.

Table **1:** Wind speed in kutubdia at 45 m height [8]

Month	Wind speed(m/s)
January	5.830
February	4.790
March	4.150
April	12.500
May	2.700
June	5.420
July	7.500
August	6.120
September	3.140
October	6.710
November	6.200
December	6.870

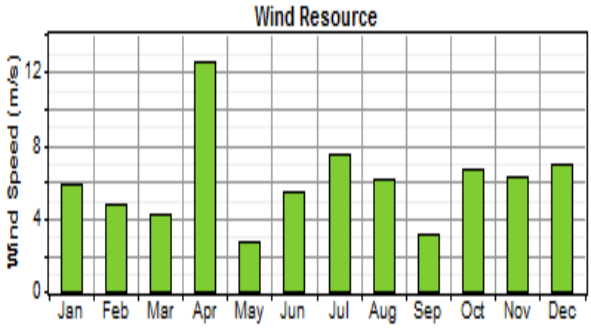

Fig. 1: Wind resource in Kutubdia Island [8]

Fig. 1 shows the wind resource in Kutubdia Island. During April the wind speed is highest, during May and September wind speed is lower. Average wind speed is 5.995 m/s, which is sufficient to generate electricity commercially.

2.1 Wind Velocity Calculation

Wind velocity changes with height. The rate of increase of velocity with height depends upon the roughness of the terrain. The variation of average wind speed can be determined from the following power law expression terrain. The variation of average wind speed can be determined from the following power law expression [9],

$$\frac{V_Z}{V_{ref}} = \left(\frac{h}{h_{ref}}\right)^{\alpha} \quad \text{.....(1)}$$

where

V_z = average wind velocity at height h meter (m/s)

V_{ref} = average wind velocity at reference height (m/s)

h = the height where the velocity of wind is to be calculated (m)

h_{ref} = reference height (m)

α = dimensional constant that varies from 0.1 to 0.4 depending on the nature of the terrain

Wind speed is measured by anemometer.

2.2 Power Generation by Wind Turbine

Power generated by a wind turbine at particular height can be calculated by using following equation [10].

Power in the Wind (watt)$=\frac{1}{2}\rho A V^3 C_p$.....(2)

where

ρ = wind power density (w/m^2)

A = area swept by the rotor (m)

V = velocity of wind (m/s)

C_p = rotor efficiency

2.3 Design of wind-diesel hybrid power system

To design the hybrid power system in Kutubdia, Diesel generator is combined with wind power generator [3]. Following figure shows block diagram of wind-diesel hybrid system.

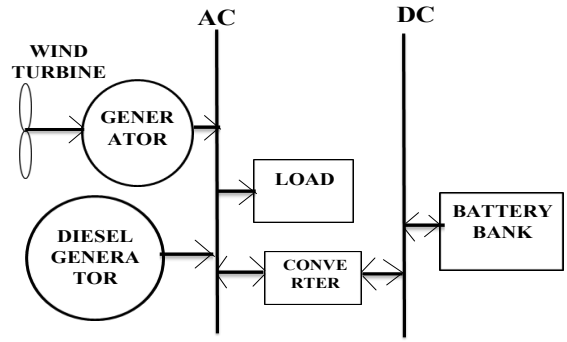

Fig. 2:Simple block diagram of wind-diesel hybrid system

Fig. 2 shows that how a diesel generator and wind turbine are connected among them with the AC system bus . Diesel generator and load are also connected to the AC bus. Battery bank and converter are used for storage of electricity and conversion of power from AC to DC and vice versa, respectively.

2.4 Electrical Demand in Kutubdia:

Following estimated data has been considered for current design:

Table 2: Estimated demand (W) of electricity per house

Appliance	Number(s)	Unit capacity
Light	2	50 W
Fan	2	80W
TV	1	100W
Other	1	40W
		Total = 400W

Kutubdia has 14,463 households in entire islands. Energy demand per day is 65 MWhr and the peak demand is 11 MW in Kutubdia.

2.5 Proposed hybrid system for Kutubdia Island:

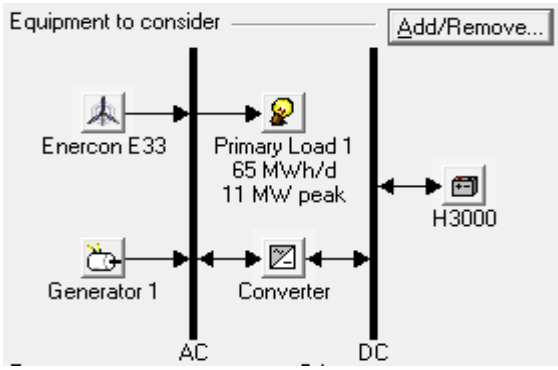

Fig. 3: Diagram of HOMER simulator.

Fig. 3 shows the proposed hybrid system for HOMER simulation. Enercon E33 wind turbine produces AC output, so it is connected to the AC bus in parallel with the diesel generator. Battery bank is connected to the DC bus. Converter is placed between the two buses. Load is connected to the system through AC bus.

Wind turbine: Enercon E33 turbine is chosen for this hybrid system because average wind speed at 45m height is 5.995 m/s in Kutubdia which goes below the average wind speed at winter, but cut-in speed of high capacity wind turbine is more than about 4 m/s. The irregularity of wind velocity can be fixed by gear system. Enercon E33 has a rated capacity of 330 kW and cut-in speed of 2.5m/s. Hence, Enercon E33 is perfect slection for low wind speed.

Diesel Generator: In the proposed system diesel generator is used to operate in parallel with the wind turbine to increase the maintenance flexibility, efficiency and distribute the electric load more optimally.

Following Table 3 shows the cost considered for this design purpose.

Table 3: Cost of different elements

Name	Cost($)
Enercon E33	500000
Diesel generator	200000/MW
Diesel	0.7/liter
Battery	1500/string
Converter	1350/MW

3. SIMULATION RESULTS AND ANALYSIS

Numerical results for wind turbine output, monthly average electricity production, cash flow summery and environmental effects are shown below.

3.1 Economic Analysis:

The simulation results depict that the production cost of electricity per KWh is 0.209$.

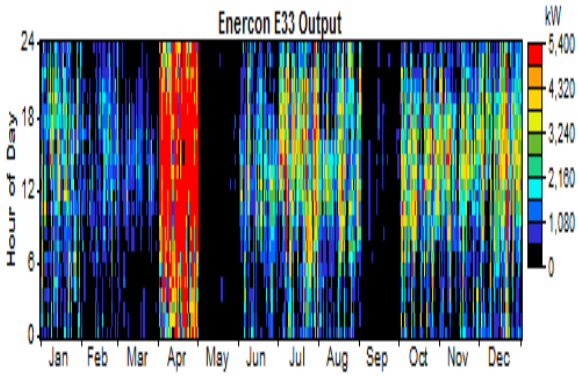

Fig. 4: Enercon E33 output

Fig. 4 shows the Enercon E33 turbine output during different months of the year. In the above figure, during April, the wind speed is higher and Enercon E33 generates more electricity. During May, due to lower wind speed Enercon E33 generates less electricity.

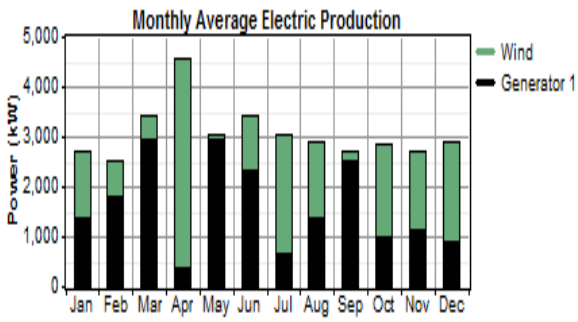

Fig. 5: Monthly average Electricity production

Fig. 5 shows electricity production by wind turbines and diesel generators. Green color indicates electricity production by wind and black color indicates electricity production by diesel. When wind speed is higher, we have to be less dependent on diesel generators. As a result cost of electricity production reduces during that time. During May the wind speed is lowest. To meet the demand of consumers, here we have to depend on diesel energy.Net present cost of different equipments are also shown in the following Fig. 3.3.

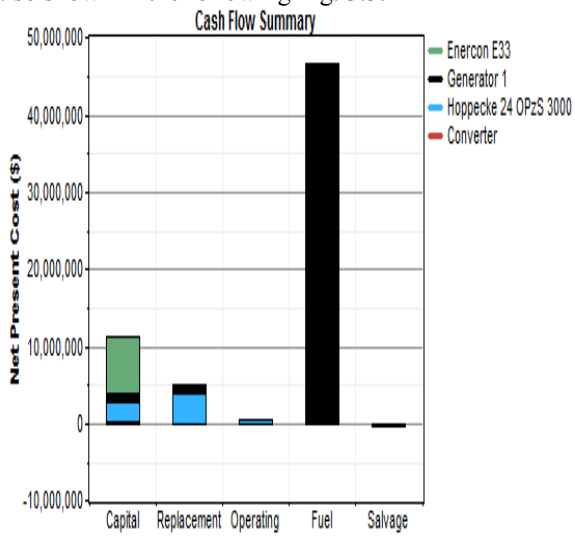

Fig. 6: Cash flow Summery

3.2 Analysis of Environmental Effects

Table 4 shows the release of different environmental pollutants per year

Table 4: Environmental pollutants

Pollutant	Emissions (kg/yr)
Carbon dioxide	9,177,737
Carbon monoxide	22,654
Unburned hydrocarbons	2,509
Particulate matter	1,708
Sulfur dioxide	18,430
Nitrogen oxides	202,143

Wind-diesel hybrid system with reduces gas emission by a significant amount due to reduced fuel consumption. If we use more wind energy, then we have to be less dependent on diesel energy. Here we have used more wind energy, so environmental pollutants are less.

4. CONCLUSIONS

In Bangladesh only 39% of the populations have access to electricity. Remote areas, like islands cannot be connected to the grid as they are discrete from main land. Due to high cost of diesel, only diesel-based power generation is not economically feasible. So, wind-diesel hybrid can be a perfect solution for electrification of the households in Kutubdia Island. The proposed production cost of electricity per KWh is 0.209$. So, per unit cost of electricity generation in kutubdia Island is lesser than the proposal of [11]. Environmental pollution in this

work is lesser in comparison with the proposal of [8] and [11], due to more use of wind energy than diesel energy. The results of HOMER simulation and modeling show that wind-diesel hybrid system is far better than a system with only diesel generator due to high cost of diesel.

5. FUTURE WORK

Future researchers may design more cost effective Wind-Diesel hybrid system and implement it in the power generation in Kutubdia island.

6. ACKNOWLEDGEMENTS

The authors thank to Abdul Khaleque, Assistant Professor, Department of Electrical and Electronic Engineering, Rajshahi University of Engineering & Technology for his support, guidance and encouragement throughout this research.

REFERENCES

[1] X. Liu and S. Islam, "Reliability Evaluation of a Wind-Diesel Hybrid Power System with Battery Bank Using Discrete Wind Speed Frame Analysis", 9th International Conference on Probabilistic Methods Applied to Power Systems KTH, Stockholm, Sweden, pp.1-7, 2006.

[2] R. Karki and R. Billinton, "Cost-Effective Wind Energy Utilization for Reliable Power Supply", IEEE Transactions on Energy Conversion, vol. 19, pp. 435-440, 2004.

[3] R. Billinton and G. Bai, "Generation Capacity Adequacy Associated with Wind Energy," IEEE Transactions on Energy Conversion, vol. 19, pp. 641-646, 2004.

[4] Maruf-ul-Karim, M. and Iqbal, M.T., "Dynamic Modeling and Simulation of a Remote Wind-Diesel-Hydrogen Hybrid Power System", IEEE International Conference on Electric Power and Energy, pp. 1-6, 2010.

[5] Raja, J., Rajan, C.C.A. and Suresh, S., "PSO Based Robust Frequency Control of Wind-Diesel Power Plant using BES", IEEE International Conference on Computational Intelligence and Computing Research, pp. 1-7, 2010.

[6] Tankari, A.M., Dakyo, B. and Nichita, C., "Improved Sizing Method of Storage Units for Hybrid Wind-Diesel Powered System", International Conference of Power Electronics and Motion Control, pp. 1911-1917, 2008.

[7] Uhlen, K., Foss, B.A., and Gjosaeter, O.B., "Robust Control and Analysis of a Wind-Diesel Hybrid Power Plant", IEEE Transactions on Energy Conversion, vol. 9, no.4, pp. 701-708, 1994.

[8] A.N.M. Mominul Islam Mukut, Md. Quamrul Islam, Muhammad Mahbubul Alam, "Prospect of Wind Energy in the Coastal Belt of Bangladesh", The Pacific Journal of Science and Technology, volume 9, Number 2, pp. 442-451, November 2008.

[9] Nahid-Al-Masood, Rifat Mirza,Jubaer Ahmed, Amina Hasan Abedin, S.R. Deeba, Faeza Hafiz, Mahmuda Begum and A. Hasib Chowdhury, "Design of a Cost Effective Off-Grid Wind-Diesel Hybrid Power System in an Island of Bangladesh", World Academy of Science, Engineering and Technology, vol 60, pp.1-4, 2011.

[10] Bindu Kansara and Prof. (Dr.) B. R. Parekh, "Modeling And Simulation of Wind- Diesel Hybrid System", National Conference on Recent Trends in Engineering & Technology, India, pp. 1-5, 2011.

[11] Alam Hossain Mondal and Manfred Denich, "Hybrid systems for decentralized power generation in Bangladesh", Energy for Sustainable Development, pp. 48–55, 2010.

Proceeding of the
International Conference on Electrical, Computer and Telecommunication Engineering
01- 02 December 2012 (ICECTE2012), RUET, Rajshahi-6204, Bangladesh

ICECTE2012: PI-0019

Performance Improvement of a Solar Cell Using Particular Window Material (GaP)

Md. Shareef Ifthekhar[1], Abu Farzan Mitul[1], Fida Hasan Md Rafi[1], Mohammad Muhiminun Islam[2]
[1, 2] Department of Electrical & Electronic Engineering, Khulna University of Engineering & Technology
shareef_ifthekhar@yahoo.com, , mitulnaya@yahoo.com, fidaeee@yahoo.com

ABSTRACT
This paper represents a model to increase efficiency beyond the theoretical limit for a single junction solar cell. Conventionally, p-i-n junction solar cell was used with addition layer p+ and n+ to increase efficiency. However, some associated problems like low conversion efficiency and materials with the appropriate band gaps that can perfectly match the broad range solar radiation remain. therefore, this proposal consists of gap as a window layer due to overcome conventional limitations by using AlGaAs as a window layer.

KEYWORDS: Window layer, AlGaAs, GaP, solar cell efficiency, antireflection coating

1. INTRODUCTION

Solar photovoltaic energy conversion is a one-step conversion process which generates electrical energy from light energy. This is one of the greatest inventions of renewable energy. As, our demand for energy consumption is increasing sharply, new methods & technologies are being used to meet up the requirements. This paper shares an idea of improving conventional solar cell efficiency. The effectiveness of a photovoltaic device depends upon the choice of light absorbing materials and the way in which they are connected to the external circuit [1]. But theoretical maximum efficiency of a silicon based solar cell is 27% [2]. Present research is proceeding at a fast clip to push the efficiencies up to 30% and beyond. The efficiency of a solar cell largely depends on its spectral response. The wider the spectrum of light that the cell can respond to (the spectral response), the more power is generated. Research is ongoing to develop techniques and materials that can use more of the light spectrum and thus generate more power from each photovoltaic cell [3]. One of the technologies used to increase efficiency of solar cell is p-i-n structure. In a p-i-n solar cell an intrinsic region is inserted between p and n-type layer of p-n solar cell. In this case, short circuit current density is higher than the conventional p-n solar cell due to the additional carrier contribution of the intrinsic region. Additionally p+ and n+ layer added to reduce front surface and back surface recombination respectfully to improve efficiency of the solar cell model.

2. MODEL OF REFERENCE CELL

Practical solar cells have a complicated structure with several layers in addition to the p-and n-layer in the simplest p-n solar cell. The purpose of these layers is to reduce front and back surface recombination and surface reflection.

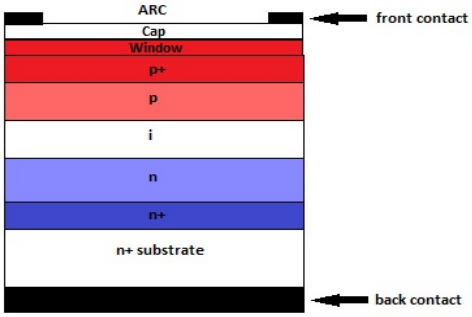

Fig. 1 Structure of reference p-i-n cell.

The model consists antireflection coating, window, p+, i, n and n+. The anti reflecting coating reduces the reflectivity. Hence, reflection losses reduce to approximately 2% [4]. The i-layer is with low background doping. It is reasonable to consider the whole i-layer as depleted with an electric field present throughout the whole i-layer. The more heavily doped p+-layer on top of the p-layer reduces the surface recombination velocity through a front surface field. The window layer made of a higher band gap material above the p+-layer. So, the effective surface recombination velocity is further reduced. More heavily doped layer placed beneath the n-layer gives a back surface field, reducing the effective rear surface recombination velocity in the same way as the front surface field. Recombination of excess carriers occurs not only within the bulk of a semiconductor crystal, but at the surface of the crystal as well. The periodicity of the atoms is interrupted at the surface of the crystal, and the surface acts as an interface between the semiconductor and another material. As a result the recombination rate at the surface is different (and usually higher) than in the bulk of the semiconductor [4]. Surface recombination is reduced by a passivating or window layer which prevents minority

carriers from reaching the surface. Surface recombination velocity is strongly dependent on the surface roughness, contamination, ambient gases used during oxidation and the annealing conditions. GaAs is used to construct this entire layer. Further reduce surface recombination they proposed AlGaAs as a window layer because in GaAs surface recombination velocity is high (10^6 cm/s). But The deposition of a thin layer of GaAIAs, however, reduces the recombination velocity at the interface to 10-10^3cm/s [3]. Therefore, we proposed GaP as a window layer for our model.

3. OUR PROPOSE MODEL

Table 1 Materials of the proposed model.

Layers	Materials
Window	GaP
p^+	GaAs
p	GaAs
i	GaAs
n^+	GaAs
n	GaAs

GaP is used as window layer in the proposed as:

a. GaP is binary and AlGaAs is ternary alloy material. It is easier to prepare binary alloy than ternary alloy. More over $Al\ x\ Ga$As is not available for all x values

b. GaAs and GaP both have zinc-blende crystal $1-x$ structure.

c. The band gap energy of the GaP is 2.26eV at 300k [5] and for Al_xGa_{1-x}As (where x=.85) 2.09eV [6] but both are indirect band gap material.

d. Two-color materials have to be transparent in both mid-wave (3-5µm) and long wave (8- 14µm) infrared region to be one color. GaP has 2-Color capability at room temperature because emittance is not significant.

e. GaP has outstanding thermal shock resistance for rapid heating environment.

f. Useful for external exposure to rain, blowing particles, rapid heating or mechanical stress. Lattice mismatch between GaP and GaAs is higher than the mismatch between AlGaAs and GaAs . This can be overcome by improving the GaAs/GaP structure quality by using special structures and growth techniques like strained super lattice, thermo cyclic growth and cyclic structure annealing [3].

4. RESULT AND DISCUSSION

4.1 Effect of Width of the Window Layer

The maximum efficiency and short circuit current density has been calculate for comparison between AlGaAs window layer device and GaP window layer device and both data are included in Table 2.

Let, Width of the window layer is W

Maximum Efficiency η_{max}

Table 2 Simulation results of varying width of the window layer.

W nm	AlGaAs as a window layer			GaP as a window layer		
	V_{oc} Volt	J_{sc} A/m^2	μ_{max}	V_{oc} Volt	J_{sc} A/m^2	μ_{max}
5	1.005	445.14	36.948	1.005	445.44	36.975
10	1.005	444.22	36.868	1.005	444.83	36.921
50	1.005	436.97	36.237	1.005	439.97	36.499
100	1.004	428.11	35.467	1.004	434.05	35.984
150	1.003	419.46	34.717	1.004	428.29	35.482

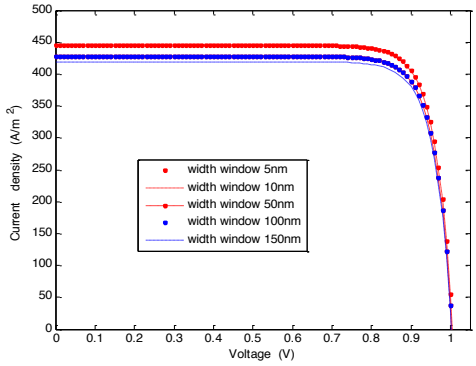

(a)

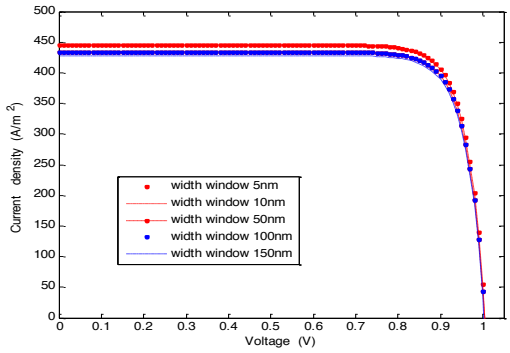

(b)

Fig. 2 V_{oc} Vs J_{sc} curve(a) AlGaAs and (b) GaP window layer.

From data table it is clear that increasing the width of the window layer causes to decrease efficiency because it increases recombination. Another cause when we use thin window layer that it's generation and recombination current can be neglected. GaP and Al_xGa_{1-x}As (where x=.804) both indirect band gap material, non radiative recombination (i.e Auger recombination) dominant here where radiative recombination is suppressed due to the need of photons in the recombination process. The Auger recombination is intrinsic to the material and for example, cannot be improved by using a purer starting material or a cleaner fabrication process. Therefore, the only way to reduce the Auger recombination rate inside the cell is to reduce its thickness. So at lower thickness device gives better performance. The efficiency variation due to

thickness of the window layer is shown in Fig. 3.

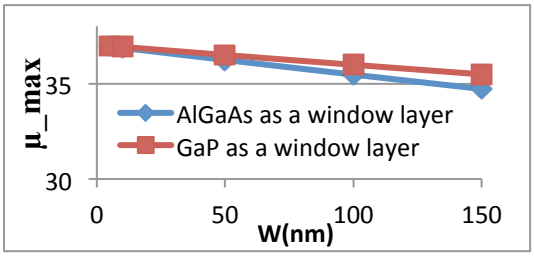

Fig. 3 Efficiency using different window layer.

4.2 Effect of Width of the p layer

Table 3 Simulation varying width of the p layer.

W nm	AlGaAs as a window layer			GaP as a window layer		
	V_{oc} Volt	J_{sc} A/m^2	μ_{max}	V_{oc} Volt	J_{sc} A/m^2	μ_{max}
100	1.002	410.90	33.970	1.002	411.19	33.995
150	1.004	428.36	35.489	1.004	428.66	35.514
200	1.005	445.14	36.948	1.005	445.44	36.975
250	1.007	461.24	38.354	1.007	461.55	38.381
300	1.008	476.67	39.711	1.008	476.99	39.740

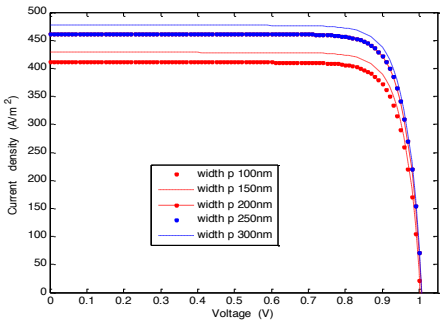

(a)

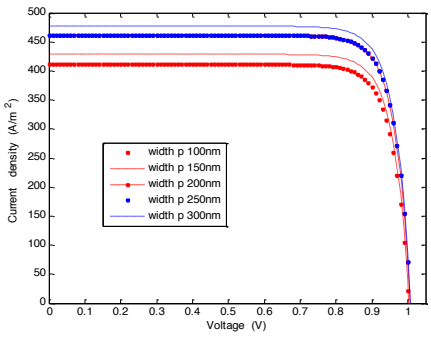

(b)

Fig. 4 Voc Vs J_{sc} for different width of the p layer (a) AlGaAs (b) GaP .

The quantum efficiency increases with the increase of the width of the p layer. As photo current is directly related to the quantum efficiency, increasing quantum efficiency results photo current also to increase.

4.3 Effect of Width of the Intrinsic Layer

Table 4 Simulation for varying width of the intrinsic layer.

W nm	AlGaAs as a window layer			GaP as a window layer		
	V_{oc} Volt	J_{sc} A/m^2	μ_{max}	V_{oc} Volt	J_{sc} A/m^2	μ_{max}
100	1.028	373.48	32.395	1.028	373.73	32.418
200	1.015	410.60	34.645	1.015	410.87	34.670
300	1.005	445.14	36.948	1.005	445.44	36.975
350	1.001	461.51	38.081	1.001	461.82	38.108
400	0.998	477.30	39.165	0.998	477.62	39.194

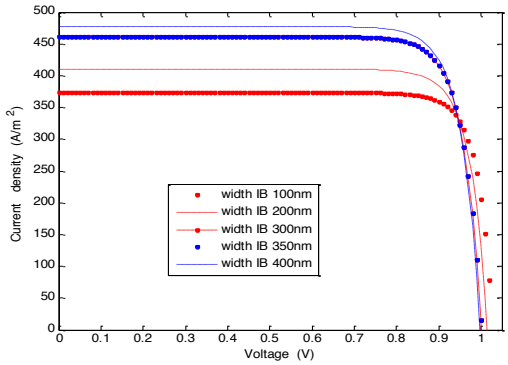

(a)

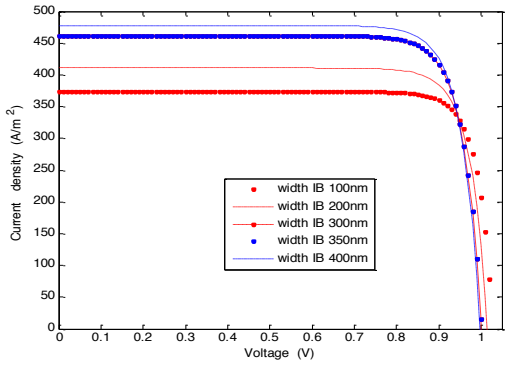

(b)

Fig. 5 Voc Vs Jsc for different width of the intrinsic layer (a) AlGaAs (b) GaP

The efficiency of the device decrease slowly due to increase in the width of GaP comparing to the AlGaAs window layer.

4.4 Effect of Width of the n Layer

Table 4 Simulation results of varying width of the n layer.

W nm	AlGaAs as a window layer			GaP as a window layer		
	V_{oc} Volt	J_{sc} A/m^2	μ_{max}	V_{oc} Volt	J_{sc} A/m^2	μ_{max}
200	1.002	416.00	34.410	1.002	416.26	34.435
250	1.004	430.97	35.715	1.004	431.27	35.741
300	1.005	445.14	36.948	1.005	445.44	36.975
350	1.007	458.54	38.117	1.007	458.85	38.145
400	1.008	471.22	39.234	1.008	471.54	39.262

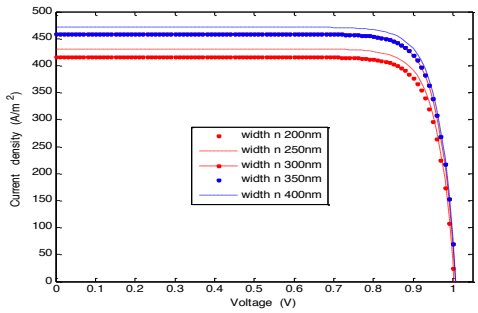

(a)

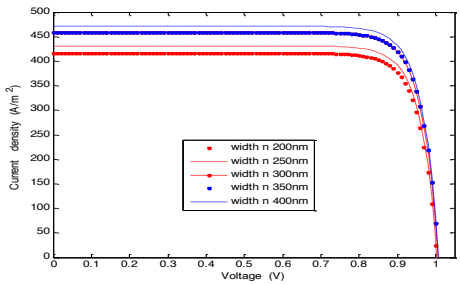

(b)

Fig. 6 Voc Vs Jsc for different width of the n layer (a) AlGaAs (b) GaP as a window layer.

It is evident that, using GaP as a window layer slightly better performance can be obtained than AlGaAs as a window layer.

4.4 Effect of thickness for all layer

The efficiency decreases with the increase of width of the window layer, but in the case of increasing width of the other layer efficiency increases. As, window layer is made of indirect band gap material, increasing thickness causes to increase auger recombination so performance decreases. Other layers are made of direct band gap material and thickness is wider than window layer. So, those layers greatly contribute to generate current. Moreover, increasing the thickness layers increase the photon absorption capacity and efficiency

5. CONCLUSION

The model optimizes the design of p-i-n reference cell for high efficiency. It shows the importance of using a window layer and heavily doped p+ and n+ layers to obtain a low effective surface recombination velocity together with an anti-reflection coating minimizing the reflection losses. By using these layers, high quantum efficiency is obtained. Due to a model of a p-i-n solar cell with the intrinsic material placed in a flat band region, a model of high efficiency solar cell is developed and high short circuit current and open circuit voltage is obtained, because additional short circuit current density comes from intrinsic region. From those simulation results maximum efficiency is obtained 40.9133% for AlGaAs as a window layer and 40.9428% is obtained for GaP. So efficiency increases 0.0295%, if GaP is used as window layer instead of AlGaAs.

6. FUTURE WORK

Placing intrinsic region between n-type and p-type short circuit current density and the open circuit voltage will be enhanced from the conventional p-n solar cell. GaP window layer that is binary compound with lattice mismatch about .03%. In future we lattice mismatch and high performance material will be used.

7. ACKNOWLEDGEMENT

Special thanks to Md. Rafiqul Islam for his constant guidance throughout our work.

REFERENCES

[1] The Physics of Solar Cells, www.icpress.co.uk/etextbook/p276/p276_ch ap1.pdf

[2] J. Nelson,"Quantum-Well Structures for Photovoltaic Energy Conversion: Thin Films", 1995.

[3] T. Markvart & L.Castaner , "Practical Handbook of photovoltaics fundamental and applications", 2008.

[4] J. P. Colinge, C. A. Colinge, "Physics of the semiconductor devices", 1981.

[5] J. R. Hauser, M. A. Littlejohn, "Approximations for accumulation and inversion space-charge layers in semiconductors", pp 667, 1968.

[6] P. D. Demoulin, M. S. Lundstrom, and R. J. Schartz, "Back-surface field design for n+ p GaAs cells. Solar Cell", pp 229, 1987.

[7] T. K. Kvanes, "Modeling of Intermediate band solar cell", Faculty of Natural Science and Technology, Department of Physics, Trondheim, June, 2009.

[8] A. Martí, C. R. Stanley, A. Luque. "Intermediate Band Solar Cells (IBSC) Using Nanotechnology", chapter 17 in Nanostructured Materials for Solar Energy Conversion, 2006.

[9] "Intermediate-band Solar Cells and the Quantum Dot Approach", Department of EEE, University of Glasgow, 2009.

Proceeding of the
International Conference on Electrical, Computer and Telecommunication Engineering
01- 02 December 2012 (ICECTE2012), RUET, Rajshahi-6204, Bangladesh

ICECTE2012: PI-0020

Design and Feasibility Study of Smart Grid System for PV Power Generation

Md. Jahangir Hossain, Md. Rafiqul Islam
Department of Electrical and Electronic Engineering, Khulna University of Engineering & Technology, Khulna
E-mail: jhossain2k2@gmail.com, rafiq043@yahoo.com

ABSTRACT
This paper briefly discuss about the design procedure and financial feasibility study of smart grid for quality power generation. The proposed smart grid has been shown satisfactory performance for enable consumers to accomplish their demand most economically and efficiently. The cost analysis procedure is clearly described and compare between on and off grid system. A techno economic feasibility analysis has done for commercial building of 10 kWp on-grid photo voltaic (PV) system at south west zone of Bangladesh. Facing the challenge of grid energy demand, climate change and carbon emissions reduction, the proposed PV system is the key obligation to ensure energy security and the balance economic growth.

KEY WORDS: Smart grid, PV system, carbon emission reduction, feasibility study, quality power.

1. INTRODUCTION

Photovoltaic (PV) system is considered as a clean and environmentally-friendly source of energy. The main applications of PV systems are in either standalone or grid connected configurations [1]. The application of on grid PV system is known as smart grid. The electrical grid essentially consists of generation, transmission and distribution system to accomplishment of the consumers demand. In a smart grid all the four subsystems are smart or intelligent [2]. A strong, smart grid is an interconnected system of electricity generation, transmission, distribution, and end-use technologies. That enables consumers to manage their power usage and choose the most economically efficient products and services [3]. The electricity delivery system's reliability and stability enhanced by using the automatic controlling system that improves the quality of services.

PV generation systems have two major problems which are related to low conversion efficiency especially in low irradiation conditions and the amount of electric power generated by PV arrays varies continuously with weather conditions [4]. In an off grid PV system require large capacity battery back up because generation of PV energy is proportional to irradiation condition. This problem will occur severely during rainy season because of cloud in sky and winter season due to fog. To avoid this redundant situation many researcher suggest taking five to three days of autonomy for off grid PV system. For this reason larger capacity storage battery requires [5]. On the other hand, for an on grid system, the grid and PV system are the alternative source for each other. Though back up power will be required to meet the peak demand as well as grid failure condition. The irradiation reduces particularly in rough weather condition, PV generation diminish. The environmental temperature decreases as well as electricity demand reduces. To accomplish the demand smaller capacity back up battery is required. In this reason initial investment, operation and periodic cost of off grid PV system is much higher than on grid system.

The smart grid enables real-time, two-way infrastructure development of the whole electrical system, among generation, transmission, distribution and end-use consumption. Smart grid also allows for real-time pricing information, so that consumers can make decisions about their timing of electricity use. This does not mean that consumers must continuously monitor pricing information; smart meter incorporating real-time pricing information helps shift consumption from times of peak usage to times of lower usage [6]. Consequently, distributed generation could decrease the risk of large scale power outages; making use of distributed space for small scale installations, and placing generation closer to consumption so as to reduce transmission losses as well as the need for new transmission capacity.

The smart grid will bring several quantifiable benefits and many other significant reimbursement exist that will not become apparent until the smart grid begins to be implemented. Many research works has been done to implement the smart grid [7]-[8]. To the best of our knowledge, there is no detail understanding about the design procedures and feasibility study of the smart grid. In this paper, the

design procedure and feasibility study analysis of smart grid system has been described for reliable and quality power generation. In addition to this a comprehensive cost analysis has been done to understand the comparison between on and off grid system.

2. DESIGN OF THE PROPOSED SYSTEM

The on-grid systems are installed in those areas where grid is present and robust, and able to accept energy feeding from the PV system. Inverter is the interfacing element of on-grid system to interface between PV source and the electrical grid. The electrical energy injected into the grid depends on the amount of power extracted from the PV system and the efficient processing of this power by the inverter [9]. The optimum power received from PV system can be directly feed to the load or grid. Operation of PV system in maximum power point condition has been done by MPPT charge controller and control back up battery charging discharging. Grid and PV system interfacing provisions are incorporate in the inverter having intelligent control of the whole process.

2.1 Procedure

The block diagram of proposed system is shown in Fig.1. This model shows that in rough weather and low irradiation condition PV energy will minimum and grid contribute to meet the consumer's energy demand. On the other hand when PV energy generation is sufficient and consumers are not able to consume the energy then excess energy is automatically exported to the grid. To evacuate the electricity to the grid it is require to voltage, frequency and phase are synchronized with the grid voltage, frequency and phase respectively. If synchronization process are properly achieved generated power are evacuated to grid. Inverter has built in self synchronization process. If it is not properly achieved generated energy will not export and charge the backup battery. Smart meter has bidirectional power measurement facility.

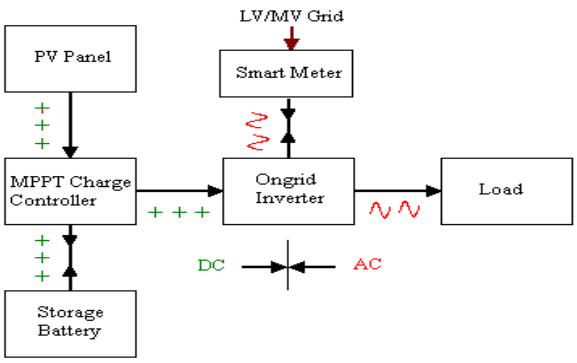

Fig.1 Block diagram of smart grid PV system

Deduction from export and import energy net energy consumption is determined. In addition, due to rough weather or any other reasons, when the PV electricity generation will not be sufficient then the load will automatically transfer to the distribution supply lines. The smart control systems are designed has been shown in Fig.2. Therefore, the system reliability and quality of service is enhanced.

a. 2.2 Flowchart

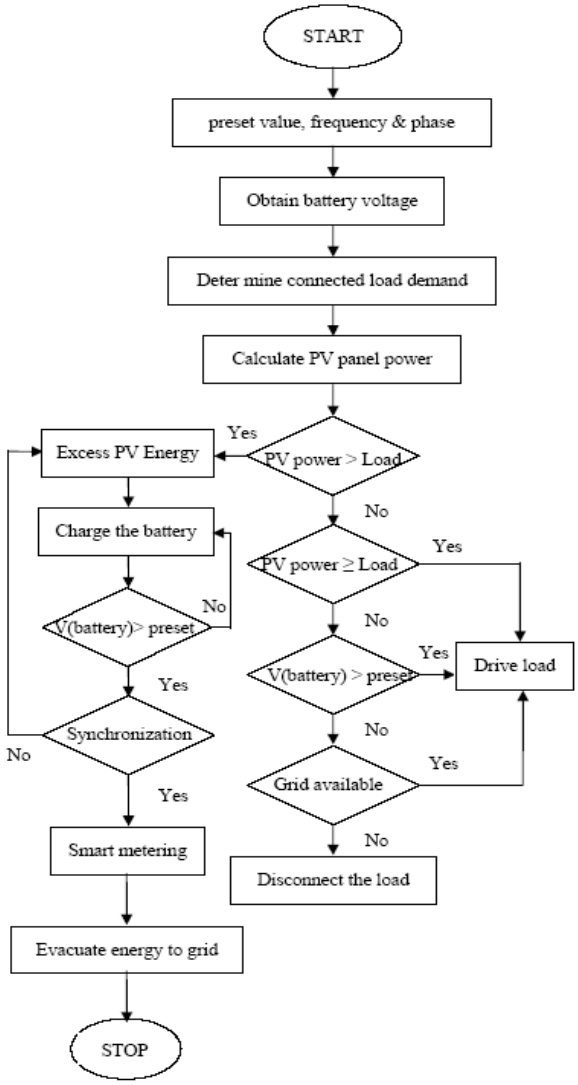

Fig. 2 Flowchart of proposed smart grid system

2.3 Technical Data

Type of the PV module used to design the system is mono-silicon; manufactured by ABC Inc. the module efficiency is 11.7%. Miscellaneous PV array loss 4% are taken, designed nominal PV array power 10kWp, PV array coverage area 85.5 m², on grid PV system inverter efficiency 90% and miscellaneous power conditioning losses 1%. Annual solar energy collected on the surface of 10kWp PV module is

16.07MWh, while renewable energy delivered in the form of electricity is estimated 14.463MWh. The location of the PV power generation project is south west zone of Bangladesh which nearest weather location is Kolkata/Alipore, where Latitude is 22.5 °N, Slope of fixed angle PV array is 30.0°N and azimuth angle is 0.0°. According to satellite data of project location annual solar radiation in horizontal surface 1.77 MWh/m² while, solar radiation in tilted surface 1.85 MWh/m² and average temperature is 26.9 °C. RETScreen computer software tools and monthly average solar radiation data from NASA are taken to feasibility study of the project. Monthly average daily temperature and radiation on the horizontal surface of the plane of PV array are given below.

Table.1 average solar energy radiation & temperature

Month	Monthly average daily radiation		Average temperature (°C)
	horizontal surface (kWh/m²)	plane of PV array (kWh/m²)	
January	3.97	5.08	20.1
February	4.89	5.78	23.0
March	5.53	5.87	27.6
April	6.22	5.94	30.2
May	6.42	5.66	30.7
June	4.92	4.29	30.3
July	4.64	4.12	29.2
August	4.47	4.16	29.1
September	4.64	4.67	29.1
October	4.53	5.08	28.2
November	4.28	5.31	24.9
December	3.83	5.05	20.8

3. COST ANALYSIS

Project costs are analyzed by RETScreen computer software tools and market price of Bangladesh. The costs are expressed by US dollar. Brief description of cost analysis is described in table 2.

Table.2 project cost analysis

Description	Quantity	Unit cost	Amount
Initial Costs			
Feasibility study	1	$ 100	$ 100
Engineering	1	$ 100	$ 100
PV module(s)	10kWp	$ 1,250	$ 12,500
Transportation	1	$ 150	$ 150
Energy equipment	1	$ 85	$ 85
Module support	85.5 m^2	$ 8	$ 684
Inverter	12.0 KW	$ 275	$ 3,300
Backup Battery	1	$ 175	$ 175
Electrical equipment	10 kWp	$ 10	$ 100
System installation	10kWp	$ 15	$ 150
Balance of equipment	1	$ 20	$ 20
Training	5 p-h	$ 50	$ 250
Contingencies	2%	$ 17,614	$ 352
Initial cost total =			$17,966
Annual Operation and Maintenance Cost			
Taxes/ Insurance	1	$ 100	$ 100
O&M labour	12	$ 80	$ 960
Other - O&M	1	$ 60	$ 60
Credit - O&M	1	$ 50	(-$ 50)
Contingencies	2%	$ 1,120	$ 22
Operation and maintenance yearly =			$1092
Periodic Cost			
Inverter replacement	13 yr	$ 3,300	$ 3,300
Battery replacement	6 yr	$ 175	$ 700

4. EVALUATION PROCEDURE

From the standard equation of project planning and feasibility study, the net present value, benefit cost ratio and pay back period are determined by the following equations. Its value is as same as the corresponding value found from RETScreen software. Where i represents the interest rate e is the inflation rate, A_o and A_n is the annual saving and annual net profit respectively. Cc is the capital cost, y denotes the project life time and O&M is the operation and maintenance cost.

4.1 Net Present Value (NPV)

$$NPV = A_n(\frac{1+e}{e-i})[(\frac{1+e}{1+i})^y - 1] - C_c \cdots\cdots\cdots \quad (1)$$

$$NPV = 1726 \times (\frac{1+0.025}{0.025-0.085})[(\frac{1+0.025}{1+0.085})^{25} - 1] - 21266$$

$$NPV = 1108$$

4.2 Benefit Cost Ratio (B/C)

$$\frac{B}{C} = \frac{benefit.of.PV}{capital.cost.of.PV + PV.operating.cost} \cdots \quad (2)$$

$$\frac{B}{C} = \frac{[A_0 - O\&M.cost] \times (\frac{1+e}{e-i})\{(\frac{1+e}{1+i})^y - 1\}}{capital.cost} \cdots\cdots \quad (3)$$

$$\frac{B}{C} = \frac{[2822-1092] \times (\frac{1+0.025}{0.025-0.085})\{(\frac{1+0.025}{1+0.085})^{25} - 1\}}{21266}$$

$$\frac{B}{C} = \frac{22426}{21266} = 1.05$$

4.3 Pay Back Period (Y)

$$y = \frac{capital.cost}{A_0 - O\&M.cost} \cdots\cdots\cdots \quad (4)$$

$$y = \frac{\log\{(\frac{C_c}{A_0})(\frac{e-i}{1+i}) + 1\}}{\log(\frac{e+i}{1+i})} \cdots\cdots\cdots\cdots \quad (5)$$

$$y = \frac{\log\{\frac{21266}{2822} \times (\frac{0.025-0.085}{1+0.085}) + 1\}}{\log(\frac{1+0.025}{1+0.085})} = 9.48$$

5. FEASIBILITY STUDY

For financial feasibility of PV system the following things should be considered. The unit electricity production cost is estimated $0.18, discount rate 8% and considering 2% electricity escalation rate annually to the grid. From the project total annual greenhouse gas emission reduction is estimated to be

12.11 t_{CO2}. The financial feasibility of on grid and off grid PV system is shown in Fig.3. The capital investment cost for on grid system is $17966, annual expenditure $1268, annual saving $2822, IRR (Internal Rate of Return) 8.8%, pay back period 10.4 year and benefit cost ratio 1.07. But for off grid system the capital cost is $36326, annual expenditure $1447, annual saving $1649, IRR -19.40% (negative), pay back period 51.1year and benefit cost ratio 0.03. Periodic maintenance or replacement cost for on grid system is $4000 but for off grid system is $30300. From the above discussion it is clear that more initial investment and periodic cost for off grid PV system IRR is negative and are not feasible. But on grid PV system is profitable and financially feasible. Cash flow statement of on grid system is shown in Fig. 4.

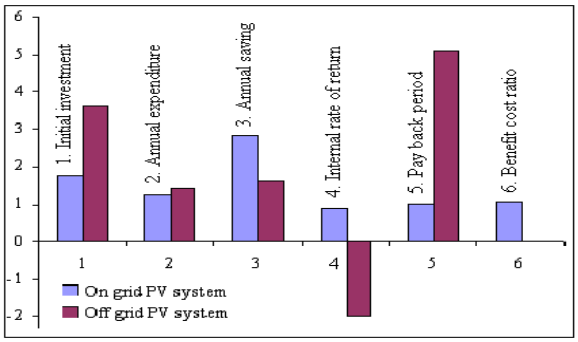

Fig. 3 Comparative study of on & off grid system

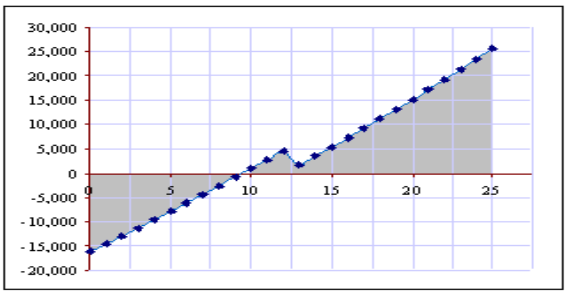

Fig. 4 Cash flow statement of the project

6. CONCLUSION

This paper represents the design procedure of smart grid PV system and its financial feasibility study. Large scale PV system application for smart grid established a contributory two way power flow and significant reduction of carbon emission. Both simulation and mathematical result of 10 kWp on-grid PV system for commercial building at South west zone in Bangladesh is financial feasible. The IRR, payback period and benefit cost ratio of the project are found 8.8%, 10.4 year and 1.07 respectively. In addition a comparative study has been done for on and off grid system. It is clear that on grid PV system shows better performance than off grid PV system. Annual greenhouse gas reduction is estimated to be 12.11 t_{CO2}. The above discussion indicates that this will be one of the key inputs for the smart grid system to meet up the future energy demand.

7. FUTURE WORK

Application of proposed PV system for smart grid will be profitable and popular to the consumer for renewable energy generation that can be the roadmap to meet up future energy demand.

REFERENCES

[1]. Tamer T. N. Khatib, A. Mohamed and N. Amin "A New Controller Scheme for Photovoltaics Power Generation Systems", *European Journal of Scientific Research,* Vol. 33 No. 3 pp. 515-524. 2009.

[2]. Abhishek Khanna, "Smart Grid, Smart Controllers and Home Energy Automation Creating the Infrastructure for Future", *Smart Grid and Renewable Energy*, Vol.3, pp. 165-174 2012.

[3]. N. A. Hidayatullah, Z. J. Paracha and A. Kalam, "Impacts of Distributed Generation on Smart Grid", *International Conference of Electrical Energy and Industrial Electronic System,* pp. 218-221, 2009.

[4]. Salas V., Barrado A., Lazaro A., "Review of the Maximum Power Point Tracking Algorithms for Stand-alone Photovoltaic Systems", *Solar Energy Materials & Solar Cells*- 90, 1555–1578. 2006.

[5]. Bogdan, S. Borowy, and Ziyed M. Salameh, "Methodology for optimally sizing the combination of a battery bank and PV array in a wind / PV hybrid system", *IEEE Transl. Energy conversion,* vol. 11, pp. 367-373, June 1996.

[6]. T. Vijayapriya1, D. P. Kothari, "Smart Grid: An Overview", *Smart Grid and Renewable Energy*, vol. 2, pp. 305-311, 2011.

[7]. P. Farhadi, M. Karimi, B. Moradi and M. Hosseini "Feasibility Study of a Photovoltaic Power Station in the Parsabad Moghan City, Iran" *International Journal of Advanced Renewable Energy Research,* Vol. 1, Issue. 3, pp. 179- 183, 2012.

[8]. Y. El-Tous, Al-Balqa, "A Study of a Grid connected PV Household System in Amman and the Effect of the Incentive Tariff on the Economic Feasibility", *International Journal of Applied Science and Technology,* Vol. 2 No. 2; February 2012

[9]. E. Koutroulis, F. Blaabjerg, "Method for optimal design of grid connected inverter", *Internal Journal on Renewable Energy Research,* Vol. 1, No. 2, pp. 54-64, 2011.

Proceeding of the
International Conference on Electrical, Computer and Telecommunication Engineering
01- 02 December 2012 (ICECTE2012), RUET, Rajshahi-6204, Bangladesh

ICECTE2012: PI-0021

Temperature, Irradiance and Parasitic Resistance Effect on the Photovoltaic Cells/Modules Parameters

Subarto Kumar Ghosh[1], Md. Rakibul Hasan[2], M. R. I. Sheikh[3]
Department of Electrical and Electronic Engineering
Rajshahi University of Engineering & Technology, Rajshahi-6204, Bangladesh
E-mail: subartoeee07@gmail.com[1], rakib071074@gmail.com[2], ris_ruet@yahoo.com[3]

ABSTRACT
This paper represents the simulation of the BP 5200 Monocrystalline solar photovoltaic module using PVsyst software. It is useful to understand the effect of the irradiance, temperature and parasitic resistance on the solar cell and module performance, in order to estimate their I-V curves, P-V curves and Efficiency curves under various climate conditions. A particular typical 170W, 12.92 percent efficiency solar panel was used for model evaluation.

KEYWORDS: Photovoltaic Module, PVsyst software, I-V curves, P-V curves, efficiency curves.

I. INTRODUCTION

Solar cells are in fact large area semiconductor diodes. Due to photovoltaic effect energy of light (energy of photons) converts into electrical current. At p-n junction, an electric field is built up which leads to the separation of the charge carriers (electrons and holes). At incidence of photon stream into semiconductor material the electrons are released, if the energy of photons is sufficient [1]. Simulation tools PVsyst software make PV generation system modeling. The performance of a PV module system depends on the operating conditions as well as the solar cell and array design quality [2]. The output voltage, current and power as well as efficiency of PV array varies as functions of solar irradiation level, temperature and parasitic resistances. Therefore the effects of these three quantities must be considered in the design of PV modules.

This paper is useful to understand the effect of the irradiance, temperature and parasitic resistance on the I-V curves, P-V curves, η-T curves and η-G curves in order to estimate their performance under various climate conditions.

II. BASIC PV CELL

A photovoltaic cell is basically a semiconductor diode whose p–n junction is exposed to light. Photovoltaic cells are made of several types of semiconductors using different manufacturing processes. The monocrystalline and polycrystalline silicon cells are the only found at commercial scale at the present time. Silicon PV cells are composed of a thin layer of bulk Si or a thin Si film connected to electric terminals. One of the sides of the Si layer is doped to form the p–n junction. A thin metallic grid is placed on the Sunfacing surface of the semiconductor. Fig. 1 roughly illustrates the physical structure of a PV cell. The incidence of light on the cell generates charge carriers that originate an electric current if the cell is short circuited [2]. Charges are generated when the energy of the incident photon is sufficient to detach the covalent electrons of the semiconductor—this phenomenon depends on the semiconductor material and on the wavelength of the incident light [2].

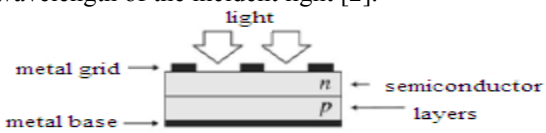

Fig. 1 structure of a PV cell

III. MATHEMATICAL MODEL OF PV CELL

PV modules are built up with series combinations of PV solar cells, which are usually represented by a simplified equivalent circuit model such as the one given in Fig. 2 and/or by an equation as in (1).

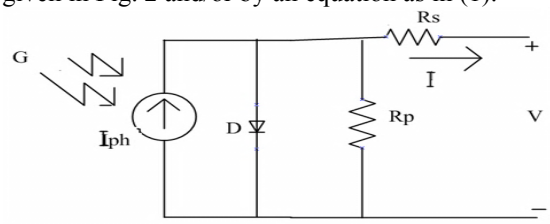

Fig. 2: circuit diagram of the PV model [3]

The voltage current characteristic equation of a solar cell is given as

$$I = I_{ph} - I_o\left(\exp\frac{q.(V + IR_s)}{N.K.T} - 1\right) - \frac{(V + IR_s)}{R_{sh}} \quad (1)$$

Where, Iph is a light-generated current or photo current, Io is the cell saturation of dark current, q (= 1.6 ×10−19C) is an electron charge, k (= 1.38 ×10−23J/K) is a Boltzmann's constant, T is the cell's

working temperature, N is an ideal factor, Rs his a shunt resistance, and Rs is a series resistance. Photo current mainly depend on the solar irradiance and cell's temperature, which is described as

$$Iph = (Iscr + Ki*(Tc + 273.15 - Tr))*G \quad (2)$$

IV. BASIC PARAMETERS OF SOLAR CELLS

There are certain parameters to be mentioned in the I-V characteristics of a solar cell [1].

IV.1 Short Circuit Current

Short circuit current is the light-generated current or Photo current, Iph. It is the current in the circuit when the load is zero in the circuit. It can be achieved by connecting the positive and negative terminals by coppr wire.

IV.2 Open Circuit Voltage

Open circuit voltage is obtained by setting I=0 in the Eq. (1) i.e I=0 when V=Voc and neglecting series and shunt resistances

$$Voc = \frac{N.K.T}{q} \ln\left(\frac{IPh}{Io} + 1\right) \quad (3)$$

The open circuit voltage is the voltage for maximum load in the circuit.

IV.3 Fill Factor

The fill factor, also known as the curve factor (Fig. 3), is a measure of sharpness of the knee in an I-V curve. It indicates how well a junction was made in the cell and how low the series resistance has been made. It can be lowered by the presence of series resistance and tends to be higher whenever the open circuit voltage is high. The maximum value of the fill factor is one, which is not possible. Its maximum value in Si is 0.88:

$$FF = \frac{Pmax}{Voc.\ Isc} = \frac{Vmax}{Voc.\ Isc} \quad (4)$$

A larger fill factor is desirable, and corresponds to an I-V sweep that is more square-like.

IV.4 Maximum Power

No power is generated under short or open circuit. The power output is defined as:

$$Pout = Vout\ .\ Iout \quad (5)$$

The maximum power Pmax provided by the device is achieved at a point on the characteristics, where the product IV is maximum. Thus:

$$Pmax = Vmax\ .\ Imax \quad (6)$$

The maximum possible output can also be given as

$$Pmax = Voc\ .Isc\ .\ FF \quad (7)$$

Where FF is the fill factor given by Eq (4).

IV.5 Solar Cell Efficiency η

The solar cell power conversion efficiency can be given as:

$$\eta = \frac{Pmax}{pin} = \frac{Vmax.\ Imax}{Pin} = \frac{Vmax.\ Imax}{I(t).\ Ac} \quad (8)$$

Where Imax and Vmax are the current and voltage for maximum power, corresponding to solar intensity I(t).

V. SIMULATION OF SOLAR PV MODULE PARAMETERS IN PVSYST SOFTWARE

The unknown parameters of the model can be obtained using PVsyst software and the parameters specified by the manufacturer. To illustrate and verify the nonlinear I-V, η-T, η-G and P-V output characteristics of PV module model is simulated for different solar insolation, temperature and parasitic resistances and shown in fig. (3-12) the specifications (at 1kW/m2, 25˚C) of the BP 5200 solar module used for simulation are given in Table 1.

Table 1 Specification of the simulated module

Parameter	Variable	Value
Maximum power	Pm	170 W
Voltage @ Pm	Vmpp	18.0 V
Current @ Pm	Impp	9.440 A
Short circuit current	Isc	10 .00 A
Open circuit voltage	Voc	22.00 V
Temp. coeff of Voc	β	0.073 %/^{0}c
Temp. coeff of Isc	α	0.024 %/^{0}c
Ideality factor	N	1.29
Efficiency /Module area	η	12.92 %

The developed model is simulated for different solar insolation level as shown in Fig. 3 and similarly for different temperature and different parasitic resistance. The results of simulation are shown in Figs. (3-12). The figures shows that with increase of working temperature, the short-circuit current of the PV cell increases, whereas the maximum power output decreases which also decreases the efficiency of solar module. In as much as the increase in the output current is much less than the decrease in the voltage, the net power and efficiency decreases at high temperatures. On the other hand, with increase of solar insolation, the short-circuit current of the PV module increases, and the maximum power output and efficiency increases as well. The reason is the open-circuit voltage is logarithmically dependent on the solar irradiance, yet the short-circuit current is directly proportional to the radiant intensity. The PV cell model of Fig. 2 has two loss representative component Rs and Rsh. The effect of increasing value of Rs can be seen under PVsyst software. Higher the value of Rs indicating the more power loss are corresponding the efficiency decreases. The resultant characteristics curve is shown Fig. 9 and 11. Also the effect of decreasing value of Rsh indicating higher power loss and low fill factor. The efficiency is directly proportional the fill factor so decreases the fill factor corresponding efficiency decreases. The

resultant characteristic curve is shown Fig. 10 and 12.

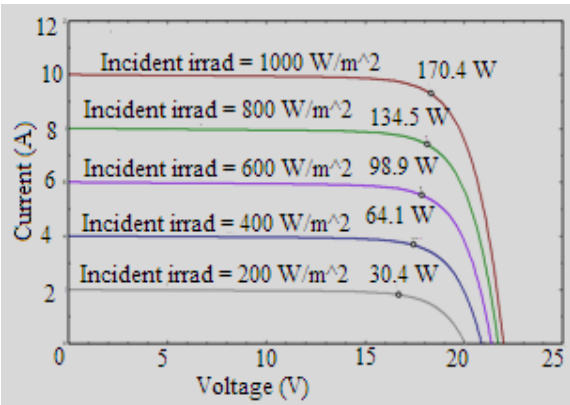

Fig. 3: I-V Characteristic curves at different insolation levels (BP 5200, G=0.2 sun, 0.4 Sun, 0.6 Sun, 0.8 sun, 1 sun)

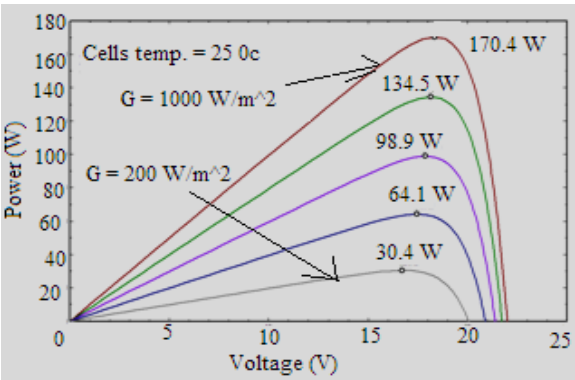

Fig. 4: P-V Characteristic curves at different insolation levels (BP 5200, G=0.2 sun, 0.4 Sun, 0.6 Sun, 0.8 sun, 1 sun)

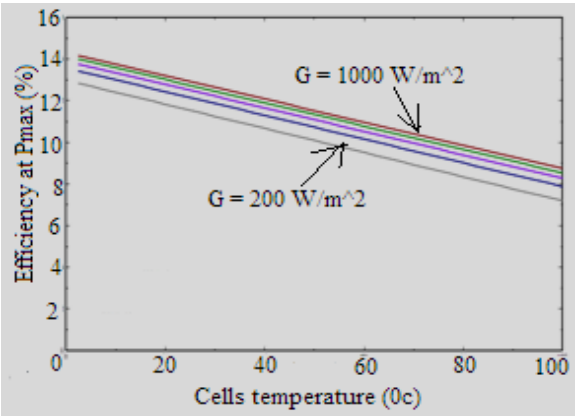

Fig. 5: η-Tc Characteristic curves at different insolation levels (BP 5200, G=0.2 sun, 0.4 Sun, 0.6 Sun, 0.8 sun, 1 sun)

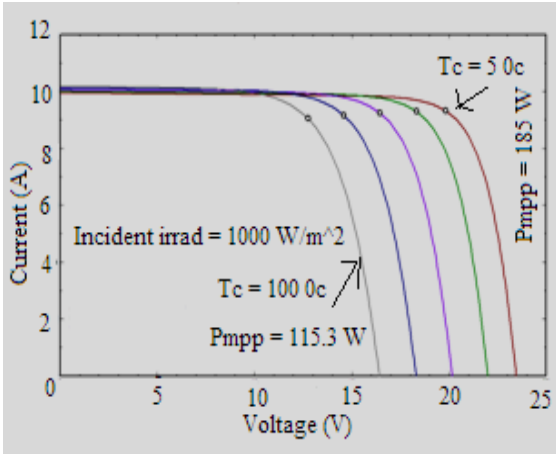

Fig. 6: I-V Characteristic curves at different cells working temperature (BP 5200, Tc = 5^0c, 25^0c, 50^0c, 75^0c, 100 ^{0}c)

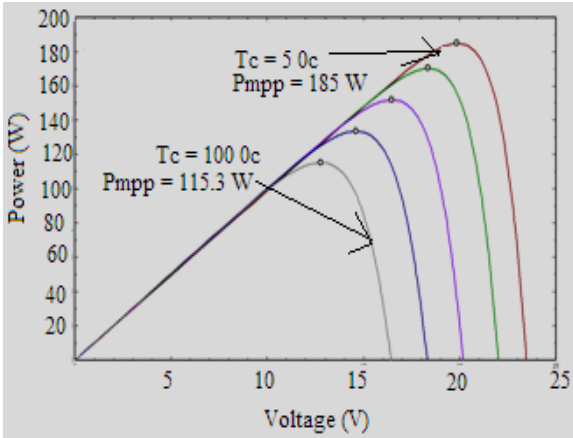

Fig. 7: P-V Characteristic curves at different cells working temperature (BP 5200, Tc = 5^0c, 25^0c, 50^0c, 75^0c, 100 ^{0}c)

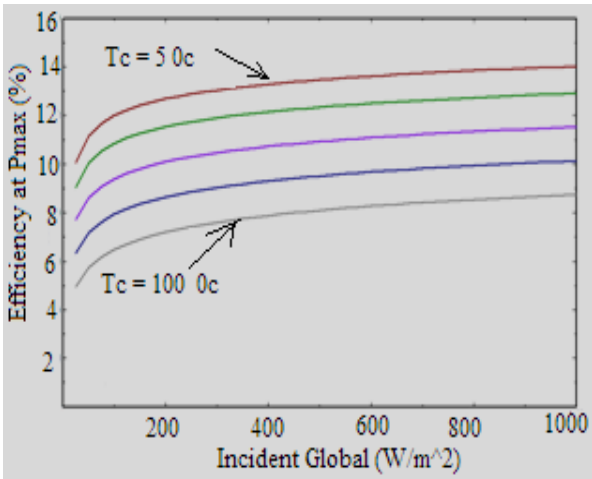

Fig. 8: η-G Characteristic curves at different cells working temperature (BP 5200, Tc = 5^0c, 25^0c, 50^0c, 75^0c, 100 ^{0}c)

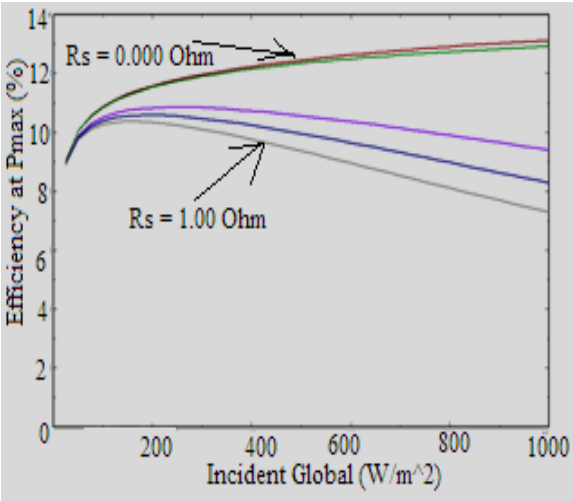

Fig. 9: η-G Characteristic curves at different series resistances (Rs = 0 Ω, 0.033 Ω, 0.6Ω, 0.80 Ω, 1.0 Ω)

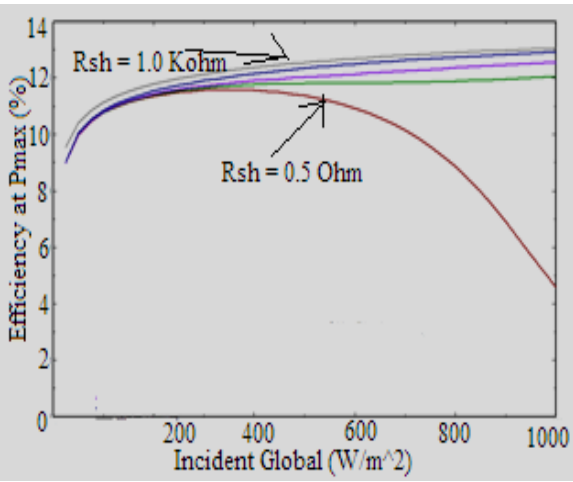

Fig. 10: η-G Characteristic curves at different shunt resistances (Rsh = 0.5Ω, 25 Ω, 50 Ω, 160 Ω, 1.0KΩ)

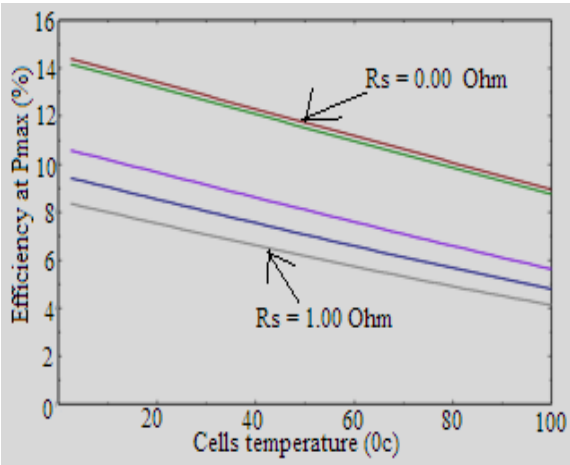

Fig. 11: η-Tc Characteristic curves at different series resistances (Rs = 0 Ω, 0.033 Ω, 0.6Ω, 0.80 Ω, 1.0 Ω)

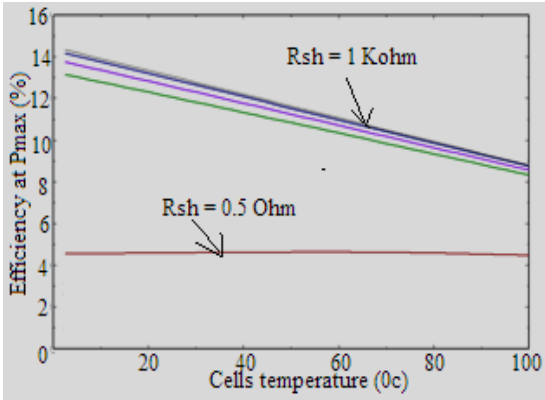

Fig. 12: η-Tc Characteristic curves at different shunt resistances (Rsh = 0.5Ω, 25 Ω, 50 Ω, 160 Ω, 1.0 KΩ)

VI. CONCLUSIONS

The PVsyst takes solar radiation intensity, cell temperature and parasitic resistance as input and outputs the I-V, P-V, η-Tc and η-G characteristics under various conditions.

VII. FUTURE WORK

The final objective is develops a general model to analyze the characteristics and problems of grid connected PV systems.

VIII. ACKNOWLEDGEMENTS

I would like to thank Dr. Md. Rafiqul Islam Sheikh, Professor, Department of Electrical and Electronic Engineering, Rajshahi University of Engineering & Technology for her effort in this research editing.

REFERENCES

[1]. A. Blorfan, D. Flieller, P. Wira, G. Sturtzer, J. Merckle, "A New Approach for Modeling the Photovoltaic Cell Using Orcad Comparing With the Model Done in Matlab",*International Review on Modeling and Simulations* Vol. 3, N. 5, PP. 948-954, Oct. 2010. 5.

[2]. J. Surya Kumari, and Ch. SaiBabu,"Mathematical Modeling and Simulation of Photovoltaic Cell using Matlab-Simulink Environment", *International Journal of Electrical andComputer Engineering (IJECE)* Vol. 2, No. 1, PP. 26-34, Feb. 2012. 7.

[3]. Sonal Panwara, Dr. R. P. Saini, "Development and Simulation of Solar Photovoltaic model using Matlab/simulink and its parameter extraction", *International Conference on Computing and Control Engineering,* 12 & 13 April, 2012.

[4]. Gwinyai Dzimanu, "Modelling of Photovoltaic System", The Ohio State University 2008.

[5]. Castañer, Luis & Santiago Silvestre, "Modelling Photovoltaic Systems,Using PSpice" John Wiley & Sons Ltd, 2002.

Proceeding of the
International Conference on Electrical, Computer and Telecommunication Engineering
01- 02 December 2012 (ICECTE2012), RUET, Rajshahi-6204, Bangladesh

ICECTE2012: PI-0022

MATLAB Programming Based Study of Photovoltaic Modules/Arrays

Subarto Kumar Ghosh[1], Md. Rakibul Hasan[2], M. R. I. Sheikh[3]
Department of Electrical and Electronic Engineering
Rajshahi University of Engineering and Technology, Rajshahi-6204, Bangladesh
E-mail: subartoeee07@gmail.com[1], rakib071074@gmail.com[2], ris_ruet@yahoo.com[3]

ABSTRACT
This paper represents the simulation of the BP SX110 Polycrystalline silicon solar photovoltaic module using MATLAB programming. Taking the effect of sunlight irradiance, cell temperature, series resistance, shunt resistance and ideality factor into consideration the output current and power characteristics of PV model are simulated and optimized using the MATLAB programming. A particular typical 110W solar panel was used for model evaluation, the results have been compared with points taken directly from the manufacturer's published curves and show excellent correspondence to the model.

KEYWORDS: Modeling and behavior, Photovoltaic module/array, MATLAB Programming.

1. INTRODUCTION

Photovoltaic's (PVs) are arrays (combination of cells) that contain a solar voltaic material which converts solar energy into electrical energy. PV cell is a basic device for Photovoltaic Systems. Such systems include multiple components like mechanical and electrical connections and mountings and various means of regulating and (if required) modifying the electrical output. Materials that are used for photovoltaic are mono-crystalline silicon, polycrystalline silicon, microcrystalline silicon, cadmium telluride and copper indium selenide [1]. The current and voltage available at the PV device terminals can be directly used to feed small loads like lighting systems or small DC motors. The output characteristics of PV module depends on the solar irradiance, the cell temperature and output voltage of PV module. Since PV module has nonlinear characteristics, it is necessary to model it for the design and simulation of maximum power point tracking (MPPT) for PV system applications. Almost all well-developed PV models describe the output Characteristics mainly affected by the solar irradiance, cell temperature, and load voltage [2]. The PV application can be grouped depend the scheme of interaction with utility grid: grid connected, stand alone, and hybrid.

The main contribution of this paper is the implementation and modeling of a BP SX110 PV module in the form of MATLAB programming on the basis of Shockley diode equation.

2. PV CELL MODEL

A general mathematical description of I-V output characteristics for a PV cell has been studied over the past four decades. Such an equivalent circuit based model is mainly used for the MPPT technologies. The equivalent circuit of the general model which consist of a photocurrent, a diode, a parallel resistor expressing a leakage current, and a series resistor describing an internal resistance to the current flow, is shown in Fig. 1 (a)

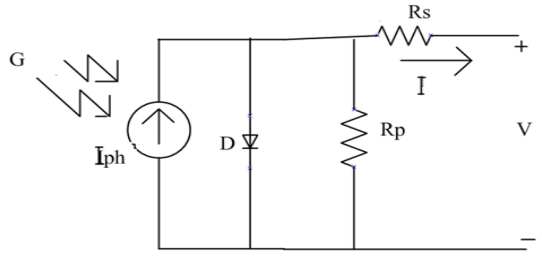

Fig. 1(a): circuit diagram of the PV model [3]

The voltage current characteristic equation of a solar cell is given as

$$I = Iph - Io\left(\exp\frac{q.(V+IR_s)}{N.K.T} - 1\right) - \frac{(V+IR_s)}{R_{sh}} \quad (1)$$

Where, Iph is a light-generated current or photocurrent, Io is the cell saturation of dark current, q (= 1.6 ×10−19C) is an electron charge, k (= 1.38 ×10−23J/K) is a Boltzmann's constant, T is the cell's working temperature, N is an ideal factor, Rsh is a shunt resistance, and Rs is a series resistance. Photo current mainly depend on the solar irradiance and cell's temperature, which is described as

$$Iph = (Iscr + Ki*(Tc + 273.15 - Tr))*G \quad (2)$$

Where, Iscr is a cell's short current at a 25^0c and $1kw/m^2$, Ki is a cell's short circuit current temperature coefficient, Tr cell's reference temperature, G solar irradiance in kw/m^2.

Also the cell's saturation current varies with cell temperature, which is described as

$$Io = I_{OR}*(\frac{TC}{TRef})^3*\exp(\frac{q*Eg(\frac{1}{TRef} - \frac{1}{TC})}{K.N}) \quad (3)$$

$$Tc = ((NOCT-20)*G/0.8) + (Ta) \quad (4)$$

Where, I_{OR} is the cell reverse saturation current at a reference temperature and a solar irradiance, NOCT is a nominal operating cell temperature, Eg is the band gap energy of the semiconductor used in the cell. The ideality factor N dependent on PV technologies. The complete behavior of PV cells are described by five model parameters (Iph, N, Is, Rs, Rsh) which is representative of a physical PV cell/module. These five parameters of PV cell/module are in fact related to two environmental parameters of solar irradiance & temperature and owing to non-linear nature of Eq. (1).

3. SOLAR MODULE AND ARRAY MODEL

Since a typical PV cell produces less than 2W at 0.5V approximately, the cells must be connected in series-parallel configuration on a module to produce enough high power. A PV array is a group of several PV modules which are electrically connected in series and parallel circuits to generate the required current and voltage. The scaling rules of voltages, currents and resistances when a matrix of $N_S \times N_P$ solar cells is considered are the following:

Iph = Np*Iph, Io = Np*Io, V = N_S*V, R_S = (N_S/N_P)*R_S. So for the new equation of PV module given following from equation (1):

$$I = Np*Iph - Np*Io\,(\exp(\frac{q\,(\frac{V}{NS} + \frac{IRs}{Np})}{N.K.T}) - 1) - (\frac{NpV}{Ns} + IRs)/Rsh \quad (5)$$

In most commercial PV products, PV cells are generally connected in series configuration to form a PV module in order to obtain adequate working voltage. PV modules are then arranged in series-parallel structure to achieve desired power output. It can be shown that Ns= Np= 1 for a PV cell, Np=1 and Ns: series number of cells for a PV module, and N_S and N_P : series-parallel number for a PV array. An appropriate equivalent circuit for all PV cell, module, and array is generalized and expressed in Fig. 1(b).

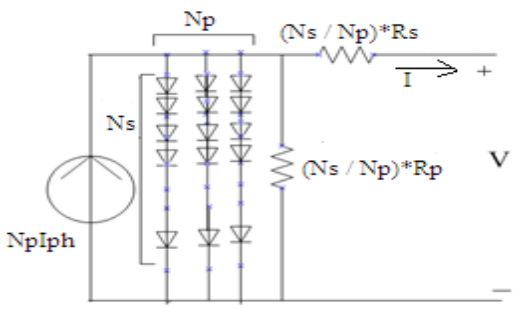

Fig. 1(b): Equivalent circuit models of generalized PV modules/array [4].

4. ROGRAMMING OF PV MODULE IN MATLAB

The circuit model of Fig. 1(a) readily offers an investigation in variation of four model parameter of which N are related to Diode model, one Iph is related to light or photon generated current and resistance Rs and Rsh represent various losses in PV cell. In this section, effect of variation of these four parameters and their influence on V-I graph of PV Cell is studied using MATLAB programming. The BP SX110 solar PV module was chosen for modeling, due is well-suited to traditional applications of photovoltaic's. The BP SX110 module provides 110 watt of nominal maximum power, and has 72 series connected polycrystalline silicon cells. The key specifications are shown in Table 1. The model of the PV module was implemented using a Matlab program. The model parameters are evaluated during execution using the equations listed on the previous section. The program calculate the current I, using typical electrical parameter of the module (I_{SC}, V_{OC}), and the Variables Voltage, Irradiation (G), and Temperature (T).

Table1

Typical Electrical Characteristics of BP SX110 Polycrystalline PV Module.

Parameter	Variable	Value
Maximum power	Pm	110W
Voltage@ Pm	Vm	32.9V
Current@ Pm	Im	3.34A
Short circuit current	Isc	3.69A
Open circuit voltage	Voc	41.2V
Temp. coeff of Voc	β	-0.38%/^{0}c
Temp. coeff of Isc	α	0.065%/^{0}c
Normal operating cell temperature	NOCT	47^{0}C

The performance of solar cell is normally evaluated under the standard test condition (STC), where an average solar spectrum at AM 1.5 is used, the irradiance is normalized to 1000W/m2, and the cell temperature is defined as 25 ºC.

5. RESULTS OF MATLAB PV MODULE MODEL

5.1 Diode Parameter (N) Variation

Fig. 2(a) shows 'V-I characteristics' of a PV cell for three different values of N corresponding to 1.5, 1.73 & 1.96 respectively. It can be observed that as we increase the value of N the open circuit voltage of cell increases and this fact may effectively be used in simulation of a PV module

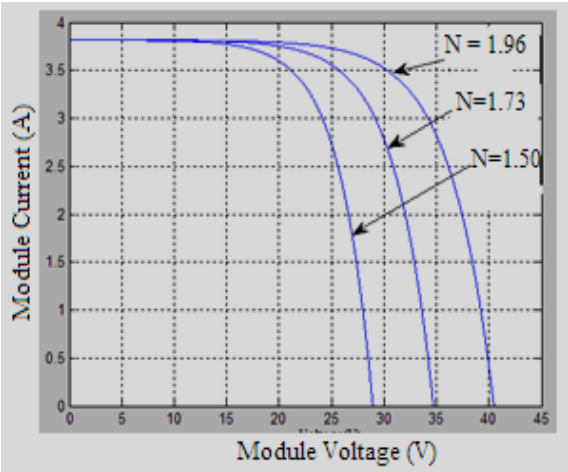

Fig. 2(a) Matlab model I-V curves, for various diode quality factors (BP SX110, G= 1 Sun, T = 25°C, N = 1.5, 1.73 and 1.96)

5.2 Variation in Rs

The PV cell model of Fig. 1(a) has two loss representative component Rs and Rsh. The effect of increasing value of Rs can be seen under MATLAB programming. The simulation is produced for three values of Rs as 0Ω, 0.007Ω, and 0.0014Ω. Higher the value of Rs indicating the more power loss. The resultant V-I characteristics curve is shown below:

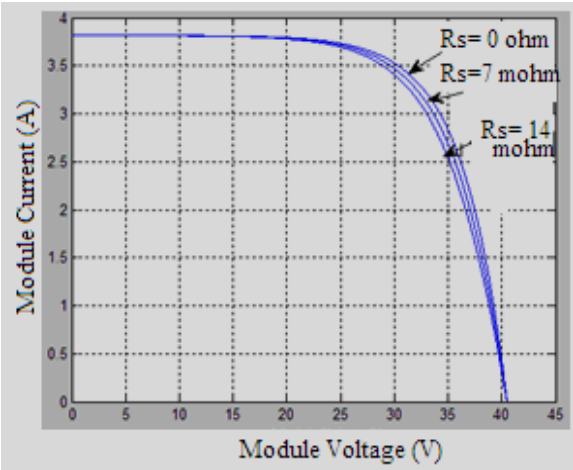

Fig. 2(b): PV Cell Characteristics for varying 'Rs'

5.3 Variation in Rsh

The simulation is produced for two different values of Rsh as 5 kΩ and 20 Ω. It is observed that the smallest value of Rsh causes PV module current to fall more steeply indicating higher power loss and low Fill Factor. The resultant V-I characteristics curve is shown below:

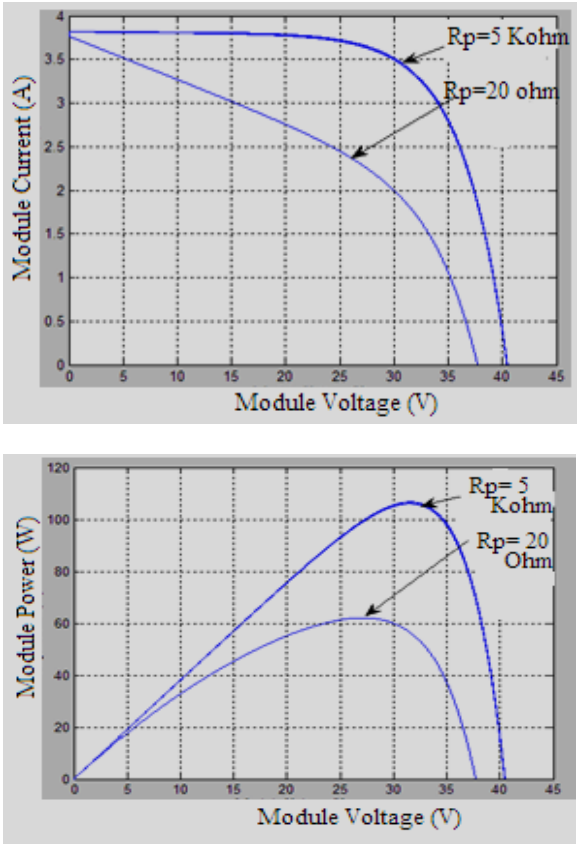

Fig. 2(c): Matlab model I-V and P-V curves, for various shunt resistance (BP SX110, G= 1 Sun, T = 25°C, Rp=20 ohm, 5 Kohm)

5.4 PV Cell under Reduced Irradiance

The two environmental conditions of Solar Irradiance and Temperature govern output of a PV Cell. The Matlab programming is used to demonstrate behavior of PV module under varying solar irradiance. The photon generated current Iph is in fact related with solar Irradiance G as in Eq. (2). The output of the Matlab function is shown various irradiation levels

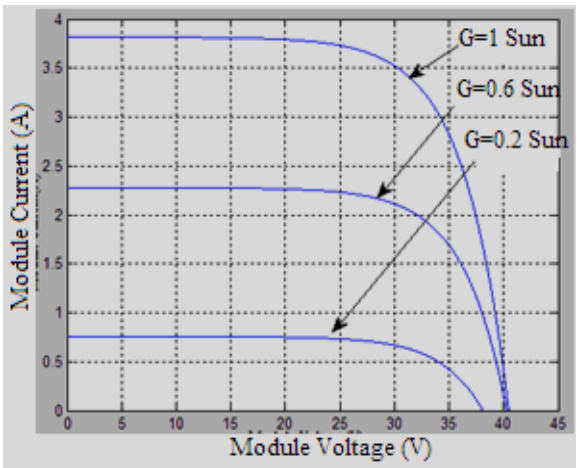

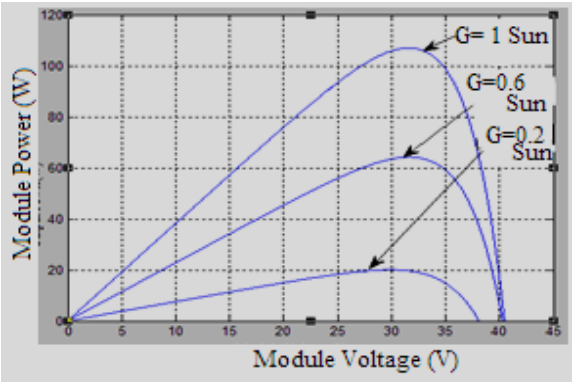

Fig. 2(d): Matlab model I-V and P-V curves for various irradiation levels (BP SX110, G=0.2, 0.6 Sun, 1 Sun, T=25^{0}C)

5.5 PV Cell under Varying Temperature

The effect of varying temperature on PV cell output is twofold: (i) It affects short circuit current 'Isc ' of Cell (ii) It changes saturation current of the diode in PV cell approximately as cubic power. Obviously from Eq. (3) the saturation current of diode of PV Cell is highly temperature dependent and it increases with increase in temperature and is taken care by Matlab programming. To study the effect of Temperature variation on PV Module output,

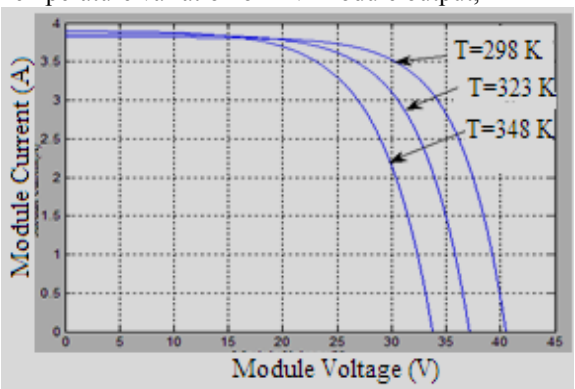

Fig. 2(e): Matlab model I-V curves for various Temperature levels (BP SX110, G=1Sun, T=25^{0}C, 50^{0}C, 75^{0}C)

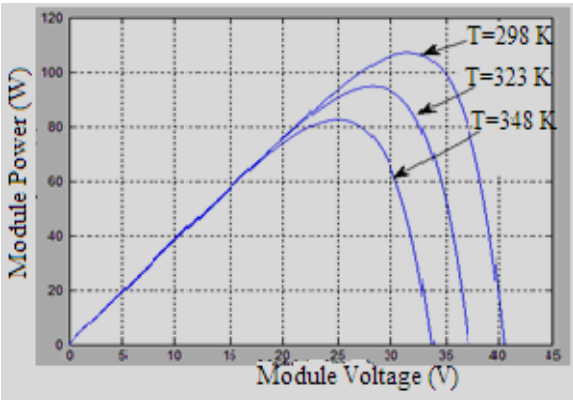

Fig. 2(f): Matlab model P-V curves for various temperatures (BP SX110, G=1Sun, T=25^{0}C, 50^{0}C, 75^{0}C)

6. CONCLUSIONS

An accurate PV module electrical model is presented and demonstrated in Matlab for a typical 110W solar panel. Given solar irradiance and temperature, the model calculates the current for a given voltage. The results from the Matlab model show excellent correspondence to manufacturer's published curves. Finally the model development was used to show the effect of irradiance, temperature, ideality factor, shunt resistance and series resistances.

7. FUTURE WORK

The MATLAB programming result in this paper verify the accuracy of the characteristics for the established solar module model. The final objective is develops a general model to simulate the electrical behavior of the PV systems in a grid connected application.

8. ACKNOWLEDGEMENTS

The authors thank to Dr. Md. Rafiqul Islam Sheikh, Professor, Department of Electrical and Electronic Engineering, Rajshahi University of Engineering & Technology for his valuable contribution to this paper.

REFERENCES

[1]. Sushen Narkhede, Rajpritam, "Modeling of Photovoltaic Array", pp. 7-21

[2]. Kinal Kachhiya, Makarand Lokhande, Mukesh Patel, "MATLAB/Simulink Model of Solar PV Module and MPPT Algorithm", *National Conference on Recent Trends in Engineering and Technology,* May. 2011. 3

[3]. R. K. Nema, Savita Nema, Gayatri Agnihotri, " Computer Simulation Based Study of a Photovoltaic Cells/Modules and their ExperimentalVerification", *International Journal of Recent Trends In Engineering*, vol.1, no. 3, pp. 151-156, 2009.5

[4]. Huan-Liang Tsai, Ci-Siang Tu, Yi-Jie Su, "Devlopment of Generalized Photovoltaic Model using MATLAB/SIMULINK", *Proceeding of the World Congress on Engineering and Computer Science*, pp. 846-854, Oct. 2008. 8

[5]. Akihiro Oi, "Design and Simulation of Photovoltaic Water Pumping System", pp. 10-26, 2005.15

[6]. J. Surya Kumari, Ch. SaiBabu, "Mathematical Modeling and Simulation of Photovoltaic Cell Matlab-Simulink Environment", *International Journal of Electrical and Computer Engineering* vol. 2, no. 1, pp.26-34, 2012.8

Renewable Energy Based Wireless Power Transmission to Electric Vehicles for Fuel Consumption

Md. SazzadHossain, AmitBarua

Electrical & Electronic Engineering, Rajshahi University of Engineering and Technology(Md. SazzadHossain)

Mechanical Engineering, Rajshahi University of Engineering and Technology (AmitBarua)

Email: samu.ruet.eee@gmail.com, amit.barua7191@gmail.com

ABSTRACT:*IN MODERN DAYS, FUEL ENERGY HAS BECOME A CRISIS BECAUSE THEY HAVE A CONCENTRATED STORAGE. SO,NOW RENEWABLE ENERGY PLANT IS NEEDED TO COVER MORE SECTORS NOT ONLY POWER BUT ALSO IN RUNNING VEHICLES. ALL TRANSPORT SYSTEM WILL BE RUN BY THIS AVAILABLE ENERGY.ELECTRICITY WILL BE TRANSFORMED INTO MICROWAVE BEAM AND THEN CHARGE THE VEHICLE AND IT WILL HELP TO RETAIN OUR ENVIRONMENT CLEAN WITHOUT POLUATION. AS WELL AS HUMAN LIFE WILL ALSO BECOME HEALTHFUL. THIS WIRELESS POWER TRANSFER SYSTEM MAY REDUCE THE DEMAND OF FOSSIL FUELS .ELECTRIC VEHICLE (EV)AND PLUG IN HYBRID EV ARE THE SAMPLE OF THIS SYSTEM. THEY CAPTURE MICROWAVE BEAM AS A REPLACEMENT OF FUEL.*

KEYWORDS:Renewable energy plant, Phased array antenna, Microwave beam, Electric vehicle(EV), Fuel consumption.

1.INTRODUCTION During the last few decades, the fuel based transport system polluted environment. So two electric vehicle (EV) Battery based electric vehicles(BEV) and Plug in hybrid vehicle(PHEV) are best idea for fuel consumption and zero emission. This sort of vehicles differ from fuel based system and it will run by renewable energy through wireless power transmission system via microwave beam. Electricity may stored using battery, flywheel and supercapacitor**[5]**. Wireless power transmission via microwave advanced from WC Brown invented microwave powered helicopter. The phased array antenna transmit microwave beam and this will be collected by rectenna used in EV. In this paper EV will charged by wirelessly microwave beam for fuel reduction and lessen CO_2emission.

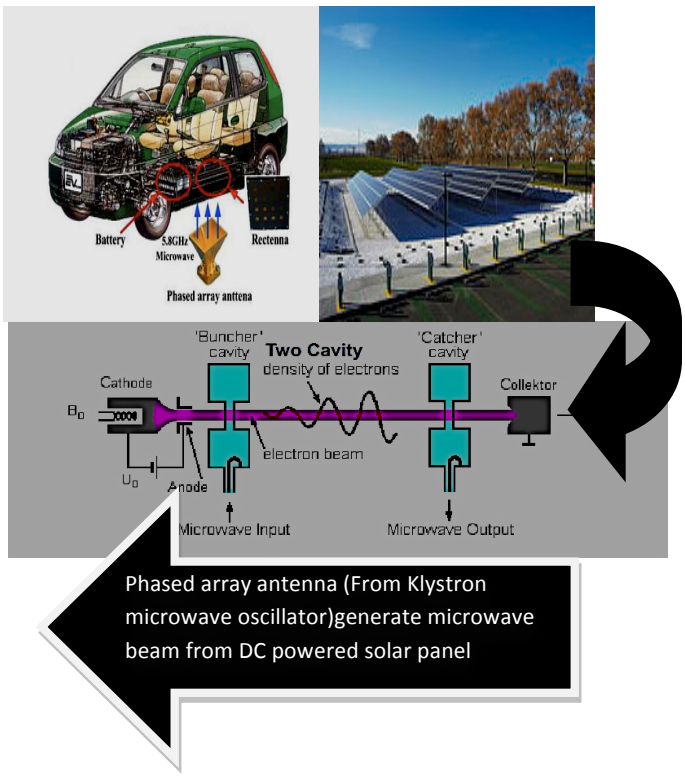

Fig 1: Concept of wireless power transmission in electric vehicle.**2 POWER FROM RENEWABLE ENERGY SOURCE**

Electrical power can be captured by renewable source such as 1. Bio-mass 2.Geo-thermal power 3. Radiant energy 4. Hydroelectricity plant 5. Wind power 6. Solar power 7.Wave power 8 .Tidal power.About 16% of global final energy

consumption comes from renewable sources, with 10% coming from traditional biomass and 3.4% from hydroelectricity. Wind power is growing at the rate of 30% annually inworldwide**[2].2.1 Renewable energy plant in recharging station** For charging vehicles there should be a renewable energy plant which need to establish in vehicle station It will charge up via microwave beam in Electric vehicle(EV) or Hybrid electric vehicle(HEV). There need some supporting station by road side from where EV or HEV can easily charge up. And this supporting station may have solar plant or wind energy plant for supplying electricity.**2.2Power transmission system**From power plant energy will transmit through multipurpose way via smart grid and a portion of power will supply to Vehicle station. Those who have vehicle own they will charge it in their house. They need to set a charge system where vehicle get power via wireless transmission system. **3 MICROWAVE BEAM PRODUCTION3.1 Phased array transmitting antenna** Phased array transmitting antenna radiate microwave beam to electric hybrid car's rectenna. Microwave beam need to be retro-directive and a PLL-Heterodyne type retro-directive system which generate microwave beam at 3.85GHz and 5.78GHz**[6].3.2Rectenna in hybrid vehicles** Arectenna is capable of receiving microwave energy and converting the received microwave power back to usable low or DC power and stored in vehicle battery. A basic rectenna consists of an antenna, a dipole rectifier and a dc bypass filter. In hybrid vehicles an aperture coupled micro-strip patch antenna (ACMPA) is suitable for capture power beam because they have more advantages and better prospects like they are lighter in weigth, low volume, low cost, low profile, smaller in dimention and ease of fabrication and conformity**[3]**.

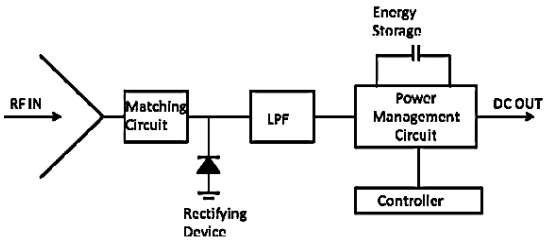

Fig 2: Schematic of rectenna associated with power management circuit in hybrid vehicle.

The RF power ***Prf*** received by the antenna is a function of the incident power density(**S**), effective area of the antenna (**A**eff), incident angle and frequency. The DC power calculated from RF power, convertion efficiency and the DC load impedence (**Z**dc).The fluctuation in the incident power density will alter the conversion efficiency and subsequently the outout***Pdc*** power at rectenna at eqn(2):

$$\mathbf{Prf} = \frac{1}{\mathrm{fhigh-flow}} \int_{\mathrm{f\,low}}^{\mathrm{f\,high}} \int_0^{4\pi} \mathbf{S}(\theta, \varphi, \mathrm{f}, \mathrm{t})\mathbf{Aeff}(\theta, \varphi, \mathrm{f})\mathrm{d}\Omega\mathrm{df} \quad (1)$$

$$\mathbf{Pdc} = \mathbf{Prf}(\mathrm{fi}, \mathrm{t})\eta(\mathbf{Prf}(\mathrm{fi}, \mathrm{t}), \rho, \mathbf{Zdc}) \quad (2)$$

3.3Rectenna specification (i)Micro-strip antenna having a HSMS 8202 Schottky diode is chosen for rectifying circuit which shows the maximum gain as 6.2dBi at the frequency of 5.8GHz with PTFI (Teflon)board. A broadband capacitor C08BLBB1X5UX is chosen as the DC pass filter**[1].**(ii)Amicrostrip harmonic rejection antenna at 2.45GHz which having maximum efficiency 77.8% using 150 ohm load resistor**[1]**(iii)Circular polarization (CP) has more fade resistant than linear polarization and low polarization loss between transmitting and receiving antennas. T.C Yo et al. proposed a compact CP which use double rectifier gives 78% of RF-DC conversion efficiency at 16.5mW/cm² incident power. The conversion efficiency of the CP rectennagivenby eqn(3)

$$\eta = \frac{\frac{Vd^2}{Rl}}{PtGtGT\left(\frac{\lambda o}{4\pi r}\right)^2 Lpol} \quad \mathbf{(3)}$$

Pt= Transmit power, Gt=Gain of transmitting antenna,GT=Gain of rectenna, Lpol=Polarization loss factor, Vd=Output voltage. (iv)For High efficiency measurement single element antenna uses a CPS band reject filter to suppress the reradiated harmonic by more than 19dB and achieve 81% RF to DC conversion efficiency at 5.71GHz. J.O Mcspadden, L.Fan and K. Chang designed a high efficient rectenna element in which they use a silicon Schottky barrier mixer diode with a low breakdown voltage as the rectifying device and its efficiency 82%. **4 ENERGY STORAGE4.1 Battery Technologies**

Transformation of microwave beam into DC power and it stored in Battery.Ultrahigh-speed flywheels appears to be a feasible means for fulfilling the energy storage requirements for EV and HEV applications.In this modern age,

unbelievable progress has been achieved on battery technologies for EV and PHEV. The batteries which are mainly used to operate EV, HEV & PHEV are consist of thelead-acid battery, nickel-based batteries such as nickel/iron, nickel/cadmium, and nickel–metal hydride batteries, and lithium-based batteries such as lithium polymer and lithium-ion batteries**[7]**.Among these available technologies, two major categories of battery chemistries can meet the PHEV & PEV goals:Nickel-Metal Hydride (NiMH) and Lithium-Ion (Li-Ion) **[8].**

Table 1: NiMH vs. Li-Ion Battery Technologies

	NiMH	Li-Ion
Power Density (W/kg)	250	540
Energy Density (Wh/kg)	57	94
Cycle Life (cycles)	>3000	>3200
Energy Efficiency (%)	70	>95

longevity and safety are still the shortcomings of Li-Ion battery in table-1 **.**

5 COMPARISON OF ENERGY EFFICIENCY

At this time, batteries are being used as the alternative energy of fossil fuels. From Fig.3**[10]**, it is clear that the net calorific values of diesel and gasoline exceed hydrogen & Li-ion. But we know that the conversion efficiency denotes the thermal output. In this case, Li-ion technology is greater than all others. But there needs further development to ensure the ultimate success of electric vehicle.

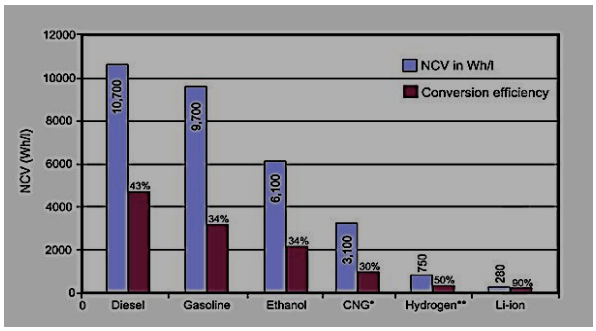

Fig.3. Net calorific values of fuels with conversion efficiencies

6 GLOBAL IMPACT

The automotive industry plays an essential role in building modern developed society. But the large number of automobiles has caused & still causing serious problems for the environment & human life. On the other hand, electric vehicles i.e. PHEVs able to increase a portion of vehicle miles to potentially low-carbon electricity sources & EVs promise to fully change transportation into the electricity system **[9].**

6.1 Fuel Storage

The vast part of our transportation system depends on the liquid fossil fuels originating from petroleum sources. As we know that global petroleum resources are finite.

Table 2 : British Petroleum 2001 estimate**[12]**

Region	Proved reserve in 2000 in Billions Tons	R/P ratio
North America	8.5	13.8
South and Central America	13.6	39.1
Europe	2.5	7.7
Africa	10	26.8
Middle East	92.5	83.2
Former USSR	9.0	22.7
Asia Pacific	6.0	15.6
Total world	142.1	39.9

In the Data Table-2, The R/P ratio refers the number of years that the reserves would last with respect to the current production rate. Another survey informs that global oil demand increased by 11% from 2005-2010 & it will be increased another 25% by 2030 **[11]**. So, in this condition BEVs & PHEVs can be a great opportunity to reduce the fuel consumption.

6.2 Fuel Cost

It is true that the primary cost of ICE vehicles remains lower than the cost of PHEV & BEV. But the fuel of EV i.e. electricity prices are less volatile than oil or gasoline prices. Since 1983, the avg. retail price of electricity in U.S.A has risen less than 2% per year **[13]**. In that time, oil prices have increased by more than 5% per **[11].**

6.3 Environmental Effect

The conventional vehicles which mainly rely on hydrocarbon fuels cause air pollution. In the combustion of fossil fuels, there not only produces CO_2 but also NO_x, CO , unburned hydrocarbons & other pollutants. Global warming is also a result of the presence of CO_2 & other gases like methane, in the atmosphere. Keeping the consequence of these effects, earth temperature results major ecological damages & natural disasters.

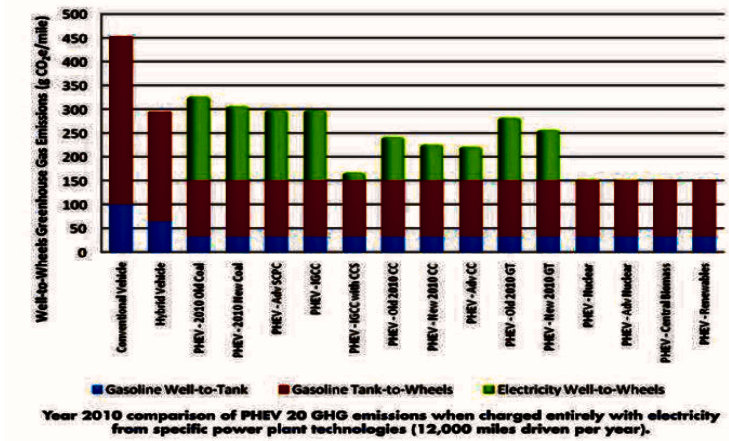

Fig.4. 12,000 Mile/Yr. PHEV 20 GHG Emissions by Fuel/Technology.

From Fig.4 we can reach a decision that HEVs, PHEVs produce comparatively less CO_2 than CVs.

As coal fuels around 45% of electricity generation in the U.S. so we can say that CO_2 is also produced to supply electricity to EVs**[11].** But it needs to ensure that the emission of EVs is less than CVs. To overcome this problem, renewable energy based charging station can be a significant solution.

6.4 FUTURE OF ELECTRIFIED VEHICLES

The Energy Technology Perspectives (ETP) 2010 BLUE Map scenario fixed a target to reduce 50% CO_2 by 2050. And this goal can be achieved in part by accomplishing an annual sale of approximately 50 million light-duty EVs & 50 million PHEVs per year by 2050**.[12]**

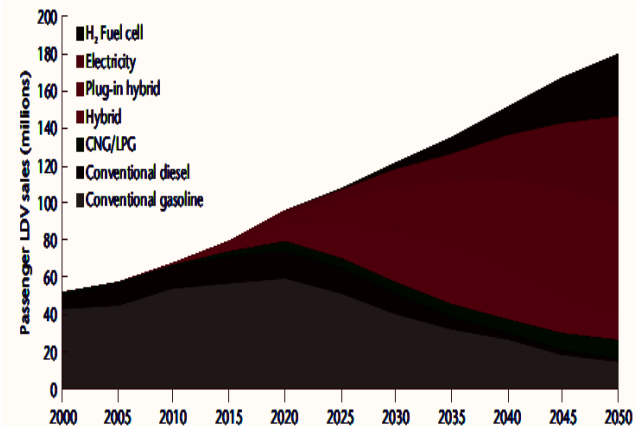

Fig.5. Annual light-duty vehicle sales by technology type, BLUE Map scenario **[12]**

Here Fig.5 indicates the roadmap of rapid light-duty vehicle technology evolution over time.

Some potential locations for renewable energy based Re-charging stations are Public Administration, Train station, Shopping Center, Park and Sports Arena .

7 CONCLUSION

In this paper we try to develop a renewable energy based Re-charging station for the electrified vehicles.The another point of our study is to build whole transport system on the basis of microwave beam via wireless power transmission. This may keep our environment green and protect it from emission of $CO_2$and also to reduce GHG gas.

REFERENCE—

1. Rakes Kumar Yadav, SushrutDas,".Rectenna design development and application",*Internationaljournalof engineering science and technology*. Vol.3 No.10 October 2011
2. Renewable energy on Wikipedia, source:*en.wikipedia.org/wiki/**Renewable_energy***
3. N.CKarmakar, P.K Weng,"Development of rectenna for microwave power reception"*9th Australian Symp on Antenna, Sydney ,Australia*, 16-17 Feb. 2005
4. ZiedHarouni, LotifOsman.Efficient,"2.45 GHz rectenna Design with high harmonic rejection for wireless power transmission",*IJCSI international journal on computer science Issues*. Vol.7, issue 5, September 2010.
5. Chang-Jun Ahn, Takeshi Kamio."Prototype of 5.8 GHz wireless power transmission system for Electric vehiclesystem*",2011 2nd International Conference on Environment Science and Technology, IPCBEE* Vol.6(2011)©(2011)IACSIT Press, Singapore
6. Naoki Shinohara, "Beam efficiency of wireless power transmission via radio waves from short range to long distance", *Journal of Korean institute of electromagnetic engineeringand science,*Vol 10, No.4, Dec 2010, JKIEES 2010-10-05
7. Y. Gao and M. Ehsani,"Investigation of battery technologies for the army's hybrid"
8. vehicle application, "*In Proceedings of the IEEE 56th Vehicular Technology Conference*",Fall 2002, pp. 1505–1509.
9. Derek M Lemoineand Daniel M Kammen,Addendum "An innovation and policy agenda for commercially competitive plug-in hybrid electric vehicles",*IOP Publishing Environmental Research Letters.Environ.* Res. Lett. **4** (2009) 039701 (3pp), doi:10.1088/1748-9326/4/3/039701, Online at stacks.iop.org/ERL/4/039701.
10. http://batteryuniversity.com/learn/article/net_calorific_value_of_fossil_fuel_and_battery
11. A symposium on: The electrification of the transportation system: issues and opportunities sponsored by the MIT Energy Initiative (MITEI) on April 8, 2010.
12. "International Energy Agency", 9 rue de la Fédération 75739 Paris Cedex 15, France, *www.iea.org*.
13. "Annual Energy Review 2008", supra note 18, at 261.

Proceeding of the
International Conference on Electrical, Computer and Telecommunication Engineering
01- 02 December 2012 (ICECTE2012), RUET, Rajshahi-6204, Bangladesh

ICECTE2012: PI-0025

Study of Two Different Receiver Antennas for Ultra Wideband Off-Body Radio Propagation Channels

Mohammad Monirujjaman Khan[1,2], Abdullah-Al-Mamun,[2] Rifat Afroze,[2]Akram Alomainy[1]
[1]School of Electronic Engineering and Computer Science, Queen Mary University of London,
Mile End Road, London E1 4NS, UK
[2]Faculty of Engineering, American International University-Bangladesh, Banani, Dhaka-1213, Bangladesh
E-mail: monirkhan@aiub.edu, mohammad.khan@elec.qmul.ac.uk

ABSTRACT
In this paper, comparison of two different receiver antennas for ultra wideband (UWB) off-body radio propagation channels in body-centric wireless communication is presented. The measurements were performed in an indoor environment using active UWB wireless tags. Two different types of receiver antennas have been used; namely a small form factor (SFF) antenna and compact co-planar waveguide (CPW)-fed tapered slot antenna (TSA) to investigate their effects on the radio channel behaviour. Results show that a reduction of 29 % path loss exponent is noticed for the SFF antenna.

KEY WORDS: Ultra wideband, off-body radio channel, path loss, body-centric wireless communications.

1. INTRODUCTION

Ultra wideband (UWB) communication is an exciting and innovative technology that has attracted much attention and experienced considerable growth in the past few years due to its distinctive characteristics. It has become a very promising candidate for future short-range indoor high speed data communication [1].

One of the most potential areas of UWB applications is the body-centric wireless network, where various units/sensors are scattered on/around the human body to measure specified physiological data i.e. patient monitoring for healthcare applications [2]. A body-worn base station will receive the medical data measured by the sensors located on/around the human body. This data will then be transmitted from the body-worn controller to the nearby access point and later to a remote medical service centre [2-3].

The rapid development of biosensors and wireless communication devices brings new opportunities for Body-Centric Wireless Networks (BCWN) which has recently received increasing attention due to their promising applications in medical sensor systems and personal entertainment technologies.

In the past few years researchers have been thoroughly investigating ultra wideband on-body radio channels. UWB on-body radio channel characterisation and system level modelling for body-centric wireless networks have been presented extensively in the open literature [3-8]. In [3-6], UWB on-body channels have been characterised and their behaviour have been investigated in indoor and chamber for stand-still and various postures of human body based on different antennas. The effect of the two different UWB antenna types on the on-body radio propagation channels has been investigated in [7-8].

Very limited work for UWB off-body radio channel characterisation is presented in the open literature [9-11]. In [10], off-body communication channel measurement was performed in the anechoic chamber placing one transmitter antenna on the access point off the body and another antenna mounted on the belt position of the human body under test where the height between transmitter and receiver antenna was the same.

In this paper a measurement campaign was performed in the indoor environment using a commercially available UWB wearable active tags and reader. Two different types of receiver antennas were used so that the effect of the antenna parameters on the radio channel is examined. The path loss exponent is extracted using least square fit techniques for both antenna cases.

The rest of the paper is organised as follows; section 2 illustrates the measurement settings and it briefly introduces the UWB tags, section 3 discusses the receiver antenna parameters. Section 4 presents the measurement results, and finally section 5 draws the conclusion of the presented study.

2. MEASUREMENT SETTINGS

In this study, measurement campaigns were performed using UWB wearable active tags and reader provided by Time Domain PLUS^{TM} [12]. Two sets of measurements were made for different receiver antennas. For the first set of measurements, a UWB reader using small form factor (SFF) antenna encased inside a loss free plastic Radome was placed on the ceiling near the wall as shown in Fig. 1(b). A real human subject was used in these measurement campaigns. The test subject was an adult male of

mass 90 Kg, height 1.68 metre and chest circumference of 114 cm. Nine UWB active tags were attached on different locations of the body including; right/left chest, right/left waist, right/left wrist, right ear and right/left ankle as shown in Fig. 1(a). Measurements were performed with the subject wearing 9 transmitter tags standing at 6 different locations with intervals of 1 metre apart in a laboratory as shown in Fig. 1(b). During the measurement, the subject was standing still on the each spot for a period of 60 seconds. The same scenario was applied for the second set of measurement replacing the receiver antenna by a TSA at the reader. Both receiver antennas were set perpendicular with the reader. The radiating element of the TSA was set facing towards the test subject.

For all measurement cases and scenarios, the subject was facing towards the reader. Measurement campaigns were performed in the Body-Centric Wireless Laboratory, Queen Mary University of London. Fig. 1(c) shows the dimensions and geometry of the laboratory.

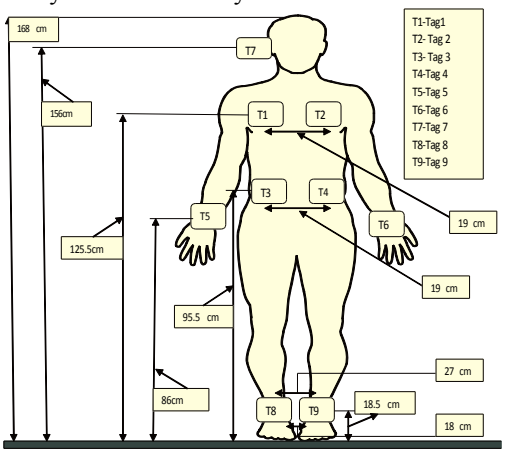

(a)

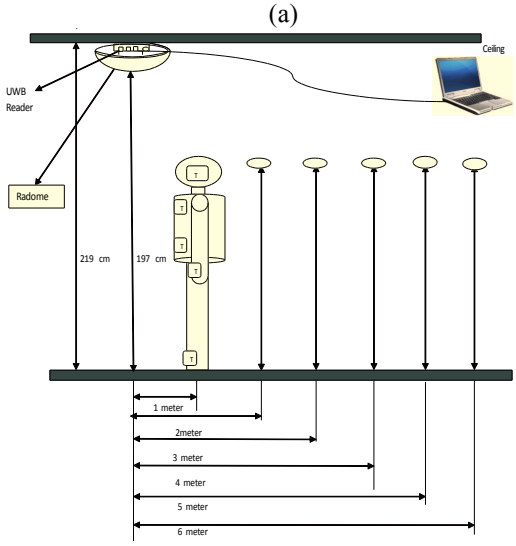

(b)

The total area of the laboratory is 45 m^2 which includes a meeting area, treadmill machine, workstations and a hospital bed for healthcare applications. Location-based software was used to save the tags transmission ID, received signal strength (RSSI) and time of arrival data from reader.

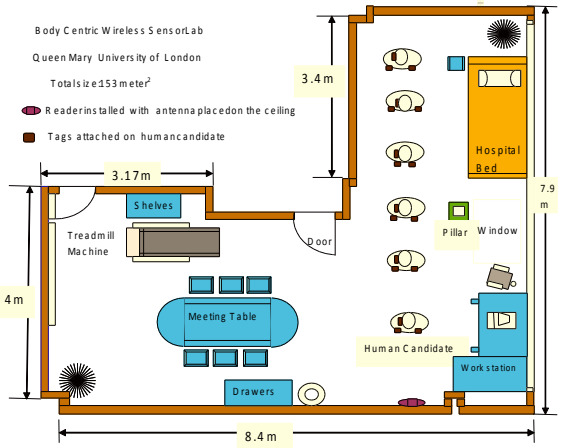

(c)

Fig. 1. (a) Front view of subject wearing nine active UWB transmitter tags on the body during measurement (b) Measurement scenario and side view during measurement; subject was standing at 1-6 metre distance locations with the interval of 1 metre (c) Dimensions and geometry of the Body-Centric Wireless Sensor Lab (housed within the Department of Electronic engineering, Queen Mary University of London, London, U.K) where the indoor off-body radio propagation measurements for the presented work is performed and also illustrated the measured scenarios locations and orientations.

The tag's transmit power is -13 dBm which is around 40 dB less than peak mobile phone transmit power. The operating frequency of the tags used for this measurement is 5.9~7.25 GHz with a centre frequency of 6.6 GHz. The UWB tag is small and durable, with a plastic housing that allows it to be attached to assets or people [12]. The dimension of the tag is (13 mm x 36 mm x 33 mm) and the weight is 0.74 oz (22 g). Figs 2(a), 2(b) and 2(c) show the UWB tag encased inside the plastic housing, the top view of the tag showing the tag antenna and the tag without plastic housing and bottom view.

The UWB tags are battery powered and the duration of the battery life is four years since the tags only transmit UWB pulses every one second. The tag antenna has monopole-like radiation patterns.

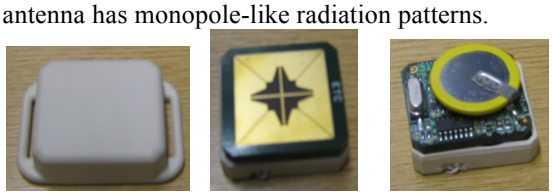

(a) (b) (c)

Fig. 2 UWB tags used in this measurement.

3. RECEIVER ANTENNAS

The Figs. 3 (a) and 3(b) show the layout of the two different receiver antennas as small form factor (SFF) and tapered slot antenna (TSA) used for this measurement. The UWB reader SFF antenna is monopole like wire antenna on the large ground plane measure 330.2 mm in diameter [13]. The total height of the radiating monopole of the SFF antenna is 12 mm while the thickness is 4 mm. The CPW-fed TSA is fabricated on RT/Duroid board with permittivity of ε_r =3 and the thickness of the board is 1.524 mm [13]. The total size of the TSA is 27 mm×16 mm. The operating frequency of SFF antenna is 4.513 GHz to 12.710 GHz, at -10 dB impedance bandwidth while the TSA works in the frequency band of 3.1~15 GHz. Comparison of the measured azimuth (XZ) plane radiation patterns of the proposed antennas are shown in Fig 4.

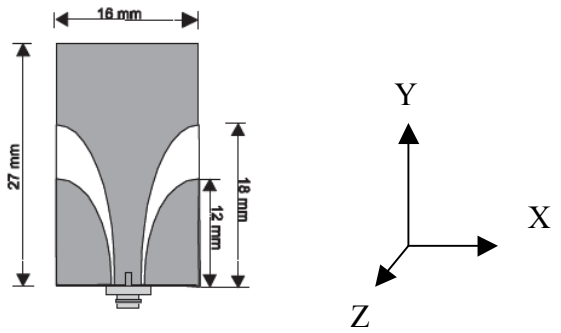

(a) Tapered Slot Antenna (TSA)

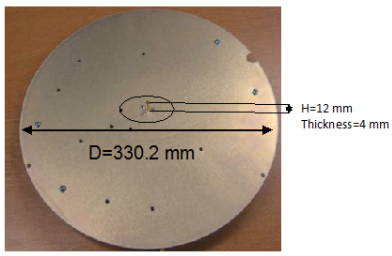

(b) SFF antenna

Fig. 3 Dimensions and geometry of the receiver antennas and the performance parameters of the receiver antennas (a) Tapered Slot Antenna (TSA) (b) Small Form Factor (SFF) antenna.

The maximum gain of the SFF antenna at 6.6 GHz is 5.86 dBi while it is 4.54 dBi for the TSA.

4. PATH LOSS VS. DISTANCE

It is well known that the average received signal decreases logarithmically with distance (for both indoor and outdoor environments). The path loss can be modelled as a linear function of the logarithmic distance between transmitter and receiver as explained in [14],

$$PL_{dB}(d) = PL_{dB}(d_0) + 10\gamma \log(\frac{d}{d_0}) + X_\sigma \quad (1)$$

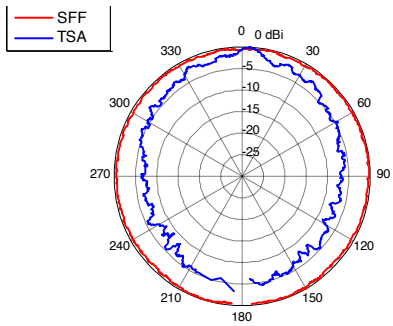

Fig. 4 Comparison of the measured azimuth (XZ) plane radiation patterns of the proposed antennas.

where d is the distance between transmitter and receiver, d_0 is a reference distance set in measurement and usually for indoor radio propagation channels it is set to be 1 metre (in this study it is set to 1metre as well), $PL_{dB}(d_0)$ is the path loss value at the reference distance, and X_σ is the shadowing fading. The parameter γ is the path loss exponent that indicates the rate at which the path loss increases with distance.

In this work, the path loss for nine different off-body channels was calculated from the measured RSSI for each transmitter tag. The path loss of nine different off-body channels for standing still measurement scenario is averaged over the measurement duration of 60 seconds. A least square fit technique is performed on the measured path loss for all 9 off-body channels as static case (1-6 metre) at 54 (6×9) different transmitter locations to extract the path loss exponent (Fig.5.a). Fig. 5(a) shows the measured value and modelled path loss for off-body channel versus logarithmic Tx-Rx separation distance showing path loss exponent for SFF and TSA.

The path loss exponent values for SFF antenna and TSA are different. Reduction of 29% in path loss exponent is noticed for SFF antenna. SFF antenna shows quite omnidirectional radiation pattern which receives more multipath reflections from the scattering objects in the indoor environment that increases the received signal strength results and thus lower path loss exponent for this antenna. Moreover, having higher gain, the SFF experiences lower path loss exponent value in comparison to the TSA.

X_σ is a zero mean, normal distributed statistical variable, and is introduced to consider the deviation of the measurements from the calculated average path loss. Fig. 5(b) shows the deviation of measurements from the average path fitted to a

normal distribution for both antenna cases. In indoor, the standard deviation of the normal distribution for SFF antenna is σ=3.10 while σ=2.74 is calculated for TSA. The difference of the standard deviation value σ in between SFF and TSA is very small.

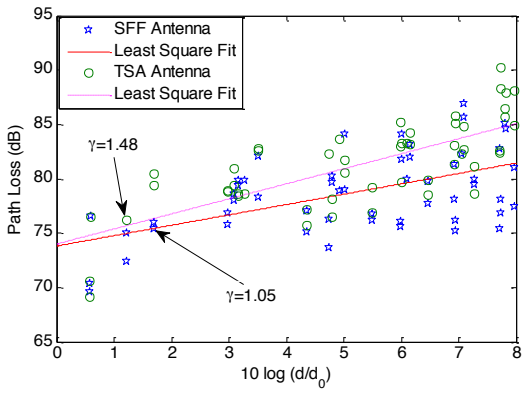

(a)

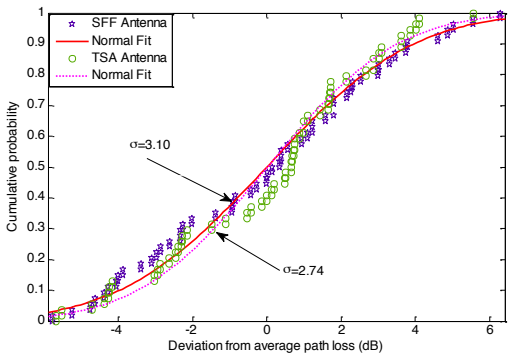

(b)

Fig. 5 Measured and modelled path loss for the off-body channels versus logarithmic Tx-Rx separation distance for both antenna cases (b) Deviation of the measurements from the average path loss fitted to normal distribution for both antennas.

5. CONCLUSIONS

UWB off-body propagation channel measurements were performed in an indoor environment using wireless tags and reader. Two different types of receiver antennas were used. Results and analysis show that SFF antenna experiences reduction of 29 % path loss exponent. Both antennas show very good off-body radio channels performances, however, due to its compact size TSA is good candidate for future body-centric wireless communications.

REFERENCES

[1] B. Allen, M. Dohler, E. Okon, W. Q. Malik, A. K. Brown, and D. Edwards, *UWB antenna and Propagation for Communications, Radar and Imaging.* John Wiley and Sons, 2007.

[2] P. S. Hall and Y. Hao, *Antennas and propagation for Body-Centric Wireless Communications.* Artech House, 2006.

[3] A. Fort, C. Desset, P. D. Doncker, and L.V. Biesen, " Ultra wideband body area propagation: from statistics to implementation,'' *IEEE Transactions on Microwave Theory and Technique*, vol. 54, no. 4, pp. 1820 1826, June 2006.

[4] Q, Wang, J. Wang, "Performances of On-Body Chest-to-Waist UWB Communication Link,'' *IEEE microwave and wireless components letters*, vol. 19, no. 2, feb.2009.

[5] Q. Wang, T. Tayamachi, I. Kimura, and J.Wang, "An on-body channel model for UWB body area communications for various postures,'' *IEEE Journal on Selected Areas in Communications,* vol. 57, no. 4, pp .991-998, Apr. 2009.

[6] A. Alomainy, Y. Hao, X. Hu, C.G. Parini, and P.S Hall, "UWB on-body radio propagation and system modelling for wireless body-centric networks, " *IEE proceedings communications*-Special Issue on Ultra Wideband Systems, technologies and Applications,'' vol. 153, no.1, pp 107-114, Feb. 2006.

[7] A. A. Alomainy, Y. Hao, C. G. Parini, and P.S. Hall, "Comparison between two different antennas for UWB on-body propagation measurements,'' *IEEE Antennas and Wireless Propagation Letter.* 2005, 4, (1), pp. 31-34.

[8] A. Sani and Y.Hao, "Modeling of Path Loss for Ultrawide Band Body-Centric Wireless Communications,'' Electromagnetics in advance applications, 2009. ICEAA '09. *International Conference on* 14-18 sept.,2009 pages(s):998-1001.

[9] P. A. Caterwood and W. G. Scanlon, "Link characteristics for an off-body UWB transmitter in a hospital environment,'' *Loughborough antennas and propagation conf.*, Nov. 2009.

[10] A. A. Goulianos, T. W. Brown and S. Stavrou, "Ultra-Wideband measurement and results for sparse off-body communication channels,'' 2008 *Loughborough Antennas and Propagation Conference,* 17-18 March, 2008, Loughborough, UK.

[11] M. M. Khan, A. Alomainy and Y. Hao, "Off-body Radio Channel Characterisation Using UWB Wireless Tags,'' *International Conference on Body Sensor Networks (BSN 2010),* June 7-9, 2010, Biopolis Singapore.

[12] (2009) Plus Asset Tag, Reader and SFF Antenna Datasheet/Time Domain. [Online]. Available: http://http://www.timedomain.com/

[13] A. Rahman, A. Alomainy and Y. Hao, "Compact Body-Worn Coplanar Waveguide Fed Antenna for UWB Body- Centric Wireless Communications,'' *Antennas and Prop., 2007. EuCAP 2007. The Second European Conference* on 11-16 Nov. 2007 Page(s):1 – 4.

[14] S. S. Gassemzadeh, R. Jana, C. W. Rice, W. Turin, and V. Tarohk, " A statistical path loss model for in-home UWB channels,'' *IEEE Conf. Ultrawide Band Systems and Technologies*, Baltimore, p. 5964, 2002.

Proceeding of the
International Conference on Electrical, Computer and Telecommunication Engineering
01- 02 December 2012 (ICECTE2012), RUET, Rajshahi-6204, Bangladesh

ICECTE2012: PI-0026

Design, analysis and comparing the performance of Microstrip single element and series feed array for X band applications

Md. Imran Hasan[1], Shah Ariful Hoque Chowdhury[2], M. A. Motin[3]
[1,2]Dept. of Electronics and Telecommunication Engineering, Rajshahi University of Engineering & Technology, Rajshahi-6204, Bangladesh.
[3]Dept. of Electrical & Electronic Engineering, Rajshahi University of Engineering & Technology, Rajshahi-6204, Bangladesh.
E-mail: imran_ruet_ete06@yahoo.com, arif.1968.ruet@gmail.com, motin_eee_06@yahoo.com

ABSTRACT
This paper demonstrates the high gain, low cost and simple microstrip antenna for applications in GHz range. In this paper microstrip single patch and series feed are designed, simulated, analyzed and compared with respect to antenna performance such as return loss, gain, directivity etc. The designed antennas are 4×1 series feed and single patch. The simulation has been performed by simulation software GEMS version 7.71.01 and designed antenna provide maximum return loss -18.52dB at frequencies around 11.875GHz and maximum gain 14.16dBi by using Taconic TLY-5 dielectric substrate with relative permittivity 2.2 and height 1.588mm. Since the resonance frequency of those antenna is 11GHz, these antenna are suitable for X band application such as satellite, radar, medical application and other wireless application etc.

KEY WORDS: Array antenna, series feed, Single patch, Microstrip array, Antenna comparison.

1. INTRODUCTION

In modern communication system everywhere required low cost, high gain, high directivity, light weight, simple structure and easy fabricated antenna. Microstrip antenna satisfied such requirements. Key feature of this antenna is, the thickness of the metallic strip is in micrometer range [1], ease of construction, light weight, low cost. This antenna provides all of the advantages of printed circuit technology. These advantages of microstrip antenna make them very popular in communication applications such as satellite communication, radar, medical application and other wireless communication etc [2].

Different array configurations of microstrip antenna can give high gain, wide bandwidth and improve efficiency [3]. The choosing of design parameters (dielectric material, height and frequency etc.) is important because antenna performance depends on these parameters. Radiation performance can be improved by using proper design structures [4]. The use of high permittivity substrates can miniaturize microstrip antenna size [5]. Thick substrates with lower range of dielectric offer better efficiency, and wide bandwidth but it requires large element size [6]. In this paper the entire antenna is designed to support 11GHz operating frequency. And simulation has been done by simulation software GEMS simulator version 7.71.01. Where used substrate height is 1.588mm, Taconic TLY-5 dielectric substrate with permittivity 2.2.

Different radar systems such as synthetic aperture radar (SAR), shuttle imaging radar, remote sensing radars and other wireless communication systems operate in L, C and X bands. Microstrip antenna is the first option for this high frequency band such as X-band due to its low cost, light weight, and robustness [7].

2. DESIGN OF MICROSTRIP ANTENNA

Microstrip antenna consists of a thin film with different shape such as rectangular or circular or triangular etc. This strip of thin film placed on ground plane where the thickness of the metallic strip is restricted by $t \ll \lambda_0$ and height is restricted by $0.000\lambda_0 \leq h \leq \lambda_0$ [3, 8]. In this paper we designed each array using rectangular patch. For a rectangular patch, the length L of the element is usually $\lambda 0/3 < L < \lambda 0/2$. There are numerous substrates that can be used for the design of microstrip antennas and their dielectric constants are usually in the range of $2.2 \leq \varepsilon r \leq 12$. To implement the microstrip antenna usually Fr-4 ($\varepsilon r = 4.9$), Rogers TMM 4 ($\varepsilon r = 4.5$), Taconic TLY-5 ($\varepsilon r = 2.2$), Alumina (96%) ($\varepsilon r = 9.4$), Teflon(PTFE) ($\varepsilon r = 2.08$), Arlon AD 5 ($\varepsilon r = 5.1$) dielectric materials are used as the substrate [3, 8, 9, 10]. The Performance of the microstrip antenna depends on its dimension. Depending on the dimension the operating frequency, radiation efficiency, directivity, return loss and other related parameter are also influenced [11].

This paper mainly includes the design and comparing the performance of two Microstrip antennas. They are-

- Single element rectangular patch
- Series feed array network

a. SINGLE ELEMENT PATCH

For an efficient radiation a practical width of the rectangular patch element becomes [3, 8, 11].

$$W = \frac{1}{2f_r\sqrt{\mu_0\varepsilon_0}} \times \sqrt{\frac{2}{\varepsilon_r+1}} \quad (1)$$

And the length of the antenna becomes [3, 8, 11]

$$L = \frac{1}{2f_r\sqrt{\varepsilon_{eff}\sqrt{\varepsilon_0\mu_0}}} - 2\Delta L \quad (2)$$

Where,

$$\Delta L = 0.41h\frac{\varepsilon_{eff}+0.3}{\varepsilon_{eff}-0.258} \times \frac{w/h+0.246}{w/h+0.8} \quad (3)$$

And,

$$\varepsilon_{eff} = \frac{\varepsilon_r+1}{2} + \frac{\varepsilon_r-1}{2\sqrt{1+12\frac{h}{w}}} \quad (4)$$

Where, λ is the wave length, fr (in Hz) is the resonant frequency, L and W are the length and width of the patch element in mm, respectively and ε_r is the relative dielectric constant.

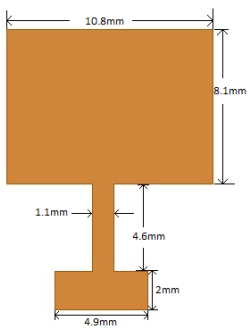

Fig 1: Single element rectangular Microstrip antenna

In the following Fig. 1, the antenna has been designed to cover 11 GHz operating frequency where the antenna dimension is in mm range and the quarter wavelength transformer method [3, 8] is used to match the impedance of the patch element with the transmission line. A probe is also used in the rectangular patch antenna.

2.2 SERIES FEED ARRAY NETWORK

The limitations of microstrip antennas are narrow frequency band and disability to operate at high power levels of waveguide, coaxial line or even strip line [12]. This can be minimized with the help of various array configurations, feeding methods, dielectric material and ground plane. In microstrip array, elements can be feed by a single line or multiple lines in a feed network arrangement [2, 13]. Based on the feeding method one of the popular array is series feed network.

A series feed microstrip array antenna is shown in Fig. 2, is formed by interconnecting the entire element with high impedance transmission line and feeding the power at the first element [13]. For series feed network the main beam direction and scan sensitivity can be calculated by following equation [13, 14]

$$d = sin\theta + \sqrt{\varepsilon}l = \lambda = \frac{c}{f} \quad (5)$$

$$\frac{\partial\theta}{\partial\lambda} = \frac{c}{\partial f^2 cos\theta} \quad (6)$$

Where, c is light velocity, d is element spacing, l is transmission line length between successive element, f is the operating frequency, θ is the beam pointing angle. The E-plane radiated field for a single element patch can be expressed as [2, 15]

$$E = j\frac{k_0 w v_0 e^{-jk_0 r}}{r\pi}\left\{\frac{sin\left(\frac{k_0 h}{2}cos\varphi\right)}{\frac{k_0 h}{2}cos\varphi}\right\}cos\left(\frac{k_0 L_e}{2}sin\varphi\right) \quad (7)$$

Here, w is width of the patch, L_e is extended length, $v_0 = hE_0$ is voltage across radiating slot, h is substrate height, r is far field distance from antenna. The array factor can be expressed as

$$FA = \frac{sin(N\pi d_x(u-u_0))}{sin(\pi d_x(u-u_0))} \quad (8)$$

Here,$u = sin\theta, u_0 = sin\theta_0$, dx is the element spacing, N is no. of elements. Combining (7) and (8) we get the total element normalized [16] radiation pattern that is

$$20log(|E/FA|) \quad (9)$$

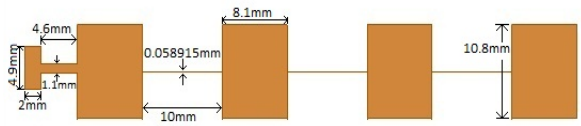

Fig 2: Series feed array antenna (4×1).

3. SIMULATION RESULT AND DISCUSSION

For each antenna, design parameter is considered that substrate permittivity is 2.2 (Taconic TLY-5), height is 1.588mm and designed frequency is 11GHz and using this consideration simulation and result is taken for each network.

a. SINGLE ELEMENT PATCH

The simulated return loss is shown in Fig. 3.The return loss at 11GHz is -7.03dB, but maximum return loss is obtained at 10.52GH is -16.61dB.

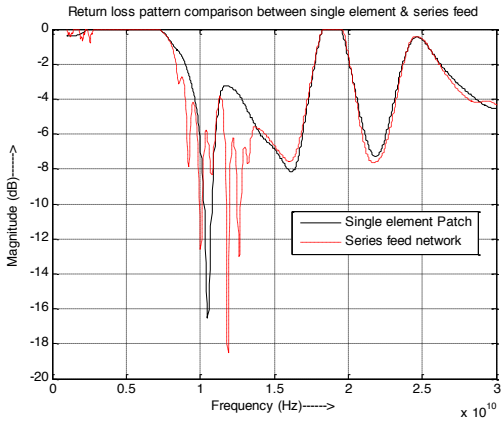

Fig. 3: Return loss pattern of single element & series feed network.

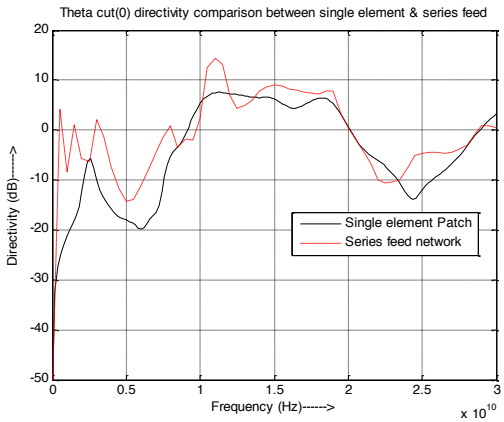

Fig. 4: Theta cut (θ=0) directivity of single element & series feed network.

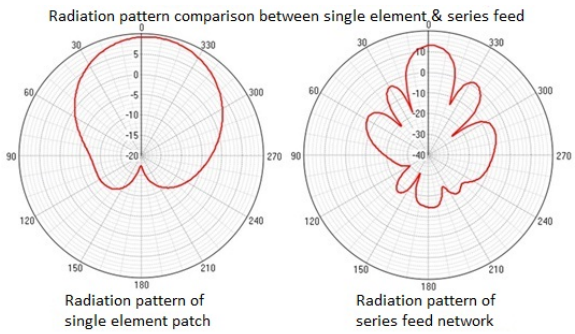

Fig 5. Radiation (polar plot) pattern of single element and series feed network.

Theta cut (θ=0) directivity at 11GHz is 7.49dB and graph is shown in Fig. 4. Accepted power and radiated power at 11GHz is 79.07mW and 115.5mW respectively. Gain at 11GHz is 9.155dBi and the polar plot of 2D radiation pattern is shown in Fig. 5.

b. SERIES FEED NETWORK

The simulated return loss is shown in Fig. 3.The return loss at 11GHz is -6.03dB, but maximum return loss is obtained at 11.88GH is -18.52dB. Theta cut (θ=0) directivity at 11GHz is 14.39dB and graph is shown in Fig. 4. Accepted power and radiated power at 11GHz is 426.9mW and 404.9mW respectively. Gain at 11GHz is 14.16dBi and the polar plot of 2D radiation pattern is shown in Fig. 5.

c. COMPARISON BETWEEN SINGLE ELEMENT AND SERIES FEED NETWORK

After observing the performance analysis parameters of both single element and series feed network antenna we can get the desirable patch antenna after comparing them. Obtained value for each antenna in different performance parameter is tabulated below for better comparing them. Here the both antenna is designed at 11GHz frequency.

Table 1: Simulation result and comparison between single element patch and series feed array network.

Performance parameter	Unit	Single element patch	Series feed array network
Obtained simulated frequency	GHz	10.52	11.875
Return loss at obtained frequency	dB	-16.61	-18.52
Return loss at designed frequency	dB	-7.3	-6.033
Theta cut (θ=0) directivity at 11GHz	dB	7.49	14.39
-3dB bandwidth	GHz	2.33	8.6018
-9dB bandwidth	GHz	0.73	0.2672
Gain at 11GHz	dBi	9.115	14.16
Radiated power at 11GHz	mW	115.5	404.9
Accepted power at 11GHz	mW	79.07	426.9

After observing the above table we get following decision-

- ✓ Return loss is always greater for series feed array than single element patch.
- ✓ Array element is used mainly for increasing gain, directivity, -3dB. We can see in above table gain, directivity, -3dB bandwidth is greater than single element patch.
- ✓ -3dB bandwidth is increased in series feed array but -9dB bandwidth goes down.

- ✓ With increasing gain, directivity the required accepted power and transmitted radiated power also increases.

According to the analysis of the simulated result and above table the overall performance of the series feed array network has better than single element patch.

4. CONCLUSION

In this paper designed antenna is very simple, low cost, high gain, high directivity, and moderate bandwidth. This antenna can easily used in any X band application, satellite communication, radar, wireless communication.

In this paper we designed a single element patch for 11GHz operating frequency and then using this single element we designed a series array to operate at 11GHz. Then using the simulated performance parameter we compare the series array with single element to get the desired one. After observing the simulated performance parameter we get a decision that the overall performance of the series feed array has batter than single element patch.

5. FUTURE WORKS

In future using this single element we designed others array network such as corporate feed, corporate- series feed. Also we will compare the performance parameter of corporate feed, corporate-series feed with this series feed to make understand which one is better for which application.

Here designed antenna is covered 11GHz operating frequency, but it is possible to design for other system such as WLAN, WiMAX, other X band etc application by changing the antenna size. In future we also use the spiral in both rectangular and circular to compare their performance.

REFERENCES

[1]. M. T. I. Huque, et al., " Design and Simulation of a Low-cost and High Gain Microstrip Antenna Arrays for the X-band Applications," In International Conference on Network Communication and Computer ICNCC 2011, New Delhi, India., March 21-23, 2011.

[2]. C. A. Balanis, Antenna Engineering, 2nd ed., Willey, 1982.

[3]. H. Cheng-Chi, et al., "An aperture-coupled linear microstrip leaky-wave antenna array with two-dimensional dual-beam scanning capability," Antennas and Propagation, IEEE transactions on, vol. 29, pp. 25-37, 1981.

[4]. Boufrioua and A. Benghalia, "Effect of the resistive patch and the uniaxial anisotropic substrate on the resonant frequency and the scattering radar cross section of a rectangular microstrip antenna", Aerospace science and technology, vol. 10, pp. 217-221, 2006.

[5]. K. C. Lo and Y. Hwang, "Microstrip antennas of very high permittivity for personal communications," 1997, pp. 253-256 vol.

[6]. J. M. Rathod, " Design Development of Antenna for TV Transmission for Connecting Outdoor Broadcasts Van to the Studio for Rural Area," International Journal of Computer and Electrical Engineering, vol. 2, pp. 251-256, 2010.

[7]. M. F. Islam, et al., "Dual band microstrip patch antenna for SAR applications," Australian Journal of Basic Applied Science, vol. 4, pp. 4585-4591, 2010.

[8]. R. Garg, P. Bhartia, I. Bahl, A. Ittipiboon, Microstrip Antenna Design Handbook, Artech House inc.,2001.

[9]. R. J. Mailloux, J. F. Mcllvenna, N. P. Kernweis, Microstrip array technology", IEEE Trans. Antenna Propagation Magazine, Vol. 29, No. 1, pp. 25-27, 1981.

[10]. Md. Tanvir Ishtaique-ul Huque, Md. Al-Amin Chowdhury, Md. Kamal Hosan, and Md. Shah Alam. " Performance Analysis of Corporate Feed Rectangular Patch Element and Circular Patch Element 4×2 Microstrip Array Antennas", International Journal of Advanced Computer Science and Applications, vol. 2, No. 7, 2011.

[11]. T. A. Millikgan, Modern Antenna Design, 2nd ed., IEEE Press, Jhon Wiley & Sons inc., 2007.

[12]. R. Mailloux, et al., "Microstrip array technology," Antennas and propagation, IEEE Transactions on. Vol. 29, pp. 25-37, 1981.

[13]. R. Garg, Microstrip antenna design handbook. Boston, mass [u.a.]: Artech house.

[14]. M. M. Alam, et, al., "Design and performance analysis of microstrip array antenna," section 5AP, p.846.

[15]. R. J. Mailloux, " Electrically Scanned Arrays," Synthesis Lectures on Antennas vol. 2, pp. 1-82, 2007.

[16]. H. J. Visser, "Array and Phased Array Antenna Basics," ed: John Wiley & Sons.

Proceeding of the
International Conference on Electrical, Computer and Telecommunication Engineering
01- 02 December 2012 (ICECTE2012), RUET, Rajshahi-6204, Bangladesh

ICECTE2012: PI-0028

Performance Analysis of LMS Algorithm for Smart Antenna Systems

Md. Masud Rana , Md. Mostafizur Rahman, A N M Enamul Kabir and Md. Moswer Hossain
Dept. of Electronics and Communication Engineering, KUET, Khulna-9203
E-mail: mrana928@yahoo.com, mostafiz963@yahoo.com

ABSTRACT
Smart antenna (SA) system is still a research area in which a lot of efforts and trials are being conducted to increase capacity and quality in mobile communication networks. Maximum utilization of limited radio frequency spectrum is only possible to use smart/adaptive antenna system. Sa radiates not only narrow beam towards desired users exploiting signal processing capability but also places null towards interferers, thus optimizing the signal quality and enhancing capacity. We have analyzed the performance of adaptive (lms) algorithm for smart antenna systems which is very important for smart antenna design. The sa incorporates this algorithm in coded form which calculates complex weights according to the signal environment. The performance of lms algorithm is compared on the basis of normalized array factor and mean square error (mse) for sa systems. It is observed that a lms algorithm is converging after 50 iterations.

KEY WORDS: Beam forming, smart antennas, LMS.

1. INTRODUCTION

A smart antenna (SA) is an antenna system, which dynamically reacts to its environment to provide better signals and frequency usage for wireless communications [1-3]. SA also known as adaptive array antennas, multiple antennas and recently multiple input multiple output (MIMO) is the antenna arrays with smart signal processing algorithms used to identify spatial signal signature such as the direction of arrival (DOA) of the signal and use it to calculate beam forming vectors to track and locate the antenna beam on the target [4-7]. Radio frequency (RF) spectrum is limited and its efficient use is only possible by employing smart/adaptive antenna array system to exploit mobile systems capabilities for data and voice communication [8]. The SA supported by signal processing capability, point's narrow beam towards the users but at the same time introduces null towards the interferers, thus optimizing the service quality and capacity [9-10]. Adaptive beam forming scheme that is least mean square (LMS) and normalized LMS (NLMS) is used to control weights adaptively to optimize signal to noise ratio (SNR) of the desired signal in look direction and minimize the mean square error.

A smart antenna system is capable of efficiently utilizing the radio spectrum and is a promise for an effective solution to the present wireless systems problems while achieving reliable and robust high speed high data rate transmission [3]. The LMS and NLMS are two adaptive beamforming algorithms use the estimate of the gradient vector from the available data. Adaptive beamforming is a technique in which an array of antennas is exploited to achieve maximum reception in a specified direction by estimating the signal arrival from a desired direction (in the presence of noise) while signals of the same frequency from other directions are rejected. This is achieved by varying the weights of each of the sensors (antennas) used in the array. The word adaptive array was first coined by Van Atta in 1959, to describe a self phase array. Adaptive algorithms form the heart of the array processing network [5]. These algorithms make successive corrections to the weight vector in the direction of the negative of the gradient vector which finally concludes to minimum mean square error (MMSE) [11-13].

In this paper, we have analyzed the performance of adaptive (LMS) algorithm for smart antenna systems which is very important for smart antenna design. The SA incorporates this algorithm in coded form which calculates complex weights according to the signal environment. The performance of LMS algorithm is compared on the basis of normalized array factor and mean square error (MSE) for SA systems. It is observed that an LMS algorithm is converging after 50 iterations.

The paper is organized as follows: the Adaptive algorithms for smart antenna systems are described in section II. The simulation results are discussed in section III. And the conclusion is given in section IV.

2. ADAPTIVE ALGORITHMS FOR SMART ANTENNA SYSTEMS

Wireless communication is one of the most rapidly growing industries. The high demand for wireless communication services had led to an increase in system capacity. Then most elementary solution would be to increase bandwidth; however, this becomes ever more challenging as the

electromagnetic spectrum is becoming increasingly congested. The ever-increasing demand is for increased the capacity in wireless communications services has led to developments of new technologies that exploit space selectivity. This is done through smart-antenna arrays and the associated adaptive beamforming algorithms. SA systems provide opportunities for higher system capacity and improved quality of service among other things [14]

The SA can atomically combine multiple antenna elements with a signal-processing capability to optimize its radiation and/or reception pattern. The SA is either switched beam or adaptive array systems [15]. In switched beam SA, a finite number of fixed, predefined patterns or combining strategies. On the other hand, in adaptive array SA system has infinite number of patterns that are adjusted in real time. It provides optimal gain while simultaneously identifying, tracking, and minimizing interfering signals as shown in Fig. 1.

An adaptive algorithm is an algorithm that changes its behaviour based on the resources available. The SA can adjust the direction pattern adaptively and reduce the interference signals using some adaptive interference algorithms, and thus enhances the performance of mobile telecommunication systems. It especially enlarges the user system capacity [14-16]. The block diagram of an adaptive array system is shown in Fig. 2.

The LMS is an iterative beamforming algorithm that uses the estimate of the gradient vector from the available data. This algorithm makes successive corrections to the weight vector in the direction of the negative of the gradient vector which finally concludes to minimum MSE. This successive correction to the weight vector is the point at which optimum value is obtained that relies on

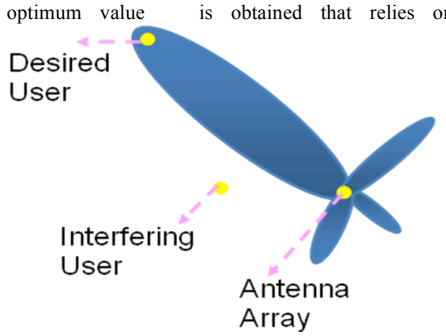

Fig. 1 An adaptive array

autocorrelation matrix R and cross correlation matrix P of the filter.

The LMS adaptive beam forming algorithm is [13]:

Fig. 2 Block diagram of an adaptive array system [3].

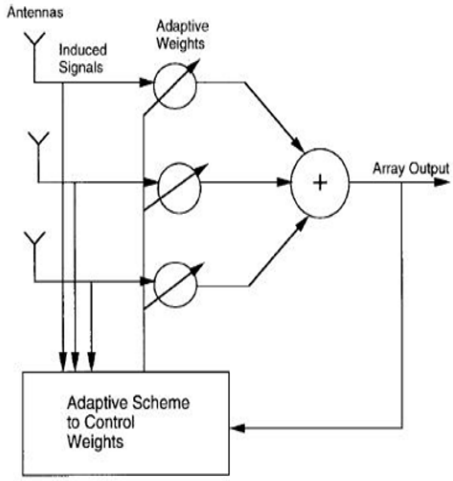

$y(n)=\omega^T(n-1)u(n)$,……..(1)

$e(n)=d(n)-y(n)$, ……....(2)

$\omega(n)=\omega(n-1)+\mu e(n)u^*(n)$, ……..…(3)

where y(n) is the filter output, e(n) is the error signal between filter output and desired signal d(n) at time n, and u(n) is the transmitted signal. In addition, w (n) is the update function for the LMS algorithm, where μ is the rate of adaptation, controlled by the processing gain of the antenna array and denotes the complex conjugate of the input signal u(n). The convergence conditions imposed on step size μ is given by

$0 \le \mu \le \frac{1}{\lambda max}$,……(4)

where λ_{max} is the largest eigen value of autocorrelation matrix R i.e., $R=E[u(n)u^T(n)]$, where E is expectation. If μ is chosen to be very small, then convergence becomes slow. If μ is kept large, then convergence becomes fast, but stability becomes a problem.

The LMS algorithm is initiated with an arbitrary value of $w(0)$ for the weight vector at time n=0. The successive corrections of the weight vector eventually leads to minimum value of the mean squared error. The next section, we describe the simulation results for SA systems.

3. SIMULATION RESULTS

The LMS algorithm was simulated using Matlab software. An N=10 element array with spacing d=0.5 has received a signal arriving at an angle θ=0°,an interferer at the angle θ1=-60°. From Fig. 3 it is observe that the final weighted array which has a

Dr Faruk 26/8/01 22:16 Formatted
Dr Faruk 26/8/01 22:16 Formatted
Dr Faruk 26/8/01 22:16 Formatted
Dr Faruk 26/8/01 22:16 Formatted
Dr Faruk 26/8/01 22:16 Formatted
Dr Faruk 26/8/01 22:16 Formatted
Dr Faruk 26/8/01 22:16 Formatted
Dr Faruk 26/8/01 22:16 Formatted
Dr Faruk 26/8/01 22:16 Formatted
Dr Faruk 26/8/01 22:16 Formatted
Dr Faruk 26/8/01 22:16 Formatted

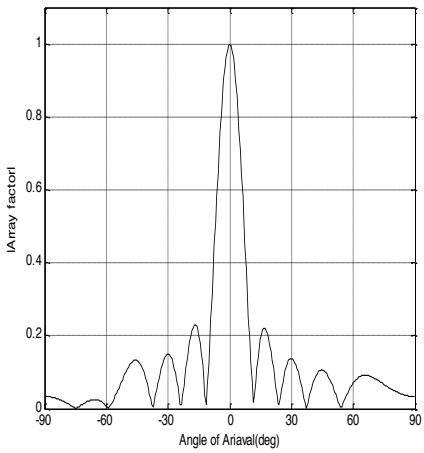

Fig. 3 The array factor using LMS algorithm

peak at the desired direction of 0º and a null at the interfering direction of -60º.

Another simulation is as shown in Fig. 4, it is observe that the array output acquires and tracks the desired signal after 50 iterations. If the signal characteristics are rapidly changing, the LMS algorithm may not allow tracking of the desired signal in a satisfactory manner.

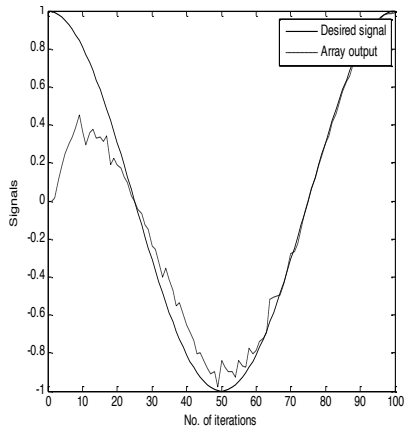

Fig. 4 Acquisition and tracking of desired signal using LMS algorithm

Another simulation result is describes the algorithmic changing the weighting in each iteration. From Fig.5 it is observed that this algorithm converge after 50, we have simulated the MSE error in all iteration. From Fig. 6 it is observed that MSE is decreases all iteration and it is converge after 50 iterations.

Finally, we have simulated the MSE error in all iteration. From Fig. 6 it is observed that MSE is decreases all iteration and it is converge after 50 iterations.

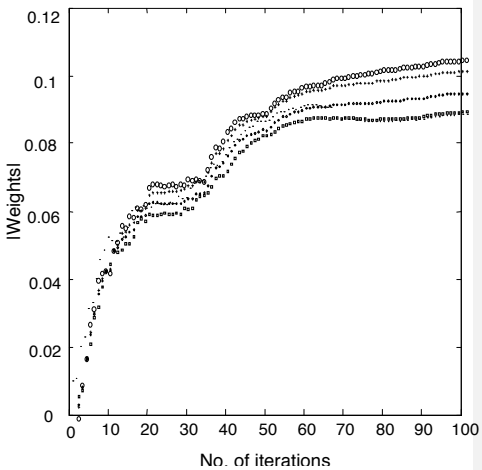

Fig. 5 Magnitude of array weights using LMS algorithm.

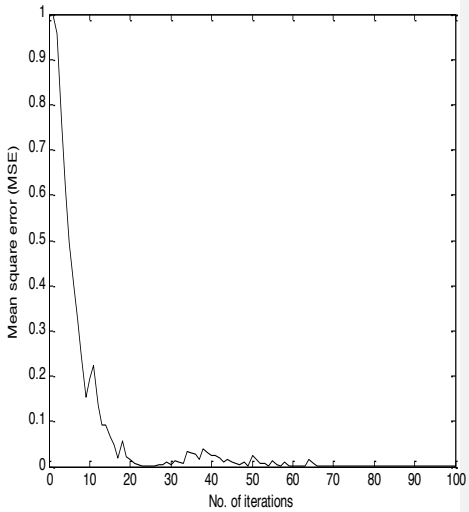

Fig.6 Shows the mean square error using LMS algorithm.

4. CONCLUSIONS

In this research we have analyzed the performance of adaptive LMS algorithm for smart antenna systems which is very important for smart antenna design. The performance of LMS algorithm is compared on the basis of normalized array factor and mean square

error (MSE) for SA systems. It is observed that an LMS algorithm is converging after 50 iterations. The attractive quality of LMS algorithm is less computational complexity. Our findings are explained in details in the above result and analysis section with graphs. Our next target is to simulate the recursive least square (RLS) algorithm for SA systems.

REFERENCES

[1]. Ch. Santhi Rani, P. V. Subbaiah, K. Chenn, T. Zervos, A.A. Alexandridis, F. Lazarakis, K. Dangakis, C. Soras"Array Factor measurements: a preliminary stage in a methodology for Smart Antenna characterization measurements " *Wseas Transactions On Communications*, Vol. 4, Issue 10, October 2005.

[2]. M. Yasin, Dr. Pervez Akhtar and Dr. Valiuddin "Performance Analysis of LMS and NLMS Algorithms for a Smart Antenna System" Published in *International journal of Computer Applications*, Volume 4-No. 9, August 2010

[3]. Ch. Santhi Rani, Dr. P.V. Subbaiah and Dr. K. Chennakesava Reddy "LMS and RLS Algorithms for Smart Antennas in a CDMA Mobile Communication Environment" Published in *International Journal of The Computer*, the Internet and Management Vol. 16.No.3 (September-December, 2008) pp 12-21.

[4]. Frank B.Gross "Smart Antennas for Wireless Communications".

[5]. Sayeed, M.S.I. Young Soo Kim "A Simple LMS Algorithm Based Smart Antenna to Solve the Reader Collision Problems in RFID System" Published in *ICIMT 2009*.

[6]. Usha Mallaparapu, K. Nalini,P. Ganesh ,T. Raghavendra Vishnu,Prof. Habib Ullah Khan, D. Lakshmi Prasanna & B.T.P. Madhav "Non-blind Adaptive Beam forming Algorithms for Smart Antennas" Published in *IJRRAS 6 (4)*, March 2011.

[7]. Ch. Santhi Rani, P. V. Subbaiah, K. Chennakesava Reddy and S. Sudha Rani "LMS and RLS Algorithms for Smart Antennas in a WCDMA mobile Communication Environment" Published in *ARPN Journal of Engineering and Applied Sciences*, Vol. 4, No. 6, August, 2009.

[8]. S.F. Shaukat, Mukhtar ul Hassan, R. Farooq, H.U. Saeed and Z. Saleem "Sequential Studies of Beamforming Algorithms for Smart Antenna Systems" Published in *World Applied Sciences Journal 6* (6): 754-758, 2009.

[9]. K.Meena alias Jeyanthi, Dr.A.P.Kabilan "A Simple Adaptive Beamforming Algorithm with interference suppression" Published in *International Journal of Engineering and Technology* Vol. 1, No. 1, April, 2009

[10]Shahriar Shirvani Moghaddam, Mahyar Shirvani Moghaddam and Roohollah Kalami Rad"A Novel Adaptive LMS-based Algorithm Considering Relative Velocity of Source" Published in IEEE 2010.

[11] Jalal Abdulsayed Srar, Kah-Seng Chung, and Ali Mansour "Adaptive Array Beam forming Using a Combined LMS-LMS Algorithm" Published in *IEEE Transaction on Antennas and Propagation*, Vol.58, No.11, November, 2010.

[12] Kazuhiko Enosawa/Dai Haruki/Chris Thron "Normalized Least Mean Square for a Smart Antenna System" Published in Document Number: *AN3351*Rev.0, 03/2006.

[13] Muhammad Salam Razzaq and Noor M. Khan "Performance Comparison of Adaptive Beamforming Algoritms for Smart Antenna Systems" Published in *World Applied Science Journal* 11(7);775-785, 2010;

[14] Sidi Bahri and Fethi Bendimerad "Performance of Adaptive Beamforming Algorithm for LMS-MCCDMA MIMO Smart Antennas" Published in the *International Arab Journal of Information Technology*, Vol. 6, No. 3, July 2009

[15] M. Yasin, Pervez Akhtar and S.H Zaheer Naqvi "Design and Performance Analysis of Blind Algorithms for Smart Antenna System Using Window Techniques" Published in *Middle-East Journal of Scientific Research* 7(4): 458-466, 2011;

[16] Seungwon Choi and Donghee Shim "A Novel Adaptive Beamforming Algorithm for a Smart Antenna System in a CDMA Mobile Communication Environment" Published in *IEEE Transaction on Vehicular Technology*, Vol.49, No.5, September, 2000.

Proceeding of the
International Conference on Electrical, Computer and Telecommunication Engineering
01- 02 December 2012 (ICECTE2012), RUET, Rajshahi-6204, Bangladesh

ICECTE2012: PI-0029

Design and Performance Analysis of Dual Band Inverted-F Antenna for Wi-Fi and WLAN Applications

Fahim Rashid, Md. Mashud Mustafiz, Mohendro K. Ghosh, Selim Hossain
Department of Electrical & Electronic Engineering
Khulna University of Engineering & Technology (KUET).
Khulna-9203, Bangladesh.

moru_balok@yahoo.com, mashudeee@gmail.com, mithuneee_069@yahoo.com, selimkueteee@yahoo.com

ABSTRACT
In this paper a modified inverted-f antenna (IFA) is designed to serve the purposes of mobile Wi-Fi and WLAN applications. The main intension of this work is to propose a dual band antenna for multi-serving purposes with good return loss characteristics, high gain as well as impedance matched and good radiation characteristics. A dual band IFA is designed with two separate bandwidth (2.4- 2.6 GHz) and (4.94-5.35 GHz) serving for Wi-Fi and WLAN operations. The proposed antenna has good gain and good radiation characteristics. As the dimensions of the proposed antenna are very small, the antenna is promising to be embedded within the different portable devices employing Wi-Fi/ WLAN applications.

KEY WORDS: Inverted-F Antenna (IFA), Dual Band, Double Inverted-F Antenna, Wi-Fi, WLAN.

1. INTRODUCTION

At present the demand of wireless local area networks (WLAN) and wireless fidelity (Wi-Fi) are increasing numerously worldwide for commercial communication because WLAN provides high speed connectivity and easy access to networks without wiring and Wi-Fi can provide a long operating range with a high data rate for wireless mobile broadband access, faultless internet access for wireless users becomes more popular. Also in recent times the function of various portable devices is increasing, so the antenna designer's encountered difficulty in designing antennas that could provide multiband operations with high gain in each operating band. In modern times, telecommunication typically involves the use of electronic transmitters such as the telephone, television, radio or computer [1]. Radio or wireless communication means to transfer information over long or short distance without using any wires. Millions of people exchange information every day using pager, cellular, laptops, telephones various types of personal digital assistants (PDAS) and other wireless communication product [2].

The official definition of the antenna according to the Institute of Electrical & Electronic Engineers (IEEE) is simply a means for radiating or receiving radio waves [3]. Now a days, many current communication services such as Global System for Mobile Communications (GSM), Digital Communication System (DCS), Personal Communication Services (PCS), Universal Mobile Telecommunications Systems (UMTS), Wireless Fidelity (Wi-Fi) & Mobile-WiMAX (Worldwide Interoperability for Microwave Access) use wireless communication that requires multiband or broadband characteristics of antennas [4]. Thus wireless devices require a sophisticated antenna design, which should focus not only on bandwidth & operating frequency but also on antenna bandwidth, where as the phase shift is also diminished.

The use of the industrial, scientific, medical (ISM) band is becoming an important means of wireless communication. The Wi-Fi operates in the 2.4 GHz band (frequency range 2.4-2.5 GHz) & 5 GHz band (frequency range 5.15-5.35 GHz, 5.47-5.725 GHz & 5.725-5.875 GHz). The mobile WiMAX operating bands are 2.3 GHz (frequency range 2.3-2.4 GHz), 2.5 GHz (frequency range 2.5-2.7 GHz) & 3.5 GHz (frequency range 3.4-3.5 GHz) [5] & WLAN operates at frequency band 2.4-2.483 GHz, 5.15-5.35 GHz & 5.725-5.85 GHz [6].

To ensure all the mentioned requirements, Inverted-F antenna is one of the good candidates. The outcome of our work is a dual band IFA designed with two separate bandwidth (2.4- 2.6 GHz) and (4.94-5.35 GHz) serving for Wi-Fi and WLAN operation. This antenna has good gain and good return loss characteristics as well as impedance matching characteristics.

2. ANTENNA DESIGN

The proposed modified inverted–FL (IFL) antenna shown in Fig.1 (a) and Fig.1 (b) for Wi-Fi and WLAN operations occupies very small area of 25×20 mm^2. The antenna is a dual band antenna which covers two Wi-Fi and WLAN operating bands of 2.4 GHz band (2.4-2.5 GHz) and 5.2 GHz band (5.15-

5.35 GHz). This provides peak gain of 5.67 dBi at 2.4 GHz band and 7.64 dBi at 5.2 GHz band.

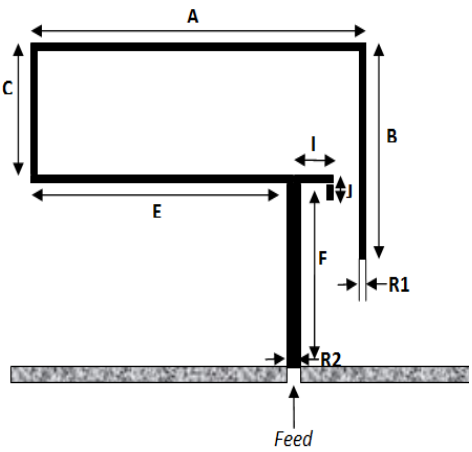

(a)

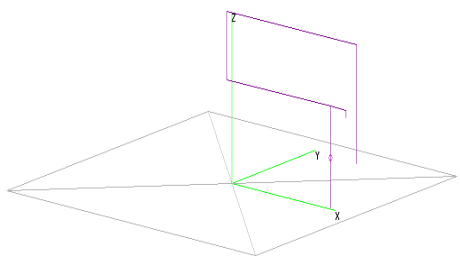

(b)

Fig.1.Structure of Inverted -F Antenna (IFA) (a) 2D and (b) 3D (software view) view.

The low profile antenna is connected to the feed by the arm F and the other arm J is 11 mm away from the ground. For the simulation we consider printed circuit board (PCB) with permittivity of ε = 2.2 and substrate thickness of 1.58 mm. In the analysis the dimensions of the ground plane considered as 60 mm × 60 mm. The F arm supports the whole antenna. In Fig.2 for B=14mm return loss and suitable bandwidth is obtained though for B=15mm we found -45 dB return loss in 2.4 GHz band but not so good in 5.2 GHz band. Varying length J does not effect that much though J=1mm is preferable in Fig.3. In Fig.4, I=3mm cause better performance than any other value of I. also A=25mm is the best taken value in Fig.5.

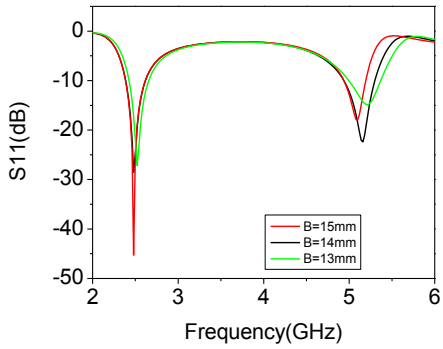

Fig.2.Variation of return loss (dB) at different values of B.

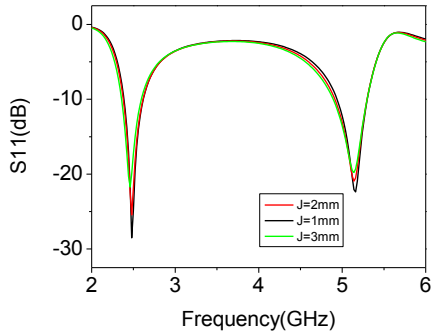

Fig.3.Variation of return loss (dB) at different values of J.

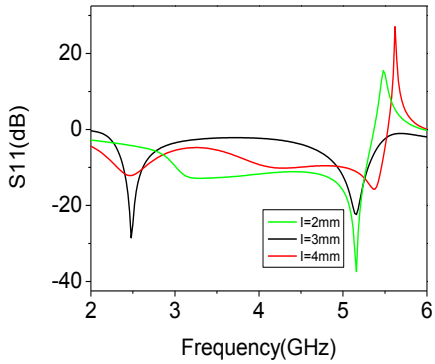

Fig.4.Variation of return loss (dB) at different values of I.

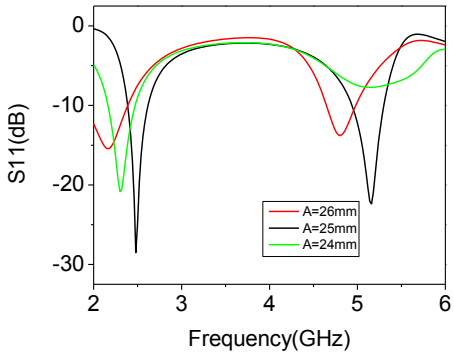

Fig.5.Variation of return loss (dB) at different values of A.

Table 1
Dimensions of the Proposed Antenna

Antenna name	Antenna parameters	Values (mm)	Dimension (mm^2)
Strip Antenna	A	25	25 × 20
	B	14	
	C	8	
	E	20	
	F	12	
	I	3	
	J	1	
	R1	.5	
	R2	1	

3. SIMULATION RESULT

The proposed low profile antenna for Wi-Fi and WLAN operations has a return loss of -21.77 dB at 2.46 GHz in the 2.4 GHz band and -22.39 dB at 5.16 GHz in the 5.2 GHz band. The return loss of this antenna is shown in Fig.6. From Fig.7, we can see that the peak gain of the antenna is 5.67dBi at 2.4 GHz band and 7.59dBi at 5.2 GHz band. The VSWR & impedance of this proposed antenna is 1.07 & 46.03 ohm at 2.48 GHz and 1.16 & 58.21 ohm at 5.18 GHz respectively. The impedance variation in Fig.9 is quite acceptable in both 2.4 GHz band as well as 5.2 GHz band. VSWR is near about 1 in the pass band in Fig.8 the phase is almost zero in the two pass bands.

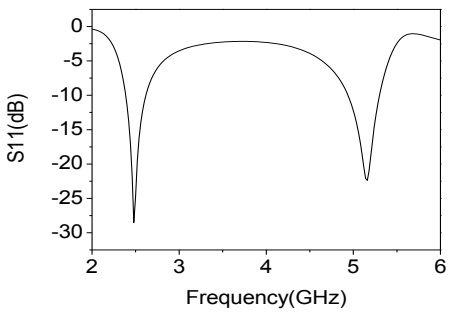

Fig.6. Variation of return loss with frequency.

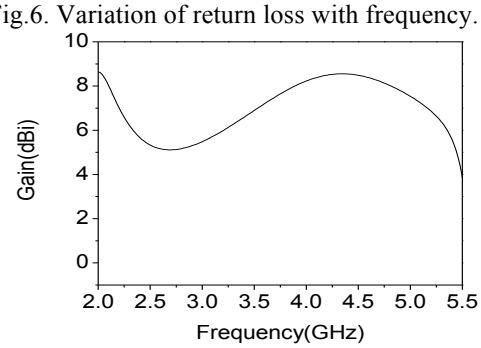

Fig.7. Variation of gain with frequency

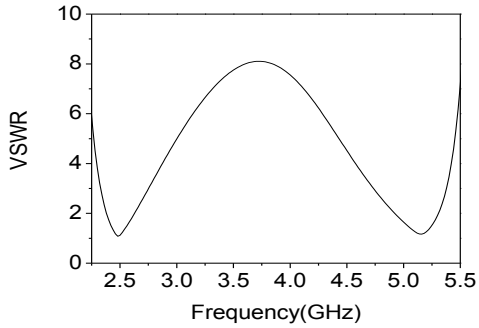

Fig.8. Variation of VSWR with frequency.

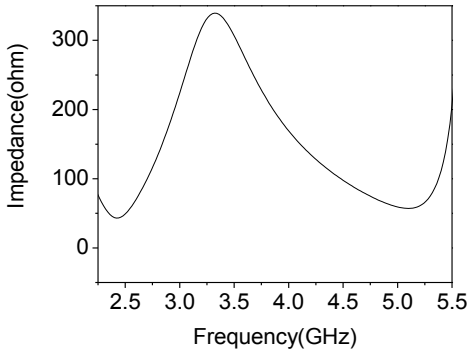

Fig.9. Variation of impedance with frequency.

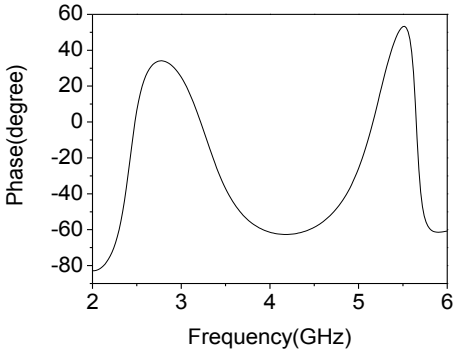

Fig.10. Variation of phase with frequency.

The radiation pattern in different plane for different frequency band is shown in figure below.

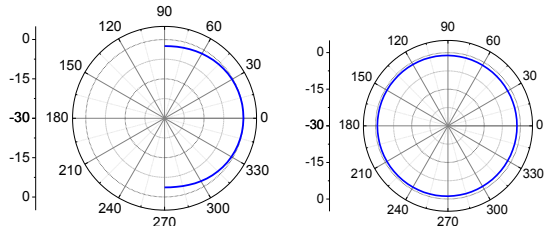

(a) (b)

Fig.11. Total gain in (a) vertical plane and (b) horizontal plane at 2.4GHz.

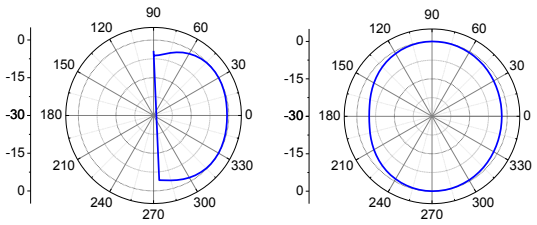

(a) (b)

Fig.12.Total gain in (a) vertical plane and (b) horizontal plane at 5.2GHz.

Table 2
Gain Comparison of Proposed Antenna and Different Reference Antennas

Antenna Name	Peak Gain (dBi)	Bandwidth
Proposed Dual band modified inverted FL(IFL) antenna	5.67 at 2.4 GHz band 7.64 at 5.2 GHz band	200MHz (2400~2600 MHz) 410MHz (4940~5350 MHz)
A Dual Band Metamaterial-Inspired Small monopole Antenna[7]	0.71 at 2.4 GHz band 1.53 at 5 GHz band	90 MHz (2420~ 2510 MHz) 3200 MHz (4520~7720 MHz)
2.4/5.2 GHz Dual-WLAN Unequal-Arms Dipole Antenna with a Chip Inductor for Omnidirectional Radiation Patterns[8]	2.9 at 2.4 GHz band 4 at 5.2 GHz band	220 MHz (2270~2490 MHz) 610 MHz (4750~5360 MHz)

4. CONCLISIONS

In this paper we have presented a dual band antenna design & its numerical simulation results, which is capable of operating in WLAN and Wi-Fi applications. We have focused to propose an antenna with good return loss characteristics, high gain, negligible phase shift, good radiation characteristics & unit VSWR. We saw our designed antenna has fulfilled all the requirements we have targeted. The simulation analysis for our proposed antenna has been carried out by applying numerical simulations in Numerical Electromagnetic Code (NEC) [9] measurements with using standard techniques. As the proposed antenna is very small in size, it is promising to be embedded within the different mobile devices & laptop computer employing Wi-Fi, & WLAN applications. As compared with others antennas proposed by different researchers, our proposed antenna is smaller in size & provide larger bandwidth with a high gain.

REFERENCES

[1] http://en.wikipedia.org/wiki/Telecommunication.

[2] http://wiki.mediaculture.org.au/index.php/wire-less History.

[3] K.D. Prasad, “Antenna and Wave Propagation”.

[4] Nobuyasu Takemura, “Inverted FLAntenna with Self-complementary Structure”,IEEETransactions on Antenna And Propagation,Vol.57,No.10, pp.3029-3034,October,2009.

[5] Lev Pazin, Nikolay Telzhensky and Yehuda Leviatan, “Multiband Flat-plate Inverted-F antenna for Wi-Fi/WiMAX Operation”,IEEE Antenna and Wireless Propagation letters,Vol.7,pp.197-200,2008.

[6] H-W.Liu,C.-H. Ku and C..-F. Yang, “Novel CPW-Fed Planner Monopole Antenna for WiMAX/WLAN Applications”,IEEE Antennas and wireless propagation letters,Vol.9,pp.240-243,2010.

[7] J.Zhu and G.V Eleftheriades “Dual band material inspired small monopole antenna for Wi-Fi applications” Electronics Letters VOl.45 , No 22 ,2009.

[8] S. H. Yeh, W. C. Yang, W. K. Su and C. Y. Wu, Information & Communications Research Laboratories, Industrial Technology Research Institute, Hsinchu 310, Taiwan Chung Cheng Institute of Technology, National Defense University Taoyuan 335, Taiwan 2007.

[9] “Numerical Electromagnetic Code” software (4NEC2) version 5.7.5.

Proceeding of the
International Conference on Electrical, Computer and Telecommunication Engineering
01- 02 December 2012 (ICECTE2012), RUET, Rajshahi-6204, Bangladesh

ICECTE2012: PI-0030

Bandwidth enhancement of a rectangular microstrip patch antenna

Rezwana Sultana[1] *Dr. Md. Mortuza Ali*[2] *and Fazle Rabbi Shalek Ahmed*[3]
[1]Lecturer, Department of Electrical and Electronics Engineering, Varendra Universtiy, Rajshahi
[2]Pro Vice Chancellor and Professor, , Department of Electrical and Electronics Engineering, Rajshahi University of Engineering and Technology (RUET) , Rajshahi
[3]Senior lecturer, Department of Computer Science and Engineering, University of Information Technology & Sciences (UITS), Rajshahi
Email : dola.ruet@gmail.com, mmali.ruet@gmail.com, bappi.paper@gmail.com

ABSTRACT
Microstrip Patch Antenna is analysed to improve its performance. The antenna is fed by a coaxial probe and is investigated with a rectangular Electromagnetic Band Gap (EBG) substrate. The substrate is made of a composite dielectric. Two different dielectric materials are used side by side to make a single substrate. Surface wave found to reduce for such a substrate. Thus an enhancement in antenna performance (gain, bandwidth and directivity) is observed.

KEYWORDS

Rectangular Microstrip Patch Antenna (RMPA), Electromagnetic Band Gap (EBG), Two-Dimensional Planar Surfaces, Return Loss, Gain, Bandwidth.

1. INTRODUCTION

Modern wireless system give greater emphasis on antenna for further development in communication technology as antenna is one of the most vital part in the RF system for receiving and transmitting the radio wave signals from and into the air. Microstrip Patch Antennas are widely used in wireless communication system as it posses attractive radiation characteristics, easy to feed, light weight, low cost and easy to analysis and fabricate [1]. But there are some drawbacks of Microstrip Patch Antenna such as low bandwidth, low gain and surface wave excitation [2-4]. Numerous techniques such as L-probe feed Patch Antenna, Reactive Impedance Substrate, Fractional Patch Antenna, and Triangular Patch Antenna Array with Hexagonal Defected Ground Substrate etc. are proposed to enhance antenna performance [5-7].

Electromagnetic Band Gap (EBG) / Photonic Band Gap (PBG) are structures useful in suppressing the surface waves and thus increase antenna performance (gain, directivity, and bandwidth) and reduces back lobe [8].

In this paper a Rectangular Microstrip Patch Antenna on two-dimensional planar EBG substrate is being proposed. Here the substrate is made of by joining two different materials of different dielectric constant according to length. Our proposed antenna gives better performance compare to conventional Rectangular Microstrip Patch Antenna on EBG surface.

2. MICROSTRIP PATCH ANTENNA

A Microstrip patch antenna consists of a radiating patch on one side of a dielectric substrate which has a ground plane on the other side as shown in Figure 1. The patch is generally made of conducting material such as copper or gold and can take any possible shape. The radiating patch and the feed lines are usually photo etched on the dielectric substrate.

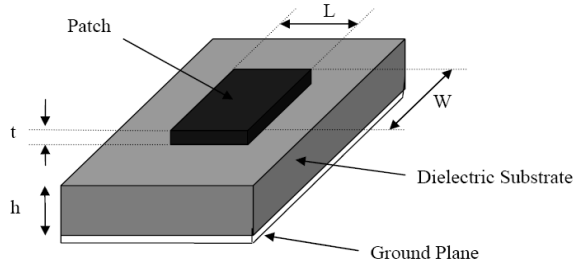

Figure 1: Microstrip Patch Antenna

A rectangular patch, the length L of the patch is usually $0.3333\lambda_0 < L < 0.5\lambda_0$ where λ_0 is the free-space wavelength. The patch is selected to be very thin such that $t << \lambda_0$, where t is the patch thickness. The height h of the dielectric substrate is usually $0.003\lambda_0 \leq h \leq 0.05\lambda_0$. The dielectric constant of the substrate (ε_0) is typically in the range $2.2 \leq \varepsilon_0 \leq 12$. Microstrip patch antennas can be fed by a variety of methods. The four most popular feed techniques are the microstrip line, coaxial probe, aperture coupling and proximity coupling. In this paper coaxial probe feed has been used due to easiness.

3. ELECTROMAGNETIC BAND GAP (EBG)

Electromagnetic Band Gap (EBG) structures can be defined as artificial periodic (or non periodic) objects that prevent or assist the propagation of electromagnetic waves in a specified band of frequency for all incident angle and polarization state. Two commonly employed features are suppressing unwanted substrate modes and acting as an artificial magnetic ground plane. The generation of surface waves degrades the antenna efficiency and radiation pattern and increases the mutual coupling of the antenna array which causes the blind angle of a scanning array [8].

EBG structures are usually realized by periodic arrangement of dielectric materials and metallic conductors. In general, they can be categorized into three groups according their geometric configuration: (a) three-dimensional volumetric structure, (b) two-dimensional planar surfaces and (c) one-dimensional transmission lines. This paper focuses on the two-dimensional planar EBG surfaces due to low profile, light weight, and low fabrication cost.

There are four main parameters affecting the performance of two-dimensional planar EBG structure such as rectangle width (w), gap width (g) substrate thickness (h) and substrate permittivity (ε_r) which are directly dependent upon the operating wavelength of the patch antenna.

4. DESIGN PARAMETERS FOR PROPOSED ANTENNA

The various design parameters of proposed Rectangular Microstrip Patch antenna which is operated at 2.96 GHz are given in the following table.

Antenna Part	Parameter	Value in cm
Patch	Length	4
	Width	3
Substrate	Length	5 Each
	Width	9
	Height	0.32
Dielectric Material 1(Rogers RT/duroid 5880(tm))	Relative Permittivity	2.2
	Dielectric Loss Tangent	0.0009
Dielectric Material 2 (Arlon AD320(tm))	Relative Permittivity	3.2
	Dielectric Loss Tangent	0.003
EBG substrate	Rectangle Width	1
	Gap Width	0.02

Table 1: Design Parameters

5. SIMULATION RESULTS AND DISCUSSION

Now a day, it is common practice to evaluate the system performances through computer simulation before real time implementation. In my job I have used the High Frequency Structure Simulator (HFSS) which very useful and user friendly. This software simulates any EM structure using Finite Element Method (FEM). The geometrical configuration of rectangular Microstrip patch antenna with EBG structure is shown in figure 2. From the figure 3 it is observed that minimum return loss is -24.81 dB. At the point of return loss -10 dB the bandwidth is 0.18 GHz. Figure 4 shows maximum gain which is 15.934 dB. Figure 5 shows maximum directivity where return loss is minimum which is 36.026.

The geometrical configuration of rectangular Microstrip patch antenna with EBG structure is shown in figure 6.From the figure 7 it is observed that minimum return loss is -22.91 dB (at 7.53 GHz). At the point of return loss -10 dB the bandwidth is 0.63 GHz. Figure 8 shows maximum gain where return loss is minimum (7.53 GHz) which is 11.047 dB. Figure 9 show

maximum directivity where return loss is minimum which 16.045 is.

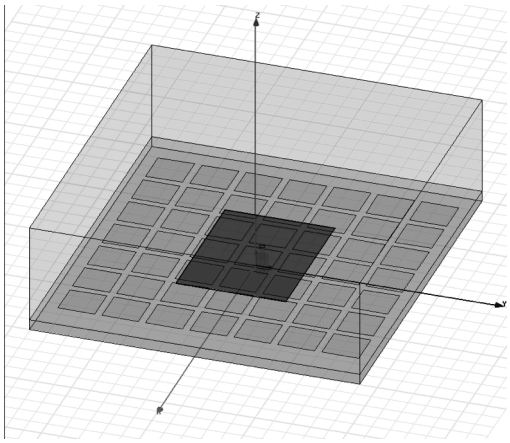

Figure 2: RMPA with EBG structure

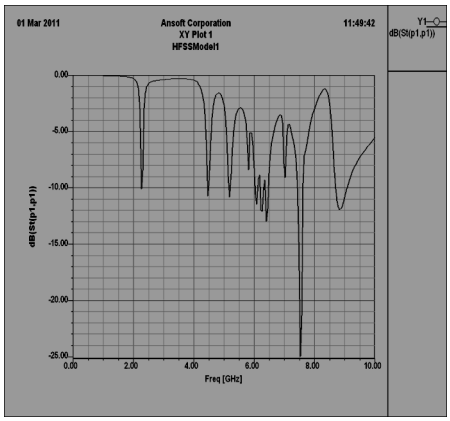

Figure 3: Return Loss of a RMPA with EBG structure.

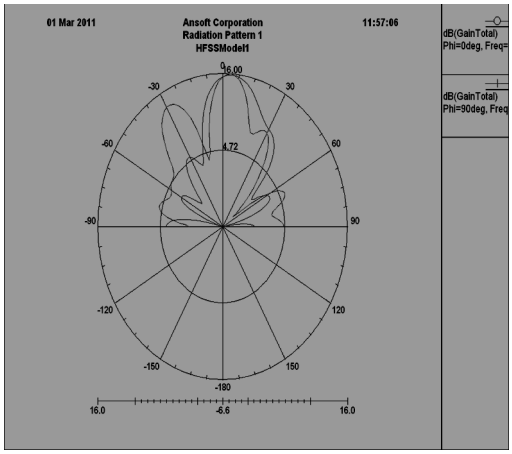

Figure 4: Maximum gain where return loss is minimum

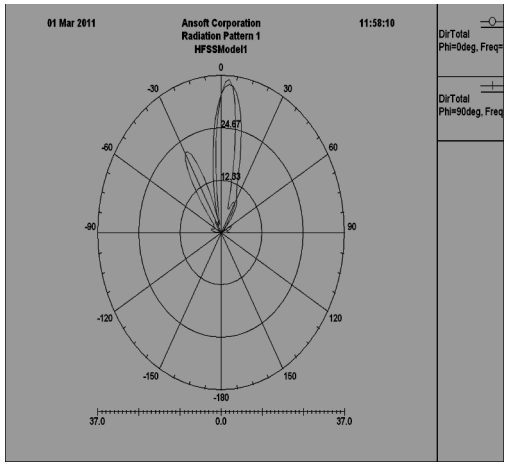

Figure 5: Maximum directivity

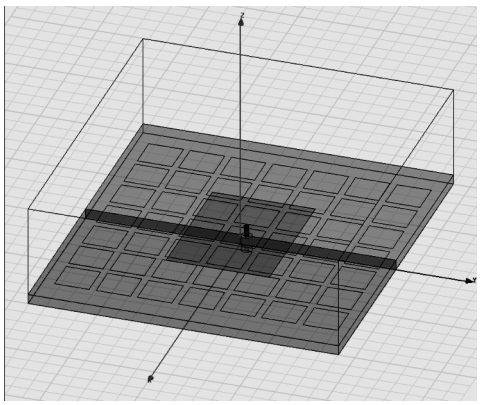

Figure 6: RMPA with EBG structure made of two piece of dielectric material

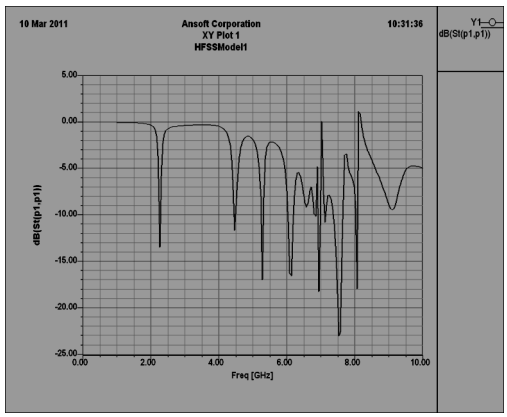

Figure 7: Return Loss of a RMPA with EBG structure made of two piece of dielectric material

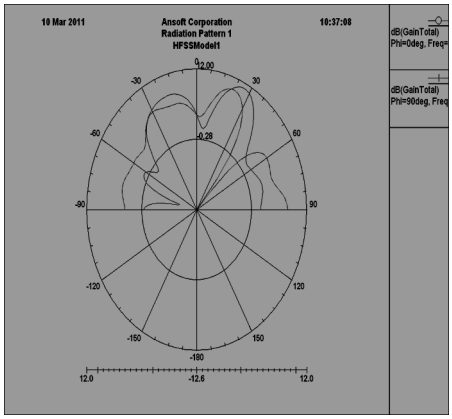

Figure 8: Maximum gain (where return loss is minimum)

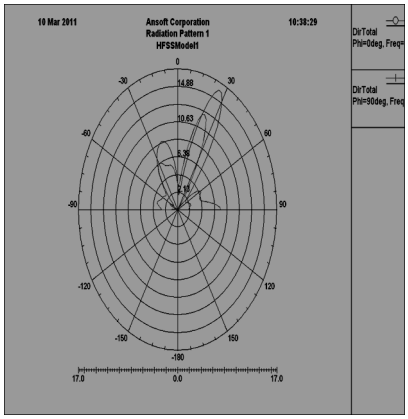

Figure 9: Maximum directivity

6. CONCLUSIONS

The objective of this paper is to design a Rectangular Microstrip Antenna which posses enhanced bandwidth. From the simulated results it is obvious that Rectangular Microstrip Antenna with conventional EBG substrate has a bandwidth of 180 MHz where as Rectangular Microstrip Antenna with EBG substrate where the substrate is made of by joining two different dielectric material with different permittivity has a bandwidth of 630 MHz . The designed antenna also possesses better gain and directivity compared to conventional Microstrip Antenna.

REFERENCES

[1] Constantine A. Balanis, (2005) "*Antenna Theory Analysis and Design*", Third Edition, John Wiley & Sons.

[2] Jing Liang & Hung Yu David Yang, (June 2007)"Radiation Characteristics of a Microstrip Patch over an Electromagnetic Bandgap Surface", IEEE Transactions on Antennas & Propagation, Vol. 55, pp.1691-1697.

[3] K. L. Wong, (2002) *Compact and Broadband Microstrip Antenna*, New York, Wiley.

[4] Mohammad Tariqul Islam, Mohammad Nazmus Sakib, Norbahiah Misran & Baharudin Yatim, (December 2008)" Analysis of Broadband Slotted Microstrip Patch Antenna", Proceeding of the International Conference on Computer and Information Technology, pp.758-761.

[5] Mohammad Tariqul Islam, Mohammad, Nazmus Sakib, Norbahiah Misran & Tiang Sew Sun, (2009) " Broadband Microstrip Patch Antenna", European Journal of Scientific Research, ISSN 1450-216X, vol. 27 No. 2 pp.174-180.

[6] Hossein Mosallaei & Kamal Sarabandi, (September 2004) "Antenna Miniaturization and Bandwidth Enhancement Using a Reactive Impedance Substrate", IEEE Transactions on Antennas & Propagation, Vol. 52, No. 9.

[7] Raj Kumar & P. Malathi, (November 2009) "On the Design of Fractional Patch Antenna & Backscattering Reduction", International Journal of Recent Trends in Engineering, Vol. 2, No.7.

[8] Fan Yang & Yahya Rahmat Sami, " *Electromagnetic Band Gap Structure in Antenna Engineering*", Cambridge University Press.

Proceeding of the
International Conference on Electrical, Computer and Telecommunication Engineering
01- 02 December 2012 (ICECTE2012), RUET, Rajshahi-6204, Bangladesh

ICECTE2012: PI-0031

Bandwidth enhancement of a rectangular microstrip patch antenna

Rezwana Sultana[1] *Dr. Md. Mortuza Ali*[2] *and Fazle Rabbi Shalek Ahmed*[3]

[1]Lecturer, Department of Electrical and Electronics Engineering, Varendra Universtiy, Rajshahi
[2]Pro Vice Chancellor and Professor, , Department of Electrical and Electronics Engineering, Rajshahi University of Engineering and Technology (RUET) , Rajshahi
[3]Senior lecturer, Department of Computer Science and Engineering, University of Information Technology & Sciences (UITS), Rajshahi
Email : dola.ruet@gmail.com, mmali.ruet@gmail.com, bappi.paper@gmail.com

ABSTRACT

Microstrip Patch Antenna is analysed to improve its performance. The antenna is fed by a coaxial probe and is investigated with a rectangular Electromagnetic Band Gap (EBG) substrate. The substrate is made of a composite dielectric. Two different dielectric materials are used side by side to make a single substrate. Surface wave found to reduce for such a substrate. Thus an enhancement in antenna performance (gain, bandwidth and directivity) is observed.

KEYWORDS

Rectangular Microstrip Patch Antenna (RMPA), Electromagnetic Band Gap (EBG), Two-Dimensional Planar Surfaces, Return Loss, Gain.

1. INTRODUCTION

Modern wireless system give greater emphasis on antenna for further development in communication technology as antenna is one of the most vital part in the RF system for receiving and transmitting the radio wave signals from and into the air. Microstrip Patch Antennas are widely used in wireless communication system as it posses attractive radiation characteristics, easy to feed, light weight, low cost and easy to analysis and fabricate [1]. But there are some drawbacks of Microstrip Patch Antenna such as low bandwidth, low gain and surface wave excitation [2-4]. Numerous techniques such as L-probe feed Patch Antenna, Reactive Impedance Substrate, Fractional Patch Antenna, and Triangular Patch Antenna Array with Hexagonal Defected Ground Substrate etc. are proposed to enhance antenna performance [5-7].

Electromagnetic Band Gap (EBG) / Photonic Band Gap (PBG) are structures useful in suppressing the surface waves and thus increase antenna performance (gain, directivity, and bandwidth) and reduces back lobe [8].

In this paper a Rectangular Microstrip Patch Antenna on two-dimensional planar EBG substrate is being proposed. Here the substrate is made of by joining two different materials of different dielectric constant according to length. Our proposed antenna gives better performance compare to conventional Rectangular Microstrip Patch Antenna on EBG surface.

2. MICROSTRIP PATCH ANTENNA

A Microstrip patch antenna consists of a radiating patch on one side of a dielectric substrate which has a ground plane on the other side as shown in Figure 1. The patch is generally made of conducting material such as copper or gold and can take any possible shape. The radiating patch and the feed lines are usually photo etched on the dielectric substrate.

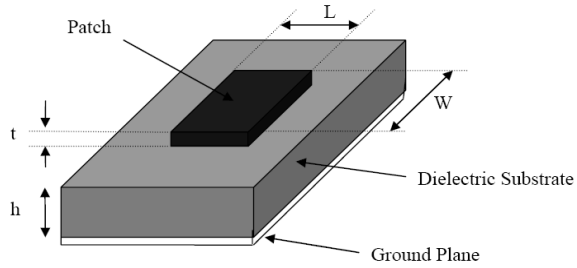

Figure 1: Microstrip Patch Antenna

A rectangular patch, the length L of the patch is usually $0.3333\lambda_0 < L < 0.5\lambda_0$ where λ_0 is the free-space wavelength. The patch is selected to be very thin such that $t << \lambda_0$, where t is the patch thickness. The height h of the dielectric substrate is usually $0.003\lambda_0 \leq h \leq 0.05\lambda_0$. The dielectric constant of the substrate (ε_0) is typically in the range $2.2 \leq \varepsilon_0 \leq 12$. Microstrip patch antennas can be fed by a variety of methods. The four most popular feed techniques are the microstrip line, coaxial probe, aperture coupling and proximity coupling. In this paper coaxial probe feed has been used due to easiness.

3. ELECTROMAGNETIC BAND GAP (EBG)

Electromagnetic Band Gap (EBG) structures can be defined as artificial periodic (or non periodic) objects that prevent or assist the propagation of electromagnetic waves in a specified band of frequency for all incident angle and polarization state. Two commonly employed features are suppressing unwanted substrate modes and acting as an artificial magnetic ground plane. The generation of surface waves degrades the antenna efficiency and radiation pattern and increases the mutual coupling of the antenna array which causes the blind angle of a scanning array [8].

EBG structures are usually realized by periodic arrangement of dielectric materials and metallic conductors. In general, they can be categorized into three groups according their geometric configuration: (a) three-dimensional volumetric structure, (b) two-dimensional planar surfaces and (c) one-dimensional transmission lines. This paper focuses on the two-dimensional planar EBG surfaces due to low profile, light weight, and low fabrication cost.

There are four main parameters affecting the performance of two-dimensional planar EBG structure such as rectangle width (w), gap width (g) substrate thickness (h) and substrate permittivity (ε_r) which are directly dependent upon the operating wavelength of the patch antenna.

4. DESIGN PARAMETERS FOR PROPOSED ANTENNA

The various design parameters of proposed Rectangular Microstrip Patch antenna which is operated at 2.96 GHz are given in the following table.

Antenna Part	Parameter	Value in cm
Patch	Length	4
	Width	3
Substrate	Length	5 Each
	Width	9
	Height	0.32
Dielectric Material 1(Rogers RT/duroid 5880(tm))	Relative Permittivity	2.2
	Dielectric Loss Tangent	0.0009
Dielectric Material 2 (Arlon AD320(tm))	Relative Permittivity	3.2
	Dielectric Loss Tangent	0.003
EBG substrate	Rectangle Width	1
	Gap Width	0.02

Table 1: Design Parameters

5. SIMULATION RESULTS AND DISCUSSION

Now a day, it is common practice to evaluate the system performances through computer simulation before real time implementation. In my job I have used the High Frequency Structure Simulator (HFSS) which very useful and user friendly. This software simulates any EM structure using Finite Element Method (FEM). The geometrical configuration of rectangular Microstrip patch antenna with EBG structure is shown in figure 2. From the figure 3 it is observed that minimum return loss is -24.81 dB. At the point of return loss -10 dB the bandwidth is 0.18 GHz. Figure 4 shows maximum gain which is 15.934 dB. Figure 5 shows maximum directivity where return loss is minimum which is 36.026.

The geometrical configuration of rectangular Microstrip patch antenna with EBG structure is shown in figure 6.From the figure 7 it is observed that minimum return loss is -22.91 dB (at 7.53 GHz). At the point of return loss -10 dB the bandwidth is 0.63 GHz. Figure 8 shows maximum gain where return loss is minimum (7.53 GHz) which is 11.047 dB. Figure 9 show maximum directivity where return loss is minimum which 16.045 is.

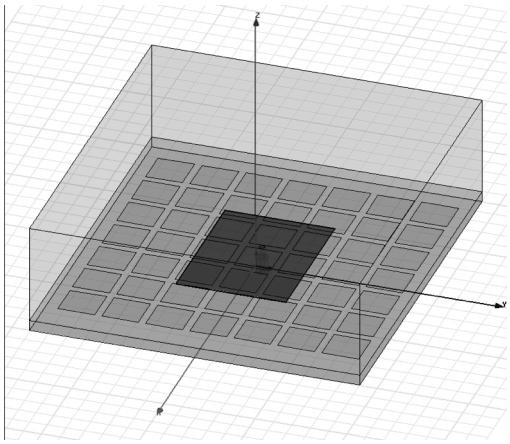

Figure 2: RMPA with EBG structure

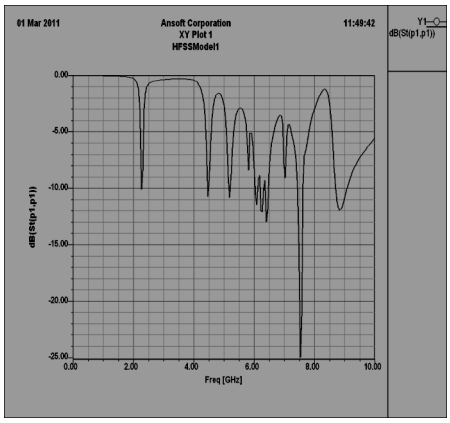

Figure 3: Return Loss of a RMPA with EBG structure.

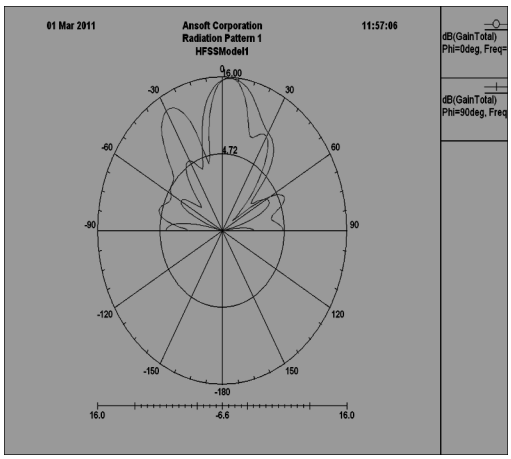

Figure 4: Maximum gain where return loss is minimum

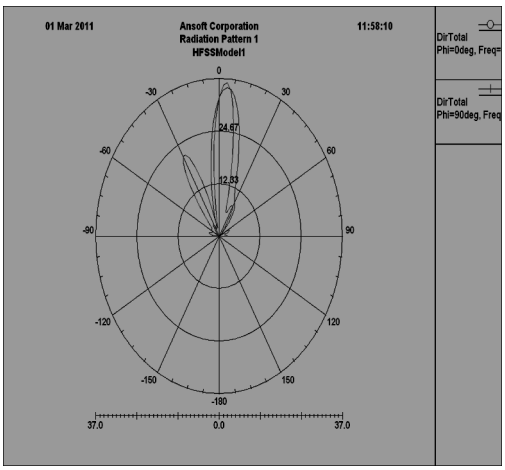

Figure 5: Maximum directivity

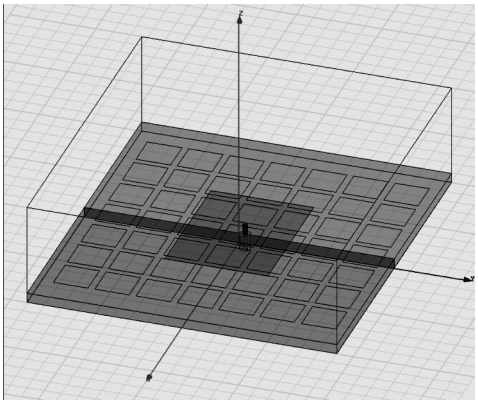

Figure 6: RMPA with EBG structure made of two piece of dielectric material

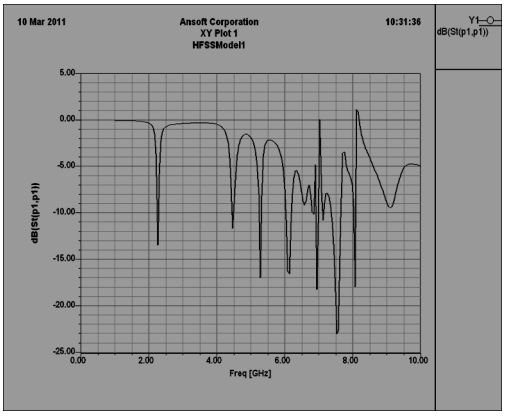

Figure 7: Return Loss of a RMPA with EBG structure made of two piece of dielectric material

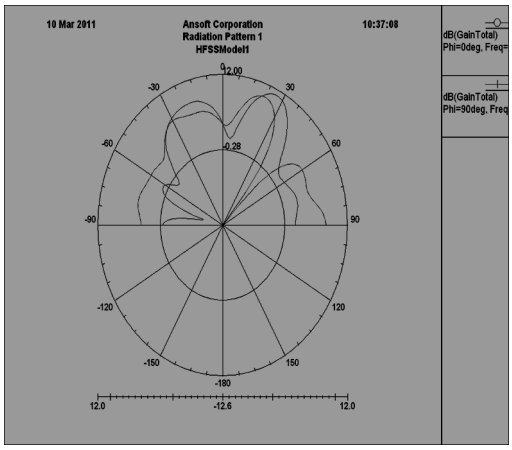

Figure 8: Maximum gain (where return loss is minimum)

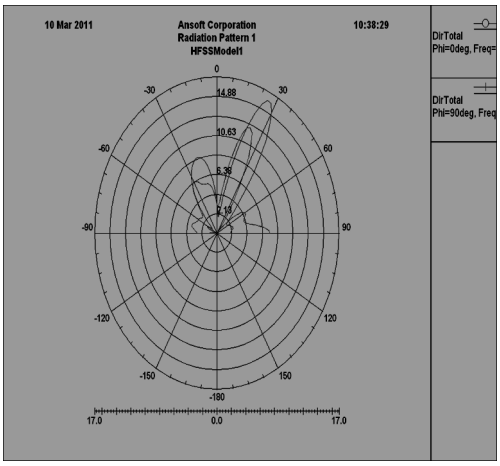

Figure 9: Maximum directivity

6. CONCLUSIONS

The objective of this paper is to design a Rectangular Microstrip Antenna which posses enhanced bandwidth. From the simulated results it is obvious that Rectangular Microstrip Antenna with conventional EBG substrate has a bandwidth of 180 MHz where as Rectangular Microstrip Antenna with EBG substrate where the substrate is made of by joining two different dielectric material with different permittivity has a bandwidth of 630 MHz . The designed antenna also possesses better gain and directivity compared to conventional Microstrip Antenna.

REFERENCES

[1] Constantine A. Balanis, (2005) "*Antenna Theory Analysis and Design*", Third Edition, John Wiley & Sons.

[2] Jing Liang & Hung Yu David Yang,(June 2007)"Radiation Characteristics of a Microstrip Patch over an Electromagnetic Bandgap Surface", IEEE Transactions on Antennas & Propagation, Vol. 55, pp.1691-1697.

[3] K. L. Wong, (2002) *Compact and Broadband Microstrip Antenna*, New York, Wiley.

[4] Mohammad Tariqul Islam, Mohammad Nazmus Sakib, Norbahiah Misran & Baharudin Yatim, (December 2008)" Analysis of Broadband Slotted Microstrip Patch Antenna", Proceeding of the International Conference on Computer and Information Technology, pp.758-761.

[5] Mohammad Tariqul Islam, Mohammad, Nazmus Sakib, Norbahiah Misran & Tiang Sew Sun, (2009) " Broadband Microstrip Patch Antenna", European Journal of Scientific Research, ISSN 1450-216X, vol. 27 No. 2 pp.174-180.

[6] Hossein Mosallaei & Kamal Sarabandi, (September 2004) "Antenna Miniaturization and Bandwidth Enhancement Using a Reactive Impedance Substrate", IEEE Transactions on Antennas & Propagation, Vol. 52, No. 9.

[7] Raj Kumar & P. Malathi, (November 2009) "On the Design of Fractional Patch Antenna & Backscattering Reduction", International Journal of Recent Trends in Engineering, Vol. 2, No.7.

[8] Fan Yang & Yahya Rahmat Sami, " *Electromagnetic Band Gap Structure in Antenna Engineering*", Cambridge University Press.

Proceeding of the
International Conference on Electrical, Computer and Telecommunication Engineering
01- 02 December 2012 (ICECTE2012), RUET, Rajshahi-6204, Bangladesh

ICECTE2012: PI-0032

Numerical Evaluation of Specific Absorption Rate and Skin Depth on Human Body Tissue Due To Electromagnetic Field Emitted From Mobile Phone Antenna

M.E.Haque[1], A.A.Suman[2] and M.M.Rashid[3]
[1]Department of Electrical, Electronics and System engineering
University Kebangsaan Malaysia, Selangor, 43600, Malaysia.
[2] Department of Electronics and Telecommunication Engineering,
Rajshahi University of Engineering and Technology, Rajshahi, Bangladesh.
[3] Department of Telecommunication, Ahsanullah Institute Of Technical and Vocational Education And Training, Dhaka, Bangladesh.
E-mail: ershadul.ruet05@gmail.com[1], suman.ete.ruet@gmail.com[2] and mamun722_ruet@ yahoo.com[3]

ABSTRACT
The development of mobile phone communication infrastructure in the world has promoted which lead public concern over possible health effects exposure to radio frequency electromagnetic energy(RFEME), emanating from mobile phone antenna . The micro-strip patch antenna plays an important role in electromagnetic energy transmitting and receiving phenomena in mobile phone. In every day human are affected by the radiation of electromagnetic field emitted from mobile phone antenna. The effect of the radiation directly calculated so difficult because the complexity of the human body structure .Two major factor are consider among many other factor when considering effect of radiation from antenna, one is the specific absorption rate (SAR) and another is the skin depth (SD) .The specific absorption rate (SAR) and skin depth (SD) are directly calculated more complex. In this paper, we evaluate the numerical analysis of the specific absorption rate (SAR) and skin depth (SD) with respect to the real life application of operating frequency of the mobile phone for GSM communication. To develop the model, MATLAB tool were used and result from the model was analysis and also compare result theoretically with the other researcher.

KEY WORDS: Electromagnetic radiation effect, skin depth, specific absorption rate, field penetration.

1. INTRODUCTION

In the recent years, the widespread use of mobile phones has given rise to a growing concern over their possible adverse effects of the electromagnetic waves emitted on human health [1]-[6].Human are being meets electromagnetic (EM) radiation in every day. Since, Electrical and electronic devices, wireless cellular telephones and other mobile communication services is the fastest growing field in the world; therefore uncertainty about the health effects of RF is major concern issue today. When human are affected by the electromagnetic field ,the electrical property of the human body is changed like conductivity and permeability and some phenomena of the electromagnetic field like attenuation, diffraction, dispersion, reflection also occurs. But, to measure those phenomena inside the human body is quite difficult. When the tissue of the human body absorb the radiation of the electromagnetic wave then the temperature of the human body tissue will increase because EM(electromagnetic) energy increase kinetic energy of the absorbing molecules. The electromagnetic energy absorb by the tissue will produce temperature that dependence on the cooling mechanism of the body tissue. When the thermoregulatory capability of the system is exceed, tissue damage result will occur. When a biological system is exposed to microwave radiation, an internal field is induced in the system. To calculation of this internal field is named as dosimetry [7]. When high frequency microwave radiation penetrates into the body exposed molecules start to move and collide each other and collision creates friction and thus heat. The properties of electromagnetic waves define neither the ionizing or non-ionizing radiation. Some electromagnetic waves carry so much energy per quantum that have the ability to break bonds between molecules. In the electromagnetic spectrum, gamma rays are given off by radioactive materials, cosmic rays and X-rays carry this property and are called 'ionizing radiation'. Fields whose quanta are insufficient to break molecular bonds are called ‘non-ionizing radiation’. Man-made sources of electromagnetic fields are found at the relatively long wavelength and low frequency end of the electromagnetic spectrum and their quanta

are unable to break chemical bonds [8]-[11]. The basic limit of exposure is expressed by the quantity called "specific absorption rate" (SAR) [12]. The penetration of the electric field current in the human body is known as skin depth. It's one of the major factor when calculating the effect of the radiation because its define how much electromagnetic field penetrate in human body.

2. SAFETY AND STANDARD

The FCC established safety guidelines and exposure limits for cell phone radiation in 1996. Every mobile phone sold in the U.S. has to be tested and meet these standards before they can be sold Radiation levels are tested based on the specific absorption rate (SAR). SAR is a way of measuring how much radio frequency energy is absorbed by the human body [13]. The maximum legal SAR level is 1.6 watts per kilogram (W/Kg). As of 2000, all cell phone manufacturers must place labels on their phones disclosing their radiation level. To find the specific radiation level of the phone you're using, you can also visit the FCC web site [14] and look it up by brand. In 2002, a two-year study performed by the Radiation and Nuclear Safety Authority in Finland, found that human cells exposed to one hour of cell phone radiation (900 MHz GSM) triggered a response that normally only occurs when cells are being damaged. This lead the cells that make up blood vessel walls to shrink, allowing tiny molecules to pass through the blood brain barrier [15].

Fig. 1 Shrink Blood Vessel Due to Effect of Radiation

Since the radiation decreases exponentially as the distance increases between human and source of the radiation like antenna, so as you can maintain large distance between you and mobile phone. But, recently you cannot do this due to the invention of the Bluetooth. There are few alternatives to ensure complete safety even though there are some common sense included [16], [17]:

1) Create small amount of time as much as possible when you talking on the phone
2) Use speakerphone instead putting the phone directly in the ear.
3) Try to use non –Bluetooth handset.
4) Try to make no call inside the building.
5) To decrease RF interference attaches a ferrite bead to the handset.

3. EMF DISTRIBUTION INSIDE BODY TISSUE

In everyday day, every time, every man are affected by EMF (Electromagnetics Field) because day by day the application of electromagnetic wave increases in house, industry, medical etc. When the E-field distribution inside body, then the SAR introduce and the rate of change of the SAR varied from organ to organ like eye, head etc. . The region with the maximum field corresponds to the region with maximum SAR value. Since, the electrical property of the human body varied from man to man because the property of the organ is varied. So, the electric field intensity inside body is different and SAR also differs because density and conductivity is changed. On the other hand, as increasing frequency, conductivity of tissue is increasing [18].

4. SKIN DEPTH INSIDE HUMAN BODY TISSUE

The skin depth provides a useful approximation for field penetration in a human body. Skin effect is the tendency of an alternating electric current to distribute itself within human body. The electric current flow mainly skin of the human body between the outer surface and a level called skin depth .The skin depth provides a useful approximation for field penetration in human body tissue for calculation the effect of the electromagnetic field radiation in the human body and the penetration of the EMF is changes in different organ because differ organ have different ability to protect EMF radiation like head, eye etc. Skin Depth is due to the eddy current

(arising from a changing H field) and it also determined by the frequency, permeability, conductivity and defines how much area of your body affected by the EMF radiation. The effective skin depth [Fig.2] is given by the following equation:

$$\delta = \sqrt{\frac{2}{2 * \pi * f * \mu * \sigma}} \qquad (1)$$

Where (N/A^2) and σ (S/m) are the permeability and electrical conductivity of the tissue and f is the operating frequency of the mobile phone. Permeability is the measure of the ability of tissue to support the formation of the magnetic field within itself and conductivity measure tissue ability to carry the electric signal. The H-field created due to the moving of the eddy current flow and cancelling the eddy current as going to the center by the H-field and pullout to the surface of the tissue [Fig.3].

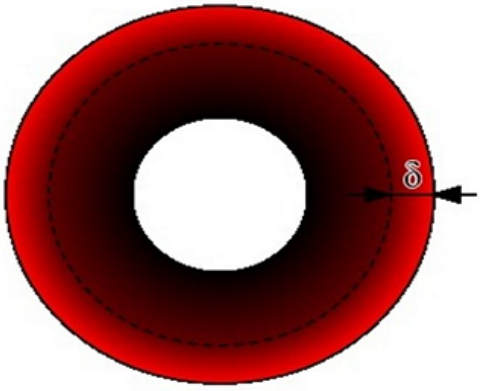

Fig. 2 Skin Depth

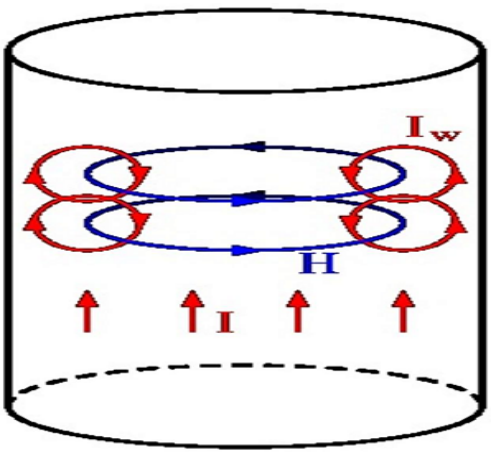

Fig. 3 Eddy Current and H-field Pattern

5. NUMERICAL ANALYSIS OF SKIN DEPTH INSIDE HUMAN BODY TISSUE

For Numerical simulation, we assume that inside body tissue the electric field intensity E=1V/m and μ = 4*Pi*10-7 N/A2, σ = 1.90 S/m and =1010 Kg/m3. Since now a day's 850MHz, 900 MHz, 1800MHz, 1900MHz and 2100 MHz frequency band are commonly used in the worldwide for GSM system whereas 2100MHz frequency band is assigned for 3G GSM system. The skin depth calculated from the equation (1) and result is given in the below table I with considerable respective frequency.

Table .1Skin Depth Calculation

Frequency f,(MHz)	Skin Depth, (δ)
850	12.5237
900	12.1708
1800	8.6061
1900	8.3765
2100	7.9677

The below graph represent the skin depth result:

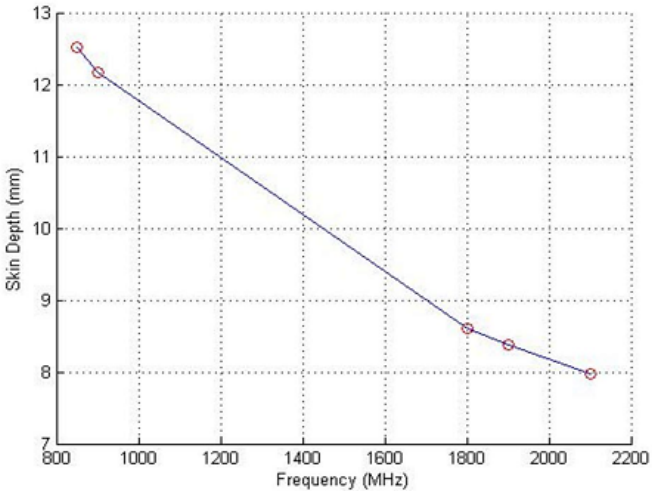

Fig. 4 Skin depth versus frequency plot

6. NUMERICAL ANALYSIS OF SPECIFIC ABSORPTION RATE

When electromagnetic wave propagates through human tissues, the energy of the electromagnetic wave is absorbed by the tissues. The rate at which electromagnetic energy is absorbed by the tissues of the human body is known as specific absorption rate (SAR). The specific absorption rate (SAR) inside the body is given by the following equation [18]:

$$SAR = \frac{\sigma E^2}{\rho} [W/kg] \qquad (2)$$

Where, E (V/m) is the electric field intensity of the electromagnetic wave in the tissue, (S/m) and (kg/m3) are the conductivity and the density of the human tissue respectively. Several method are introduces to evaluate the numerical analysis of electromagnetic energy absorption specially SAR. Among those method of moments or MOM and finite domain time difference (FDTD) are commonly used. From Yee notation (Dayawansa 2006), grid point of the body define by (i,j,k) and inside the body into δ depth ($i\delta_x$, $j\delta_y$, $k\delta_z$), the SAR given by

$$SAR = \frac{3\sigma\delta^2}{2\rho} \text{[W/kg]} \qquad (3)$$

Where δ is the skin depth of the body tissue and $\delta_x = \delta_y = \delta_z = \delta$. The SAR can be calculated from equation (3) and table II provided the SAR result with selected frequency band.

Table.2 SAR Calculation

Frequency f,(MHz)	SAR(W/kg)
50	$4.42*10^{-7}$
900	$4.18*10^{-7}$
1800	$2.09*10^{-7}$
1900	$1.98*10^{-7}$
2100	$4.42*10^{-7}$

Fig. 5 Electromagnetic field radiation inside human body.

The graphical representation of the skin depth is given below
Figure (6):

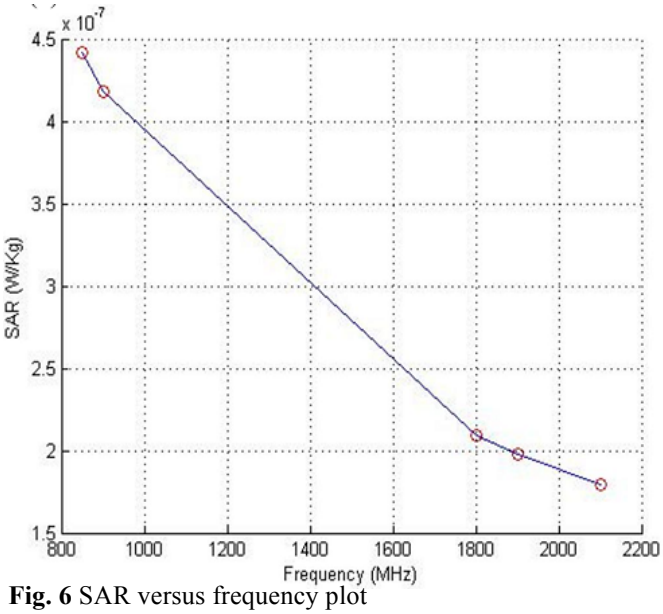

Fig. 6 SAR versus frequency plot

7. RESULTS AND DISCUSSION

We can say from table I, as the frequency is increases the skin depth is decreases that means most of the circulating current propagate through skin of the body. When, the frequency increases twice than the resultant skin depth going to half of the previous one .On the other hand, from table II, we see that the value SAR of the tissue is decreases as the frequency increases .We also plot skin depth and SAR with respect considerable frequency using MATLAB .From above graph, the value of the skin depth and SAR decreases as increases the frequency which is same result with numerical analysis. Therefore, by increasing the frequency, the propagation of the electromagnetic field is changed due to change of specific absorption rate (SAR) and also skin depth. According to FCC safety guideline our SAR results not exceed the specified value. We also compare our result with another researcher result. In telecommunication system 900 MHz and 1800 MHz frequency signal are widely used among those 900MHz signal are used to cover the large service region because its larger wavelength and small sensitive to the obstacle but its skin depth and SAR is greater than1800 MHz signal frequency band which is used for larger capacity than 900 MHz system but small wavelength is responsible for coverage and sensitive to obstacle smaller the skin depth and SAR value.

8. CONCLUSION

This paper present harmful effect of the electromagnetic field (EMF) and which factor are most important to calculate the effect of the EMF and provide some safety guideline. It's also provided numerical investigation of the SAR and skin depth, this two factor are considering when considering the effect of EMF. The result show that the electromagnetic waves can penetrate inside the body is more at lower frequency than higher frequency and assuming that the electromagnetic waves were able to propagate into the nucleus and the electromagnetic field was still high in the in the human skin tissue will become damaged. The damaged cell may cause various diseases such as skin cancer and etc. On the other hand, SAR is more at lower frequency than higher frequency even if the electromagnetic field radiation depend on many factor like antenna dimension, propagation media etc. From this finding, finally we can say that lower frequency electromagnetic field radiation is more harmful than higher frequency because skin depth and SAR is more at lower frequency than higher.

REFERENCES:

[1] Barnett, J.L Timotijevic, R. Shepherd, and V. Senior, "Public responses to precautionary information from the Department of Health (UK) about possible health risks from mobile phones," Health Policy, Vol. 82, No. 2, 240–250, 2007.

[2] Karger, C. P., "Mobile phones and health: A literature overview," Z. Med. Phys.Vol. 15, No. 2, 73–85, 2005.

[3] Wu, B. I., F. C. A. I. Cox, and J. A. Kong, "Experimental methodology for non-thermal effects of electromagnetic radiation on biologics,"Journal of Electromagnetic Waves and Applications, Vol. 21, No. 4, 533–548, 2007.

[4] Stilgoe, J., "The (co-) production of public uncertainty: UK scientific advice on mobile phone health risks," Public Underst. Sci., Vol. 16, No. 1, 45–61, 2007.

[5] Elder, A. J., C.-K. Chou and J. J. Morrissey, "Radiofrequency exposure and human health, "PIERS Online, Vol. 3, No. 2, 149–153, 2007.

[6] Sakari, L., "Recent advances in bioelectromagnetics research on mobile telephony and health — An introduction,"PIERS Online, Vol. 2, No. 2, 192–196, 2006.

[7] Bernardi, P., S. Pisa, E. Puizzi, "Specific Absorption Rate and Temperature Increases in the Head of a Cellular-Phone User," IEEE Transactions on Microwave Theory and Techniques, Vol. 48, no. 7, pp. 1118-1126, July 2000.

[8] Çelik, C.G., "EM Effects of Mobile Phone on Human being," MS. Thesis, Boğaziçi University, Istanbul, Turkey, 2001.

[9] Demirbilek, B., "Specific Absorption Rate Assessment in a Human Head Model Exposed to Radiation from Cellular Phone" MS. Thesis, Boğaziçi University, Istanbul, Turkey, 2001.

[10] Guidelines for Limiting Exposure to Time-Varying Electric, Magnetic and Electromagnetic Fields (up to 300 GHz), ICNRP GUIDELINES, Vol.74, No.4, pp.494-522, April 1998.

[11] WHO, World Health Organizations Fact Sheet No.193, "Electromagnetic Fields and Public Health, Mobile Telephones and Their Base Stations",http://www.who.int/intfs/en/fact193.html, June 2000.

[12] Stevens, N., and L.Martens, "Comparison of Averaging Procedure for SAR Distribution at 900 and 1800 MHz," IEEE Transactions on Microwave Theory and Techniques, Vol. 48, no.11, pp. 2180-2184, November 2000..

[13] Howstuffworks.com,"How cell-phone radiation works",http://electronics.howstuffworks.com/cell-phone-radiation.htm/print-able (Accessed June 27, 2007).

[14] FCC, SAR Information from individual manufacturers,http://www.fcc.gov/cgb/sar/(Accessed July 3, 2007)

[15] http://www.blackwellsynergy.com/doi/abs/10.1046/j.1432 0436.2002.700207.x (Accessed July 3, 2007).

[16] Compliance Engineering Magazine, "Filtering out interference signals with cable ferrites", http://www.ce-mag.com/archive/02/11/may.html (Accessed July 3, 2007).

[17] ELMAC Services, "Using Ferrites for interference suppression", http://www.elmac.co.uk/pdfs/ferrite.pdf (Accessed July 3, 2007).

[18] Dayawansa, M. A. A. K. a. I. J. (2006). "Energy absorption by the human body from RF and microwave emissions in Sri Lanka." Sri Lankan Journal of Physics Vol. 7 (2006), 35-47(INSTITUTE OF PHYSICS - SRI LANKA).

Proceeding of the
International Conference on Electrical, Computer and Telecommunication Engineering
01- 02 December 2012 (ICECTE2012), RUET, Rajshahi-6204, Bangladesh

ICECTE2012: PI-0034

Comparative design analysis of Microstrip single element patch and corporate feed array antenna for X band applications

Md. Imran Hasan[1], M. A. Motin[2], Shah Ariful Hoque Chowdhury[3], Abdul Khaleque[4]
[1,3]Dept. of Electronics and Telecommunication Engineering, Rajshahi University of Engineering & Technology, Rajshahi-6204, Bangladesh.
[2,4]Department of Electrical & Electronic Engineering, Rajshahi University of Engineering & Technology, Rajshahi 6204, Bangladesh.
E-mail: imranruet@yahoo.com, motin_eee_06@yahoo.com, arif.1968.ruet@gmail.com, khaleque_eee@yahoo.com

ABSTRACT
This paper present a high gain, low cost and simple microstrip single patch and array antenna for applications in X-band. Here array antennas such as corporate feed (4×1) and single element patch is designed, simulated, analyzed and compared with respect to antenna performance such as return loss, gain, directivity etc. The simulation has been performed by simulation software GEMS version 7.71.01 and designed antenna provide maximum return loss -34.528dB at 11.962GHz and maximum gain 20.3dBi by using Taconic TLY-5 dielectric substrate with relative permittivity 2.2 and height 1.588mm. Since the simulation frequency of those antenna are 10.52GHz and 11.962GHz, these antenna are suitable for X band application.

KEY WORDS: Array antenna, Corporate feed, Microstrip array, Antenna comparison, Single element.

1. INTRODUCTION

In modern communication system everywhere required low cost, high gain, high directivity, light weight, simple structure and easy fabricated antenna. Microstrip antenna satisfied such requirements. Key feature of this antenna is, the thickness of the metallic strip is in micrometer range [1], ease of construction, light weight, low cost. This antenna provides all of the advantages of printed circuit technology. These advantages of microstrip antenna make them very popular in communication applications such as satellite communication, radar, medical application and other wireless communication etc [2].

Different array configurations of microstrip antenna can give high gain, wide bandwidth and improve efficiency [3]. The proper impedance matching throughout the corporate and series feeding array configurations provides high efficiency microstrip antenna [4].The choosing of design parameters (dielectric material, height and frequency etc.) is important because antenna performance depends on these parameters. Radiation performance can be improved by using proper design structures [5]. The use of high permittivity substrates can miniaturize microstrip antenna size [6]. Thick substrates with lower range of dielectric offer better efficiency, and wide bandwidth but it requires large element size [7]. Different radar systems such as synthetic aperture radar (SAR), shuttle imaging radar, remote sensing radars and other wireless communication systems operate in L, C and X bands. Microstrip antenna is the first option for this high frequency band such as X-band due to its low cost, light weight, and robustness [8].

2. DESIGN OF MICROSTRIP ANTENNA

Microstrip antenna consists of a thin film with different shape such as rectangular or circular or triangular etc. This strip of thin film placed on ground plane where the thickness of the metallic strip is restricted by $t<<\lambda_0$ and height is restricted by $0.000\lambda_0 \leq h \leq \lambda_0$ [3, 9]. In this paper we designed each array using rectangular patch. For a rectangular patch, the length L of the element is usually $\lambda 0/3 < L < \lambda 0/2$. There are numerous substrates that can be used for the design of microstrip antennas and their dielectric constants are usually in the range of $2.2 \leq \varepsilon r \leq 12$. To implement the microstrip antenna usually Fr-4 ($\varepsilon r = 4.9$), Rogers TMM 4 ($\varepsilon r = 4.5$), Taconic TLY-5 ($\varepsilon r = 2.2$), Alumina (96%) ($\varepsilon r = 9.4$), Teflon(PTFE) ($\varepsilon r = 2.08$), Arlon AD 5 ($\varepsilon r = 5.1$) dielectric materials are used as the substrate [3, 9, 10, 11]. The Performance of the microstrip antenna depends on its dimension. Depending on the dimension the operating frequency, radiation efficiency, directivity, return loss and other related parameter are also influenced [12].

This paper mainly includes the design and comparing the performance of two popular Microstrip antennas. They are-

- Single element rectangular patch
- Corporate feed array network

2.1 SINGLE ELEMENT PATCH

For an efficient radiation a practical width of the rectangular patch element becomes [3, 9, 12].

$$W = \frac{1}{2f_r\sqrt{\mu_0\varepsilon_0}} \times \sqrt{\frac{2}{\varepsilon_r+1}} \quad \ldots\ldots\ldots\ldots\ldots\ldots\ldots\ldots\ldots (1)$$

And the length of the antenna becomes [3, 9, 12]

$$L = \frac{1}{2f_r\sqrt{\varepsilon_{eff}\sqrt{\varepsilon_0\mu_0}}} - 2\Delta L \quad \ldots\ldots\ldots\ldots\ldots\ldots\ldots\ldots\ldots (2)$$

Where, $\Delta L = 0.41h\frac{\varepsilon_{eff}+0.3}{\varepsilon_{eff}-0.258} \times \frac{W/h+0.246}{W/h+0.8}$ …....(3)

And, $\varepsilon_{eff} = \frac{\varepsilon_r+1}{2} + \frac{\varepsilon_r-1}{2\sqrt{1+12\frac{h}{w}}}$ ……..…(4)

Where, λ is the wave length, fr (in Hz) is the resonant frequency, L and W are the length and width of the patch element in mm, respectively and ε_r is the relative dielectric constant.

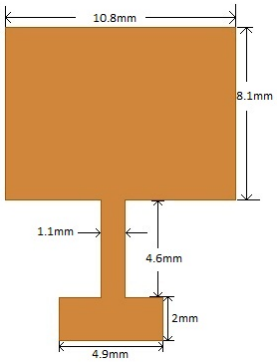

Fig 1: Rectangular Microstrip antenna

In the following Fig. 1, the antenna has been designed to cover specific 11 GHz operating frequency where the antenna dimension is in mm range and the quarter wavelength transformer method [3, 9] is used to match the impedance of the patch element with the transmission line. A probe is also used in the rectangular patch antenna. Fig. 1 is a rectangular patch without slot.

2.2 CORPORATE FEED NETWORK

The limitations of microstrip antennas are narrow frequency band and disability to operate at high power levels of waveguide, coaxial line or even strip line [13]. This can be minimized with the help of various array configurations, feeding methods, dielectric material and ground plane. In microstrip array, elements can be feed by a single line or multiple lines in a feed network arrangement [2, 14].

Based on the feeding method one of the popular array is corporate feed network.

Corporate feed are general and versatile. This method has more control of the feed of each element and is ideal for scanning phased arrays, multi beam arrays [2, 15].

The corporate feed network is used to provide power splits of 2n (i. e. n=2; 4; 8; 16; etc.). This is accomplished by using either tapered lines or using quarter wavelength impedance transformers [14, 16]. Fig 3 shows the corporate feed array, where elements are connected by quarter wavelength transformer method. The radiated field equation of it is similar to that of the series feed array and the array factor as given in [15, 17] as

$$FA = \frac{\sin^2(N\pi(d_x/\lambda)\sin\theta)}{N^2\sin^2(\pi(d_x/\lambda)\sin\theta)} \quad \ldots\ldots\ldots\ldots\ldots\ldots\ldots\ldots (10)$$

Normalized power radiation pattern can be obtained by combining the element radiation pattern and array factor [18].

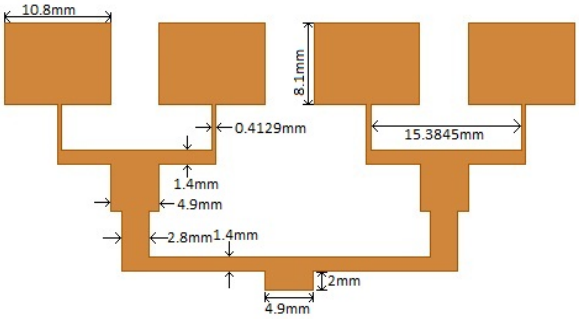

Fig 3: Corporate feed array antenna (4×1)

3. SIMULATION RESULT AND DISCUSSION

For each antenna, design parameter is considered that substrate permittivity is 2.2 (Taconic TLY-5), height is 1.588mm and designed frequency is 11GHz and using this consideration simulation and result is taken for each network.

3.1 SINGLE ELEMENT PATCH

The simulated return loss is shown in Fig. 3.The return loss at 11GHz is -7.03dB, but maximum return loss is obtained at 10.52GH is -16.61dB. Theta cut (θ=0) directivity at 11GHz is 7.49dB and graph is shown in Fig. 4. Accepted power and radiated power at 11GHz is 79.07mW and 115.5mW respectively. Gain at 11GHz is 9.155dBi and the polar plot of 2D radiation patter is shown in Fig. 5.

3.2 CORPORATE FEED NETWORK

The simulated return loss is shown in Fig. 3. The return loss at 11GHz is -0.552dB, but maximum return loss is obtained at 11.962GH is -34.528dB. Theta cut (θ=0) directivity at 11GHz is 12.47dB and graph is shown in Fig. 4. Accepted power and radiated power at 11GHz is 1181mW and 7167mW respectively. Gain at 11GHz is 20.3dBi and the polar plot of 2D radiation patter is shown in Fig. 5.

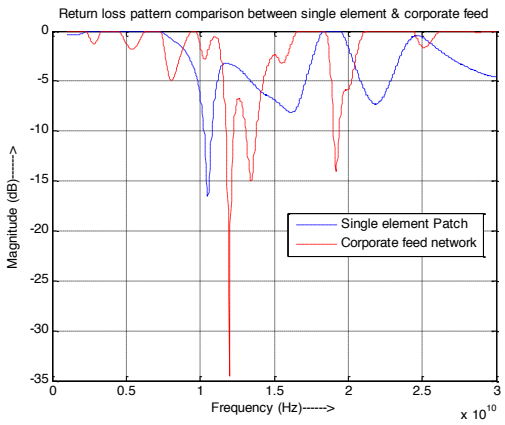

Fig. 3: Return loss pattern of single element patch and corporate feed array network.

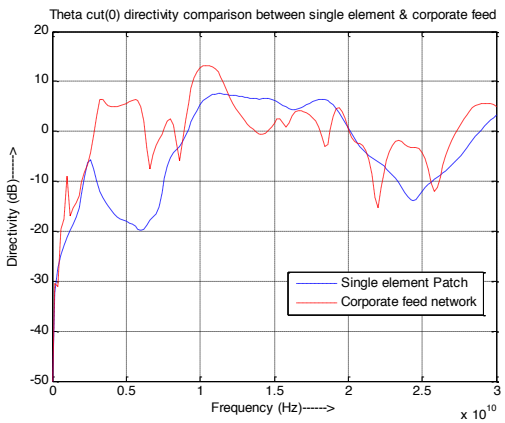

Fig. 4: Theta cut ($\theta=0^0$) directivity pattern of single element and corporate feed array network.

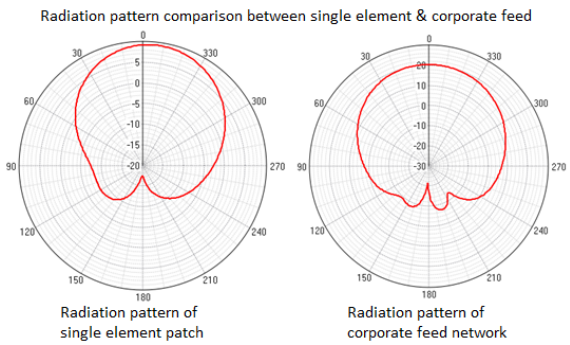

Fig. 5: Radiation pattern (polar plot) of single element and corporate feed array network.

3.3COMPARISOM BETWEEN SINGLE ELEMENT AND CORPORATE FEED

After observing the performance analysis parameters of both single element and corporate feed network antenna we can get the desirable patch antenna after comparing them. Obtained value for each antenna in different performance parameter is tabulated below for better comparison. Here the both antenna is designed at 11GHz frequency.

Table 1: Simulation results and comparison between single element patch and corporate feed network.

Performance parameter	Unit	Single element patch	Corporate feed array network
Obtained simulated frequency	GHz	10.52	11.962
Return loss at obtained frequency	dB	-16.61	-34.524
Return loss at designed frequency	dB	-7.3	-0.553
Theta cut (θ=0) directivity at 11GHz	dB	7.49	12.47
-3dB bandwidth	GHz	2.33	3.284
-9dB bandwidth	GHz	0.73	0.589
Gain at 11GHz	dBi	9.115	20.3
Radiated power at 11GHz	mW	115.5	7167
Accepted power at 11GHz	mW	79.07	1181

After observing the above table and above discussion we get following decision-

- ✓ Our operating frequency is 11GHz. For corporate feed it crosses 11GHz and for single patch almost 0.5GHz less.
- ✓ The return loss for corporate feed is almost double than single patch. So it is a big achievement to use corporate feed instead of single patch according to return loss.
- ✓ -3dB bandwidth of corporate feed is higher than single patch, not for -9dB bandwidth.
- ✓ Gain of the corporate feed is also double than single patch. So where higher gain is required corporate feed is more suitable than single patch.
- ✓ As the gain of the corporate feed is high. So its require high accepted power than single patch and that is shown in above table. Also the radiated is high for corporate feed because of high gain.

According to the analysis of the simulated result and above table the overall performance of the corporate feed array network has better than single element patch.

4. CONCLUSION

In this paper designed antenna is very simple, low cost, high gain, high directivity, and moderate bandwidth. This antenna can easily used in any X band application, satellite communication, radar, wireless communication.

In this paper we designed a single element patch for 11GHz operating frequency and then using this

single element we designed a corporate feed array to operate at 11GHz, but the simulated frequency at which the return loss is maxima, that is 11.962GHz. Using the simulated performance parameter we compare the corporate feed array with single element to get the desired one. After observing the simulated performance parameter we get a decision that the overall performance of the corporate feed array network has batter than single element patch. Specially the gain and return loss of corporate feed array is double than single element patch.

5. FUTURE WORKS

In future we design other remaining array feed network and compare among all array network and single element patch with each other. Also we will design array network for circular patch, for spiral patch and compare the performance with this rectangular array with circular array, also with spiral array feed network to make understand which one is better for which application.

Here designed antenna is covered 11GHz operating frequency, but it is possible to design for other system with operating frequency such as WLAN, WiMAX, other X band etc application by changing the antenna size. In future we also use the spiral in both rectangular and circular to compare their performance.

REFERENCES

[1].M. T. I. Huque, et al., " Design and Simulation of a Low-cost and High Gain Microstrip Antenna Arrays for the X-band Applications," In International Conference on Network Communication and Computer ICNCC 2011, New Delhi, India., March 21-23, 2011.

[2].C. A. Balanis, Antenna Engineering, 2nd ed., Willey, 1982.

[3]. H. Cheng-Chi, et al., "An aperture-coupled linear microstrip leaky-wave antenna array with two-dimensional dual-beam scanning capability," Antennas and Propagation, IEEE transactions on, vol. 29, pp. 25-37, 1981.

[4].K. Gi-Cho, et al., " Ku-band high efficiency antenna with corporate-series-feed microstrip array," in Antennas and Propagation Society International Symposium, 2003. IEEE, 2003, pp. 690-693 vol.4.

[5].Boufrioua and A. Benghalia, "Effect of the resistive patch and the uniaxial anisotropic substrate on the resonant frequency and the scattering radar cross section of a rectangular microstrip antenna", Aerospace science and technology, vol. 10, pp. 217-221, 2006.

[6].K. C. Lo and Y. Hwang, "Microstrip antennas of very high permittivity for personal communications," 1997, pp. 253-256 vol.

[7].J. M. Rathod, " Design Development of Antenna for TV Transmission for Connecting Outdoor Broadcasts Van to the Studio for Rural Area," International Journal of Computer and Electrical Engineering, vol. 2, pp. 251-256, 2010.

[8].M. F. Islam, et al., "Dual band microstrip patch antenna for SAR applications," Australian Journal of Basic Applied Science, vol. 4, pp. 4585-4591, 2010.

[9].R. Garg, P. Bhartia, I. Bahl, A. Ittipiboon, Microstrip Antenna Design Handbook, Artech House inc.,2001.

[10].R. J. Mailloux, J. F. Mcllvenna, N. P. Kernweis, Microstrip array technology", IEEE Trans. Antenna Propagation Magazine, Vol. 29, No. 1, pp. 25-27, 1981.

[11].Md. Tanvir Ishtaique-ul Huque, Md. Al-Amin Chowdhury, Md. Kamal Hosan, and Md. Shah Alam. " Performance Analysis of Corporate Feed Rectangular Patch Element and Circular Patch Element 4×2 Microstrip Array Antennas", International Journal of Advanced Computer Science and Applications, vol. 2, No. 7, 2011.

[12].T. A. Millikgan, Modern Antenna Design, 2nd ed., IEEE Press, Jhon Wiley & Sons inc., 2007.

[13].R. Mailloux, et al., "Microstrip array technology," Antennas and propagation, IEEE Transactions on. Vol. 29, pp. 25-37, 1981.

[14].R. Garg, Microstrip antenna design handbook. Boston, mass [u.a.]: Artech house.

[15].H. J. Visser, "Array and Phased Array Antenna Basics," ed: John Wiley & Sons.

[16]. R. J. Mailloux, " Electrically Scanned Arrays," Synthesis Lectures on Antennas vol. 2, pp. 1-82, 2007.

[17].M. I. Skolnik, Introduction to radar systems, 3rd ed. New York,: McGraw-Hill, 2000.

[18].W. L. Stutzman, "Estimating directivity and gain of antennas," Antennas and Propagation Magazine, IEEE, vol. 40, pp. 7-11, 1998.

Proceeding of the
International Conference on Electrical, Computer and Telecommunication Engineering
01- 02 December 2012 (ICECTE2012), RUET, Rajshahi-6204, Bangladesh

ICECTE2012: PI-0035

Multi-Layer Dipole Antenna for Implantable Biomedical Application

M.K. Hosain[1], M. F. Samad[2], M. M. Mowla[3], M. Samad[4]

[1,2] Deakin University, Australia.
[3,4] Electronics and Telecommunication Engineering,
Rajshahi University of Engineering & Technology, Bangladesh.
E-mail: mhosain@deakin.edu.au[1], mfsamad@deakin.edu.au[2] , rimonece@gmail.com[3], miti_ete_ruet@yahoo.com[4]

ABSTRACT
A compact circular stacked implantable dipole antenna is proposed for industrial, scientific and medical band of 915 MHz used in biomedical application. The antenna has dimension of $\pi * (10)^2 *2.8\ mm^3$, resonance frequency of 915 MHz and bandwidth of 10 MHz at return loss of -10 dB. In this design high permittivity dielectric of Roger RO 3210 is used as substrate and superstate. The finite element method is used to analyze electromagnetic characteristics of the dipole antenna. The radiation performance of the designed antenna in free space is evaluated in term of radiation pattern, and return loss. The paper also estimates specific absorption rate distribution in a three layer human body model to verify the feasibility of implant.

KEY WORDS: MICS, SAR, PIFA, Dipole Antenna, ISM

1. INTRODUCTION

Antenna has significant roles in implantable systems since they offer communication of the implant with the external equipment. However, the design of implantable antenna is quite challenging because of antenna size, impedance matching, biocompatibility with the body, and low-power requirements. Moreover, the biological tissue adds significant complexity to the problem due to high losses. Therefore, implantable antenna design has been limited to in silicon and *in vitro* studies [1, 2].

Medical applications of antenna have focused on medical therapy (e.g. hyperthermia for the treatment of cancer), diagnosis (e.g. monitoring physiological parameters such as temperature, blood pressure and glucose, etc), telecommunication (e.g. pacemaker, defibrillators, deep brain stimulation, etc) [3]. Low profile monopole and dipole type antennas are usually used as an internal antenna for cancer treatment [4].Though a number of research are happenings related to hyperthermia, studies on antennas used to establish telecommunication link between implanted devices and exterior instrument for biotelemetry are not widely testified [4]. Moreover, currently telecommunication has played a more and more important role in implantable device systems. For these developed systems, a more efficient implanted antenna is required to enable two-way communication between the implanted device and an external device. That's why we have designed an implantable antenna of improved performance for biotelemetry applications.

The implanted antenna should be compact, lightweight, and able to work in body dielectric environment with low power. Since this study is related to biomedical applications, the industrial, scientific and medical (ISM) band including 915 MHz is chosen as operating frequency. This band is higher than the medical implant communication service (MICS) band of 402-405 MHz [5] thus, offering small antenna in size. Since the size and weight of medical implantable device have become smaller and lighter due to the advances in implantable electronic device technology, thus one of the major challenges in designing an implantable system is to miniaturize the implanted antenna [6]. Therefore, multilayer meandered dipole antenna is a good candidate because they are flexible in design and shape, and compact in side. It is also necessary for implantable antenna to protect the human body from the heat, physical damage, or short circuiting of the antenna. Thus superstate is use to make it biocompatible and stable characteristic.
In this paper the resonance characteristic of the designed implantable antenna and its radiation performance in free space are studied. Specific absorption rate distributions are simulated inside a simple human body model for the evaluation of performances and safety issues related to implanted antennas. The SAR value is compared with American National Standards Institute (ANSI)/IEEE limitations for SAR to get some background information of biotelemetry.

2. LOW PROFILE IMPLANTED ANTENNA DESIGN AND CHARACTERIZATION

2.1 Design of the Four Layer Dipole Antenna

A circular four layers dipole antenna is designed as shown in Fig. 1(a). Fig. 1(b) shows the layer view of the designed antenna. Antenna consists of four layers. Top two layers works as one pole and bottom two layers form another pole for the dipole antenna. The layer is connected with another layer by a conductive shorting pin. Two layers in one pole are meandered in opposite to each other. The circular shape is used as it is easy to implant and it does not damage surrounded tissues. The antenna dimension is $\pi * (10)^2 * 2.8\ mm^3$. This antenna is more compact than the antennas designed by Lee et al. [7]. and Kim et al. [8]. The antenna is designed with high dielectric substrate and superstrate of Rogers RO 3210 (ε_r = 10.2, δ = 0.003). Both the substrate and superstrate have the same size of radius 10 mm. The superstrate can protect surrounded tissues against the heat from the antenna radiation. The meandered line physically lengthens the total current path. The lengthened current path can bring the resonance frequency to lower range thus reducing overall dimension of the antenna. A 50 Ohm coaxial probe is used to feed the antenna.

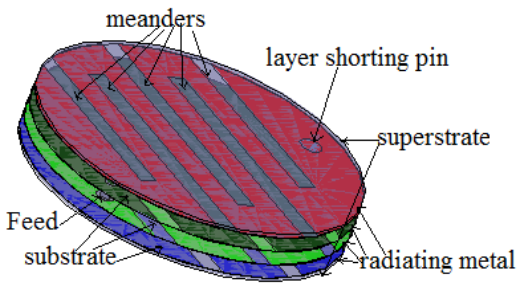

Fig. 1(a) Proposed circular meandered dipole antenna.

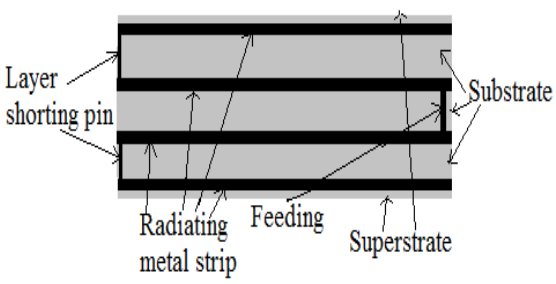

Fig. 1 (b) Layered view of the antenna.

2.2 Antenna Characteristics

The radiation characteristics including return loss response, radiation pattern are determined by using software which employs finite element method. The optimum antenna parameters are obtained by iterative simulation method. Fig. 2 shows the return loss response of the antenna. It indicates that the antenna resonates at 915 MHz which is the ISM band. Fig. 3 plots simulated input impedance of the proposed antenna. The input impedance of the antenna at 915 MHz is 49 + 4i Ω. The simulated bandwidth of the designed antenna is 10 MHz including 915 MHz resonance frequency at return loss of -10 dB. Fig. 4 indicates the 3D far field gain pattern of the designed antenna in free space. The maximum gain of value -29 dB is recorded at resonance frequency. Since the antenna is electrically very small, almost omnidirectional radiation pattern is achieved. Low gain value is recognized to the miniaturized dipole antenna. In order to assess the performances of the designed antenna, we compared the antenna parameters with those of previously reported antennas. For instance, the maximum gain value of -29 dB of our proposed antenna is much higher than the maximum gain of -55.65 dB for the miniaturized implantable PIFA reported by Kiourti et al. [9]. The bandwidth of the designed PIFA of 10 MHz is broader than the 8 MHz for the UHF PIFA reported by Louhichi et al. [10]. The simulated radiation efficiency of the proposed spiral PIFA is found to be 40.75% at 915 MHz.

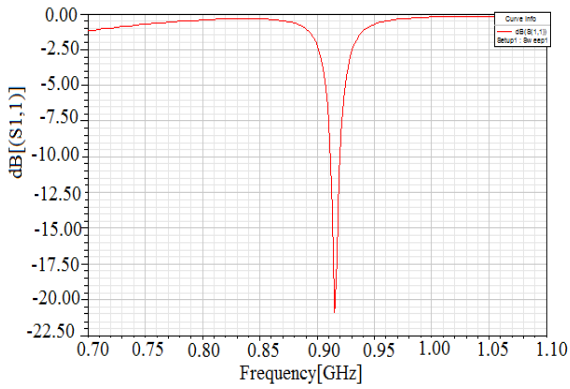

Fig. 2 Frequency response of the designed antenna.

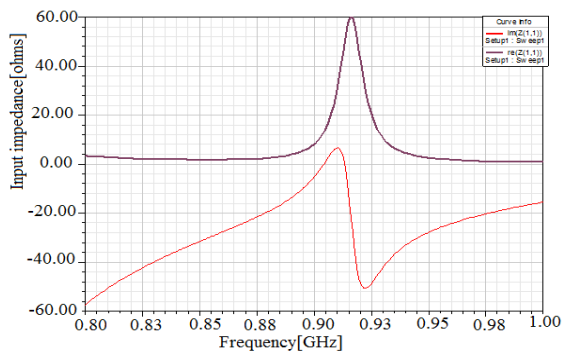

Fig.3 Input impedance versus frequency of the designed antenna.

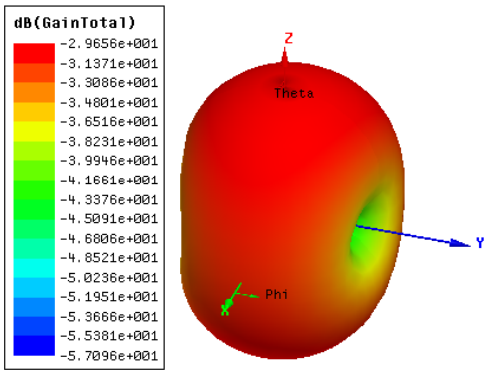

Fig.4 3D simulated gain of the antenna.

3. IMPLANTED DIPOLE ANTENNA INSIDE HUMAN BODY MODEL

The characteristics of the designed antenna have also been investigated by using the 3-layer rectangular phantom as indicated in the Fig. 5. Table I represents the dielectric properties of the human body tissues which are used in this simple rectangular model at 915 MHz. The dimension of the body model is 30 mm × 30 mm × 16 mm. In this model, the human body equivalent phantom consists of three different tissues including skin, fat, and muscle. The thicknesses of the skin, fat, and muscle are 2mm, 4 mm, and 10 mm respectively. The electrical properties of the phantom tissues are defined at 915 MHz. The antenna is embedded into the fat layer, and positioned just beneath the skin layer. In this condition, the antenna characteristics are analyzed by use of finite element electromagnetic solver.

Antenna is simulated at this location of the model since pacemakers and implantable defibrillators are generally placed between the skin and muscle tissues in the upper human chest [11]. Inside the human body model, antenna characteristic changes due to the surrounding dielectrics. The loss in antenna radiation pattern is observed. Detuning of the antenna resonance is attributed in the human body model due to the inherent dielectric loading of the surrounding tissues.

This detuning can be rectified by adequately modifying the length of the meanders. Though the actual structure of the human body is more complicated, this simple phantom make calculation easier and give some ideas.

Table 1: Dielectric Properties of the three-layer human body model [12].

Layer Name	Permittivity	Conductivity (s/m)	Mass Density (kg/m^3)
Skin (dry)	40.2	0.8	1080
Fat	11.17	0.12	920
Muscle	55.2	0.95	1040

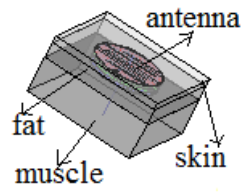

Fig. 5 Planar geometry for the design of the antenna implanted in human body.

In order to assess the safety requirement of implanted antenna, the electromagnetic power absorbed by the surrounding tissues should be calculated. A numerical analysis of SAR could examine some of the safety issues. The SAR distribution analysis was performed at 915 MHz for the simulation setup as shown in Fig. 5. Fig. 6 demonstrates the rectangular plot of the local and average SAR versus normalized distance from the antenna. The calculation method of the local and average SAR was based on the distribution of the electric field. It is clear that SAR is higher near the antenna and then rapidly decreases with the distance.

When the proposed antenna was assumed to deliver 1W, the maximum local SAR value of 285 W/kg and the average SAR value of 108 W/kg were obtained in this simulation. These values of SAR are higher than American National Standards Institute (ANSI)/IEEE C95.1-1999 (1-g average SAR<1.6 W/kg) regulation [13]. To satisfy this safety regulation, the delivered power from this implant antenna should not exceed 5.8mW. Thus the received power of the implanted antenna should be regulated accordingly.

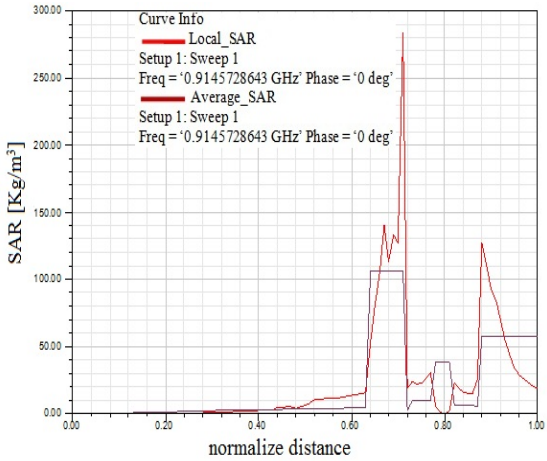

Fig. 6 Specific absorption rate distribution inside the three layer human body model.

4. CONCLUSION

In this paper a circular stacked four layers meandered dipole antenna is designed and simulated in ISM band. The antenna size reduction is achieved with meander stacked structure. In this study high permittivity substrate of Roger RO 3210 is used as substrate and superstate. The simulation result shows that operation bandwidth of the antenna is 10 MHz at -10dB return loss and radiation pattern is omnidirectional with maximum gain of -29 dB. The SAR analysis is also done in this article to verify the SAR limitation in human body set by American National Standards Institute. The designed antenna offers good physical size and performance in implantable biomedical applications. Further works are required for comprehensive study of SAR in complex human body prior to practical application.

REFERENCES:

[1]. T. Karacolak, R. Cooper, and E. Topsakal, "Electrical Properties of Rat Skin and Design of Implantable Antennas for Medical Wireless Telemetry," *IEEE Transactions on Antennas and Propagation,,* vol. 57, pp. 2806-2812, 2009.

[2]. P. Soontornpipit, C. M. Furse, and Y. C. Chung, "Design of implantable microstrip antenna for communication with medical implants," *IEEE Transactions on Microwave Theory and Techniques,,* vol. 52, pp. 1944-1951, 2004.

[3]. A. Rosen, M. A. Stuchly, and A. Vander Vorst, "Applications of RF/microwaves in medicine," *IEEE Transactions on Microwave Theory and Techniques,,* vol. 50, pp. 963-974, 2002.

[4]. J. Kim and Y. Rahmat-Samii, "Implanted antennas inside a human body: Simulations, designs, and characterizations," *IEEE Transactions on Microwave Theory and Techniques,,* vol. 52, pp. 1934-1943, 2004.

[5]. H. Fu-Jhuan, L. Chien-Ming, C. Chia-Lin, C. Liang-Kai, Y. Tzong-Chee, and L. Ching-Hsing, "Rectenna Application of Miniaturized Implantable Antenna Design for Triple-Band Biotelemetry Communication," *IEEE Transactions on Antennas and Propagation,* vol. 59, pp. 2646-2653, 2011.

[6]. W. Huang and A. A. Kishk, "Embedded Spiral Microstrip Implantable Antenna," *International Journal of Antennas and Propagation,* vol. 2011, 2011.

[7]. C. M. Lee, T. C. Yo, F. J. Huang, and C. H. Luo, "Dual-resonant π-shape with double L-strips PIFA for implantable biotelemetry," *Electronics Letters,* vol. 44, pp. 837-838, 2008.

[8]. J. Kim and Y. Rahmat-Samii, "Planar inverted-F antennas on implantable medical devices: Meandered type versus spiral type," *Microwave and optical technology letters,* vol. 48, pp. 567-572, 2006.

[9]. A. Kiourti, M. Christopoulou, S. Koulouridis, and K. Nikita, "Design of a novel miniaturized implantable PIFA for biomedical telemetry," in *Second International ICST Conference on Wireless Mobile Communication and Healthcare, MobiHealth 2010*, ed: Springer, October 2010, pp. 127-134.

[10]. O. Louhichi, D. Bechevet, and S. Tedjini, "Methodology for UHF PIFA design in harsh environment," in *2011 IEEE International Symposium on Antennas and Propagation (APSURSI)*, 2011, pp. 1201-1204.

[11]. D. Wessels, "Implantable pacemakers and defibrillators: device overview & EMI considerations," in *IEEE International Symposium on Electromagnetic Compatibility, 2002. EMC 2002*, pp. 911-915.

[12]. C. Gabriel, "Compilation of the Dielectric Properties of Body Tissues at RF and Microwave Frequencies," DTIC Document1996.

Proceeding of the
International Conference on Electrical, Computer and Telecommunication Engineering
01- 02 December 2012 (ICECTE2012), RUET, Rajshahi-6204, Bangladesh

ICECTE2012: PI-0036

Design and Simulation of a Low Cost Microstrip Patch Antenna for K Band Applications

M. A. Motin[1], Md. Asaduz-Zaman[2], Md. Imran Hasan[3], M. M. Rashid[4]
[1,2,4] Electrical & Electronic Engineering, Rajshahi University of Engineering & Technology
[3]Electronic & Telecommunication Engineering, Rajshahi University of Engineering & Technology
motin_eee_06@yahoo.com, masad_eee06@yahoo.com,
imran_ruet_ete06@yahoo.com,mrashid.eee@gmail.com

ABSTRACT

A novel rectangular microstrip patch antenna with maximum return loss of -20.5 dB at 19.25 GHz is designed .The main motto of this paper is to reduce the return loss and increase the gain. To reduce the return loss, slots of different width are inserted in different position of the patch. Mainly slot having 3mm length and 0.1mm, 0.3mm, 0.5mm, 0.7mm, 0.9mm, 1.1mm or 1.3mm width is placed in the bottom, middle and top of the patch . A single slot having 1.1mm width and 3mm length, is placed middle of the patch, shows -48.80 dB return loss at 18.35 GHz and a single slot having 1.3mm width and 3mm length is placed top of the patch shows -40.40 dB return loss at 18.45 GHz. The simulation is performed by using gems simulator which is commercially available antenna simulator. The antenna is designed by using taconic tly-5 dielectric substrate with permittivity ϵ_r =2.2 and height, h=1.588 mm. Therefore, by the result of return loss of the modified patch, it can be shown that this antenna is suitable for k- band applications.

KEY WORDS: Microstrip patch antenna, Horizontal slot, GEMS simulator, K-band, Return loss,

1. INTRODUCTION

The key features of a microstrip antenna are low profile, relative ease of construction, low weight, comfortable to planar and non planar surfaces, low cost, simple and inexpensive to manufacture by using printed circuit board. These advantages of microstrip antennas make them popular in many wireless communication applications such as satellite communication, radar, medical applications, aircraft, spacecraft, and missile applications. Many researchers have designed a single element patch in different way to gate multiband application such as double PIFA [1, 2], U-slot [3], double U slot, E slot, H slot and other structures. In this paper an investigation on the design of an optimized patch for lowest return lost is performed by matching the modified patch with probe by using the quarter wavelength transformer method. The goal of this paper is to decrease the size of the antenna and at the same time to improve the radiation performance of the patch antenna in terms of directivity, maximum radiation, return loss and efficiency. As an advantage, the resonant frequency of this antenna can be easily controlled by either increasing of decreasing some parameters such as width and length of the patch and the slot width. Here the designed antenna performs better at 18.35 GHz with minimum return loss -48.80 dB. So this designed antenna is capable to meet the demand of K-band applications.

2. MICROSTRIP PATCH ANTENNA DESIGN

Microstrip patch antennas consist of very thin metallic strip (patch) placed above a ground plane where the thickness of the metallic strip is restricted by $t << \lambda_0$ and the height is restricted by $0.003\lambda_0 \leq h \leq 0.05\lambda_0$ [4, 5]. The microstrip patch is designed so its pattern maximum is normal to the patch (broadside radiator). For a rectangular patch, the length L of the element is usually $\lambda 0/3 < L < \lambda 0/2$. The strip (patch) and the ground plane are separated by a dielectric sheet (referred to as the substrate. There are numerous substrates that can be used for the design of microstrip antennas, and their dielectric constants are usually in the range of $2.2 \leq \epsilon_r \leq 12$. The ones that are most desirable for good antenna performance are thick substrates whose dielectric constant is in the lower end of the range because they provide better efficiency, larger bandwidth, loosely bound fields for radiation into space, but at the expense of larger element size. Thin substrates with higher dielectric constants are desirable for microwave circuitry because they require tightly bound fields to minimize undesired radiation and coupling, and lead to smaller element sizes; however, because of their greater losses, they are less efficient and having relatively smaller bandwidth. The antenna has a simple structure fed by 50Ω microstrip line. The dimensions of the proposed antenna used for theoretical, simulated and practical study are in mm range. The

dielectric material selected for design is Taconic TLY-5 which has dielectric constant of 2.2 and the height of dielectric substrate is 1.588mm. The overall dimension of the antenna is 4.9 x 5.7 x 1.988mm. Here GEMS simulator is used to obtain the return loss and gain. For an efficient radiation a practical width of the Rectangular patch element becomes [5]

$$w = \frac{1}{2f_r\sqrt{\mu_0\varepsilon_0}} \times \sqrt{\frac{2}{\varepsilon_r + 1}} \qquad \text{Eq. 1}$$

And the length of the antenna becomes [4, 5, 6]

$$L = \frac{1}{2f_r\sqrt{\varepsilon_{eff}}\sqrt{\varepsilon_0\mu_0}} - 2\Delta L \qquad \text{Eq. 2}$$

Where

$$\Delta L = 0.41h\frac{\varepsilon_{eff} + 0.3}{\varepsilon_{eff} - 0.258} * \frac{\left(\frac{w}{h} + 0.264\right)}{\left(\frac{w}{h} + 0.8\right)} \qquad \text{Eq. 3}$$

And

$$\varepsilon_{eff} = \frac{\varepsilon_r + 1}{2} + \frac{\varepsilon_r - 1}{2\sqrt{1 + 12\frac{h}{w}}} \qquad \text{Eq. 4}$$

Where, λ is the wave length, f_r (in Hz) is the resonant frequency, L and W are the length and width of the patch element, in mm, respectively and ε_r is the relative dielectric constant.

3. SINGLE ELEMENT MICROSTRIP PATCH ANTENNA

Fig. 1 shows an antenna that has been designed to cover operating frequency of 19.5 GHz and quarter wave length transformer method is used to match the impedance of the patch element with transmission line.

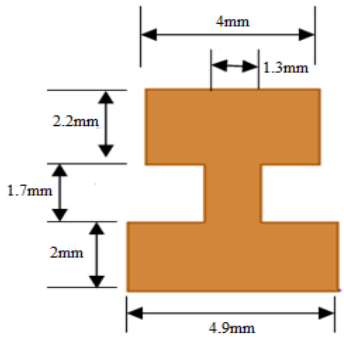

Fig. 1 Single element microstrip patch antenna without slot

The shape of the patch is 4mm x 2.2 mm. The quarter wave transformer which is used to match the patch with the probe having 1.3 mm length and 1.7 mm width. The shape of the probe is taken as 4.9 mm width and 2 mm length.

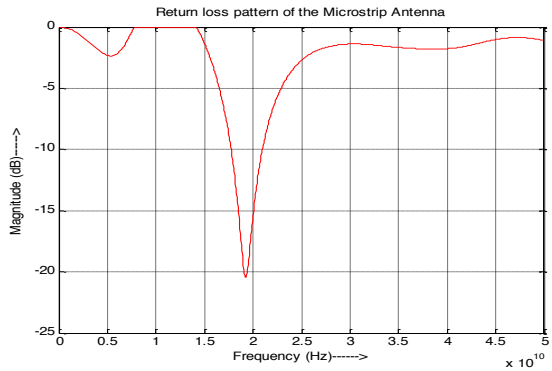

Fig. 2 Return loss of a single element microstrip patch antenna without any slot.

4. USING A SINGLE HORIZONTAL SLOT OF DIFFERENT WIDTH IN THE MIDDLE POSITION OF THE PATCH

A Single horizontal slot of 3mm length and 0.1 mm width is placed in the middle position of the patch. From the simulated result for this arrangement of patch, -21.9 dB return loss is found at 19GHz. Instead of 0.1mm slot we have also placed 0.3mm, 0.5mm, 0.7mm, 0.9mm, 1.1mm and 1.3mm slot which is shown graphically in fig .4.Then the return loss for different width of horizontal slot in the middle place of the patch which is shown graphically in fig. 3. By placing horizontal slot of different width in middle of the patch, best result is found when the horizontal slot of 1.1mm width is placed in the middle of the patch. For this case (for 1.1 mm horizontal slot) lowest return loss (-48.80 dB) is found at 18.35GHz. If the horizontal slot width is increased from 0.1mm to 1.1 mm then the return loss of the microstrip patch antenna is gradually decreased so it shows better performance gradually. If the horizontal slot width is increased more than 1.1 mm then its performance is deviated gradually which is shown in the Table 1.

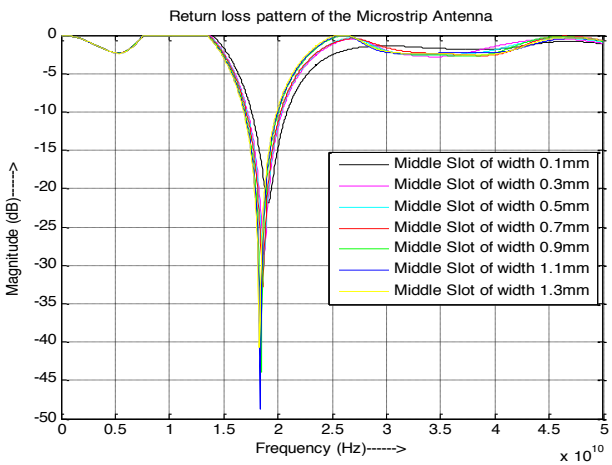

Fig . 3 Return loss of a single element microstrip patch antenna for the different horizontal slots width placed in the middle position (for 0.1mm, 0.3mm, 0.5mm, 0.7mm, 0.9mm, 1.1mm or 1.3mm slot width) of the patch.

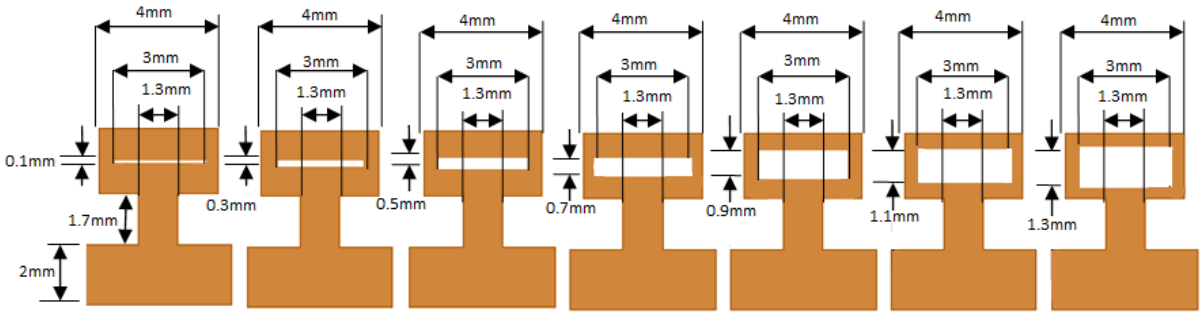

Fig . 4 Single element microstrip patch antenna having horizontal slots in the middle position for 0.1mm, 0.3mm, 0.5mm, 0.7mm, 0.9mm, 1.1mm and 1.3mm slot width respectively

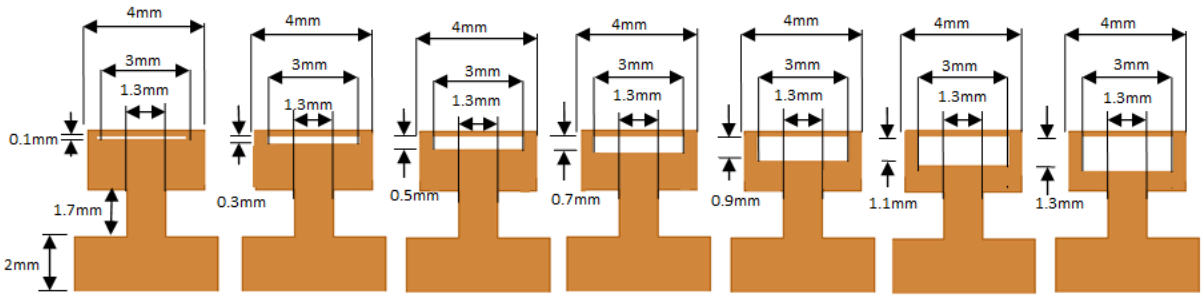

Fig . 5 Single element microstrip patch antenna having horizontal slots in the top position for 0.1mm, 0.3mm, 0.5mm, 0.7mm, 0.9mm, 1.1mm and 1.3mm slot width respectively

Table 1: Minimum return loss of a single element microstrip patch antenna for the different horizontal slots width (for 0.1mm, 0.3mm, 0.5mm, 0.7mm, 0.9mm, 1.1mm or 1.3mm slot width) placed in the different position(bottom, middle, top) of the patch.

Slot position	Lowest Return loss (slot width 0.1 mm)	Lowest Return loss (slot width 0.3 mm)	Lowest Return loss (slot width 0.5 mm)	Lowest Return loss (slot width 0.7 mm)	Lowest Return loss (slot width 0.9 mm)	Lowest Return loss (slot width 1.1 mm)	Lowest Return loss (slot width 1.3 mm)	Lowest Return loss (slot width 1.5 mm)
bottom	-27.43 dB(at 18.67 GHz)	-32 dB (at 18.6GHz)	-65 dB (at 18.35GHz)	-42 dB (at 18.25GHz)	-39.75 dB (at 18.25GHz)	-36.85 dB (at 18.25 GHz)	-31.90 dB (at 18.10 GHz)	-33.50 dB (at 18.20 GHz)
middle	-21.9 dB (at 19 GHz)	-28.75 dB (at 18.75 GHz)	-30.65 dB (at 18.65GHz)	-32.75 dB (at 18.55GHz)	-43.95 dB(at 18.40GHz)	-48.80 dB (at 18.35 GHz)	-40.70 dB (at 18.30 GHz)	-37 dB (at 18.22GHz)
top	-21.82 dB (at 19.05 GHz)	-21 dB (at 19 GHz)	-21.45 dB (at 19 GHz)	-28.75 dB (at 18.75GHz)	-30.75 dB (at 18. 57GHz)	-34 dB (at 18.50 GHz)	-40.40 dB (at 18.45 GHz)	-35 dB (at 18.18 GHz)

5. USING A SINGLE HORIZONTAL SLOT OF DIFFERENT WIDTH IN THE TOP POSITION OF THE PATCH

A Single horizontal slot of 3mm length and 0.1 mm width is placed in the top position of the patch. From the simulated result for this arrangement of patch -21.82 dB return loss is found at 19.05GHz. Instead of 0.1mm slot we have also placed 0.3mm, 0.5mm, 0.7mm, 0.9mm, 1.1mm and 1.3mm slot in top position of the patch which is shown graphically in fig .5.Then the return loss for different width of horizontal slot in the top place of the patch which is shown graphically in fig. 6. By placing horizontal slot of different width in top of the patch, best result is found when the horizontal slot of 1.3mm width is placed in the top of the patch. For this case (for 1.3 mm horizontal slot) lowest return loss (-40.40 dB) is found at 18.45GHz. If the horizontal slot width is increased from 0.1mm to 1.3 mm then the return loss of the microstrip patch antenna is gradually decreased so it shows better performance gradually. If the horizontal slot width is increased more than 1.3 mm then its performance is deviated gradually which is shown in the Table 1

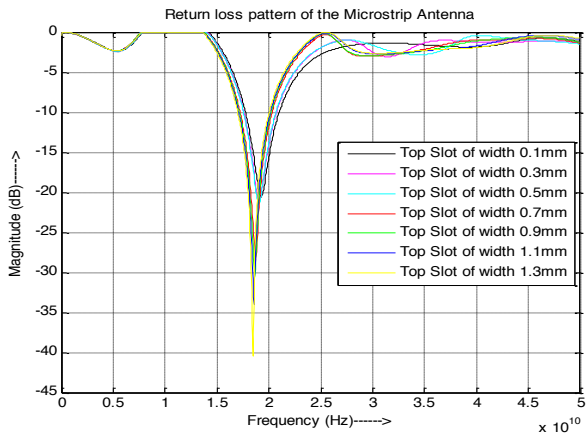

Fig . 6 Return loss of a single element microstrip patch antenna for the different horizontal slots width placed in the top position (for 0.1mm, 0.3mm, 0.5mm, 0.7mm, 0.9mm, 1.1mm or 1.3mm slot width) of the patch.

6. SIMULATION RESULT AND DISCUSSION

From the above graphical presentation it is found that if we placed slot in the middle of the patch then better performance can be found only when the width of the horizontal slot will be 1.1mm. But, if we placed slot in the top of the patch then better performance can be found only when the width of the horizontal slot will be 1.3mm which is shown in the table 2. For these two cases better performance of the microstrip patch antenna will be found when the slot of 1.1 mm width is placed in the middle of the patch which is also shown graphically in fig .7.

Table 2: Comparison between minimum return loss for slot placed in the middle of the patch and slot placed in the top of the patch

Slot position	Return loss (Minimum)	Width of slot
Middle	-48.80 dB (at 18.35 GHz)	1.1 mm
Top	-40.40 dB (at 18.45 GHz)	1.3 mm

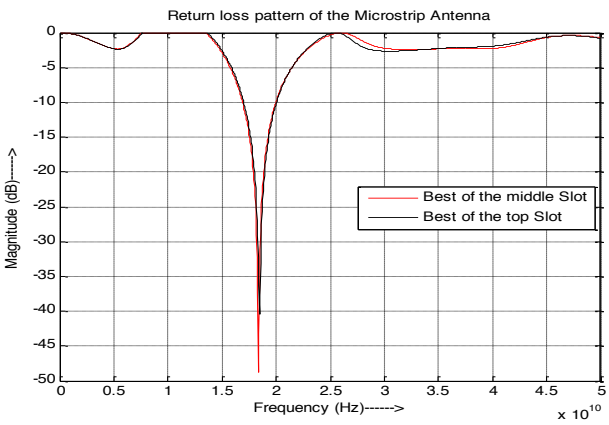

Fig . 7 Comparison between the return loss for slot placed in the middle of the patch and top of the patch

7. CONCLUSION

It would be possible to design the bands operating any other system such as in WLAN [11,13], WiMAX [12], EBAN [7,9,10] or other wireless systems by changing the dimension of the patch element. It also can be designed to operate the antenna array in ISM band. It also covers all the applications of K-band. For fulfil the K band application if we use 1.1 mm horizontal slot in the middle of the patch instead of using normal patch without slot then we get better facilities and lower return loss. In future the series feed, corporate feed and corporate-series feed array configuration can be designed by the patch having 1.1mm horizontal slot in the middle of the patch and can be simulated which can be operated at multiple frequencies and having higher directive gain and lower return loss.

REFERENCES

[1]. R. J. Mailloux, J. F. Mcllvenna, N. P. Kernweis, "Microstrip array technology", IEEE Trans. Antenna Propagation Magazine, Vol. 29, No. 1, pp. 25-27, 1981.

[2]. C. A. Balanis, Antenna Engineering, 2nd ed., Willey, 1982.

[3]. T. A. Millikgan, Modern Antenna Design, 2nd ed. , IEEE Press, John Wiley & Sons inc., 2007.

[4]. M. I. Skolnik, Introduction to RADAR System, 3rd ed., McGraw Hill Higher Education, 2000.

[5]. R. Garg, P. Bhartia, I. Bahl, A. Ittipiboon, Microstrip Antenna Design HandBook, Artech House inc., 2001.

[6]. R. J. Milloux, Electronically Scanned Arrays, Morgan & Claypool, 2007.

[7]. W. L. Stutzman, "Estimating directivity and gain of antennas", IEEE Antennas and Propagation Magazine, Vol. 40, No. 4,pp 7-11, August, 1998.

[8]. H. J. Visser, Array and Phased Array Antenna Basics, John Wiley & Sons Ltd., 2005.

[9]. Muhammad Mahfuzul Alam, Md. Mustafizur Rahman Sonchoy, and Md. Osman Goni, "Design and Performance Analysis of Microstrip Array Antenna", Progress In Electromagnetic Research Symposium Proceedings, Moscow, Russia, August 18-21, 2009.

[10]. Md. Shihabul Islam and Md. Tanvir Ishtaique-ul Huque, "Design and Performance Analysis of Microstrip Array Antenna", B.Sc. Engineering thesis, Dept. of ETE, Rajshahi University Of Engineering & Technology(RUET), Rajshahi, Bangladesh, April, 2010.

[11]. Gi-cho Kang, Hak-young Lee, Jong-kyu Kim, Myun-joo Park,"Ku-band High Efficiency Antenna with Corporate-Series-Fed Microstrip Array", IEEE Antennas and Propagation Society International Symposium, 2003.

[12]. T. F. Lai, Wan Nor Liza Mahadi, Norhayatision, "Circular Patch Microstrip Array Antenna for KU-band", World Academy of Science, Engineering and Technology, vol. 48, pp. 298-302, 2008.

[13]. K. Shambavi, C. Z. Alex, T. N. P. Krishna, "Design and Analysis of High Gain Milimeter Wave Microstrip Antenna Array for Analysis of High Gain Millimeter Wave Microstrip Anteanna Array for Wireless Application", Journal of Applied Theoretical and Information Technology(JATIT), 2009.

Proceeding of the
International Conference on Electrical, Computer and Telecommunication Engineering
01- 02 December 2012 (ICECTE2012), RUET, Rajshahi-6204, Bangladesh

ICECTE2012: PI-0037

Electric Field Distribution in a Biological Cell for Various Electrode Configurations-A Simulation Study

Md. Osman Goni
Department of Electronics and Communication Engineering,
Khulna University of Engineering & Technology
E-mail: osmanhku@gmail.com

ABSTRACT
The efficacy of Electro-permeabilization (EP) depends on a number of parameters, such as electric field strength, duration, number of pulses, size of target cell, and type of drug or DNA to be fed, to mention a few parameters. While electric field strength, duration and number of pulses are the dominant parameters for electroporation effect, the electric field distribution also depends on the shape, the size and the material of electrodes used. The electric field distribution varies with the type of electrode. This paper presents the simulation results of the electricfield distribution in biological tissues for various electrode configurations. For the same voltage applied, the triangular and arc electrode configuration developed the highest electric field strength. Specifically, we develop simulation results that enhance or enable the acquisition of information from cells.
KEY WORDS:─ Dielectrophoresis, electrodes, cell culture, HeLa cell.

1. INTRODUCTION

Electroporation is the physical process of inducing transient permeability of biological membranes by short pulses of electric fields [1-3]. The resulting high field strength in the membrane can lead to the formation of areas of increased permeability, often called pores, which allow transmembrane transport of molecules. This effect has been used in the laboratory for more than a decade as a research tool to facilitate cellular uptake of genetic material in vitro. More recently, electroporation has also been found effective for the intracellular delivery of molecules in living tissues, which led to a variety of medical applications. Some of these applications have already proceeded to clinical trials. The most important parameters for effective electroporation are the electrical field strength and the length of time the field applied (pulse length) [4,5]. A number of other parameters can affect the efficacy of electroporation, such as the shape of the electrical pulse, polarity, number of and interval between pulses, size of target cells, and thermal conditions during and after the pulse, as well as other cellular and environmental factors [4-7]. Electric field in the tissue is generated by a potential difference (voltage) between electrodes surrounding, or adjacent to, the tissue. A wide variety of electrode configurations have been developed, appropriate for each specific therapeutic goal [8, 9].

2. ELECTRODES

To manipulate cells, one must create an electric field of a certain shape and strength. The two approaches to doing this are to either integrateelectrodes within the microsystem or have them be external [14].

2.1 Internal Electrodes

Internal electrodes, uncommon in EP systems, are the predominant approach to generating electric fields for dielectrophoresis (DEP), mainly because of the superior control they offer for locally shaping the field. Electrodes act as equipotential surfaces that shape the field by controlling their location and voltage. Above, we saw that reducing the length of the electrodesfavorably affected manipulation forces, and the simplest way to do this is to place electrodes close together. This necessitates electrodes that are internal to the system. The primary consideration that arises when using internal electrodes is that the electrodes can adversely interact with the electrolyte via either gas generation or corrosion.

2.2 External Electrodes

The alternate approach is to use external electrodes. Very common in EP systems, external electrodes are rare in DEP systems. One advantage of using external electrodes is that they do not have to be fabricated with the device, resulting in a simpler fabrication process. The electrodes themselves often consist of platinum wires that are inserted into the port holes of the device. The electric field in systems that use external electrodes is shaped by using a straight channel (for EP) or inserting low polarizability obstructions (such as glass or polymer posts [15, 16]) in the channel (for DEP). There is no theoretical limit to the electric fields and forces that can be generated using external electrodes, although there are practical limits. Higher overall fields (such as for EP) are created by increasing the voltage or decreasing the spacing between the obstructions,

limited by the fact that openings cannot be made any smaller than the cells. Additionally, the fields exist throughout the volume of the electrolyte, which can lead to significant heating. Thus, published DEP devices for use with cells have typically used very-low conductivity water to minimize heating [15, 16]. Finally, fairly large voltages (approx. 0.1~1 kV) are needed to generate the required fields, and thus these devices are limited to dc or low-frequency operation. This is fine for EP, which operates at dc, but restricts DEP manipulations to only the low frequency region of the Clausius-Mossotti (CM) factor. The need to minimize solution conductivity, operate at or near dc, and minimize chamber volume make external electrodes best suited for use with robust cells—such as bacteria—that can tolerate being placed in low-conductivity buffers or as endpoint analysis on cells that are not needed for downstream use.

2.3 Effects of Electric Field on Cell

Because electrical cell manipulation exposes cells to strong electric fields, one needs to know how these electric fields might affect cell physiology. Ideally, one would like to determine operating conditions that will not affect the cells and use those conditions to constrain the design. Of course, cells are poorly understood complex systems and thus it is impossible to know for certain that one is not perturbing the cell. However, all biological manipulations—cell culture, microscopy, flow cytometry, etc.—alter cell physiology. The known influences of electric fields on cells can be split into the effects due to current flow, which causes heating, and direct interactionsof the fields with the cell.

.

3. SIMULATION MODEL

We chose the multiphysics model (conductive and dielectric media dc & electrostatics model) when using Magwel. The general model cell culture system with the HeLacell is shown in Fig. 1. Table 1 and 2 give the dimensions and other electrical data used in this simulation respectively. Modeling of cell and medium: Figure 1 shows the schematic view of the cell culture system in which Hela cell is considered as a monolayer of cell located at the bottom of the culture dish. The cell is modeled as a homogeneous sphere with a diameter of 35 mm and a thickness of 3 µm. On the other hand the culture medium is modeled as DMEM with 5 mm of height.Both the cell and the medium have their corresponding electrical parameters at different frequencies as listed in Table 1. The copper electrodes are used to apply electric field into the culture dish and are modeled as internal electrodes. The dimension and shape of the electrodes influence the generation of the E field in the vicinity of the electrodes which in turns induce field in the cell.

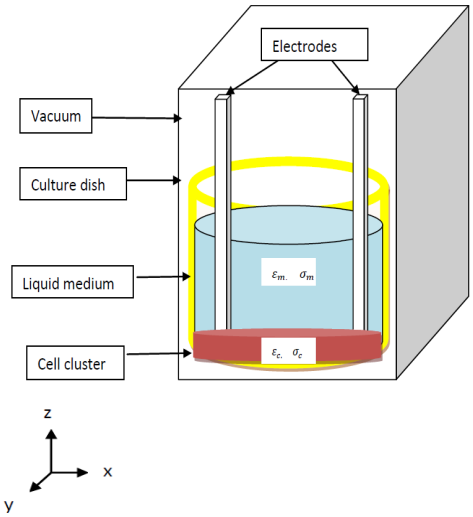

Fig. 1. 3D view of the simulation domain for the cell culture system.

Table 1: Simulation parameters

Simulation domain	50 mm X 50 mm X 15 mm
Culture dish	circular type flux, diameter= 35 mm, height= 9.5 mm
Cell culture medium	Dulbecco's Modified Eagle Medium (DMEM), height=5mm
Cell	Circular, monolayer, diameter= 35 mm, height= 3 µm
Electrodes (internal)	Copper, height=15mm (with different shape)
Spacing between electrodes	1mm
Applied voltage	10 V at f= 100 kHz (small signal)

Table 2: Dielectric properties of the HeLa cell and culture medium [17, 18]

Frequency	Cell E	Cell σ	Medium ε	Medium σ
1Hz	6.0e4	0.0001	80	1.6
100Hz	5.5e4	0.0007	78	1.55
100kHz	5 e4	0.001	76	1.5
1MHz	1.5e4	0.06	74	1.5

4. ELECTRODES TYPES

The copper electrodes are placed inclined (V-shaped) in the layer of cell and medium as shown in Fig. 2(a). The contact is facilitating the input bias to the electrodes. Here left electrode has 10 V dc while

right one is at ground state (O V). A small signal is also consider to the analysis with ac with frequency of 100 kHz. The small gap (1 mm) is maintained between the lower parts making angular orientation. The higher electric field intensity region is clearly observed at the smallest gap between the electrodes.

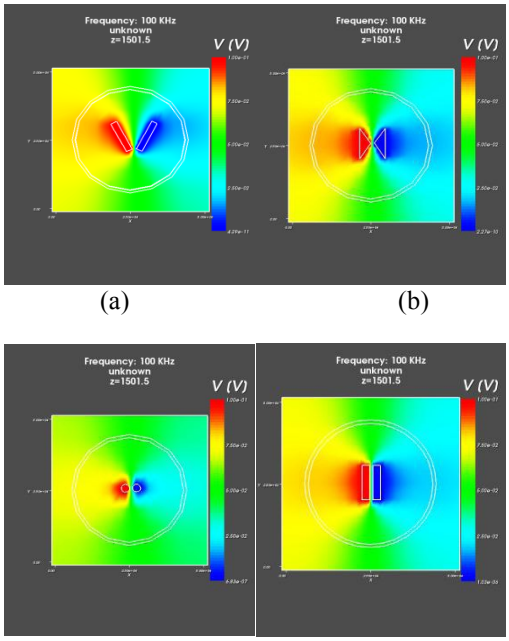

(a) (b)

(c) (d)

Fig. 2. Simulation resultsfor potential distribution of the HeLa cell using a) inclined (b) triangular (c) needle and (d) parallel electrodes configurations.

We have plotted the E field intensity in the x direction at y= 21553 µm and z=1501 µm (cell layer) as shown in Fig. 3(a). The sharp peak electric field strength at the gap of the electrodes is 64.5 V/m which is the actual field strength obtained in the center of the electrodes. The nominal field strength (voltage divided by the distance between the two electrodes) is 10 kV/m.This model is also simulated using triangular, needle, and parallel electrodes. The results of potential distribution and E field distribution are shown in Figs 2 and 3 respectively with the function of x-coordinates (micrometer).

5. RESULTS AND DISCUSSION

Table 3 summarizes the results of the simulation of HeLa cell model using different type and shape of the electrodes. The shape of the electrodes characterizes the linearity of the field distribution at the edges. The highest electric field strength due to highly non-uniformity occurs at the area closest to the sharp point.

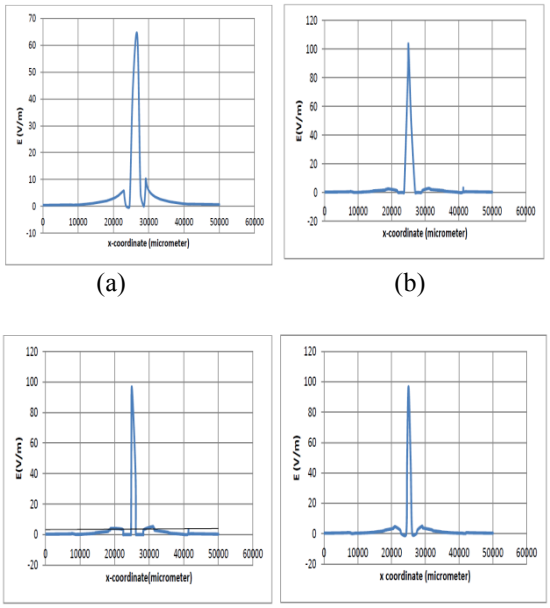

(a) (b)

(c) (d)

Fig. 3. E field variation along x axis at f=100 kHzusing a) inclined(b) triangular (c) needle and (d) parallel electrodes configurations.

Table 3: Comparison of E fields with electrode's type and their orientations.

Electrode's types and orientation	Maximum E field (V/m)	Uniformity
Flat and angular	64.5	Non uniform
Triangular	105	Non uniform
Rod (pin)	96	Non uniform
Flat and parallel	96	Uniform
Arc	134	Non uniform

Domain discretization at the structure of interest is also important for the accurate results. The peak electric field exists only at the spacing (gap) of the electrodes. Hence the location, shape and orientation of the electrodes influence the overall contribution of the E field to the cell and medium. For the monolayer of the HeLa cell, the localized electric field as obtained from the above field distribution does not affect the entire layer of the cell. Thus the average electric field should be more pronounced and effective for the polarization of the dielectric properties of the cell. In that case, the array of electrode could be a good choice where the uniform distribution is important.

6. CONCLUSIONS

The simulation of a monolayer of HeLa cell is presented here with the different types, shape and orientation of electrodes. The electric field

distribution for electroporation applications strongly depends on the electrode configurations. Parallel plate electrodes and needle electrodes of various dimensions are most commonly used for preclinical and clinical applications. Parallel plate electrodes give the most uniform electric field distribution with the simplest configuration as seen in this simulation and this correlates well with the published data. Needle electrodes need to be used for deeply-seated tumors where parallel plate electrodes cannot be used. Due to the sharp needle point, needle electrodes give non-uniform field distribution with the highest field strength near the tip of the needle as the field homogeneity depends on the shape of the electrodes. This point has to be taken into consideration during electroporation applications since the electric field in the tissue will be different for a given area and hence the efficacy of the technique will vary.The cell and the medium are equivalently characterized by their electrical constants at certain frequency. As the medium is considered to be dispersive, the results are shown to be at certain frequency namely 100 kHz. It was found that up to 100 MHz, the results does not differ significantly as the size of the cell is much less than the wavelength (low frequency problem). The work also demonstrates the proper choice of the electrodes would be significant for the cell manipulation and cell culture.The presented ideas facilitate the dielectrophoresis as a building block for lab-on-a-chip devices which can be easily fabricated using the existing microelectrode photolithography techniques. The design of the electrodes, the choice of the suspending medium, the applied peak voltage and frequency can be pre-determined to optimize the operation of the device.

REFERENCES

[1] L.M. Mir, et al., Electrochemotherapy, a novel antitumor treatment: first clinical trial. C.R. *Acad. Sci*. Paris 313, 613-618 (1991).

[2] R.H. Heller, Overview of Electroporation", *Technology in Cancer Research & Treatment*, vol. 1, no. 5, 2002.

[3] R. Heller, R. Gilbert, and M. J. Jaroszeski, "Clinical trials for solid tumors using electrochemotherapy",in *electrochemotherapy, Electrogenetherapy, and Transdermal Delivery*, New Jersey: Humana Press, pp. 137-156, 2000.

[4] M.P. Rols, et al., "In vivo delivery of drugs and other molecules to cell", in *Electrochemotherapy, Electrogenetherapy, and Transdermal Delivery*, New Jersey: Humana Press, p. 83-97, 2000.

[5] L.M. Mir and S. Orlowski., "The basis of electrochemotherapy",in *Electrochemotherapy, Electrogenetherapy, and Transdermal Delivery*, Humana Press, p. 99-117, 2000.

[6] H. Potter, "Molecular Genetic Applications of Electroporation", in *Electroporation and Electrofusion in Cell Biology*. New York: Plenum Press, p. 319-341, 1989.

[7] T. Curd, B. Vernon, C. Pauken, and R. Sundararajan**,** **"**Optimization of electroporation parameters for human ovarian cancer cells*", Proceedings of Electrostatics Society of America* (ESA) Annual Meet, University of Alberta,Edmonton, Canada 2005.

[8] G.A. Hofmann, "Instrumentation and Electrodes for in vivo electroporation", in *Electrochemotherapy, Electrogenetherapy, and Transdermal Delivery*, New Jersey: Humana Press, p. 37-61, 2000.

[9] R. Gilbert, M. Jaroszeski, and R. Heller, "Novel electrode designs for electrochemotherapy". *BiochimicaetBiophysicaActa*1334 9-14, 1997.

[10] T. Goto et al., "Combination electro-gene therapy using herpes virus thymidine kinase and interluekin-12 expression plasmids is highly efficient against murine carcinomas in vivo". *Mol. Therapy*, Vol. 10, No. 5, p. 929-937 (2004).

[11] Y. Yamashita et al., "Electroporation-mediated Interleukin-12 gene therapy for hepatocellular carcinoma in the mice model". *Cancer Res*. 61, 1005-1012 (2001).

[12] W. Mitchell, and R. Sundararajan, " Electric field distribution in biological tissues for various electrode configurations-A FEMLAB study", Proc. Of the COMSOL Multiphysics user's conf. , Boston, 2005

[13] Magwel, SolvEM User Guide, Version 3.0.0, ©Magwel, http://www.magwel.com./ Sep 2008.

[14] Joel Voldman, "Electrical forces for micrscale cell manipulation" Annu. Rev. Biomed. Eng. 8: 425-54, 2006.

[15] Chou CF,Tegenfeldt JO, Bakajin O, Chan SS, Cox EC, et al. "Electrodelessdielectrophoresis of single- and double-stranded DNA". *Biophys. J.* 83:2170–79, 2002.

[16] Lapizco-Encinas BH, Simmons BA, Cummings EB, Fintschenko Y., "Dielectrophoretic concentration and separation of live and dead bacteria in an array of insulators". *Anal. Chem.* 76:1571–79, 2004.

[17] M.H. Wang, M.K. Chen and L.S. Jang, "Electrical characterization of single HeLa cell using 2D simulation and spectroscopy measurement", *IEEE proceedings*, CIBEC 2008.

[18] Y. Nikawa and T. Michiyama, "Blood-sugar monitoring by reflection of millimeter wave", *Proceedings of Asia-Pacific Microwave Conf.* 2007.

Proceeding of the
International Conference on Electrical, Computer and Telecommunication Engineering
01- 02 December 2012 (ICECTE2012), RUET, Rajshahi-6204, Bangladesh

ICECTE2012: PI-0039

Ultra Wideband On-Body Radio Channel Measurements Using Wireless Sensors

Mohammad Monirujjaman Khan[1,2], Qammer H. Abbasi[1], Nabila Hossain[2], Abdullah-Al-Mamun[2]
[1]School of Electronic Engineering and Computer Science, Queen Mary University of London, Mile End Road, London E1 4NS, UK
[2] Faculty of Engineering, American International University-Bangladesh, Banani, Dhaka-1213, Bangladesh
E-mail: mohammad.khan@elec.qmul.ac.uk; monirkhan@aiub.edu

ABSTRACT
In this paper, experimental characterisation of on-body radio channel using ultra wideband (UWB) wireless tags is presented. The performance of wearable wireless tags on the UWB on-body radio channel characterisation has been investigated. Measurement campaigns are performed in the chamber and in an indoor environment for comparison. Statistical path loss parameters of nine different on-body radio channels for static and dynamic cases are shown and analyzed. The path loss was modeled as a function of distance for 34 different receiver locations for propagation along the front part of the body.

KEY WORDS: On-body radio channel, body-centric wireless communication, Ultra wideband (UWB), Path loss, Received Signal Strength Indicator (RSSI).

1. INTRODUCTION

Ultra wideband (UWB) communication is a low-power, high data rate technology that minimizes multipath interference due to late time-of-arrival. Its low power requirement due to control over duty cycle allows longer battery life and also introduces green radio system. One of the most potential areas of UWB applications is the body-centric wireless networks where various units/sensors are scattered on/around the human body to measure specified physiological data i.e. patient monitoring for healthcare applications [1-3].

In the past few years researchers have been thoroughly investigating narrow band and ultra wideband on-body radio channels. In [4-7], on-body radio channel characterisation was presented at the unlicensed frequency band of 2.45 GHz. UWB on-body radio channel characterisation and system level modelling for body-centric wireless networks have been presented extensively in the open literature [2, 8-18]. In [8-18] UWB on-body radio propagation channels have been characterised and their behaviour have been investigated in indoor and chamber for stand-still, various postured and dynamic human body based on different antennas.

Most UWB on-body radio channel measurements are performed using two standalone antennas and cables connecting to a vector network or spectrum analyzer which is more a controlled environment and restrictive; however, in real life scenarios potential UWB body-centric wireless network needs to be integrated with compact sensors and provides efficient and reliable communication channels. Critical issues remain with regards to indoor propagations, radio channel characterisation and human body effect which need to be addressed before the concept can be deployed for real life applications.

In this paper measurement campaigns were performed in the chamber and indoor environment using commercially available UWB wearable active tags and reader. The main aim of this study is to investigate the performance of the commercially available wireless tags on the UWB on-body radio channel characterization. Nine different UWB on-body radio channels are investigated and the effects of the body movements on the path loss are analysed. The rest of the paper is organised as follows; section II illustrates the measurement settings and it briefly introduces the UWB tags, Section III presents the measurement results and on-body radio channel parameters and modelling aspects, and finally section IV draws the main conclusion of the presented study.

2. MEASUREMENT SETTINGS

In this study, measurement campaigns were performed using UWB wearable active tags and reader provided by Time Domain PLUS^{TM} [19]. For this measurement purpose a real human subject was used. The test subject was an adult male of mass 90 Kg, height 1.68 meter and chest circumference 114 cm. Nine different ultra wideband wireless active transmitter tags were attached at different locations on the human body: left/right chest, left/right thigh, left wrist, left/right ankle, left elbow, left ear, as shown in Fig. 1, while the UWB antenna connected with the reader was placed on the left waist of the human subject for tag's signal reception. Two measurement scenarios are considered: as static and

dynamic human body. For static case, subject was standing still for a period of 60 seconds wearing nine tags on the body and, for the movement case, the subject was walking 5 steps ahead and 5 steps back, starting with the left leg and right arm as a normal walking speed. For the dynamic case, the measurement duration was again 60 seconds while the subject was doing the same walking movement for the measurement duration. Location-based software was used to save the tags transmission ID, received signal strength (RSSI) and time of arrival data from the reader. The UWB tags are battery powered and the duration of the battery life is four years since the tags only transmit UWB pulses every one second. The tag's transmit power is -13.01 dBm which is around 40 dB less than mobile phone transmit power. The operating frequency of the tags used for this measurement is 5.9~7.25 GHz with a centre frequency of 6.6 GHz. The UWB tag is small and durable, with a plastic housing that allows it to be attached to assets or people. The dimension of the tag is (13 mm x 36 mm x 33 mm) and the weight is 0.74 oz (22 g). Figs. 2(a) and 2(b) show the UWB tag encased inside the plastic housing and the bottom view of the tag without plastic housing [19].

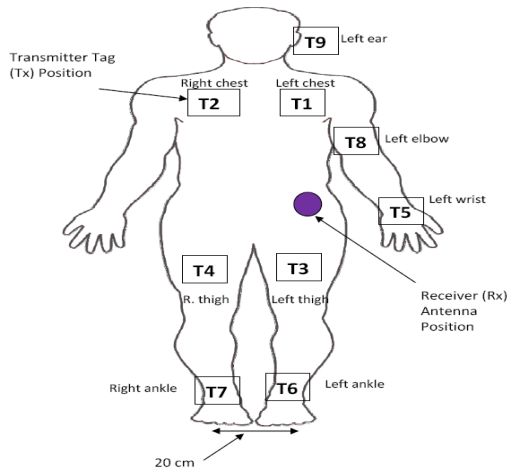

Fig. 1 On-body measurement settings showing the receiver antenna is on the left waist and nine transmitter tags are on different locations of the body (nine static and dynamic channels cases analysed).

The measurement was first performed in the anechoic chamber to eliminate multipath reflections from surrounding environment and then repeated in the Body-Centric Wireless Sensor Laboratory at Queen Mary, University of London to consider the effect of the indoor environment on the on-body radio propagation channels. Fig. 3 shows the dimensions and geometry of the Body-Centric Wireless Sensor Lab. The total area of the lab is 45 m^2 which includes a meeting area, treadmill machine, workstations and a hospital bed for healthcare applications. The measured Received Signal Strength Indicator (RSSI) level for each transmitter tag is recorded over the measurement duration of 60 seconds for each different location.

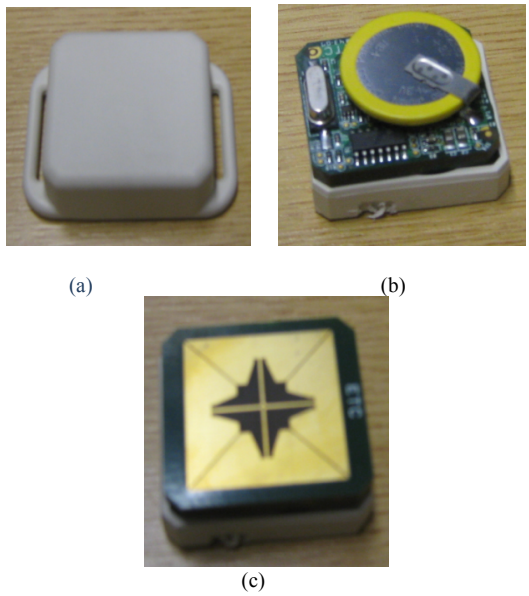

Fig. 2 (a) UWB active transmitter tag encased inside the plastic housing, (b) Tag without plastic housing and bottom view, (c) Top view of the tag showing the transmitter tag antenna.

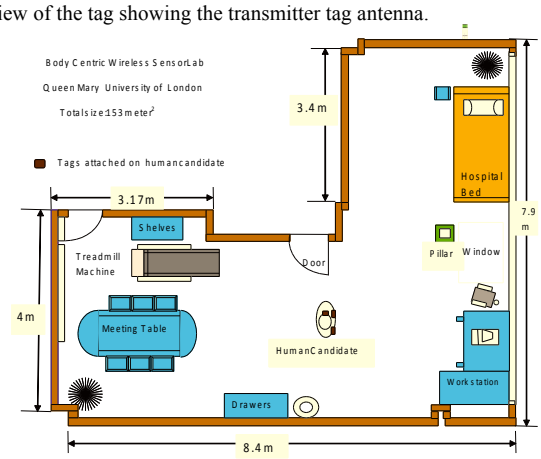

Fig. 3 Dimensions and geometry of the Body-Centric Wireless Sensor Lab (housed within the Department of Electronic engineering, Queen Mary University of London, London, U.K) where the indoor on-body radio propagation measurements for the presented work is performed.

3. UWB ON-BODY RADIO CHANNEL PARAMETERS

3.1 On-Body Radio Channel Characterisation

In this work, the path loss for nine different on-body channels was calculated from the measured RSSI for each transmitter tag. The cumulative distribution function (CDF) of the path loss variations both in the chamber and indoor environment for static and dynamic scenarios of nine different on-body radio channels is compared to well-known distributions such as Normal, Lognormal, Nakagami, Rayleigh, Weibull, Gamma and Rician. Based on the maximum likelihood test results, the lognormal distribution

provides the best fits these measured results (Fig. 4). Figs. 5 and 6 show a comparison of the measured average path loss (μ) and standard deviation (σ) of the fitted lognormal distribution that are applied to model the path loss variations for the nine on-body radio channels, for the static and walking scenarios, respectively.

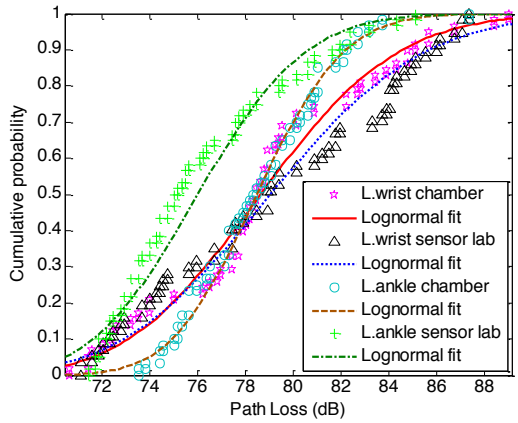

Fig. 4 Cumulative distribution function of the left wrist and left ankle on-body radio channels when subject was walking measured in the chamber and in indoor environment.

In the chamber, for both standing and walking cases, the highest path loss is noticed for the receiver to left-ear link, while the lowest is the receiver to left-thigh link (Fig. 5). For the reader to left-ear link the communication distance between the reader antenna and the transmitter tag is larger; in addition, due to the different orientation of the tag located on the left ear, non-line-of-sight (NLOS) communications exist, which cause the highest path loss value for this channel. For the left thigh link there is a clear line-of-sight (LOS) communication and the lowest communication distance between the reader and the transmitter tag.

In the indoor environment due to reflecting area and contributions of multipath reflection the right chest and left-ear (for static case) and right thigh and chest channels (for movement cases) experience the highest path loss value, while the left thigh channel experiences the lowest. Most of the on-body channels experience higher path loss value when measurements are made in the chamber, due to the non- reflecting environment. The average path loss of all nine channels in the chamber, for static and walking case, is 81.44 dB and 80.68 dB, whereas 79.22 dB and 80.00 dB are found in the indoor environment, respectively.

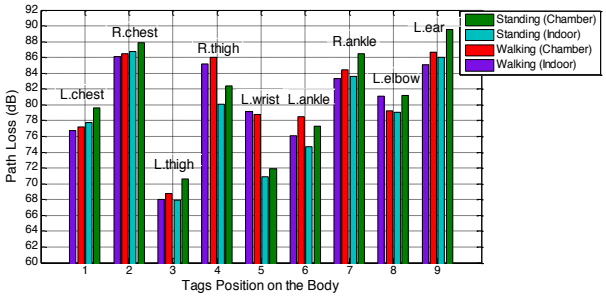

Fig. 5 Comparison of average path loss of nine UWB on-body radio channels for standing and walking scenarios measured in the chamber and in indoor.

The variation of the path loss for the nine different on-body channels is also compared for standing and walking cases, to study the trend of the changes of path loss for each channel in these two different scenarios. For the two different scenarios (i.e. standing and walking) a maximum of 8.23 dB and 6.88 dB variation of average path loss of a channel is noticed, which occurred for the left wrist channel both in indoor environment and chamber, respectively (Fig.5). During walking scenarios, the tag located on the wrist moves between to LOS and NLOS communications scenarios and the communication distance between the receiver and the transmitter is also changes greatly, causing the path loss data to vary the most with respect to the standing case for this channel.

The highest standard deviation σ value for the dynamic case is noticed for the left wrist and right ankle channels, which are considered the least stable (data spreads the most from the average path loss) channels, whereas the lowest is noticed for the left thigh and chest channels; these channels are considered the most stable (see Fig.6). Movement of the human body has the highest effect on the wrist and ankle channels and the least on chest and left thigh channels. In comparison to the chamber, the standard deviation value is found to be higher in the indoor environment due to the effects from the indoor reflecting multipath environment.

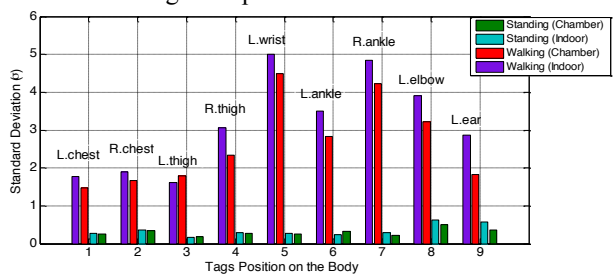

Fig. 6 Comparison of standard deviation (σ) of nine different on-body radio channels for standing and walking scenarios measured in the chamber and indoor.

4. CONCLUSIONS

UWB on-body radio propagation channel measurements were performed using ultra wideband (UWB) wireless tags and reader in the chamber and

indoor environment. Nine different UWB on-body radio channels were investigated for static and movement scenarios. Results demonstrated that lognormal distribution provides the best fits for on-body propagation channels path loss model. In this study, left thigh link shows the lowest path loss, whereas the left ear and right chest show the highest. Study shows that due to different scenarios (i.e. standing and walking) an on-body link experiences up to 8.23 dB variations in path loss.

REFERENCES

[1] P. S Hall and Y. Hao, *Antennas and propagation for Body-Centric Wireless Communications*. Artech House, 2006.

[2] J. Foerester, E. Green, S. Somayazulu and D. Leeper, " Ultra-Wideband for Short- or Medium-Range Wireless Communications,'' *Intel technology Journal*, Q 2, 2001.

[3] A. Fort, C. Desset, P. D. Doncker, and L.V. Biesen, " Ultra wideband body area propagation: from statistics to implelmentation,'' *IEEE Transactions on Microwave Theory and Technique*, vol. 54, no. 4, pp. 1820 1826, June 2006.

[4] Z. Hu, Y. Nechayev, P.S Hall, C. Constantinou, and Y. Hao, "Measurements and statistical analysis of on-body channel fading at 2.45 GHz,'' *IEEE antennas and Wireless Propag. Lett.,*. vol. 6, pp. 612-615, 2007.

[5] A. Alomainy, Y. Hao, A. Owadally, C. G. Parini, Y. Nechayev, C. C. Constantinou, and P. S. Hall, "Statistical analysis and performance evaluation for on-body radio propagation with microstrip patch antenna,'' *IEEE Transactions on Antennas and Propagation,* Vol, 55, No, 1 January 2007.

[6] S.L. Cotton, G.A. Conway & W.G. Scanlon " A time-domain approach to the analysis and modelling of on-body propagation characteristics using synchronized measurements at 2.45 GHz,'' *Ibid.*, pp. 943-955.

[7] Y. I. Nechayev, Z. H. Hu, P. S. Hall, " Short-Term and Long-Term Fading of On-Body Transmission Channels at 2.45 GHz,'' 2009 *Loughborough Antennas & Propagation Conference,* 16-17 November 2009, Loughborough, UK.

[8] A. Fort, C. Desset, J. Ryckaert, P.D. Donker, L. V. Biesen , and P. Wambackq, "Characterization of ultra wideband body area propagation channel,'' *International Conference on Ultra-Wideband*, September 2005.

[9] A. Alomainy, Y. Hao, X. Hu, C.G. Parini, and P.S Hall, "UWB on-body radio propagation and system modeling for wireless body-centric networks,'' *IEE proceedings communications*-Special Issue on Ultra Wideband Systems, technologies and Applications, vol. 153, no.1, pp 107-114, Feb. 2006.

[10] Q. H. Abbasi, A. Sani, A. Alomainy and Y. Hao, Radio Channel characterization and system-Level Modeling for Multiband OFDM Ultra Wideband Body-Centric wireless networks, *IEEE Transactions on Microwave Theory and Techniques*, Vol. 58, no. 2, pp. 3485-3492, Dec. 2010.

[11] Q, Wang, J. Wang, "Performances of On-Body Chest-to-Waist UWB Communication Link," *IEEE microwave and wireless components letters*, vol. 19, no. 2, feb.2009.

[12] Q. Wang, T. Tayamachi, I. Kimura, and J.Wang, "An on-body channel model for UWB body area communications for various postures,'' *IEEE Journal on Selected Areas in Communications,* vol. 57, no. 4, pp .991 998, Apr. 2009.

[13] A. Sani and Y.Hao, "Modeling of Path Loss for Ultrawide Band Body Centric Wireless Communications,'' Electromagnetics in advance applications, 2009. ICEAA '09. *International Conference on* 14-18 sept.,2009 pages(s):998-1001.

[14] T. Zasowski, F. Althaus, M. Stager, A, Wittneben, and G. Troster, "UWB for noninvasive wireless body area networks: channel measurements and results,'' *IEEE Conference on Ultra Wideband Systems and Technologies*, November 2003.

[15] A. A. Alomainy, Y. Hao, C. G. Parini, and P.S. Hall, "Comparison between two different antennas for UWB on body propagation measurements,'' *IEEE Antennas and Wireless Propagation Letter.* 2005, 4, (1), pp. 31-34.

[16] Q. H. Abbasi, A. Sani, A. Alomainy and Y. Hao, "Arm movements effect on ultra wideband on-body propagation channels and radio systems,'' *Antennas and Propagation Conference, 2009.LAPC.2009* Loughborough 16-17 Nov. 2009 Pages(s): 261-264.

[17] A. Alomainy, Q. H. Abbasi, A. Sani and Y. Hao, "System-Level Modeling of Optimal UWB Body-Centric wireless networks,'' *Asia Pacific Microwave Conference* (APMC) 2009, Singapore, 7-10 December 2009.

[18] A. Sani, A. Alomainy, and Y. Hao, "Effect of the Indoor Environment on the UWB On-Body Radio Propagation Channel,'' *Antennas and Propagation, 2009. EuCAP 2009. 3rd European Conference on,* 23-27 March 2009 Page(s):455 – 458.

[19] (2009) Plus Asset Tag, Reader and SFF Antenna Datasheet/Time Domain. [Online]. Available: http://http://www.timedomain.com/

Proceeding of the
International Conference on Electrical, Computer and Telecommunication Engineering
01- 02 December 2012 (ICECTE2012), RUET, Rajshahi-6204, Bangladesh

ICECTE2012: PI-0040

An Enhanced Compression Based Data Communication Scheme for Wireless Sensor Networks

S. A. Ahsan Rajon and *Md. Mahbubur Rahman*
Computer Science and Engineering Discipline, School of Science, Engineering and Technology,
Khulna University, Khulna-9208, Bangladesh.
ahsan.rajon@gmail.com, mahbubcse@yahoo.com

ABSTRACT
In this paper, we propose an effective data communication scheme for wireless sensor network. The data communication approach is mostly based on data compression. The main contribution of the proposed approach is, it makes use of the simple but efficient representation of value pairs to attain the compression. Since, providing flexible service using wireless sensor network is challenging because they usually contain a large number of resource constraint sensing nodes with small memory, lower processing capability and extremely limited battery life, the scheme is considered to be simple, computationally feasible and overall resource requirement is minimum. It is also a mentionable feature of our research that, besides consideration of resource constraints of individual sensor nodes into concern, the proposed compression based compression scheme takes the overall routing scheme into consideration which ensures efficient and minimum energy consumption of WSNs. Overall data compression scheme also ensures balanced work load distribution in sensor network.

KEY WORDS: Wireless Sensor Networks, Data Compression, Resource Constraints, Power Consumptions, Data Communication, Routing, Cluster Coordinators.

1. INTRODUCTION

Wireless Sensor Networks (WSN) have attracted lot of attention due to their multidimensional applications in both civilian and military arenas. Wireless Sensor Networks (WSN) usually consists of a large number of ultra small low-cost battery-powered devices that have limited energy resources, small computational capability, limited memory, and shorter communication capacities [1], [13]. According to different applications such as battlefield reconnaissance and homeland security monitoring, agricultural field monitoring, fire detection WSNs are often deployed in a vast terrain to detect events of interest and deliver data reports over multi-hop wireless paths to the sink. Data engineering and management is essential for these mission-critical applications to work in unattended and even hostile environments. WSNs can be used for data collection purposes in situations such that environmental monitoring, habitat monitoring, surveillance, structural monitoring, equipment diagnostics, disaster management, and emergency response [1], [2], [5], [13].

The main contributions of this paper are: firstly, it proposes an effective data communication scheme based on data compression where the workload distribution is more or less balanced and consequently, in spite of using the energy of any specific sensor especially the event reporting source sensor at a greater level, we propose to achieve the total communication at a hop by hop basis, which essentially ensures robust data delivery. Moreover, this paper employs the value-pair comparison based scheme which facilitates simple but effective solution in compressing the data.

This paper is organized into six sections. In the related literature section, we provide elementary concepts of sensor network and data routing. Recent researches regarding data compression in wireless sensor networks are presented in the section three. A detailed overview of our proposed scheme has been illustrated in section four. Section five is devoted to present an extensive analysis of the proposed scheme. This paper concludes with section six specifying future directions regarding proposed scheme.

2. RELATED LITERATURE

This section provides a glimpse on the basic concepts of wireless sensor network and data compression with investigation of the necessity of data compression for wireless sensor networks. An overview of the existing data compression schemes are also incorporated

2.1 Sensor Networks

Wireless Sensor Networks are usually composed of hundreds and thousands of individual tiny sensor nodes which are often densely deployed in a vast terrain. These nodes have the capability to collect data and to send the data to other neighboring nodes or components participating to serve the mutual goal of the system. Individual sensor node consists of four basic generic components: sensing unit, processing unit, transceiver unit, and power unit. Sensing units comprise of two subunits: sensors and analog-to-digital converters (ADCs). The analog signals are

produced by the sensors based on the sensing objects and sensing pattern and are converted into digital signals by the ADC. These digital signals are then fed into the processing unit which is generally associated with a small storage unit serving computational aspects. The processing unit also manages the applications and procedures which make the sensor node collaborate with the other nodes to carry out the assigned sensing tasks. A transceiver unit connects the node to the network. One of the most important components of a sensor node is the power unit that may be supported by power scavenging units such as solar cells. There are also other units that are Location tracking system and Power generator systems are also often integrated with the sensor nodes in order to achieve sophisticated functionalities and services.

Sensor Networks are mostly application specific and the adopted routing strategy is also considered as a design criteria. That is, each routing algorithm considers the intended observational subjects and also at the same time, the internal architecture of Sensor. However each routing technique considers several common and essential features like ensuring maximum lifetime of the sensors by minimizing energy consumption through reducing redundant data transmission or data exchange. The task of finding and maintaining routes in WSNs is nontrivial since energy restrictions and sudden changes in node status cause frequent and unpredictable topological changes [1]. A mote consumes 1 μJ for transmission and 0.5μJ for reception of a single bit while it consumes 0.8 μJ for executing roughly 100 instructions [20].

2.2 Data Compression for Wireless Sensor Networks

As the battery-powered sensor nodes cannot be frequently charged or recharged, for any application, it is essential to minimize the power consumption by reducing the radio communication and internal processing. In case of wireless sensor networks, generally two approaches are considered in reducing the radio communication namely duty-cycling and in-network processing [22]. Duty cycling schemes use coordinated sleep and wakeup schedules among nodes whereas in-network processing suggests compression and/or aggregation (clustering) techniques for reducing the total amount of data to be communicated [22].

Data compression for energy constrained devices is fundamentally different from compression of huge text [24] because –

Firstly, for energy constrained devices it is a must to minimize the number of required operations to compress the text in order to ensure normal life-time of the devices. Typical example includes the cases of data compression for wireless sensor network where the battery life is extremely limited and consequently, any algorithm for data compression should consider the energy consumption issue as the prime factor. But, in case of generic compression schemes this is not at all considered with greatest care.

Secondly, small text compression for energy constrained is normally viewed as a multi-objective optimization problem with the objective of compression ratio and compression-decompression time (i.e. performance) and energy consumption (i.e. complexity), whereas, the main target of generic compression scheme is achieving better compression ratio at a reduced compression decompression time. Usually, algorithms for small text compression for energy constrained devices compromises compression ratio for energy consumption. That is, short text compression schemes for battery powered i.e. energy constrained devices should be computationally simple to cope with the limited processing capability of the devices.

Thirdly, generic compression schemes often consider building of dictionaries on the fly, which in most researches has been discouraged for compression of short text since, construction of the dictionary on the fly will undoubtedly include additional operational cost on the devices which should be avoided.

Fourthly, the memory overhead for operation as well as for the dictionary should be reduced as much as possible for compression of text for energy constrained devices whereas, for generic text compression schemes this constraint is a secondary aspect.

Finally, recent generic text compression schemes consider (and have successfully proved and implemented) online dictionaries with the provision of sending the dictionary along with the compressed data in order to enhance the compression performance. Often the dictionary itself is made compressed and thus, for the cases of compressing large amount of text, it is beneficial. But it is of no doubt, for compression of very small text it will result into an expanded file.

That is, the compression schemes sophisticated for huge text compression often fails to compress small text successfully. For the above mentioned aspects, it is essential to devise sophisticated approaches for compression of small texts especially for energy constrained devices.

3. RELATED RESEARCH

Data compression in wireless sensor networks may be effective only at that time when the energy consumption for compressing the data along with sending the compressed data is significantly less than transmission of non-compressed data. Moreover, since generic data compression algorithms are aimed at saving storage, not energy, most of the traditional data compression algorithms fail to satisfy the requirements for wireless sensor networks.

Consequently, it requires development of sophisticated energy consumption aware data compression algorithm for wireless sensor networks in order to attain power savings. Applying specific energy efficient routing mechanism along with effective data compression for *WSNs* may offer best role in maximizing the energy savings in Wireless network and thus enhance the overall lifetime of the network.

3.1 Compression of Short Text on Embedded Systems

The recent literature regarding short text compression titled "Compression of Short Text on Embedded Systems" by Rein *et al.* [25] proposes a low-complexity version of *PPM* (Prediction by Partial Matching). A hash table technique with one-at-a-time hash function is employed in this method to design the data structure for data and context model. They use statistical models with hash table lengths of *16384, 32768, 65536* and *131072* elements requiring two bytes for each element, which result an allocation of *32, 64, 128* and *256 Kbytes* of *RAM* respectively. If this memory requirement may be substantially decreased, we may achieve more efficient compression and hence may make the scheme usable to even very low-quality cellular phones. [24].

3.2 Pipelined In-Network Compression

Pipelined In-Network Data Compression [20] is an elementary approach sophisticated for wireless sensor networks. The main underlying idea of *PINCO* is sharing common parts of the data. In the aggregation nodes, some technique is applied in combining the common parts of the correlated data which achieves the compression. The more consecutive common sensing data have the more bits can be aggregated using the common bits (known as *prefix*) and thus the better the compression. The format of sensed data is considered as *<sensing data, node ID, time-stamp>* before the compression while, after compression it is considered as *<shared prefix, suffix list, node ID list, time-stamp list>*. The revealed common part of the data is contained into the shared prefix part and the remaining parts are presented as a list of suffix. Corresponding node ids and timestamps are also presented as corresponding list. When the sensing data maintains high correlation, the approach is efficient whereas the compression ratio becomes poor for data having rare common parts. In the example, original uncompressed data was *36 bits* whereas after compression it becomes *30 bits* resulting into a savings of *6 bits* [19], [20].

3.3 Simple Huffman Algorithm

The main idea of *Simple Huffman Algorithm* is to map each symbol with some binary representation ensuring use of shorter bit-length codes for frequently appearing symbols than those occur rarely. For any sensor node, the measured data m_i is converted into its binary representation r_i comprising of R bits by an analog-to-digital converter (*ADC*), where R is the resolution of *ADC*. The compression algorithm computes $d_i=r_i—r_{i-1}$ for each new acquisition m_i. For computing d_0, it is assumed that, r_{-1} is equal to the central value among 2^R possible discrete values. Compression is performed by the entropy coder by encoding the differences d_i more compactly based on their statistical characteristics. A bit sequence bs_i composed of two parts $s_i|a_i$ is used to represent d_i, where s_i codifies the number n_i of bits needed to represent d_i and a_i is the representation of d_i. n_i is computed as $n_i = \lceil log_2(|d_i|) \rceil$ for any non-zero value of d_i ; while, $n_i=0$, for any $d_i=0$; Code s_i corresponds to a variable length symbol generated from n_i using Huffman coding. In [22], Marcelloni and Vecchio have also presented a Huffman variable length codes used for their research. The a_i part of t he bit sequence bs_i is a variable-length integer code generated as follows: [22]

1) if $d_i>0$, a_i corresponds to the n_i low-order bits of the two's complement representation of d_i;
2) if $d_i<0$, a_i corresponds to the n_i low-order bits of the two's complement representation of (d_{i-1});
3) if $d_i=0$, s_i is coded as 00 and a_i is not represented.

3.4 LZW for Sensor Nodes (S-LZW)

LZW for Sensor Nodes (*S-LZW*) proposed by Sadler and Martonosi is based on the famous Lempel-Ziv-Welch (*LZW*) compression algorithm. This lossless compression scheme is actually a dictionary based compression approach. Original Input bit stream is divided into fixed sized blocks (*e.g. 512* bytes) and then each block is compressed individually. For each new block, the dictionary is re-initialized with the codes (*256* entries) representing standard character set. With each occurrence of new string in the bit stream, the dictionary is updated. Since, this frequent update may result into memory overload, proposed measure includes getting the dictionary frozen and using it as-is for encoding remainder of the data or resetting it and starting from scratch. Apart from *LZW*, a mini-cache has been introduced in *S-LZW* which is a hash-indexed dictionary of size *N*, where N is a power of *2*, which stores recently used and created dictionary entries with an aim to take the underlying advantage of the repetitiveness characteristics of sensor data [21].

4. ENHANCED COMPRESSION BASED DATA COMMUNICATION SCHEME FOR *WSNS*

The main idea of proposed data communication scheme is to utilize the effectiveness of data compression along with the selection of appropriate routing scheme which facilitates the maximum advantage of compression. The proposed compression scheme is mostly based on three interrelated steps.

In first step of data communication, each sensing node participates into the data compression process. When the nodes are deployed, initial data are communicated

without any compression. With the course of time, the nodes develop a dictionary with the sensed data dynamically until a threshold reaches. This dictionary building process synchronizes the same dictionary entry into the cluster coordinators. Initially each node is considered to have a blank dictionary. The dictionary is supposed to map a combination of two consecutive *values* (sensor readings) onto a single *code*. Whenever any node has any sensed data (α_j), it compares it with its just previous reading (α_i). If this combination of data (α_i and α_j) doesn't exist on the dictionary, the value couple is inserted into the dictionary as a new entry. At the same time a data packet is also sent to its cluster head informing the newly explored dictionary entry and its codeword. On each cluster head end, whenever it receives any request for updating its dictionary, it updates the same and also informs it to its member nodes. That is, dictionary of both the cluster head and individual node is synchronized at the same time. On the basis of the network architecture, maximum number of entries into the dictionary is agreed upon. For our experiments, we consider maximum *256* entries (*i.e. 256* pairs of values) into the dictionary. Whenever the threshold limit exceeds, a packet informing the nodes regarding the completion of the dictionary building phase is sent to the nodes.

Whenever any node sends data to the cluster head, it maintains a certain packet format. The first entry comprise of *node_id* followed by the number of sensed data. Then for each data or value pair, *dictionary_flag* and *dictionary_entry* are placed. A *dictionary_flag* 0 indicates that, the value following the *dictionary_flag* is a single data; while a 1 as the *dictionary_flag* indicates that, *dictionary_entry* is the dictionary code for a value pair.

Whenever the cluster head have the dictionary formed, it is communicated with the sink. Since, the sink is supposed to have enough power and in most cases, it possesses enough computational capability to process huge data, maintaining separate dictionary for each cluster head is computationally feasible. Moreover, since, maintaining a single dictionary for all the cluster head requires communicating the dictionary to all the cluster head and ultimately to each node, the overall energy consumption may not be reasonable and may even result into network failure as occurs in adaptive Huffman coding. The second part includes the cluster heads where the received data from the nodes are processed to be transmitted to the sink. Whenever the cluster heads communicate the data with the sink, we adopt the pipelined in network compression approach [20]. It is notable that, the data part includes an amalgamation of both compressed and un-compressed data. Since, pipelined in network compression approach considers binary representation, it works very frequently with the data received from the first phase of the proposed scheme.

5. ANALYSIS OF PROPOSED APPROACH

Performance of the proposed scheme along with relevant schemes has been measured in terms of compression ratio.

$$Compression\ ratio = 1 - \left(\frac{bitsize\ after\ compression}{original\ size} \right)$$

Here size is usually measured in terms of bits.

The performance of our proposed scheme has been evaluated against the *PINCO* and *S-LZW* scheme. We have also evaluated the scheme considering both *256* entries and *512* entries as the threshold of the dictionary for each cluster head. We have also considered highly correlated data and low correlated data in out experiments. In *figure 1*, we have presented the compression ratio of the schemes for highly correlated data. Like other dictionary based schemes which usually perform slightly better for greater number of dictionary entries, our proposed scheme and *S-LZW* has been found better forming for *512* dictionary entries than *256* dictionary entries. Since, *PINCO* is not subjected to any dictionary mapping, varying the dictionary doesn't affect overall data compression. Moreover, our scheme and *PINCO* both exploits the correlation feature of data, performance of both the schemes for highly correlated data is better than low correlated data.

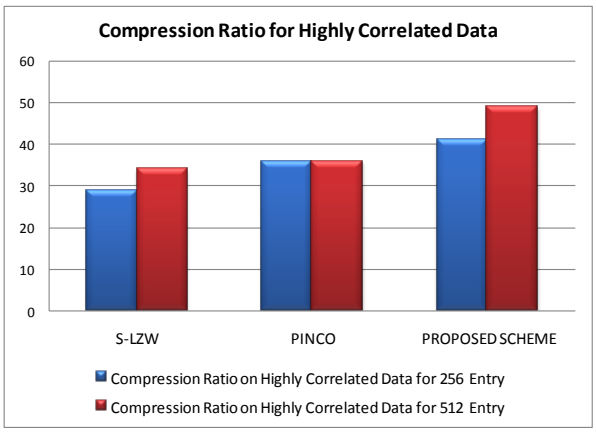

Fig. 1: Compression Ratio for highly correlated data

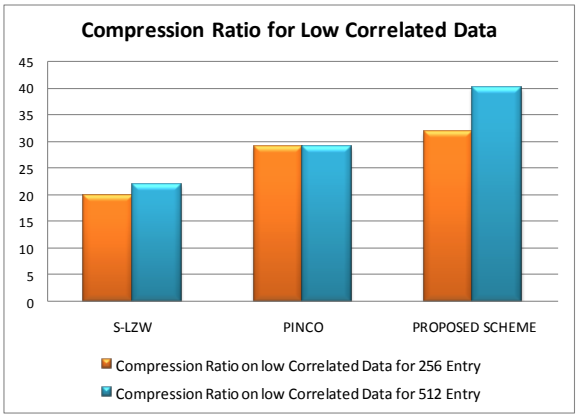

Fig. 2: Compression Ratio for low correlated data

6. CONCLUSION

In this paper, we have presented an overview of the existing researches on Sensor Network data compression approaches. This paper also proposes a compression technique which is also computationally simple and effective. We employ value-couple encoding in order to reduce the overhead of representing individual data. Our proposed scheme ensures balanced energy consumption and thus enhances the network lifetime. Future works may be dedicated to derive a more suitable way to minimizing the data transmissions involved in communicating the initial dictionary among the sensor nodes. Also the parameter of dictionary entry threshold may be standardized.

REFERENCES

[1] Abdul Gani Khan, "A Comparative Analysis: Routing Protocols For Wireless Sensor Networks", *International Journal of Research in IT & Management (IJRIM)*, Volume 2, Issue 2 (February 2012)

[2] I.F. Akyildiz, W. Su, Y. Sankarasubramaniam, E. Cayirci, "Wireless sensor networks: a survey", *Computer Networks 38 (2002) 393–422, ELSEVIER Science*, 2002.

[3] T. Venu Madhav and N V S N Sarma "Energy Efficient Routing Protocol with Improved Clustering Strategies for Homogeneous Wireless Sensor Networks", *International Journal of Computer Applications* (0975 – 8887) Volume 38– No.8, January 2012

[4] A. Bari, A. Jaekel and S. Bandyopadhyay, "Maximizing the Lifetime of Two-Tiered Sensor Networks", In the Proceedings of *IEEE International Electro/Information Technology Conference,* 2006, 222–226.

[5] V.Chandrasekaran, Dr.A.Shanmugam, "A Review On Hierarchical Cluster Based Routing In Wireless Sensor Networks", *Journal of Global Research in Computer Science (JGRCS)*, Volume 3, No. 2, February 2012

[6] Ali Norouzi, Abdul Halim Zaim, "An Integrative Comparison of Energy Efficient Routing Protocols in Wireless Sensor Network", in *Scientific Research, Wireless Sensor Network,* 2012, 4, 65-75

[7] Shabnam Zabihi, Saeed Hadidi, Maedeh Khani, "A New Energy-Efficient Reliable Data Transfer Protocol for Data Transfer in WSN", *Journal of Basic and Applied Scientific Research*, 2(2)1972-1980, 2012.

[8] Mohammad Hossein Anisi, Abdul Hanan Abdullah, Shukor Abd Razak and Md. Asri Ngadi, "An Overview of Data Routing Approaches for Wireless Sensor Networks", in *Sensors*, 2012, 12, 3964-3996;

[9] A. Manjeswar and D.P. Agrawal, "TEEN: A Protocol for Enhanced Efficiency in Wireless Sensor Networks", in the Proceedings of 15th *International Parallel and Distributed Processing Symposium*, 2002, pp. 2009 – 2015.

[10] D. Braginsky, D. Estrin, "Rumor Routing Algorithm for Sensor Networks", in the Proceedings of the *First Workshop on Sensor Networks and Applications (WSNA)*, October 2002, Atlanta, GA, pp. 141-55.

[11] N. Sadagopan *et al.*, "The ACQUIRE mechanism for efficient querying in sensor networks," Proceedings of the First International *Workshop on Sensor Network Protocol and Applications*, Anchorage, Alaska, May 2003, pp. 149 – 155

[12] W. Heinzelman, J. Kulik, and H. Balakrishnan, "Adaptive protocols for information dissemination in wireless sensor networks," Proceedings of the 5th Annual *ACM/IEEE International Conference on Mobile Computing and Networking (MobiCom'99)*, Seattle, WA, August 1999, pp.1-15.

[13] Kui Ren, Wenjing Lou, and Yanchao Zhang, "LEDS: Providing Location-Aware End-to-End Data Security in Wireless Sensor Networks", *IEEE Transactions on Mobile Computing,* vol. 7, no. 5, May 2008.

[14] S. Lindsey, C. Raghavendra,"PEGASIS: Power-Efficient Gathering in Sensor Information Systems," *IEEE Aerospace Conference Proceedings*, 2002, Vol. 3. No. 9-16, pp. 1125 1130.

[15] Intanagonwiwat, C. Govindan R. and Estrin,D. "Directed Diffusion: A Scalable and Robust Communication Paradigm for Sensor Networks". In Proceedings of the *Sixth Annual International Conference on Mobile Computing and Networks (MobiCOM 2000)*, August 2000, Boston, Massachusetts.

[16] Seokhoon Yoon, Abul K. Azad, Hoon Oh and Sunghwan Kim, "AURP: An AUV-Aided Underwater Routing Protocol for Underwater Acoustic Sensor Networks", in *Sensors*, 2012 , 12, 1827-1845.

[17] Nidhi Gautam, Prof Sanjeev Sofat, Prof Renu Vig, "Data Dissemination in Wireless Sensor Networks: A State-of-the Art Survey", *International Journal of Computer Networks (IJCN)*, Volume (4) : Issue (1) : 2012

[18] Mariam Faruque Sharif, Shalim Ahmed, Monjur-E-Mawla, Md.Roknuzzaman, and Kazi Chandrima Rahman, "An Efficient Data Aggregation Protocol Based on Dynamic Routing for Wireless Sensor Network", *International Journal of Computer and Information Technology,* IJCIT, ISSN 2078-5828 (PRINT), ISSN 2218-5224, Volume 02, Issue 02, 2012

[19] Hsing-Shao Liu, Chi-Cheng Chuang, Chih-Chung Lin, Ray-I Chang, Chia-Hui Wang and Ching-Chia Hsieh, "Data Compression for Energy Efficient Communication o n Ubiquitous Sensor Networks", *Tamkang Journal of Science and Engineering*, Vol. 14, No. 3, pp. 245-254 (2011)

[20] Arici, T., Gedik, B., Altunbasak, Y. and Liu, L., "PINCO: A Pipelined In-Network Compression Scheme for Data Collection in Wireless Sensor Networks", Proceedings of 12th *International Conference on Computer Communications and Networks* (2003)

[21] C . M. Sadler and M. Martonosi, "Data compression algorithms for energy-constrained devices in delay tolerant networks," in Proc. of *SenSys'06: 4th International Conference on Embedded networked sensor systems,* 2006, pp. 265–278.

[22] Francesco Marcelloni and Massimo Vecchio, "A Simple Algorithm for Data Compression in Wireless Sensor Networks", *IEEE Communications Letters,* Vol. 12, No. 6, June 2008

[23] S. A. Ahsan Rajon and Md. Mahbubur Rahman "Energy Efficient Routing in Wireless Sensor Network", *International Journal of Computer and*

Information Technology, IJCIT, Volume 03, Issue 01, July 2012, pp. 12—19.

[24] Md. Rafiqul Islam, S. A. Ahsan Rajon, "An Enhanced Scheme for Lossless Compression of Short Text for Resource Constrained Devices", *In the proceedings of 14th International Conference on Computer and Information Technology (ICCIT' 2011)*, December 22-24, 2011, Dhaka, Bangladesh.

[25] Stephan. Rein, F. Fitzek, M. P. G. Perucci, T. Schneider and C. Guhmann, "Low Complex and Power Efficient Text Compressor for Cellular and Sensor Networks", In 15th *IST Mobile and Wireless Communication Summit*, June 2006.

Proceeding of the
International Conference on Electrical, Computer and Telecommunication Engineering
01- 02 December 2012 (ICECTE2012), RUET, Rajshahi-6204, Bangladesh
ICECTE2012: PI-0041

Performance Analysis of LDPC Codes for MIMO 4G Mobile Communication Systems

Md. Masud Rana, Md. Mostafizur Rahman, A N M Enamul Kabir
Dept. of Electronics & Communication Engineering
Khulna University of Engineering & Technology, Khulna-9203
E-mail: mrana928@yahoo.com, mostafiz963@yahoo.com

ABSTRACT
Recently, multiple input multiple output (MIMO) transmission has been well known as one of the most important practical technique to combat fading as well as increase the channel capacity of fourth generation (4G) mobile communication system. There has been active research area on designing efficient channel codes such as turbo codes and low density parity check (LDPC) codes for MIMO fading channels. Specially, LDPC codes have great attracted substantial interests due to their capacity approaching performance and great flexibility in code design with low implementation complexity. LDPC codes are a class of linear block codes with implementable decoders, which provide near capacity performance on a large set of data transmission and data storage channels. In this paper, we have investigated the performance of LDPC codes for MIMO 4G mobile communications systems. Simulation results shows 2x2 MIMO systems provide desired bit error performance in the systems.

KEY WORDS: Channel code, LDPC, MIMO, parity check.

1. INTRODUCTION

In recent times, there has been considerable activity toward the definition of next generation wireless local area networks (WLANs), which are expected to offer high-speed Internet services with data rates exceeding 100 Mb/s and bring WLANs that are on par with wired Ethernet technology. However, the development of high data rate WLAN communication systems must cope with several implementation challenges, such as multipath fading as well as interference with limited transmission bandwidth and power. Now, it has been demonstrated that, for the predefined power and bandwidth, employing multiple transmit and receive antennas in an orthogonal frequency-division multiplexing (OFDM) system can considerably increase the spectral efficiency and the reliability of wireless transmissions over frequency-selective channels while minimizing equalization and symbol decoding complexity [1].

Wireless technology has enormous potential to change the way people and things communicate. Wireless broadband access networks allow people and devices to have high speed connections to the backbone network from any place at any time. To minimize the bit error rate (BER), error correcting codes (ECCs) can play an important role for four generation (4G) mobile communication systems. The ECC is one of many tools made available for achieving consistent data transmission with lower BER. An ECC encoder generates redundant information according to the message information. The message and redundant information are transmitted when they may be corrupted. The decoder the exploits the redundancy in the received and garbled data and determines the original message information being send.

There are two types of ECCs such as a convolution codes and block code. Both types of codes have been widely used for error control in communication systems. Block codes can be divided into two categories, linear and nonlinear block codes. Nonlinear block codes are never used in practical applications and not much investigated [2]. A code is said to be linear if any code words in the code can be added in modulo-2 arithmetic to produce a third code word in the code. The low density parity check codes (LDPCs) are linear block code that has been studied vastly in this decade. The main advantage of these codes is that they provide the performance at that very close to the capacity for a lot of different channels and linear time complex algorithms for decoding [1].

LDPC codes were invented in 1962 by Robert Gallager [3-5]. After the introduction of turbo codes, it was rediscovered by Mackay and Neal [6], [7] and Wiberg [8] in the late 90's. Gallager considered only regular LDPC codes. Regular codes are those which are represented by a sparse parity check matrix with a constant number of 'ones' in each column and in each row. In irregular LDPC codes, both weights become variable and performance of LDPC [9], [10].

The utilize of multiple antennas at the transmitter and/or receiver provides a much higher channel capacity compared to that of single antenna counterparts over wireless channels. With the current developments in iterative decoding, a number of pragmatic approaches using powerful turbo like codes such LDPC codes, repeat accumulate (RA)

codes, or turbo codes themselves have been proposed to achieve a close capacity performance under a bit interleaved coded modulation (BICM) framework. For instance, by directly transmitting signals that are coded with an outer turbo code, it was shown in that a near capacity performance can be attained in a symmetric antenna setup where the number of receive antennas equals the number of transmit antennas. However, the error performance of such turbo coded systems experiences a severe degradation when the antenna scenario is asymmetric, i.e., the number of receive antennas is smaller than the number of transmit antennas. The LDPC coded modulation scheme that performs very close to the capacity limit, even when the antenna setup is asymmetric [11]. Improvements made at the physical (PHY) layer of 4g mobile communications systems, such as the use of multiple-input multiple-output (MIMO) antennas, are capable of greatly increasing their spectral efficiency.

In radio, multiple MIMO is the use of multiple antennas at both the transmitter and receiver to improve communication performance. It is one of several forms of smart antenna technology. MIMO technology has attracted attention in wireless communications, because it offers significant increases in data throughput and link range without additional bandwidth or transmit power. It achieves this by higher spectral efficiency and link reliability or diversity (reduced fading). Because of these properties, MIMO is an important part of modern wireless communication systems.

In this paper, an overview LDPC code is presented for MIMO 4G mobile communication system. Simulation results show that 2 by 2 MIMO systems provide desired bit error performance in wireless communication systems.

The remainder of the paper is organized as follows: section II describes regular and irregular LDPC code. The communication system model is in section III. The simulation results are in section IV. The application of LDPC code in long term evolution (LTE) system in section V. Finally, some concluding remarks are given in section VI.

2. REGULAR AND IRREGULAR LDPC CODE

A regular LDPC code is a linear block code whose parity check matrix H has column weight g and row weight r, where r = g(n/m) and g<<m. If H is low density, but its row column weight are not both constant, then the code is an irregular LDPC code. For regular codes, the corresponding H matrix has β_r ones in each row and β_c one in each column. It means that every codeword bit participates in exactly β_c parity-check equations and that every such check equation involves exactly β_r codeword bits. LDPC codes have been constructed mostly using regular random bipartite graphs. A graph whose nodes may be separated into two types, with edges connecting only nodes of different types is called bipartite graph. The two types of nodes in a bipartite graph are the variable nodes (VN) and check nodes (CN). The bipartite graph of a code is drawn as follows: CN i is connected to VN j whenever element h_{ij} in H is a 1. Observe from this rule that there are m CNs in a bipartite graph, one for each check equation, and n VNs, one for each code bit. Further, the m rows of H specify the m CN connections, and the n columns of H specify the n VN connections [2].

The bipartite graph of a LDPC code acts as s blueprint for the iterative decoder in the following way. Each of the nodes acts as a locally operating processor and each edge acts as a bus that conveyed information from a given node to each of its neighbors. The information conveyed is typically probabilistic information, pertaining to the values of the bits assigned to the variable nodes. At the beginning of each half-iteration in the basic iterative decoding algorithm, each VN processor takes input from the channel and each of its neighboring CVs, and from these computes outputs for each one of its neighboring CN processors. In the next half-iteration, each CN processor takes input from each of its neighboring VNs, and from these computes outputs for each one of its neighboring VN processors. Here is an example of a regular parity check matrix with $\beta_c = 6$ and $\beta_r = 3$. The bipartite graph corresponding to this parity check matrix is shown in Fig. 1.

$$\mathbf{H} = \begin{bmatrix} 1&1&1&0&0&1&1&0&0&0&1&0 \\ 1&1&1&1&1&0&0&0&0&0&0&1 \\ 0&0&0&0&0&1&1&1&0&1&1&1 \\ 1&0&0&1&0&0&0&1&1&1&0&1 \\ 0&1&0&1&1&0&1&1&1&0&0&0 \\ 0&0&1&0&1&1&0&0&1&1&1&0 \end{bmatrix}$$

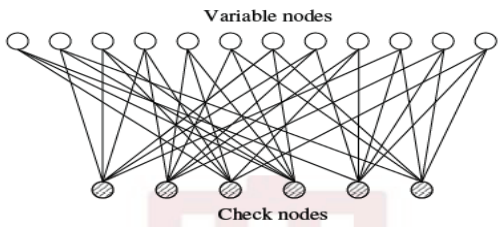

Fig. 1: Bipartite graph corresponding to a regular parity check matrix.

Here is an example of a regular parity check matrix with $\beta_c = 6$ and $\beta_r = 3$.

$$\mathbf{H} = \begin{bmatrix} 1&0&1&0&0&1&1&0&0&0&1&0 \\ 1&1&0&1&1&0&0&0&0&0&0&1 \\ 0&0&0&0&0&1&1&1&0&1&1&1 \\ 1&0&0&1&0&0&0&1&1&1&0&1 \\ 0&1&0&1&1&0&1&1&1&0&0&0 \\ 0&0&1&0&1&1&0&0&1&1&1&0 \end{bmatrix}$$

The bipartite graph corresponding to this parity check matrix is shown in Fig. 2.

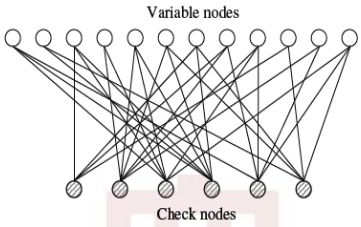

Fig. 2: Bipartite graph corresponding to an irregular parity check matrix

3. COMMUNICATION SYSTEMS MODEL

Digital communication systems are ubiquitous in our daily lives. The most obvious examples include cell phones, digital television via satellite or cable, digital radio, wireless internet connections via wireless fidelity (Wi-Fi) and worldwide interoperability for microwave access (WiMAX), and wired internet connection via cable modem. Additional examples include digital data storage devices, including magnetic disk drives, magnetic tape drives, optical disk drives, and flash drives. In the case of data-storage, information is communicated from one point in time to another rather than one point in space to another. A simplified block diagram for the communication system with channel coder is shown in Fig. 3.

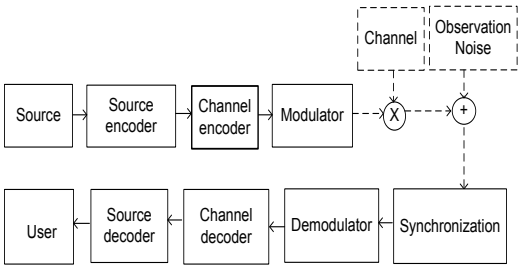

Fig. 3: Block diagram of digital communication system

The information source may be originally in analog form and then later digitized, or it may be originally in digital form. The encoder is a processor that converts the information source bit sequence into an alternative bit sequence with a more efficient representation of the information, i.e., with fewer bits. Hence, this operation is often called compression. Depending on the source, the compression can be lossless or lossy. The role of the channel encoder is to protect the bits to be transmitted over a channel subject to noise, distortion, and interference. It does so by converting its input into an alternate sequence possessing redundancy, whose role is to provide immunity from the various channel impairments. The ratio of the number of bits that enter the channel encoder to the number that depart from it is called the code rate. The modulator converts the channel encoder output bit stream into a form that is appropriate for the channel. The channel is the physical medium through which the modulator output is conveyed. Physically, the channel can include antennas, amplifiers, and filters, both at the transmitter and at the receiver at the ends of the systems [2].

The demodulation is the modulator's counterpart which recovers the modulator input sequence from the modulator output sequence. The main function of the channel encoder in spite of the presence of noise, distortion, and interference in received word. The source decoder is the encoder`s counterpart which recovers the source sequence exactly, in the case of lossless compression, or approximately, in the case of lossy compression, from the encoder`s output sequence [2].

In MIMO systems, multiple antennas are used at the transmitting end as well as at the receiving end. These systems have emerged as a most promising technology in the measures of higher data rates, better quality of service (QoS), and higher network capacity. Multiplicative increase in capacity, spectral efficiency, dramatic reductions of fading, increased system capacity (number of users), and improved resistance to interference.

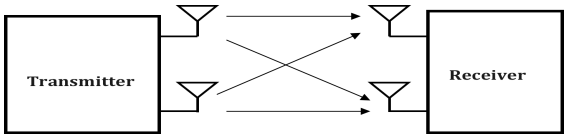

Fig. 4: MIMO communication systems

4. SIMULATION RESULTS

LDPCs are codes specified by a matrix containing mostly 0's and relatively few 1's. The implementation of LDPC decoders tends to be complex and solutions for less complex decoders are a focal point of research. Stochastic computation was introduced in the 1960's as a method to design low precision digital circuits. This method has been used for iterative decoding of some specific error-correcting codes. The main advantage of this method is that probabilities can be manipulated using very simple circuits [12]. The performance of the aforementioned is explored by performing extensive computer simulations. We used BPSK modulation, flat fading channel, and zero forcing (ZF) spatial decoding for our simulation. In addition in simulations, the receiver is assumed to know the channel exactly and employ an iterative detection and decoding algorithm. From the simulation result, it is apparent that 2x2 MIMO systems provide desired bit error performance in wireless communication systems.

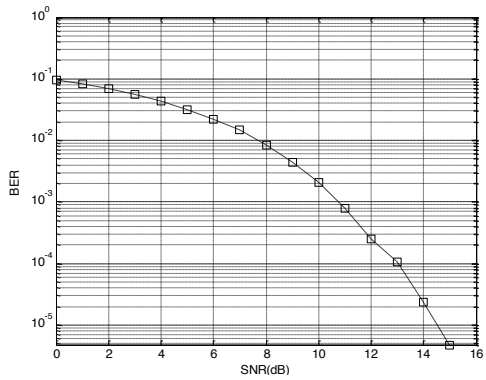

Fig.5: 2x2 MIMO Gaussian channel with BPSK modulation

5. APPLICATION OF LDPC CODE IN LTE SYSTEMS

The further increasing demand on high data rates in wireless communication systems has arisen in order to support broadband services. The third generation partnership project (3GPP) LTE members started feasibility study on the enhancement of the UTRA in December 2004, to improve the mobile phone standard to cope with future requirements. The main purposes of the 3GPP LTE are substantially improved end-user throughputs, low latency, reduced user equipment (UE) complexity, high data rate, and significantly improved user experience with full mobility. First 3GPP LTE and LTE-advanced (LTE-A) specification is being finalized within 3GPP release 9 and release 10, respectively [12], [13].

Specifically, the physical layer has become quite stable recently for a first implementation. LTE supports MIMO with 1, 2, 4, and 8 antenna elements at base station (BS) and mobile terminal. Both closed and open loop MIMO operation is possible. The target of 3GPP LTE-A is to reach and surpass the ITU requirements. One of the important LTE-A benefits is the ability to leverage advanced topology networks; optimized heterogeneous networks with a mix of macros with low power nodes such as picocells, femtocells, ensures user fairness, worldwide roaming, and new relay nodes.

LTE uses orthogonal frequency division multiple access (OFDMA) for downlink and single carrier-frequency division multiple access (SC-FDMA) for uplink transmission [1]. A highly efficient way to cope with the frequency selectivity of wideband channel is OFDMA. Turbo code is used in OFDMA systems as a tool for channel coding. But turbo coding suffers from the high decoding complexity as well as relatively high latency which make them unsuitable for some applications.

6. CONCLUSIONS

LDPC codes have great attracted substantial interests due to their capacity approaching performance and great flexibility in code design with low implementation complexity. LDPC codes are a class of linear block codes with implementable decoders, which provide near-capacity performance on a large set of data transmission and data-storage channels. In this paper, we have investigated the application of LDPC codes to MIMO channels. Simulation results shows 2x2 MIMO systems provide desired bit error performance in wireless communication system.

REFERENCES

[1] Y. Xin, S. A. Mujtaba, T. Zhang, and J. Jiang "Bypass decoding: a reduced-complexity decoding technique for LDPC-coded MIMO-OFDM systems" *IEEE Trans. On Vehicular Technology*, vol.57,no.4, pp. 2319-2333,2008.

[2] W.E. Ryan, S. Lin, "Channel codes classical and modern," *Cambridge Uni Press*, 2009.

[3] C. Prasartkaew, S. Choomchuay, "A parity check matrix design for irregular LDPC codes with 2K block length," *in Proc. International Symposium on Intelligent Signal Processing and Communication Systems*, Dec. 7-9, 2009.

[4] R. G. Gallager, "Low density parity check codes," *IRE transactions on Inform. Theory*, January 1962.

[5] R. G. Gallager, "Low density parity check codes," *Cambridge, MIT Press*, 1963.

[6] D. J. C. Mackay and R. M. Neal, "Near Shannon limit performance of low density parity check codes," *IEE Electron Letter*, vol. 32, no. 18, pp. 1645-1646, Aug. 1996.

[7] D. J. C. Mackay, "Good error-correcting codes based on very sparse matrices," *IEEE Trans. Inform. Theory*, vol. IT-45, no. 2, pp. 399-431, Mar. 1999.

[8] N. Wiberg, "Codes and decoding on general graphs," *Linkoeping studies in science and technology*, No. 440, 1996.

[9] T. J. Richardson, A. Shokrollahi, and R. Urbanke, "Design of capacity approaching low-density parity-check codes," *IEEE Trans. Inform. Theory*, vol.47, pp.619-637, 2001.

[10] M. Rakibul, J. Kim, "On the use of QC-LDPC code for data transfer using short and medium block length,"*Proc. ICACT*, Feb. 15-18, 2009.

[11] N. H. Tran, *T*. L. Ngoc, T. Matsumoto, and H. H. Nguyen, "Achieving near-capacity performance on multiple-antenna channels with a simple concatenation scheme, "*IEEE Trans. on Wireless Comm*., vol. 58, no. 4, pp. 1048-1059, April 2010.

[12]. M. Rakibul, J. Kim, "Capacity and BER analysis for Nakagami-n channel in LDPC coded wireless sensor network, "*Int. Conference on Intelligent Sensors, Sensor Networks and Information Processing*, Australia ,15-18 Dec., 2008.

[13] Q. Li, G. Li, W. Lee, M. il Lee, D. Mazzarese, B. Clerckx, and Z. Li, "MIMO techniques in WiMAX and LTE: a feature overview," *IEEE Commun. Magazine*, vol. 48, no. 5, pp. 86–92, May. 2010.

Proceeding of the
International Conference on Electrical, Computer and Telecommunication Engineering
01- 02 December 2012 (ICECTE2012), RUET, Rajshahi-6204, Bangladesh

ICECTE2012: PI-0043

SAR Calculation of Realistic Human Head for Electromagnetic Radiation Exposure from GSM-900MHz Cellular Phones Using FDTD Method

Abdul Khaleque[1], Mohammad Hasan Majumdar[2] and G.K.M. Hassanuzzaman[3]
[1, 2 &3]Department of Electrical and Electronic Engineering,
Rajshahi University of Engineering & Technology, Rajshahi-6204, Bangladesh.
E-mail: khaleque_eee@yahoo.com, hasan.majumdar@yahoo.com, g.kibria82yahoo.com

ABSTRACT
This paper presents a numerical finite difference time domain (FDTD) analysis of the electromagnetic field (EMF) penetration in structures that represent estimation of human head anatomical tissues, in specific conditions associated to mobile phone technology. Specific absorption rate (SAR) calculations have been carried out for some configurations by MATLAB simulation software. A discrete human head model derived from MRI images which is available by a total number of 24 sagital slices. The head model is considered within FDTD volume together with a discrete hand-held receiver cellular model carried out for GSM-900MHz systems with a dipole antenna, mounted on top of the hand-held cellular phone.

Key Words: Finite difference time domain (FDTD), Electromagnetic field (EMF), magnetic resonance image (MRI), specific absorption rate (SAR), MATLAB.

1. INTRODUCTION

In the past few years, very rapid development in mobile cellular communication has drawn attention to possible health risks of the electromagnetic energy (EM) emitted from the transmitters of hand-held phones [1]. Almost 70 to 80 percent of the radiation emitted from a cell phone antenna is absorbed into the head. The interaction between a human head and a hand-held phone under various conditions should be quantitatively evaluated in order to establish the safety in cellular mobile communication systems. Electromagnetic radiation/scattering problems may be modeled as initial or boundary value problem governed by partial differential equations subject to properly defined initial and/or boundary values [2]. The direct analytical solution of the problem is usually impossible. Several approximate solution techniques have been developed so far, the most important ones being FDTD method, which was introduced by K. S. Yee [3] in 1966. It has been intensively studied and widely used because of its simplicity and flexibility for various different applications. In this paper, SAR calculation has been carried out for a realistic human head. 3D FDTD MATLAB code has also been built including a Mur's boundary condition mesh truncation and human head model. The tissue distribution in a human head is extensively studied to model the object successfully.

The paper is organized in the following way: At first, the 3-D Maxwell's equations are presented in discrete form by FDTD method. Boundary conditions are then applied on it and MRI images of a human head with a cellular phone are modeled in FDTD mesh. Finally, simulation results based on FDTD method are discussed.

2. SIMULATION METHOD

FDTD method solves Maxwell's curl equation directly in time domain are [5]:

$$\nabla \times E = -\mu \frac{dH}{dt} \tag{1}$$

$$\nabla \times H = \sigma E + \epsilon \frac{dE}{dt} \tag{2}$$

Using central finite difference approximation for space and time derivatives for a uniformly spaced rectangular grid in three-dimensions, these equations are given by [6]:

$$\begin{aligned} H_x^{n+\frac{1}{2}}\left(i,j+\frac{1}{2},k+\frac{1}{2}\right) = {} & H_x^{n-\frac{1}{2}}\left(i,j+\frac{1}{2},k+\frac{1}{2}\right) \\ & + \frac{\Delta t}{\mu \Delta z}\left[\begin{array}{l} E_y^n\left(i,j+\frac{1}{2},k+1\right) \\ -E_y^n\left(i,j+\frac{1}{2},k\right) \end{array}\right] \\ & - \frac{\Delta t}{\mu \Delta y}\left[\begin{array}{l} E_z^n\left(i,j+1,k+\frac{1}{2}\right) \\ +E_z^n\left(i,j,k+\frac{1}{2}\right) \end{array}\right] \end{aligned} \tag{3}$$

$$\begin{aligned} H_y^{n+\frac{1}{2}}\left(i+\frac{1}{2},j,k+\frac{1}{2}\right) = {} & H_y^{n-\frac{1}{2}}\left(i+\frac{1}{2},j,k+\frac{1}{2}\right) \\ & + \frac{\Delta t}{\mu \Delta x}\left[\begin{array}{l} E_x^n\left(i+1,j,k+\frac{1}{2}\right) \\ -E_z^n\left(i,j,k+\frac{1}{2}\right) \end{array}\right] \\ & - \frac{\Delta t}{\mu \Delta z}\left[\begin{array}{l} E_x^n\left(i+\frac{1}{2},j,k+1\right) \\ +E_x^n\left(i+\frac{1}{2},j,k\right) \end{array}\right] \end{aligned} \tag{4}$$

$$H_z^{n+\frac{1}{2}}\left(i+\frac{1}{2},j+\frac{1}{2},k\right) = H_z^{n-\frac{1}{2}}\left(i+\frac{1}{2},j+\frac{1}{2},k\right) + \frac{\Delta t}{\mu\Delta y}\begin{bmatrix} E_x^n\left(i+\frac{1}{2},j+1,k\right) \\ -E_x^n\left(i+\frac{1}{2},j,k\right)\end{bmatrix} - \frac{\Delta t}{\mu\Delta x}\begin{bmatrix} E_y^n\left(i+1,j+\frac{1}{2},k\right) \\ +E_z^n\left(i,j+\frac{1}{2},k\right)\end{bmatrix} \quad (5)$$

$$E_x^{n+1}\left(i+\frac{1}{2},j,k\right) = \left(\frac{1-\frac{\sigma\Delta t}{2\epsilon}}{1+\frac{\sigma\Delta t}{2\epsilon}}\right)E_x^n\left(i+\frac{1}{2},j,k\right) + \frac{\frac{\Delta t}{\epsilon\Delta y}}{1+\frac{\sigma\Delta t}{2\epsilon}}\begin{bmatrix} H_z^{n+\frac{1}{2}}\left(i+\frac{1}{2},j+\frac{1}{2},k\right) \\ -H_z^{n+\frac{1}{2}}\left(i+\frac{1}{2},j-\frac{1}{2},k\right)\end{bmatrix} - \frac{\frac{\Delta t}{\epsilon\Delta z}}{1+\frac{\sigma\Delta t}{2\epsilon}}\begin{bmatrix} H_y^{n+\frac{1}{2}}\left(i+\frac{1}{2},j,k+\frac{1}{2}\right) \\ +H_y^{n+\frac{1}{2}}\left(i+\frac{1}{2},j,k-\frac{1}{2}\right)\end{bmatrix} \quad (6)$$

$$E_y^{n+1}\left(i,j+\frac{1}{2},k\right) = \left(\frac{1-\frac{\sigma\Delta t}{2\epsilon}}{1+\frac{\sigma\Delta t}{2\epsilon}}\right)E_y^n\left(i,j+\frac{1}{2},k\right) + \frac{\frac{\Delta t}{\epsilon\Delta z}}{1+\frac{\sigma\Delta t}{2\epsilon}}\begin{bmatrix} H_x^{n+\frac{1}{2}}\left(i,j+\frac{1}{2},k+\frac{1}{2}\right) \\ -H_x^{n+\frac{1}{2}}\left(i,j+\frac{1}{2},k-\frac{1}{2}\right)\end{bmatrix} - \frac{\frac{\Delta t}{\epsilon\Delta x}}{1+\frac{\sigma\Delta t}{2\epsilon}}\begin{bmatrix} H_z^{n+\frac{1}{2}}\left(i+\frac{1}{2},j+\frac{1}{2},k\right) \\ +H_z^{n+\frac{1}{2}}\left(i-\frac{1}{2},j+\frac{1}{2},k\right)\end{bmatrix} \quad (7)$$

$$E_z^{n+1}\left(i,j,k+\frac{1}{2}\right) = \left(\frac{1-\frac{\sigma\Delta t}{2\epsilon}}{1+\frac{\sigma\Delta t}{2\epsilon}}\right)E_z^n\left(i,j,k+\frac{1}{2}\right) + \frac{\frac{\Delta t}{\epsilon\Delta x}}{1+\frac{\sigma\Delta t}{2\epsilon}}\begin{bmatrix} H_y^{n+\frac{1}{2}}\left(i+\frac{1}{2},j,k+\frac{1}{2}\right) \\ -H_y^{n+\frac{1}{2}}\left(i-\frac{1}{2},j,k+\frac{1}{2}\right)\end{bmatrix} - \frac{\frac{\Delta t}{\epsilon\Delta y}}{1+\frac{\sigma\Delta t}{2\epsilon}}\begin{bmatrix} H_x^{n+\frac{1}{2}}\left(i,j+\frac{1}{2},k+\frac{1}{2}\right) \\ +H_x^{n+\frac{1}{2}}\left(i,j-\frac{1}{2},k+\frac{1}{2}\right)\end{bmatrix} \quad (8)$$

Since information out of the computational domain is not available at the boundary of FDTD cells, the fields are updated using boundary conditions. In the present paper, the first order MUR absorbing boundary conditions (ABC) is used to perform simulation [4].

3. SAR CALCULATION

It is a complex measurement of how much radiation passes through tissue during a specified time period. From the converged solutions the local SAR at $(i,j,k)^{th}$ cell inside the head is obtained from the following relation [7]:

$$SAR(i,j,k) = \frac{\sigma(i,j,k)|\hat{E}(i,j,k)|^2}{2\rho(i,j,k)} \quad (9)$$

$$= \frac{\sigma(i,j,k)\left\{\left|\hat{E}_x(i,j,k)\right|^2 + \left|\hat{E}_y(i,j,k)\right|^2 + \left|\hat{E}_z(i,j,k)\right|^2\right\}}{2\rho(i,j,k)}\text{W/kg}$$

4. HUMAN HEAD MODEL

MRI images of a adult male head are used to model the FDTD mesh. The dimensions of the head are 218.10 mm (about 29 cells) in x -direction, 156.96 mm (24 cells) in y -direction and 204.41 mm (30 cells) in z-direction. The MRI images are available slice by slice, from which the geometry, as well as the tissue type are deduced. Typical dimensions of the FDTD volume is taken as Nx= 125, Ny= 100, Nz= 100 with a total of 1,25,0000 cubic cells. The cell sizes are chosen to be Δx= 0.7520cm, Δy= 0.653cm, Δz = 0.6813cm, which means that a cubic volume of 0.7520cm×0.653cm×0.6813cm is allocated for FDTD calculations where human head is located.

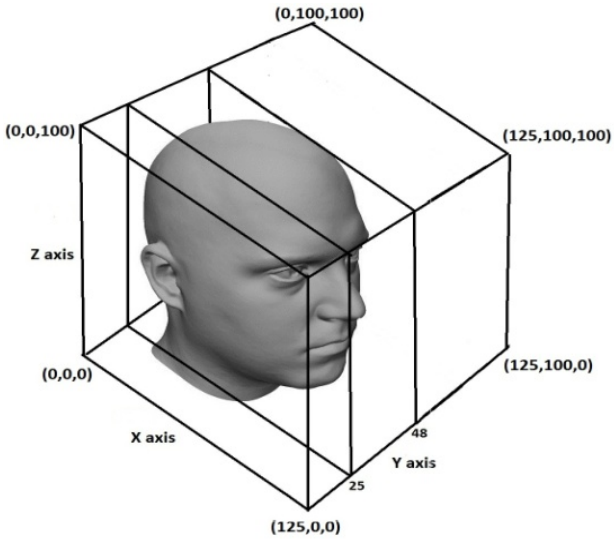

Fig. 1: 3-D geometry view of human head model

The human head model is located 36 cells away from x = 0, 24 cells away from y = 0 and 25 cells away from z = 0 planes.

Table 1: Tissue Parameters for 900 MHz [8]

Tissues	Mass Density ρ (kg/m^3)	Dielectric Constant (ε_r)	Conductivity σ (S/m)
Skin	1100	41.40	0.86
Brain	1850	16.62	0.24
Bone	1030	45.80	0.76
Michele	1040	56.87	0.99
Cerebellum	1030	57.59	1.002
Eye Humor	1010	68.63	2.41
Tongue	1040	58.2090	0.7590
Retina	1020	58.2090	0.9899
Teeth	1850	13.2770	0.0869
Spinal Cord	1040	36.065	0.4320

Above **Table 1** shows the used mass density (ρ), mass of one cell, relative dielectric constant (ε_r) and conductivity (σ) of different tissues**.**

5. CELLULAR PHONE MODEL

In this work, a cellular phone model (Fig. 2) with dimensions 3.76 cm. in *x* direction, 1.30 cm. in *y* direction and 8.272 cm. in *z* direction is used. The phone of (5×2×11) cells and a Hertzian Dipole antenna with length 3.4065 cm. (5 cells) are also considered. The antenna is placed 1 cell away from the phone in z direction. The cellular phone is made of glass, plastic and aluminum and the antenna is made of aluminum. In real case, for normal use value of radiated power from cellular phone is 250 mW but it can reach to 1 W or 2 W when the phone is far away from the mobile base station.

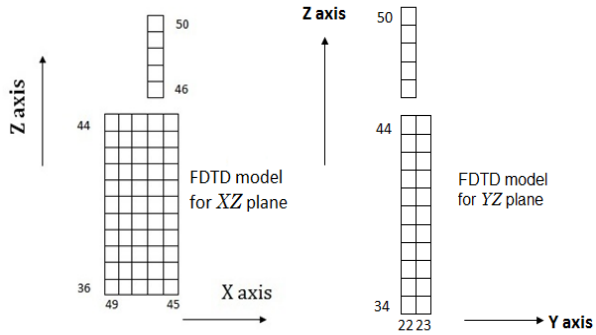

Fig. 2: FDTD phone model

6. INFINITESIMAL DIPOLE

An infinitesimal dipole ($L \ll \lambda$) is a small element of a linear dipole that is assumed to be short enough that the current (*I*) can be assumed to be constant along its length *L*. The electric and magnetic field components of this dipole are [5].

$$H = \frac{1}{4\pi} IL \sin\theta e^{-j\beta_0 r}\left(\frac{j\beta_0}{r} + \frac{1}{r^2}\right)\phi \quad (10)$$

$$E = \frac{j\eta_0 IL}{2\pi\beta_0}\cos\theta\left(\frac{j\beta_0}{r^2} + \frac{1}{r^3}\right)e^{-j\beta_0 r} r - \frac{j\eta_0 IL}{4\pi\beta_0}\sin\theta\left(-\frac{\beta_0^2}{r} + \frac{j\beta_0}{r^2} + \frac{1}{r^3}\right)e^{-j\beta_0 r}\theta \quad (11)$$

where $\eta_0 = \left(\frac{\mu_0}{\varepsilon_0}\right)^{1/2}$ is the intrinsic impedance for free space, and $\beta_0 = \omega(\mu_0\varepsilon_0)^{1/2}$ is the propagation constant.

7. RESULTS

Numerical results of the mobile phone-human head interaction for some configuration are shown below. The distance between the vertically placed mobile phone and the head is chosen zero and mobile phone is placed right side of the head.

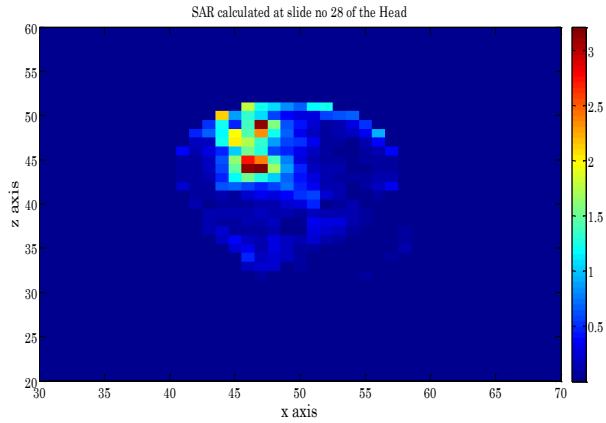

Fig. 3: SAR value distribution at y=28 plane

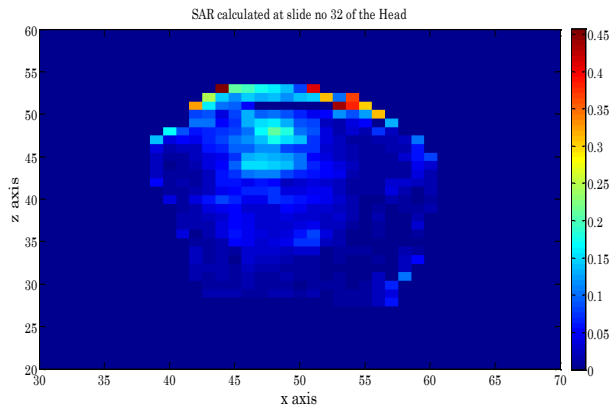

Fig. 4: SAR value distribution at y=32 plane

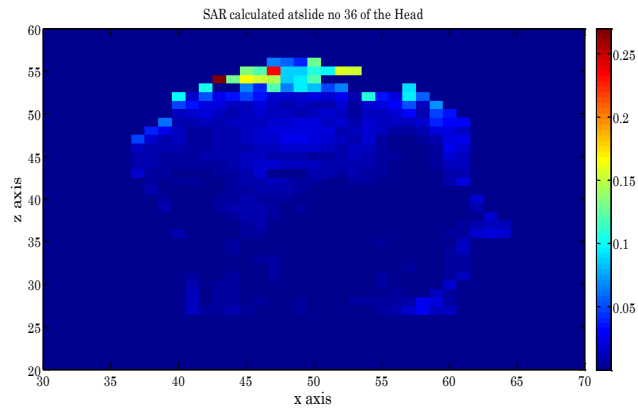

Fig. 5: SAR value distribution at y=36 plane

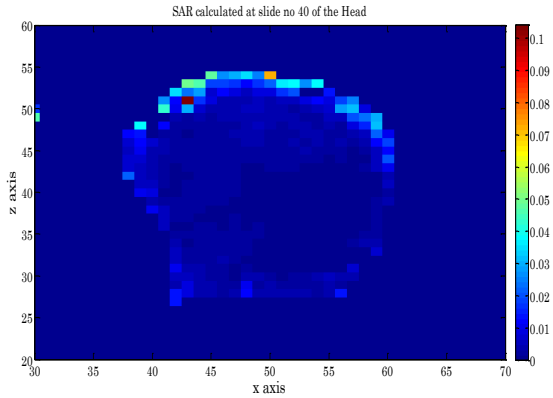

Fig. 6: SAR value distribution at y=40 plane

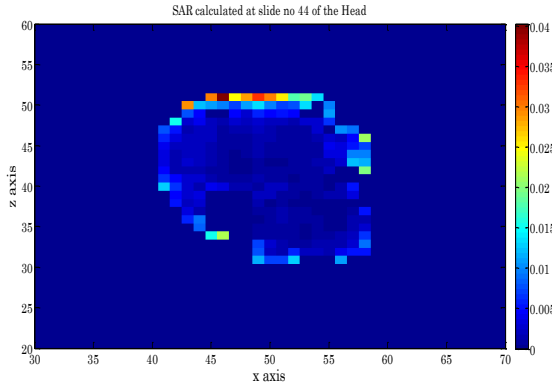

Fig 7: SAR value distribution at y=44 plane

Figs 3~7 show the SAR value distribution within the human head at y= 28, y=32, y=36, y=40 planes, respectively. A color bar is located right side of each fig. indicates the SAR value.

Fig. 3 shows the maximum SAR value (3 W/kg) but Fig. 4 represents the maximum SAR value is 0.45 W/kg. Figs. 5~7 also show the maximum SAR values are 0.25 W/kg, 0.1 W/kg and 0.04 W/kg, respectively.

8. CONCLUSIONS

In this paper, antenna feed models and phone model are developed and then combined to calculate specific absorption rate (SAR) in a realistic human head by FDTD approach which is a valuable tool in the simulation studies related to the interaction of electromagnetic waves with human tissue. 3D-MATLAB codes are developed to simulate the FDTD spatio-temporal difference equations. For safe communication purposes, the SAR number of a phone must meet the FCC established standard of 1.6 watts/kg or below. The results show the SAR value distribution within realistic human head which are within the FCC established standard except for 28 plane. Covering large areas of the phone with hand reduces its ability to send and receive signals. The phone then increases its power and transmits stronger radiation to compensate this. So hold phone as far as possible, so it can operate at low power. When reception is good the phone reduces power and radiation. If reception is poor, the phone uses maximum power and radiation.

9. FUTURE WORK

In this present thesis, Mur's 1st order boundary equation is used for FDTD code simulation. Mur's 2nd order boundary equation or perfectly matched layer (PML) boundary condition may be used in future work. The mobile phone is located vertically with respect to the head. But in actual practice mobile phone is located 15^0 or 20^0 with respect to the head. It can be done by rotating and then modeling the human head. A GSM-1800 MHz cellular phone can be used in future.

REFERENCES

[1] Chiang et al, "Health Effects of Environmental Electromagnetic Fields", Journal of Bioelectricity, Vol.8 No.1, pp.127-131, 1989.

[2] Stephen D. Gedney, "Introduction to the Finite-difference time-domain (FDTD) Method for electromagnetic", Morgan Claypool. January 2011.

[3] K.S. Yee, "Numerical Solution of Initial Boundary Value Problems Involving Maxwell's Equations in Isotropic Media", IEEE Transaction on Antennas Propagation, Vol. 14, No. 3, pp. 302,307, 1966.

[4] G Mur, "Absorbing boundary condition for the finite difference approximation of the time domain electromagnetic field equation", IEEE Transaction Electromagnetic compatibility, EMC-23pp.377-382, November 1981.

[5] D. K. Cheng, "Field and Wave Electromagnetic", Menlo Park, CA: Addison-Wesley, 1992.

[6] Dennis M. Sullivan, "Electromagnetic Simulation Using the FDTD Method", IEEE Press Series on RF and Microwave Technology. Roger D. Pollard and Richard Booton Series Editors, First Edition, July, 2000.

[7] O. P. Gandhi, Gianluca Lazzi and Cynthia M. Furse, "Electromagnetic Absorption in the Human Head and Neck for Mobile Telephones at 835 and 1900 MHz", IEEE Transaction Microwave Theory Tech., vol. MTT – 44. No.10, pp.1884-1897, October-1996.

[8] Dielectric Properties of the Human Body tissue in the Frequency Range of 10 Hz-100GHz. http://niremf.iroe.fi.cnr.it/tissprop.

Proceeding of the
International Conference on Electrical, Computer and Telecommunication Engineering
01- 02 December 2012 (ICECTE2012), RUET, Rajshahi-6204, Bangladesh

ICECTE2012: PI-0044

Performance Analysis of UMTS Cellular Network using Sectorization Based on Capacity and Coverage in Different Propagation Environment.

Jannat-E-Noor[1], Soyoda Marufa Farhana[2], Md. Shahidul Islam[3]
[1,2]Department of Electrical and Electronic Engineering, Rajshahi University of Engineering & Technology
[3]Assistant Professor, Department of Electrical and Electronic Engineering, Rajshahi University of Engineering & Technology
E-mail: farah1809@yahoo.com[1],liza.eeeruet@gmail.com[2],siruet@gmail.com[3]

ABSTRACT
PERFOMNCE ANALYSIS OF UMTS NETWORK IS OF MAJOR INTEREST, BECAUSE OF THE WCDMA TECHNIQUE USED IN UMTS, WHICH LEADS TO AN INTERFERENCE LIMITED SYSTEM WITH A DYNAMIC CELL CAPACITY AND LOAD DEPENDENT CELL COVERAGE. THE PERFORMANCE OF UMTS NETWORK DEPENDS ON SECTORIZATION; ALSO, THE COVERAGE AREA DEPENDS SIGNIFICANTLY ON THE GEOGRAFICAL NATURE AND THE PROPAGATOIN ENVIRONMENT OF THE COVERED AREA. IN THIS PAPER, THE CAPACITY AND COVERAGE OF UMTS CELLULAR NETWORK COVERING A DENSED URBAN AREA AND SUBURBAN AREA ARE SIMULATED FOR INCRISING AMOUNT OF SECTORIZATION SHOWING THE NUMBER OF USERS AND COVERAGE AREA GRADUALLY INCREASED. FOR MODELLING THE PROPAGATOIN, THE COST-231 HATA MODEL HAS BEEN USED.

KEY WORDS: UMTS, Coverage, Propagation Model, WCDMA, sectorization.

1. INTRODUCTION

Universal Mobile Telecommunications System (UMTS) is one of the standards in 3rd generation partnership project (3GPP). This thesis presents the performance of UMTS cellular network using sectorization for capacity and coverage. The major contribution is to see the impact of sectorization on capacity and cell coverage with independent dynamic parameters as energy per bit to noise spectral density ratio, soft handover factor, voice activity factor, intercell or outercell interference factor, data rates.

Bo Hagerman, Davide Imbeni and Jozsef Barta considered WCDMA 6-sector deployment case study of a real installed UMTS-FDD network [1]. Romeo Giuliano, Franco Mazzenga, Francesco Vatalaro described Adaptive Cell Sectorization for UMTS Third Generation CDMA Systems [2]. Achim Wacker, Jaana Laiho-Steffens, Kari Sipila, and Kari Heiska considered the impact of the base station sectorization on WCDMA radio network performance [3]. S. Sharma, A.G. Spilling and A.R. Nix considered Adaptive Coverage for UMTS Macro cells based on Situation Awareness [4]. A.K.M Fazlul Haque, Mir Mohammad Abu Kyum, Md. Baitul Al Sadi, Mrinal Kar and Md. Fokhray Hossain considered UMTS coverage and capacity based on sectorization[5]. Most of the works analyzed the performance considering sectors with static parameters but it is needed to analyze the performance along with all dynamic parameters and propagation environment.

This paper focuses on main factors that affect the coverage and capacity in a CDMA cell based on sectorization and on propagation prediction models COST-231 Hata model.

2. CAPACITY AND COVERAGE CALCULATIONS:

The capacity of a CDMA cell depends on many different factors, such as power control accuracy, interference power. In this present study we are considering perfect power control. We begin by calculating the signal-to-noise power [7, 8].

2.1 Initial Model for Capacity Calculation: In order to calculate the maximum number of users in a particular cell the following assumptions are made: No inter-cell and intra-cell interference is present within the cell. All signals arrive at the base station with equal power Un-limited number of spreading codes are available.

If there are N_s users in a cell and the signal is denoted by S then the interference can be calculated as $I = (N_s - 1)S + \eta$, where η is the thermal noise. Hence the *SIR* is given by

$$SNR = \frac{s}{(N_s - 1)s + \eta} = \frac{1}{(N_s - 1) + \eta / S} \quad \ldots (1)$$

Suppose the digital demodulator for each user can operate against the noise at energy per bit-to noise power density level is given by E_b/N_o , where Here $E_b = S / R$ and $N_o = I / W$

$$E_b/N_o = \frac{S/R}{I/W} \quad \ldots\ldots (2)$$

Where, W is the chip rate, R is rate of data communication and I is interference power of the cell.

Hence using equations (1) and (2) gives

$$N_s - 1 = \frac{W/R}{E_b/N_o} - \frac{\eta}{S} \quad \ldots\ldots\ldots\ldots\ldots\ldots\ldots\ldots\ldots\ldots (3)$$

For a uniform population, this reduces the average signal power of all users and consequently the interference received by each user. This results in an increase in the E_b/N_o by a voice activity gain factor, α. Similarly, the cell sectoring factor D also increases the E_b/N_o. Finally, we must evaluate the interference mathematically,

$$\beta = \frac{interference\ from\ other\ cell}{interference\ from\ given\ cell}$$

Due to the interference, the actual numbers of user will decreases. It is also necessary to consider the affects of soft handover factor (H), Array antenna gain (Ag).Thus the capacity for WCDMA in UMTS yields:

$$N_S = 1 + \left(\frac{W/R}{E_b/N_o} - \frac{\eta}{S} \right) \times \frac{D \times H \times A_g}{\alpha(1+\beta)} \quad \ldots\ldots\ldots (4)$$

2.2 Coverage versus Capacity: The analysis in the above the capacity calculation can be isolated from coverage. We can understand the performance of a WCDMA network by developing a simple expression for the ratio S as follows.

$$S = \frac{(E_b/N_o) \times R \times \eta}{W - \frac{(E_b/N_o) R \alpha (N_S - 1)(1+\beta)}{D \times H \times A_g}} \quad \ldots\ldots\ldots (5)$$

We focus on the coverage by user 1 when the number of users in the cell is Ns. Let r be the distance of user 1 from the base station. The received power at the base station from mobile user l, S, is given by, $S = S1 - P(d) - Z$ ……..…… (6)

Where, $S1$ the transmission power of the user, $P(d)$ is the propagation loss at distance d from the MS to BS, Z the shadow fading.

2.3 Coverage Area in different Propagation Environment: The propagation losses in densed urban and suburban areas are usually calculated by using propagation models. In the present study we utilized COST 231-Hata model for urban and dense urban environment. Where higher data rates need higher processing gain resulting in smaller coverage area. But increasing sectors with same parameters makes extensive coverage for higher data rates. The COST-Hata-Model is formulated as,

For densed urban environments the path loss:

$$L = 46.3 + 33.9 \log(f) - 13.82 \log h_b - 3.2 [\log(11.75 h_{UE})]^2 + 4.97 + (44.9 - 6.55 \log h_b) \log d + 3 \quad \ldots\ldots\ldots (7)$$

For suburban or rural environments the path loss:

$$L = 46.3 + 33.9 \log(f) - 13.82 \log h_b - \{(1.1 \log f - 0.7) h_{UE} - (1.6 \log f - 0.8)\} + (44.9 - 6.55 \log h_b) \log d \quad \ldots\ldots\ldots (8)$$

Where d is the coverage radius and R is the data rates. After calculating the cell range d, the coverage area can be calculated. The coverage area for one cell in hexagonal configuration can be estimated with [6]

Coverage area, $A = K.d^2$ …….... (9)

Where A is the coverage area, d is the maximum cell range, and K is a constant. K values for the site area calculation [6]: K=2.6, 1.3, 1.95, 2.6 for sector one, two, three, four respectively.

3. Simulation & Result:

The analysis has been done for capacity and coverage with sectoring cell for dense urban and suburban area using MATLAB R2008a. From this figure 1 it is observed the Number of simultaneous 384 Kbps users vs. E_b/N_o in sectors cell

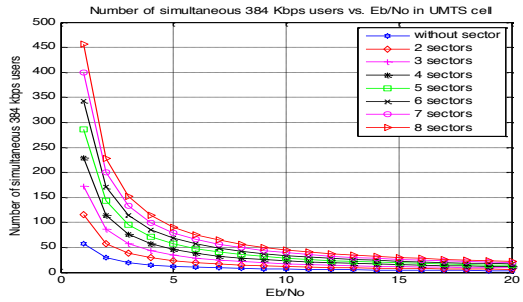

Figure 1: Number of simultaneous 384 Kbps users Vs. E_b/N_o in sectors cell

Table 1: simulated values for Figure 1

E_b/N_o	User With out sector	User with 2 sec-tors	User with 4 Sec-tors	User with 6 Sec-tors	User with 8 Sec-tors
1	58	115	229	343	457
5	12.22	23.44	45.88	68.32	90.76
10	6.5	12	23	34	45
15	4.59	8.179	15.30	22.54	29.72
20	3.636	6.271	11.54	16.81	22.09

The interference from other cell is known as inter-cell interference (β). Figure 2 represents,

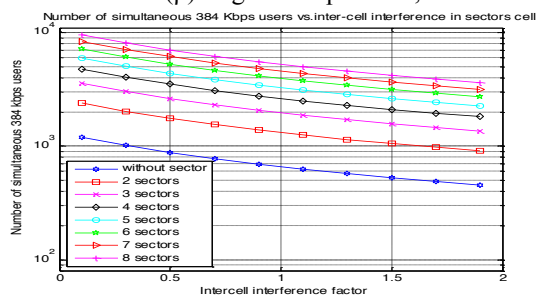

Figure 2: Number of simultaneous 384 Kbps users vs. inter-cell interference in sectors cell

Table 2: simulated values for Figure 2

β	User With out sector	User With 2 sector	User with 4 sector	User with 6 sector	User with 8 Sector
0.1	1195.4	2390	4778.5	7167.3	9556
0.5	876.9	1753	3504.5	5256.3	700.8

1	657.9	1315	2628.6	3942.4	525.6
1.5	526.5	1052	2103.1	3154.2	420.5
2	438.9	876.9	1752.8	2628.6	350.5

Figure 3 shows that for increasing H and changing value of sectorization the number of simultaneous 384 Kbps data users increases.

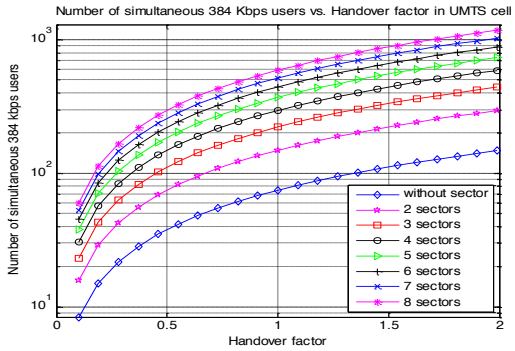

Figure 3: Number of simultaneous 384 Kbps users vs. soft handover factor in sectors cell

Table 3: simulated values Figure 3

H	User With out Sector	User with 2 sectors	User with 4 Sectors	Use with 6 Sectors	User with 8 Sectors
0.1	8.37	15.37	30.46	45.22	59.96
0.5	37.85	74.7	148.4	222.10	295.8
1	74.70	148.40	295.8	443.20	590.6
1.5	111.5	222.10	443.2	664.31	885.4
2	148.4	295.80	590.6	885.41	1180.2

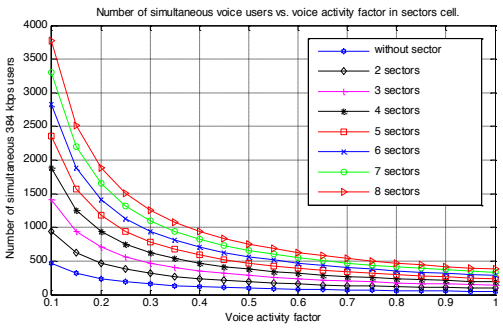

Figure 4: Number of simultaneous voice users vs. voice activity factor in sectors cell.

Table 4: simulated values for Figure 4

α	User With out Sector	User with 2 sectors	User with 4 sectors	User with 6 sectors	User with 8 sectors
0.2	236.6	472.25	943.5	1414.8	1886
0.4	118.8	236.63	472.2	707.9	943.5
0.6	79.54	158.08	315.1	472.3	629.3
0.8	59.90	118.81	236.6	354.4	472.3
1	48.12	95.251	189.5	283.8	378.0

Finally, consider for coverage vs. data rates in dense urban area and suburban area, where operating frequency is considered 2000 MHz with COST 231 Model as a radio propagation model.

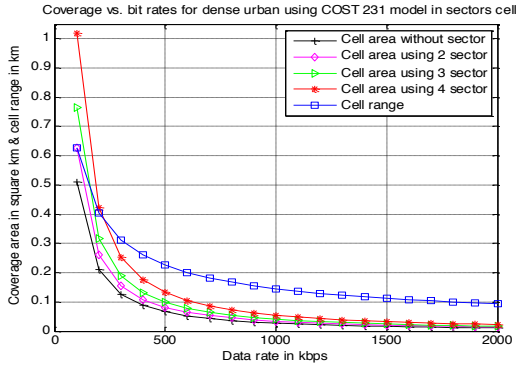

Figure 5: Coverage vs. bit rates for dense urban using COST 231 model in sectors cell

Table 5: simulated values for Figure 5

Data rate Kbps	Cell range In (km)	Area with-out sector (km^2)	Area with 2 Sec-tors (km^2)	Area with 3 Sec-tors (km^2)	Area with 4 Sec-tors (km^2)
100	0.6263	0.5099	0.6275	0.7648	1.0197
500	0.2261	0.0664	0.0818	0.0997	0.1329
1500	0.1128	0.0165	0.0203	0.0248	0.0331
2000	0.0940	0.0115	0.0141	0.0172	0.0230

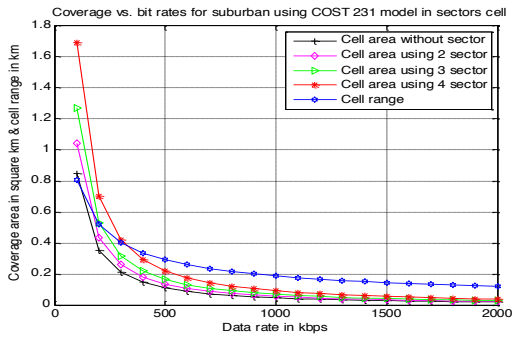

Figure 6: Coverage vs. bit rates for sub urban using COST 231 model in sectors cell

Table 6: simulated values for Figure 6

Data rate (Kbps)	Cell range in (km)	Area without sector (km^2)	Area with 2 sectors (km^2)	Area with 3 sectors (km^2)	Area with 4 sectors (km^2)
100	0.8068	0.8461	1.0414	1.2692	1.6922
500	0.2912	0.1103	0.1357	0.1654	0.2205
1500	0.1453	0.0274	0.0338	0.0411	0.0549
2000	0.1211	0.0191	0.0235	0.0286	0.0381

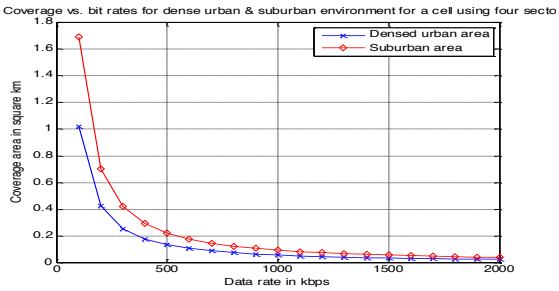

Figure7: Coverage vs. bit rates for dense urban & suburban environment for a cell using four sectors

Table 7: simulated values for Figure 7

Data rate (Kbps)	Coverage in densed Urban areas in km^2	Coverage in sub Urban areas in km^2
100	1.0197	1.6922
500	0.1329	0.2205
1500	0.0331	0.0549
2000	0.0230	0.0381

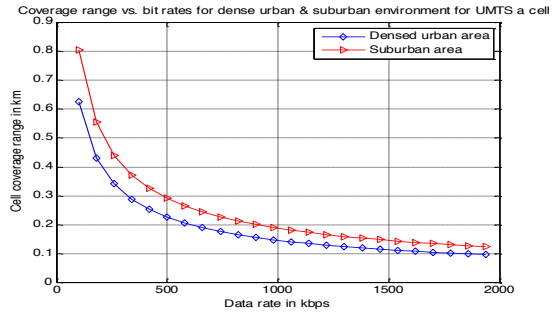

Figure8: Coverage range vs. bit rates for dense urban & suburban environment.

Table 8: simulated values for Figure 8

Data rate (Kbps)	Coverage in densed Urban areas in km	Coverage in sub Urban areas in km
100	0.6263	0.8068
500	0.2261	0.2912
1000	0.1458	0.1878
1500	0.1128	0.1453
2000	0.0940	0.1211

4. CONCLUSION:

In this paper the coverage and capacity in a CDMA cell based on sectorization and propagation prediction models COST-231 Hata model is analyzed. It has been seen that, the performance of an UMTS network can be improved using sectorization. It is also observed that, both the coverage area and coverage range is more in a suburban area than a densed urban area.

5. FUTURE WORK:

Although this research tried to give an impression of the main factors affecting the capacity and coverage. For future research more attention has to be drawn to quality of service requirements in the system and more accurate model can be used for evaluating path loss.

REFERENCES:

[1] Bo Hagerman, Davide Imbeni and Jozsef Barta "WCDMA 6 - sector Deployment-Case Study of a Real Installed UMTS-FDD Network" IEEE Vehicular Technology Conference, spring 2006.

[2] S. Sharma, A.G. Spilling and A.R. Nix "Adaptive Coverage for UMTS Macro cells based on Situation Awareness". IEEE Vehicular Technology Conference, spring 2001.

[3] A. Wacker, J. Laiho-Steffens, K. Sipila, K. Heiska, "The impact of the base station sectorisation on WCDMA radio network performance", IEEE Vehicular Technology Conference ,September 1999.

[4] Romeo Giuliano, Franco Mazzenga, Francesco Vatalaro, "Adaptive cell sectorization for UMTS Third generation CDMA systems" IEEE Vehicular Technology Conference, May 2001.

[6] Jaana Laiho, Achim Wacker, Tomas Novosad, "Radio Network Planning and Optimisation for UMTS" -Second Edition John Wiley & Sons.

[7] Rappaport T.S; Wireless Communications: Principles and Practice, Prentice Hall, 2002.

[8] Gilhousen K.S,et al; On the Capacity of a Cellular CDMA System, IEEE Trans. on VT, Vol. 40, No. 2 , pp.303-312, May 1991.

Table 9: Parameters used in our simulations

Parameter	Value
E_b/N_o	3 db
Frequency	2 GHz
Chip rate	3.84 Mcps
voice activity (α)	1
signal power (S1)	21dbm
shadow fading	8db
inter-cell interference (β)	0.1
cell range(d)	2km
base antenna height (h_b)	20m
user antenna height (h_{UE})	2m
data rate (R) in kbps	12.2,64,144,384,2000

Proceeding of the
International Conference on Electrical, Computer and Telecommunication Engineering
01- 02 December 2012 (ICECTE2012), RUET, Rajshahi-6204, Bangladesh

ICECTE2012: PI-0045

Cloud detection of satellite images by outlier removal method of single linear model

Md. Al Mamun[1], Boshir Ahmed[2] and Md. Arafat Hossain[3]
Department of Computer Science & Engineering
Rajshahi University of Engineering & Technology, Rajshahi, Bangladesh
E-mail: {cse_mamun, boshir_bd}@yahoo.com, arafat.ruet03@gmail.com

ABSTRACT
The distribution of remote sensing data for advanced analysis results in the possibility of solving problems related to the monitoring of the Earth's surface and atmosphere at different scales. As a greater amount of remotely sensed data becomes available, many of the applications will require the interpretation of images collected over a regular period. Frequently collected Satellite images mostly present strong spatial redundancies which can be exploited for the interpretation of natural phenomenon like cloud detection. Cloud pixels usually don't comply with the value of the neighboring pixels. So when the single linear regression model is applied between the odd and even pixels the cloud pixels are considered as the outliers. An iterative linear regression procedure for the odd and even pixel is proposed for outlier exclusion and is presented in detail in the paper. As the outliers are iteratively removed, the whole process converges towards the final model that better defines the spatial relationship between the pixels and the excluded outlier pixels comprise the cloud of the image. Experimental results demonstrate that the proposed method is effective, especially when the cloud pixels are not highly correlated to the other pixels.

KEY WORDS: Single linear regression, spatial correlation, outlier.

1. INTRODUCTION

Satellite images are often affected by sensor, and illumination variations, non-uniform attenuation, atmospheric absorption and other environmental effects which render system changes in them, most of these changes are gradual and incremental. Therefore, the pixels can still be predicted from the neighboring pixels. These images exhibit strong spatial correlation which makes the pixels predictable except the abruptly changed pixel. Usually sudden presence of the cloud in the images is considered as the discontinuity in the spatial correlation. In atmospheric remote sensing science, the cloud detection is an essential basis for the inversion of the parameters in atmosphere such as temperature, humidity, sea surface temperature etc [1].

Many researches are going on to effectively detect the cloud pixels. At present, the main cloud detection technologies can be divided to two categories, the method based on the different spectral characteristics of clear and cloudy area and the method based texture features of cloud relative to the earth surface [1]. In [2] PCA and genetic algorithm is applied to find a more accurate daytime cloud detection index of MODIS data. A real time procedure was proposed in [3] with the help of Spectrum and Texture Analysis Combination (STAC) approach. The Independent Component Analysis (ICA) has been developed in this purpose mainly on the concept of removing the correlation to find the mutually independent part of the images. Our proposed method highlights the same concept. Cloud pixels usually don't comply with the value of the neighboring pixels. So when the single linear regression model is applied between the odd and even pixels the cloud pixels are considered as the outliers. An iterative linear regression procedure for the odd and even pixel is proposed for outlier exclusion and is presented. As the outliers are iteratively removed, the whole process converges towards the final model that better defines the spatial relationship between the pixels and the excluded outlier pixels comprise the cloud of the image. Experimental results demonstrate that the proposed method is effective, especially when the cloud pixels are not highly correlated to the other pixels.

2. METHODOLOGY

Satellite images are highly correlated spatially due to the fact that the neighbouring pixels are homogenous in nature. The correlation value reduces only around the edges for abrupt value transition. So any pixels can be predicted from neighbouring pixels by single linear regression. The principal premise which justifies the use of single linear regression models for spatial predictions is the linear dependency between the pixels.

When the images do experience small portions of real changes or cloud, an outlier removal technique

for generating a prediction model to best fit the majority of unchanged data can be investigated. In the proposed method the pixels are evenly divided the regression analysis are performed to trace out the outlier pixels which are assumed to be cloud pixels. In the following sections correlation measure, single linear regression and the proposed method are briefly described.

2.1 SPATIAL CORRELATION

The correlation coefficient summarises the strength of the linear association between variables and actually quantifies how consistently two variables vary together. The correlation coefficient between two data sets $X = \{x\}$ and $Y = \{y\}$, is defined as

$$r_{XY} = \frac{\sum_{i=1}^{n}(x_i - \bar{x})(y_i - \bar{y})}{\sqrt{\sum_{i=1}^{n}(x_i - \bar{x})^2 \sum_{i=1}^{n}(y_i - \bar{y})^2}} \qquad \text{(Eq. 1)}$$

where $\bar{x}$ and $\bar{y}$ are the sample means of X and Y, respectively, and n the total number of observations. Though linear regression and correlation are related, a correlation calculation differs from regression analysis because it does not find the best-fit line (Motulsky and Christopoulos., 2004). However, the regression function can be chosen according to the relationship indicated by the spatial correlation.

.

2.2 SINGLE LINEAR SPATIAL REGRESSION

Regression analysis is the most common approach used for the calibration of remote sensed images to quantify the relationships between data obtained by different measurement systems in different environments (Peleg, 1998). For a given regression model, the parameters need to be estimated. The most common regression analysis finds parameters to predict the data that best fits the pixel values in a least-squares sense. This optimisation is based on minimising the sum squared error (SSE). The SSE-based least square is often preferred over other methods due to its computational simplicity and good performance in terms of distortion (Boltz *et al.*, 2006).

Given two data sets, $X = \{x_i\}$ and $Y = \{y_i\}$ where X and Y are taken from the odd and even pixel position, respectively, and $i = 1,...,n$ is the total number of observations, a regression function, $\psi(.)$, and a residual or error function, $d(.) \geq 0$, regression analysis can solve the following minimisation problem.

$$\psi^{opt} = \underset{\psi \in \lambda}{\arg\min} \sum_{i=1}^{n} d(\psi(x_i), y_i) \qquad \text{(Eq. 2)}$$

where $d(\psi(x_i), y_i) = (\psi(x_i) - y_i)^2$ is the squared difference (residuals) between the modelled result and the true value, and λ a set of candidate regression functions. Considering λ as a general polynomial function defined as

$$\lambda = \alpha_0 + \alpha_1 x^1 + \alpha_2 x^2 + \ldots\ldots\ldots\ldots + \alpha_p x^p \qquad \text{(Eq. 3)}$$

where p is the degree of the polynomial, then, when $p > 1$, λ is a non-linear function. As previously discussed, certain differences are often induced due to different environmental and imaging conditions. While these factors are complicated, a linear model is generally acceptable for describing the spatial relationship. So, as there is no strong reason for using non-linear or higher order models for multi-temporal data regression, a first-order polynomial is adopted as the prediction function for images which contain either no or only a small portion of, real changes. Taking $\alpha_0 = \beta$ and, $\alpha_1 = \alpha$ for the first-order polynomial, the candidate regression function becomes

$$\psi(x_i) = \alpha x_i + \beta \qquad \text{(Eq. 4)}$$

The optimisation process (Eq. (3.3)) is to find the model parameters α and β. In other words, a solution for the unknown parameters, α and β, that will minimise the distance between the actual and predicted values of the dependent variable, Y, needs to be determined.

2.3 ITERATIVE SINGLE LINEAR REGRESSION ANALYSIS WITH OUTLIER REMOVAL

When the images experience small portions of real changes or clouds, the regression is proposed to be conducted on only the data of the unchanged areas (majority) to make it more effective, as the frequency of the zero residual will be high. Since the data of the changed areas do not follow the rest of majority data, they are the outliers in the regression analysis. Outliers usually mislead in reporting the correlations if they are not removed because they resemble data points that don't comply with the general behavior of the data. They can seriously bias the results by 'dragging' or 'pushing' the regression line in a particular direction, thereby leading to biased regression parameters. Often, excluding just a single extreme case can yield a completely different set of model parameters.

If the pixels are paired by separating the even and odd pixels and single linear model is applied then pixel pairs which exhibit large differences from the modelled line are the outliers and are ignored in the successive iteration. So, the thresholds for outlier removal are determined based on the cumulative

histogram of the absolute values of the residual or the difference image after each iteration. The cumulative histogram can differentiate between the high percentages of small-difference values from the low percentage of large-difference values (outliers). The (real) changed pixels are identifiable due to their relatively large residuals.

After the prediction at each pass, the difference image is calculated as

$$D = \psi(x_i) - y_i \qquad \text{(Eq. 5)}$$

Now, it is considered that the discrete levels of the absolute values of the difference image belongs to the set, $\phi = \{0,\ldots\ldots,l\}$, where there are l+1 number of levels and $|D| \in \phi$. A normalised histogram of $|D|$ can be given as,

$$h(j) = \frac{n_j}{N} \qquad \text{(Eq. 6)}$$

where n_j is the total number of occurrences of level j in $|D|$ and N the total number of pixels in $|D|$. So, $h(j) \in [0,1]$ and the cumulative histogram corresponding to $h(j)$ is

$$cdf_{|D|} = c(j) = \sum_{q=0}^{j} h(q) \qquad \text{(Eq. 7)}$$

The real changed pixels are assumed as a small portion and a conservative estimate of this portion is denoted as c% from the cumulative histogram and a level j is selected as threshold T_1 such that $c(j) = 1 - c\%$. Outliers are identified if the absolute residuals are larger than T_1 and are then excluded. The remaining data, x_i^* and y_i^*, are used in the next step of prediction.

If the trimmed difference image is composed of the unchanged pixels then there are no more outliers or real change pixels left in the images and the process can be terminated. This situation is achieved when the successive iteration doesn't change. The model parameter α is used for checking the convergence. As α becomes stable, iteration will terminate. β is less important, since it does not affect the residual entropy, as discussed in next section.

3. OVERALL PROCEDURE

The consecutive steps of the overall process are detailed below.

1. Initially predict the data set, Y, from the data set, X, by single linear regression using Equation $\psi(x_i) = \alpha x_i + \beta$.
2. Calculate the difference, $D = \psi(x_i) - y_i$.
3. Generate a cumulative histogram, $cdf_{|D|}$.
4. Select a threshold, T_1.
5. Then, trim the imaged data, x_i and y_i, as follows:
   $if(|\psi(x_i) - y_i| > T_1)$,
   remove x_i from X and y_i from Y; and

the trimmed data for the next step, kth regression becomes $X = x_i^k$ and $Y = y_i^k$.

6. Run the regression again on x_i^k and y_i^k and then updated regression function is $\psi(x_i) = \alpha^k x_i^k + \beta^k$.
7. If $|\alpha^k - \alpha^{k-1}| > T_2$, repeat steps (2) to (7).
8. Find the residual, D, for all the pixels using the final model parameters.
9. Find the standard deviation SD of D.
10. Pixels values of D which are greater than $n \times SD$ are set to value 0 and the rest are set to 1, where n are selected by trial and error procedure by matching with the original image. The resultant mask indicates the location of the cloud.

T_2 is a very small value which indicates the negligible amount of change between the α values in successive iteration. The number of iterations required depends on the difference between the percentage, c%, estimated and the percentage of the real changes contained in the current image. The lower the estimate, the longer it takes to converge to the modelled line. The higher the estimate, the faster it will converge but there is a risk that the good data may be removed.

5. EXPERIMENTAL RESULTS

The proposed algorithm was applied to a part of Western Australia as shown in the image in Fig.1. The image used is MODIS (Moderate-resolution Imaging Spectroradiometer) image. Only the band number 3 image was used. Ban3 usually captures most of the features. Fig. 2 illustrates the scatter plots when the pixels are divided into odd and even part to be plotted on the same graph. The outliers are noticeable as they are distant from the central line which is assumed to be cloud pixels. Fig. 3 and Fig. 4 are the cloud masks which indicate the location pixels of the cloud. Median filter is widely used to smooth out the edges. The modified cloud masks are given in Fig.5 and Fig 6. After applying median filter.

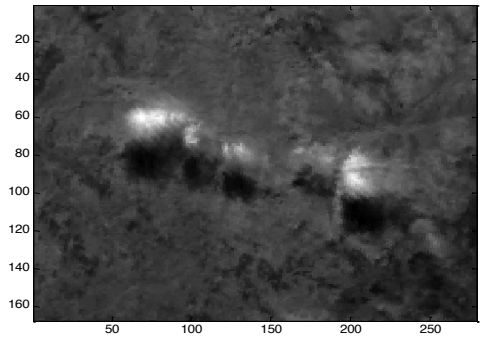

Fig 1. MODIS Image used for the experiment (Courtesy: GeoScience Australia).

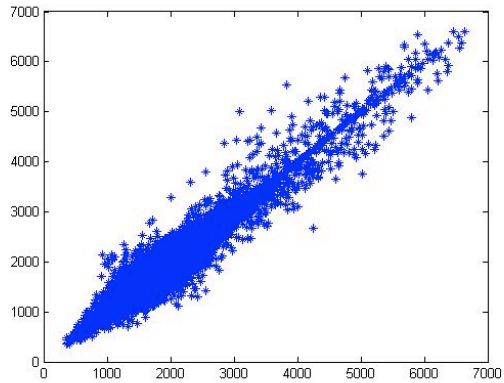

Fig. 2. Scatter plot between the odd and even pixels of the original image.

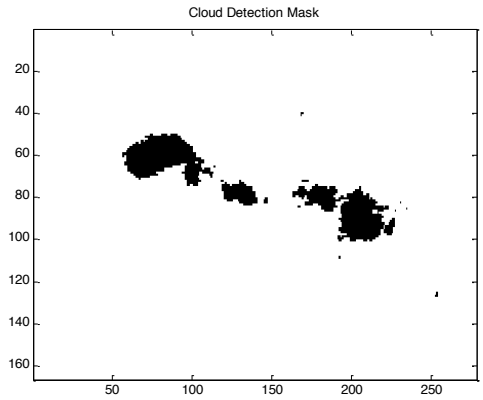

Fig. 3. Cloud detection mask obtained by taking the value of n=6.

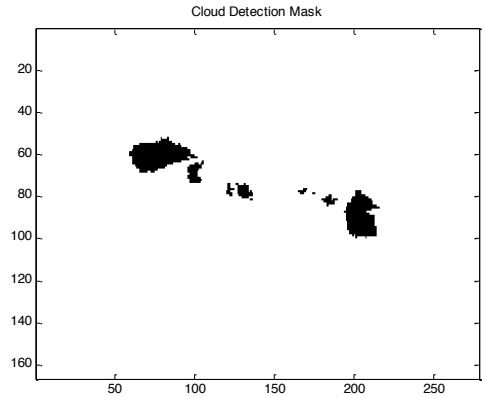

Fig. 4. Cloud detection mask obtained by taking the value of n=5.

4. CONCLUSIONS AND FUTURE WORK

Our approach is motivated by the desire to exploit the spatial correlation observed between the pixels which doesn't exhibit any change like cloud. Although de-correlation in the spatial domains is the widely adopted technique for individual image-based processing, high performance can be achieved in cloud detection by integrating them with de-correlation with outlier removal. The higher order de-correlation can be proposed for better performance in cloud detection

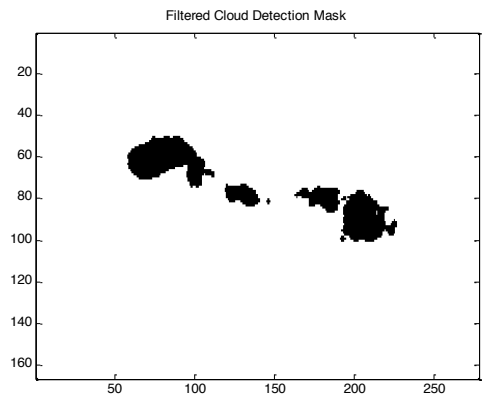

Fig. 5. Cloud mask after median filtering (n=6).

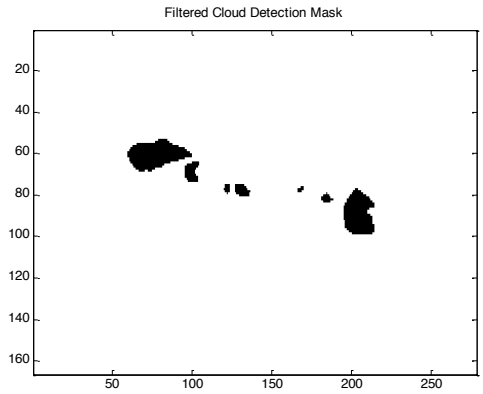

Fig. 6. Cloud mask after median filtering (n=5).

6. ACKNOWLEDGEMENTS
Sincere acknowledgements for GeoScinece Australia for their free downloadable MODIS data.

REFERENCES

[1]. D. Huadong, W. Yongqi, C. Yaming, "Studies on Cloud Detection of Atmospheric Remote Sensing Image Using ICA Algorithm", 2nd International Congress on Image and Signal Processing (CISP), 2009.

[2]. P. Kabiri, H. Ghaderi, S.K. Nejat, "Optimizing Cloud Detection Index for MODIS Imagery Using Genetic Algorithm", 2011 7th Iranian Machine Vision and Image Processing (MVIP), 2011.

[3]. N. Shan, X. Wang and Z. Wang, "Efficient FPGA implementation of cloud detection for real-time remote sensing image processing" Asia Pacific Conference on Postgraduate Research in Microelectronics and Electronics (PrimeAsia), 2010.

[4]. Motulsky, H., and Christopoulos, A. (2004). "Fitting Models to Biological Data using Linear and Nonlinear Regression: A Practical Guide to Curve Fitting". Oxford University Press.

[5]. Peleg, K. (1998). "Fast Fourier Transform based calibration in remote sensing." *International Journal of Remote Sensing*, 19(12), 2301-2315.

[6]. Boltz, S., Wolsztynski, E., Debreuve, E., Thierry, E., Barlaud, M., and Pronzato, L. (2006). "A Minimum-Entropy Procedure for Robust Motion Estimation." *IEEE International Conference on Image Processing*, 1249-1252.

[7]. Bruzzone, L., and Prieto, D. F. (2000). "Automatic analysis of the difference image for unsupervised change detection." *IEEE Transactions on Geoscience and Remote Sensing*, 38(3), 1171-1182.

[8]. Bruzzone, L., and Serpico, S. B. (1997). "An iterative technique for the detection of land-cover transitions in multitemporal remote-sensing images." *IEEE Transactions on Geoscience and Remote Sensing*, 35(4), 858-867.

Proceeding of the
International Conference on Electrical, Computer and Telecommunication Engineering
01- 02 December 2012 (ICECTE2012), RUET, Rajshahi-6204, Bangladesh

ICECTE2012: PI-0046

Maximizing Quality of Service (QoS) of Cognitive Radio Network Using Genetic Algorithm

Firoz Mahmud[1], Syed Tauhid Zuhori[2], Sheikh Abdullah Alamin[3]
[1, 2] Lecturer, Department of Computer Science & Engineering, Rajshahi University of Engineering & Technology.
[3]Department of Computer Science & Engineering, Rajshahi University of Engineering & Technology.
E-mail: fmahmud.ruet@gmial.com, tauhid.ruet@yahoo.com, alamin_cse07@yahoo.com

ABSTRACT
The rapid growth of wireless communication increases the spectrum scarcity problem in the radio network. Usually the licensed users do not utilize their allocated spectrum efficiently so there are some unused spectrums left behind. For this unused spectrum, scarcity problem occurs when an users demanded spectrum is currently unavailable in the network. One solution of this spectrum underutilization problem is the introduction of cognitive radio (CR). It can automatically sense an unused spectrum and make an intelligent decision to allocate an optimum spectrum to satisfy the users request without causing any harm to the authorized users. This paper focuses the process of maximizing a secondary users Quality of Service request by optimizing the spectrum using Genetic Algorithm.

KEY WORDS: Cognitive Radio, Genetic Algorithm, Quality of Service (QoS), Spectrum Allocation.

1. INTRODUCTION

The QoS of a network application is defined as "the set of quantitative and qualitative characteristics of the communication system required to achieve desired functionality of that application"[1]. In 1991-92 Joseph Mitola introduced a radio called "Software Defined Radio (SDR)"(Mitola 1993). SDR is defined as a radio terminal competent enough to operate with different bandwidths, that can a have wide range of operating frequencies and can use different modulation techniques and waveform formats. The SDR is able to support different communication standards like GSM, CDMA, OFDMA, WIMAX etc. SDR at times has provided the most promising solution for the interoperability and seamless connectivity problem, but QoS requirements of an application has still been under consideration. Thusc, the increasing demands of QoS have introduced Cognitive Radio (CR) [2].

Cognitive radio technology is receiving significant attention as an approach to alleviate the FCC identified problem of the scarcity of available radio spectrum [3]. Cognitive radios take advantage of the reconfigurable attributes of a conventional software defined radio (SDR) by using an "intelligent" control method to automatically adapt operating parameters based on learning from previous events and current inputs to the system. A cognitive radio uses information about the environment, and determines the best possible set of transmission parameters to use given some set of service performance objectives [2]. To solve the under utilization problem of the spectrum that means use the unused bandwidth by the secondary user without creating no harm to the communication of the primary (authorized) user a evolutionary algorithm has been introduce which has been used to solve the problem of spectrum scarcity.

This paper is organized as follows: first, preliminary concepts of cognitive radio network is described in section 2, Genetic algorithm is described in section 3, Approaches of our work are described in section 4, Implementation technique and performance evaluation of our proposed system are made in section 5 and section 6. Finally, the conclusion of this paper is described in section 7.

2. CONCEPTS OF COGNITIVE RADIO NETWORK

Basically there are three prime applications required to be added in Software define radio to make it a Cognitive radio (CR) which are:

- Optimization and management of spectrum.
- Interface with a wide variety of wireless networks, leading to management and optimization of network resources.
- Interface with a human, providing electromagnetic resources to aid the human in his or her activities. It has the ability to capture or sense the information from its radio environment and allows identifying and selecting the portion of the spectrum that is unused at a specific time or location. Also has reconfigurability that is dynamically programmable capability according to radio environment to transmit and receive on a variety of frequencies.

The cognitive radio works in a cycle i.e. observe, decide and act [3]. The cognitive radio cycle has

been shown in figure 1. The three terms we can define as follows:

A. *Observation:* Observation involves the learning and sensing of the outer world (i.e. whole radio environment). Raw data and preprocessed information helps the agent to build a knowledge base. In this context, the term environment is used in a broad sense referring to any source of information that could improve the CR's behavior.
B. *Decision:* The outputs of the observations are given as input to the CR where a decision is made on the basis of a mechanism and finally an action is taken.
C. *Action:* Finally an action is taken.

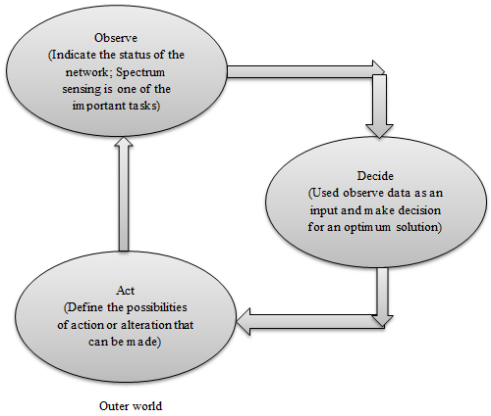

Fig. 1: The Cognitive Radio Cycle [1].

3. GENETIC ALGORITHM

A genetic algorithm (GA) is a search heuristic that mimics the process of natural evolution [4]. This heuristic is routinely used to generate useful solutions to optimization and search problems. Genetic algorithms belong to the larger class of evolutionary algorithms (EA), which generate solutions to optimization problems using techniques inspired by natural evolution, such as mutation, selection, and crossover. Crossover is performed on a single point chosen as a uniform random number with a static probability of crossover occurring. Mutation is also a single point operation chosen from a uniform random number with a static probability of crossover occurring [7]. The selection of fit chromosomes depends upon the defined fitness measures, thus fitness measures and selection are related to one another. In GA there are several techniques used to select fit chromosomes; these are elitism, roulette wheel and tournament selection. After the selection of fit chromosomes with either of the above mentioned procedures the selected chromosomes reproduce to give birth to new off-springs by crossover operation. This process might divide the individual genes into two. To have an increment in the probability of the operation occurrence, the crossover rates are usually set high [4] .After the crossover operation, the mutation process is performed in all or some bits of the chromosome. A random value will be generated and if the value is lesser than that of the mutation probability which was defined by the user, than an inversion of one of the bits in the gene will be performed. Usually the mutation is kept low otherwise it can affect the fitness level of the generated population.

4. APPROACHES

Here we explain the proposed algorithms which are used to find the spectrum utilization. The algorithm is as follow:

Begin

1) Get the user requirements.
2) Construct the proper chromosome structure
3) Generate initial population.
4) Configure the gene of the population chromosome in decimal form.
5) Find out the gene weight and define fitness point of each gene of the chromosome
6) Find out the fitness measure of each gene and the total fitness measure of the chromosome.
7) Construct the new population using selection process to select two methods crossover and mutation process.
8) Use method (7) for both crossover and mutation process.
9) Check the total fitness measure of the two new processes and display the better population set which is generated by two methods.
10) Find out the best individual from the newly generated population set.
11) Display the best result.

END

Chromosome is the collection of some parameter or gene. In this work five genes are considered. Data rate, Signal power, Error rate, Operating frequency and Modulation technique. After that initial population is generated.

Usually, to cover the whole range of possible solutions, the initial population is generated arbitrarily without having any size limitations and to attain satisfactory results. To determine the fitness measure of a chromosome we can easily find out which chromosome is fittest according to the Radio frequency environment. To determine fitness measure we have to follow some steps.

After the fitness process certain method is used to construct new population for finding the best solution from optimum solution. These steps are:

A. *Selection:* Select two chromosomes that have the best fitness level among the current population.
B. *Crossover:* The crossover is done to make new individuals for the incoming generation. So with the defined probability of crossover, selected chromosomes reproduce to form new individuals.
C. *Mutation:* The new created individual will be mutated at a definite point that means altering a binary bit of 0 to 1 or vice versa.

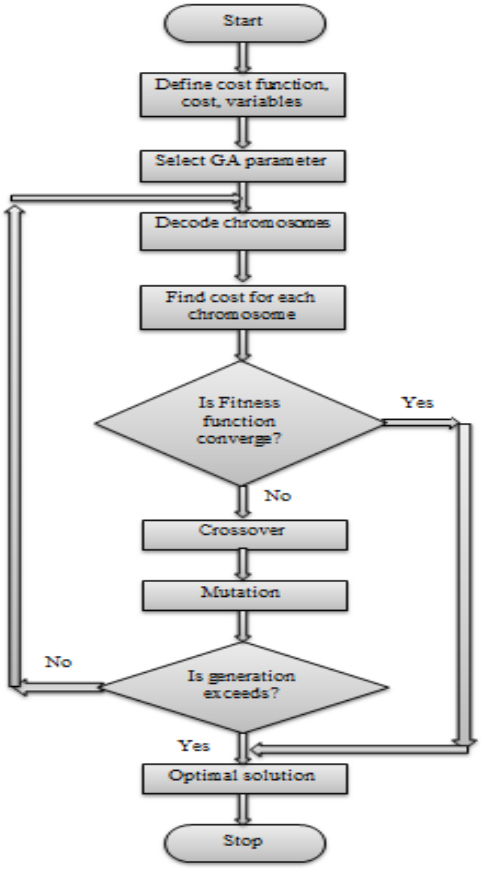

Fig. 2: Flowchart of genetic algorithm

After checking the fitness measure of two processes (Crossover and Mutation) find out the better population between the two and determine the best individual from the better population set. The overall Genetic Algorithm process is shown in Figure 2.

5. EXPERIMENTALS SETUP

At first we have to sense parameters from the environment to get the application requirement. After getting the parameters we have to construct the chromosome structure. Here, we have chosen five parameters as the gene of the chromosome ordered as follows: Data Rate, Signal Power, Error Rate, Signal to Noise Ratio, and Modulation Technique.

The ranges, integer values and the number of bit required to represent each gene is shown in table 1.

Gene	Data rate	Signal power	Error rate	Signal to noise ratio	Modulation technique
Integer range	0-15	0-60	0-10	0-7	0-8
Bit required	4	6	4	3	3
Total bits requirements				20	

Table 1: Chromosome structure representation.

So every gene in a chromosome is needed total 20 bits. The next step of our work is to construct the initial population of chromosomes. We assume the initial population size is 10 chromosomes randomly. The size can be increased up to n numbers, if the outcomes are not acceptable. This initial population is the available pool according to the users QoS requirements.

After the construction of the chromosomes and generation of the initial population we have to define a fitness function to measure fitness for each chromosome. The overall fitness function is described as follows:

$$fitness(i) = \begin{cases} \frac{Gwi * |CGi - APi|}{FPi} & if\ |CGi - APi| < FPi \\ Gwi & otherwise \end{cases} \quad \text{------(1)}$$

$$Total\ fitness = 100 - \sum_{i=1}^{5} fitness(i) \quad \text{----- (2)}$$

Where, fitness(i)=fitness of ith gene in the chromosome, Gwi=weight of ith gene, CGi=value of ith gene in chromosome, APi=value of ith parameter of the requested application, FPi=fitness point of the gene of the chromosome which is predetermined by the developer. The fitness point we have used is given in the table 2.

FP-DR	FP-SP	FP-ER	FP-SNR	FP-MT
6	20	7	4	3

Table 2: Fitness point of different gene

After obtaining the fitness value the selection operator of GA engages the selection of the best population within the pool of existing chromosomes. The probability of selection of each individual best chromosome from population, given by the equation no 3.

P (i)=fitness(i)/Σfitness(i) (3)

Where, P(i) = Probability of selection for chromosome; f(i) = Fitness measure of each chromosome and Σf(i)= total fitness of the generation.

The next step is the mutation operation and this process will generate a completely new population. Then fitness of each chromosome is measured through equation (1) and (2). Next stage we check the average fitness value of the crossover process to the mutation process .Within the generation of the

larger average fitness we find the best population as an individual solution that can maximize secondary users QoS requirements which is taken as input.

6. RESULT ANALYSIS

The secondary users Quality of service (QoS) requirements for the application that is requested is taken as input parameters for the algorithm, which is shown in Table 3.

Data rate	Signal power	Error rate	Signal to noise ratio	Modulation technique
7	34	2	40	4

Table 3: Input combination

After performing different simulation through the algorithm we get fitness values for different chromosomes, which are shown in Table 4.

Chromosomes	Normal	Crossover	Mutation
1	80	88	88
2	83	76	75
3	77	85	85
4	63	69	68
5	60	69	68
6	79	68	68
7	71	77	78
8	88	92	91
9	58	61	61
10	62	66	65

Table 4: Fitness values of different process

The solution is shown in figure 4 with respect to the QoS requirements. The top most point of the crossover process indicates the solution of maximized QoS requirements. The final output of the algorithm gives us the desired chromosome which is shown in table 5.

Data rate	Signal power	Error rate	Signal to noise ratio	Modulation technique
7	32	5	4	4

Table 5: Output combination

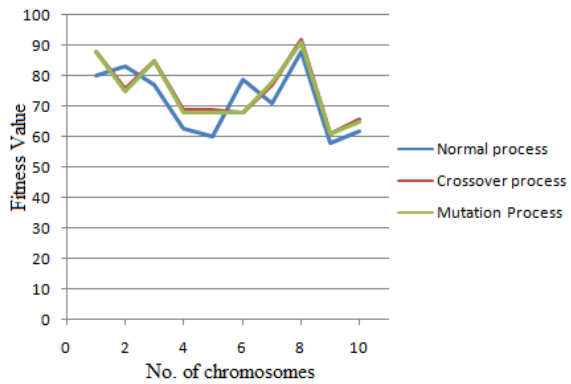

Fig. 3: Comparison of fitness measure in different process

7. CONCLUSION

This work focuses on the optimum spectrum allocation for a application. Also shows the great benefit of GA to select the perfect solution by improving performance of existing chromosomes. The above mentioned example we get 72.1% average fitness of normal process but after applying GA we get 75.40% average fitness in crossover process and 74.70% average fitness in mutation that surely provides the maximum QoS to the application. The proposed system works on a single secondary user's request. Though GA does not produce 100% accurate result but as the number generation increases GA gives more maximized output of QoS requirements.

REFERENCES

[1] "Some Principles for Quality of Service Management", Gregor v. Bochmann and Abdelhakim Hafid Université de Montréal

[2] "Cognitive radio: An integrated agent architecture for software defined radio", J. Mitola Doctor ofTechnology, Royal Inst. Technol. (KTH), Stockholm,Sweden

[3] "Cognitive Radio: Brain-Empowered Wireless Communications", S. Haykin, IEEE JSAC, vol. 23, no. 2, Feb. 2005,pp. 201–20.

[4] "Hybrid Genetic Algorithms: A Review ",Tarek A. El-Mihoub, Adrian A. Hopgood, Lars Nolle, Alan Battersby

[5] "ACognitive Radio Receiver Supporting Wide-Band Sensing", Volker Blaschke, Tobias Renk, Friedrich K. Jondral 978-1-4244-2052-0/08, IEEE

[6] "Performance Evaluation of CSMA/TDMA Cognitive Radio Using Genetic Algorithm", Maninder Jeet Kaur, Moin Uddin, Harsh K Verma, (IJSCE).

[7] "Cognitive radios with genetic algorithms: intelligent Control of software defined radios", Thomas W. Rondeau, Christian J. Rieser, Charles W. Bostian.

Proceeding of the
International Conference on Electrical, Computer and Telecommunication Engineering
01- 02 December 2012 (ICECTE2012), RUET, Rajshahi-6204, Bangladesh

ICECTE2012: PI-0047

Blind Carrier Phase Recovery Based on Partitioned Multi-Modulus Algorithm for Optical Hexagonal 16-QAM Transmission Systems

Ejarder Sabbir Hossain, Md. Saifuddin Faruk*
Department of Electrical and Electronic Engineering, Dhaka University of Engineering and Technology, Gazipur-1700, Bangladesh
**E-mail:* sabbir@duet.ac.bd

ABSTRACT
We proposed a novel carrier phase recovery scheme for optical hexagonal 16-quadrature amplitude modulation (hex-16-QAM) transmission systems which is based on a one-tap phase rotator adapted by a modified multi-modulus algorithm (MMA). Computer simulation shows that laser having several-hundred-kHz 3-dB linewidth are applicable for the 10-Gaud systems with this algorithm.

KEY WORDS: Optical fiber communication, carrier phase recovery, hexagonal 16-quadrature amplitude modulation, multi-modulus algorithm, digital signal processing.

1. INTRODUCTION

The requirement of enhancing spectral efficiency is increasing day by day. Multilevel modulation formats is one of the most effective way to mitigate this requirement. But increasing the order of modulation complicates the data recovery system. Taking all the considerations, for optical communications 16-quadrature amplitude modulation (16-QAM) is one of the most promising choices for the next generation 100G Ethernet. Most commonly used format for 16-point constellation is square 16-QAM and has been widely investigated for optical communication systems. However, hexagonal 16-QAM (hex-16-QAM) requires less energy compare to square 16-QAM to carry the same information which is close to the most energy efficient 16-point constellation [1].

Carrier synchronization in optical coherent systems can be achieved using digital phase recovery techniques. Various phase recovery algorithms have been proposed and verified for quaternary phase-shift keying (QPSK) and square 16-QAM modulation format. One of the most promising methods is M^{th} power scheme, also known as the Viterbi and Viterbi algorithm which is appropriate for QPSK modulation format [2] and can also be used for square 16-QAM with some modification. One of the modifications is QPSK partitioning which is noted in [3]. However, this modification is not applicable for hex-16-QAM due to having too many constellation points circle ring. Decision-directed carrier phase estimation has been proposed in [4], which is based on the least-mean-square (LMS) algorithm. However, without training, the result of such algorithm is unstable.

In this paper, we propose a novel blind carrier phase recovery algorithm for hex-16-QAM which is based on a modified version of MMA, which is more hardware efficient than that of proposed in [4] since we need not any symbol decision for this algorithm. We named this algorithm as Partitioned MMA (PMMA). While the conventional MMA just decompose the cost function of CMA in real and imaginary part, we include the amplitude discrimination of real and imaginary part in the cost function of MMA for PMMA. Such a partitioning enables a lower mean-square-error (MSE) and hence better performance. With computer simulation of 10-Gsymbols/s hex-16-QAM systems, we verified that with our proposed algorithm, receiver sensitivity penalty remain below 2 dB at BER=10^{-3} up to five-hundred-kHz linewidth laser.

2. PRINCIPLE OF PARTITIONED MMA BASED CARRIER-PHASE ESTIMATION

In the remainder, the subscript $(\bullet)_R$ and $(\bullet)_I$ of any variable denote the real and imaginary parts of that variable. Consider the digitized complex amplitude detected by the homodyne phase-diversity receiver input sequence is $u(n)$ and $c(n)$ is the tap coefficient which rotates $u(n)$ on the complex plane. The symbol-spaced sample index is denoted as n. The output of the carrier recovery unit is given as $v(n) = c(n)*u(n)$. The tap value is generally updated by using the stochastic gradient algorithm as

$$c(n+1) = c(n) + \mu\hat{\nabla}J(n), \qquad (1)$$

where μ is the step-size parameter and $J(n)$ is the cost function. Before explaining the operation principle of the proposed algorithm, first consider the conventional MMA.

The cost function of MMA can be written as [5]

$$\begin{aligned} J(n) &= J_R(n) + J_I(n) \\ &= E\left\{\left(R_{2,R} - v_R^2(n)\right)^2\right\} + E\left\{\left(R_{2,I} - v_I^2(n)\right)^2\right\}, \qquad (2) \end{aligned}$$

where, the parameters $R_{2,R/I}$ is given as

$$R_{2,\mathrm{R/I}} = E\left\{a_{R/I}^4(n)\right\} / E\left\{a_{R/I}^2(n)\right\}. \quad (3)$$

The cost function of proposed PMMA is same as the conventional MMA as in Eq. (2); however, instead of constant $R_{2,R}$ and $R_{2,I}$, we choose $R_{2,Rp}$ and $R_{2,Iq}$, where p=1, 2, 3 or 4 and q=1 or 2 which are calculated based on the amplitude discrimination of real and imaginary part as shown in Fig.1. The same color in the figure denotes same absolute real/imaginary value. The cost function of proposed algorithm is thus can be written as

$$J(n) = J_{Rp}(n) + J_{Iq}(n)$$

$$= E\left\{\left(R_{2,Rp} - v_R^2(n)\right)^2\right\} + E\left\{\left(R_{2,Ip} - v_I^2(n)\right)^2\right\}. \quad (4)$$

The partitioning of imaginary part is straightforward and only one amplitude decision level in imaginary side is necessary (Fig. 1b). However, the partitioning of real part requires decision from both real and imaginary part (Fig. 1a). The values of $R_{2,Rp}$ and $R_{2,Iq}$ are then decided from the constellation points inside the decision boundaries.

Figure 2 shows the block diagram of the proposed carrier phase recovery system, which is based on a one- tap phase rotator and the PMMA to control its tap coefficient. The update equation is given by

$$c(n+1) = c(n) + \frac{\mu}{|u(n)|^2} e(n) u^*(n) \quad (5)$$

$$e(n) = \left[v_R(n)\left\{R_{2,Rp} - v_R^2(n)\right\} + jv_I(n)\left\{R_{2,Iq} - v_I^2(n)\right\}\right] \quad (6)$$

3. SIMULATION RESULTS AND DISCUSSION

To investigate the performance of the algorithm for a hex-16-QAM coherent system, we used computer simulation. The output signal reconstructed from the front-end of a digital coherent receiver can be represented as

$$r(n) = a(n)e^{j\theta(n)} + w(n), \quad (7)$$

where, $a(n)$ is the data symbol such that, $\theta(n)$ is the phase noise introduced by the lasers, and $w(n)$ is an additive white Gaussian noise. The laser phase noise is considered as Gaussian distribution with a variance given by-

$$\sigma^2 = 2\pi\delta_f T, \quad (8)$$

where, δ_f is the -3dB linewidth of laser and T is the sampling period.

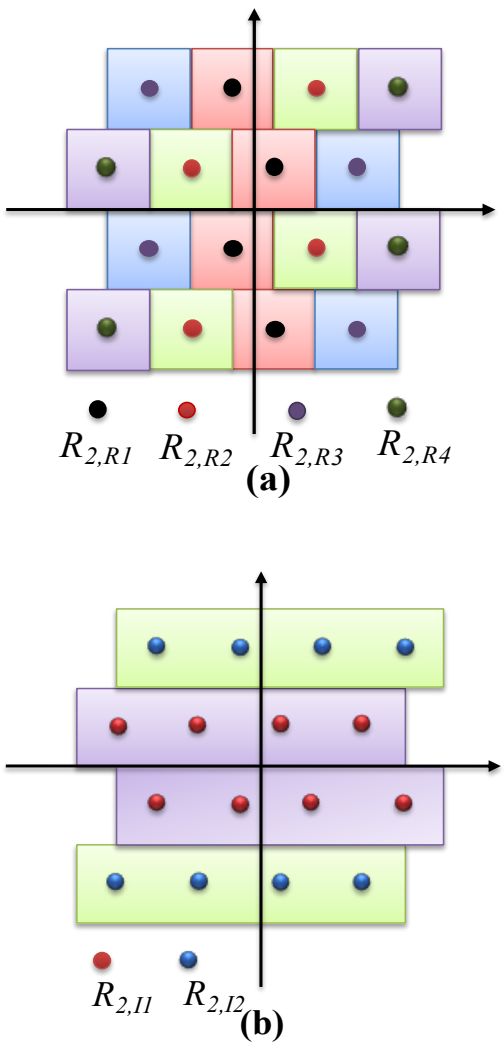

Fig.1: Partitioning technique for the proposed algorithm. (a): partitioning for real part, (b): partitioning of imaginary part.

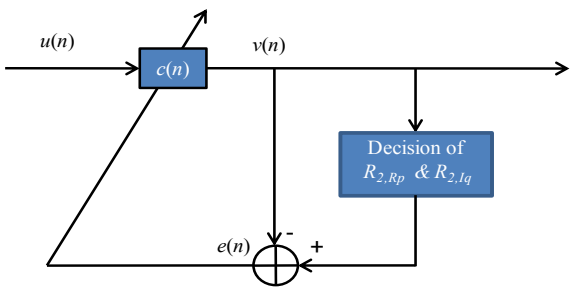

Fig.2. Block diagram of the PMMA based carrier phase recovery.

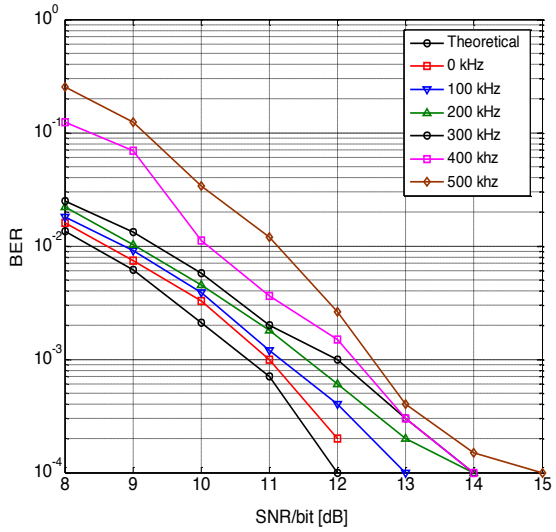

Fig.3: BER versus SNR/ bit for linewidth/laser from 0 Hz to 500 kHz.

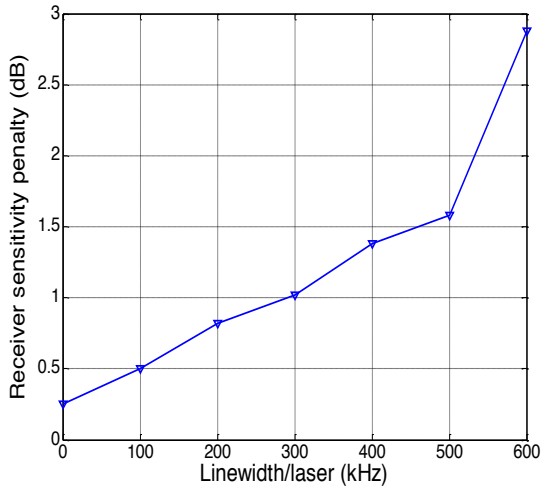

Fig.4: Receiver sensitivity penalty at BER of 10^{-3} as a function of linewidth/laser at a symbol rate of 10G.

Carrier phase recovery is performed on $r(n)$ using the proposed carrier recovery technique. Finally, symbols are decoded and BER is measured.

Figure 3 shows BER characteristics curve which is calculated as function of SNR/bit. The linewidth of lasers for the transmitter and the local oscillator (LO) is varied from 0 Hz to 600 kHz. The BER performance degrades with increasing laser linewidth. Next we measure receiver sensitivity penalty due to laser phase noise for the proposed scheme. As shown in Fig.4, the sensitivity penalty remains below 2dB up to laser linewidth 500 kHz.

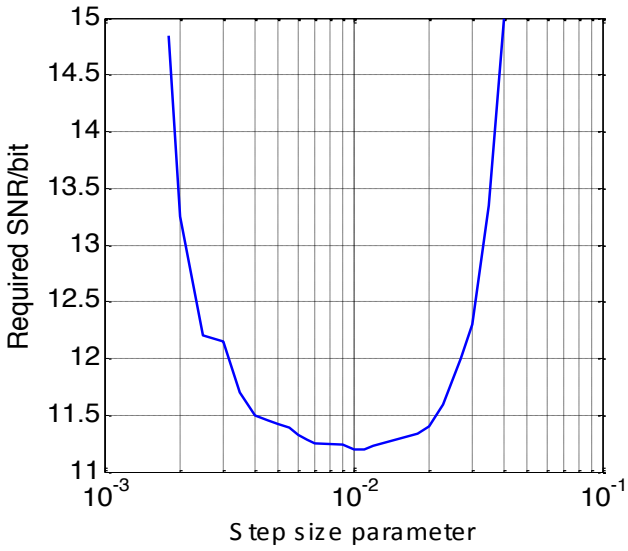

Fig.5: Required SNR/bit at **BER** of 10^{-3} as a function of μ for seeking the optimum step size parameter for linewidth/laser of 100 kHz.

For each linewidth of laser the optimum value the μ is taken. To calculate the optimum μ, we vary the value of μ up to a range and calculate the required SNR/bit at BER 10^{-3}. The optimum μ is taken for which SNR/bit is minimum. For example, as shown in Fig. 5, that optimum μ for 100 kHz laser is 0.01, as at such value the required SNR/bit is minimum.

4. CONCLUSIONS

We have proposed a novel blind carrier phase recovery algorithm named as PMMA for optical hex-16-QAM transmission systems. Computer simulation of 10-Gbaud optical hex-16-QAM systems confirms that proposed scheme is tolerant upto 500 kHz linewidth/laser with a power penalty of less than 2 dB.

5. FUTURE WORKS

Further investigation on the proposed algorithm is required to enhance the laser-linewidth tolerance.

REFERENCES

[1]. G. J. Foschini and R. D. Gitlin, "Optimization of two dimensional signal constellations in the presence of Gaussian noise," IEEE Trans.Commun., vol. COM-22, no. 1, pp. 23-38, Jan. 1974.

[2]. D.-S. Ly-Gagnon, S. Tsukamoto, K. Katoh, and K. Kikuchi, "Coherent detection of optical quadrature phase-shift keying signals with carrierphase estimation," *J. Lightw. Technol.*, vol. 24, no. 1, pp. 12–21, Jan. 2006 .

[3]. I. Fatadin, D. Ives, and Seb. J. Savory, "Laser linewidth tolerance for 16-QAM coherent optical systems using QPSK partitioning," *IEEE Photonics Technol. Lett.,* vol. 22, pp. 631-633, May. .

[4]. Y. Mori, C. Zhang, K. Igarashi, K. Katoh, and K. Kikuchi, "Unrepeated 200-km transmission of 40-Gbit/s 16-QAM signals using digital coherent receiver," *Opt. Express*, vol. 17, no. 3, pp. 1435-1441, Feb. 2009.

[5]. J. Yang, J.-J. Werner, and G.A. Dumont, "The multimodulus blind equalization algorithm," *Proc. IEEE Int'l Conf. DSP*, vol.1, pp. 127–130, 1997.

Proceeding of the
International Conference on Electrical, Computer and Telecommunication Engineering
01- 02 December 2012 (ICECTE2012), RUET, Rajshahi-6204, Bangladesh

ICECTE2012: PI-0048

BER Simulation Using MATLAB for BPSK and QPSK with Different Chip and Sampling Rates

Jishan-E-Giti, Md. Mortuza Ali

Department of Electrical & Electronic Engineering, Rajshahi University of Engineering & Technology, Rajshahi-6204

E-mail: monimala89@yahoo.com, mmali57@yahoo.com

ABSTRACT

MATLAB is an ideal tool for simulating digital communications systems, thanks to its easy scripting language and excellent visualization capabilities. One of the most frequent simulation tasks in the field of digital communications is bit-error-rate (BER) testing of various schemes. The bit-error-rate performance of a receiver is a figure of merit that allows different designs to be compared in a fair manner.in this paper BER performance for BPSK and QPSK techniques are simulated to observe the BER versus SNR characteristics for different chip rates and sampling rates of binary number generator. Both the rates are taken as 144kbps, 384kbps and 1Mbps considering WCDMA scheme which provides these data rates for highways, pedestrians and indoor respectively. The simulation results show that the BER performance for same chip and sampling rates follow a same value, also show upgradation or degradation for difference in chip and sampling rates.

KEY WORDS: BER, Chip rate, Sampling rate, BPSK, QPSK.

1. INTRODUCTION

Both higher and lower chip rate have some advantages and disadvantages. Chip rate must be higher than data rates as data bits are spread by OVSF and becomes chips. More the chips, better performance whether it is mobile communication or audio industry. The disadvantage of conveying many bits per symbol is that the receiver has to distinguish many signal levels or symbols from each other, which may be difficult and cause bit errors in case of a poor phone line that suffers from low signal-to-noise ratio. In that case, a modem or network adapter may automatically choose a slower and more robust modulation scheme or line code, using fewer bits per symbol, in view to reduce the bit error rate. [1]

Simulation using MATLAB includes some communication blocks. BPSK and QPSK baseband modulator and demodulators are chosen regarding the uplink and downlink of WCDMA respectively. For channel, AWGN channel has been chosen. For transmitting bits, Bernoulli generator is included here. The sampling rate of the generator plays the role of data rates or bit rates, and the object of the paper is to observe the BER performance for various sampling and chip rates.

1.1 Some Technical Terms

1.1.1 BER

The **bit error rate** or **bit error ratio** (BER) is the number of received bits that have been altered due to noise, interference and distortion, divided by the total number of transferred bits. BER is a unitless performance measurement that specifies the number of bit corrupted or destroyed as they are transmitted from its source to its destination. Several factors that affect BER include bandwidth, SNR, transmission speed and transmission medium.

In a communication system, the receiver side BER may be affected by transmission channel noise, interference, distortion, bit synchronization problems, attenuation, wireless multipath fading, etc. The *transmission BER* is the number of detected bits that are incorrect before error correction, divided by the total number of transferred bits (including redundant error codes). The *information BER*, approximately equal to the decoding error probability, is the number of decoded bits that remain incorrect after the error correction, divided by the total number of decoded bits (the useful information). Normally the transmission BER is larger than the information BER. The information BER is affected by the strength of the forward error correction code.

1.1.2 Chip Rate

It is the rate of encoding. In direct sequence spread spectrum technologies such as DSSS and CDMA, it is the number of bits per second (chips per second) used in the spreading signal. A different spreading signal is added to the data signal to code each transmission uniquely. The number of chips (bits) in the spreading signal is significantly greater than the data bits. [1] Chip rate is measured in "megachips per second" (Mcps), which is millions of chips per second. For example, WCDMA uses chip rate of 3.84Mcps.

chip rate=spreading factor × symbol rate

1.1.3 Binary phase-shift keying (BPSK):

BPSK is the simplest form of M-ary phase shift keying (PSK) where M=2. It uses two phases which are separated by 180° and so can also be termed 2-PSK. It does not particularly matter exactly where the constellation points are positioned, and in this figure they are shown on the real axis, at 0° and 180°. It is, only able to modulate at 1 bit/symbol. [2]

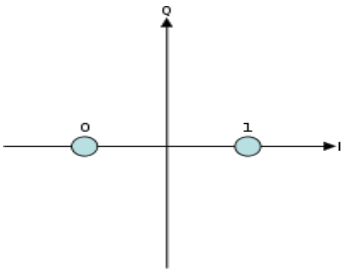

Fig.**1.1**: Constellation diagram of a BPSK system.

In the presence of an arbitrary phase-shift introduced by the communications channel, the demodulator is unable to tell which constellation point is which. As a result, the data is often differentially encoded prior to modulation.
The general form for BPSK follows the equation:

$$S_b(t) = \sqrt{\frac{2E_b}{T_b}}\cos(2\pi f_c t + \pi(1-i)), \quad i = 0,1 \qquad \text{.....(1.1)}$$

The bit error rate (BER) of BPSK in AWGN can be calculated as:

$$P_b = \frac{1}{2} erfc(\sqrt{\frac{E_b}{T_b}}) \qquad \text{.....(1.2)}$$

Since there is only one bit per symbol, this is also the symbol error rate.

1.1.4Quadrature phase-shift keying (QPSK):

QPSK is one example of M-ary PSK modulation technique (M = 4). Sometimes known as quaternary or quadriphase PSK, 4-PSK, or 4-QAM.[3] QPSK uses four points on the constellation diagram, equispaced around a circle. With four phases, QPSK can encode two bits per symbol. The basis signal for QPSK can be expressed as

$$S_b(t) = \sqrt{\frac{2E_b}{T_b}}\cos(2\pi f_c t + (2i-1)\frac{\pi}{4}), \quad i = 1,2,3,4. \qquad \text{.....(1.3)}$$

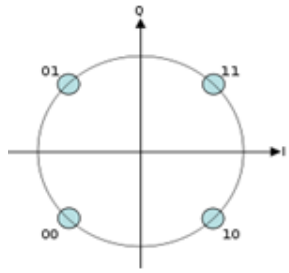

Fig.**1.2**: Constellation diagram of a QPSK system.[2]

BPSK is used on both in-phase (I) and Quadrature-phase (Q) carriers and they can be independently demodulated. As a result, the probability of bit-error for QPSK is the same as for BPSK.

1.1.5 Additive White Gaussian Noise (AWGN)

It is a basic and generally accepted model for thermal noise in communication channels, is the set of assumptions that

i. The noise is additive, i.e., the received signal equals the transmit signal plus some noise, where the noise is statistically independent of the signal.
ii. The noise is white, i.e., the power spectral density is flat, so the autocorrelation of the noise in time domain is zero for any non-zero time offset.
iii. The noise samples have a Gaussian distribution.

Mostly it is also assumed that the channel is Linear and Time Invariant. The most basic results further assume that it does not account for fading, frequency selectivity, interference, nonlinearity or dispersion.

1.1.6 SNR

It is the ratio of signal power to noise power, expressed in dB. In this simulink E_b/N_o is used as SNR where E_b is energy per bits and N_o is the power spectral density of noise. If the unit of E_b is Joules, then the unit of No is Watts per Hertz, thus making the ratio dimensionless.

2. SIMULATION OVERVIEW

2.1 Simulation Methodology

The project begins with simulation using simulink. Simulink is a software package that has the capabilities to model, simulate, and analyze dynamic systems whose outputs and states change with time. This simulation includes the following parts:

i. Transmitter
ii. Modulator
iii. Channel
iv. Demodulator
v. Receiver

The evaluation of performance is made on one user only and the thermal noise is considered negligible.

The communication blocks used here are:

- Bernoulli binary no. generator,
- BPSK/QPSK Baseband Modulator
- AWGN Channel
- BPSK/QPSK Baseband Demodulator and
- Error Rate Calculation Block

The simulink was executed and with the help of generic M-file, BER performances were plotted. [4] MATLAB 7.0 was used.

2.2 Simulation Results

BER was simulated for both BPSK and QPSK in awgn channel. Since the simulink block cannot operate with lesser sampling rate than the chip rate, with decreasing sampling rate, performance for three different chip rates were not possible to observe. However, the results found using three values for sampling (T_S) and chip rates (T_C) as 144kbps, 384kbps and 1Mbps are shown in figures and tables.

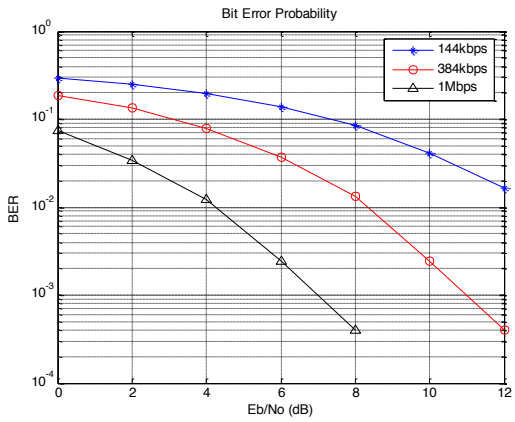

Fig. 2.1: BER for different chip rates with sampling rate 1Mbps for BPSK

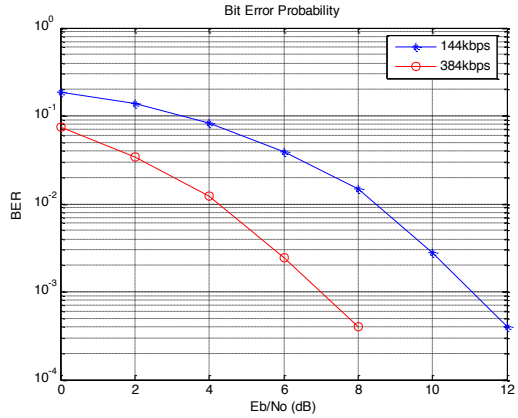

Fig. 2.2: BER for different chip rates with sampling rate 384kbps for BPSK

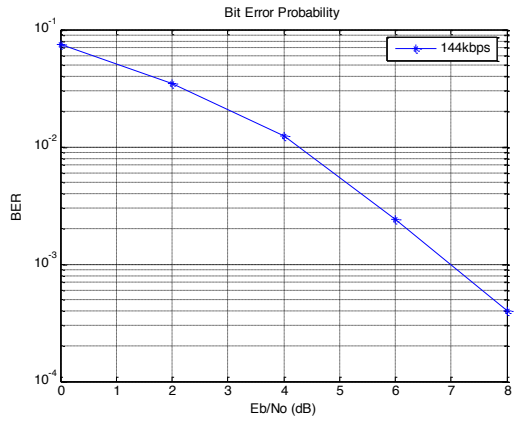

Fig. 2.3: BER for chip rate and sampling rate of 144kbps for BPSK

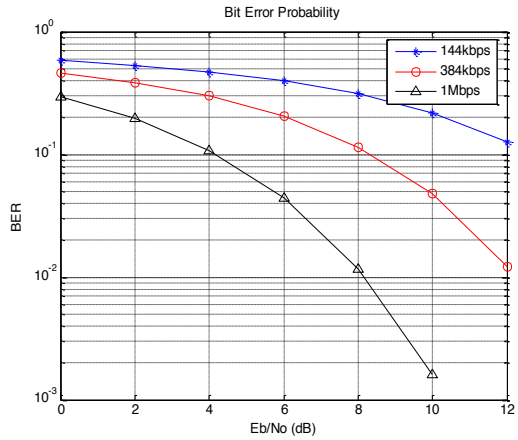

Fig. 2.4: BER for different chip rates with sampling rate 1Mbps for QPSK

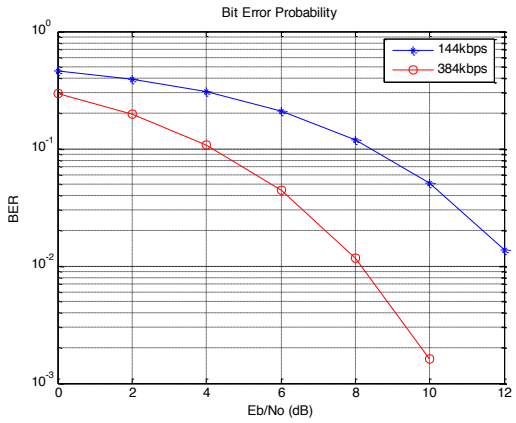

Fig. 2.5: BER for different chip rates with sampling rate 384kbps for QPSK

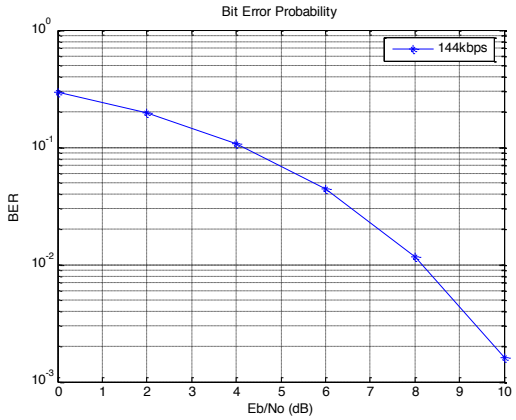

Fig. 2.6: BER for chip rate and sampling rate of 144kbps for QPSK

Table 2.1: Values obtained for BPSK

T_C / T_S	144 kbps		384kbps		1 Mbps	
	6dB $\times 10^{-3}$	8dB $\times 10^{-3}$	6dB $\times 10^{-3}$	8dB $\times 10^{-3}$	6dB $\times 10^{-3}$	8dB $\times 10^{-3}$
144 kbps	2.4	0.4				
384 kbps	39.2	14.6	2.4	0.4		
1000 kbps	139.8	86	372	13.4	2.4	0.4

Table 2.2: Values obtained for QPSK

T_C / T_S	144 kbps		384kbps		1 Mbps	
	6dB $\times 10^{-3}$	8dB $\times 10^{-3}$	6dB $\times 10^{-3}$	8dB $\times 10^{-3}$	6dB $\times 10^{-3}$	8dB $\times 10^{-3}$
144 kbps	44.4	1.6				
384 kbps	210.6	50.6	44.4	1.6		
1000 kbps	397.8	216.8	205.8	47.6	44.4	1.6

3. CONCLUSION

The simulation shows that if both sampling rate and chip rate are taken same, then the BER has the same value for considered three rates. It also shows how BER performance degrades if the difference between sampling rate and chip rate are increased. For example, for QPSK, keeping chip rate fixed at 144kbps; if we increase the sampling rate from 144 to 384 kbps, BER increases 4.7 times, and if the sampling rate is increased from 144kbps to 1Mbps then BER increases almost 9 times.

It's just mathematical observation using MATLAB tools.

4. FUTURE SCOPE

The simulation blocks were arranged considering WCDMA, but it was a simple simulink design, using higher version of MATLAB the design can be improved. The baseband modulator-demodulator blocks can be replaced by passband blocks plus x-or spreader-despreader[5], and Rayleigh or Rician channel can be used considering multipath fading.

5. AKNOWLEDGEMENTS

We are grateful to all the teachers of the Department of Electrical and Electronic Engineering, RUET for providing necessary facilities and critical suggestions during this research.

REFERENCES

[1]. www.wikipedia.com, "Symbol Rate", page last modified on 6 August, 2012.

[2]. www.wikipedia.com, "Phase-Shift Keying", page last modified on 27 August, 2012.

[3]. B. P. Lathi, "Modern Digital and Analog Communication Systems", Oxford University Press, New Delhi, 3rd edition, 2007, pp. 337-342.

[4]. Stephen J. Chapman, "MATLAB Programming for Engineers", Thomson Asia Pte Ltd, Singapore, 3rd edition, 2005, pp. 63.

[5]. Muhammad Najib Bin Ismail, "Performance Study on High Data Rates Modulation Techniques of WCDMA in Multipath Fading Channel", Project Report for M. Engg., Faculty of Electrical Engineering, University Technology Malaysia, 2005.

Proceeding of the
International Conference on Electrical, Computer and Telecommunication Engineering
01- 02 December 2012 (ICECTE2012), RUET, Rajshahi-6204, Bangladesh

ICECTE2012: PI-0049

Error Rate of ZF Equalizer on QPSK Modulation in a MIMO Rayleigh Fading Channel

Sabuj Sarkar[1], Mohammad Shaifur Rahman[2]
[1]Electrical and Electronic Engineering, Khulna University of Engineering & Technology
Khulna-9203, Bangladesh
[2]Electrical and Electronic Engineering, Khulna University of Engineering & Technology
Khulna-9203, Bangladesh
E-mail: sabujeeekuet@gmail.com, msrbitk@yahoo.com

ABSTRACT
In wireless communication fading and interference are the two most common factors that affect the bit error rate and channel performance which can be combated by equalizer. This paper introduces a novel equalizer called Zero forcing (ZF) equalizer to enhance the performance of QPSK modulation in Multiple Input Multiple Output (MIMO) channels. The performance of MIMO systems under a Rayleigh fading channel has been studied by changing the number of transmit-receive antennas. Based on bit error rates, the simulation results show that ZF equalizers with Successive Interference Cancellation and optimal ordering (ZF-SIC-Sort) have the best BER performance on QPSK modulation compared to Zero Forcing and Successive Interference Cancellation (ZF-SIC) combinations.

KEY WORDS: MIMO (Multiple Input Multiple Output), BER (Bit Error Rate), ZF (Zero Forcing), ZF-SIC (Zero Forcing Successive Interference Cancellation), ZF-SIC-Sort (Zero Forcing Successive Interference Cancellation with optimal ordering), QPSK (Quadrature Phase Shift Keying).

1. INTRODUCTION

Recent explosion in wireless technology has opened a new era to the future wireless communication. By using MIMO high data rate and high channel performance can be achieved that cannot be possible in single antenna systems [1] [2] [3]. In wireless communications, MIMO technology has attracted special attention because it offers significant increases in data throughput and link range with narrow bandwidth thus increased transmit power. This method offers higher capacity to wireless systems and the capacity increases linearly with the number of antennas. In MIMO wireless communication, an equalizer is employed in a network which makes an attempt to recover a signal that has suffered ISI. ZF equalizer is the technique in which inverse of the channel is used to restore the signal before the channel and makes ISI to zero in a noise free condition. When SNR is high its performance is best. For a 4x4 MIMO system the BER for various detection schemes like MMSE, ML and ZF has been analyzed and compared [4]. The bit error rate performance characteristics of different equalizers such as ZF, ML and MMSE for MIMO systems in wireless communication have been investigated to find out suitable equalizer [5] [6]. Different signal detector schemes such as Maximum Likelihood (ML), Minimum Mean-Square Error (MMSE), ZF, and Ordered Successive Interference Cancellation (OSIC) has been discussed and the performance of MIMO system with different modulation schemes in Raleigh Fading channels has been compared [7] [8]. The performance and the computational complexity of these schemes with other existence model have been analyzed depending on frame error rates and bit error rates.

The main purpose of present study is to analyze the different forms of ZF equalizers for QPSK modulation and different MIMO combinations. Then a comparative study is done to analyze BER vs. SNR characteristics and select that type of ZF equalizer which has a better performance in terms of BER for a given SNR.

2. MIMO CONFIGURATION

Let us consider a MIMO system containing M transmit-antennas and N receive-antennas. The received signal in the j^{th}antenna is given by

$$Y_j=\sum_{k=1}^{N} h_{jk}\ x_k+n_k \ldots\ldots\ldots\ldots\ldots\ldots \quad (1)$$

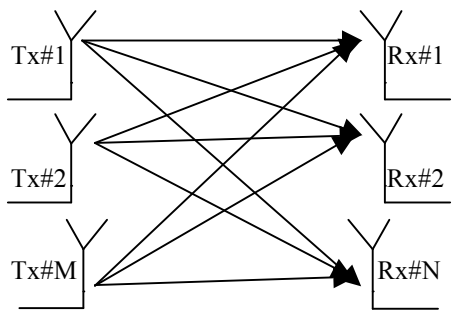

Figure**1:** Block Diagram of a MIMO system with MXN transmit-receive antennas

Where, j = 1, 2, 3…N, h_{jk} is the fading corresponding to the path from transmit antenna k to receive antenna j. $n_j$is the noise corresponding to receive antenna.

3. ZERO FORCING EQUALIZER

A Zero Forcing equalizer is a linear equalizer used in communication systems that has reduced computational complexity but suffers from noise enhancement. It applies the inverse of the channel to the received signal, to restore the signal before the channel. As the ISI becomes zero in a noise free case that is why it is called. Zero forcing equalizer. It works best when SNR is high. The solution of the ZF equalizer is given by:

$$\tilde{x} = (H^{*}H)^{-1}Hx = H^{+}x \ldots (2)$$

Where$(\,)^{+}$ represents the pseudo-inverse. The math for extracting the two symbols which interfered with each other. In the first time slot, the received signal on the first receive antenna is,

$$y_1 = h_{1,1}x_1 + h_{1,2}x_2 + n_1 = [h_{1,1}h_{1,2}][\begin{bmatrix} x_1 \\ x_2 \end{bmatrix}+n_1$$

The received signal on the second receive antenna is,

$$y_2 = h_{2,1}x_1 + h_{2,2}x_2 + n_2 = [h_{2,1}h_{2,2}][\begin{bmatrix} x_1 \\ x_2 \end{bmatrix}+n_2$$

Where, y_1,$y_2$are the received symbol on the first and second antenna respectively, $h_{1,1}$ is the channel from 1^{st}transmit antenna to 1st receive antenna, $h_{1,2}$ is the channel from 2^{nd}transmit antenna to 1^{st}receive antenna, $h_{2,1}$ is the channel from 1st transmit antenna to 2nd receive antenna, $h_{2,2}$ is the channel from 2nd transmit antenna to2^{nd} receive antenna, x_1, x_2 are the transmitted symbols andn_1,n_2 is the noise on1^{st}, 2nd receive antenna. We assume that the receiver knows$h_{1,1}$,$h_{1,2}$,$h_{2,1}$and $h_{2,2}$. The receiver also knowsy_1, and y_2 .The unknowns are x_1 andx_2.

For convenience, the above equation can be represented in matrix formation as follows:

$$\begin{bmatrix} y_1 \\ y_2 \end{bmatrix}=\begin{bmatrix} h_{1,1} & h_{1,2} \\ h_{2,1} & h_{2,2} \end{bmatrix}\begin{bmatrix} x_1 \\ x_2 \end{bmatrix}+\begin{bmatrix} n_1 \\ n_2 \end{bmatrix} \ldots (3)$$

Equivalently, $y = Hx + n$. To solve for x we need to find a matrix W which satisfies $WH = I$. The Zero Forcing (ZF) linear equalizer for meeting this constraint is given by,

$$W = [H^H H]^{-1}H^H$$

Where W- Equalization Matrix and H - Channel Matrix. This matrix is known as the pseudo inverse for a general m x n matrix. Where

$$H^H H = \begin{bmatrix} h_{1,1}^{*} & h_{2,1}^{*} \\ h_{1,2}^{*} & h_{2,2}^{*} \end{bmatrix}\begin{bmatrix} h_{1,1} & h_{2,1} \\ h_{1,2} & h_{2,2} \end{bmatrix} =$$

$$\begin{bmatrix} |h_{1,1}|^2 + |h_{2,1}|^2 & h_{1,1}^{*}h_{1,2} + h_{2,1}^{*}h_{2,2} \\ h_{1,2}^{*}h_{1,1} + h_{2,2}^{*}h_{2,1} & |h_{1,2}|^2 + |h_{2,2}|^2 \end{bmatrix}$$

Zero Forcing with Successive Interference Cancellation (ZF-SIC)

Using the ZF equalization approach, the receiver can obtain an estimate of the two transmitted symbols x_1 and x_2 i.e.

$$\begin{bmatrix} \tilde{x}_1 \\ \tilde{x}_2 \end{bmatrix} = [H^H H]^{-1}H^H\begin{bmatrix} y_1 \\ y_2 \end{bmatrix} \ldots (4)$$

Taking one of the estimated symbols (for example$\tilde{x}_2$) and subtract its effect from the received vector $y_1$and y_2 , i.e.

$$\begin{bmatrix} r_1 \\ r_2 \end{bmatrix} = \begin{bmatrix} y_1 - h_{1,2} & \tilde{x}_1 \\ y_2 - h_{1,2} & \tilde{x}_2 \end{bmatrix} = \begin{bmatrix} h_{1,1} & x_1 + n_1 \\ h_{2,1} & x_1 + n_2 \end{bmatrix}$$

$$\begin{bmatrix} r_1 \\ r_2 \end{bmatrix} = \begin{bmatrix} h_{1,1} \\ h_{2,1} \end{bmatrix}x_1 + \begin{bmatrix} n_1 \\ n_2 \end{bmatrix}$$

$$r = hx_1 + n$$

This forms the simple explanation for Zero Forcing Equalizer with Successive Interference Cancellation (ZF-SIC) approach.

Zero Forcing-Successive Interference Cancellation with optimal ordering (ZF-SIC-Sort)

In traditional Successive Interference Cancellation, the receivers arbitrarily takes one of the estimated symbols, and subtract its effect from the received symbol$y_1$and y_2. Now we try to find out the transmit symbol (after multiplication with the channel) which came at higher power at the receiver. The received power at the both the antennas corresponding to the transmitted symbol x_1 is,

$$P_{x_1} = |h_{1,1}|^2 + |h_{2,1}|^2$$

The received power at the both the antennas corresponding to the transmitted symbol x_2 is

$$P_{x_2} = |h_{1,2}|^2 + |h_{2,2}|^2$$

If $P_{x_1} > P_{x_2}$then the receiver decides to remove the effect of $\tilde{x}_1$from the received vector $y_1$and y_2. Else if $P_{x_1} \leq P_{x_2}$the receiver decides to subtract effect of $\tilde{x}_2$from the received vector $y_1$and $y_2$and then estimate $\tilde{x}_1$.

5. CONSTELLATION OF QPSK SIGNAL

QPSK implementation involves changing the phase of the transmitted waveform. Unique digital data

represents each finite phase change. A phase modulated waveform can be generated by using the digital data to change the phase of a signal while its frequency and amplitude stay constant. A QPSK modulated carrier undergoes four distinct changes in phase that are represented as symbols and can take on the values of π/4, 3π/4, 5π/4, and 7π/4. Each symbol represents two binary bits of data. The constellation diagram of a QPSK modulated carrier is shown in figure 3.

The BER of each branch is the same as BPSK:

$$P_b = Q\left(\sqrt{2\gamma_b}\right) \ldots (5)$$

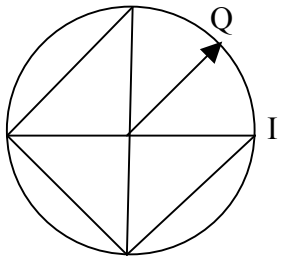

Figure 2: QPSK constellation Diagram

6. RALEIGH FADING CHANNEL

When there are many objects in the environment that scatter the radio signal, Rayleigh fading is an acceptable model before it arrives at the receiver. The central limit theorem expresses that, for sufficiently much scatter case, the channel impulse response will be well-modeled as a Gaussian process irrespective of the distribution of the individual components. If there is no dominant component of the scatter, then such a process will have zero mean and phase evenly distributed between 0 and 2π radians. The envelope of the channel response will therefore be Rayleigh distributed. In the case of random variable, the probability density function will be in the form of:

$$p_N(n) = \frac{2n}{\Omega} e^{-n^2}, n \geq 0 \ldots (6)$$

Where, $\Omega = E(N^2)$

7. SIMULATIONS AND PERFORMANCE ANALYSIS

The simulations are done for QPSK modulation and different combinations of MIMO systems using ZF equalizers. The BER values have been computed as a function of SNR. Then a comparative study for ZF equalizers with different condition has been carried out. The figure 3 shows the BER vs. average Eb/No for different MIMO systems with ZF equalizer. The simulations in this paper have been carried out using MATLAB software. From the fig. 3 it is clear that for ZF equalizer the bit error rate (BER) is lowest for 2x4 MIMO configurations in comparison to 2x3 and 2x2 MIMO configurations. For 2x4 configurations the bit error rate is similar to that of no diversity condition. As the transmit-receive antennas increase the BER vs. SNR graph shows an increased data rate by achieving minimum BER.

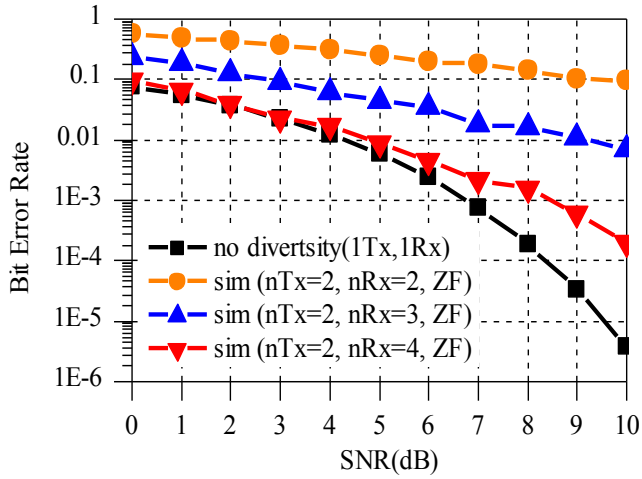

Figure 3: BER plot for QPSK modulation with MIMO and ZF equalizer

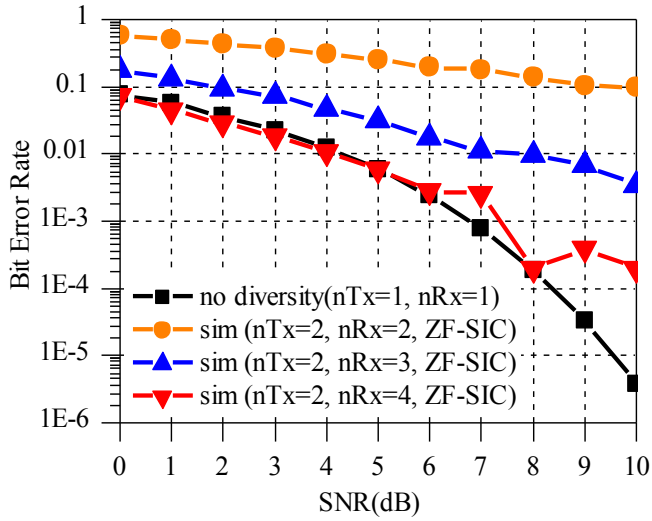

Figure 4: BER plot for QPSK modulation with MIMO and ZF-SIC equalizer

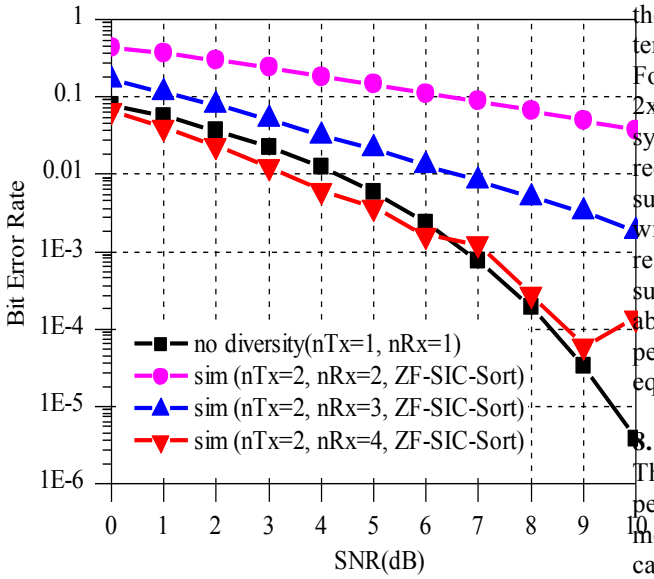

Figure 5: BER plot for QPSK modulation with MIMO and ZF-SIC-Sorted equalizer

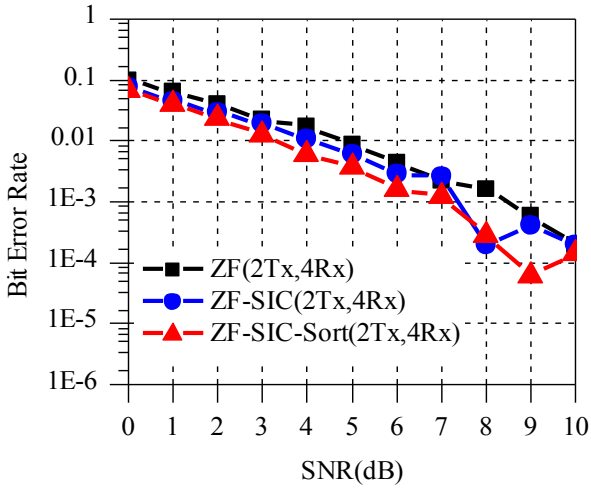

Figure 6: BER plot for QPSK modulation with 2x4 MIMO and comparison of ZF, ZF-SIC and ZF-SIC-Sort equalizers

Similarly, figure 4 and 5 shows BER vs. SNR characteristics for ZF equalizer with Successive Interference Cancellation and Successive Interference Cancellation with optimal ordering for QPSK modulation and various MIMO systems. These two figures shows that for 2x4 MIMO configurations the bit error rate (BER) shows an improvement compared to 2x3 and 2x2 MIMO configurations i.e. for higher order MIMO combinations the BER tends to decrease in terms of SNR. Finally figure 6 shows a graphical representation in which three types of ZF equalizer is compared on the basis of BER vs. SNR for 2x4 MIMO combinations. From the figure it is found that the ZF-SIC-Sort equalizer shows minimum BER in terms of SNR compared to ZF and ZF-SIC equalizer. For QPSK modulation the overall performance of 2x4 MIMO systems is better than 2x3 MIMO systems due to its improvement of transmit and receive diversity. When interference is cancelled in a successive order and arranged zero forcing equalizer with optimal order, the bit error rate is reduced with respect to simple zero forcing and zero forcing with successive interference cancelling. Hence from the above study it is evident that ZF-SIC-Sort equalizer performs better than other two forms of ZF equalizers.

8. CONCLUSION

This paper presents a comparative study on the performance of ZF Equalizer based QPSK modulation over MIMO system. From the results it can be concluded that, for a MIMO system the ZF equalizers promote in achieving better BER vs. SNR performances for QPSK modulation. From 2x3 and 2x4 MIMO combination, as the SNR increases the BER tends to decrease significantly for different forms of ZF equalizer. For higher order MIMO configurations the simulation studies show that ZF-SIC-Sort equalizer offers minimum BER than other two types of ZF equalizer.

9. ACKNOWLEDGMENT

I would like to cordial thanks to the Head, Department of Electrical and Electronic Engineering, Khulna University of Engineering and Technology (KUET). The research work was supported by communication laboratory and its annual allowance was taken from Khulna University of Engineering and Technology (KUET), Bangladesh.

REFERENCES

[1]. G. J. Foschini and M. J. Gans, "On limits of wireless communications in a fading environment when using multiple antennas," *Wireless Personal Comm.,* vol. 6, pp. 311-335, Mar. 1998.

[2]. V. Tarokh, N. Seshadri, and A. R. Calderbank, "Space-time codes for high data rate wireless communication: performance criterion and code construction," *IEEE Trans. Inf. Theory*, vol. 44, no. 2, pp. 744–765, Mar. 1998.

[3]. N.Sathish Kumar, Dr.K.R.Shankar Kumar, "Performance Analysis of M*N Equalizer based Minimum Mean Square Error (MMSE) Receiver for MIMO Wireless Channel" *International Journal of Computer Applications (0975 – 8887)* Volume 16– No.7, pp.47–50 February 2011.

[4]. Kuldeep Kumar and Manwinder Singh, "A comparison of different detection algorithms in a MIMO system," *International Journal of Advanced Engineering Sciences and Technologies,* vol. 7, no. 2, pp. 301–304, 2010.

[5]. Nagarajan Sathish Kumar, K. R. Shankar Kumar, "Bit Error Rate Performance Analysis of ZF, ML and MMSE Equalizers for MIMO Wireless Communication Receiver."*European Journal of Scientific Research ISSN 1450-216X* Vol.59 No.4 (2011), pp. 522-532.

[6]. V.Jagan Naveen, K.Murali Krishna, and K.RajaRajeswari, "Performance analysis of equalization techniques for MIMO systems in wireless communication," *International Journal of Smart Home* Vol.4, No.4, October, 2010.

[7]. Nirmalendu Bikas Sinha, R. Bera, M. Mitra "Capacity and V-BLAST Techniques for MIMO Wireless Channel, *"Journal of Theoretical and Applied Information Technology*.

[8]. Nirmalendu Bikas Sinha, S.Chakraborty, P. K. Sutradhar, R.Bera, M.Mitra, "Optimization of MIMO detectors: Unleashing the multiplexing gain" *Journal of Telecommunications,* Volume 1, Issue 1, February 2010.

Proceeding of the
International Conference on Electrical, Computer and Telecommunication Engineering
01- 02 December 2012 (ICECTE2012), RUET, Rajshahi-6204, Bangladesh

ICECTE2012: PI-0051

Bit Error Rate Analysis of QPSK modulation Technique in a MIMO Rayleigh fading channel by Maximum Likelihood Equalization

Sabuj Sarkar[1], Mohammad Shaifur Rahman[2]
[1]Electrical and Electronic Engineering, Khulna University of Engineering & Technology
Khulna-9203, Bangladesh
[2]Electrical and Electronic Engineering, Khulna University of Engineering & Technology
Khulna-9203, Bangladesh
E-mail: sabujeeekuet@gmail.com, msrbitk@yahoo.com

ABSTRACT
Multiple Input Multiple Output (MIMO) systems have recently emerged as one of the most promising technology in wireless communication systems that give tremendous advancement in achieving high data rates and improved system performance. In this paper, we discussed about the receiver structure called Maximum Likelihood (ML) Equalization and simulated this structure in a Rayleigh fading channel with QPSK modulation. Depending on bit error rates, we compared the performances of MIMO system for different combinations of transmit-receive structure. Simulation results showed that the BER can be improved by ML receiver for 2X4 MIMO Rayleigh fading channel than other lower order combinations.

KEY WORDS: MIMO; ML equalization; QPSK; MRC; BER; Rayleigh fading channel

1. INTRODUCTION

MIMO is a promising technology of modern wireless communication that uses multiple antennas at both Transmitter and Receiver and provides improved performance compared to conventional communication systems. The main idea behind MIMO is that the transmit antennas and the receive antennas are connected and combined in such a way that, the bit error rate (BER), or the data rate for each user is improved. MIMO has salient features which offers significant increases in data throughput and link range without additional bandwidth or increased transmit power. It is one of the important forms of smart antenna technology Due to these properties, MIMO is an important part of modern wireless communication standards such as IEEE 802.11n (Wi-Fi), 4G, 3GPP Long Term Evolution and WiMAX [1, 2]. The Maximum Likelihood (ML) equalization of signals transmitted over Multiple Input Multiple Output (MIMO) channels is an important technique in modern wireless communications. In this paper, the Bit Error Rate analysis of QPSK modulation technique in a MIMO Rayleigh fading channel by this technique has been performed. Maximum-Likelihood (ML) is the technique in which a search is performed over all possible symbols and the most likely one is chosen. It is the method in which the overall error probability can be minimized with lower level of complexity [3]. For a MIMO system with two-dimensional (2-D) constellations an upper bound of MLD was derived regarding the channel estimation is perfect and loose. In MIMO system maximum likelihood (ML) receiver play a vital role in determining bit error rate performance. By using ML detector a very high data rate can be achieved with little SNR penalty with a large number of receive antennas. In [4], for a 4x4 MIMO system the BER for various detection schemes like MMSE, ML and ZF has been analyzed and it showed that MIMO receiver with ML detection has the least BER for a given SNR. Depending on bit error rate, the performance of the receiver scheme indicates that the ordered SIC detector with Maximum-Likelihood (ML) detection most effectively balances the accuracy of symbol detection [5]. In [6], different signal detector schemes such as Maximum Likelihood (ML), Zero-Forcing (ZF), Minimum Mean-Square Error (MMSE), and Ordered Successive Interference Cancellation (SIC) has also been discussed. The performance of MIMO system with different modulation techniques in Raleigh Fading and AWGN channels has also been compared. Based on frame error rates and bit error rates, the performance and the computational complexity of these schemes with other existence model have also been analyzed. The ultimate target for MIMO wireless communication system is to achieve high data-rate and high performance [7], [8]. ML equalizer out performs both ZF and MMSE equalizer techniques in terms of BER performance characteristics [9].

The present study involves a number of procedures mainly simulations of the 2X2, 2X3 and 2X4 MIMO system and comparison of BER for different SNR. The aim of the study is to identify the appropriate transmit-receive techniques for ML system that gives

the best bit error rate performance for QPSK modulation.

2. MIMO CONFIGURATION

Let us consider a MIMO system containing T transmit-antennas and R receive-antennas. The received signal in the j^{th}antenna is given by

$Y_j = \sum_{k=1}^{R} h_{jk}\ x_k + r_k$ …… *(1)*

Where, j = 1, 2, 3…R, h_{jk} is the fading corresponding to the path from transmit antenna k to receive antenna j. $r_j$is the noise corresponding to receive antenna j.

$$y = \begin{bmatrix} y_1 \\ y_2 \\ \vdots \\ y_R \end{bmatrix} \cdots (2), x = \begin{bmatrix} x_1 \\ x_2 \\ \vdots \\ x_R \end{bmatrix} \ldots (3)$$

$$r = \begin{bmatrix} r_1 \\ r_2 \\ \vdots \\ r_R \end{bmatrix} \cdots (4), x = \begin{bmatrix} h_{11} & \cdots & h_{1T} \\ h_{21} & & h_{2T} \\ \vdots & \ddots & \vdots \\ h_{R1} & \cdots & h_{RT} \end{bmatrix} \ldots (5)$$

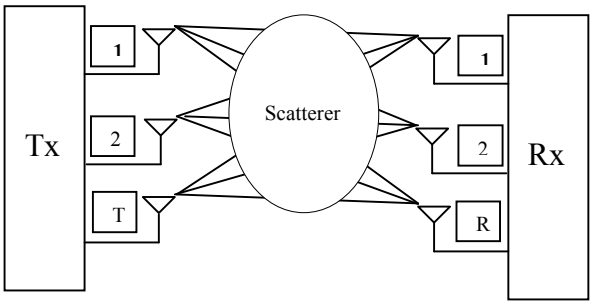

Figure1: MIMO communication system containing T transmit and R receives antennas

The above wireless channel is modulated by the theorem $y = Hx + r$ formula. Where, H is the channel matrix and r is the channel noise. For transmit/receive beam forming the diversity of order TR, is considered as full diversity. On the other hand, the antenna gain is; Max = {T, R} ≤antenna gain ≤TR.

3. MAXIMUM LIKELIHOOD (ML) EQUALIZER

The Maximum Likelihood equalizer tries to search the most likelihood one which minimizes,

$$J = |y - Hx|^2$$

$$J = \left| [\begin{bmatrix} y_1 \\ y_2 \end{bmatrix} - \begin{bmatrix} h_{1,1} & h_{1,2} \\ h_{2,1} & h_{2,2} \end{bmatrix} \begin{bmatrix} x_1 \\ x_2 \end{bmatrix} \right|^2$$

In a QPSK modulation the possible values are 11, 10, 01, and 00. In order to find the Maximum Likelihood one, we have to find the minimum from the all four combinations of

$$J_{11} = \left| [\begin{bmatrix} y_1 \\ y_2 \end{bmatrix} - \begin{bmatrix} h_{1,1} & h_{1,2} \\ h_{2,1} & h_{2,2} \end{bmatrix} \begin{bmatrix} 11 \\ 11 \end{bmatrix} \right|^2$$

$$J_{10} = \left| [\begin{bmatrix} y_1 \\ y_2 \end{bmatrix} - \begin{bmatrix} h_{1,1} & h_{1,2} \\ h_{2,1} & h_{2,2} \end{bmatrix} \begin{bmatrix} 11 \\ 10 \end{bmatrix} \right|^2$$

$$J_{01} = \left| [\begin{bmatrix} y_1 \\ y_2 \end{bmatrix} - \begin{bmatrix} h_{1,1} & h_{1,2} \\ h_{2,1} & h_{2,2} \end{bmatrix} \begin{bmatrix} 01 \\ 11 \end{bmatrix} \right|^2$$

$$J_{00} = \left| [\begin{bmatrix} y_1 \\ y_2 \end{bmatrix} - \begin{bmatrix} h_{1,1} & h_{1,2} \\ h_{2,1} & h_{2,2} \end{bmatrix} \begin{bmatrix} 00 \\ 00 \end{bmatrix} \right|^2$$

The estimate of the transmit symbol is chosen based on the minimum value from the above four values i.e. if the minimum is, J_{11} ⇒[11 11], if the minimum is, J_{10} ⇒[11 10] if the minimum is, J_{01} ⇒[01 11] and if the minimum is, J_{00} ⇒[00 00]. ML equalizer is the method which compares the received signals with all possible transmitted signal that is modified by channel matrix H and estimates transmit symbol vector x according to the Maximum Likelihood principle , which is shown as:

$$x = arg_{x_k} \epsilon \{x_1 \quad x_2 \quad \cdots \quad x_Q\} min \|q - Hx_k\|^2$$

Where, x is the estimated symbol vector. Although ML detection offers optimal error performance, it suffers from complexity issues. It has exponential complexity in the sense that the receiver has to consider $|A|^P$ possible symbols for a P transmitter antenna system with A is the modulation constellation.

4. CONSTELLATION OF QPSK SIGNAL

QPSK implementation involves changing the phase of the transmitted waveform. Unique digital data represents each finite phase change. A phase modulated waveform can be generated by using the digital data to change the phase of a signal while its frequency and amplitude stay constant. A QPSK modulated carrier undergoes four distinct changes in phase that are represented as symbols and can take on the values of π/4, 3π/4, 5π/4, and 7π/4. Each symbol represents two binary bits of data. The constellation diagram of a QPSK modulated carrier is shown in figure 2. The BER of each branch is expressed by:

P_b=Q ($\sqrt{2\gamma_b}$)

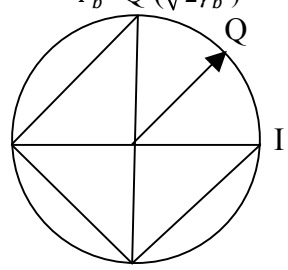

Figure 2: QPSK constellation Diagram

5. RAYLEIGH FADING CHANNEL

When there are many objects in the environment that scatter the radio signal, Rayleigh fading is an acceptable model before it arrives at the receiver. The central limit theorem expresses that, for sufficiently much scatter case, the channel impulse response will be well-modeled as a Gaussian process irrespective of the distribution of the individual components. If there is no dominant component to the scatter, then such a process will have zero mean and phase evenly distributed between 0 and 2π radians. The envelope of the channel response will therefore be Rayleigh distributed. In the case of random variable, the probability density function will be in the form of:

$$p_Q(q) = \frac{2q}{\Omega} e^{-q^2}, q \geq 0$$

Where, $\Omega = E(Q^2)$

The gain and phase elements of a channel's distortion are conveniently represented as a complex number. In this case, Rayleigh fading is exhibited by the assumption that the real and imaginary parts of the response are modeled by independent and identically distributed zero-mean Gaussian processes so that the amplitude of the response is the sum of four such processes.

6. MAXIMAL RATIO COMBINING

The bit-error rate of QPSK in a Rayleigh fading channel can be determined by MRC technique. The probability of bit-error rate for QPSK $P_b$can be determined by using the formula given below:

$$P_b = \frac{1}{\pi} \int_0^{3\pi/4} \left[det\left(\frac{\sum sin^2(\pi/4)}{sin^2\theta} \right) + I \right]^{-1} d\theta$$

For multiple eigen values the formula can be written as:

$$P_b = \frac{1}{\pi} \int_0^{3\pi/4} \sum_{n=1}^{N} \sum_{s=1}^{m_n} r_s, n \left[det\left(\frac{\overline{\gamma}_n \lambda_n \sum sin^2(\pi/4)}{sin^2\theta} \right) + I \right]^{-1} d\theta$$

The maximal-ratio combining is a method of diversity combining in which the signals from each channel are added together, the gain of each channel is made proportional to the rms signal level and inversely proportional to the mean square noise level in that channel and different proportionality constants are used for each channel. Maximal-ratio-combining is the optimum combiner for independent AWGN channels.

7. SIMULATIONS AND PERFORMANCE ANALYSIS

The performance for QPSK systems is simulated and evaluated by using MATLAB software. Depending on data generated by computer simulation of QPSK modulation techniques for BER calculation the following results are obtained.

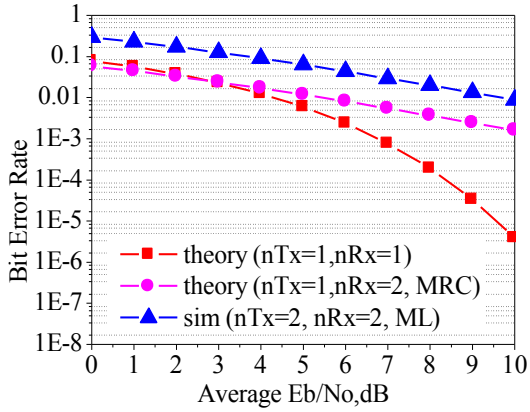

Figure 3: BER plot 2×2 MIMO Rayleigh channel with Maximum Likelihood equalization

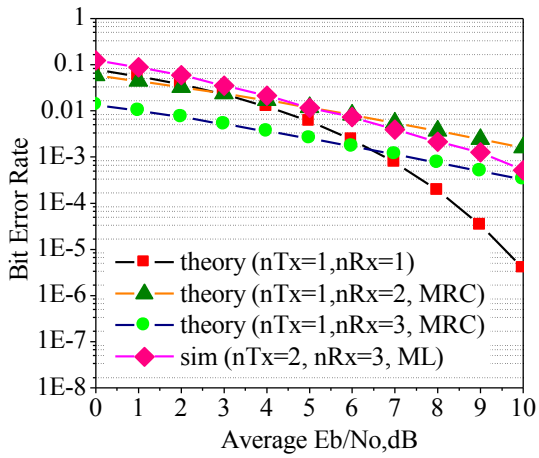

Figure 4: BER plot 2×3 MIMO Rayleigh channel with Maximum Likelihood equalization

Fig 4, 5, 6 describe Bit Error Rate (BER) versus Signal-to-Noise ratio (SNR) in a MIMO Rayleigh fading channel for QPSK modulation scheme with Maximum Likelihood equalization technique. The simulation is done for different combinations such as 2x2; 2x3; 2x4 and their theoretical and simulated performance are evaluated. The simulation and evaluation results for different combinations of MIMO with Maximum Likelihood (ML) equalization helped us to achieve a performance closely matching with the theoretical results for 1 transmit 2 receive antenna for 2x2 and 2x3 Maximal Ratio Combining

(MRC) and for 2x4 combinations the simulated performance are even better for any other theoretical performance.

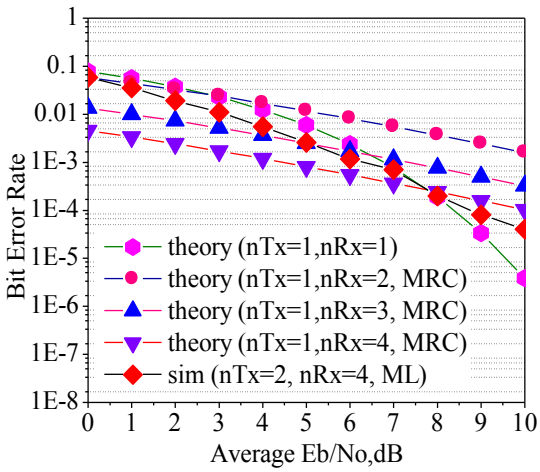

Figure 5: BER plot 2×4 MIMO Rayleigh channel with Maximum Likelihood equalization

The overall system performance of 2x4 MIMO systems is better than 2x2 and 2x3 MIMO systems for QPSK modulation due to its improvement of transmit and receive diversity. Although it is seen from the simulation that in case of higher transmit-receive antennas by MRC technique the bit-error rate performance can be improved. But by ML equalization the overall performance of 2x4 MIMO combinations the simulated results outperforms even the MRC technique i.e. it's performance can be even better. By increasing more receiving antennas the bit error rate tends to decrease in a significant manner. As it is seen from 2 transmit 4 receive antennas the bit error rate for 2 transmit 4 receive maximum likelihood equalization is closely similar to that1 transmit 3 receive antennas and 1 transmit 4 receive antennas. As the bit error rate tends to reduce in the receiver then more and more symbols i.e. data is detected in receiver stage. As a result, the performance becomes more and more accurate.

8. CONCLUSION

In this paper, we have introduced Maximum Likelihood equalization with different combination of MIMO system and compare the BER with MRC technique for QPSK modulation. The comparison of performance between 2x3 and 2x4 MIMO techniques with maximum likelihood equalization indicates that while SNR tend to increasing, bit error rate tends to decreasing. From the simulation studies, it can be concluded that the 2×4 MIMO Rayleigh channel with Maximum Likelihood equalization systems offers better BER performances for QPSK modulation, as a result improved bit error rate is achieved.

9. ACKNOWLEDGMENT

I would like to cordial thanks to the Head, Department of Electrical and Electronic Engineering, Khulna University of Engineering and Technology (KUET). The research work was supported by communication laboratory and its annual allowance was taken from Khulna University of Engineering and Technology (KUET), Bangladesh.

REFERENCES

[1].Dr.Jacob Sharony, "Introduction to Wireless MIMO–Theory and Applications", *IEEE LI*, November 15, 2006.

[2]. R Bhagya , Dr. A G Ananth" Study of Transmission Characteristics of 2x2 MIMO System Techniques and ZF Equalizer Receiver" *IJCSET* June 2011 | Vol 1, Issue 5, pp.210-213.

[3]. Xu Zhu and Ross D. Murch, "Performance Analysis of Maximum Likelihood Detection in a MIMO Antenna System" *IEEE Transactions on Communications*, Vol. 50, NO. 2, pp.187-191, February 2002.

[4]. Kuldeep Kumar* et al, "A comparison of different detection algorithms in a MIMO system" (IJAEST) *International Journal of Advanced Engineering Sciences and Technologies* Vol No. 7, Issue No. 2, 301 – 304.

[5]. Nirmalendu Bikas Sinha, S.Chakraborty, P. K. Sutradhar, R.Bera, M.Mitra,"Optimization of MIMO detectors: Unleashing the multiplexing gain" *Journal of Telecommunications*, Volume 1, Issue 1, February 2010.

[6]. Nirmalendu Bikas Sinha, S.Chakraborty, P. K. Sutradhar1, R.Bera and M.Mitra"Optimization of MIMO detectors: Unleashing the multiplexing gain" *Journal of Telecommunications*, Volume 1, Issue 1, February 2010.

[7]. G. J. Foschini and M. J. Gans, "On limits of wireless communications in a fading environment when using multiple antennas," *Wireless Personal Commun.*, vol. 6, pp. 311-335, Mar. 1998.

[8]. V. Tarokh, N. Seshadri, and A. R. Calderbank, "Space-time codes for high data rate wireless communication: performance criterion and code construction," *IEEE Trans. Inf. Theory*, vol. 44, no. 2, pp. 744–765, Mar. 1998.

[9]. Nagarajan Sathish Kumar, K. R. Shankar Kumar "Bit Error Rate Performance Analysis of ZF, ML and MMSE Equalizers for MIMO Wireless Communication Receiver."*European Journal of Scientific Research ISSN 1450-216X* Vol.59 No.4 (2011), pp. 522-532.

Proceeding of the
International Conference on Electrical, Computer and Telecommunication Engineering
01- 02 December 2012 (ICECTE2012), RUET, Rajshahi-6204, Bangladesh

ICECTE2012: PI-0052

BER Performance Analysis of OFDM System using M-PSK Modulation Scheme over AWGN Channel

Tushar Kanti Roy[1] and S M Abdur Razzak [2]
[1]Department of Electronics and Telecommunication Engineering
[2]Department of Electrical and Electronic Engineering
Rajshahi University of Engineering & Technology
Rajshahi-6204
[1]E-mail: roy_kanti@yahoo.com

ABSTRACT
Orthogonal frequency division multiplexing (OFDM) is becoming the chosen modulation technique for wireless communications. It can provide large data rates and is sufficiently robust in the face of radio channel impairments. Digital modulation techniques contribute to the evolution of our mobile wireless communications by increasing the capacity, speed and quality of wireless networks. In this paper, we concentrate on digital modulation scheme, such as M-PSK (M-Phase Shift keying) over an additive white Gaussian noise (AWGN) channel to analyze the performance of an OFDM system in terms of the bit error rate (BER). This is evaluated through a computer simulation, the results from which make it clear that when we continue to increase the E_b/N_0 value, the BER reduces.

KEY WORDS: AWGN, BER, OFDM, M-PSK.

1. INTRODUCTION

The growth in the use of information networks has led to the need for new communication techniques with higher data rates. OFDM is a powerful modulation technique used to achieve a high data rate and is able to eliminate inter-symbol interference (ISI). It is computationally efficient due to the use of fast Fourier transform (FFT) techniques for implementing modulation and demodulation functions. In an OFDM scheme, a large number of orthogonal, overlapping, narrow band sub-channels or sub-carriers transmitted in parallel and divide the available transmission bandwidth. Also it is used in many new broadband communication schemes including digital television, digital audio broadcasting, ADSL and wireless LANs. It also allows digital data to be efficiently and reliably transmitted over a radio channel, even in multipath environments [1-3]. In OFDM, although sub-carriers overlap, this does not create any problem since they are orthogonal, that is, the peak of one occurs when that of the other are at zero. This is achieved by realizing all the subcarriers together using the inverse fast Fourier transform (IFFT). BER performance of an OFDM system using BPSK modulation over AWGN and Rayleigh fading channel is analyzed in [4]. Analysis of BER performances have suggested that OFDM is better than CDMA which is currently incorporated in most existing 3G systems [5, 6]. A major problem in most wireless systems is the presence of a multipath channel. In this environment, the transmitted signal reflects off of several objectives and a result multiple delayed versions of the transmitted signal arrive at the receiver which causes the received signal to be distorted. Many wired systems also have a similar problem with reflections occurring due to impedance mismatches in the transmission line. A multipath channel will cause two problems for an OFDM system. The first is ISI which occurs when the received OFDM symbol is distorted by the previously transmitted OFDM symbol and has a similar effect to the ISI that occurs in a single-carrier system. However, in the latter systems, the interference is typically due to several symbols other than only the previous symbol and the symbol period is typically much shorter than the time span of the channel, whereas the typical OFDM symbol period is much longer than the time span of the channel. The second problem is unique to multicarrier systems and is called intra-symbol interference (ISI) which is the result of interference amongst a given OFDM symbol's own sub-carriers. The concept of OFDM is quite simple but its practical implementation involves many complexities. A single stream of data is split into parallel streams each of which is coded and modulated on to a subcarrier, a term commonly used in OFDM systems. Thus, as the high bit rates previously seen on a single carrier are reduced to lower bit rates on its. It is easy to see that ISI will be dramatically reduced. An adaptive modulation and coding technique for overcoming any ISI and analyzing the performance of the BER is proposed in [7]. Comparative BER performance of digital modulation techniques under multipath fading is addressed in [5], in which the performance of the

OFDM is tested for M-PSK and M-QAM using MATLAB. The performance of different modulation schemes for the OFDM based WLAN standard IEEE 802.11a is discussed in [8].

The main purpose of this paper is to present the commonly used modulation schemes in wireless communication systems and demonstrate the performances of the M-PSK modulated system with OFDM in the presence of a noisy channel and indicate the ways of reducing the BER. Therefore throughout this paper, we present BER performance comparisons for M-PSK modulation scheme using the OFDM technique over an AWGN channel.

The rest of this paper is organized as follows. Section 2 briefly introduces the OFDM system model in which we describe the OFDM transmit and receive signals mathematical equations, the relationship between E_s/N_0 and E_b/N_0 for the OFDM system and cyclic prefix for OFDM. Section 3 discusses the simulation results and conclusions are presented in section 4.

2. SYSTEM MODELLING

2.1 OFDM Transceiver

In this section, we describe the OFDM transceiver system. Before transmitting information bit over an AWGN channel through the OFDM transmitter, we use the M-PSK modulation scheme shown in Fig.1. The transmitter section converts the digital data to be transmitted into a mapping of the sub-carrier's amplitude and phase using modulation techniques. The spectral representation of the data is then transformed into the time domain using an inverse fast Fourier transform (IFFT) which is much more computationally efficient and is used in all practical systems [9, 10]. The addition of a cyclic prefix to each symbol solves both ISI and inter-carrier interference (ICI) [11, 12]. The digital data is then transmitted over the channel. After the time-domain signal passes through the channel, it is broken down into the parallel symbols and the prefix is simply discarded. The receiver performs the reverse operation to that of the transmitter. The amplitude and phase of the sub-carriers are then selected and converted back to digital data. In OFDM multiple sinusoidal with frequency separations $(\frac{1}{T})$ are used, where T is the active symbol period. The information (g_k) to be sent on each sub-carrier (k) is multiplied by its corresponding carrier ($g_k(t) = e^{\frac{j2\pi kt}{T}}$) and the sum of such modulated sinusoidal forms the transmit signal. Therefore, the sinusoidal used in OFDM can be defined as [13]:

$$g_k(t) = \frac{1}{\sqrt{T}} e^{\frac{j2\pi kt}{T}} w(t) \qquad (1)$$

where $k = 0, 1, \ldots N-1$ correspond to the frequency of the sinusoidal and $w(t) = u(t)-u(t-T)$ is a regular window over $[0, T]$. Since the OFDM system uses multiple sinusoidal signals with frequency separation of $\frac{1}{T}$, each sinusoidal is modulated by independent information. Mathematically we can write a transmit signal through the channel as:

$$\begin{aligned} S(t) &= \delta_0 g_0(t) + \delta_1 g_1(t) + \ldots + \delta_{N-1} g_{N-1}(t) \qquad (2) \\ &= \sum_0^{N-1} \delta_k g_k(t) \\ &= \frac{1}{T} \sum_0^{N-1} \delta_k e^{\frac{j2\pi kt}{T}} w(t) \end{aligned}$$

where δ_k is the kth symbol in the message symbol sequence for k in $[0, N-1]$, where N is the number of carriers.

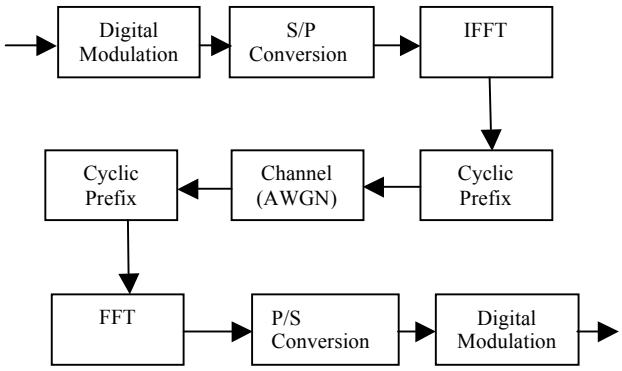

Figure 1: Block diagram of a basic OFDM transceiver

In an OFDM receiver, we multiply the received signal by a bank of correlators and integrate it over period T. Therefore, the information sent on subscriber k is:

$$\frac{1}{T}\int_T s(t) e^{-\frac{j2\pi mt}{T}} = \begin{cases} g_k, & m = k \\ 0, & m \neq k \end{cases} \qquad (3)$$

where m takes its values from 0 to $k-1$.

As we consider the AWGN channel, we can remove the frequency domain equalizer block from the above OFDM transceiver system because a frequency domain equalizer is helpful only if the channel introduces multipath fading.

2.2 Relationship Between E_s/N_0 and E_b/N_0 for OFDM System

This section presents the relationship between the E_s/N_0 and E_b/N_0 for the OFDM system. To conduct a Monte Carlo simulation of an OFDM system, the required amount of channel noise to be generated has to be representative of the required E_b/N_0. In MATLAB it is easy to generate a Gaussian noise with a zero mean and unit variance which has to be scaled accordingly to represent the required E_b/N_0 or E_s/N_0. Normally, for a simple BPSK system, the bit energy and symbol energy are the same. So E_b/N_0 and E_s/N_0 are same for a BPSK system. If we use an M-PSK modulation scheme for the OFDM system then they are not the same because, each OFDM symbol contains an additional overhead in both the time and frequency domains. In the time domain, the cyclic prefix is an additional overhead to each OFDM symbol being transmitted. In the frequency domain, not all the subcarriers are utilized to transmit the actual data bits, as a few are unused and reserved as guard bands. The relationship between the symbol energy and bit energy is [3]:

$$\frac{E_s}{N_0} = \frac{E_b}{N_0}\left(\frac{n.DSC}{n.FFT}\right)\left(\frac{T_d}{T_d + T_{cp}}\right) \quad (4)$$

If we express the above equation in db, we can write:

$$\frac{E_s}{N_0}db = \frac{E_b}{N_0}db + 10\log_{10}\left(\frac{n.DSC}{n.FFT}\right) + 10\log_{10}\left(\frac{T_d}{T_d + T_{cp}}\right) \quad (5)$$

where T_d is the data symbol duration, T_{cp} the cyclic prefix duration and $n.DSC$ the number of subscribers used in the OFDM system.

2.3 Cyclic Prefix of OFDM

This section describes the cyclic prefix of the OFDM system. Since orthogonality is an important property for an OFDM system, its synchronization in frequency and time must be extremely good. Once orthogonality is lost we experience ICI which introduces interference from one sub-carrier to another. Another reason for ICI in an OFDM system is that if we add the guard time with no transmission this creates problems for the IFFT and FFT, which results in ICI. Although a delayed version of one sub-carrier can interfere with another sub-carrier in the next symbol period, this can be avoided by extending the symbol into the guard period preceding it which is known as a cyclic prefix. It ensures that delayed symbols have integer numbers of cycles within the FFT integration interval which removes ICI providing the delay spread is less than the guard period. We should note that a FFT integration period excludes the guard period. In an OFDM transmission, we know that transmission of the cyclic prefix does not carry 'extra' information over the AWGN channel. The signal energy is spread over time T_d+T_{cp} whereas the bit energy is spread over time T_d, i.e.:

$$E_s(T_d + T_{cp}) = E_b T_d \quad (6)$$

After simplification, we obtain:

$$E_s = \frac{T_d}{(T_d + T_{cp})} E_b \quad (7)$$

3. SIMULATION RESULTS

In this section, we present the BER performances of the OFDM system for M-PSK digital modulation scheme over an AWGN channel investigated by means of a computer simulation using MATLAB. The performance of a data transmission system is usually analyzed and measured in terms of its probability of error at a given bit rate and SNR. The parameter E_b/N_0, where E_b is the bit energy and N_o the noise energy, is adjusted every time by changing the noise in the designated channel.

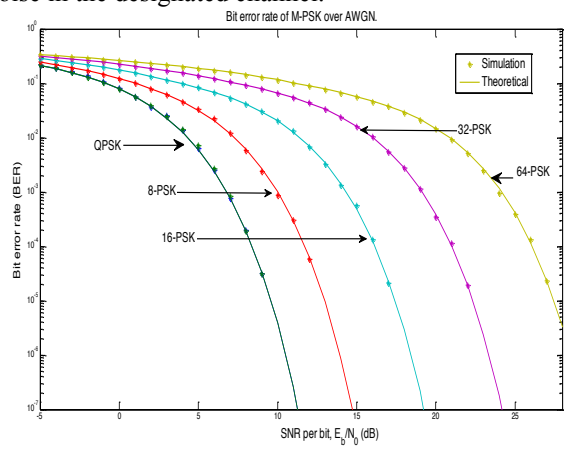

Figure 2: BER of an OFDM system using M-PSK scheme over AWGN channel

The BER performance results for an OFDM system with M-PSK modulation over an AWGN channel from the simulation results are shown in Figure 2. From the simulation result it can be observed that if we continue to increase the E_b/N_0 value, the BER reduces. In comparison of the BER performance for M-PSK also it is observed that use of a higher M-PSK is better for high capacity data transmission.

4. CONCLUSIONS

In this paper, we have evaluated the BER performance of an OFDM system for digital

modulation scheme M-PSK over an AWGN channel. OFDM is a powerful modulation technique used to achieve high data rate and is able to eliminate ISI. It is computationally efficient due to its use of FFT techniques for implementing modulation and demodulation functions. It is observed from the M-PSK BER plots that the BER is less in the case of 4-PSK for low E_b/N_0 than 8-PSK and 16-PSK cases. Hence, as a higher value of M-PSK increases spectrum efficiency, but is easily affected by noise, the OFDM system with the M-PSK scheme is used for large-capacity, long-distance applications at the cost of slight increase in E_b/N_0 while that with the QPSK scheme is suitable for low-capacity, short-distance applications.

5. FUTURE WORK

Future works will deal with the implementation of the proposed digital modulation technique on the real OFDM system to prove it feasibility in real applications.

REFERENCES

[1] J. Chuang and N. Sollenberger, "Beyond 3G: Wideband wireless data access based on OFDM and dynamic packet assignment," *IEEE Communications* Mag., vol. 38, pp. 78–87, July 2000.

[2] Saltzberg, B. R., "Performance of an Efficient Parallel Data Transmission System," *IEEE Trans. on Communications*, Vol. COM-15, No. 6, December 1967, pp. 805–811.

[3] A.G.Armada, "Understanding the Effects of Phase Noise in OFDM," *IEEE Transaction on Broadcasting*, vol. 47, No.2, June 2001.

[4] Tushar Kanti Roy,"Comparative BER Performance Analysis of OFDM System using BPSK Modulation Technique over AWGN and Rayleigh Fading Channel" International Journal of Applied Research in Computer Science and Information Technology, Vol. 1, No. 3, p. 9-16, ISSN: 1839-8480, Australia, Jul. 2012.

[5] Mehul Jain and M. Mani Roja, " Comparison of OFDM with CDMA System in Wireless telecommunication for multipath delay spread," *The 1st IEEE and IFIP International Conference in Central Asia*, 26-29 Sept., 2005, Pages 5.

[6] Bernard Sklar, Digital Communication Fundamentals and Applications, Second Edition, Pearson Education, Asia, 2000.

[7] Sami H. O. Salih, Mamoun M. A. Suliman, "Implementation of Adaptive Modulation and Coding Techniques using Matlab," *53rd International Symposium ELMAR*-2011, 14-16 September 2011, Zadar, Croatia.

[8] Sanjeev Kumar, Swati Sharma, "Error Probability of Different Modulation Schemes for OFDM based WLAN standard IEEE 802.11a", *International Journal of Engineering (IJE),* Volume: 4, Issue: 4

[9] L. Hanzo, W. Webb, and T. Keller, "Single and Multi-carrier Quadrature Amplitude Modulation", New York, USA: *IEEE Press-John Wiley*, April 2000.

[10] S. B. Weinstein and P. M. Ebert, "Data transmission by frequency division multiplexing using the discrete Fourier transform," *IEEE Transactions on Communication Technology*, vol. COM–19, pp. 628–634, October 1971.

[11] X. Cai and G. B. Giannakis, "Low-complexity ICI suppression for OFDM over time- and frequency-selective Rayleigh fading channels," *in Proc. Asilomar Conf. Signals, Systems and Computers*, Nov. 2002.

[12] Shaoping Chen and Cuitao Zhu, "ICI and ISI Analysis and Mitigation for OFDM Systems with Insufficient Cyclic Prefix in Time-Varying Channels" *IEEE Transactions on Consumer Electronics,* Vol. 50, No. 1, February 2004.

[13] M. S. Islam, G. R. Barai, and A. Mahmood, "Performance analysis of different schemes using OFDM techniques in Rayleigh fading channel," *International Journal of Fundamental Physics Science*, Vol. 1, No. 1, pp. 22-27, June, 2011.

Proceeding of the
International Conference on Electrical, Computer and Telecommunication Engineering
01- 02 December 2012 (ICECTE2012), RUET, Rajshahi-6204, Bangladesh

ICECTE2012: PI-0053

Performance Improvement of Space Time Block Coded MIMO-OFDM Wireless Communication System

Md. Mejbaul Haque[1], M.A. Motin[2], Mohammad Shaifur Rahman[3], Ki-Doo Kim[4]
[1,3]Department of Electrical and Electronic Engineering
Khulna University of Engineering & Technology
[2]Department of Electrical and Electronic Engineering
Rajshahi University of Engineering & Technology
[4]Department of Electronics Engineering, Kookmin University
Seoul 136-702, Korea
E-mail: mmhaque.eee@gmail.com

ABSTRACT
MIMO-OFDM technology is a combination of Multiple-Input Multiple-Output (MIMO) wireless technology and Orthogonal Frequency Division Multiplexing (OFDM) that has been recognized as one of the most promising techniques to support high data rate and high performance in wireless communication systems. Again, Alamouti's space time block coding scheme for MIMO system has drawn much attention in 4G wireless technologies just because of its decoding simplicity. This paper presents the performance improvement of Space-Time Block Coded (STBC) MIMO-OFDM in terms of Bit Error Rate (BER) with the variation of the number of antennas in the system. It is observed that the BER decreases significantly with the inclusion of the number of antennas in the system for a particular SNR.

KEY WORDS: MIMO, OFDM, STBC, BER.

1. INTRODUCTION

The key challenge of future wireless communication systems is to provide high data rate wireless access at high quality of service. During the last decade, many researchers have proposed Multiple-Input Multiple-Output (MIMO) wireless technology that offers increased spectral efficiency through spatial multiplexing gain and improved link reliability due to antenna diversity gain [1-2]. In addition, using multiple antennas both at transmitter and receiver end can potentially meet the growing demands for high capacity in wireless communications [3-4].The information capacity of wireless communication systems increases dramatically by using multiple transmitting and receiving antennas. Space-time coding, an effective approach for increasing data rate over wireless channels, employs coding techniques appropriate to multiple transmitting and receiving antennas. Hence, a new generalized complex orthogonal space time block code for several transmit antennas with full rate is proposed in [5-6]. In the fourth generation wireless communication systems, the data rate may be as high as 1Gbps. For that, space-time coding technique is proposed in conjunction with the Multi-Carrier Code Division Multiple Access (MC-CDMA) system to achieve very high data rate [7]. Different types of space-time trellis and block codes are proposed for MC-CDMA systems in [8]. Many literatures has proposed space-time block coding schemes for Orthogonal Frequency Division Multiplexing (OFDM) systems based on the Alamuoti's scheme [9]. In frequency selective fading channels, Space-Time Coded OFDM is a popular approach to provide transmit diversity and coding gains, which are termed as space-time trellis coded OFDM [10] and Space-Time Block Coded OFDM [11-15]. In particular, the combination of Orthogonal Space Time Block Codes (OSTBCs) and OFDM, or simply OSTBC-OFDM has drawn much attention because it attains the maximum transmit diversity and has a simple maximum-likelihood (ML) receiver structure [12-16]. OFDM has already been used successfully in standards for Digital Audio Broadcasting (DAB), Terrestrial Digital Video Broadcasting (DVB-T), and Wireless Local Area Networks (WLANs) [16]. In this paper, we present the performance of Alamouti's STBC coded MIMO-OFDM system for various antenna configurations to fulfill the demand of 4G wireless technology. A brief discussion on Alamouti's STBC is presented. Simulation results of Alamouti's STBC with various antenna configurations are analyzed to evaluate the performance in terms of BER.

2. STBC MIMO-OFDM SYSTEM MODEL

Consider a space time block coded MIMO-OFDM system [17] equipped with N_T transmit antennas and N_R receive antennas as illustrated in Fig. 1. The message bit sequence is mapped into a sequence of BPSK symbols which is then converted into N parallel symbol streams after serial-to-parallel (STP) conversion. Each of the N parallel symbol streams is then encoded by the Space-Time Block Code (STBC) encoder into $\left\{X_i^{(t)}\right\}_{i=1}^{N_T}$ $i = 1,2,3,\cdots\cdots,N_T$ where i is the antenna index and t is the symbol time index. The number of symbols in a space-time codeword is $N = N_T \times T$. Then the symbol streams are subjected to Inverse Fast Fourier Transform (IFFT) operation followed by cyclic prefix insertion between two consecutive OFDM symbols in order to reduce the effect of the delay spread of the multipath channels.

(1), where z_j^t is the noise process at the jth receive antenna during t^{th} symbol period, which is modeled as the zero mean circular symmetric complex Gaussian (ZMCSCG) noise of unit variance, and is the average energy of each transmitted signal. In general we can write in Eq. (2)

$$y_j^t = \sqrt{\frac{E_x}{N_T N_0}}\begin{bmatrix} h_{j1}^t & h_{j2}^t & h_{j3}^t \cdots h_{jN_T}^t \end{bmatrix}\begin{bmatrix} X_1^t \\ X_2^t \\ X_3^t \\ \vdots \\ X_{N_T}^T \end{bmatrix} + z_j^t \quad (1)$$

$$Y = \sqrt{\frac{E_x}{N_T N_0}} HX + Z \quad (2)$$

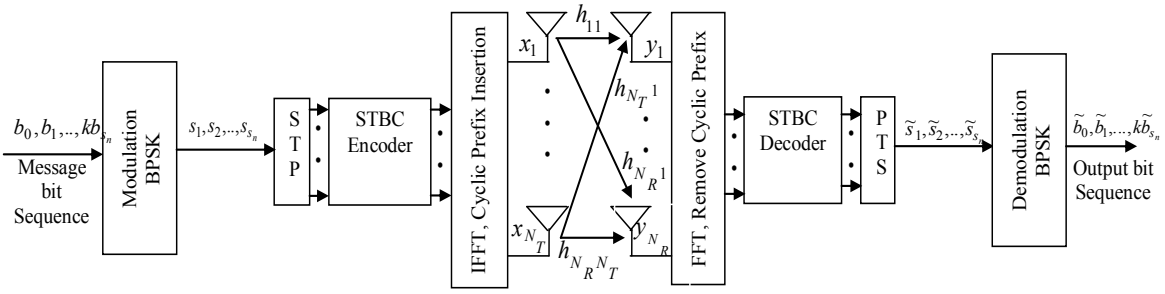

Fig. 1: Block diagram of STBC MIMO-OFDM System

The length of the CP is adjustable and is set in order to keep a bandwidth efficient system without occurring inter symbol interference or inter carrier interference. At the receiver, after removing the CP, and applying FFT, the transmitted symbol stream $\left\{\tilde{X}_i^{(t)}\right\}_{i=1}^{N_T}$ is estimated using the received signal $\left\{\tilde{Y}_j^{(t)}\right\}_{j=1}^{N_R}$. Assume the channel gain matrix h_{ji}^t follows the Rayleigh distribution from the ith transmit antenna to the jth receive antenna over the tth symbol period. If the channel gains do not change during T symbol periods, the symbol time index can be omitted and as long as the transmit antennas and receive antennas are spaced sufficiently apart, $N_T \times N_R$ fading gains $\{h_{ij}\}$ can be assumed to be statistically independent. If X_i^T is the transmitted signal from the ith transmit antenna during t^{th} symbol period, the received signal at the jth receive antenna during t^{th} symbol period is given by Eq.

Alamouti in [18]. In the Alamouti's encoder, two consecutive symbols x_1 and x_2 are encoded with the following space-time codeword matrix as follows

$$X = \begin{bmatrix} x_1 & -x_2^* \\ x_2 & x_1^* \end{bmatrix} \quad (3)$$

Alamouti's encoded signal is transmitted from the two transmit antennas over two symbol periods. During the first symbol period at $t = T$, two symbols x_1 and x_2 are simultaneously transmitted from the two transmit antennas. During the second symbol period $t = 2T$, these symbols are transmitted again, where $-x_2^*$ is transmitted from the first transmit antenna and x_1^* transmitted from the second transmit antenna. For Maximum Likelihood (ML) signal detection of Alamouti's space-time coding scheme, we assume that two channels gains $h_1(t)$ and $h_2(t)$ remain constant over two consecutive symbol periods such that

$$h_1(t) = h_1(t+T) = h_1 = |h_1| e^{j\theta 1} \quad (4)$$

$$h_2(t) = h_2(t+T) = h_2 = |h_2| e^{j\theta 2} \quad (5)$$

Where $|h_1|$ and $e^{j\theta 1}$ denote the amplitude gain and phase rotation over the two symbol periods. At the receiver the received signals y_1 and y_2 at time t and $t+T_s$ can be given as

$$y_1 = h_1 x_1 + h_2 x_2 + z_1 \quad (6)$$

$$y_2 = -h_1 x_2^* + h_2 x_1^* + z_2 \quad (7)$$

where z_1 and z_2 are the additive noise at time t and $t+T_s$ respectively.

4. SIMULATION RESULTS

Simulation results are presented to evaluate the performance of STBC oded MIMO-OFDM system with more than one antenna at the receiver.

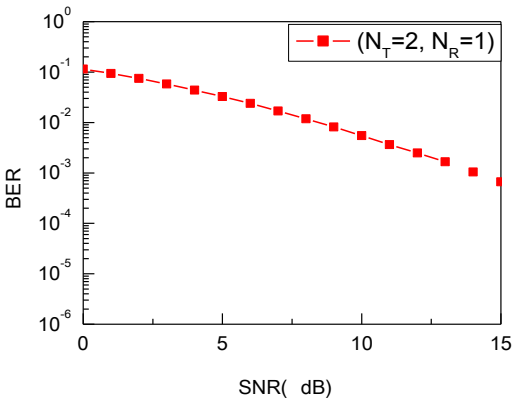

Fig. 2: Performance of STBC MIMO-OFDM system for 2-Transmit and 1-receive antennas.

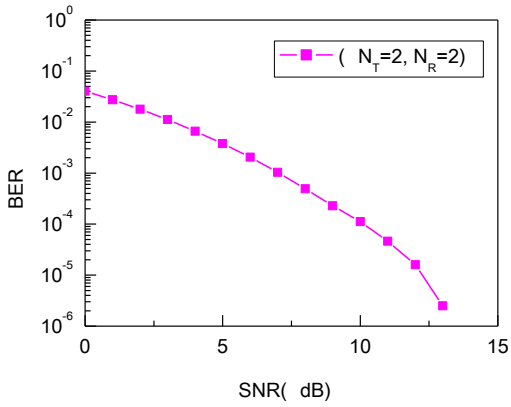

Fig. 3: Performance of STBC MIMO-OFDM system

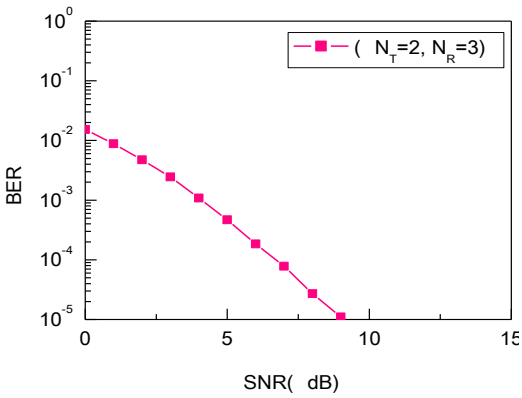

Fig. 4: Performance of STBC MIMO-OFDM system for 2-Transmit and 3-receive antennas.

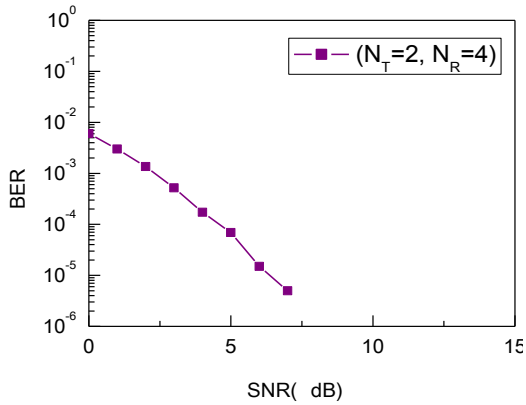

Fig. 5: Performance of STBC MIMO-OFDM system for 2-Transmit and 4-receive antennas.

Fig. 2 shows the performance of STBC MIMO-OFDM system with two antennas at the transmitter side and one antenna in the receiver side. The figure shows that the BER decreases with the increase in SNR. Fig 3~5 also shows the performance of STBC MIMO-OFDM system with two antennas at the transmitter side and different number of antennas in the receiver side. It is observed that with the increase in number of antennas in the receiver side, the BER decreases significantly. So the performance of the STBC MIMO-OFDM improves with having the increasing number of receive antenna at the receiver.

Table 1: Comparison between BER and SNR for different antenna configurations

SNR (dB)	BER			
	(N_T=2, N_R=1)	(N_T=2, N_R=2)	(N_T=2, N_R=3)	(N_T=2, N_R=4)
0	1.15e-1	4.04e-2	1.53e-2	6.01e-3
5	3.27e-2	3.78e-3	4.68e-4	6.90e-5
10	5.49e-3	1.12e-4	3.00e-6	0.0
15	6.65e-4	0.0	0.0	0.0

5. CONCLUSIONS

In this paper we evaluated the performance of the Space Time Block Coded MIMO-OFDM system under Rayleigh fading channel. We observe that the performance of two transmit antennas with more receive antennas at the receiver end is much better than that of the system with two transmit antenna and less receive antennas in term of BER due to the more diversity gain of Alamouti's code. So the performance of a system depends upon the number of receive antennas and transmit antennas. In this work the number of transmit antennas is kept

constant while the number of receive antennas is varied. It is found that the performance of the system improves with increasing the number of antennas in the receiver end. In this work the performance of 2×4 system improves significantly than 2×3**,** 2×2 and 2×1 system.

REFERENCES

[1]. C. Fellenberg and H. Rohling, "Quadrature Amplitude Modulation for Differential Space-Time Block Codes," *Wireless Personal Communications*, vol. 50 no.2, pp. 247-255, 2009.

[2]. H. Bölcskei and E. Zurich, "MIMO-OFDM Wireless Systems: Basics, Perspectives, and Challenges," IEEE Transactions on Wireless Communications, vol. 13 no. 4, pp. 31-37, 2006.

[3]. D. Gesbert, M. Shafi, D. S. Shiu, P. Smith, and A. Naguib, "An Overview Of Mimo Space-Time Coded Wireless Systems," *IEEE Journal on Selected Areas in Communications*, vol. 21, no. 2, pp. 281–302, 2003.

[4]. A. J. Paulraj, D. A. Gore, R. U. Nabar, and H. Bölcskei, "An Overview of MIMO Communications—A Key to Gigabit Wireless," *Proceedings of the IEEE*, vol. 92, no. 2, pp. 198–218, 2004.

[5]. S. H. Mei, H. G. Rui, "A New Generalized Complex Orthogonal Space-Time Block Codes," *Journal of Shanghai University*, vol. 9 no. 3, pp. 241-243, 2005.

[6]. S. Weifeng and X. Xianggen, "Two Generalized Complex Orthogonal Space-Time Block Codes of Rates 7/11 And 3/5 for 5and 6 Transmit Antennas," *IEEE Transactions on Information Theory*, vol. 49 no. 1, pp. 313-316, 2003.

[7]. Natarajan and Z. Wu., "Flexible Spectrum Coexistence at the Physical Layer ofstems via a Multicarrier Platform," *IEEE Wireless Communication*, pp. 64-71, April 2004.

[8]. L. K. Bansal and A. Trivedi, "Comparative Study of Different Space-Time Coding Schemes for MC-CDMA Systems," *International Journal of Communication, Network and System Sciences,* vol. 3 no. 4, pp. 418-424, 2010.

[9]. D. Hu, L. Yang, Y. Shi, and L. He, "Optimal Pilot Sequence Design for Channel Estimation in MIMO-OFDM Systems" *IEEE Communications Letters*, vol. 10, no. 1, 2006.

[10]. Y. Gongand, K. B. Letaief, "Low Complexity Channel Estimation for Space-Time Coded Wideband OFDM Systems," *IEEE Wireless Communications*, vol. 2, no. 5, pp. 876–882, 2003.

[11]. J. Guo, L. Jiang, Y. Gou, and X. Meng, "Blind Channel Estimator for MIMO-OFDM Systems Based on Linear Non Redundant Precoding," *Proceedings of IEEE Wireless Communication Network Conference*, New Orleans, LA, Sep. 23–26, vol. 1, pp. 44–47, 2005.

[12]. Y. Zeng, W. H. Lam, and T. S. Ng, "Semi Blind Channel Estimation and Equalization for MIMO Space-Time Coded OFDM," *IEEE Transactions on Circuits System-I*, vol. 53, no. 2, pp. 463–474, 2006.

[13]. H. Li, "Differential Space-Time Modulation over Frequency Selective Channels," *IEEE Transactions on Signal Processing,* vol. 53, no. 6, pp. 2228–2242, 2005.

[14]. Q. Ma, C. Tepedelenlioglu, and Z. Liu, "Differential Space Time Frequency Coded OFDM with Maximum Multipath Diversity," *IEEE Wireless Communications*, vol. 4, no. 5, pp. 2232–2243, 2005.

[15]. S. N. Diggavi, N. Al-Dhahir, A. Stamoulis, and A. R. Calderbank, "Differential Space Time Coding for Frequency Selective Channels," *IEEE Communication Letters*, vol. 6, no. 6, pp. 253–255, 2002.

[16]. A. Lodhi, F. Said, M. Dohler, and A. H. Aghvami, "Performance Comparison of Space-Time Block Coded and Cyclic Delay Diversity MC-CDMA Systems," *IEEE Wireless Communications*, vol. 12, no. 2, pp. 38-45, 2005.

[17]. Y. Chang, R. Zhang, and Cioffi, "Transmit Optimization for MIMO-OFDM with Delay-Constrained and No Delay- Constrained Traffic," *IEEE Transactions on signal processing*, vol. 54, no. 8, 2006.

[18]. S.M. Alamouti, "A Simple Transmit Diversity Scheme for Wireless Communications," *IEEE Journal of Selected Areas on Communication*, vol. 16, no. 8, pp. 1451–1458, 1998.

Proceeding of the
International Conference on Electrical, Computer and Telecommunication Engineering
01- 02 December 2012 (ICECTE2012), RUET, Rajshahi-6204, Bangladesh

ICECTE2012: PI-0054

BER performance analysis of a STBC encoded MIMO OFDM wireless communication system

Tanvir Ahmed[1], M.M.Ali[1]
[1]Electrical and Electronic Engineering Department, Rajshahi University of Engineering and Technology, Rajshahi -6204, Bangladesh
E-mail: tanvir_1008@yahoo.com, mmali.ruet@gmail.com

ABSTRACT
In this paper the BER performances are analyzed for a STBC encoded MIMO-OFDM wireless communication System. The 2X2 multi-antenna supported MIMO-OFDM system implements ZF and MMSE based linear channel equalization schemes with deployment of various digital modulations (16-QAM, 16-PSK and 16-DPSK) over AWGN and Rayleigh fading channel. It has been observed that the system under investigation outperforms with 16-QAM digital modulation and MMSE channel equalization scheme and shows worst performance with 16-DPSK and ZF.

KEY WORDS: MIMO-OFDM, STBC, MMSE, ZF, Rayleigh Fading.

1. INTRODUCTION

Communication systems using multiple antennas at the transmitter and/or the receiver have recently received increased attention due to their ability to provide substantial capacity improvements while achieving low error rate and/or high data rate by flexibly exploiting the attainable diversity gain and/or the spatial multiplexing gain [1].Recently much attention has been paid on transmit diversity as an efficient technique to combat fading and simplify the implementation of mobile terminals [2]. Several methods in transmit diversity are proposed in [2]-[5]. Among them, Alamouti space-time block coding (STBC) [3] is very simple and attractive due to its advantages of not requiring feedback of channel state information and easy implementation. Space-time block codes (STBC) have been integrated with orthogonal frequency division multiplexing (OFDM) by implementing STBC at a block level in a structure commonly known as ST-OFDM [6]. Since wireless communications is challenged by limited spectral resources, multi-user spacial multiplexing has recently received considerable attention. Multi-user MIMO systems can significantly improve system throughput via transceiver signal processing if the number of transmit antennas is much larger than the number of receive antennas [7].

We shall consider the case of the simple Alamouti's space-time block code as it is the only scheme which can provide full rate and full diversity for any signal constellations. Among available multiuser detection techniques [8], [9] the most popular minimum mean square error (MMSE) method is chosen in [10], [11], [12] since it can provide good performance and can be readily implemented using standard adaptive algorithms. This MMSE multiuser detector is applied for Multiuser STBC-OFDM system in [10]. In [11] the BER values were estimated to show the impact of concatenated block code (RS, BCF, Cyclic code) and interleaver with Space time trellies code (STTC) on the performance of MIMO-OFDM wireless communication system on the color image transmission with MMSE equalizer where the QAM digital modulation technique performed satisfactorily. [12] shows BER performance analysis for Zero-Forcing (ZF), Sphere Decoding (SD), Minimum mean square error (MMSE), signals detection schemes in a multi-user MIMO MCCDMA wireless communication system.

In this work the BER performances are evaluated for zero-Forcing (ZF) and minimum mean square error (MMSE) equalizers for single user MIMO-OFDM space time block coded wireless communication system with deployment of various digital modulations (16-QAM, 16-PSK and 16-DPSK) over AWGN and Rayleigh fading channel.

2. Communication System Model

The system under consideration is shown in Figure 1 where randomly generated binary message signal is encoded by a convolutional encoder of rate r =1/2, interleaved and converted to M-ary signal. This M-ary signal is modulated using various types of modulation technique such as Quadrature Amplitude modulation (QAM), Phase Shift Keying (PSK), Differentially Phase Shift Keying (DPSK) and Pulse Amplitude Modulation (PAM). The modulated digital signals are fed into the Space Time Block Encoder using Alamouti scheme. The output of the Space-time block encoder are sent up into two serial to parallel converter. The serial to parallely (S/P) converted complex data symbols are fed into each of the two OFDM modulator with 1024 sub carriers which performs an IFFT on each OFDM

block of length 1024 followed by a parallel –to-serial conversion. A cyclic prefix (CP) of length Lcp (0.1*1024) containing a copy of the last Lcp samples of the parallel –to- serial converted output of the 1024-point IFFT is added with the each OFDM symbol. The CP is essentially a guard interval which serves to eliminate interference between OFDM

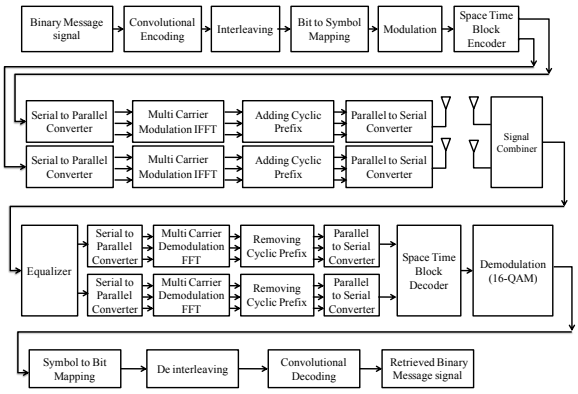

Fig.1: Block diagram of FEC encoded Space Time Block Coded MIMO-OFDM wireless communication system

symbols [12]. However, the resulting OFDM symbols of length 1024+ Lcp are lunched from the two transmitting antenna.

In receiving section, all the transmitted signals are detected with linear signal detection schemes and the detected signals are subsequently sent up to the serial to parallel (S/P) converter and fed into OFDM demodulator which performs FFT operation on each OFDM block. The FFT operated OFDM blocked signal are processed with cyclic prefix removing scheme and are undergone from parallel to serial conversion and are fed into Space time block decoder. The complex symbols are now digitally demodulated, de interleaved and convolutionally decoded to recover the transmitted data.

3. Signal Detection Schemes

Consider a N_R X N_T MIMO system. Let H denote a channel matrix with it (j,i)th entry h_{ji} for the channel gain between the ith transmit antenna and the jth receiving antenna, j=1,2,…N_R and i=1,2,….N_T. The spatially-multiplexed user data and the corresponding received signals are represented by $\mathbf{x}=[\ x_1,\ x_2,\ \ldots\ldots x_{NT}]^T$ and $\mathbf{y}=[\ y_1,\ y_2,\ \ldots\ldots y_{NR}]^T$, respectively, where x_i and y_j denote the transmit signal from the ith transmit antenna and the received signal at the jth receive antenna, respectively. Let z_j denote the white Gaussian noise with a variance of σ^2_z at the jth receive antenna, and $\mathbf{h}_i$ denote the ith column vector of the channel matrix **H**. Now, the N_R x N_T MIMO system is represented as [13]

$$\mathbf{y=Hx+z}$$

$$=\mathbf{h}_1 x_1+\mathbf{h}_2 x_2+\ldots\ldots+\mathbf{h}_{NT} x_{NT}+\mathbf{z} \qquad (1)$$

where $\mathbf{z}=[\ z_1,\ z_2,\ \ldots\ldots z_{NR}]^T$.

To facilitate the detection of desired signals from each antenna, the effect of the channel is inverted by a weight matrix **W** such that

$$\hat{x} = [\hat{x}_1, \hat{x}_2, \hat{x}_3 \ldots\ldots \hat{x}_{NT}] = Wy \qquad (2)$$

that is, detection of each symbol is given by a linear combination of the received signals. The standard linear detection methods include the zero-forcing (ZF) technique and the minimum mean square error (MMSE) technique.

3.1. ZF Signal Detection

The zero-forcing (ZF) technique nullifies the interference by the weight matrix as given by [13]

$$\boldsymbol{W}_{ZF} = (\boldsymbol{H}^H\boldsymbol{H})^{-1}\boldsymbol{H}^H \qquad (3)$$

where $(\cdot)^H$ denotes the Hermitian transpose operation. In other words, it inverts the effect of channel as [13]

$$\begin{aligned}\hat{x}_{ZF} &= W_{ZF}\, y \\ &= x + (H^H H)^{-1} H^H z \\ &= x + \hat{z}_{ZF}\end{aligned} \qquad (4)$$

Where, $\hat{z}_{ZF} = W_{ZF} z = (H^H H)^{-1} H^H z$

3.2 MMSE Signal Detection

In order to maximize the post detection signal-to - interference plus noise ratio (SINR), the MMSE weight matrix is given as

$$\boldsymbol{W}_{MMSE} = (\boldsymbol{H}^H\boldsymbol{H} + \sigma^2_z\, \boldsymbol{I})^{-1}\boldsymbol{H}^H \qquad (5)$$

Note that the MMSE receiver requires the statistical information of noises σ^2_z. It inverts the effect of channel as [13]

$$\begin{aligned}\hat{x}_{MMSE} &= W_{MMSE}\, y \\ &= x + (H^H H + \sigma_z^2 I)^{-1} H^H z \\ &= x + \hat{z}_{MMSE}\end{aligned} \qquad (6)$$

where $\hat{z}_{MMSE} = W_{MMSE} z = (H^H H + \sigma_z^2 I)^{-1} H^H z$

.

4. Simulation Result and Performance Analysis

The computer simulation has been conducted to evaluate the BER performance of the FEC encoded single user STBC encoded MIMO OFDM wireless communication system based on the parameter given in Table 1. The channel state information (CSI) is assumed to be available at the receiver only. Figure 2

to figure 4 shows the BER performance evaluation for ZF and MMSE signal detection schemes for M-ary digital modulation techniques (16-QAM, 16-PSK, and 16-DPSK). From figure 2 it is shown that for ZF signal detection scheme at the 10dB SNR the BER values are 0.0215 and 0.2870 for 16-QAM and 16- DPSK respectively. So the BER performance is improved by 25.92dB. Figure 3 shows BER performance analysis for MMSE signal detection scheme. At the BER 10^{-2} the required SNR for 16-QAM, 16-PSK and 16- DPSK are 10.10 dB, 11.50 dB and more than 14 dB respectively.

In figure 4 BER performances are evaluated for all modulation technique for ZF and MMSE signal detection schemes. The system outperforms when 16-QAM modulation technique is used with the MMSE signal detection scheme. At the 10dB SNR the BER performance is improved by 3.60dB for MMSE+16-QAM system compared with ZF+16-QAM system. An effort has been made to present the transmitted bit stream and retrieved bit stream for MMSE+16-QAM at SNR 7dB in figure 5.

Table 1: Simulated Model parameters

Parameters	Description
Type of input signal for the single user	Randomly Generated Binary Message
No. of Transmitting and Receiving antennas	2X2
Channel coding	½ rated Convolutional Encoding
Digital Modulation Techniques	16-QAM, 16-PSK and 16-DPSK
No. of OFDM subcarriers	1024
CP length	103 symbols
Signal Detection Scheme	ZF andMMSE
Channel	AWGN and Rayleigh Fading channel
Signal to noise ratio, SNR	0 to 15 dBs

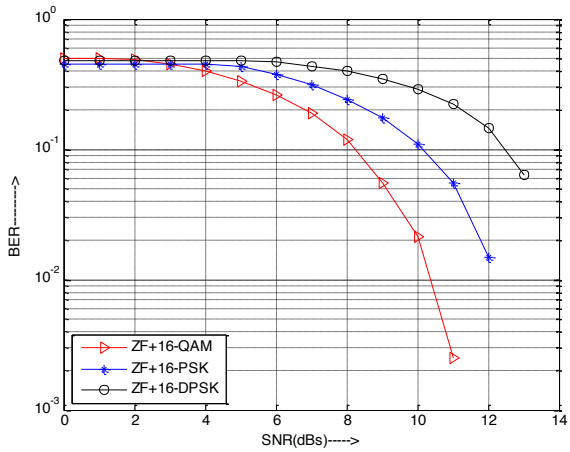

Fig. 2: BER performance analysis for ZF signal detection scheme.

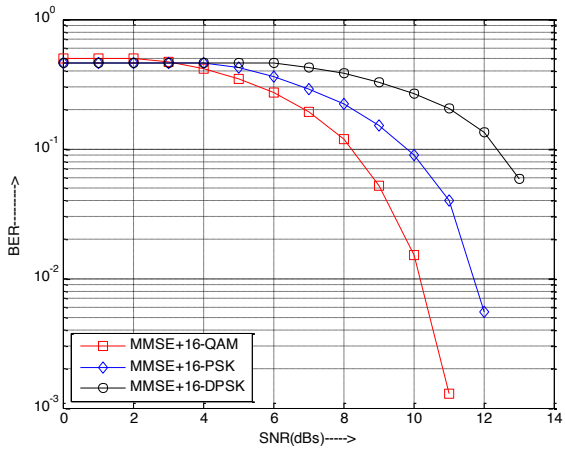

Fig. 3: BER performance analysis for MMSE signal detection scheme.

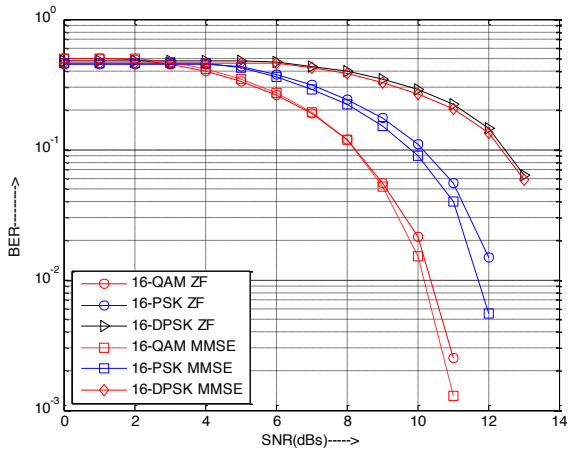

Fig. 4: BER performance analysis for ZF and MMSE signal detection schemes.

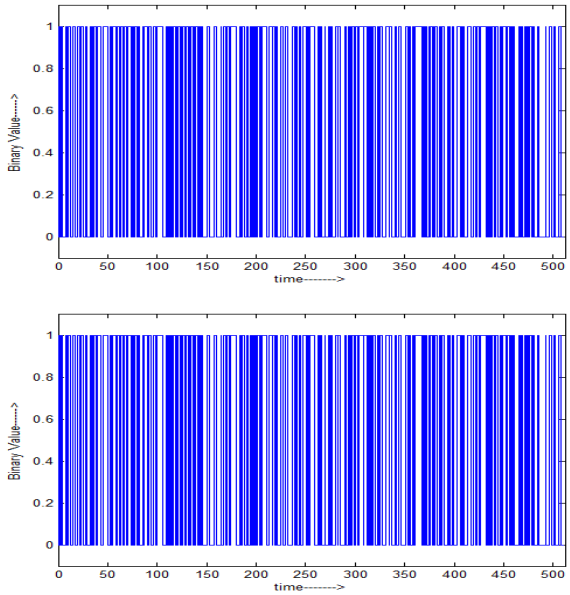

Fig. 5: Transmitted bit stream and retrieved bit stream for MMSE+16-QAM.

5. Conclusion

In this work, we have presented simulation results concerning the adaptation of various signal detection schemes in a single user STBC encoded MIMO OFDM wireless communication system. A range of system performance results highlights the impact of signal detection scheme on randomly generated binary message transmission system. In this context of system performance, it can be concluded that the implementation of 16-QAM digital modulation technique with MMSE signal detection technique provides satisfactory result for such a single user STBC encoded MIMO-OFDM wireless communication system.

REFERENCES

[1] Jiankang Zhang, Student Member, IEEE, Sheng Chen, Fellow, IEEE, Xiaomin Mu, and Lajos Hanzo, Fellow, IEEE, "Joint Channel Estimation and Multiuser Detection for SDMA/OFDM Based on Dual Repeated Weighted Boosting Search", *IEEE Transactions on Vehicular Technology*, Vol. 60, No. 7, September 2011, pp-3265-3275.

[2] Huiling Zhu,Member, IEEE,Bin Xia and Zhenhui Tan, Member, IEEE, "Performance Analysis of Alamouti Transmit Diversity with QAM in Imperfect Channel Estimation", *IEEE Journal on Selected Areas in Communications*, Vol. 29, No. 6, June 2011, pp-1242-1248.

[3] S. M. Alamouti, "A simple transmit diversity technique for wireless communications", *IEEE Journal on Selected Areas in Communications*, vol. 16, October 1998, pp. 1451 -1458.

[4] X. Y. Wang and J. Wang, "Effect of imperfect channel estimation on transmit diversity in CDMA systems", *IEEE Transactions on Vehicular Technology*, Vol.VT-53, September 2004, pp. 1400 – 1412.

[5] R. T. Derryberry, S. D. Gray, D. M. Ionescu, G. Mandyam and B. Raghothaman, "Transmit diversity in 3G CDMA systems*", IEEE Commun. Mag.*, vol. 40, April 2002, pp. 68 – 75.

[6] Dandan Wang, Student Member, IEEE, Hlaing Minn, Senior Member, IEEE,and Naofal Al-Dhahir,Fellow, IEEE, "A Robust Asynchronous Multiuser STBC-OFDM Transmission Scheme for Frequency-Selective Channels", *IEEE Transactions on Wireless Communications*, Vol. 7, No. 10, October 2008, pp-1-7.

[7] R. L. Choi, M. T. Ivrlac, R. D. Murch, and W. Utschick, "On strategies of multiuser MIMO transmit signal processing", *IEEE Transactions on Wireless Communications*, vol. 3, no. 6, November 2004, pp. 1936–1941.

[8] L. Hanzo, M. M ¨unster, B.J. Choi, and T. Keller, "OFDM and MC-CDMA for Broadband Multi-User Communications, WLANs and broadcasting", IEEE Press, John Wiley & Sons, 2003.

[9] S.Verdu, Multiuser Detection, Cambridge University Press, Cambridge 1998.

[10] Xuan Nam T RAN, Tadashi FUJINO and Yo shio KARASAWA, "An MMSE Multiuser Detector for Space-Time Block Coded OFDM", *IEICE Transactions on Communication*, Vol.E88–B, No.1 January 2005, pp-141-149.

[11] Dulal Haque, Shaikh Enayet Ullah , Md. Mahbubar Rahman and A.F.M. Zaiul Abadin, "Performance Evaluation of a FEC encoded MIMO-OFDM wireless communication System on color Image transmission", *Journal of Mobile communication*, Vol. 3(4) pp-62-67, 2009.

[12] Shaikh Enayet Ullah and Md. Mahbubar Rahman , "BER Performance Analysis of a FEC Encoded Multi-user MIMO MCCDMA Wireless Communication System", *International Journal of Hybrid Information Technology* , Vol. 4 No. 3, July 2011, pp-41-50

[13] Yong Soo Cho, Jaekwon Kim, Won Young Yang, Chung G. Kang, MIMO-OFDM wireless communications with MATLAB, John Wiley & Sons 2010.

Proceeding of the
International Conference on Electrical, Computer and Telecommunication Engineering
01- 02 December 2012 (ICECTE2012), RUET, Rajshahi-6204, Bangladesh

ICECTE2012: PI-0055

Capacity and Performance analysis of Rayleigh Fading MIMO Channels with Known CSIT

Tushar Kanti Roy[1] and S. M. Abdur Razzak [2]

[1]Department of Electronics and Telecommunication Engineering
[2]Department of Electrical and Electronic Engineering
Rajshahi University of Engineering & Technology, Rajshahi-6204
[1]E-mail: roy_kanti@yahoo.com

ABSTRACT
Due to the ever increasing demand of faster data transmission speed in recent or future wireless communication systems the multiple-input multiple-output (MIMO) is regarded as one of the most promising research area as compared to the conventional single-input single-output (SISO) systems. This is due to the high spectral efficiency of a MIMO channel and it offers a significant capacity gain as compare to a conventional SISO channel. In this paper, the capacity of Rayleigh fading MIMO channel with known channel state information (CSI) at the transmitter side is investigated. In wireless communication systems, the knowledge of CSI at either the receiver or at the transmitter or at both is consider being a vital part in information transfer across the channel. Finally a computer simulation is conducted to show the effectiveness of Rayleigh fading MIMO channel capacity over SISO channel. Our results also show that increasing the number of transmitting and receiving antennas for a wireless MIMO channel does indeed improve the channel capacity that can be obtained.

KEY WORDS: CSIT, MIMO, Multiple antennas, Rayleigh fading, SISO

1. INTRODUCTION

Compared with the wired network communication counterpart, the wireless communication offers a number of significant benefits. The rapid development of communication systems with mobile receivers at higher data rates has lead to the importance of studies on information transfer over highly time-varying channels. To meet the recent and future demand of the users, wireless networking systems continue to struggle for ever higher data rate. This is particularly challenging task for the wireless systems that are power, spectral bandwidth and complexity limited. However, another domain can be exploited to significantly increase the channel capacity: the use of multiple transmit and receive antennas. The channel capacity of a MIMO antenna system can be significantly improved without using additional transmit power and spectral bandwidth over conventional SISO antenna systems [1, 2]. The use of multiple antennas instead of single-input single-output (SISO) antenna systems is considered to overcome the limitations of SISO wireless communications due to its low capacity and inadequate data rate for demanding applications. Multiple antennas at the receiver provide diversity gain, which increases the link reliability, power gain, also called array gain so that the SNR is [7] improved. Fading channels are common in today's wireless communication systems. The term “fading" is used to describe the rapid fluctuations of the amplitudes, phases or multi-path delays of a radio signal over a short period of time or distance. This is most prominent when signal or path loss caused by the obstructions such as buildings, mountains and foliage between the transmitter and the receiver are ignored. Multipath signal propagation has long been thought an impairment limiting the system capacity and reliable communication in wireless channels together with the constraint of signal power and bandwidth. However, with the introduction of new techniques, such as MIMO systems and the use of rake receiver [3], the multipath is now viewed as a positive aspect where the receive signal can be constructed using all possible multiple waves present and as a result improved the achievable data rate and link quality [2, 9]. Unlike the wired channels that are stationary and predictable, radio channels are extremely random and the analysis is very difficult and typically done in a statistical fashion. Various probability distributions have been used to model the fading process. The most commonly used distribution is known as Rayleigh distribution, in which the time and frequency dependence of the transmitted signal is well understood [4]. Fading plays a significant role in information recovery at the receiver in wireless communication systems. In fading channels, capacity, or the maximum allowable transmission rate, depends on the information available at the transmitter and receiver of the fading process. Channel training is implemented in most cases where the channel variation during the period considered is slow.

The MIMO system provides dramatic capacity gain through an increased spatial dimension. The channel capacity gain is reduced if the channel state information (CSI) is not perfect. Many previous works in the literature have dealt with this problem with various assumptions about CSI. The channel capacity of a wireless system evaluation using Monte-Carlo method when the receiver CSI is perfectly known is given in [5]. Also [2] shows that the optimum distribution which achieves the channel capacity is circularly symmetric complex Gaussian which minimises the channel output entropy when CSI is known. In [6], the maximum capacity loss due to a lack of receiver CSI for a wideband MIMO channel in Rayleigh

fading is considered. The maximum penalty to be paid in terms of capacity not having the CSI at the receiver is shown. Furthermore, it is conjectured that on-off signalling is optimal, however no proof is given. The capacity with neither the channel state information at the receiver (CSIR) nor the channel state information at the transmitter (CSIT) has been explored in [8].

This significant capacity improvement is opened up the research activity using multi-antenna at both the transmitter and receiver sides. This is an attractive solution to the high capacity demand of future wireless systems since it increases the capacity without using the extra bandwidth or transmitted power consumption. Since the MIMO channel can offer a significant capacity gain over a traditional SISO channel, MIMO systems are today regarded as one of the promising research areas of wireless communication systems. Therefore, in this paper we analyse the capacity and performance of Rayleigh fading MIMO channel when CSI is available at the transmitter side.

The rest of this paper is organized as follows. Section 2, briefly introduces the MIMO system model with MISO and SIMO channels. The Rayleigh fading channel is discussed in Section 3. In section 4, we discuss the simulation results. Finally, the paper is concluded in Section 5.

2. SYSTEM MODEL

In this section, we describe the system model for the MIMO channel. The MIMO channel assumed to be the single user with perfect CSIT. In MIMO systems, a transmitter sends multiple streams by multiple transmit antennas. The transmit streams go through a matrix channel which consists of all N_TN_R paths between the N_T transmit antennas at the transmitter side and N_R receive antennas at the receiver sides. Then, the receiver gets the received signal vectors by the multiple receive antennas and decodes the received signal vectors into the original information. The input and output relationship of a narrow band single-user MIMO link is commonly represented by the following vector notation:

$$y = Hx + n \tag{1}$$

where, y and x are the receive and transmit vectors, respectively, and H is the channel matrix vector which represents the channel CSI and n is the noise vector. A typical MIMO wireless communication system model is shown in Fig.1 where the output vector is the spatial contribution of the input vector, channel matrix and the white Gaussian noise. In the channel matrix (H) a general entry is denoted by h_{ij} which represents the complex gain of the channel between the ith transmitter and j^{th} receiver.

For the MIMO wireless system in Eqn. (1) the channel matrix (H) is given by

$$H = \begin{bmatrix} h_{11} & h_{12} \cdot & \cdot & \cdot & h_{1N_T} \\ h_{21} & h_{22} \cdot & \cdot & \cdot & h_{2N_T} \\ h_{N_R1} & h_{N_R2} \cdot & \cdot & \cdot & h_{N_RN_T} \end{bmatrix} \tag{2}$$

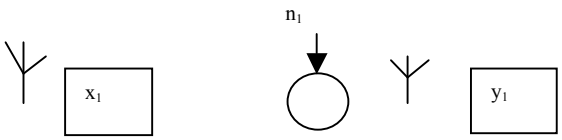

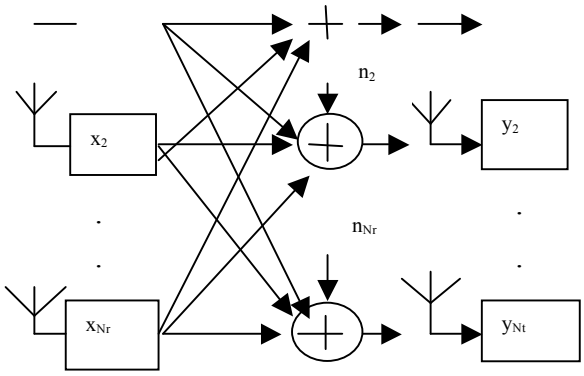

Fig.1: Wireless MIMO link comprising N_T transmit antennas and N_R receive antennas.

In this paper, we consider H is a random matrix, which means that its channel capacity is also randomly time-varying. In other words, the MIMO channel capacity can be given by its time average. In practice, we assume that the random channel is an ergodic process. Then we should consider the following statistical nation of the MIMO channel capacity

$$C = E\{C(H)\}$$
$$= E\left\{ \max_{Tr(R_{xx}) = N_T} \log_2 \det\left(I_{N_R} + \frac{E_x}{N_T N_0} H R_{xx} H^H \right) \right\} \tag{3}$$

which is frequently known as an ergodic channel capacity. Now the ergodic channel capacity without using CSI at the transmitter side is given as

$$C = E\left\{ \sum_{i-1}^{r} \log_2\left(1 + \frac{E_x}{N_T N_0} \lambda_i \right) \right\} \tag{4}$$

Similarly, the ergodic channel capacity using CSI at the transmitter side is given as

$$C = E\left\{ \sum_{i-1}^{r} \log_2\left(1 + \frac{E_x}{N_T N_0} \gamma_i^{opt} \lambda_i \right) \right\} \tag{5}$$

where, $\gamma_i = E\{|x_i|\}$ is the transmitted power for the ith transmitting antenna and λ_i is the channel gain.

2.1 Channel Capacity of SIMO and MISO Channels

In this subsection, we describe the channel capacity of SIMO and MISO channels. For the case of a SIMO with one transmit antenna and N_R receive antennas, the channel gain is given as $h \in C^{N_R \times 1}$ and thus r=1 and $\lambda_1 = \|h\|_F^{\ 2}$. Consequently, regardless of the availability of CSI at the transmitter side, the channel capacity is given as

$$C_{SIMO} = \log_2\left(1 + \frac{E_x}{N_0} \|h\|_F^{\ 2} \right) \tag{6}$$

If $|h_i|^2=1,\ i=1,\ 2,\ \ldots N_R$ and consequently $\|h\|_F^{\ 2} = N_R$ the capacity is given by

$$C_{SIMO} = \log_2\left(1 + \frac{E_x}{N_0} N_R \right) \tag{7}$$

From Eqn. (7) it is clear that the channel capacity increases logarithmically as the number of antennas increases. For the case of a MISO with one receive antenna and N_T transmit antennas, the channel gain is given as $h \in C^{1\times N_T}$ and thus r=1 and $\lambda_1 = \|h\|_F^{\ 2}$. When CSI is not available at the transmitter side, the channel capacity is given as

$$C_{MISO} = \log_2\left(1 + \frac{E_x}{N_T N_0}\|h\|_F^{\ 2}\right) \tag{8}$$

When CSI is available at the transmitter side, the transmit power can be concentrated on a particular mode of the current channel. In other words, $\left(h^H / \|h\|\right)x$ is transmitted instead of x directly. Then the receive signal can be expressed as

$$y = \sqrt{E_x}\, h \cdot \frac{h^H}{\|h\|} x + z = \sqrt{E_x}\|h\| x + z \tag{9}$$

It should be note that the received signal power has been increased by N_T times in Eqn. (9) and thus, the channel capacity is given as

$$C_{MISO} = \log_2\left(1 + \frac{E_x}{N_0}\|h\|_F^{\ 2}\right) = \log_2\left(1 + \frac{E_x}{N_0} N_T\right) \tag{10}$$

3. RAYLEIGH FADDING CHANNEL

When there are large numbers of paths, by the applying Central Limit Theorem, each path can be modeled as a circularly symmetric complex Gaussian random variable with time as the variable. This model is called the Rayleigh fading channel model. When there is no line of sight that is no direct path between the transmitter and receiver then constructive and destructive natures of the multipath component in a fading channel can be approximated by the Rayleigh distribution. A circularly symmetric complex Gaussian random variable is of the form,

$$h = X + jY \tag{11}$$

where, real X and imaginary Y parts are zero mean independent and identically distributed Gaussian random variables, respectively. For a circularly symmetric complex random variable Z,

$$E[h] = E[e^{j\theta}h] = e^{j\theta}E[h] \tag{12}$$

The statistics of a circularly symmetric complex Gaussian random variable is completely specified by the variance,

$$\sigma^2 = E[h^2] \tag{13}$$

The magnitude |Z| which has a probability density function as follows,

$$p(z) = \frac{z}{\sigma^2} e^{\frac{-z^2}{2\sigma^2}}, \quad z \geq 0 \tag{14}$$

The received signal in a Rayleigh fading channel is

$$y = z\,x + n \tag{15}$$

where, y is the received signals, h is the Rayleigh fading channel response, x is the transmitted signals and n is the AWGN. As the channel is randomly varies with time, so each transmitted signal gets multiplied by a random varying complex number h. Since h is modeled as a Rayleigh fading channel, the real and imaginary parts of the Gaussian distribution have a mean 0 and a variance of ½.

4. SIMULATION RESULTS

To compare the performances and capacity of a Rayleigh fading MIMO channel with SISO channel as a function of number of receive antennas and as a function of transmit antennas we conduct a MATLAB simulation. Here different channel configuration, such as 1x1 SISO channel, 1x2 SIMO channel, 2x1 MISO channel, 2x2 MIMO channel and 4x4 MIMO channel are used to show the advantages of 4x4 MIMO channel configuration in term of its bps/Hz and average SNR over other channels as shown in Fig.2.

Fig.4 compares the egrodic capacities for 4x4 MIMO channels with and without using CSI at the transmitter side. It shows that the MIMO system with CSI provides more capacity than the MIMO system without CSI at the transmitter. However, from this figure it is clear that the CSI availability at the transmitter side does not help to improve the channel capacity when the average SNR is extremely high.

From these plots it is obvious that the use of multiple antennas at both the transmitter and receiver significantly increases the channel capacity far beyond that of single antenna systems.

5. CONCLUSION

The theme of this paper is on the capacity and performance of MIMO channels operating over Rayleigh fading channels. From the simulation results, it is clear that the MIMO channels capacity improves with increasing the number of transmit and receive antennas far beyond that of SISO channels. The Rayleigh fading MIMO channels with 4x4 antenna configurations provide better performance in term of its bps/Hz as compared to the 2x2 antenna configuration. It is also clear that the CSI availability does not help to increase the channel capacity when the average SNR is extremely high.

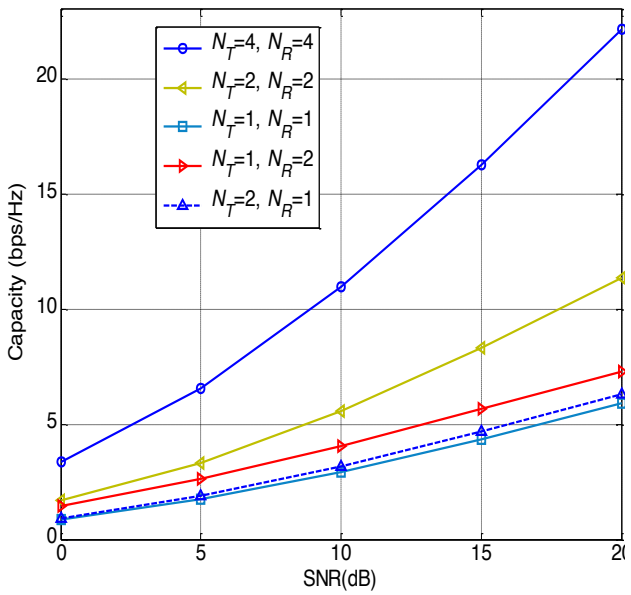

Fig.2: MIMO channel capacity when CSI is not available at the transmitter

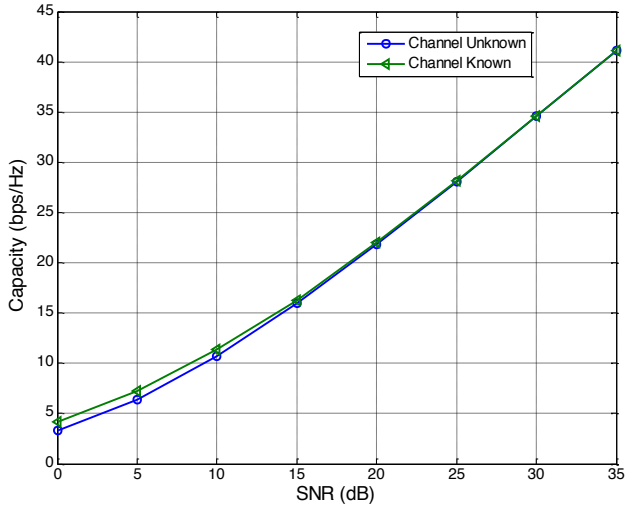

Fig.4: MIMO channel (N_T=N_R=4) capacity when CSI is available at the transmitter

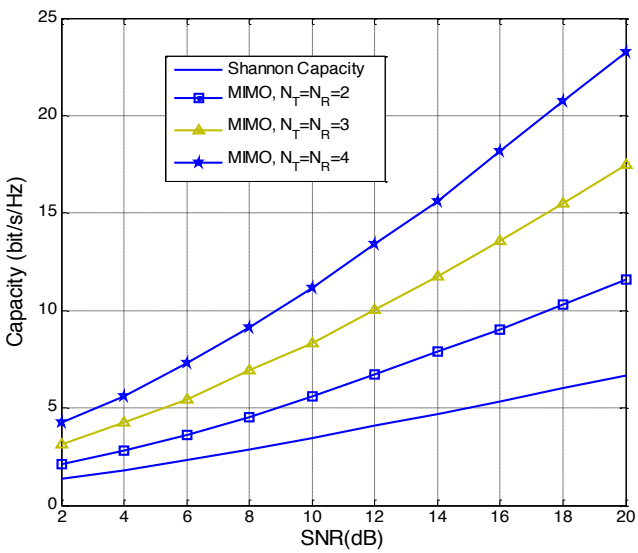

Fig.3: MIMO and Shannon channels capacity when CSI is not available at the Transmitter side

From this simulation results, it is clear that in Rayleigh fading MIMO channel the bps/Hz keeps on increasing due to MIMO antennas, when we increase the number of transmit and receive antennas.

From this figure it is also clear that having more transmit antennas than receive antennas or more receive antennas than transmit antennas provide no advantage for improving the channel capacity. We also show the comparison in between of MIMO and Shannon channels capacity in Fig.3 and it clear that the performance of Shannon channel capacity as like Rayleigh fading SISO channel.

REFERENCES

[1] G. J. Foschini, "Layered space-time architecture for wireless communication in a fading environment when using multi-element antennas," *Bell Labs Tech. J.,* pp. 41-59, Autumn 1996.

[2] I. E. Telatar, "Capacity of multi-antenna Gaussian channels," Tech. Rep. BL0112170-950615-07TM, AT& T Bell Laboratories, 1995

[3] J. H. Andersson, K. Johansson, and O. Mauritz, "A generalised RAKE receiver for WCDMA TDD," *VTC Spring* 2002, vol. 2, pp. 527-531, May 2002.

[4] M. K. Simon and M. S. Alouini, "Digital Communication over Fading Channels, A Unified Approach to Performance Analysis," John Wiley & Sons, 2000.

[5] W. Chao, W.U. Sjunjun, Z. Linrang, and T. Xiaoyan, "Capacity evaluation of MIMO systems by Monte-Carlo methods," *IEEE International Conf. on Neural Networks and Signal Processing*, pp. 1464-1466, Dec. 2003.

[6] S. Ray, M. Medard, L. Zheng, and J. Abounadi, "On the sub linear behaviour of MIMO channel capacity at low SNR," *IEEE Int. Symp. on Info. Theory*, pp. 1031-1034, Parma, Italy, Oct. 2004.

[7] Caijun Zhong, " Capacity and performance analysis of advanced multiple antenna communication systems, " PhD thesis, University college London, March 2010.

[8] T. L. Marzetta, B. M. Hochwald, "Capacity of a mobile multiple-antenna communication link in Rayleigh flat fading", *IEEE Trans. On Inform. Theory*, Vol. 45, pp. 139-157, Jan. 1999.

[9] G. J. Foschini and M. J. Gans,"On limits of wireless communications in a fading environment when using multiple antennas," *Wireless Personal Commun.*, vol. 6, no. 3, pp. 311–335, Mar. 1998.

Proceeding of the
International Conference on Electrical, Computer and Telecommunication Engineering
01- 02 December 2012 (ICECTE2012), RUET, Rajshahi-6204, Bangladesh

ICECTE2012: PI-0056

Future Data Demand: Feasibility Analysis and Suitable Solution for Future Bangladesh

Mohammad Sakib Ullah, Md. Mosaddek Hossain Adib and M Abdul Awal
Department of Electrical Engineering and Computer Science, North South University, Dhaka, Bangladesh
Email:sakib_saeem@yahoo.com, mosaddek037@eecs.northsouth.edu,abdulawal@northsouth.edu

ABSTRACT
In the communication industry, nowadays the most challenging term is to meet the future data demand. With the rapid change of the consumer communication technology like LTI, 3/4-G, Gamming, IP TV etc.; consumer data requirement is increasing very fast. In Bangladesh now Telecommunication and Internet are the growing industry. In this research we investigate for the required data demand for future Bangladesh and to find a suitable technology for it. From our analysis we figured out that 2.8TBps is the require data demand for 2030's Bangladesh which is hundred times higher than out current capacity.

KEY WORDS: Telecommunication, GDP, Internet Bandwidth, Wimax, Teledensity.

1. INTRODUCTION

At present world telecommunication and internet excess plays a vital roll for the economy of a country. From studies it is found that 10 percent increase in teledensity 0.6 percentage increase in GDP and 1 percentage increase in internet user increases 4.3 percent of toata export [1]. That is why telecommunication and internet is the most important sector in Bangladesh.

In Bangladesh teledensity was below 1 percent in the year 2000 and after that this market rised so rapidly that in 2008 it was around 32 percent. Current infrastructure of the the telecommunication sector is shown in fig. 1. In Bangladesh available service are fixed land line, mobile telephone, fixed wired internet service and newly introduce WIMAX [2]. Previously the data traffic depended on the wireless base microwave communication system and recently fiber optical trankline is introduced. Where base station or local office serve the communication service depending on their service technology i. e. mobile phone or fixed land line. Local offices are connected with the central office depending on the available technology. Few base stations are connected by fiber optic connection and other are connected by microwave as shown in fig. 1.

In this paper we investigate for the future data demand of Bangladesh in the year 2030. Here we figured out that in 2030 Bangladesh's GDP will reach more to double digit, teledensity will go more than80 percent and internet user willgo more than 70 percent. From our analysis we find that in 2030 data demand will 2.5TBps bit per second within the country and 1.8TBps bit per second in the international getaway.

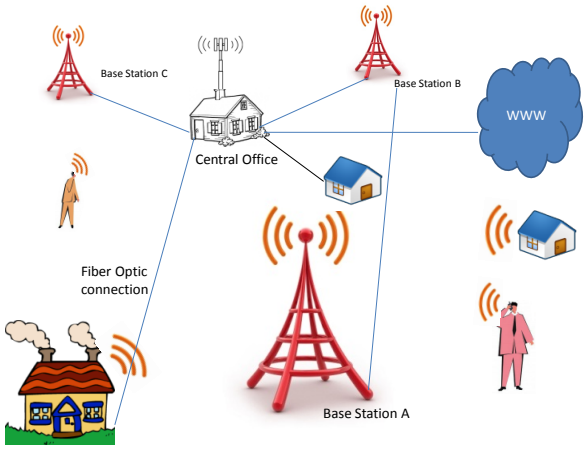

Fig. 1: Present telecommunication infrastructure of Bangladesh.

Analysis result shows that currently available STM-64, STM-16 and STM-4 optical line are not capable to meet this future demand. From the feasibility analysis we find thatnewly develop technology is the most cost effective solution to meet the challenge of 2030's.

2.BANGLADESH AND DEVELOP WORLD PERSPECTIVE

In 2002 the teledensity of Bangladesh was only 0.54% and after 2008 it reached more than 30% [1]. But in Bangladesh if we compare internet user with the teledensity; then we see that the number of internet users didn't increase that much. Currently only 0.25% people use internet [2]; which is 128 times less than current mobile or telephone users. Fig. 2, shows that the teledensity of Bangladesh in different years. From here we can see that after 2005 it changed so rapidly and it also can be observed that numbers of PSTN users are considerably low in Bangladesh. From the BTTB annual report of 2008 we find that total telecom user was 44.98 million where only 1.28 million was fixed line (PSTN) user.

If we compare figure 2 and 3 than we can find that, most of the investment happened in 2005 to 2007 and the teledensity was rapidly changed after 2006.

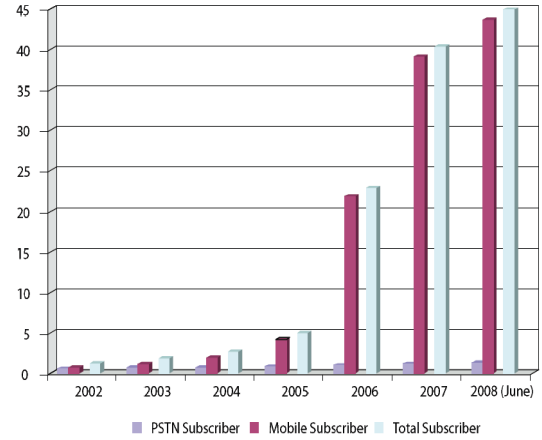

Fig. 2: Number of PSTN and Cellular user and Total user with respect to time; Along X-axis no of user in million [1].

If we compare figure 2 and 3 than we can find that, most of the investment happened in 2005 to 2007 and the teledensity was rapidly changed after 2006. After 2008 BTTB changed to BTCL and newly formed BTCL didn't introduce current statistics about teledensity. Some private organizations reported that current teledensity of Bangladesh is around 48 percent. In the comparison with developed country, it is very low.

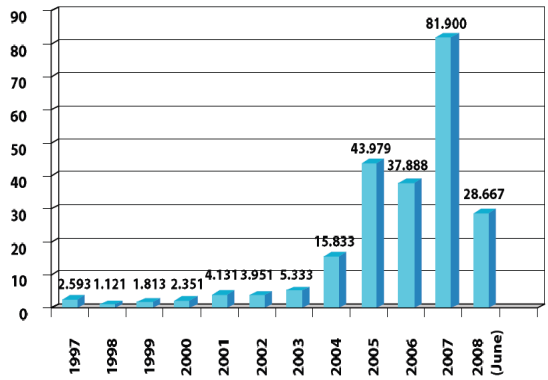

Fig. 3: Investments in telecommunication sector. Along X-axis report TK. in Billions. [1]

If we compare teledensity with human development index (HDI) of Bangladesh than we can find that In 2011 Bangladesh's HDI is 0.50 and from 2000 to now HDI increased by 0.80 percent [1]. Form fig. 4we can see that in last two decades human life expectation increased rapidly. In the year 2011 life expectancy reached almost 0.80 HDI; which is only 0.07 less than the develop world HDI. It can easily predictable that by 2020 human expectancy will touch the developed world's expectancy and in 2030 it will be parallel with the developed world. From fig. 4 we can also see that after 2000 education and gross national income (GNI) increased rapidly with compare with the last decade; and after 2000 telecommunication industry of Bangladesh increased enormously. But if we compare with India Pakistan; still Bangladesh HDI is lower than them. Recently India reported that their teledensity reached 70.89% and their HDI is over 0.55. Teledensity plays a vital role to improve HDI as well as GDP.

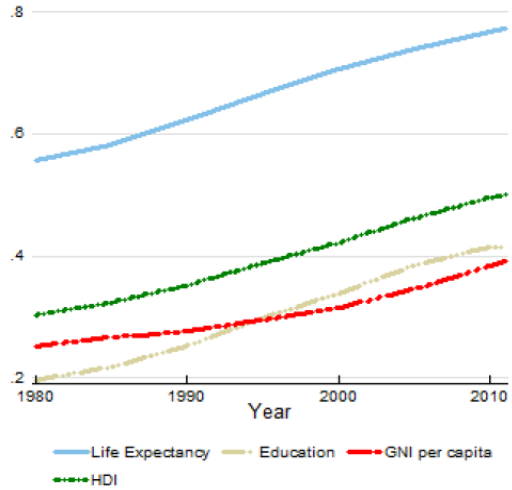

Fig. 4: Last two decade HDI of Bangladesh, here along X-axis represents HDI. [2]

In Bangladesh telecommunication industry plays an important role for HDI improvement. In fig. 4 we find that presently available fiber optical network in Bangladesh. From fig. 5 we can see currently available fiber optic network are point to point; that means thereis no alternative path to reach the destination, so if any problem occurs on the transmission cable than full network will face problem and problem facing section of the network goes outside of the network.

Internet Capacity	Satellite	48 Down + 24 Up Mbps	48 Down + 24 Up Mbps
	Submarine Cable	4 x STM4 + 8 STM1	6 x STM4 + 8 STM1
Internet Connection – Bcube Broadband (ADSL Capacity/Connection)		19,425/100	44,500/5000 (In 26 Districts)
Internet Connection – Click2Net dial-up		All Telephone Subscribers in the Country	

Present communication capacity in Bangladesh is given below which is taken from the BTCL 2011 report.

- International Internet Getaway& Trunk Exchanges (IIG/ITX): 5
- International Internet Getaway (IIG) Bandwidth : 3.34 Gbps
- International Circuits through Submarine Cable: 74176

Table 1: Fiber optic cable capacity [2]

STM4= 4 STM1= 4 X 155.52 Mbps = 622.08 Mbps
Form table 1 we find that current data transfer capability is around 9.66Gbps of the whole country. But the main drawback is only one submarine cable connection or optical fiber connection in Bangladesh. Data traffic link by this optical fiber is more than 8 Gbps. If fiber connection fails, the alternative two satellite connectiondata traffic capability is below 100Mbps; that is why it is unable to provide required service. Most of the BTCL fiber optic links are point to point. There is no alternative way if any faults occur in the backbone network.

Fig. 6 and 7 represents the current number of phone and internet user in the world. If we look carefully then we can see that in developed world percentage of mobile user is more than 100 percent and internet use almost 75 percent.

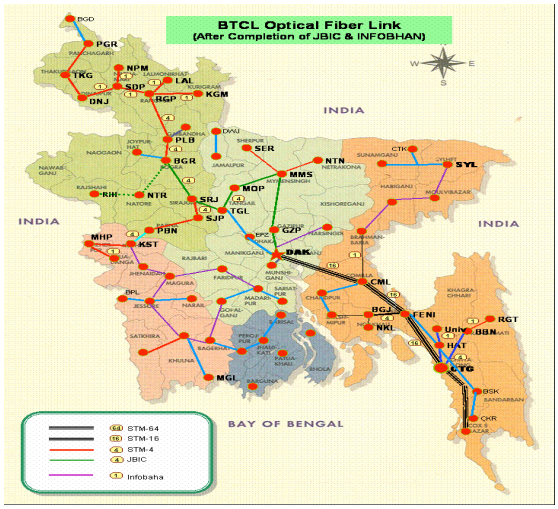

Fig. 5: Present fiber optical connection architecture in Bangladesh

In the developing country percentage of phone users and internet usersare respectively 80 and 20 percent. With respect to developed world Bangladesh's tele and internet density is very poor.Recently a private organization reported that current teledensity isaround 48 percent in Bangladesh.

Moreover, density is below 1 percent; but in Bangladesh life expectancy is very high with compare to total HDI which is reported by UNDP in the consideration of HDI [3].

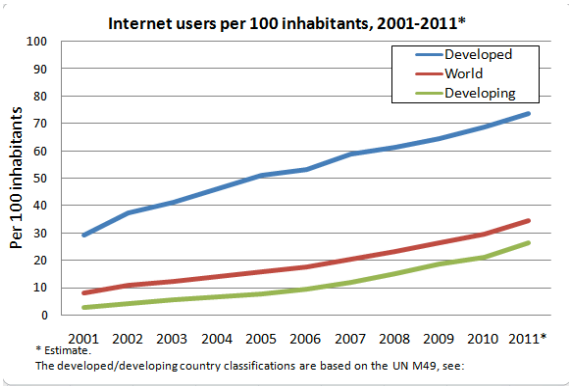

Fig. 6: Internet user in develop and the developing world [3]

3.FUTERE DATA DEMAND

In this research we are looking for the future data demand of Bangladesh. Here we consider by 2030's Bangladesh GDP will reach to double digit and mobile and internet use will be more than 80 and 70 percent. We make this assumtion depending on the HDI report. Current HDI is 0.50 but life expetancy is 0.80; which is less than 0.07 with comparing developed world HDI.

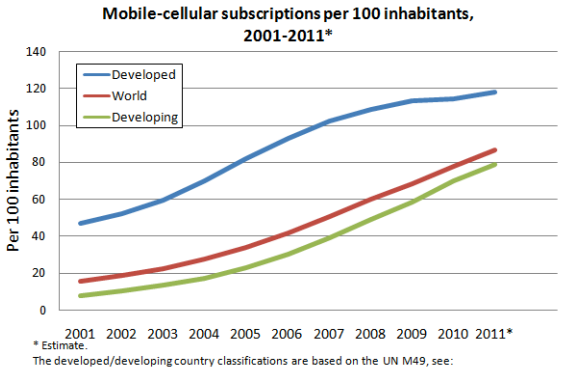

Fig.7: Percentage of Mobile user in develop and developing world [3]

So in 2030's population expected life style is more likely developed world; which increases our required data demand. But currently our capacity is around 10Gbps. But by 2030 our data demand will increase by more than 160 times of the present data demand. In this analysis we consider that by 2030's 70 percent population of Bangladesh will use internet and their minimum bandwidth on an average will be 512bps. Every dedicated IP will be shared by 5 users; that means on an average 20 percent people can get this service. From fig. 8 we can see that our required data demand is around 5Gbps for internet use; which is the 50 percent of the current capacity. If we consider that the number of internet user are linearly increasing in every year; that means we consider linear growth on internet sector and by 2030's it will be 70 percent. Then we can find that in 2030 our required data demand will be around 1.6TBps; which is 160 times of the current data demand. Currently available STM-64/16 fiber optic line cannot support this huge amount of data demand.

For telephone or mobile phone data demand is shown in fig. 9. In this simulation we considered that, 2030's mobile technology will introduce new application like video, movie, IP TV etc. Fig. 8 shows the total data traffic through the telecommunication network. Currently only 1.4 percent of the total datagoes outside the Bangladesh and we require only 4Gbps bandwidth.

If we consider our expected GDP and HDI then we can expect that international call will increase by 15 percent and in international getaway we need more than 147GBps bandwidth only for the telephone user which is the 37 times higher than the current speed

From fig. 9 we can also find that our total data traffic will be more than 950GBps and if we consider 147GBps in international getaway than we find more than 800GBps traffic within the country. From fig. 7 and 8 we find our total data demand is 1.6TBps and 0.98TBps for respectably for internet user and telephone user.

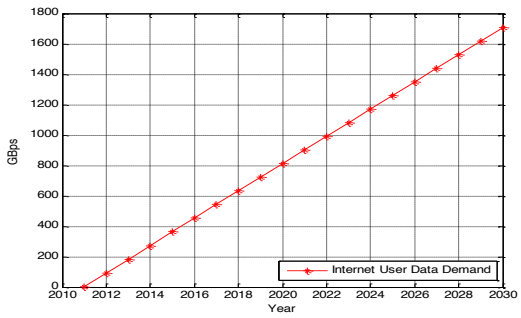

Fig. 8: Analysis result for internet user data demand through 2011 to 2030

So total data demand within the country is around 2.5Tbps and in international getawaywe require 1.8TBps; which is the hundred times higher than current data demand.

So, if we want to reach this destination we have to look for different technology as our current infrastructure is unable to serve this data demand.

So, if we want to reach this destination we have to look for different technology as our current infrastructure is unable to serve this data demand.

So, if we want to reach this destination we have to look for different technology as our current infrastructure is unable to serve this data demand. When infrastructure will available then internet density will increaseexponentially like asteledensity.

4. FEASIBLE SOLUTION

A Feasible solution is essential to overcome the problem. For overcoming the problem we figured out a model. A solution can be made by our proposed model which is given is fig 10. by blue lines.

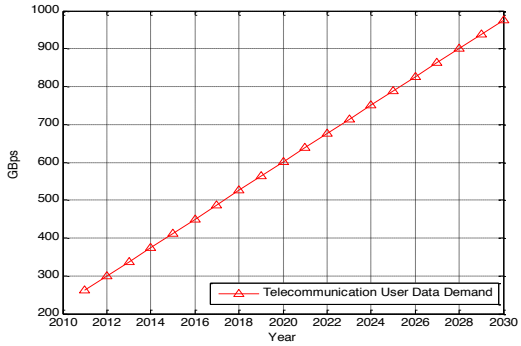

Fig. 9: Mobile user Data demand in 2030's in Bangladesh

Fig. 10: Proposed fiber optical connection architecture in Bangladesh

If we can make this happen it will help to solve the problem significantly.

5. CONCLUSION

We demonstrated the future data demand of Bangladesh which is 2.5TBps within the country and 1.8TBps in international getaway. To pick the latest technology for backbone network the best optionsthat are currently available is 400Gbps transceiver or Pol. Mux RZ-DPQPSK for future Bangladesh. If we adopt this technology for Bangladesh then we will be able to manage the future data demand of the country.

REFERANCES

[1] BTTB 2007-2008 annual report
[2] BTCL 2011annual repot.
[3] ITU report " Report to the BTRC on significant market power" 2007
[4] ICT Data and Statistics http://www.itu.int/ITU-D/ict/statistics/index.html
[5] http://www.itu.int/ITU-D/ict/publications/idi/2011/Material/MIS_2011_without_annex_5.pdf

Proceeding of the
International Conference on Electrical, Computer and Telecommunication Engineering
01- 02 December 2012 (ICECTE2012), RUET, Rajshahi-6204, Bangladesh

ICECTE2012: PI-0057

Effect of sampling rate and sensors separation on network node estimation

M. S. Anower

Department of Electrical and Electronic Engineering
Rajshahi University of Engineering and Technology
Kazla-6204, Rajshahi, Bangladesh.
md.shamimanower@yahoo.com

ABSTRACT
The number of nodes in a deployed wireless sensor network might vary due to ad hoc nature, natural disaster. Counting the number is very important in useful data collection, network maintenance, node localisation. Although protocols are being used to count the number in terrestrial networks, harsh environment limits their use in underwater networks. A statistical signal processing approach of node estimation is proposed in this paper. The nodes are considered as acoustic signal sources and their number is obtained through the cross-correlation of the acoustic signals received at two sensors. As the process of cross-correlation process might be affected by the sampling rate and the distance between sensors (sensor separation), their effects on estimation are investigated.

KEY WORDS: Cross-correlation, distance between sensors, node estimation, sampling rate, underwater acoustic sensor networks (UASN).

1. INTRODUCTION

In wireless sensor networks there may be a large number of nodes deployed over a large area for a practical purpose such as climatic data collection or pollution monitoring. Optimal performance requires a balance of the number of operating nodes, energy efficiency, and the lifetime of the network. So the number of operating nodes is a crucial factor for the networks.

However, the number of operating nodes can vary with time due to various artificial as well as natural reasons (for example, some nodes might fail, some could be damaged, or batteries might fail). So, it is a matter of great interest for a communication network to know how many operating nodes or transmitters are available in the region at any point in time to ensure proper network operation (such as routing) as well as network maintenance (such as replacement of faulty nodes). There have been many investigations regarding the estimation technique. For example, protocols [1-5] have been used to estimate the number of tag IDs in radio frequency identification (RFID) systems, which is a similar problem to the estimation of the number of nodes in wireless communication networks. Similarly, a Good-Turing estimator of node estimation for terrestrial sensor networks has been proposed in Budianu et al. [6], where each transmitting node transmits its ID in every slot according to a certain probability and the packet collection can be modeled as an i.i.d. sampling with uniform distribution by SENMA protocol (an ALOHA-like protocol). In this method they estimate the number of operating sensors by deriving an expression for it as a function of missing mass.

Although the abovementioned systems are easy to apply in RFID as well as terrestrial systems, they do not take into account the capture effect, which means that they are difficult to apply in UASN. One solution has been proposed in Howlader et al. [7], which proposes a node estimation technique taking the capture effect into account. The procedure is similar to probabilistic framed slotted ALOHA.

However all of the abovementioned procedures for the estimation of the number of nodes in RFID systems and in wireless sensor networks are similar in that they are based on protocol design. But, underwater propagation characteristics such as propagation delay, high absorption, and dispersion may make the use of protocol methods difficult.

In this paper, we propose a simple novel estimation technique based on the cross-correlation of the acoustic signals received at two sensors in the network. The cross-correlation of signals received from random signal sources at each end of the channel is an important issue in current research and this technique has been investigated by the researchers [8] to estimate the Green's function (GF), a form of cross-correlation function (CCF). However none of these investigations has focused on the estimation of the number of signal sources.

The process of cross-correlation might be affected by the sampling rate and the distance between sensors and the effects are investigated in this paper.

2. CROSS-CORRELATION PROCESS

Consider a 3D network of size *N*, where the nodes are uniformly deployed over the volume of a sphere. To estimate *N*, two identical sensors are placed inside the network as the centre of the sphere lays half way between the sensors. Assume that to respond a probe request the nodes can emit Gaussian signal.

Now, getting probe request, a node emits a very long Gaussian signal, which is recorded by the sensors with corresponding time delays. The signals in the sensors are cross-correlated, which takes the form of a delta function as it is a cross-correlation of two white Gaussian signals where one signal essentially is a delayed copy of the other. The position of this delta in the CCF will be the distance equal to the delay difference of the signals from the centre of the CCF where the position is called a bin in this paper. This holds for all nodes and the formation of CCF for *N* number of nodes can be expressed as follows.

If the transmitted signals from the nodes are denoted as $S_1(t), S_2(t), \cdots, S_N(t)$ respectively, the corresponding delays to reach the sensor 1 are denoted as $\tau_{11}, \tau_{21}, \cdots, \tau_{N1}$, and the corresponding attenuations are as $\alpha_{11}, \alpha_{21}, \cdots, \alpha_{N1}$, the composite signal at sensor 1 can be expressed as

$$S_{r_{t1}}(t) = \sum_{k=1}^{N} \alpha_{k1} S_k\left(t - \tau_{k1}\right) \tag{1}$$

Similarly, if the transmitted signals from the nodes are denoted as $S_1(t), S_2(t), \cdots, S_N(t)$ respectively, the corresponding delays to reach the sensor 2 are denoted as $\tau_{12}, \tau_{22}, \cdots, \tau_{N2}$, and the corresponding attenuations are as $\alpha_{12}, \alpha_{22}, \cdots, \alpha_{N2}$, the composite signal at sensor 2 can be expressed as

$$S_{r_{t2}}(t) = \sum_{k=1}^{N} \alpha_{k2} S_k\left(t - \tau_{k2}\right) \tag{2}$$

Assuming $\tau = d_{DBS}/c$ is the time shift in cross-correlation, and then the CCF is

$$\begin{aligned} C(\tau) &= \int_{-\infty}^{+\infty} S_{r_{t1}}(t) S_{r_{t2}}(t-\tau) d\tau \qquad (3) \\ &= \int_{-\infty}^{+\infty} \begin{matrix} \sum_{k=1}^{N} \alpha_{k1} S_k\left(t - \tau_{k1}\right) \\ \sum_{k=1}^{N} \alpha_{k2} S_k\left(t - \tau_{k2} - \tau\right) \end{matrix} d\tau \end{aligned}$$

which takes the form of a series of delta functions as it is a cross-correlation of two composite signals which are the summation of several white Gaussian signals.

One such obtained CCF with *N* (=10000) nodes is shown in Fig. 1.

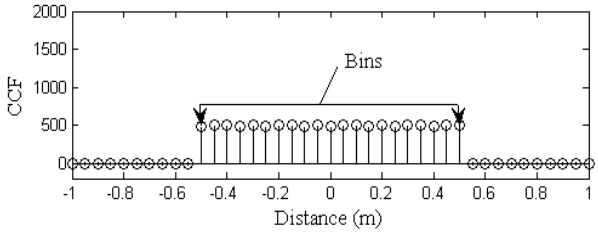

Fig. 1 Bins in the cross-correlation process positions are in meters from the CCF centre

2.1 Use of binomial distribution

Direct manipulation of the CCF is a complex problem. In this work, the cross-correlation technique is reframed to a probability problem using the well-known occupancy problem which follows the binomial probability distribution from which a parameter is chosen to estimate the number of nodes of a network. Occupancy problems deal with the pairings of objects and have a wide range of applications in different fields containing probabilistic and statistical properties. The basic occupancy problem is about placing m balls into *b* bins [9]. If one threw some balls randomly towards several bins, the bins would be randomly filled by the balls, resulting in some bins being occupied by more than one ball, some by one while some may have none. In this work, the cross-correlation process for node estimation is reframed as this occupancy problem. It describes the reframing process as follows.

- In this process to obtain a CCF, *N* nodes create *N* number of delta functions which occupy the place in the correlation length where the length is divided by *b* number of bins as shown in Fig. 1.
- Some bins are empty i.e. not occupied by any delta function; some are occupied by only one and others are more than one.

Moreover, the formation of cross-correlation function to obtain node estimation satisfies the characteristics of binomial distribution as the number of trials i.e. the number of nodes is fixed, trials are independent in that sense the nodes are sending independent Gaussian signal, there exist only two possible outcomes, success or failure, for every trial which indicates that delta for a particular node is occupying a bin or not, each trial has the same probability of success which is one on the number of bins, *b*. As the cross-correlation function follows the

binomial distribution, its mean and standard deviation are easy to obtain which is discussed in the following section.

3. ESTIMATION OF THE NUMBER OF NODES, *N*

It is discussed in the previous section that the cross-correlation function follows the binomial probability distribution in which the parameters are the number of balls i.e. nodes, N, and one on the number of bins, b. Then the expected value, i.e. the mean, m and the standard deviation, s_d of the CCF are defined as

$$m = \frac{N}{b} \tag{4}$$

and,

$$s_d = \sqrt{\frac{N}{b}\left(1-\frac{1}{b}\right)} \tag{5}$$

where b is the number of bins in the cross-correlation process.

Thus the estimation parameter, R_{msd} which is the ratio of mean and standard deviation of the CCF is obtained from (4) and (5) as follows

$$R_{msd} = \sqrt{\frac{\frac{N}{b}}{\left(1-\frac{1}{b}\right)}} = \sqrt{\frac{N}{b-1}} \tag{6}$$

which in turn gives the estimation of the number of nodes as

$$N = (b-1)\times R_{msd}^2 \tag{7}$$

4. EFFECTS OF SAMPLING RATE AND DISTANCE BETWEEN SENSORS

It can be seen in the expression (6) and (7) that the number of bins, b is a vital factor in the estimation process. The number of bins, b depends on the effective correlation length of the cross-correlation process. The effective length of the cross-correlation matrix is obtained from the experimental setup with sampling rate, S_R, distance between sensors, d_{DBS}, and speed of propagation, S_R and is defined as $\left(\frac{d_{DBS}\times S_R}{S_P}\right)\times 1$. Thus the number of bins, b in the cross-correlation process is defined by the following expression (8), as it is the cross-correlation of the two matrix of length $\left(\frac{d_{DBS}\times S_R}{S_P}\right)\times 1$.

$$b = \frac{2\times d_{DBS}\times S_R}{S_P} - 1 \tag{8}$$

It is shown that the estimation parameter is inversely proportional to one on the square root of the number of bins, b. and the value of b is directly proportional to both the sampling rate and the distance between sensors. Thus the increase of either or both the sampling rate and distance between sensors increases the value of the number of bins, b and which leads to get the higher values of the estimation parameter, R_{msd} and vice-versa.

5. RESULTS AND DISCUSSION

Simulations have been performed in the Matlab programming environment. The effects of varying the sampling rate and the distance between the sensors on the estimation parameter R (which is the inverse of R_{msd}) of CCF are shown in Fig. 2.

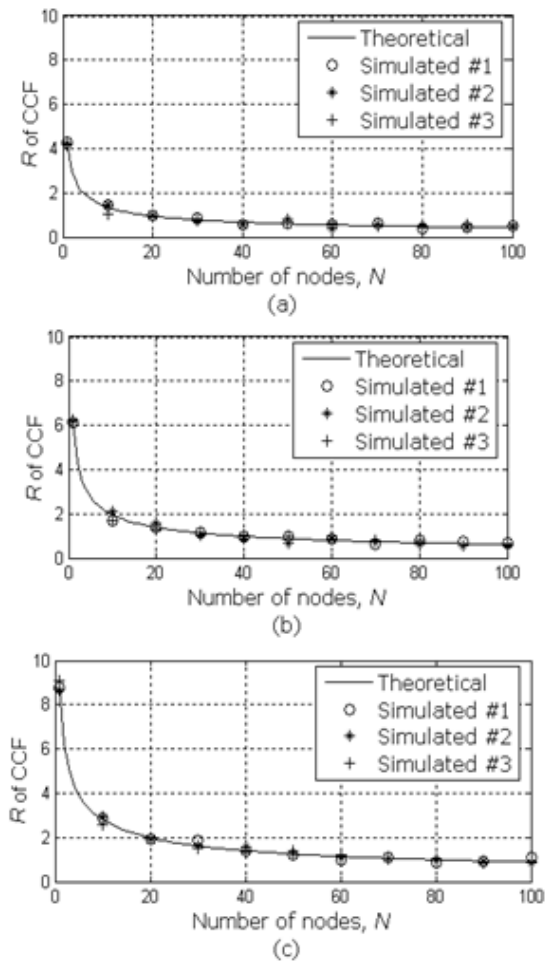

Fig. 2 R versus N: (a) b = 19; (b) b = 39; and (c) b = 79 [Simulated#1 - d_{DBS} variable and S_R fixed; simulated#2 - d_{DBS} fixed and S_R variable; and simulated#3 - both d_{DBS} and S_R variable]

There are three different plots, each comparing four different results with the same b. This figure shows comparisons of three different simulated R for b = 19

(Fig. 2 (a)), b = 39 (Fig. 2 (b)) and b = 79 (Fig. 2 (c)) using a variable d_{DBS} and a fixed S_R in simulated#1, a fixed d_{DBS} and a variable S_R in simulated#2 and both d_{DBS} and S_R variable in simulated#3 with theoretical R. The results in Fig. 2 demonstrate that, whatever the values of d_{DBS} and S_R, the estimation parameter, R, will only vary when b is varied. It is shown from the above results that, although the values of S_R and d_{DBS} change (keeping b fixed), the values of R for a particular N remain unchanged due to the unchanged b. Thus, it is possible to set suitable values for S_R and d_{DBS} by varying them oppositely to estimate N with a certain b. The results show that the simulated lines are very close to each other, which indicates that the process is good enough for estimation. Again it is obvious that the b will be larger if either or both d_{DBS} and sampling rate increases and it has an effect on the estimation parameter, which is discussed in the previous section. It is also obvious from the results that a good approximation of the number of nodes, N, can be obtained from the ration R of the CCF even when the distances between sensors are small to place them a single node.

6. CONCLUSION

This paper proposes a simple novel node estimation technique for underwater wireless sensor network. Previously proposed techniques (mostly for terrestrial wireless sensor networks and very few for underwater wireless sensor network) use routing protocols to count the number of nodes in a network. The protocol use is limited in underwater networks by the harshness of underwater environment and it requires lots of modifications which are developing stage and are inefficient and time consuming. Thus the proposed cross-correlation technique might be the useful alternate of the existing techniques. In this proposed technique, it is shown that the cross-correlation of random signal can be used to estimate the number of nodes or transmitters in underwater network. Mathematically derived expressions have been investigated by simulation and the results agree with the mathematics. The estimation parameter i.e. the estimation using cross-correlation depends on the sampling rate and the distance between sensors and is investigated with detail discussions in this paper.

REFERENCES

[1] M. Kodialam and T. Nandagopal, "Fast and Reliable Estimation Schemes In RFID Systems", Proc. Mobicom '06, September 23-26, 2006, Los Angeles, California, USA.

[2] M. A. Bonuccelli, F. Lonetti, and F. Martelli, "Tree slotted aloha: a new protocol for tag identification in RFID networks", Proc. of IEEE Int. Symposium on a World of Wireless, Mobile and Multimedia Networks, pp.603–608, Jun. 2006.

[3] M. A.-I. Center, Draft protocol specification for a 900 MHz class 0 radio frequency identification tag, http://www.epcglobalinc.org , Feb. 2003.

[4] J. Myung, W. Lee and J. Srivastava, "Adaptive binary splitting for efficient RFID tag anti-collision", IEEE Communications Letters, vol. 10 (3), pp.144–146, Mar. 2006.

[5] M. A. Bonuccelli, F. Lonetti, F. Martelli, Perfect tag identification protocol in RFID networks, http://arxiv.org/PS_cache/arxiv/pdf/0805/0805.1877v1.pdf, May 13, 2008.

[7] M.S.A. Howlader, M.R. Frater, and M.J. Ryan, "Estimation in Underwater Sensor networks taking into account capture" IEEE Oceans'07, Aberdeen, Scotland, 18-21 June 2007.

[8] P. Roux, K. Sabra, W. Kuperman, and A. Roux, "Ambient noise crosscorrelation in free space: theoretical approach", J. Acoustic Soc. Am., **117**, 79–84, 2005.

[9] W. Feller, "An Introduction to Probability Theory and its Applications, John Wiley, 1968.

Proceeding of the
International Conference on Electrical, Computer and Telecommunication Engineering
01- 02 December 2012 (ICECTE2012), RUET, Rajshahi-6204, Bangladesh

ICECTE2012: PI-0058

Practical Implementation of SS7 Signaling Link in Telecom Core Network

M. M. Mowla[1], A. A. Suman[2], L. C. Paul[3]
Electronics and Telecommunication Engineering,
Rajshahi University of Engineering and Technology, Bangladesh
E-mail: rimonece@gmail.com[1],suman.ete.ruet@gmail.com[2], litonpaulete@gmail.com[3]

ABSTRACT
Signaling System 7 (SS7) is a set of protocols that describes a means of communication between telephone switches in the international telecommunication networks. The network architecture of SS7 is greatly improved the performance of the public telephone network by facilitating faster call set up, routing, and supervision. SS7 has been traditionally used within the public switched telephone network (PSTN), but it is increasingly being used to interconnect the PSTN with wireless networks and next-generation internet protocol (IP) to support additional services as well as voice. This paper is intended to explain practical implementation of SS7 signaling links in the core network of telecommunication sector.

KEY WORDS: SS7, MTP, HLR, IN, SLC

1. INTRODUCTION

In telecommunications, the network's components must indicate (i.e. ~ signal) certain information to each other to coordinate themselves for providing services. For that, the signaling network can be considered the nervous system of telecommunication networks. It inserts life into the infrastructure. In telecommunication, core network operation is generally (In some cases, R2 signaling or other) completed by SS7. The purpose of this paper is to provide a clear explanation of how SS7 is actually implemented in core network of a telecom operation.

The rest of the paper is organized as follows. In section 2, basic concept & purpose of signaling will be discussed. In section 3, SS7 signaling network will be concisely explained. We will explain practical implementation method in section 4 and finally in section 5 we will draw conclusions.

2. BASICS CONCEPT OF SIGNALING [1]

For example, if a subscriber wishes to make a call, the call must be signaled to the subscriber's local switch. The initial signal in this process is the off-hook condition the subscriber causes by lifting the handset. The action of lifting the handset signals to the network that the subscriber wishes to engage a telephony services. The local switch should then acknowledge the request for telephony services by sending back a dial tone, which informs the subscriber that he can proceed to dial the called party number. Up to this point, the signaling is known as subscriber signaling and takes place between the subscriber and the local switch. When a complete called party number is received or enough digits are collected to allow the routing process to proceed, the calling party's local switch begins signaling to the other nodes that form part of the core network. The signaling that takes place between core network nodes is known as network signaling. In the Fig. 1, subscriber signaling and network signaling is shown for a core network.

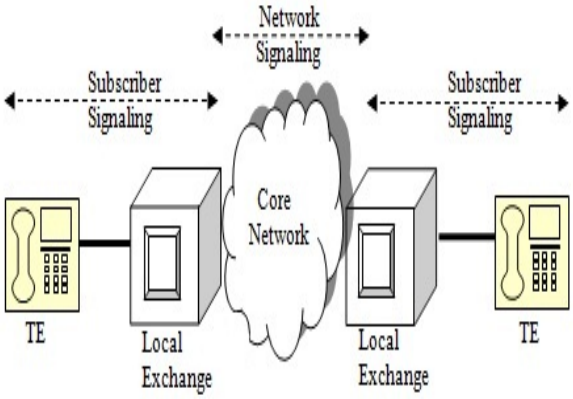

Fig. 1 Subscriber Signaling and Network Signaling

2.1 Main Purpose of Signaling

The purpose of signaling is to set up a circuit between the calling and called parties so that user traffic (voice, data for example) can be transported bi-directionally. When a circuit is reserved between both parties, the destination local switch places a ringing signal to alert the called party about the incoming call. This signal is classified as subscriber signaling because it travels between a switch (the called party's local switch) and a subscriber (the called party). A ringing indication tone is sent to the calling party telephone to signal that the telephone is ringing. This is called **set-up phase**. If the called party wishes to receive the call, the subscriber lifts the handset into the off-hook condition. This moves the call from the set-up phase to the **call phase** conditions. At some point in the call phase, one of

the parties will wish to terminate the call. The calling party typically initiates this final phase, which is known as the **release phase** conditions. The subscriber signals the network of the wish to terminate a call by placing the telephone back in the on-hook condition; hence, subscriber signaling. The local switch proceeds with network signaling to clear the call down.

3. SS7 SIGNALING NETWORK [2][3]

A signaling network is dedicated to the transmission of signaling messages. It is logically independent of the communication network. An SS7 network is essentially consists of: signaling point (SP), signaling link (SL) and signaling route (SR).

3.1 Signaling Point (SP)

SS7 network nodes are called signaling points (SPs). An SP is where the signaling messages are processed or exchanged. It functions as either the origination or the destination in signaling message transmission. Generally, an SP can be an exchange, an operation and maintenance center, or a network database. Each SP is addressed by an integer (Decimal/Hexadecimal) called signaling point code (SPC). The international network uses a 14-bit SPC. There are two types of SPCs: An originating SP (OSP) is identified with an originating point code (OPC). A destination SP (DSP) is identified with a destination point code (DPC). There are three different types of SP (signaling point):

1. Service Switching Point (SSP)
2. Signaling Transfer Point (STP)
3. Service Control Point (SCP)

3.1.1 Service Switching Point (SSP)

A Service Switching Point (SSP) is a voice switch that incorporates SS7 functionality. It processes voice-band traffic (voice, fax, modem etc.) and performs SS7 signaling. All switches with SS7 functionality are considered SSPs regardless of whether they are local switches or tandem switches. An SSP sends signaling messages to other SSPs to setup manage and release voice circuit required completing a call. It may query to central database SCP, of HLR and IN, to determine how to route a call.

3.1.2 Signal Transfer Point (STP)

A Signal Transfer Point (STP) is responsible for the transfer of SS7 messages between other SS7 nodes, acting somewhat like a router in an IP network. An STP is neither the ultimate source nor the destination. STPs are usually deployed in mated pairs in separate physical location as a backup system. Traffics are shared across all links, so if one of the links fails, the signaling traffic is re-routed over another link. STPs route each incoming message to an outgoing signaling link based on routing information contained in the SS7 message. Since STPs act as network hubs, they improve the utilization of the SS7 network by eliminating the need for direct links between signaling points. STPs also offer specialized routing functions for toll-free 800 numbers, calling card numbers, or mobile subscriber identification numbers. An STP may also be used to screen the messages exchanged with other networks.

3.1.3 Service Control Point (SCP)

A Service Control Point (SCP) acts as a central database providing information necessary for call processing. SCPs form the means to provide the core functionality of cellular networks, which is subscriber mobility. Certain cellular databases (called registers) are used to keep track of the subscriber's location so that incoming calls may be delivered used in HLR part. Other telecommunication databases include those used for calling card validation (access card, credit card) specially used in pre-paid phone's IN part.

3.2 Signaling Link (SL)

SPs are connected to each other by signaling links over which signaling takes place. The bandwidth of a signaling link is normally 64 kilobits per second (kbps). Links are typically engineered to carry only 25 to 40 percent of their capacity so that in case of a failure, one link can carry the load of two. Links between two SPs are logically grouped for administrative and load-sharing reasons.

3.2.1 Signaling Link Set (SLS)

A collection of signaling links with the same attributes is called a link set. The links to the same office may belong to one link or several link sets. The links between two adjacent SPs, however, must be configured in one link set.

3.2.2 Signaling Link Code (SLC)

Each signaling link is uniquely identified within an office with a signaling link code (SLC). All signaling links between two adjacent SPs are uniquely numbered in the same way. The SLCs of these links must be consistent at the two SPs. For signaling links to different offices, the SLCs may be identical.

3.3 Signaling Route (SR)

A signaling route is a path along which signaling messages are transmitted from an OSP to DSP. SS7 routes are statically facilitated at each SP. The selection of signaling route depends on the signaling relations and the transfer mode.

3.3.1 Signaling Route Set (SRS)

All signaling routes that correspond to a signaling relation form a route set. A given signaling message is transmitted along a specific route in normal cases. When this route becomes faulty, an alternative route is taken.

4. PRACTICAL IMPLEMENTATION [4]

Now, we will analysis practical signaling configuration of core network for an operator. Generally core network consists of several nodes (SP) like MSC, HLR, IN, VLR, EIR, AUC etc. Fig. 2 shows some SPs such as MSC, HLR and IN for a telecom operator.

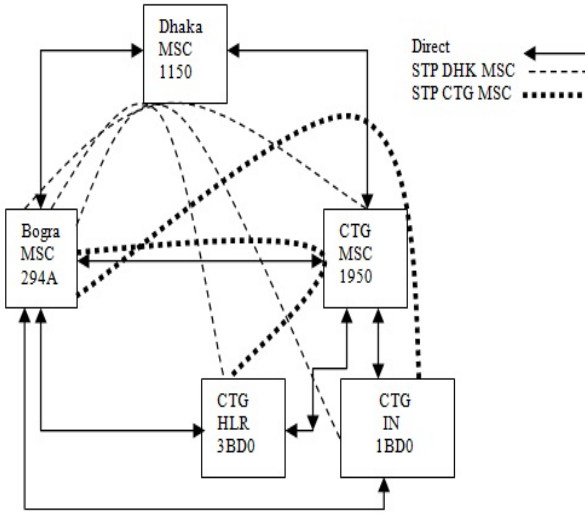

Fig. 2 Different SPs location showing direct and STP connection of a telecom core network.

Explanation:

Let, there is a telecom operator which has three core network switches (MSC) around the country named as Bogra MSC (BOG_MSC), Dhaka MSC (DHK_MSC) and Chittagong MSC (CTG_MSC). All MSC are known as SP. The Home location register (HLR) and Intelligent network (IN) of the operator are also in CTG region under CTG_MSC. HLR and IN are also treated as different SP. These all Entities are shown in Fig. 3. There is a direct connection between BOG_MSC to all other SPs as well as STP connection (Via Path) except for DHK_MSC as there is no STP link. There is also direct connection between CTG_MSC and CTG_ HLR & CTG_IN.

Let, these arrangements of data are configured in BOG_MSC. We explain here SS7 signaling configuration for BOG_MSC perspective only.

Table 1: MTP Point Code Information

DSP Index	DSP Name	OPC	DPC
1	DHK_MSC	294A	1150
2	CTG_MSC	294A	1950
3	CTG_HLR	294A	3CD0
4	CTG_IN	294A	1BD0

From the Table 1, we see that the origination point code (OPC) for Bogra MSC is 294A. It is a unique hexadecimal number for a particular SP around the country provided by Bangladesh Telecom Regularity Commission (BTRC). From Table 1, we also see point code for DHK_MSC, CTG_MSC, CTG_HLR and CTG_IN are respectively 1150, 1950, 3CD0 and 1BD0. The Destination Switching Point (DSP) is indexed here serially for those SPs from 1 to 4.

Table 2: MTP Link Table Information

Link No.	Link Name	SLC	Link Set No.
1	BOG_MSC to DHK_MSC_1	0	1
2	BOG_MSC to DHK_MSC_2	1	1
3	BOG_MSC to CTG_MSC_1	0	2
4	BOG_MSC to CTG_MSC_2	1	2
5	BOG_MSC to CTG_HLR_1	0	3
6	BOG_MSC to CTG_HLR_2	1	3
7	BOG_MSC to CTG_IN_1	0	4
8	BOG_MSC to CTG_IN_2	1	4

In the Table 2, the signaling links are configured. Link No. is indexed serially in a SP. There are two signaling links configured between BOG_MSC and DHK_MSC. Link No.1 and 2 are configured for BOG_MSC to DHK_MSC for some E1's. Generally, for each E1, timeslot-16 is kept for signaling purpose and timeslot-0 is reserved for synchronization. But, when a group of E1's are configured as a single attribute or an office, then suppose for One STM-1 (63E1), there may be used 3 or 4 signaling links (SL) are practically used. Link Set No. is same for that particular attribute or office. SLC is numbered as 0 and 1 because of uniqueness for a specific Link Set No. So, total number of signaling links in a particular attribute or office should be marked serially as SLC indexing increasing 0, 1, 2……so on.

Table 3: MTP Route Table Information

Route Name	DSP Index	Link Set	Prior -ity
DHK_MSC_Direct	1	1	0
CTG_MSC_Direct	2	2	0
CTG_MSC_STP_DHK_MSC	2	1	1
CTG_HLR_ Direct	3	3	0
CTG_HLR_STP_DHK_MSC	3	1	1

CTG_HLR_STP_CTG_MSC	3	2	2
CTG_IN_ Direct	4	4	0
CTG_IN_STP_DHK_MSC	4	1	1
CTG_IN_STP_CTG_MSC	4	2	2

In Table 3, MTP signaling links are configured for routing. For each SP to another SP, there are two types of signaling links, i.e. ~ Direct and STP links are configured.

Now, we will explain about some cases about MTP routes.

Case 1:
From BOG_MSC to DHK_MSC, there is a configuration for only direct link (DHK_MSC_Direct). From Table 1, it is already known that Dhaka MSC DSP index is 1, Signaling link set no is 1 and for direct link the priority is 0. As there is no STP connection, so there is no further configuration.

Case 2:
Now, for connection between BOG_MSC and CTG_MSC, there are two types of signaling links, i.e.~ CTG_MSC_Direct & CTG_MSC_STP_DHK_MSC. From Table 1 and Table 2, it is already known that CTG_MSC DSP index is 2, Signaling link set no is 2 and priority for direct link is 0. For STP_DHK_MSC, Signaling link set no is 1 and priority for STP link is 1.

Case 3:
For BOG_MSC to CTG HLR connection, there are three routes, i.e. ~ one direct and two STP links configured.
When connection with CTG_HLR_Direct, DSP index for CTG_HLR is always 3 (Table 1), Link Set No. is 3 (Table 2) and for direct connection the priority is 0.
For CTG_HLR_STP_DHK_MSC, DSP index is 3, Link Set No. for DHK_MSC is 1 and it is provided second priority 1.
For CTG_HLR_STP_CTG_MSC, DSP index is 3, Link Set No. for CTG_MSC is 2 and it is provided third priority 2.

Case 4:
For BOG_MSC to CTG IN connection, there are three routes, i.e. ~ one direct and two STP links configured.
When connection with CTG_IN_Direct, DSP index for CTG_IN is always 4 (Table 1), Link Set No. is 4 (Table 2) and for direct connection the priority is 0.
For CTG_IN_STP_DHK_MSC, DSP index is 4, Link Set No. for DHK_MSC is 1 and it is provided second priority 1.
For CTG_IN_STP_CTG_MSC, DSP index is 4, Link Set No. for CTG_MSC is 2 and it is provided third priority 2.

5. CONCLUSION
In this paper, the SS7 signaling network is described and explains the practical implementation of MTP links in core network of an operator. Different SP (MSC, HLR, SCP, IN, SMSC) are normally implemented in the same core network. For simplicity, we describe in this paper the MSC, HLR and IN for direct and STP connection and how the MTP links are configured in the switch. These case studies explanation helps anyone for understanding SS7 link characteristics such as link configuration and link routing.

6. ACKNOWLEDGEMENT
This network diagram is taken partially from core network department of RankTelecom Limited.

REFERENCES:

[1] Lee Dryburgh, Jeff Hewett, "Signaling System No. 7 (SS7/C7): Protocol, Architecture and Services", CISCO Press, August 2004, ISBN- 1-58705-040-4
[2] HUAWEI M800 CDMA Mobile Switching Center, Technical Manual, Vol. Signaling System, Manual Version: T2-030239-20060208-C-6.32 Product Version: V610R003, BOM: 31026239
[3] Introduction to Signaling System No. 7, publication number TEC-GEN-003 Rev. B, 2001, SUNRISE Telecom Incorporated.
[4] Core Network Department, RanksTelecom Limited.

Proceeding of the
International Conference on Electrical, Computer and Telecommunication Engineering
01- 02 December 2012 (ICECTE2012), RUET, Rajshahi-6204, Bangladesh

ICECTE2012: PI-0060

A Reliable Substation Communication Network with Reduced Ethernet Switch

Mojaharul Islam,[1],[*] *Hong-Hee Lee,*[2]

[1] Dept.of Electrical Engineering, University of Ulsan, Ulsan, South Korea & Dept. of Electronic and Telecommunications Engineering, International Islamic University Chittagong, Chittagong, Bangladesh

[2] Dept. of Electrical Engineering, University of Ulsan, Ulsan, South Korea

E-mail: mithucuet03@gmail.com , hhlee@mail.ulsan.ac.kr

ABSTRACT

Time critical monitoring and protection of power substations require very fast and reliable communication network. This paper proposes an Ethernet-based double ring Substation Communication Architecture (SCA) with reduced number of Ethernet switches without sacrificing reliability, and considering the future complexity and cost in case of expansion of substation. Instead of connecting all Intelligence Electronics Devices (IEDs) for one feeder within a bay switch, specific type of IEDs (i.e. merging unit, or protection and control IED, or breaker IED) from different manufacturer are connected to a common switch. This approach reduces the number of Ethernet switch of SCA and fixes the number of switches in case of expansion of substation. The performance of the proposed SCA is evaluated in term of End-to-End delay by modeling substation node and traffic according to IEC61850 with the Optimized Network Engineering Tool (OPNET). Experimental results demonstrate the simplicity and competency of the proposed SCA.

KEY WORDS: IEC61850, substation automation system (SAS), substation communication architecture (SCA), Ethernet, intelligent electronic devices (IEDs), protection & control (P&C)

1. INTRODUCTION

Digital Substation is one of the key nodes of future smart grid in order to meet real time monitoring, control and protection of power system. Automation in substation is prominently depending on a fast and reliable communication network and the traditional methods of automation force the customers to use single vendor equipment's due to proprietary solutions. Introduction of International Electrotechnical Commission's (IEC) standard IEC61850 makes a revolutionary change in Substation Automation System (SAS) which approaches Common Information Modeling (CIM) and common communication profile for microprocessor based Intelligent Electronic Devices (IEDs) to realize interoperability between different vendor products. [1-2] gave an overview of IEC61850 and Cagil *et al.* [3] explained the application view model of the international standard IEC61850. Expectancy of IEC61850 in process bus was described in [4-5]. As the mission critical information in process bus involves extremely high synchronization in the range of 1µs, the evaluation of time synchronization protocol IEEE1588 for critical event time synchronization in SAS is accomplished in [6] to compare the performance with IRIG-B based system. Moreover, mapping of IEC61850 services on International Standards Organization (ISO) Open System Interconnection (OSI) communication model made it highly acceptable by all over the world. Active researches have been conducted on penetration of industrial Ethernet technology into SAS [7-12]. The performance of Ethernet technology in worst situation is reported in [13-14] to verify the real time requirement.

Implementation of IEC61850 based substation automation requires very fast and reliable communication network to satisfy the P&C functions. Different types of communication network were proposed for Substation Communication Architecture (SCA) in [8, 15, 16]. All these networks are based on either share Ethernet or switched Ethernet. However, switched Ethernet seems to be fit for fast and reliable SCA because of supporting multi-port parallel link and archives concurrent data transmission among multi-node. Ethernet switch based several communication architectures were proposed in [12, 15, 16]. Among them, double ring structure was proposed in [16] as a highly reliable, fast and deterministic SCA. This paper adopt Ethernet-based double ring SCA and propose a SCA by rearranging the devices under the switches and reduced the number of Ethernet switches without sacrificing reliability of SAS and considering the future complexity and cost in case of expansion of substation. In addition, a central P&C unit is used which act as bus protection unit and backup unit for bay P&C unit in order to increase the reliability of SAS. IEDs from different vendors are considered as a reflection of interoperability. Cost effectiveness of the proposed SCA is explained in terms of number of Ethernet switches used in the SAS. Traffic within a

substation is illustrated according to IEC61850 and the performance is analysed in a heavy traffic condition. The performance of the proposed scheme is evaluated in term of End-to-End delay by using the Optimized Network Engineering Tool (OPNET) simulation software.

The rest of the paper is organized as follows. Section 2 introduces the proposed reduced Ethernet switch based SCA. Section 3 provides IED modeling and simulation study, and Section 4 analyses the cost effectiveness of the proposed SCA. Finally, Section 5 concludes the paper.

2. Reduced Ethernet Switched Based Substation Communication Architecture

SAS is distinctly separated into three levels: process level, bay level, and station level. Process level is the hardwire interface with switchyard equipment such as current transformers (CTs), potential transformers (PTs), circuit breakers (CBs) and disconnecting switches. Bay level contains the P&C IEDs. Station level comprises with Human Machine Interface (HMI), station printer, central P&C IED, GPS receiver, and remote interfaces. Fast and reliable operation of SAS depends on SCA. In planning stage of substation, the suitable communication link and communication architecture have to be chosen on cost and reliability demand of the customer. Ethernet switch based several communication architecture is proposed in [16]. In the SCA, they recommended an Ethernet switch based double ring network where one Ethernet switch is used per bay and all IEDs of the corresponding bay are connected with that switch. But in case of substation with large number of feeders this SCA needs a number of Ethernet switch. Thus, in our proposed system, similar IEDs are connected to a common Ethernet switch. The proposed SCA for an eight feeder substation is shown in Fig.1. Merging units from specific manufacturer of all feeders are connected within an Ethernet switch. Similarly, breaker IEDs of all feeders are connected to one switch and P&C IEDs of all feeders are connected to one switch. All station level devices are connected under one switch. Under the station switch a central unit is used which will act as bus P&C unit and as well as backup unit of bay P&C unit. Thus make the SAS more reliable in case of failure of bay P&C unit. Finally, the entire switches are connected in ring architecture. By using this arrangement, the number of Ethernet switch used in the substation can be reduced without sacrificing reliability. For a SCA, proposed in [16], with twenty feeder substations the required number of Ethernet

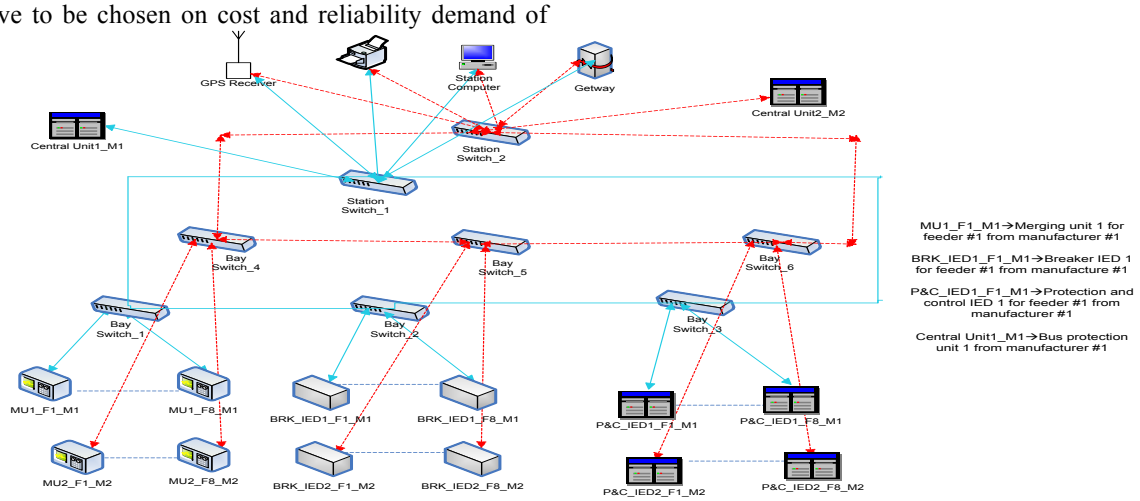

Fig. 1 Proposed Substation Communication Architecture (SCA).

switch is twenty two, whereas for our proposed arrangement it needs only eight switches. The devices can be chosen from different manufactures. In this paper, we choose the devices from two different manufactures as a reflection of interoperability. All the IEDs from one manufacturer are connected in a manner to form a common ring. The IEDs from another manufacture are connected under the second ring. As redundant devices are used, single point failure is completely avoidable. Moreover, using central unit as a backup unit of bay P&C IEDs makes the SAS more reliable. Configuration changing of any IED can be done reliably because of redundant devices and independent operation of ring structures. Interlocking, synchronous checking and auto reclosing functions can also be implemented reliably. Another advantage of this arrangement is to avoid extra switches in case of future extension of substation.

3. IED Modeling and Simulation Study

The LAN traffic in the office environment shows a random behavior. But, the real-time systems like power system control and protection have a deterministic traffic environment. Deterministic behavior makes it easy to determine the network performance in maximum load condition. In order to achieve this deterministic behavior, primarily each device in the network must have its own switch and the switches must work in the so called store and forward mode [18]. For performance study of SCA, a D2-1 type substation is considered generally [17]. It consists of two transformer bays (T1 and T2), six feeder bays, and one bus section bay. Substation communication network is shown in Fig.1. Each feeder contains two merging unit (MU) IEDs, two breaker IEDs, and two protection and control (P&C) IEDs. Message types and corresponding maximum allowable time delay for substation environment are summarized in [15] according to IEC61850 and IEC61850-8. Each merging unit sends raw data message at a specific sampling rate to corresponding P&C IEDs, and bus protection IED shown as central unit in Fig.1. The size of Ether-type application protocol data unit (APDU) for transformer bay is 98 bytes because it contains two datasets of current and voltage, whereas each APDU size of the feeder bay is 52 bytes as it contains one dataset of current and voltage [20]. Each raw message is sent once to the network. According to IEEE 802.1Q the time critical message like the raw data message should be tagged with high priority from low time requirement busload. VLAN is used to limit the broadcasting domain of data traffic [21].

As a fault can occur randomly, in order to assume the traffic in fault condition, P&C IEDs send trip message to corresponding circuit breaker in a random manner. The size of the trip message is 16 bytes. Each time trip message is sent four times to ensure correct delivery of message. The breaker IEDs also confirms its status change by GOOSE message to corresponding P&C IEDs. The size of the GOOSE message is also 16 bytes. All MUs and breaker IEDs also send updated meter values or breaker status to station server at a rate of 20 Hz. These messages are RMS voltage, RMS current and breaker status. In this case, message size is considered as 32 bytes for this study [20]. Each message is sent once to the network. For heavy background traffic, all P&C IEDs are randomly uploaded or downloaded different types of files to station server which is illustrated using FTP functions with a size of 50000 bytes.

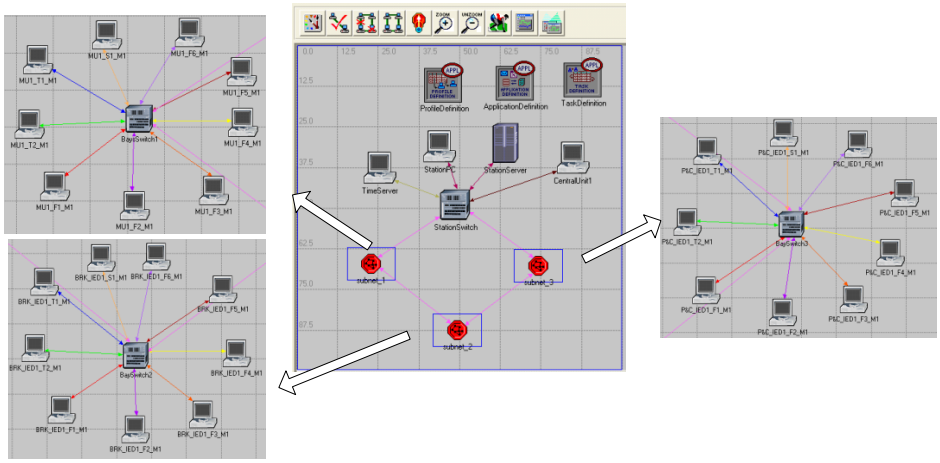

Fig. 2 Single ring arrangement of logical substation network.

As a fault can occur randomly, in order to assume the traffic in fault condition, P&C IEDs send trip message to corresponding circuit breaker in a random manner. The size of the trip message is 16 bytes. Each time trip message is sent four times to ensure correct delivery of message. The breaker IEDs also confirms its status change by GOOSE message to corresponding P&C IEDs. The size of the GOOSE message is also 16 bytes. All MUs and breaker IEDs also send updated meter values or breaker status to station server at a rate of 20 Hz. These messages are RMS voltage, RMS current and breaker status. In this case, message size is considered as 32 bytes for this study [20]. Each message is sent once to the network. For heavy background traffic, all P&C IEDs are randomly uploaded or downloaded different types of files to station server which is illustrated using FTP functions with a size of 50000 bytes.

For simulation study, OPNET modeler [21] is used to construct the models using object-oriented modeling approach. Network devices like IEDs, switches and workstations are called node models.

Fig.2 shows the single ring architecture for the proposed SCA. As two rings operate independently, it

is enough to show the performance for a single network. In OPNET, Ethernet switch is configured on port based VLAN. In Fig.2, VLANs are marked using different colour line to differentiate them from each other. After the completion of all configurations, the performance evaluation statistic is chosen as End-to-End delay. Simulation is run for 1 hour. After the completion of simulation, result can be viewed on the project editor. Table I shows the simulation result in term of maximum and average time delay with different sampling rate for the LAN speed of 10Mbps, 100Mbps, and 1000Mbps.

TABLE 1
END-TO-END DELAY FOR DIFFERENT TYPES OF CONNECTION LINK

LAN Speed	Sampling Rate Samples/s	Maximum Delay ms	Average Delay ms
10 Mbps	960	3.3215	3.2965
	1920	3.3364	2.7218
	4800	3.3139	3.2592
100 Mbps	960	0.3178	0.2592
	1920	0.1756	0.0171
	4800	0.3165	0.2562
1 Gbps	960	0.0389	0.0348
	1920	0.0176	0.0147
	4800	0.0178	0.0147

4. CONCLUSIONS

The proposed architecture for Ethernet based substation logical architecture gives a cost effective optimized solution for all type of substation. Moreover, using central P&C unit increases the reliability of SAS. Simulation results demonstrate the performance of the substation with priority tagging of time critical message and the implementation of VLAN technique in term of End-to-End with different link connection. In addition, the survivability of the arrangement is also presented in case of worst traffic situation that is mapped according to the IEC61850 standard. Time critical function and synchronized function can be implemented reliably. Thus, the proposed SCA for SAS provides a very simple, highly reliable and cost optimized solution not only in short term but also long term vision of substation by an outstanding manner.

5. ACKNOWLEDGMENT

This work was partly supported by the NRF grant funded by the Korean government (MEST) (No. 2010-0025483) and the Network-based Automation Research Center (NARC) funded by the Ministry of Knowledge Economy

REFERENCES

[1] Baigent, Drew, Adamiak, Mark & Mackiewicz, Ralph, "IEC61850 Communication Network and System in Substations: An Overview for Users," *Protection and Control journal, Vol.8, pp. 61-68,* 2009.

[2] Mackiewicz, Ralph, "Technical Overview and Benefits of the IEC 61850 Standard for Substation Automation," *in Proceedings of the Power Systems Conference and Exposition,* IEEE, Oct. 29-Nov 1, 2006.

[3] Ozansoy, C.R., Zayegh , A. & kalam, A., "The Application – View Model of the International Standard IEC61850," *IEEE transactions on Power delivery,* vol. 24, pp.1132-1139,2009.

[4] Andersson, Lars, Brunner, Christoph & Engler, Fred, "Substation Automation based on IEC 61850 with new process-close Technologies," *IEEE BPT* Bologna, 2003.

[5] Mo, J. & Tan, J.C., "Evaluation of Process Bus Reliability," *Delivered at 10th International Conference of the Institute of Engineering and Technology,* 2010.

[6] De Dominicis, C.M., Ferrari, P., Flammini, A., Rinaldi, S. & Quarantelli, M., "Experimental Evaluation of Synchronization Solutions for Substation Automation Systems," *Proceedings of I2MTC International Instrumentation & Measurement Technology Conference,* pp. 1492-1496, 2010.

[7] Skeie, T., Johanessen, S., & Brunner, C., "ETHERNET in Substation Automation," *IEEE Control System Magazine,* vol. 22, Issue 3, pp.43–5, 2002.

[8] Hoga, C., "New Ethernet Technogies for Substation Automation," *Proceedings of IEEE Power Tech conference,* pp. 707-712, 2007.

[9] Puzzuoli, M.P. and Moore, R., "Ethernet in the Substation," *Proceedings of IEEE Power Engineering General Society Meeting, 2006.*

[10] Raza, A., Ullah, K., Ahmed, S., Hyuk-Soo, Jang & Hyo-Sik, Yang , "Gigabit Ethernet Based Substation under IEC61850 standard," *Proceedings of 2nd international conference on computer, control and communication,* 2009.

[11] Jang, H.-S., Raza, A., Qureshi, M., Kumar, D. & Yang, H.-S., "Gigabit Ethernet base substation. Technical report," Myongji University, Aug. 2007.

[12] Wester, Craig, Adamiak, Mark (2010).Practical Application of Ethernet in substations and Industrial facility[online]*Available: http://www.l-3.com/wp/ieee.*

[13] Lee, K. C., Lee, S. & Lee, M. H. , "Worst case communication delay of real-time industrial switched Ethernet with multiple levels," *IEEE Trans.Ind. Electron.* , Vol. 53,issue no. 5, pp.1669–1676,2006.

[14] Mazraani, T. Y. & Parulkar, G. M., "Performance Analysis of the Ethernet under Conditions of Bursty Traffic," *Proceedings of the IEEE'92 GLOBECOM Conference, vol.1, pp. 592-596,* 1992.

[15] Kalaimani, M. and Rajmohan, C., "Simplified Protection System Architecture Based on IEC61850 for Next Generation IED's," *Proceedings of10th international conference on developments in power system protection*, 2010.

[16] Ali, I. and Mini, S. Thomas, "Substation communication networks architecture," Proceedings of POWERCON & IEEE Power India Conference, 2008.

[17] IEC61850: Communication Networks and systems in Substations, Part-1-9,2003.

[18] Mini, S. Thomas & Iqbal, Ali, "Reliable, Fast and Deterministic Substation Communication Network Architecture and its Performance Simulation*," IEEE Transaction on Power Delivery, vol.25, issue no. 4, p.2364–2370,2010.*

[19] Fodero, Ken, Huntley, Chris & Whitehead, Dave, "Secure, Wide-Area Time Synchronization," *Schweitzer Engineering Laboratories, Inc* .

[20] Sidhu, T. S. and Yin, Y., "Modeling and simulation for performance evaluation of IEC 61850-substation

communication systems," *IEEE Trans. on Power Delivery, 22, no. 3, p.1482–1489,2007.*

[21] OPNET Modeler. [Online]. Available: http://www.opnet.com.

Proceeding of the
International Conference on Electrical, Computer and Telecommunication Engineering
01- 02 December 2012 (ICECTE2012), RUET, Rajshahi-6204, Bangladesh

ICECTE2012: PI- 0061

Interference Mitigation for Femtocellular Network Deployment in Train Environment

Mostafa Zaman Chowdhury[1], Kazi Nawshad Azam[1], Ratan Kumar Mondal[1], and Yeong Min Jang[2]
[1]Dept. of Electrical and Electronic Engineering, Khulna University of Engineering and Technology, Bangladesh
[2]Dept. of Electronics Engineering, Kookmin University, South Korea
E-mail: mzceee@yahoo.com

Abstract

Owing to long distance between the base station and the users, movement of the vehicle, and the wall penetration loss, the users inside the vehicle suffer from low signal quality problem. The femtocells deployment in vehicle reduces the received signal quality problem. However, densely deployed femtocells cause serious femtocell-to-femtocell interference problem. In this paper we proposed efficient frequency allocation techniques for the moving femtocells in train environment to mitigate interference effects. The outage probability and signal quality analyses clearly demonstrate the advantage of our scheme.

Keywords: Moving femtocell, interference, frequency, and outage probability,

1. Introduction

The femtocell [1-2] is a new and emerging technology for the future wireless networks. Besides, femtocells deployment in vehicle is a new paradigm of femtocellular network deployment. Fig. 1 shows the femtocellular network deployment in the train environment. The femto access points (FAPs) are installed inside the train to make wireless connection between the users and the FAP. The FAPs and the transceiver are connected through the wired networks. The users enjoy the wireless services through the FAP. Macrocellular, satellite, or other wireless networks can be used for backhauling the femtocell traffic. .

The mobile users in the train and other vehicular environments suffer for the low quality signal from the outside wireless networks. The deployment of femtocells [1] in the vehicular environment can solve the low level signal-to-noise plus interference problem. Short distance between the user and the FAP provides better signal quality for the users. Also eliminating the wall penetration loss by the femtocellular network deployment in the train environment reduces the outage probability for the mobile users. However, dense deployment of femtocells in vehicular environment may cause serious femtocell-to-femtocell interference problem. Therefore, the frequency allocations among the femtocells of various vehicles should be properly allocated to reduce the interference effect as well as to increase the spectral efficiency. In this paper we propose an efficient scheme based on fractional frequency reuse [3] to allocate the frequency among various femtocells in train environment. The proposed scheme can reduce the inter-femtocell interferences. The concept of multi-level power transmission for each of the FAPs is applied to produce two separate coverage area. All the inner coverage areas use same frequency. However, the frequency allocations for two nearest outer coverage are different to minimize the interference effect.

The rest of this paper is organized as follows. Section II shows the proposed frequency allocation scheme. The signal-to-interference and outage probability analyses are shown in Section III. Finally, conclusions are drawn in the last section

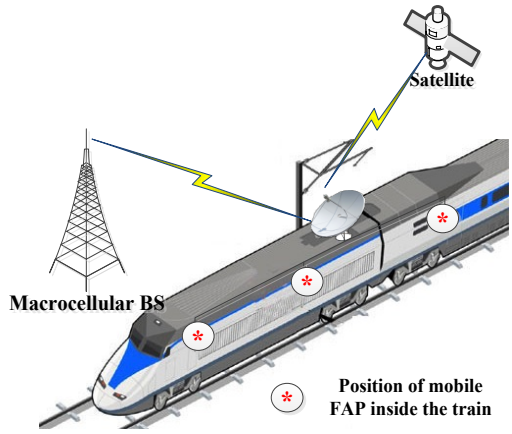

Fig. 1. Moving femtocells in train environment [4].

2. Frequency Allocation for Interference Mitigation

As femtocellular networks will co-exist with macrocellular networks, mitigation of the interferences between these two network types and also inter-femtocells is a key challenge for successful integration of these two technologies. In particular, there are several interference mechanisms between the femtocellular and the macrocellular networks, and the effects of the resulting interference depend on the density of femtocells and the overlaid macrocells in a particular coverage area. While improper interference

management can cause a significant reduction in the system capacity and can increase the outage probability, effective and efficient frequency allocation among femtocells and macrocells can result in a successful co-existence of these two technologies. Interference mitigation using the same frequency allocation scheme for the dense and the sparse moving femtocellular network deployments is not efficient. Rather, the choice of the frequency-allocation scheme to minimize the interference and to ensure maximal spectrum utilization should depend on the density of the femtocells and the relationship between the femtocells and the macrocells, which are the two parameters that we use for classification of the deployment scenarios. The different frequency-allocation schemes for moving femtocells in train environments are proposed to increase the frequency spectrum utilization, providing excellent performance in terms of cost, capacity, and outage probability.

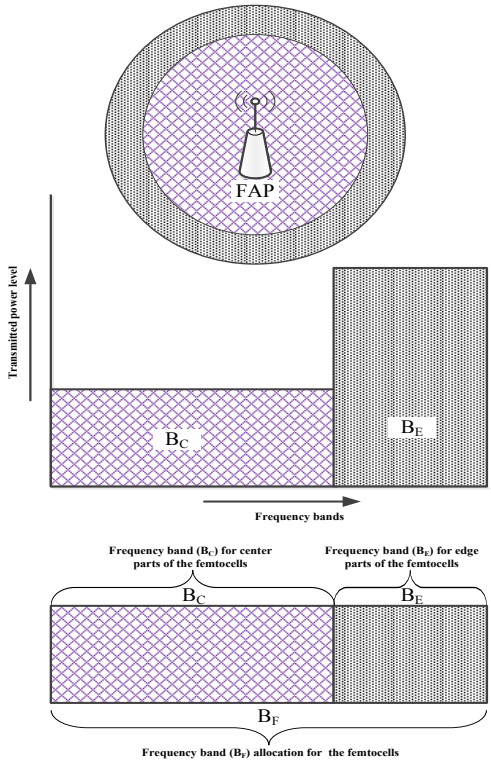

Fig. 2. Basic system model of the frequency allocation for a FAP in vehicular environment.

The basic idea behind our scheme is based on the frequency re-use concept [3], multi-level of power transmission, and the frequency allocation. Fig. 2 shows the basic system model of the frequency allocation for a FAP in vehicular environment. We use two level of power transmission for two separate bands of frequencies. As a result, the low transmission power produces a small coverage area and the higher transmission power causes the bigger coverage area. Therefore, the transmission of signal by a FAP produces two circles of coverage. The frequency allocations for the inner circle of two neighbor femtocells are same. However, the frequency allocations for the outer circle are distinct frequency bands. Even though, the two inner circles use same frequency bands, but it does not cause the interference for each other. Because, the transmission power for the inner circle is smaller. Hence two neighbor femtocells do not cause interference for each other. The interference management for the train environment is described in this section. The main issue of the interference management in train environment is the choosing of diameter for the inner circle and the outer circle. We should choose the diameters in such a way that the whole car of a train is fulfilled by femtocell coverage and the interference effect due to the inner circle is minimized.

A. Frequency band dividing for train environment

Dividing the frequency band to allocate the frequency among different femtocells in train environment is an important issue. Fig. 3 shows the dividing the frequency band to allocate the frequency among different femtocells in train environment.

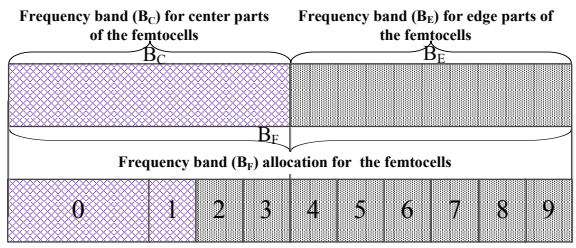

Fig. 3. Dividing the the frequency band to allocate the frequency among different femtocells in train environment.

The relation among various frequency bands are expressed as follows:

$$|B_C| = |B_E| = \frac{|B_F|}{2} \quad (1)$$

$$|B_0| = \frac{|B_E|}{2} = \frac{|B_F|}{4} \quad (2)$$

$$|B_1| = |B_2| = |B_3| = |B_4| = |B_5| = |B_6| = |B_7| = |B_8| = |B_9| = \frac{|B_E|}{6} = \frac{|B_F|}{12} \quad (3)$$

B. Two trains at two sides of a train (moving/moving or moving/static or static/static)

Fig. 4 (a) shows the frequency band separation to allocate the frequency among different femtocells in train environment when three trains are in parallel. The frequency allocations for the inner circle of all the femtocells are same. However, the frequency allocations for the outer circle are separate frequency bands. Even, the two inner circles use same frequency bands, it does not cause the interference for each other. Hence two neighbor femtocells do not cause interference for each other. Fig. 4(b) shows the

example of frequency allocation among different femtocells in train environment when three trains are in parallel.

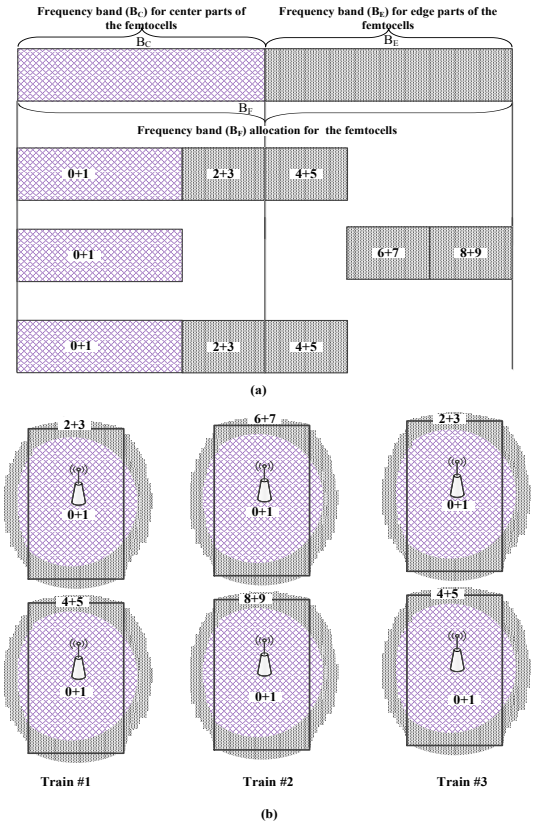

Fig. 4. (a) Frequency band separation to allocate the frequency among different femtocells when three trains are in parallel (b) frequency allocation among different femtocells in train environment when 3 trains are in parallel.

C. One train parallel to another train (moving/moving or moving/static or static/static)

Fig. 5(a) shows the frequency band separation to allocate the frequency among different femtocells in train environment when two trains are in parallel. The frequency allocations for the outer circles are separate frequency bands. Hence two neighbor femtocells do not cause interference for each other. Fig. 5(b) shows the example of frequency allocation among different femtocells in train environment when two trains are in parallel.

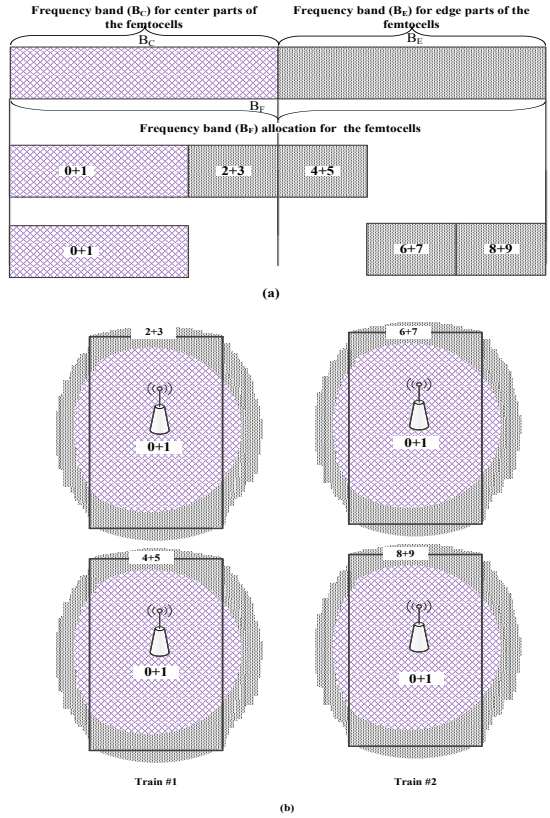

Fig. 5. (a) Frequency band separation to allocate the frequency among different femtocells in train environment when two trains are in parallel (b) frequency allocation among different femtocells when 2 trains are in parallel.

Whenever a single train with moving or static condition, the frequency allocations for the inner circle of all the femtocells are same i.e., bands B_C. However, separate frequency bands are used for the outer circles. Frequency bands B_4, B_5, and B_6 are used by outer circle of one car and the remaining B_7, B_8, and B_9 are used by outer circles of neighbor two cars.

3. Performance Analysis

The propagation model for a macrocell case is considered as [4]:

$$L = 36.55 + 26.16\log_{10} f_c - 3.82\log_{10} h_b - a(h_m) + [44.9 - 6.55\log_{10} h_b]\log_{10} d + L_{sh} + L_{pen}[dB] \quad (4)$$

$$a(h_m) = 1.1[\log_{10} f_{c,m} - 0.7]h_m - (1.56\log_{10} f_{c,m} - 0.8) \quad (5)$$

where $f_{c,m}$ is the center frequency in MHz of the macrocell, h_b is the height if the macrocellular BS in meter, h_m is the height of the MS in meter, d is the distance between the macrocellular BS and the MS in kilometer, L_{sh} is the shadowing standard deviation, and L_{pen} is the penetration loss.

Table 1: Summary of the parameter values used in analysis

Parameter	Value
Distance between macrocellular BS and MS	500 [m]

Carrier frequency	1800 [MHz]
Transmit signal power by macrocellular BS	1.5 [kW]
Transmitted signal power by a FAP	15 [mW]
Height of a macrocellular BS	100 [m]
Height of a FAP	2 [m]
Threshold value of *SNIR* for MS (γ)	12
Threshold value of *SNIR* for outside transceiver (γ)	7

The propagation model for a femtocell case is considered as as [4]:

$$L_{fem} = 20\log_{10} f_{c,f} + N\log_{10} d_1 + 4n^2 - 28 \ \left[dB\right] \quad (6)$$

where $f_{c,f}$ is the center frequency in MHz of the femtocell, n is the number of walls between the MS and the FAP, and d_1 is the distance between the FAP and the MS in meter.

The outage probability [2], [4] of a user is calculated as:

$$P_{out} = P_r(SINR < \gamma) \quad (7)$$

where γ is a threshold value of *SNIR* below which there is no acceptable reception.

Considering all the interfering neighbor macrocells and femtocells, the outage probability can be expressed as:

$$P_{out} = 1 - e^{-\frac{\gamma}{S_0}(I_f + I_m + N)} \quad (8)$$

Table 1 summarizes the values of the parameters that we used in our analysis. Three parallel trains are considered for our analysis. We assume macrocellular networks as the backhauling networks. Also, we assume that the femtocells in the trains and the overlaid macrocell are deployed through separate frequency bands [2].

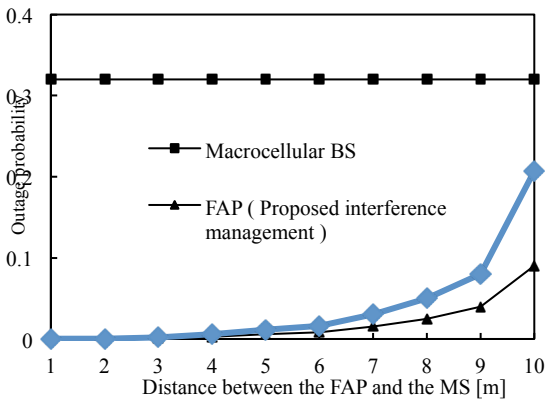

Fig. 6. Outage probability comparison.

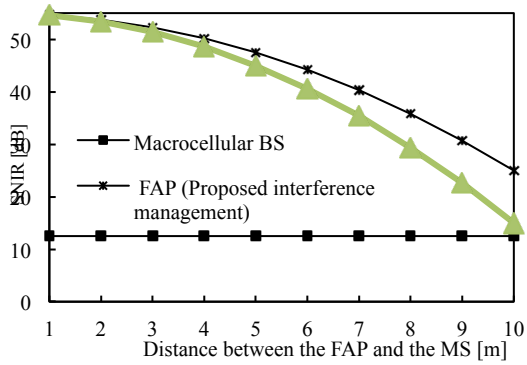

Fig. 7. Comparison of *SNIR* levels.

Fig. 6 demonstrates the outage probability comparison for different schemes. It shows that our proposed scheme performs better compared to others. Fig. 7 shows the comparison between the *SNIR* levels. The figure clearly shows the advantage of our proposed scheme especially when the distance between the FAP and the MS is comparatively higher.

4. Conclusions

The moving femtocell is promising application of femtocell technology. The moving femtocells in train environment increase the *SNIR* level, reduce the outage probability, and increase the throughput. We have shown efficient frequency allocation for interference mitigation in train environment. The proposed frequency allocation technique can increase the frequency utilization and as well as can reduce the interference effect. The performance analyses in terms of outage probability and signal quality measurement clearly illustrates the advantages of our proposed interference mitigation scheme for femtocellular network deployment in train.

References

[1] V. Chandrasekhar, J. G. Andrews, and A. Gatherer, "Femtocell Networks: A Survey," *IEEE Communication Magazine,* vol. 46, no. 9, pp. 59 – 67, Sept. 2008.

[2] M. Z. Chowdhury, Y. M. Jang, and Z. J. Haas, "Cost-Effective Frequency Planning for Capacity Enhancement of Femtocellular Networks," *Wireless Personal Communications,* vol. 60, no. 1, pp. 83-104, Sept. 2011.

[3] S. H. Ali, V. C. Leung, V. C. M. "Dynamic Frequency Allocation in Fractional Frequency Reused OFDMA Networks," *IEEE Transaction on Wireless Communication*, vol. 8, no. 8, pp. 4286-4295, Aug. 2009.

[4] M. Z. Chowdhury, S. Q. Lee, B. H. Ru,, N. Park, and Y. M. Jang, "Service Quality Improvement of Mobile Users in Vehicular Environment by Mobile Femtocell Network Deployment," in Proceeding of *IEEE International Conference on ICT Convergence (ICTC),* Sept. 2011.

Proceeding of the
International Conference on Electrical, Computer and Telecommunication Engineering
01- 02 December 2012 (ICECTE2012), RUET, Rajshahi-6204, Bangladesh

ICECTE2012: PI-0063

Performance Analysis of a Multi User Alamouti-MRC System on Secured Message Transmision over Ricean Fading Channel

Tanvir Ahmed[1], M. M. Ali[1] and Shaikh Enayet Ullah[2]
[1]Department of Electrical and Electronic Engineering ,
Rajshahi University of Engineering & Technology,
Rajshahi-6204, Bangladesh.
[2]Department of Information and Communication Engineering,
Rajshahi University
Rajshahi-6205, Bangladesh.
Email: tanvir_1008@yahoo.com, mmali.ruet@gmail.com, enayet67@yahoo.com.

ABSTRACT
This paper investigates the effect of antenna diversity for a double transmit and multiple receive antenna supported wireless communication system that employs multi user Alamouti's space time block coding (STBC) and maximal ratio combining (MRC) scheme on secured text message transmission. The FEC encoded Alamouti-MRC transmission system under investigation implements RSA cryptographic algorithm and deploys various multi-level digital modulations (16-PSK, 16-DPSK and 16-QAM) techniques over an Additive White Gaussian Noise (AWGN) and Ricean Fading Channels. It has been observed from the study that in case of without receive antenna diversity the system shows comparatively worst performance in 16-DPSK scheme and satisfactory performance in 16-QAM. It is noticeable that the system performance is improved with increase in number of receive antennas. The performance analysis shows that with implemented Alamouti-MRC scheme (6 receive antenna) under 16-QAM digital modulation, the system provides excellent performance over a significant low signal to noise ratio (SNR) values.

KEY WORDS: STBC, MRC, Ricean Fading, antenna diversity, bit error rate.

1. INTRODUCTION

Communication systems using multiple antennas at the transmitter and/or the receiver have recently received increased attention due to their ability to provide substantial capacity improvements while achieving low error rate and/or high data rate by flexibly exploiting the attainable diversity gain and/or the spatial multiplexing gain [1]. Recently much attention has been paid on transmit diversity as an efficient technique to combat fading and simplify the implementation of mobile terminals [2]. Several methods in transmit diversity are proposed in [2]-[5]. Among them, Alamouti space-time block coding (STBC) [3] is very simple and attractive due to its advantages of not requiring feedback of channel state information and easy implementation.

So far, studies on Alamouti space-time transmit diversity (STTD) have mainly assumed binary phase shift keying (BPSK) or quadrature phase shift keying (QPSK) modulation [3]-[6]. Although analytical studies have been presented for BPSK-modulated STTD systems with imperfect pilot symbol channel estimation [6]. Since wireless communications is challenged by limited spectral resources, multi-user spatial multiplexing has recently received considerable attention. Multi-user MIMO systems can significantly improve system throughput via transceiver signal processing if the number of transmit antennas is much larger than the number of receive antennas [7]. Alamouti STTD has been analyzed analytically for multi-level quadrature amplitude modulation (M-QAM), which has become very attractive for wireless communications due to its high spectral efficiency, [2]. An analytical expression for the BER of 16/64-QAM without STTD in Rayleigh fading with imperfect pilot symbol-assisted channel estimation was in [8]. However, the integration operation in the analytical formula requires heavy computation load, and thus it is impractical to extend to STTD systems. An effective approach to evaluate QAM performance analytically using the characteristic function was proposed in [9].

So far, to the best of the authors' knowledge, there is no such work published about the performance analysis presented here. We shall consider the case of the simple Alamouti's space-time block code as it is the only scheme which can provide full rate and full diversity for any signal constellations. Network security measures are provided using RSA algorithm to protect data during their transmission in the proposed scheme. Therefore, this paper focuses on the evaluation of the BER performance for the FEC encoded Alamouti-MRC transmission system for

various multi-level digital modulations (16-PSK, 16-DPSK, 16-QAM) techniques over an Additive White Gaussian Noise (AWGN) and Ricean Fading Channel with the transmit diversity technique in conjunction with receive antenna diversity.

The paper is organized as follows. Section 2 presents the system description, including the transmitter, channel, and coherent receiver models. Performance analysis is presented in Section 3. Finally, conclusions are drawn in Section 4.

.

2. The Communication System model

The MIMO wireless communication system under consideration is shown in Figure 1. In such a communication system, four users are simultaneously transmitting their secured text messages. For secret message transmission the most widely used public-key cryptosystem RSA is used here. After encryption of plaintext of each user the ciphertext is converted into binary messages. The transmitted bits of each individual user are channel encoded by a convolutional encoder of rate r = 1/2, interleaved for minimization of burst errors and then converted to M-ary signal. This M-ary signal is modulated using various types of multi level digital modulation techniques such as quadrature amplitude modulation (QAM), phase shift keying (PSK) and differentially phase shift keying (DPSK). The modulated digital signals are fed into the Alamouti Space Time Block Encoder, where the input stream is first segmented into two-symbol blocks. Each two-symbol block includes the first and second symbols x_1 and x_2, respectively. During the first symbol period, the encoder will send x_1 and x_2 to the first and second transmit antennas, respectively. During the next symbol period, x^*_1 and $-x^*_2$, where * denotes complex conjugate, will be sent to the first and second transmit antennas, respectively. These two transmit antennas can either be collocated or distributed remotely if proper symbol timing synchronization scheme is adopted. Now the space-time encoded streams are sent to the wireless channels through the two transmit antennas.

Assuming r^j_1 and r^j_2 are the received signals at the jth receive antenna at time t and $t + T$, respectively, then r^j_1 and r^j_2 are given by [2][10]-[11].

$$r_1^j = h_{j1}x_1 + h_{j2}x_2 + n_1^j$$
$$r_2^j = -h_{j1}x_2^* + h_{j2}x_1^* + n_2^j \qquad (1)$$

where h_{ji}, i=1,2, j=1,2,……N_R, is the fading coefficient for the path from transmit antenna i to receive antenna j, and n_1^j and n_2^j are the noise signals for receive antenna j at time t and $t + T$, respectively.

The receiver constructs two decision statistics based on the linear combination of the received signal. The decision statistics are given by

$$\%_1 = \sum_{i=1}^{2}\sum_{j=1}^{N_R}|h_{ji}|^2 x_1 + \sum_{j=1}^{N_R} h_{j1}^* n_1^j + h_{j2}(n_2^j)^*$$
$$\%_2 = \sum_{i=1}^{2}\sum_{j=1}^{N_R}|h_{ji}|^2 x_2 + \sum_{j=1}^{N_R} h_{j2}^* n_1^j - h_{j1}(n_2^j)^* \qquad (2)$$

The maximum likelihood decoding rules for the two independent signals x_1 and x_2 are then

$$\hat{x}_1 = arg \min_{\hat{x}_1 \in S}\left[\left(\sum_{j=1}^{N_R}\left(|h_{j1}|^2 + |h_{j2}|^2\right) - 1\right)^2 |\hat{x}_1|^2 + d^2(\%_1, \%_2)\right]$$

$$\hat{x}_2 = arg \min_{\hat{x}_2 \in S}\left[\left(\sum_{j=1}^{N_R}\left(|h_{j1}|^2 + |h_{j2}|^2\right) - 1\right)^2 |\hat{x}_2|^2 + d^2(\%_1, \%_2)\right] \qquad (3)$$

where $d^2(x, y) = (x - y)(x^* - y^*) = |x - y|^2$

The complex symbols are now digitally demodulated, de interleaved, convolutionally decoded and decrypted to recover the transmitted data for each of the four users.

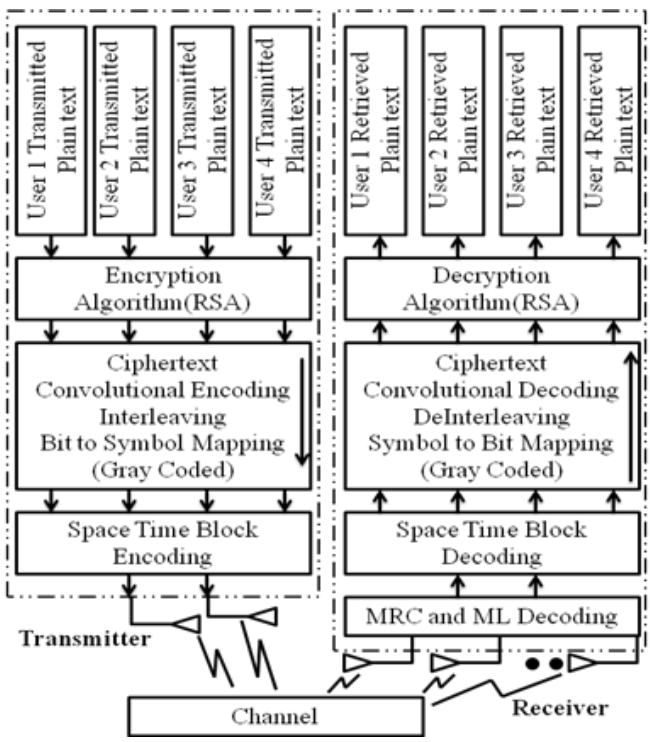

Fig1: Block diagram of FEC encoded Multi user MIMO STBC secured wireless communication system.

3. Performance Comparison and Results

The computer simulation has been conducted to evaluate the BER performance of the FEC encoded Multi user MIMO STBC secured wireless communication system based on the parameter given in Table 1.

Table 1: Simulated Model parameters

Parameters	Description
Type of input signal for the users	Secured Text Messages
Public key for user 1	{5,119}
Private key for user 1	{77,119}
Public key for user 2	{7,187}
Private key for user 2	{23,187}
Public key for user 3	{11,221}
Private key for user 3	{35,221}
Public key for user 4	{13,85}
Private key for user 4	{5,85}
No. of Transmitting and Receiving antennal	$2XN_R$; N_R =1,2…6
Channel coding	½ rated Convolutional Encoding
Digital Modulation Techniques	16-QAM, 16-PSK and 16- DPSK
Channel	AWGN and Ricean Fading channel
Signal to noise ratio, SNR	0 to 20 dBs

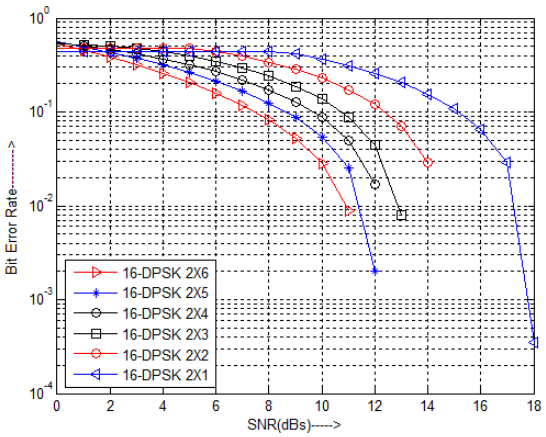

Fig. 2: BER performance analysis for 16-DPSK system with transmitter and receiver diversity.

To illustrate the effect of various multi-levels digital modulations (16-PSK, 16-DPSK, and 16-QAM) techniques over an Additive White Gaussian Noise (AWGN) and Rayleigh Fading Channel first the effect of 16-DPSK modulation technique is investigated with receive diversity. Figure 2 shows the BER performance evaluation of 16-DPSK modulation technique with the transmit diversity in conjunction with the receive diversity. With the increase in the receive diversity the system performance increases significantly. For a typical SNR value of 8dB, the BER values are 0.4341 and 0.0830 in case of 2X1 and 2X6, which is indicative of system performance improvement by 16.54 dB. The system outperforms when 2x6 antennas are adopted with the 16-DPSK modulation technique.

It is observable from figure 3 that the BER performance of 16-PSK modulation technique is improved with the transmit diversity in conjunction with the receive diversity. At the BER 10^{-2} with the receiver diversity the SNR is reduced to about 3 dB and 8dB for 2X2 and 2X6 antennas, respectively.

In figure 4 the BER performance is evaluated for 16-QAM modulation technique with the transmit diversity in conjunction with the receive diversity.

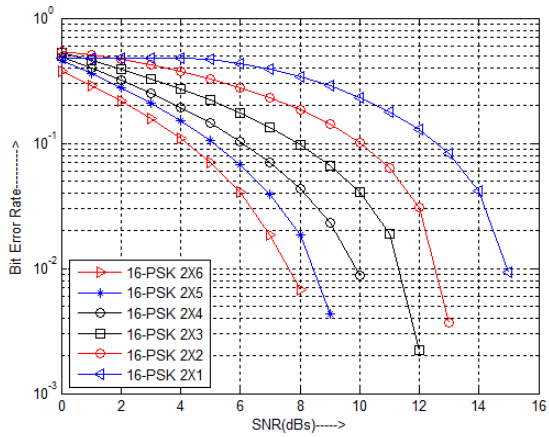

Fig 3: BER performance analysis for 16-PSK system with transmitter and receiver diversity.

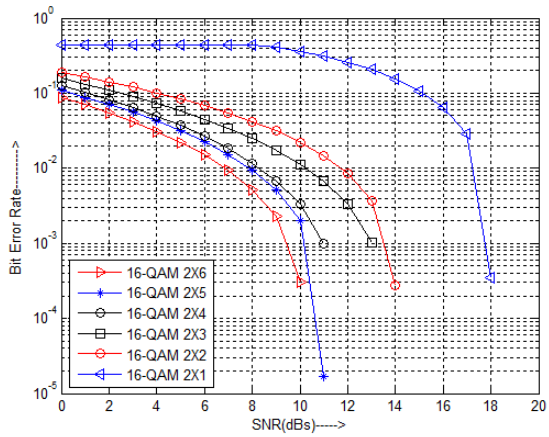

Fig 4: BER performance analysis for 16-QAM system with transmitter and receiver diversity.

It is observable that the BER values are 0.0052 and 0.4340 for a typical SNR value of 8dB in case of 2X6 and 2X1 systems viz. the system performance is

improved by 44.24 dB. From figure 5, it is noticed that at the typical SNR value of 8dB the system performance is improved by 27.70 dB for 16-QAM compared with 16-DPSK. Therefore on critical inspection of the graphical illustrations present in figure 5, it is quite obvious that the system provides most satisfactory performance in 2X6 and 16-QAM.

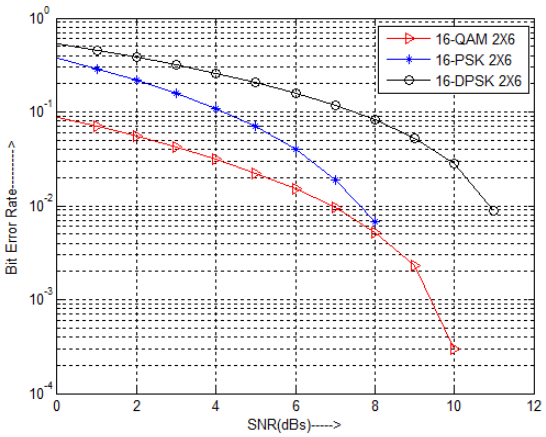

Fig. 5: BER performance analysis for 16-QAM, 16-PSK and 16-DPSK system with 2X6 antennas.

4. Conclusion

In this paper, an Alamouti's STBC-MRC transmit diversity in conjunction with the receive diversity has been studied in different receive diversity configurations for 16-DPSK, 16-PSK and 16-QAM modulation techniques. The system performance improved with the receiver diversity. The system performance improved further with the adaptation of 16-QAM compared to 16-DPSK and 16-PSK. In summary, using Alamouti's STBC-MRC transmit diversity technique in conjunction with receive antenna diversity techniques, high-level QAM can be employed even in low SNR environments.

References

[1] Jiankang Zhang, Student Member, IEEE, Sheng Chen, Fellow, IEEE, Xiaomin Mu, and Lajos Hanzo, Fellow, IEEE, "Joint Channel Estimation and Multiuser Detection for SDMA/OFDM Based on Dual Repeated Weighted Boosting Search", *IEEE Transactions on Vehicular Technology*, VOL. 60, NO. 7, September 2011, pp-3265-3275.

[2] Huiling Zhu,Member, IEEE,Bin Xia and Zhenhui Tan, Member, IEEE, "Performance Analysis of Alamouti Transmit Diversity with QAM in Imperfect Channel Estimation", *IEEE Journal on Selected Areas in Communications*, VOL. 29, NO. 6, June 2011, pp-1242-1248.

[3] S. M. Alamouti, "A simple transmit diversity technique for wireless communications", *IEEE Journal on Selected Areas in Communications*, vol. 16, pp. 1451 -1458, Oct. 1998.

[4] X. Y. Wang and J. Wang, "Effect of imperfect channel estimation on transmit diversity in CDMA systems", *IEEE Transactions on Vehicular Technology*,vol.VT-53, pp. 1400 - 1412, Sept. 2004.

[5] R. T. Derryberry, S. D. Gray, D. M. Ionescu, G. Mandyam and B. Raghothaman, "Transmit diversity in 3G CDMA systems", *IEEE Commun. Mag.*, vol. 40, pp. 68 - 75, Apr. 2002.

[6] D. Gu and C. Leung, "Performance analysis of transmit diversity scheme with imperfect channel estimation", *IEE Electron. Lett.* , vol. 39, pp. 402- 403, Feb. 2003.

[7] R. L. Choi, M. T. Ivrlac, R. D. Murch, and W. Utschick, "On strategies of multiuser MIMO transmit signal processing," *IEEE Transactions on Wireless Communications*, vol. 3, no. 6, pp. 1936–1941, Nov. 2004.

[8] X. Tang, M.-S. Alouini and A. J. Goldsmith, "Effect of channel estimation error on M-QAM BER performance in Rayleigh fading", *IEEE Transactions on Communications,* vol. 47, pp. 1856 - 1864, Dec. 1999.

[9] B. Xia and J. Wang, "Effect of channel estimation error on QAM systems with antenna diversity", *IEEE Transactions on Communications*, vol. COM-53, pp. 481 - 488, March 2005.

[10] Hamid Jafarkhan, "Space-Time Coding Theory and Practice", Cambridge University Press 2005

[11] F.Javier L´opez-Mart´ınez, Eduardo Martos-Naya, Kai-Kit Wong, J. Tom´as Entrambasaguas ,"Closed-Form BER Analysis of Alamouti-MRC Systems with ICSI in Ricean Fading Channels", *IEEE Comunications Letters*, VOL. 15, NO. 1, January 2011,pp-46-48.

Proceeding of the
International Conference on Electrical, Computer and Telecommunication Engineering
01- 02 December 2012 (ICECTE2012), RUET, Rajshahi-6204, Bangladesh

ICECTE2012: PI-0064

Vehicular ad-hoc Network(VANET) for car to car communication

Dona Basak[1], Maisuma Khatun [2], Azra Sadia Sultana[3], Md. Faruk Hossain, Md. Mortuza Ali
Department of Electrical & Electronic Engineering , Rajshahi University of Engineering & Technology
Rajshahi -6204,Bangladesh
E-mail:donaeee07_ruet@yahoo.com, amee_ruet07@yahoo.com , ushmi_eee@yahoo.com

ABSTRACT
Accident is a major phenomenon for our country as well as the whole world. As a result many lives are lost. So our purpose is to eliminate the problem using technological knowledge. Electronic circuits and communication link can be used to solve this problem. On the other hand Vehicular Ad- hoc network (VANET) becomes an scientific and commercial interest and is becoming familiar as an emerging technology. The development of VANET network is going throughout the world. Before crashing a car to another car a system is developed to alert the car so that driver become conscious of the speed of the car and if necessary can take proper step to stop the car to avoid accident.

KEY WORDS: Obstacle, VANET, Vehicle, MANET, DSRC

1. INTRODUCTION

Road accident and traffic jam are two common word to all around the world. Every day when we travel through the road we face the problem. So we want to get rid of it. In this case electronic circuit with communication link may create a vital role. For obstacle detection different systems may be followed based on requirement. Actually it is essential to detect the obstacle from a far distance so that the driver can control the car speed as motion inertia works against the driver. To cover long distance i.e. to detect long distance obstacle the frequency of system must be high..It includes internet communication such as Wi-Fi, Bluetooth which is called Dedicated Short Range Communication (DSRC) [1],[2],[3],[4],[5]. **Dedicated short-range communications** are one-way or two-way short- to medium-range wireless communication channels specifically designed for automotive use[1]. In October 1999, the United States Federal Communications Commission (FCC) allocated in the USA 75MHz of spectrum in the 5.9GHz band for DSRC to be used by Intelligent Transportation Systems ITS [3]. Also, in Europe in August 2008 the European Telecommunications Standards Institute (ETSI) has allocated 30 MHz of spectrum in the 5.9GHz band for ITS [4]. Currently its main use in Europe and Japan is in electronic toll collection[5].So the driver can interchange any information from car to car within a specific range either to avoid accident or to know any important information of any place or other things as it is associated with internet. So the total process is such a combination that helps both to avoid car-crash and to know any required information.

Other possible applications of DSRC are

- Emergency warning system for vehicles
- Cooperative Adaptive Cruise Control
- Cooperative Forward Collision Warning
- Intersection collision avoidance
- Approaching emergency vehicle warning (Blue Waves)
- Vehicle safety inspection
- Transit or emergency vehicle signal priority
- Electronic parking payments
- Commercial vehicle clearance and safety inspections
- In-vehicle signing
- Rollover warning
- Probe data collection
- Highway-rail intersection warning
- Electronic toll collection

There were many research activities on this topic and more technological improvement is going on. Annual International Conference On Ad-hoc Networks (AdHocNets) is such a conference where different research activities and relevant ideas for improvement of car to car communication is discussed. The aim of the annual International Conference on Ad Hoc Networks (AdHocNets) is to provide a forum that brings together researchers from academia as well as practitioners from industry to meet and exchange ideas and recent research work on all aspects of ad hoc networks. In this case 9th and 4th International Conference on Ad Hoc Networks is specially mentionable.

The Ninth ACM International Workshop on Vehicular Inter-NETworking [6], Systems, and Applications (VANET) is pleased to begin an association with ACM MobiSys in 2012, following

years of success at ACM MobiCom. With a track record of bringing together key researchers from academia and industry, VANET 2012 will cover a widening range of research topics related to vehicular networking applications, services and systems. The scope includes research on fundamental communication problems, design and implementation of vehicular systems and applications, as well as related topics such as the implications of VANETs on transportation efficiency and safety, liability issues, standardization efforts, and spectrum assignment.

2. MOBILE AD-HOC NETWORK (MANET) AND RELATIONSHIP WITH VANET

The primary objective of Vehicular Ad Hoc Networks (VANETs) is to provide traffic safety and efficiency. Since VANETs are an extension of Mobile Ad-hoc Networks (MANETs), a discussion of MANETs is essential to understand VANETs.

A mobile ad-hoc network (MANET) is a self-configuring infrastructure less network of mobile devices connected by wireless system. "*Ad-hoc"* is Latin word and means "for this purpose"[7]. MANETs are a kind of wireless ad hoc networks that usually has a routable networking environment on top of a Link Layer ad hoc network. Each device in a MANET is free to move independently in any direction, and will therefore change its links to other devices frequently. Each must forward traffic unrelated to its own use, and therefore be a router. The primary challenge in building a MANET is equipping each device to continuously maintain the information required to properly route traffic. Such networks may operate by themselves or may be connected to the larger Internet.

Vehicular Ah-hoc network is a part of MANET only applies for car to car communication. MANET (or self-organizing) mobile networks operate without a predefined fixed (managed) infrastructure. (VANET) Vehicular ad-hoc networks belonging to family of ad-hoc using IEEE 802.11-based standard WLAN technology have recently received considerable attention in many vehicular projects and industry groups. Vehicular Ad-Hoc Networks are a special kind of mobile Ad-Hoc networks where wireless-equipped (road) vehicles form a network with no additional infrastructure

3. TECHNOLOGIES USED FOR VEHICLE-TO-VEHICLE COMMUNICATION

There are different communication scheme used is VANET .They are-

- **Multiple-Access Wireless LAN Transmission to Vehicles** – Many different wireless technologies are currently discussed to be used for car-to-car communication. Conventional IEEE 802.11p wireless LAN (WLAN), dedicated short range communication (DSRC), and GPRS/ UMTS are just some selected technologies.
- **Inter-vehicle Communication Technology** – *Vehicle-to-vehicle communication* can be used to disseminate messages of multiple services generating their content using sensors within the vehicle. These services can include accident warning, information on traffic jams or warning of an approaching rescue vehicle. In addition, information on road or weather conditions can be exchanged. More elaborate inter-vehicle services are direct collision warning or intersection assistance with information on cross traffic.
- **Vehicle-to-Roadside Infrastructure Communication Technology** – Communication between vehicles and road side units (RSUs) can also increase safety. Traffic lights or road signs could be equipped with a communication device to actively inform vehicles in the vicinity. Hence, drivers can receive information on traffic flow, road conditions or construction sites directly from the respective RSU. In addition, static hazard areas, e.g. construction sites, could be equipped with a RSU to warn surrounding vehicles. RSU-based services will play an important role during the introduction phase, since they are almost unaffected by the penetration rate.
- **Portal-based Vehicular Infotainment Technology** – Besides the safety related services, many other services related to the vehicle or providing entertainment to the passengers can be brought to future vehicles. The on board unit (OBU) inside the vehicle collects all incoming messages and sensor information. In addition, it relies on a server-based infrastructure providing many additional services. These can include information on parking or hotels as well as sightseeing information.
- **Vehicular Business Communication Technology** – vehicles will certainly play a major role in everyday business processes that are currently handled by enterprise IT systems. Two different ways of integrating cars into business processes are considered valuable:
    - **Vehicles transmit data** such as geographical position, covered

distance or average speed may be transmitted to a company's backend system to allow for mobile asset management services. Logistics providers, for example, who nowadays run complex IT systems to manage their fleet, could feed real-time information into their applications to improve flexibility and adaptivity of their business processes.

- **Provisioning of car drivers with access to external data** is a promising possibility of applying vehicular communications as well. Business people, which are always "on the move", such as sales persons or consultants, may be highly interested in leveraging their cars' onboard systems as a conventional workplace. Via speech input, drivers could trigger their cars to remotely access a company portal and to download crucial information for their next customer visit, for example.

4 THE EXISTING SYSTEM OF CAR TO CAR COMMUNICATION

On a daily basis, the general public make journeys which may include transport by bus, car, train, plane, lorry, bike or on foot. To deliver an effective managed network all the available travel options need to be considered in the overall transport strategy for a city, region or county.

Fig.1 Various road direction indications

The Urban Traffic Management and Control Initiative was launched in 1997 by the Department for Transport and aimed to develop a more open approach to the use of Intelligent Transport Systems (ITS) in urban areas [8].

In junction point traffic control light is used as below.

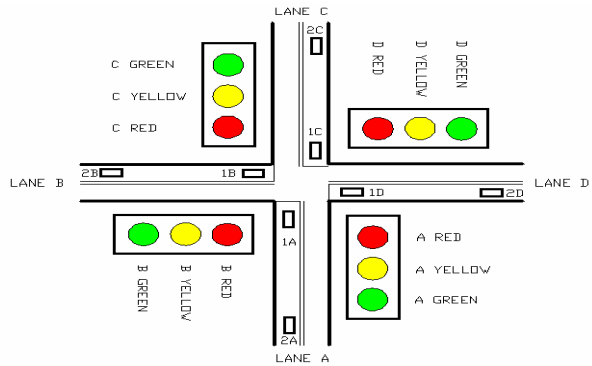

Fig.2 Traffic light model

The four ways junction is developed to display the simulation the development of the new traffic light control system. Figure 2 show the design of traffic light model. Every lane and traffic light signals have been labeled with alphabet A, B, C and D to separate each lane and traffic light. Each traffic light lane has their set of traffic light signal "Red, Yellow, and Green". This traffic light signal operates similar like common traffic light signal. It changes from red to green and then yellow and after that back to red signal [9].

In one way road if any obstacle comes in front of a car the driver wants control speed and glows backlights of the car so that the behind cars can notice it and take necessary steps and this process is going on. But in real case this manual data transfer process is slower with respect to speed of the car in highways.

In curved roads where an incoming car on the second section is not visible to cars in the first section. So in this case using VANET a system has been developed which has major applications in the developed country. When there is no inter vehicle communication between the two cars then crash would occur .But using VANET an inter vehicle warning (IVW) is transmitted to the traffic light simulator unit from the car approaching towards it and it will transmit a massage to the other unit of the second section road. As a result "Red signal" is shown in the other section so that cars must stop on that road.

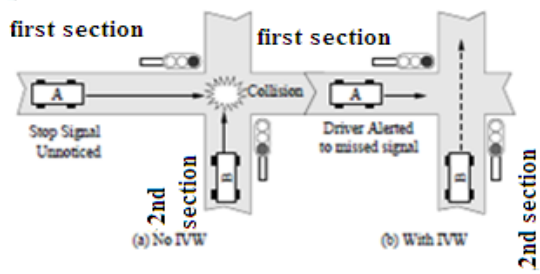

Fig.3 Inter Vehicle Communication to aviod collision

5. LIMITATION OF THE EXISTING SYSTEM

Though the existing system is giving so many facilities to the modern civilization but we find out some limitation of it which make it inconsistent in some case (some special application).It provides car to car communication in one way road even in case of curved road and helps the driver to get some necessary information about different things. But if there are more cars in road in one or more rows (the practical situation) then there becomes congestion. In that case using this technology how it is possible to congestion control by maintaining cars normal speed and as far as possible without causing any delay. Again if any emergency case such as Ambulance or Fire-service, how it will get priority to them controlling normal traffic flow. For this case we have thought of a system whose architecture is given in the following article gives the possible solution of this problem.

6. OUR PLAN AND IT'S ARCHITECTURE

When we apply VANET in roads some common cases occurs which can be approximately solved by the following ways discussed below.

Case 1: At junction point as the cars cannot pass swiftly so traffic jam causes. A base station can be placed at the middle position of the junction of more than one road . It has a specific scanning range within which any vehicle comes, base station scans step by step using DSRC and indicates the direction (using Doppler Effect) according to their priority of going to their direction. i.e. the base station displays the direction according to majority of car in any road want to cross. So that probability of passing a car to its direction will increase which reduces time delay of waiting.

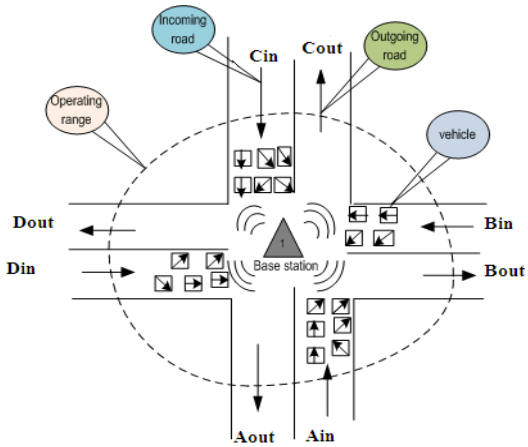

Fig.4 Schematic diagram of base station scanning in a four way junction

In fig.4 schematic diagram of base station scanning process where '→' shows the direction of vehicles. The dotted line made us understood the operating range of base station.

Consider all the 1st row of four way junction .The base station scans the first row and check the direction of the car. The direction to most of the car want to go, be the priority direction which will be shown in the base station display and the car at that direction are allowed to cross. For example for 1st row 2 cars in Aout direction,4 in the Bout direction,1 in the Cout direction and 2 in Dout direction. So the cars in Bout direction will get permission to cross. The same direction sequence is repeated. If the same number of car have direction priority such as in case of Aout and Dout then road number sequence will be followed. In this case A is before D in alphabetic sequence so Aout direction will get priority. If more than one car in any column have the same direction of selected one than those cars also allowed to cross. After that the second scanning is started and the same procedure is repeated to determine the direction. As a result car can cross the road very swiftly without any crash and time delay.

*Case 2: I*n case of emergency vehicle (ambulance, fire-service cars) it will get priority. Within the coverage area of base station when the emergency vehicle enters, it gives alarming signal to all the vehicles and the base station. At that case the cars in front of it is allowed to pass at first so that the emergency vehicle can pass smoothly. After passing it, previous system will be followed.

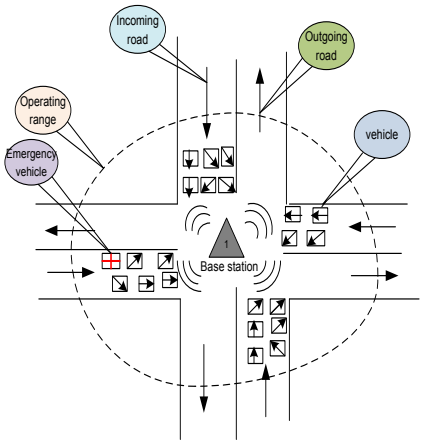

Fig.5 The schematic diagram for emergency vehicle

Fig.5 shows the schematic diagram of emergency case of vehicle. In this case when an emergency vehicle comes in the range of base station, an alarming sound will pass to the base station and the whole system will stop scanning for few times. The base station sends emergency message to all the cars so that they become alert of the position of emergency vehicle which will get priority and the vehicles in front of this is allowed to pass first without causing time delay. After passing it again the system backs to its previous strategy and a message

of informing this is send to all the cars. So the system again start scanning. So the whole system maintains a balance without any boring time delay.

7. CONCLUSION AND FUTURE WORK

Traffic jam as well as car accident are two major enemies of us. Life and time, these two important things may be lost due to this issue. But in the age of modern civilization we cannot accept it as a natural phenomenon. So our endeavour was to study the emerging technology of VANET and both apply and improve it's idea to road. In this paper we have given our idea to solve this problem. Our conventional traffic system has some limitations. To remove the limitation our proposed system is very effective. It allows very high mobility, Efficient working and is almost extreme economical. It prevents car accident and allows the vehicles to move swiftly in the road. As a result traffic jam problem is solved by our proposed system. We have submitted our idea by giving importance of all types of vehicles especially emergency vehicles such as ambulance, fire service vehicles etc. So many lives can get safety and people can do their daily work without any types of hazard because day by day people and vehicles are increasing rapidly. It also innovate some other ideas which will become the subject of research in near future. They are-

- Mobile robot as driver to control car
- Games ,Video download, Email checking etc in the running car without any risk of accident
- Automatic decision maker using logic in hazardous environment
- Necessary information and it's exchange remaining in the car to detect it's location.
- To take anti-theft action against car thief.

8. ACKNOWLEDGEMENTS

The authors would like to thank her parents. Secondly would like to thanks to Department of EEE of RUET to give the chance of doing thesis on it and for the implementation part of this work.

REFERENCES

[1] Harvey J. Miller,Shih-Lung Shaw ," *Geographic Information Systems for Transportation*" Oxford UniversityPress.

[2] "What is DSRC?". leearmstrong.com. http://www.leearmstrong.com/DSRC/DSRCHmeset.htm. Retrieved 2008-02-17.

[3] "Federal Communications Commission. News Release, October 1999". FCC. http://www.fcc.gov/Bureaus/Engineering_Technology/News_Releases/1999/nret9006.html Retrieved 2009-08-16

[4] "European Telecommunications Standards Institute. News Release, September 2008". ETSI. http://www.etsi.org/WebSite/NewsandEvents/2008_09_Harmonizedstandards_ITS.aspx. Retrieved 2009-08-16.

[5] "DSRC Standards: What's New?". standards.its.dot.gov. http://www.standards.its.dot.gov/Documents/advisories/dsrc_advisory.htm. Retrieved 2008-02-17

[6] http://www.uwicore.umh.es/vanet2012

[7] Tomas Krag, Sebastian Büettrich (2004-01-24). "Wireless Mesh Networking". *O'Reilly Wireless DevCenter*. http://www.oreillynet.com/pub/a/wireless/2004/01/22/wirelessmesh.html. Retrieved 2009-01-20.

[8] Urban traffic management and control. http://www.transporttech.mottmac.com/services/utmc/

[9] Azrulnor Bin Ahmod,"Development of Traffic Light Control System using Programmable Logic Controller",universiti melaysia pahang.

Proceeding of the
International Conference on Electrical, Computer and Telecommunication Engineering
01- 02 December 2012 (ICECTE2012), RUET, Rajshahi-6204, Bangladesh

ICECTE2012: PI-0065

Correlation between Sensorimotor Area of Central Nervous System with Peripheral Nervous System by EEG and NCV for Motor Imagery Task

Md Abdus Samad[1], Md Imanul Huq[2]
[1,2] Computer and Communication Engineering Department, International Islamic University Chittagong
E-mail: asamadece@gmail.com, imanulhuq@gmail.com

ABSTRACT
This paper investigates the future application of using peripheral nervous system in lieu of sensorimotor area of central nervous system.This study might be helpful for the people suffering problem in sensorimotor area of brain [1]. Currently, the practice of diagnosis of brain's central nervous system depends on various imaging diagnosis and it is very difficult to gain signals from brain through EEG if brain damage occur at upper lobe like cerebrum. The diagnosis of peripheral nerves relies on 'Nerve Conduction Velocity (NCV) Test' [2]. Three different tests havebeen conducted to find the correlation between EEGs from the 'sensorimotor area channel' during the MI tasks and medial nerve's conduction test as well. The correlation is calculated with respect to ERP (Event-Related-Potential [3].The events we have studied, relaxing state, motor activity and motor imagery task. Those data were then digitized, simulated and calculated the correlation in linear mode as well as in cross mode. Our study result shows thatthere are significant correlation between peripheral nervous system and sensorimotor area of human.

KEY WORDS: EEG, motor imagery task, NCV test, correlation, nervous system.

1. INTRODUCTION

The disabled patients whose motor function has taken by the diseases or other trauma their nervous system can be controlled through peripheral nervous system. The only one thing one has to do is just thinking. Brain Computer Interface (BCI) is developed to interact with people's thought with computer. This technique is especially can be used to assist sensimotor damaged people but their mental functions are not affected much [4].

2. LITERATURE REVIEW

2.1 Brain

The most remarkable part of human is the brain, which we consider as CPU of human body [5]. The brain of a vertebrate is the most complex organ of its body. In a typical human the cerebral cortex (the largest part) is estimated to contain 15–33 billion neurons, eachconnected by synapses to several thousand other neurons. These neurons communicate with one another by means of long protoplasmic fibers called axons, which carry trains of signal pulses called action potentials to distant parts of the brain or body targeting specific recipient cells.

2.2 Brain's Functional Fragment

However the brain is one single most important part of three different parts of nervous system. This includes:Brain as Central Nervous System (CNS) andthe Peripheral Nervous System (PNS)[6].The central nervous system or the CNS contains the brain and the spinal cord. All together, the brain and the spinal cord serve the nervous system's command station. When the sensory input reaches the CNS, the spinal cord and the brain figure outs what it exactly means. After, they quickly orders out the body parts that needs to move faster. Everything else but the CNS it is known as the peripheral nervous system. The peripheral nervous system or PNS contains the nerves, which leave the brain and the spinal cord and travel to certain areas of the body. The peripheral nervous system's main job is to send information gathered by the body's sensory receptors to the CNS as quickly as possible. Once the CNS has understood the information, the PNS will relay the specific orders back out the body. These nerves which carry information in a way of nerve impulses to and from the brain are called cranial nerves.

2.3 Functionality of Brain

To generate purposeful and unified action, the brain first brings information from sense organs together at a central location. It then processes this raw data to extract information about the structure of the environment. Next it combines the processed sensory information with information about the current needs of an animal and with memory of past circumstances. Finally, on the basis of the results, it generates motor response patterns that are suited to maximize the welfare of the animal. These signal-processing tasks require intricate interplay between varieties of functional subsystems:

2.3.1 Information Processing

The invention of electronic computers in the 1940s, along with the development of mathematical information theory, led to a realization that brains

can potentially be understood as information processing systems. This concept formed the basis of the field of cybernetics, and eventually gave rise to the field now known as computational neuroscience. Over the years, though, accumulating information about the electrical responses of brain cells recorded from behaving animals has steadily moved theoretical concepts in the direction of increasing realism [7].

2.3.2 Perception

One of the primary functions of a brain is to extract biologically relevant information from sensory inputs. The human brain is provided with information about light, sound, the chemical composition of the atmosphere, temperature, head orientation, limb position, the chemical composition of the bloodstream, and more.

2.3.3 Motor Control

Motor systems are areas of the brain that are directly or indirectly involved in producing body movements, that is, in activating muscles. Except for the muscles that control the eye, which are driven by nuclei in the midbrain, all the voluntary muscles in the body are directly innervated by motor neurons in the spinal cord and hindbrain. Spinal motor neurons are controlled both by neural circuits intrinsic to the spinal cord, and by inputs that descend from the brain.

2.3.4 Brain Wave

Neural oscillation is rhythmic or repetitive neural activity in the central nervous system. Neural tissue can generate oscillatory activity in many ways, driven either by mechanisms localized within individual neurons or by interactions between neurons. In individual neurons, oscillations can appear either as oscillations in membrane potential or as rhythmic patterns of action potentials, which then produce oscillatory activation of post-synaptic neurons [8]. At the level of neural ensembles, synchronized activity of large numbers of neurons can give rise to macroscopic oscillations, which can be observed in the electroencephalogram (EEG). Oscillatory activities in groups of neurons generally arise from feedback connections between the neurons that result in the synchronization of their firing patterns. The interaction between neurons can give rise to oscillations at a different frequency than the firing frequency of individual neurons. Neural oscillations were observed by researchers as early as Hans Berger, but their functional role is still not fully understood. The possible roles of neural oscillations include feature binding, information transfer mechanisms and the generation of rhythmic motor output. Over the last decades more insight has been gained, especially with advances in brain imaging. A major area of research in neuroscience involves determining how oscillations are generated and what their roles are. Oscillatory activity in the brain is widely observed at different levels of observation and is thought to play a key role in processing neural information. Numerous experimental studies indeed support a functional role of neural oscillations; a unified interpretation, however, is still lacking.

3. METHODOLOGY

3.1Task Variant Order

In the research four volunteer were selected with specific condition. This has been mention later on the slide. The aims of volunteer were to perform the tasks as: relaxing, motor activity, and motor imagery task.In every task the volunteer's EEG and NCV data were accumulated under seizure of voice stimulation. But we after becoming at alpha level the volunteer continued those tasks. This phenomenonwas not occurred when volunteer had been relaxing. The data of calm condition were taken in computation.

3.2 Channel Selection

In every task the volunteer's EEG and NCV data were accumulated under seizure of voice stimulation. But we after becoming at alpha level the volunteer continued those tasks. This phenomena did not occurred when volunteer were relaxing. The data of calm condition were taken in computation.

3.3 Relevant Calculation

Event Related Potential: The average of N trial of any signal assuming every trial is independent:

$$\bar{x} = \frac{1}{N}\sum_{k=1}^{N} x(t,k) \quad (1)$$

The correlation function (R):

$$R_{xx} = \sqrt{\frac{NCV_{Activity}^2}{NCV_{Activity}^2 NCV_{Relax}^2}} \quad (2)$$

$$R_{xx} = \sqrt{\frac{EEG_{Activity}^2}{EEG_{Activity}^2 EEG_{Relax}^2}} \quad (3)$$

Event Dependent Correlation in Percentage:

$$R_{xx} = \sqrt{\frac{EEG_{Activity}^2 NCV_{Activity}^2}{EEG_{Activity}^2 EEG_{Relax}^2 NCV_{Activity}^2 NCV_{Relax}^2}} \quad (4)$$

3.4 Data Collection Procedure

1. Both EEG and NCV data were collected in standard medical procedure.**2.** EEG data collections were made by 21 electrode electroencephalography device.**3.** The electrode placing of EEG were 20 for cutaneous nerve and other sensory nerve distribution and one for common ground.**4.** NCV data collections were made by 3stimulants NCV RMS

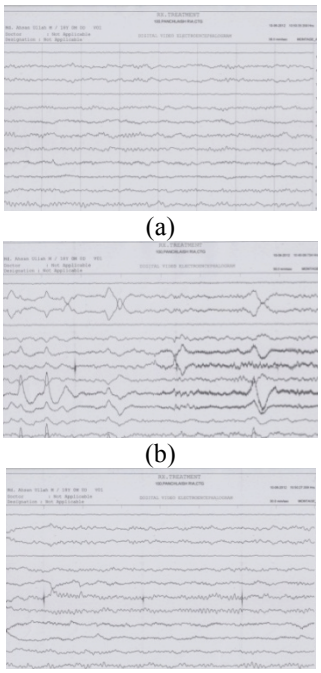

(a)

(b)

(c)

Fig. 1,(a) First volunteer's EEG at Relax State, **(b)**First volunteer's EEG at motor task activity, **(c)**First volunteer's EEG at motor imagery task activity.

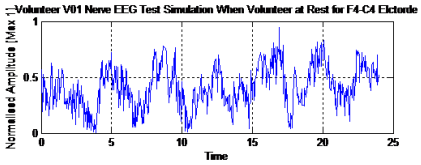

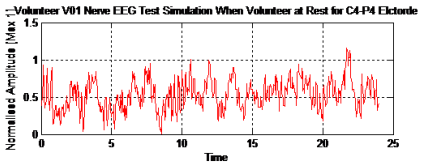

(a)

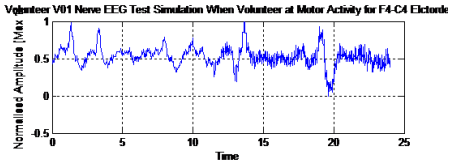

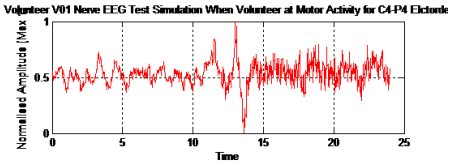

(b)

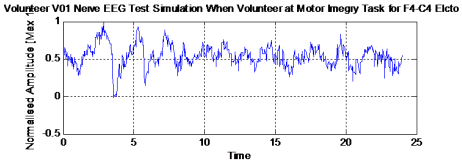

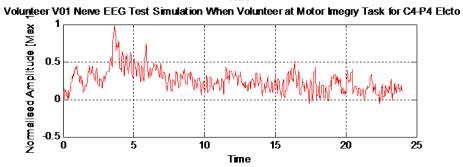

(c)

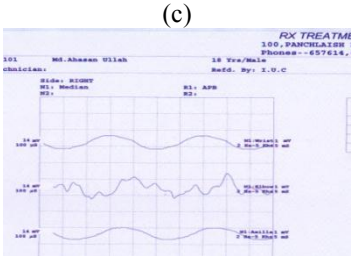

(d)

Fig. 2,(a) Simulated EEG at relax state for C4-P4 and F4-C4 channel, **(b)** Simulated EEG formotor active state for C4-P4 and F4-C4 channel, **(c)** Simulated EEG at motor imagery state for C4-P4 and F4-C4 Channel, **(d)**First volunteer's NCV data at all three state.

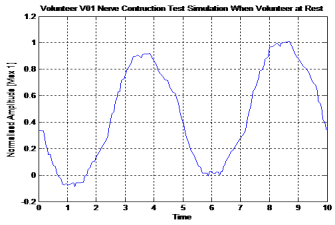

(a)

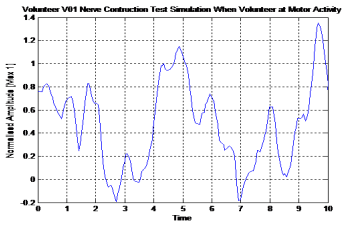

(b)

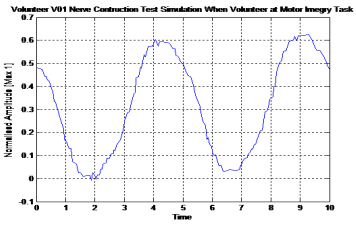

(c)

Fig. 3,(a) NCV simulated data for relax state, **(b)** NCV simulated data for motor activity state,**(c)** NCV simulated data for motor imagery activity state.

device, but in the data collection experiment no foreign stimulation were made. **5.** In data collection procedure standard coherent process were used. **6.**

For both EEG and NCV data collection process three different types of data were collected: **i.** Data were collected when volunteer were relaxing, **ii.** Data were collected when volunteer actively doing motor activity and **iii.** Data were collected when volunteer were doing motor imagery task. At motor imagery task the volunteer did the imagination of which he did on the motor activity task. Data acquisition for EEG and NCV were purely co current.

4. SIMULATION

Table 1, Cooperative Studies of Correlated Data from EEG and NCV

No.	State of Correlation	Channel	Correlation in Percentage (%)
1.	Correlation Between Relax and Motor Activity	NCV	55.9586
2.	Correlation Between Relax and Motor Imagery Task Activity	NCV	39.9906
3.	Correlation Between Relax and Motor Activity	EEG: F4-C4 Channel	57.7291
4.	Correlation Between Relax and Motor Activity	EEG: C4-P4 Channel	48.8268
5.	Correlation Between Relax and Motor Imagery Task Activity	EEG: F4-C4 Channel	56.8407
6.	Correlation Between Relax and Motor Imagery Task Activity	EEG: C4-P4 Channel	66.5576
7.	Cross Correlation for F4C4 with NCV Motor Activity	EEG: F4-C4 Channel NCV	68.1069
8.	Cross for C4P4 with NCV Motor Activity	EEG: C4-P4 Channel NCV	61.5157
9.	Cross Correlation for F4C4 with NCV MI Task	EEG: F4-C4 Channel NCV	63.2452
10.	Cross Correlation for C4P4 with NCV MI	EEG: C4-P4 Channel NCV	44.1696

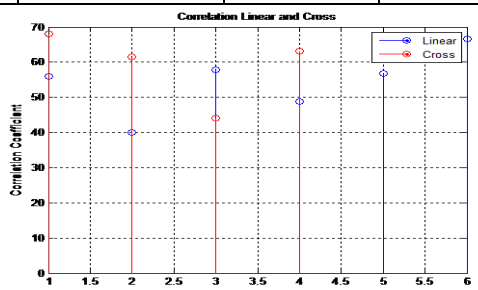

Fig. 4, Result of correlation on scale of percentage for liner and cross relation

5. CONCLUSIONS

A significant amount of correlation is observed for peripheral nervous system and central nervous system in terms of motor imagery task for right hand movement only. This paper suggested the correlation of CNS and PNS in terms of motor imagery task these values would help to model a procedure to diagnosis broken nerves would help to map brain's sensorimotor area with less effort with NCV, would make us understand the effects of thinking on peripheral nervous system, the relation of CNS and PNS would be significant to treat brain damaged person, it will also be helpful to map peripheral nervous system of a patient.

ACKNOWLEDGEMENTS

We are thankful to Dr. Fazlul Huq Associate Professor of Biomedical Sciences, University of Sydneyand Dr. Md Ataul Huq general physician of Primary Health Care of KSAfor useful help and valuable suggestions.

REFERENCES

[1]. Yoon Gi Chung, Min-Ki Kim, Sung-Phil Kim,"Inter-channel Connectivity of Motor Imagery EEG Signals for a Noninvasive BCI Application". *PRNI-11,* 2011 , pp. 49- 52

[2]. Yan Liu, HLiu, ZWei, XZhang, ZXu, ZLuan, DZhang, BLiu,"Experimental study in the function reserve of peripheral nerve repaired in different size by small gap briding". *RSETE-11*, June 2011, pp. 6839- 6842.

[3]. TianLan, Erdogmus, Black, Van Santen, "A comparison of different dimensionality reduction and feature selection methods for single trial ERP detection Engineering in Medicine and Biology Society." *EMBC-10, Annual International Conference of the IEEE*, Aug. 31 2010-Sept. 4 2010, pp. 6329 - 6332.

[4]. G.Mason, M.M.M. Jackson, G.E.Birch, "General framework for characterizing studies of bain interface technology", *Annals of Biomedical Engineering*, November, 2005, Vol. 33, No.11.

[5]. Y.M. Randall and C. O'Reilly, "Computational Exploration in Cognitive Neuroscience: Understanding the Mind by Simulating the Brain", *MIT Press London*, 2000.

[6]. Inderbir Singh, "Textbook of human neuroanatomy", Page-1-4

[7]. Churchland, PS, Koch, Sejnowski, TJ (1993). "What is computational neuroscience?" *Schwartz EL. Computational Neuroscience*. MIT Press. pp. 46–55

[8]. N A Zulkurnaini, R.S.S.A. Kadir, Z.H. Murat, R.M. Isa, "The Comparison between Listening to Al-Quran and Listening to Classical Music on the Brainwave Signal for the Alpha Band". *ISMS-2012*, 8-10 Feb.12, pp. 181 – 186

Proceeding of the
International Conference on Electrical, Computer and Telecommunication Engineering
01- 02 December 2012 (ICECTE2012), RUET, Rajshahi-6204, Bangladesh

ICECTE2012: PI-0066

Analysis of Fat Layer Effects in Ultrasound Imaging Considering the Importance of Spatial Measurement: A Simulation Study

A. B. M. Aowlad Hossain, Md. Mostafizur Rahman
Department of ECE, Khulna University of Engineering & Technology, Khulna-9203,
E-mail: aowlad0403@yahoo.com, mostafiz963@yahoo.com

ABSTRACT
Medical ultrasound imaging is safe, inexpensive and non-invasive imaging modality. Commercial ultrasound imaging systems assume average sound velocity of 1540 m/s though sound velocity varies at different tissues. Due to velocity variations, cutaneous fat layers in the imaging region cause phase aberration which may induce image distortion as well as spatial resolution degradation. The phase aberration may complicate clinical procedures particularly when imaging is used for spatial positioning of medical devices like biopsy, HIFU or other spatial measurements. This paper presents an analysis on fat layer effects in ultrasound imaging using our previously proposed inhomogeneous model. The study will be helpful for clinical imaging where spatial measurements are crucial.

KEY WORDS: Sound speeds, fat layer effects, two layer model, receive beamforming, ultrasound imaging

1. INTRODUCTION

In conventional ultrasound scanner, it is assumed that the ultrasound beam travels in a homogeneous media at a constant speed. However, human body consists of many different organs and tissues in which the sound velocity may change significantly. For example, the speed of sound in fat tissue varies between 1410 m/s and 1479 m/s., in liver between 1553 m/s and 1607 m/s, while in muscle between 1543 m/s and 1631 m/sec [1]. In abdomen imaging, the fat layer underneath the skin may have significant effects on beam focusing performance when the fat layer is very thick. The difference in sound speed and the refraction on the fat surface introduce error in phase delay calculation for transmit and receive beam formation using phase array and hence make aberration at the focal point. Aberration leads to degradation of resolution, causes a spreading in the main lobe energy and gives rise to high isolated side lobes in the beam pattern and hence off axis response become significant [1]- [2].

Some methods proposed to minimize the effect of aberration in receive beamforming [3]-[9]. For receive beamforming most of the methods process the received echo signals in the pair of different elements or elements groups to measure the deviation from expected arrival times. These deviations are used to modify time delays for received beamformer. Most of the existing methods consider the propagation medium as homogeneous and hence refraction of propagated acoustics rays in the interface of inhomogeneous tissue layers is neglected. Therefore to calculate more efficient phase delay function to achieve better focus quality and hence better resolution in ultrasound imaging through inhomogeneous media, inclusion of in vivo information about fat layer thickness and sound velocity in the medium might be helpful.

In this work, we study fat layer effects in ultrasound imaging using inhomogeneous inclined two layer model. We derive time delay function for effective beamforming using information of fat layer thickness and velocity of sound propagation through layers. We investigated the effect of fat layer on the beam focusing quality considering refraction through two layers. Finally we compare the simulated images from echo signals using homogeneous and inhomogeneous sound speeds.

2. METHODS

2.1 Time Delays Calculation Using Inhomogeneous Inclined Two Layer Model

Delayed excitation or reception of acoustic wave or echoes in transmit or receive beamforming is very important to achieve better focus quality. We followed our previously proposed inclined two layer model [10] i.e. soft tissues with fat layer to examine the effects of a cutaneous fat layer on the beam focusing and image quality. With the two layer model shown in Fig.1, the propagation delay from the i-th element to the focal point A at (x_f, y_f, z_f) is:

$$t_p = \frac{d_i}{c_1 \cos\theta_1} + \frac{F - d_i}{c_2 \cos\theta_2} \qquad (1)$$

We can calculate time delays numerically using refraction theories and geometrical information to find the values of θ_1, θ_2 and d_i which was described in details in our previous paper [10]. The time delays are calculated from the differences of propagation times between adjacent elements.

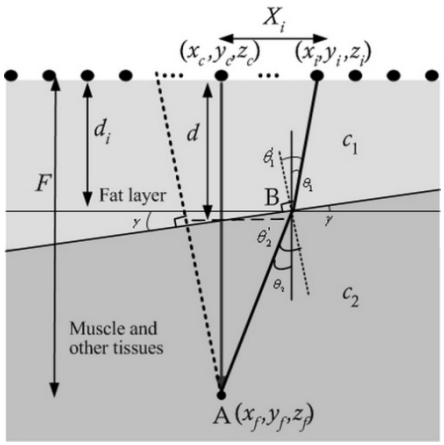

Fig. 1 Derivation of time delays from the inclined-fat-layer model

2.2 Receive Beam Profile Simulation

We first see the effect of the inclined-fat-layer in the receive beamforming by comparing the receive beam profiles obtained with and without the compensations. We estimated received beam profile by summing all delayed echoes considering refraction through fat interface. For receive beamforming taking single layer, we apply the time delay data derived from the homogeneous medium model with the nominal sound speed of 1540 m/s.

In calculating the receive beam profile, we assume uniform echogenic scatterer distribution along the lateral direction at the focal depth. The echo pulses originating from the scatterer and propagating back to the receiving array can be expressed as $q(t)e^{-2\pi f_c t}$, where $q(t)$ is the Gaussian envelope of pulse and f_c is the center frequency of the pulse [11]. The frequency spectrum of the ultrasound echo pulse can be assumed to have Gaussian shape that can be characterized by the mean (center frequency) and standard deviation (bandwidth). With arranging uniform echo sources along the lateral direction at a given focal depth, we calculate the receive beam profiles by summing up all the echo signals taking the frequency components into account. We apply the time delay data to the receive beamforming derived either from the inclined-fat-layer model or from the uniform medium model. Let r_{ij} be the geometric distance between the j-th source and the i-th receiving element. In the layered medium, the ultrasound beam refracts at the interface. Let $r_{ij,1}$ and $r_{ij,2}$ be the propagation path lengths in the top and bottom layers, respectively. Then, the normalized received beam profile is given as:

$$P(j) = \sum_{i=1}^{N}\sum_{k=1}^{O} |Q(f_k)|^2 e^{-\frac{(f_k - f_c)^2}{2\sigma^2}} e^{-2\pi f_k \left(\frac{r_{ij,1}}{c_1} + \frac{r_{ij,2}}{c_2} - t_i^F\right)}, \quad j = 1,2,\ldots,M \qquad (2)$$

where t_i^F is the time delay for receive beamforming at the focal depth F, $Q(f_k)$ is the Gaussian frequency spectrum, O is the number of discrete frequency components f_k in the bandwidth, N is the number of receiving elements, and M is the number of echo sources in the lateral direction. The time delays are derived either from the inclined-fat-layer model for the compensated case or from the uniform medium model for the uncompensated case. In the uniform medium model, uniform distribution of a non-fatty tissue with sound speed of 1540 m/s is assumed.

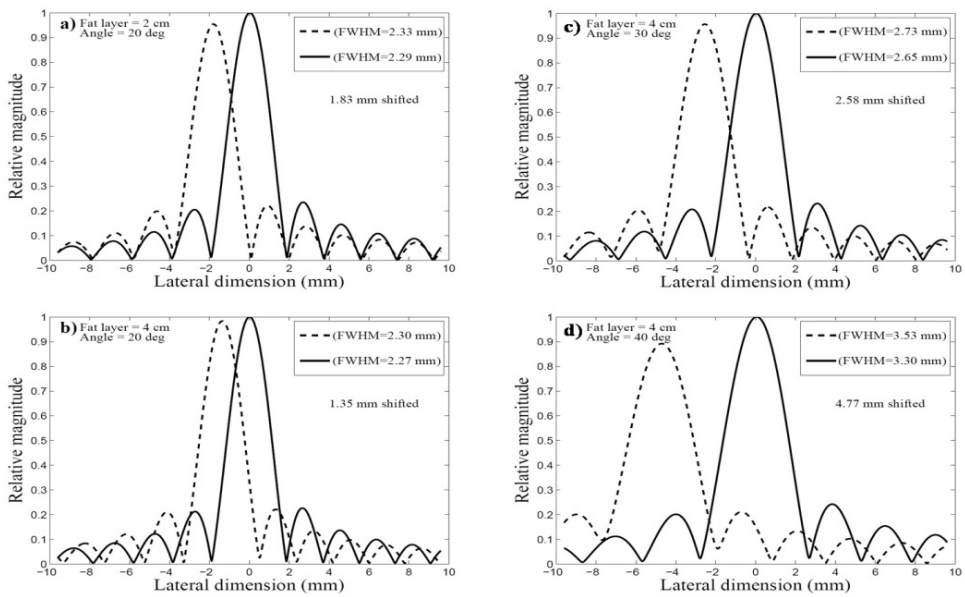

Fig. 2 Received beam profiles calculated at a focal depth of 10 cm for different thicknesses and inclination angles of the fat layers. Solid and dashed curves in **a** through **d** represent the beam profiles obtained with and without phase aberration corrections, respectively.

The calculated received beam profiles at a focal depth of 10cm with the center frequency of 6 MHz and the bandwidth of 2.5 MHz are shown in Fig. 3 for several combinations of fat layer thickness and inclination angle. In this calculation, we considered again a 64-element linear phased array with inter-element spacing of 0.3 mm. The sound speeds of the fat layer and non-fatty layer are set to 1460 m/s and 1540 m/s, respectively. The uncompensated beam profiles are shown by dashed lines while compensated beam profiles by solid lines. We can notice clear tendency that the amount of beam shift increases as the inclination angle increases. Even though it is not clearly noticeable, the fat layer effect also widens the beam profiles, which would degrade lateral resolution of ultrasound images.

2.3 Ultrasound Image Simulation

We have synthesized linear B-mode images by calculating beamformed signals emanating from randomly weighted scatterers in both layers. The number of scan lines is 64. We considered different level of echogenicity in the non-fatty and fatty tissues. We also took account of reflection from the interface which gives a contrast for the interface. The time delays data from single layer model, parallel and inclined two layer model has been used for beamformation to simulate the images. Figure 4 shows a simulated situation of a thin biopsy needle put into an inclined-fat-layer model that has the width and depth of 20mm and 60mm respectively. The top layer thickness is 30 mm at the center and the inclination angle is 30 degrees. The sound speeds of the fat layer and non-fatty layer are again 1460 m/s and 1540 m/s, respectively. The needle insertion angle is 60 degrees with respect to the horizontal axis.

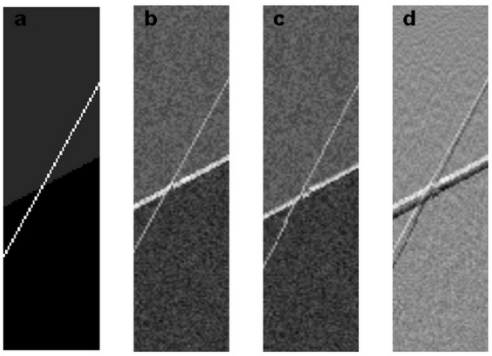

Fig. 4 Figure **a** shows the scatterer echogenicity map for a needle, a fatty layer and a non-fatty layer. Images are synthesized using the time delay data derived from the inclined-fat-layer model and single layer model are shown in **b** and **c**, respectively. Figure **d** shows the difference between **b** and **c**.

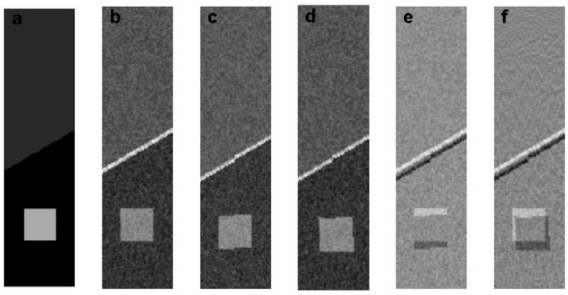

Fig. 5 Figure **a** shows the scatterer echogenicity map for a square 2D inclusion, a fatty layer and a non-fatty layer. Images synthesized using the time delay data derived from the inclined-fat-layer model, the parallel-fat-layer model, and the single layer model are shown in **b**, **c** and **d**, respectively. Figure **e** is the difference between **b** and **c**, and **f** is the difference between **b** and **d**.

To observe the image distortion effect, we place a 2D square inclusion, the size of 6mm×6mm, beneath the fat layer of Fig. 4 as shown in Fig. 5a. The inclusion has different echogenicity from the background tissue region.

3. RESULTS ANALYSIS

We calculated the amount of pixel shifts in the lateral direction by finding the received beam profile shifts as shown in Fig. 3, and the amount of pixel shifts in the axial direction by calculating the arrival times of the echoes at the receiving elements. If we assume typical lateral resolution of 0.3mm, then we observed that the amount of pixel shifts ranges up to order of 10 pixels for 4cm fat layer as shown in Fig. 3. The full-width-half-maximum (FWHM) at the main lobe of the received beam profile is reduced by 1.7-7% after the compensation. The beam shifts in the lateral direction are an order of mm, which would be noticeable in the ultrasound images. The image synthesized with the inclined-fat-layer model in the receive beamforming is shown in Fig. 4b. The image synthesized without phase aberration compensation is shown in Fig. 4c. The distortion in Fig. 4c is not so noticeable, so, we subtracted Fig. 4c from Fig. 4b. The difference image is shown in Fig. 4d. We can now see clear difference between the two images. For 2D inclusion, the images synthesized with the inclined-fat-layer model, the parallel-fat-layer model, and the single layer model are shown in Fig. 5b, 5c, and 5d respectively. To observe the distortion effect more noticeably, we calculated difference images. Figure 5e shows the difference between Fig. 5b and Fig. 5c, and Fig. 5f shows the difference between Fig. 5b and Fig. 5d. In the difference images, we can see the distortion effect more clearly.

As the fat layer has different thickness in different scan lines in ultrasound image formation, the pixel displacements may not be uniform all over the

imaging region, which cause image distortion. Therefore, Effective phase aberration correction techniques are necessary, particularly image distortion correction, to facilitate quantitative image analysis such as spatial or volumetric measuring of interested tissues as well as biopsy needle positioning.

4. DISCUSSIONS & CONCLUSIONS

We used fat layer geometry and sound velocity information which can be obtained by recent multimodal approaches or fat measurement techniques [12]-[13] to observe the effects of phase aberration caused by the fat layers. The ultrasound imaging results of a needle and 2D square shaped inclusion put into the fat-layer-soft tissue model have shown that the image quality, in terms of spatial resolution and distortion, differ notably from that of homogeneous consideration. The position shifting and distortion may misguide to locate desired region in ultrasound guided biopsy or therapy as well as results erroneous measurements. The result analysis suggests that incorporating geometry and sound velocity information can improve the phase aberration correction capability than simply homogeneous consideration. From the experience of this study, we are planning to find more efficient phase aberration correction techniques to obtain better quality abdominal ultrasound images.

In conclusion, the study has shown that fat layer introduces phase aberration due to average sound speed consideration in ultrasound imaging which in turns causes position shifting, resolution degradation and image distortion. We expect the results and analysis will be helpful in developing effective fat layer effect compensation techniques to obtain improved quality abdominal ultrasound images.

5. ACKNOWLEDGEMENTS

The authors would like to thank the Professors and members of MISL Lab, Kyung Hee University, Korea and the authority of KUET, Bangladesh.

REFERENCES

[1]. Q. Chenand, J. A. Zagzebski, "Simulation Study of Effects of Speed of Sound and Attenuation on Ultrasound Lateral Resolution", *Ultrasound in Med. & Biol.*, vol. 30, pp. 1297-1306, 2004.

[2]. D. A. Gray, "Effect of Time-Delay Errors on the Beam Pattern of a Linear Array", *IEEE Journal of Ocenic Engineering*, vol. OE-10, no. 3, pp. 269-277, 1985.

[3]. S. W. Flax, M. O'Donnel, "Phase-Aberration Correction Using Signals from Point Reflectors and Diffuse Scatterers: Basic Principles", *IEEE Trans. Ultrason. Ferroelect. Freq. Control*, vol. 35, no. 6, pp. 758-767, 1988.

[4]. D. Rachlin, "Direct Estimation of aberrating delays in pulse-echo imaging systems", *J. Acoust. Soc. Am.*, vol. 88, no. 1, pp. 191-198, 1990.

[5]. G. C. Ng, S. S. Worrell, P. D. Freiburger, G. E. Trahey, "A comparative evaluation of several algorithms for phase aberration correction", *IEEE Trans. Ultrason. Ferroelect. Freq. Control*, vol. 41, no. 5, pp. 631-643, 1994.

[6]. K. W. Rigby, C. L. Chalek, B. H. Haider, M. O'Donnell, R. S. Lewandowski, M. O'Donnell, L. S. Smith, D. G. Wildes, "Improved In Vivo Abdominal Image Quality Using Real-time Estimation and Correction of Wavefront Arrival Time Errors", in *Proc. IEEE Ultrason. Symp.*, vol. 3, pp. 1645-1653, 2000.

[7]. K. W. Rigby, "Real-time Correction of Beamforming Time Delay Errors in Abdominal Ultrasound Imaging", *in Proc. SPIE Medical Imaging*, vol. 3982, pp. 342-353, 2000.

[8]. S.-E. Måsøy, T. Varslot, B. Angelsen, "Estimation of ultrasound wave aberration with signals from random scatterers", *J. Acoust. Soc. Am.*, vol. 115, no. 6, pp. 2998–3009, 2004.

[9]. S.-E. Måsøy, T. Varslot, and B. Angelsen, "Variance analysis of arrival time and amplitude estimates from random speckle signal", *J. Acoust. Soc. Am.*, vol. 121, no. 1, pp. 286-297, 2007.

[10]. A.B.M. Aowlad Hossain, L. Kang, Y.H. Ha, M.H. Cho, and S.Y. Lee, "Compensation of fat layer effects in ultrasound imaging using an inclined-fat-layer model derived from magnetic resonance images", *Acoustical Physics (Springer)*, vol. 57, no. 2, pp. 144-150, 2011.

[11]. Szabo TL, "Diagnostic ultrasound imaging: inside out", Elsevier Academic Press, 2004.

[12]. L. Curiel, R. Chopra, K. Hynynen, "Progress in multimodal imaging: Truly simultaneous ultrasound and magnetic resonance imaging", *IEEE Trans. Med. Imag.*, vol. 26, pp. 1740-1746, 2007.

[13]. C. Orphanidou, L. McCargar, C. L. Birmingham, J. Mathieson, E. Goldner, "Accuracy of subcutaneous fat measurement: Comparison of skinfold calipers, ultrasound, and computed tomography", *Journal of the American Dietetic Association*, vol. 94, no. 8, pp. 855–858, 1994.

Proceeding of the
International Conference on Electrical, Computer and Telecommunication Engineering
01- 02 December 2012 (ICECTE2012), RUET, Rajshahi-6204, Bangladesh

ICECTE2012: PI-0067

Control of Chromatic Dispersion and Confinement Losses with Octagonal Photonic Crystal Fibers in Telecommunication Window

Md. Samiul Habib, Md. Selim Habib, S. M. Abdur Razzak, M. A. Goffar Khan, G.K.M.Hasanuzzaman*
Department of Electrical & Electronic Engineering, Rajshahi University of Engineering & Technology
E-mail: *samiul.engieee@gmail.com

ABSTRACT:

We present a Photonic Crystal Fibers (PCFs) for shaping nearly zero ultra-flattened chromatic dispersion and very low confinement loss in the entire band of interest ranging from 1.25 to 1.62 µm wavelength range. The Finite Element Method with perfectly matched layers boundary condition is used to investigate the guiding properties. A five ring octagonal PCF with low dispersion of 0 ± 0.8 ps/nm/km in the wavelength range of 1.25 to 1.62 µm with very low confinement loss of less than 10^{-6}dB/km is presented.

KEY WORDS: photonic crystal fiber, ultra-flattened dispersion, effective area, confinement loss.

1. INTRODUCTION

Photonic crystal fibers (PCFs) or holey fibers [1] have microscopic array of air channels running alone its length that makes the low index cladding around the undoped silica core. In this way, light can be well confined and guided properly through the fiber by the mechanism of either total internal reflection (TIR) or photonic band gap (PBG). One of the appealing characteristics of such fibers is that their chromatic dispersion and modal properties can be controlled significantly by varying the size of the air-holes, their number, and their positions [2]. As a result, PCFs exhibit a number of unique properties including wide range single mode operation, zero dispersion at visible wavelengths, super high or low nonlinearities, high birefringence, and ultra-flattened dispersion [3]-[4]. Therefore, PCFs are so attractive in controlling application specific dispersion and modal properties [5]. Control of fiber's chromatic dispersion is crucial for practical applications to optical fiber communication systems, dispersion compensation, and nonlinear optics [6].

Chromatic dispersion of PCFs play an important role in optical communication as it limits the data carrying capacity of the fiber. It causes light pulses to spread causing inter-symbol interference and becomes a critical issue as soon as transmission rate exceeds 10 Gb/s. Moreover, the confinement loss is also an important loss parameter in PCFs. By modulating the parameters of the holey cladding, it is possible to design application specific guiding properties [7].

Typically, in PCFs the air holes are arranged on the vertex of an equilateral triangle with six air holes in the first ring surrounding the core, named the conventional PCF or hexagonal PCF (H-PCF). Besides the hexagonal PCF structures, other structures, such as square lattice, honeycomb and octagonal-lattice were proposed to design the PCF [8]. Therefore, as part of the ongoing efforts in pursuit of a novel structure for PCFs, in this paper, investigations are made on octagonal PCF (O-PCF) so as to obtain ultra-flattened chromatic dispersion with very low confinement losses. The proposed design ensures very low confinement loss of less than 10^{-6} dB/Km with ultra-flattened dispersion of 0 ± 0.8 ps/nm/km in the entire telecommunication band.

2. DESIGN METHODOLOGY

Fig. 1 shows simple geometry of the proposed O-PCF. The air-hole diameter on the first ring is d_1, second ring is d_2 and air-hole diameter on the third to five rings is d.

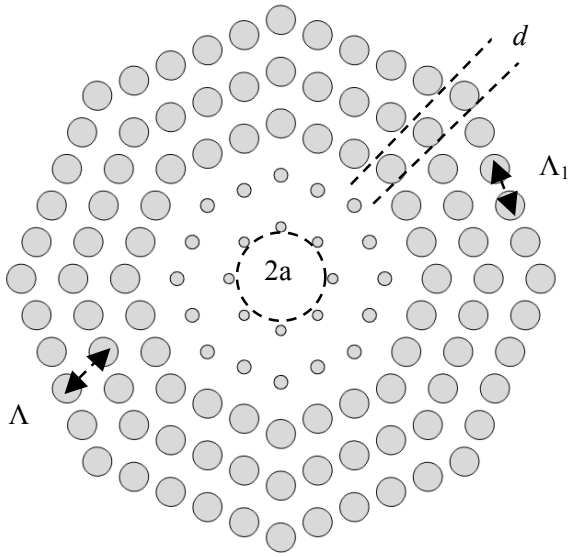

Fig. 1 Geometry of the proposed five-ring O-PCF with 1st ring air-hole diameter d_1, 2nd ring air-hole diameter d_2, air-hole pitch Λ and number of rings, Nr=5.

Pitch, Λ is the spacing between air hole centers on the adjacent rings and the spacing between air holes centers on the same ring is Λ_1. Pitch Λ_1 is related to Λ by the relation $\Lambda_1 \approx 0.765\Lambda$. In contrast to hexagonal PCFs, the octagonal structure has isosceles triangular unit lattices [9] with vertex angle of 45^0. Owing to isosceles triangular unit lattices, it contains more air-holes in the cladding region for the same number of rings compared to conventional PCFs. The number of air-holes of an octagonal structure for rings 1, 2, 3, 4, 5 is, respectively, 8, 16, 24, 32, and 40. This results a higher air-filling ratio and a lower refractive index around the core, thereby providing strong light confinement ability. The core diameter is 2a, where 'a' equals Λ-d/2. The air-holes of diameter d are located at each corner of the isosceles triangle resulting lower refractive index due to higher air-filling fractions (AFFs) around the core compared to H-PCF. This high air-filling fraction reduces the confinement loss of the O-PCF and more circular optical field distribution around the core than H-PCF.

3. SIMULATION METHODOLOGY AND EQUATION

The guiding properties of O-PCFs are numerically investigated using COMSOL 4.2 software. The finite-element method with perfectly matched boundary layers (PML) is used to calculate effective area, chromatic dispersion and confinement loss of PCFs. The FEM directly solves the Maxwell equations to best approximate the value of the effective refractive index. Once the modal effective refractive index, n_{eff} is obtained by solving an eigen value problem drawn from Maxwell equations using the COMSOL software 4.2, effective area, chromatic dispersion and confinement loss of PCFs can be easily calculated.

The effective area A_{eff} is calculated as follows [10]

$$A_{eft}=(\int_{-\infty}^{+\infty}\int_{-\infty}^{+\infty}|E|^2dxdy)^2/(\int_{-\infty}^{+\infty}\int_{-\infty}^{+\infty}|E|^2dxdy)\ldots..(1)$$

Where, E is the electric field derived by solving the Maxwell equations.

Chromatic dispersion D can be calculated by the relations [11].

$$D(\lambda)=-\lambda/c(d^2\mathrm{Re}[n_{eff}]/d\lambda^2)\ldots\ldots\ldots\ldots\ldots\ldots\ldots\ldots(2)$$

Where Re $[n_{eff}]$ is the real part of effective refractive index, n_{eff}, λ is the wavelength, c is the velocity of light in vacuum. The material dispersion given by Sellmeier formula is directly included in the calculation. Therefore, D in (2) corresponds to the chromatic dispersion of the PCF.

The confinement loss L_c is obtained from the imaginary part of n_{eff} as follows [2]

$$Lc = 8.686\times k_0\mathrm{Im}[n_{eff}]\ \ \mathrm{dB/m}\ldots\ldots\ldots\ldots\ldots\ldots\ldots(3)$$

Where $\mathrm{Im}[n_{eff}]$ is the imaginary part of the refractive index, $k_0 = 2\pi/\lambda$ is the wave number in the free space.

4. SIMULATION RESULTS

In this proposed O-PCF design, air -hole diameter of the inner two rings and hole-to-hole spacing effects, on chromatic dispersion and confinement losses are investigated. Air-hole diameters of the outer three rings are set at d/Λ=0.7. In the outer most cladding a high value air filling fraction is chosen for better field confinement and also reduce the confinement loss to a very low value. Air-hole dimension of the first ring is lowered down to flatten the dispersion characteristics. Chromatic dispersion is one of the most important modal properties of the PCFs. At shorter operating wavelengths, mode is more confined in the core region than at longer wavelengths, and the chromatic dispersion is directly affected from the inner air-hole ring and the air hole arrangements but also from the outer ring air hole sizes and hole-to-hole spacing, Λ. As shown in Fig. 1, there are three tuning parameters d_1, d_2 and Λ for shaping the dispersion behavior of the five-ring O-PCF.

From fig. 2 it has been seen that flattened dispersion is greatly depend on first ring air- filling fraction d_1/Λ. There is positive dispersion slope as d_1/Λ=0.275 , but the slope changes significantly from the positive slope to negative one near the wavelength at 1.48μm as the d_1/Λ increased from 0.275 to 0.295.

Fig. 3 shows effect of changing pitch, Λ on the dispersion level. In the outer three rings, a large value of d/Λ is chosen for better field confinement. From fig. 3 it is seen that the air-hole pitch, Λ dominantly influence the dispersion level but little effect on the slope of the dispersion.

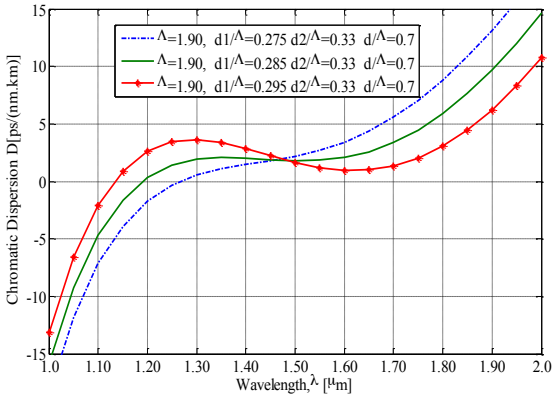

Fig. 2 Effect of changing d_1/Λ on the dispersion slope with pitch Λ=1.90 μm, d/Λ=0.7, and d_2/Λ=0.33.

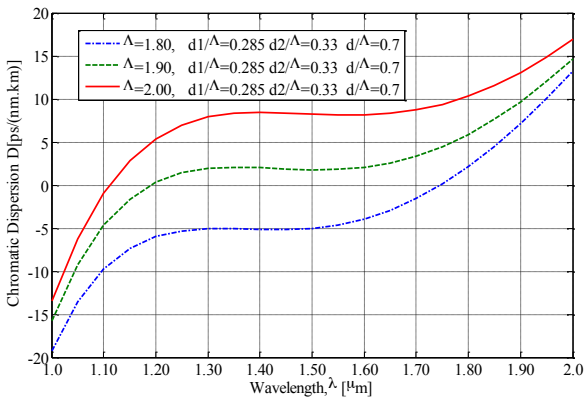

Fig. 3 Effect of pitch, Λ on the dispersion level for d_1/Λ =0.285, d_2/Λ =0.33, and d/Λ=0.7.

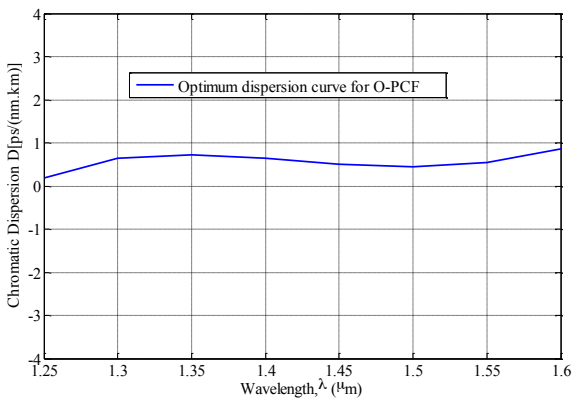

Fig. 4 Wavelength dependence of the O-PCF's chromatic dispersion for optimum parameters: d_1/Λ =0.285, d_2/Λ =0.33, d/Λ=0.7, Λ = 1.88 μm and number of ring, N_r=5.

From fig. 3 it is seen that as pitch, Λ increases level of dispersion increases due to higher effective refractive index.

An optimum dispersion curve of the proposed O-PCF is shown in Fig. 4. Air-hole pitch, Λ is varied to achieve target near-zero ultra-flattened chromatic dispersion in wide band wavelength range. Optimizing the parameters, ultra-flattened dispersion of 0 ± 0.8 ps/nm/km is obtained in a 1250 to 1620 nm wavelength range for d_1/Λ=0.285, d_2/Λ=0.33, d/Λ=0.7, Λ = 1.88 μm, and number of rings Nr = 5.

Fig. 5 shows effective area of the fiber for optimum design parameters. The effective area is 8.97 μm^2 which is small compared to that of conventional fibers at 1.55-μm wavelength. The PCFs with nearly-zero ultra-flattened dispersion has relatively small effective area and would be useful for some nonlinear applications, such as super continuum generation, soliton pulse transmission, and also in wavelength division multiplexing systems.

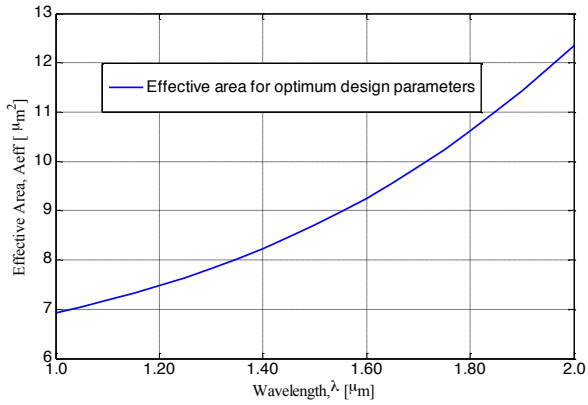

Fig. 5 Wavelength dependence of the OPCF's effective area for optimum design parameters: d_1/Λ =0.285, d_2/Λ =0.33, d/Λ=0.7, Λ = 1.88 μm and number of ring, N_r=5.

Fig. 6 shows wavelength dependence of confinement loss of the O-PCF for optimum design parameters. The confinement loss is found of the order less than 10^{-6} dB/km within the band of interest. Confinement loss in O-PCF is much lower than H-PCF due to more air-holes in the cladding region for same number of rings.

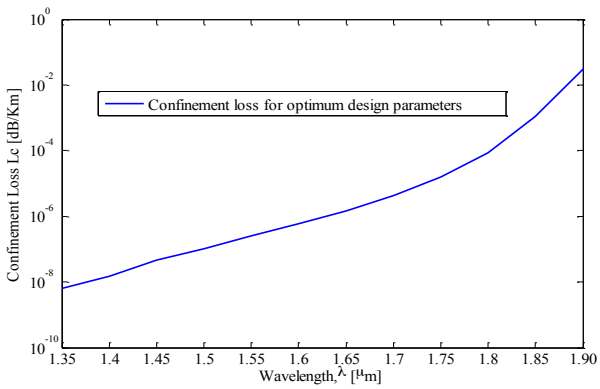

Fig. 6 Confinement loss of the proposed O-PCF's for optimum design parameters.

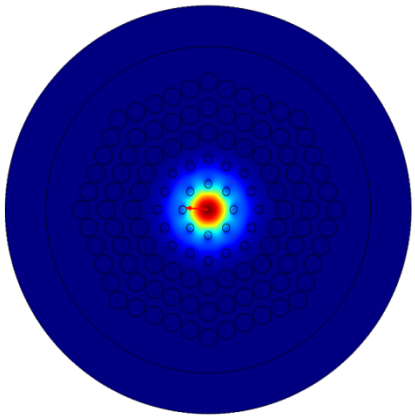

Fig. 7 Fundamental mode field distribution of the O-PCF's at 1.55 μm for optimum design parameters as a function of wavelength.

5. CONCLUSION

A near-zero Ultra-flattened chromatic dispersion with very low confinement loss for the five-ring octagonal PCF has been reported. In this proposed O-PCF design, flattened dispersion of 0±0.8 ps/nm/km from 1.25 to 1.62μm wavelength range (370 nm flat band) and confinement loss of 10^{-6} dB/km at 1.55-μm wavelength having with modest number of design parameters is numerically demonstrated.

REFERENCES:

[1] J.C. Knight, T.A. Birks, P.St.J. Russell, and D.M. Atkin: "All-silica single-mode optical fiber with photonic crystal cladding," Opt. Lett. 21,1547-1549 (1996).

[2] S M A Razzak, Y Namihira, T Kinjo, S Kaijage, N H Hai, K Miyagi (2008) "Simultaneous control of dispersion and confinement losses with octagonal photonic crystal fibers forcommunication systems ," In: International Conference of Electrical Engineering (ICEE) Okinawa, Japan, July 6-9: 2008.

[3] T. Matsui, J. Zhou, K. Nakajima, and I. Sankawa, "Dispersion-flattened Photonic Crystal Fiber with Large Effective area and Low Confinement Loss," J. Lightwave Technology, vol. 23, no. 12, pp. 4178-4183,Dec 2005.

[4] K. P. Hansen, "Dispersion flattened hybrid-core nonlinear photonic crystal fiber," Opt. Express, vol. 11, no. 13, pp. 1503-1509, June 2003.

[5] T. L. Wu and C. H. Chao, "A novel ultraflattened dispersion photonic crystal fiber," IEEE. Photon.Technol. Lett., vol. 17, pp. 67-69, 2005.

[6] K. Saitoh and M. Koshiba, "Highly nonlinear dispersion-flattened photonic crystal fibers for supercontinuum generation in the telecommunication window," Opt. Express, vol. 12, no. 10, pp. 2027-2032, May 2004.

[7] SAITOH K., FLOROUS N.J., KOSHIBA M., Ultra-flattened chromatic dispersion controllability using a defect-core photonic crystal fiber with low confinement losses, Optics Express 13(21), 2005, pp. 8365–8371.

[8] Jung-Sheng Chiang, and Tzong-Lin Wu: "Analysis of propagation characteristics for an octagonal photonic crystal fiber (O-PCF)," Opt. Commm. 258, 170-176,(2006).

[9] S. M. A. Razzak, Y. Namihira, and F. Begum, "Ultra-flattened dispersion photonic crystal fiber," Electron. Lett., vol. 43, pp. 615–617, 2007.

[10] S. M. A. Razzak, Y. Namihira, F. Begum, S. Kaijage, N. H. Hai, and N. Zou, "Design of a decagonal photonic crystal fiber with ultra-flattened chromatic dispersion," IEICE Trans. Electron., vol. E90-C, no. 11, pp. 2141-2145, Nov. 2007.

[11] K. Saitoh, M. Koshiba, T. Hasegawa, and E. Sasaoka, "Chromatic Dispersion control in photonic crystal fibers: Application to ultra flattened dispersion,"Opt. Express, vol. 11, pp. 843–852, 2003.

Proceeding of the
International Conference on Electrical, Computer and Telecommunication Engineering
01- 02 December 2012 (ICECTE2012), RUET, Rajshahi-6204, Bangladesh

ICECTE2012: PI-0068

Design of Near-Zero Ultra-Flattened Chromatic Dispersion Holey Fiber in Telecommunication Application

Md. Samiul Habib, Mahbubur Rahman, M. Ashraful Alam, A. H. Md. Mostazir, G.K.M. Hasanuzzaman*
Department of Electrical & Electronic Engineering, Rajshahi University of Engineering & Technology
E-mail: samiul.engieee@gmail.com*, engr.rumman@gmail.com, ashraful07eee@gmail.com,
hayat_eee07@yahoo.com, g.kibria82@yahoo.com

ABSTRACT:

We present a Holey fiber (HF) based on hexagonal structured cladding for tailoring near-zero ultra-flattened dispersion in a modest number of ring for wide range of wavelengths. The finite element method with perfectly matched layers boundary condition is used to investigate the guiding properties. A four ring HF with flattened dispersion of 0.82ps/nm/km from 1.25 to 1.60μm wavelength range is numerically demonstrated.

KEY WORDS: Confinement loss, effective area, finite element method, Holey fiber, ultra-flattened dispersion.

1. INTRODUCTION

Photonic Crystal fibers [1] or Holey fibers usually consist of hexagonal arrangements of microscopic air-channels. Air holes can be arranged in the cladding in a periodic (hexagonal arrangement being the common) or aperiodic fashion. Therefore, HF is a single material fiber that contains tiny air holes in silica background. The most appealing characteristics of such fibers is that their chromatic dispersion and modal parameters can be controlled significantly by varying size of the air-holes, their numbers and their positions[2]. Inclusions of air-holes in HF offer a variable index-contrast between the core and cladding which is achieved by changing dimensions of holes and cladding geometry [3]. HFs exhibit a number of unique properties such as zero dispersion at visible wavelengths, super high or low nonlinearities, high birefringence and ultra-flattened Dispersion of HFs is greatly influenced by the parameters of the silica-air microstructure namely the core diameter, air-hole diameter and position, air-hole pitch and ellipticity [4].

In broadband communications systems, fiber dispersion and confinement loss play very important roles. For example, in wavelength division multiplexing systems, it is essential to maintain a uniform response in different wavelength channels. This is strictly achieved by ensuring Ultra-flattened dispersion characteristics of fibers [5]. This novel property of HFs helps in tuning transmission characteristics namely dispersion, non-linearity and confinement losses in smart ways.

We, in this paper, propose a four-ring HF structure with nearly zero ultra-flattened dispersion in the entire band of interest ranging from 1.25 to 1.6 μm wavelength. According to simulation it is seen that our proposed design exhibits near-zero ultra-flattened chromatic dispersion throughout 350nm flat band region. Near-zero ultra-flattened dispersion of 0.82ps/nm/km is obtained in a 1.25 to 1.60-μm wavelength range.

2. DESIGN TECHNIQUE

A simple four ring structured dispersion flattened Holey fiber (DF-HF) has been proposed with optimized air-hole diameter d_1, d_2 and pitch Λ.

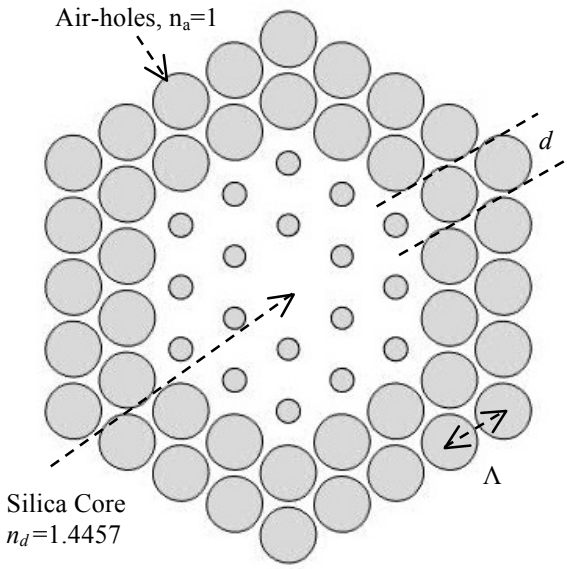

Fig. 1 Proposed Geometrical structure of four ring DF-HF. Number of ring, N_r=4.

The first and second air-hole diameter is d_1 and $d_2$respectively. The third and fourth ring diameter is same and is denoted by d. The air-hole pitch is Λ. the refractive index of fiber silica is n_s=1.4457 and refractive index of air-hole is n_a=1.

In fig. 1 there are three degrees of freedom for controlling dispersion behavior of four rings HF, namely d_1, d_2 and Λ the diameter of first and second ring is kept low for proper dispersion behavior and diameter of the outer two rings are kept large for better field confinement and for reducing confinement loss. We have shown theoretically that it possible to design a simple HF with reduced air-hole without distorting the dispersion flatness in telecom band.

3. SIMULATION TECHNIQUE

The COMSOL 4.2 version software is used as a simulation tool. Effective refractive index, effective area, chromatic dispersion and confinement loss are calculated by using finite element method (FEM) with perfectly matched boundary layers (PML). FEM has been combined with most of the other computational methods to develop more efficient hybrid computational methods. The FEM allows the MOF cross-section in the transverse $x-y$ plane to be divided into a patchwork of triangular elements, which can be of different sizes, shapes and refractive indices. FEM is suited for studying fibers with no periodic air-hole arrangements [6]. The FEM directly solves the Maxwell equations to best approximate the value of the effective refractive index. However, the modal effective refractive index, n_{eff} is obtained by solving an Eigen value problem drawn from Maxwell equations using the COMSOL 4.2 software, effective area A_{eff} can be obtained using the following equation [7].

The effective area A_{eff} is calculated by

$$A_{eff}=\left(\int_{-\infty}^{+\infty}\int_{-\infty}^{+\infty}|E|^2dxdy\right)^2/\left(\int_{-\infty}^{+\infty}\int_{-\infty}^{+\infty}|E|^2dxdy\right)\ldots..(1)$$

Where, E is the electric field derived by solving the Maxwell equations.

Chromatic dispersion D can be calculated by the relations [8].

$$D(\lambda)=-\lambda/c(d^2Re[n_{eff}]/d\lambda^2)\ldots\ldots\ldots\ldots\ldots\ldots\ldots\ldots(2)$$

Where $Re[n_{eff}]$ is the real part of effective refractive index, n_{eff}, λ is the wavelength, c is the velocity of light in vacuum. The material dispersion given by Sellmeier formula is directly included in the calculation. Therefore, D in (2) corresponds to the chromatic dispersion of the DF-HF.

The confinement loss L_c is obtained from the imaginary part of n_{eff} as follows [8]

$$Lc = 8.686\times k_0\, Im[n_{eff}]\ldots\ldots\ldots\ldots\ldots\ldots\ldots\ldots(3)$$

Where $Im[n_{eff}]$ is the imaginary part of the refractive index, $k_0 = 2\pi/\lambda$ is the wave number in the free space.

4. SIMULATION RESULTS

In this proposed HF design, Ultra-flattened zero dispersion HF can be efficiently designed by optimizing geometrical parameters, such as air hole diameters and pitch. In this design we first set air-hole diameters of the outer cladding at d/Λ=0.9. Air-hole diameter on the first ring is scaled down to shape the dispersion property while diameters of air holes on outer rings are kept larger for better field confinement. There are three optimizing parameters d_1, d_2 and Λ for tailoring the dispersion behavior of the four rings HF.

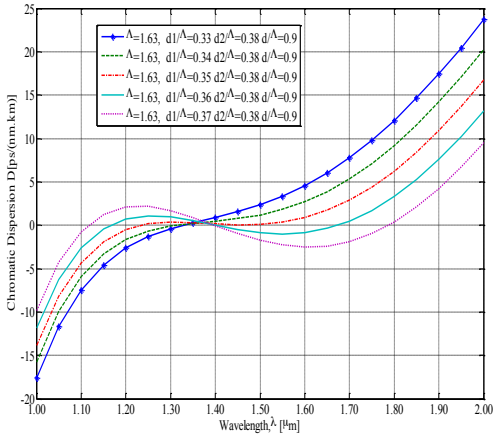

Fig. 2 Effect on dispersion due to d_1/Λ variation with d_1/Λ= 0.33, 0.34, 0.35, 0.36 and 0.37

Fig. 2 Shows an example of the effect of changing d_1/Λ on the dispersion behavior with d_1/Λ=0.33, 0.34, 0.35, 0.36 and 0.37 respectively, for a fixed air-hole pitch Λ=1.63μm and outer ring air filling fraction d/Λ=0.9. From fig. 2, it has been seen that flattened dispersion greatly depends on first ring air-filling fraction d_1/Λ. There is a positive dispersion slope as d_1/Λ=0.33 as d_2/Λ=0.34, but the slope changes significantly from the positive slope to the negative one near the wavelength 1.35μm as d_1/Λ=0.36 and d_1/Λ=0.37.

Fig. 3 shows an example of the effect of changing d_2/Λ on dispersion behavior with d_2/Λ=0.36, 0.37, 0.38, 0.39 and 0.40 respectively, for a fixed air-hole pitch Λ=1.63. From designing point of view, a large value of d/Λ=0.9 of outer ring is chosen for better field confinement. There is no effect on slope for the variation of second ring diameter. Optimum dispersion curve is obtained for Λ =1.63, d_1/Λ =0.35, d_2/Λ =0.38 d/Λ =0.9. Change in level of dispersion is obtained at d_2/Λ=0.36, 0.37, 0.39and 0.40. Optimizing the parameters, ultra-flattened dispersion is obtained in a 1.25μm to 1.60μm wavelength range.

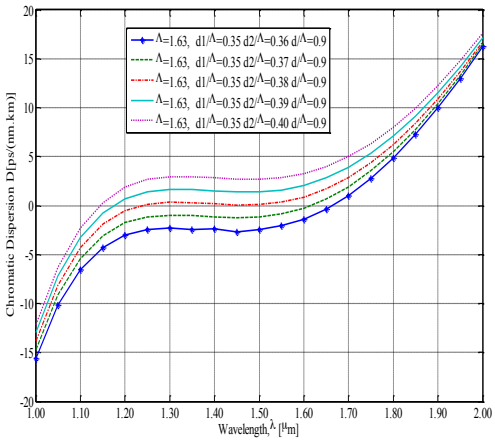

Fig. 3 Effect on dispersion due to d_2/Λ variation with d_2/Λ= 0.36, 0.37, 0.38, 0.39 and 0.40.

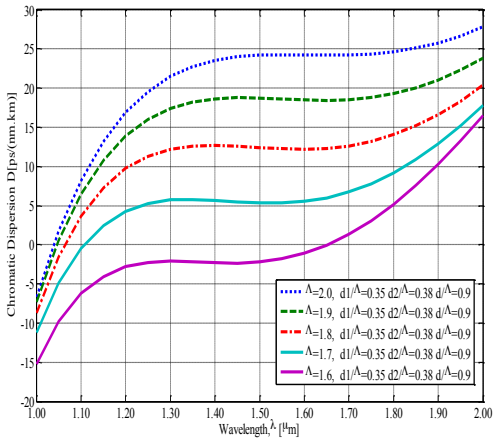

Fig. 5 Effect on dispersion due to Λ variation with Λ= 2.0, 1.9, 1.8, 1.7 and 1.6 μm.

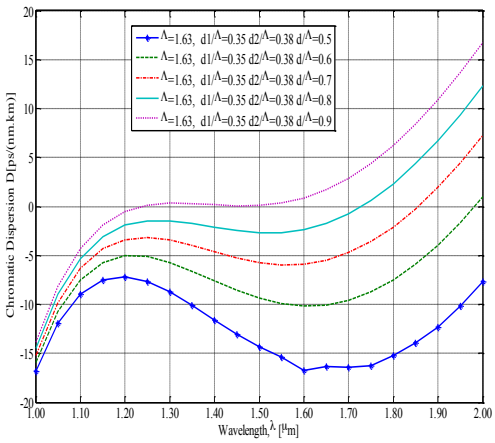

Fig. 4 Effect on dispersion due to d/Λ variation with d/Λ = 0.5, 0.6, 0.7, 0.8 and 0.9.

Fig. 4 shows the effect of changing d/Λ on dispersion level with d/Λ=0.5, 0.6, 0.7, 0.8 and 0.9 respectively for a fixed air-hole pitch Λ=1.63, d_1/Λ=0.35 and d_2/Λ=0.38.It has seen that there is a large impact on variation of slope for variation of third ring diameter. Here, optimum dispersion is obtained at pitch 1.63 d_1/Λ=0.35, d_2/Λ=0.38, d/Λ=0.9. Negative slope is obtained at other third ring diameters i.e. at d/Λ = 0.5, 0.6, 0.7 and 0.8.

Pitch dominantly influence the dispersion level but little impact on the slope of dispersion. Fig. 5 shows the effect of changing air-hole pitch Λ on the chromatic dispersion behavior with d_1/Λ=0.35, d_2/Λ=0.38, d/Λ=0.9. Air-hole pitch is varied to achieve target zero ultra-flattened chromatic dispersion in wide-band wavelength range.

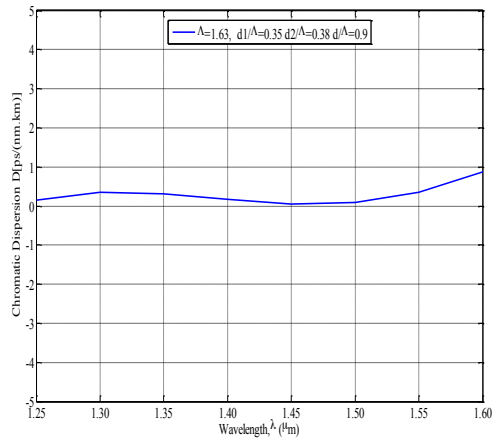

Fig. 6 Wavelength dependence of the DF-HF's chromatic dispersion for optimum parameters: d_1/Λ=0.35, d_2/Λ=0.38, d/Λ=0.9, Λ=1.63μm and N_r=4.

Optimizing the parameters, Fig. 6 shows ultra-flattened dispersion of 0.82ps/nm/km is obtained in a 1250nm to 1600nm wavelength range for d_1/Λ=0.35, d_2/Λ=0.38, d/Λ=0.9, Λ=1.63μm and number of rings= 4.

Fig. 7 shows confinement loss is increasing smoothly with the wavelength and there is no evidence of abrupt change in leakage. Increasing losses due to corresponding decrease in air-hole diameters are also consistent. In this proposed DF-HF design confinement loss at 1.55μm wavelength is less than 10^{-2} dB/km. Graph shows wavelength dependence on confinement loss of the proposed DF-HF's at 1550nm wavelength for optimum design parameters: d_1/Λ=0.35, d_2/Λ=0.38, d/Λ=0.9, Λ=1.63μm and N_r=4

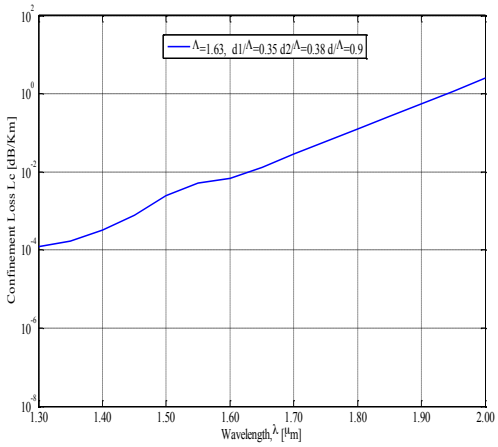

Fig. 7 Wavelength dependence of the DF-HF's confinement loss for optimum parameters: d_1/Λ=0.35, d_2/Λ=0.38, d/Λ=0.9, Λ=1.63μm and N_r=4

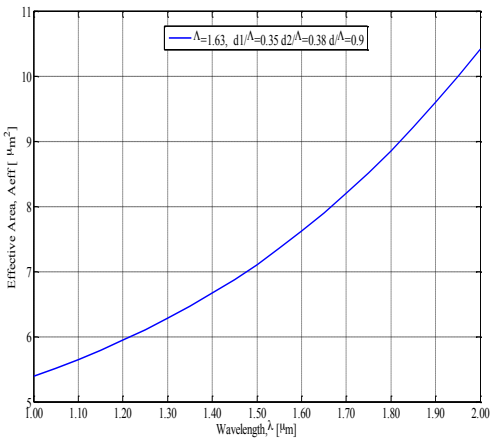

Fig. 8 Wavelength dependence of the DF-HF's effective area for optimum parameters: d_1/Λ=0.35, d_2/Λ=0.38, d/Λ= 0.9, Λ=1.63μm and N_r=4.

The effective area of the proposed fiber for optimum design parameters has been shown in Fig. 8. The effective area of the fiber at 1.55μm is 7.5μm^2.

5. CONCLUSION

A truly near zero ultra-flattened dispersion has been proposed in simple design of HF. This fiber has a modest number of design parameters, four rings, three air-hole diameters, and a common air-hole pitch. It has been shown through numerical simulation results that a four-ring DF-HF can assume nearly zero ultra-flattened dispersion of 0.82ps/nm/km in a 1.25-1.6 μm (350 nm bandwidth) wavelength range with low confinement losses of the order less than 10^{-2} dB/km. Fibers with nearly zero ultra-flattened chromatic dispersion and low confinement loss are crucial for broadband communication systems.

REFERENCES:

[1] J. C. Knight, T. A. Birks, P. St. J. Russell, and D. M. Atkin, "All-silica single-mode optical fiber with photonic crystal cladding," Opt. Lett., vol. 21, pp.1547-1549 Oct.1996.

[2] S. M. A. Razzak, Y.Namihira, T Kinjo, S Kaijage, N H Hai, K Miyagi (2008) "Simultaneous control of dispersion and confinement losses with octagonal photonic crystal fibers for communication systems ," In: International Conference of Electrical Engineering (ICEE) Okinawa, Japan, July 6-9: 2008.

[3] J. A. Buck,Fundamentals of Optical Fibers,John Wiley &Sons Inc. USA.2nd Edition,2004.

[4] *Photonic Crystal Fibers: Design and Applications* S. M. Abdur Razzak (Author), Yoshinori Namihira (Author).

[5] FERRANDO A., SILVESTRE E., MIRET J.J., ANDRES P., Nearly zero ultraflattend dispersion in photonic crystal fibers, Optics Letters **25**(11), 2000, pp. 790–792.

[6] T. M. Monro, D. J. Richardson, N. G. R. Broderick, and P. J. Bennett, "Modeling large air fraction holey optical fibers," IEEE/OSA Journal of Light wave Technology, vol. 18, pp. 50–56, Jan. 2000.

[7] S. M. A. Razzak, Y. Namihira, F. Begum, S. Kaijage, N. H. Hai, and N. Zou, "Design of a decagonal photonic crystal fiber with ultra-flattened chromatic dispersion," IEICE Trans. Electron., vol. E90-C, no. 11, pp. 2141-2145, Nov. 2007.

[8] K. Saitoh, M. Koshiba, T. Hasegawa, E. Sasaoka, "Chromatic dispersion control in photonic crystal fibers: application to ultra-flattened dispersion," Opt. Express, vol. 11, no. 8, pp.843-852, April 2003.

Proceeding of the
International Conference on Electrical, Computer and Telecommunication Engineering
01- 02 December 2012 (ICECTE2012), RUET, Rajshahi-6204, Bangladesh

ICECTE2012: PI-0069

Tailoring Nonlinear Coefficient Using Highly Nonlinear Germanium Doped Hexagonal Photonic Crystal Fiber

Md. Anwar Hossain[1], Yoshinori Namihira[1], Takuro Yasui[2]
[1]Graduate School of Engineering and Science, University of the Ryukyus
[2]Dept. of Electrical Engineering, Faculty of Engineering, University of the Ryukyus
1 Senbaru, Nishihara, Okinawa 903-0213, Japan
E-mail: anwar.ee113@gmail.com, namihira@eee.u-ryukyu.ac.jp

ABSTRACT
This paper discusses about tailoring nonlinear coefficient γ using hexagonal photonic crystal fiber (PCF). Using finite element method (FEM) with a circular perfectly matched boundary layer (PML), effects of variation of different global parameters of PCF on nonlinear coefficient γ are shown through simulation.

KEYWORDS: Nonlinear coefficients, highly nonlinear (HNL), photonic crystal fiber (PCF), finite element method (FEM).

1. INTRODUCTION

Although there are some detrimental effects of optical nonlinearities in optical communications, optical nonlinearities are found interest to be used for a number of applications including fiber amplification, wavelength conversion, multiplexing and demultiplexing, optical pulse regeneration, optical monitoring, switching and all-optical functionalities [1]. Beside the above mentioned applications, optical nonlinearity properties are also found interest to be used in biomedical optics [2] and tomographic imaging techniques such as optical coherence tomography (OCT) [3] since optical imaging of biological tissues include varieties of non-invasive optical properties. Recently, PCFs [4] as nonlinear propagating media to generate super continuum (SC) light sources [5] have attracted much more for the aforementioned applications as photonic crystal fibers (PCFs) contain a wavelength-scale morphological microstructure running down their lengths which provide PCFs tunable optical properties as per design requirements. These optical properties of PCFs have attracted researchers to think an unimaginable thinking which was quite impossible using conventional optical fibers before coming this new technology. Therefore, designing nonlinear coefficients and controlling nonlinear characteristics of PCFs become an important field of research interest [6],[7].

In this paper, a highly nonlinear hexagonal PCF (HNL-HPCF) is designed to demonstrate how nonlinear coefficient γ of a HNL-PCF can be tailored by varying different parameters of PCFs namely air-hole pitch Λ, % of Ge (Germanium)-doped rate inside the core, and 3% Ge-doped core diameter d_{ge}. The finite element method (FEM) with a circular perfectly matched boundary layer (PML) [8] is used as a numerical simulation tool to demonstrate the effect of various parameters of the design HNL-HPCF on nonlinear coefficient γ.

2. EQUATIONS FOR FIBER NONLINEARITY

When dielectric media such as optical fibers are subjected to the intense electromagnetic fields, the response of the electric dipoles (separation of positive and negative charges) in the electric field becomes nonlinear. Basically, the origin of the nonlinear response is related to anharmonic motion of bound electrons under the influence of an applied field. Therefore, induced polarization P from the electric dipoles is also nonlinear and satisfied the more general relation [9]:

$$P = \varepsilon_0 \left(\chi^{(1)}.E + \chi^{(2)}.EE + \chi^{(3)}.EEE + ... \right) \quad (1)$$

where ε_0 is the vacuum permittivity and $\chi^{(i)} (i = 1, 2, ...)$ is the *i-th* order susceptibility. The dominant contribution to P is for the linear susceptibility $\chi^{(1)}$ and its effects are included through the refractive index n and the attenuation coefficient α in optical fibers. The second-order susceptibility $\chi^{(2)}$ is responsible for such nonlinear effects and the third-order susceptibility $\chi^{(3)}$ is responsible for the phenomena such as third-harmonic generation, four-wave mixing, and nonlinear refraction. Major nonlinear effect in optical fibers originates from nonlinear refraction, a phenomenon that refers to the intensity dependence of the refractive index resulting from the contribution of $\chi^{(3)}$. Therefore, the refractive index of the fiber becomes as follows

$$\tilde{n}(\omega, |E|^2) = n(\omega) + n_2 |E|^2 \quad (2)$$

where $n(\omega)$ is the linear refractive index, $|E|^2$ is the optical intensity inside the fiber, and n_2 is the

nonlinear index coefficient related to $\chi^{(3)}$ by the relation:

$$n_2 = \frac{3}{8n}\mathrm{Re}(\chi^{(3)}_{xxxx}) \quad (3)$$

where Re stands for the real part and the optical field is assumed to be linearly polarized so that only one component χ^{3}_{xxxx} of the fourth-rank tensor contributes to the refractive index. The tensorial nature of $\chi^{(3)}$ can affect the polarization properties of optical beams through nonlinear birefringence. The intensity dependence of the refractive index leads to a large number of interesting nonlinear effects namely stimulated Raman and Brillouin scattering, harmonic generation, four wave mixing, self-phase modulation (SPM); a phenomena that occurs due to the effective refractive index dependency of a wave itself, and cross-phase modulation (XPM) [9]; a phenomena that occurs due to the effective refractive index dependency of a wave itself and other propagating waves.

3. HNL-PCF DESIGN PROCEDURE

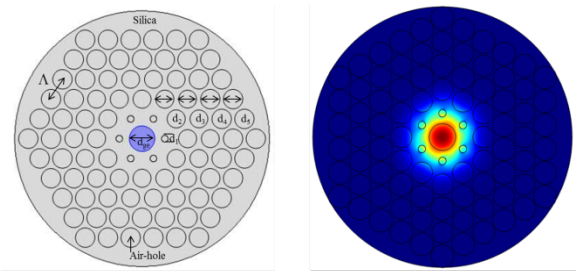

Fig. 1: (a) Ge-doped hexagonal PCF model. The diameters of air-holes of the 1st, 2nd, 3rd, 4th and 5th rings are d_1, d_2, d_3, d_4, and d_5 respectively. Λ is the pitch. (b) Mode field confinement of the HNL-HPCF**.**

Figure 1 shows the geometry and mode field confinement of the proposed HNL-HPCF with the air-hole diameters d_1, d_2, d_3, d_4, and d_5, and pitch Λ. Hexagonal lattice of air-hole structure with five rings is selected for this demonstration as it is the best arrangement to shape the dispersion curve [10]. By following simple design procedures described in Refs. [11] and [12], we successfully design this HNL-HPCF. To optimize the design parameters, a simple technique described in Ref. [12] is applied. First, a relatively higher air-filling fraction d/Λ of all air-hole dimensions is chosen in the range from 0.5 to 0.95. In particular, we have set it by observing the better field confinement to select initial guess refractive index value which is very important parameter for further processing. To evaluate more accurate effective refractive index in wider range of operating wavelength using FEM, Sellmeier equation [13] is used to determine the refractive index of fused silica. After evaluating the effective refractive index of fused silica using Sellmeier equation, the definition of relative refractive index difference Δ in Ref.[14] is used to calculate the effective index of Ge-doped core material. To damp backscattering at the boundaries of the simulation area, a circular PML is imposed inside the simulation domain since PML is the most efficient absorption boundary conditions [15] and circular design of PML is defined to improve calculations modes propagation in optical fibers [8].

4. SIMULATION RESULTS AND DISCUSSION

By modifying conventional fiber designs, values of nonlinear coefficient γ can be tailored as PCFs contain a wavelength-scale morphological microstructure running down their lengths which provide PCFs tunable light guiding properties as per design requirements. This can be done by reducing the mode field diameter of the fiber core, and using high germanium concentrations within the core which both increases the numerical aperture and enhances the intrinsic nonlinearity of the material. Both modifications act to confine light more tightly within the fiber core. As the holey cladding in PCFs makes the large difference of refractive index between the silica core and cladding, light concentrates more into a very small effective area of the core and the effective area can be defined as follows[9]:

$$A_{eff} = \frac{\left(\int_{-\infty}^{\infty}\int_{-\infty}^{\infty}|E(x,y)|^2\,dxdy\right)^2}{\int_{-\infty}^{\infty}\int_{-\infty}^{\infty}|E(x,y)|^4\,dxdy} \quad (4)$$

where E(x, y) is the electric field intensity. A small effective area provides the high optical power density necessary for nonlinear effects to be significant and the nonlinear coefficient γ is calculated by [9]:

$$\gamma = \left(\frac{2\pi}{\lambda}\right)\left(\frac{n_2}{A_{eff}}\right) \quad (5)$$

where A_{eff} is the effective area, λ is the operating wavelength and n_2 is the nonlinear refractive index. As the n_2 of pure silica is very small and nonlinear coefficient γ of pure silica is of the order of $1W^{-1}km^{-1}$ [11], we design the proposed HNL-HPCF by reducing the effective mode area and by doping higher refractive index Ge-inside the silica material to further enhance nonlinear refractive index as there are most notable physical characteristics of GeO_2; its high index of refraction and its low optical dispersion. This nonlinear refractive index n_2 [x 10^{-20} m^2/W] of higher refractive index Ge-doped composite glass fiber [14] is calculated by:

$$n_2 = 2.507 + 0.505\Delta \quad (6)$$

where Δ is the relative refractive index difference (%) defined as $\Delta = \frac{n_{core}^2 - n_{eff}^2}{2n_{core}^2} x100\%$, where n_{core} and n_{eff} denote the refractive index doped core and effective refractive index of PCF.

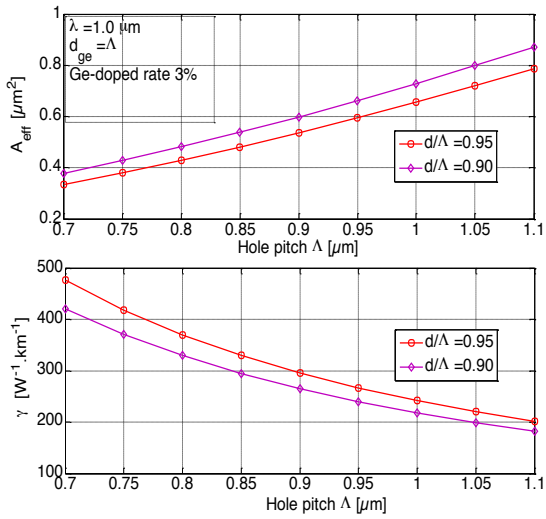

Fig. 2: Effective mode area (A_{eff}) and nonlinear coefficient (γ) as a function of hole-to-hole spacing Λ for different values of air-filling fractions d/Λ. The diameter of germanium doped core and the concentration of the core are kept at d_{ge}=Λ and 3% higher refractive index Ge, respectively.

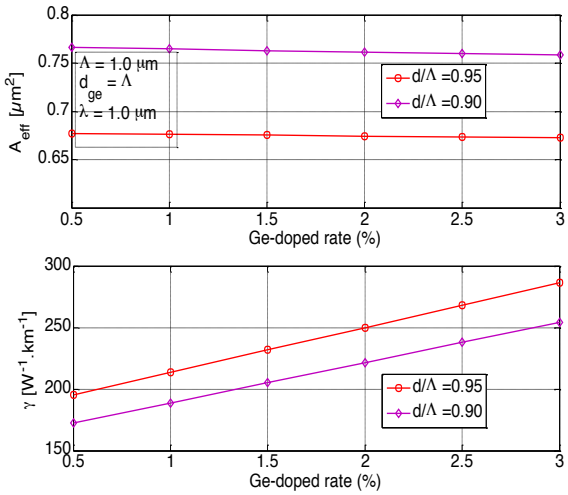

Fig. 3: Effective mode area (A_{eff}) and nonlinear coefficient (γ) as a function of Ge-doped rate for different values of air-filling fractions d/Λ. The diameter of Ge-doped core and the pitch are kept at d_{ge}=Λ and 1.0 μm, respectively.

In Fig. 2, effective mode area (A_{eff}) and nonlinear coefficient (γ) as a function of hole-to-hole spacing Λ for different values of air-filling fractions d/Λ are plotted at 1.0 μm wavelength. Fig. 2 clearly illustrates that small pitch decreases effective mode area and therefore, nonlinear coefficient increases as per eq. (5). Scaling down the structure reduces the thickness of the silica bridges between the holes. As a result, power density increases with the small core and thereby increases nonlinear coefficient γ. This figure also illustrates the effect of air-filling fraction on effective mode area and nonlinear coefficient γ. Higher air-filling fraction also decreases the effective area and thereby increases nonlinear coefficient γ. In Fig. 3, effective mode area and nonlinearity as a function of Ge-doped rate for different values of air-filling fractions d/Λ are plotted at 1.0 μm wavelength. The diameter of Ge-doped core and the concentration of the core are kept at d_{ge}=Λ and 3% higher refractive index Ge, respectively. This figure clearly indicates that more doping inside silica decreases effective mode area. Moreover, nonlinear refractive index n_2 also increases as per defined equation eq. (6). As a result, nonlinear coefficient γ increases rapidly. However, more doping inside silica creates another problem of precisely fabrication of PCFs as two materials have two different thermal expansion coefficients.

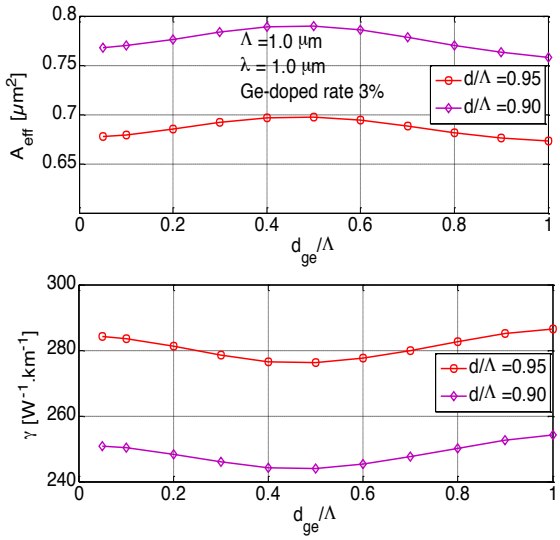

Fig. 4: Effective mode area (A_{eff}) and nonlinearity (γ) as a function of 3% Ge-doped rate core diameter d_{ge}/Λ for different values of air-filling fractions d/Λ. The pitch and the concentration of the core are kept at Λ=1.0 μm and 3% higher refractive index Ge, respectively.

Therefore, in this demonstration, doping effects are shown only for 3% higher refractive index Ge inside the silica host. This figure also shows the effect of air-filling fraction on effective area (A_{eff}) and nonlinear coefficient γ. Light concentrates more for higher air-filling fraction d/Λ. As a result, effective

mode area reduces significantly and nonlinear coefficient γ increases as per shown relationship. For constant 3% Ge-doped rate and pitch 1.0 μm, effective mode area and nonlinearity as a function of Ge-doped diameter d_{ge}/Λ for different values of air-filling fractions d/Λ are plotted in Fig. 4. Effective mode area increases with increasing d_{ge}/Λ value up to 0.5 d_{ge}/Λ. After that value of effective mode area decreases with increasing value of d_{ge}/Λ. With the fixed pitch value, small d_{ge} cannot support most of the optical power within small doping region. As a result, optical beam intensity increases within the non-doping region more. Reverse relation of nonlinear coefficient γ is found and shown in the same Fig. 4. Using higher value of d_{ge}/Λ, nonlinear coefficient γ can increase.

5. CONCLUSIONS

A HNL-HPCF is designed to demonstrate how nonlinear coefficient γ can be tailored by varying different parameters of PCFs namely air-hole pitch Λ, % of Ge-doped rate, and 3% Ge-doped rate core diameter d_{ge}. Nonlinear coefficient γ is found to be increased with decreasing the pitch value and increasing % of Ge-doped rate. With constant 3% higher refractive index Ge-doped core, effective area increases with increasing Ge-doped rate core diameter d_{ge}/Λ value up to 0.5 d_{ge}/Λ. Beyond this value, opposite characteristics of effective area is observed with increasing Ge-doped rate core diameter d_{ge}/Λ. Small pitch increases nonlinear coefficient significantly. However, too small pitch value will make PCFs very much leaky as silica bridge will reduce compared to operating wavelengths. In addition, higher % of Ge-doping inside the silica will make difficulties to fabricate PCFs precisely since two materials have two different temperature coefficients. Therefore, there should be tradeoff among all global parameters of PCFs for design of highly nonlinear PCFs.

6. FUTURE WORK

Recently, photonic crystal fibers (PCFs) based nonlinear devices are found interest for biomedical optics and optical tomographic imaging applications such as optical coherence tomography (OCT). Therefore, study is going on to retune the properties of HNL-PCFs suitable for OCT applications. Moreover, fabrication of HNL-PCFs is under consideration for doing experiments.

REFERENCES

[1]. J. Toulouse, "Optical nonlinearities in fibers: review, recent examples, and systems applications," Journal of Lightwave Technology, vol. 23, November 2005.

[2]. L. V. Wang and H. Wu, "*Biomedical optics-principles and imaging*," John Wiley & Sons, Inc., New Jersey, 2007.

[3]. M. Brezinski, "*Optical coherence tomography-principles and applications*," Elsevier Inc., San Diego, CA, 2006.

[4]. J. C. Knight, "Photonic crystal fibers," Nature, vol. 424, pp. 847-851, 2003.

[5]. J. M. Dudley and J. R. Taylor, "*Supercontinuum generation in optical fibers*," Cambridge university press, The Edinburgh building, UK, 2010.

[6]. S. M. A. Razzak, "Tailoring optical properties of index-guiding photonic crystal fibers," Doctoral Thesis, Graduate School of Engineering, University of the Ryukyus, Japan, March 2010.

[7]. S. M. A. Razzak and Y. Namihira, "Numerical design of high nonlinear coefficient of microstructure optical fibers," Optik, vol. 122, pp. 1084-1087, 2011.

[8]. H. Rogier and D. D. Zutter, "Berenger and leaky modes in optical fibers terminated with perfectly matched layer," IEEE Journal of Light wave Technology, vol. 20, pp. 1141-1148, Jul. 2002.

[9]. G. P. Agrawal, "*Nonlinear fiber optics*," Academic Press, San Diego, CA, 1995, 2nd ed.

[10]. M. A. Hossain, Y. Namihira, M. A. Islam, S. M. A. Razzak, Y. Hirako, K. Miyagi, S. F. Kaijage, H. Higa, "Tailoring supercontinuum generation using highly nonlinear photonic crystal fiber," Optics & Laser Technology, vol. 44, pp. 1889-1896, Sept. 2012.

[11]. V. Finazzi, T. M. Monro, and D. J. Richardson, "Small-core silica holey fibers: nonliearity and confinement loss trade-offs," Journal of Optical Society of America, vol. 20, pp.1427-1436, Jul. 2003.

[12]. T. L. Wu and C. H. Chao, "A novel ultra-flattened dispersion photonic crystal fiber," IEEE Photonic Technology Letter, vol. 17, pp. 67-69, Jan. 2005.

[13]. I. H. Malitson, "Interspecimen comparison of the refractive index of fused silica," Journal of Optical Society America, vol. 55, pp. 1205-1209, 1965.

[14]. K. Nakajima, M. Ohashi, "Dopant dependence of effective nonlinear refractive index in GeO_2- and F-doped core single mode fibers," IEEE Photonics Technology Letters, vol. 14, pp. 492-494, 2002.

[15]. S. Guo, F. Wu, S. Albin, H. Tai, and R. S. Rogowski, "Loss and dispersion analysis of micro structured fibers by finite difference method," Optics Express, vol. 12, pp. 3341-3352, 2004.

Proceeding of the
International Conference on Electrical, Computer and Telecommunication Engineering
01- 02 December 2012 (ICECTE2012), RUET, Rajshahi-6204, Bangladesh

ICECTE2012: PI-0070

Highly Nonlinear Hexagonal PhotonicCrystal Fiberfor Optical Coherence Tomography Light Source in Medical Imaging Applications at 1.06µm

Takuro Yasui[1], Yoshinori Namihira[2],Md. AnwarHossain[2]
[1]Dept. of Electrical and Electronics Engineering, University of the Ryukyus
[2]Graduate School of Engineering and Science, University of the Ryukyus
E-mail: y_takuro222@yahoo.co.jp,namihira@eee.u-ryukyu.ac.jp

ABSTRACT
In this paper, ahighly nonlinear hexagonal photonic crystal fiber (HNL-HPCF) is proposed to design a light source at 1.06µmfor optical coherence tomography applications suitable fordermatology and digestive organs. Nonlinearcoefficient γ is increased to a value as large as 93.3 $W^{-1}km^{-1}$ which makes it more efficient to generate supercontinuum at 1.06µm.Using finite difference method,the properties of the HNL-HPCF are simulated and slit step Fourier method is used to describe the spectral properties of the HNL-HPCF by propagating the picosecond optical pulse through it.

KEY WORDS: Photonic crystal fiber (PCF),optical coherence tomography(OCT), finite difference method (FDM),super continuum (SC).

1. INTRODUCTION

Optical coherence tomography (OCT) is a modern new imaging technique that allows noninvasive cross-sectional imaging of biological tissue by using the light sources withshort coherence length [1].The performance of OCT systems depends on longitudinal and transverse resolution, measurement speed and the center wavelength of light source [2].The main light source for OCT systemis superluminescent diodes (SLDs), butthese sourceshave a limited optical bandwidth and arerestricted to wavelength ranges. SLDs have 10-15µm longitudinal resolution which is insufficient for identifying individual cell or assessing sub cellular structures of biological tissues [3].Therefore,photonic crystal fiber (PCF) based surpercontinuum (SC) light sources are generated and used as a broadband light sources for OCT systems[3, 4].The center wavelength adopted for different biomedical tissues is different.In the case ofbiomedical tissues such as dermatology and digestive organs,the 1.3µm band can give imaging information with twice as high penetrating depth range as that at the 0.8µm band.But the power at 1.3 µm is attenuated by the scattering at biomedical tissues. At wavelength of approximately 1.06µm, itis possible to eliminate the effect of the dispersion in the depth direction due to water absorption in tissues because the zero-dispersion wavelength of biomedical tissues is approximately1.06µm[4].Therefore,a 1.06 µm center wavelength is adopted as themain wavelength of OCT system suitable for dermatology and digestive organs.

In this paper, ahighly nonlinear hexagonal PCF (HNL-HPCF) is designed to generate SC light source to obtain high resolution OCT system fordermatology and digestive organs at 1.06µm center wavelengths. Picosecond optical pulse is used to propagate through the HNL-HPCF and output optical pulse is analyzed by split step Fourier method to obtain spectral properties. Simulation results show that 410 m of the proposed HNL-HPCF can produce broadband 114 nm spectrum at 3 dB spectrum bandwidth or a full width at half maximum (FWHM). Therefore, improved OCT resolution is reported in this paper using obtained spectral properties of the proposed HNL-HPCF.

2. EQUATIONS FOR PCF DESIGN

The finite difference method (FDM) with an anisotropic perfectly matched layer (PML) is used to simulate various properties of PCFs. Once the electronic field *E(x,y)* and the model effective index $n_{eff}$are obtained by solving an eigenvalue problem drawn from the Maxwell's equation using the FDM, the chromatic dispersion parameter *D(λ)*,effective area (A_{eff}), and confinement loss (L_c)can be also obtainedas per following equations.

2.1CHROMATIC DISPERSION

Chromatic dispersion is the spreading out of light pulses as they travel along fiber. It occurs because the speed of light through a fiber depends on its wavelength. The total chromatic dispersion consists of material dispersion and waveguide dispersion. The chromatic dispersion $D(\lambda)$ of a PCF can be analyzed from the following equation[5, 6]:

$$D(\lambda) = -\frac{\lambda}{c}\frac{d^2 \operatorname{Re}[n_{eff}]}{d\lambda^2} \qquad (1)$$

where Re[n_{eff}] is the real part of n_{eff} , λ is the wavelength, c is the velocity of light in vacuum.

2.2 EFFECTIVE AREA

Effective areaA_{eff} is a parameter that represents the distribution of the intensity of light across the sectional areaof an optical fiber. This is very important thing to evaluate non-linearity of an optical fiber. Increasing air hole size, the mode becomes more confined and thus effective area is reduced. The effective area $A_{eff}$is defined as follows [5,6]:

$$A_{eff} = \frac{(\iint_{-\infty}^{\infty} |\mathrm{E}(x,y)|^2 dxdy)^2}{\iint_{-\infty}^{\infty} |\mathrm{E}(x,y)|^4 dxdy} \qquad (2)$$

2.3 NONLINEAR COEFFICIENT

Polarization will not be proportional to electric field of light as intensity of light get strong. A PCFexhibits high non-linearity when there is a high relative refractive index difference between the fiber core and the holey cladding. The nonlinearity coefficient$\gamma$is calculated with following equation [6]:

$$\gamma = (\frac{2\pi}{\lambda})(\frac{n_2}{A_{eff}}) \qquad (3)$$

wheren_2 is the nonlinear refractive index and n_2/A_{eff} is a nonlinear constant. The numerical value of nonlinear refractive index n_2 of pure silica is reported as 2.1×10^{-20} m^2/W[3].

2.4 CONFINEMENT LOSS

Leakages of light through PCFs are higher with compared to the conventional fibers since the core and the cladding of PCFs are on the same material. Light signal will be weakened as it is propagated through the PCFs.Confinement lossL_c represents numerically the leakage mode and can beobtained from imaginary part of n_{eff} as follows[6]:

$$L_c = 8.686\times k_0 \,\mathrm{Im}[n_{eff}] \qquad (4)$$

where $k_0 = 2\pi/\lambda$ is the free space wave number.

3. DESIGN PROCEDURES OF PCF

Fig.1 shows the geometry of the proposed HNL-HPCFwith the optimized air hole diameters d_1, d_2, d_3, d_4, d_5 and pitch Λ and mode field confinement of the HNL-HPCF is shown in Fig.2.Pure silica is used to design the proposed HNL-HPCF as silica material has outstanding optical properties over a wide range of operating wavelength.Hexagonal lattice of air-holes are selected as they are the best arrangement for fine tuning the dispersion curves and for PCF fabrication. Basically,first three air-holes parameters d_1, d_2, d_3 have been used to shape the desirable dispersion curve andother two outer air-hole parameters d_4, d_5 have been used to control confinement loss and single mode operation. To increase the nonlinearity, pitch Λ is reduced significantly at 0.7 µm.Optimum values of the other parameters of the HNL-HPCFare found as d_1=0.27 µm, d_2=0.65µm, d_3=0.17µm, d_4=0.68µm, d_5=0.68µm. Single mode operation is maintained using the above mentioned dimension as per definition of V parameter[7].

$$V_{eff} = k_0 \Lambda F^{1/2} (n_{eff}^2 - n_a^2)^{1/2} \qquad (5)$$

where$F$ is the average air filling fraction, $n_{eff}$is the effective refractive index, and n_a is the refractive index of the air.V parameter is obtained as V_{eff} = 1.37 which is less than that of 2.40. Therefore, the proposed HNL-HPCFis single mode PCF.

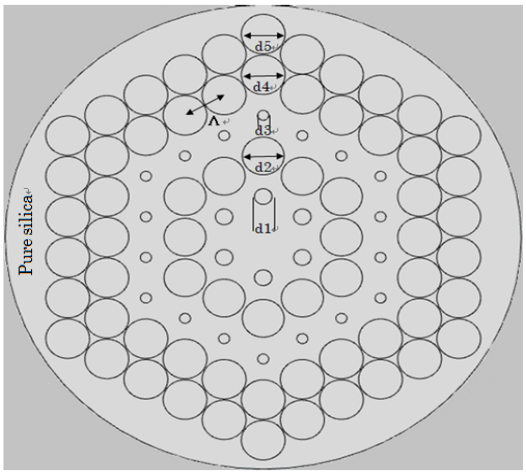

Fig.1:The proposed HNL-HPCF. The diameters of air holes of 1st, 2nd, 3rd, 4th and 5th rings are d_1, d_2, d_3, d_4, and $d_5$respectively. Λ is the pitch.

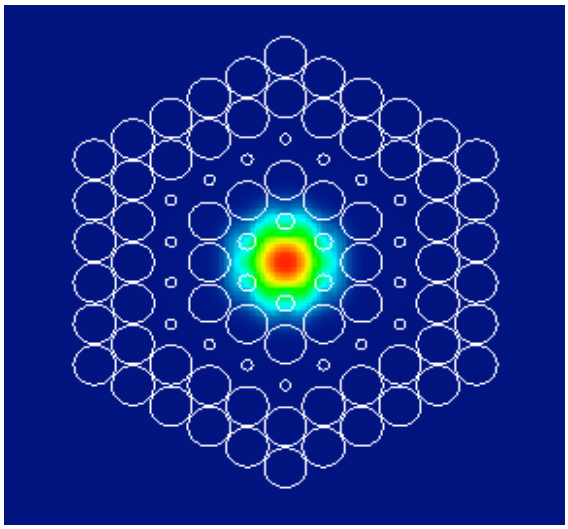

Fig.2: Mode Field Confinement of theHNL-HPCF

4. SIMULATION RESULTS

Simulation results using the FDM are illustrated in Figs.3,4,5 and 6 using the optimized value of all global parameters at d_1=0.27 µm, d_2=0.65µm, d_3=0.17µm, d_4=0.68µm, d_5=0.68µm and Λ=0.7 µm. Fig.3 shows the wavelength response of chromatic dispersion. Parabolic curve having near zero dispersion at 1.06 µm in normal dispersion region is engineered as this type dispersion curve in normal dispersion region is reported for having broad SC spectra. The value of chromatic dispersion at 1.06 µm is found about-0.13ps/(nm·km).

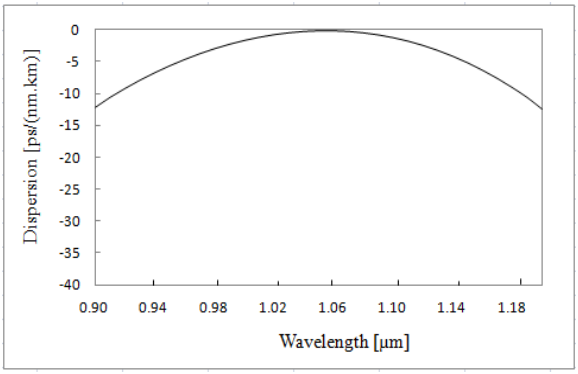

Fig.3:Wavelength response of chromatic dispersion of the proposed HNL-HPCF with optimized parameters at d_1=0.27 µm, d_2=0.65µm, d_3=0.17µm, d_4=0.68µm, d_5=0.68µm, and Λ=0.70 µm.

In Fig.4, effective area A_{eff} against wavelength is plotted.Unusual characteristic of effective area$A_{eff}$is found and shown in this fig.4. The value of effective area$A_{eff}$is about 1.34 µm^2 at 1.06µm.

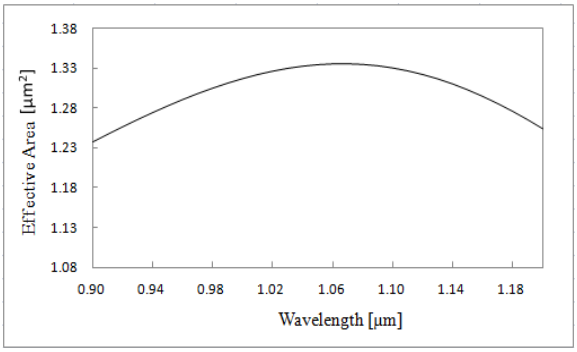

Fig.4: Wavelength response of effective area A_{eff} of the proposed HNL-HPCF with optimized parameters.

As nonlinear coefficient γ is inversely proportional to effective areaA_{eff}, opposite characteristic of the nonlinear coefficient γ is investigated and shown in Fig.5.Nonlinear coefficient γ is found about 93.3W^{-1}km^{-1}at 1.06 µm which makes it more efficient to generate desirable SC spectra.

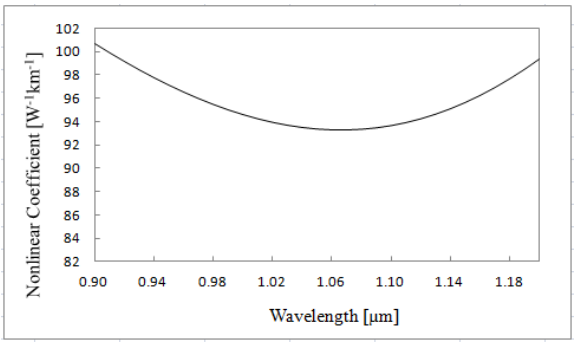

Fig.5:Wavelength response of nonlinear coefficient γof the proposed HNL-HPCF with optimized parameters.

Finally,the confinement losses in the wavelength range from 0.90 to 1.20 µm are plotted in Fig.6 in logarithmic scale with respect to wavelength in micrometer.At center wavelength 1.06 µm, this loss is found about 0.00277dB/m.

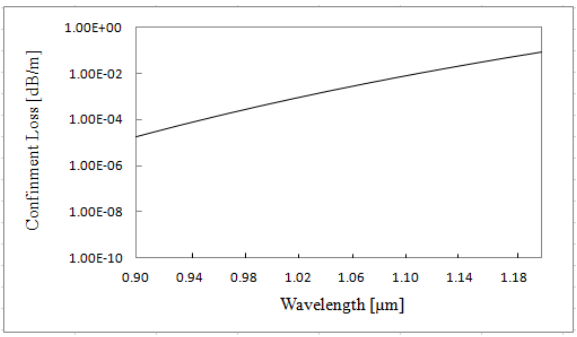

Fig.6:Wavelength response of confinement loss L_c of the proposed HNL-HPCF with optimized parameters.

5. SUPERCONTINUUM GENERATION

The generation of SC spectra using the proposed HNL-HPCF is numerically evaluated here by solving the nonlinear Schrodinger equation (NLSE) [8,9]:

$$\frac{\partial A}{\partial z}+\frac{\alpha}{2}A+\frac{i}{2}\beta_2\frac{\partial^2}{\partial T^2}-\frac{1}{6}\beta_3\frac{\partial^3}{\partial T^3} \qquad (6)$$
$$=i\gamma[|A|^2 A+i\frac{\lambda c}{2\pi c}\frac{\partial}{\partial T}(|A|^2 A)-T_R A\frac{\partial |A|^2}{\partial T}$$

where A is the complex amplitude of the optical field, α is the attenuation coefficient of the fiber, β_i (i =2 to 3) is the *i-th* order of the Taylor series expansion of the propagation constant around the carrier frequency, γ is the nonlinear coefficient, λ_c is the center wavelength, and T_R is the Raman scattering parameter. This NLSE is solved using the split-step Fourier method [8,9].We consider the

propagation of a sech^2 input pulse with a full width at half maximum (FWHM), T_{FWHM} of 2.5 ps[9]. The

fiber parameters used inthe calculation are γ = 145.2 W^{-1}km^{-1}, T_R = 3.0 fs, β_2 = 0.0613[ps^2/km], and β_3 = 0.00013[ps^3/km] and center wavelength λ_c = 1.06 µm. Fig.7 shows the spectral properties of the proposed HNL-HPCF obtained by the split-step Fourier method[8,9] where the fiber length is 410 m and the peak optical power of the incident pulse is 10 W. Spectral bandwidth $\Delta\lambda$ is found about114 nm at a FWHM. The coherent length l_c is very important in estimating the resolution in the depth direction in OCT. The coherent length l_c and spatial resolution l_r in biomedical tissues can be obtained by the following equations [4]:

$$l_c=\frac{2\ln 2}{\pi}\frac{\lambda c^2}{\Delta\lambda} \qquad (7)$$

$$l_r=\frac{l_c}{n_{tissue}} \qquad (8)$$

Heren_{tissue} is the refractive index of the biomedical tissues. It is found that l_c is 4.33µm at λ_c = 1.06 µm. Therefore, the resolution in the depth direction for OCT is obtained about3.1µm assuming a typical value of n_{tissue} of 1.41[4].

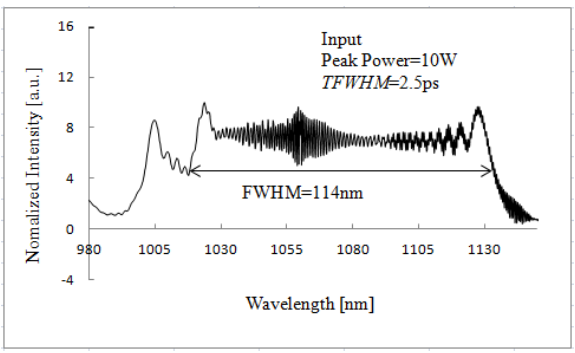

Fig. 7:Evolution of SC spectrum in the proposed HNL-HPCF at 1.06µm center wavelength.

6. CONCLUSION

A HNL-HPCF is designed at1.06µm center wavelength as this wavelength is used in OCT imaging applications for dermatology and digestive organs.The proposedHNL-HPCF has a nonlinear coefficient of γ = 93.25 W^{-1}km^{-1}at 1.06 µm. This proposed HNL-HPCF exhibits singlemode operation and around114 nm SC spectrum bandwidth is obtained at a FWHM. The coherent length l_c of the generated light source is 4.33µm at 1.06 µm wavelength.Therefore, the spatial resolution in the depth direction for OCT is found to be approximately 3.1µm. The proposed PCF with the above mentioned novel properties is expected to be applied to high-resolution OCT systems for dermatology and digestive organs.

7. FUTURE WORK

Optical coherence tomography (OCT)is intensively using for medical imaging techniques. Therefore, research is ongoing to design and fabricate HNL-PCFs for OCT system suitable fordental and eye operations as well.

REFERENCES

[1]. M. Brezinski, "*Optical Coherence Tomography Principles and Applications*", Elsevier Inc., San Diego, CA, 2006.

[2]. Y. Namihira, M. A. Hossain, T. Koga, M.A. Islam, S.M.A. Razzak, S.F. Kaijage, Y. Hirako and H. Higa, "Design of highly nonlinear dispersion flattened hexagonal Photonic crystal fibers for dental optical coherence tomography applications", *Optical Review*, vol. 19, pp.1-4, 2012.

[3]. M.A. Hossain, Y. Namihira, M.A. Islam, S.M.A. Razzack, Y. Hirako, K. Miyagi, S.F. Kaijage, H.Higa, "Tailoring surpercontinuum generation using highly nonlinear photonic crystal fiber"*Optics and Laser Technology*, vol. 44,pp.1889-1896, 2012.

[4]. T.Kinjo, Y.Namihira, K.Arakaki, T.Koga, S.F.Kaijage, S.M.A.Razzak, F.Begum, S.Nozaki, and H.Higa,"Design of Highly Nonlinear Dispersion-Flattened Square Photonic Crystal Fiber for Medical Applications"*Optical Review*, vol. 17, pp.61-65, 2010.

[5]. K. Kaneshima, Y. Namihira, N. Zou, H. Higa, and Y. Nagata,"Numerical investigation of octagonal photonic crystal fibers with strong confinement field",*IEICE Trans. Electron*. E89-C, p.830-837, 2006.

[6]. Y. Namihira, J. Liu, T. Koga, F. Begum, M. A. Hossain, N. Zou, S. F. Kaijage, Y. Hiroko, H.

Higa, and M. A. Islam,"Design of Highly Nonlinear Octagonal Photonic Crystal Fiber with Near-Zero Flattened Dispersion at 1.31 µm Waveband",*Optical Review,* vol. 18, pp. 436-440, 2011.

[7]. S.M.A Razzak, Y Namihira,"Proposal for Highly Nonlinear Dispersion-Flattened Octagonal Photonic Crystal Fibers",*IEEE Photonics Technology Letters,* vol. 20, pp. 249-251, 2008.

[8]. G. P. Agrawal, "*Nonlinear Fiber Optics*",*Academic Press, San Diego, CA*, 2nd ed, 1995.

[9]. K. Saito and M. Koshiba,"Highly nonlinear dispersion-flattenedphotonic crystal fibers for supercontinuum generationin a telecommunication window",*Optics Express*, vol.12,pp. 2027-2032, 2004.

Proceeding of the
International Conference on Electrical, Computer and Telecommunication Engineering
01- 02 December 2012 (ICECTE2012), RUET, Rajshahi-6204, Bangladesh

ICECTE2012: PI-0071

Design, Simulation & Optimization of 2D Photonic Crystal Power Splitter

**Rajib Ahmed[1], Md. Masruf Khan[2], Rifat Ahmmed[3], Abdul Ahad[4]*

[1]MAsters on Photonic NETworks engineering, Scuola Superiore Sant'Anna, Pisa, Italy
[2]School of CSE, University of Information Technology & Sciences, Dhaka, Bangladesh
[3]Dept. of ETE, Rajshahi University of Engineering & Technology, Rajshahi-6204, Bangladesh
[4]Department of Physics, Bangladesh University of Engineering and Technology, Dhaka-1000
*rajib.ahmed.apece@gmail.com[1], masrufsamgroup11@gmail.com[2], rifat.ete07@gmail.com[3], *abdulahadbbaria@hotmail.com[4]*

ABSTRACT
A very compact (80-100 μm^2) integrated power splitting devices with two output (1x2), four output (1x4) and six output (1x6) channel has been designed, simulated and optimized for Telecommunication purpose with T-Junction, Y-Junction, PC line defect waveguides integrated with multimode interference block (PCLD-MMI) and multiple line defect PC waveguides (MLDPCW) configurations. The optical modeling of these proposed structures were investigated by finite difference time domain (FDTD) simulation. With optimization of the parameters (Hole Radius, R=0.128μm, Input Diameter, D=1.02 μm, Input wavelength, λ= 1.55 μm, Substrate Reflective Index, n_{sub}= Si (1.52), Photonic Crystal Material, n_{pcs}= InAs (3.45), and Rectangular crystal structure), 1x2 for Y-Junction (100%), 1x4 for T-Junction (92.8%) and 1x6 configuration for MLDPCW (81%) show maximum power transmission.

KEY WORDS: Power Splitter, Photonic Crystals, Finite Differential Time Domain, PCLDMMI, MLDPCW.

1. INTRODUCTION

In the recent years, a lot of research has been focused on developing micro and nano photonic devices by using Photonic Crystals (PCs). Photonic Crystals (PCs) are artificial structure in which the periodic variation of dielectric constant is used to control the flow of light. PCs may be 1D, 2D & 3D crystal structure. Unlike electronic crystals (which are natural structure) that control the flow of electron by periodic variation of electron potential and follow Schrödinger equation, PCs follow Maxwell's equation [1].

Now a day, from the idea of controlling light by means of Photonic Crystal (PC) has led to many proposals and implementations for novel devices including different types of power splitters has generated wide interests in the communication field. This is possible only for periodic variation of the refractive index causes photonic band gap and artificially introduced defects to divide the input power equally into the output channels without significant reflection or radiation losses with compact in size. The traditional limitation on power splitter based optical fiber on is on transmission loss can be minimize by photonic splitter as optimal one [2]. It has many advantages such as low loss, good uniformity, insensitive to operation wavelength, polarization, large bandwidth, simple fabrication technique, larger tolerance, minimized structure, temperature and other environmental factors.

Researchers have theoretically investigated photonic crystal with array of dielectric rods in air. Based on this concept the T-junction, Y-junction and MMI effects have already been extensively studied [3, 4]. Unfortunately, the 'rod in air' approach does not provide sufficient vertical confinement and is difficult to implement for most practically useful device implementations in the optical regime. A slab waveguide structure consists of air holes etched into a dielectric medium such as silicon, GaAs/AlGaAs hetero structure or a semiconductor membrane which remedies this problem and allows waveguides with tolerable losses [5, 6]. This multimode leads to mode-mixing problem at intersection of the PCW which creates a mismatch between input and output fields and introduces large reflections at the interface.

In this paper, new power splitting techniques using 2-D and 2-D slab PC line defect waveguides are investigated. In order to achieve this, initially we investigated (a) T-junction structure for 1×2 and 1×4 applications. Then, (b) Y-junction with 1x2, 1x4, 1x6 structures are also invested. In this scheme, we have improved the power transmission and output spectrum in 1×2 application which is better than published result where as in 1×4 and 1x6 applications the power transmission and output spectrum is not good enough for practical application point of view. So, in order to improve the power

transmission and output spectrum we have investigated two new designs where one is (c) PC line defect waveguides are integrated with a multimode interference (MMI) block and multiple line defect PC waveguides (MLPCW) for 1x2,1×4,1x6 power splitting applications. In MLPCW scheme, we have investigated the three versions which are a combination of three, five and seven line defect waveguides. These two structures are more compact than the previous design but relatively broad spectrum. Among those structures Y-junction based 1×2 power splitter was found best with 100% transmission and equally splitting. Optical modeling is used to demonstrate that the power is equally divided at each output channel with a relatively broad spectrum. Moreover, FDTD simulation method is used to overcome some of the difficulties of previous works (i.e. mode mismatch, bandwidth and bending region transmission) and challenges. The structure can be applied to communication systems and also be integrated with other PC based devices.

2. LAYOUT DESIGN AND SIMULATION

We have taken SiO_2 as a wafer material (reflective index 1.447) with dimension- length- 30μm and width- 48μm, Gaussian modulated continuous wave as an input signal with wavelength 1.55 μm. Both transverse and injection type of the input is Modal. The input signal used in the simulation expressed as:

$$E_y^{inc}(x, z_{inc}) = AT(t)\, F(x, z_{inc}) \sin(wt + \theta_i) \qquad (1)$$

Where, A is the field amplitude and F (x, z_{inc}) is the transverse field location at the incident field location z_{inc}. The initial offset θ_i is the phase difference between points in the incidence plane. This offset can be adjusted to define the direction of the incident field [1]. The planar PC structure is simulated on a silicon-on-insulator substrate with a Si slab of thickness t = 220nm separated from the Si substrate by 1μm silica layer. The holes are placed in a triangular lattice and have a diameter d = 0.588Λ, where 'Λ' is the lattice constant.

The propagation of light in the waveguides is simulated by 2D Finite-difference time-domain (FDTD) method using a standard simulator. FDTD is a time-domain numerical method used for modeling the propagation of electromagnetic waves in optical media, which is based on the discretization of Maxwell's equations in differential form in free space. Time domain methods have been found to be very accurate in simulating the propagation dynamics of signals in periodic dielectric media [7].We simulate for TE mode, actual Mesh used- 0.075μm (delta X) X 0.075μm (delta Z) with number of mesh cells 400 (X) and 650 (Z). For result finalization the simulation has been done for 4000 time steps. The Anisotropic Perfectly Matched Layer (APML) boundary condition is used. PC line defect waveguides (LDWs) integrated with MMI block for power splitting has potential to transmit power from input to the output without any changes of the PC dielectric hole size. It has large optical bandwidth as compare to existing power splitter. In proposed design there are no 120^0 junctions or 60^0 bends. As a consequence the single mode operation will not be suffered. The entire structure will be formed by triangular lattice of dielectric holes so the vertical confinement will be better as compared to the triangular lattice of dielectric rod structure. In account of having all this advantages the entire structure can be considered as a 2-D slab PC configuration. Therefore, the application of power splitter by using PCLDWs integrated with MMI is attractive.

It is known that the typical Y-junction structure has poor transmission without any structural tuning at the bends and input and output ports. In addition to that the performance of the Y-junction can be improved by tuning and displacing the holes at 120^0 junction and also by bending the output ports but still difficulties exist which cannot be easily addressed for practical application. These difficulties arise from the mode-mismatch at 120^0 junction and the bending loss from the output ports. It is conspicuous from a number of researcher's work that Y-junction based power splitter itself identifies some problems in its own design. Here a unique design is proposed which will not be having any disturbances like 120^0 junction and bending loss. 2-D PC multiple line defect waveguides based power splitter is that proposed design which will be capable of addressing the issues of Y-junction based power splitter as mention before. PC multiple line defect waveguides power splitter minimizes the multimode mode problem occurred in the existing design. Therefore, this proposed scheme transmits more power as compared to the existing design. So, PC multiple line defect waveguides based power splitter should be investigated. The real motivation behind using PC waveguides over conventional dielectric waveguides for optical interconnects includes better routing capabilities with lower transmission, bending loss, coupling loss, reduced cross talk and larger design flexibility provided with the PC environment, monolithic integration with other on-chip photonic component like a PC based laser or photo-detector. A schematic representation of an optical signal distribution layer using PC based waveguides (Line defect waveguides) integrated with MMI block is shown in Figure 1. The architecture of output optical signal

consists of four PC line defect waveguides (LDWs) which is integrated with MMI block. Optical signal is equally divided at the each output channel.

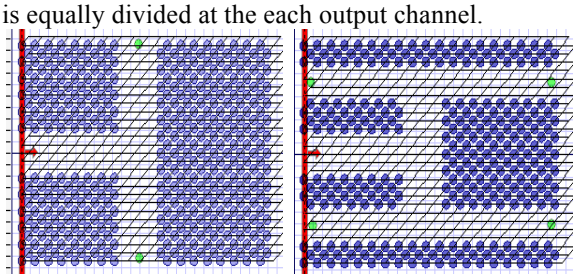

(A1) (A2)

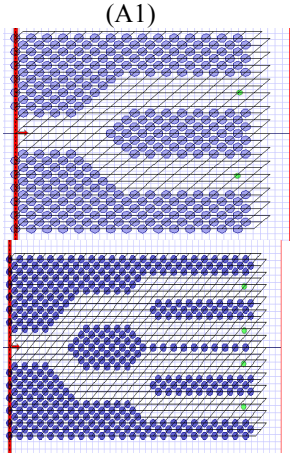

(B1) (B2)

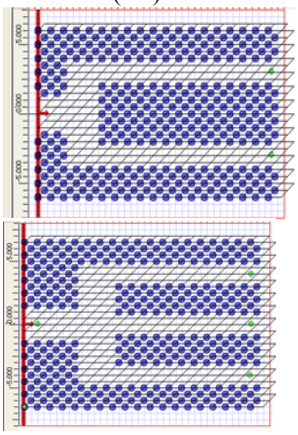

(C1) (C2)

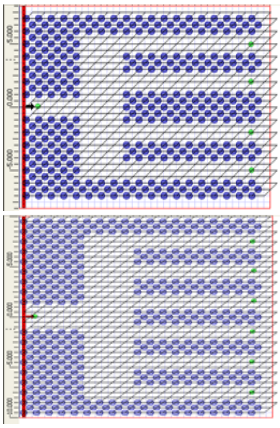

(C3) (C4)

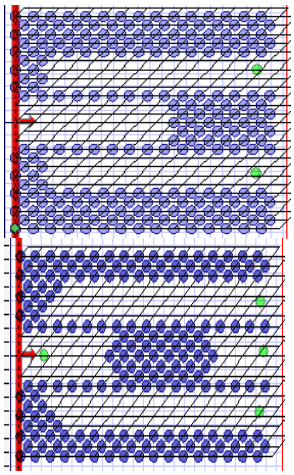

(D1) (D2)

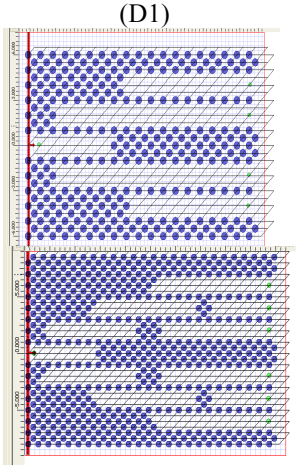

(D3) (D4)

Figure 1: Layout design of 1x2 T-Junction (A1), 1x4 T-Junction (A2), 1x2 Y-Junction (B1), 1x4 Y-Junction (B2), 1x2 PCLD-MMI (C1), 1x3 PCLD-MMI (C2), 1x4 PCLD-MMI (C3), 1x6 PCLD-MMI (C4), 1x2 MLDPCW (D1), 1x3 MLDPCW (D2), 1x4 MLDPCW (D3), 1x6 MLDPCW (D4).

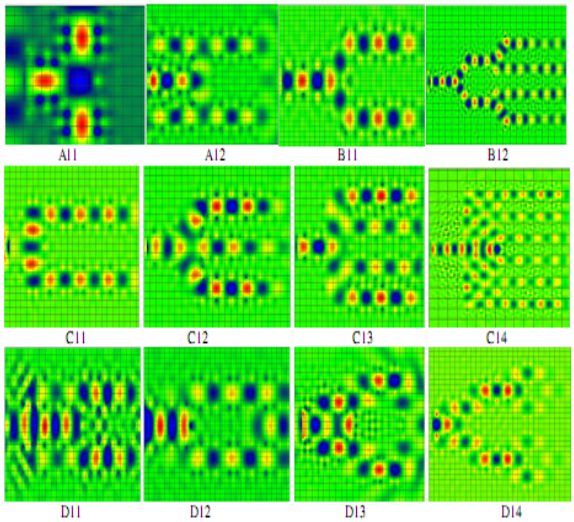

Figure 2: Simulation result of 1x2 T-Junction (A11), 1x4 T-Junction (A12), 1x2 Y-Junction (B11), 1x4 Y-Junction (B12), 1x2 PCLD-MMI (C11), 1x3 PCLD-MMI (C12), 1x4 PCLD-MMI (C13), 1x6 PCLD-MMI (C14), 1x2 MLDPCW (D11), 1x3 MLDPCW (D12), 1x4 MLDPCW (D13), 1x6 MLDPCW (D14).

3. RESULTS ANALYSIS

We try to optimization of the parameters of the splitter. For the variation of the input port diameter (0.15-1.4 μm), optimize value found for 1.02 μm (keeping fixed the Lattice constant, Λ =0.435μm and Hole Radius, R= 0.128 μm). With optimize diameter (D =1.02 μm), the hole radius of the photonic crystal (R) are varied (0.1- 0.15) to get the optimize value of hole radius, R = 0.128 μm (keeping fixed the Lattice constant, Λ =0.435μm). Similarly, from the variation of the input wavelength, λ (1.5-1.6 μm) the optimize value found λ_1 =1.55 μm (TE Mode) and λ_2 =1.6μm (TM Mode). Moreover, we take Air (n=1), Glass /Si (n=1.52), GaAs (3.40), InAs(3.45), InGaAs(3.72) as a wafer and Photonic Crystal (PC) material and found Si as wafer and GaAs(3.40) as a optimize PC materials. Similarly, with Rectangular, Hexagonal, Face-centered cubic (FCC) and Body-centered cubic (BCC), optimized structure is found for Rectangular Crystal. The decision of optimization is based maximum power transmission at the output ports.

We have investigated the transmission of the structures using 2D FDTD method with perfectly matched layer (PML) boundary condition. The output transmitted power of 1x2 T-Junction is monitored at two points on the 90^0 bend output waveguides; one at the output of channel 1 (CH1) and the other at the output of channel 2 (CH2) is indicated in Figure 1. The output spectrum indicates that a maximum of 46.4% of the input power through each channel and total 92.8% of input power is transmitted. Similarly, total 83% of input power is transmitted for 1x4 T-Junction. In this 1x2case, output ports are 90^0 bands to the inputs for single time but two times for 1x4 T-junctions and thus power reduces to 83% from 92.8%.

The improved structure of T-junction is Y-junction in which total 100% and 86% are transmitted for 1x2 and 1x4 Y-junctions splitter due to lower bends (60^0) of output ports. The structure of this Y-junction is formed by the intersection of three PCW at 120^0. The output channels have an additional 60^0 bend which is parallel to the input channel as shown in figure 1. Due to 120^0 junction and 60^0 bend; single mode operation might suffer which can cause the reflection and large transmission loss. To overcome these difficulties the junction and bend must be carefully designed. The better transmission can be achieved by the modified Y branch structure in which The 60^0 bends are modified by displacing or removing one or more holes and changing their shapes in the bend.

The PC-based Y-junction power splitter has problems with mode mismatch and bending loss which excites the higher order modes. So in order to obtain an acceptable output transmission, the bending region needs to be carefully optimized which adds difficulties in design and fabrication. To minimize mode mismatch and bending loss, many researchers have investigated theoretically on array of dielectric rods in air.

To avoid some of the above difficulties and challenges, in this thesis we have investigated a novel idea for a 1×4 power splitting technique which is a 2D photonic crystal triangular lattice of dielectric air holes line defect waveguides integrated with an MMI block. Moreover, the proposed power splitter structure overcomes the mode matching phenomena, poor transmittance of Y-junction structure and the limited bandwidth and is easier to fabricate as compared to a Y-junction structure and MMI effect dielectric rod structure. The structure can be applied to optical communication systems and also be integrated with other PC-based devices.

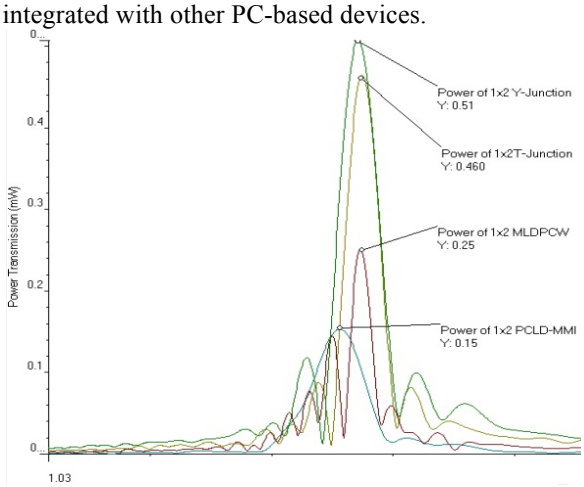

Figure 3: Power transmission mw, (Y-axis) Vs Wavelength μm, (X-axis) for 1x2 photonic splitters.

Table1: Comparison of Different 1x2 Power Splitters

Parameter	T-Junction Splitter	Y-Junction Splitter	PCLD-MMI Splitter	MLDPCW Splitter
Configuration	Holes with Rectangular lattice	Same	Same	Same
Parameters: Air fill faction = d/Λ	0.588	Same	Same	Same
Max. Power Transmission at Each Ports (%)	61	58	39	53
Equal Splitting	Yes	Yes	Yes	Yes
Device Size (Length x Width)	10 μm x 8 μm	10 μm x 8 μm	10 μm x 8 μm	10 μm x 8 μm
Spectrum	(1.48 μm-1.80μm) =0.42μm	(1.48μm-1.75μm) =0.27 μm	(1.45 μm-1.60μm) =0.15 μm	(1.47 μm-1.58 μm)=0.11 μm

Table2: Comparison of Different 1x4 Power Splitters

Parameter	T-Junction Splitter	Y-Junction Splitter	PCLD-MMI Splitter	MLDPCW Splitter
Configuration	Holes with Rectangular lattice	Same	Same	Same
Max. Power Transmission at Each Ports (%)	42(Port1&4) & 32(Port2&3)	38 Port1&4) & 30(Port2&3)	50(Port1&4) & 31(Port2&3)	38 Port1&4) & 56(Port2&3)
Equal Splitting	Yes Pair wize	Yes Pair wize	Yes Pair wize	Yes Pair wize
Device Size	10 µm x 8 µm	12 µm x 8 µm	10 µm x 8 µm	10 µm x 8 µm
Spectrum	(1.45 µm-1.56 µm)=0.11 µm	(1.47 µm-1.56 µm)=0.09 µm	(1.48 µm-1.58 µm)=0.10µm	(1.47 µm-1.55 µm)=0.08 µm

Table3**:** Comparison of various 1x6 Power Splitters

Parameter	T-Junction Splitter	Y-Junction Splitter	PCLD-MMI Splitter	MLDPCW Splitter
Configuration	Holes with Rectangular lattice	Same	Same	Same
Max. Power Transmission at Each Output Ports (%)	-	-	18(Port 1&6) 22(Port 2&5) 52(Port 3&4)	24(Port 1&6) 42(Port 2&5) 20(Port 3&4)
Equal Splitting	-	-	Yes Pair wize	Yes Pair wize
Device Size	-	-	10 µm x10 µm	10 µm x 10 µm
Spectrum	-	-	(1.48 µm-1.56µm)= 0.08 µm	(1.47 µm-1.56 µm) = 0.09 µm

4. CONCLUSIONS

T-Junction, Y-Junction, PCLD-MMI Splitters and PCLDW splitters in different lattice configurations (like rectangular, hexagonal, FCC and BCC structures) with TE and TM mode have been designed, simulated with FDTD method. Performance of each structure was characterized and compared with each other by maximum power transmission. It has shown the different types splitter have relatively higher transmission efficiency in contrast with others. Finally, with optimize parameters the output power of different and their comparison with different configuration have been done. Based on these structures optimization higher efficiency power splitters were designed which can be used in networking, modulation, transmission, switching etc. applications.

REFERENCES

[1]. J. D. Joanno poulos, R. D. Meade, and J. N. Winn, "Photonic Crystals: Molding the Flow of Light" , Princeton University Press, (1999)

[2]. Rajat Dey, "Optical Power Splitting Techniques Using Photonic Crystal Line Defect Waveguides" , Ph.D Thesis, The University of Western Ontario, (2011)

[3]. T. Yu, H. Zhou, J. Yang, X. Jiang, and M. Wang, " Ultra compact multi-way beam splitters using multiple coupled photonic crystal waveguides," *J.Phys.D:Appl. Phys*.vol.41, pp. 1-5, (2008).

[4]. S. Fan, S.G. Johnson, J.D. Joannopoulos, C. Manolatou, and H. A. Haus, "Waveguide branches in photonic crystals", *J. Opt. Soc. Am. B*. vol 18, pp 162-165, (2001).

[5]. E. Chowm S. Y. Lin, S. G. Johnson, P. R. Villeneuve, "Three-dimensional control of light in a two-dimensional photonic crystal slab," *Nature*, vol. 407, pp 983, (2000).

[6]. M.Notomi, A.Shinya, K.Yamada, J.Takahashi, "Single mode transmission within photonic bandgap of width-varied single-line-defect photonic crystal waveguides on SOI substrates," *Electron. Lett*. vol.37, pp 293, 2001.

[7]. A. Taflove, "Computational Electrodynamics: The Finite-Difference Time-Domain Method", Artech House, Boston, MA (1995).

Proceeding of the
International Conference on Electrical, Computer and Telecommunication Engineering
01- 02 December 2012 (ICECTE2012), RUET, Rajshahi-6204, Bangladesh

ICECTE2012: PI-0072

Dispersion Management in Photonic Crystal Fiber

R. R. Mahmud[1] and S. M. A. Razzak[2]
[1]Assistant Professor, Dept. of EEE, Ahsanullah University of Science and Technology (AUST), Bangladesh
[2]Associate Professor, Dept. of EEE, Rajshahi University of Engineering and Technology (RUET), Bangladesh
E-mail: [1]r.r.mahmud@gmail.com and [2]razzak91@yahoo.com

ABSTRACT
This paper presents design of a Photonic Crystal Fiber (PCF) with both ultra low dispersion and ultra flattened dispersion in a wide wavelength range of 1.23 µm to 1.78 µm. It is shown from numerical results that a new PCF design with ultra flattened dispersion of 0 ± 0.5 ps/(km·nm) can be simulated and calculated. Finite element method (FEM) with anisotropic perfectly matched layers are used to analyse the dispersion properties for a PCF with a finite number of air holes linearly placed to a straight line in a circle. Design steps, dispersion calculation and details of PCF are presented in a sequential manner that would be advantageous for the beginners as well as for the advanced readers.

KEY WORDS: Photonic Crystal Fiber, Ultra Flat Dispersion, Dispersion, Effective Area, Confinement Loss.

1. INTRODUCTION

The task of controlling the dispersion is a very important for designing practical optical communication systems and dispersion related devices. Low dispersion light guiding can be essential to maintain linear transfer function for low distortion of analog or digital signals and high bandwidth data transmission for fiber optic communication system. Photonic crystal fiber (PCF) is formed from a strand of silica glass with an array of microscopic air channels running along its length [1]. In conventional step-index fibers, group velocity dispersion (GVD) is usually dominated by the dispersion of the bulk silica. In PCF, however, the additional design parameters are hole diameter, d, hole radius r and hole-to-hole spacing pitch Λ, enable much greater flexibility in the design of dispersion to suit the required application. For example, conventional step-index fiber the zero dispersion wavelength is at ~1.3 µm. These unusual fibers have very small cores and are very efficient at generating super continuum light from fsec Ti: Sapphire laser pulses [2, 3]. Index-guiding PCF guides light by total internal reflection between a solid core and a cladding region with multiple air-holes [4]. Two micro-structured fibers showing dispersion of 0 ± 0.6 ps/nm.km from 1.24 µm-1.44 µm wavelengths and 0 ± 1.2 ps/nm.km over 1 µm-1.6 µm wavelength have been measured by W. H. Reeves [5]. K. Saitoh et al have designed a four ring PCF with flattened dispersion of 0 ± 0.5 ps/(km·nm) from a wavelength of 1.19 µm to 1.69 µm and a five-ring PCF with flattened dispersion of 0 ± 0.4 ps/(km·nm) from a wavelength 1.23 µm to 1.72 µm in 2003[6]. F. Poletti et al employed a Genetic Algorithm for the dispersion optimization of a range of holey fibers (HF) with a small number of air holes with dispersion of 0 ± 0.1 ps/nm/km in the wavelength range between 1.5 and 1.6 µm [7]. Our designed PCF can perform managed dispersion to a wide range of 1.23 µm to 1.78 µm wavelength and so far as we know, this range is one of the highest among the ultra flattened dispersion in PCF design.

2. PHOTONIC CRYSTAL FIBER

The PCF is a single material optical fiber consisting of a microscopic array of air channels running down the entire fiber length. These air-holes in a silica base constitute the low index cladding and the core is generally formed either by removing a central air hole from the structure or by creating a larger air hole in its position. In the figure 1, air holes are represented by small unfilled circles. The absence of an air hole is denoted by a dotted small circle. Inclusions of air holes in the PCF offer a variable index contrast between the core and the cladding which is achieved by changing dimension of holes and cladding geometry. Thus, PCF has a number of design freedom namely air-hole diameter, air-hole to air-hole distance (the pitch), core radius, and number of rings.

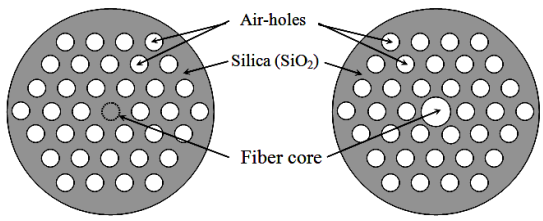

Figure 1: Schematic cross sections of PCF

3. DISPERSION, EFFECTIVE AREA AND CONFINEMENT LOSS

The dispersion in optics is a phenomenon which causes separation of a wave into its spectral components. Separations of spectral components occur due to a dependence of the wave speed on its wavelength. It is sometimes called the chromatic dispersion.

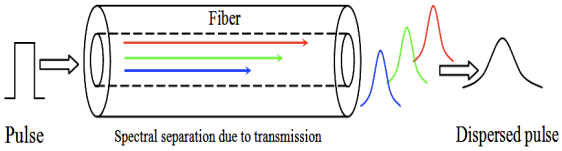

Figure 2: dispersion phenomena in optical systems

The group velocity dispersion $D(\lambda)$ is defined as the change in pulse width per unit distance of propagation (i.e., ps/km/nm), where c is the velocity of light in vacuum, λ is the wavelength and n_r is the relative refractive index of the materials.

$$D(\lambda) = d/d\lambda(1/v_g(\lambda)) = -(\lambda/c)d^2 n_r/d\lambda^2 \quad \text{----- (1)}$$

The effective area is the area where the beam intensity drops to 13.5% of the maximum value and the diameter of which is called the mode field diameter (MFD).

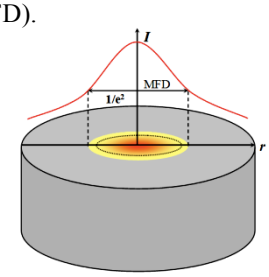

Figure 3: Mode field diameter and effective area of optical fibers

The effective area $A_{eff}(\lambda)$ is calculated by the following equation.

$$A_{eff}(\lambda) = [[\int_{-\infty}^{\infty}\int_{-\infty}^{\infty}\left(|E_x(x,y)|^2 + |E_x(x,y)|^2\right)dxdy]^2]/$$

$$[\int_{-\infty}^{\infty}\int_{-\infty}^{\infty}\left(|E_x(x,y)|^2 + |E_x(x,y)|^2\right)^2 dxdy] \quad \text{---------- (2)}$$

The guided light penetrates to the cladding region and thereby causes signal degradation. Confinement loss is treated as the loss of leaky modes. There will be no confinement losses in PCF if and only if there is infinite number of air-holes in the cladding. Theoretically, confinement losses in PCF arise from the finite size of the cladding. A fiber with infinite cladding can be free from confinement losses. This loss depends on the size of the core, air-hole dimension, pitch, and number of rings in the cladding.

Confinement losses L_c can be calculated by the following equation,

$$L_c(\lambda) = -20\log_{10} e^{-k_0 n_i} = 5.45751\times10^{-7}\times(n_i/\lambda)$$

$$= 8.686\times k_0 n_i \quad dB/m \quad \text{-------- (3)}$$

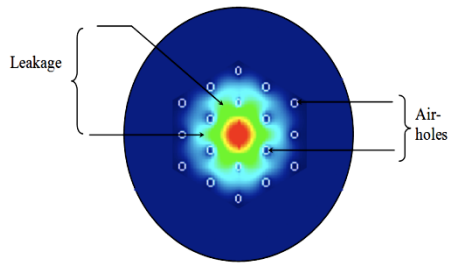

Figure 4: Confinement losses in index-guiding photonic crystal optical fibers

4. FLOW CHART AND ALGORITHM OF SIMULATION WORK

Step 1: Design the PCF
Step 2: Initialized the Refractive Index
Step 3: Run simulation by finite element method
Step 4: Check Mode Field Confinement
Step 5: If the light does not confine then change the Initial refractive index
Step 6: If light is confined then calculate dispersion. If the result is satisfactory then save the result, otherwise change the parameters of the designed PCF

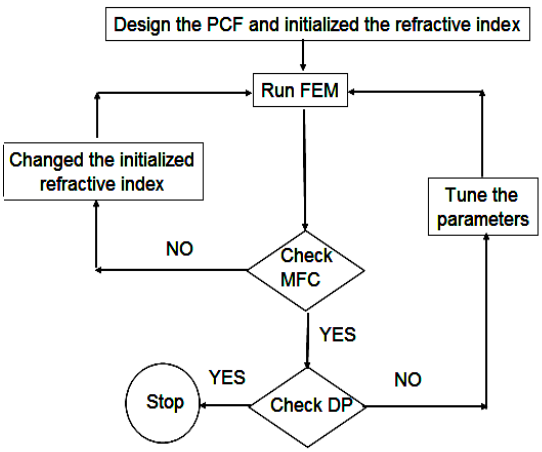

Figure 5: Flow Chart of the Simulation

5. DESIGNED PCF WITH NEAR ZERO FLATTENED DISPERSION

We have calculated PCF with ultra-flattened dispersion means low dispersion about 0 ± 0.5 ps/(km·nm) in a wide wavelength range of 1.23 µm to 1.78 µm. Pitch (p) = Λ = 1.7 µm is chosen for designed our desired PCF. Radius is measured by half of a diameter. There are 167 no of air holes are taken for the desired design and the air holes are placed to the straight line in a circle. The indicated color black block air holes are named as r_7, blue blocks are named as r_6, green blocks are named as r_5, pink blocks are named as r_4, brown blocks are named as r_3, orange blocks are named as r_2, yellow blocks

are named as r_1, bright green blocks are named as r_9, red blocks are named as r_{10}, dark gray blocks are named as r_8 given in the figure no 7. The designed parameters are given below in the table 1 where a is the center position of the circle and lam is the wavelength.

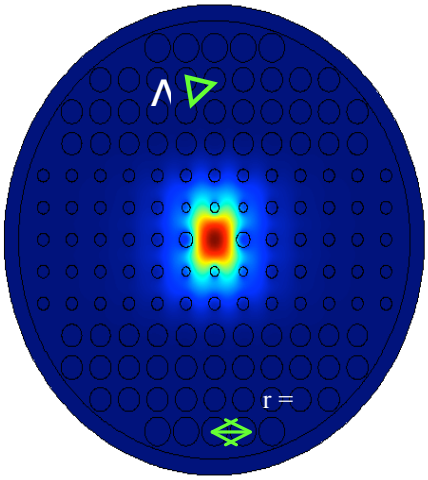

Figure 6: Parameter names of designed PCF

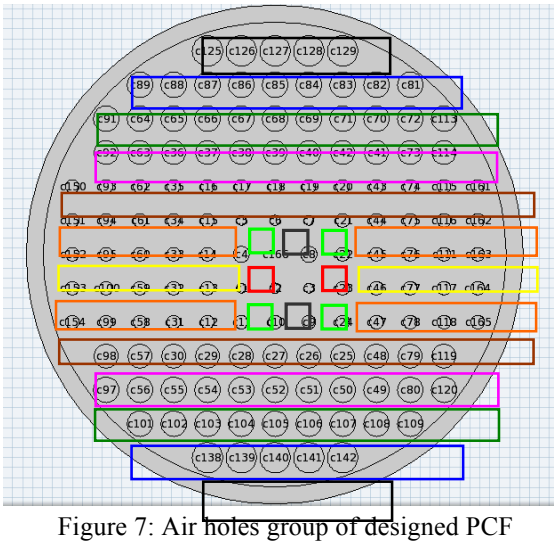

Figure 7: Air holes group of designed PCF

Table 1: Optimized Parameter Values of desired Designed PCF

Name	Expression	Value
p	1.7	1.7
r1	.4*p/2	0.34
r2	0.4*p/2	0.34
r3	0.4*p/2	0.34
r4	0.7*p/2	0.595
r5	0.75*p/2	0.6375
r10	.45*p/2	0.3825
r9	.287*p/2	0.2439
r6	0.75*p/2	0.6375
r7	0.9*p/2	0.765
r8	.302*p/2	0.2567
a	5	5
lam	1.1E-6	1.1E-6

6. EXPERIMENTAL RESULTS

The simulation has been solved for a wide range of 1.23 µm to 1.78 µm wavelengths and the fiber light is confined for all wavelengths within the range. Silica is used for our designed PCF as material which has a refractive index of 1.4457. The surround cladding air holes have 1.00 refractive index. In this way the PCF is completely index guiding. All the figures are plotted for 1.2 µm to 1.85 µm wavelengths and when the parameters are chosen in such a way that Λ=1.7µm, r_1= (0.4xΛ), r_2= (0.4xΛ), r_3= (0.4xΛ), r_4= (0.7xΛ), r_5= (0.75xΛ), r_6= (0.75xΛ), r_7= (0.75xΛ), r_8= (0.302xΛ), r_9= (0.287xΛ), r_{10}= (0.45xΛ), then ultra flattened dispersion can be plotted by the simulation value.

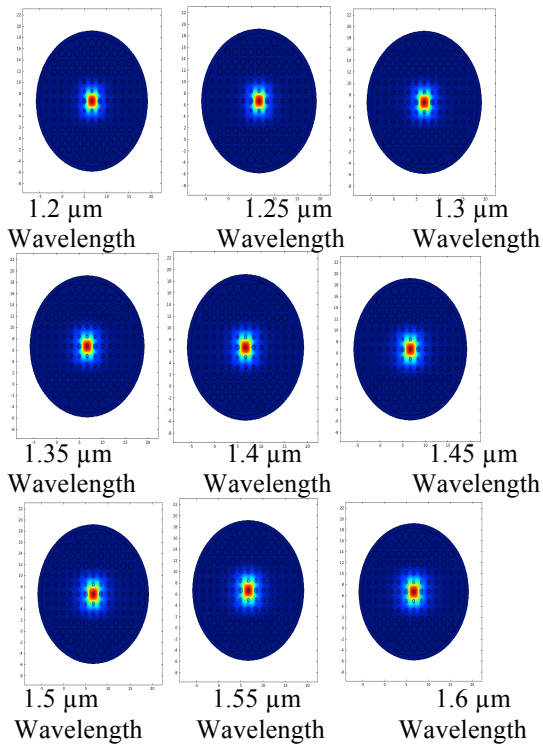

Figure 8: Simulation results of Light confinement of designed PCF for all wavelengths

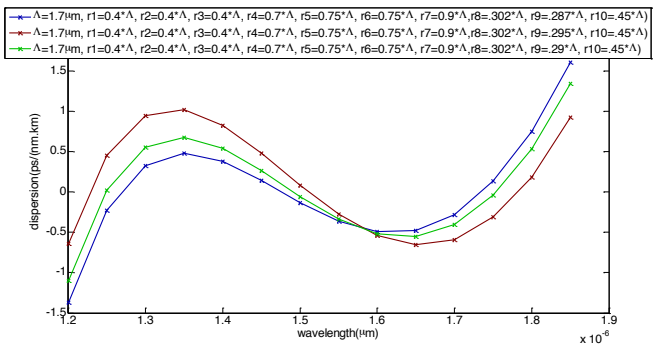

Figure 9: Dispersion when r_9 no block radius airholes are changed

Dispersion is -0.05 ps/nm.km at 1.23 µm and +0.05 ps/nm.km at 1.78 µm wavelength. So by design our

desired PCF dispersion can be managed for a wide range like 1.23 µm to 1.78 µm. When the wavelength of the light beam is increased then the effective area is also increased which is given to the figure no 12.

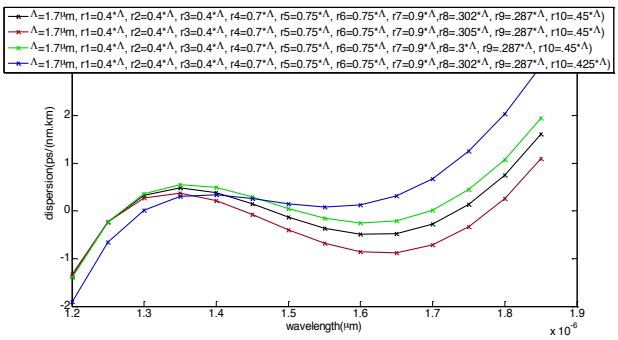

Figure 10: Dispersion at r_8 and r_{10} no block radius air holes are changed

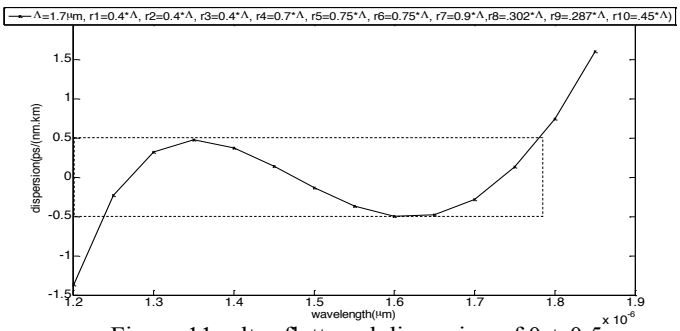

Figure 11: ultra flattened dispersion of 0 ± 0.5 ps/(km·nm) in a wide wavelength range of 1.23 µm to 1.78 µm

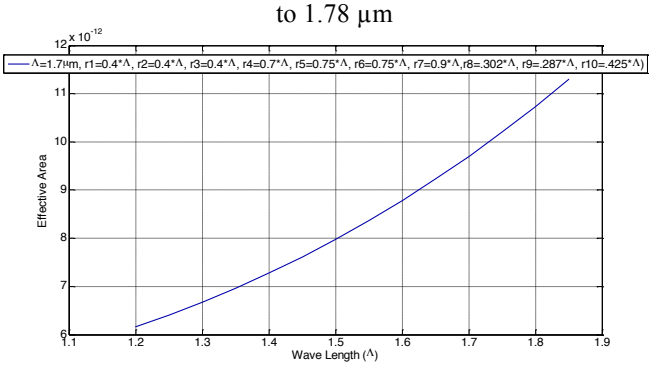

Figure 12: Effective Area of desired designed PCF

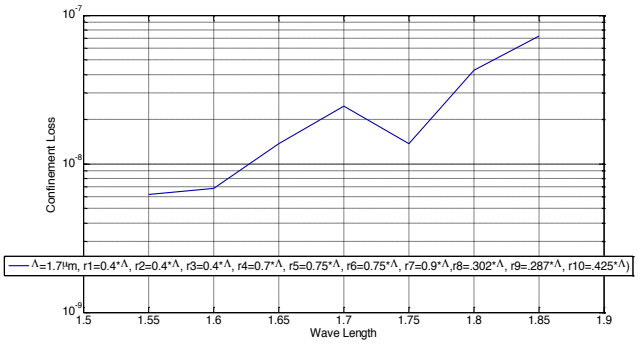

Figure 13: Confinement Loss of designed PCF

7. CONCLUSIONS

It was shown from numerical results that it is possible to design PCF with flattened dispersion of 0 ± 0.5 ps/(km·nm) from a wavelength range of 1.23 µm to 1.78 µm. Fabrication of these PCF can be under consideration now. With further optimisation of the structure and better control of the fluctuations in fiber diameter, we expect these dispersion values to be reduced still further.

REFERENCES

[1] J. C. Knight, T. A. Birks, P. St. J. Russell, and D.M. Atkin, "All-silica single-mode optical fiber with photonic crystal cladding," *Opt. Lett.,* Vol. 21, pp. 1547, 1996.

[2] W. J. Wadsworth, A. Ortigosa Blanch, J.C. Knight, T.A. Birks, T-P.M. Man and P. St. J. Russell, "Super continuum generation in photonic crystal fibers and optical fiber tapers - A novel light source," *J. Opt. Soc. Am. B in press,* 2002.

[3] J. C. Knight, J. Arriaga, T. A. Birks, A. Ortigosa Blanch, W. J. Wadsworth, and P. St. J Russell, "Anomalous dispersion in photonic crystal fiber," *IEEE Photon. Technol. Lett.,* Vol. 12, pp. 807-809, 2000.

[4] T. A. Birks, J.C. Knight, and P. St. J. Russell, "Endlessly single-mode photonic crystal fiber," *Opt. Lett.* Vol. 22, pp. 961-963, 1997.

[5] W. H. Reeves, J.C. Knight, and P. St. J. Russell, P.J. Roberts, "Demonstration of ultra-flattened dispersion in photonic crystal fibers," *Optics Express,* Vol. 10, No. 14, July 01, 2002.

[6] K. Saitoh, M. Koshiba, T. Hasegawa and E. Sasaoka, "Chromatic dispersion control in photonic crystal fibers: application to ultra-flattened dispersion," *Optics Express,* Vol. 11, No. 8, April 21, 2003.

[7] F. Poletti, V. Finazzi, T. M. Monro, N. G. R. Broderick, V. Tse and D. J. Richardson, "Inverse design and fabrication tolerances of ultra-flattened dispersion holey fibers," *Optics Express,* Vol. 13, No. 10, May 16, 2005.

[8] W. Guo, J. L. Kou, F. Xu, and Y. qing Lu, "Ultra-flattened and low dispersion in engineered microfibers with highly efficient nonlinearity reduction," *Optics Express,* Vol. 19, No. 16, August 1, 2011.

[9] S. E. Kim, B. H. Kim, C. G. Lee, S. Lee, K. Oh and C. S. Kee, "Elliptical defected core photonic crystal fiber with high birefringence and negative flattened dispersion," *Optics Express,* Vol. 20, No. 2, January 16, 2012.

Proceeding of the
International Conference on Electrical, Computer and Telecommunication Engineering
01- 02 December 2012 (ICECTE2012), RUET, Rajshahi-6204, Bangladesh

ICECTE2012: PI-0074

Compensation of Quadrature Imbalance Using Frequency-Domain Adaptive Filters in Coherent Optical Receivers

Md. Saifuddin Faruk
Department of Electrical and Electronic Engineering, Dhaka University of Engineering and Technology, Gazipur, Bangladesh
E-mail: faruk@duet.ac.bd

ABSTRACT
In this paper, a novel method for compensation of quadrature imbalance in coherent optical receivers is proposed. The method is based on a modified configuration of conventional frequency-domain adaptive filter (FDAF) used for equalization functionality. With numerical simulation of a 10-Gbaud optical quadrature phase-shift keying (QPSK) transmission system, it is verified that proposed scheme can compensate for the quadrature imbalance over a wide range without any notable performance degradation.

KEY WORDS: Optical fiber communications, equalization, quadrature imbalance, digital signal processing, adaptive filtering.

1. INTRODUCTION

Quadrature phase-shift keying (QPSK) is one of the promising candidates for the modulation format of next generation optical communication systems that will employ digital coherent receivers [1]. The received signals from inphase- (I) and quadrature phase- (Q) ports of such receivers ideally have the same average power and are orthogonal to each other. However, the slight imperfection of front-end components of the receiver such as 90-degree optical hybrid, photodetectors, trans-impedance amplifiers etc. can induce the gain and/or phase mismatch between I- and Q- port data. Such mismatch is generally termed as quadrature imbalance. The system performance can severely degrades if it is not compensated.

For compensation of the quadrature imbalance in optical communication systems, several methods have been demonstrated so far that include Gram-Schimdt orthogonalization procedure (GSOP) [2], ellipse-correction method [3] and constrained constant-modulus algorithm (CMA) quadrature imbalance equalizer [4]. All these works need a dedicated digital signal processing (DSP) circuit for quadrature imbalance compensation and these methods are not optimally applicable for high-order QAM modulation formats. Recently, we have proposed a novel quadrature imbalance compensator based on a modified time-domain adaptive finite-impulse-response (FIR) filters [5]. However, in such a time-domain approach, the computational complexity increases with the increased number of tap length. Though the frequency-domain adaptive filters (FDAF) can reduced this computational cost significantly, the conventional FDAF such as fast least-mean-square (LMS) filter [6] or frequency-domain constant-modulus algorithm (CMA)-based filter [7] cannot compensate for the quadrature imbalance.

In this paper, a new and novel configuration of FDAF based on the CMA is proposed, which can compensate for quadrature imbalance as well as can simultaneously perform other conventional tasks such as clock recovery [8, 9] and equalization. The proposed configuration has the advantage that it is applicable to any modulation format with a hardware-efficient manner. The effectiveness of the proposed algorithm is verified with 10-Gbaud optical QPSK transmission simulations. It is found that, proposed scheme can compensate for the gain and phase mismatch over a wide range without any significant receiver sensitivity penalty.

In the followings, uppercase and lowercase letters denote frequency-domain and time-domain variables, respectively, bold-face letters denote matrixes and vectors, superscript ^{T} denotes transpose operation, $\otimes$ denotes element-by-element multiplication, FFT is fast Fourier transform and IFFT is the inverse FFT.

2. PROPOSED SCHEME

The transfer matrix for the quadrature imbalance can be written as [5]-

$$\mathbf{Q} = \begin{bmatrix} \alpha_I \cos\delta_I & -\alpha_I \sin\delta_I \\ -\alpha_Q \sin\delta_Q & \alpha_Q \cos\delta_Q \end{bmatrix}, \qquad (1)$$

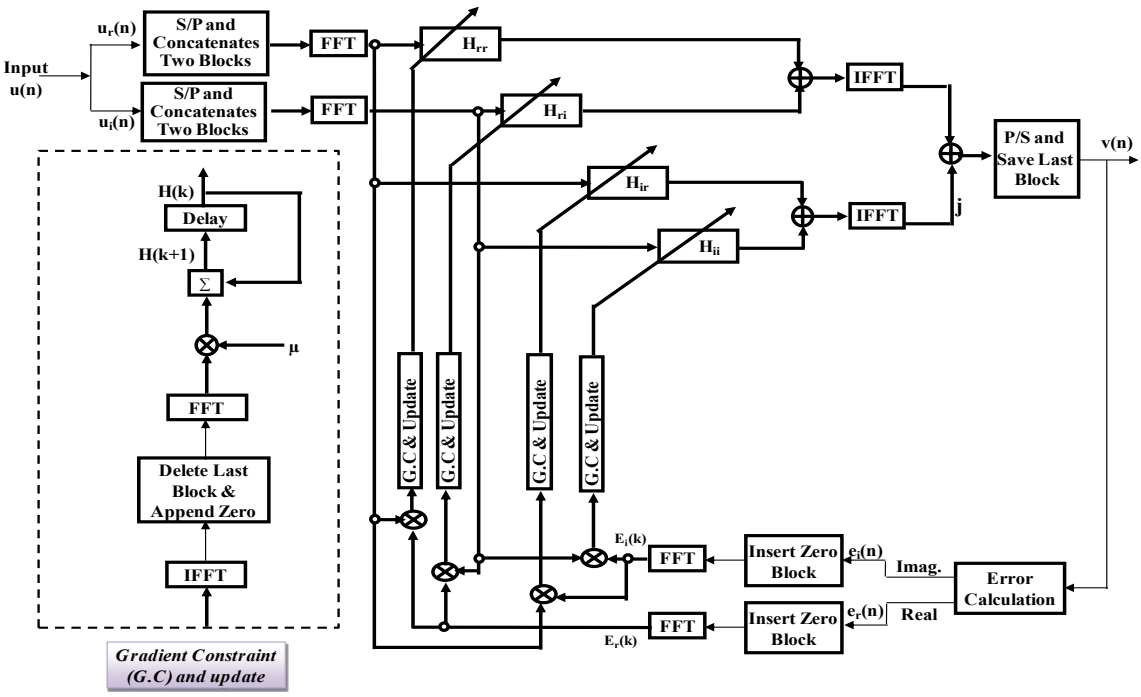

Fig.1: Schematic diagram of proposed FDAF for both equalization and quadrature imbalance compensation.

where, α_I and α_Q are the gain and δ_I and δ_Q are the phase deviation of I- and Q- port, respectively. All the elements of matrix **Q** are real-valued and frequency independent. To compensate for the quadrature imbalance, we need to evaluate the matrix $\mathbf{Q}^{-1}$ in the digital domain.

Since Eq. (1) denotes the mutual coupling between I- and Q- signals, the conventional FDAF that operates on complex input data can not compensate for the quadrature imbalance. Therefore, in order to compensate quadrature imbalance, we propose to split one conventional filter into four filters connected in a two-by-two butterfly configuration that operates on the real data (either real or imaginary part of the complex input data). With appropriate adaptive algorithm, the four filters can estimate the four elements of matrix $\mathbf{Q}^{-1}$ and thus compensate for the quadrature imbalance.

The detail of the proposed FDAF with four filters $\mathbf{H_{rr}}$, $\mathbf{H_{ri}}$, $\mathbf{H_{ir}}$ and $\mathbf{H_{ii}}$ is shown in Fig.1. First, the input sequence $u(n)$ is divided into real and imaginary sequences, $u_r(n)$ and $u_i(n)$ respectively. In the FDAF, a block of data is processed at a time instead of sample-by-sample processing in the time-domain. Considering L as the block length and k as the block index, the input sequences of the filter is denoted as $\mathbf{u}_{r/i}(k)$.

For fast implementation of linear convolution in the frequency domain, the overlap-save method with 50% overlap is chosen. By using the 50% overlapping factor, the frequency-domain input vector $\mathbf{U}_{r/i}(k)$ for four filters include L samples from the current block and L samples from the previous block and can be written as

$$\mathbf{U}_{r/i}(k) = \mathrm{FFT}[u_{r/i}(kL-L),\cdots,u_{r/i}(kL+L-1)]^{\mathrm{T}}, \quad (2)$$

Then, L tap weights of the four filters are padded with the equal number of zeros and $2L$-point FFT is executed. Let $\mathbf{H}_{pq}(k)$ be the FFT-coefficient vector of the zero-padded tap-weight vector $\mathbf{h}_{pq}(k)$ as

$$\mathbf{H}_{pq}(k) = \mathrm{FFT}[\mathbf{h}_{pq}(k);\mathbf{O}_L]^{\mathrm{T}}. \quad (3)$$

where, $pq = rr$, ri, ir or ii.

By carrying out IFFT, the output vector in the time-domain with a column length of L is given as

$$\mathbf{v}(k) = \text{last } L \text{ elements of } \mathrm{IFFT}\{\mathbf{V}(k)\}, \quad (4)$$

where $\mathbf{V}(k)$ is given as

$$\mathbf{V}(k) = \{\mathbf{H_{rr}}(k)\mathbf{U_r}(k) + \mathbf{H_{ri}}(k)\mathbf{U_i}(k)\} + j\{\mathbf{H_{ir}}(k)\mathbf{U_r}(k) + \mathbf{H_{ii}}(k)\mathbf{U_i}(k)\}$$

and the first L elements of $\mathrm{IFFT}\{\mathbf{V}(k)\}$ are discarded to implement the linear convolution. Then, the error signal for the CMA is calculated in the time

domain and the error vector with the column length of L is given as

$$\mathbf{e}(k) = [\mathbf{I}_L - \mathbf{v}(k) \otimes \mathrm{conj}\{\mathbf{v}(k)\}] \otimes \mathbf{v}(k), \qquad (5)$$

where the vector $\mathbf{I}_L$ has L columns and all of its elements are 1. After splitting $\mathbf{e}$(k) in real and imaginary part and augmenting $\mathbf{e}_{r/i}(k)$ with L zeros, we convert it to the frequency-domain vector with the column length of $2L$ as

$$\mathbf{E}_{r/i}(k) = \mathrm{FFT}[\mathbf{O}_L; \mathbf{e}_{r/i}(k)]^{\mathrm{T}} . \qquad (6)$$

Applying the overlap-save method, we calculate the gradient vector $\nabla_{pq}(k)$ as

$$\nabla_{pq}(k) = 1^{\mathrm{st}}\ L \text{ terms of } \mathrm{IFFT}[\mathbf{E}_p \otimes \mathrm{conj}\{\mathbf{U}_q(k)\}]^{\mathrm{T}}. (7)$$

Finally, tap weights are updated in the frequency-domain by using the gradient decent algorithm as

$$\mathbf{H}_{pq}(k+1) = \mathbf{H}_{pq}(k) + \mu \mathrm{FFT}[\nabla_{pq}(k); \mathbf{O}_L]^{\mathrm{T}}, \qquad (8)$$

where μ is the step-size parameter and the gradient vector $\nabla_{pq}(k)$ is augmented with L zeros to match the definition of frequency-domain filtering in Eq. (3). Equations (7) and (8) place a constraint on the gradient vector, which ensures that frequency-domain tap weights are equivalent to the time-domain counterparts.

3. SIMULATION RESULTS

To evaluate the performance of proposed algorithm, a 10-Gsymbols/s QPSK transmission systems is simulated. In the transmitter, first differentially-coded QPSK signal is generated. The signal is then band-limited by a Nyquist filter with a roll-off factor of 0.5. After that, the signal is impaired by phase noise of the transmitter laser and passes through a 100-km standard single mode fiber (SSMF) which accumulates a chromatic dispersion (CD) of 1700 ps/nm. Then additive white Gaussian noise (AWGN) and phase noise from a local oscillator (LO) are added to the signal. Both the transmitter laser and LO has the 3-dB linewidth of 500 kHz. Finally, the quadrature imbalance is intentionally added by using Eq. (1).

In the DSP, a perfect clock recovery circuit is considered that retains 1-samples per symbol. The signal is then fed to either a conventional FDAF [7] or the proposed FDAF. The number of filter taps is 16 and μ=10^{-3}. After that, M-th power carrier recovery [10] is done and symbols are decoded to estimate the BER.

Figure 2 shows the BER performance in the presence of IQ phase mismatch and no gain mismatch. In the case of conventional approach, the BER performance degrades with increasing IQ phase mismatch. However, when applying the proposed scheme, the BER curves overlaps for 0˚, 15˚ and even 30˚ of IQ phase mismatch, proving that compensation is done without any penalty.

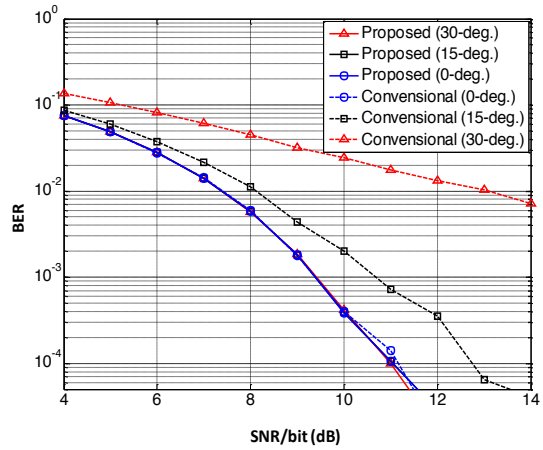

Fig. 2: The BER performance of the system as a function of SNR/bit for different IQ phase mismatch.

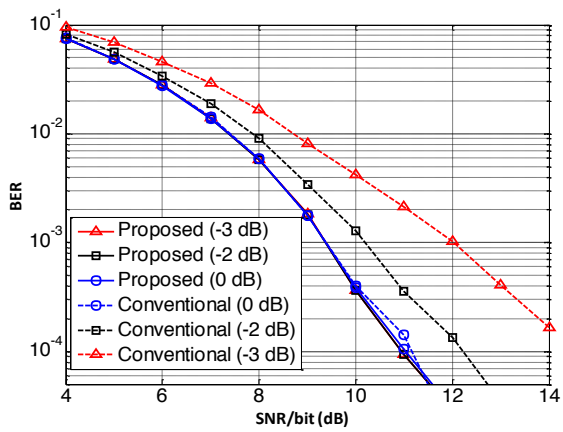

Fig.3: The BER performance of the system as a function of SNR/bit for different IQ gain mismatch.

Figure 3 shows the BER performance in the presence of IQ gain mismatch and no IQ phase mismatch. It is found that the proposed method can fully compensate for such mismatch. However, for the conventional scheme the receiver sensitivity penalty increases with the increase of IQ gain mismatch.

Next, the combined effect of phase and gain mismatch is investigated. Figure 4 shows the constellation diagram of recovered signal at SNR/bit of 9 dB in the presence of 30˚of IQ phase mismatch and -3 dB of IQ gain mismatch. It is evident from the figure that the proposed scheme provides a clear constellation compared to the conventional approach.

Therefore, it can be concluded that the conventional FDAF used for equalization cannot compensate for the quadrature imbalance. However, the modified FDAF proposed in section 2 is very tolerant to the quadrature imbalance.

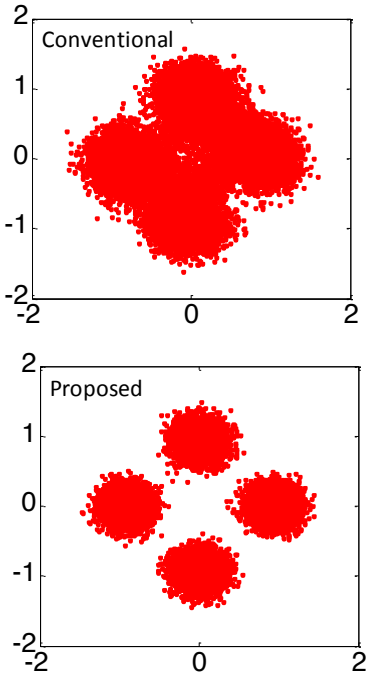

Fig. 4: Constellation diagram of recovered signal using conventional FDAF (upper) and proposed FDAF (lower) with 30˚ of IQ phase mismatch and -3dB of IQ gain mismatch.

4. CONCLUSIONS

A novel quadrature imbalance compensation scheme is proposed using a modified structure of conventional FDAF. The effectiveness of the proposed approach is verified with numerical simulation of 10-Gbaud QPSK transmission systems.

5. FUTURE WORK

For simplicity of the explanation, we do not consider the polarization multiplexed systems. However, the proposed scheme can easily be extended for such system with another 12 filters connected in proper way. Further investigation is required in this regard.

REFERENCES

[1]. K. Kikuchi, "Coherent optical communications: Historical perspectives and future directions," in *High Spectral Density Optical Communication Technology,* edited by M. Nakazawa, K. Kikuchi, and T. Miyazaki, (Springer, 2010), Chap. 2.

[2]. I. Fatadin, Seb. J. Savory, and D. Ives, "Compensation of quadrature imbalance in an optical QPSK coherent receiver," *IEEE Photon. Technol. Lett.*, vol. 20, pp. 1733-1735, 2008.

[3]. S. H. Chang, H. S. Chung, and K. Kim, "Impact of quadrature imbalance in optical coherent QPSK receiver," *IEEE Photon. Technol. Lett.,* vol. 21, pp. 709-711, 2009.

[4]. C. S. Petrou, A. Vgenis, I. Roudas, and L. Raptis, "Quadrature imbalance compensation for PDM QPSK coherent optical systems," *IEEE Photon. Technol. Lett.,* vol. 21, pp. 1876-1878, 2009.

[5]. M. S. Faruk and K. Kikuchi, "Front-end IQ-error compensation in coherent optical receiver," in *Proc. OECC' 12*, paper 4B2-5, 2012.

[6]. S. Haykin, *Adaptive Filter Theory,* 3rd ed., (Prentice Hall), 2001.

[7]. M. S. Faruk and K. Kikuchi, "Frequency-domain adaptive equalization for coherent optical transmission system," in *Proc. of IEICE society conf.,* paper B-10-71, 2010.

[8]. K. Kikuchi, "Clock recovering characteristics of adaptive finite-impulse-response filters in digital coherent optical receivers," *Opt. Express*, vol. 19, pp. 5611-5619, 2011.

[9]. M. S. Faruk and K. Kikuchi, "Adaptive frequency-domain equalization in digital coherent optical receivers," *Opt. Express*, vol. 19, pp. 12789-12798, 2011.

[10]. D. -S. Ly-Gagnon, S. Tsukamoto, K. Katoh, and K. Kikuchi, "Coherent detection of optical quadrature phase-shift keying signals with carrier phase estimation," *J. Lightwave Technol.,* vol. 24, pp. 12-21, 2006.

Proceeding of the
International Conference on Electrical, Computer and Telecommunication Engineering
01- 02 December 2012 (ICECTE2012), RUET, Rajshahi-6204, Bangladesh

ICECTE2012: PI-0075

Effect of Photon Lifetime on Lasing Conditions of InGaN Quantum Dot LASER

M. A. Humayun[1], M. A. Rashid[1], F. A. Malek[1], A. Azmi[1], M. Othman[1], M. A. Hossain[2]

[1]CERE, School of Electrical Systems Engineering, University Malaysia Perlis, Malaysia.
[2]Department of Electrical and Electronic Engineering, Jessor Science and Technology University, Jessor, Bangladesh.

E-mail: humayun0403063@gmail.com, abdurrashid@unimap.edu.my, mfareq@unimap.edu.my, azralmukmein@unimap.edu.my, muzaidi@unimap.edu.my, mahossain.eee@gmail.com.

ABSTRACT
We have analyzed theoretically the effect of photon lifetime on lasing characteristics of InGaN quantum dot laser such as: population density, feedback strength and threshold current characteristics. The photon lifetime of InN based quantum dot is higher than GaAS based quantum dot, which plays an important role to reduce the threshold current density. As the threshold current density has been reduced using InN as the active material, the other parameters required to achieve lasing action have also been improved. The other parameter improvements were achieved in terms of lower carrier population concentration and lower feedback strength required to occur population inversion and amplify light respectively.

KEY WORDS: Photon lifetime, InN, Threshold current density, Population density, Feedback strength.

1. INTRODUCTION

The effects of photon lifetime on lasing characteristics of quantum dot semiconductor laser are the subject of great current interests now a days. Recently researchers are devoted to their research on the improvement of revolutionary quantum dot lasers that are significantly superior to higher dimensional semiconductor lasers providing higher performances such as ultralow threshold current density [1], which will reduce the threshold current and improve the other parameters of the laser. If the threshold current density is minimized, the requirements to achieve the threshold current such as: feedback strength [2] to provide sufficient populations density to occur population inversion will also be improved. If the population density required for population inversion is increased so the required level of feedback for lasing will also be reduced. Finally, it will effectively reduce the biasing voltage required for pumping [3].

Earlier studies reports that the photon lifetime of GaAS based quantum dot is 1.5 ps [4], i.e. 0.015 ns. Recently it has been reported that the spontaneous radiative photon lifetime of InN based quantum dot is 0.7 ns [5, 6].So, the photon lifetime of InN based quantum dot is higher than that of GaAs.

This paper highlights the role of higher photon lifetime on threshold current, population density, feedback strength and biasing voltage to provide proper lasing action of InGaN based quantum dot laser operating at 1.55μm.

2. THRESHOLD CURRENT DENSITY

The major disadvantage of 'bulk' laser is that high current is required for the lasing action due to their large active region. The active region of a bulk laser is so large that photons are absorbed within the active region. So, it is necessary to pump a lot of electrons and holes [7].QD plays an important role to achieve low threshold current due to their $\boldsymbol{\delta}$- like density of state [8, 9] and extremely small α- parameter. The effect of photon lifetime on threshold current is described by the following equation [9]:

$$I_{th} = \frac{eVn_{th}}{\tau} \quad (1)$$

where e is the charge of electron, V is the volume of the InN quantum dot in the active layer, n_{th} is the carrier density at threshold and $\boldsymbol{\tau}$ is the carrier lifetime.

The carrier density at threshold is given by the following equation [2]:

$$n_{th} = n_0 + \frac{1}{\tau G} \quad (2)$$

where n_0 is the initial carrier density and G is the modal gain coefficient.

The threshold current density is given by the general equation as follows:

$$J_{th} = \frac{I_{th}}{A} \quad (3)$$

where A is the cross section area of the active layer of laser structure. Therefore by proper optimization of carrier lifetime the minimum threshold current density can be achieved. In order to investigate the effect of photon lifetime on threshold current density fig. 1 is plotted solving Eq. 1 to Eq. 3.

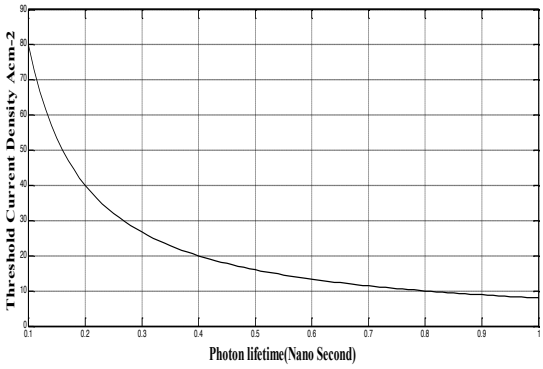

Fig. 1: Dependence of threshold current density on photon lifetime.

From Fig. 1 it is clear that the threshold current density decreases with the increase of photon lifetime. From the curve it is clear that the threshold current density of InGaN based quantum dot based laser is near about 11Acm^{-2}, which is extremely lower than that of GaAs. So, InN can be expected to be a challenging material in the field of semiconductor laser design with ultra-low threshold current density.

3. POPULATION DENSITY

Population inversion is the primary requirement for the lasing action to occur. If Quantum dot is used as the active layer of a laser the population density decays with the photon lifetime exponentially during the lasing action. So to continue the lasing action population density should maintain a certain level. The population density is given by the following equation [3]:

$$\rho_t = \rho_0 e^{-\frac{t}{\tau}} \quad (4)$$

where ρ_0 is the initial population density, t is the time and $\boldsymbol{\tau}$ is the photon lifetime.

Eq. 4 shows that the initial population (t=0) density is the maximum and it reduces with time. The population density depends on the photon lifetime and the voltage of the pump source. If the photon lifetime is higher it will be helpful to reduce the required power of the pump source.

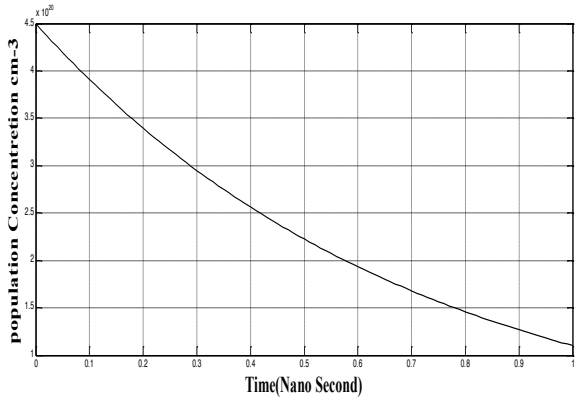

Fig. 2 Decay of Population concentration with time.

Fig. 2 shows that the required carrier population concentration to occur lasing action decreases exponentially with the carrier lifetime. From the fig. it is clear that the population density required for lasing action is near about 1.6×10^{20}cm^{-2} for InN based quantum dot, which only one-third of that of GaAs. So, if InN is used as the active layer material the required biasing voltage to achieve population inversion will also be minimized.

4. FEEDBACK STRENGTH

Feedback of light into the gain medium is the most important requirement for light amplification. Optical feedback affects noise and dynamics of laser in different ways depending on the strength of feedback [10].The feedback strength is also dependent on the photon lifetime. The dependence of photon lifetime on feedback strength is given by the following formula [2]:

$$k = \frac{(1-r_1)}{\tau\sqrt{\frac{r_2}{r_1}}} \quad (5)$$

where k is the feedback strength required for pumping r_1 and r_2 are the reflectivities of the edge mirrors of the gain medium and $\boldsymbol{\tau}$ is the carrier lifetime.

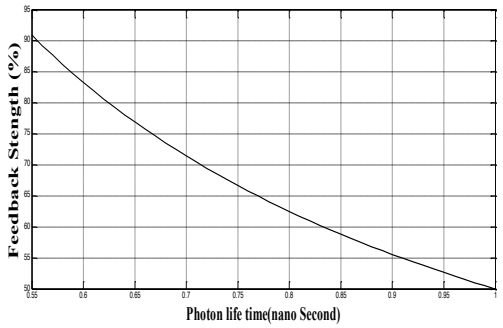

Fig.3 Effect of photon lifetime on strength of feedback required to amplify light.

Fig. 3 presents the required strength of feedback level for photon multiplication in the gain medium to amplify light. The required level of feedback strongly depends on the carrier lifetime. From fig. 3 it is clear that the feedback level required for lasing action is 72% for InN based quantum dot, which is smaller than that of GaAs. So, if InN is used as the active layer material the required level of feedback has been minimized.

5. RESULTS AND DISCUSSION

The dependence of lasing characteristics on the photon lifetime has been presented in this paper. Among the lasing characteristics we have discussed the threshold current density, population density and feedback strength required for the lasing action to occur. Results are graphically shown in Fig. 1 to Fig. 3. To determine the values of the threshold current density, density of population and feedback strength required for the lasing action. We have used the values of photon lifetime of GaAS and InN based quantum dot are 1.5 ps [4], i.e. 0.015 ns and 0.7 ns [5, 6] respectively.

Results show that the values of threshold current density, population concentration for lasing and required level of feedback strength are $11Acm^{-2}$, $1.6\times10^{20}cm^{-2}$ and 70% respectively.

6. CONCLUSION

It has been demonstrated that the lasing characteristics of a quantum dot based laser like population density, feedback strength and threshold current density decrease with the increase of photon lifetime. The photon lifetime of InN based quantum dot is 0.71 ns. The corresponding values of threshold current density, population concentration for lasing and required level of feedback strength are $11Acm^{-2}$, $1.6\times10^{20}cm^{-2}$ and 70% respectively. So, InN can be a challenging material for the fabrication of quantum dot based laser with ultralow threshold current density in future.

7. FUTURE WORK

Effect of photon lifetime on the lasing parameters has been discussed in this paper. Further study is necessary to investigate the effect of photon lifetime on other important laser characteristics like carrier recombination rate, modal gain, absorption and emission losses and finally the effect on output power. A detailed analysis of the effects of thermo ionic emission time and the thermally excited escape time of carrier on the laser dynamics is also necessary.

ACKNOELEDGEMENTS

Authors would like to acknowledge the financial and technical supports from the KTP grant from University Malaysia Perlis (UniMAP), Malaysia for the completion of the research work properly.

REFERENCES

[1] M. A. Humayun, M. A. Rashid, F. A. Malek, A.N. Hussain and I. Daut, "Design of Quantum Dot Based LASER with Ultra-low Threshold Current Density", *Applied Mechanics and Materials* Vols. 229-231, 2012, pp. 1639-1642, Trans Tech Publications, Switzerland doi: 10.4028/www.scientific.net/AMM.229 231.1639.

[2] A. N. Pisarchik and F. R. Ruiz-Olivers, "Dynamics of a semiconductor laser with external cavities", Progress *in Electromagnetics Research,* Vol.3, Issue no. 4, 2007 pp 452-56.

[3] E. A. Viktorov, G. Madden, T. Erneux, J. Pulka, P. Mandel, G. Huyet, T. Piwonski, and J. Houlihan, "Recovery time scales in a reversed-biased quantum dot absorber", *Applied Physics Letters,* Vol.94, Issue no. 263502, 2009 pp. 1-3.

[4] G. P. Agarwal and G. R. Gray, "Effect of phase-conjugated feedback on the noise characteristics of semiconductor lasers", *Physical Review A,* Vol. 46 No. 9, 1992, pp 5890-98.

[5] Luke Lester's, "The Laser Trailblazer", innovative research, the University of New Mexico School of Engineering, Fall 2008.

[6] L. V. A sryan and R. A. Suris "Theory of threshold characteristics of Quantum Dot Lasers: Effect of dot parameter & dispersion", *International Journal of High Speed Electronics and Systems,* Vol. 12, No. 1, 2002, pp 111-176 © World Scientific Publishing Company.

[7] M. M. Hossain, M. A. Humayun, M. T. Hasan, A. G. Bhuiyan, A. Hashimoto, A.Yamamoto, "Proposal of High Performance 1.55 μm Quantum Dot Heterostructure Laser using InN," *IEICE Trans Electrons*, vol. E 95-C, No.2, pp.255-261, Feb. 2012.

[8] Y. Arakawa, T. Someya and K. Tachibana, "Growth and Physics of Nitride-based Quantum

Dot for Optoelectronics Applications", *Proceedings of International Workshop on Nitride Semiconductors,* IPAP Conference Series1, 2002, pp 403-408.

[9] M. M. Hossain, M. A. Humayun, M. M. Biswas, and M. A. H. Sadi, "A Novel Design of InN Based Quantum-Dot Laser Operating at 1.55 μm", *Advanced Materials Research,* Vols. 403-408, 2012, pp 4321-4327, Trans Tech Publications, Switzerland.

[10] G. R. Gray, A. T. Rayan, G. P. Agarwal and E. G. Gage, "Control of optical feedback-induced laser intensity noise in optical data recording", *Optical Engineering,* Vol. 32, No.4, 1993, pp 739-745.

Proceeding of the
International Conference on Electrical, Computer and Telecommunication Engineering
01- 02 December 2012 (ICECTE2012), RUET, Rajshahi-6204, Bangladesh

ICECTE2012: PI-0076

Operation Algorithms of Protection for a WDM/TDM Hybrid Two-OLT PON

Fahmida Rawshan[1], Mostafa Zaman Chowdhury[2], and Youngil Park[1]
[1]Dept. of Electronics Engineering, Kookmin University, South Korea
[2]Dept. of Electrical and Electronic Engineering, Khulna University of Engineering and Technology, Bangladesh
E-mail: fahmida_rawshan@yahoo.co.in, mzceee@yahoo.com, ypark@kookmin.ac.kr

ABSTRACT

In this paper, we propose a novel architecture of passive optical network (PON) that has two optical line terminals (OLTs). The network sustains services to access area and restores normal operation in faulty conditions. We suggest existing Limited Dynamic Bandwidth Allocation (LDBA) scheme for upstream transmission in faulty condition. Performance of the proposed scheme is studied in terms of delay and throughput. Our simulation results show that the scheme can proficiently administrate the performance of the proposed network.

Index Terms - **Passive optical network (PON), WDM/TDM, Limited DBA, Two-OLT, Self-similar traffic.**

I. INTRODUCTION

Several large scale PON deployments are already underway around the world [1-2]. Protection or restoration is an important issue for these high capacity networks. A dual-homed two-OLT PON is one option to increase the resilience of such networks [3]. This architecture is very effective for protection against catastrophic failures. The way how one might enable dual homing protection and also a mechanism for the higher layers to react when there is a traffic switch to a protection OLT is described in [3]. They proposed a TDM architecture with revertive operation; the backup OLT is normally idle and thereby this resource is wasted. To improve the bandwidth utilization by using the backup OLT at normal operation we propose a WDM/TDM hybrid architecture of two-OLT PON. During fault of an OLT the other OTL restores the operation.

We provide appropriate control protocol for this novel system. Besides, appropriate dynamic bandwidth allocation (DBA) schemes can further improve the performance of the two-OLT PON in faulty situation. We suggest the existing Limited Dynamic Bandwidth Allocation (LDBA) scheme [4] for upstream transmission during fault.

The rest of this paper is organized as follows. Section II introduces system architecture of the TDM/WDM hybrid two-OLT PON system and its operation of the protection. In Section III DBA schemes for both normal operation and faulty condition are described. Section IV provides simulation results to demonstrate network performance using the suggested DBA scheme. Finally, section V concludes our work.

II. WDM/TDM HYBRID TWO-OLT PON ARCHITECTURE AND ITS OPERATION

In the proposed two-OLT PON each OLT works as backup OLT for the other one. The ONUs are divided into two groups. In normal situation, each OLT is responsible for data transmission of a group of ONUs. Figure 1 shows the architecture of the proposed network for two OLTs and sixteen ONUs. OLT_x manages data transmission to ONUs in $Group_1$ (ONU_1 to ONU_8) in λ_1 wavelength, while OLT_y manages it for ONUs in $Group_2$ (ONU_9 to ONU_{16}) in λ_2 wavelength. By exchanging control packets for ranging between OLT_x and ONU $Group_2$, and between OLT_y and ONU $Group_1$ RTT is measured continuously in some regular interval, which results in short protection time. During failure of one OLT the other OLT is responsible for data transmission of both groups. An appropriate structure of OLT and ONU is proposed for the WDM/TDM hybrid two-OLT PON. Each OLT is capable of transmitting in one of two wavelengths, λ_1 or λ_2 at a time while receiving λ_3. ONU $Group_1$ and ONU $Group_2$ receive in λ_1 and λ_2, respectively, while both of them transmit in λ_3.

In a two-OLT PON system, packets sent by each ONU are received at both OLTs. Hence, an appropriate encryption algorithm [5] should be used to ensure secured data transmission.

When failure occurs in the PON system, the protection OLT acts as a backup system for the other one. For example, during fault of OLT_x data transmission to $Group_1$ ONUs is interrupted, hence OLT_y reinstates this operation and continues data transmission to both groups until fault recovery. Similarly, OLT_x acts as backup and starts working for both groups of ONUs during fault of OLT_y. In this prospective, this scheme works like a 1:1 protection switching.

III. Bandwidth Allocation Scheme

In normal operation OLT_x and OLT_y need only a small fixed bandwidth to transmit and receive control packets. Hence, a Fixed Bandwidth Allocation (FBA) scheme is appropriate to manage the bandwidth in both upstream and downstream. During the protection of PON systems, however, the efficiency of bandwidth utilization should be maximized since the two ONU groups share the network; the FBA is not a good scheme in this case. Therefore, a new DBA scheme is suggested for upstream transmission.

In faulty condition the two-OLT PON acts like a single OLT PON. Several DBA schemes have been evolved for upstream bandwidth allocation in a single-OLT PON system. IPACT, IPACT-GE, Multi-thread polling are among them [6-7]. Limited DBA has been regarded in IPACT as a very efficient scheme with moderate complexity [6]. Therefore, we suggest the Limited scheme for upstream direction to improve the performance of two-OLT PON during fault protection.

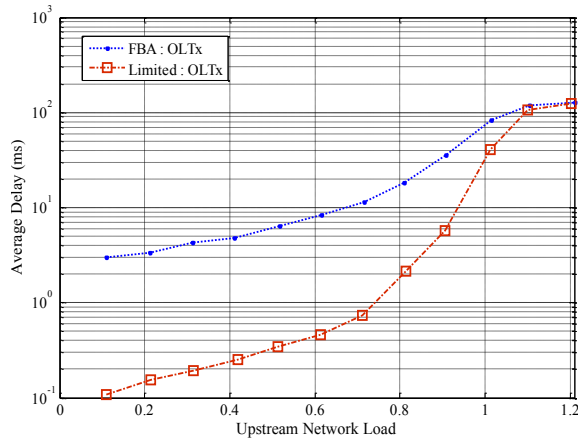

Fig. 2. Comparison of upstream delay during protection between FBA and Limited DBA.

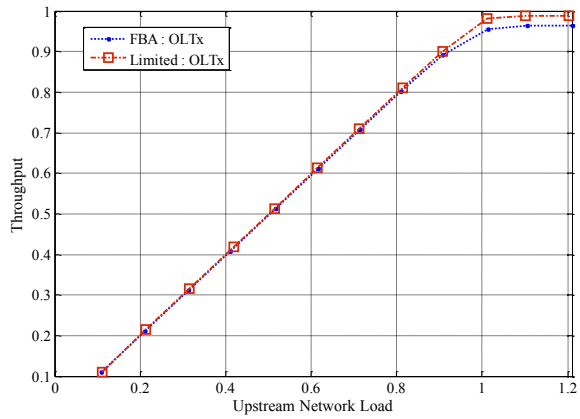

Fig. 3. Comparison of upstream throughput during protection between FBA and Limited DBA.

IV. Performance Analysis during

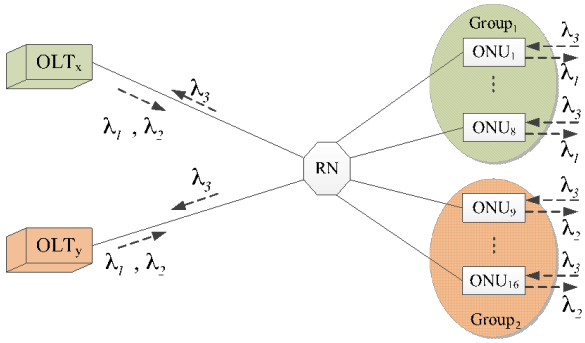

Fig. 1. The proposed architecture of a WDM/TDM hybrid two-OLT PON

PROTECTION

Performance of two-OLT PON is demonstrated during protection by investigating a system of sixteen ONUs (divided into two groups). Each ONU has a 1 MB queue, while each OLT has two separate 10 MB queues toward two groups of ONUs. Packets from queues are sent in Ethernet frames [8]. The queues are simple first-in first-out (FIFO) type. For FBA fixed cycle time of 2 ms is assumed while for Limited DBA scheme it represents the maximum length of cycle time. One cycle delay is added to the Limited DBA scheme to account for the information exchange and decision making process. Moreover, it is assumed that load is evenly distributed among 16 ONUs.

Matlab® is used for the simulation where data packets are generated by a self-similar traffic model. To generate this traffic, we used the method described in [9]. The resulting traffic is obtained by aggregating multiple sub-streams. Load distribution among sub-streams reflects real IP data traffic including recent applications such as P2P, Instant Messenger, Video, and VoIP [10].

We assumed that OLT_y is faulty and OLT_x reserves equal upstream bandwidth for both group of ONUs during protection. Average delay and throughput are analyzed and plotted with respect to total upstream load. Figures 2 and 3 compare FBA scheme with Limited DBA scheme in terms of delay and throughput performances, respectively. The performance analyses infer that the performance of a faulty two-OLT PON can be improved by Limited DBA scheme during protection.

V. CONCLUSIONS

In this paper, we proposed a WDM/TDM two-OLT PON that has two OLTs in a single network. We also presented an appropriate operation algorithm to use the network for protection purpose. We suggested the existing Limited DBA scheme to improve the performance during protection and presented it by simulation. It is estimated that the proposed protection scheme will enhance the survivability of PON system a lot, thereby it is expected that this two-OLT PON is a worthy and reliable architecture for next-generation bandwidth abundant networks like 10 Gbps or 40 Gbps PON where each OLT owns sufficient bandwidth.

ACKNOWLEDGEMENTS

This work was supported by Basic Science Research Program through NRF funded by the MEST (No.2012-0007107), Korea.

REFERENCES

[1] F. J. Effenberger, "The XG-PON system: cost effective 10 Gb/s access'' *Journal of Lightwave Technology,* vol. 29, no. 4, pp. 403-409, February 2011.

[2] T. Hills. (2009, July 3). Who makes what: 40- & 100-Gbit/s systems [Online]. Available: http://www.lightreading.com.

[3] J. Kang, M. Wilkinson, K. Smith, and D. Nesset, "Restoration of Ethernet Services over a Dual-Homed GPON System – Operator Requirements and Practical Demonstration," in *OFC/NFOEC, Optical Fiber Communication/National Fiber Optic Engineers Conference*, San Diego, CA, February 2008.

[4] G. Kramer, B. Mukherjee, and A. Maislos, "Ethernet Passive Optical Networks," in *IP over WDM: Building the Next Generation Optical Internet*, S. Dixit, ed. Hoboken, NJ: Wiley, 2003, pp. 229-276.

[5] W. Stallings, *Cryptography and Network Security: Principles and Practices*. Upper Saddle River, NJ: Prentice Hall, 2005.

[6] G. Kramer, "Interleaved polling with adaptive cycle time (IPACT): a dynamic bandwidth distribution scheme in an optical access network," *Photonic Network Communications*, vol. 4, no. 1, pp. 89-107, January 2002.

[7] J. Zheng and H. T. Mouftah, "A survey of dynamic bandwidth allocation algorithms for Ethernet Passive Optical Networks," *Optical Switching and Networking*, vol. 6, no. 3, pp. 151-162, July 2009.

[8] Ethernet in the First Mile, IEEE standard 802.3ah, June 2004.

[9] G. Kramer, *Ethernet Passive Optical Networks.* New York: McGraw-Hill, 2005, pp. 59-63.

[10] G. Xie, G. Zhang, J. Yang, Y. Min, V. Issarny, and A. Conte, "Survey on traffic of metro area network with measurement on-line," in *Proc. ITC, 20th international teletraffic conference on Managing traffic performance in converged networks,* Ottawa, June 2007, pp. 666-677.

Proceeding of the
International Conference on Electrical, Computer and Telecommunication Engineering
01- 02 December 2012 (ICECTE2012), RUET, Rajshahi-6204, Bangladesh

ICECTE2012: PI-0077

Determination of an Optimum Dispersion Level for a Reconfigurable Optical Add-Drop Multiplexer (ROADM)

Abdul Khaleque[1], Pritom Das[2] and Md. Imran Hasan[3]
[1&2]Department of Electrical and Electronic Engineering,
[3]Department of Electronic and Telecommunication Engineering,
Rajshahi University of Engineering and Technology, Rajshahi-6204, Bangladesh.
E-mail: khaleque_eee@yahoo.com, pritomeee07@gmail.com, imranruet@yahoo.com

ABSTRACT
In this paper, an optimum dispersion level for a network involving reconfigurable optical add-drop multiplexer (ROADM) is presented which will be helpful to reduce noise and increase the transmission efficiency of optical networks involving ROADMs. The result shows an optimum dispersion in which ROADM exhibits the best performance. The simulation approach is used by Optsim, an excellent optical network simulator.

KEY WORDS: Eye opening, eye closure, Q value, Bit error rate (BER), Jitter.

1. INTRODUCTION:

Dispersion is the name given to any effect wherein different components of the transmitted signal travel at different velocities in the fiber, arriving at different times at the receiver. A signal pulse launched into a fiber arrives smeared at the other end as a consequence of this effect [1]. In an optical network dispersion must occur which affects the soundness of transmission. The solution is to compensate the dispersion using extra devices such as fiber brag grating, phase conjugator etc. In case of the networks involving ROADM compensating dispersion does not end the problem. In this case there is a need to find an optimum dispersion level. This level can be determined by observing the change in some performance parameters with variation of dispersion such as Q value, BER, eye opening, eye closure and Jitter.

Q value indicates the quality of a signal with respect to its signal-to-noise ratio (SNR). It involves all physical impairments of the signal like noise, non-linear effects, and dispersion. These impairments seriously degrade the signal. Consequently, a higher value of the Q value means a better SNR [2].

Bit error rate (BER) is equally significant as Q value. In digital communication systems, the decision when to sample and whether the sampled value represents a binary 1 or 0 is affected by noise and signal distortion in the real system and there is nonzero probability of an erroneous decision. Therefore, the received signal quality is directly related to BER, which is a major indicator of the quality of the overall system.

Eye opening is another important parameter. A larger eye opening signifies less noise or distortion and therefore a higher quality of signal [3]. Eye closure is inversely related to eye opening. Smaller eye closure ensures better signal quality. Jitter can be defined as the deviation of the significant instances of a signal from their ideal location in time [4]. It is convenient to keep jitter as low as possible.

Among these parameters Q value and BER are most significant because they provide evaluation of overall signal rather than any particular optical parameter [5].

This paper is intended to outline a process to find an optimum dispersion level for a network involving Reconfigurable Optical Add-Drop Multiplexer (ROADM).

2. MODELING AND METHODS

2.1 Simulation Circuit

Fig. 1 depicts a network in which 16-channel WDM OC-192 signal is transmitted over a medium haul link. The 16 channels are spaced at 50 GHz. The signal is pre-amplified by an erbium doped fiber amplifier (EDFA) booster and transmitted over dispersion shifted fiber of 200 km. A four-channel ROADM is placed in the middle of the link. The transmitter and receiver subsystems are in compliance with the synchronous optical network (SONET) standard. The fiber dispersion is varied from 0.1 to 4.0 ps/nm.km through parametric runs. In this way the system performance can be optimized in terms of fiber dispersion. Channels 13, 14, 15 and 16 are dropped at the ROADM and channels 1, 5, 9 and 13 are detected at the receiver end. At the receiver section,

channels are monitored for the pre specified parameters.

2.2 Optical Signal to Noise Ratio

Optical signal to noise ratio is directly related to Q and BER. The logarithmic value of Q (in dB) is related to the optical signal to noise ratio (OSNR) by [6]:

$$Q_{dB} = 20\log\sqrt{OSNR}\sqrt{\frac{B_0}{B_c}} \quad \text{.....(Eq. 1)}$$

where B_0 is the optical bandwidth of the end device (photodetector) and B_c is the electrical bandwidth of the receiver filter.

Therefore, Q (dB) is shown as

$$Q_{dB} = OSNR + 10\log\frac{B_0}{B_c} \quad \text{.....(Eq. 2)}$$

In other words, Q is somewhat proportional to the OSNR**.** Again, BER is related with Q value by [6]

$$BER = \frac{1}{2}\,\text{erfc}\left(\frac{Q}{\sqrt{2}}\right) \quad \text{.....(Eq. 3)}$$

Therefore, if Q and BER can be optimized optical signal to noise ratio will also improve. This is a very important requirement for better performance of an optical network.

2.3 Shannon Capacity and Spectral Efficiency

Improvement of OSNR will also improve Shannon capacity and spectral efficiency of the network. Shannon capacity C is related with OSNR by [7]:

$$C = B\log(1 + OSNR) \quad \text{.....(Eq. 4)}$$

And, spectral efficiency S is given by

$$S = \frac{B}{\Delta f}\log_2(1 + OSNR) \quad \text{.....(Eq. 5)}$$

Here, *B* denotes the occupied bandwidth per channel, Δf denotes the channel spacing, C denotes the capacity per channel and S denotes the spectral efficiency limit.

Therefore, improved Q and BER i.e. improved optical SNR will result in increased information capacity of channels and increased spectral efficiency.

From sections 2.2 and 2.3, it can be concluded that optimizing Q and BER should be given maximum emphasis to optimize the performance of the network.

3. SIMULATION RESULTS AND ANALYSIS

Output characteristics of the pre specified parameters at different dispersion levels are obtained by simulation shows that how different parameters varies with change in dispersion. Those results are compiled in **Table 1**.

Values of the performance parameters specified before i.e Q value, eye opening, eye closure, jitter and BER corresponding to different values of dispersion are also shown in the table. The values that ensure best performance for each parameter are indicated in bold form and distinguished by asterisk symbol.

3.1 Q Value

From **Table 1** it is seen that Q for channel 1 and channel 5 is maximum at 1 ps/nm.km while that for channel 9 and channel 13 is maximum at 2 ps/nm.km and 4 ps/nm.km, respectively. The performance of maximum number of channels optimize at 2 ps/nm.km. For channel 1, 3 and 5 performance will be excellent if the dispersion value is kept between 1 ps/nm.km and 2ps/nm.km, as close to 1 ps/nm.km as possible (since performance of maximum number of channels optimize at 2 ps/nm.km). Now for channel 13, second maximum Q is obtained at 1 ps/nm.km which is same as channel 1 and 3. Differnce between maximum Q and second maximum Q is 0.922669 dB.

This is also true for channel 9. Therefore, optimum performance in terms of Q value will be obtained at 1 ps/nm.km or at between 1 and 2 ps/nm.km with a close proximity to 1 ps/nm.km.

3.2 Bit Error Rate

Like Q value, lowest BER is obtained at 1 ps/nm.km at for channel 1 and 5, at 2 ps/nm.km for channel 9 and at 4 ps/nm.km for channel 13. Howerver, it can again be assumed that optimum performance in terms of BER is obtained at 1 ps/nm.km or at between 1 and 2 ps/nm.km with a close proximity to 1 ps/nm.km.

3.3 Eye opening and Eye closure

From **Table 1**, it is clear that maximum eye opening for every channel occurs at 2 ps/nm.km. Therefore, in terms of eye opening, best performance can be obtained at 2 ps/nm.km.On the other hand, lowest eye closure occurs at 1 ps/nm.km for channel 1 and channel 5, at 2 ps/nm.km for channel 9 and at 3 ps/nm.km for channel 13. In case of channel 13, second lowest eye closure occurs at 2 ps/nm.km and difference between lowest and second lowest eye closure is 0.093192 a.u. In this case optimum performance can be obtained if dispersion level is kept between 1 and 2 ps/nm.km with a close proximity to 2 ps/nm.km.

3.4 Jitter

Lowest value of jitter is obtained at 2 ps/nm.km for channel 5 and 9 and at 4 ps/nm.km for channel 1 and 13. Therefore it will be suitable if dispersion level is chosen between 2 and 4 ps/nm.km. Considering the second and third lowest values of jitter for channel 1 and channel 13, performance

will be satisfactory enough if dispersion is kept in a proximity to 2 ps/nm.km.

4. CONCLUSIONS

An investigation has been carried out to determine optimum dispersion level for the best performance of an optical network involving ROADM. The optimum dispersion level is determined by analyzing different performance parameters. Since primary emphasis must be put on Q and BER, the dispersion level should be kept between 1 ps/nm.km with a close proximity to 1 ps/.nm.km. Again, since eye opening and closure is also important dispersion should be kept in middle point between 1 ps/nm.km and 2ps/nm.km which can be near 1.4, 1.5 or 1.6 ps/nm.km. This will also keep the jitter suitable. Thus, the performance of the network can be optimized.

The results and observations may be utilized for developing methods of improving the network performance. This will be helpful in noise reduction and distortion management.

5. FUTURE WORK

Further investigations can be carried out to find a way of determining more accurate optimum dispersion level. Also, a suitable technique can be derived to maintain the dispersion at the desired optimum level.

6. ACKNOWLEDGEMENTS

The authors thank The Almighty for this work. The authors respectfully express their gratitude to Dr. S. M. Abdur Razzak, Associate Professor, Department of EEE, RUET for his kind suggestions. The authors are also grateful to the teachers and staffs of the Department of EEE, RUET.

REFERENCES

[1]. Rajiv Ramaswami, Kumar Sivarajan, Galen Sasaki, "Optical Networks", Morgan Kaufmann, 3rd Edition September, 2009.

[2]. Vladimír Tejkal, Miloslav Filka, Jan Šporik, Pavel Reicher, "Possibilities of increasing Power Budget in optical networks" Elektrorevue, VOL 1, No 4, December 2010.

[3]. M. Niszanský, "Modeling and Optimization of Broadband Electrical Interconnects and Housing for Optical Communication System", Doctoral thesis, Erlangen Nuremberk, 2005.

[4]. Johnnie Hancock, "Jitter Understanding it, Measuring It, Eliminating It Part 1: Jitter Fundamentals", High Frequency Electronics, April 2004.

[5]. Martin Nordal Petersen, "Performance Monitoring in the Next Generation of Optical Networks", presented at Photonics in Switching Conference, 2006.

[6]. Ashwin Gumaste, Tony Antony, DWDM Network Designs and Engineering Solutions, Cisco press, 2003.

[7]. Joseph M. Kahn, Keang-Po Ho, "Spectral Efficiency Limits and Modulation/Detection Techniques for DWDM Systems", IEEE Journal Of Selected Topics In Quantum Electronics, VOL. 10, No. 2, April 2004.

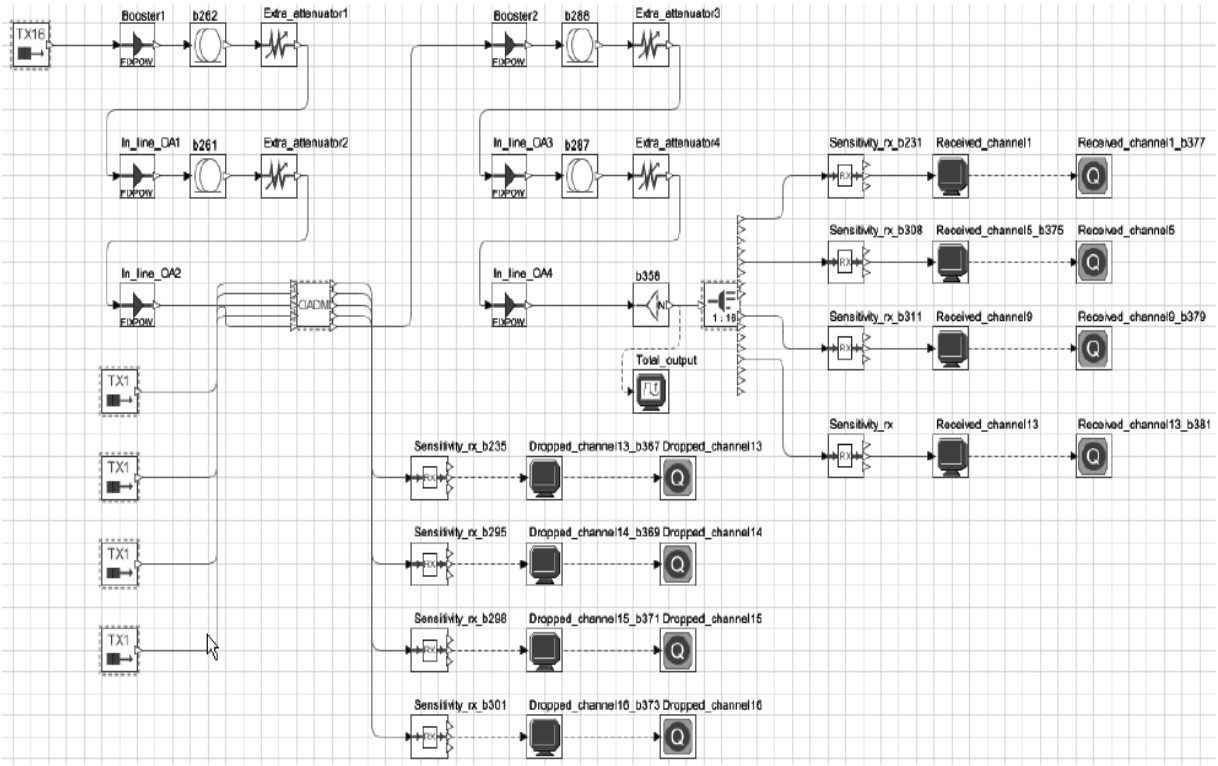

Fig. 1: Simulation circuit of an ROADM.

Table 1: Simulation results

Channel	Dispersion (ps/nm.Km)	Q value (dB)	Eye Closure (dB)	Eye opening	Jitter (ns)	BER
Channel 1	0.1	17.931901	2.404164	0.000409508	0.021238	9.945×10^{-015}
	1	**23.330528***	**0.832178***	0.000586572	0.0225275	**10^{-040}***
	2	20.707309	1.353270	**0.000703373***	0.0209409	9.56202×10^{-027}
	3	19.727075	1.228110	0.000510625	0.0208664	2.10898×10^{-021}
	4	18.469238	1.661052	0.000448739	**0.0200386***	1.67493×10^{-016}
Channel 5	0.1	14.300050	2.938833	0.000490254	0.0225512	8.28034×10^{-008}
	1	**22.896894***	**0.910247***	0.000728808	0.0190447	**10^{-040}***
	2	21.512407	0.917885	**0.000745696***	**0.0182992***	9.34982×10^{-032}
	3	19.848131	1.261258	0.00067135	0.0189719	1.75812×10^{-022}
	4	17.773205	1.578694	0.000614277	0.0186398	1.09979×10^{-014}
Channel 9	0.1	8.083592	12.434117	0.0000630552	0.0218945	0.00691968
	1	21.693342	1.143623	0.00085632	0.0198167	5.75365×10^{-034}
	2	**21.992328***	**1.047824***	**0.00088476***	**0.0185171***	**1.43101×10^{-035}***
	3	20.049059	1.339578	0.000844287	0.0200255	4.36511×10^{-023}
	4	18.249481	1.588198	0.000790099	0.019292	4.13839×10^{-016}
Channel 13	0.1	6.509753	9.184575	0.000013626	0.0221535	0.0188268
	1	16.294671	2.355173	0.000069786	0.0232394	3.3788×10^{-011}
	2	15.941647	2.015600	**0.0000805135***	0.020935	3.15487×10^{-010}
	3	16.069658	**1.922408***	0.0000756022	0.0194962	8.78934×10^{-011}
	4	**17.21737***	2.767085	0.0000710999	**0.0186944***	**2.87392×10^{-013}***

Proceeding of the
International Conference on Electrical, Computer and Telecommunication Engineering
01- 02 December 2012 (ICECTE2012), RUET, Rajshahi-6204, Bangladesh
ICECTE2012: PI-0079

Adaptive RLS Based Channel Estimation Techniques for CDMA Systems

Ratan Kumar Ghosh, Md. Masud Rana, Md. Mostafizur Rahman
Department of Electronics and Communication Engineering, Khulna University of Engineering and Technology, Khulna-9203, Bangladesh
E-mail: ghosh_ratan29@yahoo.com, mrana928@yahoo.com, mostafiz963@yahoo.com

ABSTRACT
Nowadays high speed data transformation and reliable communication is well desired. For this reason channel estimation becomes an important topic. In the last few years, many works have been done over reduced rank channel estimation. Although many of them have good performances but provide high algorithmic complexity. In this paper, we tried to describe an adaptive recursive least square (RLS) based reduced rank channel estimation technique with better performance at an acceptable complexity. We describe a reduced rank algorithm and apply this algorithm to a code division multiple access (CDMA) system. The performance of this algorithm is compared with full rank RLS algorithm. The simulated results of this algorithm shown that it may be a good solution with better performance and lower complexity at a situation where the number of samples is less.

KEY WORDS: Channel estimation, Adaptive reduced rank RLS algorithm, Full rank RLS algorithm, CDMA.

1. INTRODUCTION

In case of adaptive filtering technique [1], different algorithms have been developed with different performance and complexity. In the last few year, reduced rank signal processing technique has been applying on different applications where the numbering of filtering elements are high [2], [3]. The performance and complexity of this type algorithm depend on the full rank input data matrix r(i) of the receiver and the total number of elements M of the filter [1]. If the filter elements M are large, a large number of samples or received symbols are required to train the system. Again, in case of mobile communication adaptive filter having large number of elements provide very poor performance when the signal are highly affected by noise as well as interference.

For solving the above problem adaptive reduced rank technique has got the best dependable way. Reduced rank channel estimation technique provides better bit error rate with lower algorithmic complexity at low sample support situation [4], [5], [6]. Problem of feature selection is the source of reduced rank channel estimation [7]. The main goal of channel estimation is to represent the received data matrix in way that needs small number of symbols to represent and most of the information (as much as possible) should be preserved of the received data matrix [7]. There are different adaptive reduced rank channel estimation techniques such as eigen decomposition techniques [8, 9], the multistage wiener filter (MWF) [10, 11], the auxiliary vector filtering (AVF) algorithm [12, 13], the adaptive interpolated FIR filter with time varying interpolators [14, 15]. There are different problems with the above adaptive reduced rank channel estimation techniques. The main problem is that all the methods depend on the estimation of R. We developed an adaptive reduced rank channel estimation technique based on the interpolation, decimation and reduction. In this technique, the filtering element is reduced. As a result computational complexity decreases and provides faster convergence rate.

In our work we describe an algorithm based on interpolation, decimation and reduction. We applied this algorithm on a CDMA system and compared the performance with the performance of the rank RLS.

The rest of the paper is arranged as follows: Section 2 represents the channel estimation model, section 3 represents the simulation results and section 4 represents the conclusion.

2. CHANNEL ESTIMATION

We dealt with the adaptive reduced rank channel estimation technique based on interpolation, decimation and reduction filtering. The main function of reduced rank channel estimation techniques is to extract the most important features from the received data matrix so that the system needs to process small number of data. As a result dimensionality of the processed matrix decreases and algorithmic complexity also decreases.

This dimensionality reduction is performed by mapping the received data matrix into a new data matrix of lower dimensionality than the received data matrix. Consider the received data matrix r(i) of size M×1 and the dimensionality reduction is done by a projection matrix S of size M×D [20] than

$$\bar{r}(i) = S^H r(i) \quad (1)$$

Where r(i) is the received data matrix and $\bar{r}(i)$ is the received data matrix after dimensionality reduction.

The design of the projection matrix S is the main problem for the reduced rank channel estimation techniques. In this algorithm we designed the projection matrix based on the interpolation and decimation. Here, rank reduction is done by eliminating insignificant data during filtering. After that by using an interpolator the eliminated data samples are recreated. The input data matrix can be express as r(i)=$[r_o^{(i)} \quad r_1^{(i)} ..... r_{M-1}^{(i)}]]^T$ and the interpolator filter V(i)=$[v_o^{(i)} .....v_{N_I-1}^{(i)}]$ then the interpolated matrix $r_I(i)$ can be express as

$$r_I(i) = V^H(i)\, r(i) \qquad (2)$$

Dimensionality reduction is performed by a decimation matrix S of size D×M where D=M/L, M is the no. Of samples and L is the decimation factor. Here, we consider D as a fixed. So, the rank reduction is performed as follows

$$\bar{r}_D = S\, r_I(i) \qquad (3)$$

3. SIMULATED RESULTS

In this section we deal with the simulated results of this algorithm. We apply this adaptive reduced rank filtering scheme on DS-CDMA system to analysis the bit error rate (BER) performance, computational complexity of this adaptive algorithm with full rank algorithm of channel estimation. We also analyze the effective of increasing no. of user on the bit error rate performance and the effect of channel tab variation.

In this section we tried to discuss the simulated performance of this adaptive reduced rank filtering scheme on DS-CDMA system using MATLAB. For the simulation we consider the following consideration

Processing gain, $G_p = 32$
Bit energy, E = 1
User, U = 8
No of transmitting symbol, Nts = 1500
No of scattering elements = 20

3.1 BER Analysis

The following figure show bit error rate (BER) performance of theoretical, full rank RLS and reduced rank RLS of a CDMA system. It indicates that the theoretical BER achieves the convergence very fast. But practically it does not occur. Reduced rank reduced-RLS has got the convergence faster than full rank RLS.

Fig. 1 shows the bit error rate performance for 5-tab channel when Doppler frequency f_d = 20Hz of a CDMA system using full rank RLS and reduced rank RLS. Fig. 2 shows the bit error rate performance for 5-tab channel when Doppler frequency f_d = 40Hz of a CDMA system using full rank RLS and reduced rank RLS. Fig. 3 is for 3-tab channel when Doppler frequency 20Hz of a CDMA system.

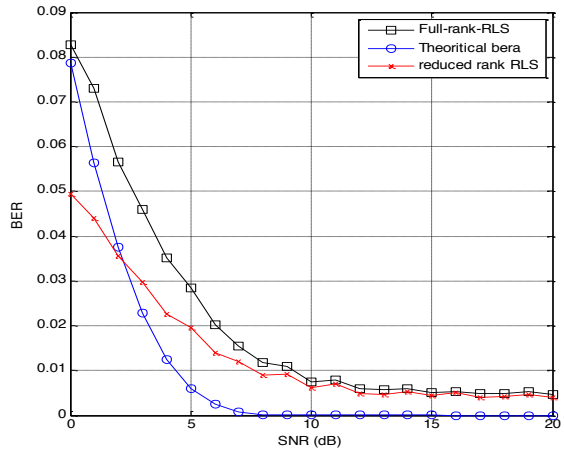

Fig. 1: Comparison of BER performance of theoretical, full rank RLS, reduced rank RLS of a CDMA system for 5-tab channel when f_d = 20 Hz

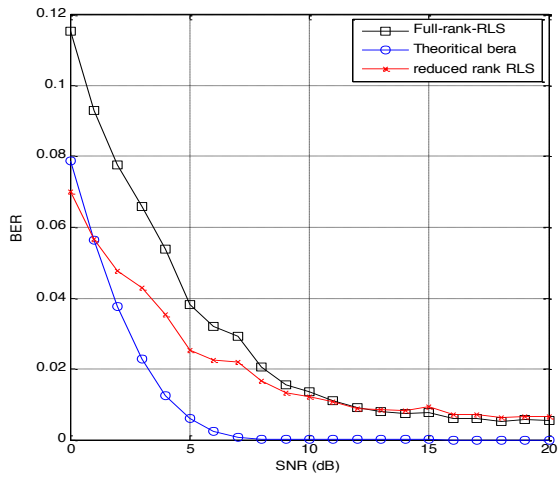

Fig. 2: Comparison of BER performance of theoretical, full rank RLS, reduced rank RLS of a CDMA system for 5-tab channel when f_d = 40 Hz.

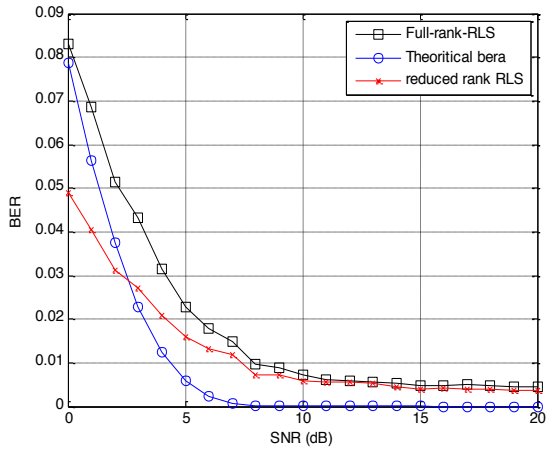

Fig. 3: Comparison of BER performance of theoretical, full rank RLS, reduced rank RLS of a CDMA system for 3-tab channel when f_d =20 Hz

Fig. 4 shows the bit error rate performance for 5-tab channel when Doppler frequency f_d = 40Hz of a

CDMA system using full rank RLS and reduced rank RLS.

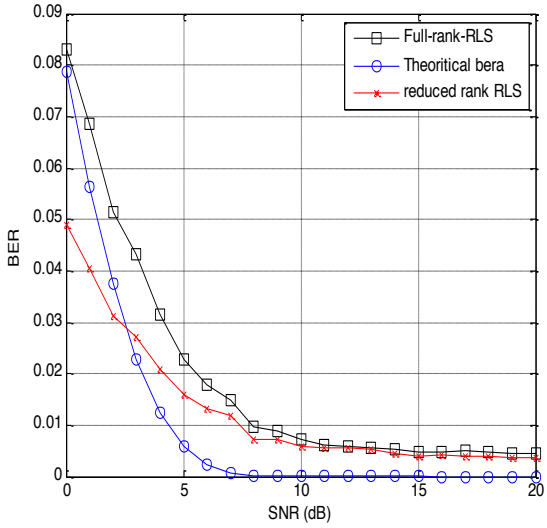

Fig. 4: Comparison of BER performance of theoretical, full rank RLS, reduced rank RLS of a CDMA system for 3-tab channel when $f_d = 40$ Hz

3.2 Complexity Analysis

Fig. 5 shows the arithmetic complexity of full rank RLS and reduced rank reduced rank-RLS. This figure represents the no. of arithmetic operations required for different no. of received symbols. The reduced rank RLS needs to perform less no of arithmetic operation than full rank RLS because the rank of the received symbols is reduced and the algorithm process less no. of symbols to train the system.

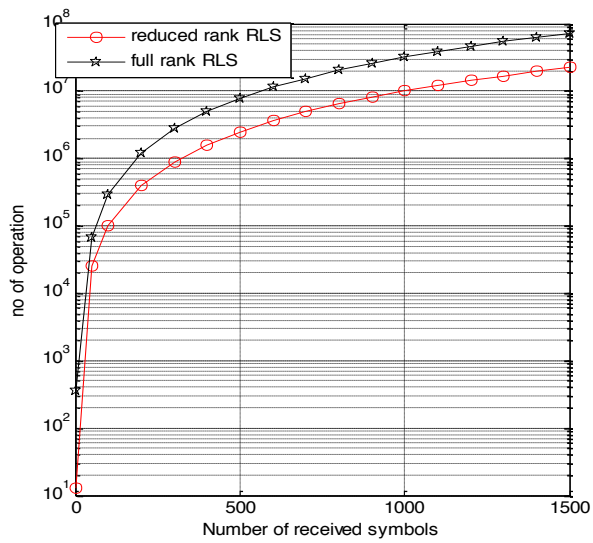

Fig. 5: Comparison of arithmetic complexity Full rank RLS and reduced rank RLS.

3.3 User Variation

The following figure (Fig. 6 and Fig. 7) shows the effect of increasing the number of user of CDMA system on bit error rate. It indicates that the bit error rate increases with the increase of the number of users because if many users transmit at the same time then there will be high collision. In case of full rank RLS the increasing rate is very high than reduced rank RLS.

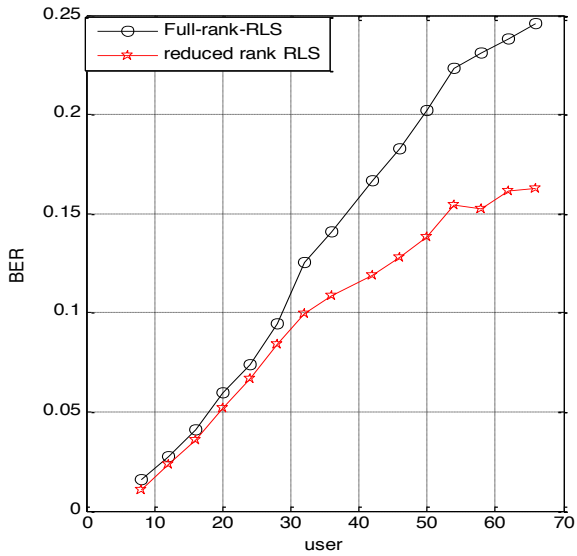

Fig. 6: The effect of user variation on BER of a CDMA system when $f_d = 20$ Hz for 3-tab channel

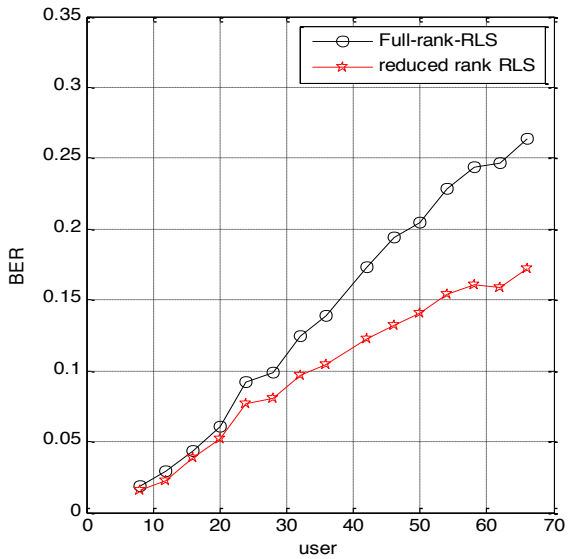

Fig. 7: The effect of user variation on BER of a CDMA system when $f_d = 40$ Hz

In the fig. 6 when number of user 60, the bit error rate for full rank RLS and reduced rank RLS for CDMA system are respectively 0.23 and 0.16 for 3-tab channel when Doppler frequency 20 Hz. The fig. 7 the represents the bit error rate performance for reduced rank RLS and full rank RLS for CDMA system with 3-tab channel when Doppler frequency 40. When the number of user is 60 the bit error rate

for full rank RLS and reduced rank RLS are 0.24 and 0.17.

4. CONCLUSIONS

This paper represents a low complexity adaptive reduced rank signal processing scheme for performing dimensionality reduction in general adaptive filtering problems which is applicable for code-division multiple-access (CDMA) systems. For adaptive filtering algorithms different tradeoffs between performance and complexity is considered. The convergence of these algorithms depends on the full-rank covariance matrix of the input data and the number of elements in the filter. Reduced-rank filtering is a very powerful technique due to its effectiveness in low-sample-support situations where it can offer improved convergence performance at a considerable complexity. The reduced rank adaptive algorithm provides better bit error rate performance with acceptable complexity and higher convergence rate even at a low sample support situation. The reduced-rank filtering scheme allows a substantially better convergence and tracking performance than existing reduced-rank and full-rank schemes. This improvement is due to the dimensionality reduction carried out by this adaptive scheme that allows the use of adaptive algorithms with very small filters. The algorithms can also be applied to other applications such as MIMO systems, equalization, GPS jammer suppression and channel estimation.

5. FUTURE WORK

In future we will try to apply our proposed adaptive reduced rank algorithm for MIMO systems and GPS jammer and compare the performance with the existing algorithms.

REFERENCES

[1]. P. S. R. Diniz, Adaptive Filtering: Algorithms and Practical Implementations, 2nd ed. Boston, MA: Kluwer, 2002

[2]. P. Clarke and R. C. de Lamare, "Adaptive set-membership reducedrank interference suppression for DS-UWB systems," in IEEE ISWCS, September 2009.

[3]. R. C. de Lamare and R. Sampaio-Neto, "Adaptive reduced-rank mmse parameter estimation based on an adaptive diversity combined decimation and interpolation scheme," in Int. Conf. on Acoustics, Speech and Signal Process., Hawaii, April 2007.

[4]. M. L. Honig and H. V. Poor, "Adaptive interference suppression," in Wireless Communications: Signal Processing Perspectives, H. V. Poor and G. W. Wornell, Eds. Englewood Cliffs, NJ: Prentice-Hall, 1998, ch. 2, pp. 64–128.

[5]. S. Verdu, Multiuser Detection. Cambridge, U.K.: Cambridge Univ. Press, 1998.

[6]. L. L. Scharf, "The SVD and reduced rank signal processing," Signal Process., vol. 25, no. 2, pp. 113–133, 1991.

[7]. L. L. Scharf and D. W. Tufts, "Rank reduction for modeling stationary signals," IEEE Trans. Acoust., Speech Signal Process., vol. ASSP-35, pp. 350–355, Mar. 1987.

[8]. L. L. Scharf and B. vanVeen, "Lowrank detectors for Gaussian random vectors," IEEE Trans. Acoust., Speech Signal Process., vol. ASSP-35, pp. 1579–1582, Nov. 1987.

[9]. A. M. Haimovich and Y. Bar-Ness, "An eigenanalysis interference canceler," IEEE Trans. Signal Process., vol. 39, pp. 76–84, Jan. 1991.

[10]. J. S. Goldstein, I. S. Reed, and L. L. Scharf, "A multistage representation of theWiener filter based on orthogonal projections," IEEE Trans. Inf. Theory, vol. 44, Nov. 1998.

[11]. M. L. Honig and J. S. Goldstein, "Adaptive reduced-rank interference suppression based on the multistage Wiener filter," IEEE Trans. Commun., vol. 50, no. 6, Jun. 2002.

[12]. D. A. Pados and S. N. Batalama, "Low complexity blind detection of DS/CDMA signals: Auxiliary-vector receivers," IEEE Trans. Commun., vol. 45, pp. 1586–1594, Dec. 1997.

[13]. D. A. Pados and S. N. Batalama, "Joint space-time auxiliary-vector filtering for DS/CDMA systems with antenna arrays," IEEE Trans. Commun., vol. 47, no. 8, Sep. 1999.

[14]. R. C. de Lamare and R. Sampaio-Neto, "Adaptive reduced-rankMMSE filtering with interpolated FIR filters and adaptive interpolators," IEEE Signal Process. Lett., vol. 12, no. 3, Mar. 2005.

[15]. R. C. de Lamare and R. Sampaio-Neto, "Adaptive interference suppression for DS-CDMA systems based on interpolated FIR filters with adaptive interpolators in multipath channels," IEEE Trans. Veh. Technol., vol. 56, no. 6, Sept. 2007.

Proceeding of the
International Conference on Electrical, Computer and Telecommunication Engineering
01- 02 December 2012 (ICECTE2012), RUET, Rajshahi-6204, Bangladesh

ICECTE2012: PI-0080

Numerical Investigation of Octagonal Holey Fibers as Dispersion Compensator

Md. Selim Habib[1], Md. Samiul Habib, S. M. Abdur Razzak, M. A. G. Khan
Department of Electrical & Electronic Engineering, Rajshahi University of Engineering & Technology, Rajshahi-6204, Bangladesh.
[1]E-mail: selim041073@yahoo.com

ABSTRACT
This paper presents octagonal holey fiber for dispersion compensation covering the entire S+C+L wavelength bands. The finite element method with circular perfectly matched absorbing layers boundary condition is used to investigate the guiding properties. This kind of fiber has large negative chromatic dispersion close to –480 ps/(nm.km) at 1.55 μm and relative dispersion slope (RDS) close to that of a conventional single-mode optical fiber (SMF). In addition to this, relative dispersion slope, residual dispersion, and effective residual dispersion of the proposed holey fiber are also reported and discussed.

KEY WORDS: Holey fiber, Dispersion-compensating fiber, Residual dispersion, Finite element method.

1. INTRODUCTION

Over the past few years, holey fibers (HFs) have become one of the most preferred platforms for the design of electromagnetic structures. Holey fibers (HFs) or photonic crystal fibers (PCFs) or microstructure optical fibers have a microscopic array of air channels running down their length that make a low index cladding around the undoped silica core [1]. Such holey claddings in HFs help tuning dispersion slope and controlling confinement losses in a way that was not possible in conventional fibers [2]. This novel property of HFs helps in tuning transmission characteristics namely dispersion, nonlinearity, and birefringence in smart ways. As a result HFs are finding applications nowadays in different areas of communication systems [3]. Such fibers are therefore, suitable for both linear and nonlinear optics applications [3]. HFs are desirable because they offer additional design parameters such as air-hole diameter *d*, air-hole rings, hole-to-hole spacing, and pitch Λ, and much greater flexibility in the design of transmission properties to achieve the requirements of various applications [4].

The dispersion must be compensated in the long-distance optical data transmission system to suppress the broadening of pulse. One way to realize this is to use the dispersion compensating fibers (DCFs), which are designed to have large negative dispersion [5]. To minimize the insertion loss and reduce the cost, the DCFs should be as short as possible, and the magnitude of negative dispersion should be as large as possible. To efficiently compensate the dispersion of all the frequencies of dense wavelength division multiplexing (DWDM), the negative dispersion of DCFs should span a wide spectrum. The dispersion and dispersion slope should be compensated at the same time [6]. So when we design a DCF, we should take into consideration dispersion, dispersion slope, relative dispersion slope, bandwidth, and mode property [7].

Various HF designs have been proposed to control different transmission properties, such as hexagonal HFs (HHFs), square HFs (SHFs), and honeycomb fibers [8],[17], [18]. It is described in the literature that exact periodic lattice arrangements for air holes are not absolutely necessary to achieve the guidance of light based on the total internal reflection mechanism. Furthermore, octagonal holey fibers (OHFs) possess the advantages of a wider wavelength range operating in the single-mode region, a more circular field distribution, and a significantly less confinement loss [9].

In this paper, we present pure silica dispersion compensating octagonal holey fibers (DC-OHFs) for optimizing the dispersion compensation of standard SMFs in the entire telecommunication band (1.46–1.64) by using full-vector finite-element method (FEM). From the numerical simulation results, it is found that it is possible to obtain larger negative dispersion, better dispersion slope, and low confinement loss in the entire telecommunication band. Another main advantage is that, compared with previously presented DC-HFs, the design procedure for this proposed novel DC-HFs structure could be more efficient and easier because relatively fewer geometrical parameters are need to be optimized.

2. GEOMETRY OF THE PROPOSED DC-OHFS

Fig. 1 shows the transverse cross-section of the proposed DC-OHFs which contains five air-hole

rings. The refractive index of the background silica is assumed to be 1.45. The cladding is formed by a triangular lattice of air-holes. The air holes are arranged in an isosceles triangle lattice with a vertex angle of 45° and geometric parameters of the air-hole diameter d, the spacing between air-holes on the same air-hole ring is Λ_1, which is related to the spacing between the adjacent rings Λ by the expression $\Lambda_1 = 0.765\ \Lambda$. In all the calculations in this work, the number of air-hole rings is assumed to be five in order to simplify as much as possible the structural composition of the HF. By keeping air-filling fractions d/Λ at bigger values, we concentrate to reduce confinement loss as much as possible and to better mode field confinement.

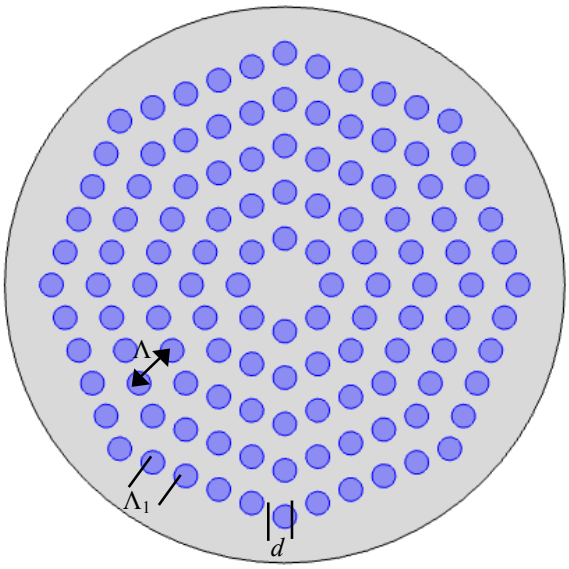

Fig. 1 Transverse cross-section of the DC-OHF showing the air-hole channels diameter, d and pitch, Λ.

3. NUMERICAL METHODS

The finite element method with circular perfectly matched boundary layers (PML) is used to calculate the effective refractive index, n_{eff}, chromatic dispersion, confinement loss, and effective area of HFs.

The effective refractive index of the base mode is given as neff $\beta = k_0$, where β is the propagation constant and $k_0 = 2\pi/\lambda$ is the free-space wave number. Once the modal effective index n_{eff} is solved, the dispersion parameter $D(\lambda)$ can be obtained as [12]

$$D(\lambda) = -\frac{\lambda}{c}\frac{d^2\,\mathrm{Re}[neff]}{d\lambda^2} \qquad (1)$$

in units of ps/(nm.km), where λ is the operating wavelength and c is the velocity of light in a vacuum. The material dispersion given by the three-term Sellmeier formula is directly included in the calculation [13].

Owing to the positive dispersion and dispersion slope of the SMF, the fundamental requirements of a DCF for WDM operation are a large negative dispersion and a dispersion slope over a broad range of wavelengths. Assuming that a fiber link consists of a transmission fiber SMF of length L_{SMF} with the dispersion $D_{SMF}(\lambda)$ and a DCF of length L_{DCF} with the dispersion $D_{DCF}(\lambda)$, the effective dispersion after compensation, $D_e(\lambda)$, on the fiber link in series can be written as [10]

$$D_e(\lambda) = (D_{SMF}\,L_{SMF} + D_{DCF}\,L_{DCF})/(L_{SMF}+L_{DCF}) \qquad (2)$$

To compensate for the accumulated dispersion of the SMF over a range of wavelengths, the following conditions must be satisfied [11]

$$\mathrm{RDS} = S_{SMF}\,/\,D_{SMF} = S_{DCF}\,/\,D_{DCF} \qquad (3)$$

S_{SMF} and S_{DCF} are the dispersion slopes for the SMF and DCF, respectively. The unit for the relative dispersion slope RDS is nm^{-1}. Once the RDS of the DCF is close to that of the single mode fiber, SMF, the design of the broadband DCF is accomplished. The RDS is used to judge DC satisfaction over a range of wavelengths.

4. NUMERICAL RESULTS AND DISCUSSION

The guiding properties of OHFs have been numerically investigated as a function of the geometric characteristics that is the hole-to-hole spacing, Λ and the air-hole diameter, d in the fiber cross-section. Fig. 2 shows the plot of effective refractive index versus wavelength for different pitch, Λ while keeping the air-filling fraction d/Λ to 0.7. It is observed that the effective refractive index decreases with the increase in wavelength and increases with increase of pitch, Λ, which is in good agreement with [14]. Fig. 3 shows the wavelength dependence properties of chromatic dispersion for the OHFs for different pitch, Λ values. It is found that in all cases the OHFs shows high negative dispersion and the dispersion coefficient monotonically decreases with the decrease of pitch, Λ providing better dispersion compensation. Fig. 4 shows the wavelength dependence of chromatic dispersion for optimum design parameters $d/\Lambda = 0.7$ and $\Lambda = 0.95$ µm. It is found that the proposed DC-HFs shows larger negative dispersion coefficients of around –330 to –620 ps/(nm.km) in the wavelength range (1.46-1.64) µm while the dispersion at 1.55 µm is –480 ps/(nm.km) far exceeding the dispersion values of conventional dispersion compensating fibers [11] [typically –100 ps/(nm.km)].

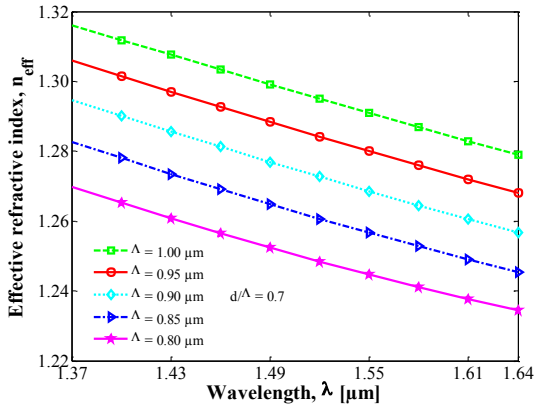

Fig. 2 Effective refractive index as a function of wavelength. The variation of effective refractive index with pitch, Λ is also shown in the figure.

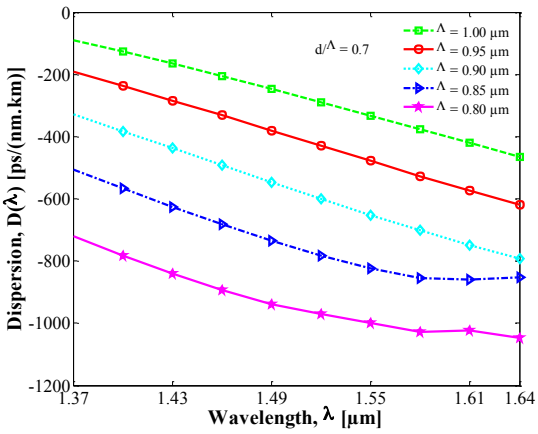

Fig. 3 Chromatic dispersion curves as a function of wavelength of the DC-HFs with d/Λ = 0.7 and different Λ values.

As we considered a simple condition for designing broadband dispersion compensation phenomena, it is worth noting that, at λ = 1.55 μm, the RDS for the dispersion curve with Λ = 0.95 μm, and d/Λ = 0.7 is close to that of the SMF (for the SMF; RDS ≈ 0.0034 nm^{-1}) [11] as shown in Fig. 5. A large negative dispersion coefficient is required to compensate for the accumulated dispersion in the SMF currently installed in WDM systems. Fig. 6 shows the calculated residual dispersion obtained after the dispersion compensation by a 1.45 km long optimized OHF for the dispersion accumulated in one span (40 km long) of the transmission fiber, SMF. It can be observed that the residual dispersion is ±50 ps/nm, which is within the range of ±64 ps/nm, enabling the proposed HF structure to be suitable for 40 Gb/s transmission system [15].

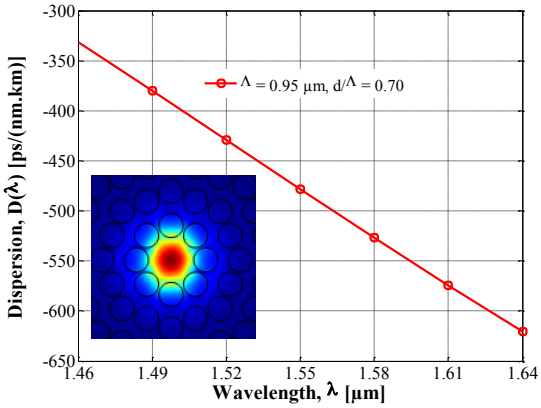

Fig. 4 Wavelength dependence of chromatic dispersion for the optimum design parameters: d/Λ = 0.7 and Λ = 0.95 μm. Insert shows the fundamental mode field at 1.55 μm.

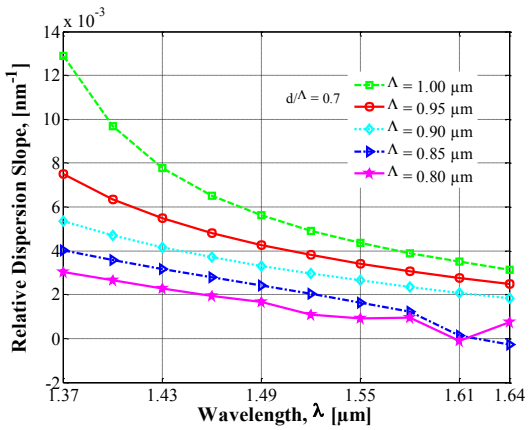

Fig. 5 Relative dispersion slope curves as a function of wavelength of the DC-HFs with d/Λ = 0.7 and different Λ values.

Fig. 7 shows the effective dispersion of the SMF + OHF for the optimum design parameters d/Λ = 0.7 and Λ = 0.95 μm. The effective dispersion should be lower than ±0.8 ps/(nm.km) to compensate for a 40 Gb/s signal [16]. As shown in Fig. 7, with an effective dispersion within a ±0.45 ps/(nm.km) range, it is clearly proved that our proposed OHF (with optimized parameters) is suitable for systems with high bit rates.

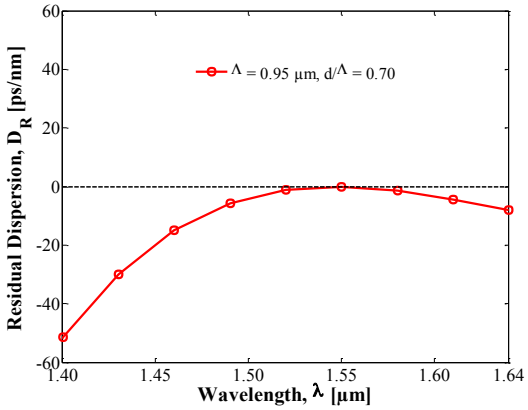

Fig. 6 Residual dispersion curve for the optimum design parameters: $d/\Lambda = 0.7$ and $\Lambda = 0.95$ μm. Here corresponding residual dispersion curve after compensating 40 km SMF link by 1.45 km long optimized HF.

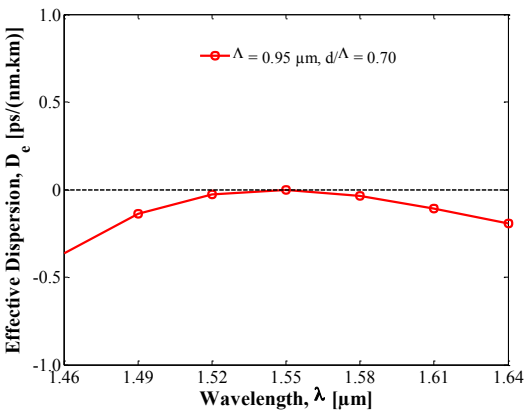

Fig. 7 Effective dispersion curve of SMF and OHF for the optimum design parameters: $d/\Lambda = 0.7$ and $\Lambda = 0.95$ μm.

5. CONCLUSION

In this paper, the chromatic dispersion, residual dispersion, and effective residual dispersion of octagonal holey fibers have been numerically investigated using FEM. The designed OHF has negative dispersion coefficient of about –330 to –620 ps/(nm.km) over the S+C+L wavelength bands and an RDS close to that of installed single mode fiber simultaneously. We also successfully achieved an effective dispersion of ±0.45 ps/(nm.km), in the entire S+C+L wavelength bands, which is suitable for 40 Gb/s transmission system. The designed fiber has a modest number of design parameters, five rings, an air-hole diameter, and an air-hole pitch.

REFERENCES

[1]. J. C. knight, "Photonic crystal fibers," *Nature*, vol. 424, pp. 847–851, 2003.

[2]. J. C. Knight, T. A. Birks, P. S. J. Russell, and D. M. Atkin, "All-silica single-mode optical fiber with photonic crystal cladding," *Opt. Lett.* vol. 21, pp. 1547–1549, 1996.

[3]. S. M. A. Razzak and Y. Namihira, "Proposal for highly nonlinear dispersion-flattened octagonal photonic crystal fibers," IEEE Photonics Technol. Lett., vol. 20, no. 4, pp. 249-251, Feb. 2008.

[4]. K. Saitoh, M. Koshiba, T. Hasegawa, and E. Sasaoka: Opt. Express **11** (2003) 843.

[5]. M. Koshiba, K. Saitoh, Optics Express 11 (2003) 1746.

[6]. S. G. Li, X. D. Liu, and L. T. Hou, "Numerical study on dispersion compensating property in photonic crystal fibers," Acta Phys. Sin. 53, 1880–1886 (2004).

[7]. B. Zsigri, J. Laegsgaard, and A. Bjarklev, "A novel photonic crystal fibre design for dispersion compensation," J. Opt. A Pure Appl. Opt. 6, 717–720 (2004).

[8]. F. Begum, Y. Namihira, S. M. A. Razzak, and N. Zou: IEICE Trans. Electron. E90-C (2007) 607.

[9]. K. Kaneshima, Y. Namihira, N. Zou, H. Higa, and Y. Nagata: IEICE Trans. Electron. E89-C (2006) 830.

[10]. L. P. Shen, W. P. Huang, G. X. Chen, and S. S. Jian: IEEE Photonics Technol. Lett. 15 (2003) 540.

[11]. L. Gruner-Nielsen, S. N. Knudsen, B. Edvold, T. Veng, D. Magnussen,C. C. Larsen, and H. Damsgaard: Opt. Fiber Technol. 6 (2000) 164.

[12]. N. H. Hai, Y. Namihira, F. Begum, S. Kaijage, S. M. A. Razzak, T.Kinjo, and N. Zon: IEICE Trans. Electron. E90-C (2007) 1627.

[13]. G. Agrawal: Nonlinear Fiber Optics (Academic Press, San Diego, CA,1995) 2nd ed., Chap. 1.

[14]. T. Matsui, J. Zhou, K. Nakajima and I. Sankawa, "Dispersion flattened photonic crystal fiber with large effective area and low confinement loss", J. Lightwave Technol. 23(12): 2005, 4178-4183.

[15]. M. N. Islam, 2004. *Raman Amplification for Telecommunications 1 and 2* (Springer-Verlag, New York).

[16]. T. Fujisawa, K. Saitoh, K. Wada, and M. Koshiba: Opt. Express 14 (2006) 893.

[17]. N. G. R. Broderick, T. M. Monro, P. J. Bennett, and D. J. Richardson:Opt. Lett. 24 (1999) 1395.

[18]. J. S. Chiang and T. L. Wu: Opt. Commun. 258 (2006), 170.

Proceeding of the
International Conference on Electrical, Computer and Telecommunication Engineering
01- 02 December 2012 (ICECTE2012), RUET, Rajshahi-6204, Bangladesh
ICECTE 2012: PI-0081

Calibration of Spectroscopic Reflectometer for Thin Film Characterization

Md.Anzan-Uz-Zaman[1], Md.Aliuzzaman[2], Md. Abul Hossion[3], Md. Nasrul Haque Mia[1], Md. Shah Alam[1], Himangshu Kumar Ghosh[1]

[1] Institute of Electronics (IE), [2] RECD, INST
Atomic Energy Research Establishment (AERE), Gonoakbari, Savar,Dhaka, Bangladesh
[3] Applied Physics, Electronics and Communication Engineering, University of Dhaka, Dhaka, Bangladesh.
E-mail: anzan.zaman@gmail.com, jonyphys@yahoo.com

ABSTRACT: *Spectroscopic reflectometer is generally used for measuring the thickness of thin films. Optical techniques are used for this purpose. Optical techniques measure the thickness of thin transparent and semi-transparent layers by analyzing white light interference. Here we have done installation and calibration of a spectroscopic reflectometer at VLSI Lab, IE, AERE. Results regarding calibration are also discussed.*

KEY WORDS: Thin film, Reflectometer, ARC, Thickness, Reflectance.

1. INTRODUCTION: A spectroscopic reflectometer is used for measuring the thickness of a thin transparent and semi-transparent layer. The instrument use optical techniques to determine thin film characteristics by measuring how the film interacts with white light. To perform the functions for which they were designed, thin films must have proper thickness, composition, roughness and other characteristics important to the particular application. These characteristics need to often be measured, both during and after thin film fabrication. Optical techniques are usually preferred for measuring thin films because they are accurate, non-destructive and require little or no sample preparation. The optical wave length range of this instrument is at a range of 380 nm to 1000 nm (White light) and repeatability ±1%. The instrument can be used in the fields of (i) Solar Cell: ARC (anti-reflective coatings) Process (ii) TFT-LCD:SiO_x,SiN_x, Photo Resists, ITO Polyimide (iii) LED: SiO_x, SiN_x, ITO etc [1,2].

2. METHODOLOGY: The two most common optical measurement methods are spectral reflectance/ transmittance and ellipsometry. Spectral reflectance measures the amount of light reflected from a thin film over a range of wavelengths, with the incident light normal to the sample surface. Ellipsometry is similar, except that it measures reflectance at non-normal incidence and at two different polarizations. In general, spectral reflectance is much simpler and less expensive than

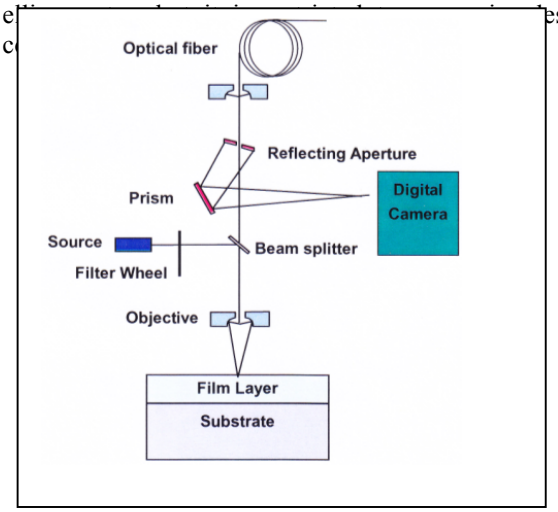

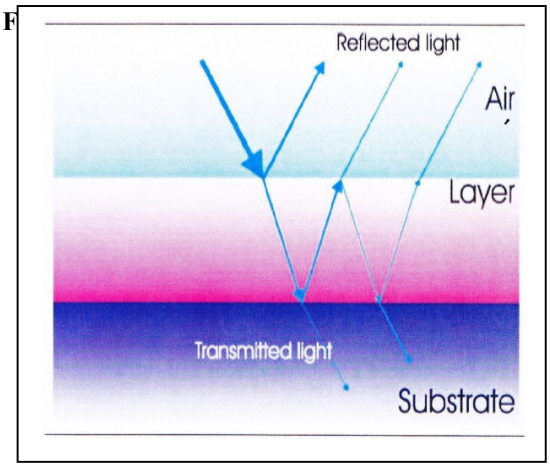

Fig.2: Principle of white Light Interference

The total system consists of five main units i.e. (i) light source (ii) PDA (Photo Diode Array) Box or Spectrometer (iii) Microscopic Unit (iv) Power supply unit for light source and (v) PC. Microscopic

unit can be divided into four parts as (i) Manual Adjustable Magnification (ii) Fiber optic coupling with spectrometer (iii) Digital visualization camera and (iv) Auto focus based on SR system [3,4].

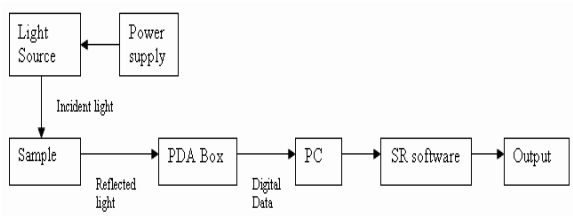

Fig.3 : A Simplified Block Diagram of the Spectroscopic Reflectometer.

The light bulb used here has a rating 6V, 20W. After turn on the lamp, it will take 10 minutes to be stable. Sample is placed to the stage under the microscope. A camera is attached to the microscope to see the view on PC screen. The stage is adjusted to focus on the sample and it is observed on PC. After stable the light source, light is incident on the sample and reflected light is carried out through the fiber optic cable to PDA Box. Fig.1 gives a basic idea how reflected light is collected by PDA Box/ Spectrometer [4]. This unit translates the optical data into digital data which is fed to the PC. SR software manipulates the digital data to measure the thickness of the film. The amplitude and periodicity of the reflectance of thin films are determined by the films thickness, optical constants and other properties such as interface roughness. In reflectometry it is not possible to solve for film properties in closed form, nor it is possible to solve for n and k at each wavelength individually. In practice, mathematical models are used that describe n (Refractive index) and k (Extinct constant) over a range of wavelengths using only a few adjustable parameters. Film properties are determined by calculating reflectance spectra based on varying trial values of thickness and the n and k model parameters, until the calculated reflectance matches the measured reflectance best (Best-Fit-Algorithm).

3. THEORY: Reflectance is defined as

$$R = \frac{I_{refl}}{I_{inc}} \text{----------} (1)$$

where I_{inc} is the incident light intensity and I_{refl} is the reflected light intensity. The tool only measures reflected light intensity I_{refl}. To determine I_{inc} , it is necessary to measure a reference sample with a known reflectance R_0 -"referencing the reflectometer". Reference I_{inc} can be easily derived from the expression [5,6].

$$R_0 = \frac{I_{r0}}{I_{inc}} \text{----------} (2)$$

Best measurements involve good knowledge of R_0 and good quality measurement of intensity. For calibrating the instrument, the stage is taken at the lowest point and then should wait for ten (10) minutes after on the light source to stable it. A small reference sample (TRF 008) is taken to the stage and the tilt part of the case of the sample is focused to check the background. If background curve is at the same range then the device is ready for next operation. The reference sample inside the plastic cover is now focused on and a measurement is done by clicking the spectrometer and reference icon of the SR software for referencing the reflectometer. Again the sample is focused on microscope and a physical measurement is done by clicking spectrometer and measurement icon. The reference sample contains a thin film layer of SiO_2 on SiCr substrate. To measure the thickness of SiO_2 film the following steps should be followed:

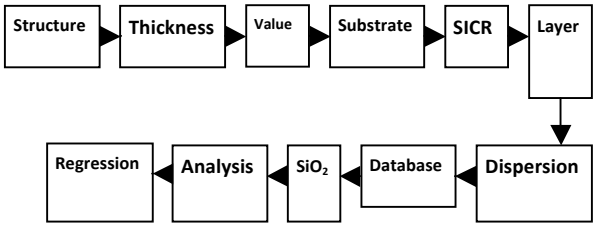

Fig 4: Flow chart for thickness measurement

4. RESULTS: The result of any measurement can be saved for further documentation. The result of calibration is given below:

Table 1: Material information

Index name	Material	Thickness µm	Type	n	K (550 nm)
Ambient	VOID			1.0	0.00
Layer-1	SiO_2	0.14709	EMA	1.466	
Substrate	SiCr			4.086	0.04

Table 2: Standard values

Material	Thickness µm	n	Wave length (λ) in µm
SiO_2	0.146 ± 0.0012	1.467	0.6238

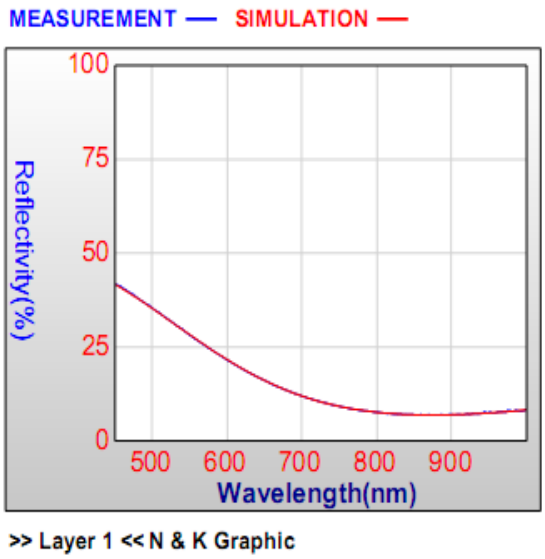

Graph 1: Reflectivity from sample for a range of incident light.

Table 3: Thickness of SiO_2 layer

No of observation	n	Thickness µm
1	1.46664	0.14702
2	1.46642	0.14701
3	1.46669	0.14699
4	1.46561	0.14708
5	1.46576	0.14708
6	1.46597	0.14706
7	1.46568	0.14704
8	1.46612	0.14703
9	1.46571	0.14709
10	1.46595	0.14709

5. DISCUSSION: The appropriate thickness of the reference sample is 146.4 nm ± 12Å and n = 1.467 at λ = 0.6238 µm as referred on the case of the sample. The calibration was taken ten times and from the table of the document it is observed that the average thickness of measurements is 0.14705 µm, minimum 0.14699 µm and maximum 0.14709 µm which are within the range of the referred thickness. The n values also approximately equal to the referred value.

Table 4: Analysis of measurements

Result	n	Thickness µm
Minimum	1.46561	0.14699
Maximum	1.46669	0.14709
Range	0.00109	0.0001
Average	1.46606	0.14705
Unification	0.00037	0.00035
Standard	0.00038	0.00003

So, it can be said the calibration of the machine has been done perfectly. All the measurements were done under X10 lens. If more precision is needed then the table should be vibration free and lenses with more amplification factor can be used. But, still X10 lens is fit for our measurement.

6. FUTURE WORK: We have collected a sample coated with TiO_2 on glass substrate and Al_2O_3 on substrate from LED industry. We will measure the thickness of TiO_2 and Al_2O_3 layer in future.

7. ACKNOWLEDGEMENT: We are thankful to Charles Lin, Application Engineer, Radiation Technology Co. LTD. Taiwan, for his presence during installation and calibration of Reflectometer.

8. REFERENCES:

[1] B. L. Sopori, Y. Zhang, W. Chen, and J. Madjdpour, "Silicon solar cell process monitoring by PV Reflectometer," *IEEE PVSC, Anchorage, AK, Sept, 2000.*

[2] Bhushan Sopori, U. S. Patent No. 6,275,295.

[3] B. L. Sopori, Reflectometer: Performance Testing / Error Analysis, 12th Workshop on Crystalline Silicon Solar Cell Materials and Processes, Aug, 2002.

[4] B. Sopori, AR Coating Thickness on Si Solar Cells, NREL/CP-520-37478, Feb 2005.

[5] B. L. Sopori, .Principle of a new reflectometer for measuring dielectric film thickness on substrates of arbitrary characteristics,. *Rev. Sci. Instrum.* **59(5)**, 725, 1988.

[6] B. Sopori, Y. Zhang, Principles and Applications of Reflectometery in PV Manufacturing, NREL/CP-520-31003, Oct, 2001.

Proceeding of the
International Conference on Electrical, Computer and Telecommunication Engineering
01- 02 December 2012 (ICECTE2012), RUET, Rajshahi-6204, Bangladesh

ICECTE2012: PI-0082

Investigation of Optical and Surface Morphological Properties of Zinc Oxide (ZnO) nanostructured films deposited on Seedless glass substrate

M.F. Hossain, Md. R. Haque, R.S. Mandal, M. Saiful Islam, M.S. Islam*
[1]Department of Electrical & Electronic Engineering, Rajshahi University of Engineering & Technology, Bang
*E-mail: faruk94_ruet@yahoo.com

ABSTRACT
Nanostructure ZnO thin films have been deposited on seedless glass by the uncovered hydrothermal method with various Hexamethylenetetramine (HMTA) Concentrations at low temperature of 85°C. The deposited ZnO films are annealed at temperature of 450°C. The optical properties of ZnO films are investigated by using ultraviolet/Visible and Photo-luminescence spectrophotometers. The nano-structured ZnO films are confirmed by atomic force microscope. The ZnO nanostructured films have the hexagonal wurtzite structure. These films show the suitable band gap (2.9-3.2eV), which is very suitable for solar cell applications.

KEY WORDS: Zinc Oxide (ZnO), Seedless, hydrothermal method, wruitzite, and hexagonal.

1. INTRODUCTION

The ZnO is one of the most important multifunctional semiconductors due to its wide range of potential photo-electrochemical applications such as light-emitting diodes, optical waveguides, dye-sensitized solar cells, conductive gas sensors and transparent electrodes, etc [1-5]. The ZnO can be used alternative to TiO_2 materials. Because, ZnO has same direct band gap (3.37 eV), and large excitation binding energy (60 meV), excellent chemical and thermal stability. Therefore, fabrication of ZnO nanostructures is of critical importance for the development of novel devices [6].

As a result, searching a new methodology to synthesize ZnO nanorods array is of great importance for both fundamental study and practical application. Up to now, various methods such as pulsed laser deposition (PLD) [7], chemical bath deposition (CBD) [8], sol–gel [9], spray pyrolysis (SP) [10], electrochemical deposition (ECD) [11], hydrothermal (HT) [12], etc. have been utilized to fabricate ZnO nanorods. Among these methods, the hydrothermal method offers advantages of being environmental friendly, large area deposition, low synthesis temperature, and low production cost. Most of the researchers used ZnO seeded glass substrate, but it has complexity to deposit ZnO seed layer on glass. This drawback is eliminated in this work. Moreover, other researchers have used autoclave system during deposition, which is very expensive. Our proposed the uncovered hydrothermal method is free from the autoclave system, which enhances the deposition process. In this work, nanostructured ZnO films have been prepared on bare glass substrate by using uncovered hydrothermal method with various HMTA and fixed Zinc nitrate (50 mM) concentrations. The Optical and surface morphological properties of these films are investigated and discussed for the application of solar cells.

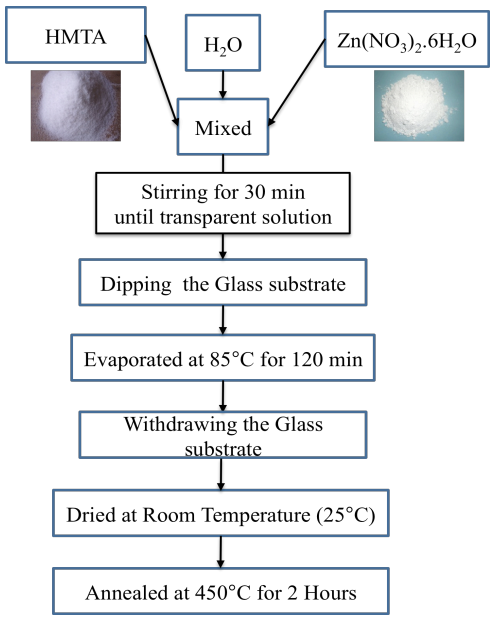

Figure 1: Schematic diagram of different steps during process of hydrothermal method.

2. EXPERIMENTAL DETAILS

2.1. Preparation of nanostructured ZnO films

The nanostructure ZnO films were prepared on seedless (bare) glass substrate by using uncovered hydrothermal method. Figure 1 shows the schematic diagram of different steps during deposition of ZnO films. For the synthesis of the ZnO nanostructures arrays, analytical grade zinc nitrate hexahydrate [$Zn(NO_3)_2.6H_2O$] and hexamethylenetetramine [HMTA, $C_6H_{12}N_4$] were used as reagent without further purification. In this experiment, 50mM of

zinc nitrate hexahydrate [$Zn(NO_3)_2.6H_2O$] was dissolved in 50 ml of deionized water, and then 40mM to 70mM of HMTA was dripped under constant stirring. The deposition process was carried out at a constant temperature (≥85ºC) using well temperature controller and 2 hours.

At the end of the growth period, the glass beaker had been cooled to room temperature naturally. The zinc oxide (ZnO) nanostructures coated substrates were removed from the solution, then immediately rinsed with deionized water to remove any residual salt from the surface, and dried at room temperature for 24 hours. After the drying process, all the samples has annealed in a highly controlled heater at 450ºC for 2 hours. Figure 2 shows the prepared ZnO films with various HMTA.

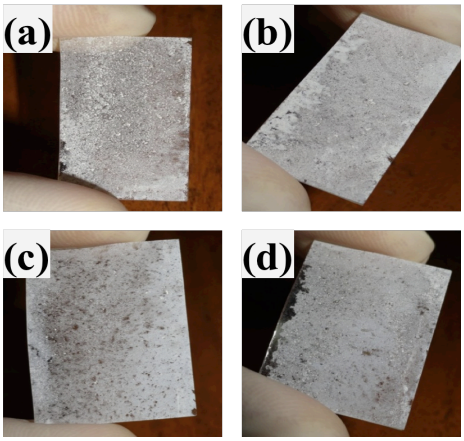

Figure 2. Images of prepared ZnO films on seedless glass substrate with (a) 40, (b) 50, (c) 60, and (d) 70mM HMTA and fixed 50mM of $Zn(NO_3)_2$.

2.2. Chemical reactions during deposition

The ZnO NRs were formed by the hydrolysis of zinc nitrate hexahydrate in water in the presence of hexamethylenetetramine (HMTA). HMTA is a nonionic cyclic tertiary amine that can act as Lewis base with metal ions and a bidentate ligand capable of bridging two zinc (II) ions in solution [13]. HMTA can also hydrolyze to generate formaldehyde and ammonia under the known reaction conditions [14]. It is considered that HMTA slowly decomposes and afford steady supply of ammonia, which can form ammonium hydroxide and complex with zinc (II) to form $Zn(NH_3)_4^{+2}$ [15-16]. Zinc (II) is thought to exist mainly as $Zn(OH)_4^{2-}$ and $Zn(NH_3)_4^{+2}$ under the given pH and temperature. Consequently, the formation of ZnO occurs by dehydration of these reaction intermediates [17].

The comprehensive chemical reactions [Eq. (1)-(2)] represent below [18]:

$$C_6H_{14}N_4 + 6H_2O \leftrightarrow 6CH_2O + 4NH_3 \quad (1)$$

$$C_6H_{14}N_4 + Zn^{2+} \rightarrow [Zn(C_6H_{12}N_4)]^{2+} \quad (2)$$

$$NH_3 + H_2O \rightarrow NH_4^+ + OH^- \quad (3)$$

$$Zn^{2+} + 4NH_3 \rightarrow [Zn(NH_3)]_4^{2+} \quad (4)$$

$$Zn^{2+} + 4OH \rightarrow [Zn(OH)_4]^{2-} \quad (5)$$

$$[Zn(NH_3)]_4^{2+} + 2OH^- \rightarrow ZnO + 4NH_3 + H_2O \quad (6)$$

$$Zn(OH)_4^{2-} \rightarrow ZnO + H_2O + 2OH^- \quad (7)$$

$$[Zn(C_6H_{12}N_4)]^{2+} + 2OH^- \rightarrow ZnO + H_2O + C_6H_{12}N_4 \quad (8)$$

3. RESULTS & DISCUSSIONS

Figure 4 shows that PL peaks of ZnO films located at 398nm can be attributed to the emission of electronic transition near the band edge of wrutzite structures. From to his peak, it is clearly understood that all the ZnO films have good crystallinity. In this work, the visible emission PL peak of ZnO nanostructures that contains different concentrations of HMTA has shown comparable crystallinity. In the inset of Figure 3, the ZnO films with 40mM of HMTA shows higher defect state than the sample with 70mM of HMTA. Therefore, the ZnO with 40mM of HMTA construct shows better crystallinity than that of the others.

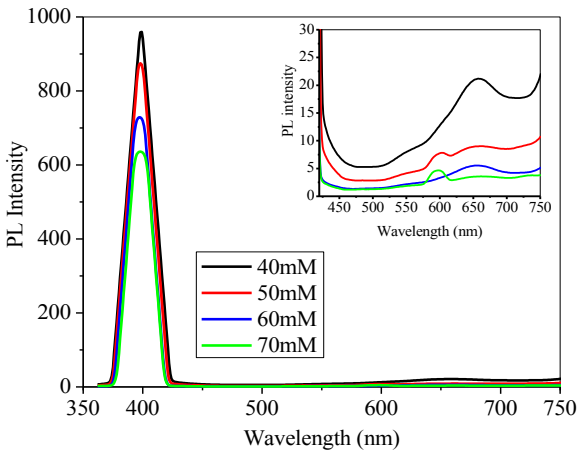

Figure 3. PL spectra of ZnO films with different HMTA concentrations and fixed (50mM) $Zn(NO_3)_2.6H_2O$. (Inset) PL spectra for 420- 750nm.

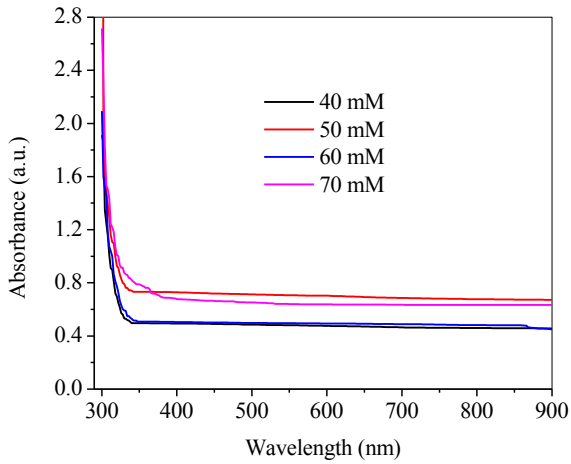

Figure 4: Absorbance of nanostructure ZnO film for different concentrations of HMTA when Zinc nitrate hexahydrate is fixed.

Figure 4 shows the optical absorbance of ZnO films. The absorbance edges of all the ZnO films are

almost at ~335nm. The ZnO films with 50mM/L shows the maximum absorbance and with the 60mM/L shows the minimum absorbance.

Figure 5 exhibits the transmittance of ZnO films prepared with various HMTA concentrations. The ZnO at 40 mM HMTA has the maximum transparency with average transmittance of 33.2%. The low transmittance occurs with 50 mM sample.

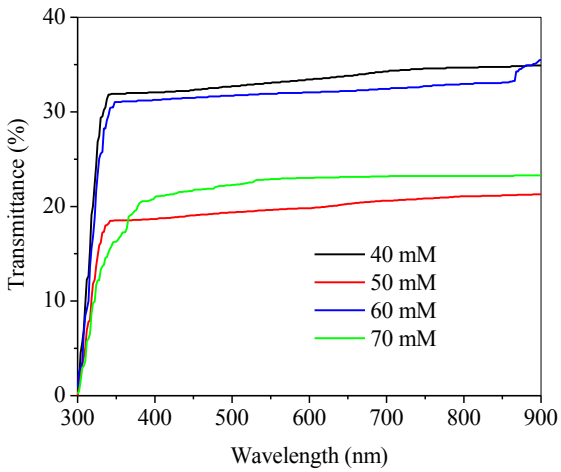

Figure 5: Transmittance spectra of ZnO films with various HMTA.

Figure 6 displays the optical band gap of ZnO nanostructure films, which has been determined from the characteristics curves of the linear plots of $\sqrt{\alpha h\nu}$ versus photon energy (eV). The photon energies are 3.15 eV, 3.08 eV, 2.98 eV and 2.95 eV for ZnO films with 40mM, 50mM, 60mM and 70mM, respectively.

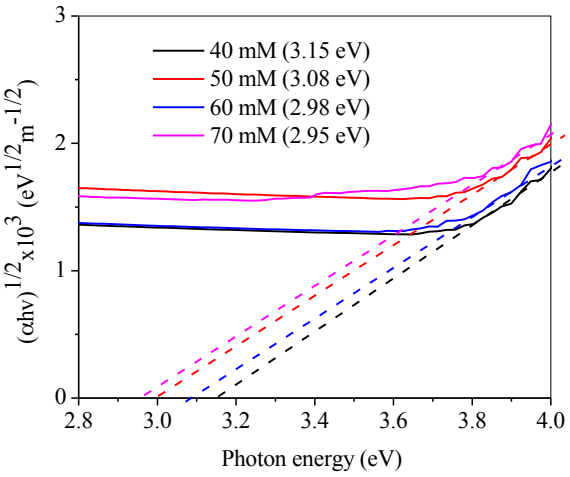

Figure 6: $(\alpha h\upsilon)^{1/2}$ versus Photon energy curve of ZnO film with different concentrations of HMTA.

Figure 7 shows that the AFM images of ZnO films with different concentrations of HMTA where 50mM of $Zn(NO_3)_2.6H_2O$ being fixed. The nanostructured ZnO films have been confirmed by these AFM images. Here, some ZnO nanostructures have verified & ZnO nanoparticles have investigated. In Fig. 7(a), the size of nanorods is approximately 2 nm, which is uniformly grown bare substrate. Figure 7(b) exhibits the large number of nanorods. The nanorods are become less due to further increase of HMTA concentration.

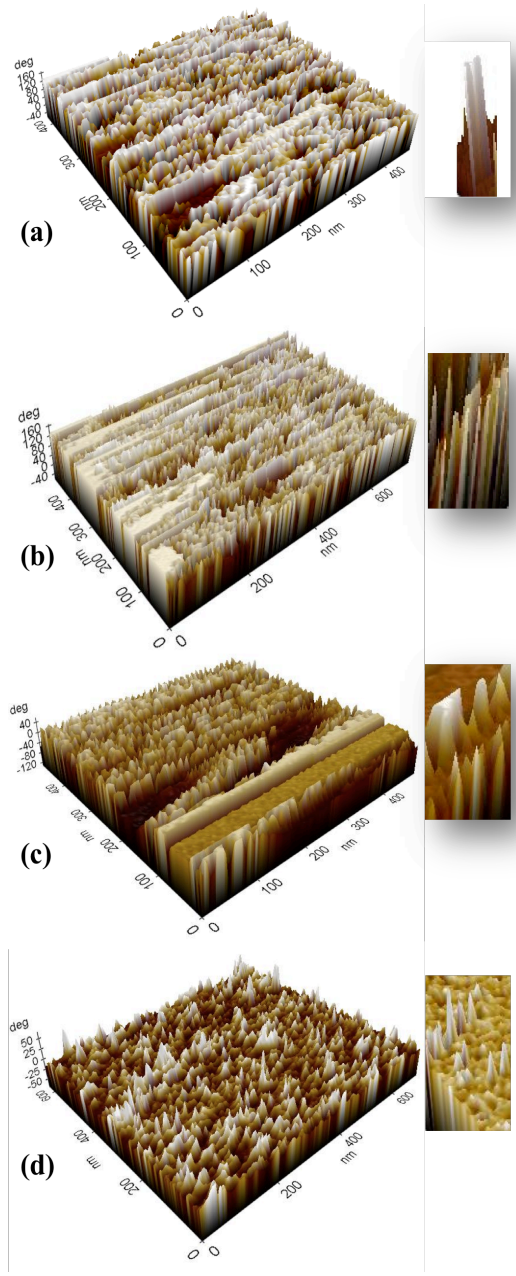

Figure 7: SEM images of ZnO nanostructures for (a) 40mM, (b) 50mM, (c) 60mM and (d) 70mM of hexamethylenetetramine (HMTA) when 50mM of zinc nitrate hexahydrate ($Zn(NO_3)_2.6H_2O$) is fixed.

Figure 7 shows the average roughness & RMS roughness of AFM image (phase) that varies with respect to different concentrations of HMTA. For Samples with 40mM, 50mM, 60mM & 70mM HMTA have the average roughness of 23.567º, 35.330º, 27.731º and 7.264º respectively. And the RMS roughness are 25.645º, 44.127º, 32.253º and 9.538º, respectively. From this figure, ZnO with

50mM HMTA shows the best average roughness and RMS roughness .

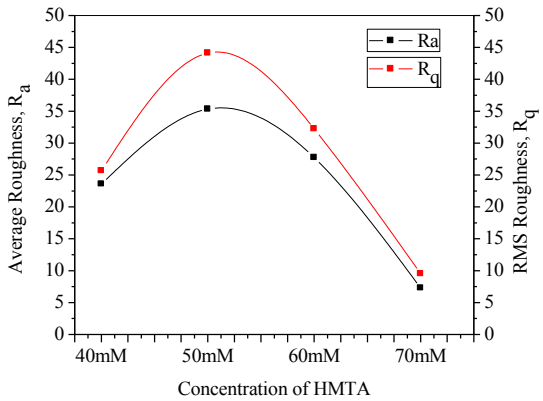

Figure 7: Average roughness & RMS roughness taking from AFM images of ZnO films with different concentrations of HMTA.

4. CONCLUSIONS

The nanostructured ZnO thin films were successfully prepared by hydrothermal method with various hexamethylenetetramine (HMTA) and fixed Zinc nitrate [$Zn(NO_3)_2.6H_2O$] concentrations. From the optical study of ZnO films exhibits good transparency and has low band gap position ~ 3.00 (2.95 to 3.15 eV. The Surface morphological properties of ZnO films were showed the nanorods like structures. The best average roughness & RMS roughness shows with 50mM HMTA sample. So ZnO films with 50mM HMTA and 50mM $Zn(NO_3)_2.6H_2O$ shows the more structures and suitable band gap of 3.08 eV, which is suitable for the dye sensitized solar cell applications.

5. ACKNOWLEDGEMENTS

This work was supported by Research project, UGC, Bangladesh.

REFERENCES

[1] R. Konenkamp, R.C. Word, M. Godinez, Nano Lett. 5 (2005) 2005- 2008.

[2] J.Y. Lee, Y.S. Choli, J.H. Kim, M.O. park, s. Im, Thin Solid Films 403 (2002) 553-557.

[3] M. Law, L.E. Greene, J.C. Johnson, R. saykally, P.D. yang, nat. matter. 4 (2005).

[4] J.X. Wang, X.W. Sun, Y. Yang, H. Huang, Y.C. Lee, O.K. Tan, L. Vayssieres, Nanotechnology 17 (2006) 4995-4998.

[5] C.D. lokhandea, P.M. Gondkara, R.S. Maneb, V.R. Shindea, S.H. Han, J. Alloy Compd. 475 (2009) 304-311.

[6] Yinglei Tao, min, Ailun Zhao, Dawei He, Yongsheng, "*The effect of seed layer on morphology of znO nanorod arrays grown by hydrothermal*," Journal of alloys and Compounds 489 (2010) 99-102.

[7] Qingwei Li, Jiming Bian, Jingchang Sun, Jingwei Wang, Yingmin Luo, Kaitong Sun, Dongqi Yu, *Controllable growth of well-aligned ZnO nanorod arrays by low-temperature wet chemical bath deposition method*, Appl. Surf. Sci. 256 (2010) 1698–1702.

[8] K. Prabakar, Heeje Kim, Growth control of ZnO nanorod density by sol–gel method, Thin Solid Films 518 (2010) e136–e138.

[9] Myo Than Htay, Yoshio Hashimoto, Kentaro Ito, *Growth of ZnO submicron single-crystalline platelets, wires, and rods by ultrasonic spray pyrolysis*, Jpn. J. Appl. Phys. 46 (2007) 440–448.

[10] Chien-Te Hsieh, Shu-Ying Yang, Jia-Yi Lin, *Electrochemical deposition and superhydrophobic behavior of ZnO nanorod arrays*, Thin Solid Films 518 (2010) 4884–4889.

[11] Seong-Jong Kim, Han-Hyoung Kim, Joo-Beom Kwon, Jong-Geun Lee, O. Beom-Hoan, Seung Gol Lee, El-Hang Lee, Se-Geun Park, *Novel fabrication of varioussize ZnO nanorods using hydrothermal method*, Microelectron. Eng. 87 (2010) 1534–1536.

[12] Li Tang, Xiao-Bo Bao, Hu Zhou, Ai-Hua Yuan, *Synthesis and characterization of ZnO nanorods by a simple single-source hydrothermal method*, Physica E 40 (2008) 924–928.

[13] L.E. Greene, B.D. Yuhas, M. Law, D. Zitoun, P. Yang, Inorg. Chem. 45 (2006) 7535.

[14] G.J. Strom, W.H. Jun, J. Pharm. Sci. 69 (1980) 1261.

[15] K. Govender, S.D. Boyle, B.P. Kenway, P. O'Brien, J. Mater. Chem. 14, 2575 (2004)

[16] Z. Wang, X.F. Qian, J. Yin, K.Z. Zhu, Langmuir 20 (2004) 3441.

[17] Q. Li, V. Kumar, Y. Li, H. Zhang, T.J. Marks, R.P.H. Chang, Chem. Mater. 17 (2005) 1001.

[18] Q. Ahsanulhaq, Jin Hwan Kim, Jeong Hyun Kim, Y. B. Hahn, Nanoscale Res. Lett. 5 (2010) 669.

Proceeding of the
International Conference on Electrical, Computer and Telecommunication Engineering
01- 02 December 2012 (ICECTE2012), RUET, Rajshahi-6204, Bangladesh

ICECTE2012: PI-0083

A New Algorithm for Partitioning with Minimum Wire-length in 3D VLSI Design

Ajoy Kumar Khan[1], Bhaskar Das[2], Rajat Kumar Pal[3]
[1]Department of Information Technology, Assam University, Silchar, India
[2]Department of Information Technology, Assam University, Silchar, India
[3]Department of Computer Science, Calcutta University, Kolkata, India
E-mail: ajoyiitg@gmail.com, bhaskardas2006@gmail.com, rajatkp@gmail.com

ABSTRACT
Partitioning plays an increasingly important role in the design process of VLSI circuits. There are partitioning problems to be solved on all levels of abstraction. The role of partitioning is exactly that of a facilitator of divide-and-conquer metaheuristics for floorplaning, timing and placement optimization. The problem is to partition the vertices of a hypergraph in k roughly equal parts, such that the number of hyperedges connecting vertices in different parts is minimized. The idea of the 3D partitioning is basically based on the initial partitioning via min cut optimization and then minimizing the interconnections between non-adjacent layers so that the wire-length and the max-cut can be minimized. Our algorithm can be used for the proper layer assignment.

KEY WORDS: Partitioning, Hypergraph, 3D Vias, Wire-length, Max-cut.

1. INTRODUCTION

Partitioning applications exist on all levels of abstraction, specifically on the functional (behavioral) and on the structural (netlist) level. In the early stages of design, far-reaching decisions have to be made how to partition a design, often based on incomplete knowledge. In particular, it has to be decided whether to implement a component in various types of hardware or software to achieve an optimal size/performance trade-off. Because the granularity is low in this application, i.e. relatively few objects of moderate to high complexities, partitioning can possibly be done by human designers based on their experience. Since fully automatic partitioning is essential for fast iterations in the design cycle, considerable effort is made in academia as well as in industry to facilitate and improve the difficult decisions on functional level.

The number of 3D-vias required in a design is determined by the tier assignment of each cell/partitions, which is performed during the cell partitioning. The initial partitioning is usually performed by hypergraph partitioning tools (since it is straightforward to map a netlist into a hypergraph) such as hMetis [1, 2]. On the other hand, hypergraph tools do not understand the distribution of partitions in the space (in 3D circuits they are distributed along in a single dimension) and fail to provide optimal It is important to results. Understand that the amount of resources used is proportional to the vertical distance of the tiers; in fact, considering that the path from a tier to an adjacent involves regular vias going through all metal layers plus one 3D-via, it is clear that any vertical connection larger than adjacency might be too expensive in terms of routing resources like wire-length and time-delay.

The paper studies about the reduction of interconnection between non-adjacent layers. As the min-cut optimization just partitions the circuit in to sub-circuits but at the time of targeting for 3D modeling the layer assignment for the partitions plays an important role as there are several other things associated with layer assignment as: wire-length, number of 3D vias etc.

So we are discussing the problem of layer assignment in this paper which will result in the minimization of wire-length and also the 3D vias. If the partitions are not assigned to proper layer it will be difficult to model the circuit, as larger interconnections between non-adjacent layers will increase the wire-length.

This paper presents a new approach for reducing interconnection between non-adjacent layers targeting wire-length reduction. In "Problem Formulation" Section, we present the problem formulation and existing work. "Proposed Algorithm" section describes a new approach for achieving the goal. "Experimental Results", "Conclusion" and "Assessment and Future scope of the Work" sections describes the experimental results and comparison with previous work, conclusion drawn and assessment and future scope of work respectively.

2. PROBLEM FORMULATION

The min-cut optimization problem just takes care about partitioning the circuit into sub-circuit based

on the edges cutting. That's a good approach for 2D partitioning or initial partitioning. But in case of 3D partitioning we have to assign the partitions obtained after initial partitioning to different layers, and for that purpose we have to take care about the interconnections between the non-adjacent layers. For 3D circuit our primary goal should be to minimize the interconnection between non-adjacent layers so that the wire-length can be minimized and hence the number of 3D vias and also the delay can be reduced.

While taking the output of initial partitioning we can assign them into various layers in different fashion, but there must be some way to minimize the interconnection between non-adjacent layers, figure1 shows two layer assignment approaches for same problem.

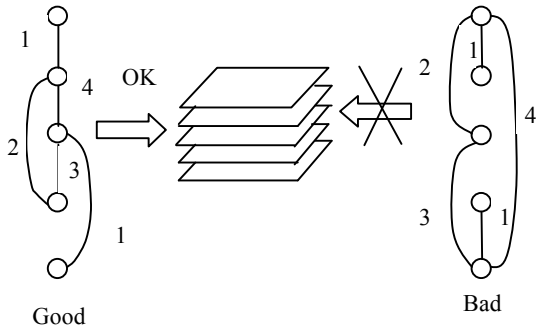

Fig. 1: Two representations for same input

3. PROPOSED ALGORITHM

For this approach, we analyze the part file given from the hMetis [1, 2] and also the hypergraph taken as input file and then find the interconnection between various partitions. And then work on to find out the sequence in which those partitions can be assigned so that the interconnections between non-adjacent layers can be minimized.

Algorithm for layer assignment is described as follows:

Algorithm <u>Minimize_Wl</u>

Input: A weighted graph with one node at each level.

Output: A weighted graph with one node at each level with minimized Wire-length.

Step 1: Analyze the graph and find the node with minimum degree and name it N1.

Step 2: Compute the BFS sequence of the graph starting from the node N1.

Step 3: make a directed graph putting the nodes at various levels based on BFS traversal starting from node N1 and the edge directed from N_i to N_j exist if there is an edge between N_i and N_j in initial graph and N_j comes after the N_i in the BFS sequence and vice-verse.

Step 4: Now find the levels with more than one node and assign effective weight (W_e) to all the nodes in that level based on:

$$W_e=W_i-W_o$$

Where, W_e is the effective weight.

W_i is the sum of weights at the inner edges from previous level.

W_o is the sum of the weight at the out-going edges to next level.

Step 5: Now assign all the nodes to different levels and for the levels having more than one node assign the nodes to different levels based on decreasing order of with effective weight (W_e) first.

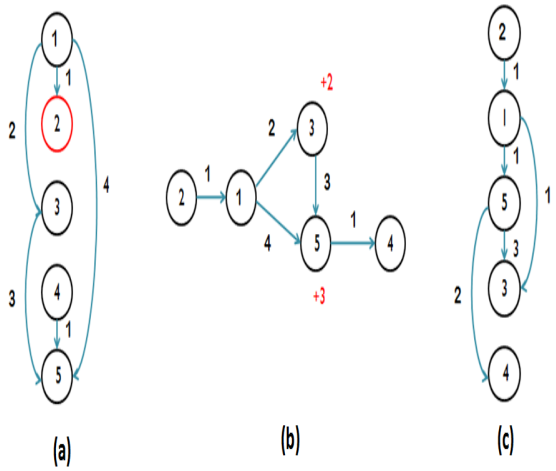

Fig. 2: Showing example of Layer assignments.

The first step of our algorithm is explained in figure2(a), which just finds the node with minimum degree. Second and third step collectively useful for making the graph directed with the nodes/partitions associated with the levels. The complexity of the steps finding the BFS and making it directed is given by O(n+e). The fourth step computes the effective weights based on the formula described above figure2(b). The final step just assigns the nodes/partitions to different layers based on te decreasing order of weights assigned figure2(c).

4. EXPERIMENTAL RESULTS

We have conducted experiments in order to verify the effectiveness of our approach. The benchmark sets used are ibm01 and s13207P. We started the experiments be recovering the experimental results of our algorithm from previous work. The proposed algorithm Minimize_WL was compared with state-of-the-art partitioning algorithm, called hMetis. The table 1 shows the comparison of wire length obtain from hMetis and Minimize_WL at different number of tiers.

The results are reported on table1. The table1 shows the comparison between the wire-length obtain from the hMetis and also by the Minimize_WL for the same number of partitions. The benchmarking circuits were partitioned in to 5, 10, 15, 20, 25, 30, 35, 40, 45 and 50 partitions and subjected to various tiers using Minimize_WL algorithm. More specifically the refinement leads to the improvement of the wire-length as compared to hMetis. This is the direct consequence of the sequence refinement step that targets at reducing the wire-length in non-adjacent connections. Therefore, the large is the number of tiers the larger is the wire-length and improvement obtain by this algorithm. Since partitioning refinement step is done after the partitions have been assigned to the tiers, it takes advantages from the knowledge of the actual partition locations, reducing the number of connections between non-adjacent tiers and increasing the number of connections between adjacent ones. This strategy yields reduce the wire-length.

IBM01			S13207P		
Number of partitions	Initial wire length(obtained using hMetis)	Final wire length (obtained using Minimize_WL)	Number of partitions	Initial wire length(obtained using hMetis)	Final wire length (obtained using Minimize_WL)
5	1199	1038	5	472	422
10	3621	2768	10	2435	2235
15	6413	5257	15	3855	3275
20	10052	8547	20	4817	3491
25	14119	11156	25	10048	7073
30	16135	15471	30	13266	10625
35	20398	19097	35	16826	15444
40	26660	21694	40	20105	17809
45	42446	29475	45	23308	17229
50	37211	33475	50	29055	21969

Table 1: Experimental result using hmetis and Minimize_WL algorithm.

The figure shows the graphical representation of the comparison between the results obtain from hMetis and Minimize_WL algorithm. The horizontal axis represents the number of tiers and vertical axis represents the wire length. The lines in the graph represent the wire-length using Hmetis and also by using our algorithm.

We compared our algorithm Minimize_WL with hMetis which is used for same purpose. And the result is very much clear to us that the wire length can be minimized using Minimize_WL. In this paper we have summarized the result till 50 partitions but our algorithm could be applied to any number of tiers.

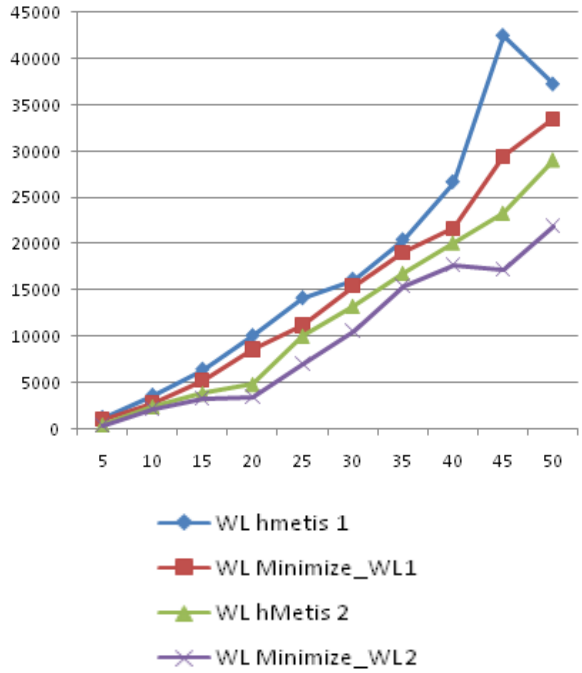

Wire-length using hMetis for IBM01.
wire-length using Minimize_WL for IBM01.
wire-length using hmetis for s13207P.
wire-length using Minimize_WL for s13207P.

Fig 4: Evolution of the wire-length obtained with hMetis and Minimize_WL

Analyzing the table1 and figure, the following topics can be observed:

- The wire-length using Minimize_WL can be reduce then hMetis as it does not concern about the sequence of the assignment of different partitions in to tiers.
- Minimizing wire-length will also minimize the 3D-vias as it will reduce the interconnections between non-adjacent layers.

So, from above discussion it's very much clear that keeping sequence in mind at the time of assigning the partitions to different layer in 3D partitioning is much important as it can lead to better results.

5. CONCLUSIONS

This paper presented a new approach for layer assignment i.e., to various layers after initial partitioning so that the interconnection between the different layers can be minimized. The methodology was based on computing BFS sequence starting from

node with minimum degree after dividing the larger circuit into smaller sub-circuits using hMetis multi-level hypergraph partitioning algorithm and placing those partitioned components in to various layers. Since sequential hMetis is not so efficient in case of wire-length minimization and max-cut optimization problem. But by refining the algorithm and working on layer assignment basing mainly on method specified in Minimize_WL makes the result i.e., wire-length and max-cut minimization a more better and more minimized way , moreover more efficient one. Our method is based on minimization of wire-length and max-cut optimization. Finally, we highlight that our heuristic was able to perform in a better way and balanced for all tiers.

Here in this algorithm we take final result of the multilevel hypergraph partitioning i.e., Dividing the larger netlist in the form of hypergraph into smaller sub-circuits using hMetis partitioning algorithm and depending on the result we draw a graph in such a way that after initial partitioning the no. of sub-circuits are assigned to different layers of equal size. Mainly on BFS methodology the graph is redesigned based on the node with minimum degree and then computing BFS to the graph we obtain some results. This algorithm gives a better result for wire-length minimization and max-cut optimization as compared to the previous approach on weighted or non-weighted directed graph of equal size.

REFERENCES

[1]. G. Karypis et al, "Hypergraph Partitioning: Application in VLSI domain", In: *Proceedings of 34th Annual Conference on Design Automation*, DAC 1997, pp. 526–529, 1997.

[2]. G. Karypis, R. Aggarwal, V. Kumar, S. Shekhar, "Multi-level Hypergraph Partitioning: Applications in VLSI Design", *Proc. ACM/IEEE DAC,* pp. 526-529, 1997.

[3]. F. M. Johannes, "Partitioning of VLSI Circuits and Systems", *Institute of Electronic Design Automation, ECE Department, Technical University of Munich, Arcisstr. 21, D-80333 Munich, Germany,* 1996.

[4]. S. CHENa, C. K. CHENG, "Tutorial on VLSI Partitioning", *VLSI DESIGN,* Vol. 00, No. 00, pp. 1 – 43, 2000.

[5]. S. Sawicki, G. Wilke, M. Johann, R. Reis, "3D-Via Driven Partitioning for 3D VLSI Integrated Circuits", *CLEI ELECTRONIC JOURNAL*, VOLUME 13, NUMBER 3, PAPER 1, 2010.

[6]. C. Ababei, H. Mogal, K. Bazargan, "Three-dimensional Place and Route for FPGAs," *IEEE*, 2004.

[7]. S. Sawicki, R. Hentschke, M. Johann, "An Algorithm for I/O Pins Partitioning Targeting 3D VLSI Integrated Circuits", *Circuits and Systems, MWSCAS '06, 49th IEEE Inernational Midwest Symposium on*, Volume 2, pp. 699-703, 2006.

[8]. R. F. Hentschke, "Algorithm for Wire length improvement of VLSI Circuits With concerns to Critical paths", pp. 64-67, 2007.

Proceeding of the
International Conference on Electrical, Computer and Telecommunication Engineering
01- 02 December 2012 (ICECTE2012), RUET, Rajshahi-6204, Bangladesh

ICECTE2012: PI-0084

Linear Asymmetric Pocket Profile Based Threshold Voltage Model for Nano Scale n-MOSFET

Muhibul Haque Bhuyan and Quazi D. M. Khosru*
Department of Electrical and Electronic Engineering
Green University of Bangladesh, Dhaka, Bangladesh
E-mail: muhibulhb@gmail.com, qdmkhosru@eee.buet.ac.bd

ABSTRACT
This paper presents an analytical threshold voltage model of the pocket implanted nano scale n-MOSFETs incorporating the drain and substrate bias effects using an asymmetric linear pocket profile at the source side of the device. Linear equation is used to simulate the pocket profile along the channel at the surface from the source edge toward the center of the n-MOSFET. Then the effective doping concentration is derived and is used in the threshold voltage equation that is obtained by solving the Poisson's equation in the depletion region at the surface. Threshold voltages are simulated for various gate lengths, pocket lengths, peak pocket doping concentrations, oxide thicknesses as well as for various bias conditions. The results show that the proposed threshold voltage model with linear pocket profile can be utilized to study and characterize the pocket implanted advanced ULSI devices.

KEY WORDS: Linear Asymmetric Pocket Profile, n-MOSFET, Threshold Voltage.

1. INTRODUCTION

As the channel length of MOSFETs is scaled down to deep-submicrometer or sub-100 nm regime, short-channel effects (SCE) [1] and hot carrier reliability problems [2] have been observed. Lateral channel engineering utilizing halo/pocket implant [3-5] surrounding the drain and/or source regions is effective in suppressing SCE. An extension of the homogeneous model to the nonhomogeneous impurity pileup in the vertical direction has been reported previously [3, 6]. However, the reported model cannot be extended further to the pocket implantation where inhomogeneity along the channel is the main cause for the reverse short channel effect (RSCE) [7]. This pocket implantation can be either symmetric [3-5] or asymmetric [8-9].

The increased doping concentration at the drain side increases the electric field strength and thus hot carrier reliability problems become more serious [2] and reduces the voltage gain. On the other hand, drive current improves in asymmetric devices with noise trade-offs [10]. The asymmetry in the channel can be obtained by incorporating pocket at the source side only.

In [11], threshold voltage (V_{th}) model is presented that solves the 2-D Poisson's equation analytically and predicts threshold voltage shift (ΔV_{th}) accurately as a function of drain bias, substrate bias, channel length, oxide thickness and substrate concentration. This model is then transformed to short channel n-MOSFET assuming the step doping profile along the vertical direction of the channel. Since the pocket implanted MOSFETs are non-uniformly doped laterally, therefore, one of the key factors to model threshold voltage accurately is to model its non-uniform doping profile and then to transform it to an effective doping concentration that can be applied directly to the V_{th} expression incorporating the ΔV_{th} due to bias and channel length dependence. Short channel V_{th} equation from [11] is used for the case of pocket implanted n-MOSFET. Simulation results using the proposed linear asymmetric pocket profile show that the V_{th} model prediction is agreeable. Thus it proves the usefulness and validity of the proposed V_{th} model for circuit simulation.

2. THRESHOLD VOLTAGE MODEL

The asymmetric pocket implanted at the source side n-MOSFET structure, shown in Fig. 1, is considered for this work. The assumed co-ordinate system is shown at the right side of the structure.

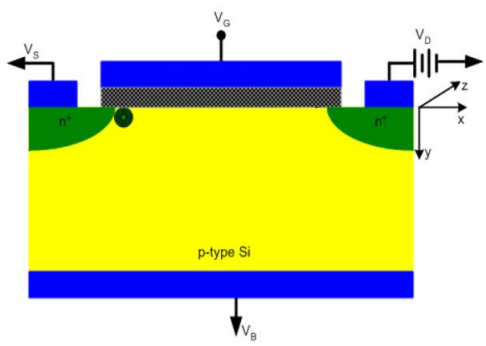

Fig. 1 Pocket implanted n-MOSFET structure with asymmetric pocket at the source side only.

All the device dimensions are measured from the oxide-silicon interface. In the structure, the junction depth (r_j) is 25 nm. The oxide thickness (t_{ox}) is 2.5 nm, and it is SiO_2 with fixed oxide charge density of 10^{11} cm^{-2}. Uniformly doped p-type Si substrate is used with substrate doping concentration, N_{sub} = 4.5×10^{17} cm^{-3}, pocket implantation at the source with peak pocket doping concentration, N_{pm} = 2.5×10^{18} cm^{-3}, pocket length, L_p = 25 nm and source/drain doping concentration, $N_{sd} = 9.0\times10^{20}$ cm^{-3}.

To preserve the long channel threshold voltage behavior for the short channel device, pocket implantation, which causes the reverse short channel effect (RSCE), is done by adding donor atoms at the source edge. The peak pocket doping concentration (N_{pm}) gradually decreases towards the substrate level concentration (N_{sub}) with a pocket length (L_p) from the source edge. The basis of the model of the pocket is to assume a linear doping profile from the source edge across the channel as shown in Figs. 2-3. The pocket parameters, N_{pm} and L_p, play important role in determining the RSCE.

At the source side, the pocket profile is given as:

$$N_s(x) = -\frac{N_{pm} - N_{sub}}{L_p}x + N_{pm}$$

$$\text{or, } N_s(x) = N_{sub}\frac{x}{L_p} + N_{pm}\left(1 - \frac{1}{L_p}x\right) \qquad (1)$$

,where x represents the distance across the channel.

Since the pocket profile is due to the direct pocket implantation at the source side only, it is an asymmetric device. This conceptual pocket profile is integrated mathematically along the channel length (L) and then divided it by the channel length to derive an effective concentration as in equation (2).

$$N_{eff} = \frac{1}{L}\int_0^L \left[N_s(x) + N_{sub}\right]dx$$

$$\text{or, } N_{eff} = \frac{1}{L}\int_0^{L_p} N_s(x)dx + \frac{1}{L}\int_{L_p}^{L} N_{sub}dx \qquad (2)$$

Putting the expression of $N_s(x)$ from equation (1) in to equation (2), the effective doping concentration is obtained as given in equation (3).

$$N_{eff} = N_{sub}\left(1 - \frac{L_p}{2L}\right) + \frac{N_{pm}L_p}{2L} \qquad (3)$$

When $L_p << L$ for long channel device then pocket profile has no effect on V_{th}, but when L_p is comparable with L then pocket profile affects V_{th}.

The threshold voltage model derived in [11] incorporated the effects of substrate and drain biases on threshold voltage for vertically non-uniform doping profile. Based on that concept, a threshold voltage model is obtained for the proposed linear pocket doping profile along the channel. This model incorporates the effective doping concentration of equation (3) to get the V_{th} model as in equation (4).

$$V_{th} = V_{th,L} + \gamma_B\left[\frac{N_{sub}}{N_{eff}}(2\varphi_F) - V_{BS}\right]^{\frac{1}{2}} - \gamma_A\frac{N_{sub}}{N_{eff}}(2\varphi_F)^{\frac{1}{2}}$$
$$-\frac{6t_{ox}}{d_1}\left[2(\varphi_{bi} - V_{BS}) + V_{DS}\right]\exp\left(-\frac{\pi L}{4d_1}\right) \qquad (4)$$

,where $V_{th,L}$ is the long channel threshold voltage, the second and the third parts include the threshold voltage due to both the effect of substrate bias and effective doping concentration, the fourth part incorporates the effect of drain and substrate biases as well as the short channel effect. The long channel threshold voltage, $V_{th,L}$ for the pocket implanted n-MOSFET is given by the equation (5).

$$V_{th,L} = V_{FB} + 2\varphi_F + \gamma_A(2\varphi_F)^{\frac{1}{2}} \qquad (5)$$

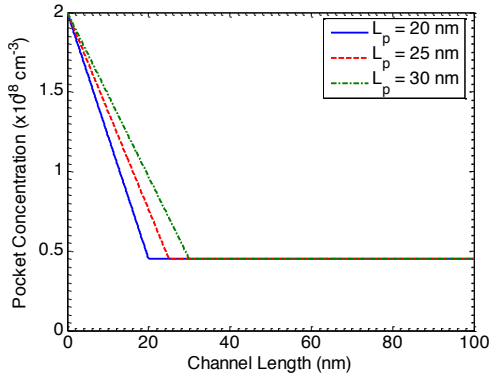

Fig. 2 Simulated pocket profiles at the surface for different pocket lengths, L_p = 20, 25 and 30 nm, peak pocket doping concentration, $N_{pm} = 2.0\times10^{18}$ cm^{-3}.

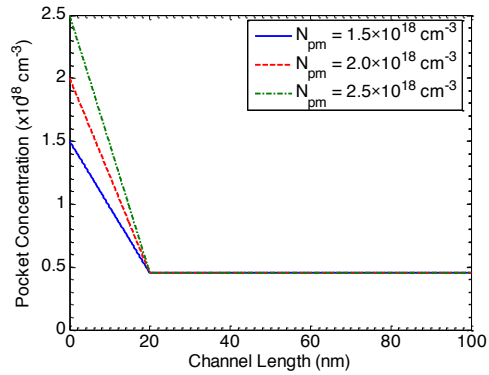

Fig. 3 Simulated pocket profiles at the surface for various peak pocket concentrations, N_{pm} = {1.5, 2.0, 2.5}$\times10^{18}$ cm^{-3}, pocket length, L_p = 20 nm.

,where V_{FB} is the flat band voltage. φ_{FA}, γ_A and γ_B are the Fermi potential due to pocket implantation, threshold sensitivity due to back bias for effective doping concentration along the channel and body

factor corresponding to bulk doping respectively and are given in equations (6)-(8).

$$\varphi_F = \frac{kT}{q} \ln \frac{N_{eff}}{n_i} \tag{6}$$

$$\gamma_A = \frac{\left(2q\varepsilon_{Si} N_{eff}\right)^{\frac{1}{2}}}{C_{ox}} \tag{7}$$

$$\gamma_B = \frac{\left(2q\varepsilon_{Si} N_{sub}\right)^{\frac{1}{2}}}{C_{ox}} \tag{8}$$

The depth (where band bending of $2\varphi_F$ occurs) of the pocket doping vertical to the channel and the built-in potential at the source/drain to channel junction are given by the equations (9) and (10) respectively.

$$d_1 = \left(\frac{2\varepsilon_{Si}}{qN_{eff}}\right)^{\frac{1}{2}} \left(2\varphi_F\right)^{\frac{1}{2}} \tag{9}$$

$$\varphi_{bi} = \frac{kT}{q} \ln \frac{N_{sd} N_{eff}}{n_i^2} \tag{10}$$

,where N_{sd} is the source/drain doping concentration and n_i is the intrinsic carrier concentration of Si.

3. RESULTS AND DISCUSSIONS

The simulated V_{th} vs. L curve is shown in Figs. 4-8 for different drain bias (V_{DS}) and substrate bias (V_{BS}) as well as pocket and device parameters. It is observed that with the increasing drain bias V_{th} decreases at shorter channel device as in Fig. 4. Because drain induced barrier lowering (DIBL) effects come in to play. V_{th} increases when substrate bias increases in the negative direction as in Fig. 5 due to the increment of the depletion layer charge. But in short channel case the opposite phenomenon occurs due to the increment of the inversion carriers.

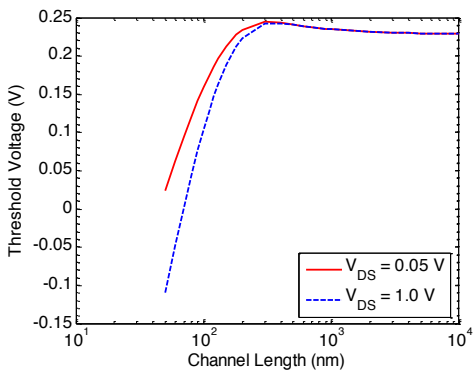

Fig. 4 Threshold voltage vs. gate length curves for various drain biases at zero substrate bias

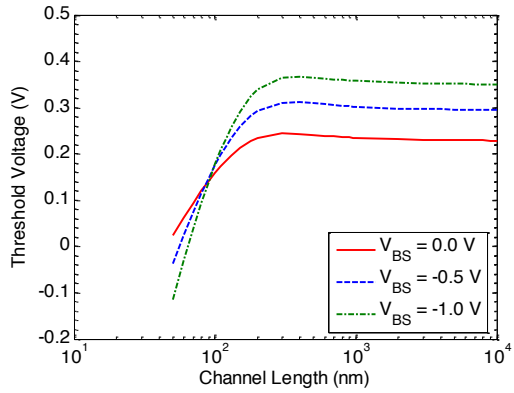

Fig. 5 Threshold voltage vs. gate length curves for various substrate biases at drain bias of 0.05 V

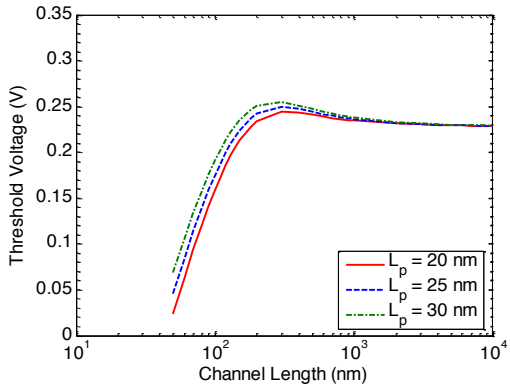

Fig. 6 Threshold voltage vs. channel length curves for various pocket lengths with V_{DS} = 0.05 V and V_{BS} = 0.0 V

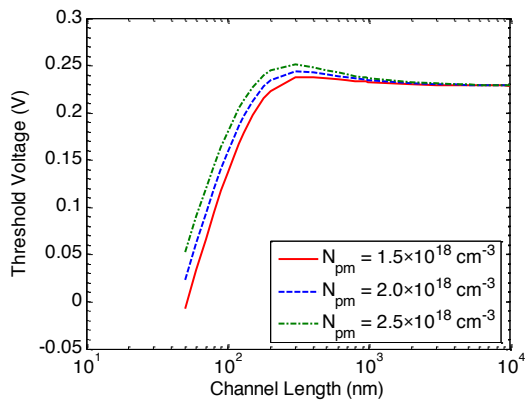

Fig. 7 Threshold voltage vs. channel length curves for various peak pocket doping concentrations with V_{DS} = 0.05 V and V_{BS} = 0.0 V

In Figs. 6-7, pocket lengths and peak pocket doping concentrations are increased, and it is observed that the peak of the curve increases and the onset of threshold voltage (V_{th}) roll-up happens at a longer channel length and also the onset of V_{th} roll-off happens at a shorter channel length and exhibits strong reverse short channel effect (RSCE) with the increased L_p and N_{pm}. If these are increased further by keeping the other parameters constant then V_{th} roll-off starts to vanish exhibiting only RSCE.

In Fig. 8, oxide thickness is increased, and it is observed that the V_{th} increases due to less control on the inversion channel charge by the gate.

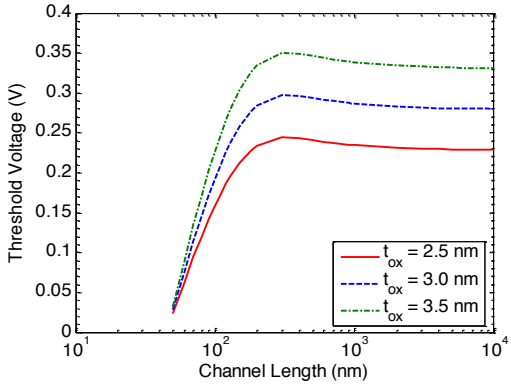

Fig. 8 Threshold voltage vs. channel length curves for various oxide thicknesses with V_{DS} = 0.05 V, V_{BS} = 0.0 V

4. CONCLUSIONS

A threshold voltage model for ultra-thin oxide and nano scaled pocket implanted n-MOSFET has been developed with asymmetric linear pocket doping profile at the source side of the device. The well-known reverse short channel effect (RSCE) has been observed through the proposed model. The proposed threshold voltage model has been simulated for different parameters and bias conditions. It is found that our model efficiently determines the threshold voltages of the nano scaled n-MOSFETs. Therefore, this model is very useful for circuit simulation.

5. FUTURE WORKS

This model can be used in to the other MOS devices, such as, SOI or double-gate MOSFETs. Besides, more efficient models can be developed for the bulk device. Pocket profile type may be changed and comparative study may be carried out among the various types of pocket doping profiles to determine the performance of the simulator.

REFERENCES

[1]. M. Miura-Mattausch, M. Suetake, H. J. Mattausch, S. Kumashiro, N. Shigyo, S. Oganaka and N. Nakayama, "Physical modeling of the reverse short channel effect for circuit simulation," IEEE Transactions on Electron Devices, vol. 48, no. 10, pp. 2449-2452, Oct. 2001.

[2]. A. Hokazono, S. Balasubramanian, K. Ishimaru, H. Ishiuchi, H. Chenming and L. T.-J. King, "MOSFET Hot-Carrier Reliability Improvement by Forward-Body Bias," IEEE Electron Device Letters, vol. 27, no. 7, pp. 605-608, July 2006.

[3]. B. Yu, C. H. Wann, E. D. Nowak, K. Noda and C. Hu, "Short Channel Effect improved by lateral channel engineering in deep-submicrometer MOSFETs," IEEE Transactions on Electron Devices, vol. 44, pp. 627-633, Apr. 1997.

[4]. M. H. Bhuyan and Q. D. M. Khosru, "Linear Pocket Profile Based Threshold Voltage Model for Sub-100 nm n-MOSFET," International Journal of Electrical and Computer Engineering, vol. 5, no. 5, pp. 310-315, May 2010.

[5]. Y. S. Pang and J. R. Brews, "Models for subthreshold and above subthreshold currents in 0.1 μm pocket n-MOSFETs for low voltage applications," IEEE Transactions on Electron Devices, vol. 49, no. 5, pp. 832-839, May 2002.

[6]. Y. Cheng, T. Sugii, K. Chen and C. Hu, "Modeling of small size MOSFETs with reverse short channel and narrow width effects for circuit simulation," Solid State Electronics, vol. 41, pp. 1227-1231, 1997.

[7]. M. K. Khanna, M. C. Thomas, R. S. Gupta and S. Haldar, "An analytical model for anomalous threshold voltage behavior of short channel MOSFETs," Solid State Electronics, vol. 41, pp. 1386-1388, 1997.

[8]. C. Bulucea, S. R. Bahi, W. D. French, Y. Jeng-Jiun, P. Francis, T. Harjono, V. Krishnamurthy, J. Tao and C. Parker, "Physics, Technology and Modeling of Complimentary Asymmetric MOSFETs," IEEE Transactions on Electron Devices, vol. 54, no. 11, pp. 2969-2974, Nov. 2007.

[9]. J. P. Kim, W. Y. Choi, J. Y. Song, S. W. Kim, J. D. Lee and B.-G. Park, "Design and Fabrication of Asymmetric MOSFETs using a Novel Self-Aligned Structure," IEEE Transactions on Electron Devices, vol. 57, no. 10, pp. 2363-2380, Oct. 2010.

[10]. A. Cathignol, S. Bordez, A. Cros, K. Rochereau and G. Ghibaudo, "Abnormally high local electrical fluctuations in heavily pocket implanted bulk long MOSFET," Solid State Electronics, vol. 53, no. 2, pp. 127-133, Feb. 2009.

[11]. K. N. Ratnakumar and J. D. Meindl, "Short-Channel MOST Threshold Voltage Model," IEEE Journal of Solid State Circuits, vol. 17, no. 10, pp. 937-948, Oct. 1982.

Proceeding of the
International Conference on Electrical, Computer and Telecommunication Engineering
01- 02 December 2012 (ICECTE2012), RUET, Rajshahi-6204, Bangladesh

ICECTE2012: PI-0085

Via Minimization in VLSI Design – A Brief Survey

Ajoy Kumar Khan[1], Dhurjati Dev[2], Tapas Kumar Bayen[3]
[1]Department of Information Technology, Assam University, Silchar, India
[2]Department of Information Technology, Assam University, Silchar, India
[3]Computer Science and Engineering, National Institute of Science and Technology, Orissa, India
E-mail: ajoyiitg@gmail.com, devdhurjati@gmail.com, tapas.bayen@gmail.com

ABSTRACT
In VLSI circuit when two conducting layers are available for interconnection, the simplest way to route the signal nets is by assigning all horizontal wire segments to one of the layer and all vertical segment to another layer. However this method of interconnection uses large number of vias. Vias are necessary to connect wires of same net on different layers. These vias gives rise to increased area, decreased yield and reliability and poor electromagnetic characteristics. In this paper we study some of the algorithms used in minimizing vias in VLSI. Unconstrained, constrained and layout modification are some of the algorithm used for via minimization. Later we also study how via can be minimized in two layer channel routing, three and four sided switch-box routing, color constrained three layer channel routing and by layout modification.

KEY WORDS: channel routing, switch-box routing, permutation graph, maze router, restricted terminals, layout modification.

1. INTRODUCTION

A VLSI circuit consists of a set of modules, where each module is a collection of active devices, and a set of nets. Again each net specifies a subset of points on the boundary of modules, called terminals. A VLSI circuit layout problem has the involvement of stages like placement, i.e., finding a proper placement of the modules in the plane, and routing, i.e., interconnecting the terminals as specified by the nets. The region of the plane where routing is done (but not in the modules) is called routing region. Again this routing region is partitioned into simpler sub-regions, called channels. In its most general form a channel is a rectilinear polygon. However the method of interconnection of horizontal and vertical wire segments uses large number of vias. Vias are necessary to connect the wires of the same net on different layers. Vias are usually made up of tungsten. In solving the routing problem of an enclosed region with pins on the perimeter, unnecessary vias are undesirable for reasons of increased area, decreased yield and reliability, and poor electromagnetic characteristics. So in order to minimize the number of vias in a circuit there are many type of techniques used. Via minimization are mainly of two kinds namely unconstrained or topological via minimization and constrained via minimization.

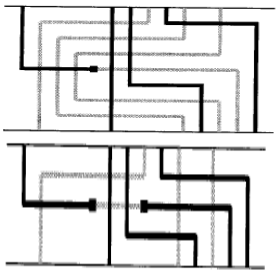

(a) (b)

Figure1. (a) Geometrical mapping with one via.
(b) A more compact layout with two vias.

Unconstrained via minimization-where the routing topology of the layout can be changed, whereas in constrained via minimization the routing topology of the layout cannot be disturbed only the layers of wire segment and position of vias can be changed.

2. UNCONSTRAINED VIA MINIMIZATION ALGORITHM IN CHANNEL ROUTING

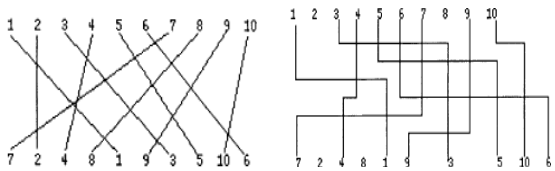

(a) (b)

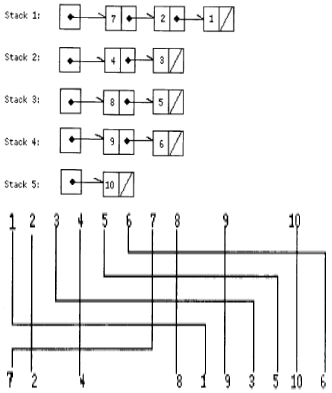

(d) **(e)**

Figure 2. [2] (a) Permutation Diagram. (b) Two-Terminal Channel Routing Problem.(c) Linear Link List. (d) Routing Of Maximum Abutment Set Of Fig.(a).

Haklin Kim proposed an algorithm for via minimization in channel routing. In this paper the problem of via minimization in VSLI routing can be solved in *0(n log n) b*y the help of the algorithm finding maximum independent set in a permutation graph. We know that minimization of via in channel is equivalent in finding maximum independent set in a permutation graph. Now again the problem of finding maximum number of independent set in a permutation graph is also equivalent in finding longest up sequence[3] in the algorithm. So now, here the algorithm which will be used in finding the longest up sequence can be used in reduction of time complexity of minimization of via with the movable terminals [1].

Now let us consider routing problem as shown in fig.1 (a) [2]. Now with the help of this figure we can find the longest up sequence[3], in the permutation. Now finding a maximum independent set in this matching diagram which is equivalent in finding longest up sequence in a given permutation

π= (7, 2, 4, 8, 1, 9, 3, 5, 10, 6).

Now considering fig.2(a), let us process the top row of the permutation diagram fig.2[2]. Now fig.2(c), first 1 is placed on stack1 , then as 2 intersects 1 it goes in front of 1 in stack1. Now 3 cannot go in stack1 as 3 does not intersect 2 in stack1, so we will have to put it in stack2. Then 4 is placed in front of 3 on the stack2 since 4 does not intersect 2 but intersect 3. The 5 goes in stack3 as 5 does not intersect 4 and 2 which are the front of stack1 and satck2. Like wise 6,7,8,9 and 10 goes in stack4, stack1, stack3, stack4 and stack5 respectively. Now if we scan the tree we generated from top to bottom, we find a selective decreasing subsequence. That is 10 from stack5, 9 from stack4, 8 from stack3, 4 from stack2 and 2 from stack1. The generated stacks are shown in fig.2.[2]. Then {10,9,8,4,2} maximum independent set of G[π] and longest up-sequence of a given permutation. Now the maximum abutment set of the given example will be wired by moving terminal from left to right horizontally in order to minimize the vias.

3. UNCONSTRAINED VIA MINIMIZATION WITH MOVABLE TERMINALS

Jitender S. Deogun and Bhargab B. Bhattacharya proposed this algorithm for via minimization in two layer VLSI channel and switch-box with movable terminals. In this algorithm a unified graph-theoretic approach for minimizing the number of via is used. Now a brief description of two channel routing, three and four side switch-box routing.

Two channel routing: - two horizontal rows of terminals which can be moved freely without any sort of constraints, keeping their relative order unchanged.

Three sided switch-box routing:- two horizontal rows of movable terminals with a vertical column of fixed terminals.

Four sided switch-box:- two horizontal rows of movable terminals and also two vertical rows of movable terminals.

3.1. Two-Row Channel Routing

Consider a two-row multi-terminal routing problem as shown in fig.3(a)[4], in which the number of vias is to be minimized. The connectivity can be represented by a bipartite graph G as shown in Fig.3(b[4]). In multi-terminal net selecting one vertical abutment reduces the number of via holes by 1. However realization of two terminal net by an abutment lowers the count by 2. To solve this a weighted bipartite graph G, such that all the edges in G receive a weight equal to either 1 or 2. In G an edge (u, v) , u € X 1, and v € X2, is said to be isolated if degree c *(u)* = 1 , and degree c *(v)* = 1 . The graph G is constructed by giving weight of value 1 and value 2 to isolated edges and other edges respectively.

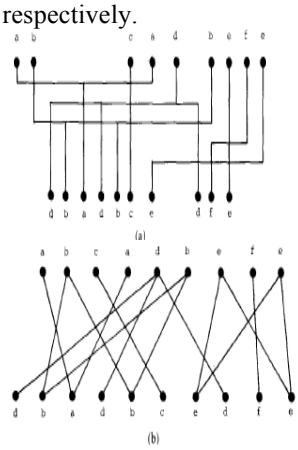

Figure 3 [4] (a) A Two-Row Multi-Terminal Routing Problem. (b) Its Bipartite Graph.

3.2 Three-Sided and Four-Sided Switch-Box Routing Problem.

The problem of via minimization in a switch-box environment can be managed by solving at most two independent maximum parallel set (MPS) problems. One in horizontal direction and another in vertical direction. Both three sided and four sided switch-box routing problem are similar.

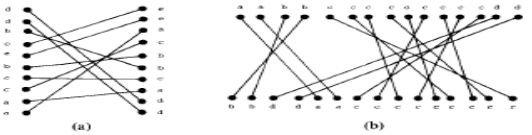

Figure 4. [4](a) Horizontal Permutation Diagram. (b) Vertical Permutation Diagram.

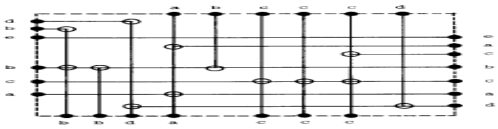

Figure.5. [4] Optimal Solution Of Four Way Switch-Box Routing.

Let us consider the routing problem. Now here it partitioned the problem into two equivalent weighted MPS problems for bipartite graphs, in vertical and horizontal connectivities. Also the number of vias necessary for connectivity is independent of their placement. The equivalent permutation diagram of the horizontal and vertical bipartite graph are fig.4(a) & (b)[4]. As soon as the maximum independent sets in these two graphs are found, it determines the maximum sets of abutment in both directions. Layouts of horizontal and vertical connectivities are shown in fig4[4]. Now the horizontal and vertical layouts are to be superimposed and thus we get to connect the terminals. The final routing is shown in fig.5[4], which minimizes the number of via by 13.

4. VIA MINIMIZATION WITH ASSOCIATED CONSTRAINTS

This paper proposes a via minimization algorithm with associated constraints in VLSI. In this paper a algorithm to globally eliminate the vias in three layer channel routing has been proposed[5,6]. Some associated constraints here are restricted terminals and adjacent limitation. Sung-Chuan Fang, Kuo-En Chang, and Wu-Shiung Feng proposed this algorithm. In three layer routing a large number of vias come up, so we have limit the number of vias in the routing algorithm.

Before we go to the algorithm, we have to know about transient routing. So transient routing is an incomplete physical routing in which topology of nets is done but wire segments have not been assigned. The transient routing represented by graph called segment crossing graph(SCG) denoted as Gs = (Vs, Ev U Ec), where vertex Vs represent wire segment, Ev and Ec represented as via-edges and cross-edges respectively. Also A(u) and C(u) are the adjacent list and cluster of vertex u respectively. Moreover each layer in three layer routing is represented by one color. Now the color painted on vertex u is different from the color on the vertex in C(u) and same that of the vertex in A(u) as shown in fig6(b)[7].

Now in constrained via minimization (CVM) algorithm the segment-crossing graph Gs = (Vs, Ev, Ec) and two sets of vertices associated with each vertex u € Vs. The two sets of vertices is adjacent to u and another is cluster of u as shown in fig 6 (a)[7]. The color assigned to the vertices A(u) are recommended colors of vertex u. If the vertex u is colored with one of the recommended colors of A(u), some of the vias can be eliminated. But the colors assigned to the vertex of C(u) are constrained colors that is this colors cannot be changed in order to eliminate some of the vias. Therefore in order to eliminate some of the vias we have to concentrate to the assigned colors but not in the constrained colors. Now a colors that has been assigned to a vertex u is called active vertex denoted by a(u) and the vertex where color has numbers been assigned is called inactive vertex. Here r(u),c(u) and e(u) are collections of recommended colors, constrained colors and expected colors respectively. r(u),c(u) and e(u) can be expressed in the following formulas.

$r(u) = \{ a(i) \mid 1 \le i \le n \text{ and } i \in A(u)\}$

$c(u) = \{ a(i) \mid 1 \le i \le n \text{ and } i \in C(u)\}$

$e(u) = r(u) - (r(u) \cap c(u))$.

At first all the vertices of Gs are inactive. After that one of the vertices will have to be selected where color will be assigned. As this algorithm is dependent on the mode of selecting the inactive vertices, a priority function is estimated in Gs. Each inactive vertices are 0C, 1C,2C,3C kinds when three colors are used in three layer routing. The highest priority vertex is obviously 3C and the lowest one is 0C. Again if some of inactive vertices are of same type than we will have to select the vertex with highest degree of constraint.

Now we have to decide the active color assigned to the vertex selected. Here L = (0, 1,2) be a set of colors corresponding to the three layers used in the routing. The active color of vertex, a(u), must be one in the set of L =c(u). Here $r\alpha$ be the number of color α in r(u) and α € L. For eliminating the maximum number of vias, the color assigned to an inactive vertex u will be a(u) satisfying the feasible condition that is defined below.

$a(u) = \alpha$, α € e(u) and $r\alpha(u)$ is maximum.

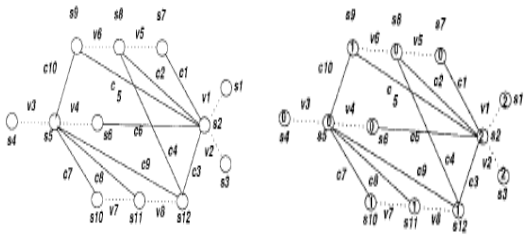

(a) (b)

Figure. 6(a)[7]Segment Crossing Graph.
(b)Color Assignment On Segment Crossing-Graph.

5. VIA MINIMIZATION USING LAYOUT MODIFICATION.

Layout modification proposes a new approach to the via minimization problem which combines the advantages of both UVM and CVM. This method is based on the observations that same routing problem can have different layouts where each layout requires lesser number of via. In this approach Khe-Sing The, D.F. Wong and Jingsheng Cong proposes a method of eliminating vias by systematically modifying the routing layout. In this layout modification method it uses two procedures to modify the layout. The first one will eliminate a via provided that this method of layout can have a new path to maintain the connection of the nets without using via. The new path should be prepared without any new via. Now in order to enhance the reconnecting process, it introduces another process to change the layer of wire segments by shifting vias along wire segments and thus reducing number of vias. This algorithm investigates the possibility of eliminating each via. It searches for a new route to connect the net components which become disjoint if the via is removed. Now as shown in fig.7a[9], a reconnecting path to replace via v is shown in fig.7b[9]. Via v will be eliminated without having to alter the connectivity of nets.

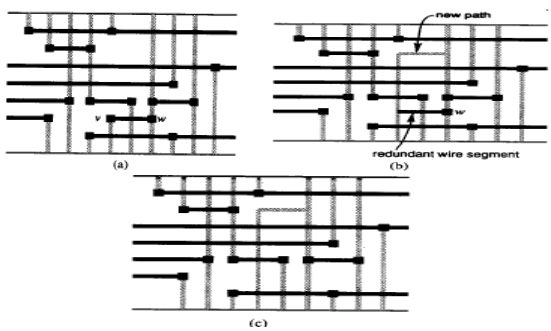

Figure.7[9] (a) Original Layout .(b)The New Path And Redundant Wire Segments.(c) Final Layout.

This algorithm considers the possibility of eliminating each via in the layout. For each of the via v, this algorithm makes an attempt to reconnect the components defined by via v. Now the search for the reconnecting path should be conducted twice, where each one starts from a different components. Before going for the search all other vias are shifted to facilitate the search. Now from the two search results, the one with the better results (in terms of number of eliminated vias and also the wire length of the reconnecting path) shall be adopted. Now if the search is successful , then the layout is actually have to modify or will be modified. Here some of the steps are involved. They are, at first reconnecting of the two net components with wire segments along new path. Secondly, eliminating the via. Thirdly, deleting wire segments and other vias that become more redundant after via v has been eliminated.

Now here are some of the steps for high level description of the algorithm:

It is assumed that via v belongs to net N. Then it finds the components of net N as defined by via v. Then it finds an alternate path reconnecting the two components of net N. Now it shifts all other vias to maximize the wire segments of net N on layer 1 and minimize wire segments of other nets on this same layer 1.Now starting from layer1 it uses a maze router to find a new path to reconnect the two components. Then it shifts all other vias in order to maximize of net N on layer 2 and minimize wire of other nets on this same layer2 and again uses a maze router to reconnect the components here too. Now it compares in terms of the number of vias eliminated and also wire length of the reconnect components. Based on the comparison , the one with better rerouting path is selected.

If the components are reconnected then eliminate via v and delete redundant wire segments. The time complexity for the above algorithm in the worst case is o (vn). Where v is number of via and n is number of grid points in layout. Since the maze routing and via shifting procedure takes only $o(1)$ time for dense layouts. The algorithm practically runs in o(v) time.

6. CONCLUSION

Here we have discussed about some two layer channel routing, three & four sided switch-box routing, color constrained three layer channel routing and layout modification via minimization algorithms to minimize the number of vias in a VLSI circuit.

We have seen that constrained via minimization gives better reduction than the unconstrained minimization and also in some case the layout modification give better reduction of vias than constrained algorithms. Hopefully, the paper could be able to give a glimpse of performance factor by the minimization of via in VLSI circuit and the challenges that are to be taken by the VLSI designers.

REFERENCES

[1]. I.S. Gopal, D. Coppersmith and C.K. Wong, "Optimal wiring of movable terminals, *IEEE Trans. Computer,* vol. C-32, pp.845-850,1983

[2]. Kim, H.; , "An application algorithm for the via minimization problem in channel routing," Applied Computing, 1990., *Proceedings of the 1990 Symposium on* , vol., no., pp.150-154, 5-6 Apr 1990.

[3]. R.B.K. Dewar, S.M. Merritt and M. Sharir, !!Some modified algorithms for Dijikstra'*s* longest up-sequence problem, *Acta Informatica 18*, pp. 1-15, 1985

[4]. Deogun, J.S.; Bhattacharya, B.B.; , "Via minimization in VLSI routing with movable terminals," Computer-Aided Design of Integrated Circuits and Systems*, IEEE Transactions on ,* vol.8, no.8*,* pp.917-920, Aug 1989]

[5]. Y. K. Chen and M. L. Liu, "Three-layer channel routing," *IEEE Trans. Computer-Aided Design,* vol. *CAD-3,* no. 2 pp. 156-163, Apr. 1984.

[6]. F. P. Preparata and W. Lipski, "Optimal three-layer channel routing," *IEEE Trans. Comput.,* vol. *C 33,* no. 5, pp. 427-437, May 1984.

[7]. Sung-Chuan Fang; Kuo-En Chang; Wu-Shiung Feng; , "Via minimization with associated constraints in three-layer routing problem," Circuits and Systems, 1990., *IEEE International Symposium on ,* vol., no., pp.1632-1635 vol.2, 1-3 May 1990.

[8]. D.N. Deutsch," compacted channel routing", *in Proc. Int. Conf. CAD*,1985,pp. 223-225.

[9]. Wong D.F.; Jinsheng Cong ;"A Layout Modification Approach to Via Minimization", *IEEE Trans. CAD* vol 10 no. 4,pp.536-41,April 1991.

Proceeding of the
International Conference on Electrical, Computer and Telecommunication Engineering
01- 02 December 2012 (ICECTE2012), RUET, Rajshahi-6204, Bangladesh

ICECTE2012: PI-0086

FCC Compliant CMOS IR-UWB Transmitter for Bio-sensing

Sagar K. Dhar[1], Quazi D. Hossain[2] and Palash K. Bhowmik[3]
[1]Department of EEE, Premier University, Chittagong, Bangladesh
[2]Department of EEE, Chittagong University of Engineering and Technology, Bangladesh
[3]Department of Instrumentation and Communication, Eastern Refinery Ltd., Bangladesh
E-mail: sagar378@puc.ac.bd

ABSTRACT
This paper presents an FCC (Federal Communications Commission) compliant impulse radio (IR) ultra-wideband (UWB) indoor Gaussian pulse transmitter for bio-sensing specially targeted for vital sign monitoring system. Exact spectrum tuning is a challenge in IR-UWB system while it has the highest level of prospects in contactless continuous monitoring. In this paper, the transmitter is designed for the most desirable feature of IR-UWB that is exact spectral tuning which is solved using underdamped operation of RLC circuit incorporated with three step amplitude tuning. Amplitude tuning enables adaptable output spectral density for different transmission band in order to meet the FCC spectral mask. Simulation results of the presented design are carried out in Advanced Design System 2009 where exact spectrum generation with center frequency 5, 7 and 9GHz of 2GHz bandwidth is tested.

KEY WORDS: Impulse Radio, UWB, Gaussian Pulse,Bio-sensing, Transmitter

1. INTRODUCTION

A pervasive healthcare system invariably refers to the system that is non-invasive, contactless and networkable in a wireless manner. Such systems proposed generally have two parts: a sensor of some kinds and a communication infrastructure such as transceiver and protocols to share data collected by the sensor. Among different possible sensing and imaging technologies, UWB detection and imaging is preferable for non-invasive and contactless biomedical sensing due to its resolution. It can be used for a perfect radar that is possible to deploy for short range detection (that offers contactless bio-sensing) and because it has resistance to multipath (a consequence of its resolution), it is possible to use for communication with high speed; and both tasks can be performed using the same design (i.e. same pulse shape, same frequency, transmitted power) [1]. It is also beyond questioning the impact of UWB radiation on health because UWB radar sensing is possible with even approximately 1μW [2] which is about three orders of magnitude lower than most international standards for continuous human exposure to microwaves. These issues make UWB as an appropriate selection for bio-sensing. And to meet the low power requirement, carrier less IR-UWB system is preferable. Moreover, IR-UWB is an inherently duty cycled system which allows to turn off the output buffer of the transmitter during the intervals between two impulses which reduces average power consumption. However, the main problem with IR-UWB is the exact controlling of output spectrum while meeting the FCC mask.

During the past ten years after FCC permitted the commercial development of UWB technology from 3.1-10.6GHz in 2002, more and more advancement have been attracted on this rising technology. IR-UWB is a duty cycled system and the most commonly used pulse shape is Gaussian pulse because of its good performance in frequency domain [3]. But it is required to meet the FCC restrictions which alternatively calls for IR-UWB pulses of tight requirements such as pulse width ~ 1ns and pulse amplitude < 1V. Early reported pulse generators (PG) used analog techniques [4, 5] which do not meet the low power and low cost requirements. [6] reports 1.7ns, 313pJ/pulse Gaussian pulse generated and centred at 5GHz with 550MHz bandwidth using complicated analog topology consumes high power. [7] presents a traditionally modulated 17ns PG in 7-9GHz band with programmable carrier where the pulse width would extremely limit the data throughput when the same transmitter would like to be used for detection and communication. On the other hand, [8] reports a 2nd derivative Gaussian PG requiring off chip band pass filters to deliver FCC compliant 1.5ns 63pJ/pulse over 0.5-5GHz. And [9] and [10] present 4 and 8-delay cell type 5th derivative all digital PG that will require very low chip area but unfortunately would suffer from process variation.

In this paper, an ultra-low power CMOS IR-UWB transmitter is presented with exact spectrum tuning tested for 3 bands centred at 5, 7 and 9GHz under the FCC restrictions having maximum average power of -41dBm per MHz. The proposed design eliminates the complexity of integrating exact R values using active circuit alternatives. The key point in meeting

low power requirement of Gaussian pulse generation yet applying mixed signal technique is the highly selective underdamped circuit. This technique actually reduces the sideband power in the Gaussian pulse compared to the digital circuits that actually operate on the basis of differentiating a Gaussian pulse.

2. METHODS

A simplified form of IR-UWB system for heart rate monitoring is in general a transmitter incorporated with a receiver section. In the transmitter, the fundamental issue is a Gaussian pulse generator under FCC power restriction [11] shown in Table Iand the main concern is yet to generate exact transmitting spectrum. The mathematical expression for a Gaussian pulse and its first and second order derivatives are shown in Eq. (1-3). But the spectrum of the pulses shown in Fig. 1 does not meet the FCC restriction. However, it is evident from Fig. 1 that if the pulse is differentiated to higher orders, the centre frequency of the pulse in frequency domain is shifted without changing its total bandwidth.

$$x(t) = \frac{A}{\sqrt{2\pi}\sigma}\exp(-\frac{t^2}{2\sigma^2}) \quad (1)$$

$$x'(t) = -\frac{At}{\sqrt{2\pi}\sigma^3}\exp(-\frac{t^2}{2\sigma^2}) \quad (2)$$

$$x''(t) = (\frac{At^2}{\sqrt{2\pi}\sigma^5} - \frac{A}{\sqrt{2\pi}\sigma^3})\exp(-\frac{t^2}{2\sigma^2}) \quad (3)$$

TABLE I
FCC POWER RESTRICATIONS FOR INDOOR APPLICATIONS

Frequency (GHz)	Max. Power in dBm/MHz	Frequency (GHz)	Max. Power in dBm/MHz
0.5-0.96	-41.3	1.99-3.1	-51.3
0.96-1.61	-75.3	3.1-10.6	-41.3
1.61-1.99	-53.3	10.6-50.6	-51.3

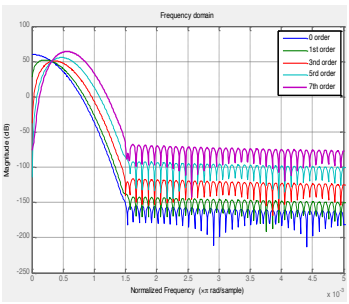

Fig. 1 Spectrum of different order Gaussian pulse

On the other hand, if the duration of the pulse in time domain is increased by increasing σ in (1) as shown in Fig. 2 (sd1<sd2<sd3), the bandwidth is decreased and vice versa.But the spectrum of Gaussian pulse and its derivatives do not meet the precise spectrum tuning requirement. One possible solution to this problem is to modulate the Gaussian pulse with a carrier signal instead of using derivatives to have a precise spectrum. But this approach would drastically increase the power consumption in transmitter unit. This paper presents under-damped operation of a second order system as a possible solution for modulating the Gaussian pulse without carrier signal generation.

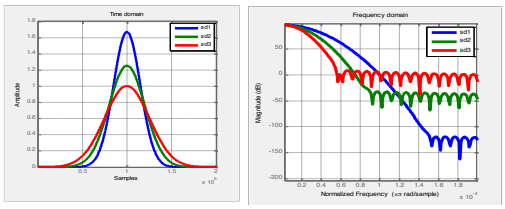

Fig. 2 Pulse width vs. bandwidth: time (left) and frequency domain (right).

In this paper, at first the Gaussian pulse is generated combining the edges of digital signals which excites an under-damped RLC circuit for generating modulated Gaussian pulse. The duration of the pulse could be precisely controlled by R value and oscillation frequency which is controlled by varying C value as shown in Fig. 3 in this work.

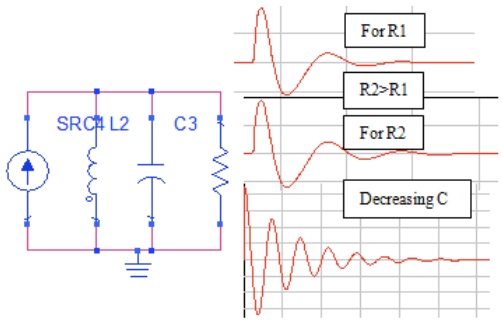

Fig.3 Controlling pulse shape and hence the bandwidth varying R and C

However, such an FCC compliant IR-UWB transmitter could be useful in sensing physiological information such as heart and respiration rate. And based on these bio-information, survivor detection in disasters and surveillance system are possible to develop. The heart of an adult person if considered as 12cm in length, 8 to 9cm in breadth and 6cm in thickness [12],it can be approximated as a sphere of radius 6cm. [13] presents the feasibility of heart rate monitoring 15cm apart under FCC power restrictions considering total attenuation of 30dB from body surface to heart and heart to body surface again although this range 15cm could be increased to about 1m for gated pulse as shown in [11] as presented in this paper still meeting the FCC restrictions.

3. TRANSMITTER ARCHITECTURE

The The block diagram of the transmitter presented, shown in Fig. 4 is comprised of 4 major parts: a) Gaussian pulse generator, b) amplitude tuning, c) frequency tuning and d) output buffer.

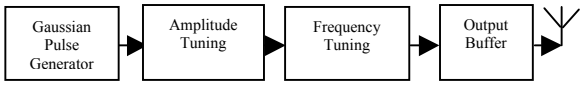

Fig. 4 Transmitter block diagram

3.1 Gaussian Pulse Generator

Two categories of pulse generator exist: analog pulse generators and digital pulse generators. [4] presentsanalog pulse generator that employs square and exponential functions of transistors biased in saturation and weak inversion region respectively. The main disadvantage of such pulse generators is the extremely low pulse amplitude. On the other hand, digital pulse generators combine the edge of a digital signal with its inverted version that eliminates the problem of low amplitude of analog pulse generators. In this paper, the Gaussian pulse is generated with XNOR operation of a digital signal and its inversion as shown in Fig. 5.

3.2 Amplitude Tuning

Amplitude tuning is optimised for meeting the FCC mask and designed in this paper with common source amplifier with current source load as shown in Fig. 6. Attenuation for different transmission frequency band is different which demands amplitude tuning to maintain FCC restrictions. In this paper, the gain and hence the amplitude is controlled with the trans-conductance of MOSFET 1-6. Three step amplitude control is obtained by applying 1 or 0 to the vctrl1-vctrl3 for three band of testing spectrum centred at 5, 7 and 9GHz.

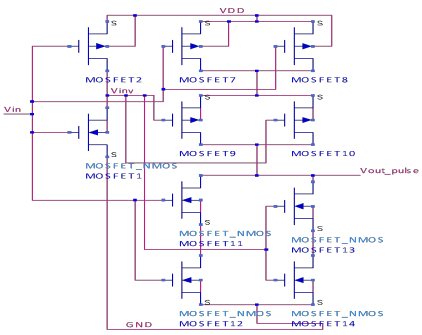

(b)

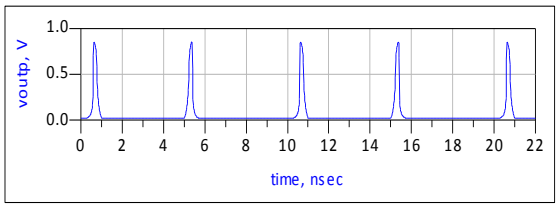

(b)

Fig. 5 Gaussian Pulse: (a) CMOS implementation, (b) pulse waveform.

3.3 Frequency Tuning

Frequency tuning of transmitted pulse can be obtained by digital or analog circuits. [9-10] present IR-UWB system using digital circuits where 4 pulses are combined successively to form fifth derivative of Gaussian pulse which alternatively offers modulated Gaussian pulse without a carrier signal. Moreover, this method eliminates inductor and reduces the chip area in a great manner. But unfortunately, these methodshave higher side lobe spectral component and severely suffers from process variation. In this paper, an under damped RLC network is used for up-conversion and spectrum control is realised triggering three capacitors C4-C6 with Fctrl1-3 in Fig. 7.

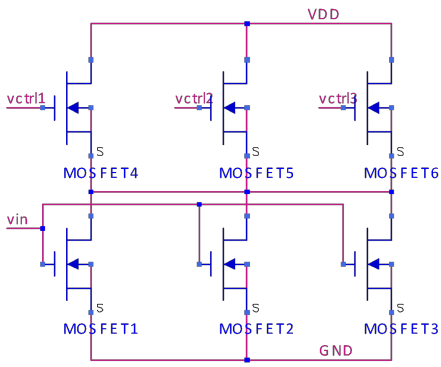

Fig. 6 Amplitude tuning circuit

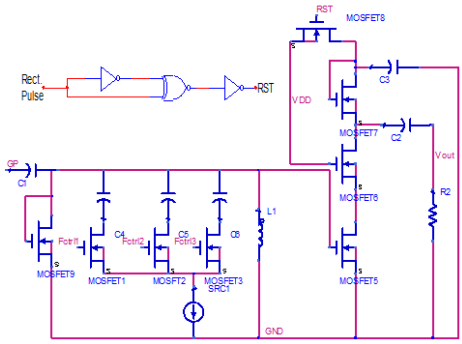

Fig. 7 Frequency tuning and output buffer circuit

3.4 Output Buffer

In this paper, an output buffer is designed for generally two purposes: a) driving the antenna and b) gated transmission. A cascode arrangement is applied for antenna driving and input-output isolation. On the other hand, the gated transmission is implemented with a PMOS switch (MOSFET8) in Fig. 7 which provides no static current consumption. The RST signal generation circuit for blocking the transmitter power consumption during off pulse period is also shown in Fig. 7. Capacitor C_3 is used to cancel out the noise generated from switching on/off and capacitor C1 is used for minimising low frequency side lobe components.

4. RESULT

The IR-UWB transmitter is designed and simulated in Advanced Design System 2009. Exact spectrum generation for IR-UWB system is tested at 5, 7 and 9GHz centre frequency meeting the FCC regulation with no static current. A finally shaped Gaussian pulse of the transmitter unit is shown in Fig. 8.

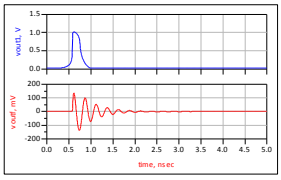

Fig. 8 Gaussian pulse after frequency tuning and buffer circuit

Fig. 9 shows the power spectral density with FCC masks of generated Gaussian pulses by the proposed transmitter. The amplitude is perfectly controlled for FCC restrictions and possible to tune within the range 3.1-10.6GHz range. The inductor L1 in Fig. 7 is carefully designed for high selectivity and C1 along with MOSFET9 and capacitors provide bandwidth selection.

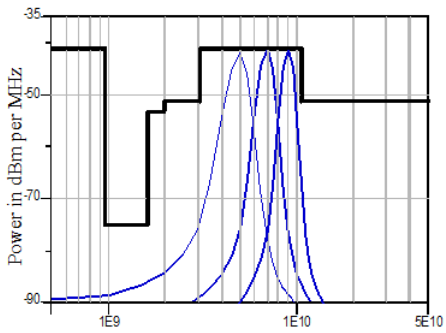

Fig. 9Power spectrum density with FCC mask for centre frequency: (a) 5GHz, (b) 7GHz and (c) 9GHz.

5. CONCLUSION

An ultra-low power, low complexity and spectrum tuneable CMOS IR-UWB transmitter without any static current consumption is presented meeting the FCC spectral regulations which is of frequent demand for continuous and contactless monitoring of vital sign monitoring. Such transmitters would be equally applicable not only for medical application such as heart and respiration rate monitoring but on the basis of these kinds of information, rescue operation and surveillance systemis also possible to develop for remote monitoring along with a receiver.

REFERENCES

[1] Hussain, M.G.M, "Ultra-wideband impulse radar- an overview of the principles," IEEE Aerospace and Electronics Systems Magazine, Vol.13, No.9, pp.9-14, Sept, 1998.

[2] McEwan, T.; Azevedo, S.; "Micropower Impulse Radar"; Science & Technology Review; Lawrence Livermore National Labora-tory, US; Jan./Feb. 1996.

[3] X. Chen and S. Kiaei, "Monocycle shapes for ultra wideband system", IEEE Int, Symp. Circuits And Systems (ISCAS), bol.1, pp.597-600, May 2002.

[4] Y. Zheng, Y. Tong, C. W. Ang, et al., "A CMOS carrier less UWB transceiver for WPAN applications," IEEE Int. Solid-State Cir. Conf., pp.116-117, 2006.

[5] J. Han and C. Nguyen, "A new ultra-wideband ultra short monocycle pulse generator with reduced ringing", IEEE Microwave and Wireless Components Letters, vol.12, no.6, pp.206-208, 2002.

[6] D. Wentzloff and A. Chandrakasan, "Gaussian pulse generators for subbanded ultra wideband transmitters", IEEE transactions on UWB, Zurich, Switzerland, pp1647-1655, 2006.

[7] J. Ryckaert, G. Van der Plas and et al., "A 0.65 to 1.4nJ/burst 3-10GHz UWB all digital TX in 90nm CMOS for IEEE 802.15.4a", IEEE JSSC, vol.42, no.12, pp2860-2896, 2007.

[8] L. Smaini, C. Tinella and et al., "Single chip CMOS pulse generator for UWB systems", IEEE JSSC, vol.41, no.7, pp.1551-1561, 2006.

[9] Q. Bo, C. Hongyi and et al., "An ultra low power FCC compliant 5th Derivative Gaussian Pulse generator for IR-UWB Transceiver", Chinese Journal of Electronics, vol. 18, no. 4, pp605-609, Oct 2009.

[10] H. Kim, Y. Joo, "Fifth derivative Gaussian pulse generator for UWB system," IEEE Radio Frequency Integrated Circuit Symp., pp.671-674, 2005.

[11] Freescale semiconductor, "UWB opportunities under the new FCC Waiver," Doc. #UWBOPPFCCWVRWP rev.1, March, 2005.

[12] Gray, Henry, *Anatomy of Human Body*, Philadelphia: Lea &Febiger, 1918, Bartleby.com, 2000.

[13] Carlos G. Bilich, "Feasibility of dual UWB heart rate sensing and communications under FCC power restrictions," PhD Proposal, Dept. of Information and Telecom. Tech., University of Trento, Italy, 2006.

[14] B. Razavi, *Design of Analog CMOS Integrated Circuit,* McGraw-Hill Higher Education, International Edition, 2001, pp.505-509.

Proceeding of the
International Conference on Electrical, Computer and Telecommunication Engineering
01- 02 December 2012 (ICECTE2012), RUET, Rajshahi-6204, Bangladesh

ICECTE2012: PI-0087

Effects of electrolyte composition, current density and heattreatment on the microstructure and magnetic properties of electrodeposited Fe-Ni alloy coating

Mohammad Fuad Nur Taufique, Ashraful Azamand Dr.Kazi Md. Shorowordi
Department of Materials and Metallurgical Engineering, Bangladesh University of Engineering and Technology
E -mail: taufiquemme@gmail.com, ndcboys@gmail.com and kmshorowordi@mme.buet.ac.bd

ABSTRACT
Iron-nickel (Fe-Ni) alloys are of great commercial interest in the field of electronics as they possess good soft magnetic property. In the present study, Fe-Ni alloy coating were electrodeposited on the Cu substrate from one simple bath containing $NiSO_4$, $FeSO_4$, Na_2SO_4 *and* H_3BO_3 *of varying compositionand two complex baths containing ascorbic acid and citric acid separately in addition to the simple baths. All baths contain the sameFe-Ni ratio as 1:12 and electrodeposition were carried out in different current densities under constant pH value.Heattreatment at the temperature range of* 350^0*cto* 500^0 *c in presence of inert atmosphere was done onsome selective samples. The Morphology and composition of the deposited Fe-Ni film were investigated by scanning electron microscope (SEM) and energy dispersive x-ray analyzer (EDX)respectively. The magnetic propertieswere determined using vibrating sample magnetometer (VSM).It was found that high nickel content and addition of complexing agent suppresses the anomalous nature of the Fe-Ni alloy electrodeposition. Maximum Saturation magnetization value of 114.2emu/gm was obtained from simple bath. Coating obtained from complex bath showed maximum saturation magnetization value 109.36emu/gm,and after heattreatmentcoercivity decreased. It was also observed that in simple and complex bath with increasing current density, anomalous deposition behavior of Fe-Ni alloy suppressed.*

KEYWORDS: Fe-Ni coating, complexing agent, current Density, heattreatment, coercivity.

1.INTRODUCTION

There has been a great research interest in the development and characterization of iron-nickel (Fe-Ni) thin films due to their operational capacity, economic interest and magnetic properties [1]. Fe-Ni alloys of certain compositions are preferable for high sensitivity applications since they exhibit high magnetic permeability at low intensity magnetic fields because of their low magnetic anisotropy and magnetoelastic energy [2] Therefore, it has a wide application in the field of electronic device manufacturing such as read-write heads for magnetic storage, magnetic actuators, magnetic shielding, high performance transformer cores.

There are various methods for deposition of iron-nickel magnetic film such as electrodeposition, vacuum evaporation plating, sputtering, cold rolling. But a simple and inexpensive technique for the production of alloy coatingis electrodeposition. In the case of electroplating, magnetic property of iron-nickel alloy coating depends on several factors. In the experiment effects of molar ratio of Fe and Ni ,current density, grain size, addition of complexing agent over the Fe-Ni electrodeposited coating were investigated. Effects of heattreatment on the property of electrodeposited Fe-Ni alloy coatings were also observed.

One serious drawback of the electrodeposition process is the generation of internal stresses resulting in the formation of microcracks [3]. However, the internal stress level can be reduced by heat treatment or the addition of inhibitors [4]. In addition, Fe-Ni electrodepositing exhibits the phenomenon of anomalous codeposition. This term introduced by Brenner is being used to describe the preferential deposition of the less noble metal, Fe, to the more noble metal, Ni. In other words, the reduction of nickel is inhibited while the deposition of iron is enhanced when compared with their individual deposition rates. Thus electrodepositing of Fe-Ni alloys has attracted considerable attention because of its special characteristic nature and wide range of unique properties. An important feature of the Fe-Ni alloy system is its structural evolution, with a change from bcc for the Fe-rich alloy to fcc for the alloy with higher Ni content.

The focus of this study, however, is not the mechanism of anomalous codeposition but the major aim is to investigate the influence of complexing agents, currentdensity, molar concentration of Ni and Fe and heattreatment on magnetic property and surface morphology of the electrodeposited Fe-Ni alloy coating.

2. EXPERIMENTAL PROCEDURE

Commercial copper sheets were used as substrates in the experiment of this study. Platinum anodes were used for electrodeposition. Dimension of the Cu substrate were 50mm x 15 mm x 1 mm.The Cusubstrates were degreased, mechanically and electrochemically cleaned by maintaining polishing with emery papers, pickling, rinsing and acid dipping process.

Electrodepositing was carried out in a laboratory type electrodepositing set-up consisting a beaker, a D.C power supply, cathode and anode electrode and a Perspex electrode holder cathode. Two platinum anodes were used on both sides of the cathode at a same distance for uniform deposition on both sides of the cathode. Schematic of the electrodepositing set up is illustrated in Fig. 1.

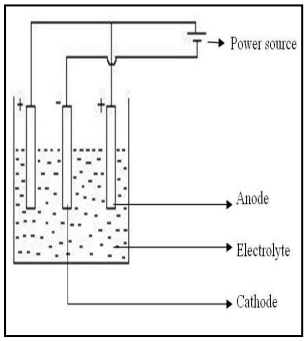

Fig.1: Schematic of the set-up used for electrodepositing.

Both simple and complex baths were used. Analytical reagent grade chemicals and deionized water were used to prepare baths. Sulfate baths composing of $NiSO_4$, $FeSO_4$, H_3BO_3 and Na_2SO_4 in varying composition comprise the simple baths. $(NH_4)_2SO_4$ and H_2SO_4 were added to control the value of pH.Two Complex baths were prepared by adding ascorbic acid and citric acid separately in same composition to the simple baths. Details of the simple and complex bath compositions are shown in Table 1. All depositions were carried out at room temperature and at constant current densities viz. 30, 50, 70 and 100 mA/cm^2.Each deposition was continued for a predetermined time period of 2 hours and without any stirring action. Initial pH value of each bath was 2. Chemical analysis of the deposit was determined by energy dispersive x-ray analyzer (EDX).Scanning Electron Microscopy (SEM) was used to study the morphology of Fe-Ni alloy coatings. Magnetic properties of the Fe-Ni coatings were measured by aVSM (vibrating sample magnetometer). After that some selective samples were heattreated at the temperature range from 350^{0}c to 500^{0}c in presence of inert (N_2 gas) in a muffle furnace. Effect of heattreatment on the magnetic property also studied.

Table1: Overall bath compositions.

Bath identification	Bath composition gm/L	Complexing ingredients (gm/l)	Ni/ Fe ratio
B1	$NiSO_4$=53.3 $FeSO_4$=4.44 H_3BO_3=25 Na_2SO_4=49.7		12 :1
B2(a)		ascorbic acid =4	
B2(b)		citric acid=4	

3. RESULTS AND DISCUSSION

3.1 Chemical analysis of the coating

Chemical analysis of the coatings was carried out by energy dispersive x- ray analyzer (EDX) respectively. Percentage of nickel in the deposit as a function of current density is shown in Fig. 2. For all cases neglecting a small deviation, with increase in current density % of Ni in the coating increases. The standard electrode potential for reduction of pure Ni2+ (-0.257 V) is relatively more positive than that of Fe2+ (-0.447 V). According to normal deposition theory, an element with a higher positive standard electrode potential is expected to deposit preferentially than the one with a less positive standard electrode potential [5]. Again according to Brenner's definition of anomalous codeposition [6], the less noble metal (here Fe) is deposited preferentially. So increase in current density and high molar percent of Ni in the bath suppressed the anomalous nature of theelectrodeposition.

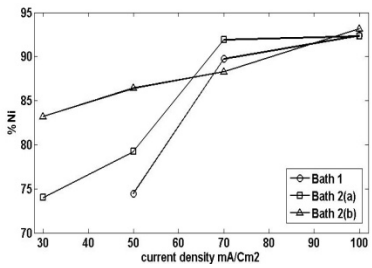

Fig. 2: Current density vs. % Ni

3.2 Morphology of the coating

The influence of current density and bath composition on the morphology of Fe-Ni coatings were evaluated by Scanning Electron Microscope (SEM). The topographies of Fe-Ni coatings were analyzed concerning their uniformity, porosity and the presence of cracks.In case of the coatings deposited from bath B-1 [Fig. 3(a), 3(b)], grains are roughly spherical and the average grain size decreased with increasing current density. Thus structure of the Fe-Ni coatings is strongly influenced by current density.It is known that high current density gives rise to a high degree of adatoms saturation at the electrode surface and high degree of adatoms decreases the grain size. With the presence of only citric acid as complexingagent in bath B2(b) , the film was highly porous [Fig. 4(a)] probably due to the hydrogen bubbles formed during co-deposition. Addition of ascorbic acid as complexing agent in bath B 2(a) increased nucleation rates that helped form crack-free, uniform and fine grained structures as is seen in Fig. 4(b) and 4(c)

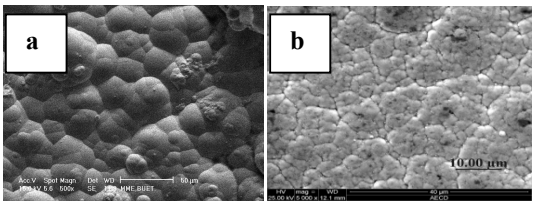

Fig. 3: SEM images of the deposit obtained from simple bath B-1 at current density (a) 30 ma/cm^2 (b)70 ma/cm^2

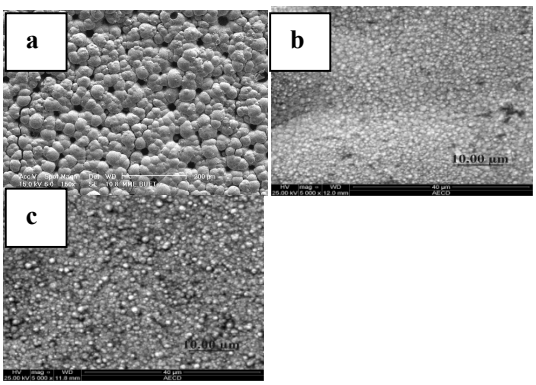

Fig. 4: SEM images of the deposit obtained from (a) bath B2(b) at current density 100 ma/cm^2 (b)bath B2(a) at current density 70 ma/cm^2(c)bath B2(a) at current density 30 ma/cm^2

3.3 Magnetic property of the coating

Soft magnetic thin films with high saturation magnetization are highly desired in a wide range of applications from magnetic write heads to high frequency inductors. The demand of saturation magnetization for soft magnetic materials is increasing steadily and that the saturation magnetization 135 emu/gm is satisfactorily acceptable for the write head materials [7]. Magnetization loops of the Fe-Ni films deposited from various simple and complex baths were measured using a vibrating sample magnetometer (VSM). The variation of saturation magnetization (Ms) with %Ni of coatings from different baths is shown in Table 2 and effect of heattreatment (annealing) on magnetic saturation of the bath B 2(a)(ascorbic acid bath) is shown in Table 3. In all cases value of Ms increases with increasing the % Ni in the coating. The reason behind this may be the presence of $FeNi_3$ phasewith increasing the Ni content. Highest Ms value of 109.36 (emu/gm) is observed for the sample of B 2(b) at current density 100 ma/cm^2. After annealing the sample of bath B 2(a) at current density 100 ma/cm^2, increase in Ms value is observed.With increasing the annealing temperature highest Ms value of 115.10 emu/gm is found at annealing temperature 500^{0}c whose before heattreatment value was 101 emu/gm. Due to annealing coercivity decreased and the BH loop became more soft magnetic[Fig.5 (b)]. The reason behind this may be the increasing of gain size due to annealing.

Table2: Saturation magnetization of different baths

Bath identification	Current density ma/cm^2	%Ni	Ms(emu/gm)
B 1	50	74.46	72.48
	70	89.73	98.48
	100	92.39	114.2
B 2(a)	30	74.02	74.81
	50	79.22	77.36
	70	91.9	89.1
	100	92.3	101
B 2(b)	30	83.19	69.46
	50	86.4	85.81
	70	88.27	97.42
	100	93.16	109.36

Table2: Saturation magnetization after heattreatment

Bath B2(a)coating at current density cd=100 ma/cm^2	Annealing temperature, ^{O} celcius	Ms(emu/gm)
	350	102.07
	400	109.38
	450	113.624
	500	115.10

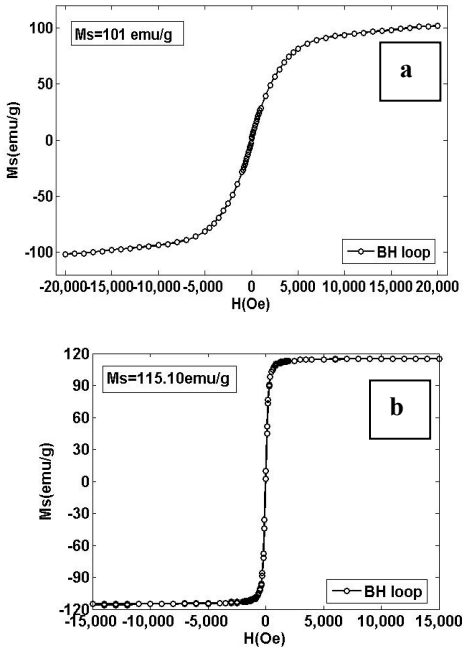

Fig 5:BH loop of (a) sample B2(a) at current density 100 ma/cm^2, before heattreat ment . (b) SampleB2 (a) at current density100 ma/cm^2, after heattreat ment at 500^{0}c.

4. CONCLUSIONS

The electrolytic compositions, current density of depositing baths and annealing temperatures are considered as varying parameters in this work. The conclusions drawn from the study are:

1. Variation of applied current density affected deposit compositions for both simple and complex baths. Percentage Ni into the coating increased with increasing current density for both simple baths and complex baths.
2. High Ni content in the bath, high current density and addition of complexing agents suppress the anomalous behavior of the Fe-Ni alloy coating.
3. The morphology of the Fe-Ni films obtained from simple baths is characterized by coarse-grained, non-smooth surface with /without microcracks onto it. On the contrary, coatings from ascorbic acid added complex baths are fine-grained with smooth surfaces. But in case of, citric acid added complex bath film is highly porous.
4. For all baths magnetic saturation (Ms) increases with increasing the %Ni in the coating.
5. Heattreatment (annealing) increases the magnetic saturation and decreases coercivity and increasing the annealing temperature increases the grain size which also help to decreases the coercivity as a result more soft magnetic property enhanced.

5. ACKNOWLEDGEMENTS

The authors thank the project of Development of Materials for Tools and Bio Metallic Implant(DMTBI) under Bangladesh Council of Scientific and Industrial Research(BCSIR) for using their laboratory. The assistance of Dr. Abdul Gafur and Engg. Rakibul Qadir of BCSIR and Engg. Al Mamun of Bangladesh Atomic Energy Commission with the VSM, SEM and EDX analysis is gratefully acknowledged.

REFERENCES

[1] Li, H., Ebrahimi, F., "*Mater. Sci. Eng.*" Vol. 93, p. 347, 2003.
[2] Ovari, T.A., Tibu, M., and Chiriac, H., "*Sensors Actuat. A106*", Vol. 267, 2003.

[3]Czerwinski, F., Kedzierski, Z., "*J. Mater. Sci.*", Vol. 32, p. 2957, 1997.

[4] Szewczyk, R., Bienkowski, A., Salach, J., Fazakas, E., Varga, L. K., "*J. Optoelectron. Adv. Mater.*"
Vol. 5, p. 705, 2003.
[5] M. M. Abu-Krisha, A. M. Zaky and A. A. Toghan," *J. Corr. Sci. and Egg.*", Vol. 7, 2005.

[6] A. Brenner," Electrodeposition of Alloys, Academic Press", New York, Vol. 2, 1963.

[7] N. X. Sun and S. X. Wang, "*Soft High Saturation Magnetization (Fe 0.7 Co 0.3)1- x N x Thin Films forInductive Write Heads*", Vol. 36, 2506, 2000.

Proceeding of the
International Conference on Electrical, Computer and Telecommunication Engineering
01- 02 December 2012 (ICECTE2012), RUET, Rajshahi-6204, Bangladesh

ICECTE2012: PI-0088

Preparation of ZnO film by an optimum and automatic control system of spray-pyrolysis

M. A. Munjer, M.F. Hossain, M. Firoj Ali, Shadhon Chandra Mohonta*
Department of Electrical and Electronic Engineering, Rajshahi University of Engineering & Technology (RUET), Rajshahi-6204, Bangladesh.
*faruk94_ruet@yahoo.com

ABSTRACT
The aim of this paper is to fabricate an optimum and automatic control system for spray pyrolysis. The spray pyrolysis technique is more suitable, simple and cost-effective than other methods. As a result spray-pyrolysis technique has chosen for the present work to deposit film. This optimum and automatic control system of spray-pyrolysis system consists of precursor chamber, spray nozzle unit, electric heater, air compressor, display unit and spray-dry controlling unit. The whole controlling system is controlled by using microcontroller. The good transfer ability of ZnO films has confirmed using this automatic system.

KEY WORDS: Spray-pyrolysis, thin film, Spray-dry controller, ZnO film.

1. INTRODUCTION

There are a number of physical and chemical routes for preparing thin films, like pulsed laser deposition, ion beam sputtering, thermal evaporation, vacuum deposition, chemical vapor deposition, co-precipitation, sol-gel, chemical bath deposition etc. Among these processing methods, a spray pyrolysis is one of the most promising techniques, where the thin film formation is carried out in air by a simple apparatus [1] and this technique is also applicable to produce thin film in large scale. Moreover, the complicated vacuum system (like in CVD and sputtering systems) is no longer necessary for this technique [2].

The film properties are sensitive not only to their structure but also to many other parameters including thickness, surface states, morphology etc [3]. The quality and properties of the films depend largely on the process parameters. The most important parameter is the substrate surface temperature. The properties of deposited films can be varied and thus controlled by changing the spray-dry time during deposition to vary the substrate surface temperature.

In this paper, an automatic controlling arrangement has been proposed to prepare thin film from precursor and organic solvent of ZnO. A microcontroller based circuit is used in this arrangement. This controlling arrangement is low-cost and has no mechanical arrangement. This arrangement also offers a display and keyboard unit for easy handling and maintenance to the user. Detailed analysis of the film formation mechanisms have been discussed in this work. An excellent performance have confirmed by using this controlling arrangement for depositing of ZnO thin films by spray-pyrolysis technique.

2. SPRAY-PYROLYSIS TECHNIQUE

Spray pyrolysis is a deposition process whereby heat is used to break molecules into elemental sources that are then spray deposited on a substrate. This coating technique was the predecessor of the chemical vapor deposition (CVD) techniques. The coating is applied at elevated temperatures by spraying droplets of liquid precursors onto hot substrates. It is used for depositing a wide variety of thin films, which are used in devices like solar cells, sensors, solid oxide fuel cells etc. It has evolved into an important thin film deposition technique and is classified under chemical methods of deposition.

Spray Pyrolysis technique involves spraying a solution of the desired compound onto a heated substrate. Typical CSP equipment consists of an atomizer, a substrate heater, temperature controller and a solution container. Additional features like solution flow rate control, improvement of atomization by electrostatic spray or ultrasonic nebulization can be incorporated into this basic system to improve the quality of the film. To achieve uniform large area deposition, moving arrangements are used where either nozzle or substrate or both are moved.

Only crude models about the mechanism of spray deposition and film formation have been developed. There are too many processes that occur sequentially or simultaneously during the film formation by CSP. These include atomization of precursor solution, droplet transport, evaporation, spreading on the

substrate, drying and decomposition. Understanding these processes will help to improve film quality.
Deposition process in CSP has three main steps: atomization of precursor solutions, transportation of the resultant aerosol and decomposition of the precursor on the substrate. Atomization of liquids has been investigated for years. It is important to know which type of atomizer is best suited for each application and how the performance of the atomizer is affected by variations in liquid properties and operation conditions. Air blast, ultrasonic and electrostatic atomizers are normally used. Among them, air blast atomization is the simplest.

The precursor solution comes to the spray nozzle through a pipe with controlling system. The spray nozzle is fixed at an appropriate distance from the substrate. The precursor solution is sprayed on to the substrate in air and around a high temperature zone where thermal decomposition and possible reaction between solutions occur, through compressed air, which is used as carrier gas with a flow rate controlled through air compressor regulator.

Thin film deposition using spray pyrolysis can be divided into three main steps: atomization of the precursor solution, transportation of the resultant aerosol and decomposition of the precursor on the substrate. However, four types of processes that may occur during highest temperatures, the metallic compound vaporizes before it reach the substrate and the chemical reaction takes place in the vapor phase [4]. Deposition is shown in Fig. 1.
In step 01, the droplet splashes on the substrate, vaporizes, and leaves a dry precipitate in which decomposition occurs fig.1(a). In step 02, the solvent evaporates before the droplet reaches the surface and the precipitate impinges upon the surface where decomposition occurs fig.1(b).

In step 03, the solvent vaporizes as the droplet approaches the substrate, then the solid melts and vaporizes (or sublimes) and the vapor diffuses to the substrate to undergo a heterogeneous reaction there. This is true CVD fig.1(c).

In step 04, at the highest temperatures, the metallic compound vaporizes before it reaches the substrate and the chemical reaction takes place in the vapor phase [4] fig.1(d)..

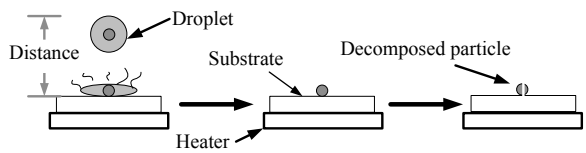

(a) Step 01

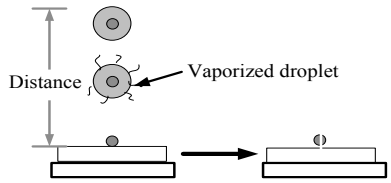

(b) Step 02

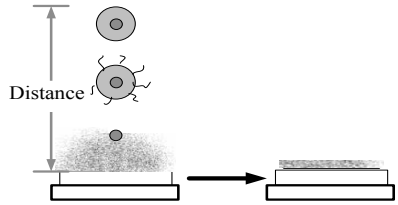

(c) Step 03

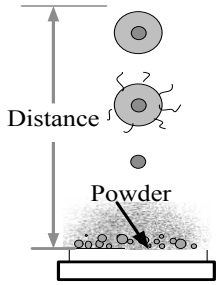

(d) Step 04

Fig. 1: Spraying with different distance between droplets to substrate.

3. EXPERIMENTAL MODEL

The experimental model of the automatic system of spray-pyrolysis contains with wooden chamber and control unit which are discussed in the next articles.

3.1WOODEN CHAMBER

At first a perfect wooden box was made in which an electric heater, the spray nozzle and the substrate are arranged as shown in fig. 2. The spraying system and furnace were kept inside wooden chamber of size 50x30x70 cm^3 and the outlet of the box is fitted with an exhaust fan to remove the toxic gases produced during the decomposition of the spray solution. The inner surface of the box is painted by epoxy liquid, to reduce the heat loss through the surface.

As the box was made of wood, it was a duty to think about the burning of it. So the heater was placed about 15cm far from each of the wall of the box.

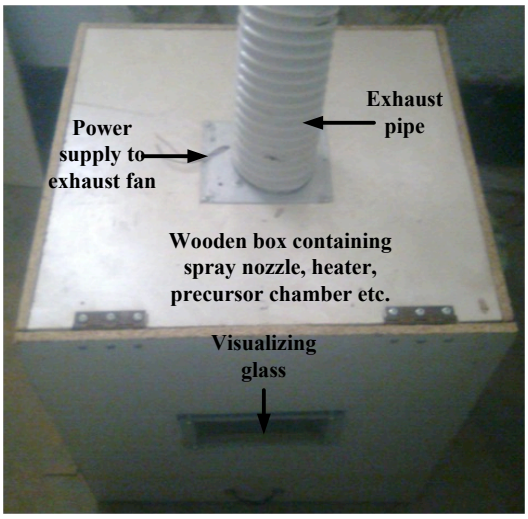

Fig. 2 Photograph of Wooden chamber.

For spraying the solution on the substrate wih the flow of air a spray nozzle is used. A spray nozzle is a precision device that facilitates dispersion of liquid into a spray.

An air compressor was used to provide the flow of air through the spray nozzle to spray the liquid on substrate. A rack was designed at a 20cm distance from top to place the spray nozzle efficiently on the heater. A glass plate is attached with the door of the box to visualize inside the box. A fan was placed on the top wall of the box to exhaust the evaporating gas from the wooden chamber. The rating of the relay was 12V to operate the 12V DC cooling fan.

3.2AUTOMATIC CONTROLLING UNIT

Spray-dry controller is the main units of the proposed system of automatic spray-pyrolysis system.

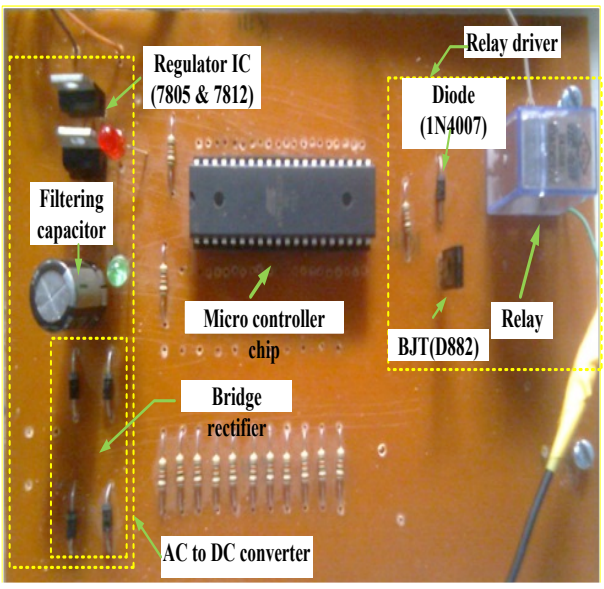

Fig. 3 internal circuit diagram of Controlling unit.

display, the key board arrangement, relay, BJT, transformer, one of 5V and 12V regulator IC. Each resistor of 1KΩ was used with the switch to ground to protect the microcontroller IC. The BJT was used to switch the relay at the specific time controlled by the MCU. The MCU operated by the program written in BASCOM AVR software.

Fig. 4 shows the photograph of automatic controlling unit.

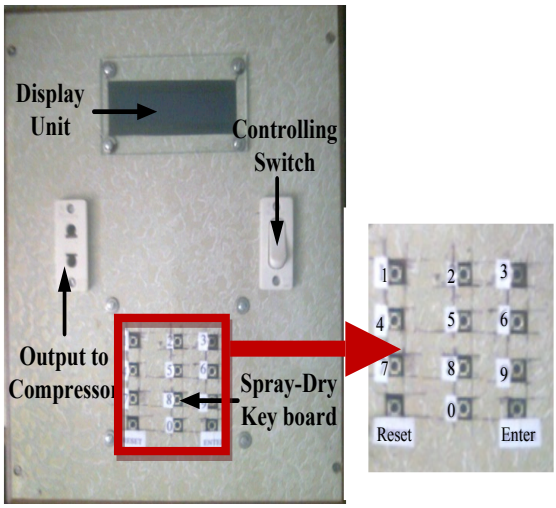

Fig. 4 Photograph of Automatic Controlling unit.

When the compressor is being switched on, the flow of air impinge the liquid situated inside of the spray nozzle. As a result the flow of air sprays the solution on the substrate which is placed on the heater jacket. The compressor is controlled by the controlling unit. The controlling unit takes a spray and a dry time through the key board. The compressor is switched on and off until the spray and dry time and the cycle is repeated. As a result the solution is sprayed and dried continuously.

At first the system will ready for taking the input time of spray and dry of the substrate and this time the display unit will show the message that ‘’Enter spray time Enter dry time’’ . This time a red light will switch on to signal that the MCU is ready for taking the input from key. After that the MCU will check the time is valid or not. Invalid will show only when the input time given by the user is more than 100 or less than 1. This time the display unit will show the message that ‘’0s spray time is not valid’’.But if the time given by the user is correct the display will show the message with spray and dry time. After being successfully input of spray and dry time, the system will wait for the permission of the user to start and this time the display unit will show the message that ‘Please press the enter button’’ .

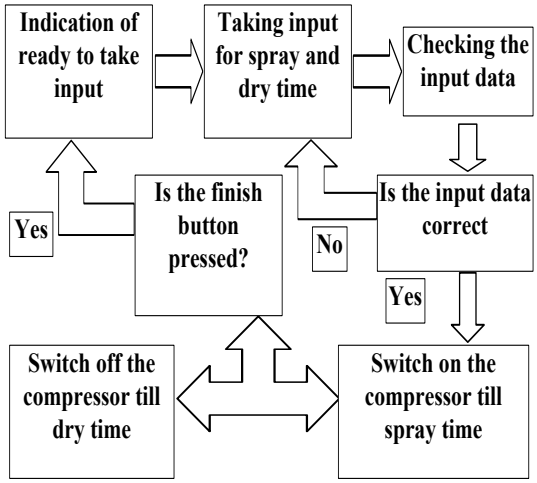

Fig. 5 Flow chart of Operating Principle of Controlling Unit

Fig. 5 shows the flow chart of operating principle of control unit.

3.3 PRECURSOR REACTANTS

The reactants of precursor of the present work are Ethanol, Zinc Acetate and Di-ethylamine (DEA). The table 1 shows the amount of each reactant used in the preparation of precursor of ZnO.

Reactants	Amount
Ethanol	25 ml
Zinc Acetate	5.487 gm
Di-ethylamine (DEA)	2.41 ml

Table 1 Amount of different reactants.

3.4 FEATURES OF THE DEPOSITION

Table 2 shows the different features about the current deposition. From this table it can be seen that the spray and dry time were 10 and 11 s respectively.

Contents	Amount/value
Spray time	10 s
Dry time	11 s
Spray-dry within	2 min
Substrate temperature	250 °C
Room temperature	31°C
Distance between nozzle and substrate	19 Cm
Solution	3 ml

Table 2 Features of the current deposition

4. CONCLUSION

The continuous spray and dry on the substrate was carried out within 2 min. In the mean time the substrate temperature was about 250 °C and room temperature was 31°C. After finishing the continuous spray and dry for 2 min, the substrate was kept on the heater plate for drying the solution sprayed on to it. The distance between spray nozzle and the substrate was 19 Cm. there were 3 ml solutions needed for current deposition. After passing about 6 min the substrate color turn to the black. And the existences of the ZnO particles on the substrate were confirmed easily. This was because the crystalline temperature of the ZnO is 450°C. But in the current work the substrate temperature was about 250°C. So the particle on the substrate could not grow the crystal structure.

Fig. 6 shows the photograph of the prepared ZnO film on the glass substrate.

(a) (b)

Fig. 6 Photograph of the depositing film

In the figure 6(a) it is clear to see that, the ZnO particles are situated on the substrate. On the other hand in figure 6(b) it is tried to show the transparency ability of the film of ZnO grew on the glass substrate.

5. FUTURE WORK

Depositing the film by the variation of the distance,between the spray nozzle and the glass substrate. Characterizing the films prepared by the present system, improving the heating ability of the heater and displaying and controlling the temperature.

6. ACKNOWLEDGEMENTS

The authors would like to thank the Rajshahi University of Engineering & Technology (RUET) for giving the chance to use the different equipment of the photovoltaic and nano technology lab.

REFERENCES

[1]. G.K. Wehner and G.S. Anderson, *Handbook of Thin Film Technology*, McGraw-Hill, New York, 1970

[2]. M.F. Hossain, T. Takahashi, *The Effect of Substrate Temperature on the Spray-Deposited TiO_2 Nanostructured Films for Dye-Sensitized Solar Cells*, J. Nanosci. Nanotechnol. Vol. 11, pp. 3222-3228, June 2011.

[3]. Kikuo Okuyama et al., *Preparation of Nanoparticle via Spray route*, chemical engineering Sciences, 58, pp.537-547, 2003.

[4]. J.C Viguie, J Spitz. Chemical Vapor Deposition at Low Temperatures. *Journal of*

The Electrochemical Society. 1975 122: 585-8.

Proceeding of the
International Conference on Electrical, Computer and Telecommunication Engineering
01- 02 December 2012 (ICECTE2012), RUET, Rajshahi-6204, Bangladesh

ICECTE2012: PI-0089

Synthesis and Investigation of Microstructure, Resistivity and Dielectric Properties of Vanadium penta-oxide (V_2O_5) Doped Ni-Zn Ferrite

*Abdul Ahad [1], Rajib Ahmed[2], Rifat Ahmmed[3]

[1]Department of Physics, Bangladesh University of Engineering and Technology, Dhaka-1000, Bangladesh
[2]Dept. of EEE, University of Information Technology & Science, Dhaka-1000, Bangladesh
[3]Dept. of ETE, Rajshahi University of Engineering & Technology, Rajshahi-6204, Bangladesh
E-mail: *abdulahadbbaria@hotmail.com[1], rajib.ahmed@uits.edu.bd[2], rifat.ete07@gmail.com[3]

ABSTRACT
Vanadium penta-oxide (V_2O_5) Doped $Zn_{1-x}Ni_xFe_2O_4$ Ferrite Samples (x=0, 0.1, 0.2, 0.3 and 0.4) have been prepared by conventional ceramic technique. The effect of Zn and Ni substitution on the electrical properties and microstructure has been investigated .Temperature dependent graphs show that the resistivity increases with increasing temperature upto the Curie temperature and then decreases gradually. The frequency dependent curves indicate that with increasing frequency, the dielectric constant (ε) and dielectric loss tangent (tanδ) decrease while the A.C conductivity ($\sigma_{a.c}$) and Q-factor increase. The $Zn_{0.7}Ni_{0.3}Fe_2O_4$ has the highest Q-factor (Q=9.60 at 2 MHZ).Finally, the best electrical and dielectric properties have been found for the sample $Zn_{0.7}Ni_{0.3}Fe_2O_4$ with maximum quality factor, Q=9.60 at 2 MHZ. Moreover, microstructure of the samples (Five) has been analyzed based on the average grain size. Hence, this locally produced low cost Ni-Zn ferries can be used in electronics and discrete microwave devices.

KEY WORDS: Ni-Zn ferrite, Resistivity, Curie temperature, Q-factor, Microstructure.

1. INTRODUCTION

Ferrite constitutes a special branch of ferromagnetic material which is considered as highly important electric materials used widely in electronic industries, information and communication technology. In the modern society of today, a constant challenge is being posted by ever increasing demands for ferrite materials in home communication appliance, computer etc area. A handsome number of papers related to this field have been published. But we describe the synthesis of V_2O_5 doped Ni-Zn Ferrite and hence study the electrical and dielectric properties of Ni-Zn ferrites.

Crystallographic and Magnetic Properties of V_2O_5 -doped Titanium Cobalt Ferrites were investigated by Woo Hyun Kwon, Seung Wha Lee, Jae-Gwang Lee and Kwang Pyo Chae *et al*[1] and found that the average grain size of the samples increases with V_2O_5 concentration [1]. Microstructure and magnetic properties of Ni-Zn ferrites doped with MnO_2 have been studied by SU Hua, ZHANG Huai-wu, TANG Xiao-li, JING Yu-lan, *et al*[2]. The average grain size, sintering density and real permeability gradually decrease with the increase of the MnO_2 content [2]. Substituted Ni-Zn ferrites for passive sensors application were synthesized by Jozef Slámas, Anna Grusková, Mariana Ušáková, Elemír Ušák, Ján Šubrt, Jozef Lukáč *et al* [3]. The influence of small be and/or Cu substitution on various magnetic properties of Ni-Zn ferrites has been analyzed by means of various experimental methods and interpreted from the point of view of preparation technology optimization and possible applications of such materials in sensor technology. A strong correlation between the substituent content and resulting properties has been observed [3].

The effect of additive on the microstructure and complex permeability of Ni-Zn ferrites were investigated by B. Parvatheeswara Rao, K. H. Rao, P. V. Ramana, O. F. Caltuna et al [4] with the formula $Ni_{0.65}Zn_{0.35}Fe_2O_4 + x.Nb_2O_5 / V_2O_5$ where x values ranging from 0.0 wt% to 1.5 wt% has been prepared by conventional ceramic technique and observed vanadium additions results infine grain structures with grain sizes of 4.9 μm whereas niobium additions promoted grain growth with an increase in grain size from 5.7 μm to 13.2 μm [4].

The present study has been undertaken to synthesize V_2O_5 doped Ni-Zn Ferrite by conventional ceramic technique and study on their intrinsic properties (such as D.C electrical resistivity, Curie temperature, semiconducting behavior, activation energy as a function of temperature and A.C electrical conductivity, dielectric constant, dielectric loss tangent, Q-factor as a function of frequency & the morphology analysis) of the five sintered specimens with the series of $Zn_{1-x}Ni_xFe_2O_4$ (x=0,

0.1, 0.2, 0.3 and 0.4).The best electrical and dielectric properties have been found for the sample $Zn_{0.7}Ni_{0.3}Fe_2O_4$ with maximum Q-factor; Q=9.60 at 2MHz.Not much information is yet available in literature on Ni-Zn ferrites, the present investigation has been undertaken to give an idea on the electrical properties of locally prepared materials that can be tailored for the requirement of further investigation in future.

2. METHOD AND SAMPLE PREPARATION

Fine powder of ZnO, NiO and Fe_2O_3 were used as raw materials for the preparation of the Ni-Zn ferrite five samples using the formula, $Zn_{1-x}Ni_xFe_2O_4$ (x=0, 0.1, 0.2, 0.3 and 0.4).After raw materials weighing dry mixing is done and pre-sintered at 700°C for 3-hour.Dry Milling is completed after pre-sintering. The required quantity of pre-sintered powder is taken separately in a small glass vessel and mixed well some drops of poly-vinyl alcohol of .01% as binder and V_2O_5 of .01% used as additive. After making desired samples, these samples sintered at 1200°C for 3-hour and then are pasted with air dying type silver paste for electrical contacts. Finally, synthesized five samples are collected to complete the experiment.

3. EXPERIMENTAL SETUP

We take a varaic (0 to 300V) for the control of the temperature of the tube furnace. Three digital multi-meters are used to measure the D.C (one is used to measure the voltage against the fixed resistance, the second to measure the voltage against the sample and the third for measuring the temperature that temperature given from the external agency, as shown in figure.

Figure 1: Experimental Setup for D.C resistivity measurement

Three different types of experiments are used to measure the electrical property (D.C and A.C) and microstructure of the samples.

(A) D.C Electrical Property Measurement

To measure the D.C electrical property of the synthesized ferrite samples, we have measured (1) temperature dependent D.C resistivity (2) Curie temperature (3) Semiconducting behavior and (4) Activation energy.

For D.C resistivity measurement, we used a constant D.C current source, fixed resistance, etc. After obtaining the D.C resistivity, we plotted the graphs lnρ versus 1000/T for each sample where ρ defines the D.C resistivity in Ω-m and T defines the given temperature in °C. These graphs show the Curie points, after passing the Curie points the magnetic domains are broken and the alignment of the dipoles are also in different directions in which ferromagnetic substances converted into paramagnetic substances for a certain temperature .This temperature is termed as the Curie temperature(T_c), as shown in figure . Thus we get the Curie temperature for five samples.

After the Curie temperature, the resistivity decreases gradually with increasing temperature, therefore, shows the excellent semiconducting behavior and obeys the following formula

$$\rho=\rho_0 \exp(E_p/K_в T_c) \quad \text{.....(1)}$$

Where, ρ_0 =Resistivity at room temperature
E_p =Activation energy
$K_в$=Boltzmann constant = 8.62×10^{-5} eV/ ^{0}K
T_c=Curie temperature

At Curie temperature the energy of the thermal motion of the atoms is sufficient to overcome the interactions forces between the atomic moments. Because at this temperature the magnetic alignment within the domains is fully destroyed by thermal agitation and as a result the saturation flux density falls and the material becomes paramagnetic. Near T_c, some of the intensive parameters such as magnetization, susceptibility, thermal & electrical conductivities are known to behave differently than predicted by classical molecular field theory.

Knowing the values of ρ_0, ρ, T_c, we can determine the Activation energy (E_p) from the equation of $\rho=\rho_0 \exp(E_p/K_в T_c)$.

(B) A.C Electrical Property Measurement

To determine the A.C electrical property of the synthesized ferrites we have determined the Q-factor, A.C electrical conductivity ($\sigma_{a.c}$), dielectric constant (ε) and dielectric loss tangent (tanδ) with the help of a LCR-Q meter which gives automatically the resistance (R_p in KΩ) of the samples by changing frequencies ranging from 75 KHz to 2MHz.

(C) Microstructure Measurement of the Samples

The surface morphology of the samples are measured by high resolution Scanning Electron Microscope (SEM-Hitachi, S- 3400N).

4. RESULT ANALYSIS

(A) D.C Electrical Property Analysis

The lnρ versus 1000/T curves have been plotted for each sample, as shown in Figure2 .The Curie temperature for the samples of 1, 2, 3, 4 and 5 are 215°C,150°C, 165°C, 295°C and 310°C respectively, as shown in the figures. At these temperatures the magnetic alignment within the domains is fully destroyed by thermal agitation and as a result the saturation flux density falls and the material becomes paramagnetic from ferromagnetic.

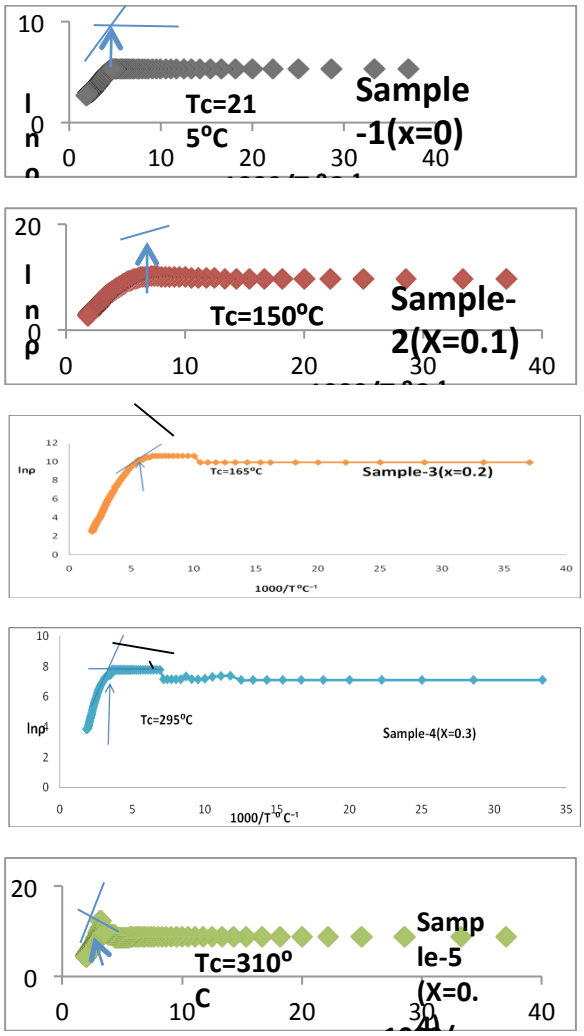

Figure 2: The lnρ versus 1000/T curves for Samples

Table-1: Electrical Properties of samples

Sample No.& Chemical formula	Curie Temperature in °C.	Resistivity, ρ in Ω-m at room temperature	Resistivity, ρ in Ω-m at Tc	Activation energy, Ep in eV at Tc
Sample -1(x=0) ($ZnFe_2O_4$)	215	$1.960x10^2$	$1.978x10^2$	$3.840x10^{-4}$
Sample -2(x=0.1) ($Zn_{0.9}Ni_{0.1}Fe_2O_4$)	150	$1.690x10^4$	$2.369x10^4$	$1.231x10^{-2}$
Sample -3(x=0.2) ($Zn_{0.8}Ni_{0.2}Fe_2O_4$)	165	$2.090x10^4$	$3.598x10^4$	$2.0509x10^{-2}$
Sample -4(x=0.3) ($Zn_{0.7}Ni_{0.3}Fe_2O_4$)	295	$1.201x10^3$	$1.650x10^3$	$1.555x10^{-2}$
Sample -5(x=0.4) ($Zn_{0.6}Ni_{0.4}Fe_2O_4$)	310	$6.895x10^3$	$2.363x10^5$	$1.776x10^{-2}$

This table is given the Curie temperature, D.C resistivity (at room and Curie temperature) and activation energy (Ep) at Tc for the samples. From the above result we find the maximum Curie temperature 310^0C for sample-5 and minimum 150^0 C for sample-2. Resistivity **(ρ),** $2.363x10^5$ Ω-m at Tc for sample-5 which is the maximum of all the samples.

(B) A.C Electrical Property Analysis

The result of the frequency dependent A.C electrical Property (Q-factor, A.C electrical conductivity ($\sigma_{a.c}$), dielectric constant (ε) and dielectric loss tangent (tanδ)) of the five Ni-Zn ferrite samples given as follows-

Table2: A.C Electrical Property

Sample No. / Freq.	Conductivity, ($\sigma_{a.c}$) in mho/m		Dielectric Constant (ε)		Dielectric Loss Tangent (tanδ)		Q-Factor	
	75(KHz)	2(MHz)	75(KHz)	2(MHz)	75(KHz)	2(MHz)	75(KHz)	2(MHz)
Sample -1(x=0)	$0.327x10^{-3}$	$1.412x10^{-3}$	104.52	53.33	0.8018	0.239	1.25	4.18
Sample -2(x=0.1)	$0.097x10^{-3}$	$0.561 x10^{-3}$	60.71	32.38	0.403	0.156	2.48	6.37
Sample -3(x=0.2)	$0.095x10^{-3}$	$0.699x10^{-3}$	58.78	29.77	0.420	0.204	2.33	4.74
Sample -4(x=0.3)	$0.082x10^{-3}$	$0.338x10^{-3}$	44.66	29.29	0.393	0.102	2.34	9.60
Sample -5(x=0.4)	$0.043x10^{-3}$	$0.613x10^{-3}$	53.22	30.55	0.350	0.170	3.10	6.50

Q-factor, A.C electrical conductivity ($\sigma_{a.c}$), Dielectric constant (ε), and Dielectric loss tangent (tanδ) Vs frequency graphs have been plotted for all samples as shown in Figure3-6.

Frequency dependent graphs (Figure3-6) show that with increasing frequency Dielectric constant (ε) and Dielectric loss tangent (tanδ) decrease but Q-factor and A.C electrical conductivity ($\sigma_{a.c}$) increase with increasing frequency. The above result indicates, the $Zn_{0.7}Ni_{0.3}Fe_2O_4$ (sample-4; x=0.3) has the maximum Q-factor (Q=9.60 at 2 MHz)

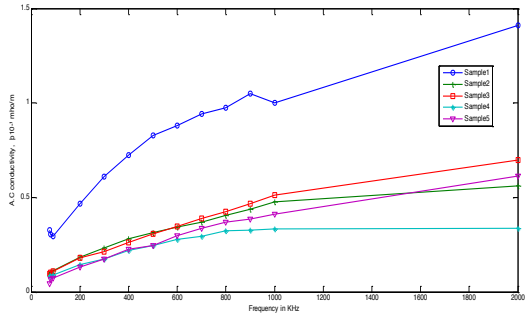

Figure 3: A. C conductivity Vs frequency graph

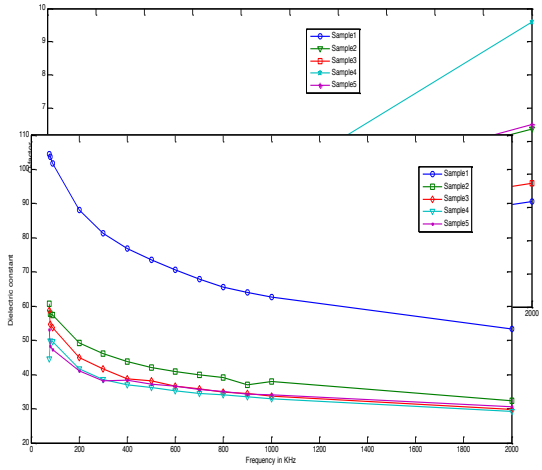

Figure 4: Q-factor Vs frequency graph

Figure 5: Dielectric constant Vs frequency graph

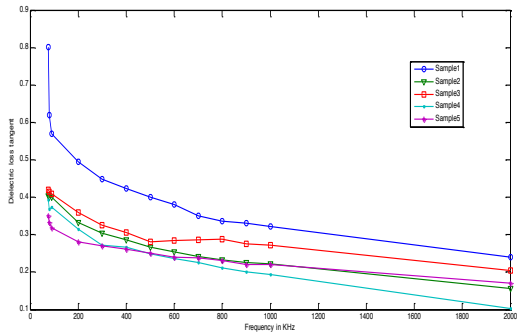

Figure 6: Dielectric loss tangent Vs frequency graph

(c) Microstructure Analysis

The microstructure of the samples has been measured by using the Scanning Electron Microscope. The scanning electron micrographs of Ni-Zn ferrite samples sintered at 1200^{0}C given as follows-

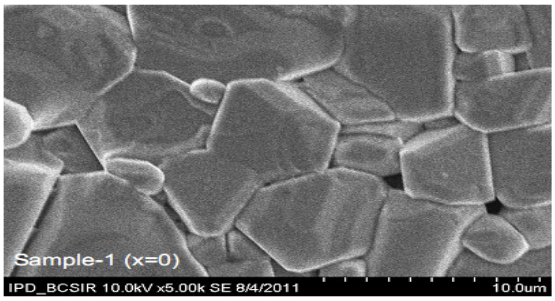

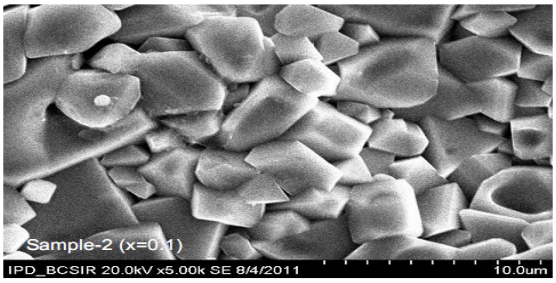

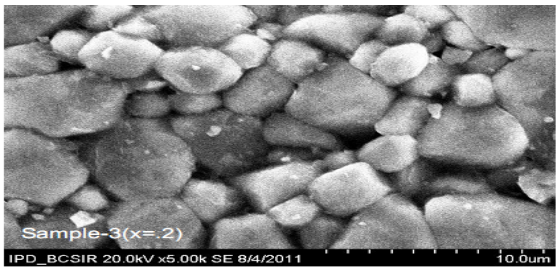

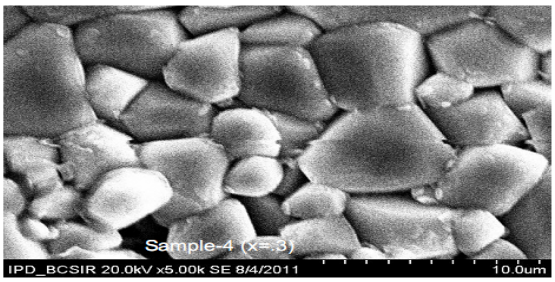

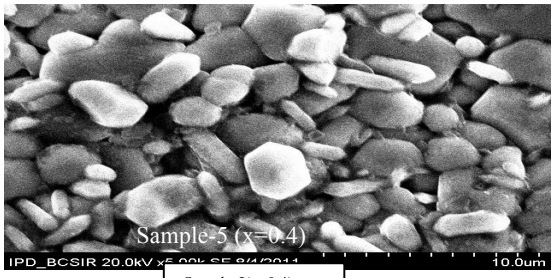

Sample-5(x=0.4)

Figure 7: Scannin aphs of five samples

5. CONCLUSIONS

Present research work demonstrates the intrinsic properties of Ni-Zn ferrite samples are strongly dependent on chemical composition, sintering temperature and site locations of various cations. It has been investigated in the case of five samples that the D.C resistivity increases with increasing temperature up to the Curie temperature, T_c and then

decreases gradually. It has been observed that A.C electrical conductivity and Q-factor were found to be higher for higher frequency. Comparing the electrical properties of five compositions can be said that the mixed $Zn_{0.7}Ni_{0.3}Fe_2O_4$ ferrite**,** sample-4(x=0.3)**,** shows the highest Q-factor of all and therefore more elaborate investigation should be needed with this composition. The micrographs of the samples show that the average grain size increases with decreasing Zn content but decreases with decreasing Ni content. The results indicate that the sample-5(x=0.4) is characterized by large grain, smallest porosity on the boundary and on the surface of the grains which features the highest magnetic performances. So the locally prepared low cost Ni-Zn ferrite materials have the advantages of high resistivity, high Curie temperature, low relative loss, good high permeability feature which can be used in telecommunication technology, electronics industries and discrete microwave devices.

6. FUTURE WORK

The next goal of our research would focus on exploring applications on different types of ferrites e.g. Magnesium-Manganese ferrites, Yttrium-iron garnet, Aluminium–iron garnet whose have applications in microwave gyrators, phase shifters, isolators and memory cores. Moreover, we want to work on Li-Zn and Ni-Zn ferrites.

ACKNOWLEDGEMENTS

I would like to express my heartily gratefulness to Nurzaman Ara Ahmed, PSO, Syeda Nasmin Rahman ,SSO, BCSIR Laboratory, Dhaka, Professor Ishrat Jahan, Head of the Physics Department , Govt. Titumir College Dhaka and Dr. A.K.M Akhter Hossain , Department of Physics, BUET.

REFERENCES

[1]. Woo Hyun Kwon, Seung Wha Lee, Jae-Gwang Lee and Kwang Pyo Chae, "Crystallographic and Magnetic Properties of V_2O_5 – doped Titanium Cobalt Ferrites" *Journal of the Korean Physical Society*, Vol. 55, No. 4, October 2009, pp. 1548~1552 .

[2]. SU Hua, ZHANG Huai-wu, TANG Xiao-li, JING Yu-lan, "Microstructure and magnetic properties of Ni-Zn ferrites doped with MnO2" Science Direct, Trans. Nonferrous Met. Soc. China 21(2011) 109-113.

[3]. Jozef Slama, Anna Gruskova, Mariana Usakova, Elemir Usak, Jan Subrt, Jozef Lukac , *Journal of Electrical Engineering*, Vol 57. NO 8/S, 2006, 159-162.

[4]. Mustaffa Abdullah and Ahmed Nazlim Yosoff, Microstructure and Dielectric Properties, Faculty of physical and applied Science, University Kebangsaan, Malaysia, Pertanika J. Science and Technology, Vol-6, No-2, year-1997.

[5]. B. Parvatheeswara Rao, K. H. Rao, P. V. Ramana, O. F. Caltuna, *Journal of Optoelectronics and Advanced Materials,* Vol. 7, No. 2, April 2005, p. 733 – 737.

Proceeding of the
International Conference on Electrical, Computer and Telecommunication Engineering
01- 02 December 2012 (ICECTE2012), RUET, Rajshahi-6204, Bangladesh

ICECTE2012: PI-0090

Use of Silvaco TCAD Simulator to Determine the Base Transit Time of $Si_{1-y}Ge_y$ Heterojunction Bipolar Transistor for Different Base Profiles for Low Level of Injection

*Ayed Al Sayem[1], *Yeasir Arafat[1] and M.Z.R. Khan[1]*
[1]Department of EEE,BUET, Dhaka 1000, Bangladesh
E-mail: ayedalsayem143@gmail.com, *arafat@eee.buet.ac.bd

ABSTRACT
In this work, the most important factor of transit time of a SiGe heterojunction bipolar transistor (HBT) has been analysed for different mole fraction profiles in base with Gaussian doped base for low level of injection considering band gap narrowing, doping dependent mobility, velocity saturation with the help of SilvacoTCAD. It has been found that base transit time varies with different profiles in the base.The calculated base transit time shows similar variations as found in literature for BJT.

KEY WORDS:Base transit time, HBT, Gaussian doping, bandgap narrowing,SilvacoTCAD.

1. INTRODUCTION

For high speed applications, Heterojunction Bipolar transistors are considered as potential devices. In general, HBT devices can give a number of advantages over their homojunction counterparts; especiallySiGe-base HBTs are efficient alternative to III-V HBTs [1]-[2]. These are the first practical bandgap-engineered silicon devices. By using a narrow-gap material for base region results in extremely high values of emitter efficiency and introduces an additional degree of freedom in device design. Device performance can be improved further by introducing a compositional grading in the base region. This base grading creates a drift field that sweeps the electrons towards the collector reducing transit time. The addition of Ge with Si, leads to a strained SiGe base layer but the strain tolerable provided that the layer thickness is less than a critical value [3]. Band gap is reduced by introducingGe to the base region, compared to that in Si BJT [4]. Because of high speed performance and mature silicon process, SiGeHBTs have emerged as the technology of the choice for RFICs [5].

Base transit time plays a very critical role in determining aTransistor's high frequency performance as it is more than 70% of a bipolar transistor's total transit time [6]. A number of studies have been done on the base transit time of SiGe HBTs [6]-[7].

In this work, the base transit time is found by simulation in Atlas for a Gaussian doped base by considering heavy doping and Ge induced band gap narrowing effect, doping dependent and electrical field dependent minority carrier mobility, change in density of states and modification in velocity saturation at the base collector junction. The result of this simulation showed similar trends of base transit time that is found in literature for BJT.

2. TRANSISTOR FABRICATION AND DOPING

For the Fabrication of SiGeHBT, Athena has been used. Silvaco Athena is device fabrication software. The most important thing in fabrication was the doping in the base. As we wanted to find the similarities of transit time found in literature for Gaussian doped base it was necessary to dope the base in Gaussian Shape. Ion Implantation and diffusion process was used to do this Gaussian doping.Emitter and Collector were doped in conventional manner.

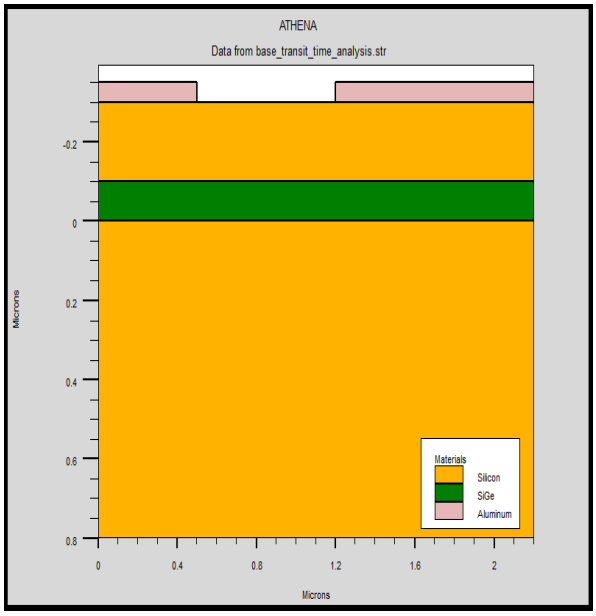

Figure1: SiGeHBT Structure shown in Silvaco simulator

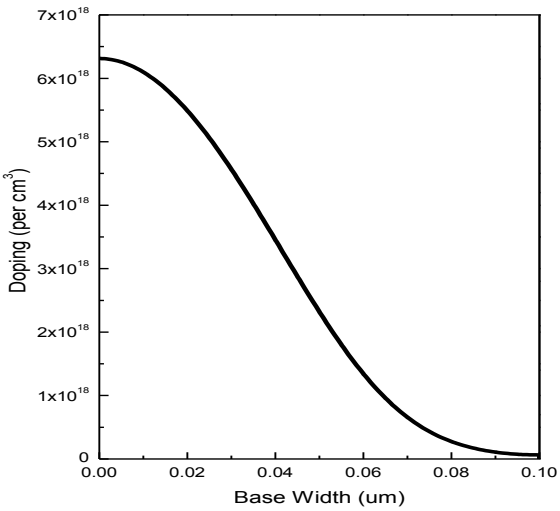

Figure2: Gaussian doping in the baseregion of an HBT

3. THEORY

The Basic advantage of SiGe HBT over conventional Si BJT comes from the bandgap engineering technology. Bandgap engineering technology is a very fascinating technology to improve several importantcharacteristics for a bipolar transistor. The main difference in working principle of anHBTfromBJT can be understood from the energy band diagram. The energy band diagram for a forward biased ideal graded-baseSiGe HBT with constant doping in the emitter, the base and the collector regions, and a Si BJT are shown in Fig. 3. The Ge content is linearly graded from 0% from the emitter–base (EB) junction to some maximum (permissible) value of Ge content near the collector–base (CB) junction, and then rapidly rampedback down to 0% Ge.

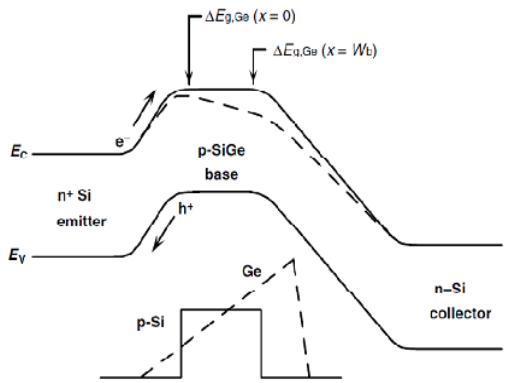

Figure3: Energy band diagram for graded base SiGeHBT and normal Si BJT

The effect of introducing a graded Ge profile into the base region is shown in the band diagram above. $\Delta E_{g,Ge}(x = 0)$and $\Delta E_{g,Ge}(x = W_b)$Ge represent the germanium-induced bandgap narrowing at the emitter end of the base (x = 0) and the germanium-induced bandgap narrowing at the collector end of the base ($x = W_B$) respectively.

The Ge mole fraction (y) distribution profiles of an *npn*SiGe-base HBT is shown in Fig.4. For a trapezoidal profile, y can be expressed as a function of distance (x) along the neutral base width W_B, as

$$y(x) = m_{GE}x + y_E \quad (1)$$

where,$m_{GE} = (y_C - y_E)/W_B$, y_C *and* y_E are Ge fraction at the collector and emitter respectively $y_E = 0$,Eq. 1represents triangular profile. For $y_E = y_C$, Eq. 1 represents box shape profile [8].

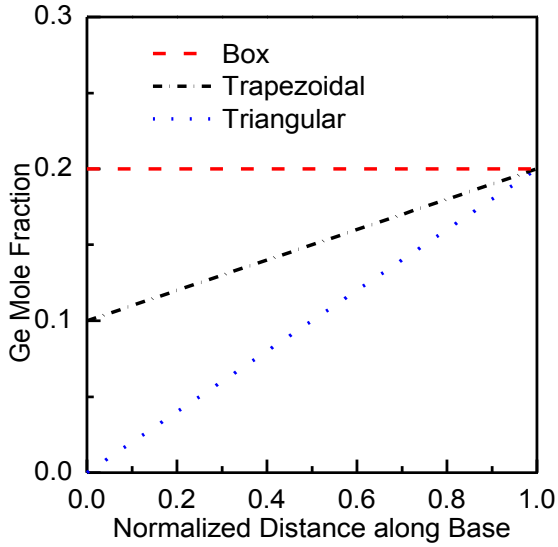

Figure4: Mole fraction distribution within the SiGe base for various geometric profiles

Total Ge content within the base is called Ge dose and is calculated as [9]

$$y_D = y_{AV}W_B \quad (2)$$

where, $y_{AV} = (y_E + y_C)/2$ (3)

For HBT, the base transit time can be found by using the following relation [10]

$$\tau_B = q\int_0^{W_B} \frac{n(x)}{J_n(x)}dx \quad (4)$$

where, n(x) is the minority carrier concentration and $J_n(x)$ is the electron current density within the base, q is the charge of an electron.

4. SIMULATION AND RESULTS

Atlas was used for device simulation. For base-emitter voltage from 0.6V to 0.8V data of minority current density and electron concentration in base was collected. Using Eq. 4and the collected data we got the transit time by using MATLAB.

Minority carrier current density J_n is a function of base-emitter voltage. This relation is plotted for different shape of Ge profiles and shown in Fig. 5. For triangular and trapezoidal profile, J_n increases with V_{BE} maintaining a constant logarithmic slope but for the box shape the slope of the curve decreases after V_{BE}=0.75V. $J_n$for box shape Ge (0 gradient) is higher than that of triangular (maximum gradient) and $J_n$for trapezoidal (moderate gradient) profile remains in-between. The reason for this is that the current gain in the SiGe HBT is maximum for the box-type profile and minimum for the triangular profile [4].

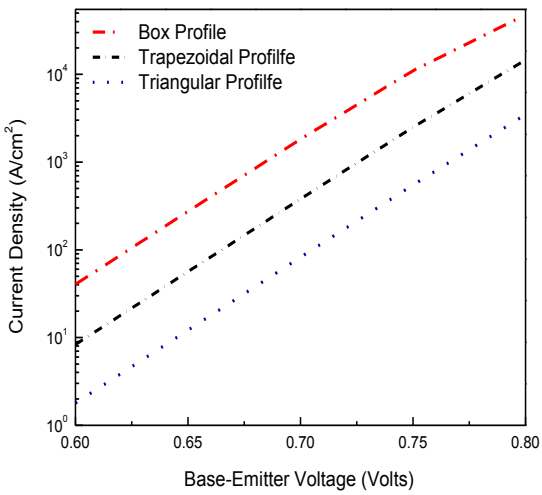

Figure5: Current densities (J_n) as a function of base-emitter voltage (V_{BE}) for different shape of Ge profiles. Gefractions at boundaries are similar

Base transit time for an *npn*SiGe base HBT has been calculated Eq. 4 where $n(x)$ and$J_n(x)$ data were found from simulation for Gaussian doped base and differentGe profiles under low level of injection. Changing the value of y_E, triangular or box or trapezoidal Ge effects are incorporated. The results are shown in Fig.6 which illustrates the plots ofτ_B as a function of V_{BE} for different shape of Ge profiles. For triangular and trapezoidal profile, τ_B becomes smaller and remains almost constant but for box profileτ_B starts to increase after 0.75V. Box shape Getakes higher transit time than triangular to pass the electron to the collector and the trapezoidal Ge takes in-between time. This result is also verified by [4] which shows that transit through the base is minimum when the triangular Ge profile is chosen.

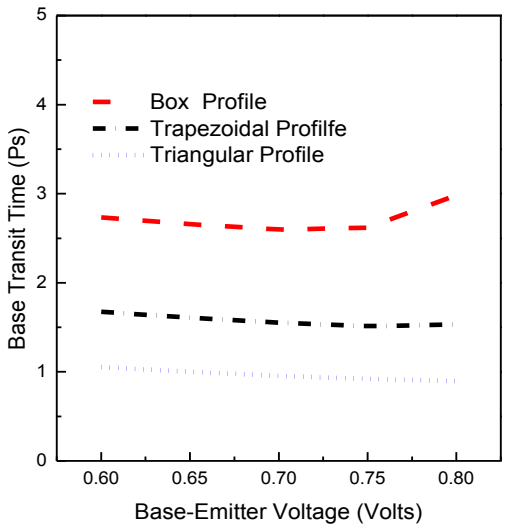

Figure6: Base transit time variation with base-emitter voltage for different Ge profiles in the base. Ge % at boundaries are: for triangular profile y_E=0%;y_C=20%, for trapezoidal profile y_E=10%; y_C=20% and for box profiley_E=y_C=20%.

5. Conclusions

Base transit time for a SiGe HBT with Gaussian doped base is analysed for different Ge profiles using TCAD simulator. It was found that the transit time decreases as the profiles change from box to triangular types. In this work we show that device simulation can be a very powerful tool to find out very specific characteristics of device and fabrication which can be helpful to produce specific quality device.

6. Acknowledgment

Authors of this work would like to thank the Department of EEE, BUET, for its various supports during the preparation of this manuscript.

References

[1]. N. Zerounian, F. Aniel, B. Barbalat, P. Chevalier, and A. Chantre, "500 GHz cutoff frequency SiGe HBTs," *Electronics Letters,* vol. 43, July 2007.

[2]. Z. Xu, G. Niu, L. Luo, P. S. Chakraborty, P. Cheng, D. Thomas, and J. D. Cressler, "Cryogenic RF Small-Signal Modeling and Parameter Extraction of SiGe HBTs," *IEEE Topical Meeting on Silicon Monolithic Integrated Circuits in RF Systems, SiRF'09*, pp. 1-4, Jan 2009

[3]. S. C. Jain, Germanium-Silicon Strained Layers and Heterostructures: Academic Press, Inc. USA, 1994.

[4]. M. K. Das, N. R. Das, and P. K. Basu, "Effect of Ge content and profile in the SiGe base on

the performance of a SiGe/Si HBT," *Microwave and Optical Technology Letters*, vol. 47, pp. 247-254, Nov 2005

[5]. K. Lee, D. H. Cho, K. W. Park, and B. Kim, "Improved VBIC Model for SiGe HBTs With a Unified Model of Heterojunction Barrier Effects," *IEEE Tran. on Electron Devices*, vol. 53(4), p. 743, 2006.

[6]. S. K. Mandal, G. K. Marskole, K. S. Chari, and C. K. Maiti, "Transit time components of a SiGe-HBT at low temperature," *Proc. 24th International Conference on Microelectronics*, vol. 1, pp. 315-318, May 2004

[7]. V. S. Patri and M. J. Kumar, "Profile Design Considerations for minimizing base transit time in SiGe HBT's," *IEEE Tran. on Electron Devices*, vol. 45, pp. 1725-1731, Aug 1998.

[8]. Z. R. Tang, T. Kamins, and C. A. T. Salama, "Analytical and experimental characteristics of SiGe HBT with thin α-Si: H emitters," *Solid-State Electron.*, vol. 38, pp. 1829-1834, 1995.

[9]. K. H. Kwok and C. R. Selvakumar, "Profile design considerations for minimizing base transit time in SiGe HBTs for all levels of Injection before onset of Kirk effect," *IEEE Tran. on Electron Devices*, vol. 48, pp. 1540-1549, 2001.

[10]. H. Kroemer, "Two integral relations pertaining to electron transport through a bipolar transistor with a nonuniform energy gap in the base region," *Solid-State Electron.,* vol. 28, pp. 1101–1103, 1985

Proceeding of the
International Conference on Electrical, Computer and Telecommunication Engineering
01- 02 December 2012 (ICECTE2012), RUET, Rajshahi-6204, Bangladesh

ICECTE2012: PI-0091

The effect of inter-electrode distance on TiO_2 Nanotube Arrays fabricated by Anode Oxidation method

R.S. Mandal, M.F. Hossain, Md. R. Haque and M.S. Islam
Department of Electrical and Electronic Engineering, Rajshahi University of Engineering & Technology, Rajshahi-6204, Bangladesh
E-mail: faruk94_ruet@yahoo.com

ABSTRACT
TiO_2 nanotube arrays have an important role on the potential application like solar cells, air purification, dust water cleaning and hydrogen fuel generation. Highly aligned titanium oxide (TiO_2) nanotube (NT) arrays have been grown on titanium sheet by using a self organized anodic oxidation method at different inter-electrode distance (1.5 cm to 2.5 cm) in a NH_4F and ethylene glycol based electrolyte. The temperature has been maintained to room temperature (RT). The formation and growth mechanism of TiO_2 NTs have been discussed with proposed experimental system and observe the effect of changing inner-electrodes distance on the inner diameter of NTs. The optical property of TiO_2 NTs is investigated PL spectra. The surface morphology has been confirmed by atomic force microscopy (AFM).

KEY WORDS: Inter-electrode distance, Fluoride-based electrolytes; Titanium dioxide nanotubes; Electrochemical anodization.

1. INTRODUCTION

Titanium nanotubes have drawn extraordinary attention for their applications in photovoltaic cell [1], photocatalysis [2], sensing [3], and biomedical industry [4], air purification, waste water cleaning due to their unique physical and chemical properties [5].

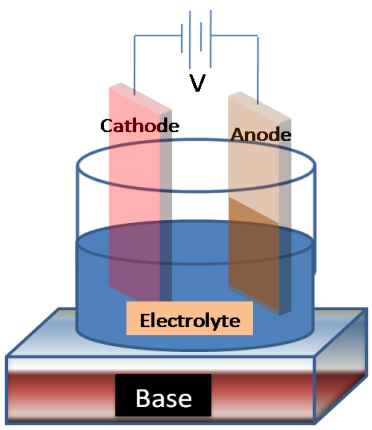

Fig 1: Schematic simple set-up for anodization experiments

Many approaches such as templating synthesis, hydrothermal reactions, and anodic oxidization have been developed to prepare TiO_2 nanotube. Among them the anodic oxidization is the relatively simple technique that can be easily automated to fabricate high-oriented uniform nanotube arrays shown in Fig 1[6]. Titanium oxide (TiO_2) is an important material in the construction of DSC, because of its suitable energy band position, and high photoelectric response as a porous photoelectrode material of DSC [7, 8]. In 1991, Zwilling and co-workers [9] reported the porous surface of titania films electrochemically formed in fluorinated electrolyte by titanium anodization. A decade later Grimes and co-workers [10] first reported formation of uniform titania nanotube arrays via anodic oxidation of titanium in an hydrofluoric (HF) electrolyte. Varying pH and electrolyte concentration, this same research group achieved a 6.4 mm long nanotube array using a fluoride solution of pH 5.5 [11]. Recently, Schmuki and co-workers [12, 13] also reported the formation of long nanotubes during anodization of titanium in neutral fluoride solutions.

So, in this work, TiO_2 nanotube arrays have been prepared on Ti metal sheet in ethylene glycol and NH_4F based electrolyte by anodic oxidation method in a less expensive way and observe the effect of inner-electrode distance.

2. FORMATION & GROWTH OF TIO_2 NT

In general the anodic growth of oxides on Ti metal surface as well as formation of Nanotube is the simplest approach done by the following reaction shown in (1)

$$Ti + 2H_2O \rightarrow TiO_2 + 4H^+ + 4e^- \quad (1)$$

and chemical dissolution of the oxide as soluble fluoride complexes, e.g.;

$$TiO_2 + 6F^- \rightarrow [TiF_6]^{2-} \quad (2)$$

Respectively direct complexation of high-field transported cations at the oxide electrolyte interface,

$$Ti^{4+} + 6F^- \rightarrow [TiF_6]^{2-} \quad (3)$$

Figures 2 (a-d), shows the schematic diagram of anode oxidation method with growth, electrochemical etching mechanism, and anodization

current behaviour respectively. TiO_2 NT arrays were fabricated by using self organized electrochemical anodization method [6, 14] in NH_4F and ethylene glycol (EG) based electrolyte.

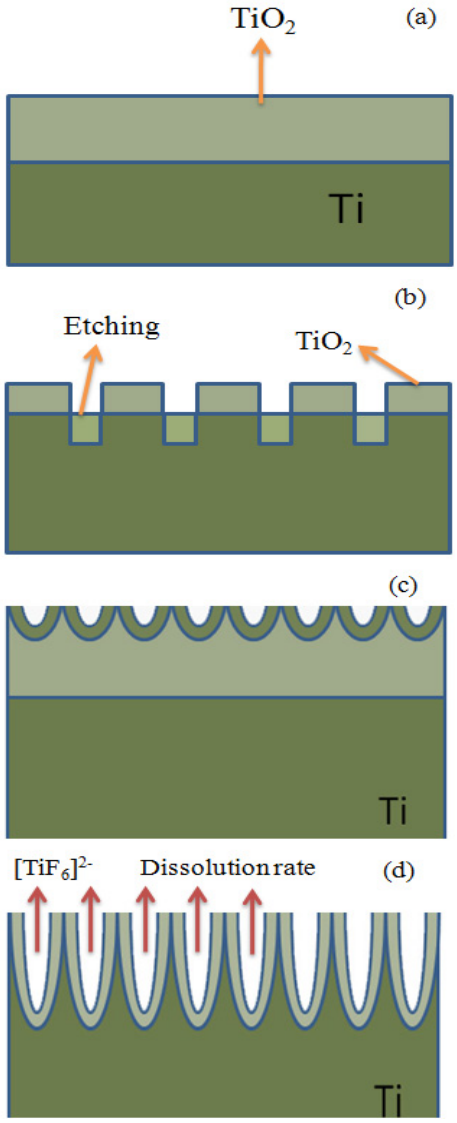

Fig 2(a-d): Schematic representation of the growth mechanism of TiO_2 NT arrays.

The F^- ions in electrolyte have two effects including the ability to form water-soluble $[TiF_6]^{2-}$ and the small ionic radius that makes them suitable to enter the growing TiO_2 lattice and to be transported through the oxide by the applied field (thus competing with O^{2-}). Under the sufficient applied voltage magnitude (growth factor $f_g \approx$ 1-5 nm/V) is reached then the field-assisted oxidation occurs at the TiO_2/Ti interface, where the oxygen ions (O^{2-}) are transported from the solution to the oxide layer.

3. FABRICATION OF T_IO_2 NT ARRAYS

The electrochemical anode oxidation method to fabricate the TiO_2 NT arrays. The schematic diagram of electrochemical anode oxidation experimental set-up with variable dc supply system for TiO_2 NT array growth is given in Fig. 3. The titanium (Ti) sheet of 99.6% purity, 0.2mm thickness. Prior to anodization, the Ti sheet was first mechanically polished with different abrasive papers and rinsed in an ultrasonic bath of cold distilled water for 10 min. Then the cleaned Ti sheet was soaked in a mixture of HF, HNO_3 acids and H_2O (the mixing ratio of HF:HNO_3:H_2O is 1:4:5 in volume) for 30 sec.

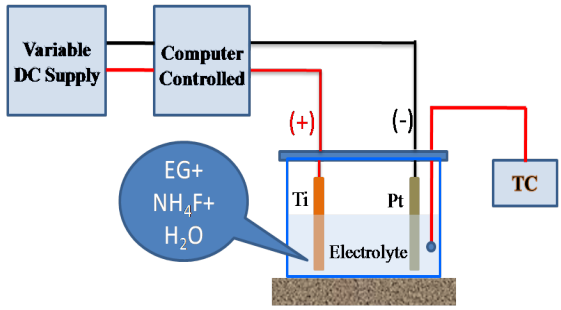

Fig 3: Schematic diagram of computer controlled anode oxidation experimental system set-up.

After rinsed with acetone and distilled water for 20 min, the Ti sheet was dried in a flow of pure nitrogen stream. The TiO_2 NTs were fabricated in a cylindrical electrochemical reactor. A conventional two-electrode system was employed with Ti sheet as the anode and Pt foil as the cathode and the inner-electrode distance of these electrodes was varied from 1.5 cm to 2.5 cm. The time-dependent current behavior under constant potential was recorded using a computer-controlled system. All the anodization experiments were carried out in an electrolyte of ethylene glycol (EG), 0.3wt% NH_4F and 3vol% of water. Samples were prepared without any cooling system. Each set of sample was prepared at Anodization potentials of 50V. The sample was cleaned in EG and then distilled water, and was dried with N_2 steam flow. The TiO_2 NT arrays were subsequently crystallized by annealing in dry oxygen at 450ºC for 15 min with a heating and cooling rate of 2ºC/min.

4. RESULT AND DISCUSSION

Fig.4 shows the anodization current (mA/cm^2) with respect to time (sec). In this figure three curves are shown at an inner-electrode distance 1.5 cm, 2.0 cm and 2.5 cm. The Anodization potential in all those three distance variation is 50V. It also shows the original sample image at those three distances. At the starting of the anodization process the current is high because of only titanium metal sheet but as the time passes TiO_2 is formed on the metal sheet as it began to form the anodization currents starts to decay, when etching shown in Fig 2(b) is started than rapid reduction in the current density. This compact oxide layer on the titanium surface leads to a rapid reduction in the current density due to its poor

electrical conductivity, which at constant potential brings a decrease in current in the circuit [14] and at the same time depth of porous structure, is also increased vertically shown in Fig 2(c).

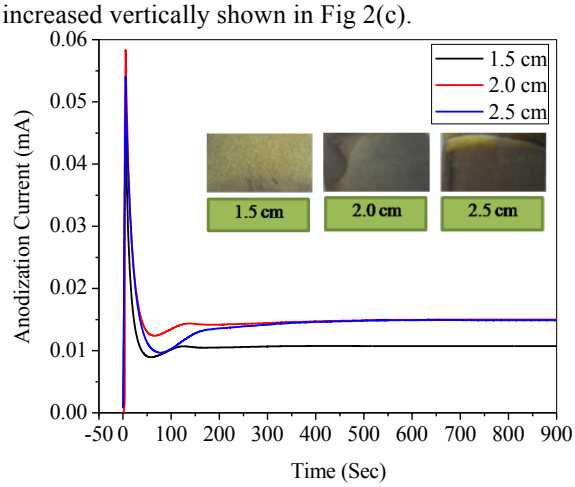

Fig 4: Anodization current behavior during anode oxidation of TiO_2 NT at different inner-electrode distance.

In anodization process, the chemical dissolution is the key for the formation of TiO_2 NT arrays, which reduces the thickness of the oxide layer (barrier layer) keeping the electrochemical etching process active. If the chemical dissolution is too high or too low no NTs can be formed. The electrochemical etching rate depends on the anodization potential as well as electrolyte concentrations. The length of TiO_2 NT array increases until the electrochemical etching rate equals to the chemical dissolution rate.

The PL spectra of the TiO_2 films prepared with different distance between electrodes have shown in figure 5. The UV PL peak exhibits due to the recombination of photo-generated electrons and holes, while the visible emission PL peak ranging from 400 to 700 nm associated with defects related to deep-level emission such as oxygen vacancies. The PL peaks locked 324nm (≈ 3.827 eV). It can be attributed to the emission of electronic transition near the band edge.

In this PL spectrum visible emission PL peak is much weaker than the peak at 372nm (≈3.33eV), so all the TiO_2 films have low defect concentrations. But in case of 2.0 cm distance between two electrodes there is no such peak in visible range. So TiO_2 sample prepared in this condition is no defect state, so it can be conclude that 2.0 cm distance between electrodes is the optimized distance to fabricate TiO_2 films.

From figure 6(a-c) shows the AFM image of surface (amplitude) of TiO_2 sample prepared at 1.5 cm, 2.0 cm, 2.5 cm distance between electrodes respectively. Here other variable is kept constant at the standard value to find which one is the best inner electrode distance to fabricate TiO_2 NTs. From the AFM image average roughness for 1.5 cm, 2.0 cm and 2.5 cm is found 0.130nm, 0.352nm and 0.041nm and the rms roughness is found 0.163nm, 0.546nm and 0.051nm respectively. As the roughness is more at 2.0 cm and because of large inner diameter more dye is absorbed by the TiO_2 NTs so that the more electron can be generated by the incident light in the visible range and a result the efficiency of DSSC trend to increase.

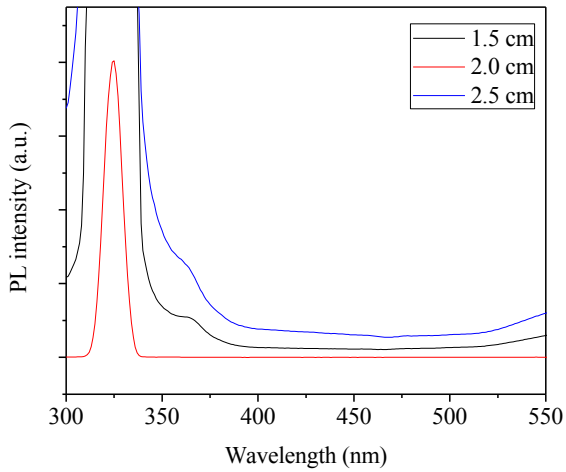

Fig 5: The photoluminescence (PL) spectra with 1.5, 2.0 and 2.5 cm distance between electrodes.

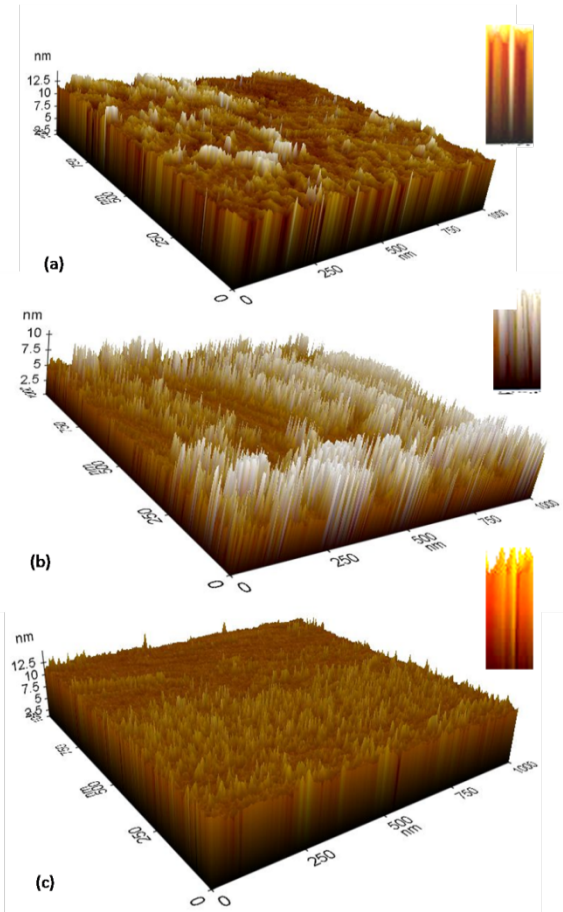

Fig 6(a-c): AFM image of surface of TiO_2 NTs at (a) 1.5 cm (b) 2.0 cm and (c) 2.5 cm distance

5. CONCLUSIONS

The main purpose of this dissertation is to fabricate TiO_2 NTs by electrochemical anode oxidation method with NH_4F and ethylene glycol based electrolyte at room temperature with an optimized inner-electrode distance. From the SEM surface morphology clears that the inner diameter at 2 cm inner-electrode is found 150nm which is better than other two distance variations. PL spectra shows that at 2 cm distance oxygen deficiency is lesser than other two variations but crystallite is found better than others. So 2 cm inner-electrode distance is the optimized distance for further applications.

6. ACKNOWLEDGEMENTS

Authors like to thank the authority of Central Lab Rajshahi University for the measurement of PL spectra measurement.

REFERENCES

[1]. LI.D, XIA Y.N, "Fabrication of titania nanofiber by electrospinning", *Nano Lett.*, 2003, 3, 555-560.

[2]. H. D. Jang, S.K. Kim, S.J. Kim, "Effect of particle size and phase composition of titanium dioxide nanoparticles on the photocatalytic properties", *J. Nanopart. Res.*, 2001, 3, 141-147.

[3]. O. K. Varghese, D. Gong, M. Paulose, K.G. Ong, C.A. Grimes, "Hydrogen sensing using titania nanotubes",*Sens. Actuators B*, 2003, 93, 338-344.

[4]. R. Rodriguez, K. Kim, J.L. Ong, J. Biomed, "In vitro osteoblast response to anodized titanium and anodized titanium followed by hydrothermal treatment", *Mater. Res. A*, 2003, 65, 352-358.

[5]. S. Hrapovic, B.L. Luan, M.D'amours, G. Vatankhan, G. Jerkiewicz, " Morphology, chemical composition and electrochemical characteristics of colored titanium passive layers", *Langmuir*, 2001 17(10), 3051-3060.

[6]. R.S. Mandal, M.F. Hossain, Md.R. Haque and M.S. Islam**,** "Fabrication of TiO_2 Nanotube Arrays in room temperature by Anode Oxidation method". *ICECE 2012, BUET, Bangladesh.* Accepted.

[7]. B.O. Regan, M.Grätzel, "A low-cost, high-efficiency solar cell based on dye sensitized colloidal TiO_2 films", *Nature* 1991, 353, 737-740.

[8]. M.F. Hossain, S. Biswas, T.Takahashi, Y.Kubota, A.Fujishima, "Investigation of sputter-deposited TiO_2 thin film for the fabrication of dye-sensitized solar cells", *Thin Solid Films* 2008, 516, 7149-7154.

[9]. V. Zwilling, M. Aucouturier, E. Darque-Ceretti, "Anodic oxidation of titanium and TA6V alloy in chromic media. An electrochemical approach",*Electrochim. Acta* 1999, 45, 921.

[10]. D. Gong, C.A. Grimes, O.K. Varghese, W. Hu, R.S. Singh, Z. Chen, E.C. Dickey, "Titanium Oxide Nanotube Arrays Prepared By Anodic Oxidation," *J. Mater. Res.* 2001, 16, 3331.

[11]. Q.Cai, M. Paulose, O.K. Varghese, C.A. Grimes, "The effect of electrolyte composition on the fabrication of self-organized titanium oxide nanotube arrays by anodic oxidation", *J. Mater. Res.* 2005, 20, 230.

[12]. J.M. Macak, H. Tsuchiya, P. Schmuki, "High-aspect-ratio TiO_2 nanotubes by anodization of titanium", *Angew. Chem. Int. Ed.* 2005, 44, 2100.

[13]. M. Macak, H. Tsuchiya, L. Taveira, S. Aldabergerova, P. Schmuki, "Smooth anodic TiO_2 nanotubes", *Angew. Chem. Int. Ed.* 2005,44, 7463.

[14]. A. Elsanousi, J. Zhang, H. M. H. Fadlalla, F. Zhang, H. Wang, X. Ding, Z. Huang, C.Tang, "Self-organized TiO_2 nanotubes with controlled dimensions by anodic oxidation", *J. Mater. Sci.* 2008, 43, 7219.

Proceeding of the
International Conference on Electrical, Computer and Telecommunication Engineering
01- 02 December 2012 (ICECTE2012), RUET, Rajshahi-6204, Bangladesh

ICECTE2012: PI-0093

Design, Construction and Performance Test of a Water Wave Power Plant

Md. Abdur Rahim[1], A.K.M Abdul Hamid [2], Md. Anamul Haque[3], Md. Enamul Hoque[4]
[1,2,3,4]Department of Mechanical Engineering, Rajshahi University of Engineering and Technology
E-mail: rahimruet05@gmail.com, mahamid_ruet@yahoo.com, haque.me05@gmail.com, enam_ruet@yahoo.com

ABSTRACT
This paper describes the design, construction and performance test of a water wave power plant. The rise and fall of the waves is converted to mechanical motion by heavy floating body driving a rack and pinion. This runs the shaft. As the rotational motion of shaft is discrete motion, flywheel is used to make its continuous motion for its inertia. The gear boxes are used to increase the speed. This rotational speed is used to rotate the rotor of generator. Thus we can get electrical power from the generator.

KEY WORDS: Renewable energy, rack and pinion, ratchet mechanism, gear box, generator.

1. INTRODUCTION

In modern age, the demand of electrical energy is increasing day by day. The conventional sources of energy such as coal, oil and gas cannot fulfill adequate demand of electrical energy. So it is so important to think about renewable energy such as water wave energy. A plant that produces power (electricity) is called power plant. Water wave power plant produces power (electricity) using water wave. Wave power is the transport of energy by ocean surface waves, and the capture of that energy to do useful work—for example, for electricity generation, water desalination, or the pumping of water (into reservoirs). Though often co-mingled, wave power is distinct from the diurnal flux of tidal power and the steady gyre of ocean currents. Ocean waves represent a considerable renewable energy resource. They travel great distances without significant losses and so act as an efficient energy transport mechanism across thousands of kilometers.

1.1 Formula for wave power, energy and energy flux

In deep water where the water depth is larger than half the wavelength, the wave energy flux [2, 3] is

$$P = \frac{\rho g^2}{64\pi} H^2{}_{m0} T_e \qquad \text{(Eq. 1)}$$

Here, P is wave power
T is time period
H is height of deflection
ρ is density of water

In a sea state, the average energy density per unit area of gravity waves on the water surface is proportional to the wave height squared, according to linear wave theory [1, 5].

$$E = \frac{1}{16} = \rho g H^2{}_{m0} \qquad \text{[Eq. 2]}$$

Where, E is the mean wave energy density per unit horizontal area (J/m^2

The wave energy flux [6], through a vertical plane of unit width perpendicular to the wave propagation direction, is equal to:

$$P = E c_g \qquad \text{[Eq. 3]}$$

Here, c_g the group velocity (m/s).

1.2 Airy wave theory

Airy wave theory is often applied in ocean engineering and coastal engineering for the modeling of random sea states — giving a description of the wave kinematics and dynamics of high-enough accuracy for many purposes[4]. Further, several second-order nonlinear properties of surface gravity waves, and their propagation, can be estimated from its results. This linear theory is often used to get a quick and rough estimate of wave characteristics and their effects.

2. DESCRIPTION OF WATER WAVE

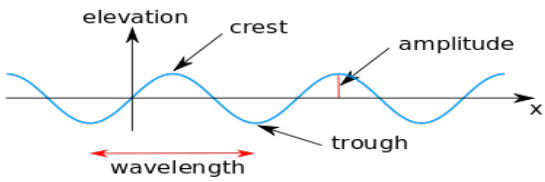

Fig. 1: Wave characteristics.

Airy wave theory is a linear theory for the propagation of waves on the surface of a potential flow and above a horizontal bottom. The free surface elevation $\eta(x,t)$ of one wave component is **sinusoidal,** as a function of horizontal position x and time t:

$$\eta(x,t) = a\cos(kx - \omega t) \qquad \text{(Eq. 4)}$$

Where,

a is the wave amplitude in metre,
cos is the cosine function,
k is the angular wave number in radian per metre.

3. DESCRIPTION OF PARTS

3. 1 Floating Body

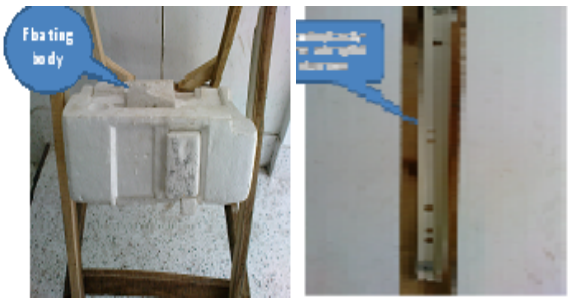

Figs. 2~3: Floating body

It is our designed floating body which moves up and down by water wave. It is made of corcksheet. It is 25 cm length.16cm width and 10cm height. It volume is 4000 cubic cm.

It is channel through floating body moves up and down. It is made of aluminium sheet. it is 43cm long and 2.1 cm width we used it, because it has small friction and due to plastic bearing can rotate easily.

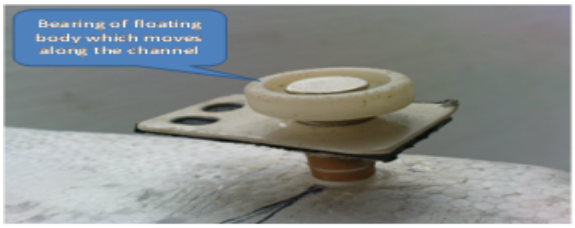

Fig. 4: Bearing of floating body which moves along the channel

It is a bearing attached with floating body. It can moves along the channel. It is made of plastic material. Its diameter is 1.8 cm. its thickness is .6 cm. It was selected because of its small weight, small friction, small density, no corrosion effect in water etc.

3.2 Rack and Pinion

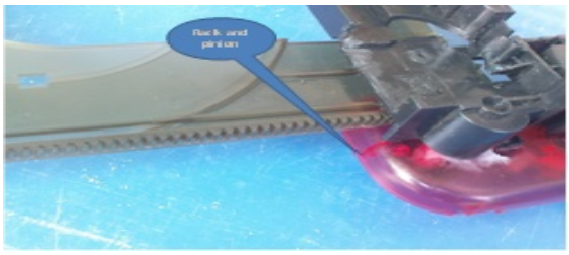

Fig. 5: Rrack and pinion

It is our designed rack and pinion. The teeth of gear are 30 and teeth of pinion are 12. Both rack and pinion is made of plastic material. It is 30.5 cm long and thickness is 1 cm .

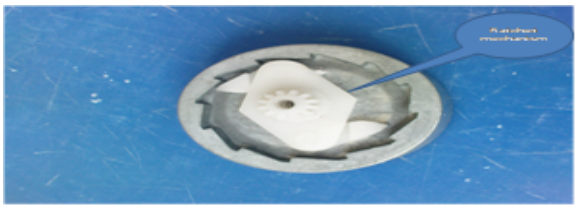

Fig. 6: Ratchet mechanism

It is used as a device that allows continuous linear or rotary motion in only one direction while preventing motion in the opposite direction. The ratchet mechanism is also made of plastic material.

3.3 Gear and Flywheel

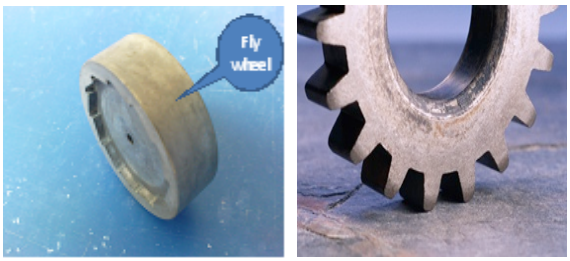

Fig. 7~8: flywheel and spur gear.

Spur gear is to change the speed of rotation from one shaft to another and/or change the direction of rotation (clockwise to counter-clockwise, or vice-versa).

Flywheel is made of cast iron. For flywheel inertia is main factor. Its diameter is about and thickness 3 cm and thickness is 1 cm.

3.4 Gear Box

It is a combination of different sized gears. It is a device which increases rotational speed and vice

versa. It is specially used in lathe machine . In this project, it is used for increasing rotational speed.

3.5 Generator

It is a small size electric generator that converts mechanical energy into electrical energy. The main components of this generator are stator, rotor, armature coil and electromagnet. In its simplest form, the rotor consists of a single loop of wire made to rotate within a magnetic field.

Fig. 9: DC Generator

4. DESIGN AND CONSTRUCTION

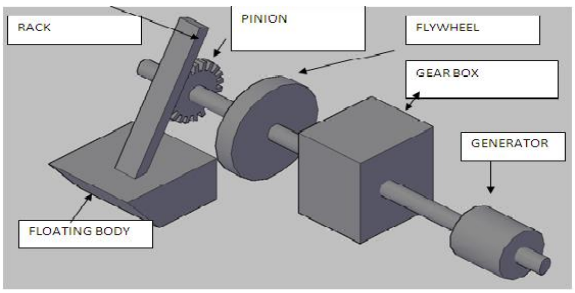

Figs. 10~11: Total figure of the project.

5. EXPERIMENTAL PROCEDURE

For sample performance test, we used water tank. At first the tank was filled with water. Then the water wave apparatus was immersed in water. Then water wave was created by manually .The water wave forced the floating body to move up and down on the water. Then the reciprocating motion of the floating body converted into rotational speed by ratchet mechanism. The motion is gone to generator. We took the time of 5 deflection of water wave and measured height of deflection by steel rule. Then, reading of current and voltage by multimeter was taken. Thus the process was repeated for 5 the time.

7. EXPERIMENTAL CALCULATION

Data table 1:

Sample calculation:

Height of deflection, H=6cm=0.06 m

Time for 5 deflection = 5.7sec

Time required for each deflection, T =5.7/5=1.14sec

No of obs.	Height of Deflection (cm)	Input power (watt)	Output power (watt)	Efficiency (%)
1	2	0.214	0.1134	52.9
2	3	0.494	0.21605	43.72
3	4	0.9018	0.3257	36
4	5	1.49	0.421	28
5	6	1.96	0.397	20.25

Wave power formula:

Wave power, $p = \rho g^2 H^2 T / 64\pi$

$= (1000*9.8^2*0.06^2*1.14/64*3.14)$

=1.96 watt

Input power=1.96 watt

Output power:

Voltage =4.03 volt, Current, I=0.0986 amp

Output power =V*I =4.03*00986 = **0** .397 watt

Efficiency:

ň =output power /input power

= (0.397/1.96) *100=20.25%

8. RESULT AND DISCUSSION

Using the experimental data of water wave, the theoretical graph of power of input Vs height deflection of water wave is plotted. From the performance test graph power input and output was increased with geometry rate. The maximum input power was 1.96 watt and output power was 0.397 watt for 6 cm height .The efficiency of this power plant is about 20.25 to 52.9 percent. For 2 cm height of deflection efficiency was 52.9%. But the efficiency was decreasing with increasing height .Because the teeth of gears were made of plastic and one tooth was broken, which was slipped during operation. Other losses may be as friction loss, vibration, loss in power transmission etc.

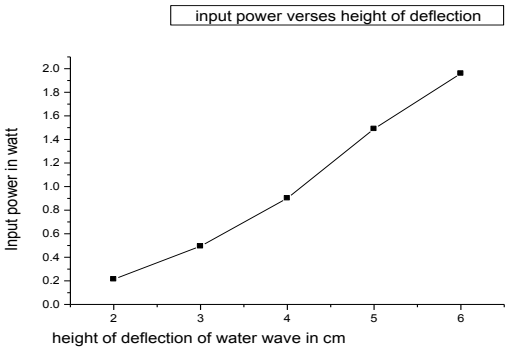

Fig. 12: Power input $v_{s.}$ height of deflection of water wave

In curve, it is seen that power input increases almost linearly with respect to height of deflection of water wave.

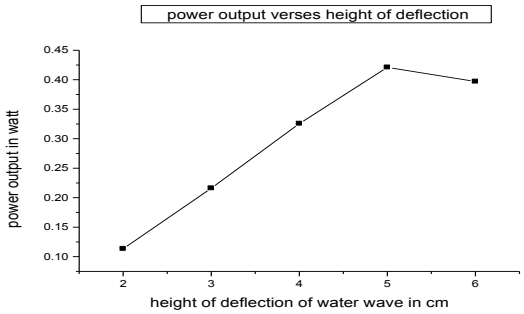

Fig. 13: power output verses height of deflection of water wave

In this curve ,output power was increased almost linearly with increase of height of deflection .Initial power output is not increased at the same rate because initial input power is not increased due to static inertia.

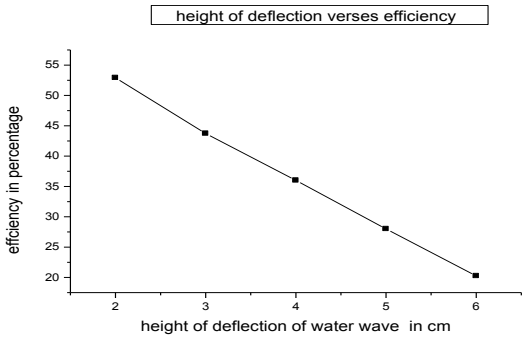

Fig. 14: efficiency verses height of deflection of water wave

In this curve efficiency was decreased with increase in height of deflection of water wave .

9. CONCLUSIONS

The water wave power plant is suitable for deep water such as sea water. But this project was designed to work in shallow water .The characteristics of such is that; it produces more power in more height of water wave. The project is completed very finely. We get the efficiency up to 20.25 to 52.9%. First the project is designed. According to dimension the water wave power plant was constructed. But it is true that there is a little difference between theoretical calculation and practical calculation. As the Evaluation of the water wave power plant continued, the height of deflection of water wave became one of the major factors for efficiency.

12. REFERENCES

[1]. Phillips, O.M. (1977). *The dynamics of the upper ocean* (2nd ed.). Cambridge University Press. ISBN 0 521 29801 6.

[2]. "Wave Power". *University of Strathclyde*. http://www.esru.strath.ac.uk/EandE/Web_sites/01-02/RE_info/wave%20power.htm. Retrieved 2008-11-02.

[3]. "Wave Energy Potential on the U.S. Outer Continental Shelf" (PDF). *United States Department of the Interior*. http://www.ocsenergy.anl.gov/documents/docs/OCS_EIS_WhitePaper_Wave.pdf. Retrieved 2008-10-17.

[4]. Goda, Y. (2000). *Random Seas and Design of Maritime Structures*. Advanced Series on Ocean Engineering. 15. Singapore: World Scientific Publishing Company. ISBN 981-02-3256-X. OCLC 45200228.

[5]. Goda, Y. (2000). *Random Seas and Design of Maritime Structures*. World Scientific. ISBN 978 981 02 3256 6.

[6]. Reynolds, O. (1877). "On the rate of progression of groups of waves and the rate at which energy is transmitted by waves". *Nature*16:343–44.

Proceeding of the
International Conference on Electrical, Computer and Telecommunication Engineering
01- 02 December 2012 (ICECTE2012), RUET, Rajshahi-6204, Bangladesh

ICECTE2012: PI-0094

Power System Stability Enhancement Using Fuzzy Logic Controller

Md. Asaduz-Zaman[1], M. A. Motin[2], Md. Rezwanul Haque[3]
[1]Dept.of Allied Engineering, Bangladesh University of Textiles
[2,3]Dept.of Electrical and Electronic Engineering, Rajshahi University of Engineering and Technology
masad_eee06@yahoo.com, motin_eee_06@ yahoo.com, rezwanul.ruet@yahoo.com

ABSTRACT
Fuzzy logic controller(FLC) is the most powerful tool for power system stability. It gives a quick and autonomous output based on various system inputs. In this paper the application of FLC for power system stability enhancement is presented. The performance of FLC in comparison with automatic voltage regulator(AVR) has been investigated. The whole procedure has been implemented by MATLAB simulation.

KEYWORDS: Fuzzy logic control, fuzzification, fuzzy processing, defuzzification, scaling factor, AVR.

1. INTRODUCTION

The concept of Fuzzy Logic (FL) was conceived by Lotfi Zadeh, a professor at the University of California at Berkley, and presented not as a control methodology, but as a way of processing data by allowing partial set membership rather than crisp set membership or non-membership. Fuzzy logic is a technique to embody human like thinking into a control system. It is a system of logical operators defined by a calculus of interaction, that attempts to construct a model for the various modes of human reasoning, which are approximate rather than exact. In its broad sense, fuzzy logic refers to a general class of fuzzy set theories, describing a family of classes with unsharp fuzzy boundaries.

2. ELEMENTS OF A FUZZY CONTROLLER

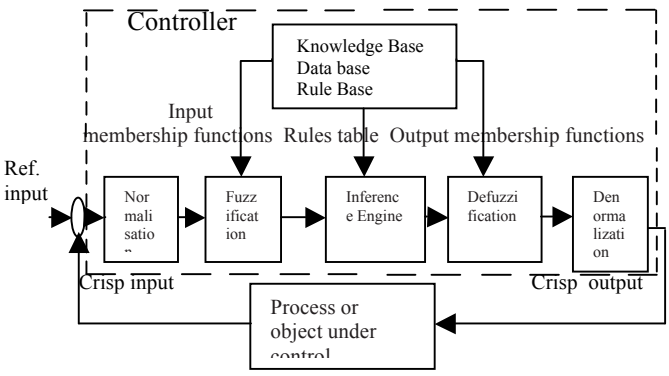

Fig. 1 Block diagram of a typical fuzzy logic controller

A fuzzy logic controller's control process consists five principal elements. These elements are:

•Fuzzification module (fuzzifier).
•Knowledge base.
•Rule base.
•Inference engine.
•Defuzzification module (defuzzifier).

When a fuzzy controller receives input data, it translates it into a fuzzy form. This process is called fuzzification. The controller then performs fuzzy processing which involves the evaluation of the input information according to IF…THEN rules created by the user during the fuzzy control system's design stage. Once the fuzzy controller finishes the rule processing stage and arrives at an outcome conclusion, it begins the defuzzification process. In this final step, the fuzzy controller converts the output conclusions into "real" output data (e.g., analog counts) and sends this data to the process via an output module interface.

2.1 Fuzzification

Fuzzification is a process of producing a fuzzy input on the base of a crisp one. Fuzzification consists of two main components:
• membership functions
• labels

2.1.1 Membership Functions:

During fuzzification, a fuzzy logic controller receives input data, also known as the fuzzy variable, and analyses it according to user-defined charts called membership functions. Membership function are system dependent.. The controller assigns the input data a grade from 0 to1 based on how well it fits into each membership function. Membership functions can have many shapes, depending on the data set, but the most common are the Γ, S, L,A, Gaussian and ∏ function shown in fig.2. To choose membership functions, first of all we need to consider the universe of discourse for all the linguistic variables, applied to the rules formulation. For example, if we specify a range which is too small, regularly occurring data will be off the scale, that may impact on an overall system performance. Conversely, if the universe for the input is too large, a temptation will often be to have wide membership functions on the right or left to capture the extreme input values.

Membership functions consist of connected line segments defined by the lines' end points.

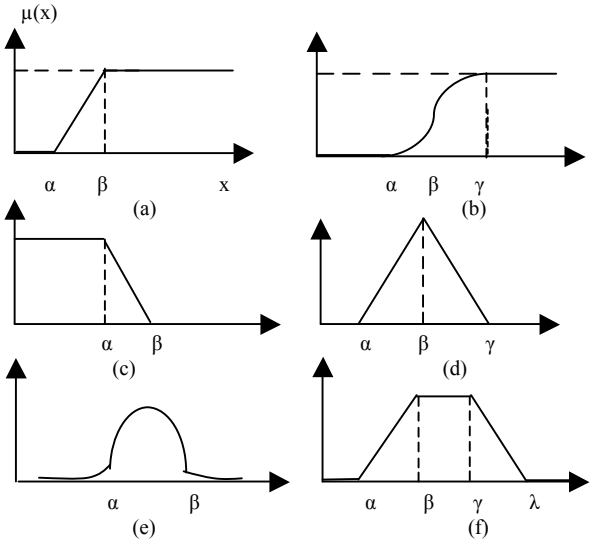

Fig.2**:** Types of membership functions: (a) Γ-function; (b) *S*-function; (c) *L*-function; (d) Λ-function;(e) Gaussian function; (f) Π-function

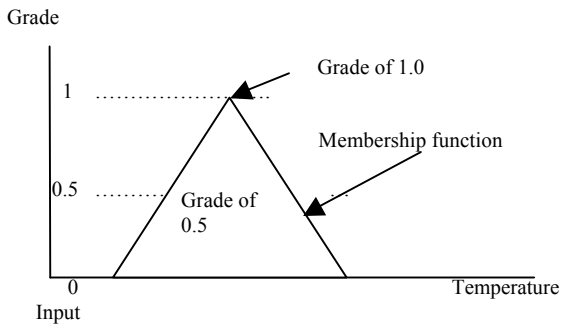

Fig.3**:** Membership function chart.

Each membership function can have up to three line segments with a maximum of four end points. The grade at each end point must have a value of 0 or 1. A membership function's shape does not have to be symmetrical.

2.1.2 Labels:

Each fuzzy controller input can have several membership functions, with seven being the norm, that define its conditions. Each membership function is defined by a name called a label For example, an input variable such as temperature might have five membership functions labeled as cold, cool, normal, warm, and hot. Generically, the seven membership functions have the following labels, which span from the data range's minimum point (negative large) to its maximum point(positive large):

- NL (negative large)
- NM (negative medium)
- NS (negative small)
- ZR (zero)
- PS (positive small)
- PM (positive medium)
- PL (positive large)

Fig.4 shows an example of an input variable with seven-shaped membership functions using all of the possible labels. A group of membership functions forms a fuzzy set. Although most fuzzy sets have an odd number of labels, a set can also have an even number of labels. For example, a fuzzy set may have four or six labels in any shape, depending on how the inputs are defined in relationship to the membership function.

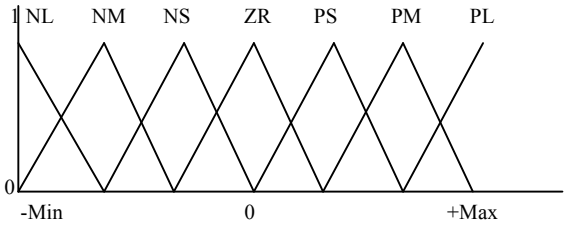

Fig. 4: Fuzzy logic input with seven membership functions

2.2 Knowledge Base

The knowledge base consists of a database of the plant. It provides all the necessary definitions for the fuzzification process such as membership functions, fuzzy set representation of the input–output variables and the mapping functions between the physical and fuzzy domain.

2.3 Rule Base

The rule base is essentially the control strategy of the system. It is usually obtained from expert knowledge or heuristics and expressed as a set of IF-THEN rules. The rules are based on the fuzzy inference concept and the antecedents and consequents are associated with linguistic variables. For example: IF error (e) is Positive Big (PB) THEN output (u) is Negative Big (NB).Error (e) and output (u) are linguistic variables while Positive Big (PB) and Negative Big (NB) are the linguistic values. The first part of the rule is called antecedent part and the second part of the rule (the result part) is called consequent part. The rules are interpreted using a fuzzy implication technique. In fuzzy control theory, this is normally Mamdani's implication technique.To understand the design of rule base consider the following Fig.5.

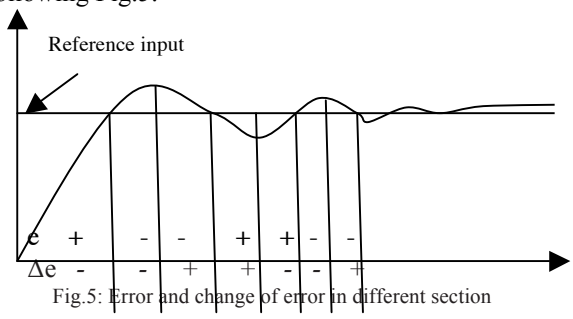

Fig.5: Error and change of error in different section

In this figure it is evident that when the sign of error and the change of error are of same sign then the output curve moves away from the reference value. So to keep the output close to the reference value a large excitation of opposite polarity of error is to be applied. For opposite polarity of error and change of error the output curve moves towards the reference value. In this case a moderate excitation of same polarity of error is to be applied.

A convenient form to write down rules is proposed here. This table form is suitable with two inputs and one output. On the top side of the table the possible linguistic values for the change-of-error (Δe) and on the left side, the error (e) are written. Let us consider two inputs where both inputs and an output have a set of possible linguistic values {NL, NM, NS, ZR, PS, PM, PL}

TABLE I

Δe / e	PL	PM	PS	ZR	NS	NM	NL
PL	NL	NL	NL	NL	NM	NS	ZR
PM	NL	NL	NL	NM	NS	ZR	PS
PS	NL	NL	NM	NS	ZR	PS	PM
ZR	NL	NM	NS	ZR	PM	PM	PL
NS	NM	NS	ZR	PS	PM	PL	PL
NM	NS	ZR	PS	PM	PL	PL	PL
NL	ZR	PS	PM	PL	PL	PL	PL

So the rule will be as follows where the Δu indicate output.

if e is **PL** and Δe is **PL** then Δu is **NL**

if e is **PL** and Δe is **NL** then Δu is **ZR**

and so on.

2.4 Fuzzy Inference System

Fuzzy inference is the process of formulating the mapping from a given input to an output using fuzzy logic. The mapping then provides a basis from which decisions can be made, or patterns discerned. The process of fuzzy inference involves all of the pieces which are membership functions, fuzzy logic operators, and if-then rules. There are two types of fuzzy inference systems that can be implemented in the Fuzzy Logic Toolbox: Mamdani-type and Sugeno-type. These two types of inference systems vary somewhat in the way outputs are determined.

2.5 Defuzzification

Defuzzification is a process of producing a crisp output on the base of a fuzzy input. There is no systematic procedure for choosing a good defuzzification strategy. Selection of defuzzification procedure depends on the properties of the application. Different defuzzification methods have been developed and applied. These are:

- Centre-of-area/gravity defuzzification.
- Centre-of-largest-area defuzzification.
- Mean of maxima.
- First-of-maxima defuzzification.
- Middle-of-maxima defuzzification.
- Height defuzzification.

The most well-known defuzzification method is the centre-of-area/gravity defuzzification.

3. RULES FOR TUNING PARAMETERS OF A PI-LIKE FUZZY CONTROLLER

The output de-normalization factor has the most influence on stability and oscillation tendency. Because of its strong impact on stability, this factor is assigned to the first priority in the design process. Input scaling factors have the most influence on basic sensitivity of the controller with respect to the optimal choice of the operating areas of the input signals. Therefore, input scaling factors are assigned the second priority. The shape and location of input and output membership functions may influence positively or negatively the behavior of the controlled system in different areas of the state space provided that the operating areas of the signals are optimally chosen. Therefore, this aspect is the third priority. For the PI like fuzzy controller the rules for tuning parameters are shown in the following table.

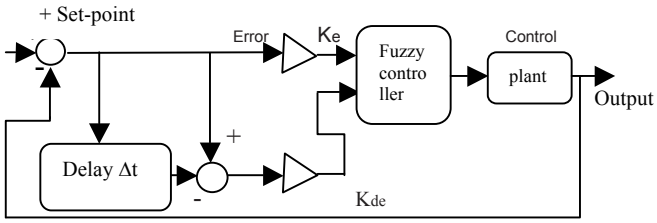

Fig.6: A block diagram of a PI fuzzy control system

4. SIMULATION OF AVR WITH FUZZY LOGIC CONTROLLER

Automatic voltage regulators are part of excitation systems of synchronous machines. Over the past decades the excitation system and AVRs have been developed into several different versions and designs. generator is accompanied by a drop in the terminal voltage magnitude. The voltage magnitude is sensed through a potential transformer on one phase. This voltage is rectified and compared to a dc set. This point signal. The amplified error signal controls the exciter field and increases the exciter terminal voltage. Thus the generator terminal voltage is increased which results in an increase in the desired value. Block diagram of automatic voltage regulator with fuzzy logic controller in Matlab file is shown in figure 5-7. Excitation system and voltage regulators of generator regulate the terminal voltage within

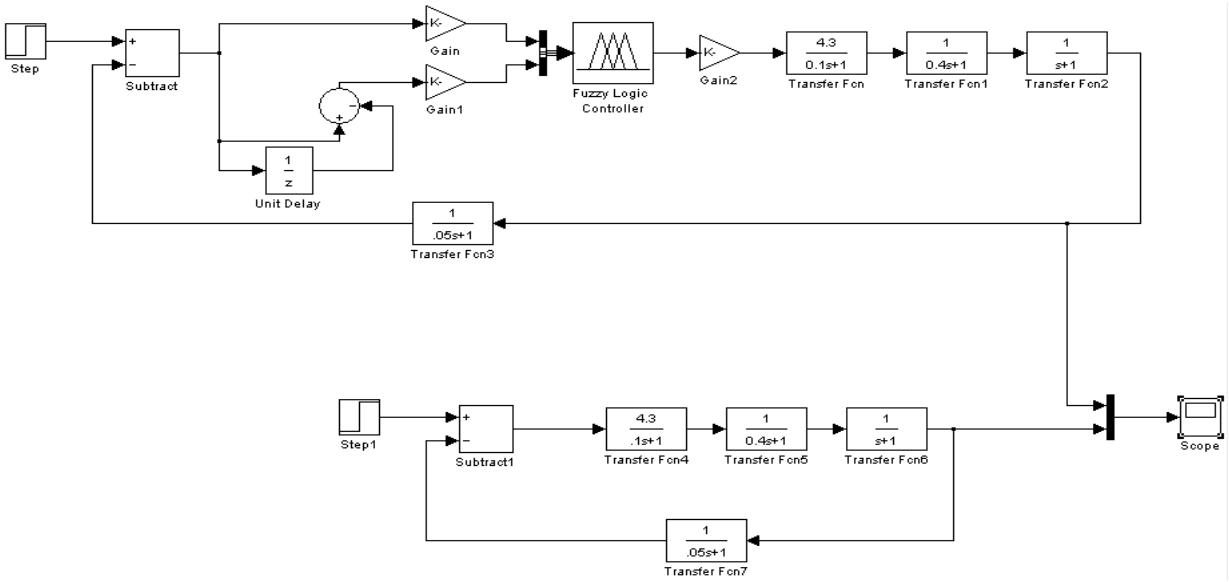

Fig. 7: Combine block diagram of AVR with FLC and without FLC

specified limit during normal load variation and improve transient stability during disturbances. Additional limiting and controlling, protective stabilizing features are also provided within excitation systems and automatic voltage regulator. During terminal voltage fall, the excitation current is rapidly increased by field forcing. During voltage rise, the excitation current is rapidly reduced by field forcing. As a result the rated terminal voltage of generator is recovered within a few seconds to ensure the transient stability. This transient stability can be increased if Automatic voltage regulator is used with a fuzzy logic controller shown in Fig.8

.

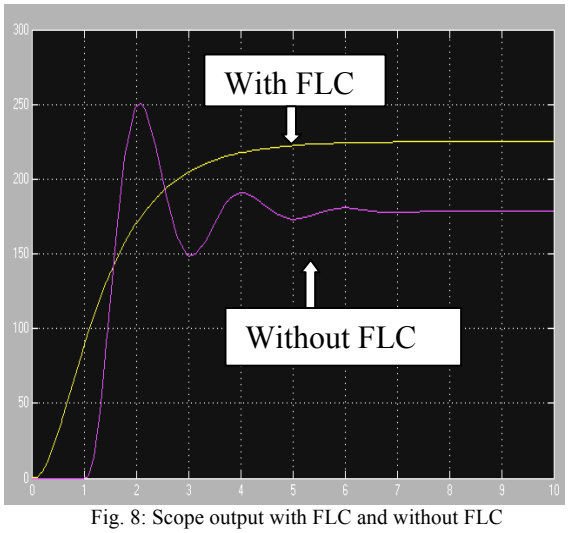

Fig. 8: Scope output with FLC and without FLC

5. CONCLUSIONS

An automatic voltage controller based on fuzzy logic has been designed and compared with the classical one(AVR).The output obtained from both has been compared with a reference input. The output obtained from classical one contains overshoots, undershoots and large settling time to be stable. Whereas the FL based controller removes overshoots, undershoots and reduce the settling time. Another advantage of FLC is it's cheapness. Due to robustness and effectiveness of FLC it is worthy to use FLC instead of classical controller and it's application is still proliferating in the control system applications.

REFERENCES

[1] M.N. Cirstea, A. Dinu, J.G. Khor M. McCormick, *Neural and Fuzzy Logic Control of Drives and Power Systems,* First published 2002, Newnes,London, ISBN 0 7506 55585.

[2] LEONID REZNIK, *Fuzzy Controllers,*First published 1997, Newnes,London, ISBN 0 7506 3429 4.

[3] P. M. Anderson and A. A. Fouad, *Power system control and stability*, 2nd edn, IEEE Press,1993, New Jersey.

[4] H. Saadat, *Power System Analysis*, McGraw Hill Book Company, 1999, New York.

[5] P. W. Sauer and M. A. Pai, *Power Systems Dynamics and Stability*, Prentice-Hall, Inc., 1998,New York.

[6] M. E. El-Hawary, *Electric power applications of fuzzy systems*, IEEE Press, 1998, New Jersey.

[7] http://en.wikipedia.org/

[8] http://www.seattlerobotics.org/

Proceeding of the
International Conference on Electrical, Computer and Telecommunication Engineering
01- 02 December 2012 (ICECTE2012), RUET, Rajshahi-6204, Bangladesh

ICECTE2012: PI-0095

Stabilization of Wind Farm Integrated Power System by Using Static Synchronous Compensator (STATCOM)

M J Rana[1], M R I Sheikh[2], M F Rahaman[3], M M Rashid[4], M S R Ashrafi[5]
[1,2,3,4,5] Department of Electrical and Electronic Engineering , Rajshahi University of Engineering & Technology
E-mail: jewel.eee33@gmail.com, ris_ruet@yahoo.com

ABSTRACT
Due to continuously varying nature of wind speed, the active and reactive power along with terminal voltage of a wind farm fluctuates continuously. In this paper, a STATCOM with wind farm integrated power system has been presented which can maintain both voltage and power fluctuations to the desired level. MATLAB/SIMULINK program has been used for this purpose. Terminal voltage and active power under short circuit faults has been analyzed. The simulation result shows that STATCOM acts as a good reactive power compensator and thus relieves the main supply system from the burden of reactive power supply to the induction generator.

KEY WORDS— wind energy, active power, wind farm, voltage, reactive power, STATCOM**.**

1. INTRODUCTION

Global wind power production has increased rapidly in the recent years. World wind generation capacity more than quadrupled between 2000 and 2006, doubling about every three years [7]. Due to proliferation of wind power penetration into the grid, the impact of power quality is emerging as a crucial issue. One of the important power quality issue is the flicker. Voltage flicker describes dynamic variations in the network voltage. The flicker emission produced by grid connected wind turbines during continuous operation is mainly caused by fluctuations in the output power due to wind speed variations, the wind gradient and the tower shadow effect. Flicker mitigation can be realized by appropriate reactive shunt compensation. The most commonly used device for flicker mitigation is the Static Var Compensator (SVC). However, the STATCOM has received much more attention recently. Compared with the SVC, the STATCOM has many advantages, such as overall superior functional characteristics, better performance, faster response, smaller cost reduction, and capable of providing both active and reactive power [1].

In this paper, a wind farm using induction generators modeled using MATLAB/SIMULINK and reactive power compensation of grid connected wind turbines fed induction generators is investigated during normal and faulty condition. Simulation results prove that STATCOM is an effective means for the reactive power compensation.

2. STATCOM

STATCOM is a static synchronous generator operated as a shunt-connected static var compensator whose capacitive or inductive output current can be controlled independent of the ac system voltage [4]. The STATCOM (or SSC) is capable of generating and/ or absorbing reactive power and in which the output can be varied to control the specific parameters of an electric power system [2]. Furthermore, a STATCOM has the following advantages [3]:

1. Faster response
2. Requires less space as bulky passive components (such as reactors) are eliminated
3. Inherently modular and relocatable
4. It can be interfaced with real power sources such as battery, fuel cell or SMES (superconducting magnetic energy storage)

2.1. OPERATION OF STATCOM

The basic voltage-source converter scheme is shown in figure 3. The charged capacitor C_{dc} provides a DC voltage to the converter, which produces a set of controllable three-phase output voltages with the frequency of the AC power system.

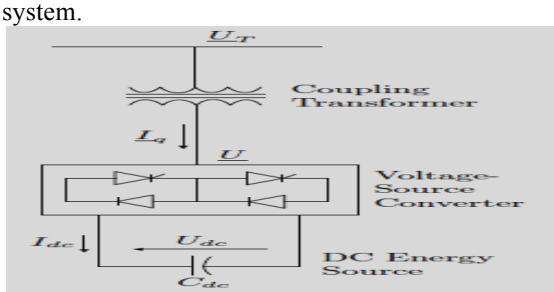

Fig. 1. Operation STATCOM

By varying the amplitude of the output voltage $\underline{U}$, the reactive power exchange between the converter and the AC system can be controlled. If the amplitude of the output voltage $\underline{U}$ is increased above that of the AC system $\underline{U}_T$, a leading current is produced, i.e. the STATCOM is seen as a

conductor by the AC system and reactive power is generated. Decreasing the amplitude of the output voltage below that of the AC system, a lagging current results and the STATCOM is seen as an inductor. In this case reactive power is absorbed. If the amplitudes are equal no power exchange takes place.

A practical converter is not lossless. In the case of the DC capacitor, the energy stored in this capacitor would be consumed by the internal losses of the converter. By making the output voltages of the converter lag the AC system voltages by a small angle, the converter absorbs a small amount of active power from the AC system to balance the losses in the converter. The mechanism of phase angle adjustment can also be used to control the reactive power generation or absorption by increasing or decreasing the capacitor voltage Udc, and thereby the output voltage U. [5]

To establish the rotating magnetic field of the stator of the induction generator, reactive power must be supplied from the network to the stator winding. This is undesirable particularly in case of large wind turbine and weak grids. Therefore, reactive power consumption of the induction generator is partly compensated by capacitor bank in order to achieve power factor close to one in steady state condition [6].

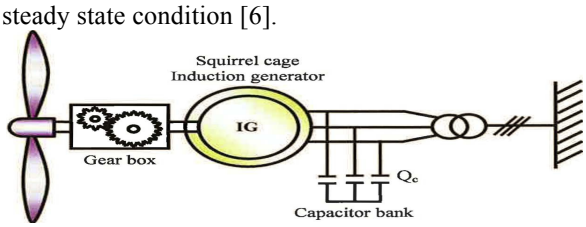

Fig. 2. Reactive power compensation by capacitor bank

3. MODEL SYSTEM

In model system a wind farm consisting of six 1.5-MW wind turbines was connected to a 25-kV distribution system exporting power to a 120-kV grid through a 25-km 25-kV feeder. The 9-MW wind farm was simulated by three pairs of 1.5 MW wind-turbines. Wind turbines used squirrel-cage induction generators (IG). The stator winding was connected directly to the 60 Hz grid and the rotor is driven by a variable-pitch wind turbine. The pitch angle was controlled in order to limit the generator output power at its nominal value for winds exceeding the nominal speed (9 m/s). In order to generate power the IG speed must be slightly above the synchronous speed. Speed varies approximately between 1 per unit (pu) at no load and 1.005 pu at full load. Each wind turbine had a protection system monitoring voltage, current and machine speed.

Reactive power absorbed by the IGs was partly compensated by capacitor banks connected at each wind turbine low voltage bus (400 kvar for each pair of 1.5 MW turbines). The rest of reactive power required to maintain the 25-kV voltage at bus B25 close to 1 pu was provided by a 3-Mvar STATCOM with a 3% droop setting. Short circuit faults were applied at the terminal of wind turbine 2.

4. SIMULATION RESULTS

CASE A: In this case, only capacitor bank supply the reactive power. From the fig.3 it is seen that active power of first turbine becomes zero at t=13.5 sec. Due to the insufficient supply of reactive power and reduction of electrical torque the turbine becomes unstable and shut down by the protection system.

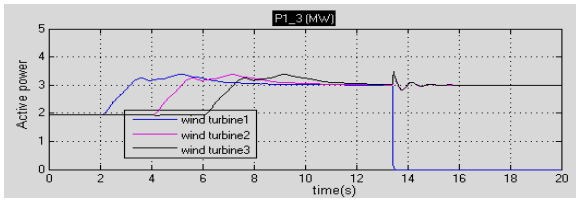

Fig.3. Active power of three pair of wind turbine without STATCOM and without fault

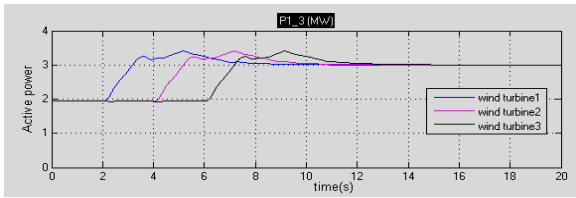

Fig.4. Active power of three pair of wind turbine with STATCOM and without fault

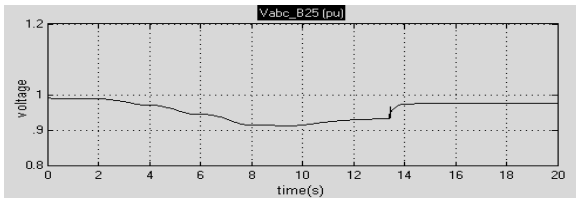

(a) Voltage at the bus

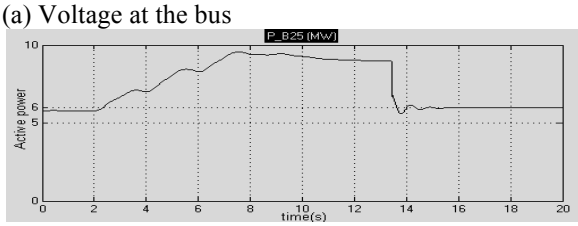

(b) Active power at the bus B_25

Fig.5. Voltage and active power of bus B_25 without STATCOM during single line to ground fault.

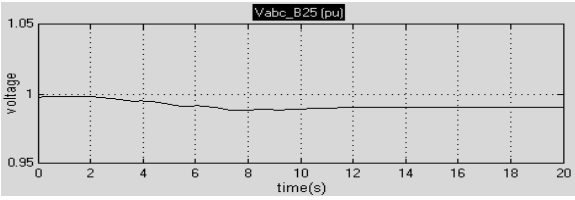

(a) Voltage at the bus B_25

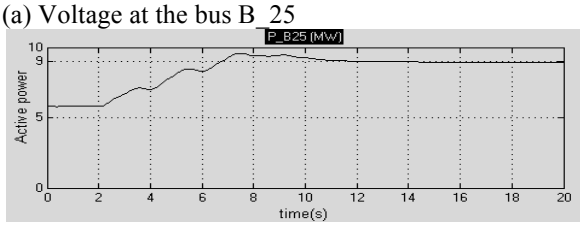

(b) Active power at the bus B_25

Fig.6. Voltage and active power of bus with STATCOM during single line to ground fault.

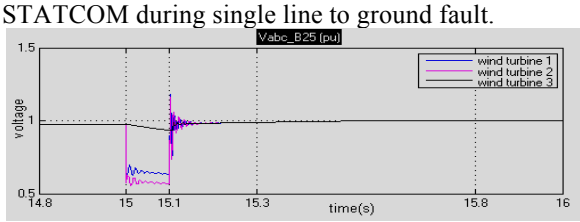

(a) Voltage at the bus B_25

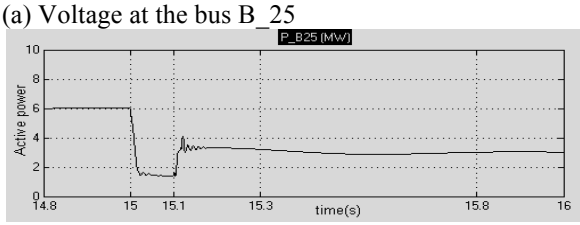

(b) Active power at the bus B_25

Fig.7. Voltage and active power of bus without STATCOM during double line to ground fault.

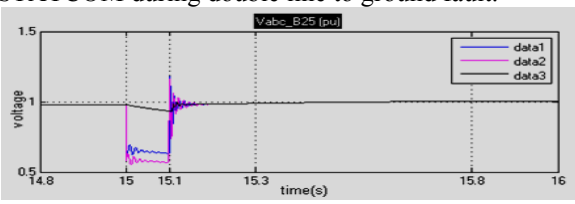

(a) Voltage at the bus B_25

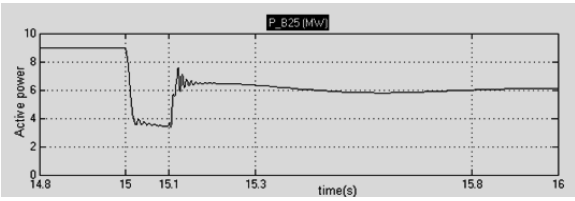

(b) Active power at the bus B_25

Fig.8. Voltage and active power of bus B_25 with STATCOM during double line to ground fault.

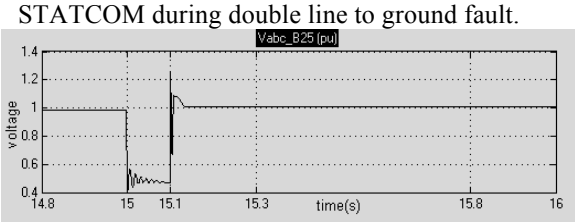

(a)Voltage at the bus B_25

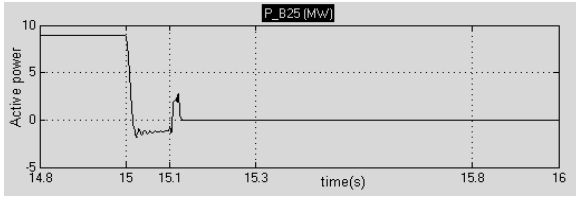

(b) Active power at the bus B_25

Fig.9. Voltage and active power of bus with STATCOM during three phase fault

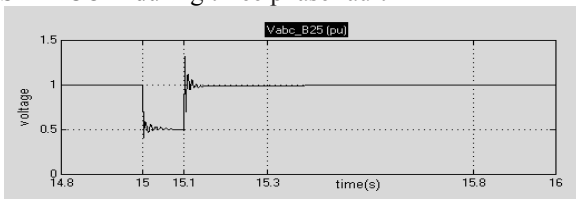

(a) Voltage at the bus B_25

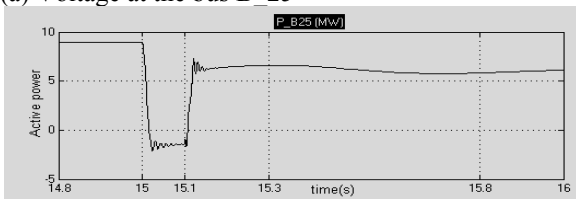

(b) Active power at the bus B_25

Fig.10. Voltage and active power of bus B_25 with increased STATCOM value during three phase fault

CASE B: With STATCOM and without fault the active power of the three pair of wind turbine as shown in fig.4. In this case, each turbine runs smoothly and gives rated power of 3MW. This happens due to the sufficient supply of reactive power by the STATCOM as required by induction generator.

4.1. Fault Analysis

Faults were applied at t=15sec and cleared at t=15.1sec

4.1.1. Single Line to Ground Fault

CASE A: Without STATCOM due to single phase to ground fault voltage and active power have reduced by about 2% and 33% respectively as shown in fig.5.

CASE B: With STATCOM single line to ground fault has little effect on the system due to the reactive power compensation of the STATCOM. Fig.6 shows that active power of the bus is at rated condition (9MW).

4.1.2. Double Line to Ground Fault

CASE A: Without STATCOM due to double line to ground fault bus voltage and active power drop largely during fault period and turbine 1 and turbine 2 shuts down due to the insufficient absorption of reactive power as shown in fig.7. After clearance of the fault voltage remains at 1pu

but active power falls to 3MW as only turbine 3 supplies power to the bus.

CASE B: As shown in fig.8 with STATCOM active power of the bus is 6MW after clearance of the fault. Due to the reactive power support of the STATCOM only one turbine shuts down and remaining two turbines supply power to the bus.

4.1.3. Three Phase Fault

CASE A: During three phase fault the STATCOM of 3Mvar cannot meet the reactive power requirement of the induction generators. As a result, all the turbines shut down and active power of the bus becomes zero as shown in the fig.9.

CASE B: When value of STATCOM is increased from 3Mvar to 6Mvar the active power of the bus becomes 6MW at the steady state. Also the voltage drop during fault period is lesser than with 3Mvar STATCOM. These are shown in the fig.10.

5. CONCLUSION

In this work, the role of STATCOM as a reactive power compensator has been demonstrated. The analysis of the simulation result shows that the use of STATCOM ensures better voltage regulation and active power supply from wind farm to the grid. From the fault analysis it obvious that by supplying reactive power STATCOM combats the transient period of the fault and accelerates the recovery of system after the fault. So, it is concluded that STATCOM improves the stability of wind farm integrated power system to an effective manner.

6. FUTURE WORK

1. Stability control of wind farm using multimass shaft drive train modeling.
2. Analysis of the utility of this wind farm in respect of Bangladesh.
3. Analysis of interconnected system of different types of renewable energy so that proper utilization of renewable energy can be achieved instead of conventional energy.
4. Comparison of performance of STATCOM with other reactive power compensator such as SVC.

7. ACKNOWLEDGMENTS

Thanks to Allah for His blessing without which nothing is possible. In addition to that we are really grateful to teachers of Electrical and Electronic Engineering department of Rajshahi University of Engineering and Technology for their valuable suggestion throughout the work. Last but not least we want to thank our friends for their inspiration, help and support.

REFERENCES

[1]. V.Suresh Kumar, Ahmed F.Zobaa , R.Dinesh Kannan , and K.Kalaiselvi "Power Quality and Stability Improvement in Wind Park System Using STATCOM". Jordan Journal of Mechanical and Industrial Engineering Volume 4, Number 1, Jan. 2010.pp. 169-176

[2]. Yuvaraj and Dr. S.N. Deepa. "Improving Grid Power Quality With FACTS Device on Integration of Wind Energy System." *Student Pulse Academic Journal*. Vol. 3,Issue 4, April 2011.pp. 5

[3]. K. R. Padiyar.2007. "FACTS Controllers in Power Transmission and Distribution." New Age International (P) Ltd., India. PP. 173

[4]. Pavlos S. Georgilakis and Peter G. Vernados."Flexible AC Transmission System Controllers: An Evaluation." *Trans Tech Publications, Switzerland. Materials Science Forum*. 2011.Vol. 670. pp 399-406

[5]. Gabriela Glanzmann."FACTS -Flexible Alternating Current Transmission Systems." EEH Power Systems Laboratory ETH Zurich. January 2005. pp.7-8. http://www.eeh.ee.ethz.ch/uploads/tx_ethpublications/Glanzmann_FACTS_internal.pdf

[6]. Md. Rafiqul Islam Sheikh.. Stabilization of a Grid Connected Wind Farm by Using SMES.pp. 21 https://kitir.lib.kitamiit.ac.jp/dspace/bitstream/10213/1744/1/Sheikh.pdf

[7]. Wind power.14 May 2012. http://en.wikipedia.org/wiki/Wind_power#Wind_power_capacity_and_production

Proceeding of the
International Conference on Electrical, Computer and Telecommunication Engineering
01- 02 December 2012 (ICECTE2012), RUET, Rajshahi-6204, Bangladesh

ICECTE2012: PI-0096

Damping improvement of SMIB System by STATCOM and UPFC

Abdul Khaleque[1], Feroz Ahmmed Bhuyan[2] and M. A. Motin[3]
[1, 2&3] Department of Electrical and Electronic Engineering,
Rajshahi University of Engineering & Technology, Rajshahi-6204, Bangladesh.
E-mail: khaleque_eee@yahoo.com, ferozeee@gmail.com, motin_eee_06@yahoo.com

ABSTRACT
This paper presents two different techniques for damping undesirable electromechanical oscillations in a single machine infinite bus (SMIB) system. A comparison between static compensators (STATCOM) and unified power flow controllers (UPFC) is performed for this purpose. However, disturbances are simulated on single machine infinite bus system and rotor angle or speed deviations are investigated without and with flexible Alternating current transmission system (FACTS) devices. MATLAB SIMULINK is used for dynamic simulations.

KEY WORDS: Flexible a.c. transmission system (FACTS), static compensators (STATCOM), unified power flow controller (UPFC), single machine infinite bus (SMIB).

1. INTRODUCTION

FACTS devices (STATCOM, SSSC, UPFC, IPFC, etc.) are a powerful technology that can solve many outstanding problems in power systems. They provide the opportunity to influence power flows and voltages and therefore are able to enhance the system security, e.g. by improving the voltage profile or increasing the transfer capacity of a system without the need of new lines. Better utilization of the existing power system to increase capacities by installing FACTS devices becomes imperative [1~2]. Along with power system stabilizers now FACTS stabilizers are used for damping oscillations in the power system. It is important to arrive at the transient rating of the FACTS controller.

STATCOM is a shunt connected reactive-power compensation device that is capable of generating or absorbing reactive power and in which the output can be varied to control the specific parameters of an electric power system [3].

Unified Power Flow Controller is the most versatile FACTS controller developed so far, with all encompassing capabilities of voltage regulation, series compensation and phase shifting. It can independently control both the real and reactive power flows in a transmission line. It comprises two voltage sourced converters coupled through a common DC terminal. One Voltage Source Converter (VSC) is connected in shunt with the line through a coupling transformer and the other VSC inserted in series with the transmission line through an interface transformer. This paper proposes the use of controlled active loads to increase damping of such electro-mechanical oscillations by using FACTS devices such as STATCOM and UPFC.

2. MODELING OF THE POWER SYSTEM WITH AND WITHOUT FACTS DEVICE

Consider a simple Single Machine Infinite Bus (SMIB) system shown in Fig. 1 without any FACTS device.

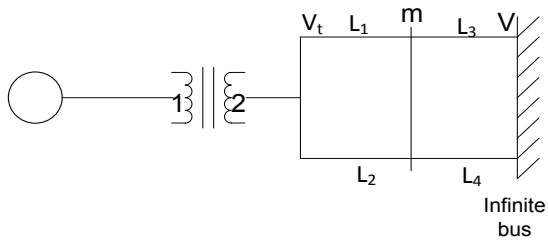

Fig. 1: Single Machine Infinite Bus system.

The system consists of a single machine connected to an infinite bus through two identical transmission lines.

The equivalent circuit of the system is shown in Fig. 2, where X_1 represent the equivalent reactance between machine internal bus and the impedance bus m. and X_2 represent the equivalent reactance between the bus m and the infinite bus [3].

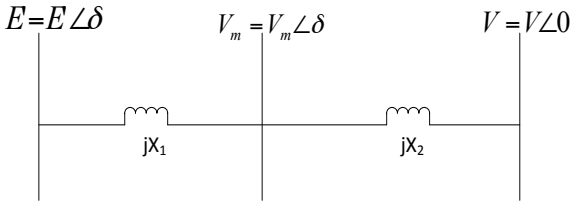

Fig. 2: Equivalent circuit of SMIB system.

The magnitude of the machine internal voltage and the infinite bus voltage is represented by E, and V, respectively. The dynamics of the machine in the classical model can be represented by the following equations [3] as

$$\frac{d\delta}{dt} = \omega \quad \text{..... (1)}$$

$$\frac{d\omega}{dt} = \frac{1}{M}(P_m - P_e - D_\omega) \quad \text{(2)}$$

Here δ, ω, M, P_m and D are the rotor angle deviation, rotor speed deviation, moment of inertia, input mechanical power and damping coefficient, respectively of the machine. The electrical output power of the machine in Fig. 2 can be written as [3]

$$P_e = P_{\max} Sin\delta \quad \text{(3)}$$

where

$$P_{\max} = \frac{E'V}{X_1 + X_2} \quad \text{(4)}$$

2.1 Modeling of STATCOM

Figs. 3 and 4 depict the schematic diagram and equivalent circuit, respectively, of the SMIB system with STATCOM.

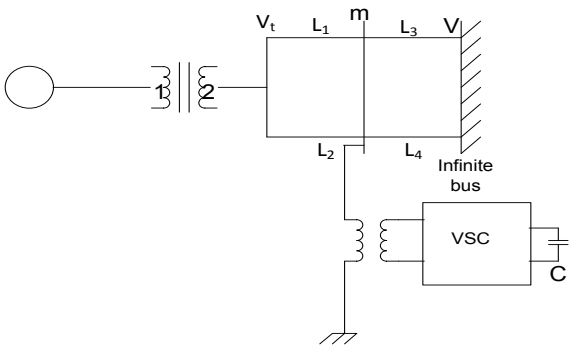

Fig. 3: Schematic diagram of the SMIB system with STATCOM.

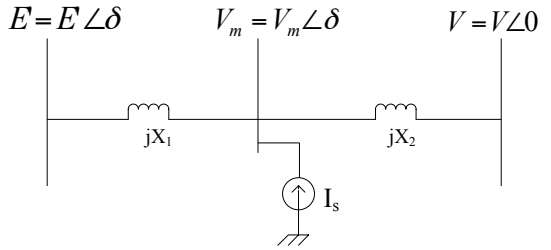

Fig. 4: Equivalent circuit of SMIB system with STATCOM.

The STATCOM is placed in the bus m and is represented by a shunt reactive current source I_s as [4-5]

$$I_s = I_s e^{j(\delta_m \pm \pi/2)} \quad \text{(5)}$$

where,

$$\delta_m = \tan^{-1}\left(\frac{E'X_2 Sin\delta}{VX_1 + E'X_2 Cos\delta}\right) \quad \text{(6)}$$

With the STATCOM the output power P_e of the machine can be written as

$$P_e = P_{\max} Sin\delta + f1(\delta) I_s \quad \text{(7)}$$

where

$$f1(\delta) = \frac{E'X_2}{X_1 + X_2} Sin(\delta - \delta_m) \quad \text{(8)}$$

is positive when δ oscillates in between zero and π. Equation of P_e suggests that it can be modulated by modulating the shunt reactive current I_s.

For enhancement of power system damping the shunt reactive current can be modulated in propagation to the rotor speed deviation ω. With this control signal I_s can be expressed as [3]

$$I_s = K_1 \omega, \quad -I_s^{max} \le I_s \le I_s^{max} \quad \text{(9)}$$

where K_1 is a positive constant.

2.2 Modeling of UPFC

Fig. 5 shows the single line diagram of the SMIB system with UPFC.

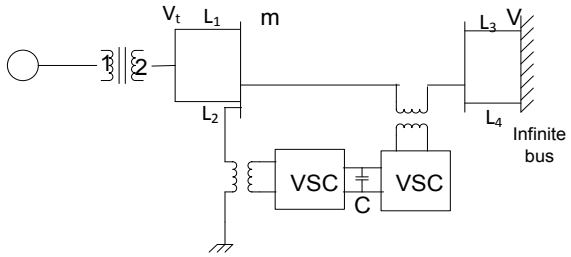

Fig. 5: Schematic diagram of the SMIB system with UPFC.

The series converter exchanges both real and reactive power within the transmission line. The shunt connected converter 1 is used mainly to supply the real power demand of converter 2, which derives from the transmission line itself [3]. The shunt converter maintains constant voltage of the DC bus. Thus the net real power drawn from the AC system equal to the losses of two converters and their coupling transformers.

The equivalent circuit of UPFC can be represented as a shunt current source and a variable voltage source as shown in fig. 6.

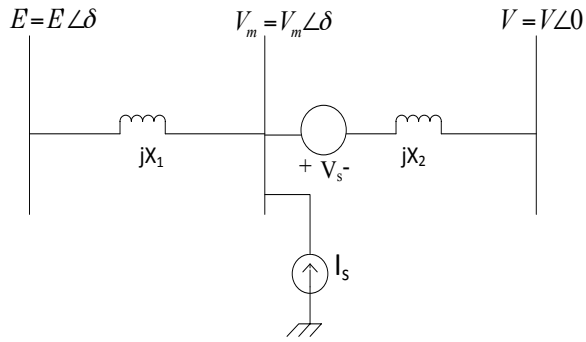

Fig. 6: Equivalent circuit of SMIB system with UPFC.

The mathematical expression of Static Synchronous Series Compensator (SSSC) and Static Compensator (STATCOM) will be combined to show the damping

improvement of the system with UPFC. With the UPFC the machine power P_e can written as [4]

$$P_e = P_{\max} Sin\delta + f1(\delta)I_s + f2(\delta)V_s \ldots \quad (10)$$

where the value of $P_{\max}$, δ, $f1(\delta)$ and $f2(\delta)$ are given in the previous sections.

3. SIMULATION BLOCK DIAGRAM OF THE SYSTEM

3.1 Simulation diagram of the system with STATCOM

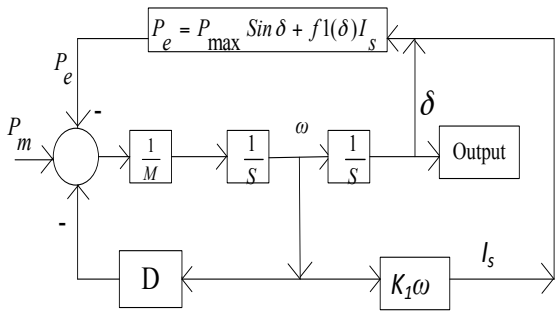

Fig. 7: Simulation diagram with STATCOM

where
P_m = change in mechanical Input to the turbine.
P_e = Electrical power output of the machine.
M = Machine moment of inertia.
ω = Rotor speed deviation.
δ = Rotor angle deviation.
D = Damping coefficient.

3.2 Simulation diagram of the system with UPFC

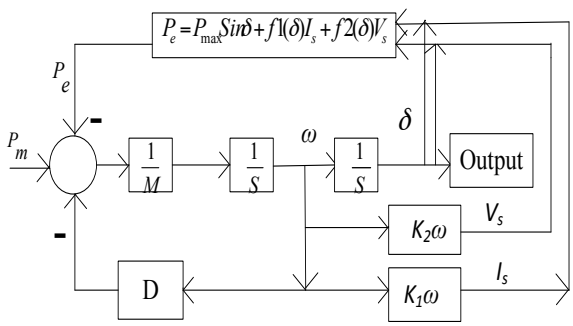

Fig. 8: Simulation diagram with UPFC

Figs. 7 to 8 represent the simulation model for dynamic analysis of power system with STATCOM and UPFC, respectively. With UPFC both the loops $K_1\omega$ (shunt current modulation) and $K_2\omega$ (series voltage modulation) are present.

4. RESULTS AND DISCUSSION

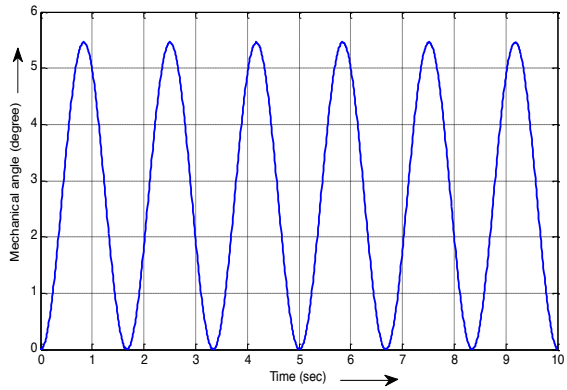

Fig. 9: Rotor angle deviation without FACTs for step change in the turbine mechanical input, Δpm = 0.1 p.u.

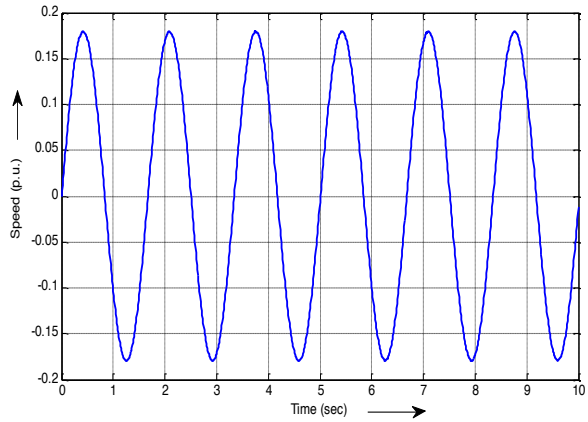

Fig. 10: Rotor speed deviation without FACTs for step change in the turbine mechanical input, Δpm=0.1 p.u.

Figs. 9 to 10 it is clear that there are sustained rotor angle oscillations with poor damping. The peak value rotor angle deviation is 5.4 mechanical degrees and 0.155 p.u. for rotor speed deviation.

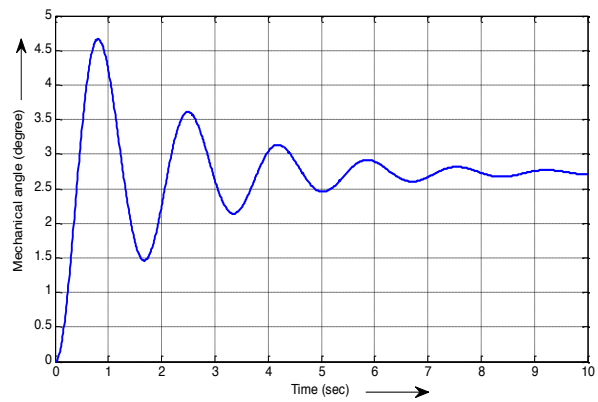

Fig. 11: Rotor angle deviation with STATCOM for step change in the turbine mechanical input, Δpm = 0.1 p.u.

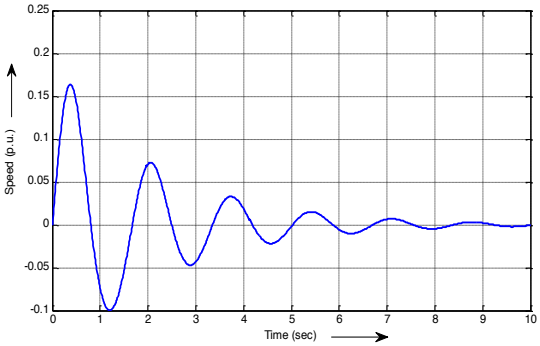

Fig. 12: Rotor speed deviation with STATCOM for step change in the turbine mechanical input, Δpm = 0.1 p.u.

Figs. 11 and 12 show the peak value of rotor angle deviation is 4.7 mechanical degrees and the speed deviation damp out in 9.8 seconds, respectively, for step change in the turbine mechanical input, Δpm = 0.1 p.u when STATCOM is connected with SMIB.

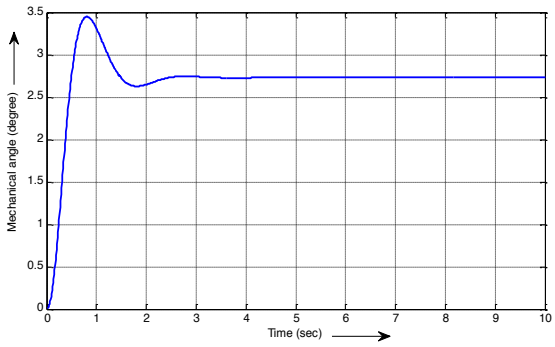

Fig. 13: Rotor angle deviation with UPFC for step change in the turbine mechanical input, Δpm = 0.1 p.u.

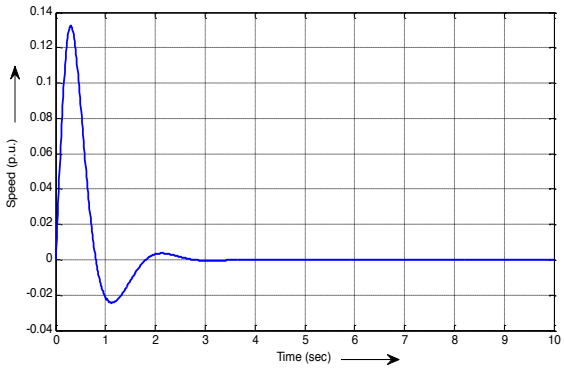

Fig. 14: Rotor speed deviation with UPFC for step change in the turbine mechanical input, Δpm = 0.1p.u.

Figs. 13 to 14 it is clear that as UPFC is connected to the system, the peak value of rotor angle deviation is 3.4 mechanical degrees and the speed deviation damp out in 3.2 seconds.

5. CONCLUSIONS

In this work, the performance of STATCOM and UPFC with respect to rotor angle deviation and rotor speed deviation are shown when both devices are with SMIB system. The performance of SMIB system without FACTs is also investigated. The results show that the peak value of rotor angle deviation (4.7 mechanical degrees) with STATCOM is higher than the peak value of rotor angle deviation (3.4 mechanical degrees) with UPFC. When STATCOM and UPFC are connected with SMIB, the rotor speed deviation damp out in 9.8 seconds and 3.2 seconds, respectively. However, the transient rating of UPFC is found to be better than STATCOM. The results will give useful information on the transient rating of the FACTs controllers for small or large disturbance stability enhancement.

6. FUTURE WORK

Future researchers may use IPFC and PID controller to make system stable quickly and to damp out electro-mechanical oscillations.

REFERENCES

[1]. S. Gerbex, R. Cherkaoui, and A. J. Germond, "Optimal location of multi-type FACTS devices in a power system by means of genetic algorithms", IEEE Trans. Power Systems, vol. 16, pp. 537-544, August. 2001.

[2]. F. D. Galiana, K. Almeida, M. Toussaint, J. Griffin, and D. Atanackovic, "Assessment and control of the impact of FACTS devices on power system performance", IEEE Transaction Power Systems, vol. 11, no. 4, Nov. 1996.

[3]. N. Senthil Kumar, R. Srinivasan, M. Abdullah Khan, "Damping Improvement by FACTs devices: A comparison between STATCOM, SSSC and UPFC", International Journal on Electrical and Power Engineering, vol 2(3), pp. 171-178, 2008.

[4]. Klein, M. G. J. Rogers, P. Kundur, "A Fundamental Study of Inter-Area Oscillations ", IEEE Trans. Power System, vol. 6, 1991.

[5]. Mathur R.M. and R.K. Verma, "Thysistor based FACTs controller for Electrical transmission systems", IEEE press, Wiley and Sons Publications, 2002.

Proceeding of the
International Conference on Electrical, Computer and Telecommunication Engineering
01- 02 December 2012 (ICECTE2012), RUET, Rajshahi-6204, Bangladesh

ICECTE2012: PI-0097

Rice Husk Gasification: An Alternative to Rural Electrification in Bangladesh

Barun Kumar Das[1], S.M. Najmul Hoque[1], Syed Mamun R Rasid[1], Md. Abdul Kader[1] and Md. Abdulla-Al-Mahmood[2]

[1] Department of Mechanical Engineering, Rasjshahi University of Engineering and Technology, Rajshahi, Bangladesh.
[2] Department of Glass and Ceramics Engineering, Rasjshahi University of Engineering and Technology, Rajshahi, Bangladesh.

E-mail: barun_ruet@yahoo.com, shumon99234@gmail.com, mamunruet05@gmail.com kader_042017@yahoo.com, abdulla2038@yahoo.com.

ABSTRACT
In recent year, Bangladesh is facing severe power crisis all over the country, but the rural area is the most vulnerable. Bangladesh is an agricultural country and produces huge quantity of paddy every year. Husk is the waste biomass produce during the rice processing on average it accounts for 20% of the paddy produced, on weight basis. The husk production per annum is about 6.57 million tonnes which is used to produce producer gas through gasification process with heating value of 4~6 MJ/Nm^3 for application in internal combustion engines. In this paper the prospects of rice husk gasification and the technological aspects of the gasification process have been studied

Key words: Rice husk, Gasification, Electricity, Biomass, Producer gas

1. INTRODUCTION

The supply of sustainable energy is one of the main challenges that mankind will face over the coming decades, particularly because of the need to address climate change. Biomass can make a substantial contribution to supplying future energy demand in a sustainable way.

About 80% of the populations of Bangladesh live in rural areas. The rural economy is characterized by slow growth, high unemployment, insufficient infrastructure and widespread poverty. Due to the lack of electricity supply in rural areas, the rural population depends mainly on biomass as a source of energy. Over 70% of total primary energy consumption is covered by biomass, mainly agricultural waste and wood. Only about 6% of the entire population has access to natural gas, primarily in urban areas. Biomass fuels, such as wood, cow dung and agricultural residues are collected mainly from the local environment and have become a traded commodity as cooking fuel as access to local biomass becomes ever more difficult. Today only an estimated 43% of the Bangladesh population is connected to the electricity grid. The electricity supply is not reliable though and peak demand cannot be met. In the rural areas, where more than 70% of the population lives, only about 25% have electricity [1].The installed capacity in Bangladesh as increased by roughly 2,000MW between 2009-2011 and is now about 6,900MW (August 2011) [2]. According to reports, Bangladesh at present generates 5000 MW power. Peak hour demand of 6,000 MW everyday and increases on hot summer days.Bangladesh´s electricity supply strongly relies on gas: More than 80% of the power plants are fired by gas. Hydro power is responsible for 4.4% of the total electricity supply. The acute gas shortage causes a loss in production of around 600MW [2].

Bangladesh has strong potential for biomass gasification based electricity. More common biomass resources available in the country are rice husk, crop residue, wood, jute stick, animal waste, municipal waste, sugarcane bagasse etc. This technology can be disseminated on a larger scale for electricity generation. Rice husks are among the most common agricultural residues in the world accounting for about one-fifth of unmilled rice dry wet. Indonesia, Vietnam, Malaysia, Myanmar, China, India, Philippine and Bangladesh produces large amount rice husk which can be a potential source of energy. Rice husk gasifiers have been successfully operated in Indonesia, China, Mali and India

A large rice-husk power generation plant coming up at the north-western Thakurgaon district of Bangladesh will generate 400 KWh of electricity mainly for small and medium sized rice mills. The project, first of its kind in the country, is in line with such power generation plants in the neighbouring India and China.The private sector venture undertaken by Sustainable Energy & Agro-resources Ltd (SEAL) will use the same technology employed in India, and will be in fully operation.

2 . RICE HUSK IN BANGLADESH

Bangladesh is an agricultural country and it's economy largely depends on agriculture. About 70% people earn their livelihood by agriculture and agri-based industry. Total area of Bangladesh is about 144000 km², where the total agricultural land is about 90500km² which is 62.8% of the total area. Total arable land is 79700km² and is 55.3% of the total area.Aus, amon and boro are the main three types of rice are produced in Bangladesh. Total aus, aman and boro production of 2010-2011 has been estimated at 2.12 million metric tones, 12.77 million tones and 17.99 million tones respectively. Total rice production in 2011 was around 32.88 million tones [3]. The rice husk is the outer cover of the rice and on average it accounts for 20% of the paddy produced, on weight basis and is accounted 6.58 million tones.

3. CHARACTERISTICS OF RICE HUSK

The husk surrounding the kernel of rice accounts for about 20%, by weight of the harvested grain (paddy). In modern two-stage mills, the husk and the bran layer inside the husk are removed in separate stages; these mills generate about 200 kg of husk for each tonne of paddy. In most of the very numerous small mills in developing countries, some or all of the bran is removed with the husk in a single-stage milling operation. The resulting husk mixture often represents 25% or more of the paddy.

The energy content or caloric value of the husks varies somewhat with the rice variety, the amount of bran mixed with the husks, and the moisture content of the husks (usually 8 to 10%). Most of the approximate fuel values cited in the literature on rice husks are close to 6,000 BTU/lb, 3000 kcal/kg, or 15 MJ/kg. The energy in 3 kg of husk approximately equals that in 1 kg of fuel oil or 1.5 kg of coal [4]. Somewhat higher fuel values have been indicated in tests of husks from small mills in developing countries; the inclusion of some bran with the husks tends to increase the percentage of carbon and dilute the ash in the mixture.

Most rice husks contain between 15% and 20'% ash, although even higher ash contents hive been recorded in some cases. The ash is 92% to 95% silica. The high ash contents and the characteristics of the ash impose several severe requirements on the design of the combustion or the gasification systems for the use of rice husk.

3.1 Proximate and Ultimate analysis of Rice Husk:

Proximate analysis gives information about feedstock suitability in terms of moisture content, volatile matter content and fixed carbon content. Chemical compositions of the solid wastes are identified by the determination of elemental contents in the sample such as Carbon, Nitrogen, Sulfur and Hydrogen. Table 1 shows the proximate analysis and Table 2 shows the ultimate analysis of rice husk.

Table 1: Proximate analysis of Rice Husk

	Rice Husk
Moisture	10.79 %
Ash	16.73%
Volatile Matter	56.46%
Fixed Carbon	16.02%

Table 2: Ultimate analysis of Rice Husk

	Rice Husk
C%	33.95
H%	5.01
N%	0.91
S%	0.09
O%	32.52
Cl%	0.16
Mineral Matter	16.73
GCV (Kcal/kg)	3568

4. Gasification

During a gasification process, biomass is directly converted to synthesis gas (syngas) in a gasifier under a controlled amount of air.Syngas can be used in internal combustion (IC) engine to produce heat, or in a cogeneration system to produce heat and electricity. Previously, Kapur et al. calculated the unit cost of electricity of using rice husk gasifier based power generation system and evaluated its financial feasibility with utility supplier and diesel generated electricity [5]. Abe et al. [6] discussed the potential of rural electricity generation via biomass gasification system. The results suggest that even though agricultural residues such as rice husks may contain high energy potential, however, to supply a biomass gasification system in the long term may require tree farming in order to provide sufficient amount of resources [6]. These researches imply that the feasibility of these large scale projects is greatly dependent on the plant location that affects the

resource availability and the incurred logistic costs of the selected biomass feedstock. On an industrial scale, biomass gasification and power generation systems have been well-established. Table. 3 shows the different types of gasifier with thermal capacity.

Table 3 Thermal capacity of different gasifier designs [7]

Downdraft	1 KW – 1MW
Updraft	1.1MW – 12MW
Fluidized-bed gasifiers	1 MW – 50MW
Cross-draft gasifiers	10 MW – 200MW

Classification of biomass gasifiers based on the density factor (ratio of dense biomass phase to total reactor volume) is a simple and effective method of classification. The gasifiers can be classified into a) dense phase gasifiers b) lean phase gasifiers. In lean phase gasifiers e.g. fluidized bed, the biomass occupies very little reactor volume i.e. 0.05 -0.2. Most of the gasifiers employed for decentralized applications in developing countries are dense phase reactors, mostly fixed bed reactors, they have typical density factor of 0.3 -.08 [8]. There are two main types of fixed bed gasifiers:

Fixed Beds

Fixed bed gasifiers typically have a grate to support the feed material and maintain a stationary reaction zone. They are relatively easy to design and operate, and are therefore useful for small and medium scale power and thermal energy uses. The two primary types of fixed bed gasifiers are updraft and downdraft.

In a downdraft gasifier, air is introduced into a downward flowing packed bed or solid fuel stream and gas is drawn off at the bottom. The air/oxygen and fuel enter the reaction zone from above decomposing the combustion gases and burning most of the tars. Downdraft gasifiers are not ideal for waste treatment because they typically require a low ash fuel such as wood, to avoid clogging.

In an updraft gasifier, the fuel is also fed at the top of the gasifier but the airflow is in the upward direction. As the fuel flows downward through the vessel it dries, pyrolyzes, gasifies and combusts. The main use of updraft gasifiers has been with direct use of the gas in a closely coupled boiler or furnace. Because the gas leaves this gasifier at relatively low temperatures, the process has a high thermal efficiency and, as a result, wet MSW containing 50% moisture can be gasified without any pre-drying of the waste.

Slagging fixed bed gasifier, which is high-pressure and oxygen-injected, has commercial potential for gasifying MSW. In theory, the high temperatures crack all tars and other volatiles into non-condensable, light gases. Also under these conditions, the ash becomes molten and is tapped out, as is done in iron blast furnaces.

Fluidized Beds

Fluidized beds are an attractive proposition for the gasification of MSW. In a fluidized bed boiler, a stream of gas (typically air or steam) is passed upward through a bed of solid fuel and material (such as coarse sand or limestone). The gas acts as the fluidizing medium and also provides the oxidant for combustion and tar cracking. Waste is introduced either on top of the bed through a feed chute or into the bed through an auger. Fluidized-beds have the advantage of extremely good mixing and high heat transfer, resulting in very uniform bed conditions and efficient reactions. Fluidized bed technology is more suitable for generators with capacities greater than 10 MW because it can be used with different fuels, requires relatively compact combustion chambers and allows for good operational control. The two main types of fluidized beds for power generation are bubbling and circulating fluidized beds.

In a Bubbling Fluidized Bed (BFB), the gas velocity must be high enough so that the solid particles, comprising the bed material, are lifted, thus expanding the bed and causing it to bubble like a liquid. As waste is introduced into the bed, most of the organics vaporize pyrolytically and are partially combusted in the bed. Typical desired operating temperatures range from 900° to 1000 °C.

A circulating fluidized bed (CFB) is differentiated from a bubbling fluid bed in that there is no distinct separation between the dense solids zone and the dilute solids zone. The capacity to process different feedstock with varying compositions and moisture contents is a major advantage in such systems.

5. ELECTRICITY GENERATION FROM RICE HUSK

Electricity generation from rice husk depends on the availability of raw materials and technology for conversion of rice husk to electricity. Gasification converts a traditional, low quality fuel to a modern day energy carrier i.e. combustible gas. Such conversion occurs at relatively high efficiencies and results in total convenience and process control. The process can be applied over a very wide range of output ratings (a few kilowatts to tens of megawatts) with only a small variation in overall efficiency and investment. Gasifiers with individual units being capable of supporting power generation at upto 500-800 kWe level; larger outputs need paralleling of more than one unit. Complete power generation systems including gasifiers, gensets, fuel handling sub-systems and grid paralleling sub-systems, as needed and effluent treatment.

The process is equally applicable for electricity generation and a variety of thermal applications. Raw material availability is also a concern for larger plants. Other than 4 distinct cluster areas for rice mills in Bangladesh, it will be difficult to keep the continuous supply to the plant [9].So, it's need to coupled with local availability of biomass, it provides for a truly distributed energy/power system at various output levels. The process is equally applicable for stand-alone utility and grid feeding. Almost all environmental pollution associated with biomass use can be eliminated. Various researcher shows that the downdraft gasifier is suitable for small scale rice husk gasification base power plant [10, 11]. For gasification based power plant consumption of rice husk is 1.86kg per kWh electricity generation [12]. If considering half of the total husk is used for parboiling of rice and domestic purposes;the rest of the husk could be produced 200MWe electric power. The power plant to be installed near the large rice mills `cluster areas' in Dinajpur, Bogra, Naogaon, Chapainawabganj and Ishwardi with the surplus rice husk.

6. CONCLUSION

Bangladesh has a good potential for power generation from rice husk gasification and has estimated around 200 MWe. There are seasonal, geographical distribution and other variations in the availability of this potential. Establishment of rice husk based power plants in rural areas will be led to an enormous change in the lifestyle of the local communities. Increased lighting would also be indirectly helped the community by increasing the business hours in the market area, reducing thefts, improving health conditions and encouraging new business developments like computer shops and photo studios. Gasification could reduce significantly reduce the GHG emission. Each Megawatt of power generated from rice husk plant has resulted in reduction of carbon dioxide (CO_2) emissions by about 5800 tonnes every year.

REFERENCES

[1] http://www.energybangla.com/

[2] BPDB- Bangladesh Power Development Board, "Key Statistics", June, 2011

[3] Infrastructure Development Company Ltd. (http://www.idcol.org/energyProject.php)

[4] Schaffer & Associates International, *"Rice Husk to Energy: A Preliminary Assessment for the Republic of Mali"*, USA, 2005

[5] Kapur T, Kandpal TC, Garg HP. *Electricity generation from rice husk in Indian rice mills: potential and financial viability.* Biomass Bioenergy 1996;10:393–403.

[6] Abe H, Katayama A, Sah BP, Toriu T, Samy S, Pheach P, et al. *Potential for rural electrification based on biomass gasification in Cambodia.* Biomass Bioenergy 2007;31:656–64.

[7] Dayton, D. 2002. *A Review of the Literature on Catalytic Biomass Tar Destruction, Milestone Completion Report* , NREL, Golden, Colorado, USA, NREL/TP

[8] Kishore V V N (editor). 2008. *Renewable Energy Engineering and Technology a knowledge compendium.* New Delhi: The Energy and Resources Institute.

[9] M. Ahiduzzaman. "Rice Husk Energy Technologies in Bangladesh" *Agricultural Engineering International: the CIGR Ejournal*. Invited Overview No. 1. Vol. IX. January, 2007.

[10] Environmental Protection Agency Combined Heat and Power Partnership (EPA-CHP), 2007, Biomass conversion technologies in biomass combined heat and power catalog of technologies, Environmental Protection Agency, United States.

[11] Bhattacharya, S. C., Salam, P. A., 2006, *A review of selected biomass energy technologies, Asian Regional Research Programme in Energy, Environment and Climate (ARRPEEC)*,Asian Institute of Technology (AIT), Thailand.

[12] Singh. R.I (2007), *Combustion of Biomass in an Atmospheric Fbc: An Experience and Study*. Paper presented at the International Conference in Advances on Energy Research Indian Institute of Technology Bombay, December, 12-15, 2007.

Proceeding of the
International Conference on Electrical, Computer and Telecommunication Engineering
01- 02 December 2012 (ICECTE2012), RUET, Rajshahi-6204, Bangladesh

ICECTE2012:PI-0098

Prospects of Wave power in Bangladesh

Md.Monjur Ellahi Rafi, Shah Md. Salimullah , M.R.I. Sheikh , S.M. Showybul Islam Shakib , F.A. Bhuyan
Department of Electrical & Electronic Engineering,
Rajshahi University of Engineering & Technology, Rajshahi-6204, Bangladesh.
E-mail: rafiruet@yahoo.com, ris_ruet@yahoo.com

ABSTRACT
This study deals with the idea of wave power to produce electricity in coastal areas of bangladesh. The graphical representation of power vs. Wave height and power vs. Wave period in different locations in bangladesh has been showen by matlab simulation. A self made prototype for wave energy harnessing and its experimental output has also been presented. From many other wave energy conversion technique which one is most suitable for bangladesh is predicted here. Last of all the cost estimation for a small wave plant has been discussed.

KEY WORDS: Oscillating water column(OWC), Wave energy converter(WEC).

1. INTRODUCTION

The purpose of this paper is to demonstrate that Bangladesh can be enriched in power sector and can reduce the power crisis using wave power. Because wave energy is essentially a non-depleting source of emission free power. Waves are free and will not run out so the cost is in building the power station. It causes less environmental impact on the local communities compared to conventional thermo electrical power generation.There are very few safety risks with wave power generation.

The earth is moving time to time. The surface of earth becomes warm more or less due to sunlight and differential heat is absorbed by land and water. These temperature variations cause density variations which influenced by gravity and the moving globe cause winds. This wind creates ripples on still water. As the wind continues to blow the ripples turn into waves and if the fetch is long enough, the waves develop into the great ocean swells . Once formed ocean waves can travel great distances with minimal loss of energy until they break on some distant shore. Thus wave energy is constantly renewed[1]. It varies in intensity, but it is available twenty-four hours a day, 365 days a year.For utilizing this constantly renewed energy, in this paper, we've gathered various information like site choice, simulation of wave power with height, design of a wave plant, and experimental output of own created prototype.

2. HARNESSING WAVE ENERGY

WEC is required to take off wave energy. Of them three major techniques are vitally used.

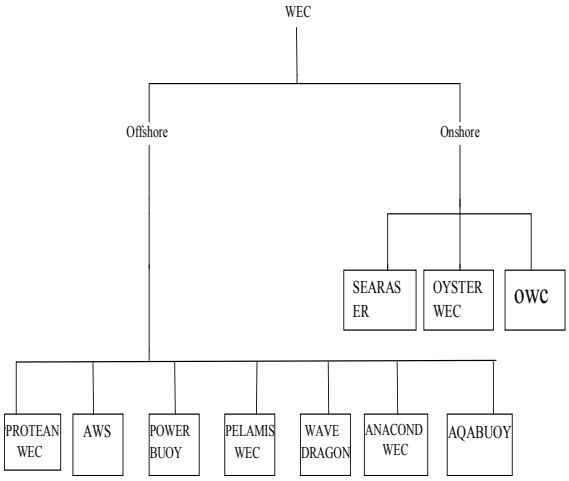

2.1 Oscillating Water Column

OWC consists air filled chamber above the water line. By wave action the water level inside the chamber rises and falls, alternately pressurising the air. This pressurised air escapes from the chamber through a turbine-generator unit producing electrical power. As the water level in the chamber falls air is drawn back through the turbine-generator assembly to continue power production. Wells turbines are self rectifying so that the direction of turbine rotation remains constant throughout the power cycle[2].

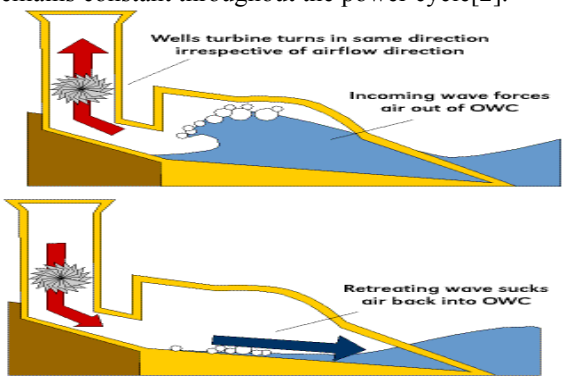

Fig. 1 Oscillating Water Column[4]

2.2 Pelamis

It is a semi submerged, articulated structure consisting cylindrical sections linked by hinged joints and is held on station by a compliant mooring system that allows the machine to weathervane to align itself head-on to incoming waves. As waves travel down the length of the machine they cause the structure to articulate around the joints. The induced motion of these joints is resisted by hydraulic rams that pump high-pressure oil through hydraulic motors which drives electrical generators to produce electricity[2].

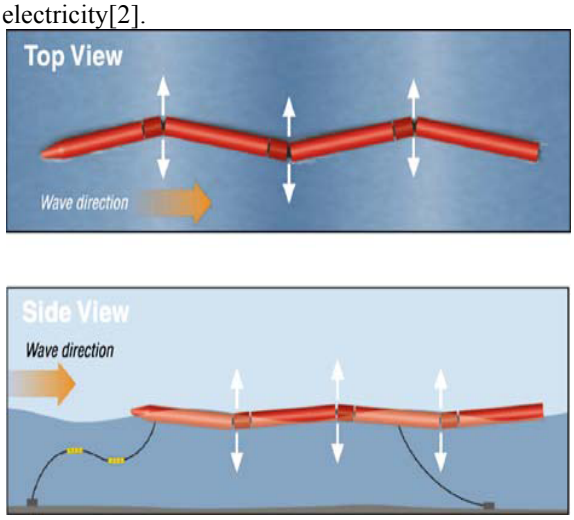

Fig. 2 Pelamis[5]

2.3 Archimedes Wave Swing

It is a fully submerged, bottom standing point absorber.It consists out of a cylindrical shaped floater containing entrapped air which oscillates due to pressure differences caused by surface wave action. The relative motion of the floater is converted into electricity through a linear direct induction generator. One unit is rated at 4 MW depending on the wave climate. The floater component has a diameter of 9.5 m and the device is designed for deployment in water depths ranging from 50-100 m[2].

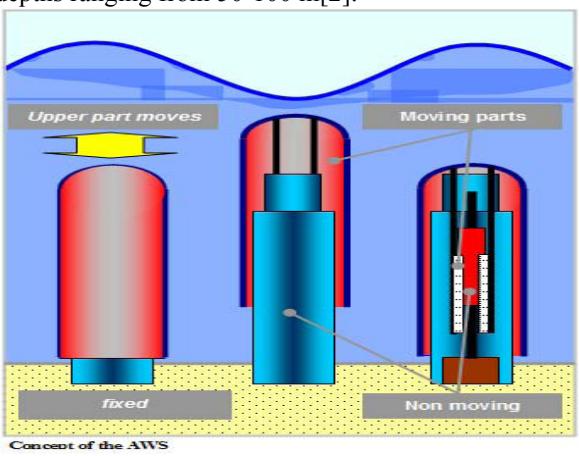

Fig. 3 Archimedes Wave Swing[2]

3.WAVE POWER IN BANGLADESH

Wave energy is a potential energy resource for electrification. But this is a matter of great regret that there is no wave plant in Bangladesh that has been yet built. Wave height in the Bay Of Bengal is of maximum 2.9m from recorded data.The approximate average wave height is 2.6m.And the wave period is about 8-9second. From where by energy calculation we can easily get 27kw from a single unit. At the same time we can think about the Saint Marteen. All this recorded data with simulation will be discussed here.

3.1 Recorded Data Of Wave Height In Different Region Of Bangladesh

3.1.1 Cox'sbazar

Local date	Monday, Jun 04								Tuesday, Jun 05							
Local time	00h	03h	06h	09h	12h	15h	18h	21h	00h	03h	06h	09h	12h	15h	18h	21h
Wave height (m)	2.6	2.6	2.6	2.6	2.6	2.6	2.6	2.7	2.7	2.8	2.8	2.9	2.8	2.8	2.8	2.8
Wave period (s)	8	8	8	8	9	9	9	9	9	9	9	9	9	9	9	9

3.1.2 Saint Marteen

Local date	Wednesday, Jun 06								Thursday, Jun 07							
Local time	02h	05h	08h	11h	14h	17h	20h	23h	02h	05h	08h	11h	14h	17h	20h	23h
Wave height (m)	1.5	1.5	1.6	1.6	1.6	1.6	1.6	1.7	1.8	1.9	1.9	2.0	2.0	2.0	2.0	2.0
Wave period (s)	5	5	5	5	6	6	6	6	6	6	6	6	7	7	7	7

3.2 Wave Power Formula

In deep water where the water depth is larger than half the wavelength, the wave energy flux is

$$P = \frac{\rho g^2}{64\pi} H_{m0}^2 T \left(0.5 \frac{KW}{m^3.s}\right) H_{m0}^2 T \ldots\ldots\ldots\ldots\ldots\ldots\ldots\ldots\text{(I)}$$

Where, P the wave energy flux per unit wave crest length (kW/m),$Hm0$ is the significant wave height (meter),T is the wave period (second),ρ is the mass density of the water (kg/m^3), and g is the acceleration by gravity (m/s^2).

3.3 Wave Power Characteristics By Matlab Simulation

3.3.1 Cox's bazar,Bangladesh

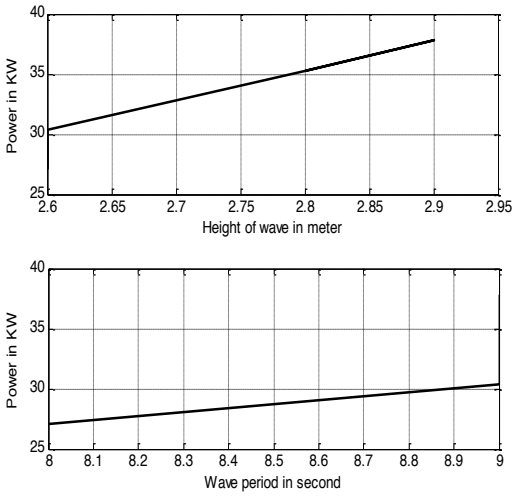

Fig. 4 Power vs wave height and wave period.

3.3.2 Saint Marteen,Bangladesh

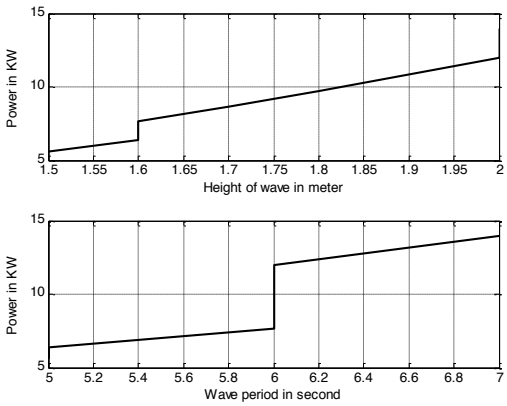

Fig. 5 Power vs wave height and wave period.

3.4 Suitable Wec's For Bangladesh

For onshore power take-off system the suitable one is OWC. The reason behind this as follows:

I) OWC uses Wells Turbine inside of it whose direction of rotation remains same whether the wave propagate in one direction first and then in reverse direction.
II) Produce a high air pressure.
III) Simple construction.
IV) No maintenance required.

For offshore power take-off system the suitable one is Pelamis. The reason behind this as follows:

I) In this type of WEC cyclinderical tube section's movement does not depend on the direction of wave.
II) Less cost required.
III) The Pelamis has a similar output to a modern wind turbine.
IV) Minimum environmental impact.
V) Survivability - 100 year wave.

4. COST ANALYSIS

It's vitally important that whenever we want to go with some new idea for realistic implementation whether it is cost effective or not. For this purpose before realistic implementation the cost should be analysed truly. In this chapter we will forgo with a sample of 500MW wave farm and then we will design our required one.

4.1 Construction Costs for 500-MW Wave Farm, 2008 [3]

Cost Category	Amount
Onshore transformers and grid	$8,283,50
Cables	$6,130,000
Mooring	$38,089,000
Power conversion modules	$202,701,000
Concrete structures	$77,878,000
Building/facilities	$21,379,000
Installation work	$19,973,000
Total	**$374,433,500**

Source: *ECONorthwest analysis of EPRI data.*

4.2 Cost For Our Proposed 1.5MW Wave Plant

Pelamis power conversion module	$2,930,000
Pelamis manufactured steel sections	$1,641,000
Pelamis mooring	$4,86,000
Installation	$1,000,000
Subsea cables	$1,635,000
Grid interconnection	$1,90,000
Total cost	**$7,882,000**

5. PROTOTYPE SIMULATION

This section deals about the practical implementation of our research in a little space. All of the step done is as follows.

5.1 Apparatus Used

i. 7.5 foot long wood made box.
ii. Four piece dc motor(each of 6volt)
iii. Four piece small fan.
iv. Wood stand.
v. Multimeter.
vi. Light emitting diode.
vii. Connecting wire.
viii. Single phase induction motor.

5.2 Construction

First of all a 7.5ft long box using wood is made. The dc motors is made water proof by plastic

prevailings. Now the four motors are placed in the wood stand perfectly. All the motors are connected in series. After making the wood box water proof by polythyene it is filled with water. And the wave is produced by Single phase induction motor with 220volt ac supply. Now the prototype is ready.

5.3 Working Principle

The wave energy we are discussing about is basically wind generated wave. In our prototype the artificial wind is produced by Single phase induction motor. Whenever this wave flows it acts upon the small fan or blade of the dc motor. As the armature of dc motor is connected with the blade and it starts rotating hence the armature starts to rotate across the magnet prevailing it. That the dc motor acts like a generator and produce voltage.

5.4 Experimental Output

Table 1 Experimental data from the prototype

Sl. no.	1-phase induction motor speed (rpm)	6v motor speed (rpm)	Wave height (m)	Wave period (s)	Voltage output (v)
01	2609	150	0.01	1	0.95
02	3200	225	0.015	1	1.2
03	3608	350	0.02	1	1.5

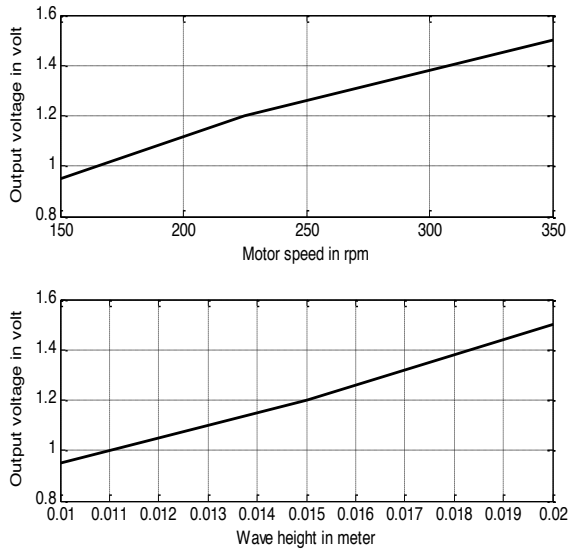

Fig 6 Output voltage vs motor speed and wave height.

We've used four motors(6v rating) in series and the output voltage(1.5v) is enough to glow a LED. From our experiment we can conclude that if we use more motors in series then more voltage will be generated.

6. CONCLUSION

The wave power plant is suitable for deep water such as sea water. The sea is not confined within a box. But in our prototype we've created wave within a confined region. Hence the wave reflected back, which can't be happened in the sea. At the same time our wave height created was not fair. For this reason we've got less output(only 1.5volt). But it is clear from this research that the output power is proportional to the square of wave height. Our wave height was only 0.02m and output voltage was 1.5volt whereas the wave height in cox'sbazar is 2.8m. So it is no doubt that hopeful result will be get in Cox'sbazar , Saint Marteen.

7. FUTURE WORK

Future researchers may create animated film based on wave power plant to present a clear view to the society to make a wave power plant & can give proposal to the government with the feasibility study to set a wave power plant.

8. ACKNOWLEDGEMENTS

The authors thank to Dr. Md. Rafiqul Islam Sheikh, Professor, Department. of Electrical and Electronic Engineering, Rajshahi University of Engineering & Technology for his support, guidance and encouragement throughout this research. We wish to thank our friend Abdul Aziz who help us to construct our prototype box.

REFERENCE

[1]. Tom Heath,"Realities of wave technology ", ART 1727.doc Page 1.

[2]. J.R Joubert,"An Investigation Of The Wave Energy Resource On The South African Coast, Focusing On The Spatial Distribution Of The South West Coast", *Stellenbosch-2008,*page2-26,27,2008.

[3]. A Report to Oregon wave Energy Trust, "Economic Impacts of wave Energy to Oregon's Economy",ECONorthwest-2009.

[4]. http://www.eepe.murdoch.edu.au/resources/info/Tech/wave/index.html

[5]. http://www.coppercanada.ca/Electrical/Wave/wavepowerS4.html

Proceeding of the
International Conference on Electrical, Computer and Telecommunication Engineering
01- 02 December 2012 (ICECTE2012), RUET, Rajshahi-6204, Bangladesh

ICECTE2012: PI-0099

A Modified Method of Coherency Identification for Large Multi-Machine Power System

Rahman Shaikh Rashedur, Hussain Md. Yeakub and Ali Md. Sekendar

Department of Electrical and Electronic Engineering
University of Asia Pacific
shaikhrahman77@gmail.com, yhussain1951@yahoo.com, sekendarali@hotmail.com

ABSTRACT
This paper is based on a modified method of coherency identification, which is very much simple and reliable. The modified method actually not a new method but a simple modification gives a new look of this method which presents in this paper. The technique involves the electrical proximity index, inertia condition index and a power variation index under faulted condition to select the coherent groups. The main focus of this paper is to transient stability study of a large multi-machine power system. And to check the stability, here a slightly modified coherency identification method is used. To replace coherent group by a single machine dynamic equivalent construction method is used. For transient stability study 20 M/C, 118 bus IEEE test power system has been chosen.

KEY WORDS: Transient stability study, coherent generators, dynamic equivalents, swing curve, 118-bus power system.

1. INTRODUCTION

The power system industry is a field where there are constant changes. Power industries are restructured to cater to more users at lower prices and better power efficiency. Power systems are becoming more complex as they become inter-connected. Load demand also increases linearly with the increase in users. Since stability phenomena limits the transfer capability of the system, there is a need to ensure stability and reliability of the power system due to economic reasons [1].

The large interconnections that constitute the present day power networks has further added to its complexity hence requiring a simplified but accurate method of transient stability analysis with minimum computing time and memory space. For this reason a design of a self-healing strategy with emphasis on a new two-level load shedding scheme to deal with large disturbances has been presented [2].

The method of transient stability analysis of a large power system via simplified dynamic equivalents is one of the attracting methods of system reduction, so less computer memory and time are required in solving the swing equations.

The coherent generator technique is an elegant and powerful tool for system simplification through construction of simplified reduced order dynamic models which can represent the entire system without loss of system significant characteristic. The reduction is based on the impact of large disturbances in a particular area known as the study system, while system external to study area are not of direct interest in stability analysis; and are thus represented by dynamic equivalents in recognition of its influence on the response of the study area to disturbances.

The concept of power variation of the generators at the instant of initiating fault is applied to classify the machines into inner circle (study area) machines and outer circle (external area) machines [3]. The study sub-system is modeled in detail whereas approximate modeling is carried out for the external sub-system.

For transient stability study of 118-bus IEEE test power system, a modified coherency identification method based construction of dynamic equivalent is used in this paper.

2. COHERENCY IDENTIFICATION METHOD BASED ON EQUAL ACCLERATION AND VELOSITY

This method was proposed by Hussain & Rau in 1992 [4], [5]. According to this method coherent group of generators can be identified by using Electrical Proximity index and Inertia Condition index.

2.1 Electrical Proximity and Inertia Condition Index

Electrical proximity index α_{ij} is defined by the expression:

$$\alpha_{ij} = [(n-1) * | Y'_{ij} | / |Y'_{ii} |] \geq 1.0 \quad (1)$$

for j=1,..,n where j ≠ i,

Where,

Y'_{ij} = Actual system admittance matrix elements.

$$And, \qquad Y'_{ii} = -\sum_{\substack{j=1 \\ j\neq i}}^{n} Y_{ij}$$

Only such generators which satisfy equation (1) are considered as candidates for coherency grouping test with the ith machine.

Now another normalized index, β_{ij} (Inertia condition index) can be evaluated which will give an estimate of the coherency between the generators i and j. The β_{ij} is defined as:

$$\beta_{ij} = | M_i - M_j | / \text{Max}(M_i, M_j) = \beta_{ji} \qquad (2)$$

Where, $M_i - M_j =$ Inertia difference between machine no i & j.

3. MODIFIED COHERENCY IDENTIFICATION METHOD BASED ON POWER VARIATION

This method is the modification of the previous method [4].

The Swing Equation (pu) of a generator is given as:

$$\frac{H}{\pi f}\frac{d^2\delta}{dt^2} = P_m - P_e \qquad (3)$$

From the above equation it is clear that, the nature of rotor angle variation of a machine is depended on its power variation. So a new coherency index, named power variation index may be evaluated by using this power variation of the machines at the instant of initiating fault. This index may be used further in coherency group identification test. This index is based on normalized value of power variation among the machines in faulted condition. It is defined as:

$$PV_{(ij)} = \left| \frac{|P_{e(i)}| - |P_{e(j)}|}{Max(p_{e(i)}, P_{e(j)})} \right| \leq 0.3 \qquad (4)$$

Where, i= 2, 3, 4….n & j= 1, 2, 3… (i-1)

Here, (Real Power)

$$P_{e(i)} = |V_i| * \sum_{k=1}^{n} |V_k|\,|Y_{ik}| \cos(\delta_{ik} - \theta_{ik})\,;$$

For, i=1,2,3…n

Where,
$n =$ Total number of machines.
$Y_{ik} =$ During fault bus admittance matrix.
$\delta_{ik} =$ Initial rotor angle (δ°_{ik})

3.1 Stepwise Procedure of This Modified Coherency Identification Method

Step-1; Machines are classified into study and external areas depending upon their power variation at the instant of initiating fault. The machines with power variation less than 30% are grouped together as external area machines. The external area machines are considered for coherency grouping test.
Step-2; Choosing a reference machine in the external area, all other machines in that area which satisfy Equation (1) are grouped together.
Step-3; For those machines, obtained from step-2, the elements of the inertia index β_{ij} are evaluated. Generators satisfying the inequality $\beta_{ij} \leq 0.5$ are tested further in step-4.
Step-4; The power variation index, PV_{ij} is evaluated for the machines carried over from step-3. If the inequality $PV_{ij} \leq 0.3$ is satisfied then the machines will from a coherent group.

4. CONSTRUCTION OF DYNAMIC EQUIVALENTS

The concept of dynamic equivalent in this paper is based on Kimbark's method [6]. Also the property of power invariance [4], [7] is included.

4.1 Mathematical Formulation

Formulas for construction of dynamic equivalents are given below:

$$E_e = \left(\sum_{i=1}^{m} (E_i^* I_i / I_e)^* \right) \qquad (5)$$

Where,

$$I_e = \sum_{i=1}^{m} I_i\,; \text{ vector sum of currents.}$$

E_e = The voltage of the equivalent machine. And m is the number of machines in the coherent group. The inertia constant (H_e), damping coefficient and mechanical power of the equivalent machine are obtained respectively as:

$$H_e = \sum_{i=1}^{m} H_i \qquad (6)$$

$$D_e = \sum_{i=1}^{m} D_i \qquad (7)$$

$$P_{me} = \sum_{i=1}^{m} P_{mi} \qquad (8)$$

The modified transient reactances are:

$$X'_{dei} = [(E_e - V_i)/(E_i - V_i)]\, X'_{di} \qquad (9)$$

5. RESULTS AND DISCUSSION

The modified coherency identification method was applied to a large multi-machine power system. More over construction of dynamic equivalents were done for the system. The one line diagram of the power system is given below.

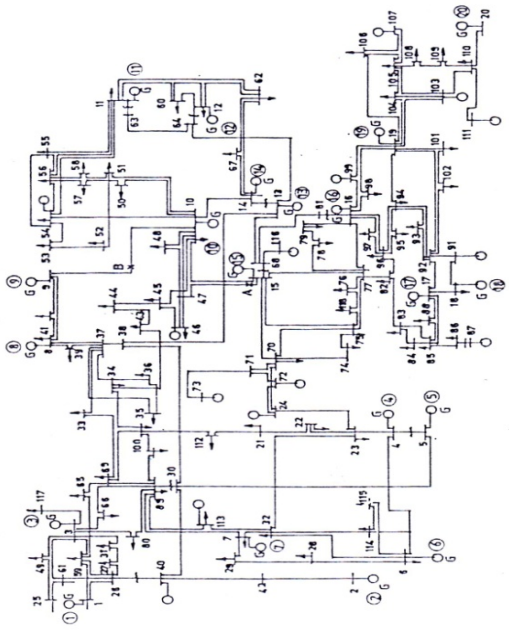

Fig: 1 Single line diagram of 20-M/C, 118-bus, IEEE test power system.

A 3-phase to ground fault was assumed to occur at bus-15 and the fault was cleared automatically at 0.1 sec. Power variation of generator 15 was more than 30% at the instant of initiating fault, so it was in study area and rest of the generators were in external area. Generator 20 was assumed as a reference. By using equations 1, 2 and 4 α , β and PV indices were evaluated. After satisfying the conditions of α , β and PV indices,

Coherent groups: Group I (gen 4 & 5); Group II (gen 6 &7); Group III (gen 8 & 9);

Group IV (gen 10, 11 &12); Group V (gen 13 & 14) were found (According to the modified method of coherency identification).

After solving the swing equations [8], [9], swing curves for both full and equivalent systems are given below:

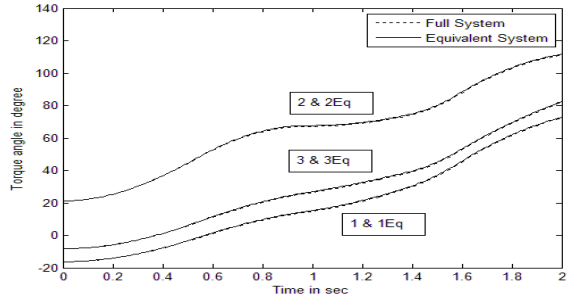

Fig: 2 Swing curves

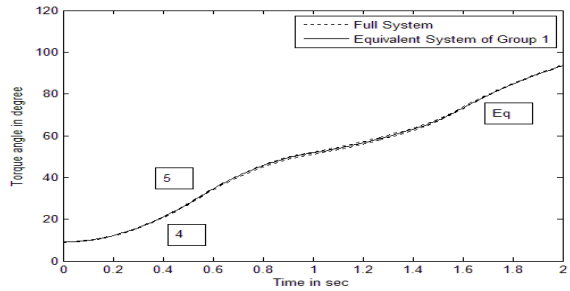

Fig: 3 Swing curves

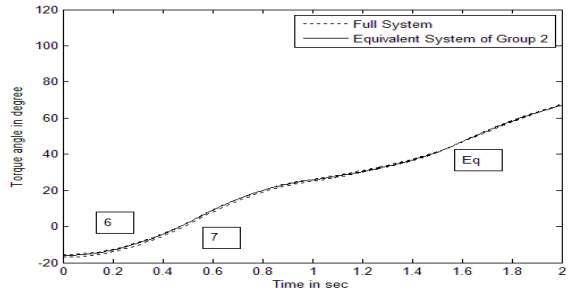

Fig: 4 Swing curves

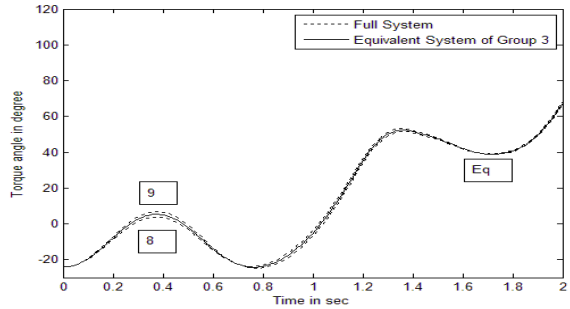

Fig: 5 Swing curves

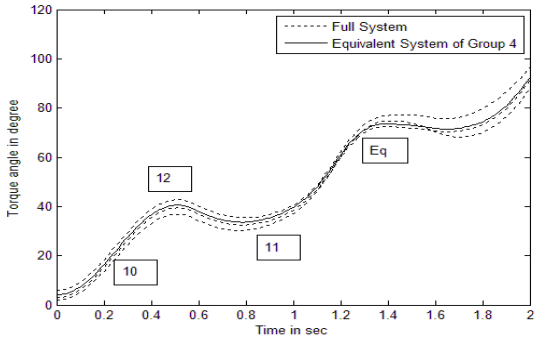

Fig: 6 Swing curves

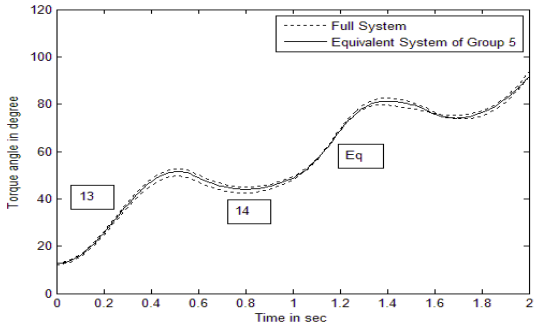

Fig: 7 Swing curves

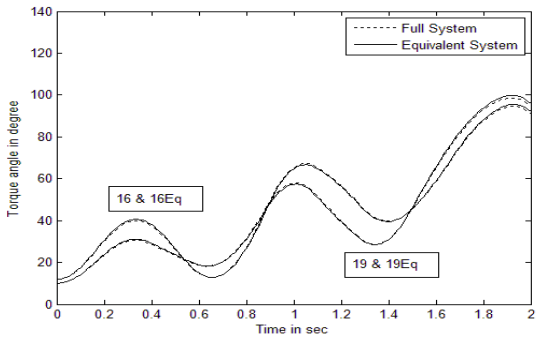

Fig: 8 Swing curves

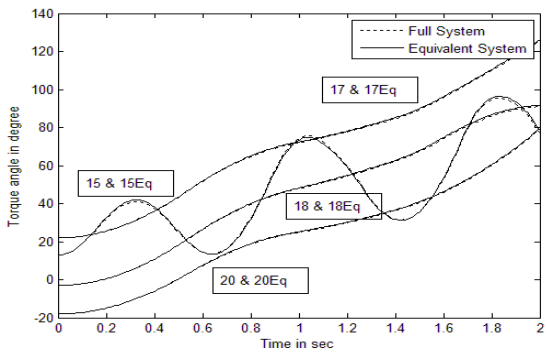

Fig: 9 Swing curves

6. CONCLUSIONS

This paper deployed the dynamic generators aggregation technique to perform transient stability analysis of 20-M/C, 118-bus IEEE test power system. The principle is based on a modified coherency identification technique, in which electrical proximity, inertia condition and power variation index at the instant of initiating fault are involved to define the degree of coupling between two or more generators. According to modified method the system is reduced from 20 machines to 14 machines. And the identified coherent groups are perfect, because from the swing curves it is clear that both full and equivalent systems are showing the similar characteristics.

REFERENCES

[1]. I.J. Nagrath, and D.P. Kothari, *"Modern Power System Analysis"*, 3rd Edition, New Delhi, Tata McGraw-Hill Publishing Company Limited, 2003.

[2]. H. You, V. Vittal, and Z. Yang, "Self-healing in power systems: An approach using islanding and rate of frequency decline based load shedding," *IEEE Trans. Power Syst.*, vol. 18, pp. 174–181, Feb. 2003.

[3]. S. T. Y. Lee and F.C. Schweppe, "Distance measures and Coherency Recognition for Transient Stability Equivalents", *IEEE Trans. Vol. PAS-82,*Sept./Oct., pp. 1550-1557, (1993).

[4]. V. G. Rau and M. Y. Hussian, *"Coherent Generators",* Allied Publishers Limited, New Delhi, (1998).

[5]. M. Y. Hussian and V.G Rau, "A New and Simple Method of Identifying Coherent Generators for Large Power System" 9th *International Conference on Electric Power Supply Industries,* Hongkong,1992,Vol.4,pp.193-202.

[6]. E. W. Kimbark, *"Power System Stability, vol.1: Synchronous Machine",* John Wiley & Sons (1948)

[7]. M. Y. Hussian and V. G. Rau, 'Coherency Identification and Construction of Dynamic Equivalent for large Power System', *Proceedings of 2nd Inter. Confr. on Advances in Power Sys. Control, Operation and Management*, Hongkong, Dec (1993).

[8]. W.D. Stevenson, *"Elements of Power System Analysis",* 3rd Edition, McGrawHill, 1975.

[9]. Website, *http://www.mathworks.com* [online]

Proceeding of the
International Conference on Electrical, Computer and Telecommunication Engineering
01- 02 December 2012 (ICECTE2012), RUET, Rajshahi-6204, Bangladesh

ICECTE2012: PI-0100

Electrical Power Profile Prediction by Using Rice Statistics in Bangladesh

Sabina Yasmin[1], M. A. Hossain[2], M. A. Humayun[3]

[1, 2]Department of Electrical & Electronic Engineering, Rajshahi University of Engineering & Technology
[3]CERE, School of Electrical Systems Engineering, University of Malaysia Perlis

[1]syasmin.ruet@gmail.com, [2]mahossain.eee@gmail.com, [3]humayun041024@gmail.com

ABSTRACT
IN DEVELOPING COUNTRY LIKE BANGLADESH, THE DEMAND OF ELECTRICAL POWER IS VERY HIGHER THAN THE AVAILABLE PRODUCTION. BANGLADESH IS AN AGRICULTURE BASED COUNTRY AND THE PRODUCTION OF RICE IS INCREASING IN TREMENDOUS AMOUND IN THE LAST DECADE. RICE HUSK BASED POWER PLANT IS ALREADY INSTALLED IN INDIA, INDONESIA, SOUTH KOREA. HOWOVER THERE ARE SOME LOCATIONS IN WHICH RICE HUSK BASED POWER STATION PROJECTS COULD BE FEASIBLE IN BANGLADESH. BY ANALYZING THE PREVIOUSLY COLLECTED DATA ON THE SELECTED LOCATIONS, THIS WORK HAS BEEN CARRIED OUT TO PREDICT IF THESE RESOURCES ARE SUFFICIENT FOR RICE HUSK POWER, IN THE HOPE TO EXTRACT ELECTRICAL POWER.

KEYWORDS: Rice Husk, Rice Clusters, Parboiling, Plants, Bangladesh**.**

1. INTRODUCTION

Bangladesh is situated between 20.30 - 26.38 degrees north latitude and 88.04 - 92.44 degrees east latitude. Placed between the Bay of Bengal and the Himalayas, Bangladesh is a South Asian country with a land area of 144,000 sq. kms. populated by around 150 million people. During summer, the rural areas face a severe load shedding. Three quarters of Bangladesh population live in the rural areas. Development of rural areas as well as expanding rural electrification is the key to the prosperity. The country's main endowments are fertile agricultural land, vast human resources, relatively abundant water, and natural gas. The agricultural land here is devoted mainly to rice and jute cultivation, although wheat and maize production has increased in recent years. Electricity and natural gas are the major sources of power in Bangladesh. Biomass is by far the dominant energy source in Bangladesh [1]. Approximate land use for agriculture is 54.5%, while the forest covers 17.6% of total land area of the country. About 46% of traditional biomass energy is supplied from agricultural residues such as rice straw and rice husk from rice plants, bagasse from sugarcane and jute stick [2]. Rice straw and rice bran are used as feed for cattle, poultry, fish etc. where the rice husk is used as energy. Husk Power Systems (HPS) lighted the first village from its first 100% biomass based power plant that uses discarded rice husks to generate electricity in August 2007. On an average, each power plant serves about 400 households and replaces approximately 42,000 litres of kerosene and 18,000 litres of diesel per year. The rice husk is one of the agriculture-based fuel materials in the world that can be feasibly collectible. Rice husk is a by-product of major food crop rice. The husk is the coating for the seeds of the rice plant. The husk is mostly indigestible to human being.

Rice husk have the following properties: Dimension is approximately 6 to 10 mm x 3 to 4 mm; Bulk density is around 100-120 kg/m3; Moisture content is approximately 10-14%; Net calorific value is approximately 14 MJ/kg. The chemical components of rice husk are cellulose (44.83%), hemicelluloses (35.3%), and lignin (19.87%). The lower heating value of rice husk is considered fairly as 14 MJ/kg, where the higher heating value of rice husk is considered fairly as 19 MJ/kg. Rice milling industry generates a lot of rice husk during milling of paddy which comes from the fields. This rice husk is mostly used as a fuel in the boilers for processing of paddy.

2. BACKGROUND AND MOTIVATION

As of 2011, Husk Power Systems provides power approximately 25,000 households in more than 250 villages serves 150,000 people through its 60 mini-power plants systems that each generate 35 to 100 kilowatts of power in villages in India's states of Bihar, Tamil Nadu and West Bengal, providing up to eight hours of power, primarily during the evening hours when illumination is needed [3] [4].

In global context, annual rice husk production is 137 million tonnes whereas, in Bangladesh, about 9.0 million tonnes of rice husk is produced. Figure 1 shows the top ten rice husk producing country in the world in 2007 [6]. Figure 2 shows the projection of future rice production in Bangladesh. Over last 30 years, there has been an increasing trend of rice husk energy production [5].

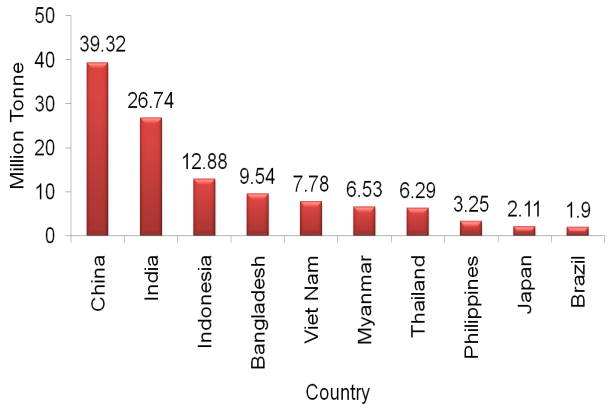

Fig. 1: Top ten rice husk producing country in 2007

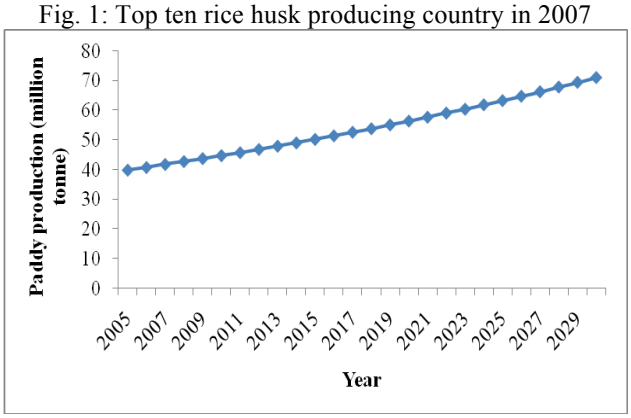

Fig. 2: Projection of future rice production in Bangladesh

The production of rice is projected using the growth of 2.35%. The growth is calculated from the average growth of rice production data from 1971 to 2009.

3. METHODOLOGY

There are main two sectors of rice process such as household level process and processed in rice mills. Husk obtained from household level process cannot be collected due to its wide spread localization. Therefore, husk from household level process is not considered as supply source of husk for electricity generation. Paddy processed in rice mill is considered the source of husk supply. There are several rice processing zones in the country. Major rice processing zones or 'cluster' areas are distinguished as - (i) Dinajpur (North Bengal) (ii) Sherpur (near Bogra) (iii) Ishawardi (Pabna) (iv) Naogaon and (v) Kaliakoir (near Dhaka), where most of the rice mills are located in close proximity to each other. To conduct the investigation three rice processing zones were selected to estimate potential husk available for electricity generation. The selected rice clusters are located at Naogaon, Bogra, and Ishawrdi. A survey questionnaire was used to collect the information on monthly quantity of paddy processed, amount of husk produced, amount of husk consumed for rice processing purposes and the surplus amount of rice husk. Another study is conducted to estimate the total electricity generation from rice husk in Bangladesh. LEAP (Long-range Energy Alternative Planning System) tool is used to make three different scenarios for consumption of energy.

4. RICE HUSK CLUSTERS IN BANGLADESH

About 4 – 4.5 million metric tons (MT) of paddy is annually produced in the Bangladesh [2]. A 20% yield of input paddy leads to a production of 8 - 9,000,000 metric tons rice husk annually. There are over one hundred thousand rice mills located in a scattered manner all over the country with four 'cluster' areas according to the Rice Mill Owners' Association of Bangladesh. Over ninety percent of these rice mills are reported to be in smaller capacity ranges, i.e. < 20 – 25 MT/day of paddy processing capacity. The number of lower-midsized rice mills (with paddy processing capacity range : > 25 - 50 MT/day) are reported to be about 490 and that of mid to large sized rice mills (30- 120 MT/day) are about 50 units. IDCOL already financed two such projects in Kapasia, near Dhaka and recently one in Thakurgaon sadar, Thakurgaon. Hence, based on preliminary surveys by Bangladesh Rice Research Institute, BRRI and information from Rice Mill Owners' Association, typically at least over 500 rice mills are located in these cluster areas [2]. Taking an average (lower-mid) capacity range of about 100-200 kW, there is a 50-100 MW power market in these cluster areas. Areas like Dinajpur, Sherpur etc. are having intermittent power supply which often leads to less production for these rice mills and also other energy craving small enterprises and local dwellers are potential consumers for future rice husk based biomass power plant. Figure 3 shows rice husk clusters in Bangladesh [2] [7].

Fig. 3: Rice husk clusters in Bangladesh (Red Stars)

5. ASSUMPTIONS AND MODEL

Bangladesh has reportedly over one hundred thousand Rice Mills - large, medium and small. They process paddy, using mostly the parboiling practice. The rice mills use the thermal energy of steam generated in boilers, which are fired by rice husk - a by-product's of paddy processing in the rice mills and which is globally well-known as very convenient source of dry biomass energy of reasonable heat value. With a few exceptions, presently most of the 'boilers', used in these rice mills of Bangladesh are very inefficient. This results in a huge wastage of rice husk, which is an important source of biomass. Preliminary estimates are indicative that at least 50% of the rice husk produced could be saved and made surplus for its better use as input for small power generation. Figure 4 shows the improved rice parboiling boiler which consumes less rice husk to boil each tonne of paddy. Rice husk consumption can be reduced by using improved parboiling boiler.

Fig.4: Improved rice parboiling boiler

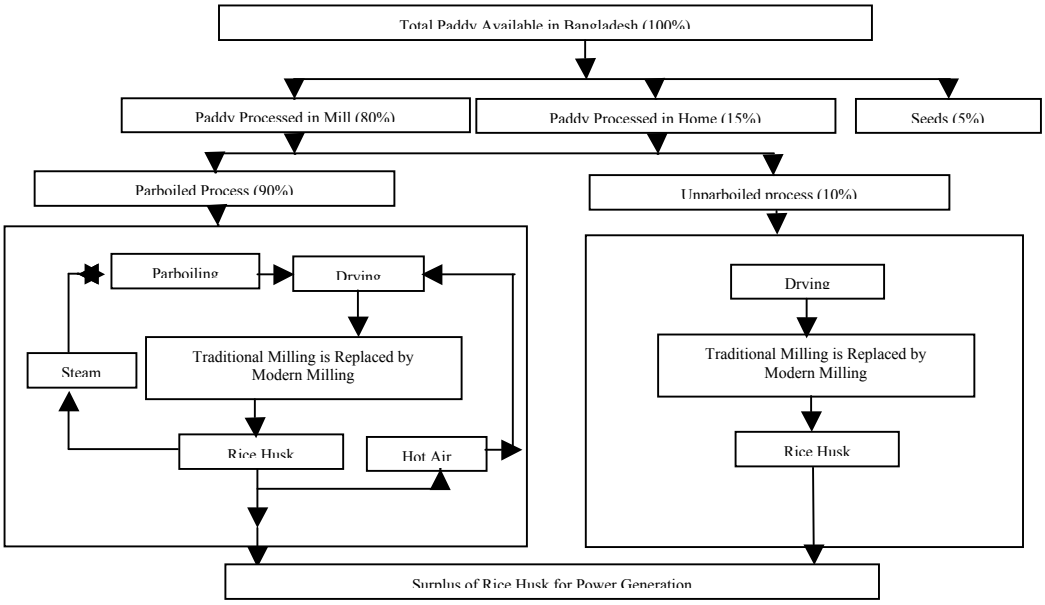

Fig. 5: Schematic of Rice Husk Collection for Power Generation

Figure 5 shows the simple schematic of Rice Husk Collection for power generation.At present all boilers used are traditional type. In scenario-1, it is assumed that 95% of traditional boiler is to be replaced by improved boiler to reduce the husk consumption for parboiled process. In scenario-2, coverage of parboiled process is reduced to 50% from 90% (reference scenario). The husk consumption is reduced to 4.55 million tonnes (Scenario-1) and 3.20 million tonne (Scenario-2) from 6.48 million tonnes (reference).

TABLE I: Utilization of Rice Husk

Paddy Activity level	Reference scenario	Scenario 1	Scenario 2
Processed in mill	70%	90%	90%
Parboiled processed	90%	90%	50%
Unparboiled processed	10%	10%	50%
Traditional parboiling	100%	5%	5%
Improved parboiling	0	95%	95%

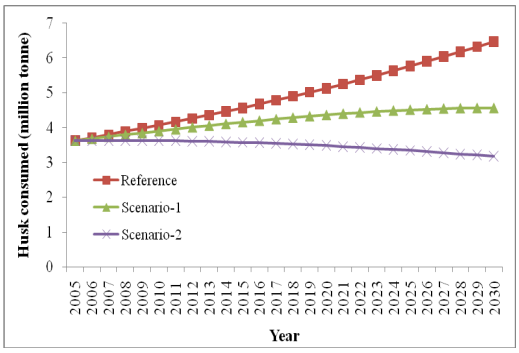

Fig. 6: Rice husk consumption scenarios

Utilization of rice husk is shown in Table I. Rice husk consumption can be reduced by some assumptions. Figure 6 shows the rice husk consumption scenarios. In scenario – I husk consumptions is less than reference, where husk consumption is very low in scenario – II. The surplus amount of husk is calculated deducting the consumed amount of husk from total potential of husk. There is a huge potential to save rice husk by changing the technology for parboiling. Surplus of rice husk can be collected to generate power.

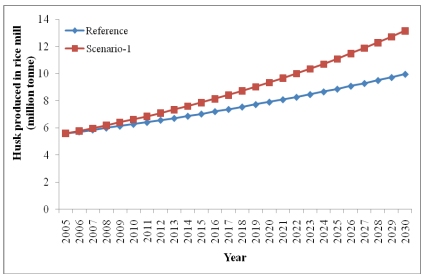

Fig. 7: Husk production in rice mill

Husk produced in rice mill could be increased by increasing the amount of processed paddy in mill. As a result the husk production is increased from 9.96 million tonnes (reference scenario) to 13.16 million tonnes.

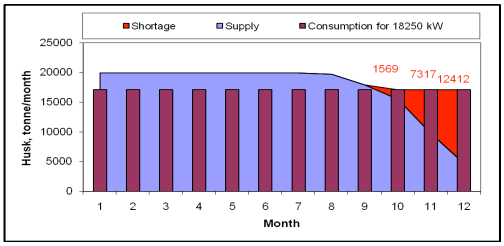

Fig. 8: Potential for steam turbine technology at Naogaon

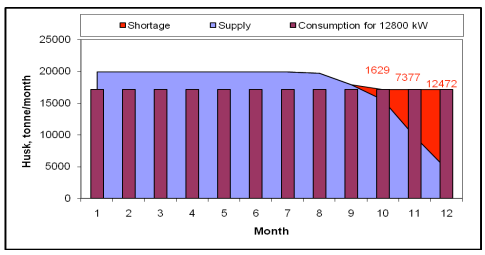

Fig. 9: Potential for gasification technology at Naogaon

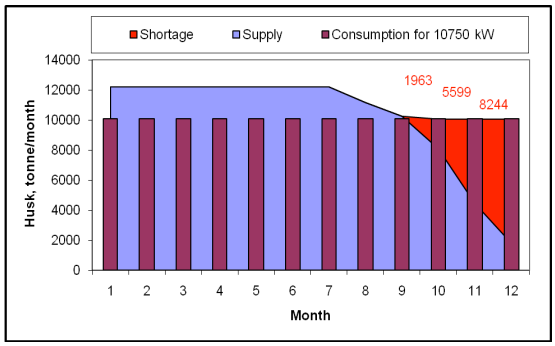

Fig. 10: Potential for steam turbine technology at Ishurdi

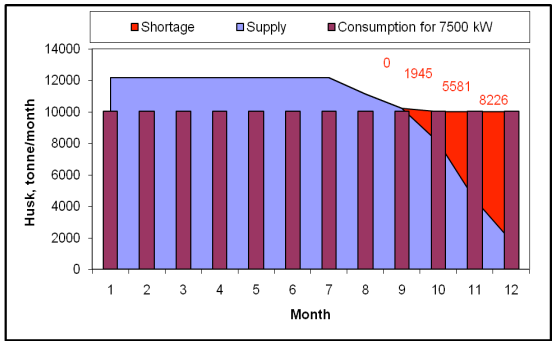

Fig. 11: Potential for gasification technology at Ishurdi

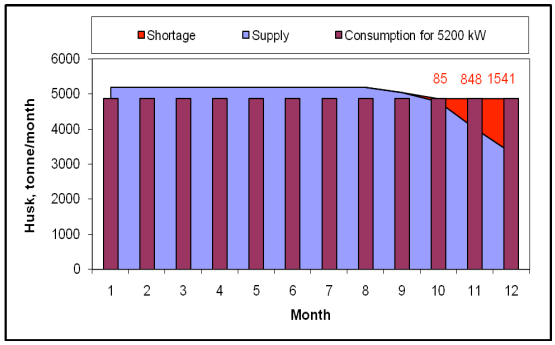

Fig. 12: Potential for steam turbine technology at Bogra

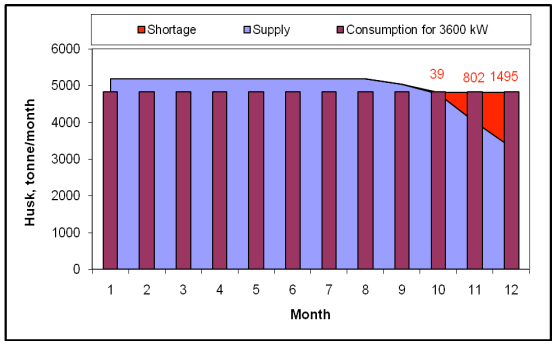

Fig. 13: Potential for gasification technology at Bogra

6. Conclusions

The study results conclude that there is a potential to produce electricity from rice husk based on the available surplus husk after their own consumption in selected rice processing zones in Bangladesh. Power generated from rice husk is sufficient to meet the power needed for rice processing purposes. The selected rice clusters, Naogaon has better potential than Ishawrdi and Bogra. Before launching a husk based power generation technology, it is important to know the production and distribution of available rice husk resource at different location. Another important issue is the sustainable supply of rice husk in future for husk based power generation plant. The technological improvement is going on; however, there are some constraints for dissemination of the new technologies. The policy makers, technologists, extension personnel of government and non government organization need to give an urgent thrust for enhancing the dissemination of new renewable energy technologies among the stakeholders.

7. Future Work

More detailed study can be done by collecting data from other rice clusters zone such as Dinajpur, Sherpur, Gazipur. Generated rice husk ash (RHA) can be analyzed or tested for a wide variety of applications like: green concrete, high performance concrete, refractory, ceramic glaze, insulator, roofing shingles, and bio fertilizers industries.

References

[1] M. Ahiduzzaman. “Rice Husk Energy Technologies in Bangladesh” Agricultural Engineering International: the CIGR Ejournal. Invited Overview No. 1. Vol. IX. January, 2007.

[2] Arif Md. Waliullah Bhuiyan, Md. Rejwanur Rashid Mojumdar and A K M Kamrul Hasan, “An Improved Method to Generate Electricity and Precipitated Silica from Rice Husk: Perspective Bangladesh”, International Journal of Environmental Science and Development, Vol. 2, No. 4, August 2011.

[3] Nerenberg, Jenara."Husk Power Systems Wants to Lead 'a Revolution in Electricity'", Fast Company (magazine), January 5, 2011. Retrieved January 12, 2011.

[4] (2012) The Husk Power System website. [Online]. Available: http://www.huskpowersystem.com

[5] BBS (2008): Statistical Year Book of Bangladesh. Bangladesh Bureau of Statistics. Planning Division, Ministry of Planning, published in December 2008.

[6] (2010) The IRRI website. [Online]. Available: http:// www.irri.org

[7] Dasgupta, N., Baqui, M. A., Dhingra S., Raman, P., Ahiduzzaman, M. And Kishore, V.V. N., Benefits of Improved Rice Husk Combustion, Bangladesh. NRI report no. 2764. p. 8, 21, 67, 2003

Proceeding of the
International Conference on Electrical, Computer and Telecommunication Engineering
01- 02 December 2012 (ICECTE2012), RUET, Rajshahi-6204, Bangladesh

ICECTE2012: PI-0101

Evaluating Currents at Different Portion of a Tower (60m) Model and Analysing Surge Impedance

Fida Hasan Md Rafi[1], Mashrur Washid Nabil[1], Nazmush Shahid[1], Abu Farzan Mitul[1]
Department of Electrical & Electronic Engineering, Khulna University of Engineering & Technology
fidaeee@yahoo.com,nabil_2k7@yahoo.com , nstamalmail@yahoo.com, mitulnaya@yahoo.com

ABSTRACT
Knowledge about surge impedance & currents in different parts of a tower during lightning is very important for the design purpose of protective devices. the operating time of these devices must be designed accurately in order to avoid damages in the transmission system. for this purpose we have designed a voltage source with step waveform to represent the lightning and 60 m tall metal structure to represent a transmission tower in network simulator nec-2.simulation using nec-2 shows currents in different parts of the tower. Utilizing the results from these analyses is useful for designing protection schemes against surges on transmission tower.

KEY WORDS: Surge Impedance, NEC-2, tower height, reliability, MOM.

1. INTRODUCTION

Surge impedance can be expressed by the ratio of instantaneous values at the top voltage to the current into the vertical conductor at the moment of voltage peak. The knowledge of this surge impedance is extremely important in order to know the transient current and voltage in a circuit. It gives the idea about the amount of voltage and current far away from the point of fault. The oscillating voltage produced would be dangerously high if the value is larger than predefined limit and would cause severe outages in the transmission lines. Conventionally circuit theory is used for this kind of analysis of transmission system tower model but for tall structures & three dimensional structures this theory will not be applicable. There are many others simulation tools available like the EMTP, VSTL, FDTD, NEC-2 and NEC-4. We have used NEC-2 in our analysis as it gives more accurate results especially for analysing a tall geometrical structure. Due to unavailability of student version of NEC-4, we had to analyse using NEC-2.However, the NEC-2 uses the method of moment (MOM) for analysis which is more accurate than other simulation tools. There are many formulas available for surge impedance analysis but we have used empirical formula of Hara et al for surge impedance analysing which is shown in **Eq. (1).**

$$Z= 60 \{\ln ((2h\sqrt{2}) /r0) - 2\}\Omega \qquad \text{Eq. (1)}$$

There is another popular formula as shown in **Eq. (2).**

$$Z= 60 \{\ln ((2h\sqrt{2})/ r0) - 1.54\}\Omega \qquad \text{Eq. (2)}$$

Previously some used a tall structure resembling a practical tower and considering some buried wire in the footings of the tower [2]. But this type of simulation can be done with NEC-4 only which is not available for student version as said before. Some authors simulated using magnitude data in frequency domain only [3]. Authors in [5] used the PSCAD/EMTDC for their simulation. They used different models for grounding impedance for the analysis of surge which resulted complexity in the analysis. Using NEC-2 60 cm geometry was analysed [6].They investigated surge with and without ground plane for both vertical and horizontal conductor. Authors in [7] were concerned about the antenna rather than transmission tower using NEC-2. Some measured the voltage at different parts of the tower and analysed in time domain [8].

Comparing previous works, our designed model and method of analysis is more useful for lightning engineering. Our model consist 60m tall transmission tower and analysing this kind of tall tower is quite troublesome and inaccurate. But our experimental results are quite reliable and resemble the theoretical result even though there were some limitations regarding tower height in NEC-2 simulator. Covering maximum limitations of previous, our designed model shows reliable analysis result for surge impedance in transmission tower.

2. SURGE IMPEDANCE BY NEC-2

Using NEC-2 the transmission tower model was designed consisting wire elements in the geometry structure for approximate accurate

analysis. These elements were divided into segments. The number of segment into which the elements is divided depends upon the wavelength. If ΔL is denoted as the segment length & λ as wavelength then the segment length should be between $0.001\ \lambda < \Delta L < 0.1\lambda$ [10]. Moreover, the length of the wire i.e. the coordinates of its ends, its radius, number of segment, frequency range, input data etc. were precisely given as input in order to get accurate results. The output results were in frequency domain which was converted into time domain using by fft and ifft command in MATLAB. Excitation was imposed as a voltage source or a plane wave on one of the tower segment. The internal impedance of the pulse generator was taken as 500Ω [8]. The MOM is usually used to determine the current on every segment due to the source and all the other currents by numerically solving the electric field integral equation. To evaluate the conductor top voltage the waveform of the current flowing through the resistor was calculated. The ground was considered as perfectly conducting grounds. After considering all these factors, we measured the surge impedance which is the ratio of instantaneous values of the top voltage to the current into the vertical conductor at the moment of peak voltage [8]. Fig.1 shows the working flowchart of the solution by NEC-2.

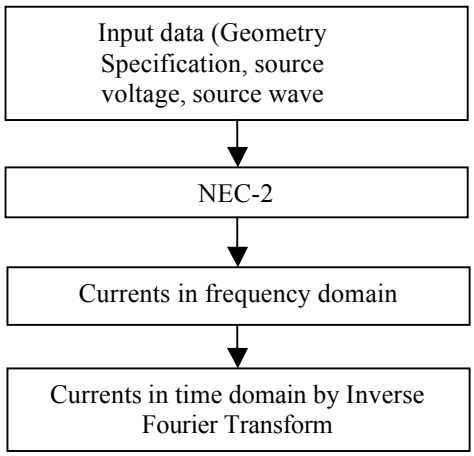

Fig.1 Flow chart for the simulation of the designed model.

3. SIMULATION MODEL AND GEOMETRY DESCRIPTION

The modeling of the structure is very important.
As we have said, the tower of height is 60 meter and it has crossings above also. This complex arrangement was designed to make the model more realistic and reliable. The tower consists four foots and the distance between them is 1 meter.

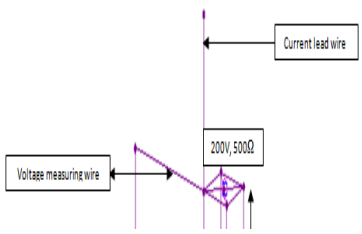

Fig.2 Simulation model.

There is a vertical conductor above the tower model which acts as a current lead wire to inject the wave into the tower. There is also a horizontally arranged conductor with the model. It is connected to the ground and works as the voltage measuring wire.

4. SIMULATION RESULTS

The influence of the reflected wave from the ground reaches the top of the conductor in $t = (2h/c) \approx 0.4\ \mu s$ [8] which means the travelling wave is propagating at the velocity of light.
We have also measured the voltage of the conductor top by voltage measuring wire which is shown in Fig. 3. From the graph we can see that the voltage rise time is near about 0.08 µs and wave reflected from the ground at 0.4 µs.
From Fig. 2 we have further measured the current from different heights i.e. at top, middle and bottom of the tower model.
From Fig. 3, we can see that at the top of the tower model current goes to flat after rising at 0.08 µs and stays flat till wave is reflected from the ground.

Fig. 3 Propagating currents observed at different heights from the tower model.

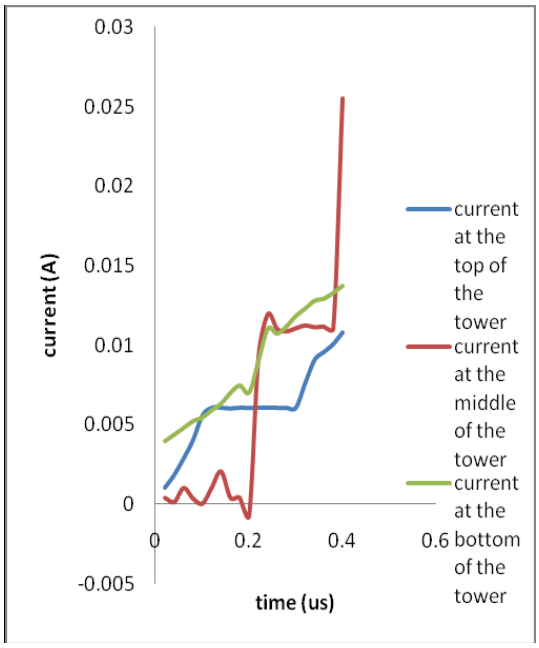

5. COMPARISON BETWEEN THEORETICAL AND SIMULATION RESULT

From the graphical representation we can see that at 0.4 µs the magnitude of the surge impedance is 607Ω which was recorded for comparison purpose. Using **Eq. (1)** the surge impedance is calculated.

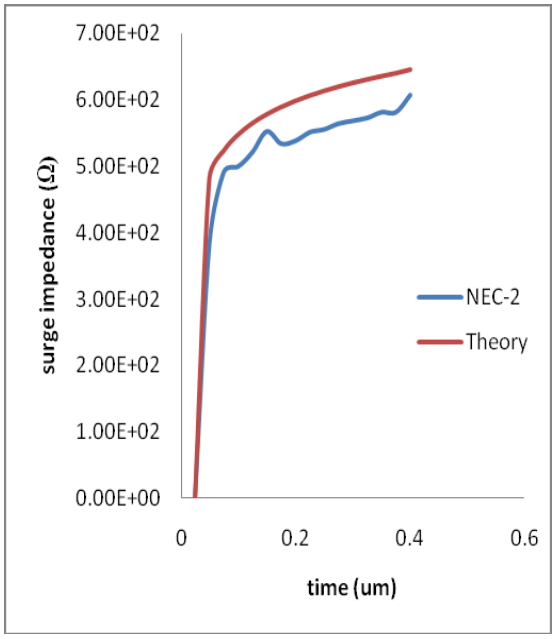

Fig. 4 Theoretical value and simulated result of NEC-2 for surge impedance.

From Fig. 4, we can see that our simulated result by NEC-2 nearly agrees with the theoretical value calculated using Hara et al theory. Although at 0.4us time there is slight disagreement in the results by 5.74%.

Table 1. Surge Impedance values

Determination Process	Impedance
Calculated	644 Ω
NEC-2	607 Ω

6. SIMULATION FOR REDUCED SCALE

If the height of the geometrical model is 0.6cm instead of 60m then the curve of current at different point of the model would be as shown in Fig. 5.

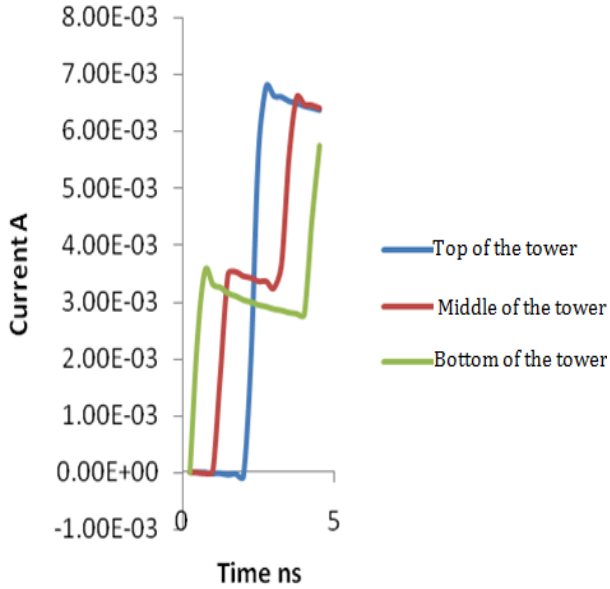

Fig. 5 Currents at Different Position of a Reduced Scale Model.

From this analysis we can see that the shape of the current waveform is the same weather we take a large tower or a small tower. But the only difference is the re striking time. For tall towers, it take more time for the re-strike phenomena to occur which is quite logical and important for practical tower designing.

From the Fig. 6 below, we can see there are similarity between conventional tall tower model and reduced scale model. Previous many authors found that reduced scale gives a sharper curve which makes it possible to take decisions practically. As the larger scale & reduced scale results show similarity, we can say our designed model is quite realistic and can be implemented for practical purpose.

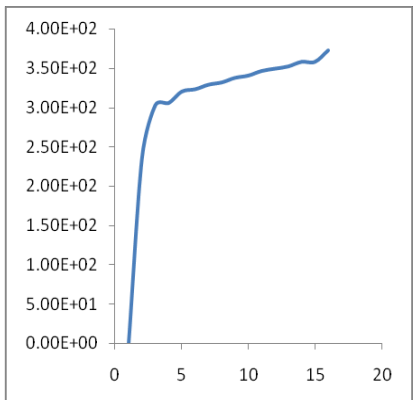

Fig. 6 Impedance Curve for Reduced Scale.

7. CONCLUSION

In our work we have used a 60 meter tall tower model which is very much similar to a practical implemented transmission tower in power systems. The results we have obtained also resembles with the results obtained from different appreciated theories. Therefore our designed method of surge impedance analysis using NEC-2 can be employed in practical surge analysis in power system. This way we can protect our valuable protective schemes of the power stations from unwanted damages occurred from surges.

8. FUTURE WORK

We can see from our model there is no transmission line in it as we have concentrated mainly on the tower rather than the line. However in future we will analyse this model considering the transmission line for more realistic implementation.

9. ACKNOWLEDGEMENT

Special thanks to Md. Salauddin Yusuf for his constant guidance throughout our work.

REFERENCES

[1] P. Kirawanich, N. E. Islam,"An Electromagnetic Topology Approach: Crosstalk Characterization of the Unshielded Twisted-Pair Cable", *Progress In Electromagnetics Research, PIER 58,* pp 285–299, 2006.

[2] E. Petrache, W.A. Chisholm, A. Phillips,"Evaluating the Transient Impedance of Transmission Line Towers",*IX International Symposium on Lightning Protection,November ,* Foz do Iguaçu, Brazil, 2007.

[3] U. Kumar, P. K. Nayak, "Investigations on Voltages and Currents in Lightning Protection Schemes Involving Single Tower", *IEEE Transactions on Electromagnetic Compatibility*, vol. 47, no. 3, August, 2005.

[4] J.B. Aizenberg, Prof. Dr.Vnisi, Korobko A.A., Dr. Npsp "Svetoservice", "Principal New Hollow Light Guide system "Heliobus" for Daylighting and Artificial Lighting of Central Zones of Multi Storey Buildings", Russia.

[5] G. Radhika, Dr. M. Surya kalavathi, "Lightning Surge Analysis on Grounding Models of a Transmission Lines", *Journal of Theoretical and Applied Information Technology*, pp 87-93, 2009.

[6] Md. S. U. Yusuf, M.F. Hossain, M.O. Goni,"Electromagnetic Simulation of a Lightning Surge on a Vertical Conductor Model",*3rd International Conference on Electrical & Computer Engineering*, pp 163-166,December, 2004, Dhaka, Bangladesh.

[7] A. M. N. A. Mobin, M. H. Rahman, M. N. A. Rahim, M. O. Goni, "Design of Antennas Using MoM for the Wireless Applications", *International Journal of Wireless Communication and Information Systems (IJWCIS),* vol 1, no 1, pp 34-41, April, 2011.

[8] M. Ishii, Y. Baba, "Advanced Computational Methods in Lightning Performance the Numerical Electromagnetics Code (NEC-2)", *IEEE Power Engineering Society Winter Meeting*, pp 2419 – 2424, vol.4, 2000.

[9] V.K. Mehta, R. Mehta, S. Chand, "Principles of Power System", 4th revised edition book, 2009.

[10] J. L. Smith, "Basic NEC".

[11] Lightning Center, "Myths and Facts About Lightning",http://myweathercontent.myweather.net/webhd/pkg/v2/template1.html?host=keyc&section=9&page=36&story=317, 2010.

Proceeding of the
International Conference on Electrical, Computer and Telecommunication Engineering
01- 02 December 2012 (ICECTE2012), RUET, Rajshahi-6204, Bangladesh

ICECTE2012: PI-0102

Potentials of Biomass Gasification & Power Generation in Bangladesh

T.Mondal[1], *M. S. Islam* [2].
[1]Officer, Engineering Department (RENATA Limited).
[2]Department of Electrical & Electronic Engineering, Rajshahi University of Engineering & Technology (RUET), Rajshahi-6204, Bangladesh.
E-mail: tonueee2007ruet@gmail.com, siruet@gmail.com

ABSTRACT
Electricity generation by biomass gasification can solve the problems of our day-to-day life at a great extent. Even it also serves the purpose of rural electrification which is the crying need of Bangladesh. Besides producing electricity it is beneficial to the agricultural and industrial production. Some small enterprises trying to ensure energy security at countryside using biomass gasification by rice husk. This paper includes availability, proper selection and quality of biomass trough-out the country and utilization of by-product released by the plant. A case study showing how power generation using only rice husk as fuel is also discussed. In addition it includes how ash generated from the husk is processed to produce silica and calcium carbonate through silica precipitation method in order to minimize the production cost.

KEY WORDS: Biomass gasification, Electricity generation by rice husk, Product utilization, Silica precipitation.

1. INTRODUCTION

Energy is the basic necessity for the development of a country and electrical energy is superior to all other forms of energy. The modern society is so much dependent upon the use of electrical energy that it has become a part and parcel of our life. In fact the advancement of a country is measured in terms of per capita consumption of electrical energy. Bangladesh is one of the most densely populated countries with about 80% of the population living in rural areas. However, only about 38% of its total population has access to the electricity. Without the development of rural electrification it is impossible to fulfill Bangladesh Governments vision of ensuring access to affordable and reliable electricity for all by 2020. The main energy sources of Bangladesh are biomass and natural gas. Where biomass energy is about 70% of the total energy consumption in Bangladesh [1].In rural areas normally direct combustion is the most common method of biomass utilization. Because of its poor efficiency and limited supply alternative techniques of resource utilization can meet the energy demand in this case.

South and Southeast Asia account for over 90% of the world's rice production [2].Rice husk is a major by-product of the rice-milling industries and is abundantly available. However, rice husks have been considered a waste, causing disposal problems. Like most other biomass materials, rice husk contains a high amount of organic volatiles. Thus, rice husk is recognized as a potential source of energy. Moreover, its 20 wt. % ash content comprising of over 95% amorphous silica makes a rice husk utilization system economically and environmentally attractive.

Gasification of biomass has been known as one of the effective technology options for the utilization of this renewable energy resource. Many interesting investigations concern the subject of biomass gasification from the points of view of fuel used, gasifier type, kinetic, and product specifications and uses. Other neighboring Asian countries especially India and China have already undertaken gasification programs on large scale. On the other hand, only a demonstration biomass gasification of 200 kW based on rice husk is being set up by Local Government Engineering Department (LGED) at Dinajpur. The first commercial rice husk based power plant is established by a private entrepreneur in Kapasia, near Dhaka, with financial assistance from Infrastructure Development Company Limited (IDCOL).

2. BIOMASS GASIFICATION BASICS

Biomass gasification is the process of converting solid fuels into a combustible gas mixture. This is achieved by reacting the material at high temperatures (>700 °C), without combustion, with a controlled amount of oxygen and/or steam. The resulting gas mixture is called syngas or producer gas and is itself a fuel. The power derived from gasification of biomass and combustion of the resultant gas is considered to be a source of renewable energy. The calorific value of this gas varies between 4.0 and 6.0 MJ/Nm3 or about 10 to 15percent of the heating value of natural gas [3]

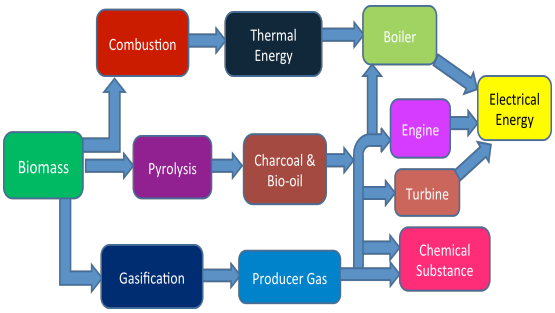

Figure-2.1: Biomass conversion into energy [4]

Biomass can be converted into electrical energy by 3 ways as: combustion, pyrolysis and gasification.

- Gasification process starts as auto thermal heating of the reaction mixture.
- Then in the second stage, combustion gases are pyrolyzed by being passed through a bed of fuel at high temperature.
- Initial products of combustion, carbon dioxide (CO_2) and (H_20) are reconverted by reduction reaction to carbon monoxide (CO), hydrogen (H_2) and methane (CH_4).

.

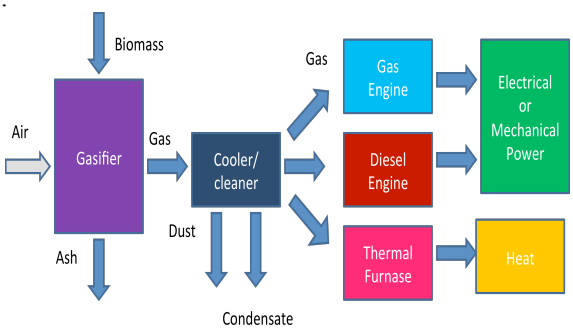

Figure-2.2: A flow diagram of BGT

3. AVAILABILITY AND USE OF BIOMASS IN BANGLADESH

Bangladesh is an agriculture-based country and the available biomass is mainly of agricultural residues like rice husk & rice straw from rice plants, Baggasse from sugarcane, Jute stick, residues from Wheat, potato, oilseeds, spices etc. In addition to the agricultural wastes the other sources are dry materials such as dry wood, dried leaf, charcoal, coconut shells etc.

Over last 30 years, there has been an increasing trend of biomass fuel supply in Bangladesh. The total supply of biomass fuel was 236.08 PJ in 1980 and has increased over next 20 years to 356.66 PJ. Traditional fuel supply usually comes from main three sources viz. crop residues, animal dung and trees [5].

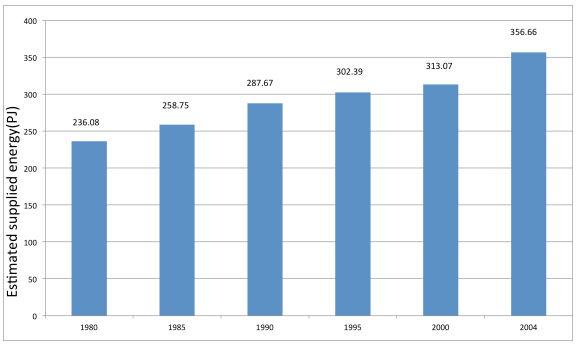

Figure-3.1: Trends of traditional fuel supplied during 1980 to 2004

The percentages of different traditional energy were as follows: cow-dung 20.4%, jute stick 7.5%, rice straw 11.6%,rice husk 23.3%, bagasse 3.2%, fire wood 10.4%, twigs and leaves 12.5% and other wastes 11.1%. Rice husk contributes biggest share of biomass energy and it was 83.04 PJ in 2003-2004. Energy production from rice husk is steadily increasing. In 1991, the production of rice husk energy was 76.35 PJ and it increased to 106.1 PJ in 2004 (Figure 3.2) [5].

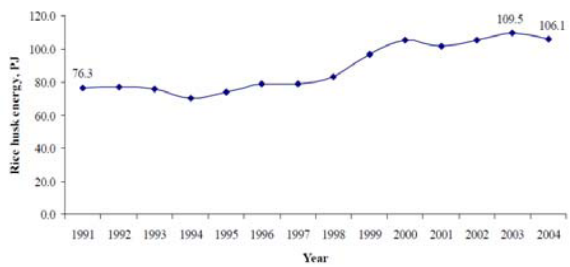

Figure-3.2: Trends of traditional fuel supplied during 1980 to 2004[5]

4. BIOMASS CHARACTERISTICS

Gasification technology requires some important biomass characteristics the moisture content of biomass should be as low as possible. No of volatile matter content, ash content and composition must be considerably low. Morphology and bulk density should be constant.

Figure-4.1: Rice husks & wood chips

5. ELECTRICITY GENERATION BY RICE HUSK GASIFICATION

Several types of gasifiers e.g. fixed-bed updraft and downdraft gasifier, fluidized bed gasifier and bubbling bed gasifier are available in the existing market with different sets of pros and cons. However, the downdraft gasifier is a comparatively cheap and the gasification in this type of gasifier can produce a product gas with very low tar content [4]. Keeping the process in mind, fixed-bed downdraft gasifier is thus recommended for small-scale rice husk biomass plant. Here, biomass fuel is fed at the top of the reactor/gasifier. The fuel then slowly moves down and during this time, the fuel reacts with air, which is supplied by the suction of a blower or an engine and is converted into combustible producer gas in a complex series of oxidation, reduction, and pyrolysis reactions [3].Generated ash is then removed from the bottom of the reactor for silica production.

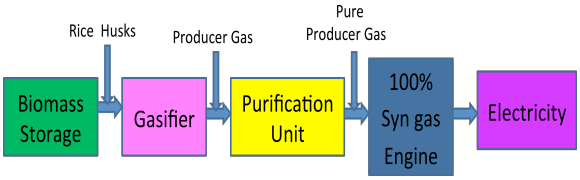

Figure-5.1: Electricity generation by rice husk gasification

6. PROGRESS OF TECHNOLOGY INCLUDING A CASE STUDY

Over the years a considerable number of gasification systems for demonstration purposes have been financed worldwide. A large diversity of fuels and equipment was experimented with.

A decade of experience with modern biomass technologies for thermal, motive power and electricity generation applications exists in India. Over 1600 gasifier systems, having 16 MW total capacity, have generated 42 million Kilo Watt hour (KWh) of electricity, replacing 8.8 million liters of oil annually (CMIE, 1996) [6]. Like India in China 150 set of gasifier used for generating electricity,160 set for cooking & 370 set for drying woods.

The only gasification plant in our country namely "Dreams Power Limited" located in gaspur in kapasia, Gazipur. IDCOL provided concessionary loans and grants to Dreams Power Private Limited (DPPL), the Project Sponsor, for setting up the plant. Ankur Scientific Energy Technologies Pvt. Ltd, India is the equipment supplier of the project, although some of its parts come from Germany and Italy.

The main parts of the plants are:

a) Two Downdraft gasifier, b) A dual-fuel generator, c) Four Electric motor & d) A spray pond.

A mini grid has been constructed to sell the power to the adjacent area. The plant is able to deliver power to at least 200 households and over 100 commercial entities of that area. At present only one unit is on running condition from two, and this unit produces 56-KW only. The plant is no longer capable of supplying more than 50 houses.

Figure-6.1: Rice Husk fired 250 kW Gasifier power plant and Spray pond at Kapasia, Bangladesh.

Dreams Power Limited now supplies about 333 unit/day (56-KW * 6-hr=336 KW-hr or unit). It runs 6hrs a day. The sales cost of each unit is 5 TK. Therefore the monthly income of the plant equals to 333 * 5 * 30 =49950 i.e. about 50000 TK. But it cost pretty more than income. The loss of the existing plant can be minimized in two ways:

1. By establishing plant at rice mill cluster areas &
2. By utilizing the ash generated from rice husk.

According to the Rice Mill Owners' Association of Bangladesh there are over one hundred thousand rice mills located in a scattered manner all over the country with four 'cluster' areas. These four distinct 'cluster' areas are distinguished as - (i) Dinajpur (ii) Sherpur (iii) Inshawerdi and (iv)Kaliakoir, where most of the rice mills are located in close proximity to each other.

Figure-6.2: Districts with rice mill clusters (red marked) in Bangladesh [7]

Based on preliminary surveys at least over 500 rice mills are located in these cluster areas. Taking an average capacity range of about 100-200 kW, there is a 50-100 MW power market in these cluster areas [8].

Silica generation is a separate independent process not dependent on electricity generation, although the

input ash is dependent on gasification process. Provision will be taken in the design so that external ash is used also as input thus increase silica production. The process along with three major steps of production is depicted in below mentioned figure.

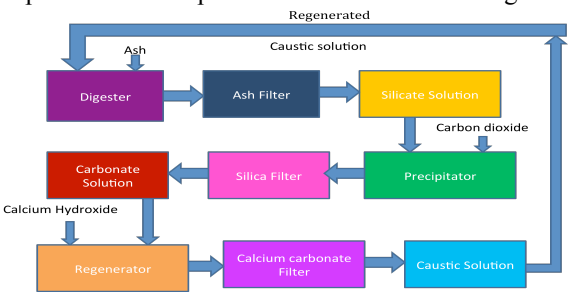

1.Digestion

This step involves the digestion of the rice husk ash with caustic to formulate sodium silicate solution at specific condition.The solution is filtered & then clear filtrate is then taken for precipitation.

Ash + NaOH (l) $Na_2O.xSiO_2$ (l) + Undigested ash

2. Precipitation

This step involves precipitation of silica from sodium silicate solution in presence of CO_2. The precipitated silica is then filtered, washed with water to remove the soluble salts and dried to form silica powder[10].

$Na_2O.xSiO_2$ (l) + CO_2 (g) $xSiO_2$ (s) + Na_2CO_3

3. Regeneration

Regeneration is the step where calcium compound reacts with the sodium carbonate to form calcium carbonate and sodium hydroxide. The resulting solution is filtered to remove the solid calcium carbonate and the aqueous sodium hydroxide is used for digestion again [9].

Na_2CO_3 (l) + $Ca(OH)_2$ (s) $CaCO_3$ (s)

$CaCO_3$ (l) $Ca(OH)_2$ (s) + CO_2

7. CONCLUSION & FUTURE WORK

The Biomass power plant in Kapasia is a milestone in country's history to promote and develop renewable energy. These sorts of off-gird power plant are needed as the government cannot meet the electricity demand alone.

In order to flourish this technology in near future following factors should be considered:

- Recognition,
- Attitudinal Barriers to shift,
- Available Loan facility,
- Cost of installation,
- Type of fuel to be used and its availability,
- Efficiency,
- By-product utilization.

REFERENCES

[1]. M. Rofiqul Islam, M. Rabiul Islam and M. Rafiqul Alam Beg,"Renewable energy resources and technologies practice in Bangladesh", *Renewable and Sustainable Energy Reviews (2006)*, doi:10.1016/j.rser.2006.07.003.

[2]. T.B. Reed, "Biomass Gasification Principles and Technology", Noyes Data, Park Ridge, NJ, 1981.

[3]. S.K. Patra and P.P. Datta, "Technical Digest, Insights into Biomass Gasification Technology".

[4]. J. Waewsak, M. Mani, P. Buaphet and P. Panichayunon, "A Biomass Gas Engine System for Power Generation of OTOP Building in Southern Thailand", *Renewable Energy System Research and Demonstration Center (RERD)*, Department of Physics, Faculty of Science, Thaksin University, Thailand.

[5]. M. Ahiduzzaman. "Rice Husk Energy Technologies in Bangladesh" *Agricultural Engineering International: the CIGR Ejournal.* Invited Overview No. 1. Vol. IX. January, 2007.

[6]. P.R. Shukla Published in The Social Engineer, "Biomass Energy in India: Transition from Traditional to Modern", Vol. 6, No. 2.

[7]. Dasgupta, N., Baqui, M. A., Dhingra S., Raman, P., Ahiduzzaman, M. And Kishore, V.V. N., "Benefits of Improved Rice Husk Combustion, Bangladesh", NRI report no. 2764. p. 8, 21, 67, 2003.

[8]. APCTT-UNESCAP, Bangladesh Renewable Energy Report.

[9]. CGPL, Indian Institute of Science, "Precipitated Silica from Rice Husk Ash", India. Available: http://cgpl.iisc.ernet.in/site/Portals/0/Technologies/PrecipitatedSilica.pdf.

[10]. D.N. Subbukrishna, K.C. Suresh, P.J. Paul, S. Dasappa, N.K.S. Rajan, Precipitated Silica From Rice Husk Ash by IPSIT Process, *15th European Biomass Conference & Exhibition*, Berlin, Germany, 7-11 May, 2007.

Proceeding of the
International Conference on Electrical, Computer and Telecommunication Engineering
01- 02 December 2012 (ICECTE2012), RUET, Rajshahi-6204, Bangladesh

ICECTE2012: PI-0103

Multi area Tie-line Frequency Deviation Control using Thyristor-Controlled-Phase-Shifter

Asaduzzaman[1], Hasan Sheikh[2], M.R.I. Sheikh[3] ,Ar Rafiul Faisal[4]
EEE department, Rajshahi University of Engineering & Technology
E-mail: asad3e@rocketmail.com[1],hasan.eee.69@gmail.com[2],ris_ruet@yahoo.com[3] ,mfaisaleee@yahoo.com[4]

ABSTRACT
Frequency deviation and inter-area tie power fluctuations from their respective predetermined values following a local load disturbance are a source of great concern in interconnected power system operation and control. In this paper, a new model is proposed to minimize such deviations and thereby enhance the performance of Automatic Generation Control (AGC) of an interconnected power system. Thyristor-Controlled-Phase-Shifter (TCPS) with Automatic Generation Control (AGC) are proposed to reduce frequency fluctuations. Finally it is compared with only AGC based simulation. The simulation results show that AGC with TCPS performs more effective to reduce frequency deviations and compared to AGC with normal systems.

KEY WORDS: Tie line, AGC, TCPS.

1. INTRODUCTION

Automatic generation control is one of the most important issues in electrical power system design and operation. For proper design of AGC with other controller performs effectively to maintain the frequency of each area and to keep tie-line power close to the scheduled, the AGC generator so as to accommodate fluctuating load demands. For proper design many past and present control strategies have been developed to perform for reducing it. But due to highly change of load variation and errors in modeling in industry only AGC is not suitable to perform better. So some techniques are applied to solve these problems.[4]

In multi-area power system, if a load variation occurs at any one of the areas in the system, the frequency related with this area is affected first and then that of other areas is also affected first and then of other areas is also affected from this perturbation through tie-lines. When a small load disturbance occurs, power system frequencies oscillations continue for a long duration even in the case with optimized gain of supplementary controllers. So to damp out the oscillations in the shortest possible time, the fast acting energy storage device are expected to be the most effective counter measure due to increase the overall cost, energy storage device does not apply in the power system. For this reason, the concept of utilizing power electronic devices as for power system control has been widely accepted in the form of Flexible AC Transmission Systems (FACTS) which provides more flexibility in power system operation and control. A Thyristor-Controlled-Phase-Shifter (TCPS) is expected to be an effective apparatus for power system.[4]

2. TIE_LINE INCREMENTAL POWER FLOW MODEL WITH TCPS

The AGC system investigated comprises of an interconnection of two areas, both areas comprising of a non reheat thermal units. Figure 1 shows the schematic of two area interconnected thermal power system with TCPS. Two areas are connected by a weak tie line and the tie line resistance is neglected. TCPS is placed in series with the tie line near area-1.[5]

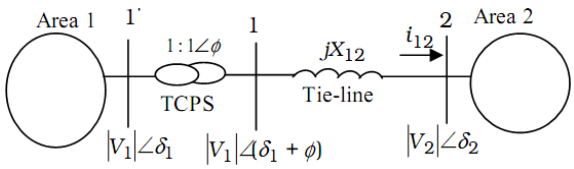

Figure 1: Two-area Power system with TCPS

A TCPS is a device that changes the relative phase angle between the system voltages. Therefore the real power flow can be regulated to mitigate the frequency oscillations and enhance power system stability.[5] without TCPS, the incremental tie line power flow from area-1 to area-2 can be expressed as

$$\Delta p^0_{tie12} = \frac{2\pi T^0_{12}}{s}(\Delta f_1 - \Delta f_2) \quad \ldots\ldots\ldots\ldots\ldots\ldots\ldots\ldots\ldots (1)$$

When a TCPS is placed in series with the tie line as in fig-2 the current flowing from area-1 can be written as

$$i_{12} = \frac{|V_1|<(\delta_1+\varphi) - |V_2|<(\delta_2)}{jX_{12}} \quad \ldots\ldots\ldots\ldots\ldots\ldots (2)$$

From fig-2 we can also write,

$P_{tie12} - jQ_{tie12} = V_1^* \times i_{12} = |V_1| < -(\delta_1 + \varphi)\left[\frac{|V_1|<(\delta_1+\varphi)-|V_2|<(\delta_2)}{jX_{12}}\right]$ …….…… (3)

Therefore,

$P_{tie12} - jQ_{tie12} = \frac{|V_1||V_2|\sin(\delta_1-\delta_2+\varphi)}{X_{12}}$ - j$\left[\frac{|V_1|^2 - |V_1||V_2|\cos(\delta_2-\delta_1-\varphi)}{X_{12}}\right]$…….…… (4)

Separating the real part of equation (4)

$P_{tie12} = \frac{|V_1||V_2|\sin(\delta_1-\delta_2+\varphi)}{X_{12}}$ ……..…… (5)

$\Delta P_{tie12} = T_{12}(\Delta\delta_1 - \Delta\delta_2 + \Delta\varphi) + T_{12}\Delta\varphi$…..… (10)

But $\Delta\delta_1 = 2\pi\int \Delta f_1 dt$ and $\Delta\delta_2 = 2\pi\int \Delta f_2 dt$ ..… (11)

And hence $\Delta P_{tie12} = 2\pi T_{12}(\int \Delta f_1 dt - \int \Delta f_2 dt) + T_{12}\Delta\varphi$ ……. (12)

Laplace transform of equation (12) is

$\Delta P_{tie12}(s) = \frac{2\pi T_{12}}{s}\left(\Delta F_1(s) - \Delta F_2(s)\right) + T_{12}\Delta\varphi$ (s) …….. (13)

As per eq.(12) tie line power flow can be controlled by controlling the phase shifter angel Δj . The phase shifter angle Δj(s), can be represented as [13, 15]

$\Delta\varphi$ (s) = $\frac{K_\varphi}{1+sT_{PS}}\nabla F_1(s)$ ……..… (14)

where Kφ and TCPS are the gain and time constants

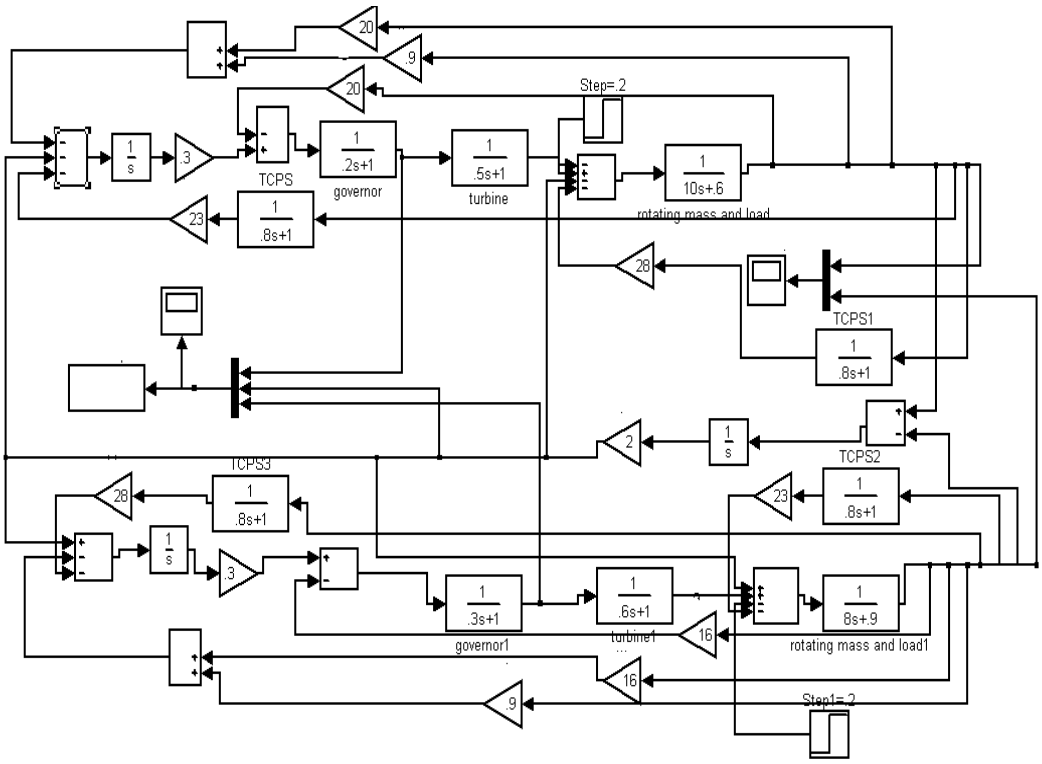

Figure 2: Simulation model for two-area Power system with TCPS

In eq.(5) perturbing δ_1 , δ_2 and φ from their nominal values ,we get

$\Delta P_{tie12} = \frac{|V_1||V_2|}{X_{12}}\cos(\delta_1^0 - \delta_2^0 + \varphi^0)\sin(\Delta\delta_1 - \Delta\delta_2 + \Delta\varphi)$ …….. (6)

But $((\Delta\delta_1 - \Delta\delta_2 + \Delta\varphi))$ is very small. Hence

$\sin(\Delta\delta_1 - \Delta\delta_2 + \Delta\varphi) \approx (\Delta\delta_1 - \Delta\delta_2 + \Delta\varphi)$

$\Delta P_{tie12} = \frac{|V_1||V_2|}{X_{12}}\cos(\delta_1^0 - \delta_2^0 + \varphi^0)(\Delta\delta_1 - \Delta\delta_2 + \Delta\varphi)$ …… (7)

Considering $T_{12} = \frac{|V_1||V_2|}{X_{12}}\cos(\delta_1^0 - \delta_2^0 + \varphi^0)$…… (8)

Thus $\Delta P_{tie12} = T_{12}(\Delta\delta_1 - \Delta\delta_2 + \Delta\varphi)$…… (9)

And hence

of the TCPS. Thus Δf_1 is the frequency deviation of the area-1 and is given as an input to the TCPS control logic

Thus, eq. (14) can be written as

$\Delta P_{tie12}(s) = \frac{2\pi T_{12}}{s}\left(\Delta F_1(s) - \Delta F_2(s)\right) + T_{12}\frac{K_\varphi}{1+sT_{PS}}\nabla F_1(s)$ …….…… (15)[2]

3. MODELING OF TWO-AREA POWER SYSTEM INCLUDING TCPS

When there is sudden rise in power demand in a control area, the governor control mechanism starts

working to set the power system to the new equilibrium condition. Similar action happens when there is a sudden decrease in load demand. Basically the operation speed of governor turbine system is slow compared with that of the excitation system. As a result fluctuations in terminal voltage can be corrected by the excitation system very quickly, but fluctuations in generated power or frequency are corrected slowly. Since load frequency control is primarily concerned with the real power frequency behavior the excitation system model line power interchange at the scheduled value .thus supplementary controller with integral gain kill is therefore made to act on area control error (ACE), which is a signal obtained from tie-line power flow deviation added to frequency deviation weighted by a bias factor β as eq.(16)[4]

$$ACE_i = \sum_{j=1}^{n} \Delta P_{tie,i,j} + \beta_1 \Delta f_1 \quad \ldots\ldots\ldots\ldots\ldots\ldots (16)$$

here the suffix I refer to the control area and j refer to the number of generator.

4. SIMULATION RESULTS

To demonstrate the usefulness of the proposed controller, computer simulations were performer using the MATLAB environment under different operating conditions. The system performance with AGC including TCPS is shown in figure. The system performances without TCPS with are also shown in the same figures. It is seem form figure that, the frequency deviations are more reduced with the AGC including TCPS than the AGC without TCPS.

5. CONCLUSION

The LFC performance of a two-area interconnected power system is investigated in the presence of a coordinated AGC and TCPS combination. The result shows that the scheme is more powerful in reducing the frequency deviation under a variety of load perturbations. On line adaption of supplementary controller gain associated with TCPS makes the proposed intelligent controller s more effective and are expected to perform optimally under different operating conditions.

REFERENCES

[1] Hadi Saadat, "Power System Analysis", Tata McGraw-Hill Publishing Company Limited, New Delhi.

[2] Sunil S. Rao, "Switchgear Protection & Power System".

[3] Willaim D. Stevenson Jr., "Elements of Power System Analysis", McGraw-Hill Book Company, New Delhi.

[4] M.R.I. Sheikh, R. Takahashi & J. Tamura, "Multi-Area Frequency & Tie-line Power Flow Control by Coordinated Operation of FGS-AGC with TCPS".

[5] K. Subbaramaiah, V.C. Jagan Mohan, V.C. Veera Reddy, "Comparison of Performance of SSSC & TCPS in AGC by Coordinated Operation of Hydrothermal System under Deregulated Scenario".

[6] P. Kumkratug & M.H. Haque, "New Model of a TCPS in Simple Power System".

[7] Duane Hanselman & Bruce Littlefield, "Mastering MATLAB 7" .

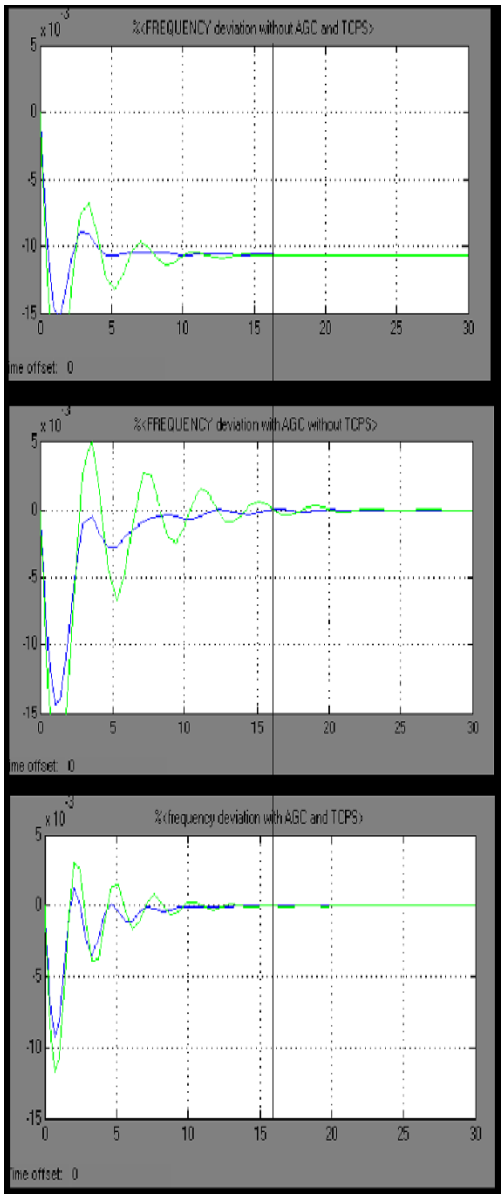

Proceeding of the
International Conference on Electrical, Computer and Telecommunication Engineering
01- 02 December 2012 (ICECTE2012), RUET, Rajshahi-6204, Bangladesh

ICECTE2012: PI-0104

Design and Analysis of a Three Element Boiler Drum Level Control System

P. K. Bhowmik[1], P. Dutta[2], S. K. Dhar[3] and M. Dey[4]*
[1]Department of Instrumentation & Communication, Eastern Refinery Limited, Chittagong, Bangladesh
[2]Department of Energy Auditing Unit-2, Bangladesh Power Development Board, Chittagong, Bangladesh
[3]Member Institute of Electrical and Electronics Engineers, Chittagong, Bangladesh
[4]Department of EEE, Chittagong University of Engineering & Technology, Bangladesh
E-mail: pkbcuet@yahoo.com, dpinky42@yahoo.com, sagar378@gmail.com, mrinmoyeee@gmail.com

ABSTRACT
This paper presents design and analyze of three elements boiler drum level control system for ensuring system reliability, safety and robustness in a cost effective way. The control system contains a feedfoward loop using the steam flow signals and a feedback PID loop using feed water flow and drum level signal. Output of the two loops is summed to establish set point for the actuator. In this way, feedwater flow tracks steam flow and any disturbances in the system will be arrested quickly. A feedback PID controller plus adapt feedfoward compensator can be successfully employed for the level control in such a plant.

KEY WORDS: Three element control, boiler drum level control, feedforward control, feedback control.

1. INTRODUCTION

Boiler drum level control is one of the critical control loop for ensuring un-interruption of operation, protection and safety of boiler system [4]. For boiler drum level control by manipulating the feed water flow to the boiler, three elements: drum level, main steam flow and feed water flow; the primary inputs are normally being considered. In addition, drum pressure, main steam pressure and temperature are also considered for compensation [3]. The three-element system provides tighter control for drum level with fluctuating steam load, rapid change in steam demand or system having multiple boilers and multiple feedwater pumps or where the feedwater has variations in pressure or flow. In the boiler the steam flow changes according to the load demand that will change ultimately the water level in the boiler drum. The drum level controller manipulates the feedwater flow setpoint in conjunction with feedforward signal from the steam flow measurement [1]. The boiler drum water level control of 3MW STG Unit-II of Eastern Refinery Limited, Chittagong, Bangladesh is taken as the reference model applied in this study. It is analyzed in a systematic way and the simulation result of the system give the clear understanding about the system.

2. PROCESS SCHEMATIC DIAGRAM

The boiler drum level control system is as follows [1]-

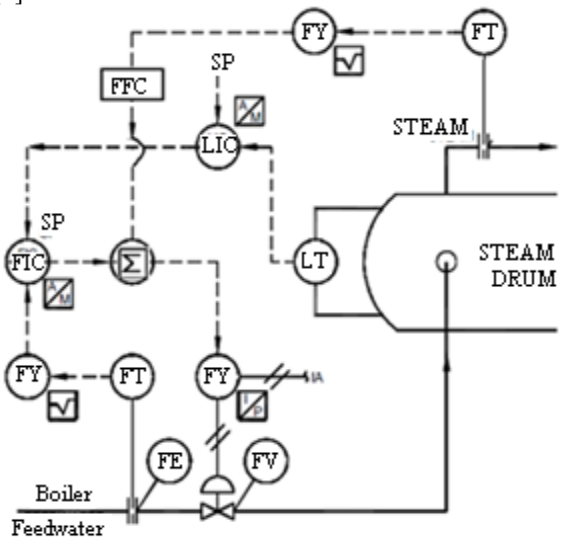

Fig. 1. Schematic diagram of boiler drum level control system

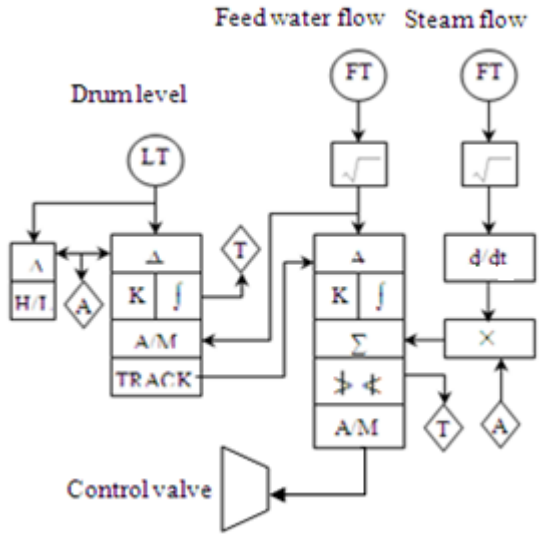

Fig. 2. Logic diagram of boiler drum level control system

3. PROCESS MODEL DEVELOPMENT

The performance of the three-element control system during transient conditions makes it very useful for general industrial and utility boiler applications. Plants which exhibit load characteristics of this type are those with mixed, continuous, and batch processing demands [5][6]. Figure 1 and 2 shows the control scheme for three-element drum level control. In this system the output signals of the level controller (LIC) use as a cascade set-point input to feedwater flow controller (FIC). Feedwater flow and steam flow are measured by the differential pressure transmitters. The output signal of the flow transmitter is linearized by a square root extractor (FY). The feedwater flow controller produces the necessary corrective signal to feedwater flow control valve to maintain feedwater flow. The steam flow signal which is act as a disturbance in boiler drum level control system is computed by feed forward compensator adds to the flow controller output [1].

4. CONTROL LOOP OF BOILER DRUM LEVEL CONTROL SYSTEM

The control loop of three element boiler drum level control system is shown in figure 3. Here, the primary control loop consists of LIC and secondary control loop having FIC are connected in cascade mode. The output of primary control loop controller is the input or set value to the secondary control loop. The feedback compensators both for primary and secondary loop are used to improve the control action of the whole control loop. The combination of primary and secondary loop is the feedback control design of boiler drum level control system. The feed forward compensation which main objective is to minimize the effect of disturbance, the steam flow in drum level control system is sum with the output of secondary loop controller (feedback control) and finally gives actuating signal to the final control element, the feed water flow control valve.

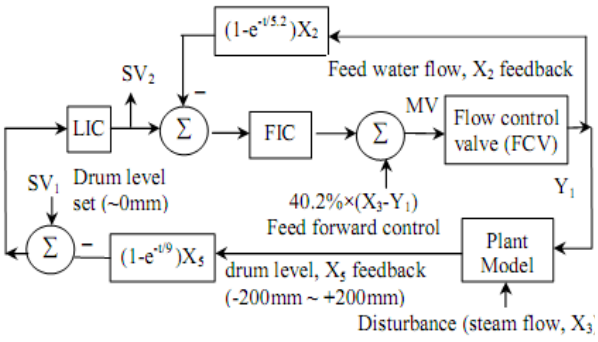

Fig.3. Control loop with associated feedback compensator of boiler drum level control system

5. CONTROLLER CONFIGURATION AND PROGRAM DEVELOPMENT

In this paper the system analysis is performed using YOKOGAWA YS1700 controller which is configured and programmed by YS1000 software. Thus the system analysis requires the following steps [2]:

- System configuration:- this is mainly configures the controller model and required system, input and output.
- Parameter settings:- it consist of settings of PID, controller actions, alarms, units, input & output range
- Writing tax program:- writing program for the respective system according to the programming instruction.
- Upload all settings and tax program from YS1000 software to YS1700 controller & run the controller.

5.1 Parameter settings and configuration

References In figure 4 the parameter settings of the controller are given. PID1 and PID2 are the proportional–integral-derivative settings for primary and secondary control loop respectively. In the config2 the control action of controller, controller output type and the input/ output signal settings are presented [2].

PID 1

	Name	Setting Value	
SV1	Setpoint value 1	0.0	
PB1	Proportional band 1	39.5	%
TI1	Integral time 1	32	S
TD1	Derivative time 1	4	S
SFA1	Adjustable setpoint filter alpha1	0.000	
SFB1	Adjustable setpoint filter beta1	0.000	
GW1	Non-linear control gap width 1	0.0	%
GG1	Non-linear control gain 1	1.000	
PH1	High limit alarm setpoint for PV1	247.7	
PL1	Low limit alarm setpoint for PV1	-247.7	
HH1	High-high limit alarm setpoint for PV1	247.7	
LL1	Low-low limit alarm setpoint for PV1	-247.7	
DL1	Alarm setpoint for deviation variable 1	0.0	
VL1	Velocity alarm setpoint for PV1	0.0	
VT1	Velocity alarm time setpoint for PV1	1	S
HYS1	Alarm hysteresis 1	8.8	
MH1	High limit setpoint of MV1	106.3	%
ML1	Low limit setpoint of MV1	-6.3	%
MR1	Manual reset 1	-6.3	%
RB1	Reset bias 1	0.0	%
PMV1	Preset output 1	-6.3	%

PID 2

	Name	Setting Value	Unit
SV2	Setpoint value 2	12.50	
PB2	Proportional band 2	63.4	%
TI2	Integral time 2	61	S
TD2	Derivative time 2	0	S
SFA2	Adjustable setpoint filter alpha2	0.000	
SFB2	Adjustable setpoint filter beta2	0.000	
GW2	Non-linear control gap width 2	0.0	%
GG2	Non-linear control gain 2	1.000	
PH2	High limit alarm setpoint for PV2	26.58	
PL2	Low limit alarm setpoint for PV2	-1.58	
HH2	High-high limit alarm setpoint for PV2	26.58	
LL2	Low-low limit alarm setpoint for PV2	-1.58	
DL2	Alarm setpoint for deviation variable 2	0.00	
VL2	Velocity alarm setpoint for PV2	0.00	
VT2	Velocity alarm time setpoint for PV2	1	S
HYS2	Alarm hysteresis 2	0.50	
MH2	High limit setpoint of MV2	106.3	%
ML2	Low limit setpoint of MV2	-6.3	%
MR2	Manual reset 2	-6.3	%
RB2	Reset bias 2	0.0	%
PMV2	Preset output 2	-6.3	%

CONFIG 2

	Name	Setting Value
CMOD1	C-mode 1	CAS
BMOD1	Backup mode 1	BUM
CNT1	Control type 1	PID
ALG1	Control operation formula 1	PI-D
ACT1	Control operation direction 1	RVS
VDIR1	Valve direction 1	C-O
SCH1	100% value of scale 1	2200
SCL1	0% value of scale 1	-2200
UNIT1	Engineering unit 1	mmH2O
TAG1	Tag number 1	---LIC501--
CMOD2	C-mode 2	CAS
BMOD2	Backup mode 2	BUM
CNT2	Control type 2	PID
ALG2	Control operation formula 2	PI-D
ACT2	Control operation direction 2	RVS
VDIR2	Valve direction 2	C-O
SCH2	100% value of scale 2	2500
SCL2	0% value of scale 2	0
UNIT2	Engineering unit 2	T/H
TAG2	Tag number 2	---LIC-501--

Fig. 4. Parameter settings of controller (PID1, PID2 and Configure-2) for boiler drum level control system

5.2 Parameter settings and configuration

For developing the text program for boiler drum level control system the respective program instructions of YSS100 software are used keeping in mind that text program should easily understandable to new user. The developed program instruction for the described system is given bellow with explanation.

```
; Start program
  LD Y1      Read output (Y1) of the controller.
  ST T3      Store Y1 in temporary register T3
  LD T2      Recall and load in temporary register
  ST P4      Store in variable parameter P4
  LD X3      Read input-3, Main steam flow
  ST P5      Store X3 in variable parameter P5
  ST T2      Store X3 in temporary register T2
  CHG        Status register interchange
  -          Subtraction
  ST P6      Store X3-Y1 in variable parameter P6
  LD P11     Load variable parameter (40.2%)
  *          Multiplication
  ST FF2     Store in Feedforward compensator
  LD X5      Read input-5, Drum level
  ST P1      Store X5 in variable parameter P1
  LD P12     Read variable parameter P12 (T1=9 sec)
  LAG1       Computing first order lag 1/ (1+T1S)
  ST P2      Store (1-e^(-t/9))X5 in variable parameter P2
  LD X2      Read input-2, Feed water flow
  ST P3      Store X2 in variable parameter P3
  LD P13     Read variable parameter P13 (T2=5.2 sec)
  LAG2       Computing first order lag 1/ (1+T2S)
  ST P7      Store (1-e^(-t/5.2))X5 in variable parameter P7
  LD P2      Read variable parameter P2
  CHG        Status register interchange
  CSC        Cascade Control
  ST Y1      Store output to output-1
             terminal (4~20mA)
  ST Y2      Store output to output-  terminal (1~5V)
  LD T3      Read temporary register T3
  LD X4      Read Control valve position (feedback)
  -          Subtraction
  ABS        Absolute Value of subtracted value
  LD P9      Load variable parameter P9
  LD P10     Load variable parameter P10
  HAL1       High Alarm output
  ST T1      Store in temporary register T1
  END        End of Program
```

Fig. 5. Test program of boiler drum level control system in YSS1000 software.

5.3 Program execution and simulation

After writing the text program in YSS100 software then the program is uploaded to the YS 1700 YOKOGAWA controller and run the program [3]. In AUTO mode controller always scan its input address and give output signals according to the program instruction loaded to it.

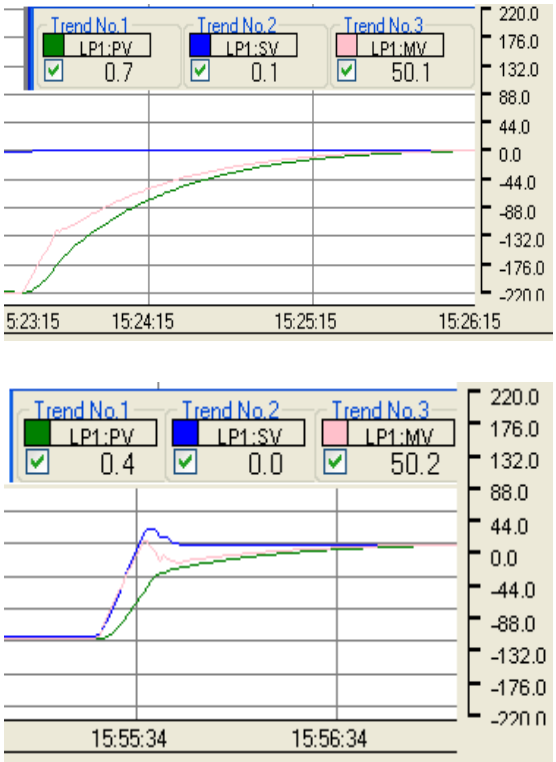

Fig. 6. Simulation result of boiler drum level controller (a) Start from no level to set level, (b) Step set level change

For checking the control loop performance at first assume that there is no water level in the drum, so the controller will give control signal to the control element according to the program instruction to increase the feed water flow to maintain the drum level. Thus result is shown in figure 6(a). The output response of the controller for step change in level set value is shown in figure 6(b). The response of the controller for steam flow change without changing the drum level set value is also excellent.

6. RESULT AND DISCUSSION

The simulated result of the boiler drum level control system ensure that it will track the set point without having considerable overshoot combining the effect of both LIC and FIC which are connected in cascade.

The simulation result also ensures the ability of the system to minimize the effect of disturbance (stem flow) by taking preventive action called feedforward compensation. Thus the control system offers precise set point tracking and effective disturbance rejection which is the desired goal of any control system.

7. CONCLUSION

To cope with the technological advancement and to ensure higher efficiency, effectiveness and reliability of boiler drum level system control in a more economical way, the system presented in this paper would be a great scope. It will also provide better flexibility in customization of operation, error checking and modification with minimum effort. The paper has furnished itself to study the integral parts of the entire process, their implementation and the problems that can occur have also been investigated with due importance.

8. ACKNOWLEDGEMENT

The author would like to thank Mr. Sharafat Ali, Assistant General Manager, Dept. of Instrumentation and Communication, Eastern Refinery Ltd., Bangladesh for his valuable guideline to complete the task. Also thanks to Md. Ali Zulquarnain, Member, Planning, Bangladesh Atomic Energy Commission for his valuable review and comments.

REFERENCES

[1]. Operation Guideline of Boiler of STG Unit-2 of Eastern Refinery Limited, Chittagong, Bangladesh.

[2]. YOKOGAWA YSS1000 Programmable Controller Software, YSS1000 programming instruction Manuals.

[3]. "Combustion Management Solutions Boiler Drum Level (Feedwater) Control" AD353-105, Rev-2, January 2005, Siemens Energy and Automation.

[4]. Mingliang WU, Lili WEI, Jiankang HUANG, Mingyong WU, "The Cascade Three-elements Fuzzy auto-adapted PID Control System for Boiler" Advanced Materials Research Vols. 139-141 (2010) pp 119-1923.

[5]. Tatang Mulyana, Mohd Nor Mohd Than, Dirman Hanfi, "A Disctrete Time Model of Boiler Drum and Heat Exchanger QAD Model BDT 921", International Conference on Instrumentation, Control and

[6]. A Guide to Boiler Drum Level Equipment and Control Concept- presented by Clark Relience Corporation, Strogsville, Ohio.

Proceeding of the
International Conference on Electrical, Computer and Telecommunication Engineering
01- 02 December 2012 (ICECTE2012), RUET, Rajshahi-6204, Bangladesh

ICECTE2012: PI-0105

Power System Stability Improvement By Using SVC With PI And PD Controller

[1]*Habibur,* [2]*Emdadul,* [3]*Dr.MRI Sheikh,*[4]*Harun*
[1,2,3]Department of EEE, Rajshahi University of Engineering & Technology, Bangladesh
E-mail:habibieee@yahoo.com,emdad_0813@yahoo.com,ris_ruet@yahoo.com,harun.h.eee@gmail.com

ABSTRACT
THIS PAPER PRESENTS THE PERFORMANCE OF A STATIC VAR COMPANSATOR(SVC) WHICH IS CONTROLLED EXTERNALLY BY USING PROPORTIONAL INTEGRAL& PROPORTIONAL DERIVATIVE CONTROLLERS FOR THE IMPROVEMENT OFAN ONLINE POWER SYSTEM STABILITY.CONTROLLER PARAMETERS HAS BEEN SELECTED BY USING ZIEGLAR-NICHOLS CLOSE LOOP TUNING METHODS & THE POWER SYSTEM NETWORK HAS BEEN SIMULATED FOR SINGLE PHASE & THREE PHASE FAULTS.SIMULATION RESULTS SHOWS THAT,EVERY PARAMETERSI.E. VOLTAGE ,CURRENT, POWER, MACHINES OSSCILLATION BECOMES STABLE &ONLY A SMALL RATING OF SVC CAN REGAIN THE SYSTEM STABILITY IN FASTER WAYS THEN WITHOUT CONTROLLERS.SO, SVC WITH BOTH CONTROLLERS,THE SYSTEM PERFORMANCE ARE GREATLY ENHANCED.

KEY WORDS:SVC,TCR,PI,PD,MATLAB Simulink

1. INTRODUCTION

Power system stability improvements is very important for large scale system..SVC is an electrical device for providing fast-acting reactive power compensation on high voltage transmission networks and it can contribute to improve the voltage profiles in the transient state and therefore[1,2].An SVC can be controlled externally by using properly designed different types of controllers which can improve voltage stability of a large scale power system. In previous study[3]authors has designed a PI controller by setting the tuning parameters by using trial & error method. However, in this study, With a view to get better performance, PI & PD controller parameters has been designed by Ziegler-Nichols method for SVC to injects V_{qref}externally. Therefore, thyristor based SVC with PI & PD controllers has been used to improve the performance of 2-machine power system.

2.CONTROL CONCEPT OF SVC

An SVC is a controlled shunt susceptance(B) which inject reactive power (Q_{net}) into thereby increasing the bus voltage back to its net desired voltage level. If bus voltage increases, the SVC will inject reactive power, and the result will be to achieve the desired bus voltage[Fig.1].Here, $+Q_{cap}$ is a fixed capacitance value, therefore the magnitude of reactive power injected into the system, Q_{net}, is controlled by the magnitude of $-Q_{ind}$ reactive power absorbed by the TCR. SVC based control system is shown in Fig.1[2].

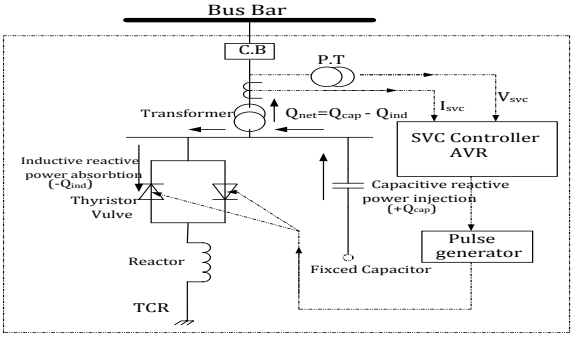

Fig.1 SVC based control system

3. POWER SYSTEM NETWORKMODELLING

This example described in this section illustrates modelling of a simple transmission system containing 2- hydraulic power plants. SVC has been used to improve transient stability and power system oscillations damping.A single line diagram represents a simple 500 kV transmission system is shown in Fig.3.

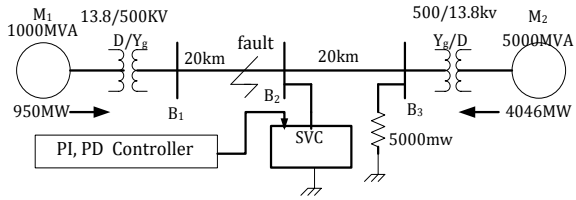

Fig.3 Single line diagram of 2-machine power

To maintain system stability after faults, the transmissionline is shunt compensated at its centre by a 200MVAR SVC. The SVC doesnot have any controller unit. Machine & SVC parameters has been taken from[5].The complete simulink model of this network is shown in Fig.3.1.To maintain system stability after faults, the transmissionline is shunt compensated at its centre by a 200MVAR Static VAR Compensator (SVC). Thetwo machines are equipped with a hydraulic turbine and governor (HTG),Excitation system, and power system stabilizer (PSS).

3.1.Simulation Results (SVC Without Controller)

3.1.1 Single Phase Faults

Consider a 1-phase fault occurred at 0.1s & circuit

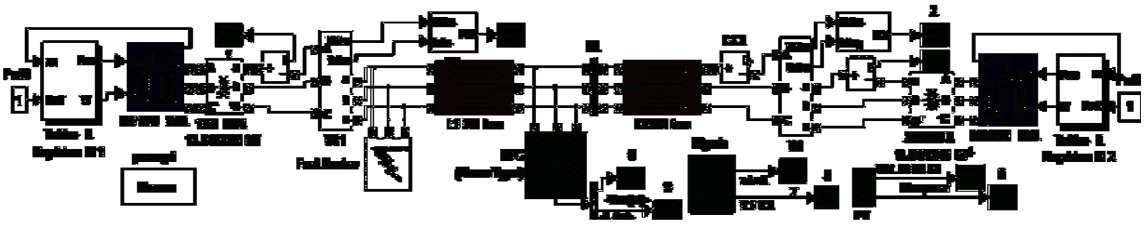

Fig.3.1 Complete simulink model of 2-machine power system

SVC, the system parameters goes on unstable[Fig.3(a-c-e)].But if SVC(without controller) is applied then voltage becomes stable within 3s [Fig.3(b)],power becomes stable within 3s[Fig.3(d)] & machines oscillation becomes stable within 4.5s [Fig.3(f)].

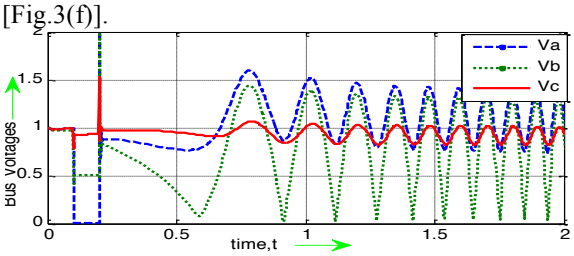

Fig. 3(a) Bus voltages in p.u (without SVC)

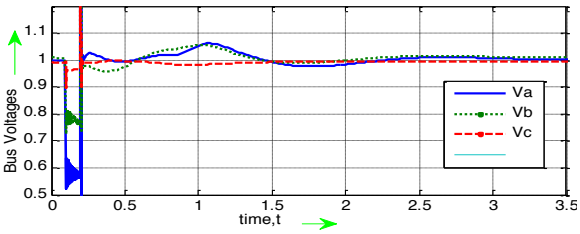

Fig.3(b) Bus Voltages in p.u (with SVC)

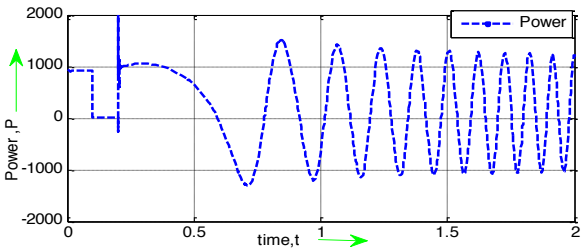

Fig.3(c) Bus power,P in MW (Without SVC)

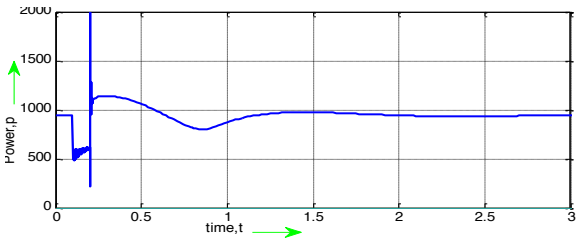

Fig.3(d) Bus Power(P)in MW (with SVC)

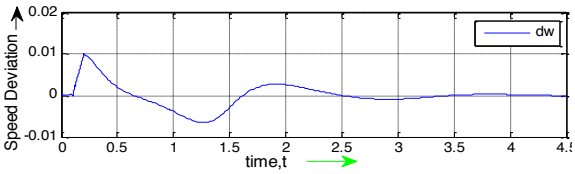

Fig.3(f) Speed oscillations (with SVC)

3.1.2Three Phase (Line-Line) fault

During 3-phase faults, If no SVC is applied then system becomes unstable But when SVCis applied then the system voltage becomes stable within 5s [Fig.3(g)] & machines speed deviation becomes stable within 5s [Fig.3(h)].

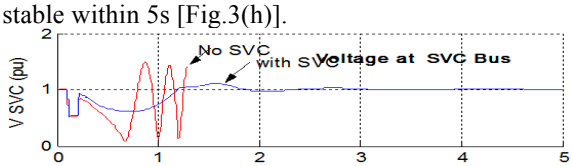

Fig.3(g) Bus Voltage(Va) in p.ut

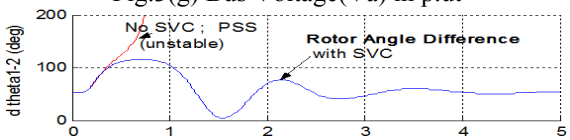

Fig.3(h) Machines speed deviation for L-L fault

4. DESIGNE OF PI CONTROLLER

Proportional Integral(PI) controller parameters has been designed by Ziegler-Nichols close loop tuning method.The PI controller has two term control signal[4],

$$u(t) = K_p e(t) + \frac{K_p}{T_i}\int e(t)dt \quad \ldots\ldots(1)$$

In Laplace Form,

$$Gc(s) = K_p\left(1 + \frac{1}{T_i s}\right) \quad \ldots\ldots(2)$$

Ziegler and Nichols assumptions are,

$K_p=0.6K_{cr}$, $T_i=0.5P_{cr}$,

$$Gc(s) = 0.6K_{cr}\left(1 + \frac{1}{0.5P_{cr}s}\right) \quad \ldots\ldots(3)$$

The critical gain (K_{cr}) for which the plant output gives a sustained oscillation is determined for this network(K_{cr}=200) & corresponding period of P_{cr}[Fig.3(a)] has been found0.2s.So, PI controller parameters becomes,

$$Gc(s) = 120\left(\frac{S+10}{S}\right) \quad \ldots\ldots(4)$$

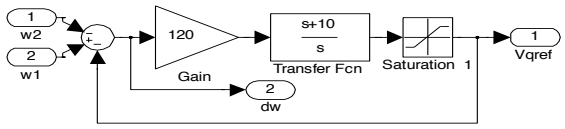

Fig.4(a) Internal Structure of PI controller (dω input)

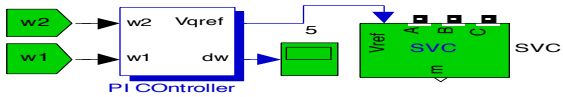

Fig.4(b) PI controlled SVC Model with dω input

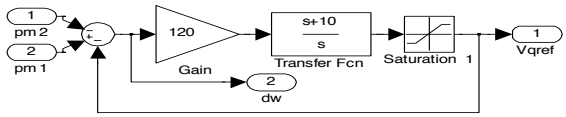

Fig.4(c) Internal Structure of PI controller (pm input)

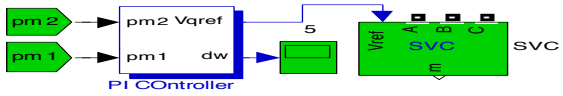

Fig.4(d) PI controlled SVC Model with pm input

4.1 Simulation Results (SVC with PI Controller)

4.1.1 Single Line to Ground Fault

If PI is used as SVC controller then, the system voltage becomes stable within 2s [Fig.4(e)] & power (P) becomes stable within 1s [Fig.4(f)] & Machines speed deviation becomes stable within 2.5s [Fig.4(g)].

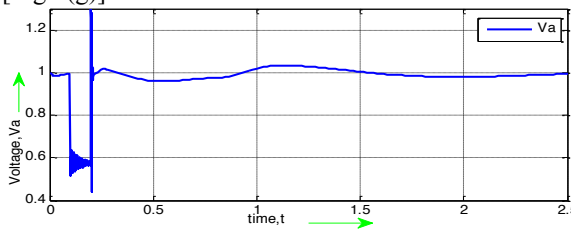

Fig.4(e) Voltage(Va) in p.u (SVC with PI)

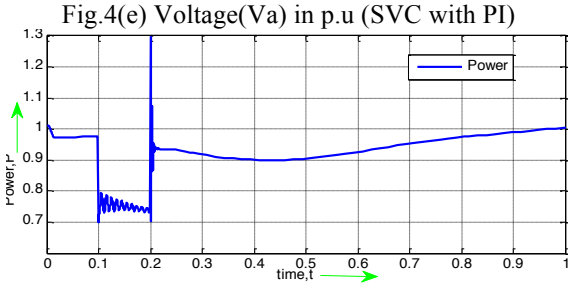

Fig.4(f) Bus Power(P) in p.u (SVC with PI)

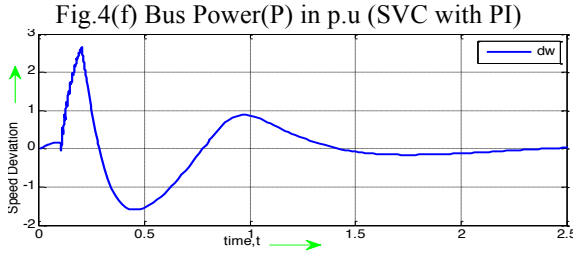

Fig.4(g) Speed deviation (SVC with PI)

4.1.2 Three Phase (line-Line) Fault

If PI is used as SVC controller then, the system voltage becomes stable within 3.1s[Fig.4(h)] & Power (P) becomes stable within 2s [Fig.4(i)]& Machines speed deviation becomes stable within 4s [Fig.4(j)].

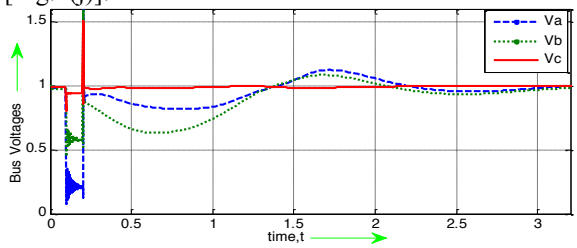

Fig.4(h) Bus voltages in p.u for L-L faults (with PI)

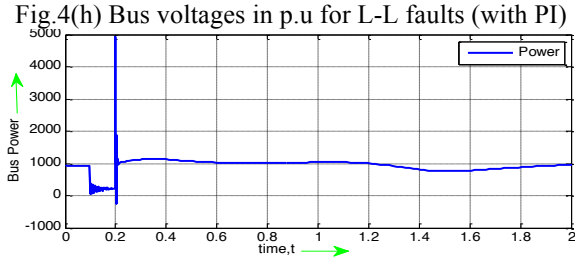

Fig.4(i) Bus power in MW (with PI)

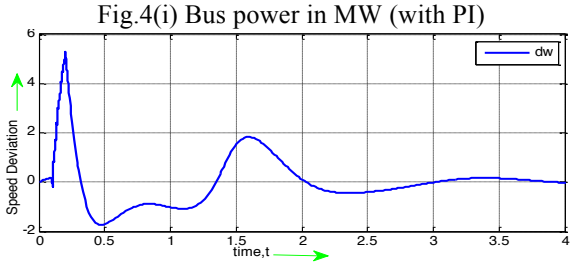

Fig.4(j) Machines speed deviation (with PI)

5. DESIGNE OF PD CONTROLLER

Similarly,The PD controller has two term control signal[4],

$$u(t) = K_p e(t) + K_p T_d \frac{de(t)}{dt} \quad \text{.....(5)}$$

$$G_c(s) = K_p(1 + T_d s) \quad \text{.....(6)}$$

Ziegler and Nichols assumptions are,

$K_p = 0.6K_{cr}$, $T_d = 0.125P_{cr}$,

Thus, Transfer Function,

$$G_c(s) = 0.6K_{cr}(1 + 0.125P_{cr}s) \quad \text{.....(7)}$$

$$Gc(s) = 120\left(\frac{S+40}{40}\right) \quad \text{.....(8)}$$

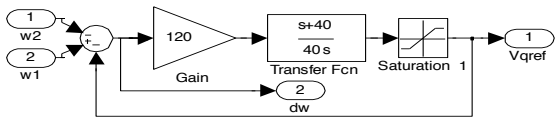

Fig.5(a) Internal Structure of PD controller

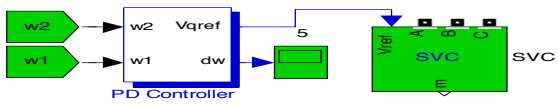

Fig.5(b) PD controlled SVC Model with dω input

5.1 Simulation Results (SVC with PD Controller)

5.1.1 SingleLine To Ground Fault

If PD is used as SVC controller then, the system voltage becomes stable within 1.5s[Fig.5(c)] & power (P) becomes stable within 1.6s [Fig.5(d)] & Machines speed deviation becomes stable within 1.3s

[Fig.5(e)].

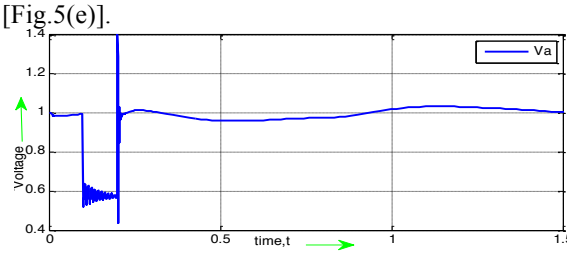

Fig.5(c) Voltage(Va) in p.u (SVC with PD)

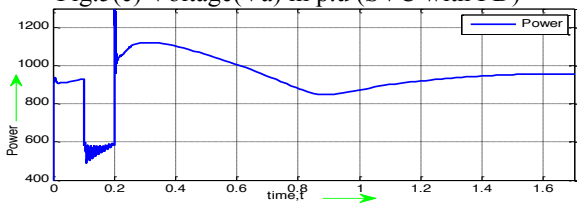

Fig.5(d) Bus Power(P)in p.u (with PD)

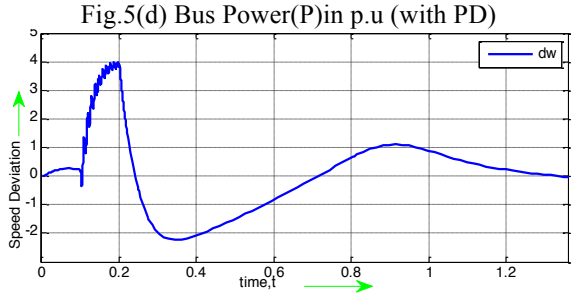

Fig.5(e) Speed deviation (SVC with PD)

5.1.2 Three Phase (line-Line) Fault

If PD is used as SVC controller then, the system voltage becomes stable within 1.4s with 0% damping [Fig.5(f)] & Power (P) becomes stable within 0.62s [Fig.5(g)]& Machines speed deviation becomes stable within 3s [Fig.5(h)].

6.RESULTS & DISCUSSIONS

The performance of both proposed PI & PD controller of power system network with SVC has been summarized in the table1

Table-1:

Performance Comparison of PI & PD Controllers

		1-Øfault (Stability time)			L-L fault(st. time)		
Controller	**SVC rating**	**Volt**	**P**	**dω**	V	**P**	**dω**
No SVC	200 MVA	inf	inf	inf	inf	inf	inf
SVC	200	3s	3s	4.5s	5s	5s	5s
SVC +PI	50 MVA	2s	1s	2.5s	3.1	2s	4s
SVC +PD	50 MVA	1.5s	1.6s	1.3s	1.4	0.6s	0.6

7. CONCLUSION

This paper presents the stability improvement of apowersystem network& performance of SVC with or without properly tuned PI & PD controllers for different types of faulted conditions. Both are very cheapest &efficient controllers for SVC to enhance the power system stability.If a externally(PI & PD) controlled SVC is connected in the network, then a small rating SVC can damp out all types of oscillation & the system becomes stable in faster way. From above results, this proposed PI & PD controllers which is properly & easily tuned by using Ziegler-Nichols tuning method may be highly suitable as SVC controller. Compared to those two controller, PD controller may be highly suitable

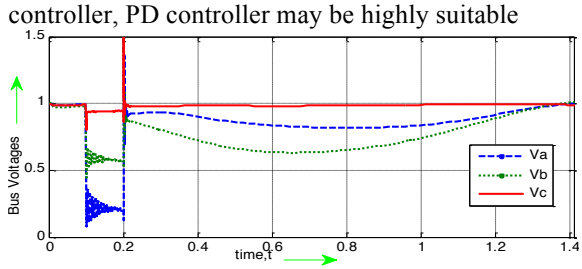

Fig.5(f) Bus voltages in p.u (with PD)

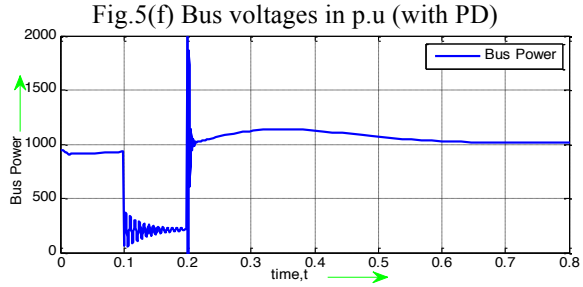

Fig.5(g) Bus power in MW (with PD)

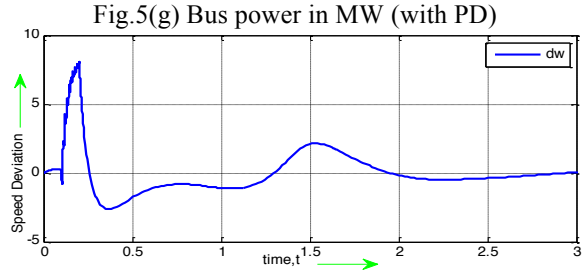

Fig.5(h) Machines speed deviation (with PD)

8. FUTURE WORK

Different tuning methods may be applied &Another FACTS devices namely SSSC, STATCOM, UPFC which may be controlled externally forfurther stability improvement of a power system.

REFERENCES

[1]. AmitGarg ,"Modeling and Simulation of Static VAR Compensator for Improvement of Voltage Stability in Power System"ISSN:2249-071X,Vol.2,Issue-2

[2]. Ali M. Yousef "Transient stability Enhancement of multi machine using Global deviation PSS" *Journal of Engineering sciences,* Faculty of Engineering, Assiut University, Vol. 32-No.2 April 2004 pp. 665-677

[3]. **Habibur,Dr.Fayzur,Harun,**"Online Voltage level Improvement by using SVC &PSS.*International Journal of System & Simulation*,ISSN-0975-4814,Vol.06,No.02(Dec-2012)Issue.

[4]. K.Ogata,"*Modern Control Engineering*,(Fourth Edition,Princes Hall,2002,Chapter,10)

[5]. "MATLAB Math Library User's Guide",by the Math Words, Inc.

Proceeding of the
International Conference on Electrical, Computer and Telecommunication Engineering
01- 02 December 2012 (ICECTE2012), RUET, Rajshahi-6204, Bangladesh

ICECTE2012: PI-0106

Hybrid Power System for Rural Areas of Bangladesh

M.F. Hossain, Shuva Paul, Md. Tariful Islam , Monojit Sarkar*
Department of Electrical and Electronic Engineering, Rajshahi University of Engineering & Technology
*E-mail: faruk94_ruet@yahoo.com

ABSTRACT
Hybrid system can produce synergistic benefits in which the "whole is greater than the some of its parts". Conventional hybrid power systems generally employ solar cell, wind turbine and other renewable energy sources. But in Bangladesh wind energy is not available at the same rate throughout the year except during monsoon (March to September). Again wind generally blows heavily in the coastal areas, which are located at the southern part of Bangladesh, and in the islands like Sandwip, Kutubdia, Saint Martin. Hence in this paper a hybrid power system have been proposed mainly for the rural areas of Bangladesh based on Solar energy, Biomass, Biogas, and Micro Hydro power plant which are rurally available throughout the year. The proposed system generally integrates renewable energy sources with fossil fuel to provide electric power which feeds directly into the grid. A solar tracking system has also been proposed to improve the efficiency of Hybrid Power System.

KEYWORDS: Hybrid Power System, Solar energy, Biomass, Biogas, Micro hydro power plant.

1. INTRODUCTION

Bangladesh is a developing country and lying below the poverty line. Here there are lack of raw materials, technologies, capital to ensure continuous power supply and proper electrification. The demand of power in our country is about 8500MW. On the contrary the available power is about 7000MW only [7]. Only 20% people of Bangladesh are now grid connected and only 42% people have electricity accessibility. Per capita electricity consumption is only 146.5kwh. Whereas for any high-income country, the average per capita electricity consumption is 9789kwh[3]. About 16% of global final energy consumption comes from renewable, with 10% coming from traditional biomass, which is mainly used for heating, and 3.4% from hydroelectricity. New renewables (small hydro, modern biomass, wind, solar, geothermal, and biofuels) accounted for another 3% and are growing very rapidly [4].

About 70% of total population of Bangladesh lives in rural areas. There are more than 87,319 villages in Bangladesh, and most of them are not connected to the national grid [8]. Due to the lack of electricity supply in rural areas, the rural population depends mainly on biomass as a source of energy. Over 70% of total primary energy consumption is covered by biomass, mainly agricultural waste and wood. By properly using the biomass available in rural areas it possible to establish hybrid power system based on solar cell, biomass and biogas which can mitigate power demand for rural areas and power also can be supplied to national grid. In this paper the hybrid power system has been proposed for rural areas is based on Solar energy, Biomass, Biogas and Micro-hydro power plant. Moreover, a solar tracking system has also been introduced to improve the efficiency of Hybrid Power System.

2.1 POWER STATISTICS OF BANGLADESH

Bangladesh is one of the world's lowest energy producers. The government's vision of electrifying the entire country by 2020 through grid expansion may not be realistic due to inaccessibility and low consumer density in many rural areas, as well as financial constraints [5].

Table 1: power statistics of Bangladesh

Area	About 145,000 sqkm
Population	About 155 Million
Per capita energy consumption	251 kwh
Share of traditional energy	About 60%
Access to electricity	30% of population (Rural area with 85% of population: 20% Remote area with 15% of population: <5%)
Area coverage by electrification	About 40% (as estimated by 2009)

2.2 PRESENT SCENARIO OF ENERGY SECTOR IN BANGLADESH

Power generation in Bangladesh has been dependent on natural gas and still now, 79.331% of electricity is being produced from our gas reserve. However, our

net remaining gas reserve (proven and probable) is only 13.53 Trillion Cubic Feet (TCF) and present proven reserve of indigenous gas will be exhausted by 2030.

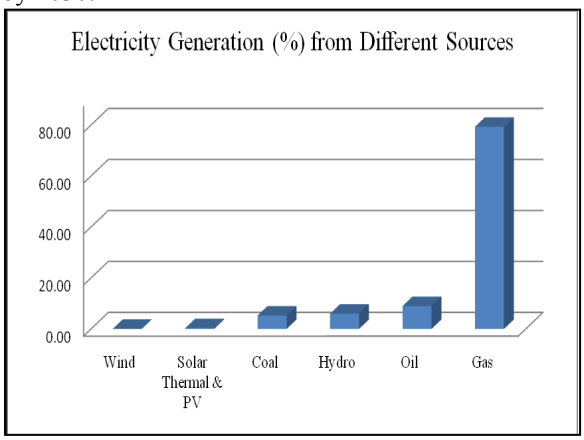

Figure 1: Percentage of electricity generation in Bangladesh from different sources.

Figure 1 shows the percentage of electricity production in Bangladesh from various sources. It can be observed that only 6.359% of electricity is coming from non-carbon sources (hydro, solar and wind) and 93.64% of energy is coming from hydrocarbon sources (gas, oil and coal) in Bangladesh [2].

3. HYBRID POWER SYSTEM

Hybrid power systems generally integrate renewable energy sources with fossil fuel powered diesel generator to provide electric power where the electricity is either fed directly into the grid or to batteries for energy storage. The role of integrating renewable energy in a hybrid power system is primarily to save diesel fuel. Figure 2 shows solar and wind based hybrid power system which is mostly used for electrification of a house [9].

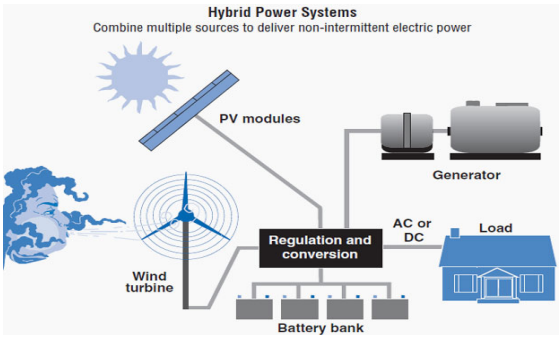

Figure 2: Most widely used hybrid power system for electrification of a house.

The prime negative point of traditional way of producing electrical energy is that it pollutes the environment severely and is too much expensive. But hybrid power system is extremely environment friendly and less expensive. In some cases where transportation and distribution of electrical energy is about to impossible, hybrid power system is blessing for that location.

4. PROPOSED HYBRID POWER SYSTEM

The proposed hybrid system is designed for both on grid and off grid operation to reduce dependency on the national grid for electrical supply.

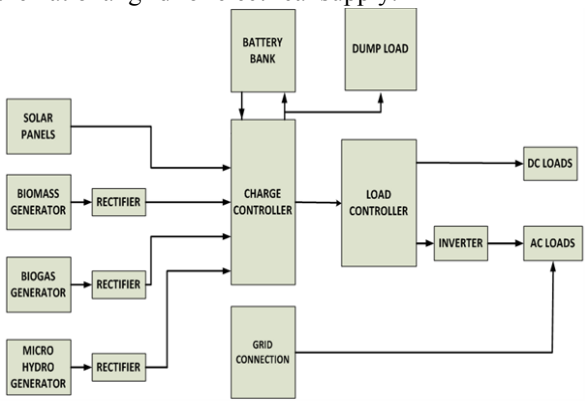

Figure 3: The configuration of proposed hybrid power system.

Figure. 3 shows that the hybrid power system consists of PV generators, biogas generator, biomass (rice husk) generator, micro-hydro generator, battery bank, battery charge controller and the dump load. The provisions for the availability of both AC and DC buses are made using converters. Here the dump load is used to put power when the batteries are fully charged. Then the output from charge controller is used to control loads and inverter, so that we may get both DC and AC output. The DC loads are directly supplied from load controller whereas an inverter is used to supply to the AC loads.

5. PRESENT STATUS OF RENEWABLE ENERGY IN BANGLADESH

The government has instituted a policy to meet five percent of the country's total electricity demand by 2015 and 10 percent by 2020 from renewables.

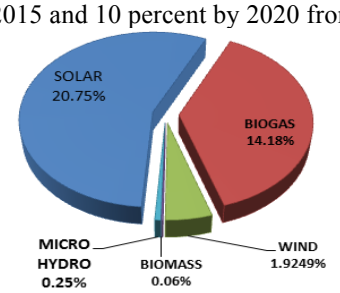

Figure 4: Contribution of renewable sources in Bangladesh.

Figure 4 shows the contribution of different implemented renewable sources in Bangladesh where solar energy contributes maximum of 20.75% and micro hydro contributes minimum of 0.25%.

5.1 SOLAR POWER

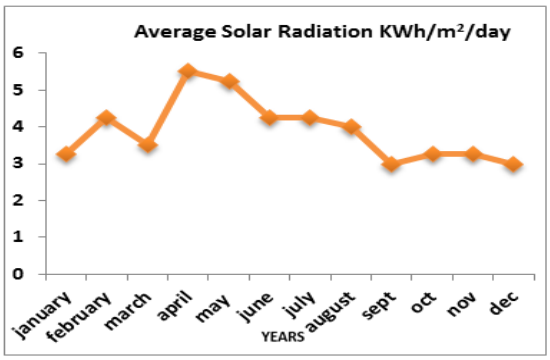

Figure 5: Monthly average solar radiation profile in Bangladesh

Figure 5 shows monthly average solar radiation profile in Bangladesh it is found that average solar radiation KWh/m^2/day is maximum at April and minimum at December.

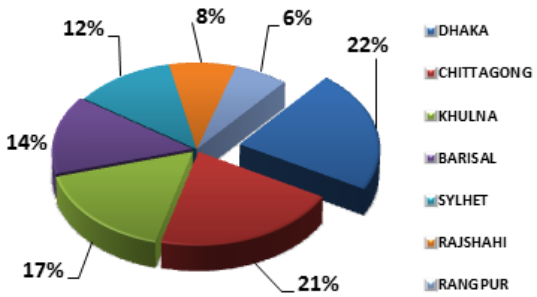

Figure 6: Distribution of the SHSs (Solar Home System) in seven divisions in Bangladesh.

Figure 6 shows the distribution of the Solar Home System in seven divisions in Bangladesh. Maximum solar home system is implemented at Dhaka of about 22% and minimum at Rangpur of about 6%.

According to [1], in Bangladesh about 376MW and 1480MW of electricity generation is possible to harness from solar energy by 2015 and 2020 respectively.

5.2 BIOMASS

Bangladesh is a major rice producing country. It produces on the average about 35,000,000 MT of Paddy per Year. If only 20% of this paddy i.e. 7,000,000 MT could be made useful through the gasification technology; then the Power generation from Rice Husk could be of a significant amount [6]. By using the gasification technology the output equation for a biomass generator is given by (considering 50% efficiency):

$$P_{biomass} = \frac{50\%\ of\ 7{,}000000\frac{MT}{year}\ rice\ husk * 1000\frac{kgs}{MT} * 1000}{2\ kgs\frac{husk}{kwh} * 16\ hours\ operation\ a\ day * 300\ days\ /year} \quad (1)$$

This is approximately 364 MW of power generation. Where we assume that, 2 Kgs of husk is needed in an hour to produce 1 KW of power. [1 MT = 1,000kgs]

Figure 7 shows rice production in Bangladesh in pase eleven years where it is found that rice produced in year (2010-11) maximum and it is 35000 thousand metric ton [2].

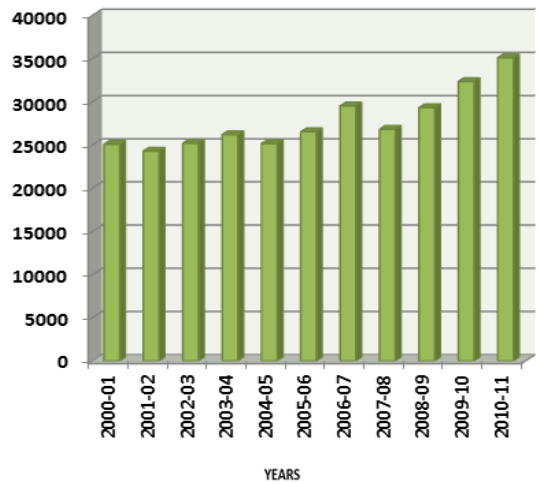

Figure 7: Rice production (Thousand Metric Ton) in Bangladesh in past eleven years

5.3 BIOGAS

The total electricity in kWh that can be produced from biogas can be found with the following equation.

$$e\ biogas = Ebiogas\ [BTU] \times 0.00293 \times \eta (inKW) \quad (2)$$

Where, Ebiogas is unconverted raw energy in the biogas typically listed in BTUs(Biogas Technologies Unlimited); e biogas is the total electricity that can be generated from biogas, and η is the overall conversion efficiency.

From view point of temperature and raw materials Bangladesh is a best suitable country for biogas. Along with government several NGO's like Grameen Shakti has completed 13,500 biogas plants, Seed Bangla Foundation has proposed a 25 KW Biogas based Power Plant, IDCOL fixed a target to set up 37,669 biogas plants in Bangladesh by 2012. Form biomass and biogas it is possible to get 60MW and 120MW of electricity by 2015 and 2020 respectively [1]

5.4 MICRO HYDRO

By installing micro and mini hydro power plant in hilly area of Bangladesh it is possible to get 20MW of electricity by 2020 [1]. A recent study has been carried out on micro hydro power plant starting capacity from 3KW to 30KW. These plants are in:

- NunchariTholipara, Khagrachari
- Chang-oo-Para, Bandarban

• Bangchari, Bandarban
• Liragaon, Bandarban
• Kamalchar, Rangamati
•ThangKhrue, Rangamati
• Monjaipara, Bandarban

6. SOLAR TRACKING SYSTEM FOR IMPROVING EFFICIENCY

The proposed PV panel is based on following components: a DC motor, voltage mode driven, with current monitoring, without movement sensors (speed or position), a motor control system, completely digital, a measurement system for light intensity applied to the PV panel which is shown in figure 8.

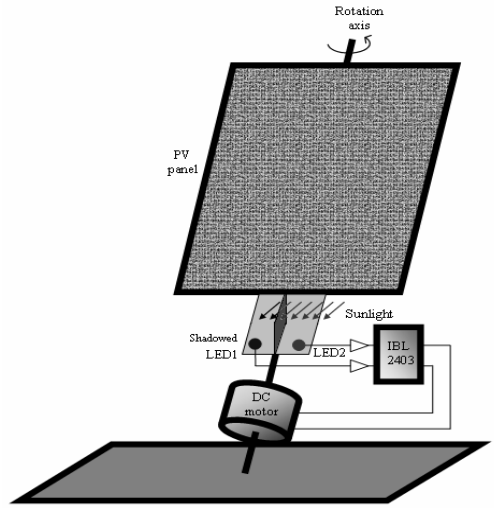

Fig. 8: Principle of light sensors and motion control of PV panel

6.1 MOTOR DRIVE SYSTEM

The parameters of the DC motor used as the movement execution element are: rated voltage 24V, rated current 3A, maximum speed 3000rpm, gear box with a speed reduction ratio of 1:20.

6.2 LIGHT INTENSITY SENSOR

To command the PV panel motion, two light intensity sensors was used, execute dusing two luminescent diodes of LED type, placed so that the signal they generate is correlated with the light intensity applied to the PV panel. When the motor is not active the power circuit of the IBL2403 drive can be completely deactivated and minimizing energy consumption.

6.3 EXPERIMENTAL MODEL AND RESULT

Based on the design configuration a completely operational small scale experimental model of a single axis solar tracking system has been executed. With this model specific control components have been evaluated using the Technosoft Easy Motion Studio Platform. Starting from this small scale equipment the proposed technology can be implemented in larger power PV systems.

7. CONCLUSION

In this paper, a novel model of an effective, convenient and robust hybrid system has been proposed especially for the rural and remote areas of Bangladesh where it is difficult to provide a continuous power supply from national grid connection. A contemporary scenario of Bangladesh's renewable energy sector has been presented using data and illustrations, on the basis of careful literature review and fieldworks. It can be an excellent, cost effective and also a reliable solution to mitigate the existing power crisis if we can implement this project properly. It has a great impact on improving the socio-economic condition of rural people as well as will be a good sign of green energy technology.

8.REFERENCES

[1] D. M. Rahman, F. M. Mohammedy, A. R. Rume, and N. Nahar, "Prospects of renewable energy and its current status in Bangladesh", *International Conference on Climate Change Effects and Energy Development.* Germany, Jul.2011.

[2] Dewan Mowdudur Rahman[1,*], Navid bin Sakhawat[2], Riasad Amin[1], and Faisal Ahmed[3], "A Study on Renewable Energy as a Sustainable Alternative for ensuring Energy Security in Bangladesh and Related Socio-Economic Aspects", *Engineering Journal,* Vol 16, No 2(2011).

[3] Md. Zunaid Baten, Md. Amin, Raisul Islam, Shahriar A. Chowdhury, "Renewable Energy Scenario of Bangladesh: Physical Perspective", ICDRT-2009, Dhaka, Bangladesh.

[4] REN21 "Renewables 2011: Global Status Report", p. 17, 18 (2011). .

[5] I. Sharif, "Renewable Energy Development in Bangladesh," Executive Exchange on the use and Integration of Renewable Energy in the Power Sector, Madrid, Spain, 2009.

[6] Md. Tariful Islam, Monojit Sarkar, " Study of Hybrid Power System in the Present Prospect of Bangladesh", B.Sc dissertation, EEE, RUET, 2012.

[7] http://www.powerdivision.gov.bd/endex.php/

[8] http://www.lged-rein.org

[9] http://www.bestpowerinverter.com/blog/2012/03/

Proceeding of the
International Conference on Electrical, Computer and Telecommunication Engineering
01- 02 December 2012 (ICECTE2012), RUET, Rajshahi-6204, Bangladesh

ICECTE2012: PI-107

A Novel Technique for Initial Fragmentation of Distributed Database

Shahidul Islam Khan[1], Dr. A. S. M. Latiful Hoque [2]
[1]Department of CSE, International Islamic University Chittagong (IIUC), Chittagong, Bangladesh
[2]Department of CSE, Bangladesh University of Engineering & Technology (BUET), Dhaka, Bangladesh
E-mail: nayeemkh@yahoo.com, asmlatifulhoque@cse.buet.ac.bd

ABSTRACT
An efficient way of improving performance of a database management system is distributed processing. Distribution of data involves fragmentation, replication and allocation process. Previous research works provided fragmentation solution based on empirical data which are not applicable at initial stage of distributed database. In this paper we have presented a fragmentation technique that can be applied at the initial stage as well as in later stages of a distributed database system for partitioning the relations. Experimental results show that our proposed technique can solve the initial fragmentation problem properly.

KEYWORDS: D***istributed system, Initial fragmentation, Allocation, MCRUD matrix, Attribute ocality precedence***

I. INTRODUCTION

A distributed database management system (DDBMS) is defined as the software system that provides the management of the distributed database system and makes the distribution transparent to the users. The sites of the distributed database can have the same network address and may be in the same room but the communication between them is done over a network instead of shared memory. Design of efficient distributed databases is one of the major research problems. Primary concern of distributed database design is to making fragmentation of the relations, allocation of the fragments in different sites of the system, and local optimization in sites [1], [2].

Fragmentation is a design technique to divide a single relation or class of a database into two or more partitions such that the combination of the partitions provides the original database without any loss of information. [1]. Fragmentation can be horizontal, vertical or mixed/hybrid. Horizontal fragmentation (HF) allows a relation or class to be partitioned into disjoint tuples. Vertical fragmentation (VF) partitioned a relation or class into disjoint sets of columns or attributes except the primary key [1], [2]. Combination of horizontal and vertical fragmentations to form mixed or hybrid fragmentations (MF) are also proposed [3]. Allocation is the process of assigning the fragments of a database on the sites of a distributed network.

The main reasons of fragmentation of the relations are to: increase locality of reference of the queries, improve reliability and availability of data and performance of a system [1]-[4]. Combined problem of fragmentation and allocation is NP-hard [5].

HF using minterm predicate is first proposed by Ceri et al. (1982) [6]. Navathe et al. (1984) used attribute usage matrix (AUM) and Bond energy algorithm to produce vertical fragments [7]. Navathe and Ra (1989) improved the previous work on VF by proposing an algorithm using a graphical technique [8]. Shin and Irani (1991) proposed knowledge based approach in which user reference clusters are derived from the user queries [9]. Ra (1993) presented a graph based algorithm for HF in which predicates are clustered based on the predicate affinities [10]. Navathe et al. (1995) first proposed MF technique[3]. Ozsu and Valduriez (1999) proposed an iterative algorithm COMMIN to generate a complete and minimal set of predicates from simple predicates [1].

Cheng et al. (2002) presented a genetic algorithm based fragmentation approach that treats horizontal fragmentation as a traveling salesman problem [11]. Bai˜oo et al. (2004) inputted predicate affinity matrix to build a predicate affinity graph [4]. Ma et al. (2006) used an attribute uses frequency matrix (AUFM) and a cost model for VF [12]. Abuelyaman (2008) proposed a static algorithm StatPart for initial VF [13]. Runceanu A. (2008) presented a partition evaluator that used AUM to select attributes for VF [14]. Mahboubi H. and Darmont J. (2009) used predicate affinity for HF in data warehouse [15].

In this paper we have presented a novel technique for horizontal fragmentation of the relations of a distributed relational database that is capable of taking proper fragmentation decision at initial stage. The work of this paper is to extend our work in [16].

The rest of this paper is organized as follows. In section II we have described our developed technique. Our results and discussion are presented in Section III. Finally Section IV concludes the paper with further research directions.

II. MCRUD MATRIX BASED FRAGMENTATION

To solve the problem of taking proper fragmentation decision at the initial stage of a distributed database, we have developed a new fragmentation technique namely MCRUD Matrix based Fragmentation technique (MMF). Instead of using empirical data, we have developed Modified Create, Read, Update and Delete (MCRUD) matrix to obtain fragmentation decisions. That is to fragment a relation horizontally according to locality of precedence of its attributes.

Attribute locality precedence (ALP) can be defined as the value of importance of an attribute with respect to sites of distributed database. ALP table will be constructed by database designer for each relation of a DDBMS at the time of designing the database using MCRUD matrix and cost functions. A block diagram of our system is depicted in Fig. 1.

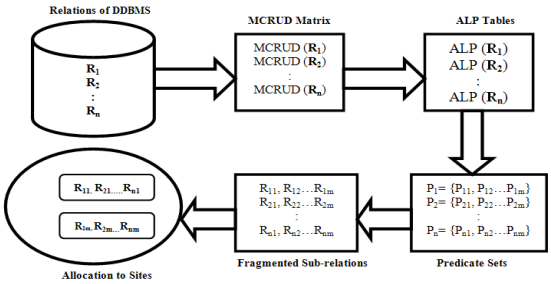

Figure 1. Block diagram of MMF Technique

A data-to-location CRUD matrix is a table of which rows indicate attributes of the entities of a relation and columns indicate different locations of the applications [17], [18]. We have modified the existing CRUD matrix according to our requirement of HF and name it MCRUD matrix. It is a table constructed by placing predicates of attributes of a relation as the rows and applications of the sites of a DDBMS as the columns [16]. We treated cost as the effort of access and modification of a particular attribute of a relation by an application from a site. To calculate precedence of attributes we took MCRUD matrix as input and use following cost functions:

$$C_{i,j,k,r} = f_C C + f_R R + f_U U + f_D D \quad (1)$$

$$S_{i,j,k} = \sum_{r=1}^{A_{ijk}} C_{i,j,k,r} \quad (2)$$

$$S_{i,j,m} = \text{Max}\,(S_{i,j,k}) \quad (3)$$

$$ALP_{ij} = S_{i,j,m} - \sum_{k \neq m}^{A_{ijk}} S_{i,j,k} \quad (4)$$

$$ALP_{i} = \sum_{j=1}^{J} ALP_{i,j} \quad (5)$$

Here f_C = frequency of create operation
f_R = frequency of read operation
f_U = frequency of update operation
f_D = frequency of delete operation
C = weight of create operation
R = weight of read operation
U = weight of update operation
D = weight of delete operation
$C_{i,j,k,r}$ = cost of predicate j of attribute i accessed by application r at site k
$S_{i,j,k}$ = sum of all applications' cost of predicate j of attribute i at site k
$S_{i,j,m}$ = maximum cost among the sites for predicate j of attribute i
ALP_{ij} = actual cost for predicate j of attribute i
ALP_i = total cost of attribute i (locality precedence)

After construction of ALP table, predicate set P is generated for the attribute with highest precedence value. Finally each relation is fragmented horizontally using the predicates of P as selection predicate. The procedures can be understood from the following algorithm of Fig. 2. The space and time complexity of MMF have been discussed in following subsections.

Input: *Total number of sites: $S = \{S_1, S_2, \ldots, S_n\}$*
Relation to be fragmented: R
Modified CRUD matrix: MCRUD[R]
Output: Fragments $F = \{F_1, F_2, F_3, \ldots, Fn\}$
Step 1: Construct ALP[R] from MCRUD[R] based on Cost functions
Step 2: For significant highest valued attribute of ALP table
a. Generate predicate set $P=\{P_1, P_2, \ldots, P_m\}$
b. Fragment R using P as selection predicate

$$\forall_p \mid \sigma_p(R)$$

c. Allocate F to S
*Step 3: For non-significant-highest-value (Max-Highest<1.5*2nd-Highest) in ALP[R]*
a. REPLICATE R to $\sum_{j=1}^{n} S_j$ *if R is an entity set*
b. Derive Horizontally Fragment R using its owner relation if R is a relationship set

Fig. 2. FragmentationAllocation algorithm

A. Memory Cost Analysis

To store the MCRUD matrices of different relations in the system, we have used four dimensional arrays. For calculating ALP values we have to store four things: site number, application number, attribute number and predicate number. These values will be stored in 4D arrays and ALP tables are constructed using the arrays. Cost of each cell of MCRUD matrix is computed by the cost function of equation 1.

This is represented in pseudo-code of Fig.3in [17] as:

$$C[i][j][k][r] = f_c*C + f_r*R + f_u*U + f_d*D,$$

Where i: attribute number, j: predicate number, k: site number and r: application number. In this thesis number of sites is denoted by S, number of applications is denoted by N, number of Predicates is denoted by P and number of attributes is denoted A. So space requirement to store an MCRUD matrix will be O(S*N*A*P) or O (n^4) if S≈ N≈ A ≈P ≈ n.

B. Computational Cost Analysis

Creation of MCRUD matrix for every relation and calculation of ALP from each matrix adds some additional cost in our system. Its maximum computational cost is dominated by the computation within four nested loops. The code is as follows:

```
for ( i =1; I <= TotalAttributes; i++){
```

```
for ( j =1; j <= TotalPredicates[i]; j++){
        for ( k =1; k <= TotalSites; k++){
for ( r =1; r <= TotalApplications[k]; r++)
        C[i][j][k][r] = fc*C + fr*R + fu*U + fd*D
S[i][j][k] + = C[i][j][k][r]
```

So computational order is O (i*j*k*r). As i_{max} =A, j_{max}=P, k_{max}=S and r_{max}=N, so we can rewrite the order as or O (n^4) if we treat S≈ N≈ A ≈P ≈ n.

Actual problem of horizontal fragmentation and allocation is O (k^{2^n}) where there are *n* simple predicates and *k* sites. This is impossible in practical large database systems [8]. We have reduced it to O (n^4) by providing solution based on heuristic that use MCRUD matrix. Our cost can be ignored because ALP calculation from MCRUD matrix will be performed *offline* during analysis phase.

III. Result and Discussion

We have implemented a distributed banking database system in the post-graduate lab of BUET using three DELL computers each with Core-two Duo 2.80 processors and 2GB RAM. We have used Oracle 10g for database creation. Initially number of sites of the distributed system is three as shown in Fig.3.

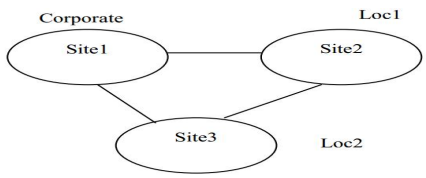

Figure 3. Distributed banking database system

A. Construction of MCRUD Matrix

We have constructed the MCRUD matrix for each relations in the requirement analysis phase.

B. Calculation of ALP values

We have calculated locality precedence of each attribute from the MCRUD matrix. Using the ALP values we have constructed ALP table for each relation. Detail calculation is explained in [16].

C. Generation of Predicate Set & Fragmentation

Predicate set was generated for the attributes with highest locality precedence of all relations respectively. According to predicate set, fragmentations of all relations were performed.

We have executed twenty queries in each site with a total of sixty selected queries in the distributed system according to Pareto Principle [19], [20] to see the performance of MMF.

The queries were selected from following *query domain*:

Insertion e.g. Insert into RRR values (xxx, yyy, zzz)

Selection (Point) e.g. Select A_1, $A_{2...}$ A_n from RRR where xxx= P

Selection (Range) e.g. Select A_1, $A_{2...}$ A_n from RRR where xxx< BBB

Selection (Join) e.g. Select A_1, $A_{2...}$ A_n from R_1, R_2 where $R_1.A_i$=$R_2.A_j$ AND $R_1.A_k$=CCC

Selection (Aggregation) e.g. Select Sum (AA) from RRR where P

Update e.g. Update RRR set A_i = xxx where A_j = yyy

Deletion e.g. Delete * from RRR where P

We define *hit* as a result of a query of any type accessed records of local fragment of the site where the query was initiated and *miss* as a result of a query of any type accessed records of one or more remote fragments of other sites. Table I shows the overall performance of the distributed system after fragmenting the relations using MMF technique.

TABLE I: Overall System Performance of MMF

Site Name	Queries executed	Access fragment stored in local site	Access fragment stored in remote site	Percentage of Hit	Percentage of Miss
$Site_1$	20	18	2	90%	10%
$Site_2$	20	16	4	80%	25%
$Site_3$	20	17	3	85%	15%
DDBMS	60	51	9	85%	15%

We have named the techniques deals with fragmentation problem of distributed database without addressing the initial stage problem as Techniques without Initial Fragmentation (TWIF) as in [1] – [12], [14] - [15]. TWIF uses the model in general as shown in Fig. 4.

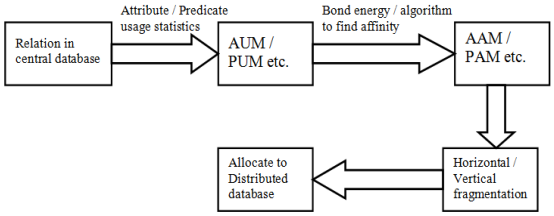

Figure. 4 Model of Non-initial Fragmentation Techniques (TWIF)

We have implemented the above model in our lab and execute the same sixty queries with the assumption that at the initial stage the centralized database is stored at Site1. During a long period before reasonable amount of statistical record are available to construct decision matrix and to fragment and allocate the database among the three sites, percentage of hit of the overall system is only 33.33% which is much less in comparison with our achieved 85% hit rate. The reason of poor performance of all other fragmentation techniques (TWIF) is that, all sites other than central site have no data. So all queries that are generating in those sites requires remote data access thus scores *miss*. Comparison of MMF and TWIF by their hit ratio shown in Fig. 5.

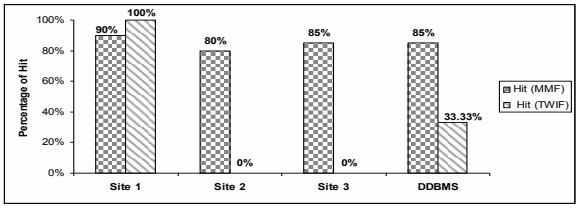

Figure.5 Comparison of Hit between MMF & TWIF for 3 Sites

Fig. 6 shows the hit ratio of MMF and TWIF with the increase of number of sites in the distributed system. We can see that MMF shows much better and quite steady performance as sites increases from three to ten. In the same time performance of TWIF falls gradually as new sites are added to the system.

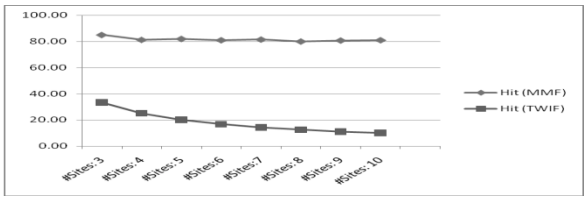

Fig. 6: Comparison of Hit between MMF and TWIF with #Site Increase

Existing technique that provided a solution of initial fragmentation is StatPart described in [13]. To fragment a relation, it starts with a randomly generated matrix called reflexivity matrix. it always suggests two binary vertical fragments independent of number of sites of the DDBS. So this technique is not suitable for a distributed system with more than two allocation sites. Also as it starts with a random matrix steady fragmentation decision cannot be provided using StatPart algorithm.

IV. CONCLUSIONS

Making proper fragmentation of the relations and allocation of the fragments is a major research area in distributed systems. Many techniques have been proposed by the researchers using empirical knowledge of data access and query frequencies. But proper fragmentation and allocation at the initial stage of a distributed database has not yet been addressed. In this paper we have presented a fragmentation technique to partition relations of a distributed database properly at the initial stage when no data access statistics and query execution frequencies are available. Performance of a DDBMS can be improved significantly by avoiding frequent remote access and high data transfer among the sites. This research can be extended to support fragmentation in distributed object oriented databases as well.

REFERENCES

1. M. T. Ozsu and P. Valduriez, *Principles of Distributed Database Systems,* 2nd ed., New Jersey: Prentice-Hall, 1999.
2. S. Ceri and G. Pelagatti, *Distributed Databases Principles and System,* 1st ed., New York: McGraw-Hill, 1984.
3. S. Navathe, K. Karlapalem, and M. Ra, "A mixed fragmentation methodology for initial distributed database design," *Journal of Computer and Software Engineering* Vol. 3, No. 4 pp 395–426, 1995.
4. F. Bai˜ao, M. Mattoso, and G. Zaverucha, "A distribution design methodology for object DBMS," *Distributed and Parallel Databases, Springer*, Vol. 16, No. 1, pp. 45–90, 2004.
5. R. Blankinship, A. R. Hevner, and S. B. Yao, "An Iterative Method for Distributed Database Design," *Proc. 17th Int'l Conf. on Very Large Data Bases,* pp. 389–400, 1991.
6. S. Ceri, M. Negri, and G. Pelagatti, "Horizontal data partitioning in database design," in *Proc. ACM SIGMOD,* 1982, pp. 128–136.
7. S. B. Navathe, S. Ceri, G. Wiederhold, and J. Dour, "Vertical partitioning algorithms for database design," *ACM Transactions on Database Systems (TODS),* Vol. 9, No. 4, pp. 680–710, 1984.
8. S. B. Navathe, and M. Ra, "Vertical partitioning for database design: A graphical Algorithm," *ACM SIGMOD Record,* Vol. 14, No. 4, pp. 440-450, 1989.
9. D. G. Shin, and K. B. Irani, "Fragmenting relations horizontally using a knowledge based approach," *IEEE Transactions on Software Engineering (TSE)*, Vol. 17, No. 9, pp. 872–883, 1991.
10. M. Ra, "Horizontal partitioning for distributed database design," *In Advances in Database Research, World Scientific Publishing*, pp. 101–120, 1993.
11. C. H. Cheng, W. K. Lee, and K. F. Wong, "A genetic algorithm-based clustering approach for database partitioning," *IEEE Transactions on Systems, Man, and Cybernetics*, Vol. 32, No. 3, pp. 215–230, 2002.
12. H. Ma, K. D. Schewe, and M. Kirchberg, "A heuristic approach to vertical fragmentation incorporating query information," in *Proc. 7th International Baltic Conference on Databases and Information Systems (DB&IS)*, 2006, pp. 69–76.
13. E. S. Abuelyaman, "An optimized scheme for vertical partitioning of a distributed database," *Int. Journal of Computer Science & Network Security,* Vol. 8, No. 1, 2008.
14. A. Runceanu, "Fragmentation in Distributed Databases," *Innovations and Advanced Techniques in Systems, Computing Sciences and Software Engineering, Springer*, pp. 57–62, 2008.
15. H. Mahboubi and J. Darmont, "Enhancing XML Data Warehouse Query Performance by Fragmentation," in *Proc. ACM SAC09,* 2009, pp.1555-1562.
16. S. I. Khan, and A. S. M. L. Hoque, "A new technique for database fragmentation in distributed systems," International Journal of Computer Applications (IJCA), Vol. 5, No. 9, pp. 20-24, 2010.
17. J. Whitten, L. Bentley, and K. Dittman, *Systems Analysis and Design Methods*, 6th Ed, McGraw-Hill, 2004.
18. P. Surmsuk, "The integrated strategic information system planning Methodology," *IEEE Computer Society Press*, pp. 467-475, 2007.
19. A. Silberschatz, H. F. Korth, and S. Sudarshan, *Database Systems Concepts.* McGraw- Hill, 2001.
20. C. S. Mullins, Defining Database Performance [Online] Available: *http://www.craigsmullins.com/cnr_db.htm*.

Proceeding of the
International Conference on Electrical, Computer and Telecommunication Engineering
01- 02 December 2012 (ICECTE2012), RUET, Rajshahi-6204, Bangladesh

ICECTE2012: PI-0108

Traffic Road sign detection and recognition for Automotive Vehicles

Md. Safaet Hossain[1], Zakir Hyder[2]
Department of Electrical Engineering and Computer Science
North South University, Dhaka Bangladesh
E-mail: safayeth@gmail.com, voodoox33@yahoo.com

ABSTRACT
Traffic road sign detection and recognition is important for transport system with a robotic eyes or camera while driving in the road. This paper presents an overview of the traffic road sign detection and recognition system. We have developed and implemented the procedure to extract the road sign from a natural complex image. The main objective of this paper is to design and construct a computer based system which can automatically detect the direction of the road sign. This paper is based upon a major approach to detect the direction. In this paper, we will demonstrate the basic idea of how to detect the area and extract it. This system will play an important role for the detection purpose of specific domains like island, schools, traffic sign, universities, hospitals, offices etc.

KEY WORDS: Advanced driver information systems, color/shape processing, computer vision, neural networks, traffic signs recognition.

1. INTRODUCTION

The sign which is placed at the side of roads to impart information to road users is known as road signs or traffic signs. There are four types of traffic signs that are shown in the traffic code: a) warning; b) prohibition; c) obligation and d) informative. Depending on the form and the color, the warning signs are equilateral triangles with one vertex upwards. They have a white background and are surrounded by a red border. Prohibition signs are circles with a white or blue background and a red border. Both warning signs and prohibition signs have a yellow background if they are located in an area where there are public works. To indicate obligation, the signs are circles with a blue background. Informative signs have the same color. Finally, there are two exceptions: a) the yield sign, an inverted triangle; and the stop sign, a hexagon. To detect the position of the sign in the image, we must know the two properties i.e., color and shape.

The applications and the difficulty of road sign detection make road sign detection an interesting problem. In terms of applications, road sign detection is quite important for the road sign recognition problem, since it is the most important step for a road sign recognition system. So far, the researchers have mainly focused on the road sign recognition problem, in which the task of finding road sign in an arbitrary background is usually avoided by either manual segmentation of the input image, or by capturing faces against a known uniform background. In the last decade, road sign detection has attracted great attention, as road sign recognition system requires automatic road sign detection as a first step, especially for images with cluttered background. Road sign detection also has potential applications in human computer interface and surveillance systems. Road sign detection is difficult due to three main reasons. First, there is a large component of non-rigidity and textural differences among road sign. Second, road sign detection is also made difficult because of additional features, such as dust, which can either be present or totally absent from a road sign. All these additional features increase the variability of the road sign patterns that a road sign detection system should handle. Third, the presence of unpredictable imaging conditions in an unconstrained environment increases the difficulty of the task. A change in light source distribution can cause a significant change in the appearance of the road sign image. All these things should be taken into consideration when designing a road sign detection system.

2. Methodology

Real time road sign detection system has been developed by sequence of operations. To achieve a successful road sign detection system we use following methodologies:

- Studying literature on different road sign detection methods and image processing.
- Studying the existing method for road sign detection. Analyze and design for the proposed system.
- Implement the proposed design of the road sign detection. Carrying out experiment and evaluate the system.

The performance of the system has been tested and achieved its desired goal. It was captured by a digital camera and able to detect road sign properly with in a natural image.

3. RELATED WORK

There are many researches in the literature deal with Road Sign Recognition (RSR) problem. In this section, we will explore some of those approaches.

i) Fast grey scale road sign model matching and recognition

Mobile Mapping is a standard technique for compiling cartographic information from a mobile vehicle. [1] author proposes a novel method for modeling the recognition in a Mobile Mapping process that consists in fitting a model to recover the sign distortion and applying recognition techniques on weak classifiers cascade results. High variance of sign appearance has made the detection and recognition of road signs a computer vision problem over which many studies have lately been performed. There are two main approaches in this field, the color-based and the grayscale-based sign recognition. Color-based approach allows reducing false positives results in the recognition process whereas grayscale methods concentrate on the geometry of the model to recognize it. The color-based studies are based on segmentation by thresholding in color space [2][3][4]. Ghica [5] study focused exclusively on neural networks that are used for image filtering and sign recognition, while other approaches are based on genetic algorithms [6]. The studies on gray-scale images use geometric reasoning [7][8] and most of them on the Hough transforms, and usually color is used as a complementary technique to eliminate false positive results of the classification method.

ii) Detection by Adaboost

The Adaboost algorithm presents a general framework to combine classifiers in order to solve the supervised pattern recognition problem [9]. This approach consists of a) choosing a (weak) classifier, b) modifying example weights in order to give priority to examples where the previous classifiers fail, and c) combining classifiers in a multiple classifier. As a result, each state of the boosting process, which selects a new weak classifier, can be viewed as a feature selection process where features correspond to the image pixels values [10]. The input images of our recognition procedure are provided by the weak classifiers cascade detection process [11].

iii) Road Traffic Sign Detection and Classification

[16] author suggest for road vehicles can have three main roles: a) road detection; b) obstacle detection; and c) sign recognition. The first two have been studied for many years and with many good results, but traffic sign recognition is a less-studied field. Traffic signs provide drivers with very valuable information about the road, in order to make driving safer and easier. They think that traffic signs must play the same role for autonomous vehicles. They are designed to be easily recognized by human drivers mainly because their color and shapes are very different from natural environments. The algorithm described in this paper takes advantage of these features. It has two main parts. The first one, for the detection, uses color thresholding to segment the image and shape analysis to detect the signs. The second one, for the classification, uses a neural network. Some results from natural scenes are shown. On the other hand, the algorithm is valid to detect other kinds of marks that would tell the mobile robot to perform some task at that place.

iv) Traffic sign detection

There are four types of traffic signs that are shown in the traffic code: a) warning; b) prohibition; c) obligation; and d) informative. Depending on the format of the color, the warning signs are equilateral triangles with one vertex upwards. They have a white background and are surrounded by a red border. Prohibition signs are circles with a white or blue background and a red border. Both warning signs and prohibition signs have a yellow background if they are located in an area where there are public works. To indicate obligation, the signs are circles with a blue background. Informative signs have the same color. Finally, there are two exceptions: a) the yield sign, an inverted triangle; and b) the stop sign, a hexagon. They were not studied here. To detect the position of the sign in the image, we must know the two properties we talked about before, i.e., color and shape.

v) Color Thresholding

The most intuitive color space is the RGB system. The color of every pixel is defined by three components: red, green, and blue. Because of this, the color threshold has the following expression:

$$g(x,y)=k_1 \quad \begin{cases} R_a \leqslant f_r(x,y) \leqslant G_b \\ G_a \leqslant f_g(x,y) \leqslant G_b \\ B_a \leqslant f_b(x,y) \leqslant G_b \end{cases}$$

$g(x,y)=k_2$ in any other case

where $f_r(x,y)$, $f_g(x,y)$ and $f_b(x,y)$ are, respectively, the functions that give the red, green, and blue levels of each point of the image. One of the greatest inconveniences of the previous color space is that it is very sensitive to lighting changes.

(a)

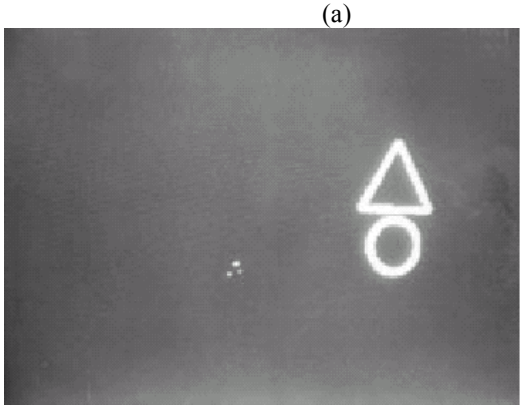

(b)

Figure 1: Color threshold (a) Original image (b)

3.6 Experimental Results

In this section, we will present some results for the red (prohibition) signs. The first row of Figure 2 shows samples of road images. The second row shows the results of the Bayes classifier on the road images set. The third row shows the gray level labels for the red color in the captured images. The last row shows the matching results.

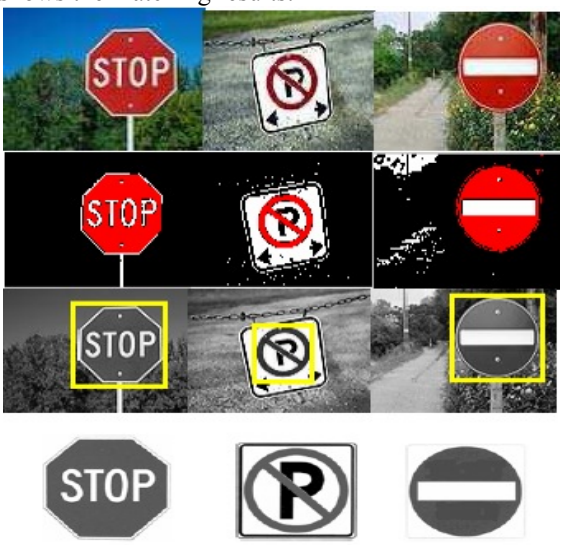

Figure 2: Sample results

4. SYSTEM ARCHITECTURE

Following figure shows the system architecture

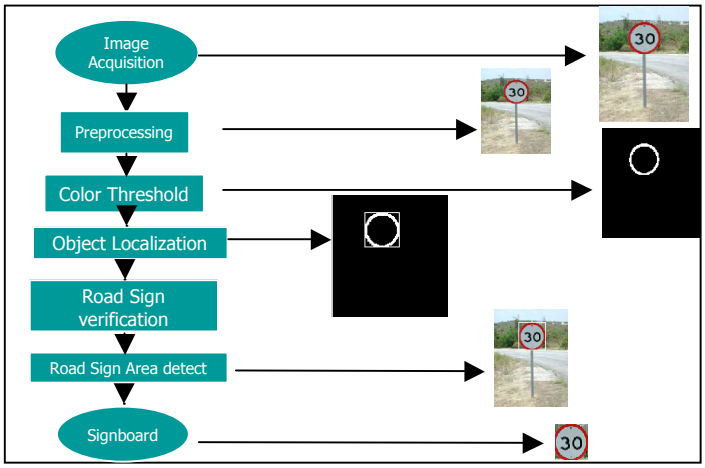

Figure 3: System Architecture

i) Experimental Result:

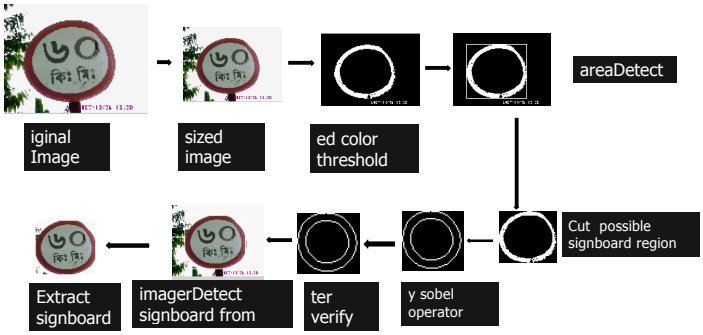

Figure 4: Experimental results with sign detection

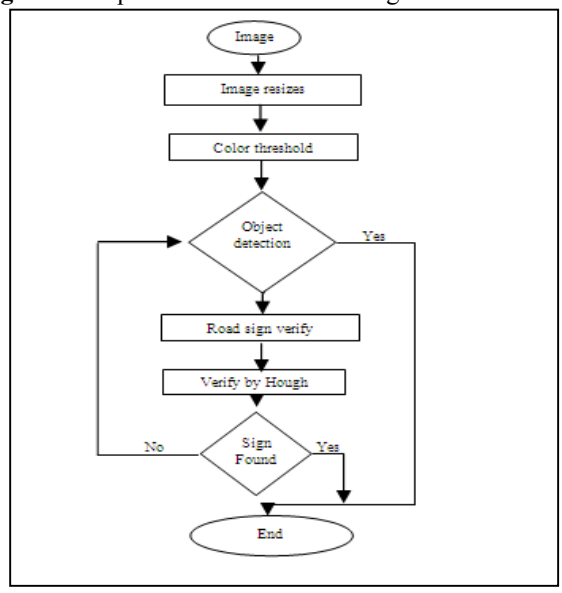

Figure 5: System Flow chart

This paper deals with object detection in outdoor an environment which is usefulness for Driver Support systems and Intelligent Autonomous Vehicles to take some decisions about their speed, trajectory and send

a warning signal indicating over speed, warn or limit illegal ma-noeuvres.

ii) Breadth first search

Bredth first search (BFS) is a searching technique that searches all the space area to locate the region of interest. This technique is widely used for searching. In this project we use to find the problem space where the destination object is road sign.

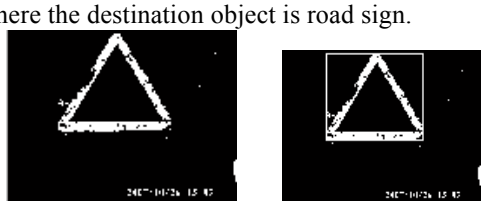

Figure 6: Object detection (a) Threshold image

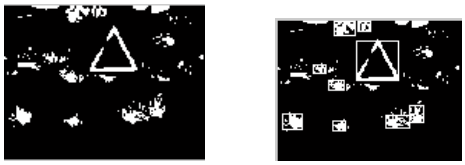

Figure 7: Object detection (b) detect by BFS

iii) Edge detection

Where intensity change abruptly in an image is called edge. In edge detection technique the longest connected component are determine by various operator. In this project work we use sobel operator for detecting edges.

Figure 8: Edge detection

iv) Extract our desired road sign

After verify the detected sign by applying sobel edge detection operator we extract the road sign from background.

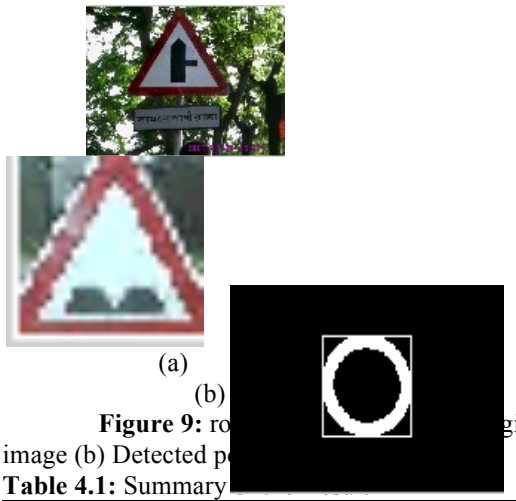

(a)

(b)

Figure 9: ro ginal image (b) Detected p

Table 4.1: Summary

Captured in	No. of Image	Correct result	Error result
Morning	50	85%	15%
Noon	50	90%	10%
Evening	50	82%	18%
Night	50	50%	50%
Total	200	76.75%	23.25%

v) Sample result

Experiment no 1:

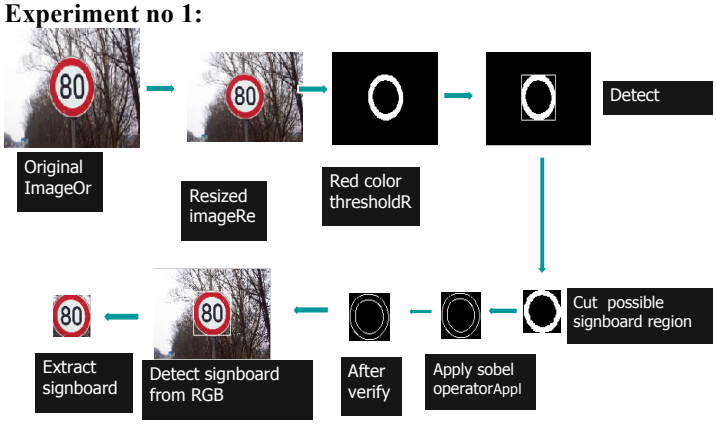

Experiment no 2:

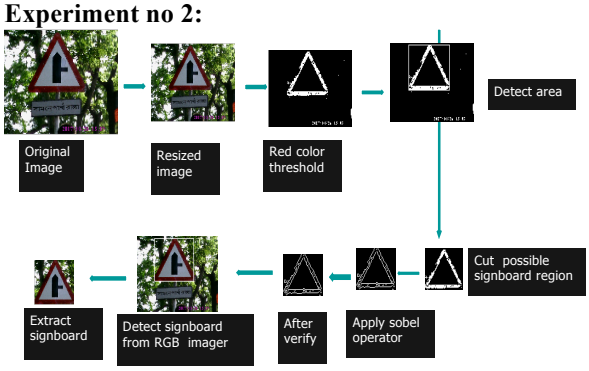

Experiment no 3:

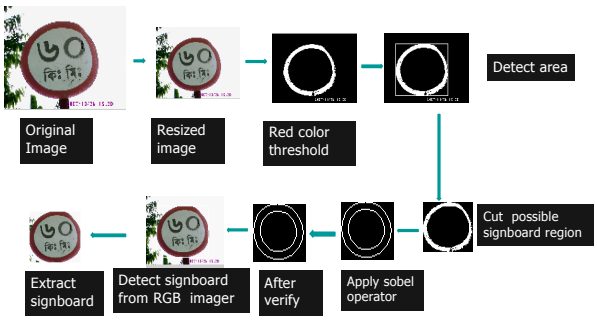

Experiment no 4:

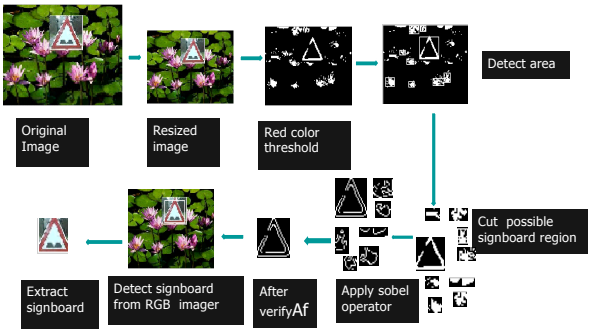

5. CONCLUSION

This paper deals with object detection in outdoor environments which are usefulness for Driver Support systems and Intelligent Autonomous Vehicles to take some decisions about their speed, trajectory and send a warning signal indicating over speed, warn or limit illegal ma-oeuvres. It works only red object detection. This technique is deferent for detecting road sign. It helps researchers because it is time effective one.

6. FUTURE WORK

Automatic Signboard Recognition using Neural Network All colors Signboard Recognition and Text and symbol recognition and Automatic speed warning.

REFERENCES

[1] Sergio Escalera, Alicia Fornés, Oriol Pujol, Josep Lladós, Petia Radeva: Circular Blurred Shape Model for Multiclass Symbol Recognition. IEEE Transactions on Systems, Man, and Cybernetics, Part B 41(2): 497-506 (2011)

[2] D. Kellmeyer and H. Zwahlen. "Detection of highway warning signs in natural video images using color image processing and neural networks." In IEEE Proc. Int.Conf. Neural Networks 1994, volume 7, pages 4226–4231, 1994.

[3] M. de Saint Blancard. "Road sign recognition: A study of vision-based decision making for road environment recognition." In Vision-based Vehicle Guidance, Springer Series in Perception Engineering. Springer-Verlag, 1992.

[4] Arturo de la Escalera, Luis E. Moreno, Miguel Ángel Salichs and José María Armingol "Road Traffic Signs Detection and Classification," CICYT Project TAP94-0711-C03-02, jul. 1996.

[5] R. Ghica, S. Lu, and X. Yuan. "Recognition of traffic signs using a multilayer neural network," In Proc. Can Conf. on Electrical and Computer Engineering, 1994.

[6] A. de la Escalera, J. M. Armingol, M.A. Salichs. Traffic Sign Detection for Driver Support Systems. *3rd International Conference on Field and Service Robotics*, Espoo, Finlandia. June 11-13 (2001).

[7] G. Piccioli, E. D. Michelli, and M. Campani. "A robust method for road sign detection and recognition." In Proc. European Conference on Computer Vision 1994, pages 495–500, 1994.

[8] G. Piccioli, E. D. Michelli, P. Parodi, and M. Campani. "Robust road sign detection and recognition from image sequences." In Proc. Intelligent Vehicles'94, pages 278–283, 1994.

[9] Yoav Freund and Robert E. Schapire. "A decision-theoretic generalization online learning and an application to boosting," Computational Learning Theory: Eurocolt '95, pages 23-37. Springer-Verlag, 1995.

[10] Paul Viola and Michael J. Jones, "Robust Real-time Object Detection," Cambridge Research Laboratory, Technical Report Series, CRL 2001/01. Feb. 2001.

[11] Xavier Baró and Jordi Vitrià Traffic sign detection on grayscale images. Recent advances in artificial intelligence research and development, Frontiers in Artificial Intelligence and Applications, Vol. 113, pp. 209-216. ISBN: 978-1-58603-466-5. October 2004..

[12] Gareth Loy and Alexander Zelinsky, "Fast Radial Symmetry for Detecting Points of Interest," IEEE Transactions on Pattern Analysis and Machine Intelligence, vol. 25, no. 8, Aug. 2003.

[13] Andrew Ditzgibbon, Maurizio Pilu, and Robert B. Fisher, "Direct Least Square Fitting of Ellipses," Tern Analysis and Machine Intelligence, vol. 21, no. 5, may. 1999.

[14] R. Brunelli and T. Poggio, "Face Recognition: Features vs. Templates," IEEE Trans. Pattern Analysis and Machine Intelligence, vol. 15, no. 10, pp. 1,042- 1,053, oct. 1993.

[15] Peter N. Belhumeur, Joao P. Hespanha, and David J. Kriegman, "Eigenfaces vs. Fisherfaces: Recognition Using Specific Linear Projection,"

IEEE Transactions on Pattern Analysis and Machine Intelligence, vol. 19, no. 7, jul. 1997.

[16] Arturo de la Escalera, Luis E. Moreno,"Road Traffic Sign Detection and Classification", IEEE Transaction on Industrial Electronics, VOL 44, NO 6, pp. 848–859 December 1997

[17] L. Dreschler and H. Nagel, "Volumetric model and 3-D trajectory of a moving car derived from monocular TV-frame sequence of a streetscene," in Proc. IJCAI, 1981, pp. 692–697.

[18] M. Shah and R. Jain, "Detecting time-varying corners," Comput. Vision, Graph., Image Processing, vol. 28, no. 3, pp. 345–355, Dec. 1984.

[19] L. Kitchen and A. Rosenfeld, "Gray-level corner detection," Pattern Recognit. Lett., vol. 1, pp. 95–102, 1982.

[20] O. A. Zuniga and R. Haralik, "Corner detection using the facet model," in Proc. IEEE CVPR Conf., 1983, pp. 30–37.

[21] David G. Lowe, ìObject Recognition from Local Scale Invariant Featuresî, ICCV 1999, pp. 1150-1157, 1999.

[22] K. Rangarajan, M. Shah, and D. Van Brackle, "Optimal corner detector," Comput. Vision, Graph., Image Processing, vol. 48, no. 2, pp. 230–245,Nov. 1989.

[23] J. Torresen, J. W. Bakke, and L. Sekania. Efficient recognition of speed limit signs. In Proc. IEEE Conf. on Intelligent Transportation Systems (ITS), Washington, DC, 2004.

[24] P. Viola and M. J. Jones. Robust real-time object detection. Technical Report CRL 2001/01, Cambridge Research Laboratory, 2001.

[25] B. Xie, D. Comaniciu, V. Ramesh, T. Boult, and M. Simon.Component fusion for face detection in the presence of heteroscedastic noise. In 25th Pattern Recognition Springer Verlag.

[26] M. M. Zadeh, T. Kasvand, and C. Y. Suen. Localization and recognition of traffic signs for automated vehicle control systems. In Proc. SPIE Vol. 3207, Intelligent Transportation Systems, pages 272–282, 1998.

[27] Y. Zhu, D. Comaniciu, M. Pellkofer, and T. Koehler. An integrated framework of vision-based vehicle detection with knowledge fusion. In IEEE Intelligent Vehicles Symposium (IV), Las Vegas, NV, 2005.

[28] M. de Saint Blancard. "Road sign recognition: A study of vision-based decision making for road environment recognition." In Vision-based Vehicle Guidance, Springer Series in Perception Engineering. Springer-Verlag, 1992.

Proceeding of the
International Conference on Electrical, Computer and Telecommunication Engineering
01- 02 December 2012 (ICECTE2012), RUET, Rajshahi-6204, Bangladesh

ICECTE2012: PI-0109

Intelligent Eye: Sound Based Event Detection and Camera Control

Md. Rokunuzzaman [1], Md. I. H. Bhuiyan[1], Md. Abul Munjer[1], Md. Monjur Elahi[2], M.A. Kader[1]
[1]Department of Mechanical Engineering, [2]Department of Electrical & Electronic Engineering
Rajshahi University of Engineering & Technology
E-mail: rzaman_mctr@yahoo.com, saddam_6@yahoo.com

ABSTRACT
An intelligent eye always responds when the intensity of sound changes due to some event. This capability can nicely complement vision to help localize a person or an interesting event in the environment. Event detection using audio streams presents a hierarchical approach for audio based event detection. In this paper, we present a sound source localization method in three-dimensional space using an array of microphones sensor. The proposed method is based on time delay of arrival estimation and position estimation. Our proposed system can localize in real time different types of sound sources over a significant range and respond accordingly.

KEY WORDS: Sound source localization, Event detection, Camera control.

1. INTRODUCTION

Sound is an important cue for perception, especially when the vision system is unable to detect events occurring at a high speed. To become intelligent, systems or robots should have to understand situation, make decisions and interact accordingly. It is very difficult to understand situation using only vision sensor, because vision sensor must be able to collect necessary information of the event. Moreover, the collected information needs to process so that it can represent some concept of the event. The processing of high level knowledge and recognition algorithms needs sufficient amount of time. Furthermore, to focus on interesting event, special algorithms need to develop in the system. Therefore, we develop some simple systems which can localize the sound source and guide the camera to focus on that event instantly. This will help the vision system to restrict its search area and lowers down its computational cost of information processing.

The main purpose of the paper is to develop some sensing and controlling systems for the mobile robots for detecting an intense sound in the 3D space and locate the region by pointing a camera towards it. Sound source localization for mobile robots is very interesting research topic. Different approaches are proposed in [1], [2]. The sound source localization is useful for surveillance based applications such as in Hazardous situations [3], event detection in acoustic activities [4],[5], or anti-social behavior detection [6]. Camera control according to sound events are discussed in [7], [8]. Sound based event detection is the technology to detect sound sources with the help of the installed sensors in a definite platform and respond accordingly to transmit a signal to a specific place as required.

2. FORMULATION

Our sound source localization is based on time delay of arrival estimation [9] which is very popular and simple technique for this area of research.

Let $s(n)$ be the source signal, and $x_1(n)$, $x_2(n)$ be the signals received at the two sensors under additive noise conditions. The following relations hold assuming no multi-path distortions.

$$x_1(n) = \alpha s(n-D) + n_1(n) \tag{1}$$

$$x_2(n) = \beta s(n) + n_2(n) \tag{2}$$

Where n_1 (n) and n_2 (n) represent noise signals received at the two sensors. The cross correlation of the signals received at the two sensors is

$$R_{x_1x_2}(\tau) = \alpha\beta R_{ss}(\tau - D) + R_{n_1n_2}(\tau) \tag{3}$$

Assuming that the source signal is not correlated with the noise. D represents the delay of signal arrival between the two sensors. The cross power spectrum (The Fourier Transform of Equation (3))

$$G_{x_1x_2}(\omega) = \alpha\beta G_{ss}(\omega)e^{-j\omega D} + G_{n_1n_2}(\omega) \tag{4}$$

We assume that the background noise is stationary, but might be correlated (such as the noise from a ceiling fan or an overhead projector, etc). Background noise $G_{n1n2}(\omega)$ is estimated for each frequency during a period when the source signal is not present. Subtracting the background noise, the cross spectrum becomes

$$G'_{x_1x_2}(\omega) = G_{x_1x_2}(\omega) - G_{n_1n_2}(\omega) = \alpha\beta G_{ss}(\omega)e^{-j\omega D} \tag{5}$$

The normalized cross correlation, i.e. the Phase Transform [7] is therefore given by

$$\hat{R}_{x_1x_2}(\tau) = \frac{1}{2\pi}\int_{-\pi}^{\pi} \frac{G'_{x_1x_2}(\omega)}{\left|G'_{x_1x_2}(\omega)\right|} e^{j\omega\tau} d\omega \tag{6}$$

$$= \delta(\tau - D)$$

The time delay is estimated as the time lag that has the maximum cross-correlation coefficient

$$D = \arg\max_{\tau} \hat{R}_{x_1x_2}(\tau) \tag{7}$$

3. SOUND BASED EVENT DETECION

In this paper, we define an event is the occurrence of sound pulse created by clapping of hand, speaking in front of microphone sensor or dropping of any object..

3.1 Experimental Setup

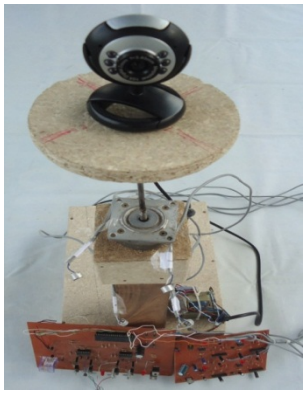

Fig. 1 Experimental setup

Figure 1 shows the experimental setup for camera panning mechanism for event detection system. In this setup, a stepper motor is used to orient the camera toward the sound source when there is any event around microphone sensors. This setup carries sound sensing circuitry, motor driver circuitry and stepper motor with disc which carries a web camera. All the components are covered inside the wooden and partex boards which is rugged in construction and low in weight.

3.2 Sound Sensing Circuitry

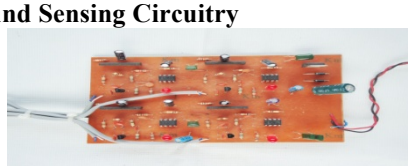

Fig. 2 Sound sensing circuitry

Figure 2 shows the sound sensing circuitry for 4 microphone sensors. For each sensor, we have one circuit which is shown in Figure 3.

In this circuit we use KA2284 IC which converts sound signal to an electric signal. It is then fed to the IC 555 to trigger the driving circuit for controlling the camera.

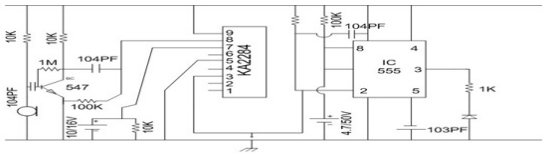

Fig. 3 Circuit diagram for microphone sensor

3.3 Driver Circuitry for Camera Panning

The project consists of a webcam with pan mechanism on an installed platform to detect the sound source for monitoring. Sensors surrounding the webcam will receive the audio streams from the sources of sound and then convert it to electric signal. Here four microphone sensors are used to sense the sound from the surrounding in order to cover 360^0. The installed circuit provides good gain to weak audio signals. The sound sensing is done with the ADC of the ATmega as shown in Figure 4. A simple program reads the analog value of the amplifier over and over. If the value (loudness) exceeds a specific level, an LED is lit responding to the sound.

Then the amplified signal is fed into the microcontroller. Microcontroller input determines the direction of sound source. There are four inputs to the MCU each of which indicates East, West, North and South respectively. Then according to the MCU input degree of rotation is calculated in accordance with the program burnt on the microcontroller for the stepper motor.

Fig. 4 Driver circuitry for camera panning

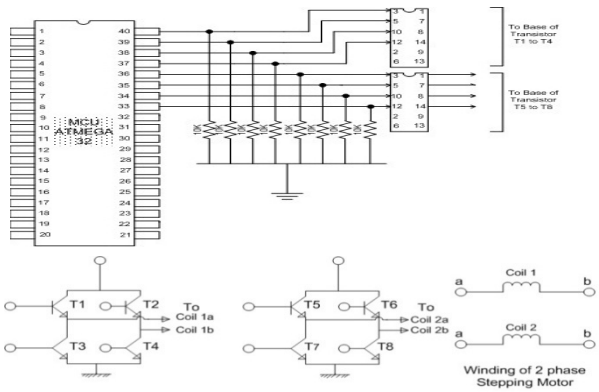

By this time MCU will check the direction of sound source whether in line with the webcam position or not. If the direction of sound source is in line with the webcam position, MCU will not generate any pulse to drive the stepper motor. Otherwise MCU will generate required number of pulse to rotate the stepper motor at a desired angle which eventually rotates the webcam. Then webcam is moved to source of sound smoothly and show the image in the monitor.

The LM324 chip acts as a connector between the controller and the driving circuit as well as to protect the controller from any uncertainty.

3.4 Methodology

Figure 5 shows the methodology of sound detection and camera control with the help of a block diagram. First the sound is generated by any event, for example, lapping of hands or shouting in front of the microphone. Then the sound is processed through the sound processing circuit. The processed sound signal is fed into a microcontroller circuit. The MCU (Micro-Controller Unit) computes the necessary pulses for the driver circuit to control the stepper motor. A shaft is connected to the motor shaft of the

stepper motor. The shaft also carries a disc which carries a web camera. This mechanism is named as Pan Mechanism. This mechanism makes an orientation of the webcam to focus on to the source of the sound.

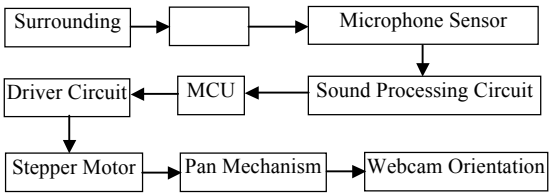

Fig. 5 Method of sound based event detection

3.5 Algorithm of sound based event detection

Figure 6 shows the algorithmic flow chart of sound based event detection.

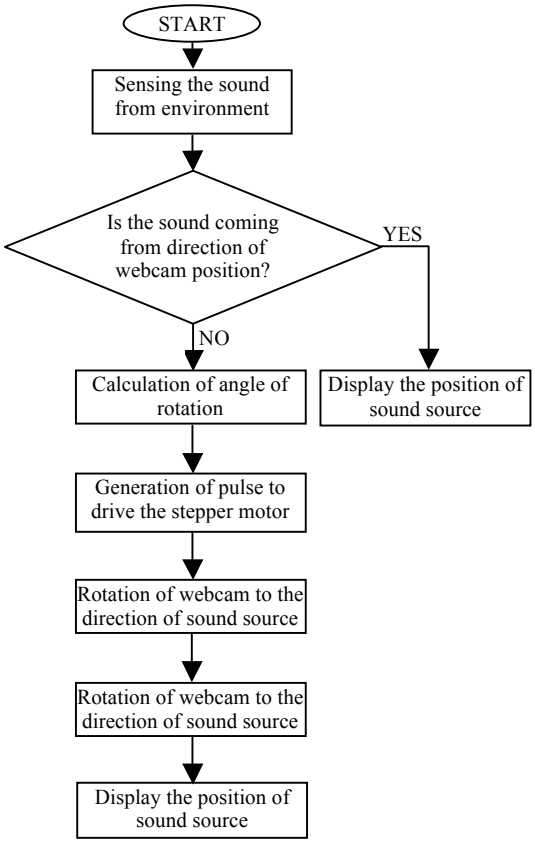

Fig. 6 Algorithm of sound based event detection

4. EXPERIMENTAL RESULTS

In order to evaluate our project we conduct several experiments. The performance of the project depends on the sensitivity or accuracy of the microphone sensors when there are sound events in front of the microphone sensors. Figure 7 shows the arrangement of microphone sensors and sound events.

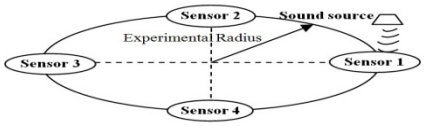

Fig. 7 Experimental arrangement of sensors

Table 1: Performance of sensor 1 for various experimental radii

Experimental Radius	Distance between Sound Source & **Microphone Sensor 1**	Minimum Sound Intensity(dB)				Accuracy
		Mic1	Mic2	Mic3	Mic4	
0.25m	0.25m	**64**	62	61	62	0%
	0.50m	**66**	64	63	64	25%
	0.75m	**69**	67	65	67	50%
	1m	**71**	69	68	69	100%
0.50m	0.25m	**64**	61	60	61	25%
	0.50m	**66**	63	62	63	50%
	0.75m	**69**	66	64	66	50%
	1m	**71**	68	67	68	100%
0.75m	0.25m	**64**	60	59	60	25%
	0.50m	**66**	62	61	62	50%
	0.75m	**69**	65	63	65	50%
	1m	**71**	67	66	67	100%
1m	0.25m	**64**	58	57	58	50%
	0.50m	**66**	60	59	60	100%
	0.75m	**69**	64	62	64	100%
	1m	**71**	67	66	67	100%

Table 2: Performance of sensor 2 for various experimental radii

Experimental Radius	Distance between Sound Source & **Microphone Sensor 2**	Minimum Sound Intensity(dB)				Accuracy
		Mic1	**Mic2**	Mic3	Mic4	
0.25m	0.25m	66	**68**	66	65	25%
	0.50m	68	**70**	68	66	25%
	0.75m	70	**72**	70	68	50%
	1m	71	**73**	71	69	100%
0.50m	0.25m	65	**68**	65	64	25%
	0.50m	67	**70**	67	65	50%
	0.75m	69	**72**	69	67	25%
	1m	70	**73**	70	68	100%
0.75m	0.25m	64	**68**	64	63	25%
	0.50m	66	**70**	66	64	50%
	0.75m	68	**72**	68	66	100%
	1m	69	**73**	69	67	50%
1m	0.25m	63	**68**	63	62	50%
	0.50m	65	**70**	65	63	100%
	0.75m	67	**72**	67	65	100%
	1m	70	**73**	70	68	100%

Table 3: Performance of sensor 3 for various experimental radii

Experimental Radius	Distance between Sound Source & **Microphone Sensor 3**	Minimum Sound Intensity(dB)				Accuracy
		Mic1	Mic2	**Mic3**	Mic4	
0.25m	0.25m	66	67	**70**	67	25%
	0.50m	69	70	**73**	70	25%
	0.75m	70	71	**75**	71	50%
	1m	71	72	**76**	72	100%
0.50m	0.25m	65	66	**70**	66	50%
	0.50m	68	69	**73**	69	50%
	0.75m	69	70	**75**	70	50%
	1m	70	71	**76**	71	100%
0.75m	0.25m	64	65	**70**	65	25%
	0.50m	67	68	**73**	68	50%
	0.75m	68	69	**75**	69	100%
	1m	69	70	**76**	70	100%

1m	0.25m	62	63	**70**	63	50%
	0.50m	65	66	**73**	66	50%
	0.75m	66	67	**75**	67	100%
	1m	67	68	**76**	68	100%

Table 4: Performance of sensor 4 for various experimental radii

Experimental Radius	Distance between Sound Source & **Microphone Sensor 4**	Minimum Sound Intensity(dB)				Accuracy
		Mic1	Mic2	Mic3	**Mic4**	
0.25m	0.25m	72	70	72	**76**	25%
	0.50m	76	74	76	**78**	25%
	0.75m	78	76	78	**81**	50%
	1m	81	79	81	**83**	100%
0.50m	0.25m	71	69	71	**76**	25%
	0.50m	75	73	75	**78**	50%
	0.75m	77	75	77	**81**	50%
	1m	80	78	80	**83**	100%
0.75m	0.25m	70	68	70	**76**	50%
	0.50m	74	72	74	**78**	50%
	0.75m	76	74	76	**81**	50%
	1m	79	77	79	**83**	100%
1m	0.25m	69	67	69	**76**	50%
	0.50m	73	71	73	**78**	100%
	0.75m	75	73	75	**81**	100%
	1m	78	76	78	**83**	100%

Table 1, 2, 3 and 4 shows the performances of sensor 1, 2, 3 and 4 respectively w.r.t. various experimental radii when sound event occurs at various heights from the sensors. The accuracies are computed on the basis of microphone responses with sound events. The accuracy is 100% when the nearest microphone from sound source responds. If two microphone responds at the same time, then the accuracy reduces to 50%, for three microphone response, the accuracy becomes 25% and if the entire microphone responds then the accuracy is considered as 0%. The average accuracy found in our system is 83.33%, which seems quite satisfactory for the desired purpose.

5. CONCLUSIONS

Analyzing the results, it is evident that when the experimental radius is high (in our case, 1m), the accuracy of the sensor becomes high. This is because, when the experimental radius is high, then the distance between sensors becomes high and this helps to reduce interference of sounds. Therefore, it may be concluded that, best results can be achieved when the sensors are placed as apart as possible.

6. FUTURE WORK

In our system, we have been able to point the camera toward the sound source. However, one of the limitations of our system is, we have to make sound in front of the microphone, not in between the microphone sensors. In the practical case, it is not possible to fix the sound source in front of the sensor. In order to improve the sensing system, we can increase the number of sound sensor so that it can response from any direction to the sound sensor. Another way of improving the sensing system is to develop algorithm so that it can compute the location of sound source using interpolation of distances between two sound sensors. After computing the location, the microcontroller sends the required pulses to the stepper motor to orient the camera to the required position.

REFERENCES

[1]. J. M. Valin, F. Michaud, J. Rouat, and D. Letourneau, "Robust sound source localization using a microphone array on a mobile robot", *Proc. IEEE/RSJ IntConf on Intelligent Robots and Systems (IROS 2003)*, vol. II, pp. 1228-1233, 2003

[2]. Y. Sasaki, S. Kagami, and H. Mizoguchi, "Main-lobe canceling method for multiple sound sources localization on mobile robot", *IEEE/ASME IntConf on Advanced intelligent mechatronics*, pp. 1-6, 2007

[3]. S. Ntalampiras, I. Potamitis, N. Fakotakis, "On Acoustic Surveillance of Hazardous situations", *IntConf on Acoustics, Speech, and Signal Processing (ICASSP)*, pp. 165-168, 2009

[4]. C. Clavel, , T. Ehrette, and G. Richard, , "Event Detection for an Audio-Based Surveillance System," *Proc. of IEEE IntConf on Multimedia and Expo*, pp. 1306-1309 , 2005

[5]. F. Alan, , M. Mike, " Towards event detection in an audio-based sensor network", *Proc. 3rd ACM Workshop on Video surveillance & sensor networks*, pp.87-94, 2005

[6]. K. Joglie, "Anti-social behavior detection in audio-visual surveillance systems" *Workshop on Pattern Recognition and Artificial Intelligence for Human Behavior Analysis*, 2009

[7]. A. Ranjan, J. Birnholtz, R. Balakrishnan and D. Lee, "Automatic Camera Control Using Unobtrusive Vision and Audio Tracking", *Proc. Graphics Interface Conference* , pp.47-54, 2010

[8]. H. Wang, P. Chu, " Voice Source Localization for Automatic Camera Pointing System in Video Conferencing", Proc. *IEEE IntConf on Acoustics, Speech and Signal Processing (ICASSP'97)*, vol.1, pp.187-190, 1997

[9]. C. H. Knapp and G. C. Carter, "The Generalized Correlation Method for Estimation of Time Delay", *IEEE Trans. ASSP,* volume 24, pp. 320-327, 1976

Proceeding of the
International Conference on Electrical, Computer and Telecommunication Engineering
01- 02 December 2012 (ICECTE2012), RUET, Rajshahi-6204, Bangladesh

ICECTE2012: PI-0111

Performance Analysis of Different Feature Matching Techniques in Iris Recognition System

Md. Hedayetul Islam Shovon[1], Jesmin Aktar Mousumy[2]
[1]Lecturer, Department of Computer Science and Engineering, RUET, Rajshahi, Bangladesh.
[2]Department of Computer Science and Engineering, RUET, Rajshahi, Bangladesh.
E-mail: hedayet04@yahoo.com, jesmin_mou07@yahoo.com

ABSTRACT
Biometric technology—the automated recognition of individuals using biological and behavioral traits. This paper presented an iris recognition system in order to verify both the uniqueness of the human iris and also its performance as a biometric identification and also focus on the iris feature matching in iris recognition system. For feature Matching we used different methods (hamming, Euclidean, Manhattan, Correlation) and we also measure performance and success rate of those methods. . Experimental results show that, in iris recognition these method can be used for human identification in efficient manner.

KEY WORDS: Biometrics Identification, Iris segmentation, Iris normalization, Feature Matching, Iris recognition.

1. INTRODUCTION

A biometric system provides automatic recognition of an individual based on some sort of unique feature or characteristic possessed by the individual. Biometric systems have been developed based on fingerprints, facial features, voice, hand geometry, handwriting, the retina and the one presented in this thesis, the iris. Biometric systems work by first capturing a sample of the feature, such as recording a digital sound signal for voice recognition. Most biometric systems allow two modes of operation. An enrolment mode for adding templates to a database, and an identification mode, where a template is created for an individual and then a match is searched for in the database of pre-enrolled templates.

Fig1: Front view of the human eye.

A front-on view of the iris is shown in Figure 1. Formation of the unique patterns of the iris is random and not related to any genetic factors . The average diameter of the iris is 12.

2. IRIS RECOGNITION BLOCK DIAGRAM

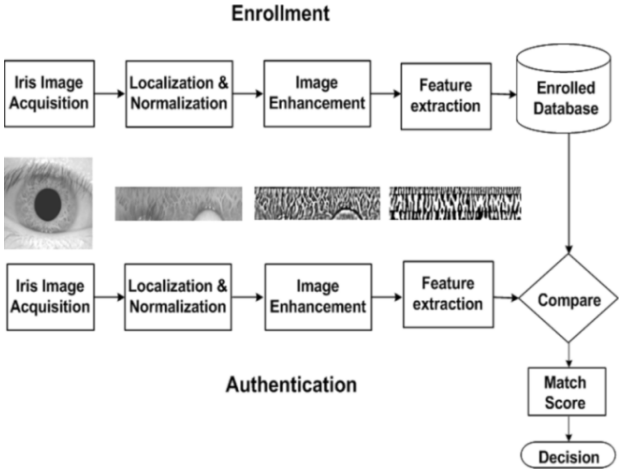

Fig.2 Block diagram of iris recognition.

3. IRIS ACQUISITION

Iris image acquisition is a vital and first step of any iris recognition system. In most iris recognition system 2-D image of the eye is obtained using a monochromatic CCD camera sensitive to near infrared (NIR) light spectrum. NIR imaging is used because it helps emphasize the iris texture that can be difficult to image under visible light (i.e., texture is richer for dark pigmented eyes under NIR compared to visible). Furthermore, NIR is used because the human eye is not as sensitive to NIR wavelengths as it is to visible light. Image quality of the iris depends on the image acquisition. Image quality plays an important role in automated biometric systems for two reasons: 1) system performance and 2) interoperability.

4. IRIS SEGMENTATION

The first stage of iris recognition is to isolate the actual iris region in a digital eye image. The iris region, can be approximated by two circles, one for the iris/sclera boundary and another, interior to the first, for the iris/pupil boundary. A technique is

required to isolate and exclude these artifacts as well as locating the circular iris region. The success of segmentation depends on the imaging quality of eye images. The segmentation stage is critical to the success of an iris recognition system, since data that is falsely represented as iris pattern data will corrupt the biometric templates generated, resulting in poor recognition rates.

A. Hough transformation

The circular Hough transform can be employed to deduce the radius and centre coordinates of the pupil and iris regions. The parameters are the centre coordinates x_c and y_c, and the radius r, which are able to define any circle according to the equation

$$x_c^2 + y_c^2 - r^2 = 0 \quad (1)$$

Usually, inner boundary is clearly, which is easy to choose a threshold transforming grayscale image into binary image. Outer boundary has low contrast, depending on the pupil centre position and the true inner radius of iris. An Iris segmentation result is shown as fig 3.

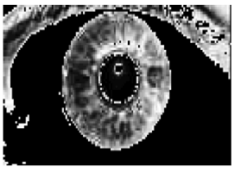

Fig.3 Iris segmented image after multiplication result.

5. IRIS NORMALIZATION

Once the iris region is segmented from an eye image, the next stage is to transform the iris region so that it has fixed dimensions. The rubber sheet model takes into account pupil dilation and size inconsistencies in order to produce a normalized representation with constant dimensions. It convert the Cartesian coordinate to polar coordinate.

A. Daugman`s Rubber Sheet Model

The homogenous rubber sheet model devised by Daugman remaps each point within the iris region to a pair of polar coordinates (r,θ) where r is on the interval [0,1] and θ is angle [0,2π].

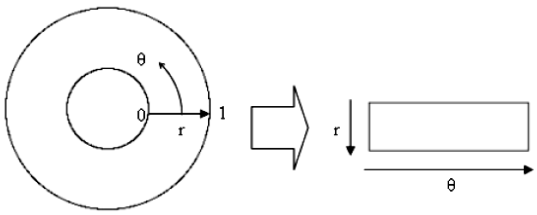

Fig.4 Daugman's rubber sheet model.

The normalization process proved to be successful and some results are shown in Fig 5. In this paper, the rectangular representation is constructed from M*N data points in each iris region.

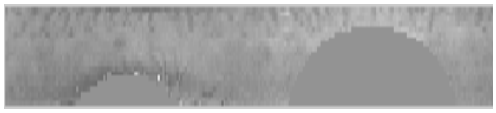

Fig.5 Iris normalization (with noise) result.

6. FEATURE ENCODING

In order to provide accurate recognition of individuals, the most discriminating information present in the iris pattern must be extracted.

A. Laplacian of Gaussian Filters

In order to encode features, the Wildes et al. system decomposes the iris region by application of Laplacian of Gaussian filters to the iris region image. The filters are given as

$$\nabla G = -\frac{1}{\pi\sigma^4}\left(1-\frac{\rho^2}{2\sigma^2}\right) \quad (2)$$

where σ is the standard deviation of the Gaussian and ρ is the radial distance of a point from the centre of the filter.

Fig.6 Laplacian of Gaussian filtered image .

Then this feature extracted image is encoded by converting the image into binary image using thresholding

Fig 7: Feature encoded image.

7. FEATURE MATCHING

After features have been extracted, they must be compared to the features of other images in a very efficient manner.

A. Hamming distance

The Hamming distance gives a measure of how many bits are the same between two bit patterns. In comparing the bit patterns X and Y, the Hamming distance, HD, is defined as the sum of disagreeing bits (sum of the exclusive-OR between X and Y) over N, the total number of bits in the bit pattern.

$$HD = \frac{1}{N}\sum_{j=1}^{N} X_j (XOR)\, Y_j \quad (3)$$

B. Weighted Euclidean Distance:

The weighted Euclidean distance (WED) can be used to compare two templates, especially if the template is composed of integer values. This metric is employed by Zhu et al. [9] and is specified as

$$\text{WED(k)} = \sum_{i=1}^{N} \frac{(f_i - f_i^{(k)})^2}{(\delta_i^{(k)})^2} \qquad (4)$$

Where f_i is the ith feature of the unknown iris, and $f^{(k)}$ is the ith feature of iris template, k, and δ^{th} is the standard deviation of the ith feature in iris template k. The unknown iris is found to match iris template k, when *WED* is a minimum at k.

8. PERFORMANCE ANALYSIS

Time Complexity

Number of Iris Template	Different Methods (Time in ms)	
	Hamming Distance	Weighted Euclidean Distance
5	0.1716	0.0468
10	0.2964	0.0468
20	0.4992	0.0312
30	0.6084	0.0468
40	0.8112	0.0936
50	0.8580	0.0780
60	0.9516	0.1404
70	1.2636	0.1404
80	1.4196	0.1092
90	1.5444	0.1404
100	1.7628	0.1872

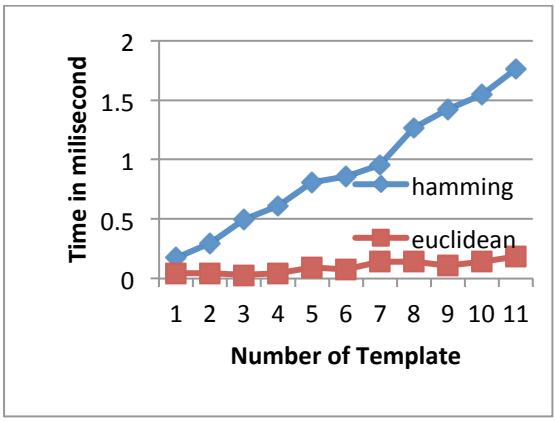

Fig. 7 Compare time (millisecond) for different matching methods.

B. Success Rate

Number of Iris Template	Different Methods (Time in ms)	
	Hamming Distance	Weighted Euclidean Distance
5	5	5
10	10	10
20	20	17
30	30	25
40	40	32
50	49	44
60	59	52
70	68	61
80	77	70
90	87	78
100	95	86
Avg.	97	87

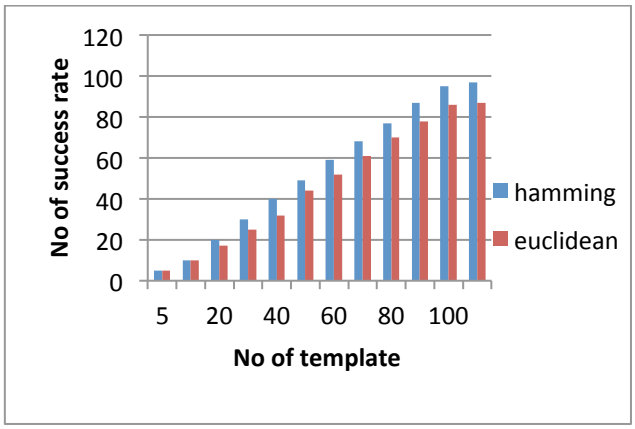

Fig. 8: Measure success to identify for different matching methods.

9. CONCLUSION AND FUTURE WORK

Iris recognition as a biometric technology has a great advantage such as variability, stability and security. This thesis has presented an overview of Iris Recognition technology and calculates the success rate to analyze performance. Comparison those feature matching methods and calculating EER(error rate) into hierarchical phase based matching.

10. ACKNOWLEDGEMENT

We would like to thank Dr.S.prabhakar,S.Pankanti and A.K. Jain ,Dr. John Daugman (Cambridge University, UK), Dr. Richard Wildes (York University, Canada), and Dr. Li Ma (Chinese Academy of Sciences) for their efficient references. And also thanks to Rajshahi University of Engineering & Technology in Bangladesh.

REFERENCES

[1] S. Prabhakar, S. Pankanti, and A.K. Jain, "Biometric Recognition: Security and Privacy Concerns," IEEE Security & Privacy, vol. 1, no. 2, 2003, pp. 33–42.

[2] Watson, "Biometrics: Easy to Steal, Hard to Regain Identity," Nature, vol. 449, 2007, p. 535.
[3] S. Sanderson, J. Erbetta. Authentication for secure environments based on iris scanning technology. IEE Colloquium on Visual Biometrics, 2000.
[4] J. Daugman. How iris recognition works. Proceedings of 2002 International Conference on Image Processing, Vol. 1, 2002.
[5] E. Wolff. Anatomy of the Eye and Orbit. 7th edition. H. K. Lewis & Co. LTD, 1976.
[6] R. Wildes. Iris recognition: an emerging biometric technology. Proceedings of the IEEE, Vol. 85, No. 9, 1997.
[7] J. Daugman. Biometric personal identification system based on iris analysis. United States Patent, Patent Number: 5,291,560, 1994.
[8] J. Daugman. High confidence visual recognition of persons by a test of statistical independence. IEEE Transactions on Pattern Analysis and Machine Intelligence, Vol. 15, No. 11, 1993.

Proceeding of the
International Conference on Electrical, Computer and Telecommunication Engineering
01- 02 December 2012 (ICECTE2012), RUET, Rajshahi-6204, Bangladesh

ICECTE2012: PI-0112

PCA based Gradient Descent Variable Learning Rate BPN Algorithms in terms of Face Recognition

Rizoan Toufiq[1], Md. Rabiul Islam[1] and M. Abdus Sobhan[2]*
[1]Department of Computer Science & Engineering
Rajshahi University of Engineering & Technology, Rajshahi-6204, Bangladesh
[2]School of Engineering & Computer Science, Independent University, Bangladesh
E-mail: rizoantoufiq@yahoo.com, rabiul_cse@yahoo.com and sobhan30@gmail.com

ABSTRACT
Artificial neural network has been highly used to classify data set in recent activities, especially in pattern classification technique. This paper introduces about the face recognition system based on different back-propagation algorithm where features are extracted by using image pre-processing techniques and dimensionality of the feature vector are reduced using pca technique. Experimental results shows that the performance of the recognition system is varied based on the trained multilayer perceptron back-propagation algorithm because of using various parameters to enhance the learning efficiency based on the memory, speed or other criterion in terms of face recognition system. The performance of variable learning rate back-propagation algorithm can achieve higher recognition rate than constant learning rate algorithm with maintaining desired time limit.

KEY WORDS: Artificial Neural Network, Principal Component Analysis, Back-propagation Algorithm, Learning Rate and Momentum Constant.

1. INTRODUCTION

Artificial Neural Networks (ANNs) are being designed to solve a variety of problems in pattern recognition, prediction, optimization, associative memory, and control [1]-[2].In recent year, a lot of research has been done on Neural Networks used in pattern recognition to the purpose of classification. P. Latha., Dr. L. Ganesan and Dr. S. Annadurai has been developed a system where ANN is used to classify the facial pattern [3]. C. Kotropoulos el. has been described a front face recognition system where two methods i.e. support vector machine and back-propagation feed forward neural network are used for detecting faces and their performance has been thoroughly measured with respect to the false acceptance and false rejection rates [4].Y. Lecun el. designed a recognition system where Back-propagation applied to handwritten zip code recognition [5]. L. Ma and K. Khorasani described a new technique for facial expression recognition which uses the two-dimensional (2-D) discrete cosine transform (DCT) over the entire face image as a feature detector [6]. Christine L. Lisetti and David E. Rumelhart recognized and interpret facial expression in terms of signalled emotions and level of expressiveness. A face recognition system has been described based on Back-propagation neural network to reduce the redundancy on the image and genetic algorithm also included [7]-[9].

In this work, we want to focus the face recognition system performance based on different Back-propagation algorithms and the effect on learning and recognition stage based on various parameters that is the contribution of this paper.

2. OUTLINE OF THE SYSTEM

The neural network based recognition methods are found to be particularly promising, since the neural networks can easily implement the mapping from the feature space of face images to the facial expression space. However, determining a proper network size has always been a frustrating and time consuming experience for neural network developers. This is generally dealt with through a series of long and costly trial and error simulations [6]. Motivated by these limitations and drawbacks, in this paper we want to select, overcome the limitations of the problems and propose the highest efficient algorithm by analyzing different types of Back-propagation learning Neural Networks with the variations of different parameters which in shown in Fig. 1

3. METHODOLOGY OF FACE RECOGNITION SYSTEM

In the proposed system, the dimensions of the images are reduced by PCA technique. After the images are trained and the recognition rate of the system has been determined in testing phase. The following steps will focus the implementation strategies of the proposed system.

3.1 Facial Image Acquisition

Standard image database, ORL has been used to measure the performance of the proposed face recognition system. In this work, three face images

per person have been used for learning and other two different facial images of that person have been used for testing. Fig. 2 shows some ORL database images.

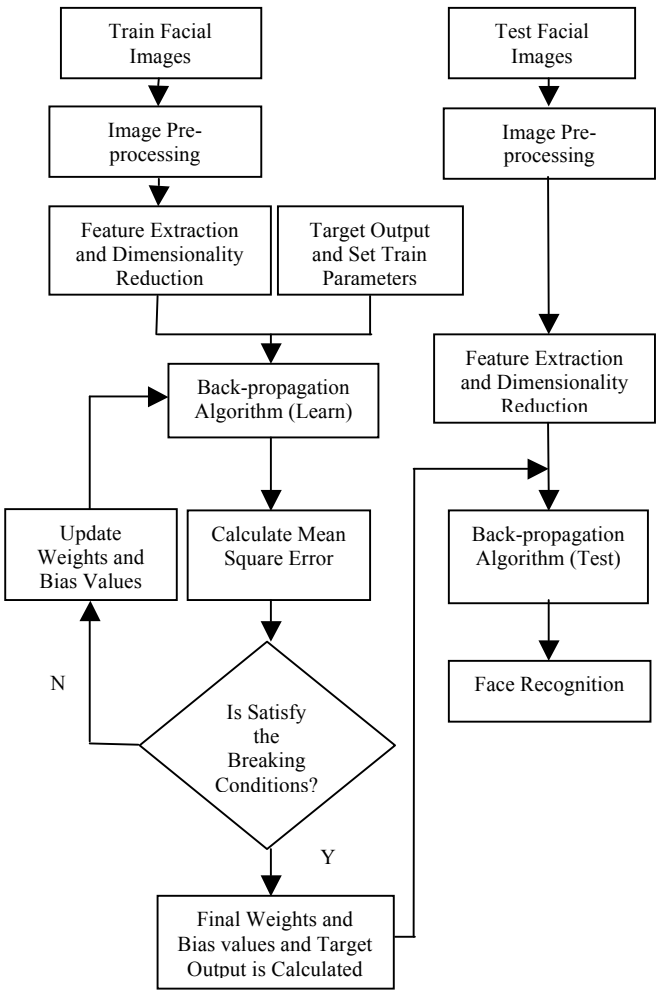

Fig. 1 Proposed block diagram of the face recognition system based on BPN.

Fig. 2 Sample images of ORL database.

3.2 Image Filtering for Noise Reduction

The main idea of the median filter is to run through the image pixel values, replacing each pixel with the median of neighbouring pixel. Median filter are particularly effective in the presence of impulse noise, also called *salt-and-paper* noise [10] which is shown in Fig. 3.

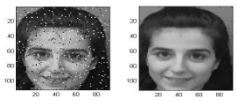

Fig. 3 Effects of median filtering.

3.3 Feature Extraction

A face image $I(x,y)$ is a two dimensional N by N array of intensity values. An image may also be considered as a vector of dimension N^2. Let the training set of face images be $\Gamma_1, \Gamma_2, \Gamma_3 \ldots \Gamma_M$. The average face of the set is defined by

$$\Psi = \frac{1}{M}\sum_{i}^{M}\Gamma_i \tag{1}$$

Each face differs from the average by the vector,

$$\Phi_i = \Gamma_i - \Psi \tag{2}$$

$$\lambda_k = \frac{1}{M}\sum_{n=1}^{M}(\mu_k^T \Phi_n)^2 \tag{3}$$

$$\mu_l^T \mu_k = \delta_{lk} = \begin{cases} 1, & if \quad l = k \\ 0, & otherwise \end{cases} \tag{4}$$

The vectors μ_k and scalars λ_k are the eigenvectors and eigenvalues respectively of the covariance matrix

$$C = \frac{1}{M}\sum_{n=1}^{M}\Phi_n \Phi_n^T \tag{5}$$

$$= AA^T$$

where $A = [\Phi_1, \Phi_2 \ldots \Phi_M]$. The matrix C, however, is N^2 by N^2, and determining the N^2 eigenvectors and eigenvalues is an intractable task for typical image size. Fortunately, we can solve for the N^2 dimensional eigenvectors in this case by first solving for the eigenvectors of a M by M matrix and then taking appropriate linear combinations of the face images Φ_i. Consider the eigenvectors v_i of A^TA such that

$$A^T A v_i = \mu_i v_i \tag{6}$$

$$AA^T A v_i = \mu_i A v_i \tag{7}$$

From which, we see that Av_i are the eigenvectors of $C = AA^T$. Following this analysis, we construct the M by M matrix $L = A^TA$ where, $L_{mn} = \Phi_m^T \Phi_n$ and find the M eigenvectors, v_l, of L. These vectors determine linear combinations of the M training set face images to form the eigenfaces μ_l,

$$\mu_l = \sum_{k=1}^{M} v_{lk}\Phi_k, \quad l = 1,2\ldots, M \tag{8}$$

Some sample eigenfaces are shown in Fig. 4.

.

Fig. 4 Examples of eigenfaces.

With this analysis, the calculations are greatly reduced from the order of the number of pixels in the images (N^2) to the order of the number of images in the training set (M) [11-14]

3.4 Learning and Recognition Model of Face Recognition System based on Back-propagation Algorithmame(s)

An ANN that is found to be useful in addressing problems requiring recognition of complex patterns and performing nontrivial mapping functions is the back-propagation network [15]. The network that has been used in this system is a feed-forward network with tan-sigmoid transfer functions in both the

hidden layer and the output layer which is shown in Fig. 5.

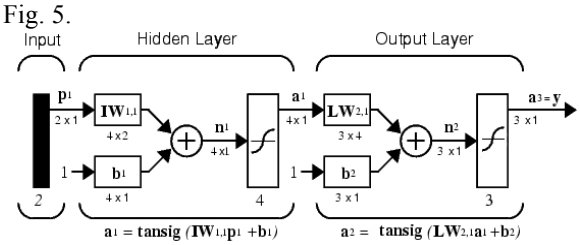

Fig. 5 Architecture of Back-propagation neural network.

If the input vector is $I = [p_1, p_2 ... p_n]$, then the output of hidden layer has been calculated as following,

$$n = IW + b \tag{9}$$

$$a = f(n) = \frac{2}{(1+e^{(-2*n)})^{-1}} \tag{10}$$

Where, W = weight vector and b = bias input. The error is calculated as the difference between the target output and the network actual output. The goal is to minimize the average of the sum of these errors.

$$mse = \frac{1}{M}\sum_{k=1}^{M} e(k)^2 = \frac{1}{M}\sum (t(k) - a(k))^2 \tag{11}$$

Here, *mse* means mean square error, *t(k)* represents the target output and *a(k)* represents the network output. The weights and bias values are updated based on the goal average error value.

In face recognition system, the final weights and bias values are calculated in training stage. In test phase, the output of the network has been calculated for the new input image and compared with the target output to select the class of the input facial image.

4. EXPERIMENT RESULTS AND PERFORMANCE ANALYSIS

Learning rate coefficient determines the size of the weight adjustments made at each iteration and hence influences the rate of convergence. There is another possible way to improve the rate of convergence by adding some initial or momentum to the gradient expression. This can be accomplished by adding a fraction of the previous weight change to the current weight change. This addition of such a term helps to smooth out the descent path by preventing extreme changes in the gradients due to local anomalies.

Fig. 6 shows the performance of the network according to the learning rate. From the figure, it is observed that the learning performance has been increased based on the largest value of the learning parameter. When the learning rates are 0.1, 0.5, and 0.9, the error rate is 0.0806, 0.0357 and 0.0200 respectively. In other way, we can say that the desired performance is reached when we use large value of the learning rate.

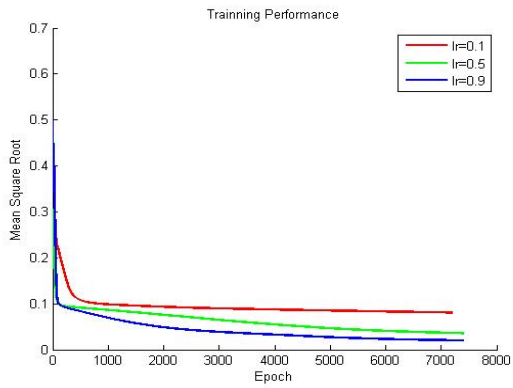

Fig. 6 Performance of network based on the learning rate.

Table 1
Comparison of Performance among Different Back-propagation Algorithm

Different type of BPN Algorithms	No. of Trained Images, A	No. of Test Images, B	No. of Correctly Recognized Images	Recognition Rate (%)
Batch Gradient Descent Back-propagation	30	20	15	75
Batch Gradient Descent Back-propagation with Momentum	30	20	16	80
Batch Gradient Descent Variable Learning Rate Back-propagation	30	20	19	95

There different Back-propagations has been developed based on the learning rate and momentum in learning stage of the network. We have compared three different algorithms of Back-propagation algorithm with different dimensions and various changed parameters in face recognition system. Fig. 7 shows the recognition rate of different Back-propagation algorithm. From where, we can make a decision that gradient descent with variable learning rate back-propagation algorithm gives the highest recognition rate (95%) than other algorithm.

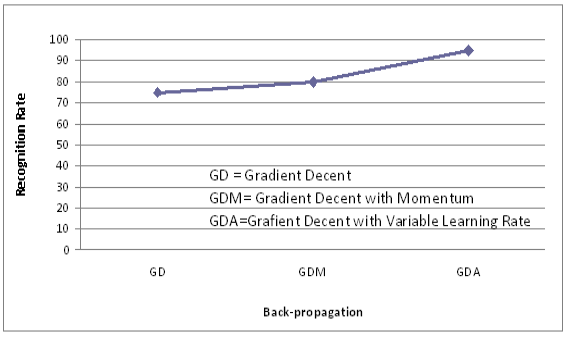

Fig. 7 The recognition rate of different Back-propagation algorithm.

5. CONCLUSIONS AND OBSERVATIONS

In the experimental results and performance analysis, we can conclude that the face recognition rate is highly depending on the trained network where the network was perfectly trained or not. Basically the performance of the training of Back-propagation network depends on two parameters namely learning rate and momentum factor. If we fixed the learning rate then the running time of the algorithm is very slow and it takes more time to converge the network. In this work, we set maximum 120s training time for the network. In constant learning rate Back-propagation algorithm could not achieve the goal performance and the recognition rate is relatively low. In variable learning rate back-propagation algorithm could achieve the target performance within the time limit and the recognition rate is very high.

REFERENCES

Anil K. Jain, Jianchang Mao, K. Mohiuddin, "Artificial Neural Networks: A Tutorial", *IEEE Computer Special Issue on Neural Computing*, March, 1996.

James C. Bezdek, James Keller, Raghu Krisnapuram and Nikhil R. Pal, "Fuzzy Models and Algorithms from Pattern Recognition and Image Processing", Springer, 2005.

P.Latha, Dr. L. Ganesan and Dr. S. Annadurai, "Face Recognition using Neural Networks", *Signal Processing: An International Journal (SPIJ)* Vol. 3, Issue 5, pp. 153-160.

Kotropoulos Bassiou Kosmidis, C. Kotropoulos, N. Bassiou, T. Kosmidis, and I. Pitas, "Frontal Face Detection using Support Vector Machines and Back-propagation Neural Network", *Conference of Proc. Int. Conf. Image Processing*, pp. 1026-1029, 2001.

Le Cun, B. Boser, J. S. Denker, D. Henderson, R. E. Howard, W. Hubbard, and L. D. Jackel, "Backpropagation Applied to Handwritten Zip Code Recognition*", Journal Neural Computation*, Vol. 1, Issue 4, Winter,1989, pp. 541-551, MIT Press Cambridge, MA, USA.

L. Ma and K. Khorasani, "Facial Expression Recognition Using Constructive Feedforward Neural Networks", *IEEE Transactions on Systems, Man, and Cybernetics, Part B: Cybernetics*, Vol. 34, Issue: 3, pp.1588 – 1595, June, 2004.

Christine L. Lisetti and David E. Rumelhart, "Facial Expression Recognition Using a Neural Network", *Proceedings of the Eleventh International Florida Artificial Intelligence Research Society Conference*, pp. 328 – 332, 1998.

Zhengjun Pan , Alistair Rust and Hamid Bolouri, "Image Redundancy Reduction for Neural Network Classification using Discrete Cosine Transforms", *Proceedings of the International Joint Conference on Neural Networks Conference*, Vol. 3, pp. 149-154, 2000.

Sarawat Anam, Md. Shohidul Islam, M.A. Kashem, M.N. Islam, M.R. Islam and M. S. Islam, "Face Recognition Using Genetic Algorithm and Back Propagation Neural Network", *Proceedings of the International Multi-Conference of Engineers and Computer Scientists*, Vol.1, IMECS 2009, March 18-20,2009, Hong Kong.

Rafael C. Gonzalez and Richard E Woods, "Digital Image Processing", Prentic Hall, Second edition, 2002.

Matthew Turk and Alex Pentland, "Eigenfaces for Recognition", *Journal of Cognitive Neuroscience* Vol. 3, No. 1, Massacbusetts Institute of Technology,1991.

Matthew Turk and Alex Pentland, "Face Recognition Using Eigenfaces, Vision And Modeling Group", *The Media Laboratory, Massachusetts Institute of Technology*, CVPR'91.

Jon Shlens, "A Tutorial on Principal Component Analysis, Derivation, Discussion and Singular Value Decomposition", Version 1, 25 March, 2003.

Alok Sharma, Kuldip K. Paliwal and Godfrey C. Onwubolu, "Splitting Technique Initialization in Local PCA", *Journal of Computer Science 2(1)*: pp.53-58, 2006.

[1]. James A. Freeman, David M. Skapura, "Neural Networks, Algorithms, applications and Programming Techniques", Addison-Wesley Pub (Sd), June, 1991.

Proceeding of the
International Conference on Electrical, Computer and Telecommunication Engineering
01- 02 December 2012 (ICECTE2012), RUET, Rajshahi-6204, Bangladesh

ICECTE2012: PI- 0113

A Survey of Image Edge Detection Techniques

Md. Sujan Ali
Assistant Professor, Department of Computer Science and Engineering, Jatiya Kabi Kazi Nazrul Islam University,
Trishal, Mymensingh,Bangladesh.
E-mail: msujanali@gmail.com

ABSTRACT— For image segmentation and object identification edge detection is the main pre-processing step. Many edge detection techniques have previously been proposed for enhancing the performance of image segmentations and object detections. This paper reviews different edge detection algorithms. All of the algorithms have some advantages and disadvantages, but some performs better than others for specific regions and specific type of images. This paper indicates the advantages and disadvantages, differences and similarities of the reviewed algorithms and compares their performances. The experiment is carried out using MATLAB 7.10.0 (R2010a). The experimental results showed that Canny's edge detection algorithm performs comparatively better than other algorithms.

Keywords— edge detection, image segmentation, object detection, derivative filters, comparison of algorithms.

I. INTRODUCTION

In the field of computer vision edge detection is a fundamental operation in image processing. Edge detection is one of the most commonly used techniques in digital image processing [1]. In an image edges are points where there is a boundary between two image regions. The boundaries of object surfaces in a scene often lead to oriented localized changes in intensity of an image, called edges. In practice, edges are usually defined as sets of points in the image which have a strong gradient magnitude. Edge detection is the first step in image segmentation, has fueled a long search for a good edge detection algorithm to use in image processing [2]. Edge detection refers to the process of identifying and locating sharp discontinuities in an image. The discontinuities are abrupt changes in pixel intensity which characterize boundaries of objects in a scene. Classical methods of edge detection involve convolving the image with an operator (a 2-D filter), which is constructed to be sensitive to large gradients in the image while returning values of zero in uniform regions. There are an extremely large number of edge detection operators available, each designed to be sensitive to certain types of edges. Variables involved in the selection of an edge detection operator include Edge orientation, Noise environment and Edge structure. The geometry of the operator determines a characteristic direction in which it is most sensitive to edges. Operators can be optimized to look for horizontal, vertical, or diagonal edges. Edge detection is difficult in noisy images, since both the noise and the edges contain high frequency content. Attempts to reduce the noise result in blurred and distorted edges. Operators used on noisy images are typically larger in scope, so they can average enough data to discount localized noisy pixels. This results in less accurate localization of the detected edges. Not all edges involve a step change in intensity. The operator needs to be chosen to be responsive to such a gradual change in those cases. So, there are problems of false edge detection, missing true edges, edge localization, high computational time and problems due to noise etc. Therefore, the objective is to do the comparison of various edge detection techniques and analyze the performance of the various techniques in different conditions. In this paper the most commonly used Gradient and Laplacian based Edge Detection techniques are reviewed. For experiment a set of test images are taken and evaluate the performance of various edge detection techniques by developing software using MATLAB 7.10.0 (R2010a). The advantages and disadvantages of various techniques are discusses in section 4. After analysis and visual comparison of experimental results of various edge detection techniques the performance of the techniques are compares in conclusion section.

II. SURVEY OF IMAGE EDGE DETECTION ALGORITHMS

2.1 First derivative gradient edge detection

The first derivative assumes a local maximum at an edge. For a continuous image $f(x, y)$, where x and y are the row and column coordinates respectively, we typically consider the two directional derivatives

$\partial_x f(x,y)$ and $\partial_y f(x,y)$. The first derivative of gray level is negative at the leading edge of the transition, positive at the trailing edge, and zero in the areas of constant gray levels. The presence of an edge in the image is detected by the magnitude of the first derivative. The gradient magnitude is defined as

$$mag\Delta f(x,y) = \sqrt{\left(\partial_x f(x,y)^2 + \partial_y f(x,y)^2\right)} \quad (1)$$

In an image edge pixels have higher intensity values than its surrounding pixels. If the value of the gradient exceeds some threshold value then the pixel position is identified as an edge position. The convention for 3 by 3 regions to denote image points of an input image is as follows:

Z1	*Z2*	*Z3*
Z4	*Z5*	*Z6*
Z7	*Z8*	*Z9*

Fig.-1 A 3 by 3 region of an image

Where *Z5= f(x, y), Z1= f(x-1, y-1), Z2= f(x-1, y)*
Z3= f(x-1, y+1), Z4= f(x, y-1), Z6 = f(x, y+1)
Z7=f(x+1, y-1), Z8= f(x+1,y), Z9= f(x+1, y+1)

2.1.1 Sobel edge detection

The Sobel operator consists of a pair of 3 by 3 convolution kernels as shown in Fig.-2. One kernel is simply the other rotated by 90^0.

-1	0	+1
-2	0	+2
-1	0	+1

a

-1	-2	-1
0	0	0
+1	+2	+1

b

Fig.-2: a) Sobel mask for vertical direction
b) Sobel mask for horizontal direction

The Sobel operator is given by the equations [3], [4], [5]:

$$\partial_x f(x,y) = (Z7 + 2Z8 + Z9) - (Z1 + 2Z2 + Z3) \quad (2)$$

$$\partial_y f(x,y) = (Z3 + 2Z6 + Z9) - (Z1 + 2Z4 + Z7) \quad (3)$$

Where Z1 to Z9 are pixel values in a sub image as shown in Fig.-1.

The kernels are used separately to the input image and produce separate measurements of the gradient component in each direction. The results then combined to find the absolute magnitude of the gradient at each point and the orientation of that gradient [6]

2.1.2 Robert edge detection

The mask of Robert operator is very simple and can measure the gradient components of an image rapidly. It thus highlights regions of high spatial frequency which often correspond to edges. In its most common usage, the input to the operator is a grayscale image, as is the output. Pixel values at each point in the output represent the estimated absolute magnitude of the spatial gradient of the input image at that point [1]. The Robert masks are shown in Fig.-3. The Robert operator is given by the equation [7]:

$$\partial_x f(x,y) = Z9 - Z5 \quad (4)$$
$$\partial_y f(x,y) = Z8 - Z6 \quad (5)$$

0	-1
+1	0

a

-1	0
0	+1

b

Fig.-3: a) Robert mask for vertical direction
b) Robert mask for horizontal direction

2.1.3 Prewitt edge detection

The magnitude of an edge can measure efficiently by the Prewitt operator. Prewitt operator [3] is very similar to Sobel operator and is used for detecting vertical and horizontal edges in images. Prewitt operator is given by the equations [7]:

$$\partial_x f(x,y) = (Z7 + Z8 + Z9) - (Z1 + Z2 + Z3) \quad (6)$$

$$\partial_y f(x,y) = (Z3 + Z6 + Z9) - (Z1 + Z4 + Z7) \quad (7)$$

-1	0	+1
-1	0	+1
-1	0	+1

(a)

-1	-1	-1
0	0	0
+1	+1	+1

(b)

Fig.-4 : (a) Prewitt mask for vertical direction
(b) Prewitt mask for horizontal direction

2.1.4 Canny edge detection

The Canny edge detection algorithm is very optimal edge detector. In this algorithm a list of criteria is followed [10] for the betterment of current methods of edge detection. The first one is to ensure the edges occurring in images and no responses to non-edges. The distance between the edge pixels as found by the detector and the actual edge is to be at a minimum is the second one. In this criterion the edge will be well localized. The third criterion is the response for an edge should not be multiple. In other words, the response should be one for a single edge. Based on

the criteria, Canny edge detection algorithm follows the following steps:

1. In first step the original image is passed through a filter to filter out any noise before trying to locate and detect any edges. To remove the noise Gaussian filter is comprehensively used in this algorithm.
2. Find the edge strength by taking the gradient of the image. Sobel operator (Fig.-2) is used to measure the gradient of an image.
3. Calculate Edge direction using the gradient in the x and y direction. Once the edge direction is computed, subsequently relate the edge direction to a direction that can be traced in an image
4. Trace along the computed edge direction and suppress non-edge pixel value and set it equal to zero.
5. Remove streaking using hysteresis [11]. If a single threshold, T1 is applied to an image, and an edge has an average strength equal to T1, then due to noise, there will be instances where the edge dips below the threshold. Equally it will also extend above the threshold making an edge. To avoid this, hysteresis uses 2 thresholds, a high and a low. Any pixel in the image that has a value greater than T1 is assumed to be an edge pixel, and is marked as such immediately. Then, any pixels that are connected to this edge pixel and that have a value greater than T2 are also selected as edge pixels. If you think of following an edge, you need a gradient of T2 to start but you don't stop till you hit a gradient below T1.

2.2 Second-Order Derivative Gradient Edge Detection

2.2.1 Laplacian of Gaussian (LoG)

The edge points of an image can be detected by finding the zero crossings of the second derivative of the image intensity. The idea is illustrated in Fig.-5 [3]. However, calculating 2nd derivative is very sensitive to noise. This noise should be filtered out before edge detection. To achieve this, "Laplacian of Gaussian" is used. This method combines Gaussian filtering with the Laplacian for edge detection.

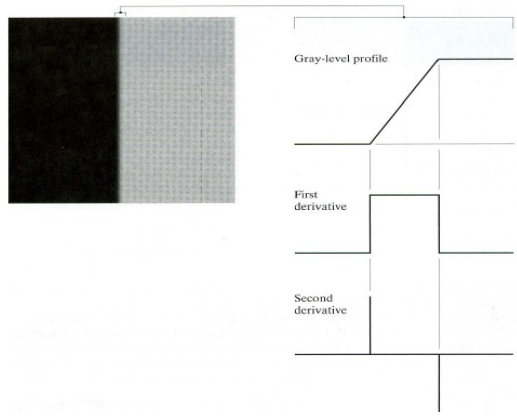

(a) (b)

Fig.-5: (a) two regions separated by a vertical edge (b) detail near the edge, showing a gray level profile and, the first and second derivative of the profile.

In Laplacian of Gaussian edge detection there are mainly three steps:

1. Filtering
2. Enhancement
3. Detection.

Gaussian filter is used for smoothing and the second derivative of which is used for the enhancement step. The detection criterion is the presence of a zero crossing in the second derivative with the corresponding large peak in the first derivative. In this approach, firstly noise is reduced by convoluting the image with a Gaussian filter. Isolated noise points and small structures are filtered out. With smoothing; however; edges are spread. Those pixels, that have locally maximum gradient, are considered as edges by the edge detector in which zero crossings of the second derivative are used. To avoid detection of insignificant edges, only the zero crossings whose corresponding first derivative is above some threshold, are selected as edge point. The edge direction is obtained using the direction in which zero crossing occurs.

As Laplace operator may detect edges as well as noise (isolated, out-of-range), it may be desirable to smooth the image first by convolution with a Gaussian kernel of width

$$G_\sigma(x,y) = \frac{1}{\sqrt{2\pi\sigma^2}}\exp[-\frac{x^2+y^2}{2\sigma^2}] \quad (8)$$

to suppress the noise before using Laplace for edge detection:

$$\Delta[G_\sigma(x,y) * f(x,y)] = [\Delta G_\sigma(x,y)] * f(x,y) = LoG * f(x,y) \quad (9)$$

The first equal sign is due to the fact that

$$\frac{d}{dt}[h(t) * f(t)] = \frac{d}{dt}\int f(\tau)h(t-\tau)d\tau = \int f(\tau)\frac{d}{dt}h(t-\tau)d\tau = f(t) * \frac{d}{dt}h(t) \quad (10)$$

So we can obtain the *Laplacian of Gaussian* $\Delta G_\sigma(x,y)$first and then convolve it with the input image. To do so, first consider

$$\frac{\partial}{\partial x}G_\sigma(x,y) = \frac{\partial}{\partial x}e^{-(x^2+y^2)/2\sigma^2} = -\frac{x}{\sigma^2}e^{-(x^2+y^2)/2\sigma^2} \quad (11)$$

and

$$\frac{\partial^2}{\partial^2 x}G_\sigma(x,y) = \frac{x^2}{\sigma^4}e^{-(x^2+y^2)/2\sigma^2} - \frac{1}{\sigma^2}e^{-(x^2+y^2)/2\sigma^2} = \frac{x^2-y^2}{\sigma^4}e^{-(x^2+y^2)/2\sigma^2} \quad (12)$$

Note that for simplicity we omitted the normalizing coefficient $1/\sqrt{2\pi\sigma^2}$. Similarly we can get

$$\frac{\partial^2}{\partial^2 y}G_\sigma(x,y) = \frac{y^2-\sigma^2}{\sigma^4}e^{-(x^2+y^2)/2\sigma^2} \quad (13)$$

Now we have LoG as an operator or convolution kernel defined as

$$LoG = \Delta G_\sigma(x,y) = \frac{\partial^2}{\partial x^2}G_\sigma(x,y) + \frac{\partial^2}{\partial y^2}G_\sigma(x,y) = \frac{x^2+y^2-2\sigma^2}{\sigma^4}e^{-(x^2+y^2)/2\sigma^2} \quad (14)$$

The Gaussian $G(x,y)$and its first $G'(x,y)$ and second derivatives $\Delta G(x,y)$ are shown here:

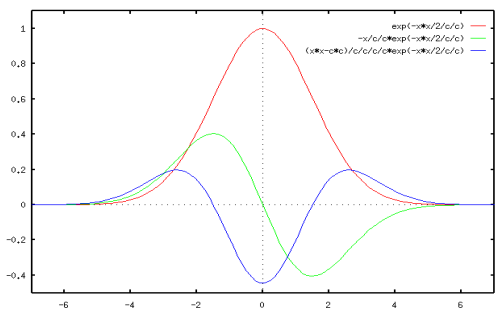

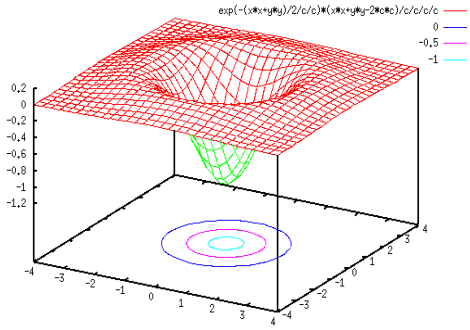

This 2D LoG can be approximated by a 5 by 5 convolution kernel such as

$$\begin{bmatrix} 0 & 0 & 1 & 0 & 0 \\ 0 & 1 & 2 & 1 & 0 \\ 1 & 2 & -16 & 2 & 1 \\ 0 & 1 & 2 & 1 & 0 \\ 0 & 0 & 1 & 0 & 0 \end{bmatrix}$$

The kernel of any other sizes can be obtained by approximating the continuous expression of LoG given above. However, make sure that the sum (or average) of all elements of the kernel has to be zero (similar to the Laplace kernel) so that the convolution result of a homogeneous regions is always zero. The edges in the image can be obtained by the following steps. The last step is needed to suppress the weak zero-crossing most likely caused by noise.

i) Applying LoG to the image
ii) Detection of zero-crossings in the image
iii) Threshold the zero-crossings to keep only those strong ones (large difference between the positive maximum and the negative minimum)

III. EXPERIMENTAL RESULTS

For experiment in this paper a set of images has been taken from the database of images *Berkely Segmentation Dataset* for training and corresponding ground truth images for objective evaluations. This database contains a set of 500 images of natural scene and their ground truth produced manually. In this experiment images are processed by MATLAB 7.10.0 (R2010a). In pattern recognition and information retrieval, precision is the fraction of retrieved instances that are relevant.

The precision or positive predictive value is defined as the proportion of the true positives against all the positive results.

$$Precision = \frac{True\ Positive\ (TP)}{True\ positive\ (TP) + False\ Positive(FP)} \quad (15)$$

Balanced Error Rate (BER) is also calculated for each submitted result. BER is the average of the proportion of wrong classifications in each class.

Balanced Error Rate (BER) = 100 * (1 - BCR) (16)

Where, Balanced Classification Rate (BCR) = 0.5 * (Sensetivity + Specificity).

In this experiment the precision and balanced error rate of the edge images comparing with the ground truth images are measured. Table 1 compares the performance of different edge operators. According to comparison performed, the Canny operator has the best overall performance with precision and balanced error rate. Fig.-6(a) shows the original image. The edge images of the original image using different operators are shown in Fig.-6 (b)- 1(f).

Table-I

	Precision	BER (%)
Canny	0.90187	35.41293
LoG	0.89807	35.66351
Sobel	0.89286	35.74236
Prewitt	0.89244	35.87267
Roberts	0.88870	36.85616

(a) Original Image

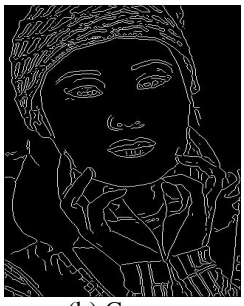

(b) Canny

(c) LoG

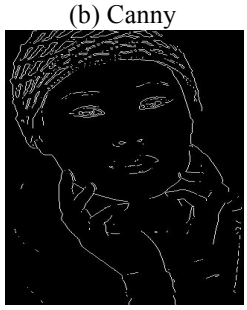

(d) Sobel

(e) Prewitt

(f) Roberts

Fig.-6: Edge images on the original image using different operators.

IV. MERITS AND DEMERITS OF EDGE DETECTORS

In computer vision, edge detection is the basic step. To get the best results it is necessary to point out the true edges. So, selection of edge detector is important. All the edge detection techniques presented in this paper has advantages and disadvantages [11], [12]. The classical edge operators (Sobel, Prewitt etc.) are very simple but noise sensitive and sometimes show inaccurate results. Although the Laplacian of Gaussian (LoG) finds correct edge, malfunctions at the corners, curves and where the intensity function varies. The LoG uses Laplacian filter that's why do not find the orientation of edge. The Canny edge operator performs comparatively well especially in noise conditions. The demerits of the Canny operators is that its computation is complex and takes more time.

V. CONCLUSION

In this paper, both first-order and second-order derivative edge detection techniques are reviewed. For objective evaluation the test images are taken from *Berkeley Segmentation Dataset*. The software is developed using MATLAB 7.10.0 (R2010a). The edge images are produced on the original image by different operators. Comparing the edge images with its ground truth image, precision and balanced error rate are measured. Drawbacks and advantages of the different operators are observed. None of the edge operator is perfect for edge detection. This paper concludes that after objective evaluation based on precision and balanced error rate the performance of the Canny edge detection technique is better than other techniques.

REFERENCES

[1] N. Senthilkumaran and R. Rajesh, "Edge Detection Techniques for Image Segmentation - A Survey", *Proceedings of the International Conference on Managing Next Generation*

Software Applications (MNGSA-08), 2008, pp.749-760.

[2] Mantas Paulinas and Andrius Usinskas, "A Survey of Genetic Algorithms Applicatons for Image Enhancemen and Segmentation", *Information Technology and Control*, Vol.36, No.3, 2007, pp.278-284.

[3] R. C. Gonzalez, R. E. Woods, "Digital Image Processing", 2nd edition, Upper Saddle River, New Jersey, Prentice-Hall Inc. (2002).

[4] Cyganek, C., Siebert, J. P., "An Introduction to 3D Computer Vision Technologies and Algorithms", John Wiley & Sons, Ltd (2009).

[5] Sobel, I. E., "Comera Models and Machine Perception", *PhD dissertation*, Stanford University, Palo Alto, California, 1970.

[6] L. G. Roberts, "Machine Perception of 3D Solids", *Optical and Electro-optical Information Processing*, MIT Press, 1986.

[7] Roberts, L. G., Tippet, J. T., Machine "Perception of Three-Dimensional Solids", Cambridge, Mass, MIT Press (1965).

[8] Prewitt, J. M. S., Lipkin, B. S., and Rosenfeld, "Object Enhancement and Extraction", New York, Academic Press (1970).

[9] J. F. Canny, "A Computational Approach to Edge Detection", *IEEE Trans. Pattern Anal. Machine Intell.,* vol PAMI-8, no. 6, pp. 679-697, 1986.

[10] J. Canny, Finding Edges and Lines in Image, Master's Thesis, MIT, 1983

[11] Raman Maini, HImashu Aggarwal, "Study and Comparison of Various Image Edge Detection Techniques", *International Journal of Image Processing (IJIP),* volume (3), Issue (1).

[12] M. C. Shin, D. Goldgof, and K. W. Bowyer, "Comparison of Edge Detection Performance through Use in an Object Recognition Task", *Computer Vision and Image Understanding,* vol (84), no (1), pp. 160-178, October 2001.

Proceeding of the
International Conference on Electrical, Computer and Telecommunication Engineering
01- 02 December 2012 (ICECTE2012), RUET, Rajshahi-6204, Bangladesh

ICECTE2012: PI-0114

Face Recognition using Self-Organizing Mapping Technique

Rizoan Toufiq[1], Md. Rabiul Islam[1], M. Abdus Sobhan[2] and Md. Fayzur Rahma[3]*
[1]Department of Computer Science and Engineering, Rajshahi University of Engineering & Technology
[2]School of Engineering & Computer Science, Independent University, Bangladesh
[3]Department of Electronics and Telecommunication Engineering, Daffodil International University, Bangladesh
Email: rizoantoufiq@yahoo.com, rabiul_cse@yahoo.com, m.sobuj.cse@gmail.com, mfrahman3@yahoo.com

ABSTRACT
Face recognition has been one of the most interesting and important research fields in the past few decades. It has been identified as one of the attracting research areas and it has drawn the attention of many researchers due to its varying application such as security and surveillance system, medical system, and entertainment etc. It is natural, robust and non-intrusive. These researches involve knowledge and researchers from disciplines such as neuroscience, psychology, computer vision, pattern recognition, image processing and machine learning, etc. Face recognition is a very complicated process since the human faces changes depending on their age, expression and pose. There are some difficulties to learn all types of facial features. In this paper, a recognition system for human faces using kohonen self organizing network has been developed and illustrated. The objectives of this procedure is to obtain a model that is easy to learn i.e. minimization of learning time, react well with different facial expression and pose with noisy input and optimizing the recognition as possible.

KEY WORDS: Self-Organizing mapping, Artificial Neural Network, Face Recognition, Features Extraction, Dimension Reduction etc.

1. INTRODUCTION

Pattern (i.e face) recognition can be defined in different way that is, it has two parts: feature selection (i.e some distinguish characteristic of pattern) and classifier design (i.e. classify the data set based on some criteria) [1]. Face recognition has been designed based on different classifier (i.e. GA-fisher, Back propagation Neural Network, Support Vector Machine, PCA etc) [2]-[6]. A self-organization map has been proposed by Teuvo Kohonen, where speech recognition system has been designed successfully in very noisy environment [7]. Self-Organization Mapping has been used in Natural Language Processing and Symbol Processing where word category maps have been organized according to word similarities [8]-[9]. It is difficult and time consuming to find the structures in vast multi-dimensional data sets. Exploratory data analysis and data mining has been reviewed and developed by the methodology of using Self-Organization Maps (SOMs) [10]. SOM Algorithm has been used in creating order where word categories are extracted by the "semantic" SOM and the textual context of the document is encoded based of the histograms of words formed on the word category map [11]. Another type of SOM algorithm named WEBSOM has been developed to document collection of various types [12]. Here SOMs algorithm has been used to classify the facial data sets based on the feature of the facial image in trained stage and after that, in recognition stage, new facial image has been classified to determine the similarity between the database facial images and the new entered facial image.

In this paper, the main contribution is to use the Self-organization mapping methods to recognize the facial images and find out the recognition rate. The next section describes the more details about the methodology of the Self-Organizing Mapping based on face recognition system. In section 3, Experimental result and performance analysis are described. The section 4 focuses the conclusion and observation of the work.

2. METHODOLOGY OF THE SELF-ORGANIZING MAPPING BASED FACE RECOGNITION SYSTEM

The self-organizing map, or SOM, introduced by Teuvo Kohonenis an unsupervised learning process which learns the distribution of a set of patterns without any class information that have become very popular for discovery of significant patterns or features in the input data. Using SOM as a feature extraction method in face recognition applications is a promising approach, as the learning is unsupervised; no pre-classified image data are needed at all. In the self-organizing mapping based face recognition system, facial images has been preprocessed before classifying the facial data sets by SOMs algorithm. Features have been extracted by using the self-organization neural network methods and the information formed in trained stage, has been

used in recognition stage. The main methodology of the work are shown in fig. 1

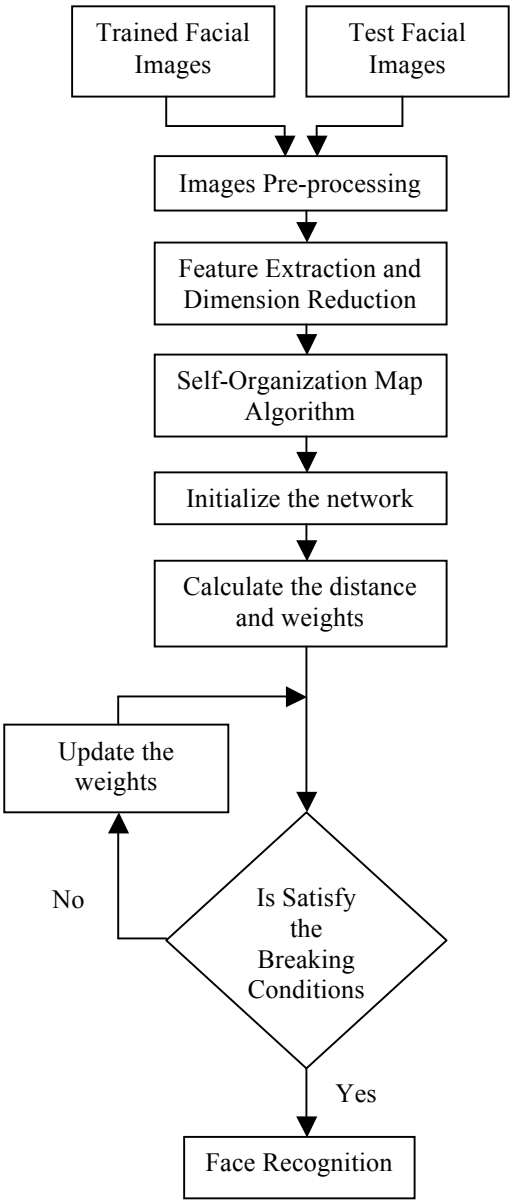

Fig. 1 Proposed face recognition system based on self-organizing mapping algorithm

2.1 Facial Image Acquisition

Indian Face database (captured in February, 2002 in the campus of Indian Institute of Technology Kanpur) has been used to test the system. The images are in JPEG format. The size of each image is 640x480 pixels, with 256 grey levels per pixel. This database contains images of 40 distinct subjects with eleven different poses for each individual. All the images have a bright homogeneous background and the subjects are in an upright, frontal position. Some sample images shown in fig. 2.

Fig. 2 Sample images of facial database

2.2 Image Filtering for Noise Reduction

Median filter technique has been used for the reduction of the noise isolated with images. This technique is very effect for 'salt & pepper' noise reduction [13]. In this stage, we lose some feature of the image to reduce the noise. Fig.3 shows the noise reduction technique.

Fig. 3 (a) Noisy image (b) Filtered image

2.3 Feature Extraction Based on Self-Organizing mapping

Recently, Self-Organizing mapping (SOMs) has been used for the dimensionality reduction. SOMs have been used as the feature extraction technique in this work, which is used to recognition stage. The steps of feature extraction are given below:

Step1: Initialize network

Define $w_{ij(}(t)$ $0 \le i \le n-1$ to be the weight from input *i* to node *j* at time t. Initialize weights from the n inputs to the nodes to small random values. Set the initial radius of the neighborhood around node *j*, $N_j(0)$, to be large.

Step 2: Present Input

Present input $x_0(t), x_1(t), ..., x_{n\ 1}(t)$, where $x_i(t)$ is the input to node *i* at time *t*.

Step 3: Calculate distance

Compute the distance d_j between the input and each output node *j*, given by

$$d_j = \sum_{i=0}^{n-1} (x_i(t) - w_{ij}(t))^2 \qquad (1)$$

Step 4: Select minimum distance

Designate the output node with minimum d_j to be j^*.

Step 5: Update weights

Update weights for node j^* and its neighbors, defined by the neighborhood size $N_{j^*}(t)$. New weights are

$$w_{ij}(t+1) = w_{ij}(t) + \eta(t)(x_i(t) - w_{ij}(t)) \qquad (2)$$

For j in N_{j^*}, $0 \le i \le n-1$

The tern $\eta(t)$ is a gain term ($0<\eta<1$) that decreases in time so slowing the weight adaption.

Here, the neighborhood of $N_{j^*}(t)$ decrease in size as time goes on thus localizing the area of maximum activity i.e shown in fig. 4 [15]

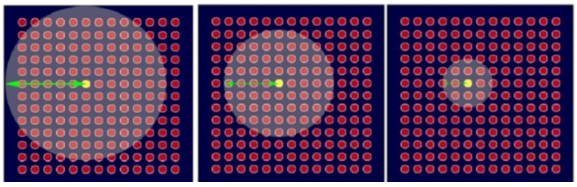

Fig.4. Examples of topological neighborhood

2.4 Face Recognition

In this stage, the new facial image has been taken as input and the feature has been extracted by using self-organizing mapping technique and find out the closing facial image from the database. The sample output of system is shown the below figure,

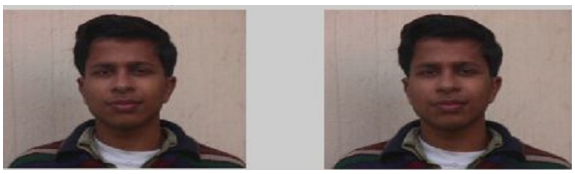

(a) Input Image **(b) Equivalent Image**

Fig 5 Sample output of the face recognition stage

3. EXPERIMENTAL RESULT AND PERFORMANCE ANALYSIS

In the experiment, Recognition rate is not less than 93% and execution time of only few milliseconds. The face recognition using Kohonen SOM has been provided more robust in accuracy and fast in execution time. The result is shown in table 1

Table 1 Recognition Rate and Execution Time for Various Number of Train Images.

No. of Train Image	No. of Test Image	No. of Recognized images	Reco-gnition rate (%)
10	20	16	80
20	20	17	85
30	20	17	85
40	20	18	90

Recognition rate Vs no. of train image line chart is shown in fig. 6.

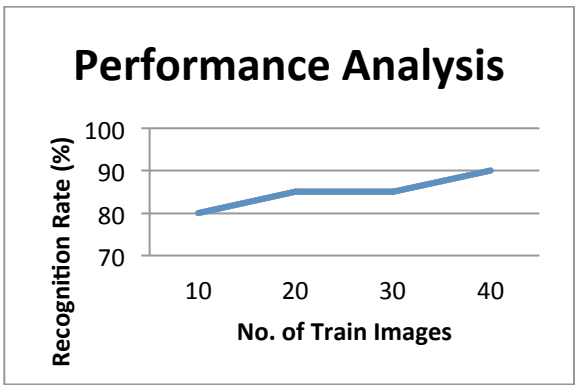

Fig.6. Recognition rate Vs no. of train image line chart

4. CONCLUSIONS AND OBSERVATION

As unsupervised learning technique, Self-Organizing Mapping has been used to classify the facial data set and the classified facial data set has been used in recognition stage to determine an unknown face is in trained data set. Previously this technique has been used to reduce dimensionality of data set. In this work, we focused on the recognition of face with high recognition rate.

REFERENCES

[1]. James C. Bezdek, James Keller, Raghu Krisnapuram and Nikhil R. Pal, "Fuzzy Models and Algorithms from Pattern Recognition and Image Processing", Springer, 2005.

[2]. Kotropoulos Bassiou Kosmidis, C. Kotropoulos, N. Bassiou, T. Kosmidis, I. Pitas, "Frontal Face Detection Using Support Vector Machines and Back-propagation Neural Networks", *Conference of Proc. Int. Conf. Image Processing*, p. 1026—1029, 2001.

[3]. P. Latha, Dr. L. Ganesan & Dr. .S. Annadurai, "Face Recognition Using Neural Networks", *Signal Processing: An International Journal (SPIJ),* Volume (3): Issue (5), p. 153-160.

[4]. Wei-Shi Zheng, Jian-Huang Lai, and Pong V. Yuen, "GA-Fisher: A New LDA-Based Face Recognition Algorithm with Selection of Principal Components", *IEEE Transactions on Systems, Man, and Cybernetics- Part B: Cybernetics,* Vol. 35, No. 6, December 2005.

[5]. Matthew Turk and Alex Pentland, "Eigenfaces for Recognition", *Journal of Cognitive Neuroscience,* Vol. 3, No. 1, Massacbusetts Institute of Technology, 1991.

[6]. Sarawat Anam, Md. Shohidul Islam, M.A. Kashem, M.N. Islam, M. R. Islam and M. S.

Islam, "Face Recognition Using Genetic Algorithm and Back Propagation Neural Network", *Proceedings of the International Multi-Conference of Engineers and Computer Scientists*, Vol.1, IMECS 2009, March 18-20,2009, Hong Kong.

[7]. TeuvoKohonen, "Self-Organizing Map", *Proceeding of the IEEE* vol. 78, No.9, 1990.

[8]. Timo Honkela, "Self-Organizing Maps of Words for natural Language Processing Application", *Proceedings of International ICSC Symposium on Soft Computing*, Nimes, rance, Setempber 1719, 1997, ICSC Academic Press, Millet, Alberta, Canada, pp. 401-407.

[9]. Timo Honkela, "Self-Organizing Map in Symbol Processing, Springer, 2000, pp. 348-362.

[10]. Kaski, S., "Data Exploration Using Self-Organizing maps", *Acta Polytechnica Scandinavica, Mathematics, Computing and Management in Engineering Series*, No.82, Espoo 1997, pp. 57, Published by the Finnish Academy of Technology. ISBN 952-5148-13-0. ISSN 1238-9803.

[11]. Samuel Kaski, Timo Honkela, Krista Lagus, and Teuvo Kohonen, "Creating an Order in Digital Libraries with Sel-Organizing Maps", *Proceeding of WCNN'96, World Congress on Neural Networks, September 1518, San Diego, California, Lawrence, Erlbaum and INNS Press, Mahwah NJ*, pp. 814-817.

[12]. Krista Lagus, "Generalizability of the WEBSOM Method to Document Collections of Various Types", *In Proc. Of 6th European Congress on Intelligent Techniques & Soft Computing (EUFIT'98)*, 1998, Vol. 1, pp. 210-214.

[13]. Rafael C. Gonzalez and Richard E Woods, "Digital Image Processing", Second edition, Prentic Hall, 2002.

[14]. Dinesh Kumar, C.S. Rai, and Shakti Kumar, "Dimensionality Reduction using SOM Based Technique for Face Recognition", *Journal of Multimedia*, Vol. 3, No. 1, May, 2008.

[15]. R Beale and T Jackson, "Neural Computing: An Introduction", IOP Publishing Ltd, 1990, ISBN 0-85274-262-2.

Proceeding of the
International Conference on Electrical, Computer and Telecommunication Engineering
01- 02 December 2012 (ICECTE2012), RUET, Rajshahi-6204, Bangladesh

ICECTE2012: PI-115

A Hybrid Feature Selection Method Using Lempel-Ziv Complexity & Principle Component Analysis

Mobarakol Islam[1], Md. Mehedi Hasan[2], Arifur Rahaman[3], M. M. Farhad[4]
[1,2,3]Dept. of Electronics & Communication Engineering,
[4]Dept. of Electrical & Electronic Engineering,
Khulna University of Engineering & Technology,
E-mail: {mobarak.islam, mehedi_ece, arifur_ece, ronieee08}@yahoo.com

ABSTRACT
Feature selection is a preprocessing step to machine learning. In this paper, we proposed a new improved hybrid filter based feature selection method called Hybrid Feature Selection with Principle Components Analysis (PCA) and Lempel-Ziv Complexity (LZC) measure (LZPC). Principal Components Analysis (PCA) is a way of identifying patterns in data, and expressing the data in such a way as to highlight their similarities and differences. The main use of PCA is to reduce the dimensionality of a data set while retaining as much information as is possible. On the other hand, LZC measure counts the number of different patterns in a sequence, starting from short patterns to the longer ones. In a data set, the variation of data means it contains more features. So from the time series LZC is measured. The features are ranked according to their values of LZCs. Here the features with higher valued LZCs are picked out and lower valued LZCs are deleted. LZPC is tested on ten real world benchmark classification problems such as Lung-cancer, Isolet, Splice, CoIL2000, Chemical, USCensus90, Arrhythmia, Musk2, Multi-Features and Promoters are used identification. The efficiency and effectiveness of our method is demonstrated through extensive comparisons with other methods using these real world data of high dimensionality. The comparison results confirm that LZPC leads to promising improvement on feature selection.

KEY WORDS: Feature selection, Filter based methods, Principle Components Analysis, Lempel-Ziv complexity, Classification.

1. INTRODUCTION

Feature selection is a frequently used as a preprocessing step to machine learning [1]. It is a process of choosing a subset of original features so that the feature space is optimally reduced according to a certain evaluation criterion [2]. Feature selection is used to reduce the cost of extracting features, to improve the classification accuracy and to improve the reliability of the estimate of performance. Feature selection also increases the generalization ability, convergence and comprehensibility of the learning mode [3]. Feature selection becomes very necessary for machine learning tasks when facing high dimensional data because high dimensional data can contain high degree of irrelevant and redundant information which may greatly degrade the performance of learning algorithm.

There are so many feature selection methods that approach the task as a search problem, where each state in the search space specifies a distinct subset of possible features [4]. The feature selection methods are classified as wrapper and filter methods [5]. In wrapper method, the learning model is run on a specific subset of features and after that test set is used to measure the accuracy. And the features with higher accuracy are selected. In filter method, the features are filtered out which are irrelevant to the target concept [6].

There are many filter based algorithms in literature. By measuring correlations among the features together with classes features can be selected [7]. For this case the highly correlated features may be converged when selecting them if less correlated features are deleted. For this reason this is not well performed in all cases. Information theoretic measure has been used in ranking the features [8]. In this case, the mutual information among the features together with classes is computed and the redundant features are deleted.

In a set of data there are so many features. And among these features there are some major components which define the characteristics of the data set. The principal component analysis (PCA) technique has been investigated before by researchers for signal and image processing [9], [10]. Principle component analysis is a popular tool for data analysis and dimensionality reduction. Dimensionality reduction transformations can have a variety of optimality criteria, and ten of them discussed in [11] lead to the principal component solutions, which is one reason for the popularity of this analysis. Essentially, in PCA a set of correlated variables are transformed into a set of uncorrelated variables which are ordered by reducing variability. The uncorrelated variables are linear combinations of the original variables, and the last of these variables can be removed with minimum loss of real data. The

main advantage of PCA is to reduce the number of dimensions, without much loss of information.

Complexity tends to be used to characterize something with many parts in intricate arrangement. Complexity of any system is measured to solve real world problems [12]. Lempel and Ziv proposed a useful complexity measure, which can characterize the degree of order or disorder and development of spatiotemporal patterns [13]. After normalization the relative Lempel-Ziv complexity measure (L-Z measure) reflects the rate of new pattern occurrences in the investigated series of the symbols. L-Z values range from near 0 to 1. Lempel-Ziv Complexity (LZC) is a good mathematical tool to compute the number of unique patterns in a time series [14].

In this paper, a new improved hybrid filter based FS technique (LZPC) is proposed. LZPC requires low computational efforts. It is the combination of PCA and LZC measure. PCA finds the principle features from a data set and store these features. After that, LZC computes the complexity from the stored features. The feature with higher value of LZC is selected and the lower one is deleted. In order to justify LZPC, the selected features are applied to neural network (NN) learning model [15]. In the experiments, several benchmark classification problems such as Lung-cancer, Isolet, Splice, CoIL2000, Chemical, USCensus90, Arrhythmia, Musk2, Multi-Features and Promoters are used. It is shown that the selected features with LZPC produce more accuracy than some other FS algorithm in neural network learning.

The rest of the paper is organized as follows. The proposed LZPC is described in section II. Section III includes the experimental studies. The discussion on LZPC is presented in section IV. Section V concludes the paper.

2. PROPOSED METHOD

LZPC is the hybrid form of PCA and LZC measure. LZPC first finds the principle features from the data sets and then LZC compute the complexity of the principle features. The features with higher complexity are selected and the features with lower complexity are deleted. And these selected features are applied to the NN learning model.

2.1 Principle Components Analysis

Principle component analysis is a popular tool for data analysis and dimensionality reduction. Selecting the most representative features as inputs to the machine condition monitoring system presents another challenge. PCA reduces dimension from a given data set. The consecutive steps of PCA are given below.

Step 1) Get data
Step 2) Subtract the mean
Step 3) Calculate the covariance matrix
Step 4) Calculate the Eigen vectors and Eigen values of the covariance matrix
Step 5) Choosing top components and forming a feature vector by projection
Step 6) Driving the new data set by using following equation:

Final data = Row feature vector * Row data adjust

2.1 Lempel-Ziv Complexity

Complexity means a large number of parts in intricate arrangement. Lempel-Ziv complexity is a measure of unique patterns in a given data set or a set of features. The Lempel-Ziv algorithm objectively and quantitatively estimates the system complexity through the change process of system structure, and has overcome the limitation of depicting the complexity through characteristic quantities of statistical complexity. A standard algorithm is given below for computing the complexity of data set. Here N denotes the number of feature and P denotes the number of pattern.

Step 1) Begin
Step 2) i varies from 1 to N with an increment 1
Step 3) S varies from 1 to P an increment 1

```
If (x(s) <a)
    x(s) =0;
Else
    x(s) =1;
End step 3 & go to step 4
```

Step 4) Save first value in a string
Step 5) Run step 6 to 9 until Z=Pattern (Z increases by 1 for each iteration until the loop end)
Step 6) Take next input in a new string
Step 7) Compare it with previous string
Step 8) if same then take next input in the string until it became different from other strings
Step 9) Move to step 6
Step 10) Exit

The values of a feature selected from PCA are the floating values in the range of zero to unity. If a value is greater than 0.5, it is considered as one, otherwise zero. So a binary string is formed for a feature. The LZC of the string is computed and it is considered as the LZC of corresponding feature. By the same way, LZCs of all the features are computed. The features with higher complexity are used to train the NN learning and also from the learning network accuracy is computed.

3. EXPERIMENTAL STUDIES

3.1 Representative Feature selection algorithms

In our experiments, we choose four representative feature selection algorithms in comparison with LZPC. One is Fast Correlation Based Filter Solution (FCBF) which introduces the concept of predominant correlation and a fast filter method that can identify relevant features as well as redundancy among relevant features without pairewise correlation

analysis. Another one is a feature weighting algorithm, ReliefF (an extension to Relief) which searches for several nearest neighbors to be robust to noise and handles multiple classes; the other two are subset search algorithms which exploit sequential forward search and utilize correlation measure or consistency measure to guide the search, denoted as CorrSF and ConsSF respectively. To evaluate the accuracy on selected features we trained and tested a NN learning algorithm for each feature selection method.

3.2 Characteristics of Benchmark datasets

LZPC is applied on ten benchmark classification problems – Lung-cancer, Isolet, Splice, CoIL2000, Chemical, USCensus90, Arrhythmia, Musk2, Multi-Features and Promoters identification. Some characteristics of the datasets are listed in Table 1. For example, Lung-cancer problem is a classification problem having a total examples or patterns of 32 with 57 attributes and 3 classes. Other problems are arranged in a similar fashion. The total examples of a dataset are divided into training examples and testing examples. The training examples are used to train the NN and the trained NN is tested with the testing examples.

Table 1: Characteristic of Benchmark Datasets

Datasets	Number of		
	Instances	Features	Output Classes
Lung-cancer	32	57	3
Isolet	1560	618	26
Splice	3190	62	3
CoIL2000	5822	86	2
Chemical	936	151	3
USCensus90	9338	68	3
Arrhythmia	452	280	16
Musk2	6598	169	2
Multi-Features	2000	650	10
Promoters	106	59	2

3.3 Experimental Process and Comparison

Table 2 records the number of selected features for each feature selection algorithm. From the experimental results it is clear that LZPC achieves the highest level of dimensionality reduction by selecting the least number of features, which is consistent with our theoretical analysis about LZPC's ability to identify redundant features. For example, the selected features for arrhythmia problem is 6 by FCBF, 25 by ConSF, 25 by ReliefF, 24 by ConsSF where as only 5 features are selected by LZPC.

Table 2: Number of selected features for each feature selection algorithm

Title	Selected Features				
	FCBF	CorrSF	ReliefF	ConsSF	LZPC
Lung-cancer	5	8	5	4	4
Isolet	2	137	2	11	2
Splice	6	6	1	10	7
CoIL2000	3	10	1	29	6
Chemical	4	7	7	11	4
USCensus90	2	1	2	13	2
Arrhythmia	6	25	2	24	5
Musk2	2	10	2	11	2
Multi-Feature	14	87	14	7	8
Promoters	4	4	4	4	4

On the other hand, Table 3 shows the learning accuracy of NN on different feature sets. From the averaged accuracy over all data sets we observed that, LZPC improves the accuracy of NN. From individual accuracy values, it is certified that for most of the data sets LZPC can maintain or even increase the accuracy.

Table 3: Accuracy of neural network learning algorithm on selected features for each feature selection method

Title	FCBF	CorrSF	ReliefF	ConsS F	LZP C
Lung-cancer	87.50	84.17	80.83	84.1	88.5
Isole	75.77	80.70	52.44	69.2	82.6
Splice	93.48	93.48	89.25	93.9	93.6
CoIL2000	94.02	94.02	94.02	93.9	94.0
Chemical	95.51	96.47	93.48	95.7	96.5
USCensus90	98.08	97.95	98.08	98.2	97.9
Arrhythmia	72.79	68.58	65.90	67.4	75.7
Musk2	91.33	95.56	94.62	95.3	91.4
Multi-Features	95.06	94.95	80.45	90.8	95.1
Promoters	87.73	87.73	89.64	84.0	88.1
Average	89.13	89.36	83.87	87.2	90.3

The above experimental results suggest that LZPC is practical for feature selection for classification of high dimensional data.

We have also applied this method on a human face. From which it first extracts the principle features of that image by applying PCA. Then the PCA image has been run by the LZC algorithm to reduce the feature. We have used a threshold value to select the complexity. The features which contain high complexity have been taken as the final feature. Figure 1(a) shows the actual image where as figure 1(b) and figure 1(c) shows the image after applied PCA and LZC respectively. The first figure is 515 X 952 pixels, when PCA was applied the pixels were reduced to 215 X 742 and when LZC was applied to the PCA image then the pixels became 215 X 300.

Fig. 1 (a): Actual image

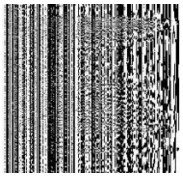

1(b)

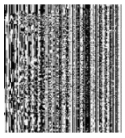

1(c)

Fig. 1(b) 1(c): PCA applied image and LZC applied image

4. DISCUSSION

Feature selection is an essential task for high dimensional data set. LZPC combines the PCA and LZC to select features. Here by using PCA the major features are selected and from the selected data complexity is measured by using LZC. The difference between LZPC and other feature selection methods is that they only reduce features from the whole data set where as LZPC first selects the principle components and then measuring the complexity, it again reduces the features. So it reduces the features in two ways and so that the number of selected feature is less than from other methods.

5. CONCLUSION

This paper proposes a hybrid filter based feature selection method, called LZPC which introduce an efficient way of analyzing feature redundancy. In LZPC, the major features are selected by PCA and LZC computes the complexity of those features. In fact LZC is a good tool to determine the number of unique patterns in a feature and so that LZPC selects the features which have higher number of unique patterns. LZPC is tested on several real world benchmark classification problems such as Lung-cancer, Isolet, Splice, CoIL2000, Chemical, USCensus90, Arrhythmia, Musk2, Multi-Features and Promoters to compare with other feature selection algorithms. Our approach demonstrates its efficiency and effectiveness in dealing with high dimensional data for classification. So LZPC is capable to train NNs with reduced features and highest accuracy than that of other feature selection algorithms.

REFERENCS

[1] Tang Lei, Liu Huan, Bias analysis in text classification for highly skewed data, *In the proc. of Fifth IEEE International Conference on Data Mining,* pp. 4, 2005.

[2] Zitao Liu Wenchao Yu Wei Chen Shuran Wang Fengyi Wu, Short text feature selection for micro-blog mining, *In the proc. of International Conference on Computational Intelligence and Software Engineering,* pp. 1-4, 2010.

[3] R. Kohavi and G. John,"Wrappers for feature subset selection", *Artificial Intelligence*, vol. 97, pp. 273-324, 1997.

[4] Avrim Blum and Pat Langley, "Selection of relevant features and examples in machine learning," *Artificial Intelligence*, vol. 97, no. 1-2, pp. 245-271, 1997.

[5] M. Dash and H. Liu, "Feature selection for classifications", *Intelligent Data Analysis: An International Journal*, vol. 1, pp. 131-156, 1997.

[6] I. Guyon and A. Elisseeff, "An Introduction to variable and feature selection", *Journal of Machine Learning Research*, vol. 3, pp. 1157-1182, 2003.

[7] L. Yu and H. Liu, "Feature Selection for High-Dimensional Data: A Fast Correlation-Based Filter Solution", *Proceedings of the Twentieth International Conference on Machine Learning*, Washington DC, 2003.

[8] P. E. Meyer, C. Schretter, and G. Bontempi, "Information-Theoretic Feature Selection inMicroarray Data Using Variable Complementarity", *IEEE trans. selected topics in signal processing, vol. 2, no. 3*, pp 261-274, June 2008.

[9] V. Algazi, K. Brown, and M. Ready, "Transform representation of the spectra of acoustic speech segments with appliances, part I: General approach and application to speech recognition," *IEEE Trans. Speech Audio Process.*, vol. 1, pp. 180–195, 1993.

[10] L. Sirovich and L. Keefe,"Low dimensional procedure for characterization of human faces," *J. Opt. Soc. Amer.*, vol. 4, pp. 519–524, 1987.

[11] G.P. McCabe. Principal variables. *Technometrics*, 26:127-134, 1984.

[12] T. D. Jorgensen and B. P. Haynes, "Pruning artificial neural networks using neural complexity measures", *International Journal of Neural Systems,* vol. 18, no. 5, pp. 389-403, 2008.

[13] Lempel A, Ziv J. "On the complexity of finite sequences". IEEE Trans Inform Theory, 1976; 22(1): 75-81.

[14] Willi-Hans Steeb, "*The Non linear Work Book*"- World Scientific Publishing Co. Third Edition, Chapter 2, pp. 107.

[15] Q. Song, Y. C. Soh, and L.Zhao, "A robust extended Elman backpropagation algorithm", *In the Proc. of International Joint Conference on neural network (IJCNN 2009)*, pp. 2971-2978, 2009.

Proceeding of the
International Conference on Electrical, Computer and Telecommunication Engineering
01- 02 December 2012 (ICECTE2012), RUET, Rajshahi-6204, Bangladesh

ICECTE2012: PI-0116

An Enhanced Circular and Non-circular Iris Segmentation and Localization using Circle Hough Transform and Arched Hough Transform Algorithm

Jannatul Ferdous[1], Md. Arafat Hossain[2]
Department of Computer Science and Engineering
E-mail: shimul072426@gmail.com, arafat.ruet03@gmail.com

ABSTRUCT
Iris segmentation, including localization and noise removal, is a fundamental step in iris recognition systems as the performance of the system is highly depend on this step. There are a few existing techniques for iris segmentation in which iris detection using Circular Hough Transform is the most reliable and popular But it does not gives high accuracy with images containing noise or occlusions caused by eyelids. So sour proposed method enhanced the Circular Hough Transform and gives a better result. This method is only applied in circular eye. In this paper, we also propose a new localization algorithm for non circular iris. Inner boundary is detected by using a set of morphological operators and canny edge detector are applied to the square region, which surrounds the pupil. Outer boundary is divided into right and left sides in which they are detected by arched Hough transform and finally merged together.

KEY WORDS: Iris Localization, Segmentation, Boundary, Circular Hough transform, Arched Hough Transform, Morphology.

1. INTRODUCTION

Nowadays, Iris recognition, as of the most accurate biometric system, has been received more attentions. Iris segmentation is the first and, probably, the most important step in an iris recognition system. The performance of the system is highly depending on this step and mishandling it leads to error in the task of identification. Iris segmentation consists of two sub steps: localization and noise removal. The task of localization is to detect inner (iris/pupil) and outer (sclera/iris) boundaries. Noise removal is the post-processing stage, which excludes any non-iris regions such as which excludes any non-iris regions such as eyelids, eyelashes and specular reflections. There are two classical ways to do iris localization: using intensity information [1,2] and edge information [3]. First approach, which is proposed by Daugman, find the circle parameters, radius(r) and center coordinates (x0,y0), from the smoothed image I(x,y) by Gaussian function Gσ(r), for inner and outer boundaries. Second approach, which is developed by Wildes, used edge detection techniques plus Hough transform to fit a circle for each of boundaries. Unfortunately, both of these methods take long time due to search in the whole image. In order to accelerate localization process, some researchers utilized coarse to fine strategy. Ren et al. [4] used the point that pupil is the darkest region in the image, improved the performance of Daugman's algorithm. Ma et al. [5] and Monro et al. [6] presented improved algorithms based on wildes' method by using of the above point to confine the search space of the Hough transform. Furthermore, some researchers proposed other methods for localization. In [4] authors used intensity threshold to binarize the eye image. In order to fill holes caused by bright spots on the pupil and eliminating the effects of eyelashes in the binary image, they applied Morphological operators such as erosion and dilation. Then they attempted to fit a circle for each of the boundaries by miscellaneous methods such as using sudden change in the intensity derivative [7], statistical properties [2], geometrical method based on circle vertical bisector intersection points [6] and mapping into a complex domain [5].

2. CIRCULAR IRIS LOCALIZATION

The whole process is divided into 4 steps[1]:

2.1 ENHANCED PUPIL BOUNDARY DETECTION ALGORITHM

Step 1: Transform the original grey scale eye image into a binary image by applying global threshold to segment the pupil whose grayscale values are much smaller than other eye components. This threshold computes the constant of the threshold using the image space; transforming an image to a binary image g as thus

$$g(x,y)=\int_{1}^{0} \quad \begin{matrix} if\ (x,y)>1 \\ 0 \end{matrix} \qquad \text{.....(Eq. 1)}$$

T is the threshold value.

Step 2: Inversion of the dark color pupil to white to make it visible since it is the area interest.

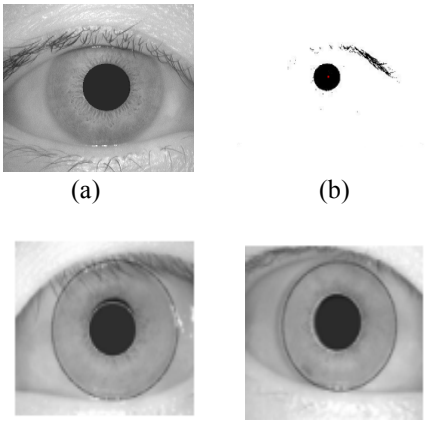

(a) (b)

(c) (d)

Fig.1. (a) Input image (b) Binarized image (c) Applying Hough Transform (d) Removed Eyelids and Eyelashes.

2.2 FINDING PUPIL CENTER ALGORITHM

Step 1: Scan through the binary image starting from the top left horizontally, using 8 mark the first and last 8-neigbour encountered whose value is 1, that should form a vertical bisector of the pupil circle at 0^0 and 180^0 respectively.

Step 2: Scan vertically through the image this time, and repeat step 1.

Step 3: Connect these two opposite point; whose midpoint half of the length of the opposite connected pixel is an assumed radius of the pupil.

Step 4: Use the assumed center and radius detected to localize the pupil circular shape.

2.3 DETECTION OF IRIS BOUNDARY USING HOUGH TRANSFORM ALGORITHM

Step 1: Remove the noise on the eye image by applying minimal blurring to avoid making the boundary difficult to avoid making the boundary difficult to visualize.

Step 2: Apply 5 by 5 average filter for smoothing the image on the original intensity image.

Step 3: Feed the pupil center parameter as detected in section 3 to circle Hough transform to detect the iris boundary.

2.4 DETECTION AND REMOVAL OF EYELIDS AND EYELASHES

Step 1: Apply canny edge operator on the eye image

Step 2: Locate four different edge point pixels on the top (left and right) and bottom (left and right respectively lying on the edge map of the eyelids detected by canny edge operator.

Step 3: Use the center of the pupil which is also the center of the iris, to exclude it from the iris.

3. NONCIRCULAR IRIS LOCALIZATION

In this paper we use two separate localization Algorithms for inner and outer boundaries without any assumption for their shapes.

3.1 FINDING INNER BOUNDARY

Step 1: Finding approximate location of pupil: Pupil and sometimes eyelashes and eyebrows are the darkest regions in the iris images. In this step, the original image is divided into identical square blocks and the first one with the minimum average intensity is found. Size of the blocks should not be too small.

Step 2: Finding the optimum window: Nevertheless, if we can find sub image, which surrounds the pupil and then threshold the sub image, in the binarized sub image, the presence of eyelashes would minimized. In this step, we are looking for the optimum window, which completely surrounds the pupil and including the least regions from other parts of the image. In so doing, we define the windows with different sizes and origins.

Step 3: Threshold: To attain binary version of the sub image in the optimum window, a threshold is required.

Step 4: Detecting exact inner boundary: At first, we applied canny edge detector to the sub image to extract the edges of the pupil as shown in Figure (d). The previous works which are based on edge detection, extracted the edges of the pupil .Therefore, they used curve-fitting techniques, such as the Hough transform and geometrical methods, to fit a circle or an ellipse for the inner boundary based on the extracted edges.

Step 5: In this step, the inner boundary is detected with no assumption for the shape of it.

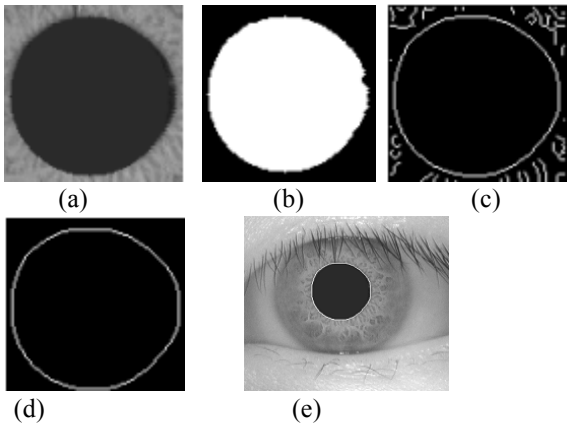

(a) (b) (c)

(d) (e)

Fig 2. (a) Sub-image of original image, (b) binarized sub-image (c) Canny Edge operator (d) Edge removed (e) Extract inner boundary

3.2 FINDING OUTER BOUNDARY

In order to detect outer boundary, three main steps are used as mention below:

Step 1: In order to reduce the effect of the eyelashes and the iris patterns in the extracted edges, we apply a median filter to original image. The result of applying median filter is portrayed in Fig. 3 (a).

Step 2: Canny edge detector is used to extract the edges of smoothed image, which was produced in the previous step. This process is depicted in Fig. 3(b). Because the occlusion by eyelids and eyelashes, the edges in the upper and lower of the iris are corrupted and not be valid in the evidence-gathering procedure of the Hough transform. So we removed these edges based on the location of the optimum window. In so doing, all edges placed in the window and upper and lower parts of the window is deleted as shown in Fig. 3 (c).

Step 3: The outer boundary is divided into right and left sides and supposed each of them to be arched. Therefore, we applied the arched Hough transform based on located the pupil for each side as they not included visible arc scope of opposite side as shown in Fig. 3 (d). This process is used to form intersection points in order to merge two arcs together. So this process makes the outer boundary. Fig. 3 (d) shows the detected outer boundary of the iris.

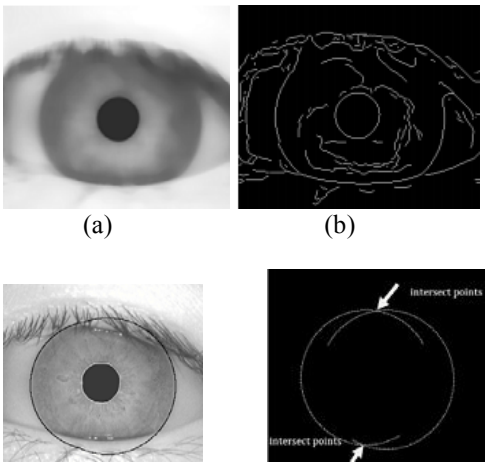

(a) (b)

(c) (d)

Fig.3. (a) Apply median filter (b) Canny edge Operation (c) Aarched Hough transform (d) detected Outer boundary.

4. EXPERIMENTAL RESULTS

4.1 RESULT of CIRCULAR IRIS DETECTION

By using enhanced Hough Transform algorithm iris localized and segmented in five stages and every stage we use one algorithm, these algorithms are already discussed in previous chapter and now we just show the result after applying these algorithm. The technique of Circular Hough Transform discussed in implemented for finding the radius of iris and pupil and centre of iris. A grayscale image using appropriate threshold. This step was done to remove some noise from image. Then edges were found using any edge detection technique. This step is required since Hough Transform requires edge points. There are various edge detectors like Canny, Sobel, Prewitt[2]. For our purpose Canny edge Operator was used. A range of radius was chosen.

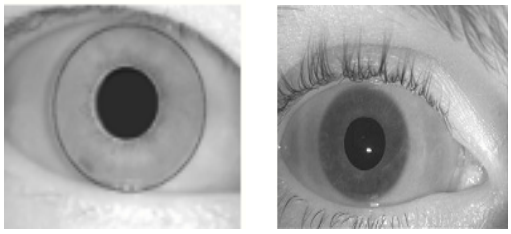

(a) (b)

Fig.4. (a) Input image (b) Detected the circular iris

4.2 RESULT of NON-CIRCULAR BOUNDARIES

Proposed method for Noncircular Iris Boundaries using Morphology and Aarched Hough Transform is Segmented and Localized by following two algorithms. One algorithm is using for detecting inner Boundary of iris and another algorithm is used for outer boundary. Though these algorithms have some steps that are discussed in implementation chapter so here we show only the final result.

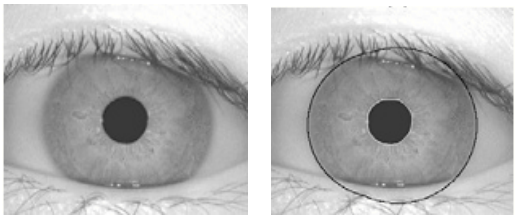

(a) (b)

Fig.5. (a) Input image (b) Localized non circular iris boundaries

5. CONCLUSION

The paper introduced an efficient iris localization algorithm without any assumption for the shape of the iris boundaries. In order to find the inner boundary, a new algorithm was presented which used of intensity and edge information with threshold. The paper introduced an efficient iris localization algorithm without any assumption for the shape of the iris boundaries. In order to find the inner boundary, a new algorithm was presented which used of intensity and edge information with threshold.

REFERENCES

[1]. L. Ma, T. Tan, Y. Wang and D. Zhang, "Personal Identification based on Iris Texture Analysis", IEEE Transactions on Pattern

Analysis and Machine Intelligence, Vol. 25, No. 12, pp. 1519-1533, 2003.
[2]. Bhola Ram Meena, "Personal Identification based on Iris Patterns", Ph.DThesis,Department of Computer Science and Engineering, Indian Institute of Technology, Kanpur, 2004.
[3]. M. Vatsa, R. Singh, and A. Noore, "Reducing the False Rejection Rate of Iris Recognition Using Textural and Topological Features", International Journal of Signal Processing, Vol. 2, No. 2, pp. 66-72, 2005.
[4]. R.Woods,R.Gonzales,Digital image processing using matlab,2nd edition,Prentice Hall.
[5]. P. Gupta et al," Iris Recognition using Corn Conference on Research and Developing Systems', pp.169-172, 2002.
[6]. Nabti M and Bouridane A, "effective and fast iris recognition based on a combined multiscale feature extraction technique", Proceedings of Pattern Recognition, Vol: 41, pp: 808 – 879, 2008.

Proceeding of the
International Conference on Electrical, Computer and Telecommunication Engineering
01- 02 December 2012 (ICECTE2012), RUET, Rajshahi-6204, Bangladesh

ICECTE2012: PI-0117

Feature-based Image Registration Technique

Md. Baharul Islam[1], *Mir Md. Jahangir Kabir*[2]
[1]School of Computer Engineering, Nanyang Technological University, Singapore
[2]Department of Computer Science & Engineering, Rajshahi University of Engineering & Technology
E-mail: md3@e.ntu.edu.sg, mmjahangir.kabir@gmail.com

ABSTRACT
Image registration (IR) is one of the important operation of image processing system which is the process of aligning two or more images into one coordinate system that are taken at different times, from different sensors or viewpoints. It has a lot of applications especially medical imaging and remote sensing. The main purpose of this paper is to provide a comprehensive review of existing literature's available on image registration system and proposed a new feature-based IR technique using edge of images. I believe that it will be a useful document for researchers who will work on feature-based image registration regardless for specific applications.

KEY WORDS: Feature detection, image registration, feature extraction, transformation

1. INTROCUCTION

Images need to geometrically align to one another to get better observation for image registration. There are a lot of applications of IR such as motion correction, correcting of geometric distortion, formulation of composite functional maps, mapping of Positron Emission Tomography (PET) or Single Photon Emission Computed Tomography (SPECT) to Magnetic Resonance Imaging (MRI) and many more. Reference [1] are given the details applications of IR in different fields. There are a lot of image features that can be used for feature-based image registration. I preferred edge as a feature of an image that covered surrounding of images. Edge detection is divided by two categories gradient and Laplacian. The gradient method detects the edges by finding for the maximum and minimum in the first derivative of the image whereas the Laplacian method searches for zero crossings in the second derivative of the image. I took gradient method for edge detection in my experiment because of two filters like horizontal and vertical. Fig. 1 is shown the concepts of image registration system. Basically there are four steps involving in image registration system.

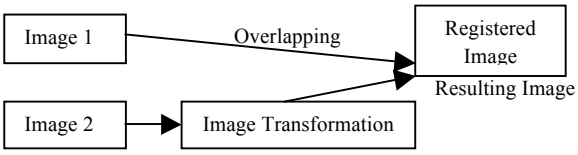

Fig. 1 Concepts of image registration

1.1 Feature Detection

Feature detection is usually performed as the first operation on an image and examines every pixel to see if there is a feature present at that pixel. It involves finding features in the two or more images that to be registered. It may be point, edge, corner, pixels, textures, colours, histogram etc. The resulting features will be subsets of the image domain, often in the form of isolated points, continuous curves or connected regions. Selecting image features depend on the problem of image registration and the type of application on it. A feature is defined as an interesting part of an image. Since features are used as the starting point and main primitives for subsequent algorithms. The overall algorithm will often only be as good as its feature detector. Consequently the desirable property for a feature detector is repeatability; whether or not the same feature will be detected in two or more different images of the same scene.

1.2 Feature Matching

After the strong feature points detected from reference and sensed images, a corresponding mechanism is required between two feature point sets. This correspondence mechanism fulfils the requirement of pairing the feature point of reference image with its correspondent one in the sensed image. References [2] [3] are worked on feature point matching using on Zernike moment. It is a very important step because the percentage of correct matches depends on how well the transformation can be estimated in the next step. Common matching methods include simple city block distance, Euclidean distance matching and nearest neighbour based matching.

1.3 Transformation

The mapping function is constructed after the feature correspondence has been established. It should transform the sensed image to overlay it over the reference one. The transformation could be rigid, affine, projective or nonlinear [1]. The first broad category of transformation models includes linear transformation which includes translation, rotation, scaling, and other affine transforms. The second category of transformations allows 'non-rigid' transformations. These transformations are capable

of locally warping the target image to align with the reference image. Non-rigid registration using Free Form Deformation (FFD) shows on [4] [5].

1.4 Image Re-sampling

The last step of any image registration system involves the correct mapping of the one image to another using the transformation model estimated in previous step. Point-by-point will be corresponding one image to another in one coordinate system. Each pixel from the sensed image can be directly transformed using the estimated mapping functions. Reference [6] published a survey article covering main interpolation methods for re-sampling with the emphasis on medical imaging applications. There are no re-sampling functions necessarily interpolate the image gray levels [7].

2. LITERATURE REVIEW

Image registration is widely used in different important areas. References [8] [9] were reviewed on medical image registration techniques. A phase-based and some feature-based image registration algorithms were implemented by [10]-[13]. A new registration algorithm based on Newton-Raphson iteration is proposed to align images with rigid body transformation [14]. PET/CT and MR Image registration using Normalized Cross Correlation (NCC) algorithm and Spatial Transformation (ST) techniques introduced on [5] [15] [16]. 3D real-time elastic image registration and multimodal medical image registration algorithm implemented by [6] [17]. Comparisons of edge-based and ridge-based registration of CT and MR brain images done by [18]. Algorithms based on Q-shift, entropy, automatic robust implemented in [19]-[21]. Reference [22] proposed invariant image recognition by Zernike moment. Image registration using correlation techniques introduced by [23]-[25]. High resolution remote sensing image registration by combination of feature-based and area-based proposed by [26]. Image and surface registration using neural network implemented by [27]-[32]. References [33] [34] proposed genetic image registration techniques. Non-rigid image matching and registration were implemented from some of author's [35]-[38].

3. EXPERIMENTAL FRAMWORK

We are implemented a feature-based image registration technique. We used edge as features of image. Fig. 2 is shown the proposed technique for feature-based image registration.

This project was the requirements of Master of Science degree in Nanyang Technological University, Project No. SCE/DMT/10/039

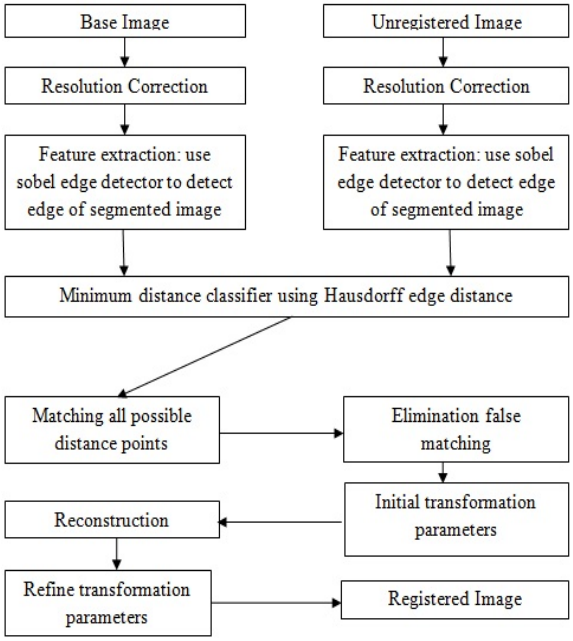

Fig. 2 Proposed image registration technique

3.1 Feature Extraction

Feature extraction involves simplifying the amount of resources required to describe a large set of data accurately. There are many ways to extract features from an image. Low-level features to be those basic features that can be extracted automatically from an image without any shape information. Low level feature is called edge of image and it aims to produce a line drawing. High-level feature extraction concerns finding shapes in an image. Shape extraction implies finding their position, orientation and their size.

3.1.1 Image Segmentation

Image segmentation for the purpose of obtaining boundaries is an important step in a feature-based registration system. There are many segmentation techniques available that could be used. However, there is no unique segmentation technique that can perform best on all types of images, and most segmentation techniques are image-dependent. The goal of segmentation is to simplify and/or change the representation of an image into something that is more meaningful and easier to analyze. It is typically used to locate objects and boundaries in images. More precisely, image segmentation is the process of assigning a label to every pixel in an image such that pixels with the same label share certain visual characteristics. For intensity images, there are four popular approaches such as threshold techniques, edge-based methods, region-based techniques, and connectivity-preserving relaxation methods. We are applied here edge-based methods for image segmentation that are shown in Fig. 3.

Fig. 3 Image segmentation

3.1.2 Sobel Edge Detector

We are used to detect edge feature of images using sobel edge detector. The sobel operator performs a 2D spatial gradient measurement on an image. Typically it is used to find the approximate absolute gradient magnitude at each point in an input grayscale image. The sobel edge detector uses a pair of 3x3 convolution kernel, one estimating the gradient in the x-direction and the other estimating the gradient in the y-direction. A convolution kernel is usually much smaller than the actual image. As a result, the kernel is slid over the image and manipulating a square of pixels at a time. The sobel operator consists of a pair 3×3 convolution kernel is shown in Fig. 4. One kernel is simply rotated by 90° to get another kernel.

-1	0	+1
-2	0	+2
-1	0	+1

Gx

+1	+2	+1
0	0	0
-1	-2	-1

Gy

Fig. 4 Sobel convolution kernel

3.2 Hausdorff Distance Measurements

We used hausdorff distance to measure image difference according to their edges. Hausdorff distance from set A to set B is a maximum minimum function defined as

$$H(A, B) = \max_{a \in A} \{\min_{b \in B} \{d(a, b)\}\} \quad (1)$$

Where a and b are points of set A and B respectively and d (a, b) is the distance between these points. For simplicity, we took d (a, b) as the Euclidian distance between a and b. Fig. 5 is shown hausdorff distance classifier between two images.

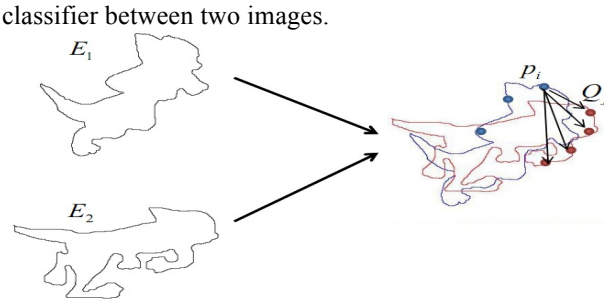

Fig. 5 Hausdorff distance of two images

$$\text{Distance} = \max(H(E1, E_2), H(E2, E_1)) \quad (2)$$

$$H(E1, E_2) = \max_{Pi \in E1}(\min_{Qj \in E2}(\|P_i - Q_j\|)) \quad (3)$$

3.3 Finding the Matching Pairs

Now we are ready to find the matching feature point pairs between $f_1(x, y)$ and $f_2(x, y)$. The first step of the process is to rotate all the points in $f_1(x, y)$ to their new positions located in F1(X, Y) where,

$$X = x\cos\theta + y\sin\theta \quad (4)$$

$$Y = -x\sin\theta + y\cos\theta \quad (5)$$

If an edge point in f_1 is rotated to a new position in F_1, the angle θ is also adjusted to suit the coordinates of F_1.

3.4 Eliminating the False Matching Pairs

Reference [39] proposed an iterative scheme that could not remove false pairs completely and efficiently. A new method is proposed to eliminate the incorrectly matched pairs. We present a non iterative scheme based on the idea that the distance between two points in the same image will be preserved when it undergoes a rigid transform. If all the matching pairs are correct then the following equation should hold

$$P_i = Sq_i + T \text{ for } i = 1, 2 \ldots N_m \quad (6)$$

Where S and T are scalar and translation vector respectively.

4. EXPERIMENTAL RESULTS

We will see some resulting images that are used in our experiments. Fig. 6-7 is showing some images that used our proposed IR technique whereas first two images were reference and sensed image and last one was registered image respectively.

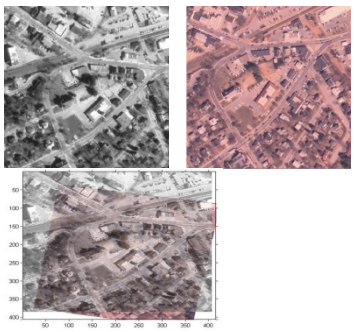

Fig. 6 Reference image, sensed image and resulting registered images (aerial)

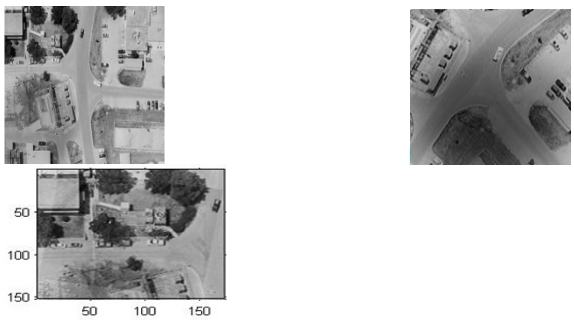

Fig. 7 Reference image, sensed image and resulting registered image (aerial)

5. CONCLUSIONS

We used Intel core i3 processor with 4GB RAM to run our experiment. The timing complexity was 1.2 seconds to come output results using MATLAB 2008a. Our proposed technique for image registration is used edge as a feature of an image. There are a lot of image registration systems using other features rather than edge as a feature of image.

REFERENCES

[1]. M. V. Wyawahare, P. M. Patil, H. K. Abhyankar, "Image registration techniques: an overview", *International Journal of Signal Processing,Image Processing and Pattern Recognition*, vol. 2, issue 3, 2009.

[2]. J. Sarvaiya, S. Patnaik, H. Goklani, "Image Registration using NSCT and Invariant Moment", *International Journal of Image Processing*, vol. 4, issue 2, pp. 119-130.

[3]. A. Khotanzad, Y. H. Hong, "Invariant Image Recognition by Zernike moment", *IEEE Transactions on Pattern Analysis and Machine Intelligence*, vol. 12, issue. 5, pp. 489-497, 1990.

[4]. D. Rueckert, L. I. Sonoda, C. Hayes, D. L. G. Hill, M. O. Leach, D. J. Hawkes, "Nonrigid Registration Using Free-Form Deformations: Application to Breast MR Images", *IEEE Transactions on medical imaging*, vol. 18, no. 8, 1999.

[5]. C. R. C. Pareja, "Real-time 3D elastic image registration", *Dissertation, Doctor of Philosophy in the Graduate School of The Ohio State University*, 2004.

[6]. T. M. Lehmann, C. Gonner, K. Spitzer, "Survey: interpolation methods in medical image processing", *IEEE Transactions on Medical Imaging*, vol. 18, pp. 1049–1075, 1999.

[7]. P. Venaz, T. Blu, M. Unser, "Interpolation revisited", *IEEE Transactions on Medical Imaging*, vol. 19, pp. 739–758, 2000.

[8]. J. B. A. Maintz, M. A. Viergever, "A Survey of Medical Image Registration", *Medical Image Analysis*, vol. 2, no. 1, pp. 1–36, 1998.

[9]. R. Shams, P. Sadeghi, R. A. Kennedy, R. I. Hartley, "A Survey of Medical Image Registration on Multicore and the GPU", *IEEE Signal Processing Magazine*, pp50-60, 2010.

[10]. A. Nikaido, K. Ito, T. Aoki, E. Kosuge, R. Kawamata, "A phase-based image registration algorithm for dental radiograph identification", *IEEE Conference on Intelligent Signal Processing*, 2007.

[11]. K. Krish, S. Heinrich, W. E. Snyder, H. Cakir, S. Khorram, "A new feature based image registration algorithm", *ASPRS Annual Conference*, Portland, Oregon, 2008.

[12]. M. S. Yasein, P. Agathoklis, "A Feature-based Image Registration Technique for Images of Different Scale", *IEEE*, 978-1-4244-1684-4/08/2008, 2008.

[13]. S. Boda, "Feature-based image registration", Department of Electronics & Communication Engineering, *National Institute of Technology*, 2009.

[14]. W. Chu, L. Ma, J. Song, T. Vorburger, "An Iterative Image Registration Algorithm by Optimizing Similarity Measurement", *Journal of Research of the National Institute of Standards and Technology*, vol. 115, no. 1, 2010.

[15]. P. J. Kostelec, S. Periaswamy, "Image Registration for MRI", *Modern Signal Processing*, MSRI Publications, vol. 46, 2003.

[16]. B. Balasubramanian, K. Porkumaran, "PET/CT and MR Image Registration using Normalized Cross Correlation Algorithm and Spatial Transformation Techniques", *International Journal of Computer and Network Security*, vol. 2, no. 5, 2010.

[17]. A. Almhdie, C. Léger, M. Deriche, R. Lédée, "Multimodal medical image registration using a novel implementation of the ICP algorithm", *15th European Signal Processing Conference,* 2007.

[18]. J. B. A. Maintz, P. A. Elsenyz, M. A. Viergever, "Comparison of edge-based and ridge-based registration of CT and MR brain images" *Medical Image Analysis*, Chapter 4, pp 96-114.

[19]. H. S. Own, "An Efficient Image Registration Algorithm Based on Q-Shift Complex Wavelet Transform (Q-Shift CWT)", *ICGST-GVIP Journal*, vol. 5, 2, pp. 9-12, 2005.

[20]. M. R. Sabuncu, "Entropy-based Image Registration" *Dissertation, Doctor of Philosophy, Department of Electrical Engineering, Princeton University*, 2006.

[21]. G. Yang, C. V. Stewart, M. Sofka, C. Tsai, "Automatic robust image registration system: Initialization, estimation, and decision", *Proceedings of the Fourth IEEE International Conference on Computer Vision Systems*, 2006.

[22]. C. Harris, M. Stephens, "A combined corner and edge detector", 4th Vision Conference, pp. 147-151, 1988.

[23]. K. Takita, T. Aoki, Y. Sasaki, T. Higuchi, K. Kobayashi, "High-accuracy subpixel image registration based on phase-only correlation," *IEICE Trans. Fundamentals*, vol. E86-A, no. 8, pp. 1925–1934, 2003.

[24]. B. Pan, K. Qian, H. Xie, A. Asundi, "Two-dimensional digital image correlation for in-plane displacement and strain measurement: a review", *IOP publishing*, 2009.

[25]. W. K. Pratt, "Correlation techniques of image registration", *IEEE Transactions on Aerospace and Electronic Systems*, vol. 10, pp. 353–358, 1974.

[26]. G. Hong, Y. Hang, "Combination of feature-based and area-based image registration technique for high resolution remote sensing image", *IEEE international symposium on Geosciences and remote sensing*, pp. 377-380, 2007.

[27]. L. Ramirez, N. G. Durdle, V. J. Raso, "Medical Image Registration in computational Intelligence framework: A review", *Proceedings of CCECE, pp.* 1021-1024, 2003.

[28]. T. Sabisch, A. Ferguson, Bolouri, "Automatic registration of complex images using a self organizing neural system," *International Joint Conference on Neural Networks,* pp. 165-170, 1998.

[29]. H. Liua, J. Yan, D. Zhang, "Three-dimensional surface registration: A neural network strategy", *Neurocomputing,* vol. 70, pp. 597–602, 2006.

[30]. M. Li , W. Cai, Z. Tan, "A region-based multi-sensor image fusion scheme using pulse-coupled neural network", *Pattern Recognition Letters*, vol. 27, issue 16, pp. 1948–1956, 2006.

[31]. L. Shang, J. C. Lv, Z. Yi, "Rigid medical image registration using PCA neural network", *Neurocomputing*, vol. 69, pp. 1717–1722, 2006.

[32]. J. Zhang , Y. Ge , S.H. Ong , C.K. Chui, S.H. Teoh , C.H. Yan, "Rapid surface registration of 3D volumes using a neural network approach", *Image and Vision Computing*, vol. 26, pp 201-210, 2007.

[33]. J.J. Jack, C. Roux, "Registration of 3-D images by genetic optimization", *Pattern Recognition Letters*, vol. 16, pp. 823-841, 1995.

[34]. Z. Janko, D. Chetverikov, A. Ekart, "Using a genetic algorithm to register an uncelebrated image pair to a 3D surface model", *Engineering Applications of Artificial Intelligence*, vol. 19, pp. 269–276, 2006.

[35]. R. S. Mitra, N. N. Murthy, "Elastic maximal matching", *Pattern Recognition*, vol. 24, pp. 747–753, 1991.

[36]. R. Szeliski, S. Lavall, "Matching 3-D anatomical surfaces with nonrigid deformations using octree-splines", *IEEE Workshop on Biomedical Image Analysis*, pp. 144–153, 1994.

[37]. W. Peckar, C. Schnorr, K. Rohr, H.S. Stiehl, "Two step parameter free elastic image registration with prescribed point displace-ments", *Journal of Mathematical Imaging and Vision*, vol. 10, pp. 143–162, 1999.

[38]. G. Wollny, F. Kruggel, "Computational cost of nonrigid registration algorithms based on fluid dynamics", *IEEE Transactions on Medical Imaging,* vol. 21, pp. 946–952, 2002.

[39]. B. Zitova, J. Flusser, "Image registration methods: a survey", *Image and Vision Computing,* vol. 21, pp. 977–1000, 2003.

Proceeding of the
International Conference on Electrical, Computer and Telecommunication Engineering
01- 02 December 2012 (ICECTE2012), RUET, Rajshahi-6204, Bangladesh

ICECTE2012: PI-0118

Determination of the Effect of Having Energy Drinks on Tachycardia and Bradycardia by Analyzing HRV of ECG Signal

Md. Nafiur Rahman[1], Fatema Khatun[2], Md. Dulal Haque[3], Muhammad Muinul Islam[4]
[1,2,3]Dept. of Telecommunication and Electronic Engineering, Hajee Mohammad Danesh Science and Technology University, Dinajpur, Bangladesh
[4]Dept. of Biomedical Engineering, Khulna University of Engineering and Technology, Khulna, Bangladesh
E-mail: [1]protik69@hotmail.com, [2]fatema.tee.08@gmail.com, [4]mmi.kuet@gmail.com

ABSTRACT
In this work, heart rate variability (HRV) of ECG signal was analyzed to determine the effect of having energy drinks on tachycardia and bradycardia by observing 12 healthy human subjects. Tachycardia and Bradycardia are two abnormalities of ECG signal where Tachycardia happen when R-R interval < 0.6s and Bradycardia happen when R-R interval > 1s. After having energy drink it is observed that heart beat rate is increasing and that is 80 per minute whereas 75 per minute at the normal condition. Average R-R interval of QRS peak is also decreased here by increasing heart beat rate. By this we can said that after having energy drinks though heart beat increased but no tachycardia and bradycardia abnormalities are happened because the R-R interval is greater than 0.6s and smaller than 1s.

KEY WORDS: AcqKnowledge software, bradycardia, Energy drinks, HRV, Tachycardia.

1. INTRODUCTION

Ventricular tachycardia is a fast but regular rhythm. With ventricular fibrillation, the heart beats are so fast and irregular that the heart stops pumping blood. Ventricular fibrillation is a leading cause of sudden cardiac death. An electrocardiogram is a tracing of the electrical activity of your heart [7]. Having bradycardia means that heart beats very slowly. It means that the heart's natural pacemaker is not working right. In severe forms of bradycardia, the heart beats so slowly that it does not pump enough blood to meet the body's needs. This can cause symptoms and can be life-threatening [8]. The recording of the heart's electrical activity is known as the ECG. The deviations in the normal electrical patterns indicate various cardiac disorders. Cardiac cells, in the normal state are electrically polarized [1].

The aim of the study is to determine any effect present or not on ECG abnormalities. For this here we analyze the ECG signal components and HRV to determine the effect present or not after having energy drinks.

2. MATERIALS AND METHOD

2.1 ECG signal

The heart is divided into four chambers that are connected by heart valves. The lower two chambers of the heart are called ventricles. They are separated by a septum into the left ventricle and the right ventricle. The upper two heart chambers are called atria. Atria receive blood returning to the heart from the body and ventricles pump blood from the heart to the body. Fig. 1 shows the cross sectional view of heart.

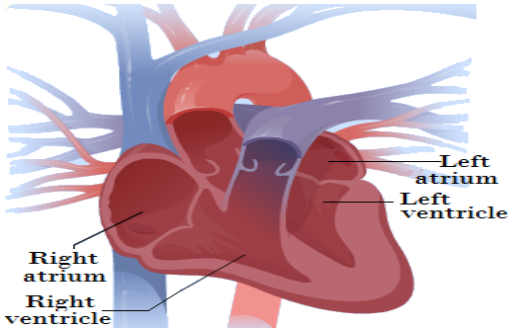

Fig. 1: Cross sectional view of heart [7]

Fig. 2 shows a normal ECG waves. The P-wave represents the activation of the upper chambers of the heart, the atria, while the QRS complex and T-wave represent the excitation of the ventricles- the lower chamber of the heart.

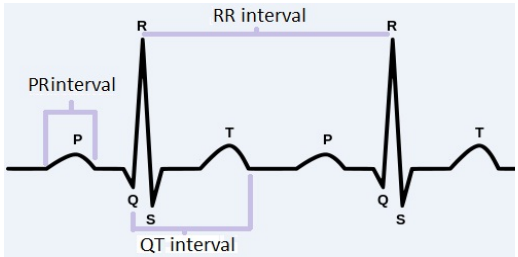

Fig. 2: Normal ECG waves.

Normally, the frequency range of an ECG signal is of 0.05–100 Hz and its dynamic range of 1–10 mV. TABLE 1 shows range of the interval of ECG peaks.

So, from the recorded shape of the ECG, we can say whether the heart activity is normal or abnormal.

TABLE 1. ECG peaks interval and their range

Event\Interval(Range)	Corresponds to
P-R interval (0.12 -0.20 s)	AV nodal delay
R-R interval (0.6-1 s)	Time between beats
QRS interval (0.09 s)	Ventricle depolarization

Any change in the above indicates the abnormality of the heart. Among various abnormalities here discussed two abnormalities –one is Tachycardia(R-R interval < 0.6 s) and the other is Bradycardia(R-R interval >1 s). Among all the waves, QRS complex is the most significant wave [3] of an ECG signal through which R-R interval can be determined. Using this R-R interval [4] [5] one can find the irregularity of the heart beat and the number of beats per minute. The normal value of heart beat lies in the range of 60-100 beats/minute.

2.2 Subjects

Twelve healthy, male subjects were enrolled between the age of 23 and 31 years old and their Mean ±SD (range) for age, weight, height and Body Mass Index (BMI) were given in TABLE 2. The subjects had not taken any medication during the week prior to the study. None of the subjects were smokers and they refrained from alcohol and caffeine containing drinks at least 4 h prior to the study or had a history of cardiovascular disease or other illness. Exclusion criteria included: obesity (body mass index >30 kg/m2), under weight (body mass index <18.5 kg/m2) and history of cardiovascular disease or other illness. The study was approved by the local Ethics Committee.

TABLE 2. Participants demographic characteristics

Para-meter	Age (yrs)	Weight (kgs)	Height (cms)	BMI (kg/m)
Value (N=12)[a]	23.33 ±2.87	63.67± 10.61	165.89± 8.03	22.27± 3.30

[a] Values are Mean ±SD.

2.3 Energy drinks:

Energy drinks, unlike "sports" drinks that contain water, sugar and salts, have high levels of caffeine and taurine aimed at increasing "energy" or alertness. In this experiment we have used drinks of serving size of 250ml/can which contains caffeine 62.5mg/250ml of, 27 gm sugar per 250ml can and other ingredients e.g. water, acidity regulators: citric acid and sodium citrate, carbon dioxide, taurine (0.4%), flavor, inositol (0.02%), colours: E 150d, riboflavin, enriching substances: vitamins (niacin, panthotenic acid, vitamin B6, vitamin B12).

2.4 Experimental setup

The study was performed in a quiet room with the temperature kept at 22°C (21-23). The subjects were resting in the supine position throughout the whole experimental period. ECG is performed with ECG100C amplifier directly connected to biopac data acquisition unit, MP150 (Biopac, USA) through universal interface module, UIM100C (Biopac, USA).

2.5 Testing Procedure

Food intake was restricted to a light meal 2 hour prior to the test. ECG measurements were carried out in a room in which the temperature was maintained constant at 22°C (21-23) with the subjects in a supine position. At least 20 minutes were allowed for acclimatization before the measurements were performed on the skin of middle finger tip. ECG was measured immediately before and after the taking of energy drinks for 30 minutes.

3. RESULT

3.1 Recording and analyzing ECG signal

Any ECG gives two kinds of information. One is the duration of the electrical wave crossing the heart which in turn decides whether the electrical activity is normal or slow or irregular and the second is the amount of electrical activity passing through the heart muscle.

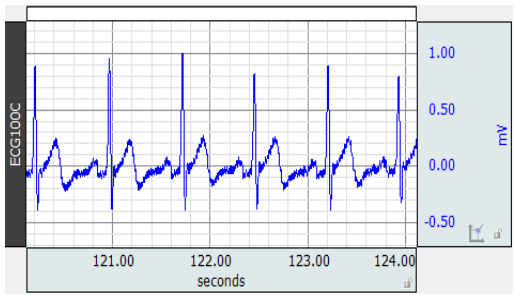

(a)

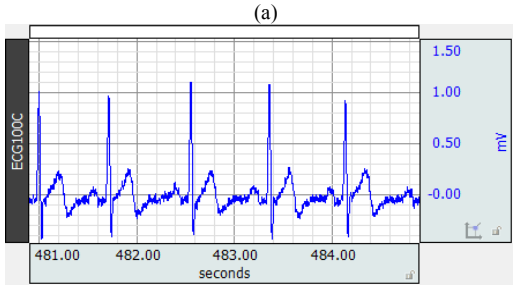

(b)

Fig. 3: ECG wave pulse train (a) before taking energy drinks (b) after taking energy drinks

The pulse train of ECG wave before and after taking energy drinks is shown in Fig. 3(a) and 3(b) respectively. At normal condition, the maximum amplitude (peak value of R wave) of ECG wave is about 1 mV (at 121.71 second). After having energy drinks, the maximum amplitude (peak value of R wave) of ECG wave is about 1.09 mV (at 482.59 second). From TABLE 3 we observed that, the maximum amplitude of R wave in ECG signal increases about 0.10 mV after having energy drinks with respect to normal condition. Not only R peak but also there is a significant increase in Q peak & S peak in ECG signal after having energy drinks.

TABLE 3. Peak amplitude of R(peak) wave

Peak amplitude of R wave (mV)	
Before having energy drink	after having energy drink
0.86	0.99
0.95	0.95
0.99	1.09
0.81	1.04
0.88	0.90

The duration of the QRS complex is another useful calculation. Once the QRS complex has been identified a more detailed examination of ECG signal including the heart rate can be performed [2].

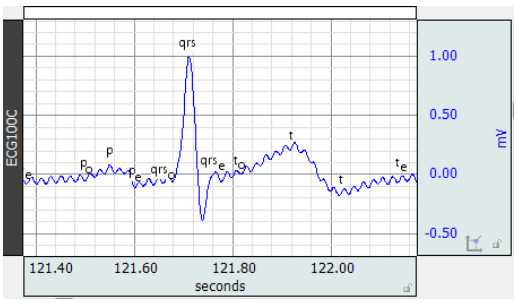

(a)

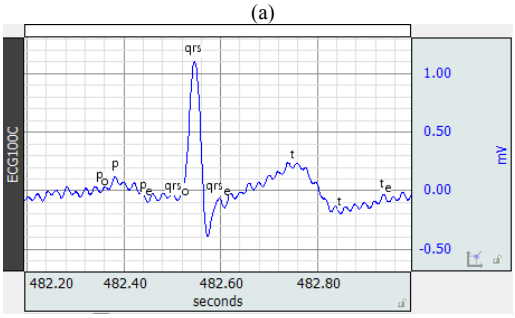

(b)

Fig. 4: ECG wave of single pulse with complex boundary (a) before taking energy drinks (b) after taking energy drinks

From Fig. 4(a) and 4(b) we can see that, the maximum amplitude of P, QRS (especially R peak) & T waves of ECG signal increase about 0.03, 0.10 & 0.03 mV respectively after having energy drinks with respect to normal condition.

3.2 Analysis Heart rate variability

The HRV analysis QRS detector uses a modified Pan-Tompkins algorithm. The algorithm normalizes the ECG data to 1 whereby the peak amplitude of the highest R-wave represents 1. The default threshold level of 0.5 should place the threshold in the middle of the R-wave [6].

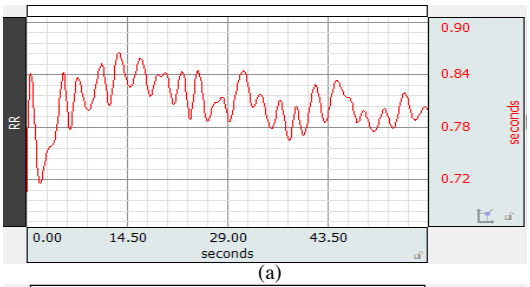

(a)

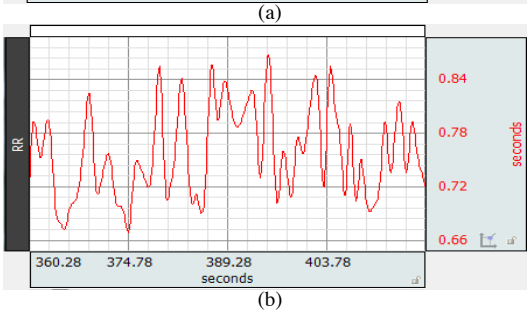

(b)

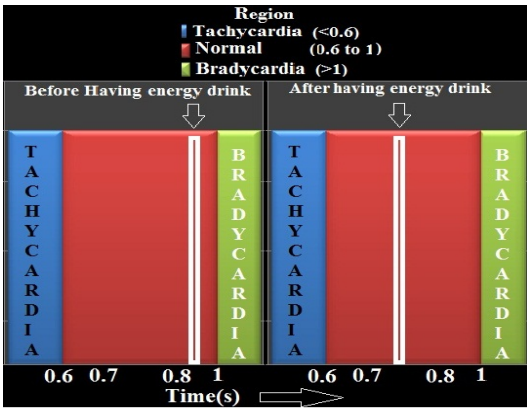

Fig. 6: Average R-R interval (QRS Peak event) before and after having energy drink

shown that maximum events of QRS peak occur at the average time of 0.806s, whereas in Fig. 5(b) QRS peak happened on average time of 0.755s after having energy drinks. Here after having energy drink the R-R interval is 0.755s which is faster than normal condition but also not nearer to Tachycardia and Bradycardia. Fig. 6 shows that normal heart beat happened around 0.8s to 1s where after having

energy drinks this heart beat happened around 0.7s to 0.8s which is faster than before. Table 4 shows that the average heart beat and R-R interval values after 1 minute observation.

TABLE 4. Average heart beat and R-R interval per minute before and after having drinks

	Before	After
Heart beat	75	80
R-R interval(QRS Peak event)	0.806 s	0.755 s

3.3 Statistical analysis

The significance was determined at 95% confidence level. The measured p-value is smaller than 0.0001 ($p<0.0001$) which was measured by two tailed paired T-test. This summary of the test is shown at TABLE 5.

TABLE 5. Significance of R-R interval of before and after having energy drinks

95% confidence level	Paired T-test	p-value	Significant
	two tailed	< 0.0001	***(extremely)

4. DISCUSSION

This research shows that heart beat rate was increased after having energy drinks than the normal condition. But this increasing of heart beat rate has no effect on two abnormalities tachycardia and bradycardia. This is showed by analyzing the ECG signal components and also by analyzing the HRV of ECG signal.

The results also showed that:

- Heart rate increased by 7.25 per cent after having energy drinks.
- After having energy drinks, the average observation on ECG signal it was found that heart rates went up between 5 and 7 beats per minute.
- Significant ECG R-R interval is occurred.
- No effect present on tachycardia and bradycardia.
- Heart rate function is increased but this is at normal condition not on abnormality events.

Although the heart rate increases observed in this study were not dangerous for healthy volunteers, the results suggest that the drinks could be dangerous to patients if drinking more than two cans a day.

5. CONCLUSION

To analyze the effect of having energy drinks on tachycardia and bradycardia we analyze the component and HRV of ECG signal. By analyzing them it was found that, no effect present on tachycardia and bradycardia though heart beat rate was increased. Also an extremely significant difference was found.

6. ACKNOWLEDGEMENTS

Authors wish to thank all participants in this study and cordially grateful to the Department of Biomedical Engineering, KUET, Khulna, where the measurements were done and also thanks for their most constructive remarks and suggestions.

REFERENCES

[1]. Brian, 2004, November 23rd, "Energy Drinks: Ingredients & Dangers", *Citynet Magazine.* http://www.citynetmagazine.com/nightlife/energy-drinks.html

[2]. Somers VK, Dyken ME, Mark AL, Abboud FM. Sympathetic-nerve activity during sleep in normal subjects. N Engl J Med 1993;328(5): 303–7.

[3]. M.A. Khayer, M.A.Haque "ECG Peak Detection using Wavelet Transform", 3rd International Conference on Electrical Computer Engineering (ICECE 2004), ISBN 984-32-1804-4, 28-30, 2004, Dhaka, Bangladesh, pp. 518-521.

[4]. A. Ghodrati, S. Marinello,"Statistical Analysis of RR interval Irregularities for Detection of Atrial Fibrillation", IEEE Transactions on Computers in Cardiology, ISSN 0276-6574, Vol. 35, pp. 1057-1060, 2008.

[5]. M G. Tsipouras, D I Fotiadis, D Sideris , "Arrhythmia Classification using the RR-interval Duration Signal",IEEE Transactions on Computers in Cardiology, Vol. 29, 485-488, 2002.

[6]. Pan J and Tompkins WJ. A real –time QRS Detection algorithm.IEEE transaction on biomedical engineering 32(3):230-236, 1985.

[7]. http://www.webmd.com/heart-disease/tc/ventricular-tachycardia-topic-overview

[8]. http://www.webmd.com/heart-disease/tc/bradycardia-slow-heart-rate-overview

[9]. http://www.medicalnewstoday.com/articles/88066.php

Proceeding of the
International Conference on Electrical, Computer and Telecommunication Engineering
01- 02 December 2012 (ICECTE2012), RUET, Rajshahi-6204, Bangladesh

ICECTE2012: PI-0119

Disease Prediction Based on Genome Sequence

Kawsar Ahmed[1], Abdulla-Al-Emran[2], Md. Zamilur Rahman[1], Tasnuba Jesmin[1], Md. Farhad Ali[1]
[1]Department of Information and Communication Technology, Mawlana Bhashani Science and Technology University, Bangladesh
[2]Department of Biotechnology and Genetic Engineering, Mawlana Bhashani Science and Technology University, Bangladesh
E-mail: kawsar_it08050@yahoo.com, emran_geb@yahoo.com, zamiljitu@gmail.com, tasnuba_it08005@yahoo.com, farhad_ict17@yahoo.com

ABSTRACT
Lung cancer, one of most deadly, disabling and costly diseases is mainly caused by smoking which is increasing at alarming rate. The diagnosis of lung cancer is a vital and tedious task. The accumulation of genomic alterations mainly causes lung cancer. So analysis of genome sequences and structures are helpful for detection and prevention of lung cancer. Collected genome sequences are BLAST, MSA to detect Conserved region where mutation occurs. SNP for each gene is taken to implement tools which are able to detect where, how and why mutation occurs and to give the consciousness even before affected by cancer.

KEY WORDS: Conserved region, BLAST (Basic local alignment searching tool), MSA (multiple sequence alignment), and SNP (Single Nucleotide Procedure), Mutation.

1. INTRODUCTION

Personalized medicine requires a test that fairly accurately predicts disease risk, particularly when interventions are invasive, expensive or have major side effects. Recent studies on the prediction of common diseases based on multiple genetic variants alone or in addition to traditional disease risk factors showed limited predictive value so far, but all have investigated only a limited number of susceptibility variants [1].

Genetic mutation is one of the many topics that are highly debated in our society, it can produce harmful anomalies. At a basic level, mutation causes a gene or genetic sequence to change from its original or intended purpose [2].

The goal of those projects is to provide an understanding of how genotype is associated with disease, how it affects our response to drugs and how it affects the protein products of genes.

- Disease predict based on genome sequence.
- Try to find out How, Where and Why mutation in genome sequence are occurred.
- Implemented tools that can predict disease and also can find out pre-position of a disease.
- Provide the implemented tools through Internet so that people can easily use this and be conscious about his/her diseases and provide cost effective tools.

2. BACKGROUND

A gene mutation [3] is a permanent change in the DNA sequence that makes up a gene. Mutations range in size from a single DNA building block (DNA base) to a large segment of a chromosome. Mutations may occur in a single cell within an early embryo. As all the cells divide during growth and development, the individual will have some cells with the mutation and some cells without the genetic change. This situation is called mosaicism [3].

DNA sequencing [4] is the process of determining the exact order of the bases A, T, C and G in a piece of DNA. In essence, the DNA is used as a template to generate a set of fragments that differ in length from each other by a single base.

Single nucleotide polymorphisms, frequently called SNPs (pronounced "snips"), are the most common type of genetic variation among people. Each SNP represents a difference in a single DNA building block, called a nucleotide [5]. Single nucleotide polymorphisms, or SNPs, the tiny differences between individual genomes, make each of us unique. At the same time, however, they are partly responsible for individual differences in the effectiveness and tolerability of drugs. SNPs have therefore become one of the most important objects of medical research, especially as they could also provide clues to new targets [6].

In biology, conserved sequences are similar or identical sequences that occur within nucleic acid

sequences (such as RNA and DNA sequences), protein sequences, and protein structures or within different molecules produced by the same organism. Since sequence information is normally transmitted from parents to progeny by genes, a conserved sequence implies that there is a conserved gene. It is widely believed that mutation in a "highly conserved" region leads to a non-viable life form [7] [8] [9].

3. METHODOLOGY

Here we will discuss about the whole working process of our research. Firstly we show the flow diagram of our process.

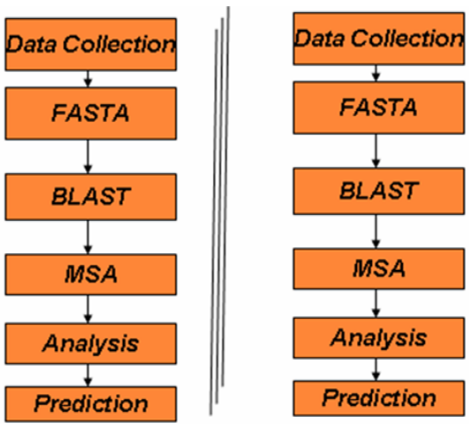

Fig. 1 Flowchart of working process with DNA & Protein Sequences

3.1 Data Collection (DNA & PROTIEN)

For data collection maintains some procedure that is discussed briefly below. Firstly we know the name of genes that are responsible for lunch cancer. Then we collect two types of sequences for each gene from NCBI (National Center of Biotechnology Information) http://www.ncbi.nlm.nih.gov/. One is DNA sequence and another is PROTEIN sequence. We take both type sequences in FASTA format for our working purpose. FASTA is a DNA and protein sequence alignment software package and is a text-based format for representing either nucleotide sequences or peptide sequences.

3.2 BLAST

BLAST searches for all matching sequence of length k where k is any positive number. The main working principal of BLAST is to identify that the sequence is valid or not. We use BLAST for every sequence .Now why to check the validation of that sequence which we choose .That means the sequence which we take is really a correct gene sequence or a normal line of English alphabet. We put collected sequence on the exact space in BLAST page.

3.3 MSA (Multiple Sequence Alignment)

Collecting gene sequences are done MSA using CLUSTALW algorithm because it is easy to use and capable to adjust the length of different sequence and give the approximately correct result. Putting all collected sequence on the exact space in clustalw page and determine conserve region from CLUSTALW result where CONSERVE region is what that indicate or help to understand the pattern of mutation or position of mutation.

3.4 Algorithm

The output of CLUSTALW algorithm will be the input of our implemented software. This will find the position of mutation and also find substituted base (such as A, T, G, C) at conserve region by maintaining a pattern that shown in Fig. 7.

4. RESULTS

The identification of the conserved regions of a genome is fundamentally important.

4.1 DNA and Protein Sequences

First find the DNA, PROTEIN sequences from NCBI following the 3.1 article procedure. Those sequences are saved at FASTA format that shown at Fig. 3.

4.2 BLAST Results

Every sequence has been done BLAST to check the validation of that sequence which we choose. That means the sequences which are taken are really a correct gene sequence or a normal line of English alphabet and shown by Fig. 4 & Fig. 6 respectively.

4.3 MSA Results

MSA determines conserve region from CLUSTALW result where the star (*) marking places denote the conserve region of those three sequences at Fig. 5. MSA helps to understand the position of mutation or pattern of mutation.

4.4 Algorithm Results

Here we find some patterns (such as A replace by T and vice versa when there is 2 same base pair like AA, TT, GG, CC within five length,1 base consider length1, both left to right from mutation point details are shown at see Fig. 7) that are responsible for mutation and causes lung cancer.

Our proposed algorithm firstly finds out mutation point and then checks all mutation points whose will be changed or not according to following Fig. 7.

Example: if there is C in Conserved point then our algorithm will follow the 2nd, 4th and 6th row of Fig. 7. And if there is 2 same base pair within length (Both left and right from conserved point) equal to 4 then C replace by T or length equal to 6 then C replace by A or G . Otherwise this conserved point will not be mutated.

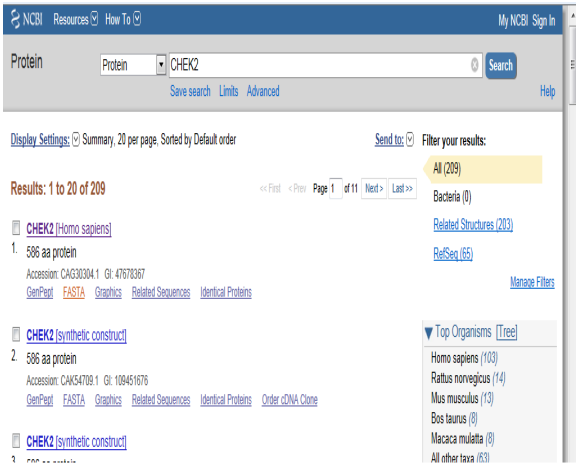

Fig. 2 Selection procedure of CHEK2 gene

Fig. 3 CHEK2 gene at FASTA format

Sequences producing significant alignments:

Accession	Description	Max score	Total score	Query coverage	E value	Max ident
Transcripts						
NM_145862.2	Homo sapiens CHK2 checkpoint homolog (S. pombe) (CHEK2), transc	3278	3278	100%	0.0	100%
NM_007194.3	Homo sapiens CHK2 checkpoint homolog (S. pombe) (CHEK2), transc	1995	3283	100%	0.0	100%
NM_001005735.1	Homo sapiens CHK2 checkpoint homolog (S. pombe) (CHEK2), transc	1288	3286	100%	0.0	100%
NR_038836.1	Homo sapiens CHK2 checkpoint homolog pseudogene (LOC646096), r	918	918	37%	0.0	92%
Genomic sequences [show first]						
NT_011520.12	Homo sapiens chromosome 22 genomic contig, GRCh37.p5 Primary As	603	3231	96%	4e-169	100%
NW_001838745.1	Homo sapiens chromosome 22 genomic contig, alternate assembly Hu	603	3231	96%	4e-169	100%
NT_010393.16	Homo sapiens chromosome 16 genomic contig, GRCh37.p5 Primary As	429	1805	36%	8e-117	98%
NW_001839404.1	Homo sapiens unplaced genomic contig, alternate assembly HuRef SC	429	574	18%	8e-117	98%
NT_167230.1	Homo sapiens unplaced genomic contig, GRCh37.p5 Primary Assembly	412	705	23%	8e-112	98%
NT_011519.10	Homo sapiens chromosome 22 genomic contig, GRCh37.p5 Primary As	412	705	23%	8e-112	98%
NW_001839651.1	Homo sapiens unplaced genomic contig, alternate assembly HuRef SC	411	697	23%	3e-111	97%
NW_001841247.1	Homo sapiens unplaced genomic contig, alternate assembly HuRef DE	411	556	18%	3e-111	98%
NW_001838735.2	Homo sapiens chromosome 22 genomic contig, alternate assembly Hu	411	697	23%	3e-111	98%
NT_037852.6	Homo sapiens chromosome 15 genomic contig, GRCh37.p5 Primary As	405	1178	39%	1e-109	98%
NT_034508.2	Homo sapiens chromosome 2 genomic contig, GRCh37.p5 Primary Ass	405	690	23%	1e-109	98%

Fig. 4 Similarity of given sequences as percent

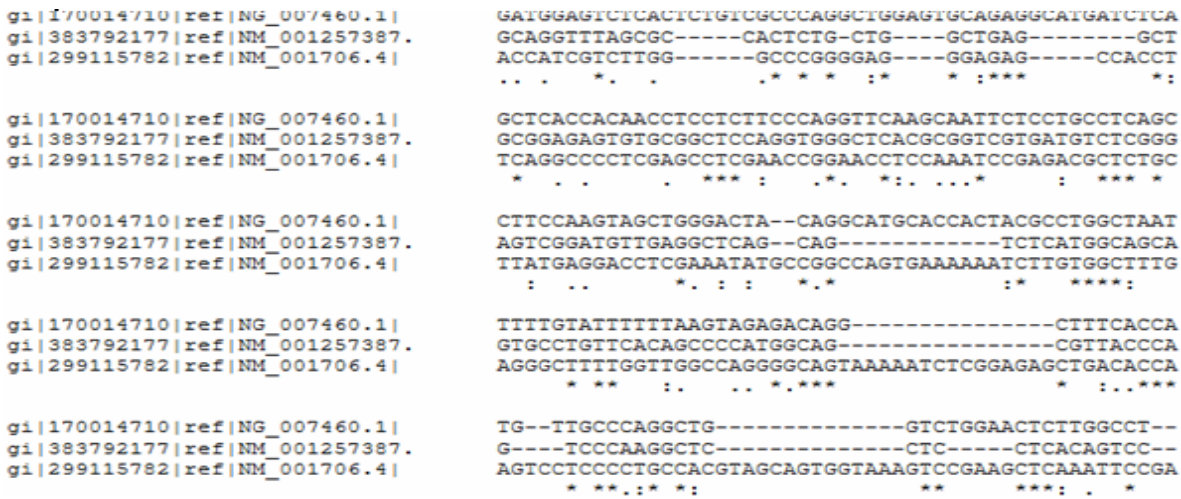

Fig. 5 Conserved region of given sequence

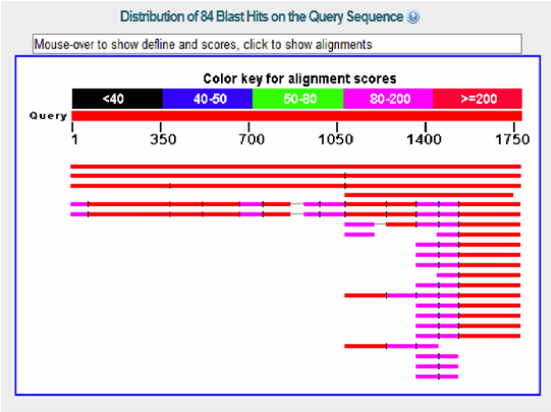

Fig. 6 Graphical Similarity of given sequence

Substitution	Length (Both Left Right)
A/T	5
A/C	6
A/G	4
T/C	4
T/G	5
C/G	6

Fig. 7 Some Patterns of Analysis result

When MSA output given as input of this algorithm and click ok. Then get output message as warning by following the predicted patterns. The Fig. 8 shows which conserved point will be mutated or not. This also shows that what will be new base pair in that mutated point.

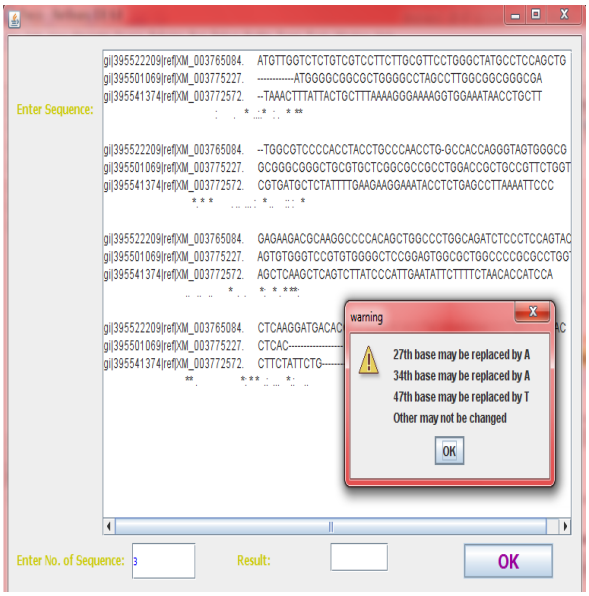

Fig. 8 Final output for given sequence

5. CONCLUTIONS

Uncontrolled cell growth causes diseases that are known as cancer. Lung cancer occurs for this out-of-control cell growth and begins in one or both lungs. Now dividing the lung tissue creates tumors that interfere with the main function of the lung, which is to provide the bloodstream with oxygen to be carried to the entire body. A person can keep healthy by stopping uncontrolled cell growth. So prevention of lung cancer we must be capable to know where, why and how cells are dividing.

6. FUTURE WORK

In future we will also look at the upstream and downstream regulatory region of gene as in many diseases regulatory regions like promoters are frequently mutated.

But up to now it is analyzed only for lung cancer and with a limited data set. If it had taken large data set for lung cancer then result may be more accurate and the tools also are able to give accurate result which is demanded. In future we will do analyzing for all gene sequences which are required for lung cancer as well as other diseases also to upgrade our thesis.

REFERENCES

[1] A. Cecile J.W. Janssens and Cornelia M. van Duijn, "Genome-based prediction of common diseases: advances and prospects", *Oxford Journals, Life Sciences & Medicine, Human Molecular Genetics*, Volume 17, Issue R2, Pp. R166-R173.

[2] "How can gene mutations affect health and development - Genetics Home Reference", *A service of the U.S. National Library of Medicine®*, Published: August 7, 2012.

[3] www.wisegeek.com/what-is-a-gene-mutation.htm accessed on 28 October-2012.

[4]http://ghr.nlm.nih.gov/handbook/mutationsanddisorders/neutralmutations accessed on 28 Oct. 2012.

[5] http://www.What are single nucleotide polymorphisms (SNPs) - Genetics Home Reference.mht accessed on 28 October-2012.

[6] Chakravarti A, "Single nucleotide polymorphisms: … to a future of genetic medicine", Nature 409, 2001, pages 822-823.

[7] S. R. Myers and R. C. Griffiths, "Bounds on the minimum number of recombination events in a sample history", *Genetics*, 163:375–394, 2003.

[8] Y.S. Song and J. Hein., "Parsimonious reconstruction of sequence evolution and haplotype blocks: Finding the minimum number of recombination events", *In Proc. of 2003 Workshop on Algorithms in Bioinformatics*, 2003, pages 287-302.

[9] Y.S. Song, Y. Wu, and D. Gusfield, "Efficient computation of close lower and upper bounds on the minimum number of needed recombinations in the evolution of biological sequences", *Proc. of ISMB 2005*, *Bioinformatics*, 2 1, 2005, i413–i422.

Proceeding of the
International Conference on Electrical, Computer and Telecommunication Engineering
01- 02 December 2012 (ICECTE2012), RUET, Rajshahi-6204, Bangladesh

ICECTE2012: PI-0120

IRIS RECOGNITION SYSTEM FOR BIOMETRIC IDENTIFICATION

MD. Golam Robbani[1], Md. Azahar Ali[2], Md. Shamsur Rahman PK[3]
[1]Dept. of EEE, University of Information Technology & Sciences, Rajshahi-6000, Bangladesh.
[2]Dept. of CSE, Frankfurt University of Applied Sciences, Frankfurt am Main, Germany.
[3]Dept. of EEE, Rajshahi University of Engineering & Technology, Bangladesh.
Email: **robbani.uitsbd@gmail.com, azaharali28@yahoo.com, rick_eee06@yahoo.com**

ABSTRACT

The work presented in this paper involved developing an iris recognition system in order to verify both the uniqueness of the human iris and also its performance as a biometric. Here, emphasize is given on software based implementation of the system and not on the hardware part. The feature of the iris region is extracted and encoded using laplacian of Gaussian filter to create a biometric template. The objective will be to implement an open-source iris recognition system in order to verify the claimed performance of the technology. The development tool used will be MATLAB, and emphasis will be only on the software for performing recognition, and not hardware for capturing an eye image

KEY WORDS: Biometric system, Iris Recognition, Image Restoration, Machine Vision.

1. INTRODUCTION

Biometric systems work by first capturing a sample of the feature, such as recording a digital sound signal for voice recognition, or taking a digital colour image for face recognition. The biometric template will provide a normalized, efficient and highly discriminating representation of the feature, which can then be objectively compared with other templates in order to determine identity. Biometric technology—the automated recognition of individuals using biological and behavioral traits—has been presented as a natural identity management tool that offers "greater security and convenience than traditional methods of personal recognition." Indeed, many existing government identity management systems employ biometrics to assure that each person has only one identity in the system and that only one person can access each identity. The iris recognition system consists of an automatic segmentation system that is able to localize the circular iris and pupil region, occluding eyelids and eyelashes, and reflections. In this thesis, thresholding technique is used for extracting the iris region. Normalization is avoided by capturing same size of images for database and for comparison. Iris recognition is regarded as the most reliable and accurate biometric identification system available. Most commercial iris recognition systems use patented algorithms developed by Daugman, and these algorithms are able to produce perfect recognition rates.

2. IRIS RECOGNITION

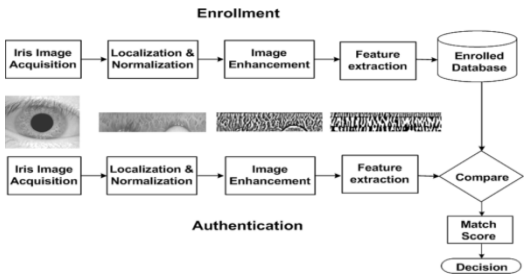

The iris is an externally visible, yet protected organ whose unique epigenetic pattern remains stable throughout adult life [5]. These characteristics make it very attractive for use as a biometric for identifying individuals. Figure 1.2 shows, most iris recognition systems consist of five basic module leading to a decision: The image acquisition module obtains 2-D image of the eye using a monochromatic camera.

Fig 1: Block diagram of iris recognition system

The *iris* is an internal organ of the eye that is located just behind the cornea and in front of the lens. It's function is to control the size of the pupil, which in turn regulates the amount of light entering the pupil and impinging the retina. The iris consists of a number of layers, the lowest is the epithelium layer, which contains dense pigmentation cells. The stromal layer lies above the epithelium layer, and contains blood vessels, pigment cells and the two iris muscles. The density of stromal pigmentation determines the colour of the iris [1].

The externally visible surface of the multi-layered iris contains two zones, which often differ in colour. An outer *ciliary zone* and an inner *pupillary zone*,

and these two zones are divided by the *collarette* – which appears as a zigzag pattern.

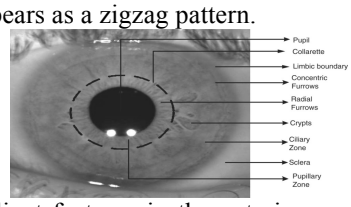

Fig 2: Salient features in the anterior portion of the iris

As the pupil dialates and contracts, *crypts*-pit like oval structures in the zone around the collarette-permits fluid to quickly enter and exit the iris. Concentric lines near the outer ciliary zone become deeper as the pupil dialates, causing the iris to fold. These are *concentric furrows.* The *limbus* and *pupilary* boundaries define iris's spatial extent and, in 2-d images of the eye help delineate it from other ocular structures, such as the eyelashes, eyelids, sclera, and pupil.

3. IMAGE ACQUISITION

Iris image acquisition is a vital and first step of any iris recognition system. In most iris recognition system 2-D image of the eye is obtained using a monochromatic CCD camera sensitive to near infrared (NIR) light spectrum. NIR imaging is used because it helps emphasize the iris texture that can be difficult to image under visible light (i.e., texture is richer for dark pigmented eyes under NIR compared to visible). Furthermore, NIR is used because the human eye is not as sensitive to NIR wavelengths as it is to visible light. Image quality of the iris depends on the image acquisition. Image quality plays an important role in automated biometric systems for two reasons: 1) system performance and 2) interoperability. The quality of the image is affected by the following factors:

Defocus blur, Off-angle, Occlusion, Lighting variation, Iris resolution.

3.1 Defocus blur

Defocus blur can result from many sources, but in general, defocus occurs when the focal point is outside the "depth of field" of the object to be captured. The farther an object is from the depth-of-field interval, the higher the degree of defocus. Defocus primarily attenuates high spatial frequencies. In order to collect varying levels of defocused images, subjects were initially positioned 6 in. from the lens, with their chins being lined up at the edge of the chin rest. This was the initial position that the ideal images were collected at (the camera was manually focused in at this position). Subjects were then instructed to slide their head back along the chin rest, and frames were recorded at approximately 1/8, 1/4, and 3/4 inches from the edge of the chin rest. (Figure: 3.1).

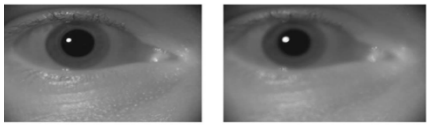

(a) (b)

Fig 3.1: Sample images of defocus blur at
(a) defocus distance = 1/4 in
(b) defocus distance= 3/4 in

3.2 Off-angle

Off-angle means iris is at some angle with the camera. Iris images that are not of frontal view have significant effect on the image quality. To evaluate the effect of off-angle, we train recognition systems on frontal-view images and test on off-angle images. Examples of off-angle is given in the figure. (Figure: 3.2)

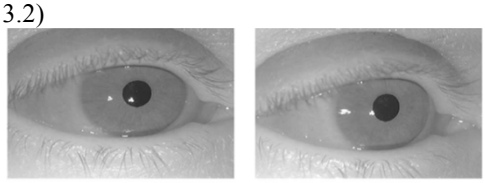

(a) (b)

Fig 3.2: Sample images of off-angle at angle (a) 15^0 and (b) 30^0

3.3 Iris resolution

The amount of information within an iris is a function of its resolution. Capturing iris at a distance can result in variable resolutions. With that notion in mind, The ISO iris image standard states that 200 pixels across the iris is considered good quality for recognition. We wanted to explore lower resolutions because iris at a distance is gaining much more interest, and capturing high-resolution images of the iris can be problematic (Figure 3.3).

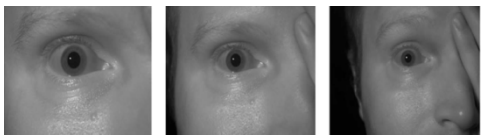

Fig 3.3: Iris images at different resolution

4. METHODS ANALYSIS

There are several methods to localize the iris. They are:

- Hough transform,
- Daugman's integro-differential operator,
- Active contour models

4.1 Hough transform

The Hough transform is a standard computer vision algorithm that can be used to determine the parameters of simple geometric objects, such as lines

and circles, present in an image. The circular Hough transform can be employed to deduce the radius and centre coordinates of the pupil and iris regions. An automatic segmentation algorithm based on the circular Hough transform is employed by Wildes et al.[2], Kong and Zhang [3], Tisse et al.[4], and Ma et al.[5]. Firstly, an edge map is generated by calculating the first derivatives of intensity values in an eye image and then thresholding the result. From the edge map, votes are cast in Hough space for the parameters of circles passing through each edge point. These parameters are the centre coordinates x_c and y_c , and the radius r, which are able to define any circle according to the equation

$$x_c^2 + y_c^2 - r^2 = 0 \quad \text{..... (4.1)}$$

A maximum point in the Hough space will correspond to the radius and centre coordinates of the circle best defined by the edge points. Wildes et al. and Kong and

Zhang also make use of the parabolic Hough transform to detect the eyelids, approximating the upper and lower eyelids with parabolic arcs, which are represented as;

$$(-(x - h_j)\sin\theta_j + (y - k_j)\cos\theta_j)^2 = a_j((x - h_j)\cos\theta_j + (y - k_j)\sin\theta_j) \quad \text{..... (4.2)}$$

where a_j controls the curvature, (h_j, k_j) is the peak of the parabola and θ_j is the angle of rotation relative to the x-axis. In edge detection horizontal gradient is used for detecting the eyelids, and in the vertical gradient is used for detecting the outer circular boundary of the iris. There are a number of problems with Hough transform method. First of all, it requires threshold values to be chosen for edge detection, and this may result in critical edge points being removed, resulting in failure to detect circles/arcs. Secondly, the Hough transform is computationally intensive and thus may not be suitable for real time applications.

4.2 Daugman's integro-differential operator

Daugman makes use of an integro-differential operator [6] for locating the circular iris and pupil regions, and also the arcs of the upper and lower eyelids. The integro-differential operator is defined as

$$max_{(r,\, x_p,\, y_0)} \left| G_\sigma(r) * \frac{\partial}{\partial r} \oint_{r, x_0, y_0} \frac{I(x,y)}{2\pi r} ds \right| \quad (4.3)$$

where $I(x,y)$ is the eye image, r is the radius to search for, $G_\sigma(r)$ is a Gaussian smoothing function, and s is the contour of the circle given by r, x_0, y_0. The operator searches for the circular path where there is maximum change in pixel values, by varying the radius and centre x and y position of the circular contour.

The integro-differential can be seen as a variation of the Hough transform, since it too makes use of first derivatives of the image and performs a search to find geometric parameters. Since it works with raw derivative information, it does not suffer from the thresholding problems of the Hough transform. However, the algorithm can fail where there is noise in the eye image, such as from reflections, since it works only on a local scale.

5. IMPLEMENTATION

Our goal is to implement iris recognition system using MATLAB. In this section we will discuss on the software based implementation of the iris recognition system and analysis the recognition performance. We implemented iris recognition system using simple and efficient methods for each task in the iris recognition system. There are several steps in implementing iris recognition system.

First step can be considered is image acquisition. As we emphasize on the software, the detail description of image acquisition is beyond the scope of this paper. In this implementation image is obtained using camera of a cellular phone with fixed dimension of 320x240.

After obtaining iris image the next step is iris segmentation or localization. Before segmentation obtained image is converted to gray scale image from RGB image using the function *rgb2gray*.

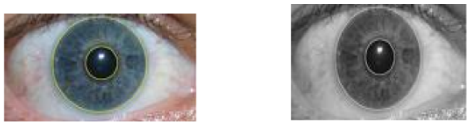

Fig 5.1: (a) RGB image, (b) Gray scale converting image

Then the histogram of the image is equalized to enhance the image using the function *histeq*.

Fig 5.2: Enhanced image using histogram equalization.

For iris segmentation there are various methods have discussed in previous section but for simplicity and less computational burden we used threshold-ding technique for iris segmentation. We determine the threshold value on the basis of the average pixel value of the image. After threshold-ding we obtained a binary image. This binary image is then multiplied with the enhanced image of figure 5.2 to extract the iris region.

Fig 5.3: Binary image after thresholding

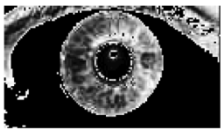

Fig 5.4: Segmented image after multiplication

After the iris region is extracted, the next task is normalization of the iris region. Daugman's rubber sheet model, image registration, virtual circles are the most common methods of normalization. Since obtained images are of fixed dimension (320x240) normalization has not applied in this system. We can obtain iris region of equal dimension by using the function *imresize*.

The next process is feature encoding which plays an important role in the recognition performance. Feature encoding means extraction and encode of most discriminating characteristic of an iris. In our system we used Laplacian of Gaussian filter for feature extraction.

Fig 5.5: Laplacian of Gaussian filtered image

Then this feature extracted image is encoded by converting the image into binary image using thresholding.

Fig 5.6: Feature encoded image

The next step is matching between the acquired image and database images. So before matching we need to create a database. Database is created with several iris images of different person. All images are taken with the camera of the cellular phone with the fixed dimension stated earlier. The database images goes through the same processing step as acquired image stated above during comparison. We created database of 15 people. Some sample database images are shown in the figure below.

Fig 5.7: Sample database images

6. RESULT

This paper has presented an iris recognition system, which was tested using grayscale eye images in order to verify the claimed performance of iris recognition technology. Firstly, an automatic segmentation algorithm was presented, which would localize the iris region from an eye image and isolate eyelid, eyelash and reflection areas. Automatic segmentation was achieved through the use of threshold-ding technique. Next, features of the segmented iris region were encoded by convolving the iris region with Laplacian of Gaussian filter and threshold-ding the output in order to produce a bit wise biometric template. The Hamming distance is used for comparing acquired biometric template and reference biometric template of the database. Thus when the lowest Hamming distance is below a predefined threshold, the system is considered to be found match for the acquired iris image. The system is performed perfect recognition on a set of 15 eye images. Here, normalization is avoided as images were obtained with same size.

7. CONCLUSION & FUTURE WORK

The system presented in this publication was able to perform accurately, however there are still a number of issues which need to be addressed. First of all, the automatic segmentation was not perfect, since it could not successfully segment the iris regions for all of the eye images in the database. In order to improve the automatic segmentation algorithm, a more elaborate and computationally intensive method could be implemented, such as the one suggested by Kong and Zhang [3].

Since the system is implemented in MATLAB, which is an interpreted language, speed benefits could be made by implementing computationally intensive parts in C or C++. Speed was not one of the objectives for developing this system, but this would have to be considered if using the system for real-time recognition.

Another extension to the system would be to interface it to an iris acquisition camera. Now rather than having a fixed set of iris images for recognition, a frame grabber can be used to capture a number of images, possibility improving the recognition rate.

REFERENCES:

[1] E. Wolff. *Anatomy of the Eye and Orbit*. 7th edition. H. K. Lewis & Co. LTD, 1976.

[2] R. Wildes, J. Asmuth, G. Green, S. Hsu, R. Kolczynski, J. Matey, S. McBride. A system for automated iris recognition. *Proceedings IEEE Workshop on Applications of Computer Vision*, Sarasota, FL, pp. 121-128, 1994.

[3] W. Kong, D. Zhang. Accurate iris segmentation based on novel reflection and

eyelash detection model. *Proceedings of 2001 International Symposium on Intelligent Multimedia, Video and Speech Processing*, Hong Kong, 2001.

[4] C. Tisse, L. Martin, L. Torres, M. Robert. Person identification technique using human iris recognition. *International Conference on Vision Interface*, Canada, 2002.

[5] L. Ma, Y. Wang, T. Tan. Iris recognition using circular symmetric filters. National Laboratory of Pattern Recognition, Institute of Automation, Chinese Academy of Sciences, 2002.

[6] J. Daugman. How iris recognition works. Proceedings of 2002 International Conference on Image Processing, Vol. 1, 2002.

[7] N. Ritter. Location of the pupil-iris border in slit-lamp images of the cornea. *Proceedings of the International Conference on Image Analysis and Processing*, 1999.

[8] J. Daugman and C. Downing, "Epigenetic Randomness, Complexity, and Singularity of Human Iris Patterns," Proc. Royal Soc., vol. B, no.268, Biological Sciences, 2001.

[9] J. Daugman, "Probing the Uniqueness and Randomness of Iris Codes: Results from 200 Billion Iris Pair Comparisons," Proc. IEEE, vol. 94, no. 11, 2006, pp.1927-1935.

[10] S. Prabhakar, S. Pankanti, and A.K. Jain, "Biometric Recognition: Security and Privacy Concerns," *IEEE Security & Privacy*, vol. 1, no. 2, 2003, pp. 33–42.

[11] Watson, "Biometrics: Easy to Steal, Hard to Regain Identity," *Nature*, vol. 449, 2007.

BIBLIOGRAPHIES:

Md. Golam Robbani was born in Rajshahi, Bangladesh on 20th October, 1992. He is currently a Bachelor of Science in Engineering student in the Department of Electrical and Electronic Engineering, University of Information Technology & Sciences(UITS), Rajshahi-6000, Bangladesh. He has been actively involved in the study, research and Electronics project works. His research interests are Wireless, Image Processing, Renewable Energy, Power system, Nanotechnology and Information Technology.

Md Azahar Ali was born in Rajshahi, Bangladesh on March 05, 1985. He received his B.Sc. Engineering Degree from Rajshahi University of Engineering & Technology (RUET), Bangladesh, in November, 2010 in the department of Electronics and Telecommunication Engineering. He published two conference papers. He is currently a Master of Engineering student in the Department of CSE, Frankfurt University of Applied Sciences, Frankfurt am Main, Germany. Also he is working as a Lecturer(study leave) in Electrical and Electronic Engineering Department, UITS, B**angladesh**. His research interests are Wireless, Communication, Image Processing and Information Technology. He is also interested in Electronics project, circuit design & control monitoring of mechanical instrument.

Md. Shamsur Rahman PK was born in Rajshahi, Bangladesh on 28th May, 1987. He received his B.Sc. Engineering Degree from Rajshahi University of Engineering & Technology (RUET), Bangladesh, in July 25, 2011 in Electrical and Electronic Engineering. He is a part-time M.Sc(Engineering) student in the department of EEE in RUET. He is currently working as a Full-time Lecturer in the Department of Electrical and Electronic Engineering, University of Information Technology & Sciences(UITS), Rajshahi, Bangladesh. He has been actively involved in the study, research, teaching and consulting project works to undergraduate students. His research interests are Wireless, Image Processing, Renewable Energy, Power system and Nanotechnology.

Proceeding of the
International Conference on Electrical, Computer and Telecommunication Engineering
01- 02 December 2012 (ICECTE2012), RUET, Rajshahi-6204, Bangladesh

ICECTE2012: PI-0121

Weeds Classification through Digital Image

Md Mursalin[1], Md. Mesbah-Ul-Awal[2]
[1] Computer Science and Engineering Department, Pabna Science and Technology University
[2]Information Technology Department, Ranks Telecom Limited
E-mail: mursalin.mithu@gmail.com, mesbah_ul_awal@yahoo.com

ABSTRACT
Throughout the time of conventional organic agriculture, weeds are often one of the biggest problems encountered by farmers. With proper management of weeds can maximize the productivity of crops. Applying excessive herbicide uniformly throughout the field has an adverse effect on the environment. An automated weed control system which can differentiate the weeds and crops from the digital image could be a feasible solution for this problem. This paper demonstrates the classification of weeds and crops according to ten extracted features. 400 sample images over five species were taken where each and every species contains 80 images. Minimizing the computation cost and achieving high accuracy rate, Naïve *Bayes classification algorithm has been proposed as it gains 99.3% accuracy over 400 sample image.*

KEY WORDS: Image processing, herbicide, environment pollution, weed classification, Naïve Bayes classifier.

1. INTRODUCTION

Weeds are those unwanted plants which grow in the area not belongs to them and cause more negative impact on economy income. It competes with the crop for resource such as soil, water, sunlight and fertilizer. So the production efficiency and quality of economic crops would decrease when the weeds are out of control. Statistics has been shown that the worldwide estimated potential loss due to all kinds of pests was at 40%-80%; besides them the potential losses for weeds were found 34% which is the highest of all pests [8]. As a result, better weed control system must be deployed to sustain the productivity without hampering the environment. Currently several weed control policies exist e.g. removing weeds manually by human laborers, crop rotation, mechanical cultivation, and chemical herbicides.

The huge rate of herbicide in the world causes negative impact on the ecological environment and the survival of species. It has also arises some economic concern. In year of 2005, the total estimated cost of applied herbicides was $16 billion in United States [8]. The main cost ineffective and strategic problems in herbicides system is that they are applied uniformly on the field. Generally the volumes of weeds are more in some specific region but herbicides are still applied regardless. In addition, applying herbicides manually is very costly and time consuming. Statistics has been shown that if same kinds of herbicides are applied repeatedly for reducing the unwanted weeds then there is a good possibility that they become tolerant to those types of herbicides [6]. Moreover some herbicides contaminate the ground water even though it applied in the soil. Thus farmers need more sophisticated alternative weed control techniques which will reduce the usages of chemicals and provide safety for the overall ecosystem.

Several researches have been done for investigating fruitful solution for controlling the weeds without collapsing down the environment. The machine vision technique has the ability to differentiate the crops from weeds so that herbicides can be applied effectively. In this technique image are captured by a digital camera from different parts of a crop field so that weeds can be identified properly. Shearer, et al. [10] has developed a photo sensor plant detection system which has the ability of detecting and spraying only the green plant. Jiang Zhengrong, et al [7] has proposed automatic weed identification based on image processing technology. They have investigated the spectrum analysis, color identification, texture assessment for weed identification. In [3], weeds and crops are classified by SVM and achieved 98% where using Bayesian classifier achieved 95% accuracy over 224 test images. Weis et al, proposed a sensor related analysis techniques of weed detection system [14]. In [12], comparison of different classification algorithms has been shown for weed detection based on shape features. For selective herbicide application a model has been proposed [1] with 95% accuracy, which categorizes images into narrow and broad classes based on the Histogram Maxima using a thresholding technique. In [13] calculation of various shape features for identifying weeds in digital images has been shown. Active shape models can identify young

weed seedlings with the accuracy of 65% to 90% [11].

The aim of this paper is to demonstrate a model for classifying weeds and crops in digital images using Naïve Bayes classifier to evaluate its performance in an automated weed control system. Naïve Bayes classifier has been selected because of its simplicity, effectiveness and fastness among other image classification algorithms.

2. METHODS

2.1 Process Flow

Fig: 1 has demonstrated the overall procedures of this paper. Images were captured by a digital camera with 4.9-24.5 mm lens. The position of camera was 90 degree angle form the ground that means vertically towards the ground. The distance between camera lens and the ground was 1.3 feet. Photo shed was used for keeping same light intensity. 1024x768 photo resolution was set for capturing the color image of weeds and crops. All images were taken from the capsicum filed. There were five species including the capsicum. Other four species were considered as weed for the capsicum.

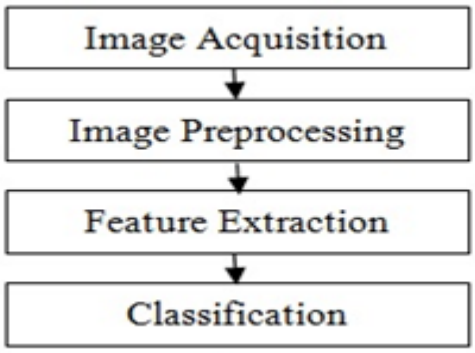

Fig 1: Step by step procedure.

2.2 Image Preprocessing

The high resolution image was converted to 225x175 pixels in order to minimize the computation cost. Color segmentation based image-processing has been done for distinguishing plants from background objects where objects are one of two classes as plants and background. The plants in the field images must be properly segmented otherwise extraction of features will give improper results. Each and every pixel of rgb (red, green, blue) image an exhibitor value 'e' was calculated for enhancing the green plant in compare to the background:

$$e = 2 \times g - r - b \qquad \text{(Eq. 1)}$$

The rgb color plant images were converted to grey images after calculation of e value. Binarization technique with global threshold was performed on these images to separate plants form the background. Composite Laplacian mask was used for further enhancement of the grey-scale image [3]. As the sharpening procedure is sensitive to noise, a linear smoothing method known as median filter was used which successfully reduce impulse noise [4]. Otsu's method [9] an effective technique was used to select the proper binarization threshold value. If the pixel value 'p' is smaller than threshold value 't' were referred as soil in the binary image. In binary image '0' indicates the background where '1' indicates the plant.

The binary image contains some noise. This noise is reduced by first applying morphological opening. In this operation, an erosion operation is followed by a dilation operation. It makes smooth the image by eliminating small pixel regions. The erosion and dilation were combined in reverse order for morphological close operation. This close operation fills the small holes in image [5].

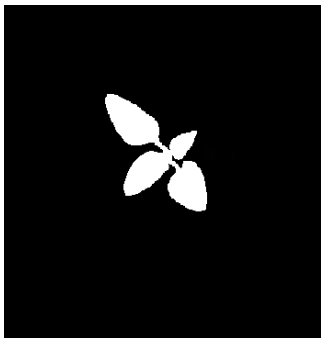

Fig 2: Binary image after open-close operation.

2.3 Features Extraction

Ten features were extracted from the binary images (Fig 2). These features were decomposed as shape, color and moment invariants. The shape features were divided into two categories: size dependent and size independent. Size dependent descriptors are area, perimeter, thickness, convex area and convex perimeter. The size dependent features were combined to present size dependent shape features:

$$formfactor = 4 \times \pi \times \frac{area}{perimeter^2} \qquad \text{(Eq. 2)}$$

$$elongatedness = \frac{area}{thickness^2} \qquad \text{(Eq. 3)}$$

$$convexity = \frac{convex_perimeter}{perimeter} \qquad \text{(Eq. 4)}$$

$$solidity = \frac{area}{convex_area} \qquad \text{(Eq. 5)}$$

For making the color features consistent with various lighting conditions, each and every color component was divided by sum of all the three color components. Here the color features were mean value and the standard deviation.

The scope of an object area is measured by moment invariant (N_1, N_2, N_3, N_4) [2] which consists of geometric transformation such as scaling, translation and rotation. Here in this study only central moments are considered.

2.4 Classification

The Naïve Bayes classifier is a simple but effective classifier has been used here to minimize the computation cost. Let $\vec{a}$ be a vector we want to classify and c be a possible class. Using Bayes formula first we transform the probability $P(c \mid \vec{a})$:

$$P(c \mid \vec{a}) = P(c) \times \frac{P(\vec{a} \mid c)}{P(\vec{a})} \qquad \text{(Eq. 6)}$$

P(c) can be estimated from training data. Considering the conditional independence of the elements of a vector $P(\vec{a} \mid c)$ is decomposed as follows,

$$P(\vec{a} \mid c) = \prod_{i=1}^{D} P(a_i \mid c) \qquad \text{(Eq. 7)}$$

Where, a_i is the ith element of $\vec{a}$. Now, combining both equations we get:

$$P(c \mid \vec{a}) = P(c) \times \frac{\prod_{i=1}^{D} P(a_i \mid c)}{P(\vec{a})} \qquad \text{(Eq. 8)}$$

From this final equation we can calculate $P(c \mid \vec{a})$ and classify $\vec{a}$ into the class with the highest $P(c \mid \vec{a})$.

A classification process in Naïve Bayes classifier requires first train the classifier using labeled data. Then classify unlabeled examples with assigning probabilistic labels to them. In this paper we consider binary classification as weed and crops.

Let k_i be the probabilistic label of ith example illustrate the probability that it belongs to weed class. If the proportion of weed class examples in unlabeled data is different form labeled data then the probabilistic labels were calibrated. The main theme of the calibration is to shift all the probability values of unlabeled data to the scope that the class distribution of unlabeled data becomes alike to that of labeled data. In [15] the whole calibration process has shown.

3. RESULT AND DISSCUSSION

In this paper, each setting is evaluated by using 10-fold cross-validation procedure. 10-fold cross-validation procedure needs portioning the whole training set into 10 subgroups. Each and every subgroup has an equal number of instances. In this training process, one subgroup is tested with the remaining nine subgroups. As a result, over-fitting protection is ensured and smooth outcome for the actual computing is achieved.

Three hundred sample image data were trained and one hundred sample image data were tested. The result of 10-fold cross-validation of Naïve Bayes classifier using ten features was found 99.3% accurate. In [2], they have shown that 97% accuracy be achieved using 10-fold cross-validation of SVM classifier with eleven features. According to [2], we selected eleven features and found the optimal features using forward-selection and backward-elimination methods. We have observed that 10 features achieved the above accuracy rate. Selected features were convexity, mean value of 'r', mean value of 'b', standard deviation of 'r', standard deviation of 'b', $\ln(N_1)$ of area, $\ln(N_2)$ of area, $\ln(N_3)$ of area, $\ln(N_4)$ of area, $\ln(N_2)$ of perimeter.

In present study the capsicum, cogon grass and marsh herb were successfully classified. Other two species had some misclassifications. **Table 1** shows the comparative accuracy rate for each species. Here each and every species has trained with 60 samples and 20 sample images were used for testing whether the classifier can successfully classify or not.

Plants Name	*Accuracy (%)*
Capsicum	100
Burcucumber	98.5
Cogongrass	100
Marsh herb	100
Pigweed	98
Average Accuracy Rate	**99.3**

Table 1: Classification result using Naïve Bayes classifier

4. CONCLUSIONS

Our main goal of this work is to find a solution which will minimize the operating cost as well as maximize the result. Naïve Bayes classifier has been successfully satisfied our goal. In this paper 400 sample images were experimented to classify whether the image is crop or weed. Naïve Bayes classifier with 10-fold cross-validation provides 99.3% accuracy.

5. FUTURE WORK

To get more accurate result, noise must be handled properly. So in future we will emphasize on image preprocessing steps more precisely. We want to analyze wavelet transformation for reducing the noise level.

6. ACKNOWLEDGEMENTS

With due homage and honor we wish to express our gratitude to Almighty. We wish to express our love and gratitude to our beloved families; for their understanding & endless love, through the duration of studies. We are grateful for their continuous support and help, which taught us to be more responsible for own good and for others.

REFERENCES

[1]. Irshad Ahmad, Abdul Muhamin Naeem, Muhammad Islam, Shahid Nawaz, "Weed Classification using Histogram Maxima with Threshold for Selective Herbicide Applications", *In the Proceedings of the 19th International Conference on Computer, Information and Systems Science and Engineering (CISE 2007), Bangkok (Thailand)*, 19: 2007, 331-334.

[2]. Faisal Ahmed, Hawlader Abdullah Al-Mamun, A.S.M Hossain, Emam Hossain, Paul Kwan, "Classification of crops and weeds from digital images: A support vector machine approach", *Crop Protection*, Volume 40, ISSN 0261-2194, 10.1016/j.cropro.2012.04.024, October 2012, Pages 98-104.

[3]. Faisal Ahmed, A.S.M Hossain, Emam Hossain, Hawlader Abdullah Al-Mamun, Paul Kwan, "Performance Analysis of Support Vector Machine and Bayesian Classifier for Crop and Weed Classification from Digital Images", *World Applied Sciences Journal*, Volume 12 (4), ISSN 1818-4952, IDOSI Publications, 2011, Pages: 432-440.

[4]. Fu, J.C., J.W. Chai, S.T.C. Wong, J.J. Deng, J.Y. Yeh, "De-noising of left ventricular myocardial borders in magnetic resonance images", *Magnetic Resonance Imaging*, Volume 20(9), 2002, Pages: 649-657.

[5]. Rafael C. González, Richard Eugene Woods, "Digital Image Processing", Pearson Education, Singapore, 2nd edition, pp: 528, 2004.

[6]. "International survey of herbicide tolerant weeds", *http://www.weedscience.org/in.asp* (accessed on 2, June, 2012).

[7]. Jiang Zhengrong, Li Zhengxi, "Automatic Weed Identification Based on Image Processing Technology", *the 3rd International Conference on Machine Vision*, ISBN: C 978-1-4244-8889-6, 2011.

[8]. E. –C. Oerke, "Crop losses to pests" *The Journal of Agricultural Science*, Volume 144(1), doi: 10.1017/S0021859605005708, 2006, pp: 31-43.

[9]. Otsu, "A Threshold Selection Method from Gray-Level Histograms", *IEEE Transactions on Systems, Man and Cybernetics*, SMC-9(1): 62-66, 1979.

[10]. Shearer, S.A. and P.T. Jones, et al., "Selective Application of Post-Emergence Herbicides Using Photoelectric", *ASABE Technical Library, Transactions of the ASAE*, Volume 34(4), 1991, pp: 1661-1666.

[11]. Sogaard, H.T., "Weed Classification by Active Shape Models", *Biosystems Engineering*, Volume 91(3), 2005, pp: 271-281.

[12]. Weis, M., T. Rumpf, R. Gerhards, L. Plumer, "Comparison of different classification algorithms for weed detection from images based on shape parameters", *In the Proceedings of the 1st International Workshop on Computer Image Analysis in Agriculture, Potsdam, Germany, 2009*, Volume 53, pp : 460-463.

[13]. Weis, M., R. Gerhards, "Feature extraction for the identification of weed species in digital images for the purpose of site-specific weed control", *In the Proceedings of the 6th European Conference on Precision Agriculture, Skiathos, Greece*, Volume 6, 2007, pp: 537-544.

[14]. Weis, M., C. Gutjahr, V. Rueda, R. Gerhards, C. Ritter, F. Scholderle, "Precision Crop Protection - the Challenge and Use of Heterogeneity", 1st Edition, Chapter Detection and identification of weeds, Springer Dordrecht Heidelberg London, New York, pp: 119-134, 2010.

[15]. Yoshimasa Tsuruoka and Jun'ichi Tsujii, "Training a Naive Bayes Classifier via the EM Algorithm with a Class Distribution Constraint",*www.acl.ldc.upenn.edu/W/W03/W03-0417.pdf.*

Proceeding of the
International Conference on Electrical, Computer and Telecommunication Engineering
01- 02 December 2012 (ICECTE2012), RUET, Rajshahi-6204, Bangladesh

ICECTE2012: PI-0122

Fingerprint Recognition by using Minutiae Extraction Technique

Nahida Sultana[1], Md. Arafat Hossain[2]
Department of Computer Science & Engineering
E-mail: nahida.ruet07@gmail.com, arafat.ruet03@gmail.com

ABSTRACT
The development of Biometrics technologies are gained most popularity in both academic research community and industrial sectors. The goal of Fingerprint recognition is to develop a complete system for fingerprint verification through extracting and matching minutiae. To achieve good minutiae extraction in fingerprints with varying quality, pre-processing in form of image enhancement and binarization is first applied on fingerprints before they are evaluated. Many methods have been combined to build minutiae extractor and a minutiae matcher. Minutiae marking with special consideration of the triple branch counting and false minutiae removal methods are used in the work. An alignment-based elastic matching algorithm has been developed for minutiae matching. This algorithm is capable of finding the correspondences between input minutia pattern and the stored template minutiae pattern without resorting to exhaustive search. Performance of the developed system is then evaluated on a database with fingerprints from different people.

KEYWORDS— Minutiae Matching, Crossing Number Method, FAR(False Acceptance Rate), FRR(False Rejected Rate), Biometrics.

1. INTRODUCTION

High security authentication system is necessary for safe access. Traditional password and token based authentication schemes are insecure. Due to the vulnerability of conventional authentication system, cybercrime has increased in the past few years. Identity authentication, which is based on biometric feature such as face, iris, voice, hand geometry, fingerprints can significantly decrease the fraud. So they are being replaced by biometric authentication mechanisms. Among biometrics, fingerprint systems have been one of most widely researched and deployed for their easy access, low price of fingerprint sensors, significant because of their easy access, non-intrusive scanning, and relatively good performance.

2. Literature Review

In recent years, significant performance improvements have been achieved in commercial automatic fingerprint recognition systems. However, current fingerprint recognition technologies are vulnerable to poor quality images. It is imperative to continue research on improving the reliability, stability, performance and security of fingerprint recognition systems. Low quality fingerprint image, distortion, the partial image problems, large fingerprint databases are all major areas of research needed to improve the accuracy of current systems.

3. What is Fingerprint?

Skin on human fingertips contains ridges and valleys which together forms distinctive patterns. These patterns are fully developed under pregnancy and are permanent throughout whole lifetime. Prints of those patterns are called fingerprints. Injuries like cuts, burns and bruises can temporarily damage quality of fingerprints but when fully healed, patterns will be restored[1].

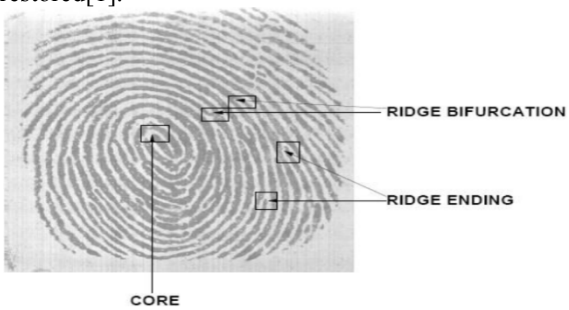

Fig.1 Fingerprint Image

There are three main fingerprint features. They are-

i). Global Ridge Detail: There are two types of ridge flows: the pseudo-parallel ridge flows and high-curvature ridge flows which are located around the core point and/or delta point(s). This representation relies on the ridge structure, global landmarks and ridge pattern characteristics.

ii). Local Ridge Detail: This is the most widely used and studied fingerprint representation. Local ridge details are the discontinuities of local ridge structure referred to as minutiae. They are used by forensic experts to match two fingerprints. There are about 150 different types of minutiae. Among these minutiae types, ridge ending and ridge bifurcation are the most commonly used. Some of them are following-

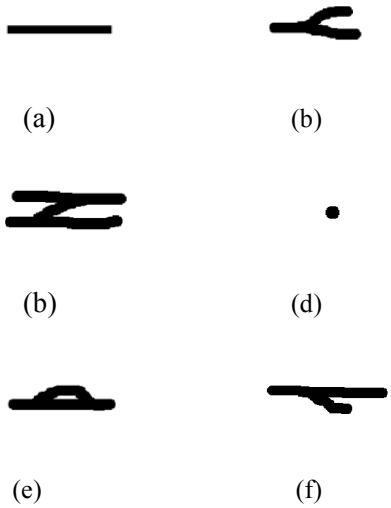

Fig.2 Types of minutiae

iii). Intra Ridge Detail: On every ridge of the finger epidermis, there are many tiny sweat pores and other permanent details. Pores are distinctive in terms of their number, position, and shape. However, extracting pores is feasible only in high-resolution fingerprint images and with very high image quality. Thus the cost is very high. Therefore, this kind of representation is not adopted by current automatic fingerprint identification systems (AFIS) [2].

3.1 Fingerprint Recognition?

The method that is selected for fingerprint matching was first discovered by Sir Francis Galton. In 1888 he observed that fingerprints are rich in details also called minutiae in form of discontinuities in ridges. He also noticed that position of those minutiae doesn't change over the time. Therefore minutiae matching are a good way to establish if two fingerprints are from the same person or not [4].

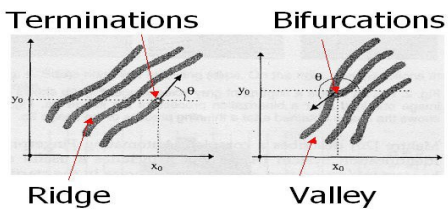

Fig.3 Minutiae of Fingerprint

The advantages of fingerprint recognition system are-

(a) They are highly universal as majority of the population have legible fingerprints.

(b) They are very reliable as no two people (even twins) have same fingerprint.

(c) Fingerprints are formed in the fetal stage and remain structurally unchanged throughout life.

(d) It is one of the most accurate forms of biometrics available.

(e) Fingerprint acquisition is non intrusive and hence is a good option [3].

3.2 Objectives

The objective is to implement fingerprint recognition algorithm. Also for accuracy for security, easy to recognize and To make invariant to translation, rotation and scale changes. The Region of Interest (ROI) for each fingerprint image is extracted after enhancing its quality. The concept of Crossing Number is used to extract the minutia, followed by false minutiae elimination. An alignment based matching algorithm is then used for minutiae matching.

4. System Design

Two methods for Fingerprint recognition:

4.1 System Level Design:

A fingerprint recognition system constitutes of fingerprint acquiring device, minutia extractor and minutia matcher [4].

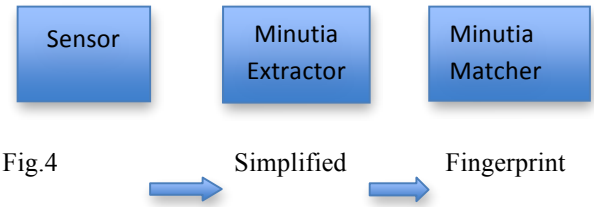

Fig.4 Simplified Fingerprint Recognition System

4.2 Algorithm Level Design:

To implement a minutiae extractor, a three-stage approach is widely used by researchers. They are preprocessing, minutiae extraction and post-processing stage.

Minutia Extractor

Pre-processing	• Image Enhancement • Image Binarization • Image Segmentation
Minutia Extraction	• Thinning • Minutiae Marking
Post: Processing	• Remove False Minutiae

Fig.5 Minutiae Extractor

For the post-processing stage, a more rigorous algorithm is developed to remove false minutiae. Also a novel representation for bifurcations is proposed to unify terminations and bifurcations.

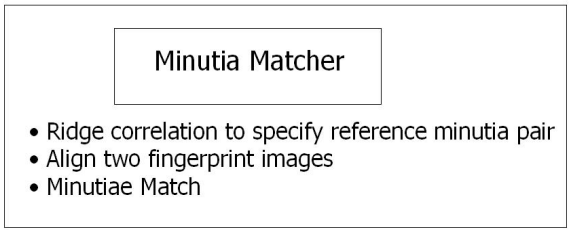

Fig.6 Minutiae Matcher

4.3 Minutiae Algorithm:
Here step1-5 are pre-processing, 6-7 are Minutiae extraction and 8-9 are post-processing stages.

Step1: Input
In this step we take a fingerprint of a person as input and process it.

Step2: Histogram Equalization
Histogram equalization is to expand the pixel value distribution of an image so as to increase the perceptional information. The histogram after the histogram equalization occupies all the range from 0 to 255 and the visualization effect is enhanced.

Step3: Enhancement using FFT
We divide the image into small processing blocks (32 by 32 pixels) and perform the Fourier transform according to :

$F(u,v)=\sum_{x=0}^{M-1} \sum_{y=0}^{N-1} f(x,y)\times \exp\{-j2\pi\times(\frac{ux}{M}+\frac{vy}{N})$....(1)
Where, u = 0, 1, 2, ..., 31 and v = 0, 1, 2, ..., 31.
In order to enhance a specific block by its dominant frequencies, the FFT of the block was multiplied by its magnitude a set of times.
Where, the magnitude of the original-

FFT = abs(F(u,v)) = |F(u,v)|…(2)
The enhanced block is obtained according to-

$g(x,y)=F^{-1}\{F(u,v)\times\left|F(u,v)^{K}\right|\}$ ...(3)
Step4: Binarization
This transform the 8-bit Gray fingerprint image to a 1-bit image with 0- value for ridges and 1-value for furrows [5].

Step5: Ridges Detection
The direction for each block of the fingerprint image with WxW in size (W is 16 pixels by default) is estimated by following algorithm:

- The gradient values along x-direction **(gx)** and y-direction **(gy)** for each pixel of the block is calculated by using two Sobel filters.
- Use the formula $tg2ß=2\sum\sum(g_x*g_y)/\sum\sum(g_x^2-g_y^2)$ for all the pixels in each block.

Use the formula to discard ridges and furrows by comparing with the threshold value.

$E=\{2\sum\sum(g_x*g_y)+\sum\sum(g_x^2-g_y^2)\}/)\}/W*W*\sum(g_x^2+g_y^2)\}/)$
Step6: ROI
Two Morphological operations called 'OPEN' and 'CLOSE' are adopted. The 'OPEN' operation can expand images and remove peaks introduced by background noise. The 'CLOSE' operation can shrink images and eliminate small cavities.
Step7: Thinning
Ridge Thinning is to eliminate the redundant pixels of ridges till the ridges are just one pixel wide. An iterative, parallel thinning algorithm is used.

Step8: Minutiae Marking
Crossing Number method is used for each 3x3window.

- If the central is 1 and has only 1 one-valued neighbor, then the central pixel is a termination.
- If the central is 1 and has 3 one-value neighbors, then the central pixel is a bifurcation.
- If the central is 1 and has 2 one-value neighbors, then the central pixel is a usual pixel.

Step9: Remove false Minutiae
Removal of false minutiae is given below [8]:

- If the distance between one bifurcation and one termination is less than D and the two are in the same ridge. Remove both. D is the average distance between two parallel neighbouring ridges.
- If the distance between two same bifurcations is less than D remove the both.
- If two terminations are within a distance D and directions are coincident with a small angle variation and no other termination is located between the two terminations. Then the two terminations are regarded as false minutiae are removed.

Step10: Minutiae Matching
Stage1: Alignments

If the similarity is larger than a threshold, each set of minutia is transformed to a new coordination system whose origin is at the referenced point and whose x-axis is coincident with the direction of the referenced point .

Stage2: Match
After obtaining two set of transformed minutia points, the elastic match algorithm is used to count the matched minutia pairs by assuming two minutia having nearly the same position and direction are identical .

Fig.7 Orginal Image

Fig.8 Histogram Equalization

Fig.9 FFT

Fig.10 Binarization

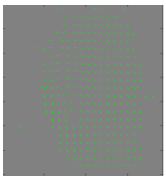

Fig.11 Direction

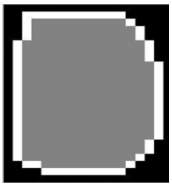

Fig.12 ROI

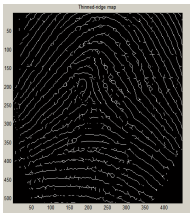

Fig.13 Thinned Image

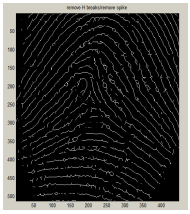

Fig.14 Remove h-breaks

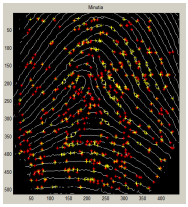

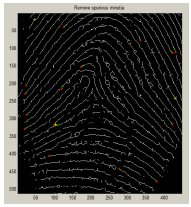

Fig.15 Marking Minutiae Fig16 Unify Minutiae

5. Results

The final match ratio for two fingerprints is the number of total matched pairs divided by the number of minutiae of the template fingerprint. The score is 100*ratio and ranges from 0 to 100. If the score is larger than a pre-specified threshold (typically 80%), the two fingerprints are from the same finger. However, the elastic match algorithm has large computation complexity and is vulnerable to spurious minutiae. We use CASIA database. FAR and FRR are calculated with respect to threshold value.

Threshold value	FAR	FRR
7	0.07%	7.1%
8	0.02%	9.4%
9	0.01%	12.5%
10	0	14.3%

6. Conclusion

Here we accurately mark a thinned image to a single pixel width. Improve verification rate. It also done matching accurately.

The future scope of the work is to improve the quality of image by improving the image enhancement technique and develop better feature extraction and matching technique. Also improve the recognition speed.

7. References

[1]. Jain, R. Bolle, and S. Pankanti, “Biometrics Personal Identification in Networked Society”, Kluwer Academic Publishers New York, Boston, Dordrecht, London, Moscow, pp. 1-64, 2002.

[2]. A. K. Jain, F. Patrick, A. Arun, “Handbook of Biometrics”, Springer Science+Business Media, LLC, 1st edition, pp. 1-42, 2008.zz

[3]. Handbook of Fingerprint Recognition by David Maltoni, Dario Maio, Anil K. Jain and Salil Prabhakar , Springer, New York, pp. 2003.

[4]. D. Maio, and D. Maltoni, “Direct gray-scale minutiae detection in fingerprints”, IEEE Transactions Pattern Analysis and Machine Intelligence, vol. 19(1), pp. 27-40, 1997.

[5]. K. Nallaperumall, A. L. Fred, and S. Padmapriya, “A Novel Technique for Fingerprint Feature Extraction Using Fixed Size Templates”, IEEE 2005 Conference, pp. 371-374, 2005.

Proceeding of the
International Conference on Electrical, Computer and Telecommunication Engineering
01- 02 December 2012 (ICECTE2012), RUET, Rajshahi-6204, Bangladesh

ICECTE2012: PI-0123

Human Facial Expression Detection using Genetic Algorithm

Tasnuva Haque[1], Md. Rabiul Islam[1], Rizoan Toufiq[1]*
[1]Department of Computer Science & Engineering
Rajshahi University of Engineering & Technology, Rajshahi-6204, Bangladesh
E-mail: reya.ruet@gmail.com, rabiul_cse@yahoo.com and rizoantoufiq@yahoo.com

ABSTRACT
This paper presents a robust and adaptable facial expression detection system in human computer interaction environment. In this work, a method has been proposed to detect the expressions of a facial image from an image database regardless of changes in the position and orientation of a face using the genetic algorithm. Facial expression parameters are assigned to the genes of an individual in a population. The fitness function of genetic algorithm which evaluates to what extent the real and synthesized face images are similar to each other is calculated. After the repetition of the process for sufficient generations, the parameter estimation is obtained from the genes of the individual with the best fitness. Finally, expression is detected by matching the recognized image with properties of database image which is previously defined. Experimental results and performance analysis demonstrate the effectiveness and versatility of the proposed method.

KEY WORDS: Facial Expression Detection, Image scaling, Image filtering, Fitness Function, Genetic Algorithm.

1. INTRODUCTION

Facial expression analysis and emotion recognition has gained much attention by the engineering community in the last twenty years. Recently, there has been a growing interest in improving all aspects of the interaction between humans and computers. The reasons include the need for quantitative facial expression description as well as automation of the analysis process which is strongly related to one's emotional and cognitive state [1]. This paper presents an approach to determine the human facial expression using genetic algorithm. Facial expressions are micro expressions which indicate the mental and physical state of a person. Human gestures can be identified by observing the different movements of eyes, mouth nose and hands [2]. It plays an important role in smooth communication among computer and their user. Because understanding the emotion and knowing how to react to people's facial expression greatly enrich the human computer interaction. Basically face and its expression recognition system are mainly used in security aspect because the facial expression of a person indicates his next action. For example, observing the gesture of a driver when he/she is driving and alerting him/her when in sleepy mood will be quite useful [2]. For this reason facial expression recognition system is widely used in security, surveillance, authentication and criminal identification.

The research for improving facial expression detection system has been performed since many years by many researchers. Essa and Pentland created the "face space" by performing Principal Component Analysis of eigenfaces from 128 face images. Face is detected in the image if its distance from the face space is acceptable [3]. Essa and Pentland also proposed temporal approach to the problem of facial expression analysis. They used the multiscale coarse-to-fine Kalman filtering. Pantic and Rothkrantz selected a set of facial points from frontal and profile face images. They introduced the expert system with rule based classifier which can recognize 31 action units with accuracy rate of 89% [4]. Kobayasi and Hara used 234×50×6 neural back propagation network for recognition of 6 basic emotions and achieved recognition accuracy is 85% [5]. Facial expression is either interpreted as a human universal with basic expressions represented in all known human populations or it is conceptualized as the natural outgrowth of cultural differences, with little overlap in expression from population to population [6]. Not only the above researches are performed but also many other researchers try to develop facial expression detection system. According to the Ekman's theory [7], there are six basic emotion expressions that are universal for people of different nations and cultures. Those basic emotions [8] are happy, sad, anger, fear, disgust and surprise which are shown in figure 1.

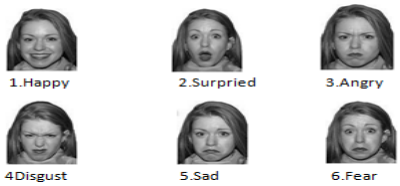

Fig. 1 Several facial expressions.

Our aim is to present a system which can detect facial expression from verities of images in comparatively shorter time. So, our objective is to speed up the recognition process. In this work, we have considered static facial expression detection technique in which image is recognized from an image database. Genetic Algorithm has been used in this proposed system which can search in a large space within a small amount of time and can produce an optimal result. This system is based on probabilistic based approach which does not gives preference to facial features such as eyes and mouth. It gives preference in random distribution of image intensities. The experimental results reflect the efficiency of the proposed method of facial expression.

2. PROPOSED TECHNIQUE FOR FACIAL EXPRESSION DETECTION

At first facial images have been captured and take as input to the system. Then some image pre-processing techniques have been used to prepare the facial image to the system and noise reduction techniques have been used to reduce the noise from the facial images. Genetic algorithm has been used to classify the unknown facial pattern with the learned template and finally get the facial expression detection results. Figure 2 shows block diagram of the proposed method for facial expression detection system.

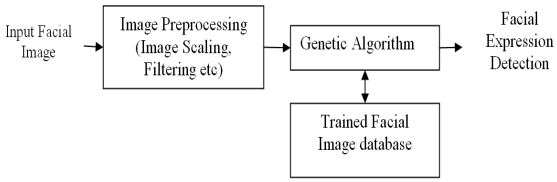

Fig. 2 Block diagram of the proposed facial expression detection system.

2.1 Facial Image Acquisition

The first step of this system is image acquisition; that is to acquire a digital face image by using high regulation digital camera. To do so, an imaging sensor along with signal digitization capability is required so that captured image can be converted to digital form directly. Digital camera is being used to capture image and to get the digital form of face images. Better digital camera must be used for good face image [9]. Then the image can be saved into various formats such as Bitmap, JPEG, GIF and TIFF. Figure 3 shows a sample facial image.

2.2 Image Pre-processing:

To prepare the captured image into the system requirements i.e. image size, color, contrast etc have been changed by using some image pre-processing techniques. Noise reduction technique has also been used to create a noise free facial image of the system.

Fig. 3 Sample facial image.

2.2.1 Image Scaling

After acquisition of face image, it was being scaled. In this work, scaling on the face image was being done to get the actual shape of face from its original image. It was observed that the background color of the original form of face image was black or like shadow and the original shape of face (i.e. foreground color) was not actually black which means there was some dissimilarity between the foreground and background color. So, using scaling technique, we removed the background color from the original image and obtained the actual shape of face image [9]. There are various techniques for scaling of the image. Here shrinking technique has been used to get the image dimension 92×112. Figure 4 shows the results after applied scaling technique.

(a) Before scaling **(b) After scaling**

Fig. 4 Effects of image scaling.

2.2.2 Image Filtering

The input face image of the system may contain noise and garbage data that must be removed. Salt and pepper noise is of the common form of noise typically seen on images. It represents itself as randomly occurring white and black pixels. An effective noise reduction method for this type of noise involves median filter. In our system, median filter is used to remove salt and pepper noise. In median filtering, after applying mask the pixel values are arranged in ascending order. Then middle pixel value is identified and output pixel is replaced by median value. Figure 5 shows the results after applying median filtering technique.

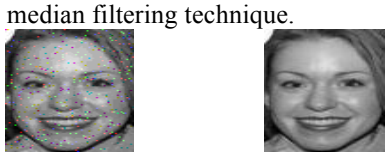

(a) Before filtering **(b) After filtering**

Fig. 5 Image filtering output.

2.3 Recognition Model

This processed image is utilized to identify certain optimum parameters through Genetic Algorithm.

These parameters are employed in the interpretation of emotion characteristics. Three different genetic operators such as selection, crossover and mutation have been used to search the matching for the unknown pattern from the learned template that was already saved to the system. Different numbers of generations have been applied to optimize the search results. Effective fitness function has been adopted for the proposed system for the successfully mapping unknown image with the learned images. By performing cross-over according to the fitness value various numbers of generations have been created. If optimal solution is not found by cross-over operation then mutation is performed to get the accurate match.

3. IMPLEMENTATION OF THE PROPOSED FACIAL EXPRESSION DETECTION SYSTEM

Implementation has been done in some different phases which are focuses below:

Step 1: Assumptions taken

- There are M images in the training set.
- There is K most significant faces using which we can satisfactorily approximate a face. Needless to say $K<M$.
- All images are $N \times N$ matrices, which can be represented as $N^2 \times 1$ dimensional vectors.
- An image can be represented simply as a point in a dimensional space.

The same logic would apply to images that are not of equal length and width. For example: an image of size 92×112 can be represented as a vector of 10304 dimensions or simply as a point in a 10304 dimension space.

Step 2: Prepare facial image database

ORL facial database has been used to evaluate the proposed system performance. ORL database contains a set of face images taken between April 1992 and April 1994 at the lab. There are ten different images of each of 40 distinct subjects in the database. For some subjects, the images were taken at different times, varying the lighting, facial expressions (open/closed eyes, smiling/not smiling) and facial details (glasses/no glasses). All the images were taken against a dark homogeneous background with the subjects in an upright, frontal position (with tolerance for some side movement). There is some variation in scale of up to about 10%. The images are gray scaled with a resolution of 92×112.

Step 3: Recognition using genetic algorithm

For recognition using genetic algorithm we have used,

Maximum number of generations = *5*

Type of selection = Rank selection

At first summation of all pixel values of the input image is calculated. Then for each database image, the summation of all pixel values has been calculated. The absolute difference between summation of all pixel values of an input image and train database image is used as fitness value for that image. If the total database image is *100* we will find the *100* fitness values.

The fitness function can be defined as,

F = Minimum absolute difference between input image and train database image

$$= Min\left(\sum_{i=0}^{n-1}\sum_{j=0}^{n-1} S_{input}(x_i, y_j) - \sum_{i=0}^{n-1}\sum_{j=0}^{n-1} S_{train}(x_i, y_j)\right) \quad (1)$$

After getting fitness values for every database image the values are sorted. Then select those values are nearest to the fitness values for the next generation. After each generation, 3 rows and 3 columns are eliminated and again fitness value is calculated. Finally after 5 numbers of generations, the similar fitness valued equivalent image is selected with the input image. The recognized facial image according to the input image is shown in figure 6.

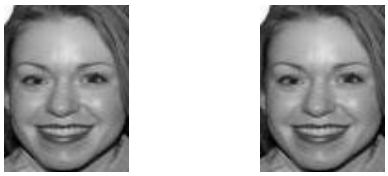

(a) Input image (b) Recognized image

Fig. 6 Output of the system.

4. EXPERIMENTAL RESULTS AND PERFORMANCE ANALYSIS

To measure the performance of the proposed facial expression detection system, various numbers of parameters such as crossover rate, number of generations, different lighting conditions, facial expression with adverse condition etc have been considered. Searching time has also been captured to measure the time complexity of the proposed system. Six different images of facial expression have been considered for the testing phase of the system. Table I shows the experimental results of genetic algorithm based face recognition system. System performance according to recognition rate and average elapsed time is shown in figure 7 and figure 8 respectively.

Table 1 Results of the proposed facial expression detection system

No. of test images	No. of correctly detected images	No. of incorrectly detected images	Average elapsed time per searching image (in seconds)	Recognition rate (in %)
10	10	0	2.46	100
20	20	0	4.61	100
30	30	0	6.22	100
40	39	1	8.46	97.5
50	49	1	10.79	98
60	59	1	13.44	98.33
70	69	1	15.12	98.57
80	78	2	17.33	97.5
90	88	2	18.24	97.78
100	98	2	20.59	98

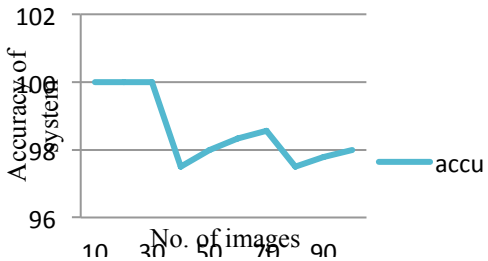

Fig. 7 Recognition rate according to the number of images.

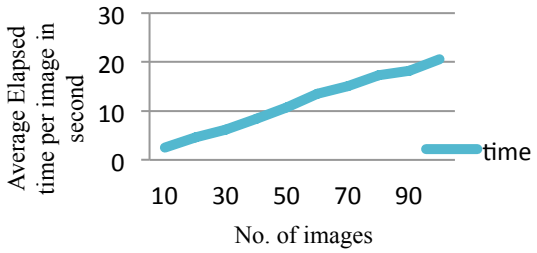

Fig. 8 Performance of average elapsed time per image.

5. CONCLUSIONS AND OBSERVATIONS

In this paper, we have proposed a simple and robust genetic algorithm based facial expression detection technique has been proposed where different lighting variations, various facial expressions has been considered. Experimental results and performance analysis reflects the veracity of the proposed system which can be used in any practical system. Though the system performs well enough, the system performance can also be increased by using different image pre-processing techniques and noise removing techniques. The system performance can also be enhanced by using different classification techniques such as neural networks, support vector machine, hidden markov model etc which may be the further work of the developed system.

REFERENCES

[1]. Spiros Ioannou, George Caridakis, Kostas Karpouzis, and Stefanos Kollias, "Robust Feature Detection for Facial Expression Recognition", *EURASIP Journal on Image and Video Processing*, Vol. 2007, Article ID 29081, November 2007.

[2]. Jagdish Lal Raheja, Umesh Kumar, "Human Facial Expression From Detected In Captured Image Using Back Propagation Neural Network", *International journal of computer science & information technology(IJCSIT),* Vol.2, No.1, pp. 116-123, February 2010.

[3]. Essa, I., Pentland, "Coding, analysis, interpretation,and recognition of facial expressions." *IEEE Trans. Pattern Anal. Machine Intell. 19 (7),* pp.757–763, 1997.

[4]. Pantic M, Rothkrantz L. "Automatic Analysis of Facial Expressions: The State of the Art." *IEEE Transaction on Pattern Analysis and Machine Intelligence*, pp. 1424–1445, 2000.

[5]. Kobayashi H, Hara F. ,"Facial Interaction between Animated 3D Face Robot and Human Beings." *Proceedings of International Conference on Systems, Man, Cybernetics*, pp. 732–7371997.

[6]. Karen L. Schmidt, Jeffrey F. Cohn, **"**Human Facial Expressions as Adaptations:Evolutionary Questions in Facial Expression Research", *Yearbook Of Physical Anthropology*, Vol. 44:3–24, pp. 50, 2001.

[7]. P. Ekman, T. Huang, T. Sejnowski, J. Hager, "Final Report To NSF of the Planning Workshop on Facial Expression Understanding", 1992.

[8]. Ewa Piatkowska, "Facial Expression Recognition System", pp. 7, 2010.

[9]. Abu Sayeed Md. Sohail, Md. Rabiul Islam and Kaushik Roy, "Real Time Face Recognition Using Artificial Neural Networks: A Secure Personnel identification system," *3rd international conference on Electrical & Computer Engineering*, pp. 120-123, December 28-30, 2004.

Proceeding of the
International Conference on Electrical, Computer and Telecommunication Engineering
01- 02 December 2012 (ICECTE2012), RUET, Rajshahi-6204, Bangladesh

ICECTE2012: PI-0125

Web Testing Methodology and Performance Assessment of University Web Sites

Md. Safaet Hossain
Department of Electrical Engineering and Computer Science
North South University, Dhaka Bangladesh
E-mail: safayeth@gmail.com

ABSTRACT
The worldwide internet audience of any Web Browser Enabled Application makes its eminence and trustworthiness vital factors in its success. Correspondingly, the nature of automated testing poses inimitable software testing challenges. Webmasters, Web applications developers, and WebSite quality assurance managers need tools and methods that congregate their precise needs. Some of the other test types are functional tests (makes sure features work), stress tests (site is tested on computers with different hardware specifications), and regression tests (defines how site will be tested in the next phases), boundary analysis (tests the limitations of site such as entering information in forms). Sometimes the best way to test university web site is by having an actual person to go through the site and get the problems he encountered. Some of these software run test that simulate testers. However, few tools are provided to directly support the software testing on Web-based applications. In this paper, an automated online website evaluation http://safaethossain.comze.com is proposed to support the automated testing for scenario of web-based applications. Testers can evaluate performance comparison and evaluate with other websites and can precisely express the existing websites and find out what are the modifications required. The tool can elevate the automated level of functional testing for web applications. Our technical approach, based on existing Web browsers, offers a clear solution to most of the technical needs for assuring WebSite quality.

KEY WORDS: Total Page Download Time, page link, page response time, Total Page Size, Total Size by Object Type

1. INTRODUCTION

In recent years, Web portals are attracting more and more users and escalating in reputation. Web portal is a site (often a system) that creates a solitary summit of entrance to information collected from different sources. It offers a structured approach for navigating through the information. This portal may restrain assortment of Web pages, images, videos or other digital assets that are hosted on one or several Web server(s), usually available via the Internet. As a result, web portals suitable increasingly complex as more and more services like videos, downloads, images and dynamic information like reservations are made available over the Internet. At the same time, the correctness of sites has become vital for the success of businesses and organizations. Therefore it is not an easy job for web administrator to keep it up to date. Thus testing plays a prominent role in the maintenance of such software.

These Web portals mainly focus on the information publication, searching and indexing. Thus compared to traditional software, they have weaker functionalities but quicker updating speeds in their contents and techniques. We need to validate the normal running of Web portals in such aspects as functionality, performance, compatibility, usability, safety and so on. Here we are focusing on testing the functionality of a web portal. As an important method to ensure the quality of Web portals, the Web portal testing attracts more and more attention by researchers and users. They have proposed some important research methods and obtained numerous results [1], [2]. So far traditional testing methodologies were used for web portal testing as they are treated similar to software. But these traditional testing methods cannot meet the demands of Web portal and a unique suit of testing system is needed to fulfill the task of web testing due to their special properties like numerous users, heterogeneity, autonomous environments and their dynamic nature.

The developing process of Web portal is generally in the style of RAD (Rapid Application Development) and it has shorter emergent time, which can amend to the frequent changes of user demands. But this puts greater pressure on the preservation and makes the Regression testing especially important. Once the changes take place in the Web portal, we must retest all the existing functions to ensure whether the changes are consistent with the previous functions, in addition to the new test cases which are needed to test

the new or modified functions. This paper focuses on improving the existing Web testing tools by developing a tool based on Regression Testing Technique. Our tool analyses the Web portals and also provides a GUI for search and navigation facilities. The web portal structure is organized as a set of pages and links between pages.

A key challenge for university is to spread information about various topics and subjects and to develop their Web presence and back-office operations accordingly. Any University or any education institute with a Web site that is difficult to use and interact with will project a poor image on the Internet and weaken the institution's position. It is therefore important that an education institute be able to make an assessment of the quality of their website information density, as perceived by their customers and in the context of the industry. In doing so, education institution can improve their offerings over time and benchmark against competitors and best practice in any industry. This research utilizes the integrated approach to assess university websites. Typically, the tool allows comparisons to be made between different university websites over time. The structure of the paper is as follows. The paper is organized as the following: Section II provides related works, section III presents Web test models, section IV describes Web evaluation methodologies and finally section V draws conclusion. The discussions are interpreted in section V. The last section provides a summary and makes recommendations for future work.

2. RELATED WORK

The testing process for traditional software is generally consisted of different steps: firstly determine the testing objects and targets, such as the required testing coverage ratio; next, generate the testing input, and this input is generated by the specification and structure of the software; then produce the expected output results; subsequently, execute the test cases and validate output; This series of steps and flows are suitable for the general software testing, and the differences, which can directly influence the ultimate testing effect.

In order to evaluate the quality of Web application and the efficiency of testing process, we can measure and evaluate a lot of testing results for Web applications and give the guidelines to the development of Web applications. In the existed research work, P.Warren [10,11] mainly focused on the Website evolution and Web application maintenance, and they pointed out that all kinds of problems occurred in the Website development, usage and maintenance are caused by disobey the rules of software engineering, and they put forward the metrics to indicate the evolvement of Websites; Devanshu Dhyani presented the origins, measurement functions, formulations and comparisons of well-known Web metrics for quantifying Web graph properties, Web page significance, Web page similarity, search and retrieval, usage characterization and information theoretic properties [9]. However, there are short of the related metrics criterions and indexes to the testing, so it is difficult to directly evaluate the testing effect.

After we obtain the web testing result from different sources, the modification and maintenance to the Web application are needed due to the testing results, so as to eliminate the influences caused by the faults in the system, satisfy all kinds of actual demands of users, improve the system quality actual demands of users, improve the system quality and the degree of users' satisfactions and feed back the related testing information into the Web applications themselves, thus we can know the existed problems in Web applications and the difficulties of their modifications and improvements, then we can guide the development and evolvement of Web applications directly and exactly especially in the aspects of system reliability, usability and safety.

3. WEB TEST MODEL

Website building and testing needs to follow several ways of experiments and it needs to follow several methods to ensure the quality of Web applications and it hard working and become crucial after applications raises new problems and faces very high challenges

Faults are obtained through a process similar to one defined and used in previous research in testing techniques [2,3,4] whereby faults are inserted, which are as realistic as possible and based on user experience. The following fault types are investigated:

- Web page faults: This includes web page faults according to the Web Content Accessibility Guidelines and World Wide Web consortium.
- HTML faults: This includes HTML tag opening and closing error.
- Link Error: This includes page link error.
- Page Link status: This includes page link status according to the benchmark.
- Response time testing: This includes response time of each page link.

4. WEB EVALUATION METHODOLOGY

Testing of web-based applications in particular deserves further examination due to economic considerations and companies are choosing not to test due to resource constraints. Like any complex piece of software there is no single, all inclusive quality measure that fully characterizes a WebSite (by which we mean any web browser enabled application).

The process of website designing can be divided into different stages. The stages are Information Gathering,

Apply methods, Website evaluation, Result Analysis.

Figure 1: Web Assessments Model

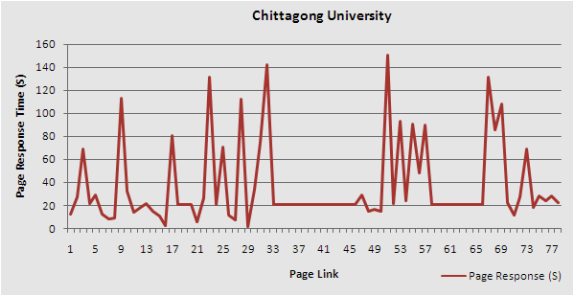

Figure 2: Chittagong University website testing according to page response time

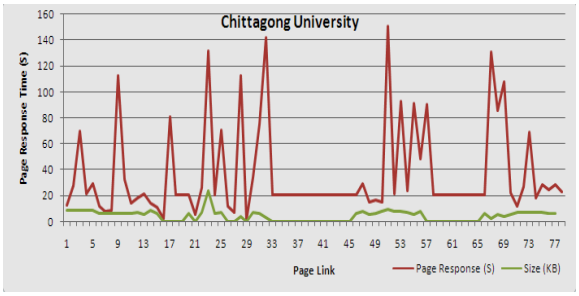

Figure 3: Chittagong University website testing according to page response time and page size of each page

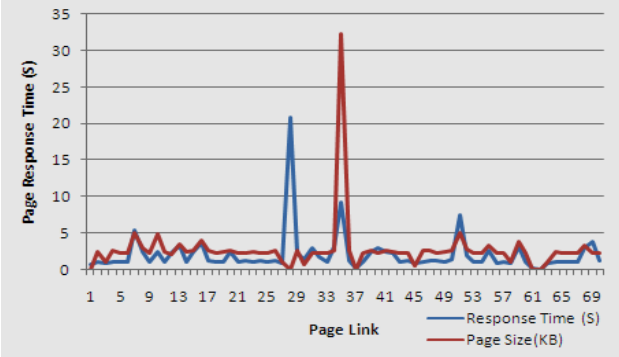

Figure 4: BUET University website testing according to page response time and page size of each page

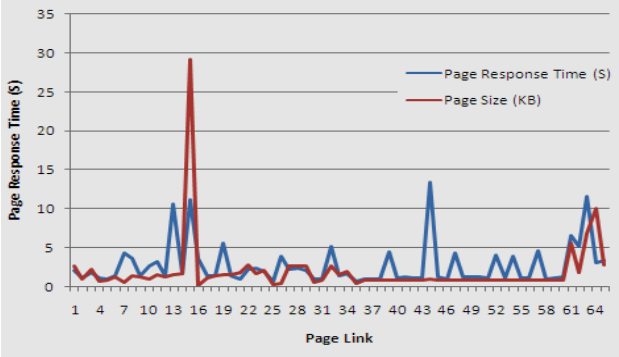

Figure 5: Dhaka University website testing according to page response time and page size of each page

5. Page Testing Methodology

Web Page Link Response Time

The end-to-end time elapsed to response a web page link. This includes the response time (millisecond) and response time (second) and page size (KB) with every page link of the web sites. A screenshot is as follows:

LINK	MS	Response Time (S)	Page Size(KB)
1	780	0.78	0.017
2	1070	1.07	2.45
3	850	0.85	1.02
4	1100	1.1	2.531
5	1023	1.023	2.26
6	1080	1.08	2.228
7	5456	5.456	5.12
8	2437	2.437	2.955
9	1079	1.079	2.316
10	2426	2.426	4.946
11	1031	1.031	2.385
12	2188	2.188	2.142
13	3291	3.291	3.457
14	1122	1.122	2.438
15	2437	2.437	2.676
16	3671	3.671	3.945
17	1161	1.161	2.556
18	1072	1.072	2.243
19	1093	1.093	2.387
20	2389	2.389	2.564
21	1082	1.082	2.33
22	1138	1.138	2.32
23	1111	1.111	2.415
24	1133	1.133	2.326

Figure 7: BUET University Evaluation with all page links

Website performance (response time vs page size)

The time it takes from the server to the client and every page link to load according to the web page size can be generated from the data sheet which was generated by the site: http://safaethossain.comze.com.

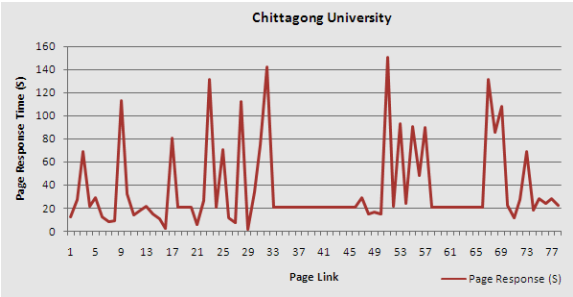

Figure 8: Sample Page Response assessment

Performance analysis

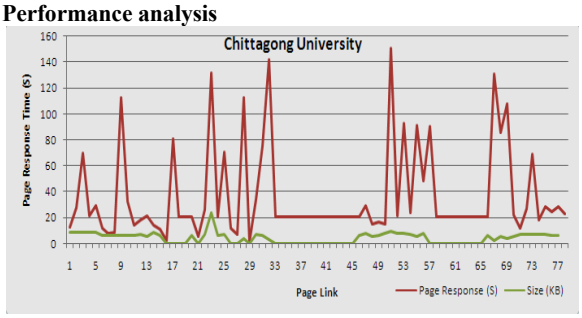

Figure 9: Sample Page Response assessment with page size

Chittagong University	
Average Response Time	36.74 seconds
Average Page Size	4.25 KB
BUET	
Average Response Time	2.04 seconds
Average Page Size	2.73 KB
Dhaka University	
Average Response Time	2.50 seconds
Average Page Size	2.34 KB

Table 1: Performance evaluation of different university web sites based on response time and Page size

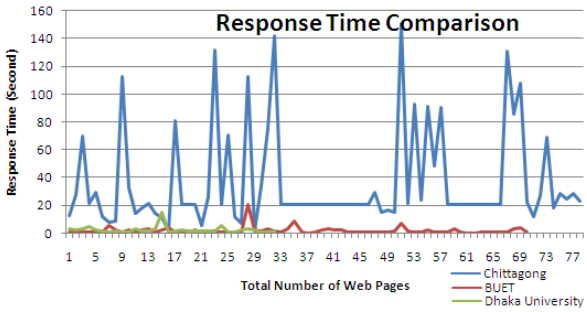

Figure 10: Page Response time performance graph Chittagong University vs BUET vs Dhaka Unioversity

Page Response Time:

The total size, or weight, of each page link is compared with different websites and get the average page response time including all objects and third-party content. There is a correlation between the Total Page Size and Total Page Load Time, and therefore Total Page Size can impact customer experience and behavior

Web Site	Average Response Time (Sec)
Chittagong University	**36.74**
BUET	**2.04**
Dhaka University	**2.50**

Table 2: Response time comparison different web sites

Web Site	Average Page Size (KB)
Chittagong University	4.25
BUET	2.73
Dhaka University	2.34

Table 3: Average Response time comparison web sites

Web Page Response time

The comparison between different websites by analyzing all the pages response time and get the average response time.

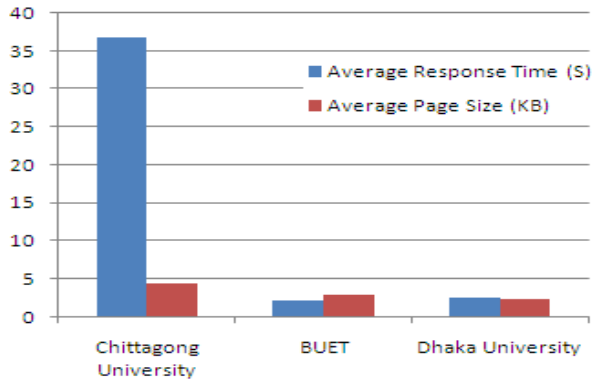

Figure 11: Average Page and Response time comparison

6. Procedure Analysis

Web-based analysis and test tools have been also developed the integrated model the underlying structure for web applications. By implementing the integrated step to create a program that can scan a web site and check the broken links, broken images, client side script errors and other web site common errors. Performance of web sites has addressed in order to ensure the reliability and speedy access of web sites performances. White box testing approach build system models from inspection of code, identify test requirements from those models, and require extensive human participation in the generation of test cases to fulfill those requirements. These approaches focus on the internal structural aspect and involve in the details of a web application.

By developing an integrated prototype tool allowing users to run the test cases to test the functionality, security and find faults in the web application. The test cases should specify the input conditions and expected output of each test as specified. It should be generated to be extensible and allow enhancements to be made for more complex and customizable tests. Load test the newly generated test cases to test the performance of the web application and generate a test report.

7. CONCLUSIONS

This paper aims to investigate into various measures required for quality Website design. A focused approach has been made to identify all possible errors in developing Website so that before going to use any qualitative measure, it is necessary to verify whether all aspects of Website design are considered in quality assessment or not. This would enable to adjudge the quality status of Web design of the various universities and would indicate the necessity of improvement in the design of the Website. The integrated web testing evaluates effective testing methodology for web application and can improve the performance testing of web application.

Using a series of online diagnostic tools, we examined many dimensions of quality, and each dimension will be measured by specific test online. To get results on the quality of a Web site, we measure sample data extracted from different web sites and calculate response time, page size, number of item, and load test, mark validation, and broken link, number of link test. Moreover because the ultimate determinant of quality website is the users, future directions for this research also involve the objective and subjective views of the website from user's perspective. Finally, the practical experiment of application of our methodology has been described; we believe that this experiment provides encouraging results concerning the validity, correction and agility of the method.

TOOL AVAILABILITY

The tool has been released online for public use. More information about the tool can be found at the following location: ***http://safaethossain.comze.com***

REFERENCES

[1]. C. Kallepalli, J. Tian, "Measuring and Modeling Usage and Reliability for Statistical Web Testing", IEEE Trans Software Engineering, 2001,27(11): 1023-1036.

[2]. L. Xu, B. W. Xu, and Z.Q. Chen, "Survey of Web Testing", Computer Science (in Chinese), 2003, 30(3): 100-104.

[3]. Xu L, Xu BW, Chen HW. "Website Evolution based on Statistic Data", Proceedings of the Ninth IEEE International Workshop on FutureTrends of Distributed Computing Systems (FTDCS 2003), Page(s):301-306.

[4]. J. Gao, C. Chen, Y. Toyoshima and D. Leung, "Engineering on the Internet for Global Software Production", IEEE Computer, 1999, 32(5):38-47.

[5]. F. Ricca and P. Tonella, "Web Site Analysis: Structure and Evolution", Proc. of International Conference on Software Maintenance (ICSM'2000), 2000, pp. 76-86.

[6]. Rohit Dhand, "Web Services: A Trend Shift from conventional Distributed Computing Model" IEEE Computer, 2009, DOI 10.1109/ICCEE.2009.26:313-317.

[7]. Bo Song and Huaikou Miao, "Modeling Web Applications and Generating Tests: "A Combination and Interactions-guided Approach", IEEE Computer, 2009, DOI 10.1109/TASE.2009.54:174-181.

[8]. K. Y. Cai, "Optimal software testing and adaptive software testing in the context of software cybernetics", Information and Software Technology, 2002, 44, pp. 841-855.

[9]. D. Dhyani, W. K. Ng, and S. S. Bhowmick, "A survey of Web metrics", ACM Computing Surveys, 2002, 34(4): 469-503.

[10]. P. Warren, C. Boldyreff, and M. Munro, "The Evolution of Websites", Proc. of the Int. Workshop on Program Comprehension, 1999, pp. 178-185.

[11]. P. Warren, C. Gaskell, C. Boldyreff. Preparing the ground for website metrics research. Proc of the 3rd International Workshop on Web Site Evolution, 2001, pp. 78-85.

[12]. http://www.gomez.com/website-performance-test/, last access on January 15, 2012

Proceeding of the
International Conference on Electrical, Computer and Telecommunication Engineering
01- 02 December 2012 (ICECTE2012), RUET, Rajshahi-6204, Bangladesh

ICECTE2012: PI-0126

A Comparison of Distributed Transaction Technologies and Protocols for Mobile Database Systems

Shahidul Islam Khan
Department of CSE, International Islamic University Chittagong (IIUC), Bangladesh
E-mail: nayeemkh@yahoo.com

ABSTRACT
With the advent and increasing popularity of mobile devices, new challenges arise in mobile databases. Now a day databases are hosted by a growing number of lightweight intelligent devices like palmtops, cellular phones, car computers and even smart cards. That's why uses of mobile databases are also increasing. In this paper I have compared different technologies and protocols of transaction management of Mobile Database System (MDS) such as Two Phase Commit (2pc), Transaction Commit On Timeout (TCOT), Mobile 2PC (M-2pc), UCM, OCC-UTS.

KEY WORDS: Mobile Database System, Distributed Database, Commit protocol and Transaction management.

1. INTRODUCTION

Mobile computing is one of the most challenging areas for database systems recently. Database Management Systems are commonly hosted by laptops to serve as storage area for disconnected computing. More recently, databases come forward in the world of lightweight smart devices such as palmtops, cellular phones, smart cards etc [7]. Mobile Database System (MDS) is a system with the following structural and functional properties: Distributed system with mobile connectivity, Full database system capability, Complete spatial mobility, Built on GSM/ PCS platform, Wireless and wired communication capability. The problems that MDS faces are limited wireless bandwidth, wireless communication speed, limited energy source (battery power), less secured, vulnerable to physical activities. In a mobile environment, transactions may be initiated by mobile units (MU) and distributed among a set of mobile or fixed units [8, 3, 4].

This paper deals with the transactional properties in this context. It compares atomic commitment protocol that eases the integration of lightweight database users in a distributed transaction.

2. UNILATERAL COMMIT FOR MOBILE PROTOCOL (UCM)

To understand UCM [6], the execution phase and the termination phase of a transaction have to be considered together. Five types of components interact in the execution and termination of a transaction, namely the *Application* that asks for the execution of a sequence of operations, the *LogAgent* that logs each operation before execution, the *Participants* that execute these operations, the *Coordinator* that pilots the termination protocol and the *PAgents* (one per participant) that represent the participants in the termination protocol and play an active role during recovery. These components may be co-located or not depending on the hardware and software configuration. Note that the Coordinator is still located on the fixed network while the other components can be potentially hosted by a mobile.

The commit scenario produced by UCM is depicted in **Fig. 1**. To simplify the figure, only the actions executed by a single participant P_k are shown. In the following, T_{ik} denotes the local branch of transaction T_i executed at participant P_k.

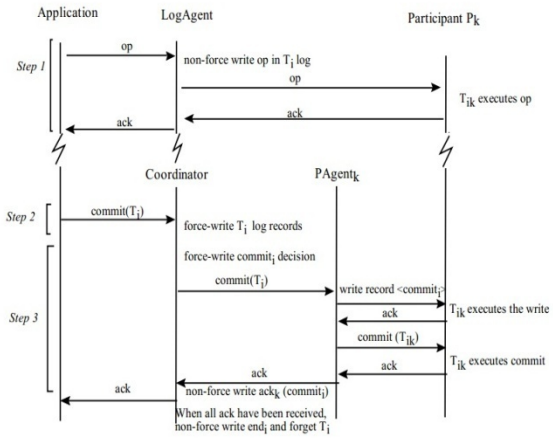

Figure 1: The commit scenario produced by UCM

In **Fig. 1**, Step 1 represents the sequence of operations executed on behalf of T_{ik}. The LogAgent registers in its log each operation that is to be executed. Note that this registration is done by a non-forced write. Non-forced writes are buffered in main

memory and do not generate blocking I/O. Operations are then sent to and locally executed by *P* k. Every operation is acknowledged up to the application.

Step 2 corresponds to the termination of the transaction from the application point of view. Once all the acknowledgments are received by the application, it issues a commit request. At this point, properties ACI are locally guaranteed by the participants for all the local transaction branches 1. However, since participants are not aware of the termination of the transaction, they cannot guarantee the Durability property. Durability is ensured by the coordinator itself, which gets the T_i log produced by the LogAgent and force-writes it on stable storage. Once Step 2 is achieved, the ACID properties are guaranteed altogether for all the transaction branches. Thus, the coordinator takes a Commit decision and force-writes this decision on stable storage (Step 3). Note that, in order to improve performances, T_i 's log records (Step 2) together with the Commit decision (Step 3) can be forced on stable storage at the same time, thereby generating a single blocking I/O. Then, the coordinator broadcasts the Commit decision to all participants and waits for their acknowledgments. When all acknowledgments are received, the coordinator forgets the transaction. If transaction T_i is to be aborted, Step 2 and Step 3 are simpler than their committing counterparts. The coordinator discards all T_i 's log records and broadcasts an Abort decision message to all participants. A presumed abort protocol is assumed, so abort messages are not acknowledged and the *Abort* decision is not recorded in the coordinator's log.

3. MOBILE TWO PHASE COMMIT PROTOCOL (M-2PC)

M-2PC protocol commits a mobile transaction T_m globally which is being executed over more than one host [9]. It is assumed that a transaction T_m is issued at an MH called Home-MH and the BS where it is attached is called Home-BS. While MH moves from a cell to another, it attached to a new BS that is Current-BS. At commit time a commit-request is issued by Home-MH [3]. The transaction initiator is called a client, the servers are called participants and the commit-BS is the Coordinator. **Fig. 2** illustrated M-2PC protocol.

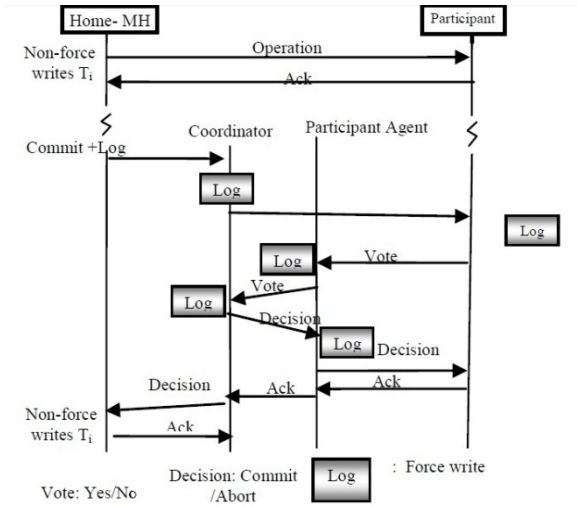

Figure 2: M-2PC Protocol

The coordination resides in the fixed part of the network to be directly reachable by the fixed participants. The coordinator must also be reachable by the client residing on the MH, thus it resides on the current-BS. It executes on the same commit-BS even if the MH changes cell during the commitment process. To handle disconnections, client delegates its commit duties to the coordinator which is always available during execution. The client sends request for commit to the coordinator along with its logs. The coordinator sends vote messages to all participants and decides on whether to commit or abort according to the traditional 2PC principal. After receiving acknowledgements the coordinator informs the client about the result. The coordinator waits for the clients' ack before forgetting about the transaction. M-2PC protocol requires only the coordinator permanently knows about the client current location in order to forward the results to it.

4. TRANSACTION COMMIT ON TIMEOUT PROTOCOL (TCOT)

Here a transaction T_i commits if the Coordinator does not receive a failure message from a node in the commit set within a predefined timeout period [5]. It is well known that finding the most appropriate value of a timeout is not always easy because it depends on a number of system variables, which could be difficult to quantify. However, it is usually possible to define a value for timeout, which performs well in all cases. Two types of timeout are defined in TCOT: Execution Timeout and Update Shipping Timeout.

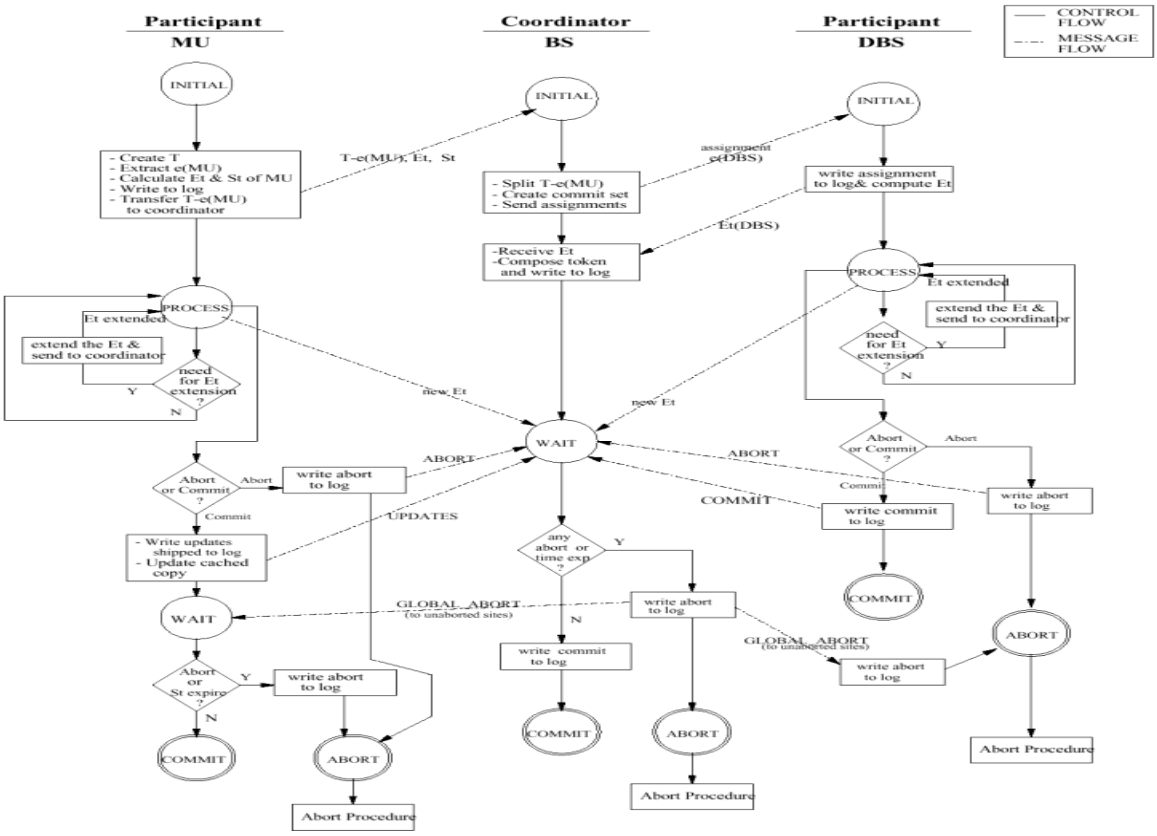

Figure 3: TCOT Protocol

Execution Timeout (Et) defines an upper bound timeout value within which a node of a commit set completes the execution of its ei. Shipping timeout (St) defines the upper bound of shipping time from H-MU to DBS. Thus, at the end of Et the Coordinator (CO) expects the updates to be shipped to the DBS and logged there within St. St is computed as Time to compose updates (Ut) + Time for the updates to reach CO (Sh).

Fig. 3 shows how TCOT works. A commit decision by a CO is said to be "correct" if the decision to commit is unanimous. The contrary is assumed here. Suppose the CO decides to commit Ti when at least one member of the commit set is undecided. This is possible only if the CO decides commit before the expiration of either St or the expiration of Et and the absence of "commit message" from DBSs. This cannot happen. Further, suppose that the MU failed and could not send updates to the CO within St or the CO does not receive the "commit message". In this situation, the CO will abort Ti. Since our algorithm is based on timeout, it is not possible that at any stage the CO will enter into an infinite wait.

5. OPTIMISTIC CONCURRENCY CONTROL WITH UPDATE TIME STAMP (OCC-UTS)

In OCC-UTS [10] each data item has a timestamp. Here invalidation report is broadcasted by the server. On transaction commit, server verifies that execution is serializable. Two forms of validation are done in OCC-UTS: Backward: Check if commiting transaction invalidated by commit of another. Forward: Check if commiting transaction conflicts with any other active transaction. Data has time stamp associated with it. Mobile client checks transactions upon receiving commit operation:
Mobile client sends RequestToCommit message. Mobile client listens to CommitList and AbortList to determine outcome of transaction.

6. COMPARISON OF ABOVE PROTOCOLS

M-2PC protocol does not modify the 2PC basics. So it keeps the advantages and drawbacks of 2PC. As no assumption is made about local concurrency and consistency mechanism, M-2PC can co-exist with other traditional ACPs. M-2PC protocol considers the mobility problem as a matter of maintaining the communication between the participating entities in the protocol in terms of message exchange.

TCOT protocol is based on timeout approach to reach a final transaction termination decision. It can commit transactions with minimum number of uplink by allowing each processing unit participating in the

transaction to have independent decision making capability based on the timeout mechanism. TCOT is designed for a system offering a connectivity mode called mobile connectivity that allows clients to remain connected all the time to the network through the wireless channel irrespective of their states.

The idea of OCC-UTS is to verify that a transaction is serialize-able before taking decision if it should be committed or aborted. The transaction executes locally offline before committing at the server. Timestamps are associated with data items and used to determine if a transaction is serialize-able by compare the client data stamp with the last update stamp maintained at the server. To validate its data, a transaction checks invalidation reports that are broadcast periodically by the server. A request to commit message is sent to the server after positive validation. This protocol is suitable for PDAs or portable computers relatively well equipped in order to provide local application execution, generally offline execution.

UCM aims to support off-line processing of transactions and moving client. A transaction executing offline can commit as soon as its log has been approaches. It exhibits the following properties:

1. It supports off-line transactions and minimizes risks of abortion of transaction at reconnection time.
2. It can commit a transaction despite the disconnection of one or more participants.
3. It can be applied to any kind of servers and it does not waste the local resources of lightweight servers.

7. DECISION

In our analysis, UCM appears to be the best candidate among the four protocols to manage distributed transactions in mobile environment. It has the best message complexity in terms of wireless messages, though assumptions about the local concurrency and recovery have to be made. As in Bangladesh the providers have to focus more on inexpensive technology than hi-quality because most of the users are of low income group. So UCM should be the better choice of them when providing transaction services of mobile database system.

8. CONCLUSIONS

In distributed database systems, an atomic commitment protocol (ACP) is needed to terminate distributed transactions. The assumptions of 2PC protocol are not valid in the mobile distributed environment where a typical architecture includes portable and small devices equipped with more or less limited resources (CPU, memory, battery power etc.) and communicating over wireless links. In this paper I have analyzed some popular ACPs those overcome the shortcomings of 2PC protocol for mobile database transaction.

REFERENCES

[1] Silberschatz, Korth, Sudarshan "Database System Concepts", 5th Ed., McGrawHill-2005.

[2] J. Gray, "Notes on Database Operating Systems, Operating Systems: An Advanced Course", *LNCS, vol.60, Springer Verlag*, 1978.

[3] M. Mouly, M-B. Pautet, "The GSM System for Mobile Communications", *Cell and Sys*.1992.

[4] Le Gruenwald · Shankar M. Banik · Chuo N. Lau "Managing real-time database transactions in mobile ad-hoc networks" *Distrib Parallel Databases-2007,* 2:27–54.

[5] Kumar, V., Dash, K., Dunham, M.H. and SeydimA.Y. "A timeout-based mobile transaction commitment protocol." *ADBIS-DASEAA 2000*, in cooperation with ACM SIGMOD.

[6] Bobineau, C. Pucheral, P. and Abdallah, M. "A unilateral commit protocol for mobile and disconnected computing", *Proc. of the 12th int. conf. on parallel and distributed computing Systems (PDCS)-2000,* Las Vegas, USA.

[7] Dunham, M., Hellal,A., Balakrishan S. "Mobile computing and databases: anything new?" *Proc. of the ACM SIGMOD-95,* Rec 24(4).

[8] P. K. Chrysanthis, "Transaction Processing in Mobile Computing Environment", *IEEE Workshop on Adv. in Parallel and Dist. Sys.-93,* pages 77–82.

[9] Nadia Nouali, Anne Doucet, Habiba Drias, "A Two-Phase Commit Protocol for Mobile Wireless Environment", *Proceedings of the 16th* Australasian Database Conference, Volume 39 Pages: 135 – 143, 2005.

[10] M. Perron and B. Bai, "Low Cost Commit Protocol for Mobile Computing Environments", accessed from *http://webdocs.cs.ualberta.ca/~baochun*

Proceeding of the
International Conference on Electrical, Computer and Telecommunication Engineering
01- 02 December 2012 (ICECTE2012), RUET, Rajshahi-6204, Bangladesh

ICECTE2012: PI-0128

Effective and Uninterrupted Execution of Numerical Integration through Computational Grid

Ashis Kumar Mandal[1], Md. Delowar Hossain[2], Rikta Sen[3] , Tangina Sultana[4]
[1]Department of CEN, Hajee Mohammad Danesh Science and Technology University, Dinajpur, Bangladesh.
[2] Department of CIT, Hajee Mohammad Danesh Science and Technology University, Dinajpur, Bangladesh.
[3]Department of ETE, Rajshahi University of Engineering and Technology, Rajshahi, Bangladesh.
[4] Department of TEE, Hajee Mohammad Danesh Science and Technology University, Dinajpur, Bangladesh.
E-mail: ashis.62@gmail.com, delowar.cit@gmail.com, rikta.sen06@gmail.com,dristy.043@gmail.com

ABSTRACT
Numerical integration is essential for virtually all fields of scientific research. Traditionally numerical integration is carried out sequentially in a single computer where trade-off has to be made between computing time and precision of numerical value. For reduction of computing time and betterment of precision, numerical integration problems may require a significant amount of computational effort; in this situation, using distributed computing to share task might be a solution. Therefore, this project set up a computational grid based on the Alchemi middleware and use multiple Simpson's 1/3 rules with a sample numerical integral. For uninterrupted execution, fault-tolerance method is also implemented. Result show that this approach reduces computing of numerical integration a significant amount with ensuring better precession.

KEY WORDS: Numerical integration, Grid Computing, Alchemi middleware, fault-tolerance.

1. INTRODUCTION

For many engineering problems require the evaluation of the integral frequently. However, the function *f(x)* may be a complicated continuous function that is difficult or impossible to integrate in the closed form. In some cases, *f(x)* may not have a known analytical form; it may be known only in a tabular form [1]. The limits of integration may be infinite or the function *f(x)* may be discontinuous or the function may become infinite at certain points in the interval *a* to *b*. In all these cases, the integral can be evaluated only numerically. To solve the problems numerically, there are many algorithms. In this project, the Multiple-Application Simpson's 1/3 Rule [2] is used as this equation is effective in many cases. However, when scientific research demands exact result in many significant digit, number of segments of the Multiple-Application Simpson's 1/3 Rule have to be increased in many times. This indicates much more calculation , and employment of one processing unit takes huge time to complete the task. This computation time can be reduced significantly if distributed computing resources are used. Therefore Grid computing, a branch of distributed computing, can be considered.

Grid comuting creates the illusion of a simple yet large and powerful self managing virutal computer out of a large collection of connected heterogenous systems sharing various combinations of resources[3]. One of the key technologies in the development of grid networks is the middlewares. Among them Alchemi [4] is a .NET-based framework that provides the runtime machinery for building a Grid. In our application we use this framework in windows platform.A particular numerical integration is distributed and executed parallely by the help of manager and executors of the framework respectively. Since any problems of manager or executors might hamper the performance of numerical integration , we suggest folt tolerance approach so as to uninterruted execution of numerical integration can be ensured.

2. LITERATURE REVIEW

2.1 Alchemi

Alchemi is a .NET-based framework that provides the runtime machinery and programming environment required to construct desktop grids and develop grid applications [3]. There are four types of distributed components (nodes) involved in the construction of Alchemi grids including manager, executor, owner, and cross platform manager. Owner node generates application and creates threads which are submitted in manager node. Manager node provides services such as storing thread in a pool and distributes threads to the executor. Executor accepts threads from the Manager and executes them and sends result back to the manager node. After finishing all threads, the manager aggregates them and sends ultimate result to the owner node.

2.2 Multiple-Application Simpson's 1/3 Rule

Simpson's rule is improved by dividing the integration interval into a number of segments of

equal width which is called multiple-Application Simpson's 1/3 Rule. So, overall result of integration is as follows [2]:

$h = \frac{b-a}{n}$, where n=segments number and

$$I = \frac{h}{3}\left(f(x_0) + 4\sum_{i=1,3,5...}^{n-1} f(x_i) + 2\sum_{j=2,4,6...}^{n-2} f(x_j) + f(x_n) \right) \quad (2)$$

This Numerical Integration equation is certainly a subject that can be executed in distributed computing. That is, this equation lends itself to parallel computation because it can be easily divided into smaller problems, such that these sub-problems are independent of each other's results.

2.3 Related Works

Many integration packages have been implemented based on different algorithms and computer architectures. Some are sequential [5] programs for standalone computers; the others are parallel [6] programs that are executed by multiple processing elements such as those of a cluster. One work such as, Distributed numerical integration is proposed in [7] where a software module named ParInt is developed for multivariate numerical integration. Similarly Shujun Li et al., [8] describes a distributed numerical integration paradigm using Web Service where they propose an XML data format for the exchange of integration related data among different computing unit.

3. METHODOLOGY

3.1 Application Modeling

Before implementing our numerical integration application in Grid, A Grid system have to be constructed using Alchemi.Net grid framework.Now procedure to model and implimentation are described as follows:

- Specify the integration for which solution have to be calculated
- Now divide the total integral into sub-integrals of equal range
- Implement Multiple-Application Simson's 1/3 Rules for all sub-integrals
- Execute each sub-integral in particular executor of Alchemi.Net grid system
- Finally, total integral is calculated by taking all the results of sub-integrals in manager of Alchemi.Net grid

This test application basically use the concept of multithreading where the large size job is divided into some small sub-jobs. Here these sub-jobs are known as sub-integrals. Manager basically create a thread for each sub-integral and migrate these threads into various resources (executor).Each executor accept threads as input and compute its assigned part properly and submit the result toward the manager. Manager receives all results as input and provides appropriate result. Manager has a scheduler to control over all threads.

During the distributed execution of numerical integration some failures may happen in the Grid environment such as failure of the executor node, failure of the Grid manager nodes or both. For uninterrupted execution following methods is used.

3.2 Failure of the Executor and recovery method

If a thread is scheduled on an executor and due to some reasons, the executor crashes, the thread running on this executor also crashes, in such case, the manager reschedules this thread on another executor but it does not keep any track of the percentage of the work that has already been done. For betterment of computing, a file based Grid thread was implemented to overcome this executor failure problem [9]. Here the file keeps track of the last resultant values of the thread and the executor is responsible for saving these values into the file that is on manager. Whenever a crashed thread is rescheduled on different executor, the manager node will extract the values form the file and will pass it to the thread so that it can resume its operations.

3.2 Failure of the Manager and recovery method

Failure of the manager may happen if the manager gets disconnected from the network or if the manager gets crashed for any reason. Under this circumstance, all the executors registered with the failed manger will stop executing, and the whole system will come to halt. For uninterrupted execution, we need backup manager. This can be achieved by secondary manager at one of the executor [10]. Usually an executor can register itself only with one manager. If the manager fails, secondary manager notify all executors to reregister with the new manager. This new Alchemi manager can continue functioning from the point of failure providing previous. manager stores all required information in a file and this file needs to be replicated to that secondary manger. Periodic updating of file is required so as to maintain the consistency of the system.

4. EXPERIMENTAL RESULT AND DISCUSSION

4.1 Evaluation Test Setup

The test bed of this Alchemi Grid Computing for Numeric Integration consisted of five Executors of Pentium (R) 4 CPU 2.26GHz desktop computers with 512MB physical memory running Windows XP Professional operating system. As for the designated Alchemi manager is set on desktop computer of Pentium (R) 4 CPU 2.26GHz machines with 512MB physical memory also running Windows XP Professional. All the six computers are linked together with a switch to form Local Area Network

as Grid Environment. With this evaluation set up, one of the main assumptions is that every connected computer (executors) will have equal chance of receiving a thread task from manager.

We used the following integral to evaluate the procedures described above

$$\int_0^1 \sqrt{x^2 + 1}dx$$

We compute it with ε<0.00001.

There are two parts in evaluating the performance of numerical integration in grid environment. System using above numerical integration application and execution time was measured at the elapsed clock time for the integral processing to complete on the manager node. This application of the Alchemi grid thread model system is based on different number of executors performing the task with different number of segments and different number of split threads set.

4.2.Increasing Executors with Different segment size

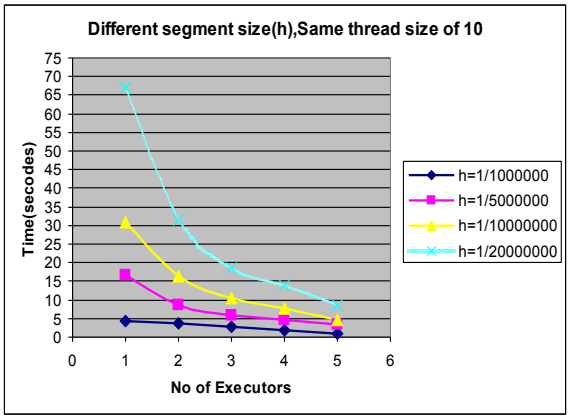

Fig. 1 performances of varying numbers of executors enabled with different segment size with same thread size.

First part of the test is to calculate the integration with increasing number of executors at different segments maintaining at 10 threads to compare and observed the affect execution time. Figure 1 shows the time taken to perform 10 threads with different amount of segment size against different number of executors.

4.3 Evaluation on Different segment size and its Observation Result.

Based on the evaluation outcome from Figure 1 on different size of segments performance on the Alchemi grid system, it is observed in showing significance improvement in execution time with increasing number of executors enabled for the task. The amount of processing time has improved by almost half when using 2 executors as compare to 1 executor. On the whole evaluation on segment number with 5 executors can shorten execution time by up to above 80% as compare to single computer processing as shown in Table 1.

Table 1. Comparision for no. of segments executions time efficiency improvement

No. of Segments (n) h=1/(x*1000000)	Standalone Computer Execution Time(s)	2 Executors Grid System		5 Executors Grid System	
		Execution Time(s)	Percentae Improve (%)	Execution Time(s)	Percentage Improve (%)
1	4.21	3.56	19.40	1.02	77
5	16.70	8.54	49	3.25	81
10	30.92	16.39	47	4.73	85
20	67	31.60	53	8.75	87

4.4 Increasing Executors at Different Thread Size

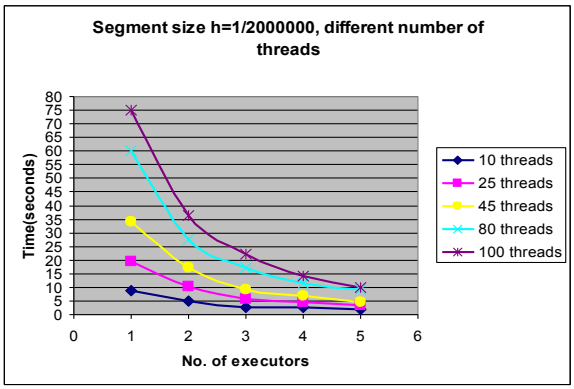

Fig. 2 performances of varying numbers of executors enabled with same number of segment and different thread size.

The second part of the evaluation test involved in increasing up to 5 executors performing with different workloads being sliced into thread size of 10, 25, 45, 80 and 100 in order to observed the affect on execution time maintaining same segment number of 2000000. Figure 3 shows the time taken to complete the various numbers of threads size against varying numbers of executors enabled.

4.5 Evaluation on Different Thread Size and its Observation Result

Figure 2 shows the processing time of different workloads of thread size over the grid system with increase number of executors. The resulting trend for this is similar to graph 1 but graph 2 shows obvious improvement in the processing time over the grid network. At low workload of 10 threads for this case, there is little difference between the execution time with different number of executors. This is so as the total overhead involved in managing the distribution of the thread task is proportion to the actual

computation time. So if the number of executors continues to increase, there will have no further significant decrease in the computational time on the workload.

Table 2. Comparison for Threads size executions time efficiency improvement

Thread Size	Standalone Computer Execution Time	2 Executors Grid System		5 Executors Grid System	
		Execution Time (s)	Percentage Improve (%)	Execution Time(s)	Percentage Improve (%)
10	8.78	5.01	42	1.89	78.4
25	19.52	10.19	48	3.4	83
45	33.94	17.23	49	4.56	87
80	60	27.55	54	9.25	85
100	75	36.40	51	10.02	87

On the other hand with increasing thread size, significant different in the execution time can be observed with more executors enable to handle the grid job. Of course looking at the first two-alchemi executors there will be obvious decrease in computational time of up to 50% with the increase in workloads thread size. Table 2 shows the improvement in the execution time for 2 executors is 50% and with 5 executors efficiency can improve up to above 80% as compare to one executor over the grid system.

5. CONCLUSIONS

Numerical Integration is used extensively in engineering, sciences, economics, technology and other fields. As intensive computing is required for executing this integration while ensuring better precession, we present one-dimensional numerical integration scheme in computational grid to reduce executing times. In this paper we develop this grid environment by Alchemi framework. At the same time, we consider fault-tolerance methods for uninterrupted execution of numerical integration. Further enhancement could be achieved by establishment of cross platform Global grid together with multidimensional Numerical Integration.

REFERENCES

[1]. N. Arnold, "Introduction to Numerical Analysis", Cambridge University Press, 2001.

[2]. S. C. Chapra , Raymond P. Canale, "Numerical Methods for Engineers with Programming and Software Applications", *Tata McGraw-Hill Edition, 2000.*

[3]. R. Buyya , B. Kris, "Market Oriented Grid and Utility Computing", *Wiley ISBN 9780470287682 ,2009.*

[4]. A. Luther, R. Buyya, R. Ranjan, S. Venugopal ,"Alchemi: A .NET-Based Enterprise Grid Computing System*", Proc. 6th Int'l Conf. on Internet Computing (ICOMP'05),* Las Vegas, USA, 2005.

[5]. K. Tobimatsu ,S. Kawabata, "Multi-dimensional integration routine DICE", *Technical Report 85*, Ko-gakuin University,1998.

[6]. R.Cools, D.Laurie, L.Pluym, "Cubpack++: A C++ package for automatic two-dimensional cubature*",ACM Trans. Math. Software,23:1–15,1997.*

[7]. E. de Doncker ,A. Gupta, "Distributed adaptive integration, algorithms and analysis",in proceedings of Transputers 94*, 1994, 266-277.*

[8]. S. Li, K. Kaugars, E. de Doncker, "Massive Scale Distributed Numerical Integration Using Web Service", *The Hawaii International Conference on Computer Sciences*, CDROM Proceedings (2003).

[9]. V. Sharma, M. Vardhan, S. Mishra, D. S. Kushwaha, "A Generalized Approach for Fault Tolerance and Load Based Scheduling of Threads in Alchemi. Net", *The Second International Conference on Cloud Computing, GRIDs, and Virtualization 2011 .211-216*

[10]. A. Hussain, A. A. Shoeb, A. N. Bikas, M. K. Hasan, "File Based GRID Thread Implementation in the .NET-based Alchemi Framework", *Appeared in IEEEXplore, Link: http://ieeexplore.ieee.org/stamp/stamp.jsp?arnumber=04777784.*

Proceeding of the
International Conference on Electrical, Computer and Telecommunication Engineering
01- 02 December 2012 (ICECTE2012), RUET, Rajshahi-6204, Bangladesh

ICECTE2012: PI-0129

Can Rural Telecentre Reduce Poverty in Developing Countries?

Md. Baharul Islam[1], *Md. Jalilur Rahman*[2]
[1]Research Fellow, James Cook Australia Institute of Higher Learning Pte Ltd, Singapore
[2]Faculty of Science & Information Technology, American International University-Bangladesh
E-mail: bahar_mag@yahoo.com or baharul.islam@jcu.edu.au, rahul_cse03@hotmail.com

ABSTRACT
Telecentre is to provide information to villagers based on their needs in developing countries. Telecentre pays special attention to the use of IT and media technology with the province level and commune level especially for the benefit of farmers who are its target customers. The main objective of rural telecentre is to improve public services in agriculture and small business by sharing information. This paper explores the impact on villagers specially farmers for using Rural Telecentre's (RT's). The paper gives emphasis to motivate rural communities to use RTs facilities and improve their livelihood by reducing poverty. RT's meets the demands of the poor villagers in rural areas by accessing and sharing information. This paper will find out the answer of the above question.

KEY WORDS: Telecentre, Information and Communication Technology (ICT), social and digital inclusion

1. INTROCUCTION

Information technology is considered the backbone of national economy in the field of national development. There are some weaknesses and drawbacks of agricultural production in rural areas such as: unsystematic formation of viewpoints and arguments related to developing agriculture, farmers and rural areas; non-synchronous and lack of breakthroughs in the policy of developing agriculture; unrealistic and inappropriate policies that are not corrected over time; low investment from the national budget in developing agriculture, farmers and rural areas; and weak national management and implementation.

A telecentre can be established for community and rural development purposes if it is available for full public access to information technology for educational, social and personal development. In spite of building telecentre's in rural area, it is not sure that villagers can use them and share knowledge that could help to reduce poverty. They need to know that telecentre help them to increase their income and to develop social economic effects in villagers. Telecentre's are considered as a powerful engine of rural development [1]. Science and IT are working as a driver of socio-economic development.

There are no ways to meet the demand on specific information for farmers before telecentre foundation. Telecentre's are located at commune so that they can provide specific information which is related to local demand. Telecentre establishment is also based on successful experiences of telecentre network development in several countries in Asia with the same socio-economic conditions. They are proceeding with national programmes for telecentre's, mostly aimed at delivering information and communication facilities to their rural populations who represent the majority of the poor people in the country. Such programmes are under way in India, Pakistan, Malaysia, Bangladesh, Sri Lanka, Philippines etc. In India, "Mission 2007" - every village a knowledge centre. Mission 2007 is a national alliance for access to ICTs for all India's 600,000 villages. It is targeting 100,000 telecentre's, each to serve six villages on average [2]. The Government of Pakistan is planning for 10,000 telecentre's to be established in the rural areas of the country. The government of Malaysia is implementing a programme to install telecentre in all 927 mukims (local government districts). The government of Bangladesh has established "Mission 2011" to set up the Bangladesh Telecentre Network (BTN) consisting of 40,000 Telecentre's across the country by the 40th anniversary of independence so that every villager can access to livelihood services through ICTs. The Sri-Lankan government, with the support of the World Bank has established the E-Sri-Lanka programme that includes more than 350 Telecentre's, known as Nenasalas, to disseminate knowledge and share information through the Internet, with the goal of reducing poverty, peace building, economic and social development and improving the IT literacy rate of the country. The government of Philippines has a programme for "Jumpstarting the e-Local Government Unit Project (e-LGU)" which includes 100 Telecentre's [3]-[5].

There are some effective factors for using rural telecentre's [6]. Telecentre works as a role model for community building. About 80% of users agree that telecentre have a positive impact on community building [7]. Telecentre can work to provide

telemedicine services [8]. The big challenges for telecentres are the sustainability issue. Telecentre's are working as a role of knowledge network. It will be success or more challenges depend on some factors [9]-[11]. Telecentre evaluation in different countries is discussed details based on participation, gender, social impact, sustainability [12].

It is evident that each of telecentre's project displayed some common characteristics like Multi-sector partnerships, High-level sponsor, Co-ordination among government ministries, Multiple models of telecentre, Training staff, Networking, International links, Connected to national development goals etc. The pilot of 13 RTs at commune level was designed in 2006 as a subcomponent of the support to administration reform at Ministry of Agriculture and Rural Development (MARD) under United Nation Development Program (UNDP) in Vietnam. The pilot's objective is to identify an appropriate model which is technically and financially sustainable and capable to provide farmers with information supporting production development and income improvement. After 3 years, 13 RTs came into sustainable operation and introduced benefits for the local community. The main tool of this study is questionnaires from 1000 villagers after using telecentre's.

Basically, the key objective of the assessment is to assess the results and impact of the RTs in supporting production development and income improvement for local farmers. It is important to make a perfect model for wider replication by making an evaluation and analysis on the financial aspects and the local people to ensure the long term existence and effectiveness of the RTs.

2. EVALUATION FRAMWORK

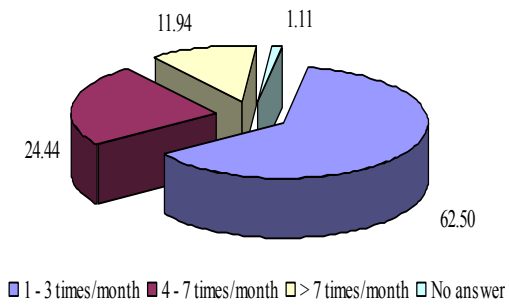

Fig. 1 Frequency of the service usage

The data in charts 1 and 2 show that the demands to use information of the people are very high; nearly 90% of respondents use the services of the centre because of their needs for information, and 62.50% customers use the service of the centre from 1 to 3 times per month. It can be seen that the existence of the centre has contributed actively to meet the real demand of information of the people. In addition to the demand of information, the number of customers visiting the centre because of their desire to studying goes up to 51.18% that is a relatively high rate. However, the number of customers going to the centres with the purpose of entertainment is low. This could be explained by the two reasons: 1st is that the rural people do not have any demand for entertainment by the centre service yet, 2nd is that the services provided by the centre are not aimed at entertainment, just merely providing information that is practical to their social life and farm production

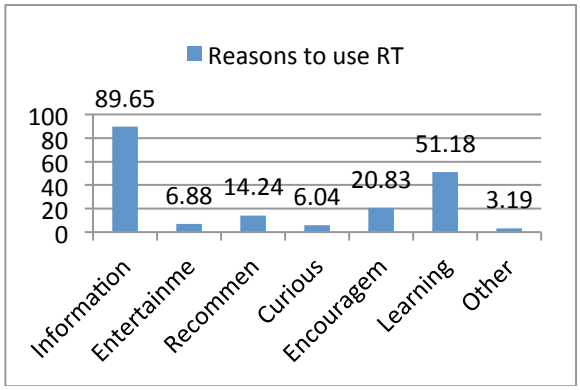

Fig. 2 The reason to use rural telecentre services

2.1 Before the Existence of the RT

The local people mainly collected information about culture, society, economy, science and technology through oral communication (63.2%), via radio / television and through agricultural cadres such as agricultural extension officers, fishery extension staff and veterinary officials, while a very small part of information is from the internet. Except the information from the internet, information from these sources is not updated regularly.

2.2 After the Establishment of the RT

- The local people go to the RT to directly receive updated information or to leave their requirements of information for the staff to search on the Internet.
- People go to the centre to read books and newspapers and to learn the techniques of growing seed trees.
- The RT actively collects information on good models of production and then presents this to the people. This model is highly welcomed due to its high effectiveness of observation and illustration.
- The local people send requests through collaborators usually the head of village/ hamlet. The collaborators will collect these requirements

and submit them to the centre and then transfer the information back to local people.

Table 1 Information channels employed by farmers before and after the establishment of rural telecentre
Unit: Percentage %

Source of information / Percentage	RTs	By words of mouth	Press	TV and radio	Internet	Agricultural extension and veterinary officers	Communal officers	Other sources
Percentage of farmers using the source before the operation of RT		63.19	25.63	54.38	8.19	45.42	33.47	0.97
Percentage of farmers using the source after the operation of RT	95.21	20.00	20.76	40.42	46.04	55.69	33.96	1.18

The Table 1 above summarises the general information system at the communes. Before the establishment of the RT, word of mouth was the most popular channel to spread the information. Moreover, the local people are more active to go to the RT to access the internet, read materials and participate in the agricultural technical trainings held by the RT's staff with agriculture officers and the farmer association. It can be concluded that the RTs, as represented by the name, have become a prestigious and reliable source of information for farmers which meet their practical need.

2.3 The Information Needs of the Residents

In rural areas, there have been shortages of information to residents, especially price forecasts, so residents still produced their products by comparing prices on the market. As a result, they invested in produce which promised high prices without considering the actual market demand. Living in rural areas which are located far from the cultural, political, economic centre and with difficult traffic conditions and slow economic development, farmers are unable to gain access to sources of social information. They need a lot of information in terms of law, policy, technical production, and education, health, economics, etc for applying in their daily life, ensuring food security and alleviating poverty. Although traditional means of communication (television, radio, etc) have made contributions to popularizing information to the community, they are unable to meet the increasing need for information of farmers, especially those living in remote areas and under economic difficulties.

The RT model established in the pilot project in rural areas has met the information needs of people in these communes. Information on breeding technology, cultivation, fisheries, agriculture, aquaculture market prices, animal feeds, newly issued policies and laws, aquaculture export and import markets, predicted pests, etc. make up the interests of most farmers. This information is applied effectively to prevent diseases in animals and plants, help residents reduce production costs, limit use of chemicals and antibiotics in treatments, and improving the quality of their products. Aside from the purpose of providing information to support production to farmers, RTs were also established with the aim of reducing poverty in rural areas. By applying IT and communication technology, RTs provide information, knowledge, improved production capacity and increase quality of agricultural products to people living in rural areas.

3. ANSWER OF THE QUESTION

As farmers are the targeted beneficiaries of the project, RTs have significantly contributed to enhancing the awareness of the people and reduce the information gap between rural and urban areas. Farmers are able to receive necessary information and scientific knowledge. Much of the information is applied effectively by farmers and is popularized to many farmers to bring practical benefits to them. Teleentre is helping people raise their awareness by providing them with the necessary information for production and socio-economics, RTs have also helped to improve people's living standard and income.

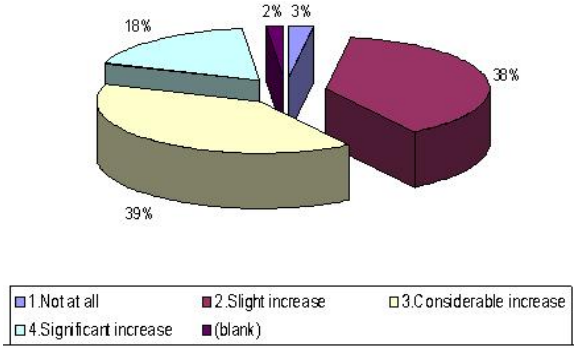

Fig. 3 Percentage of farmers having income improvement with support of rural telecentre

According to data from the survey, 95.76% people said the RT has helped them increase their income. The improved income may vary but generally the RT has had a practical effect on people. Farmers can apply the experiences and technical science to enhance cultivation and production productivity as well as avoid the negative consequences caused by natural disasters and epidemics.

4. CONCLUSIONS

Access to information technology is vital in improving the livelihoods of rural communities. It will help to save time and in the long run and save costs, benefiting the agriculture sector as a whole and increasing incomes and production efficiency for farmers. Results of the review show that operation of telecentre is of practical use to farmers (62.50% of those interviewed said telecentre's are very useful). The achievements of the rural telecentre model can be summarised as:

- Telecentre's are effective in seeking and propagating information on production and cultivation techniques to local people, helping them gradually change traditional production practices. Also market prices are provided, helping farmers avoid being forced in terms of price and minimizing risks incurred by epidemics calamity and market changes;
- Telecentre's help local people update their socio-economic, education and legal information and contributing to their improved awareness and livelihoods;
- Telecentre's are successful in changing the awareness of local people in project communes, showing them the usefulness and effectiveness of information technology to normal life.
- Telecentre's form a 2–way information channel that both provide information on production techniques to improve production conditions and increase income.
- Telecentre's have offered several services which help develop information knowledge and awareness in rural areas such as informatics training and internet access.

Despite the above mentioned major achievements, it is important to manage finance for maintaining the current telecentre's that are not an easy task. RTs make a bridge between information and communication technologies and rural poverty reduction. So, Villagers can access information, knowledge sharing and increase their income using RTs.

REFERENCES

[1]. C. Ruth, R. Soraino, "Exploring the ICT and Rural Poverty Reduction Link: Community Telecentres and Rural Livelihoods in Wu'an, China", *Electronic Journal on Information Systems in Developing Countries*, vol. 32, pp. 1-15, 2007.

[2]. Fourth Annual Convention, "Every Village A Knowledge Center", *National Alliance for Mission 2007*, The Grameen Gyan Abhiyan, Mission 2007, India,http://www.mission2007.in/iec-pub/pubfile/ Transitiontoaknowledgesociety.pdf

[3]. M. Hasan, "Mission 2011: A Multi-Sakeholder Partnership to create a knowledge based Society in Bangladesh", 2011 http://www.unescap.org/idd/_events/ADB-CeC-Bangladesh-2008/Pdf/Bangladesh %20Telecentre%20Network.pdf

[4]. R._Harris, "Session 6: Structuring Public Private Partnerships for Telecentres Projects", http://www.itu.int/ITU-D/asp/CMS/ASP-CoE/2010/IRD/S6-Dr_Roger_Harris.pdf

[5]. Salman Ansari Technology Consultants (Pvt) Ltd ,"Telecentres and Community Resource and Information Centers in Pakistan", *World Bank*, 2007.

[6]. Farhad Lashgarara, Alieh Karimi and Seyyed Mehdi Mirdamadi, "Effective factors on the villagers' use of rural telecentres (case study of Hamadan province, Iran)", *African Journal of Agricultural Research,* vol. 7, issue 13, pp. 2034-2041, 2012.

[7]. Z. Ibrahim, S. Ainin, "The Influence of Malaysian Telecentres on Community Building." *Electronic Journal of e-Government,* vol. 7, Issue 1, pp. 77-86 2009.

[8]. S. Puşcoci, H. Costin, C. Rotariu, B. Dionisie, F. Şerbanescu, "TELMES - Regional Medical Telecentres", *World Academy of Science, Engineering and Technology*, vol. 23, 2006.

[9]. A. Bailey, "Issue Affecting the Social Sustainability of Telecentres in Developing Contexts: A Field Study of Sixteen Telecentres in Jamaica", *Electronic Journal on Information Systems in Developing Countries*, vol. 36, issue 4, pp. 1-18, 2009.

[10]. M. L. Best, R. Kumar, "Sustainability Failures of Rural Telecentres: Challenges from the Sustainable Access in Rural India (SARI) Project", *Journal of Information Technologies & International Development*, vol. 4, Issue 4, pp. 31–45, 2008.

[11]. A. Ahmad, R. A. Razak, W. R. S. Osman, A. R. B. Rahmat, M. S. Abdullah, A. B. M. Ali, "Business Intelligence Model for Sustainability of the Malaysian Rural Telecentres", *Journal of Southeast Asian Research*, vol. 2011, Article ID 492934, pp. 12, 2011.

[12]. K. Reilly, R. Gomez, "Comparing Approaches: Telecentre Evaluation Experiences in Asia and Latin America", *Electronic Journal on Information Systems in Developing Countries*, vol. 4, issue 3, pp. 1-17, 2001.

Proceeding of the
International Conference on Electrical, Computer and Telecommunication Engineering
01- 02 December 2012 (ICECTE2012), RUET, Rajshahi-6204, Bangladesh

ICECTE2012: PI-0130

Filtering a specialized Meta Search Engine for Domain Specific Organization

Fazle Rabbi Shalek Ahmed[1], Rezwana Sultana[2],Mobasseer M. Hossain[3]
[1]Senior lecturer, Department of Computer Science and Engineering, University of Information Technology & Sciences (UITS), Rajshahi
[2]Lecturer, Department of Electrical and Electronics Engineering, AhsanullahUniverstiy of Information technology (AUST), Rajshahi
[3]Lecturer, Department of Computer Science and Engineering, University of Information Technology & Sciences (UITS), Rajshahi
E-mail:bappi.paper@gmail.com, dola.ruet@gmail.com,duke_ruetbd@yahoo.com

ABSTRACT
Automated search engines that rely on keyword matching usually return too many low quality matches. To make matters worse, some advertisers attempt to gain people's attention by taking measures meant to mislead automated search engines. In this paper, we are presenting such type of search engine and such type of prototype of a large-scale search engine which makes heavy use of the structure present in hypertext. This is designed to crawl and index the Web efficiently and produce much more satisfying search results especially for domain specific organizations.

KEY WORDS: Search engine, web pages, domain, crawler, filteringalgorithm.

1. INTRODUCTION

This paper addresses the question of how to build a practical large-scale [1] system which can exploit the additional information present in hypertext. Also we look at the problem of how to effectively deal with uncontrolled hypertext collections those are based on that organization where anyone can publish anything they want.

Our main goal is to improve the quality of web search engines. Some people believed that a complete search index would make it possible to find anything easily. Anyone who has used a search engine recently can readily testify that the completeness of the index is not the only factor in the quality of search results.

In section 1, already we have discussed about the goal and the concept of developing filtering search engine. In section 2, we discuss some related works and fundamental ideas in the field of information extraction and summarization. Section 3 focuses on our proposed system architecture, followed by necessary operations and algorithms in section IV. In section V, we conclude and brief on our research direction.

2. RELATED WORKS IN THE FIELD

Many other works have been done in the field on in-formation extraction from web pages. But most of these works are done to serve specific purposes. However, analyzing the research works on similar fields helped us to build our concept on different issues. OrkutBuyukkokten, Hector Garcia-Molina and An-dreasPaepcke worked on how information can be summarized [2] before displaying in a handheld device like PDA or palm top computer as the information are to be displayed in a small screen. Adam Jatowt, KhooKhyou Bun and Mitsuru Ishizuka worked on the changes of dynamic web pages [3] When the content of a web page is changed partially or completely, to provide the user the flexibility to keep track of the changes, they researched on summarizing the changes and providing information about the change to the user. Inderjeet Mani, Eric Bloedorn, and Barbara Gates pro-posed an interesting approach on information extraction from web page by constructing a graph [4] where the nodes of the graph are words of sentences and the links between the nodes are the different types of relations between the words. Yutaka Matsuo, Yukio Oh-sawa and Mitsuru Ishizuka researched on the relation-ship of the links [5] that exists in the web pages.

3. PROPOSED SYSTEM ARCHITECTURE

The entire fetched URL must be filtered before storing to the store server. The filter will follow some method that is defined only for this architecture to find out the relevant information about specific domain. We will use some technique to filter the all process. Our first approach for finding out the related information is matching some defined key words and having some regular expressions. Here is the figure of filter based search engine.

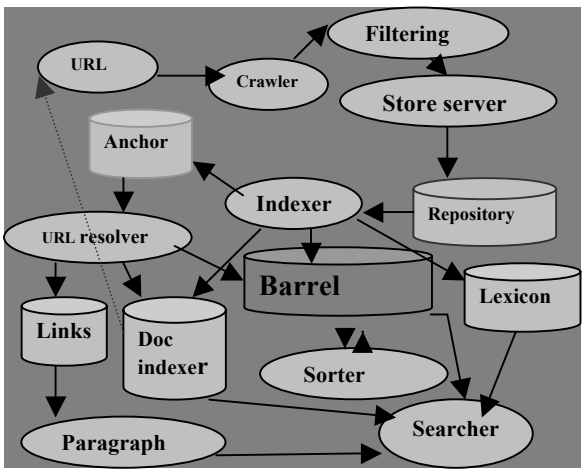

Fig. 1:Filter Based architecture

3.1 Filter Based Crawler

A normal crawler is used to find out all the information from the whole internet based connection and download all of those into store server. Filter based crawler refers that it will search or download only all of those pages or documentsthat is defined by the filtering techniques. Below is the figure of proposed filter based crawler:

FOM attempts to understand an authors' intention by identifying the object's function and category. In FOM, objects are classified in to a Basic Object (BO), which is the smallest information body that cannot be further divided, or a Composite Object (CO) which is a set of objects (BO or CO) that perform some function together. An example of a BO is a jpeg file. In HTML contents a BO is a non-breakable element within two tags or an embedded object. There is no other tag inside the content of a BO. According to this criterion, it is easy to find out all the BO's inside the Web pages. Likewise, COs can be detected by a layout analysis of web pages. The basic idea is that objects in the same category generally have consistent visual styles so that they are separated by apparent visual boundaries, such as table boundaries, from the objects in other categories. After detecting all the BO's and CO's in a Web page, we could identify the category of each object according to some heuristic rules. The categories of objects include:

Information Object: This object presents contentInformation.**Navigation Object:** This object provides navigationGuide.**Interaction Object:**This object provides user side interaction. **Decoration Object:** This object serves for decoration purpose.

Special Function Object: This object performs special performs special functions such as AD, Logo, Contact, Copyright, Reference etc.

Among these objects, only information objects will have to be extracted and stored in separate page to perform further operations. Further information

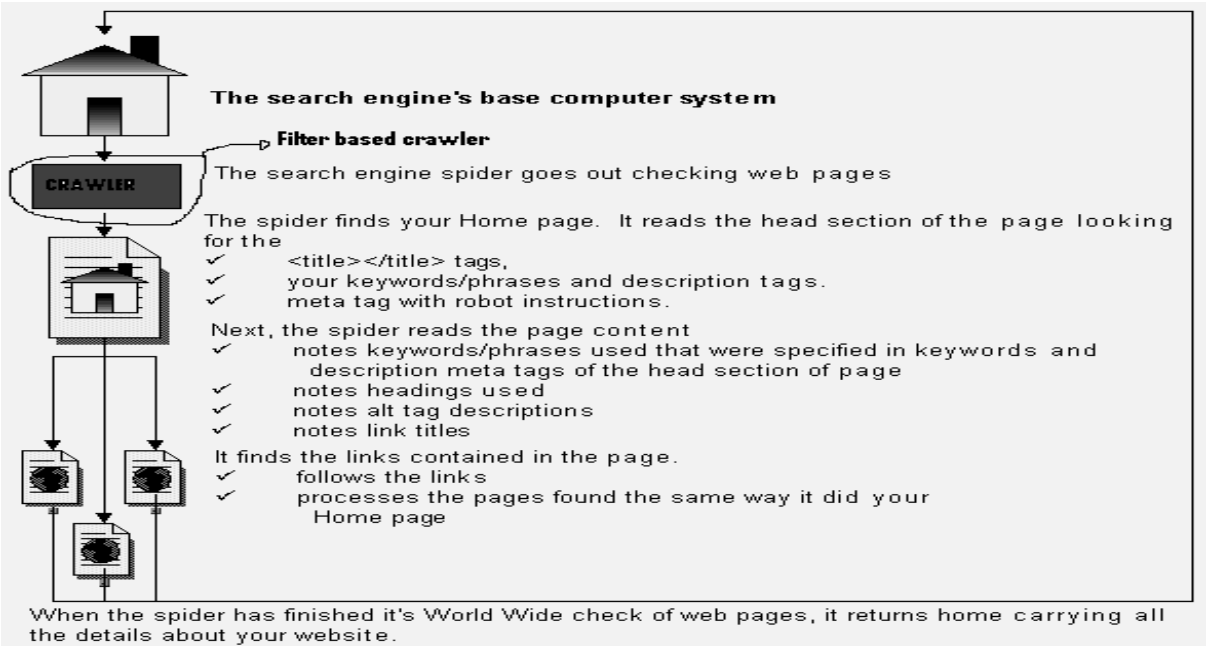

Fig. 2:Filter Based Crawler

4. NECESSARY OPERATIONS AND ALGORITHMS

4.1 Removing Noises and Extracting Important Information from the Web Pages

In order to utilize the structure information of Web pages, we can employ a simplified version of the Function-Based object Model (FOM). In a nutshell,

means we have to find out all of those single objects and compare with our defined keywords.

4.2 Identifying the Keywords from the Document

We will implement the "Keyword Extraction from a Single Document using Word Co-occurrence Statistical Information" algorithm proposed by Matsuo & Ishizuka [6], with a little modification to extract the keywords. In this algorithm, they considered each sentence as a basket containing some words, ignoring their order or other grammatical relations. At first, the frequent terms in the documents are identified. Then the frequency of co-occurrence of each non-frequent term (will be denoted as the "general term" from now on) with each general term is determined. Here co-occurrence only means that the two terms appear in the same sentence, they need not be situated one after another. The main idea behind their proposal is, a general term that is distributed evenly throughout the document is less significant than a term that shows a significant bias of co-occurrence with a particular subset of frequent terms. In order to measure this degree of bias, they proposed an equation [7]:

$$X^2(\omega) = \left[\sum_{g \in G} \frac{(freq(\omega, g) - n_w p_g)^2}{n_w p_g} \right] \ldots \text{Eq. 1}$$

Here the equation no. 1 is referring the following aspects,

- $X^2(\omega)$ is a measure of degree of co-occurrence of a general term *w* with a frequent term g
- G is the set of the frequent terms
- n_w is the number of terms in the sentences where w appears
- p_g is the sum of the total number of terms in sentences where *g* appears divided by the total number of terms in the document
- freq (*w*, g) is the actual number of co-occurrences between w and g.

The details of the process can be found in the paper submitted by the developers of the algorithm [7].

Now by implementing this equation for all the general terms, we will get the X^2 values for all the general terms. Among them, we will take a certain number of terms with the highest X^2 values.

Note that, if we want to implement this algorithm, we must ensure that the terms mentioned in the search string are included in the list of keywords, as these words must be important on the context of the user's perspective. For example, if the user runs a search on "the Big Bang theory", it is logical that the terms "Big", "Bang" and "theory" all should be identified as key-words. Though because of the way the current search engines work, there is a high probability that these words will be frequent in the found web pages, we will still manually ensure that these words are included in the list of the keywords.

So in a nutshell, the steps of keyword identification process are:

- **Preprocessing:** Remove all the articles (a, an, the), prepositions (on, of, at etc.), conjunctions (and, but etc.) and auxiliary verbs (is, was, were etc.) from the document. Then remove the stop words (For example: punctuation marks).
- **Selection of frequent terms:** Select the top frequent terms up to N% of the number of running terms. Here N is an integer; its value comes from the experiment.
- **Calculation of the X^2 values:** Now for each general term, find the X^2 value from the equation stated above. Make a list of general terms along with their X^2 values in descending order.
- **Select the keywords:** From the list of the general terms, select the top N%. Here N is an integer; its value comes from the experiment.
- **Add the terms in the search string:** Take the search string given by the user and include the terms in it (except the articles, prepositions, conjunctions, auxiliary verbs etc.) to the set of keywords. If a term is already there, it is overwritten.

4.3 Crawling Algorithm

For each and every search engine we need a crawler which crawls all the pages from internet based connection. There are some restrictions it may find not to be authenticated into those sites. For this reason every crawler should have that much of knowledge what it should do at that time. This is basically defined by the Robot Protocol. However, this is not so much concern for us as it is already defined inside the crawling algorithm.

***1**. Get the user's input: the starting URL and the desired file type. Add the URL to the currently empty list of URLs to search. While the list of URLs to search is not empty,*

***1.1** Get the first URL in the list.*

***1.2** Move the URL to the list of URLs already searched.*

***1.3** Check the URL to make sure its protocol is HTTP (If not, break out of the loop, back to "While").*

***2.** See whether there's a robots.txt file at this site that includes a "Disallow" statement.*

***2.1** If so, break out of the loop, back to "While".*

***2.2** Try to "open" the URL (that is, retrieve that document From the Web).*

***2.3** If it's not an HTML file, break out of the loop back to "While."*

***3.** Step through the HTML file. While the HTML text contains another link,*

3.1 *Validate the link's URL and make sure robots are allowed*
3.2 *If it's an HTML file,*
3.2.1 *If the URL isn't present in either the to-search list add it to the to-search list.*
3.2.2 *If it's the type of the file the user requested, add it to the list of files found.*
4.*After the defined time it will crawl again from the step 1.*

4.4 Webpage Content Retrieving and Individualizing Keyword

This module is responsible for retrieving contents of the web pages and individualizing useful information chunks in the forms of paragraph. We will form the paragraph with some logic as keyword and we needthat keyword because of comparing with some defined keyword. But in this cases there are some problem that we may fall that sentences are not independent of their position within the pages. For getting this we have applied the underlying algorithm:

1. *Search the pages (requested) using a popular search engine on the internet*
2. *Search all the top N ranked web links from the search results.*
3. *Get the contents of each of the web pages and store them locally.*
4. *Remove comments, unnecessary tags such as <HTML>.<HEAD>,etc.*
5. *Individual the paragraphs and make them as keyword from the whole internet.*

4.5Filtering algorithm

This is the basic part of this paper to make it filtered for a domain specific organization. From the general view it is very easy to get that the idea of filtering process. Obviously, there should have predefined keyword and some comparison and at last store to the data server.

1. *Extract all the keyword from the keyword techniques (crawled by the crawler)*
2. *We will define our predefined keyword.*
3. *Matching between extracting keyword and pre-defined keyword*
3.1 *If match*
Then store all the links and info into the server.
3.2 *Else*
Skip that part and remove from the temp memory.
4. *Start again from the step 3.*

5. CONCLUSION

A major part of this algorithm is needed to be changed for the filtering section. We changed the algorithm of the crawling to extract the related info. Unlike other search engines (yahoo, Google) our approach is to search on specific domain.

There is no way of denying that our proposed approach is a robust one for increasing user convenience in searching. Basically whatever we have proposed in this paper will work for the domain specific search, but for the time being we have completed some filtering part as well as the skeleton of a search engine. We hope that it will increase the possibility of finding desired information within a very short time and less effort.

References

[1] Monica Peshave,."Modeling the Internet and the Web: Probabilistic Methods and Algorithms, 2003."
[2] OrkutBuyukkokten, Hector Garcia-Molina and Andreas Paepcke, Digital Libraries Lab (InfoLab), Stanford University, Stanford, CA 94305, USA - "Seeing the Whole in Parts: Text Summarization for Web Browsing on Handheld Devices", 10th In international WWW Conference, 24 feb 2001.
[3] KhooKhyou Bun and Mitsuru Ishizuka, Dept. of Information and Communication Engineering, The University of Tokyo – "Emerging Topic Tracking System", Proc. Web Intelligence (WI2001), LNAI 219(Springer), Maebashi, Japan (2001.10), pp.125-130.
[4] Inderjeet Mani, Eric Bloedorn, and Barbara Gates, The MITRE Corporation – "*Using Cohesion and Coherence Models for Text Summarization*", In Proceedings of AAAI Spring Symposium on Intel-ligent Text Summarization, Stanford, March '98.
[5] Yutaka Matsuo, Yukio Ohsawa and Mitsuru Ishi-zuka – "Discovering Hidden Relation Behind a Link", Knowledge-based Intelligent Information Engineering Systems & Applied Technologies (KES2001), Osaka, Japan (2001.8), pp.1183-1187.
[6] Yutaka Matsuo and Mitsuru Ishizuka, Dept. of Info and Communication Engg, The University of Tokyo– "Keyword Extraction from a Single Document using Word Co-occurrence Sta-tistical Information", Proc. 16th Int'l FLAIRS Conf., Florida, (2003.5), pp. 392-396.
[7] Md. ShafayatRahman, AshequlQadir, Md. Mohsin Ali Khan, Abdullah Azfar - "Summarization of Web Pages by Keyword Extraction and Sentence Vector", International Conference of Computer And Information Technology (ICCIT-2006), IndependentUniversity (IUB), Bangladesh, 21-23 December2006, pp 432-436.

Proceeding of the
International Conference on Electrical, Computer and Telecommunication Engineering
01- 02 December 2012 (ICECTE2012), RUET, Rajshahi-6204, Bangladesh

ICECTE2012: PI-0131

Automatic Phase Sequence Corrector with Prevention of Single Phasing

Md. Nafiz Imtiaz[1], Md. Samiul Habib[2], Mafin Muntasir Rahman[3]
Dept. of EEE, Rajshahi University of Engineering & Technology
E-mail: nafizeee07@gmail.com, samiul.engieee@gmail.com, mafin_eee.ruet@yahoo.com

ABSTRACT:
This paper presents the difficulties of phase reversal and single phasing and proposed a design which is a remedy of these problems at very low cost. Phase reversal and single phasing are very frequent problem in our country. A 3-phase motor does not start if any one phase fails. However if a phase fails during the running condition, it will be overloaded, which may damage the motor winding. If phase reversal occurs then the motor will rotate in the reverse direction of the original direction. If a generator is connected with the motor shaft, then the generator brush or slip ring will be damaged. For many other industrial applications we need to rotate motors in a definite direction only. In this project, a very simple automatic phase sequence corrector with single phasing preventer is designed.

KEY WORDS: Phase Sequence indicating circuit, AND gate, ATMEGA 8, Transistor, Relay

1. INTRODUCTION

A 3-phase motor does not start if any one phase fails. However if a phase fails during the running condition, it will be overloaded, which may damage the motor winding. Because synchronous motor consume constant power as voltage is constant so current will be increased. On the other hand, in induction motor, at the running condition when single phasing is occurred, the motor will rotate if the load is more than half rated of the motor but slower speed and lower efficiency but if the load is more than half rated of the motor winding, the motor will shut down and it will act as a short circuited secondary of transformer and for this reason, high current will flow through the motor windings and those windings will be damaged. If an induction motor is connected with phase sequence ACB then the motor will rotate in the reverse direction of the original direction. If a generator is connected with the motor shaft to generate electricity the generator shaft will rotate also in the reversed direction. Then the motor brush or slip ring will be damaged. For many other industrial applications we need to rotate motors in a definite direction only. So we need to automatically correct the phase sequence so that the motor will rotate in a definite direction only. So it becomes necessary to provide a "Automatic Phase Sequence Corrector With Prevention Of Single Phasing".

2. OBJECTIVES

1. To Design a circuit that can detect and protect the system from single phasing.
2. To design a circuit that can automatically correct the phase sequence.
3. To design a circuit that allows only rotation in a definite direction for a motor.

3. WAYS

We can make the project by 2 ways

1. By using basic electronic element
2. By using microcontroller

4. PHASE SEQUENCE INDICATING CIRCUIT

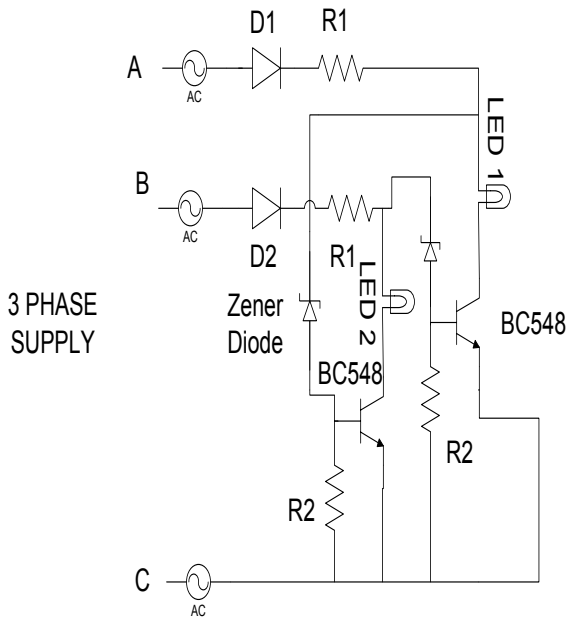

Fig 4: Phase Sequence Indicating Circuit

4.1 : Operation

These is phase sequence indicating circuit. Here A,B,C terminals are connected with 3 phase supply.If supply phase sequence is ABC or equivalent then only LED 1 will be on. If supply phase sequence is ACB or equivalent then only LED 2 will be on.

Phase Sequence ABC = CAB = BCA = LED 2

Phase Sequence ACB= CBA = BAC = LED 1

If Single phasing occurs then both LED 1&2 will be off.

5 . BY USING BASIC ELECTRONIC ELEMENT

5.1 Circuit Element

1. Phase Sequence indicating Circuit
2. And Gate
3. Relay
4. NPN Transistor

5.2 Description

The first circuit is connected to the second circuit. The first circuit is for preventing single phasing & the second circuit is for automatic phase sequence correction. Same phase sequence indicating circuit is used for both circuit because we need various And operation here. All of the relays are connected accordingly. Relay 1,2,3 are used to supply phase voltages when no single phasing occurs. Relay 4,5 are used to invert the phases if supply phase sequence is ACB. So all time out phase sequence of the circuit is ABC.

5.3 Circuit Operation

Three phase supply is given to the phase sequence indicating circuit. Then the light of the phase sequence indicating circuit switches the light dependent resistor. So, the input of the and gate changes. If single phasing occurs then lights of the phase sequence indicating circuit is kept off so that relay 1,2,3 will be energized so that three phase supply will be opened from the motor. If no single phasing occur then relay 1,2,3 will be de-energized so that three phase supply will be reached to the second section. Now, if supply phase sequence is ABC then led 1 is turned on, that switches the LDR so that AND gate output is turns off, so that relay 4,5 is remain de-energized. Now, if supply phase sequence is ACB then led 2 is switched on, so LDR is kept unchanged so that the output of the And gate is high, that enables the driver circuit so that relay 4,5 will be energized, so that the phases are inverted so output of the phase sequence corrector will be ABC whether supply phase sequence is ACB.

5.4. Circuit Diagram 1

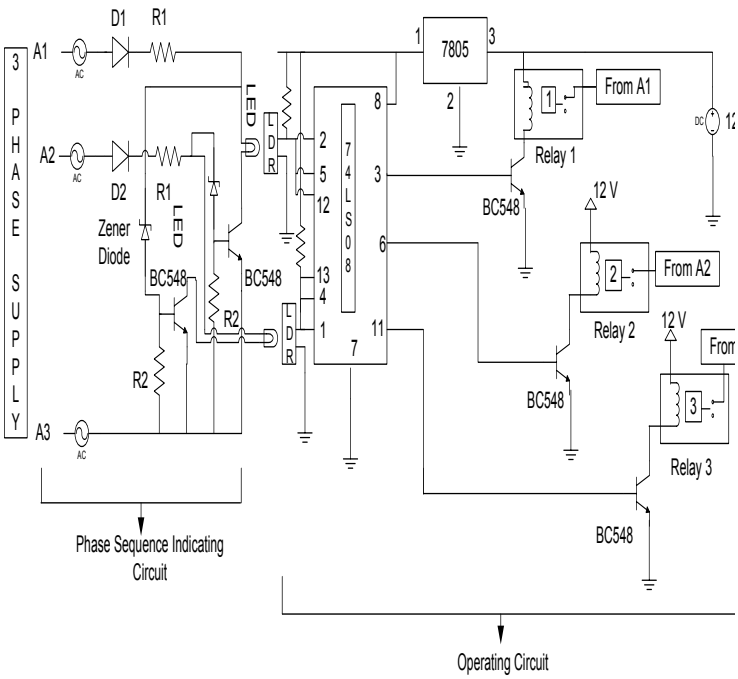

Fig 5.4: Single phasing prevention circuit

5.5 Circuit Diagram 2

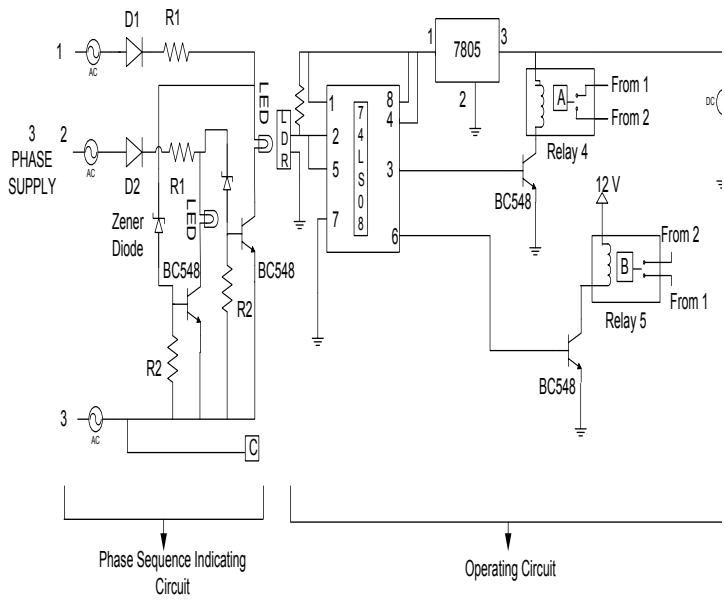

Fig 5.5 : Phase sequence corrector circuit

6. BY USING MICROCONTROLLER

6.1 Circuit Diagram:

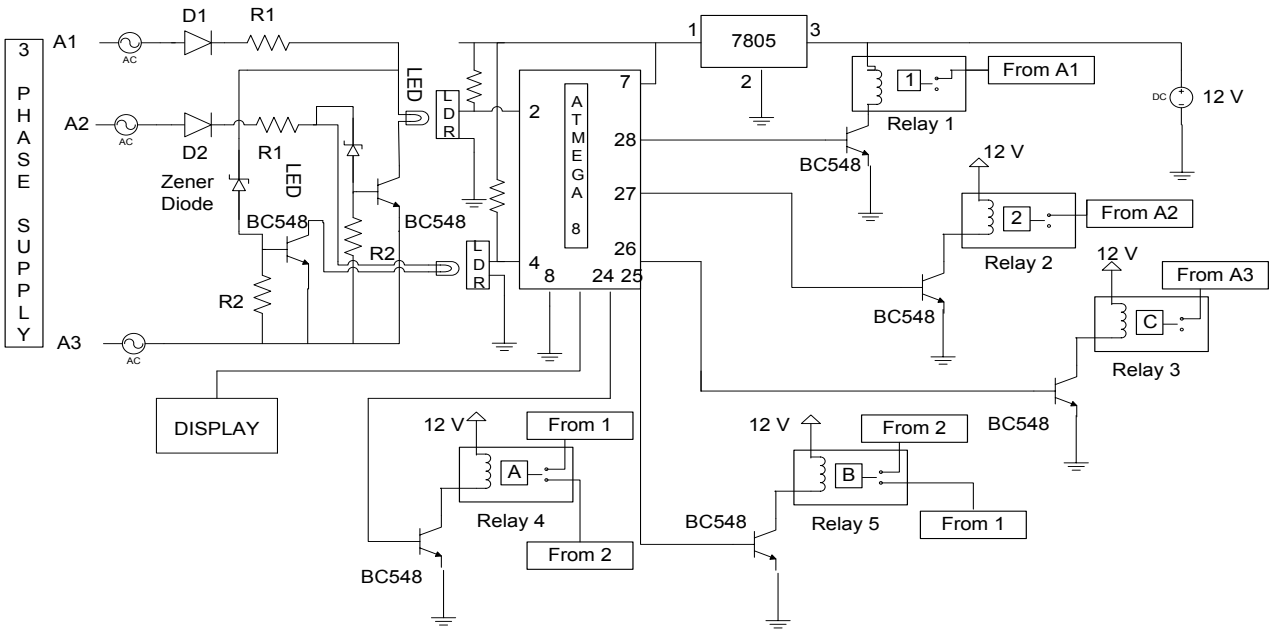

Fig 6.1: Automatic phase sequence corrector with single phasing preventer by Using Microcontroller

6.2 Circuit Element

5. Phase Sequence indicating Circuit
6. Microcontroller AT MEGA 8
7. Relay
8. NPN Transistor

6.3 *Description*

Led 1 & Led 2 of phase sequence indicating circuit is used to change the state of two LDR. These LDR is connected as input of microcontroller ATMEGA 8. According to the input the output of ATMEGA 8 is used to switch the transistor therefore the relays.

6.4 *Operation*

Three phase supply is given to the phase sequence indicating circuit. Then the light of the phase sequence indicating circuit switches the light dependent resistor. So, the input of the ATMEGA 8 changes. If single phasing occurs then lights of the phase sequence indicating circuit is kept off so that relay 1,2,3 will be energized so that three phase supply will be opened from the motor. If no single phasing occur then relay 1,2,3 will be de-energized Now the program will reach to the second section. Now, if supply phase sequence is ABC then led 1 is turned on, that switches the LDR so that AND gate output is turns off, so that relay 4,5 is remain de-energized. Now, if supply phase sequence is ACB then led 2 is switched on, so LDR is kept unchanged so that the output of the And gate is high, that enables the driver circuit so that relay 4,5 will be energized, so that the phases are inverted so output of the phase sequence corrector will be ABC whether supply phase sequence is ACB.

6.5 Proteus Simulation :

6.5.1 If Single Phasing Occurs:

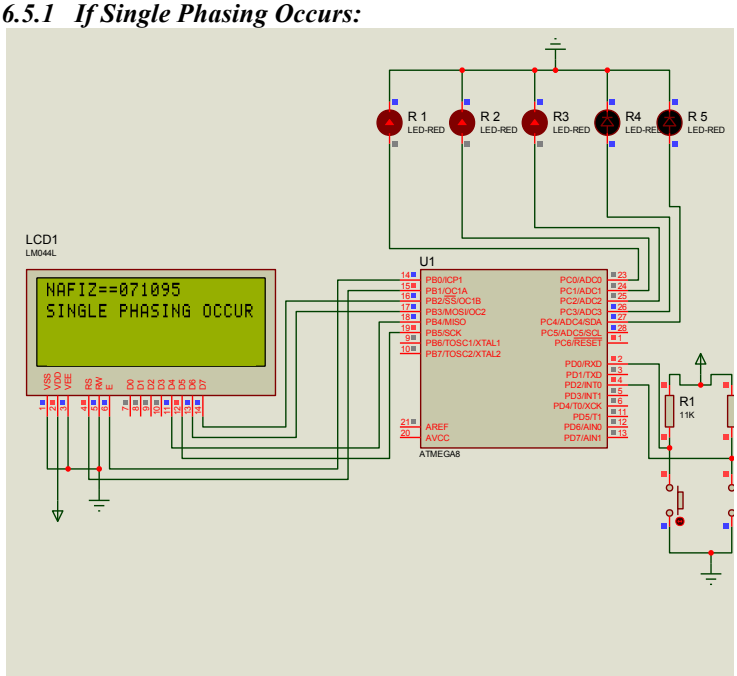

6.5.2 If Phase Sequence is ABC

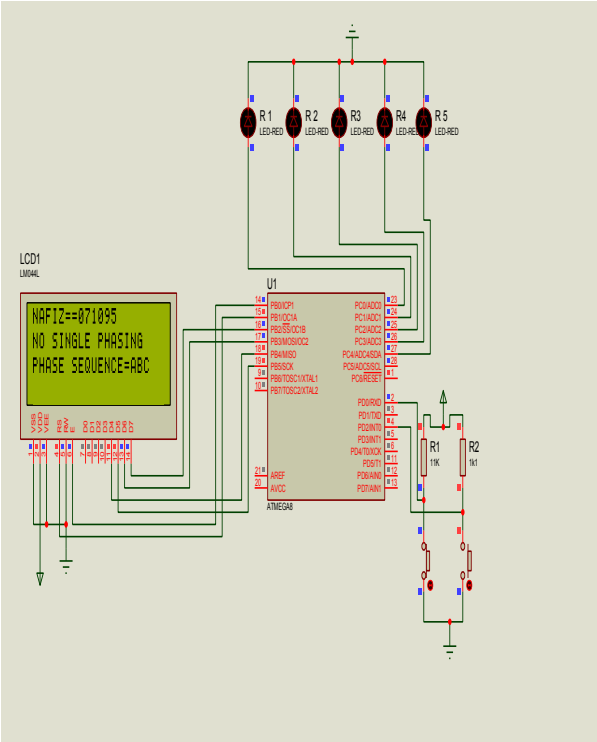

6.5.3 *If Phase Sequence is ACB*

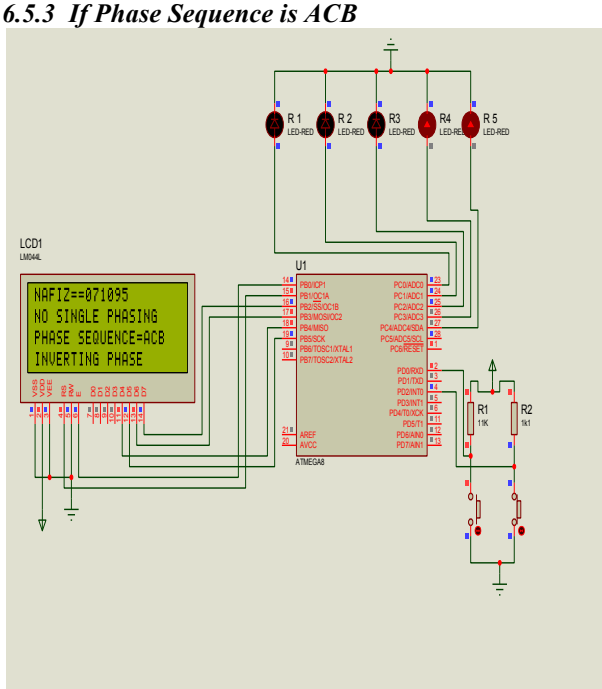

7. Conclusion

1. If Terminal A1,A2,A3 are not supplied with proper 3 phase supply or single phasing occurs then Relay 1,2,3 will be energized and no supply will reach to the phase sequence corrector circuit.
2. If Terminal A1,A2,A3 are supplied with proper 3 phase supply or no single phasing occurs then Relay 1,2,3 will remain de-energized and 3 phase supply will reach to the phase sequence corrector circuit.
3. If 3 phase supply comes from single phasing preventer circuit then if supply phase sequence is ABC then Relay 4,5 will remain de-energized and Terminal A,B,C supply 3 phase supply at phase sequence ABC.
4. If 3 phase supply comes from single phasing preventer circuit then if supply phase sequence is ACB then Relay 4,5 will be energized and so Relay 4,5 corrects the wrong phase sequence and Terminal A,B,C supply 3 phase supply at phase sequence ABC.

8. FUTURE WORK

We can reduce the complexity of the project. We can also reduce the transition time of the project.

9. ACKNOWLEDGEMENT

I also wish to express my heartiest gratitude and respect to the lab assistants of RUET who helps me to successfully complete the project.

REFERENCES:

[1]. Robert L. Boylestad, Louis Nashelsky " Electronic Devices and Circuit Theory ", Published by Pearson Education(Singapore) Pte. Ltd., Indian Branch, 482 F.I.E. Patpargang, Delhi 110 092,India. EighthEdition.Website:www.prenhall.com/boylestad.

[2]. B.L. THERAJA & A.K. THERAJA "A TEST BOOK OF ELECTRICAL TECHNOLOGY IN S.I UNITS Volume II AC & DC MACHINES ", Published by S.CHAND & COMPANY LTD.RAM NAGAR, NEW DELHI – 110 055.

[3]. ROSENBLATT & FRIEDMAN " DIRECT AND ALTERNATING CURRENT MACHINERY ", Published by S.K. Jain for Publishers & Distributors, 4596/1 Darya Ganj, New Delhi- 110 002 (India). Second Edition

[4]. IRVING L. KOSOW " ELECTRIC MACHINERY AND TRANSFORMERS " , Published by Prentice – Hall of India Private Limited, M-97, Connaught Circus, New Delhi-110001.Second Edition.

[5]. RONALD J. TOCCI & NEAL S. WIDMER & GREGORY L. MOSS " DIGITAL SYSTEM " , Published by Prentice – Hall of India Private Limited New Delhi- 110001.Tenth Edition.

Proceeding of the
International Conference on Electrical, Computer and Telecommunication Engineering
01- 02 December 2012 (ICECTE2012), RUET, Rajshahi-6204, Bangladesh

ICECTE2012: PI-0132

Design and Fabrication of a Temperature Controller

M.F.Hossain, Sajal Chaklader, Mithun Kabiraj, Asheque Newaz*
Department of Electrical and Electronic Engineering, Rajshahi University of Engineering & Technology (RUET), Rajshahi-6204, Bangladesh.
*E-mail: faruk94_ruet@yahoo.com

ABSTRACT
In thin films deposition, temperature is a vital factor. Different thin films deposition method needs different temperature for proper growth of thin films. . Deposition criteria and property of thin films depend on temperature. When a current passes through a heater coil then the electrical energy is converted into heat energy. If the current of the heater is controlled then its temperature is also be controlled. An AC control device Triac is used to control the current of the heater. The control of current of the Triac depends on the triggering pulse which is properly applied to its gate terminal. The triggering pulse is varied by a variable resistance of the triggering circuit. The different amount of currents from 2A to 3.8A is allowed to pass the heater coil by varying the variable resistance,. The constant temperature has been observed after 25 minutes. The 64, 134 and 215°C are obtained during 2A, 3A, 3.8A respectively.

KEY WORDS: Include at DC power supply unit, triggering pulse generating, driver circuit triac, Opto coupler, heater.

1.INTRODUCTION

The properties of the thin films grown by the different deposition technique depends on the temperature of the substrate, among other parameters. During growth the vaccum evaporated materials condense on the substrate and the further nucleation and growth formed films depends on the impinged energy at arrival and on the energy obtained from the substrate. Atoms mobility produced by the high temperature, promotes a better crystalline structure and large grain size in poly crystalline materials [1]. High temperature during growth reduce the selection of the type of material to be used as substrate heater. Besides high temperature can soften materials ,changing the geometry of the component.

The control of the temperature of a substrate heater is a requirement in simplementation of a simple and low cost substrate heater and it's temperature controller is presented. Substrate temperature plays a major role in determining the properties of the films formed. It is generally observed that higher substrate temperature results in the formation of better crystalline films [2, 3]. Grain size is primarily determined by initial nucleation density and recrystallization. Recrystallization into larger grains is enhanced at higher temperature [4].

By increasing the substrate temperature, the film morphology can be changed from cracked to dense and then to porous [5].Variation of substrate temperature over different points results in non-uniform films. Composition and thickness are affected by changes in substrate temperature which consequently affect the properties of deposited films. For example, while preparing SnS films using CSP, single phase films are obtained only in a narrow range of temperatures. Secondary phases like Sn2S3, SnS_2, SnO_2 etc. are present in filmsprepared at lower and higher temperatures [6].High substrate temperature can also result in the re-evaporation of anionicspecies as in the case of metal sulfide films [7].

In metal sulfides, re-evaporation of sulfur from film occurs at high substrate temperature, leaving metal rich surface,which may react with oxygen to form oxides.Though surface temperature is a critical factor, most investigators have not known the actual surface temperature of the substrate. Also, maintenance of substrate temperature at the preset value and its uniformity over large area are challenging. Liquid metal baths offer good contact at the interface and are widely used. But when solid surfaces are used, the actual area of contact is less than 1% of the surface area. Hardness and elastic modulus, residual stress, r.m.s surface friction coefficient etc are function of the annealing temperature.

In the study of carbon film as deposition, the hardness and elastic modulus of carbon film are decreased with the increasing of the annealing temperature. The adhesion behavior of carbon increases with decreasing of annealing temperature.

2.BLOCK DIAGRAM

The block diagram of proposed temperature controller is given in Fig. 1.

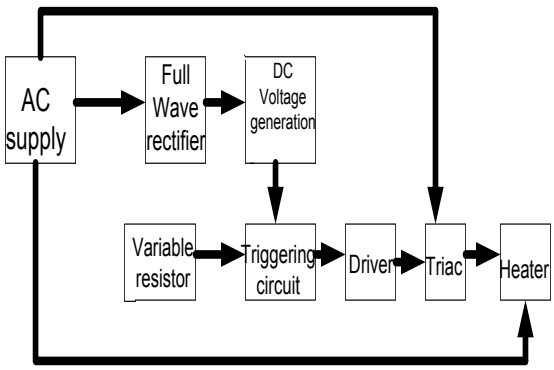

Figure 1. Block diagram of the controller.

2.1 AC supply

AC supply is essentially required for heater and also required for generation of DC voltage. Generally AC supply is available 230v.

2.2 Full wave rectifier:

Full wave rectifier is needed to convert AC signal to dc signal. It is also necessary for the switching purpose of the transistor that we used.

2.3 DC voltage generation:

DC voltage is necessary to generate for the biasing purpose of IC and different electronic devices.

2.4 Variable resistor:

This equipment is needed to vary the width of the pulses. By varying resistance we can vary the DC level at the input of the comparator.

2.5 Triggering circuit:

Triggering circuit is necessary to produce the triggering pulse for the AC controller i,e triac. It includes the comparator.

2.6 Driver :

This part includes the opto coupler. Normally pulse produced in the triggering circuit is small in voltage level compared to the AC voltage of the AC controller. So an isolation is required between the triggering circuit and the triac.

2.7 Triac:

This device is needed to control the AC power. To control the AC power a small triggering pulse is required to apply it's gate terminal.

2.8 Heater:

It consists of high resistive coil. When current passes through it electrical energy is converted into heat energy.

3. LIST OF COMPONENTS.

The components are used for design purpose of the controller their ratings and number are shown in a Table 1. These components are available in local market.

Table 1. list of components

SL. No.	Name of components	Specification	Quantity.
1.	Transformer	230/9-0-9	1
2.	IC	LM 324	1
3.	Diode	IN 4007	5
4.	Transistor	C 828	3
5.	Resistor (KΩ)	220,.470,1,10,15,22, 100,33	2,5,6,4,2, 2,1,1
6.	Capacitor (μF)	1000,10,2.2	1,1,1
7.	Optocoupler	MOC 3021	2
8.	Triac	BTA 16A	2
9.	Heater Coil	1000W	1

4. COMPLETE CIRCUIT DIAGRAM:

The complete circuit diagram and the operation of the circuit is described in Fig.2. LM 324 IC consists of four operational amplifier. we used three of these as a comparator. The first comparator compares full wave rectified signal with dc voltage. The output of this comparator is square wave. This signal is fed to a transistor with which a capacitor is connected at output terminal. By charging discharging method of capacitor another signal wave is produced. This signal is applied at input of the second comparator which compared with a dc voltage at other terminal of the comparator. This dc voltage level can be changed by a variable

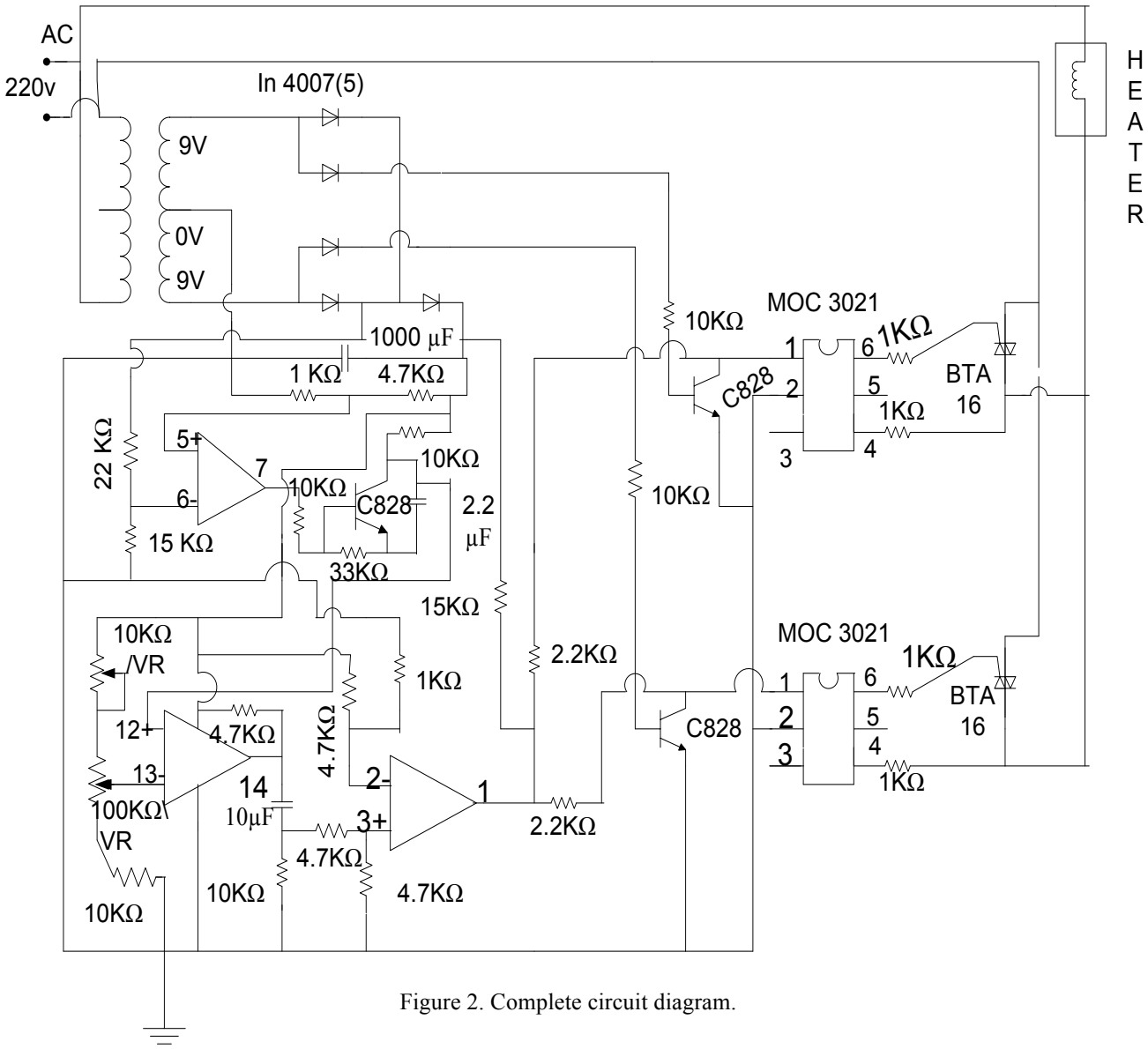

Figure 2. Complete circuit diagram.

resistor and the width of the pulse is changed. The output of this comparator is applied to a filter circuit. The output of the filter is finally compared with a dc voltage in the last comparator. the output of this comparator is the modulated pulses. These modulated pulses are applied to the gate terminal of triac. These pulses are drived to gate of triac by a optocoupler . If the width of the pulse is varied then the output of the triac is also varied and finally the current of the heater will be varied.

5. RESULT

Figure 3 shows the temperature of the heater, which are measured for different values of current. Starting from current 2A to3.8A we measured the current with interval of two minutes until the temperature becomes fixed. The temperature become saturated after 26 minute and maximum temperature is 64ºC for 2A current. The temperature became saturated after 24 minute and maximum temperature is 134ºC for 3A current. The temperature became saturated after 32 minute and maximum temperature is 215ºC for 3.8A current.

6. CONCLUSION

A temperature controller was successfully designed and fabricated by varying trigger pulse, which depended on a variable resistance of the trigger circuit. Three temperatures of 64, 134, and 215 ºC are getting by the currents of 2A, 3A, and 3.8A, respectively.

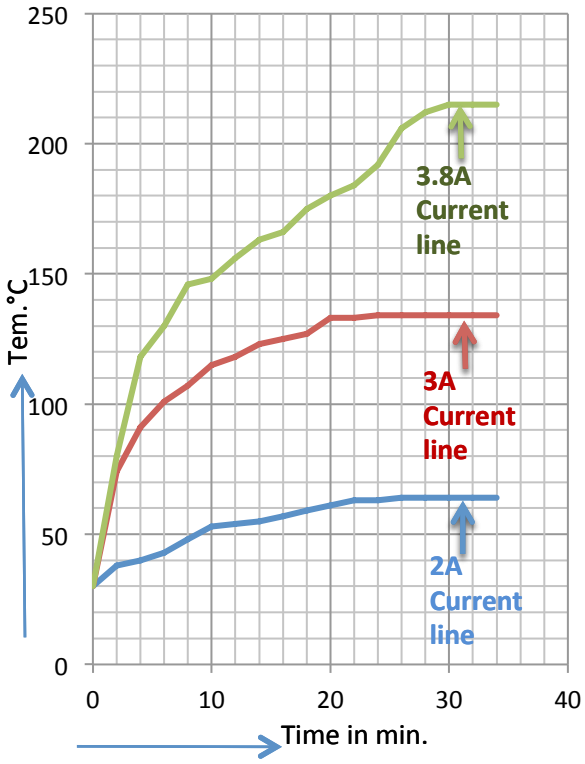

Figure 3. Temperature curve for 2A, 3A, 3.8A currents.

7. ACKNOWLEDGEMENT

The authors would like to thank the Rajshahi University of Engineering & Technology (RUET) for giving the chance to use the different equipments of the photovoltaic and nanotechnology lab and electronic lab.

REFERENCES

[1] K.S. Sree Harsha ,"Principles of physical vapor deposition of thin films.",vol.513,issue no.1-2 2006,pp.1-24 Elsevier, 2006.

[2] L.D. Partain, Solar cells and their Applications, John Wiley and Sons (1995).

[3] M.D. Archer, R. Hill, "Clean electricity from photovoltaics", Imperial College, Press, London, UK (1998).

[4] G. Zoppi, K. Durose, S.J.C. Irvine, V. Barrioz, "Grain and crystal texture properties of absorber layers in MOCVD-grown CdTe/CdS solar cells" Proc.of IOP Science,vol.21,issue num. 6,2006

[5] Edwards P.R. et al., Proceedings of 2nd World Conference in Photovoltaic Solar Energy Conversion, Vienna, Austria (1998).

[6] Jensen D.G. et al., Proceedings of 25th IEEE Photovoltaic Specialists Conference, Washington, USA (1996).

[7] D. Rudmann, D. Brémaud, A.F. da Cunha, G. Bilger, A. Strohm, M. Kaelin, H. Zogg, A.N. Tiwari, "Thin Solid Films"pp. 480-481 (2005) 55.

[8] .V.K. Mehta & Rohit Mehta," Principles of power system"4th revised edition,page no 2.

[9] Ramakant A. Gayakward,''Op-Amps and Linear Integrated Circuit," 4th edition,315-317.

[10] Muhammad H. Rashid,''Power electronics'', 3rd edition,page no 791,792.

[11] Robert L. Boylestad & Louis Nashelsky "Electronic device & circuit theory" 9th edition, page no. 79-81.

Proceeding of the
International Conference on Electrical, Computer and Telecommunication Engineering
01- 02 December 2012 (ICECTE2012), RUET, Rajshahi-6204, Bangladesh

ICECTE2012: PI-0133

Effect of Capacitance & Load on Rectifier DC Output Voltage

Mohammad Kamruzzaman Khan Prince[1], Md. Nafiz Imtiaz[2], Muhammad Abdul Goffar Khan[3]
Dept. of EEE, Rajshahi University of Engineering & Technology
E-mail: kzaman.eee@gmail.com[1], nafizeee07@gmail.com[2], agmagk@gmail.com[3]

ABSTRACT

In our practical life AC to DC conversion is frequently necessary. One way to do so is to use full wave bridge rectifier. But ripple components are always there when bridge rectifier is used solely. So, to improve the output DC level, filter capacitors can be used. Here the effect of capacitances and load has been examined.

.

KEY WORDS: capacitance, Load, Bridge rectifier, Ripple voltage, DC output voltage.

1. INTRODUCTION

1.1 Why Rectifier Circuit Is Needed

Alternating current (AC) is the most efficient way to deliver electrical power. But most electronic devices need direct current (DC) to function

An AC voltage is continually changing between positive (+) and negative (-).

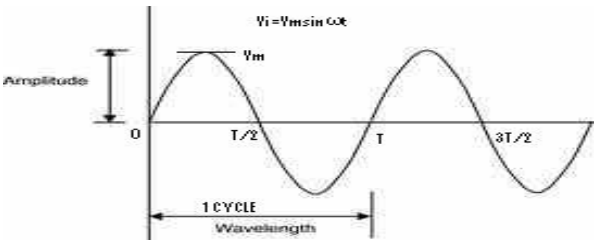

Fig. 1~1 AC supply voltage wave shape

Over one full cycle, defined by the time period T in Fig 1~1 the average value (the algebraic sum of the areas above and below the axis) is zero.

However by using rectifier circuit an average value (dc level) can be obtained. Here, the dc level can be improved 100% using a process called full-wave rectification.

1.2 Full Wave Bridge Rectifier Circuit

A rectifier is a circuit that converts an ac signal into a unidirectional signal.

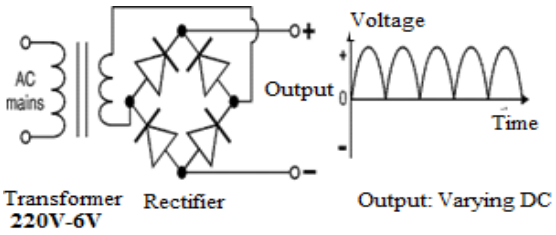

IN4007 diodes are used.

Fig. 1~2 Full wave bridge rectifier & it's output

This varying DC output is suitable for lamps, heaters and standard motors. But a supply of this nature would not be of any use for powering circuits because any analogue circuits would have the huge level of ripple superimposed on the output, and any digital circuits would not function because the power would be removed every half cycle [1].

By smoothing process (using filter capacitor) this pulsating dc have to be improved much more.

1.3 Smoothing Process

After the smoothing process the smooth DC output got very small amount of ripple contents. It is suitable for most electronic circuits.

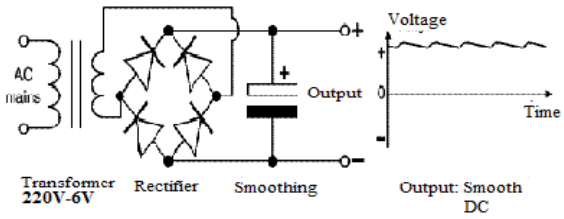

IN4007 diodes are used.

Fig. 1~3 Bridge rectifier circuit with filter capacitor and the corresponding output

Here, ripple voltage is the small unwanted residual periodic variation of the DC output.

The relation between smoothing capacitor and ripple voltage for full wave rectification is,

$C = I_{dc}/(2*f*V_{ripple})$ (Eq. 1~1)

Here, I_{dc} is dc load current and f is the supply frequency, which was 50Hz.

i.e. By using larger value of smoothing capacitor this ripple contents can be greatly minimized.

Since larger capacitor requires smaller time to charge to the peak value of the AC supply and they slowly

discharges because the discharging period of the capacitor is determined by the time constant, ($C*R_L$). Here, C is the value of the capacitance and R_L is the load resistance.
So filter capacitor acts as a reservoir & supply current to the output when the varying DC voltage from the rectifier is falling.

2. EFFECT OF CAPACITANCE

Effect of capacitances on full wave bridge rectifier circuit with RL load (Bulb of motor cycle head light (6V) in series with the 6V inductive coil of 220V-6V*2 XFMR) is shown by presenting the DC output wave shape from bridge rectifier for different values of capacitance with corresponding input wave shape.

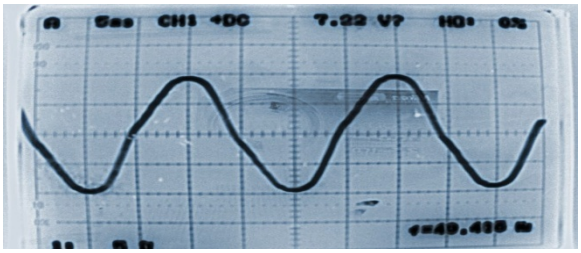

Fig. 2~1: 6V AC input voltage wave shape

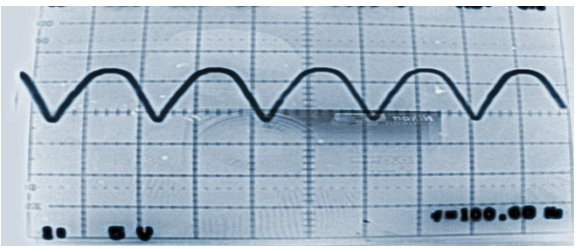
Fig. 2~2 DC output wave shape with 100uF filter capacitor.

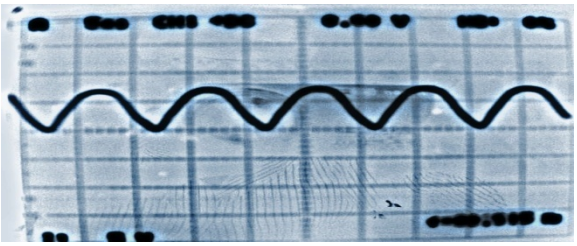
Fig. 2~3 DC output wave shape with 220uF filter capacitor.

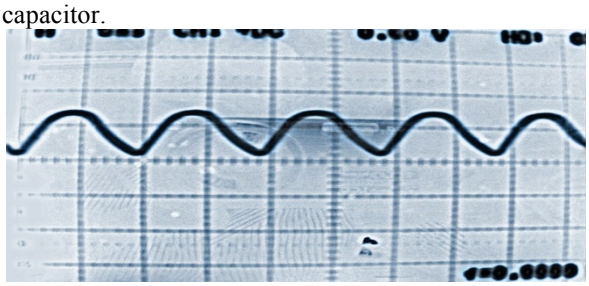
Fig. 2~4 DC output wave shape with 330uF filter capacitor.

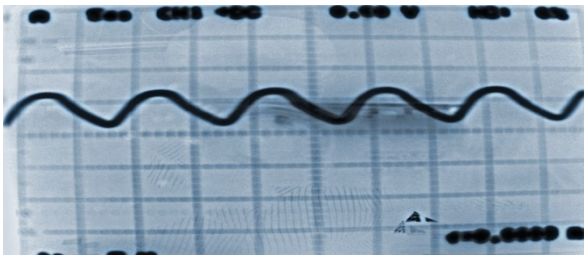
Fig. 2~5 DC output wave shape with 470uF filter capacitor.

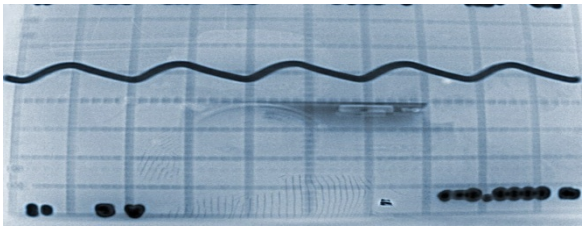
Fig. 2~6 DC output wave shape with 1000uF filter capacitor.

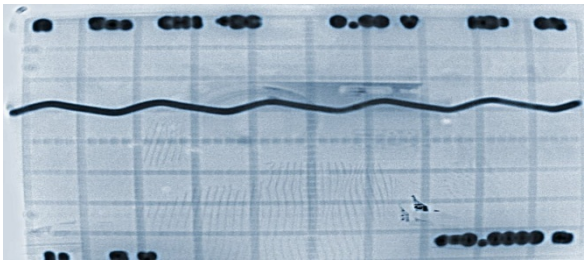
Fig. 2~7 DC output wave shape with 1800uF filter capacitor.

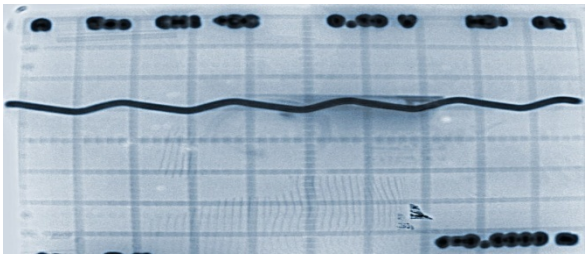
Fig. 2~8 DC output wave shape with 2200uF filter capacitor.

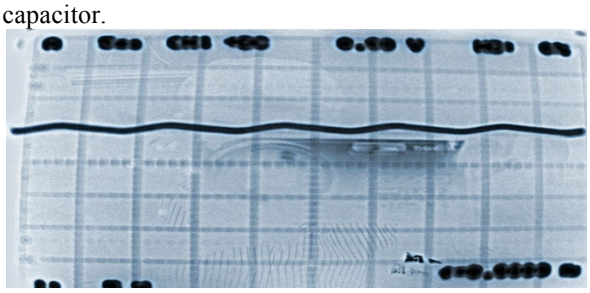
Fig. 2~9 DC output wave shape with 3300uF filter capacitor.

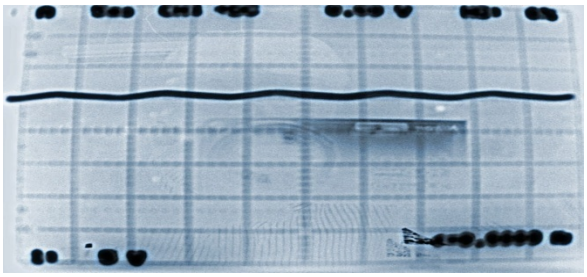

Fig. 2~10 DC output wave shape with 4700uF filter capacitor.

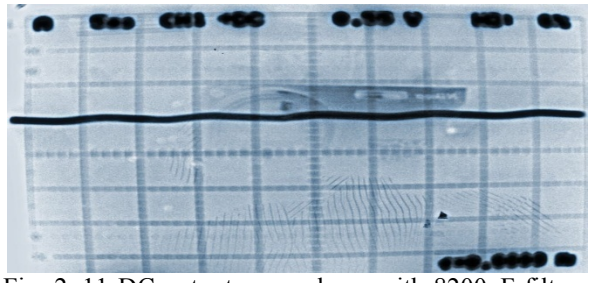

Fig. 2~11 DC output wave shape with 8200uF filter capacitor.

All the wave shapes are taken from oscilloscope with scale 5V in vertical axis and 5ms in horizontal axis for every small square. With zero supply voltage, minimum output has been found and peak output occurs when the supply was in it's peak value (positive or negative).

In this case negative voltage (-1.2V) appears when 100uF capacitance is used. Because inductor is an energy storing device. Due to inductive load, the conduction period of the diodes will increase. Because the current through an inductor can not change instantaneously [2]. When the negative half cycle of the supply commences the current in the inductor can not dissipate immediately, so the diode remains forward biased and conducting until the current coming from the supply is greater than the current in the inductor at which point the diode switches off. This is why a negative voltage is developed across the load. The greater the inductance the more of the negative half cycle is seen by the load [3]. But if freewheeling diode were used then it would prevent the development of the negative voltage [4].

This type of negative voltage doesn't appear for capacitances higher than 100uF, because later the increased value of capacitance will improve the $V_{O(DC)}$ and reduces ripple content.

3. EFFECT OF LOAD

Different types of loads also affect the output of the rectifier circuit.

As R load and motor load, 4.7ohm resistor and DC motor (6V) is used respectively.

3.1 Comparison Among Wave Shapes

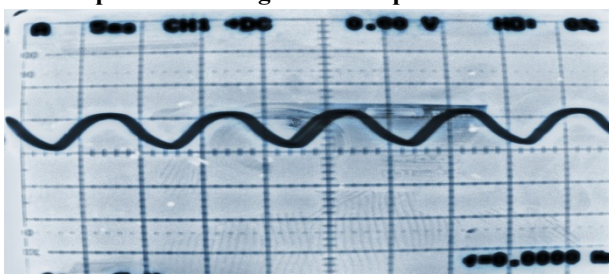

Fig. 3~1 DC output wave shape with R load

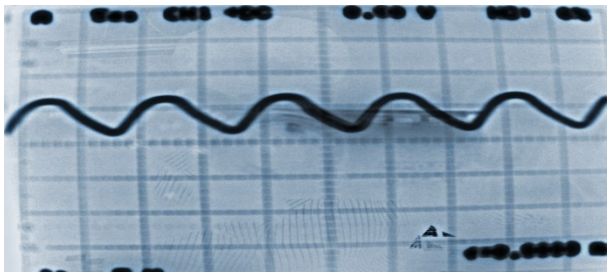

Fig. 3~2 DC output wave shape with RL load

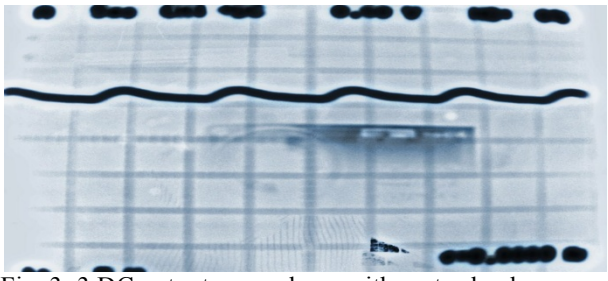

Fig. 3~3 DC output wave shape with motor load

In all cases 470uF capacitor is used as filter capacitor. From here it is seen that greater ripple is associated with R and R-L loads. Ripple is very small amount in case of motor load since DC motor is highly inductive in nature. An inductance in the load offers a high impedance for the harmonic currents and acts like a filter in reducing the harmonics. Also depending on the load time constant ($\zeta=\omega L/R$) the load current may be discontinuous but it might be made continuous with very high inductive.[4]

Same scale is also used here.

3.2 Comparison Among Capacitance VS $V_{O(DC)}$ Graphs

The effect of different types of load can also be realized from capacitance vs $V_{O(DC)}$ graphs.

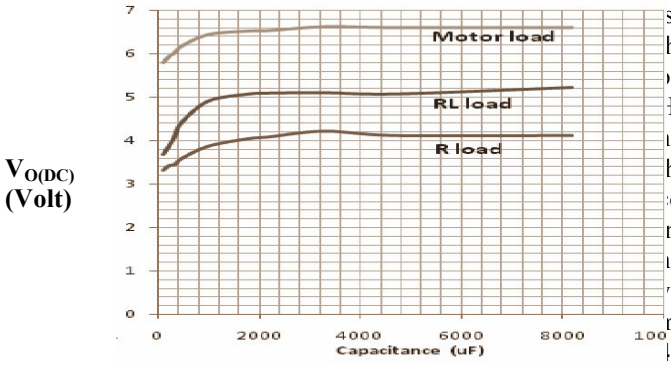

Fig. 3~4 Comparison among outputs of bridge rectifier with R, RL & Motor load.

The corresponding data table from which above curves are drawn is given below;

Data table 3~1 DC output with corresponding capacitor values for different types of loads

Capacitors (uF)	Voltage across the load, $V_{O(DC)}$(Volt)		
	R load	RL load	Motor load
100	3.32	3.67	5.78
220	3.43	3.87	5.93
330	3.45	4.09	6.01
470	3.59	4.41	6.17
1000	3.87	4.90	6.44
1800	4.04	5.06	6.52
2200	4.08	5.08	6.53
3300	4.21	5.09	6.62
4700	4.11	5.06	6.60
8200	4.11	5.21	6.60

All the $V_{O(DC)}$ values are measured by multimeter.
Here, in all cases capacitances vs $V_{O(d.c)}$ curves start from a minimum value and then gradually increases with the increase of capacitance as shown in Fig. 1~18.
In the end, all the curves got nearly constant values when capacitances are increased sufficiently and didn't change much then. In case of motor load (dc motor; 6V), most successful AC to DC conversion is found. Here $V_{O(DC)}$ is very close to the peak value of the supply voltage ($6*\sqrt{2}=8.49V$).
But, for R (4.7 ohm) and R-L load (Bulb of headlight of motor cycle (6V) in series with the 6V inductive coil of 220V-6V*2 XFMR), the curves got lower position than that, found for motor load. Between R and R-L load, R-L load got much improved $V_{O(DC)}$ since they are more close to 8.49V (peak value of the AC supply voltage) than R load. This is occurred because R-L load got some amount of inductance. Here, inductive load offers a high impedance for the harmonic currents and acts like a filter in reducing the harmonics and load current might be made continuous [4]. On the other hand, ripple voltage is inversely proportional to the sole resistance [7], and here the used resistance has very small value (i.e. very high load is used), so $V_{O(DC)}$ didn't improve much.

4. CONTRIBUTION & ACHIEVEMENTS:

For a particular load, most successful AC to DC conversion will occur on which capacitance value, that can easily determined from the graph obtained. It is proved that inductive load is better than any other load. With increasing capacitance, $V_{O(DC)}$ gradually increases. But in the end $V_{O(DC)}$ doesn't continue to increase. From this experimental work that particular capacitance value can be easily determined, for which, $V_{O(DC)}$ get's saturated value.

5. CONCLUSION

However, from the experimental work it is seen that with the increase of the capacitance the dc output voltage from the bridge rectifier circuit is improved gradually. It is because, capacitor with larger value will store more charge and their discharging period is also much longer. These capacitors will make the output steady & smooth. The output also improved when the resistive load was replaced by the inductive one. Inductive load doesn't allow the load current to change instantly. So they make the output current more smooth, more ripple free. That's why with high inductive load, like dc motor, the dc output voltage of the rectifier circuit is so improved, and inductive load like DC motor can be used with very small values of capacitor.

REFERENCES

[1]. http://www.kpsec.freeuk.com/powersup.htm
[2]. Charles K. Alexander & Matthew N. O. Sadiku, "Fundamentals of Electric Circuits", Chapter: 06 "Capacitors and Inductors", Second Edition.
[3]. www.csupomona.edu/~prnelson/courses/ece469/469hw1-revised.pdf
[4]. Muhammad H. Rashid, "Power Electronics Circuits, Devices, and Applications", Chapter: 03 "Diode Rectifiers", Third Edition.
[5]. http://wiki.answers.com/Q/What_is_the_effect_of_load_resistance_on_ripple_voltage_in_presence_of_filter_capacitor

Proceeding of the
International Conference on Electrical, Computer and Telecommunication Engineering
01- 02 December 2012 (ICECTE2012), RUET, Rajshahi-6204, Bangladesh

ICECTE2012: PI-0134

Efficiency Characteristics of a Combined π- and T-type Immittance Converter for Constant Current Applications

Sumaiya B. Afzal[1], Meeyad M. Shabab[1], Adnan Moin[1], Deepa Barua[1], Tajnin K. Turna[1], Sameya Shahnaj[1], Sheikh R. Reza[1], Taohid Latif[1], M. A. Razzak[2]
[1]Department of Electrical Engineering & Computer Science, North South University
[2]School of Engineering & Computer Science, Independent University, Bangladesh
E-mail: sumaiya.b.afzal@gmail.com, shabab.eee@gmail.com, adnan_m360@yahoo.com, deepa_jus4u@yahoo.com, tajnin_turna@yahoo.com, sameya_shahnaj@yahoo.com, taohidlatif@gmail.com, razzak_1971@yhaoo.com

ABSTRACT
Impedance-admittance converter is shortly written as immittance converter. In this converter, the output current is proportional to the input voltage and the output voltage is proportional to the input current. This simulation-based paper proposes the π-CLCL configuration of the immittance converter, which is a combination of the π- and T-type configurations, for constant current output applications. The input/output characteristics and efficiency characteristics are analyzed and simulated. The characteristics are compared to that of the π- and T-type converters which shows that the proposed configuration provides higher efficiency than the typical π- and T-types of immittance converters.

KEY WORDS: Immittance converter circuit, LC lumped immittance circuit, power electronics, efficiency characteristics, constant current output.

1. INTRODUCTION

The term 'immittance' combines the words 'impedance' and 'admittance'. Impedance-admittance converter is shortly written as immittance converter. The main characteristic of this converter is that the input impedance is converted into the admittance of the load at the output terminals; the output current is proportional to the input voltage and the output voltage is proportional to the input current [1]. This converter has functions in many power electronics applications especially where constant currents are needed. It is used to convert voltage sources into current sources and current sources into voltage sources. Some power electronics applications of this converter are photovoltaic inverters [2], dc-dc converters with constant current outputs[3], induction heating and plasma generation [4].

A lumped-constant reactor L and capacitor C can be used for the implementation of an immittance converter in a compact design [1]. In this article, a π-CLCL configuration of the immittance converter is proposed, which is a combination of the π-type and the T-type converters. The input/output voltage and current characteristics and the efficiency characteristics of the proposed π-CLCL immittance converter are analyzed. The characteristics are simulated and the simulation results are compared to that of the typical π-CLC type and T-LCL type immittance converter.

2. L-C LUMPED IMMITTANCE CIRCUIT

The immittance converter can be represented by the block diagram as shown in Fig. 1. There are four typical configurations of the immittance circuit namely T-LCL type, π-CLC type, T-CLC type and π-LCL type. Figure 2 shows the circuit diagram of the above-mentioned four types of immittance converter.

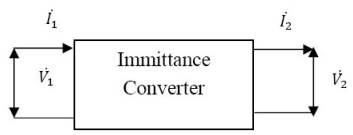

Fig. 1: Four-terminal immittance converter.

The four-terminal matrix of the immittance converter can be represented by:

$$\begin{bmatrix}\dot{V}_1\\ \dot{I}_1\end{bmatrix}=\begin{bmatrix}\dot{A} & \dot{B}\\ \dot{C} & \dot{D}\end{bmatrix}\begin{bmatrix}\dot{V}_2\\ \dot{I}_2\end{bmatrix} \quad (1)$$

At resonance frequency and under ideal conditions (Q_1, Q_2>>1), the immittance converter can be described as follows:

$$\begin{bmatrix}\dot{V}_1\\ \dot{I}_1\end{bmatrix}=\begin{bmatrix}0 & jZ_0\\ j\frac{1}{Z_0} & 0\end{bmatrix}\begin{bmatrix}\dot{V}_2\\ \dot{I}_2\end{bmatrix} \quad (2)$$

where $Z_0(=\sqrt{\frac{L}{C}})$ is the characteristic impedance.

From Eq. 2, it can be seen that the input voltage is proportional to the output current and input current is proportional to the output voltage.

$$\dot{V}_1 = \pm jZ_0 \dot{I}_2$$
$$\dot{I}_1 = \pm j\frac{1}{Z_0}\dot{V}_2 \quad (3)$$

Figure 3 shows the output characteristics of the ideal immittance circuit. If the input voltage is constant then a constant output current proportional to the input voltage is achieved and if the input current is constant, a constant output voltage proportional to the input current is achieved.

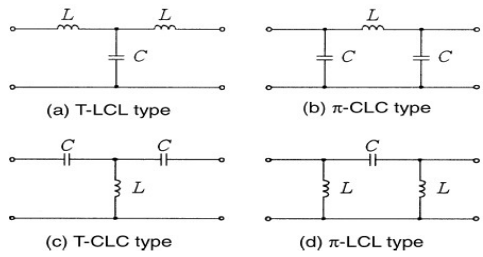

Fig. 2: Typical configurations of immittance converter (a) T-LCL type (b) T-CLC type (c) π-CLC type (d) π-LCL type.

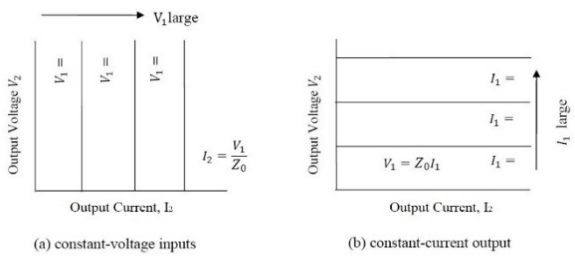

Fig.3: Output characteristics of immittance converter.

2.1 π-CLC Immittance Converter

By analyzing the respective immittance converter circuit with Kirchoff's laws, we find that at resonant condition the four-terminal matrix of π-CLC immittance converter can be written as:

$$\begin{bmatrix}\dot{V}_1\\ \dot{I}_1\end{bmatrix} = \begin{bmatrix} j\frac{1}{Q} & jZ_0 \\ j\frac{1}{Z_0} & j\frac{1}{Q}\end{bmatrix}\begin{bmatrix}\dot{V}_2\\ \dot{I}_2\end{bmatrix} \quad (4)$$

where, Q is the quality factor and Q>> 1.
From Eq. 4, by applying the binomial theorem the load current equation is:

$$I_2 \cong \frac{V_1}{Z_0}\left(1 - \frac{1}{Q}\frac{Z_2}{Z_0}\right) \quad (5)$$

where, the load impedance $\dot{Z}_2 = \frac{\dot{V}_2}{\dot{I}_2}$

Using Eq. 4 and Eq. 5, the efficiency of the π-CLC converter is

$$\eta \cong \frac{1}{1+\frac{1}{Q}\frac{Z_2}{Z_0}+\frac{1}{Q}\frac{Z_0}{Z_2}} \quad (6)$$

2.2 T-LCL Immittance Converter

Similar to π-CLC configuration, at resonant condition the four-terminal matrix of T-LCL immittance converter can be written as:

$$\begin{bmatrix}\dot{V}_1\\ \dot{I}_1\end{bmatrix} = \begin{bmatrix} j\frac{1}{Q_1} & jZ_0 \\ j\frac{1}{Z_0} & j\frac{1}{Q_2}\end{bmatrix}\begin{bmatrix}\dot{V}_2\\ \dot{I}_2\end{bmatrix} \quad (7)$$

From Eq. 7, by applying the binomial theorem the load current equation is:

$$I_2 \cong \frac{V_1}{Z_0}\left(1 - \frac{1}{Q_1}\frac{Z_2}{Z_0}\right) \quad (8)$$

Using Eq. 7 and Eq. 8, the efficiency of the π-CLC converter is

$$\eta \cong \frac{1}{1+\frac{1}{Q_1}\frac{Z_2}{Z_0}+\frac{1}{Q_2}\frac{Z_0}{Z_2}} \quad (9)$$

For the case $Q_1=Q_2=Q$ and $Z_0=Z_2$ the efficiency characteristic of both the π-CLC and T-LCL configurations is the same.

$$\eta \cong \frac{1}{1+\frac{2}{Q}} \cong 1 - \frac{2}{Q} \quad (10)$$

3. PROPOSED π-CLCL IMMITTANCE CONVERTER

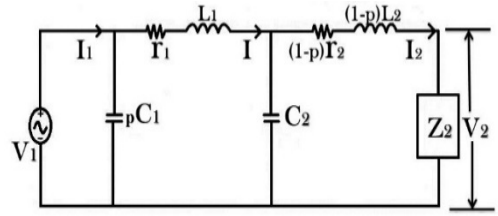

Fig. 4: π-CLCL type immittance converter.

The proposed π-CLCL immittance converter is shown in Fig. 4, where p is an arbitrary coefficient in the range of 0 to 1. This π-CLCL converter correspond to the T-LCL type converter at p=0, and to the π-CLC type at p=1 as shown in Fig. 2(a) and Fig. 2(b), respectively.

3.1 Resonant Frequency Characteristics

By analyzing the proposed π-CLCL immittance converter circuit using Kirchoff's laws, the $\dot{A}$, $\dot{B}$, $\dot{C}$,

$\dot{D}$ parameters in Eq. 1 at resonant frequency ω are found to be:

$$\dot{A} = j\omega C r_1 \quad (11)$$

$$\dot{B} = j\omega C(r_1+j\omega L)(r_2+j\omega L)(1-p) + (r_1+j\omega L) + (r_2+j\omega L)(1-p) \quad (12)$$

$$\dot{C} = \omega^2 C^2 r_1 p + j\omega C \quad (13)$$

$$\dot{D} = -\omega^2 C^2 p(r_1+j\omega L)(r_2+j\omega L)(1-p) + j\omega Cp(r_1+j\omega L) + j\omega C(r_2+j\omega L)(1-p) + j\omega Cp(r_2+j\omega L)(1-p) + 1 \quad (14)$$

The resonance frequency, ω, the characteristic impedance, Z_0 and the quality factor, Q are defined as:

$$\omega = \frac{1}{\sqrt{LC}} \quad (15)$$

$$Z_0 = \omega L = \frac{1}{\omega C} = \sqrt{\frac{L}{C}} \quad (16)$$

$$Q_1 = \frac{\omega L}{r_1} \quad (17)$$

$$Q_2 = \frac{\omega L}{r_2} \quad (18)$$

Using Eq. 15~18, the $\dot{A}$, $\dot{B}$, $\dot{C}$, $\dot{D}$ parameters in Eq. 11~14, at resonant condition can be rewritten as:

$$\dot{A} = j\frac{1}{Q_1} \quad (19)$$

$$\dot{B} = jZ_0\left(1 + \frac{1-p}{Q_1 Q_2} + j\frac{p}{Q_1}\right) \quad (20)$$

$$\dot{C} = j\frac{1}{Z_0}\left(1 + j\frac{p}{Q_1}\right) \quad (21)$$

$$\dot{D} = j\frac{1}{Q_2} + jp\left(\frac{p}{Q_1} - \frac{1}{Q_2}\right) - \frac{p(1-p)}{Q_1 Q_2} \quad (22)$$

Since Q_1, Q_2>> 1, the real part of these parameters becomes very close to zero. Therefore, the following approximation can be made:

$$\begin{bmatrix} \dot{V}_1 \\ \dot{I}_1 \end{bmatrix} = \begin{bmatrix} j\frac{1}{Q_1} & jZ_0 \\ j\frac{1}{Z_0} & j\frac{1}{Q_2} + jp\left(\frac{p}{Q_1} - \frac{1}{Q_2}\right) \end{bmatrix} \begin{bmatrix} \dot{V}_2 \\ \dot{I}_2 \end{bmatrix} \quad (23)$$

If Q_1 and Q_2 are high (>100) then A=D=0 at any value of p which is the properties of an ideal immittance converter as shown in Fig. 2.

3.2 Input / Output Characteristics

When the load impedance $\dot{Z}_2$ is connected to the output terminals, $\dot{V}_1$ and $\dot{I}_1$ are as follows:

$$\dot{V}_1 = j\dot{I}_2\left(1 + \frac{1}{Q_1}\frac{Z_2}{Z_0}\right) \quad (24)$$

$$\dot{I}_1 = j\frac{1}{Z_0}\dot{V}_2\left[1 + \left\{\frac{1}{Q_2} + p\left(\frac{p}{Q_1} - \frac{1}{Q_2}\right)\right\}\frac{Z_0}{Z_2}\right] \quad (25)$$

where $\dot{Z}_2 = \frac{\dot{V}_2}{\dot{I}_2}$

Taking the magnitude of the input voltage and current and using the binomial theorem and ignoring the higher order terms of Q, Eq. 24~25 become:

$$I_2 \cong \frac{V_1}{Z_0}\left(1 - \frac{1}{Q_1}\frac{Z_2}{Z_0}\right) \quad (26)$$

$$V_2 \cong I_1 Z_0\left[1 - \left\{\frac{1}{Q_2} + p\left(\frac{p}{Q_1} - \frac{1}{Q_2}\right)\right\}\frac{Z_0}{Z_2}\right] \quad (27)$$

The first term of the output current and output voltage is the ideal term while the second term is the loss term resulting from the internal resistance of the inductance. When the internal resistance is negligible or zero, the quality factor becomes infinity. Under this condition, the second term becomes zero giving the ideal immittance condition.

3.3 Efficiency Equation

From Eq. 24~27 and ignoring higher order terms of Q since Q_1, Q_2>>1, the efficiency of the proposed π-CLCL immittance converter is:

$$\eta \cong \frac{1}{1 + \frac{1}{Q_1}\frac{Z_2}{Z_0} + \left\{\frac{1}{Q_2} + p\left(\frac{p}{Q_1} - \frac{1}{Q_2}\right)\right\}\frac{Z_0}{Z_2}} \quad (28)$$

For the case Q_1=Q_2=Q and Z_0=Z_2 the efficiency characteristic of the π-CLCL converter becomes:

$$\eta \cong \frac{1}{1 + \frac{1.75}{Q}} \cong 1 - \frac{1.75}{Q} \quad (29)$$

4. SIMULATION RESULTS AND DISCUSSIONS

4.1 Load Current Characteristics

Fig. 5 shows the load current versus load impedance for the proposed π-CLCLC immittance converter at different values of quality factor Q considering Q_1=Q_2=Q and with characteristic impedance Z_0=20Ω. The load current I_2 is independent of p. The output current remains fairly constant over a wide range of load impedance. The higher the quality factor the less is the effect of the loss term of output current.

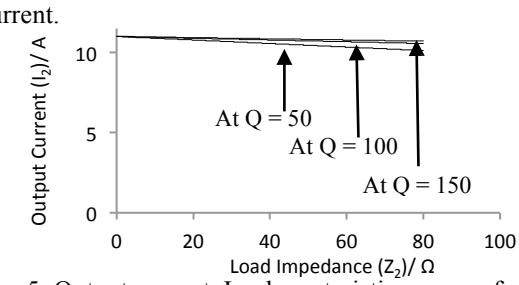

Fig. 5: Output current, I_2, characteristics curve of π-CLCL type immittance converter.

4.2 Efficiency Characteristics

The efficiency characteristics (efficiency versus load impedance) of the proposed π-CLCL immittance converter at different values of quality factor Q are compared with that of the π- and T-type immittance converters in Fig. 6~8. For p=0.5, the π-CLCL converter has higher efficiency than that of the

typical two configurations for all three cases as can be seen from the graphs.

Thus, according to our simulation results, it is observed that the proposed π-CLCL converter is more efficient than the typical π-CLC and T-LCL type converter. The higher the value of Q the higher the efficiency achieved. With Q=150 peak efficiency close to 99% can be achieved.

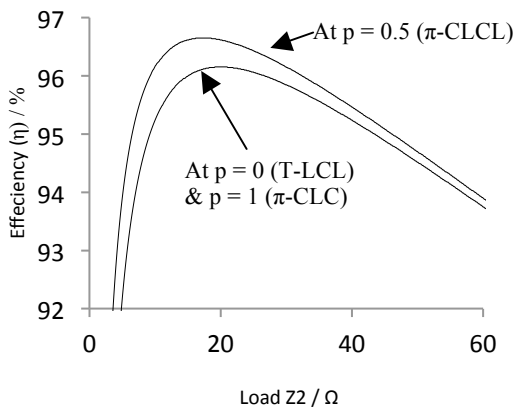

Fig. 6: Efficiency characteristics curve of π-CLCL for different values of p and Q = 50.

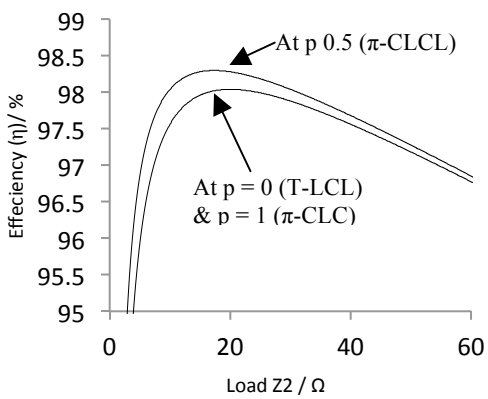

Fig. 7: Efficiency characteristics curve of π-CLCL for different values of p and Q = 100.

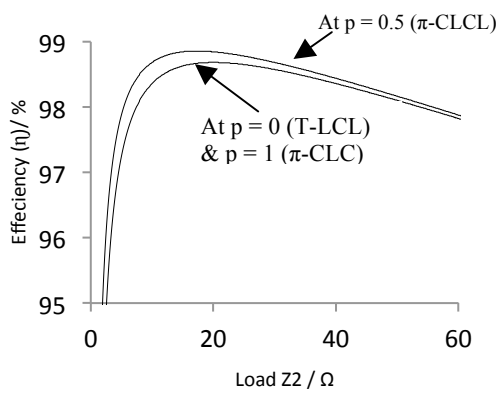

Fig. 8: Efficiency characteristics curve of π-CLCL for different values of p and Q = 150.

5. CONCLUSION

In this paper, a π-CLCL configuration of the immittance converter is proposed which is a combination of the π- and T-type converters. The study ensures immittance conversion of the circuit at resonant frequency. The simulation results show that the output current remains fairly constant for any dynamic load. The efficiency characteristics for different Q values shows that a better performance can be achieved with the proposed π-CLCL immittance converter with a value of p=0.5 than that of the typical π- or T-type immittance converters. Therefore, a highly efficient converter can be built with a Q value greater than 100.

6. FUTURE WORK

In future the simulation results will be compared to the experimental results by building the prototype of the proposed converter.

REFERENCES

[1]. Ohnishi K et al. Efficiency characteristics of immittance converter. Proc 1998 Japan IAS Conference, No. 215.

[2]. Irie H et al. Utility interactive inverter using immittance converter for photovoltaic power system. Trans IEE Japan, Vol.120-D, pp. 410–416.

[3]. Yamana H, Irie H. Immittance converter in a switching mode power converter. National Convention Record of IEEJ, No. 817, 1996.

[4]. M. A. Razzak et al., Efficient Radio Frequency Inductive Discrges in Near Atmospheric Pressure Using Immittance Conversion Topology, J. Plasma Fusion Res, Vol. 81, No. 3, pp. 204-211, 2005.

Proceeding of the
International Conference on Electrical, Computer and Telecommunication Engineering
01- 02 December 2012 (ICECTE2012), RUET, Rajshahi-6204, Bangladesh

ICECTE2012: PI-0135

Design and Implementation of a PC Based Single Channel Online Data Logger using USB Port

Muhammad Abdul Goffar Khan [1], Md Rabiul Islam [2], Sarim Khan[3]
[1]Department of Electrical & Electronics Engineering
[2]Department of Computer Science & Engineering
[3]Department of Electronic & Telecommunication Engineering
Rajshahi University of Engineering & Technology

E-mail: agmagk@gmail.com, rabiul_cse@yahoo.com

ABSTRACT
Data loggers are used in research laboratories as well as in industries to observe the change of any physical quantity such as pressure, temperature, density, velocity etc. for a longer period of time. Such instruments are mostly imported one, suffers from different disadvantages such as lacking of user defined operating scheme, future modification and overall cost. Moreover such data loggers use parallel port of the computer. But now-a-days personal computers and laptops do not have parallel ports. In this paper an indigenously developed data logger has been reported which can be connected to the pc using USB port. A microcontroller based electronic board receives the analog signal, which is converted to digital form, using the inbuilt ADC available in the microcontroller. Using separate protocol, the received data is sent to the computer, as and when requested from it. Separate software are developed for the microcontroller as well as the pc to complete the entire task. The designed electronic board is fabricated in the laboratory, using all the necessary parts from the local market, which makes the data logger most cost effective. The fabricated circuit is tested in the laboratory and the observed result is compared with that obtained by using a pc based multimeter. The observed performance of the proposed data logger agrees with the theoretical expectation as well as the practically measured values using commercially available meters.

KEY WORDS: Online data logger,

1. INTRODUCTION

The need for small, online data loggers and data acquisition systems are becoming more essential for both academia and industry, especially for remote monitoring. Modern data loggers are being designed based on stand-alone and low power or energy consumption. A smart data logger is the convergence of the sensing features of a sensor with the intelligence and decision making abilities of the entire system. The data logger has to be a portable, hand-held, battery-operated data collection device for collecting "real world" data which can be used as an interface to a computer [1]. The block diagram of the proposed data logger is shown in Fig.1.

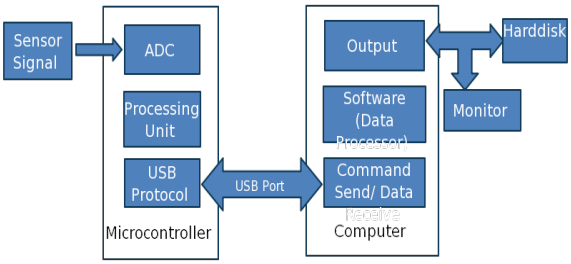

Fig.1. Block diagram of the proposed data logger

2. BLOCK DIAGRAM

The physical signal under monitor, such as temperature, pressure etc. is converted to an equivalent analog signal by using proper sensors and/or transducers. The analog signal thus obtained is fed to the ADC, built-in in the microcontroller. A Ten bit digital signal is thereby obtained. By using proper protocol and developing required software, a virtual USB controller is developed within the microcontroller, because the microcontroller which we selected does not have built-in USB controller. The USB controller sends the digital data to the PC as and when requested by it. Separate software is developed for the PC to control the entire operation. The time interval between two consecutive samples and the total number of samples to be monitored can be preset by the operator through keyboard of the PC. At the end of the session a graph is displayed which can be saved in the PC for further use/processing. Print out of the graph can also be taken using a printer with the PC. The Flow starts from the software, the software sends a command to send a data to the MC. This command translates to usb protocol and travels through the USB port to MC. inside MC, the USB protocol translator translates the command and send it to MC's

Processing Unit, which then instructs the ADC to read a data. ADC reads the data and send it to MC, the data is 10bit. this 10bit is splited to 2 bytes using the following formula. byte 1 = data \ 256 byte 2 = data % 256 This bytes (data) is translated to usb protocol and send to computer. Where it again translates to bytes and the Data processor of the Software converts it to 10 bit integer using the following formula. Resultant data = byte 1 * 256 + byte 2 This data is the raw result of the ADC, it is then scaled using the scaling factors and shown as graph in monitor and also optionally saved to the HDD. Depending on the interval set in the software, the software again send the command to MC and the whole process is kept repeating and the data is stored cumulatively.

3. DESIGN AND FABRICATION

The printed circuit board is designed using Express PCB, commercially available software for this purpose. The PCB layout is shown in Fig.2.

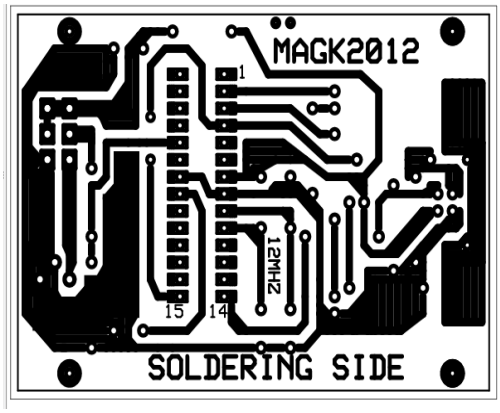

Fig.2. PCB layout of the electronic board

The microcontroller and the necessary components are collected from the local market and fixed on the PCB. The view of the electronic board is shown in Fig.3.

Fig.3. View of the electronic board after fabrication (left) without casing (right) with casing

4. TEST RESULT

The fabricated data logger is tested in the laboratory for temperature measurement of a water jar. An immersion heater is used to heat up water in a jar. A conventional 'mercury in glass tube' thermometer is used for calibration. Commercially available temperature sensor is used to convert temperature into equivalent electrical signal. The test setup is shown in Fig.4. The test is performed in two steps.

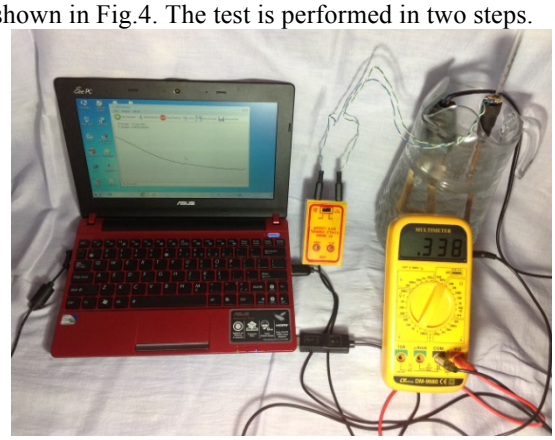

Fig.4. View of the Test setup

Step 1 : The output of the sensor is connected with the input of a commercially available pc linked multimeter, Model to observe the temperature change over a period of 5 minutes, at an interval of 100 millisecond. The change of temperature is also recorded by a conventional mercury in glass tube thermometer. Step 2 : The output of the sensor is connected with the input of the proposed data logger through USB port and the temperature change is observed in the similar manner as above. The change of temperature is also recorded by a conventional mercury in glass tube thermometer. Result : The obtained graphs are shown in Fig. 5. It is revealed from the graphs that the performance of the proposed data logger is similar to that of the commercially available pc linked meter.

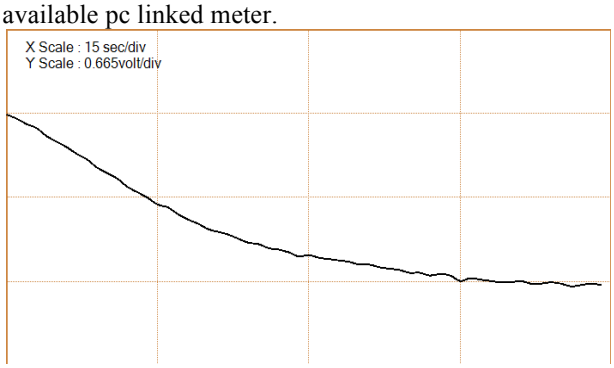

Fig.5. Test Result

5. CONCLUSIONS

A pc based data logger is presented in this paper. It is designed and fabricated using components available in the local market, which makes it cost effective, compared to similar devices imported from outside the country. It is tested in the laboratory and the results are compared with that obtained using an

imported one. The observed results are found to be in consistent with theory as well as practical observations. The device can be further improved for multichannel input signals.

REFERENCES

[1]. Krishna Kanth, "Computer based Industrial Control", PHI, New Delhi, 2004.

[2]. www.control.com.

[3]. Mirza Nazrul Alam, Md. Woalid Hossain and A K M Moinul Islam, ".A low cost pc based real time signal analysis technique", *Proceedings of 3rd International conference on Electrical , Electronics and Computer Engineering*, 22-24 December,2003, pp.272-274.

[4]. R Anand, "A versatile digital thermometer", Electronics projects, EFY enterprises Ltd., New Delhi, Vol. 19, pp. 7-10.

[5]. M F Rahman, M F hossain and M A Goffar Khan, "Microprocessor based temperature Monitoring and display system", *Proceedings of 3rd International conference on Electrical , Electronics and Computer Engineering*, 22-24 December,2003, pp.254-261.

[6]. Debashis Chandra Saha, Md. Ruhul amin, Md. Nasirul Hasan and Md. Zulfiquar Ali Bhotto, "Design and implementation of PC based real time data acquisition and visualization system", *Proceedings of 3rd International conference on Electrical , Electronics and Computer Engineering*, 22-24 December,2003, pp. 77- 83.

[7]. S Rajendran and P Swaminathan, "Capture analogue signals on your PC using printer port", Electronics projects, EFY enterprises Ltd., New Delhi, Vol. 18, pp. 3-8.

Proceeding of the
International Conference on Electrical, Computer and Telecommunication Engineering
01- 02 December 2012 (ICECTE2012), RUET, Rajshahi-6204, Bangladesh

ICECTE2012: PI-0136

Experimental Investigation and Optimization of a 270W Low Cost Sub-Woofer Amplifier

Md. Ifthekhar Hossain[1], BishwajitBanik Pathik[2]
[1, 2]Dept. of Electrical and Electronic Engineering, American International University-Bangladesh (AIUB)
E-mail: ifte.hsn@gmail.com, bishwajit.b.pathik@gmail.com

ABSTRACT
This article is about the design of a low cost, noise freeHiFi audio power amplifier and it's optimization for subwoofer operation.In this paper, we have represented an IRFP250 and IRFP9140 MOSFET (Metal Oxide Semiconductor Field Effect Transistor) based low cost high power amplifier with frequency response of 10 Hz to 40 kHz which has been suitably optimized for a sub-woofer using a specially designed filter. The whole study has been conducted in few steps like reviewing previous works, designing and simulating the circuits using software, constructing PCB (Printed Circuit Board) layout and practical implementation, performance analysisand optimization etc.After analyzingthe performance and additional optimization with trial and error approach, we have found anamplifier which is quite suitably capable of driving two12", 8Ω sub-woofer speakers in the frequency range of 15 to 200Hz.

KEY WORDS: Sub-woofer amplifier, noise free amplification, low cost sub-woofer, frequency response, amplifier architecture.

1. INTRODUCTION

A high quality audio power amplifier is a circuit in which the output voltage is an (almost) exact replication of the input voltage, without any modification of phase relationships, harmonic integrity, transient response, or frequency. There are essentially three areas of quality evaluation for an audio amplifier: performance, reliability and construction. Considering performance, a high quality amplifier should be extremely low in distortion across the entire audio bandwidth with low –noise specifications and rock-solid stability under all practical load conditions. From the reliability stand point, it should be able to protect itself under a wide variety of adverse condition and operator mistakes. Finally the overall construction of power amplifier should include adequate bracing for heavy power supply components, and shield the user from any injurious electrical potential.

Upon considering the three factors of high quality audio power amplifiers, the researchers attempt to construct a system that can fulfill the demand of listener both technologically and economically. The ultimate target of the authors is to build up a 7.2 channel home theater system with the facilities like remote control, USB, equalizer,VU meter etc.To accomplish this goal,designing a low cost noise free subwoofer amplifier is a major step. Existing low cost IC based sub-woofer amplifiers available in the local markets are subjected to poor low-frequency response and tremendous noise. Again, imported quality amplifiers are too costly for the low income community of Bangladesh. This experimental study is a novel approach to build step by stem IRFP250 and IRFP9140 MOSFET based economically cheap but quality subwoofer amplifier.

2. RELATED STUDY

2.1 Audio Power Amplifier

Power amplifier is an amplification device which boosts the level of a line-level signal(the signal from modern source device like CD, DVDs. In the range from 0.1V to 3V) in order to supply sufficient power to directly drive a speaker.[10]

2.2 Architecture of an Audio Amplifier

Almost all solid-state amplifiershave three-stagearchitecture.[1][2][3]Two-stage and three stage architectures have occasionally been used,but their distortion performance is not very satisfactory.[2]

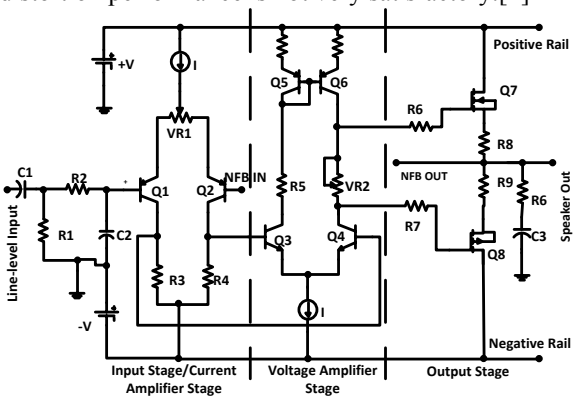

Fig. 1: Three stage amplifier structure

In the three stage architecture topology, the first being a trans-conductance stage, the second a trans-impedance stage this stage provide all the voltage gain and therefore it is called Voltage-amplifier Stage (VAS).The third stage is a unity voltage-gainoutput stage.

2.2.1 Input Stage (IPS)[2][3]

The input stage of an amplifier is the first stage of an audio power amplifier. Its primary function is to convert a line-level signal voltage input to an amplified current signal which is then coupled to the VAS. In addition, it performs the critical duty of

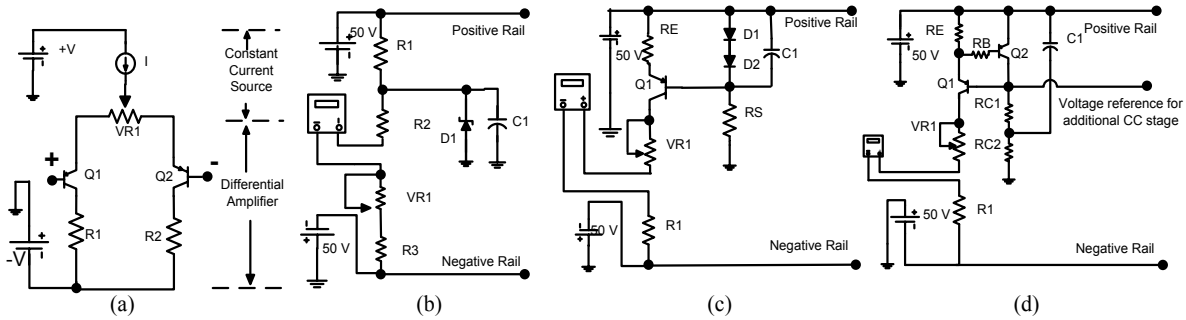

Fig.2: IPS and 3 topologies of CCS (b) Pseudo CCS, (c) Common transistor-diode CCS, (d) Dual transistor CCS

generating an error signal by subtracting the feedback signal from the input.

The schematic of input stageis represented in Fig. 2 (a). This stage consists of constant current source and differential amplifier. To accommodate the multidimensional characteristics of high quality input stages, a variety of common electronic building blocks can be incorporated for optimum performance.

(a) Constant Current Source (CCS): The constant current source is a major part in almost any audio amplifier design. They are commonly used to supply tail current in differential stages, improving the stability, speed, gain, and common mode rejection characteristics. [1]

(i) *Pseudo Constant Current Source:*A pseudo-constant current source has been illustrated in Fig. 2(b). R_1 and D_1 make up a simple Zener voltage regulator with C_1 used to smooth out load and power supply variations. R_2 simulates the current source internal resistance. The performance of such a constant current source is far from ideal, but it is adequate for some input stage.

(ii) *Common transistor-diode constant current source:* Fig. 2(c) is a common form of constant current source with two forward-biased series diodes D_1 and D_2 as the voltage regulating elements. The design of fig. 2(c) provides current regulation over 12.7 times superior to that of fig.2(b). [1]

(iii) *Dual transistor current source:* Fig 2(d) represents a different approach to constructing a constant current source, incorporating transistor $Q_1$and Q_2, resistors R_E, R_B, R_{C1}, and R_{C2} and smoothing capacitor C_1. The constant current source of fig 2(d) is a much better design than the observed previously. The dual transistor action greatly reduces the variation in voltage regulation inherent with forward biased diodes or zener diodes. This approach is over six times better than the current source of fig.2(c) and about 84 times better than the current source of fig. 2(b). [1]

(b) Differential Amplifier: In its simplest form, a two transistor circuit that shares a common emitter load or current source. If the output is taken between transistor collectors, differential amplifier will provide high common mode rejection. However their common use in audio power amplifiers is due to the way they fit into the Lin topology.

2.2.2 Voltage Amplifier Stage (VAS)

The Voltage Amplifier Stage (VAS) is responsible for all of the voltage gain within a typical audio power amplifier. The VAS receives a buffered and current amplified output signal from the input stage and converts it to large-signal voltage to be applied to the output stage. [1]4]

There are different types of VAS topologies. A simple differential amplifier for VAS has been illustrated in fig. 3. It takes the current as input from input stage and converts it to voltage. Like input stage, the VAS also has differential amplifier and constant current source.[2][3][

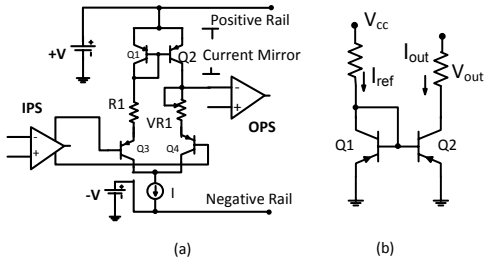

Fig. 3(a) Voltage amplifier stage (b) Current mirror

A current mirror is also incorporated in Voltage Amplifier Stage (VAS) to improve its stability. The incorporation of current mirror as the collector load for a differential amplifier creates significant improvements in linearity and virtually doubles the amplifier's output current capability and slew rate[1]. The current mirror is shown in the fig. 3(b) consisting of Q_1, Q_2, R_{E1}, and R_{E2}. Important aspect of the operation of the current mirror is that the current from the constant current source is split evenly between the two current mirror legs.

2.2.3 Output Stage (OPS)

The purpose of output stage is to receive the high level voltage from the Voltage Amplifier Stage (VAS) and interface it to a low-impedance reactive load i.e. a speaker system. The OPS is typically a unity voltage gain current amplifier. Output stage classes are:

(i) *Class A:* In a Class-A amplifier current flows continuously in all the output devices, which enables

thenonlinearities of turning them on and off to be avoided.[4]

(iii) *Class B:*Class B push-pull system is the same as that for class A system, except that the devices are biased approximately at cut-off. The advantages of class B compared with class A operation is that it is possible to obtain greater power output, its efficiency is higher, and there is negligible power loss at no signal. [4]

(ii) Class AB: class AB is intermediate between class A and Class B, with better power efficiency and less distortion than class B. The two active devices conduct more than half of the time, producing less cross-over distortion than class-B amplifier. [4][6]

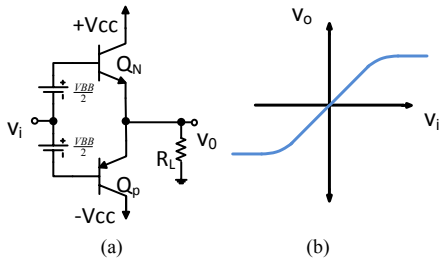

Fig. 4:(a) Class AB amplifier (b) VTC curve

(iv) *Class C:*Class-C implies device conduction for significantly less than 50% of the time, and is normally onlyusable in radio work, where an LC circuit can smooth out the current pulses and filter harmonics.[4]

2.3 Sub-Woofer

A speaker designed exclusively for low-frequency reproduction. A true subwoofer should be able to at least reach into the bottom octave (20-40Hz). [6]The typical frequency range for a subwoofer is about 20–200 Hz for consumer products, [8] below 100 Hz for professional live sound.

2.4 Low Pass Filter (LPF)

By definition, a low-pass filter is a circuit offering easy passage to low-frequency signals and difficult passage to high-frequency signals. [4] Ideally, lowpassfilter passes all frequencies below its cut-off frequency and rejects those above the cut-off.[5][11]

3. METHODOLOGY

There are several synchronous steps involved to complete this research fruitfully. Such as-

Step 1:Identifying the target and clarifying the objectives for the study which are designing a low cost, noise free subwoofer amplifier.

Step 2:Checking previous works from various sources, i.e. books, conference papers, articles from prestigious journals, websites etc.

Step 3:Stepwise designing and analyzing the performance of the amplifier circuit virtually using circuit simulation software like *NI Multisim*, *Proteous*, and *PSpice*.

Step 4:Designing PCB (Printed Circuit Board) layout using *Diptrace*software.

Step 5:Preparing the PCB and soldering the components on the board designed.

Step 6:Analyzing the frequency response of the amplifier in laboratory with sophisticated equipment.

4. THE AMPLIFIER

The schematic of the power amplifier is demonstrated in fig. 5. It incorporates the IRFP250 and IRFP9140, MOSFET devices. The amplifier operates from +50V/-50V DC. It is able to deliver output of 270 watt RMS into 8Ω load.

Resistor R_2 limits the input current to Q_1 and C_7 bypasses any high frequency noise from the input. Constant current source is built by using the transistor Q_9 and Q_{10} to supply about 1.34mA current. Q_1 and Q_2 form the input differential pair. C_3 is rail decoupling capacitor and its value is standard for such type of current source. For current 1.34mA the value of R_1 was chosen 470Ω (0.65V/470Ω=1.34mA). The value of R_{12} and R_{13} is such that current flows through them which is roughly half of the desired current flow. The value of rail decoupling capacitor is standard for this type of current source. R_f and R_i establishes the closed loop AC voltage gain of the amplifier.

From Ohm's Law, for 270 watt RMS output into 8Ω speaker, gain must be 46.5 [(46.5x46.5) ÷ 8=270]. R_f and R_i value are specified as 47 kΩ and 1kΩ respectively for voltage gain of about 47 [(R_f ÷ R_i) +1=47]. This is a good choice since it establishes that AC voltage gain a little higher than needed. Preset V_{R1} is used for adjusting the voltage at the output of the amplifier.

The second differential stage is formed by transistors Q_3 and Q_4 while transistors Q_{14} and Q_{15} forms a current mirror which makes the second differential pair to drain an identical current. This is done in order to improve linearity and gain.

Output stage is based on Q_7 and Q_8 which operates in the class AB mode. Preset R_8 is used for adjusting the quiescent current of the amplifier. The network comprising of capacitor C_4 and resistor R_6 improves high frequency stability and prevents the chance of oscillation.The frequency response curve without and with low pass filter (LPF) have been illustrated in fig. 6. There is also PCB layout of the circuit in fig 7.

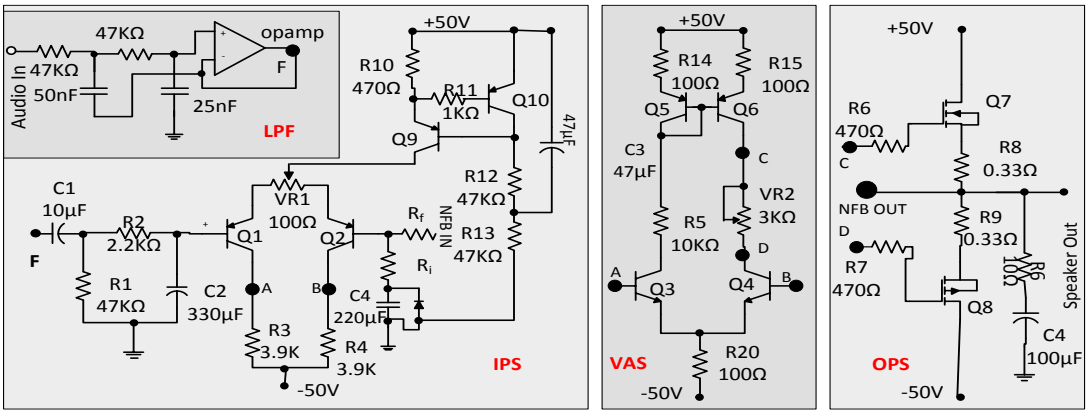

Fig 5: SchematicDiagram of Sub-Woofer Amplifier

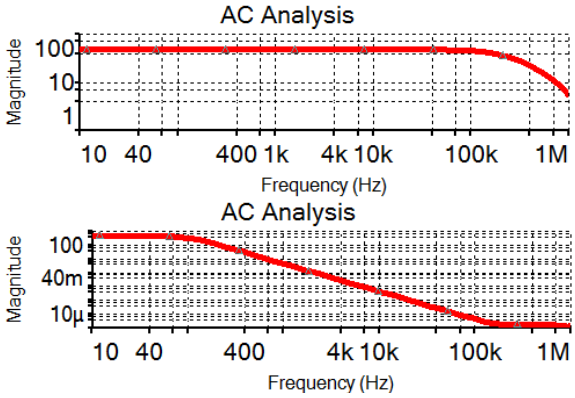

Fig. 6: Frequency response of amplifier without LPF (top) and with LPF (bottom).

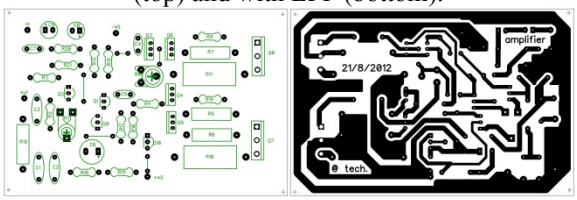

(a) (b)

Fig. 7: PCB layout (a) Top layer (b) Bottom Layer

5. FUTURE WORK

The circuit designed can be further modified to build a 7.2 channel home theater system. We have a plan to add additional features like remote control, USB, 10-band Graphic Equalizer, 20x20 LED array audio VU meter etc. with this existing amplifier. The ultimate target would be developing a low cost wireless Hi-Fi audio system with locally available components.

6. CONCLUSION

The main objective of this research work was to design and implement a low cost subwoofer amplifier that can drive two 10" sub-woofer speakers without any humming and noise which will be a part of uniquely designed 7.2 channel wireless home theater system in future. In this paper, theinvention and fabrication of asub-woofer amplifier has been described, which is the main challenge to build the above mentioned sound system. By analyzing the performance at 10Hz to 1MHz frequency span it is clear that the designed amplifier, as the result of systematic trial and error process, ensures a high quality and powerful (270 Watt) subwoofer amplifier in the frequency range of 15 to 200 Hz without being distorted at high amplification and produces noiseless sound.

REFERENCES

[1] G. R.Slone, "High-Power Audio Amplifier Construction Manual",McGraw-Hill, USA, 1999, ISBN: 0-07-134119-6.

[2] D. Self, "Audio Power Amplifier Design Handbook", Focal Press, USA, 5th Ed., 2009.

[3] B, Cardel, "Designing Audio Power Amplifiers", McGraw-Hill, USA.

[4] J. Millman, C. C. Halkias, "Integrated Electronics", Tata-McGraw-Hill Publishing Company Ltd., New Delhi, ISBN 0-07-46245-5.

[5] Coughlin, R. F. "Operational Amplifiers and Linear Integrated Circuits (6th Edition)", Prentice-Hall of India Pvt. Ltd., New Delhi, ISBN-81-203-2096-4

[6] Audio Glossary, viewed 29 September,2012, <www.audioc.com/library1/glossary.htm>

[7] Barstow, Loren (January 18, 2010). "Home Speakers Glossary", Learn: Home. Crutchfield New Media, LLC. Retrieved April 24, 2010.

[8] Young, Tom (December 1, 2008), "In-Depth: The Aux-Fed Subwoofer Technique Explained", Study Hall, ProSoundWeb, pp. 1–2. Retrieved March 3, 2010.

[9] Low Pass Filter, viewed 29 September, 2012, <http://www.allaboutcircuits.com/vol_2.html>.

[10] M. E. V. Valkenburg, "Analog Filter Design (Oxford Series in Electrical and Computer Engineering)", Oxford University Press, USA, ISBN-978-0195107340.

[11] F. Taylor, "Electronic Filter Design Handbook", Fourth Ed., McGraw-Hill, USA.

Proceeding of the
International Conference on Electrical, Computer and Telecommunication Engineering
01- 02 December 2012 (ICECTE2012), RUET, Rajshahi-6204, Bangladesh

ICECTE2012: PI-0137

Polarization Encoded Optical Shadow Casting Logic Units: Design of Trinary Combinational Arithmetic Units Using Various Input Coding Scheme

Abdullah Al Hadi[1], Jamal Uddin Ahmed[2], Md. Mahim Muntasir[3], Saiful Islam Chowdhury[3], Tawsif Aqib[3]
[1]Graduate Student, Universitat Politecnica de Catalunya, 08034 Barcelona, Spain
[2]Faculty of Electrical and Electronic Engineering Department, Ahsanullah University of Science and Technology (AUST), Dhaka-1215, Bangladesh
[3]Electrical and Electronic Engineering Department, AUST, Dhaka-1215, Bangladesh
Email:abdullah.al.hadi.bd@gmail.com,jamaluddinahmedjua@gmail.com,mahim1800@gmail.com,im_shuvo@yahoo.com,tawsif.aqib@gmail.com

ABSTRACT
In this paper we evolve several input pixel pattern scheme for trinary half adder design. The POSC[1] modified algorithm is used to design and implement trinary half adder. A set of POSC equation are obtained from the truth table of the desired arithmetic unit. Different input coding schemes are calculated by changing the minterm grouping conditions. Three different pixel patterns are designed which are more efficient for integrating larger complex design. Each design has various merits on other designs. This will help to implement larger design conveniently using these various design of half adder.

KEY WORDS: Polarization Encoded Optical Shadow Casting (POSC), Trinary logic design, Optical Computing, Half Adder design.

1. INTRODUCTION

The speed of computers was achieved by miniaturizing electronic components to a very small micron-size scale, but they are limited not only by the speed of electrons in matter (Einstein's principle that signals cannot propagate faster than the speed of light) but also by the increasing density of interconnections necessary to link the electronic gates on microchips. The optical computer [2] comes as a solution of miniaturization problem. In an optical computer, electrons are replaced by photons, the subatomic bits of electromagnetic radiation that causes light. If we can replace electronic system by photonic system then we should have a computing system thousands of times faster than the electronic system. Electronic signals in chips travel at snail speed compared to light speed. Moreover, there is no such thing as a short circuit with light, so beams could cross with no problem after being redirected by pinpoint-size mirrors in a switchboard. In a pursuit to probe into cutting-edge research areas, optical technology[3] is one of the most promising, and may eventually lead to new computing applications as a consequence of faster processor speeds, as well as better connectivity and higher bandwidth.

With the advent of mass-produced binary components for computers, trinary components have diminished to a small footnote in the history of computing. However, elegance and efficiency of trinary logic is predicted by Donald Knuth. Possible ways of solving this issue is by the combination of an optical computer with the trinary[4],[5],[6] logic system. The simple way to explain this phenomenon is to compare it with the binary system. Binary system, normally used in electronic computing, has two values 1 or ON and 0 or OFF. A trinary computer could use three values: 0 or OFF, 1 or Semi ON and 2 or Full ON. Hence, ternary or trinary is the base-3 numeral system. Analogous to a bit, a ternary digit is known as trit (trinary digit). One trit contains $log_2 3$ (about 1.58496) bits of information, increasing the efficiency of the system. Although ternary most often refers to a system in which the three digits 0, 1, and 2 are all nonnegative integers are difficult to configure by electronic system. So, the implementation of trinary system should be much easier in optical method. In electronic system there is no such value Semi-ON or Full-ON

Yet, in optical method light could be either horizontally polarized or vertically polarized to distinguish between Semi-ON and Full-ON. Therefore, the three nonnegative values are represented by 0 or dark, 1 or horizontally polarized, 2 or vertically polarized light.

First Trinary adder and subtractor were designed using POSC scheme by A. A. S. Awwal et. el., 1987[4]. Later on, modification on this design was done by R. A. Rizvi et. el., 1991[5]. In this paper we introduced further improvement and modification in the design with different types of input pixel patterns for trinary half adder. Here all together four different designs were introduced out of which design 1 was introduced by R. A. Rizvi. Three new various design alternatives will help in integrating larger complex design.

In the next section the shadow-casting setup and consequent design algorithm are elaborated. Then various design examples of trinary half adder are described.

2. POSC METHOD AND ALGORITHM

The optical shadow casting system is considered to be promising for optical digital computing because of the relative ease with which it can be implemented to utilize fully parallel communication and noninterfering interconnection capability of optics. The scope of optical shadow casting was broadened by polarization-encoded optical shadow casting. By Including polarized pixel codes as additional design variables for encoding the input, source, and the decoding mask the capability of optical shadow-casting system has been improved drastically. This improved technique, is called polarization-encoded optical shadow casting (POSC) scheme. In the POSC scheme, the geometry of the system is identical to that of the OSC method. Here, the logical inputs as well as the LED sources can be coded by the sense of polarization. To display the basic features of the POSC scheme, we consider a simple POSC system shown in Fig.1.

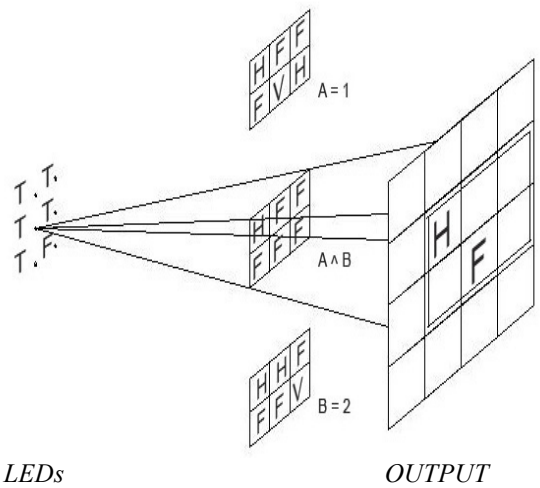

Figure 1: A Polarization-encoded Optical Shadow-Casting (POSC) system.

POSC Algorithm:

A POSC design scheme involves determining the encoding patterns of the input, the source LED pattern and the decoding mask which will produce the desired output of any arithmetic and/or logic unit. An algorithm for the design of POSC logic unit utilizing truth table partitioning is described as follows:

Step 1: The truth table of the to-be-designed logic unit is determined.

Step 2: The truth table is then partitioned into two sections, taking at least two input columns in primary section. The remaining inputs form the secondary section. For multiple output functions, each output is treated separately.

Step 3: The outputs assigned the polarization codes: T/ V for 2 in trinary system, H for trinary 1 and F for trinary 0. The non-zero outputs are thus assigned either V code for 2 or H code for 1. Trinary logical values 1 and 2 are decoded by horizontally polarized H and vertically polarized V masks respectively of a same micro pixel occupying half part of the pixel each. Zero outputs are not usually considered in the treatment, as they would always occur by default whenever a 1 or 2 is not generated.

Step 4: The overlap of the primary inputs in each row of the truth table is assigned the same code as that of the corresponding output.

Step 5: The overlap of the secondary inputs is assigned a POSC code so that its overlap with the code of the overlap of the primary inputs produce the code for the desired output the overlap of the secondary inputs is thus assigned either T, F, or "don't care" code. A don't care means that the variable could have any one of the codes T, V, H, or F for any of its trinary values.

Step 6: The input coding pattern is determined from the solution of the corresponding POSC overlap equations.

Step 7: If more than one output exists, the next output is generated from the existing codes of the primary inputs. If this is not possible, step 4, 5 and 6 are repeated to provide new assignments for the overlap of either primary and/or secondary inputs. This step may increase the size of the input pixel.

Step 8: The POSC overlap equations involving (i) the primary input variables and the code of their overlap and (ii) the secondary input variables and the code of their overlap are solved to provide the codes for all of the inputs.

Step 9: The source LED pattern for each output is determined.

Step 10: The output decoding mask are identified.

The basic overlap (AND) operation is governed by the following set of rules: (a) the overlap of transparent code and an input code leaves the input code unchanged, while the overlap of opaque code destroys all input code resulting in an opaque output. (b) The overlap of orthogonal codes results in opaque output. F is found to be orthogonal to all variables including it. (c) The overlap of any one of the codes of itself results in the same code. The overlap operations are represented by:

$$x \wedge T = x$$
$$x \wedge F = F$$
$$x \wedge x = x$$
$$V \wedge H = F$$
$$H \wedge V = F$$

Where ∧ indicates the overlap operation, and x may be any one of the codes T, F, V and H. It is to be noted that (a) F and T, and (b) H and V are complementary to each other. A complementary operation is represented by a bar overhead. Complementary pairs are also orthogonal since their overlap produces opaque output. However, while all complementary pairs are orthogonal, pairs are not complementary.

2.1 Half Adder:

The truth table for the trinary half adder is characterized in table 1. Let us consider two trinary input variables A and B, each represented by a 2 X 3 spatial matrix and a source plane characterized by a 3 X 2 matrix:

$$A = \begin{bmatrix} a_{11} & a_{12} & a_{13} \\ a_{21} & a_{22} & a_{23} \end{bmatrix}$$
$$B = \begin{bmatrix} b_{11} & b_{12} & b_{13} \\ b_{21} & b_{22} & b_{23} \end{bmatrix}$$
$$L = \begin{bmatrix} L_{11} & L_{12} \\ L_{21} & L_{22} \\ L_{31} & L_{32} \end{bmatrix}$$

The decoding mask, thus, would be represented by a 4 X 4 spatial matrix:

$$\begin{bmatrix} D_{11} & D_{12} & D_{13} & D_{14} \\ D_{21} & D_{22} & D_{23} & D_{24} \\ D_{31} & D_{32} & D_{33} & D_{34} \\ D_{41} & D_{42} & D_{43} & D_{44} \end{bmatrix}$$

Output pattern is detected at micro pixels say, D_{22} and D_{33}, if we are dealing with a combinational logic element having two outputs. It can be seen that the output pattern at D_{22} is produced from the overlap of L_{21}, L_{22}, L_{31}, and L_{32} with input pixel subcells {11}, {12}, {21}, and {22} respectively. Likewise at D_{33}, it is generated by the overlap of L_{11}, L_{12}, L_{21} and L_{22} with input pixel subcells {12}, {13}, {22}, and {23} respectively. This situation can be represented in terms of an equation called an input-output equation. For D_{22} and D_{33} respectively, we can write

$$L_{21} \wedge O_{11} + L_{22} \wedge O_{12} + L_{31} \wedge O_{21} + L_{32} \wedge O_{22} = D_{22} \ldots\ldots\ldots\ldots\ldots\ldots\ldots (1)$$
$$L_{11} \wedge O_{12} + L_{12} \wedge O_{13} + L_{21} \wedge O_{22} + L_{22} \wedge O_{23} = D_{33} \ldots\ldots\ldots\ldots\ldots\ldots\ldots (2)$$

Where, O_{ij} represents the overlap of the input pixel subcell, i.e. $O_{ij} = a_{ij} \wedge b_{ij}$

Sub cells a_{ij} and b_{ij} can be assigned any values from the POSC variables T, V, H, and F. In the same way, the LEDs in the source plane are also characterized by the POSC code variables. The overlap rules and algorithm summary are already given.

Table 1: Truth Table for Trinary Half-Adder

Condition number	A	B	S	C
1	0	0	0	0
2	0	1	1	0
3	1	0	1	0
4	2	1	0	1
5	1	2	0	1
6	1	1	2	0
7	0	2	2	0
8	2	0	2	0
9	2	2	1	1

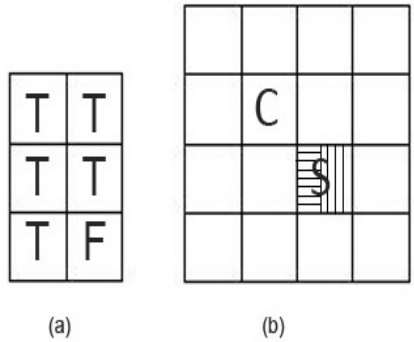

Figure 2: Trinary half-adder: (a) source plane and (b) decoding mask.

The sum and carry outputs are detected at micro pixels D_{33} and D_{22} respectively on the decoding mask. The projected trinary logical values 1 and 2 for the sum output are decoded by horizontally polarized (H) and vertically polarized (V) masks respectively i.e. by using a mixed polarized (HV) mask. The left half part of D_{33} would detect trinary logic 1 and the right half will decode trinary logic 2. As carry output does not involve trinary logic 2, the only true logical value is 1 that can be detected by a transparent mask; i.e. any transparent, vertically polarized and horizontally polarized input pixel projected at D_{22} would represent the true output and otherwise false output (F). The input-output equations for SUM (D_{33}) and CARRY (D_{22}) are given before. Using Eq. (1) and (2) the procedure starts by writing POSC logic equations, preferably obtaining more than one appropriately chosen true operation from a single pixel. If this causes any problem of emergence of some unwanted input condition or cross-decoding, some of the LEDs in the source plane can be polarized in such a way that cross-decoding does not occur.

Different grouping condition in different pixels, we can design different input coding scheme. The designs are described below.

Only one input pixel pattern was developed in 1991[2], which is shown below as design 1. We

developed three more new possible designs of input pixel pattern shown in design 2, design 3 and design 4.

Design 1: Introduced by R. A. Rizvi et al., 1991.

$$\overline{A} = \begin{bmatrix} F & F & F \\ F & V & H \end{bmatrix}; A = \begin{bmatrix} F & F & V \\ H & H & F \end{bmatrix};$$
$$\bar{\bar{A}} = \begin{bmatrix} H & H & F \\ F & F & V \end{bmatrix}$$
$$\overline{B} = \begin{bmatrix} F & F & F \\ F & H & V \end{bmatrix}; B = \begin{bmatrix} H & F & V \\ F & F & H \end{bmatrix};$$
$$\bar{\bar{B}} = \begin{bmatrix} F & H & F \\ H & V & F \end{bmatrix}$$
$$L = \begin{bmatrix} T & T \\ T & T \\ T & F \end{bmatrix}$$

Design 2: An alternate design of design 1.

$\overline{X_{ij}}$, X_{ij} and $\overline{\overline{X_{ij}}}$ respectively, represent trinary 0, 1 and 2 of the ijth pixel subcell of input X. POSC logic equations are written by grouping conditions 2 and 8 through pixel {13} ,

$$L_{12} \wedge [\overline{a_{13}} \wedge b_{13}] = H \ldots\ldots\ldots (3)$$
$$L_{12} \wedge [\overline{\overline{a_{13}}} \wedge \overline{b_{13}}] = V \ldots\ldots\ldots (4)$$

As both equations (3) and (4) have orthogonal logical output and L_{12} is common in both equations, it is kept unpolarized. Also, in both these equations, one of the inputs inside the brackets can be transparent and the other can be polarized, or both can be correspondingly polarized. We chose $\overline{a_{13}} = b_{13} = H$ and $\overline{\overline{a_{13}}} = \overline{b_{13}} = V$. Similarly for condition 3 and 7 through pixel {23},

$$L_{22} \wedge [a_{23} \wedge \overline{b_{23}}] = H \ldots\ldots\ldots (5)$$
$$L_{22} \wedge [\overline{a_{23}} \wedge \overline{\overline{b_{23}}}] = V \ldots\ldots\ldots (6)$$

Again, light source L_{22} is common to both equation (5) and (6), so it is assigned a transparent code and $a_{23} = \overline{b_{23}} = H$, $\overline{\overline{b_{23}}} = \overline{a_{23}} = V$. As we have more four empty pixels, conditions 4, 5, 6 and 9 are obtained through independent pixels. For condition 5 through pixel {11}, we have,

$$L_{21} \wedge [a_{11} \wedge \overline{\overline{b_{11}}}] = H \ldots\ldots\ldots (7)$$

As no other LED projects this pixel at D_{33}, we can keep L_{21} unpolarized and select $\overline{\overline{b_{11}}} = a_{11} = H$.The equation for condition 6 through pixel {22}, we have,

$$L_{21} \wedge [a_{22} \wedge b_{22}] = V \ldots\ldots\ldots (8)$$

L_{21} is already assigned a transparent code, hence,

$$a_{22} = b_{22} = V.$$

It can be noted that L_{32} also projects {22} at D_{22}, which is undesirable, therefore, we make L_{32} = F. In the same way we can satisfy the equation for condition 4 through pixel {21} and for condition 9 through pixel {12} respectively,

$$L_{31} \wedge [\overline{\overline{a_{21}}} \wedge b_{21}] = H \ldots\ldots\ldots (9)$$
$$[L_{11} + L_{22}] \wedge [\overline{\overline{a_{12}}} \wedge \overline{\overline{b_{12}}}] = H \ldots\ldots\ldots (10)$$

Now, from equation (9), we have, L_{31}=T as no other LED projects this pixel at D_{33}, and $\overline{\overline{a_{21}}} = b_{21} = H$. From equation (10), we have, $\overline{\overline{a_{12}}} = \overline{\overline{b_{12}}} = H$ and Since L_{22} is already unpolarized and L_{11} can be assigned a transparent or a horizontally polarized code, it is chosen to be unpolarized to keep the source plane unpolarized. The new half adder design is now complete. The coding scheme thus obtained is,

$$\overline{A} = \begin{bmatrix} F & F & H \\ F & F & V \end{bmatrix}; A = \begin{bmatrix} H & F & F \\ F & V & H \end{bmatrix};$$
$$\bar{\bar{A}} = \begin{bmatrix} F & H & V \\ H & F & F \end{bmatrix}$$
$$\overline{B} = \begin{bmatrix} F & F & V \\ F & F & H \end{bmatrix}; B = \begin{bmatrix} F & F & H \\ H & V & F \end{bmatrix};$$
$$\bar{\bar{B}} = \begin{bmatrix} H & H & F \\ F & F & V \end{bmatrix}$$
$$L = \begin{bmatrix} T & T \\ T & T \\ T & F \end{bmatrix}$$

By using same procedure two more possible input coding schemes are shown in design 3 and design 4.

Design 3: One more alternate design of design 1.

$$\overline{A} = \begin{bmatrix} F & F & V \\ F & F & H \end{bmatrix}; A = \begin{bmatrix} F & F & H \\ H & V & F \end{bmatrix};$$
$$\bar{\bar{A}} = \begin{bmatrix} H & H & F \\ F & F & V \end{bmatrix}$$
$$\overline{B} = \begin{bmatrix} F & F & H \\ F & F & V \end{bmatrix}; B = \begin{bmatrix} H & F & F \\ F & V & H \end{bmatrix};$$
$$\bar{\bar{B}} = \begin{bmatrix} F & H & V \\ H & F & F \end{bmatrix}$$
$$L = \begin{bmatrix} T & T \\ T & T \\ T & F \end{bmatrix}$$

Design 4: Yet another alternate design of design 1.

$$\overline{A} = \begin{bmatrix} F & F & F \\ F & H & V \end{bmatrix}; A = \begin{bmatrix} F & F & V \\ H & F & H \end{bmatrix};$$
$$\bar{\bar{A}} = \begin{bmatrix} H & H & F \\ F & V & F \end{bmatrix}$$
$$\overline{B} = \begin{bmatrix} F & F & F \\ F & V & H \end{bmatrix}; B = \begin{bmatrix} H & F & V \\ F & H & F \end{bmatrix};$$
$$\bar{\bar{B}} = \begin{bmatrix} F & H & F \\ H & F & V \end{bmatrix}$$
$$L = \begin{bmatrix} T & T \\ T & T \\ T & F \end{bmatrix}$$

The grouping condition of input pixel for design 2, design3 and design 4 are given in figure 3,

5	9	2,8

4	9	3,7

4	9	6

4	6	3,7

(a)

5	6	2,8

(b)

5	2,8	3,7

(c)

Figure 3: Input pixel grouping condition: (a) design 2, (b) design 3 and (c) design 4.

Design 2, 3 and 4 were nowhere introduced before. Here the light source in every design is kept constant (same pattern). Only input pixel patterns are changed. Also the output pixel position did not alter to make the output part compatible to each other. One might use this scheme for alternative output pixel position and make more alternate design for half adder. Multiple design schemes will help a designer to integrate larger complex design efficiently.

3. DISCUSSION

The POSC system is more versatile and flexible, since the polarization directions are considered. Moreover, the POSC system is suitable not only for the single-instruction multiple-data (SIMD) application but also for the multiple-instruction multiple-data (MIMD) applications. Implementation of trinary logic in a polarization encoded optical shadow casting scheme was designed for only one input pixel pattern. In this paper we used the same method to design three more possible schemes of input pixel pattern.These new schemes are more easy and efficient than previous design. The calculation of making new input coding schemes is very easy and simple. These different input coding schemes can be used in different applications and can be very helpful to design more complex logic units with more grouping conditions. There is a disadvantage in decoding mask with this method that is the horizontally polarized code and vertically polarized codes are detected by the same micro pixel. This can be minimized by using separate decoding output pixel for SUM outputs and have to consider different type of grouping condition which we did not use in this paper for different type of input coding scheme. The smallest design for half adder was published by A.A.S. Awwal et. el., 1987, which is not able to implement an integrated larger complex design because it may, requires alternative coding schemes for the complete functionality and faster computation as well as accurate result. Various alternate designs of input pixel array for this compact scheme is very difficult rather could be impossible. So using this new scheme such design problem is solved. A complex design may need many alternate half adder designs to complete the functionality and hence these new designs are the only solutions for the successful design of a large optical system. Although the input pattern size and light source increased by 50%, various design versions have increased by 300%, which is a significant advantage for this new scheme.

4. ACKNOWLEDGMENT

We would like to thank the faculty of Electrical and Electronic Engineering (EEE) department of Ahsanullah University of Science and Technology (AUST) to provide us all sufficient components and their kind help to make this work possible. We would like to thank Dr. Kazi Shariful Alam, Vice Chancellor, AUST and Professor Md. Abdur Rahim Mollah, Head of the department of EEE, AUST, for their support which has enabled us to complete our work.

REFERENCES

[1]. Y. Li, G. Eichmann, and R. R. Alfano, "Optical Computing Using Hybrid Encoding Shadow Casting," Appl. Opt. 25, 2036 (1986).

[2]. Tanida, J., & Ichioka, Y. (1983). Optical logic array processor using shadowgrams. J. Opt. Soc. Am. , 73 (6), 800-809.

[3]. M. A. Karim, A. A. S. Awwal, and A. K. Cherri, “Polarization Encoded Optical Shadow Casting Logic Units: Design,” Appl. Opt. 26, 2720 (1987).

[4]. A. A. S. Awwal, M. A. Karim, and A. K. Cherri, "Polarization- Encoded Optical Shadow-Casting Scheme: Design of Multi- Output Trinary Combinational Logic Units," Appl. Opt. 26,4814 (1987).

[5]. Rizvi, R. A., Zaheer, K., & Zubairy, M. S. (1991). Implementation of trinary logic in a polarization encoded optical shadow-casting scheme. Appl. Opt. , 30 (8), 936-941.

[6]. R. A. Rizvi, K. Zaheer, and M. S. Zubairy, "Separate and Simultaneous Generation of Multioutputs in a Polarization-Encoded Optical Shadow-Casting Scheme: Design of Half- and Full Adders and Subtractors," Appl. Opt. 27, 5176 (1988).

Proceeding of the
International Conference on Electrical, Computer and Telecommunication Engineering
01- 02 December 2012 (ICECTE2012), RUET, Rajshahi-6204, Bangladesh

ICECTE2012: PI- 0138

Microcontroller Based Remote Control of Home Appliances

Abu Farzan Mitul[1], Fida Hasan Md Rafi[1], Md. Manirul Islam[1], Mohiuddin Ahmad[1]
[1, 2] Department of Electrical & Electronic Engineering, Khulna University of Engineering & Technology
mitulnaya@yahoo.com, fidaeee@yahoo.com, mmislam@gmail.com

ABSTRACT
Automatic control of home appliances is highly demand now a day .In this work, we have designed, constructed a circuit which specially meet the requirement of control the home appliances through any remote control device that is portable within the periphery of the room. The device is able to control a load of high power rating from remote area. Any equipment can be made password protected through this device. The system works satisfactorily and it is also considered to be a cost effective system.

KEYWORDS: Microcontroller, password protected, home appliances, automatic control, cheap installation cost.

1. INTRODUCTION

In Bangladesh, control of home appliances using remote control is not a common phenomenon. But, with the advancement of technology, it is possible to develop an automatic control of home appliances in Bangladesh also in quite a reasonable cost. Not only that, this project work can be implemented to control industrial heavy loads from remote area. We are working for the development of the project so that automatic control system can be implemented in every spheres of our country at reduced cost.

Authors in [1] proposed an internet based wireless home automation system for multifunctional devices. This paper proposed a low cost and flexible web-based solution. Authors in [2] developed microcontroller based IR remote control signal decoder for home application. The authors only used Sony IR remote as IR remote transmitter. They used ATMEL AVR Atmega8 microcontroller as decoder. Authors in [3] developed a microcontroller based home security system. They designed an IR transmitter section for their work and in the receiver section, they used AT89C51 microcontroller for the work of protection. Compared to this work, we could make every equipment password protected to provide the security facility. Authors in [4] designed remote controlling of home appliances using mobile telephony. They have used X10 technology to carry out the control of home appliances. Authors in [5] developed a cell phone based remote control system to control home appliances and systems. They have used the GSM technology to control home appliances. Authors in [6] presented a design and implementation of SMS based control for monitoring systems. The paper had three modules involving sensing unit for monitoring the complex applications. A processing unit, that is microcontroller and a communication module that uses GPRS modem or cell phone via serial port RS-232. The SMS is used for status reporting such as power failure. Authors in [7] developed a microcontroller based home automation system with security. They have also used ATMEL`s AT89S52 microcontroller to control and security purpose. But, their overall system was not cost effective.

The main objectives of our proposed project are (i) To sense the existing status of the remote devices and obtain information in the display, (ii) To control the remotely operated devices using control signals, (iii) To take corrective action automatically as per requirement, and (iv)To protect the equipments from unwanted operations.

2. PROPOSED IDEA

The work consists of blocks namely IR transmitter, IR receiver, microcontroller as bit selector, level changer, and switch. IR sensor module receives the IR signal. The output of the IR receiver is not very high. So, an amplifier amplifies the signal to digital form 1 & 0 level. Now, the microcontroller stores the bit pattern of the IR transmitter and compares with pre-defined bit pattern.

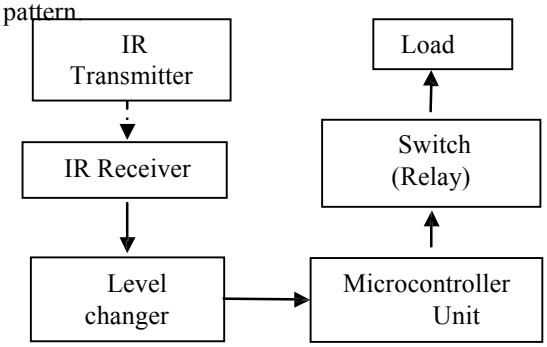

Fig. 1 Block diagram of our developed system.

The microcontroller will give decision to drive the specific load.

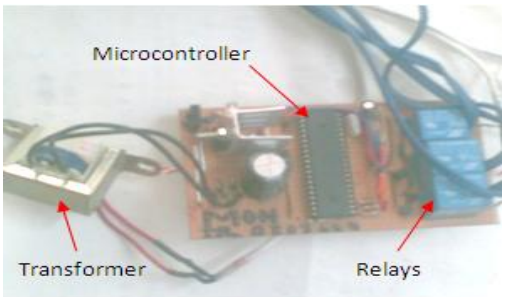

Fig. 2 Pictorial view of our developed system.

3. DESIGN OF HARDWARE

3.1 IR Remote Transmitter

In present system, we have used universal TV remote. Every remote has its own protocol. But, one of the biggest advantages of using universal remote controller is that it can learn of brand new remote controllers, which did not exist yet while the universal remote was created. The specialty of our project is that, any remote can be used to drive different loads. But, the condition is bit pattern of the specific remote should be stored in the microcontroller. Microcontroller stores the bit pattern for specific buttons of remote and finally, it just compares with the pre-defined bit pattern to drive the load. We have already taken Sony, Phillips and other remotes in our analysis and in all the cases; we have found quite satisfactory results to drive different loads.

3.1.1 Sony SIRC protocol

In the project, we have used IR remote switch which uses 12-bit SIRC protocol as shown in Fig. 3. The code starts with a header of 2.4ms followed by 7-bit command and 5-bit device address in which least significant bits (LSB) are transmitted first. Then the commands are repeated every 45ms for as long as the key on the remote control is held down. The address and commands exist of logical ones and zeros. A space of 600µs or 1Tand a pulse of 1200 µs or 2T form logical one. A logical zero is formed by a space of 600 µs and a pulse of 600 µs as shown in Fig. 4 [10].

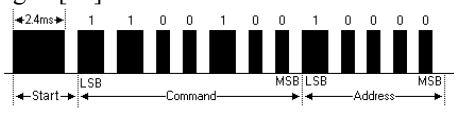

Fig. 3 12-bit SIRC protocol.

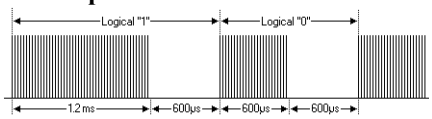

Fig. 4 IR transmitter protocol (Sony).

3.1.2 Philips RC-5

5 bits is used as address and 6 bit is used as command length. The coding technique of this remote control is Bi-phase coding. Carrier frequency is of 36 KHz. Constant bit time is1.778ms. The typical pulse train of RC-5 message is illustrated in **Fig. 5**. And the IR transmitter protocol is shown in **Fig. 6** [11].

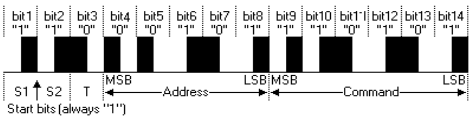

Fig. 5 Pulse train of RC-5 message.

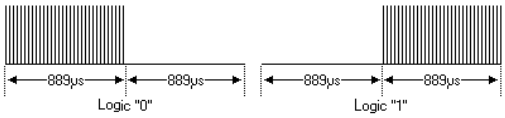

Fig. 6 IR transmitter protocol (Phillips).

3.2 Microcontroller as a Bit Selector

The system circuit diagram shown in Fig. 7 has been designed around the ATMEL 89C52 microcontroller [8]. It consists of the arithmetic and the logic unit, I/O Unit, control unit and other various components. Microcontrollers are designed in a single chip, which typically includes a microprocessor, certain byte of R/W memory, from 1K to 2K bytes of ROM, and several signal lines to connect I/O lines. We have used ATMEL 89C52 microcontroller in our project.

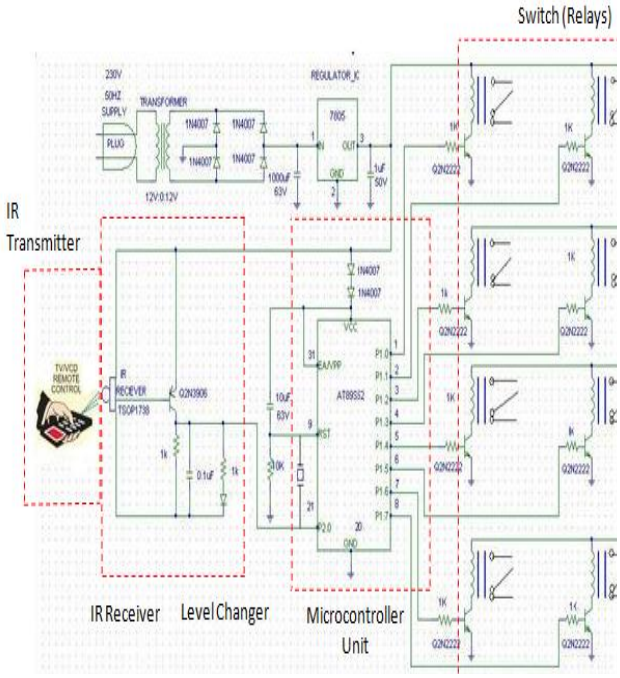

Fig. 7 Experimental setup of the system.

One of the 8051 based microcontrollers is the most popular and widely used chip named as AT89C51. But because of the higher size of ROM as well as RAM needed in our project, we have used AT89C52, which consists of 8KB of ROM and 256 bytes of RAM. The AT89C52 provides the following standard features timer/counter, five vector interrupt architecture with two levels, full duplex serial port, on-chip oscillator and clock circuitry, In addition, the AT89C52 is designed with static logic for operation down to zero frequency and supports two software selectable power saving modes [8]. These features of ATMEL 89C52 make the project a low cost, efficient and reliable. In our project, we have used crystal oscillator of 12 MHz for the proper operation of the device. TSOP-1738 receiver module is used to receive the IR signal from transmitter. When any IR signal is transmitted, microcontroller matches the transmitted bit pattern with the pre-defined bit pattern. In our present system, 12v:0v:12v transformer & IC-7805 are used to bias the microcontroller. Thus, it remains connected with the AC mains.

3.3 Switch

Microcontroller will give the decision about which load has to be driven depending on the pressed button from remote. Any load of any power rating can be driven using this project. In case of load of high power rating, the relay switch has to be changed.

4. SOFTWARE PART

The operation of MCU is written in embedded-C language. In **Fig. 8**, the basic flow chart of the system software is shown.

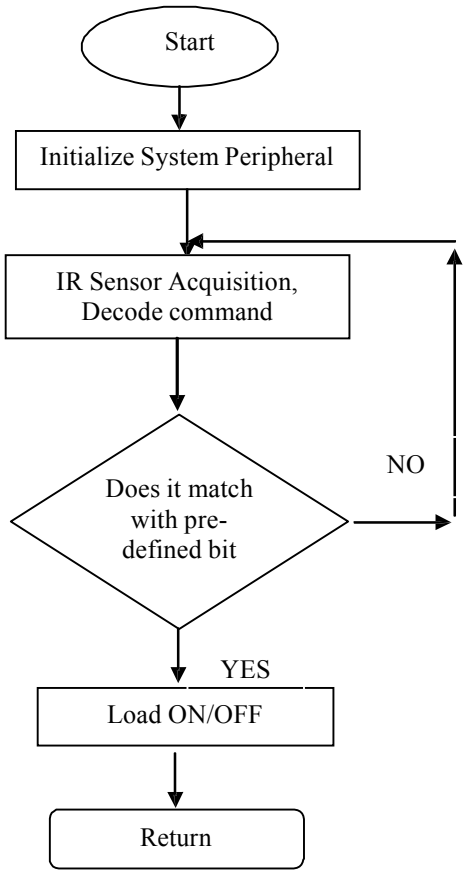

Fig. 8 Flow chart of proposed system.

When the device is powered –up, the initialization part of the device software biases various on-chip peripherals such as interrupts, port, timer etc.

5. REAL SYSTEM ANALYSIS

This simulation architecture is used for driving several loads using remote control. In our work, as a part of trial, we implemented our project to drive a tube light, fan and multi-plug. Using multi-plug, we were able to drive various loads (rated: 230v (50 Hz), 5A).

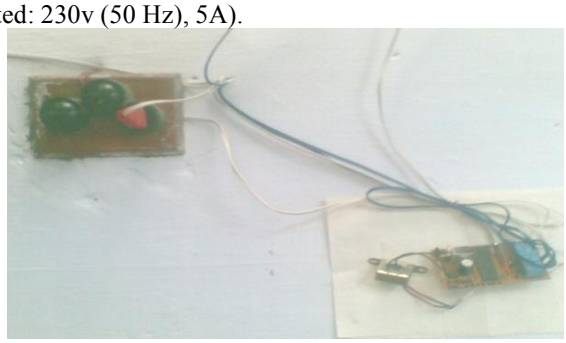

Fig. 9 Experimental analysis of the project

Meanwhile, we have increased load driving capability from 3 to 8 by changing the program in microcontroller. To drive loads of 1 MW, we just changed the relay configurations. So, to drive loads of several MW, the project does not depend on the rating of power. Rather, changes in relay configurations make the project possible to drive loads of any power ratings.

A part from these, we have also fixed a display board on the project to provide timer facility for driving different loads. Using this timer facility, we can fix a specific time (say 15 min, 30 min etc.) for which the load will remain on/off. If anyone wants to drive a load at a particular time, then the person can do it using the timer facility through the remote control. In short, load on/off can be made fully time dependent through this project using the remote control.

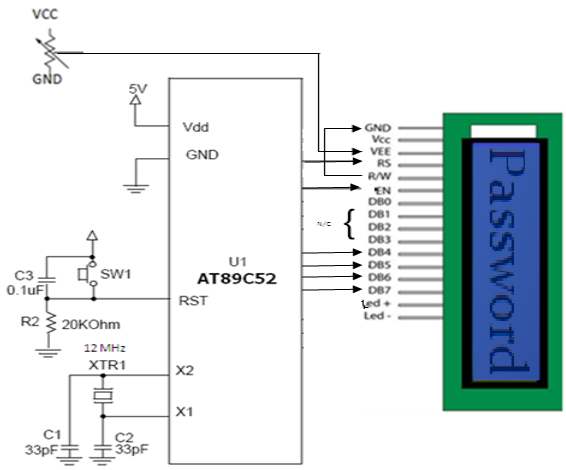

Fig. 10 Microcontroller interfaced with 16×2 LCD.

Our project can also protect any equipment to turn on/off instantaneously. If any user wants to make his equipment password protected, then he just needs to ON the password protection option through the display board (LCD). The user can specify any password for his equipment. In this case, other user will not be able to turn ON the equipment without knowing the password. Now, if the user wants to withdraw the password protection option, then he can also do the same.

6. RESULT AND ANALYSIS

6.1 Proper Decoding

IR receiver could decode transmitted IR signal for the operation of microcontroller. Load on/off is tested about 100 times using the remote control. Due to different bit pattern in different buttons make the circuit possible to switch to different loads.

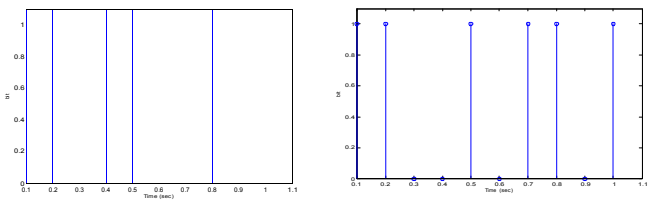

Fig. 11 Bit pattern of button 1 (left) & 6 (right).

Similar bit pattern simulations for different buttons shows, how microcontroller is able to differentiate the transmitted IR signal to drive different loads.

6.2 Life Time

The project is able to drive a load without any kind of damage for about 2 years. The performance of the device is quite satisfactory. It is desirable that it can work properly for any kind of loads of any power ratings quite satisfactorily.

6.3 Password Protection

The project is tested to verify its protection ability and it is found that, in every case, the microcontroller grants access only for the right password. In case of wrong password, the project does not response. These results have proved password protection ability of our project.

6.4 The Project in Perspective of Bangladesh

The cost required for the implementation of the project is estimated. The estimated cost is shown in **Table 1**.

Table 1 Total Cost of the overall project implementation

Name of component	Number (pieces)	Cost in Tk
Microcontroller	01	90.00
Crystal oscillator	01	10.00
Remote controller	01	120.00
Transformer	01	90.00
Diode	04	6.00
IR receiver	01	25.00
IC Regulator	01	20.00
Heat sink	01	50.00
Capacitor	03	24.00
Transistor	10	100.00
Relay	08	240.00
R & Variable R	23	23.00
LCD display	01	240.00
PCB and wires		50.00
Total		=1115.00 =USD 14 (app.)

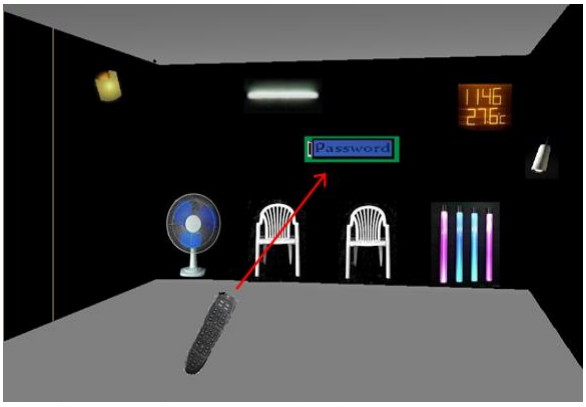

Fig. 12 Plan of implemetation in a room.

In **Fig. 12**, we can see the design of the work in a room. Our purpose is to take control over every equipments of a room.

7. CONCLUSION

In our work, we tried to develop an automatic control system which is not dependent on the power rating if the load. Timer facility of the project provides an extra advantage to the user. Timer facility allows the user to on/off the load for any specific time. Our target is to develop an automatic control system for home appliances where the project will be able to decide to turn off all the loads after leaving the room. In this project, the user can be able to get the security facility. For example, in case of fire in house, the security system will provide an alarm. Not only that, other security facility can also be included in our project.

8. FUTURE WORK

In near future, automation will cover every industries and homes for driving different loads and facilitate the livelihood of human being.

9. ACKNOWLEDGEMENTS

Special Thanks to Dr. Mohiuddin Ahmad for his supervision on this project.

REFERENCES

[1] A. Z. Alkar, U. Buhur, "An Internet Based Wireless Home Automation System for Multifunctional Devices," *IEEE Consumer Electronics*, vol. 51, no. 4, pp. 1169-1174, 2005.

[2] G. S. Nhivekar and R.R.Mudholkar, "Microcontroller Based IR Remote Control Signal Decoder for Home Application", *Advances in Applied Science Research*, vol. 2 no. 4, pp. 410-416, 2011.

[3] http://www.123eng.com/projects/microcontroller_based_home_security_project.html, *Web.*

[4] R. Shahriyar, E. Hoque, S. M. Sohan, I. Naim, M. M. Akbar, and M. K. Khan, "Remote Controlling of Home Appliances using Mobile Telephony", *International Journal of Smart Home*, Vol. 2, No. 3, July, 2008.

[5] C. K. Das, M. Sanaullah, H. M. G. Sarower and M. M. Hassan, "Development of a cell phone based remote control system: an effective switching system for controlling home and office appliances", *International Journal of Electrical & Computer Sciences IJECS*, Vol. 9, No. 10, pp. 37-43, 2009.

[6] M. S. H. Khiyal, A. Khan, and E. Shehzadi, "SMS Based Wireless Home Appliance Control System (HACS) for Automating Appliances and Security", *Issues in Informing Science and Information Technology*, vol. 9, pp. 887-894, 2009.

[7] I. Kaur, "Microcontroller Based Home Automation SystemWith Security", *International Journal of Advanced Computer Science and Applications (IJACSA)* ,Vol. 1, No. 6, December 2010.

[8] www.atmel.com

[9] Bergmans S., Oisterwijk, Sony SIRC Protocol [online].

[10] http://www.sbprojects.com/knowledge/ir/rc5.php.

Proceeding of the
International Conference on Electrical, Computer and Telecommunication Engineering
01- 02 December 2012 (ICECTE2012), RUET, Rajshahi-6204, Bangladesh
ICECTE2012: PI-0139

Microcontroller Operated Intelligent Vehicle using Artificial Neural Networks

Md. Rabiul Islam[1], Rizoan Toufiq[1], Md. Nahid Hasan[1] and M. Abdul Goffar Khan[2]*
[1]Department of Computer Science & Engineering
Rajshahi University of Engineering & Technology, Rajshahi-6204, Bangladesh
[2]Department of Electrical & Electronic Engineering
Rajshahi University of Engineering & Technology, Bangladesh
.E-mail: rabiul_cse@yahoo.com, rizoantoufiq@yahoo.com, nahid_043019@yahoo.co.in, agmagk@gmail.com

ABSTRACT
In this paper, a microcontroller operated intelligent motor has been developed which can be maintained itself automatically by observing road arrows. Error back-propagation neural networks algorithm has been used to provide intelligence for the motor. High resolution digital camera has been used to capture the road side arrow images and different image pre-processing techniques have been applied to process those images. To reduce or eliminate the noises from the captured image, filtering technique has been adopted and feature extraction technique has been used to extract the features. Principal component analysis technique has been applied to reduce the dimensionality of the feature vector. The extracted image features are then fed into the neural network for learning. The recognition of unknown road arrow image is then performed by comparing this unknown pattern to the pattern for which an image module is already built. Experimental results and performance analysis shows the superiority of the system with various dimensions.

KEY WORDS: Microcontroller Operated Intelligent Vehicle, Artificial Neural Networks, Image Pre-processing, Feature Extraction, Pattern Classification.

1. INTRODUCTION

The use of power electronics for the control of electric machines offers not only better performance caused by precise control and fast response but also maintenance and ease of implementation [1]. In parallel with the advance in power electronic there have been great advances in microcontroller based control systems due to the microcontroller flexibility and versatility [2].

In this system, digital camera has been placed on the motor car. The motor car will move automatically to capture road side arrow images and make decisions according to the learned image which has already been developed by Back-propagation learning neural networks algorithm. Three different types of arrow images have been used for learning and various noises have been added to those arrow images to measure the performance of the system.

2. HARDWARE REQUIREMENTS AND CIRCUIT CONNECTIONS FOR THE MICROCONTROLLER OPERATED SYSTEM

To operate the motor, a microcontroller, voltage level converter chip and high current driving transistor are required. PIC16F628A microcontroller has been used to provide USART interface for the car circuit and external crystal facility connection for high baud rate [3]-[5]. The microcontroller is equipped with various ports which can be used as control logic output an interfacing to USART. Fig. 1 and Fig. 2 show the pin configuration and internal block diagram of PIC16F628A microcontroller respectively.

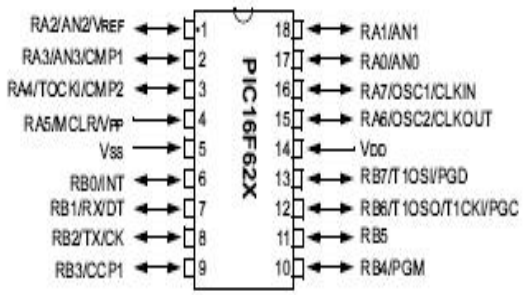

Fig. 1 Pin configuration of PIC16F628A [6].

The following sub-section focuses the configuration techniques of the microcontroller, data transmission algorithm, data reception algorithm and controlling and driving circuits for motor.

2.1 Data Transmission and Reception Circuits

For data transmission and reception, asynchronous data transfer mode has been used here where the USART uses standard non-return to zero (NRZ) format (one START bit, eight or nine data bits and one STOP bit). The most common data format is 8 bits. A dedicated 8-bit baud rate generator is used to derive baud rate frequencies from the oscillator. The USART's transmitter and receiver are functionally independent but use the same data format and baud rate. Data transmission and reception circuits are shown in Fig. 3 and Fig. 4.

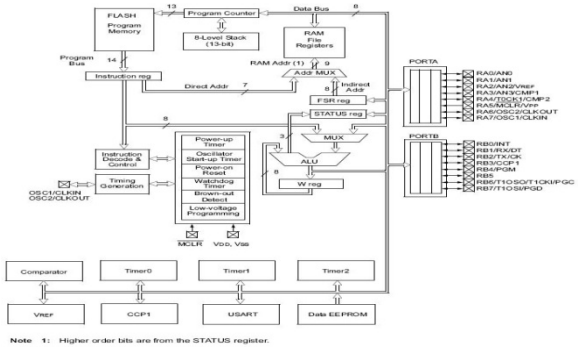

Fig. 2 Block diagram of PIC16F628A [6].

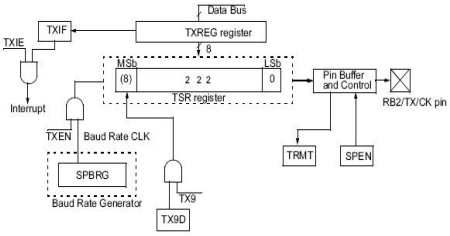

Fig. 3 Data transmission circuitry.

2.2 Controlling and Motor Driving Circuits

Data are sent to the microcontroller of the car through serial port. According to the captured data, microcontroller takes decision for movement. Logic control circuit schematic of microcontroller is shown in Fig. 5.

Motor drive circuit schematic is shown in Fig. 6 where two push-pull configurations is used to drive both clockwise and anticlockwise direction. Inverting buffers are used to drive the bases of motor drive transistor. Fig. 7 is used for distributing voltage and current to various circuit units.

3. IMAGE PRE-PROCESSING AND FEATURE EXTRACTION

In image pre-processing phase, images are converted from true colour RGB image to gray scale intensity image. Then edges from the images are detected by using canny mask. The next sub-sections will focus the image pr-processing parts of the system.

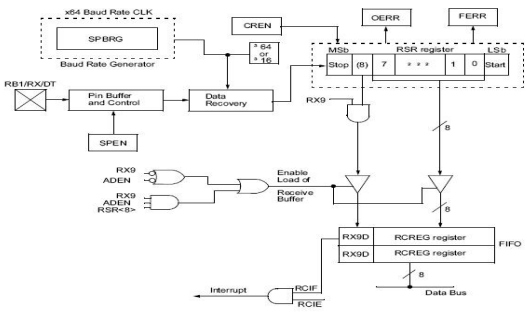

Fig. 4 Data reception circuitry.

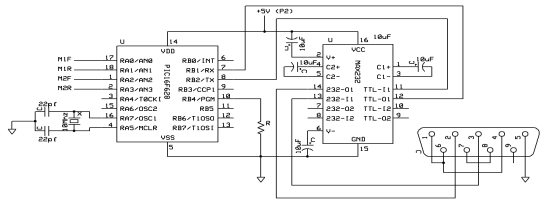

Fig. 5 Car control logic circuit schematic.

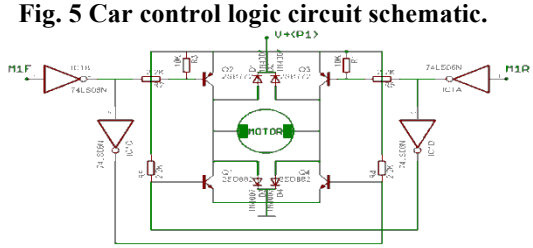

Fig. 6 Motor driving circuit.

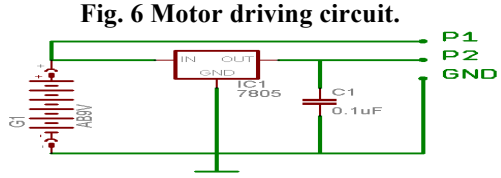

Fig. 7 Power distribution circuit.

3.1 Conversion from RGB Image to Grayscale Image

Greyscale image is also known as an intensity or gray level image whose pixel values specify intensity values. A true colour image is an image in which each pixel is specified by three values one each for the red, blue, and green components of the pixel scalar [7]. The conversion from RGB image to gray scale image can be expressed as following,

$$I(x,y) = T[f(x,y)] \tag{1}$$

Where *f(x,y)* is a color input image, *g(x,y)* is the transformed or processed grayscale output image and *T* represents an operation on a spatial neighbourhood of *(x,y)* [8]. There are different types of transformation, one is the lightness method where average the most prominent and least prominent colours:

$$I(x,y) = \frac{\max[f_R(x,y), f_g(x,y), f_b(x,y)] + \cdot\cdot \max[f_R(x,y), f_g(x,y), f_b(x,y)]}{2} \tag{2}$$

Where $f_r(x,y)$ is the intensity of the pixel *(x,y)* in the red channel, $f_g(x,y)$ is the intensity of pixel *(x,y)* in the green channel, and $f_b(x,y)$ is the intensity of pixel *(x,y)* in the blue channel. Another transformation is the average method that is,

$$I(x,y) = \frac{f_R(x,y) + f_g(x,y) + f_b(x,y)}{3} \tag{3}$$

In this paper, we used luminosity method which is a more sophisticated version of the average method [3]-[4],

$$I(x,y) = 0.2989\, f_R(x,y) + 0.5870\, f_g(x,y) + 0.1140\, f_b(x,y) \tag{4}$$

The resultant image is shown in Fig. 8.

(a) (b)

Fig. 8 Conversion form RGB image to grayscale image (a) RGB image (b) Grayscale image.

3.2 Dimensionality Reduction and Feature Extraction

To reduce the dimension Principal Component Analysis method has been used in this work. Let, *I(x,y)* represents an image of $M \times N$ dimension. We have L images which can be represented L number of $MN \times 1$ vector images i.e. $\Gamma_1, \Gamma_2 ... \Gamma_L$. So, the average face vector,

$$\Psi = \frac{1}{L} \sum_{i=1}^{L} \Gamma_i \tag{5}$$

The deviation image vector,

$$\Phi_i = \Gamma_i - \Psi \tag{6}$$

$$A = \lfloor \Phi_1 \quad \Phi_2 \quad .... \quad \Phi_L \rfloor \tag{7}$$

The covariance matrix of A can be calculated as follows:

$$C = AA^T \tag{8}$$

The dimension of C is $MN \times MN$. Fortunately, we can solve for the MN dimensional eigenvectors in this case by first solving for the eigenvectors of an L by L matrix and then taking appropriate linear combinations of the face images Φ_i. Consider the eigenvectors v_i of A^TA, such that

$$A^T A v_i = \mu_i v_i \tag{9}$$

$$AA^T A v_i = \mu_i A v_i \tag{10}$$

From which, we see that Av_i are the eigenvectors of $C = AA^T$. Following this analysis, we construct L by L matrix $Y = A^TA$ where, $Y_{mn} = \Phi_m^T \Phi_n$ and find the L eigenvectors, v_l of Y. These vectors determine linear combinations of the L training set face images to form the eigenfaces μ_l,

$$\mu_l = \sum_{k=1}^{L} v_{lk} \Phi_k, \quad l = 1,2..., L \tag{11}$$

Here, the image dimension has been reduced to $L \times L$ dimensions [9]-[11].

4. CLASSIFICATION TECHNIQUES WITH BACK-PROPAGATION NEURAL NETWORKS ALGORITHM

In recent, Back-propagation neural network algorithm has been widely used for classification of pattern. An ANN that is found to be useful in addressing problems requiring recognition of complex patterns and performing nontrivial mapping functions is the back-propagation network [12]. In this work, we used back-propagation algorithm to classify the arrow images. In recognition stage, vehicles determine the way to move based on the current input arrow image and the classified learned pattern.

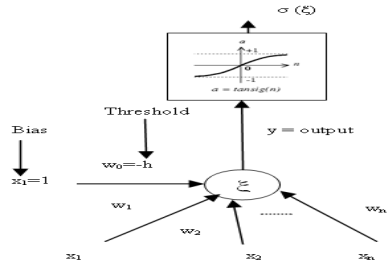

Fig. 9 Model of the neuron.

A neuron computes the weighted sum of its n input signal, x_i, $I = 0, 1, 2 \ldots n$ and generates an output based on the tan sigmoid function where the threshold values is h. The output of the neuron in hidden layer or output layer is calculated as follows:

$$\xi = \sum_{i=0}^{n} w_i x_i \qquad i = 0,1,2...n \tag{12}$$

$$\sigma(\xi) = \frac{2}{(1 + e^{(-2\xi)})^{-1}} \tag{13}$$

The error is calculated as the difference between the target output and the network actual output. The goal is to minimize the average of the sum of these errors.

$$mse = \frac{1}{M} \sum_{k=1}^{M} e(k)^2 = \frac{1}{M} \sum_{k=1}^{M} (t(k) - \sigma(k))^2 \tag{14}$$

Here, *mse* means mean square error, *t(k)* represents the target output and *σ(k)* represents the network output. The weights and bias values are updated based on the equation,

$$w_i(t+1) = w_i(t) + \eta \times mse \times x_i \tag{15}$$

Here, η $(0.0<\eta<1.0)$ is the gain term (i.e. step size) and t is the iteration number [13].

5. EXPERIMENT RESULTS AND PERFORMANCE ANALYSIS

The performances of the system depend on two different levels, one is microcontroller based hardware system and another is the pattern recognition stage. We have used Back-propagation neural network algorithm to train and classify the input arrow images. The training performance of the algorithm is given the Fig.10.

To measure the performance of the system, four different groups of images have been used in this system. First group contains the noise free images which are typically called Env-I. Second group contains blurred images namely Env-II, some additional lines have been added with the arrows in third group (called Env-III) and finally in group four (i.e. Env-IV), edges are broken down in some places. Env-I group image has been used for learning because this group contains noise free images. Some

sample images of different group are shown in Fig. 11.

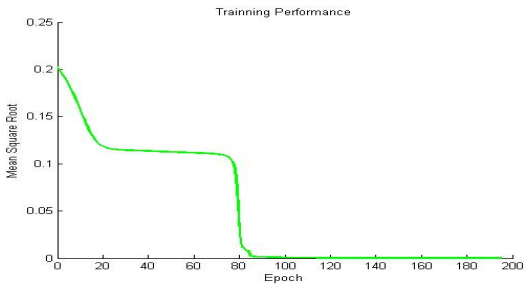

Fig. 10 Performance of the trained back-propagation neural network.

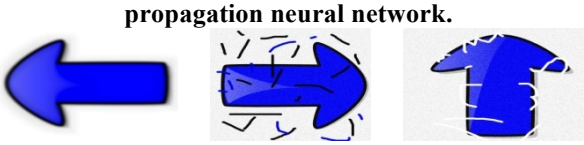

(a) (b) (c)

Fig. 11 Sample images of group (a) Env-II, (b) Env-III and (c) Env-IV.

According to four different groups, the recognition rate of the system is shown in table Table 1 and graphically in Fig. 12.

T able 1 Performance of the system

Group	Number of test images	Number of correctly recognized images	Recognition rate (in %)
Env-I	3	3	100%
Env-II	18	18	100%
Env-III	18	18	100%
Env-IV	9	8	88.89%

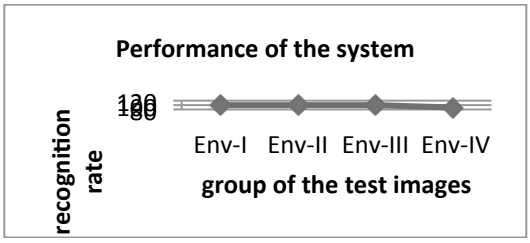

Fig. 12 Performance of the system.

6. CONCLUSIONS AND OBSERVATIONS

In this paper, a microcontroller operated intelligent motor has been developed where four different types of road side arrow images have been used to measure the performance of this system. To focus the superiority of this system, various noises is added to measure the performance of the system and get sound performance which is shown in Table 1. Though four different arrow images have been used, actually in road side there are various types of arrow images exists. As a result this system can be learned and tested with other types of arrow images with hybrid intelligence techniques.

REFERENCES

[1]. Singh Shilpi Ramprasad and V.S.Nandanwar, "Design and Implementation of Performance Monitoring of DC Motor Based on Microcontroller and Temperature Control of Heat Sink", *International Conference on Advanced Computing, Communication and Networks'11"*, pp. 158-160, 2011.

[2]. T.Castabnet and J. Nicolai, "Digital Control for Brush DC Motor", *IEEE Transaction on Industry Application*, Vol, 30, No 4, July-August 1998.

[3]. AT89C Series Hardware Description (Atmel Corporation), http://www.csd.uoc.gr/~hy325/spring2006/docs/doc0499.pdf

[4]. Microcontroller Based System Design, http://www.tuxmaniac.com/work/abstracts/uCTrainerKit.pdf

[5]. Application Note AP-155, *Oscillators for Microcontrollers*, 1983. (Intel Corporation), http://ecewww.colorado.edu/~mcclurel/iap155.pdf

[6]. *PIC Microcontroller Instruction Sets, PIC16F628 Datasheet.*

[7]. Tarun Kuma, Karun Verma, "A Theory Based on Conversion of RGB image to Gray image", *International Journal of Computer Applications (0975 – 8887),* Vol.7, No.2, September 2010.

[8]. Rafael C. Gonzalez and Richard E Woods, "*Digital Image Processing*", Second edition, Prentic Hall, 2002.

[9]. Matthew Turk and Alex Pentland, "Eigenfaces for Recognition", *Journal of Cognitive Neuroscience* Vol. 3, No. 1, Massacbusetts Institute of Technology,1991.

[10]. Matthew Turk and Alex Pentland, "Face Recognition Using Eigenfaces, Vision And Modeling Group", *The Media Laboratory, Massachusetts Institute of Technology*, CVPR'91.

[11]. Jon Shlens, "A Tutorial on Principal Component Analysis, Derivation, Discussion and Singular Value Decomposition", Version 1, 25 March, 2003.

[12]. James A. Freeman, David M. Skapura, "*Neural Networks, Algorithms, applications and Programming Techniques*", Addison-Wesley Pub (Sd), June, 1991.

[13]. Anil K. Jain, Jianchang Mao, K. Mohiuddin, "Artificial Neural Networks: A Tutorial", *IEEE Computer Special Issue on Neural Computing*, March, 1996.

Proceeding of the
International Conference on Electrical, Computer and Telecommunication Engineering
01- 02 December 2012 (ICECTE2012), RUET, Rajshahi-6204, Bangladesh

ICECTE2012: PI-0142

Microcontroller Based DC Motor Speed Control Using PWM Technique

Md. Kamruzzaman Russel[1], Muhibul Haque Bhuyan[2]
[1]Department of Electrical and Electronic Engineering, Daffodil International University, Dhaka, Bangladesh
[2]Department of Electrical and Electronic Engineering, Green University of Bangladesh, Dhaka, Bangladesh
E-mail: russel_eee@ymail.com, muhibulhb@gmail.com

ABSTRACT
This paper reports a microcontroller based control system to change the speed and direction of rotation of DC motor. Armature voltage is varied by pulse width modulation (PWM) of input DC voltage by using the developed microcontroller's program. Thus the speed of the DC motor is changed. Direction of rotation of DC motor is changed by initiating an interrupt signal to the microcontroller using push switches. To drive the DC motor, a four channel monolithic integrated buffer circuit was used. PCB of the control circuit has also been designed and fabricated. Test data shows very good agreement with the expected results.

KEY WORDS: Microcontroller, DC motor speed, PWM signal.

1. INTRODUCTION

DC motors are being used in many control systems now a days [1-3]. For the fractional horsepower and variable speed drive systems, DC motor is a good choice. Because, torque of DC motor is also quite high and its speed regulation is very low. Development of rare earth magnet advances in brush commutator technology and advanced manufacturing techniques of the Permanent Magnet (PM) dc motor with ironized rotor and rotor with very low inertia extends its use in several types of control system [4].

With the development of technology, microcontroller is becoming more suitable chip to control various electro-mechanical devices [5-6]. Microcontrollers are used in automatically controlled products and devices. By reducing the size and cost, microcontrollers make it economical to digitally control even more devices and processes [7].

To obtain variable speed of DC motor, usually armature voltage and field currents are varied. But the range of speed variation is good if armature voltage can be varied. To get variable DC voltage chopper or PWM circuit can be used. PWM is routinely used to control the speed of DC motors. But designing and implementing the chopper or PWM circuit is very cumbersome [8-10].

This paper reports a microcontroller based control system to change the speed and direction of rotation of DC motor. Armature voltage is varied by pulse width modulation (PWM) of DC input voltage by using the microcontroller that sends the signals at the microcontroller's PWM terminal. Thus the speed of the DC motor is changed. Direction of rotation of DC motor is changed by switching the signals at armature terminals of the DC motor by initiating an interrupt signal to the microcontroller. Hardware implementation was done using an 8 bit ATmega16 microcontroller and its software was written in C language using the AVR Butterfly that makes the hex file to be sent to the microcontroller by the Ponyprog software through the ISP port (DB 25) [11]. Since its output current is very low, a four channel monolithic integrated buffer circuit (L293) was used. This IC is capable of handling high voltage and high current and of driving the inductive loads. A separate DC power supply unit was also designed for the various ICs of the system. PCB of the control circuit has also been designed using Proteus software and then the PCB was fabricated. Finally, the designed circuit was tested by controlling the DC motor and results are recorded for various speeds. Measured data show very good agreement with the expected output.

2. HARDWARE SYSTEM DESIGN

The block diagram of the microcontroller based display system is shown in Fig. 1. It has four units, such as, a control unit, a driver unit, a DC power supply unit and a switching unit. The control unit part consists of an 8 bit ATmega16 microcontroller [12]. Its function is to get input signals from the different switches of the switching unit (SW0, SW1 and SW2) through its interrupt inputs (PB0, PB1 and PB2) respectively and then to send the appropriate output ports (PC0, PC1 and PD5). Ports PB0 and PB1 are used to increase and decrease the duty cycle of the output DC signals respectively while port PB2 is used to change the direction of rotation. Ports PC0 and PC1 are used to send the signals for the two terminals of the DC motor depending on the signal at port PD5. Port PD5 is connected to the driver IC's

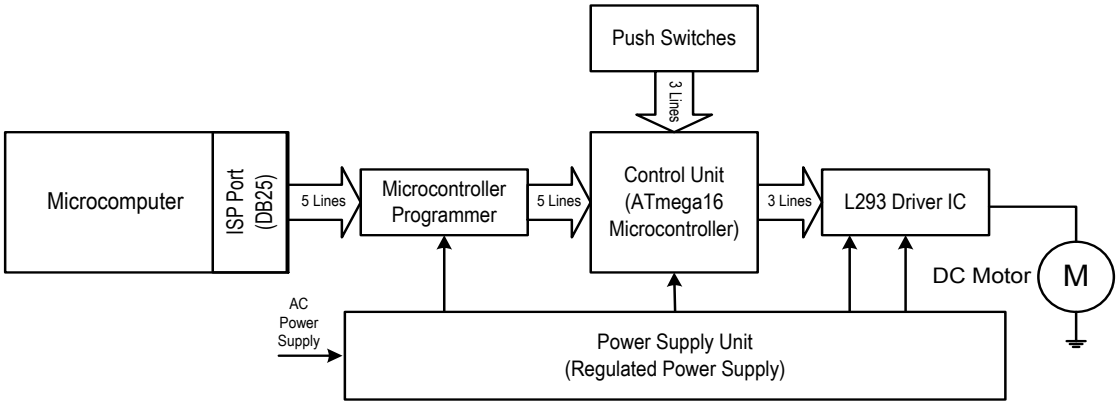

Fig. 1 Block Diagram of the DC Motor's Speed Control System

EN input. When SW0 or SW1 are pressed then microcontroller sends an appropriate signal to the port PD5 so that the duty cycle of the chopped output at the ports PC0 or PC1 can be increased or decreased respectively. DC motor's rated voltage, current, power and speed are 200 V, 1.5 A, 300 W and 1500 rpm respectively.

For the driver unit, a push-pull type four channel driver IC (L293) was used [13]. This is a monolithic integrated high voltage, high current driver designed to accept standard DTL or TTL logic levels and drive inductive loads (such as, relays, solenoids, DC and stepping motors) and switching power transistors. To simplify use as two bridges each pair of channels is equipped with an enable input. A separate supply input is provided for the logic, allowing operation at a lower voltage and internal clamp diodes are included. This device is suitable for use in switching applications at frequencies up to 5 kHz. Each of its output channels has the current capability up to 600 mA. It has enable (EN) facility.

The power supply unit is designed by using a step down transformer, bridge rectifier, capacitors and regulated power supply ICs of 7805 and 7812 to get the DC voltages of 5 V and 12 V respectively [14].

The switching unit has three push type switches (SW0, SW1 and SW2) to send inputs or interrupts to the microcontroller's PB0, PB1 and PB2 ports respectively.

The complete circuit diagram drawn using Proteus software is shown in Fig. 2. Finally, the PCB was designed using Proteus software and implemented on the copper board but it is not shown here for brevity.

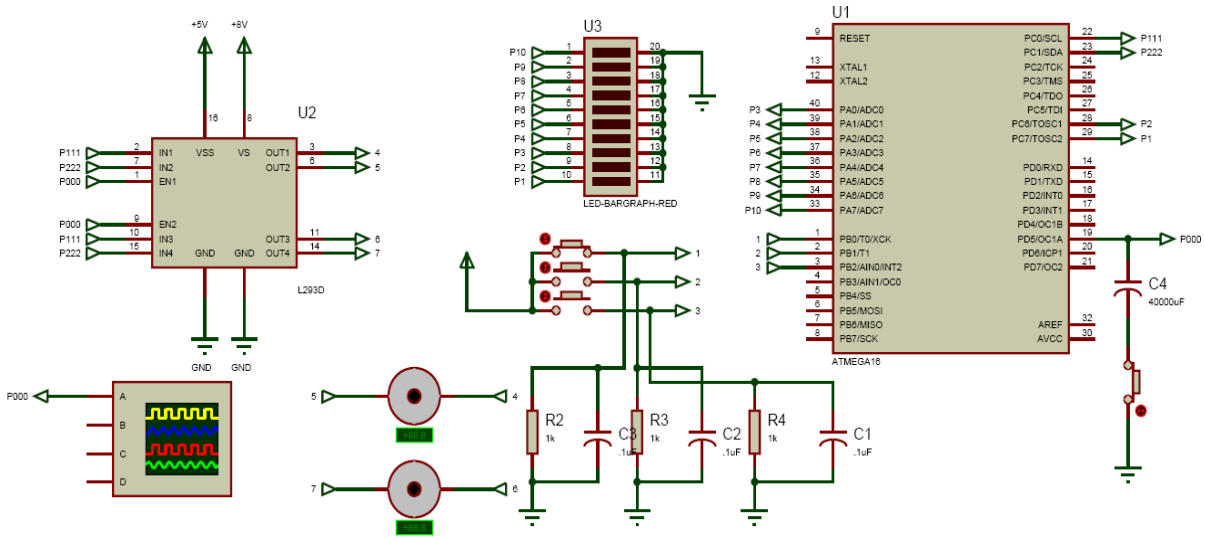

Fig. 2 Circuit Diagram of the contol system

3. SOFTWARE DEVELOPMENT

The program is developed for the microcontroller using the WinAVR Butterfly software [15] in C language, then debugged and edited as required and finally the hex codes are generated using a microcomputer. The hex codes of the developed program are sent to the microcontroller through the parallel port (DB25) of the microcomputer by the Ponyprog software. Parallel port was connected to the miso, mosi, ack, reset and gnd terminals of ATmega16 microcontroller. The ISP Programmer was also developed specially for this work to download the hex codes to the microcontroller.

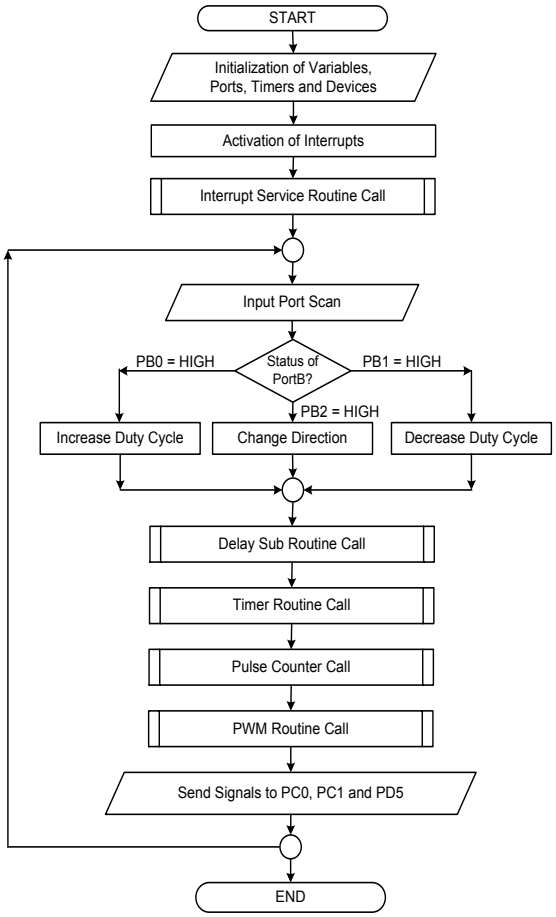

Fig. 3 Flow chart of the program

C is a general-purpose programming language that can work on any microprocessor that has a C compiler written for it. C abstracts the concepts of what a computer does and provides a text based logical and readable way to get computers to do what computers do. WinAVR is a set of tools for C programming. The AVR microcontroller family is a suite of executable, open source software development tools for the ATMEL AVR series of RISC microprocessors hosted on the Windows platform. Ponyprog works as burner software for the microcontroller.

In this work, we need to develop and use interrupt service routine, delay sub-routine and PWM function to make change the DC voltage of the armature and hence the speed of the DC motor and also to change the direction of rotation. The main programs have been developed to calculate the appropriate number of pulses and amount of time required for the pulses. The flow chart of the program is shown in Fig. 3.

4. RESULTS

The whole system is implemented in the laboratory in bread boards and the photograph of the whole system with DC motor is shown in Fig. 4. The armature voltage is measured using voltmeter and speed of the motor is measured using optical digital tachometer. The recorded results are shown in Table 1. When armature voltage is varied the field coil is separately excited with a constant voltage of 200 V. The measured field current is 476 mA. It has been observed that as the armature voltage increases due to the increment of the duty cycle speed of the DC motor also increases.

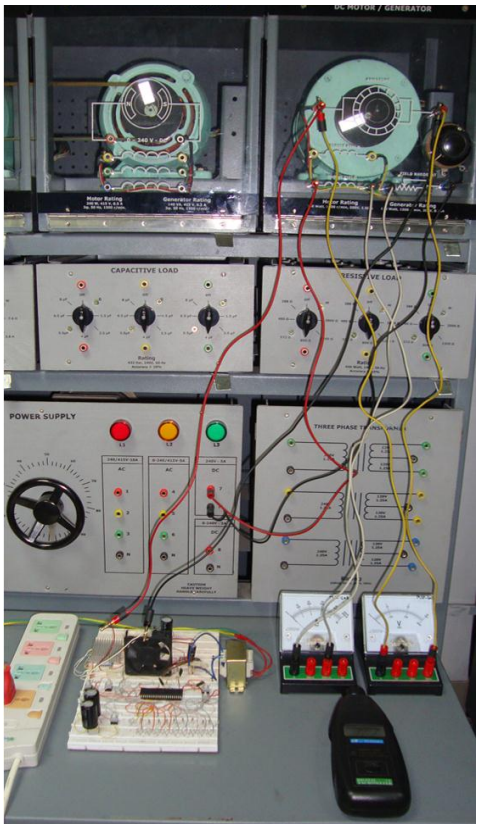

Fig. 4 Photograph of the DC motor control system

Table 1 Observed armature voltage and shaft speed

No of observations	Armature Voltage (Volt)	Shaft Speed (rpm)
1	10	77
2	18	138

3	24	193
4	33	265
5	41	325
6	48	380
7	56	450
8	61	483
9	70	569
10	86	693
11	98	785
12	114	920
13	122	998
14	143	1156
15	174	1425

5. CONCLUSIONS

In this work, a microcontroller based DC motor control system design is described to change the speed and direction of rotation of DC motor. Armature voltage is varied by pulse width modulation (PWM) of input DC voltage. Direction of rotation of DC motor is changed by initiating an interrupt signal to the microcontroller. To drive the DC motor, a four channel monolithic integrated driver circuit with diode clamps was used. PCB of the control circuit was been designed and the whole system is implemented on it. Test results are presented in tabular form and it shows very good agreement with the expected output.

6. FUTURE WORKS

Field flux can be controlled to vary the speed of the DC motor using the same circuit. In that case driver circuit may be required. Feedback may be incorporated in the system to make it close loop control system. Protection from the maximum input voltage, maximum speed of DC motor etc. may be incorporated in the software.

REFERENCES

[1]. P. K. Saha, S. S. Ahsan, M. H. Bhuyan, K. Islam and AHM Z. Alam, "Microcomputer Based Dish Antenna Position Control System," Proceedings of International Conference on Computing and Information Technology, Dhaka, Bangladesh, December 18-20, 1998, pp. 273-277.

[2]. P. K. Saha and M. H. Bhuyan, "Microcomputer Based Dish Antenna Position Control System with Auto Calibration", Proceedings of International Conference on Computing and Information Technology, Dhaka, Bangladesh, December 28-30, 2005, pp. 417-421.

[3]. M. H. Bhuyan, "Wireless Control System for DC Motor to Position a Dish Antenna Using Microcomputer," Daffodil International University Journal of Science and Technology (DIUJST), Dhaka, vol. 2, issue 1, pp. 44-49, January 2007.

[4]. M. A. Rahman, "Special section on permanent magnet motor drive: Guest editorial," IEEE Transactions on Industrial Electronics, vol. 43, no.2, pp. 245, April 1996.

[5]. M. H. Bhuyan, M. A. Rabby, M. A. Parvez and M. M. G. Tarik, "Microcontroller Based Display System Design using LED Array," Proceedings of the Conference on Engineering Research, Innovation and Education, Shahjalal University of Science and Technology, Sylhet, Bangladesh, 11-13 Jan 2010, pp. 417-420.

[6]. M. H. Bhuyan, M. A. Rabby and M. M. G. Tarik, "Microcontroller based Automatic Traffic Light Control System Design," Proceedings of the National Conference on Electronics and Telecommunications for Digital Bangladesh, Bangladesh Electronics Society, Dhaka, 2-3 June 2010, pp. 139-142

[7]. M. A. Mazidi, R. McKinlay and D. Causey, "PIC Microcontroller and Embedded Systems: Using Assembly and C for PIC18," Prentice-Hall, USA, 2007.

[8]. C. S. Siskind, "Electrical Machines Direct and Alternating Current," McGraw-Hill Book Co., 1959, ch. 6, pp. 207-210.

[9]. C. A. Schuler and W. L. McNamee, "Industrial Electronics and Robotics," McGraw-Hill Co., 1986, ch. 3, pp. 42-45.

[10]. M. H. Rashid, "Power Electronics Circuits, Devices and Applications," Prentice Hall Inc. USA, 2010.

[11]. J. Axelson, "Parallel Port Complete: Programming, Interfacing and using the PC's Parallel Printer Port," Lakeview Research, USA, February 1997, ch. 2, pp. 17- 31.

[12]. www.atmel.com

[13]. Datasheets of L293, SGS-Thomson Microelectronics, Italy, 1996.

[14]. R. Boylestad and L. Nashelsky, "Electronic Devices and Circuit Theory," Prentice-Hall, 10th Edition, USA, 2008.

[15]. J. Pardue, "C Programming for Microcontrollers," Smiley Micros, TN, USA, http://www.SmileyMicros.com, 2005.

Proceeding of the
International Conference on Electrical, Computer and Telecommunication Engineering
01- 02 December 2012 (ICECTE2012), RUET, Rajshahi-6204, Bangladesh
ICECTE2012: PI-0143

Digital Water Level Indicator and DC Motor Control Device for Alarming Purpose

Md. Mamorej Hossen[1], *Md. Azahar Ali*[2]
[1]Dept. of EEE, University of Information Technology & Sciences, Rajshahi-6000, Bangladesh.
[2]Dept. of CSE, *Frankfurt University of Applied Sciences*, Frankfurt am Main, Germany.
E-mail: momrej09eee@yahoo.com , azaharali28@yahoo.com

ABSTRACT
Water is an essential resource for all life on the planet. Successful management of any resources requires accurate knowledge of the resource available, the uses to which it may be put, the competing demands for the resource, measures to and processes to evaluate the significance and worth of competing demands and mechanisms to translate policy decisions into actions on the ground. This process is concerned about water management in daily life. To reduce the wastage of water "WATER LEVEL SENSOR" is developed and with the help of "Dc Motor Controlling System" proper use of pump is ensured. DC motor alarming system is used to get knowledge about appropriate use of attached devices with this system so that any kinds of failure could be easily detected. This alarming system has an intelligence to detect failure of the system and producing different sound for specific problem. With the combination of these devices an attempt of the automation of centrifugal pump is taken. Besides, with the proper use of this system it is expected it will reduce the operating cost in our daily life.

KEY WORDS:- Water level sensor, back emf, operation of dc motor , Dc Motor Controlling System, Fleming's left hand rule.

1. INTRODUCTION

The importance of water to life can never be overstated. The quality of life of the population and the consequent growth of any nation depend on its water. After all, the efficient management of water can lead to the reduction of the cost of water and energy, while making sure that quality is not affected. There is lots of work done on automatic water pump controller. The main objectives of this water pump controller are to minimize the wastage of water from the overhead tank due to overload.

Agriculture is the largest user of the world's freshwater resources, consuming 70 per cent. An assessment of water management in agriculture was conducted in 2007 by the International Water Management Institute in Sri Lanka to see if the world had sufficient water to provide food for its growing population[1]. To avoid a global water crisis, farmers will have to strive to increase productivity to meet growing demands for food, while industry and cities find ways to use water more efficiently [2]. Water management is the activity of planning, developing, distributing and managing the optimum use of water resources [3]. Elias Santiago &Bayarnon[4] constructed an automatic pump control system, such as for boat which including a battery operated main motor and pump unit and a backup motor and pump unit. Robert F. Gibb, San Diego, Calif [5] constructed an automatic pump control system, which can distinguish between water and oil so that a pump can be controlled to pump water and deactivated before oil is pumped. Anton Belehradek, Downers Grove, II, (US) [6] constructed an automatic pump control system which incorporates a programmed processor and respond to input from multiple floats. IIumbertoV.Meza, Tustin, CA (US); Nikhil Jitendro Gandhi , Anaheim, CA (US) ; Quang Minh Iruoag, West Covia, CA (US) [7] constructed an automatic pump control system. The apparatus includes pistons integrally formed in a diaphragm and coupled to the diaphragm by convolutes. Robert M. Koehl, Lakemoor, IL (US) [8] constructed an automatic pump control system. Dc motors feature a speed, which can be controlled smoothly down to zero, immediately followed by acceleration in the opposite direction without power circuit switching. And dc motors respond quickly to changes in control signals due to the dc motor's high ratio of torque to inertia. Water can also be electrolyzed into oxygen and hydrogen gases but in the absence of dissolved ions this is a very slow process, as very little current is conducted. While electrons are the primary charge carriers in water (and metals), in ice the primary

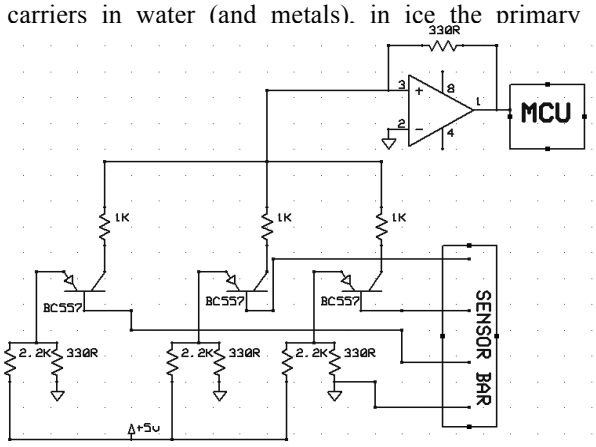

Fig 1.1: Water level sensor circuit

Dc motors feature a speed, which can be controlled smoothly down to zero, immediately followed by acceleration in the opposite direction without power circuit switching. And dc motors respond quickly to changes in control signals due to the dc motor's high ratio of torque to inertia.

2. WATER LEVEL SENSOR

Water level sensor is such kind of a device which produces a certain voltage due to change of water level. This sensor consists of two parts

1. Water level sensor bar
2. Water level sensor circuit

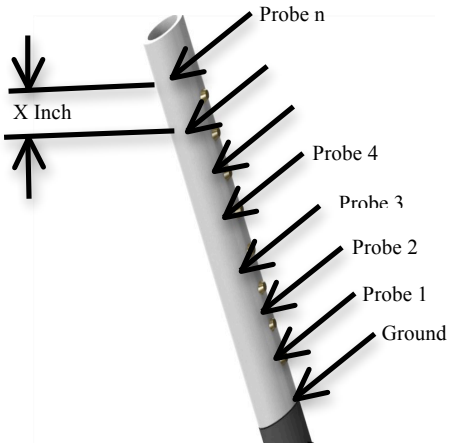

Fig 2.1: A typical water level sensor bar

2.1Water level sensor bar

Water level sensor bar consists of a long tube having some extended probes for sensing water level. The height of the water level sensor bar is determined from the design of the water reservoir (shown in figure 2.1).

2.2 Water level sensor circuit

Water level sensor circuit consists of three parts(shown in figure 1.1).

1. Voltage divider circuit
2. Transistor circuit
3. Op-amp circuit

2.2.1 Voltage divider circuit

Microcontroller unit operates 0v to 2.56v. So it is necessary to maintain voltage level within this level for sensing purpose. For operating microcontroller 5 volt dc supply is required. So to operate sensor with this volt voltage dividing rule is applied in sensor design (shown in fig 2.2).

$$V_{out} = \frac{R_2}{R_1+R_2} V_{in} \quad \text{.....(1)}$$

2.2.2 Transistor circuit

In a grounded-emitter transistor circuit, such as the light-switch circuit shown in fig 2.3, as the base voltage raises the base and collector current rise exponentially, and the collector voltage drops because of the collector load resistor. The relevant equations:

$V_{RC} = I_{CE} \times R_C$, the voltage across the load (the lamp with resistance R_C)

$V_{RC} + V_{CE} = V_{CC}$, the supply voltage shown as 6V

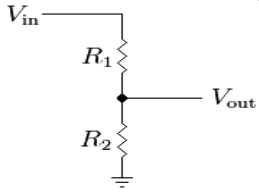

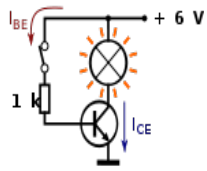

Fig2.2:Voltage divider circuit **Fig2.3**: BJT used

If V_{CE} could fall to 0 (perfect closed switch) then Ic could go no higher than V_{CC} / R_C, even with higher base voltage and current. The transistor is then said to be saturated. Hence, values of input voltage can be chosen such that the output is either completely off, or completely on. The transistor is acting as a switch, and this type of operation is common in digital circuits where only "on" and "off" values are relevant. A negative portion of 5 volt DC source is placed inside the reservoir lower portion. When the level of water is raised it contains the negative voltage of DC source. This voltage is used to switch the transistors attached to the different probes of the sensor bar. Three PNP transistors are used in this experiment where base is connected to the probes of sensor bar.

2.2.3 Op-amp circuit

An operational amplifier ("op-amp") is a DC-coupled high-gain electronic (shown in fig 2.4) voltage amplifier with a differential input and, usually, a single-ended output. An op-amp produces an output voltage that is typically hundreds of thousands times larger than the voltage difference between its input terminals.

Using op-amp as Summing amplifier in water level sensor.

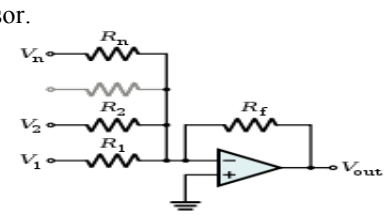

Fig2.4: Op-amp act as summing amplifier in water level sensor

Equation for above diagram:

$$V_{out} = -R_f\left(\frac{V_1}{R_1} + \frac{V_2}{R_2} + \cdots + \frac{V_n}{R_n}\right) \text{.....(2)}$$

In this experiment three voltage sources are used to calibrate the water level and voltage for each level is same. Voltage is getting from transistor where transistor acts as switch.

3. METHOD ANALYSIS

All motors require two magnetic fields, one produced by the stationary part of the motor (the stator, or field), and one by the rotating part (the rotor, or armature). These are produced either by a winding of coils carrying a current, or by permanent magnets. If the field is a coil of wire, this may be connected in a variety of ways, which produces different motor characteristics.

3.1 Fleming's left hand rule

The basic law of a motor, the reason why they rotate, is governed by Fleming's left hand rule (in fig 3.1). This tells you the direction of the force on a wire that is carrying current when it is in a magnetic field.

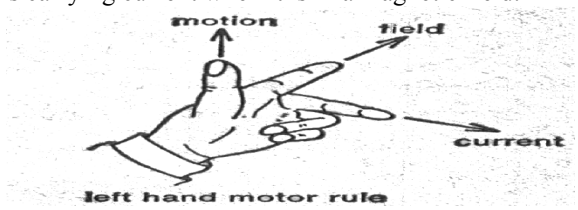

Fig 3.1: Fleming's left hand rule

The next diagram shows the force acting on a wire carrying current, obeying the left hand rule:

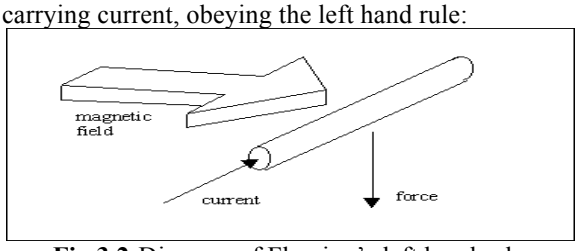

Fig 3.2: Diagram of Fleming's left hand rule

If we now bend the wire round in a loop, and place it in a magnetic field caused by two permanent magnets, we have the situation shown in the fig 3.3.

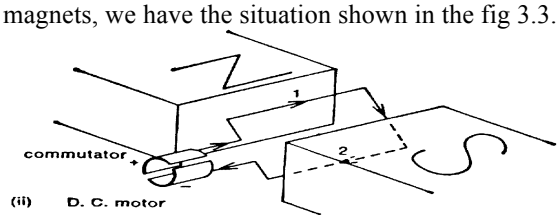

Fig 3.3: Supplying current through commutator

Here, both sides of the wire loop will have a force on them, trying to make the wire loop rotate. The current is applied to the loop through the commutator, which is shown as two pieces of metal formed into a ring in the figure. Current is applied to the commutator by stationary graphite blocks, called brushes, which rub against the commutator ring.

3.2Calculation of back emf

The back emf is dependent on the speed of the motor, and is given by the equation.

$$e_a = k\omega_{m\varphi} \quad \ldots\ldots\ldots\ldots\ldots\ldots\ldots\ldots\ldots\ldots\ldots(3)$$

Where, k is a constant for the motor, Ω_m is the speed of the motor, and Φ is the strength of the magnetic field generated by the field coils or magnets. From this equation you can see that when the motor starts, and its speed is zero, then the back emf will be zero, and so the current taken by the motor will be very large. This is also true when the motor is stalled.

When a load is put on the motor, the speed drops, and so the back emf drops, so the current drawn from the battery will increase.

4. SIMULATION & RESULT

To verify our program will work, simulation is required which presents a hardware abstraction to the programmer & hence one can decide whether it will work or not. Displays the simulator window (shown in Fig 4.1) in which one can simulate a compiling program.

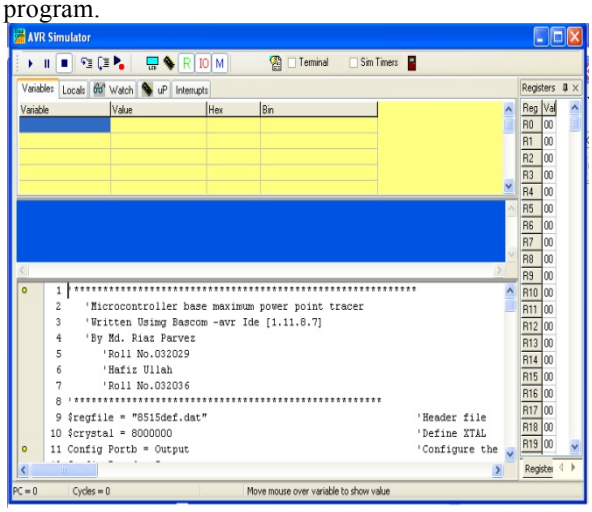

Fig.4.1: Simulating Window

When the source code is saved without compiling, one will be warned that the debug file differs from the source code. One has the option to compile it before simulate or continue without recompiling.

While programming the Microcontroller the Reset pin of the microcontroller must be connected to the Parallel Port, which is accomplished by opening the RISC Switch. After programming the RISC Switch is connected to the Vcc for start operation [10].

Calibration of voltage against water level of a sensor is shown in figure 4.2.

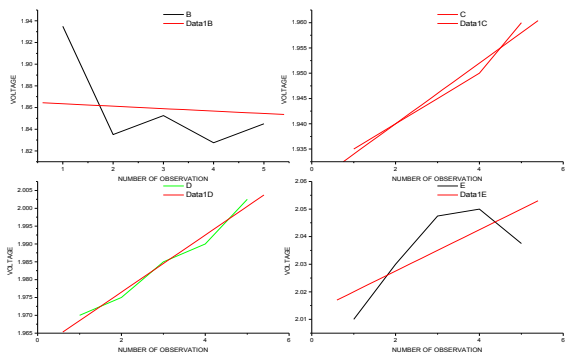

Fig 4.2: Calibration of voltage against water level

Voltage versus Number of water level graph of a water level indicator is shown in figure 4.3.

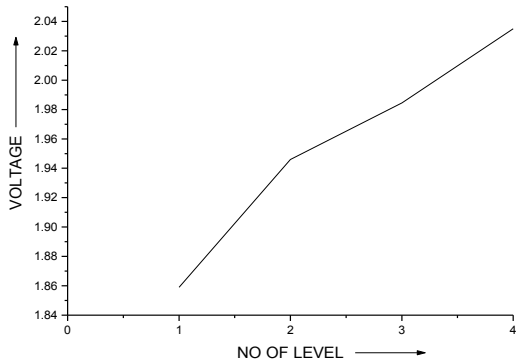

Fig 3.8: Voltage versus Number of water level graph

5. CONCLUSION

In this paper, digital water level senor is constructed for indicating 3 levels that's mean it can sense three levels of water. More level can be introduced by adding transistors according to described sequences. However, three levels sensor is enough to sense water level in reservoir. Motor control device is employed in alarming system. This type of alarm has an intelligence to detect the reason of failure of the system. By varying motor speed different sound is produced in this paper so that it indicates distinct operation of the system. Finally, a schematic design of centrifugal pump is shown at the end of this paper which is based on digital water level sensors and variable speed alarming motor for producing different sounds for this type of control system.

6. FUTURE WORK

In this paper, motor control device is employed in alarming system. This type of alarm has an intelligence to detect the reason of failure of the system. By varying motor speed different sound is produced in this paper so that it indicates distinct operation of the system.

REFERENCES

[1] Molden, D. (Ed). *Water for food, Water for life: A Comprehensive Assessment of Water Management in Agriculture.* Earthscan / IWMI, 2007.

[2] Chartres, C. and Varma, S. *Out of water. From Abundance to Scarcity and How to Solve the World's Water Problems* FT Press (USA), 2010

[3] Water Management, ISSN: 1751-7729 (electronic) 1741-7589 (paper), Thomas Telford

[4] Malvino, A. P. Electrical Principle, New York, McGraw-Hill Book Company, 1998.

[5] Bansal Dr. R.K. A textbook of fluid mechanics & hydraulic machines, Ninth edition,New Delhi, 2005.

[6] Holman J.P. Experimental Methods for Engineers, Seventh edition, TATA McGraw-Hill Bo New delhi, 2001.

[7] David G. Ullman, The mechanical Design Process, Second edition McGraw-Hill, 1992.

[8] Robert B. McKee, Fundamental of Mechanical Component Design McGraw-Hill, 1991.

[9] A. Crofts (1996). "Lecture 12: Proton Conduction, Stoichiometry". University of Illinois at Urbana-Champaign. http://www.life.uiuc.edu/crofts/bioph354/lect12.html. Retrieved 2009-12-06.

[10] Claus kuhnel, BASCOM programming of_Microcontrollers_with_Ease, 2001

BIBLIOGRAPHIES

Md. Mamorej Hossen was born in Rajshahi, Bangladesh on 23th November, 1989. He is currently a Bachelor of Science in Engineering student in the Department of Electrical and Electronic Engineering department, University of Information Technology & Sciences (UITS), Rajshahi-6000, Bangladesh. He has been actively involved in the study, research and Electronics project works. His research interests are Wireless, Renewable Energy, and Power system.

Md Azahar Ali was born in Rajshahi, Bangladesh on March05, 1985. He received his B.Sc. Engineering Degree from Rajshahi University of Engineering & Technology (RUET), Bangladesh, in November, 2010 in the department of Electronics and Telecommunication Engineering. He has published two conference papers. He is currently a Master of Engineering student in the Department of CSE, Frankfurt University of Applied Sciences, Frankfurt am Main, Germany. Also he is working as a Lecturer(study leave) in Electrical and Electronic Engineering Department, UITS, B**angladesh**. He has been actively involved in the study, research, teaching and consulting project works to undergraduate students. His research interests are Wireless, Communication, Image Processing and Information Technology. He is also interested in Electronics project, circuit design & control monitoring of mechanical instrument.

Proceeding of the
International Conference on Electrical, Computer and Telecommunication Engineering
01- 02 December 2012 (ICECTE2012), RUET, Rajshahi-6204, Bangladesh

ICECTE2012: PI-0144

An FPGA-Based Semi-Automated Traffic Control System Using Verilog HDL

Anik Mallik, Sanjoy Kundu, Md. Ashikur Rahman
Department of Electronics & Communication Engineering, Khulna University of Engineering & Technology
E-mail: anikmallik@yahoo.com, sanjoykundu.ece@gmail.com, ashik_ece_kuet@yahoo.com

ABSTRACT
Traffic Congestion is one of the severe problems in heavily populated countries like Bangladesh where Automated Traffic Control System needs to be implemented. An FPGA-based Semi-automated system is introduced in this paper including a completely new feature "Safe State" to avoid sudden unwanted collision. Here we used sequential encoding which has made the program much simpler and so that easy to control and modify. The experimental result showed the automated change in traffic lights according to the specified timing sequences which would be able to conduct maximum possible transitions of vehicles occur at different directions simultaneously without facing any accident.

KEY WORDS: FPGA, Verilog HDL, Mealy Machine, Sequential Encoding

1. INTRODUCTION

Traffic Congestion problem is a common misery to the busy lives of the heavily populated countries like Bangladesh. Weak urban planning and Traffic Control System are mainly responsible for this problem. To form methods which will control the Congestion of traffic in the roads in urban and sub-urban areas remained the most challenging issue for the engineers [1]. So, research on this issue continues and various methods have been proposed by the researchers. The classical methods had mainly two drawbacks- one is, due to lack of perfect adjustments in the signal-timings, vehicles had to wait for a long time without any reason [2], and the other is, there was no such way in which ambulances, fire brigades, police vehicles and other emergency vehicles could pass with high level of priority [3]. Some of the recent methods used Fuzzy Logic to implement an intelligent system which would monitor and control the Traffic system [4]. These methods could set time adjustment and lead the cars with the help of arrival parameters through camera type sensors and image processing or electromagnetic sensors [5]. Fuzzy Logic is of a great use for systems whose appropriate mathematical modeling is not possible or very expensive to implement. However, the system may suffer from noticeable error if the input-output relation & the set of rules are weakly defined. So, there is a need to design a system, simple to operate, using FPGA based, cost effective technology which can eradicate these problems and can provide much greater speed.

Recently a Traffic Control System has been developed using Mealy State Machines [6]. But, the system grown in that research, has limited Emergency States for passing vehicles on the roads, which had different switches for different roads and had no "Safe State" (i.e. all roads having alert signal to avoid sudden unwanted collisions) between an emergency and normal or ordinary state. The system also suffered from inadequate Green signals for various directions and signal for human-passing on Zebra-crossings. In our proposed design, an input of 3 binary bits has been provided which is used for defining the states, including a new idea of "Safe State". Emergency states are changed manually and too easy to handle. The major or minor roads can be defined manually and the system can run that way. Timings are specified here based on our assumptions. This can also be changed by a statistical approach depending upon the necessity of the roads in practical. We also have included signals for Zebra-crossing into the system and this design allows the maximum possible transitions of vehicles on different directions without facing any accident along with the basic features found in any control system, which can be fabricated into one single chip.

The system has been written in Verilog HDL [7] & designed, tested and evaluated using the ISE 6.0 tool of Xilinx and VeriloggerPro 6.5 [8]. Then the design has been implemented on Xilinx Spartan-2 FPGA (XC2S150). In the following sections, the methodology, the implementation technique of this system, designed circuit schematic and the result of the experiment will be discussed in brief.

2. METHODOLOGY

2.1 Mealy State Machine & State Machine Style

State machines can be classified into two categories: Mealy machines and Moore machines. Basically, the process of generation of the output differentiates between Mealy and Moore machines. In a Mealy

machine, the outputs are generally a function of both the state and the inputs [9].

The State Machine Style can be of various forms. One of these forms combines the next-state logic and the state register. This style is good to use since the next-state logic and state register here are related quite inseparably. If the state machine has many inputs which change frequently, this style is efficient enough to use [9].

2.2 Sequential Encoding

State encoding has a great effect on the size and performance of a circuit, and also influences the amount of electronic glitches produced by a circuit. This can also be of several kinds: Sequential Encoding, Gray Encoding, One-Hot or One-Cold Encoding etc.

In Sequential Encoding, state comes one after another according to the sequence of bit pattern and makes the system simpler and efficient. But glitches may occur when we deal with a circuit with huge dimensions. In case of Gray Encoding, the simplicity in program code along with the circuitry is missed as it does not change the bit pattern sequentially and provides speed little bit slower. One-Hot or One-Cold Encoding is very efficient when we need to consider faster operation but in this case the area of circuitry becomes huge [9].

In this design, we have used Sequential Encoding as our concern was to simplify the operation. The proposed circuitry is not huge, so this scheme gave us the optimized performance.

2.3 Field Programmable Gate Array (FPGA)

A Field Programmable Gate Array (FPGA) is an integrated circuit and its configuration is generally defined using a Hardware Description Language (HDL), and in this case, it is same as an Application Specific Integrated Circuit (ASIC). This name 'FPGA' is given as it is structured like a gate array configuration of an ASIC [10]. This regular structure is interconnected which is under the designers' extreme control, which means that the user can design, modify or make any change to his circuit easily [11]. FPGAs can be used to implement any logical function that can be performed by an ASIC, and it should also be noted that FPGA design is more cost-effective than that of ASIC [12]. They have lots of advantages over microcontrollers, such as greater speed, number of I/O ports and performance [13].

3. SYSTEM IMPLEMENTATION

3.1 States

The simplest form of traffic light is introduced with a single or a pair of colored aspects that warns any vehicle of the shared right of way of a possible conflict or danger [14]. But, in case of a complex form, the scenario is a bit different.

3.1.1 Traditional States

Now, we have to imagine a junction of four roads. In this complex state, each road will have six lights (Red, Yellow, Green for going straight, Green for turning Left and Green for turning Right and Green for Zebra-crossing) which are illustrated in **Fig. 1**. The timing sequence is shown in the **Table 1**.

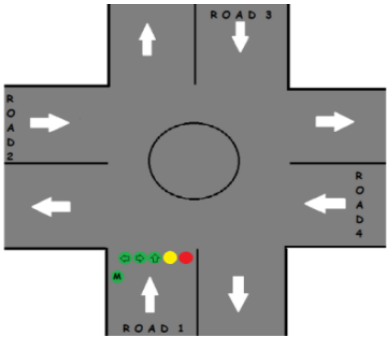

Fig. 1: A Four way road each having six lights

Table 1: Timing Sequence of Traditional States (Only Road 1 is shown here)

Timing Sequence	R 1	Y 1	G 1 ↓	G 1 →	G 1 →	M 1	HEX (for all the four roads)
60 sec	0	0	1	1	0	0	3218A6
15 sec	0	1	0	0	0	0	410820
60 sec	1	0	0	1	1	0	98C862
15 sec	1	0	0	0	0	0	810420
60 sec	1	0	0	0	1	0	8A6321
15 sec	1	0	0	0	0	0	820410
60 sec	1	0	0	0	0	1	86298C
15 sec	0	1	0	0	0	0	420810

3.1.2 Emergency States

In some special cases, like emergency states, the controlling would be different from the traditional one. For example, we can easily open Road 1 for having an emergency in this way, and can block the others which are shown in the **Table 2**.

Table 2: Timing Sequence of Emergency-1 State (Only Road 1 is shown here)

3.1.3 Safe State

The Safe State is needed to occur between the transitions of traditional state and emergency one.

Timing Sequence	R 1	Y 1	G 1 ↓	G 1 →	G 1 ←	M 1	HEX (for all the four roads)
15 sec	0	1	0	0	0	0	410410
≥ 60 sec	0	0	1	1	1	0	3A0822

This is shown in **Table 3**.

Table 3: Timing Sequence for "Safe State" (Only Road 1 is shown here)

Timing Sequence	R 1	Y 1	G 1 ↓	G 1 →	G 1 ←	M 1	HEX (for all the four roads)
≥ 15 sec	0	1	0	0	0	0	410410

3.2 System Flow Chart

The proposed system can be expressed through the Flow Chart in **Fig. 2**.

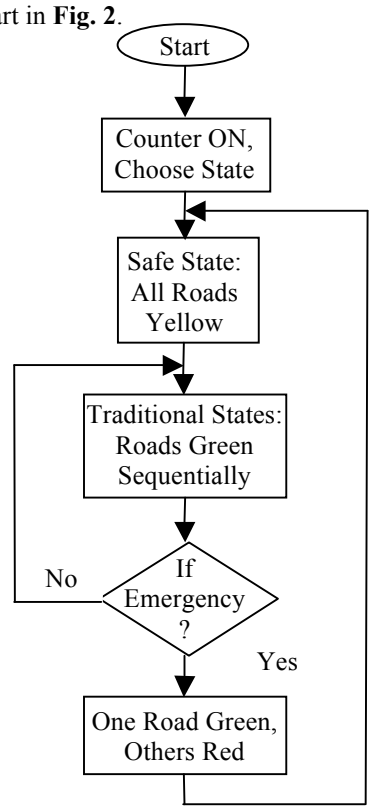

Fig. 2: Flow Chart for our prescribed System

3.3 Circuit Schematic

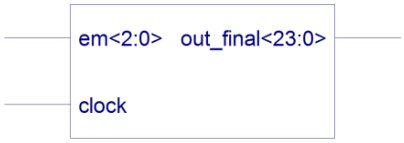

Fig. 3: Block Diagram of FPGA-Based Semi-Automated Traffic Control System

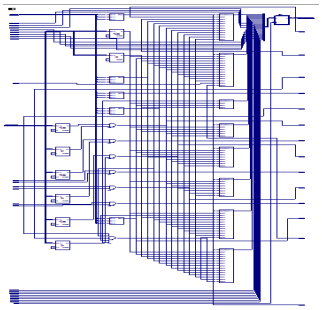

Fig. 4: RTL Schematic of one of the system blocks

4. RESULTS

We used the Verilog as HDL to design this system and then verified it in VeriloggerPro 6.5 software. The timing diagram achieved from Testbencher showed that the traffic lights were being ON and OFF automatically according to the timing sequences. Then we tested it in the Xilinx FPGA where it also gave the correct output. The timing diagrams are provided in the next sub-section. The 24 bits of outputs are converted here into 6-digits Hexadecimal numbers.

4.1 Timing Diagrams

4.1.1 Traditional State

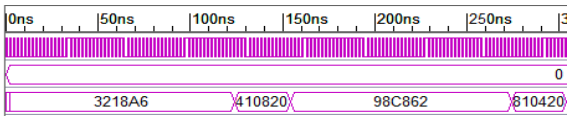

Fig. 7: Timing Diagram of Traditional State Output (from 0ns to 300ns)

4.1.2 Emergency State

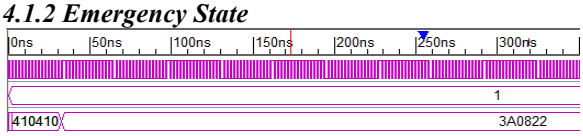

Fig. 8: Timing Diagram of Emergency-1 State Output (from 0ns to 350ns)

4.1.3 "Safe State"

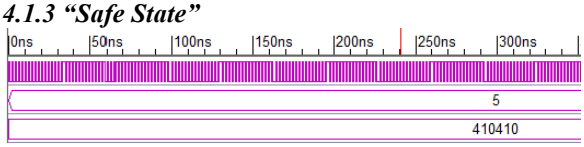

Fig. 9: Timing Diagram of "Safe State" Output (from 0ns to 350ns)

5. CONCLUSION

We have presented an FPGA-Based Semi-Automated Traffic Control System, where we used Verilog as

the HDL. We have named this design as "Semi-Automated" because we could not make the emergency-state input system fully automated. We used the Mealy State Machine and the Sequential Encoding made the program simplest. This design allows the maximum possible transportation of vehicles in different directions simultaneously. One of the salient features of this design is any addition of different lights for different purposes can take place easily just by adding bits to the output ports. Again, we have left two more states in this design which can be used for other necessary purposes. The whole design needs only two inputs- one is Clock and the other is for different states, which can be controlled fluently. The most effective feature of this design is the use of 15sec "Safe State" which is able to avoid the sudden unwanted collision between vehicles in the transitions of states easily. Any kind of step for the improvement of this system can easily be taken for this design because the logic is made simpler than ever.

6. FUTURE WORK

We have a plan to include a feature to this system which will be able to count the number of the vehicles in a road. This can be accomplished using a number of Heat-sensors or IR-sensors placed in different positions in a road. Each road will be timed automatically according to the number of vehicles.

7. ACKNOWLEDGEMENTS

We want to acknowledge gratefully Mr. Robin Sarker (B.Sc. Engr.), Mr. Shumit Saha (Lecturer) and Dr. A. B. M. Aowlad Hossain (Asst. Professor) from Dept. of Electronics & Communication Engineering, Khulna University of Engineering & Technology, for their valuable suggestions & also for providing the facilities to implement the design on FPGA.

REFERENCES

[1]. Tehshnehlab, M., Afyooni, D., "An artificial intelligent system for traffic forecasting in virtual stations of highways", *Iranian Journal of Science and Technology, Transactions B: Engineering*, vol. 28, pp. 395-400, 2004.

[2]. Z. Yuye, Y. Weisheng, "Research of Traffic Signal Light Intelligent Control System Based On Microcontroller", *First International Workshop on Education Technology and Computer Science*, 2009.

[3]. W. M. E. Medany, Mr Hussain, "FPGA-based Advanced Real Traffic Light Controller System Design", *IEEE International workshop on Intelligent Data Acquisition Computing Systems: Technology and Applications*, Germany, September, 2007.

[4]. Osigwe Uchenna Chinyere, Oladipo Onaolapo Francisca, Onibere Emmanuel Amano, "Design and Simulation of an Intelligent Traffic Control System", *International Journal of Advances in Engineering & Technology (IJAET)*, Nov 2011.

[5]. Behnam Barzegar, Siyavash Ghanbari, Hossein Bozorgi, Mahmoud Rahmani, "Modeling and simulation of traffic lights and controller unit systems by colored Petri net", *International Journal of the Physical Sciences*, vol. 6(34), pp. 7760-7770, December 2011.

[6]. M. Ali Qureshi, Abdul Aziz, S. Hammad Raza, "A Verilog Model of Adaptable Traffic Control System Using Mealy State Machines", *International Journal of Computer and Electrical Engineering*, vol. 4, no. 3, June 2012.

[7]. J. Bhasker, "Verilog® HDL Synthesis: A Practical Primer", Star Galaxy Publishing, 1998.

[8]. Xilinx, Internet site address: http://www.xilinx.com.

[9]. James M. Lee, "Verilog® Quickstart: A Practical Guide to Simulation and Synthesis in Verilog", 3rd Edition, pp. 169-186, Kluwer Academic Publishers, Boston, 2002.

[10]. Bob Zeidman, "Designing with FPGAs and CPLDs", CMP Books, CMP Media LLC, 2002.

[11]. Programmable Logic Design (Quick Start Handbook), Xilinx, 2006, pp. 17.

[12]. El-Medany, W.M., Hussain, M.R., "FPGA-Based Advanced Real Traffic Light Controller System Design", *4th IEEE Workshop on Intelligent Data Acquisition and Advanced Computing Systems: Technology and Applications, 2007 (IDAACS 2007),* pp. 100-105, September 2007.

[13]. Liu Zhenggang, Xiong Jialong, Zhou Mingyun, Yang Jun, Ding Hongwei, "FPGA-Based Dual-Mode Traffic Lights System Design", *1st International Conference on Information Science and Engineering (ICISE),* pp. 558-561, December 2009.

[14]. Akshansh Kaushik, "Advanced and Intelligent Traffic Light Controller", *International Journal of Research and Practices in Engineering Sciences (IJRPES)*, vol. 1, issue 1, pp. 27-32, Mar-May 2012.

Proceeding of the
International Conference on Electrical, Computer and Telecommunication Engineering
01- 02 December 2012 (ICECTE2012), RUET, Rajshahi-6204, Bangladesh

ICECTE2012: PI-0145

Prospects of Cloud Computing in Bangladesh and Its Security Challenges

Muhammed Samsuddoha Alam[1], Ahsan Raja Chowdhury[2]
[1]Department of Computer Science & Engineering, Northern University Bangladesh
[2]Department of Computer Science & Engineering, University of Dhaka
E-mail: msdohanub@yahoo.com, farhan717@yahoo.com

ABSTRACT
The popularity of Cloud Computing has grown spectacularly in the recent years, and assumed to be a form of "Green computing". It promises Information Technology (IT) services with cost-efficiency and flexibility. Presently, Cloud Computing is a new wave of IT for individuals, companies, universities and governments. Use of Cloud Computing technology can ensure the capabilities of IT at low cost which can create great opportunities in the field of ICT in Bangladesh. In Cloud Computing, the data have to be released to the Cloud and thus leaves the protection-sphere of the data owner. For any technological advancement we must consider its disruptive possibilities and potential risks. This paper points out the way to implement Cloud Computing in Bangladesh especially in universities and provides suggestions for overcoming the security issues in order to make the Cloud Computing more reliable and secure. The proposal can make innovative impact in the concept of Digital Bangladesh and hence in ICT.

KEYWORDS*: Cloud Computing, Information Technology, Security.*

1. INTRODUCTION

Cloud Computing is a dynamically scalable shared resources accessed over a network [1]. It is a pay-per-use model for enabling available, convenient, on-demand network access to a shared pool of configurable computing resources. These resources, like networks, servers, storage, applications, and services can be rapidly provisioned and released with minimal management effort or service provider interaction. In Cloud Computing, the users will pay for what they use, which can be shared internally or with other computer users via Internet or internal network. The main goal of the Cloud Computing is to share resources with cost efficiency and flexibility. Any computer user can access the cloud via Internet protocol from any computer. The best feature of the Cloud is to enable user's full self-online service.

2. LITERATURE REVIEW

The concept of Cloud Computing dates back to the 1960s, when John McCarthy said that "computation may someday be organized as a public utility". Cloud applications extend their accessibility through the Internet by using large data centers and powerful servers that host web applications and services. Anyone with a suitable Internet connection and a standard Internet browser can access a cloud application [2]. A cloud service has three distinct characteristics that differentiate it from traditional hosting. It is sold on demand, typically by minute or hour; it is elastic -a user can have as much or as little of a service as they want at any given time; and the service is fully managed by the provider (the consumer needs nothing but a personal computer and Internet access). Significant innovations in virtualization and distributed computing, as well as improved access to high-speed Internet and a weak economy, have accelerated the interests in Cloud Computing. A Cloud can be private or public; where a public Cloud sells services to anyone on the Internet. Currently, Amazon Web Services is the largest public cloud provider. A private cloud, on the other hand, is a proprietary network or a data center that supplies hosted services to a limited number of people. When a service provider uses public cloud resources to create their private cloud, the result is called a virtual private cloud. Private or public, the goal of Cloud Computing is to provide easy, scalable access to computing resources and IT services [3]. The architecture of a typical Cloud Computing is shown in Fig. 1, while its categories are shown in Fig. 2.

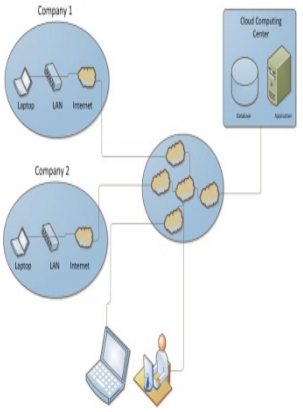

Fig. 1 General Cloud Computing Architecture

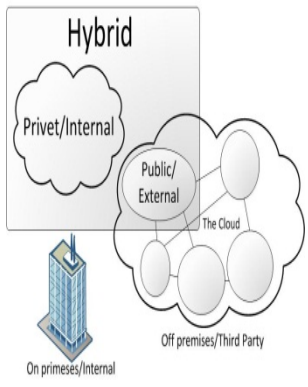

Fig. 2 Cloud Computing Types

3. CLOUD COMPUTING ARCHITECTURE

Cloud Computing encompasses many aspects of computing (from hardware to software) that a single solution is not able to support them all. In general, Cloud Computing applications incorporate the combination of the following functional service models [4-6]:

- SaaS – Software as a Service-Network-hosted application (shown in Fig. 3).
  In the software-as-a-service cloud model, the vendor supplies the hardware infrastructure, the software product and interacts with the user through a front-end portal.
- DaaS – Data as a Service-Customer queries against provider's database.
- PaaS– Platform as a Service-Network-hosted software development platform in the cloud is defined as a set of software and product development tools hosted on the provider's infrastructure.
- IaaS – Infrastructure as a Service-Provider hosts customer VMs or provides network storage.
  For example, Amazon Web Services.

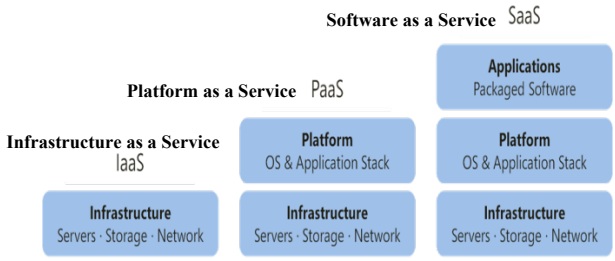

Fig. 3 Architectures of Iaas, PaaS and SaaS

4. CLOUD COMPUTING PROSPECTS IN BANGLADESH

Cloud Computing is a new area of computing technology in Asia region. In developing countries like Bangladesh, Cloud Computing is still in its infancy. The lack of a national ICT/IT policy remains a barrier in the development and advancement of Cloud Computing infrastructure in Bangladesh. Notwithstanding the advantages offered by Cloud Computing technologies with identification and proper exploration of all relevant legal issues pertaining to Cloud Computing activities in developing countries is therefore imperative if Cloud Computing is to be implemented within governmental, education and industrial sectors [7]. If Bangladesh wants to emerge as a Digital Country then Cloud Computing can be a very effective medium for the go in public and private sectors due to the following outcomes:

- It can improve the government's ability to create a transparent, open and participatory government
- Organize solutions around the constituent groups being served
- Continue the migration towards a services-based environment that is interoperable and standards-based.
- Enable rapid deployment of technology solutions for government without developing stove-pipes.
- Enable scalability for existing and new capabilities.
- Increase savings through virtualization and economies of scale.
- Potentially reduce cost of infrastructure, buildings, power, and staffing (Sample analysis is shown in Fig. 4).

The pharmaceutical industry can offer some good examples of the power of using computing in the cloud [8]. For example, scientists at a drug company of different countries are using Amazon's cloud services to dramatically shrink the time to analyze data and determine how to treat diseases. They cut the time to analyze a large data set from 140 days (on a desktop computer/laptop computer) to six days (in the cloud). Another example comes from the manufacturing sector, where, Cloud Computing is viewed as a superior tool to link factory information systems to those of suppliers, distributors and customers, resulting in fewer supply chain disruptions.

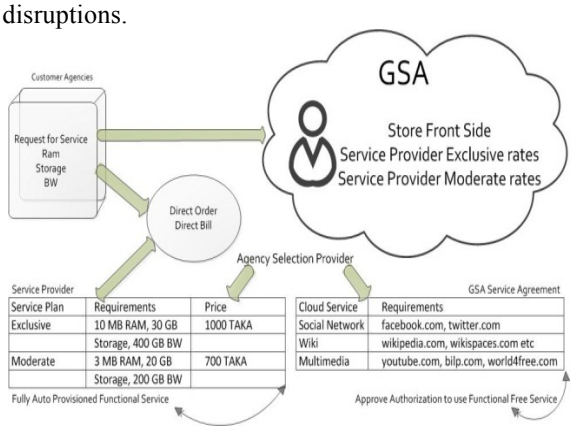

Fig. 4 A sample Cloud Computing architecture [Conceptual]

Indeed, some new cloud-based services, such as providing advice to rural doctors, are set up to require only mobile connectivity [9]. Specially, I want to highlight our education sector. In Bangladesh, there are many public and private universities but still the authorities aren't capable of creating sufficient IT infrastructure due to financial support and operational complexity. I want to say that the Use of Cloud Computing on universities can solve this problem and can bring many benefits such as accessing the file storages, e-mails, databases, educational resources, university management or virtual university, library, research applications and tools from anywhere for faculty, administrators, staff, students and other users in university, on demand. In

addition, cloud computing reduces universities' IT complexity and cost. Cloud Computing could be a technological innovation that both reduces IT costs for the university and eliminates many of the time-related constraints for students, making learning tools accessible for a larger number of students. I want to share the way by which cloud computing paradigm in the universities can be benefited [10].

- ✓ Reduced administrative and academic function.
- ✓ Can make learning environment more effective and interesting for the students.
- ✓ Task distribution and coordination may be easier.
- ✓ Reduced deployments time.
- ✓ Via cloud computing, universities can open their own technology infrastructures to businesses and industries for research advancements.
- ✓ The efficiencies of cloud computing can help universities keep pace with ever-growing resource requirements and energy costs.
- ✓ The extended reach of cloud computing enables institutions to teach students in new way [blended learning], different ways and help them manage projects and massive workloads.
- ✓ When students enter the global workforce they will better understand the value of new technologies.
- ✓ Cloud computing allows students and teachers to use applications without installing them on their computers and also allows access to saved files from any computer with an Internet connection.

Here is the cloud university architecture and details infrastructure layer.

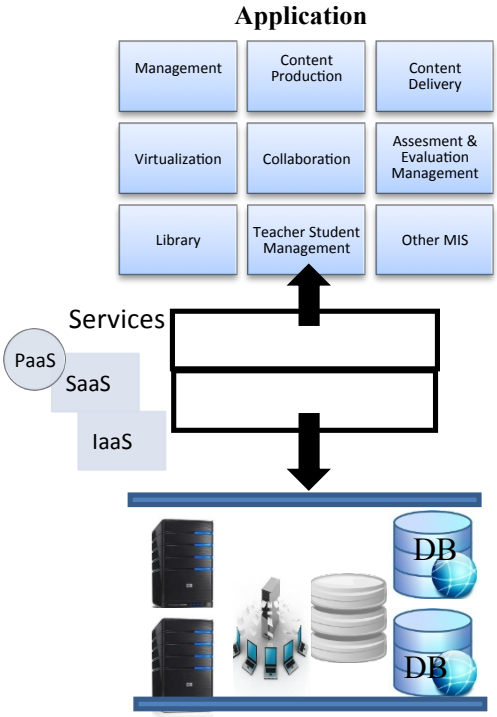

Fig. 5 University Cloud Architecture

Fig. 6 Infrastructure Layer for University Cloud

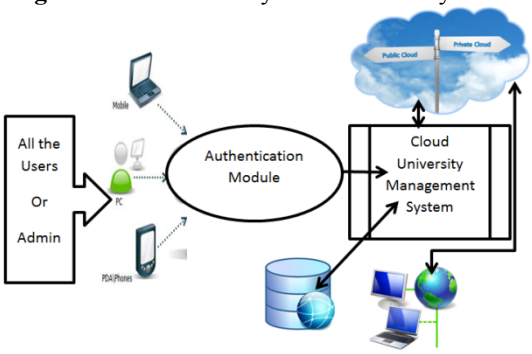

Fig. 7 Interaction with Users and University Cloud

The above university cloud architecture shown in Fig. 5 can be divided into the following layers: Infrastructure layer as a dynamic and scalable physical host pool, software resource layer that offers a unified interface for university system developers, resource management layer that achieves loose coupling of software and hardware resources, service layer, containing three levels of services (software as a service, platform as a service and infrastructure as a service), application layer that provides with content production, content delivery, virtual laboratory, collaborative learning, assessment and management features[11].

Infrastructure layer is composed of information infrastructure and teaching resources shown in Fig. 6 and Fig. 7. Information infrastructure contains

Internet/Intranet, system software, information management system and some common software and hardware; teaching resources is accumulated mainly in traditional teaching model and distributed in different departments and domain. This layer is located in the lowest level of cloud service middleware, the basic computing power like physical memory, CPU, memory is provided by the layer. Through the use of virtualization technology, physical server, storage and network form virtualization group for being called by upper software platform. The physical host pool is dynamic and scalable, new physical host can be added in order to enhance physical computing power for cloud middleware services.

Software resource layer mainly is composed by operating system and middleware. Through middleware technology, a variety of software resources are integrated to provide a unified interface for software developers, so they can easily develop a lot of applications based on software resources and embed them in the cloud, making them available for university cloud computing users.

Resource management layer is the key to achieve loose coupling of software resources and hardware resources. Through integration of virtualization and cloud computing scheduling strategy, on-demand free flow and distribution of software over various hardware resources can be achieved.

Service layer has three levels of services namely, SaaS (Software as a service), Paas (Platform as a service), IaaS (Infrastructure as a service).

Application layer is the specific applications of integration the teaching resources and other managerial resources in the cloud computing model, including interactive courses and sharing the teaching resources. The interactive programs are mainly for the teachers and administrative managers Sharing of teaching resources include teaching material resources, teaching information resources (such as digital libraries, information centers), as well as the full sharing of human resources. This layer mainly consists of content production, educational objectives, content delivery technology, assessment and management component for the university.

5. SECURITY RISK FACTORS IN CLOUD COMPUTING

Cloud security threats come in all shapes and sizes where the biggest one is the distributed denial of service (DDoS) attacks in application layer. These attacks threaten the very availability of cloud infrastructure itself [12]. If a cloud service is not even available, all other security measures, from protecting access to ensuring compliance is of no value whatsoever. Hackers have found and are actively exploiting weaknesses in cloud defenses, utilizing cheap, easily accessible tools to launch application-layer attacks. A major reason behind the success is that enterprise data centers and cloud operators are not well prepared to defend against them [13].

Abuse and Nefarious Use of Cloud Computing- IaaS offerings have hosted the Zeus botnet, InfoStealertrojan horses, and downloads for Microsoft Office and Adobe PDF exploits, Spam. The safe initiatives are stricter initial registration and validation processes, enhanced credit card fraud monitoring and coordination, comprehensive introspection of customer network traffic, monitoring public blacklists for one's own network blocks.

Insecure Interfaces and APIs- Anonymous access and/or reusable tokens or passwords, clear-text authentication or transmission of content, inflexible access controls or improper authorizations, limited monitoring and logging capabilities, unknown service or API dependencies. Safe initiatives analyze the security model of cloud provider interfaces, ensure strong authentication and access controls are implemented with encrypted transmission, and understand the dependency chain associated with the API.

Malicious Insiders- The threat of a malicious insider is well-known to most organizations. This threat is amplified for consumers of cloud services by the convergence of IT services and customers under a single management domain, combined with a general lack of transparency into provider process and procedure. Safe Initiatives are enforce strict supply chain management and conduct a comprehensive supplier assessment, specify human resource requirements as part of legal contracts, require transparency into overall information security and management practices, as well as compliance reporting, determine security breach notification processes.

Shared Technology Issues- IaaS vendors deliver their services in a scalable way by sharing infrastructure. Often, the underlying components that make up this infrastructure (e.g., CPU caches, GPUs, etc.) were not designed to offer strong isolation properties for a multi-tenant architecture. To address this gap, a virtualization hypervisor mediates access between guest operating systems and the physical compute resources.

Data Loss or Leakage- Some examples to compromise data are 1) operational failures (e.g., improper data deletion or alteration); 2) inconsistent use of encryption and software keys (or loss of encryption keys); 3) unreliable data storage; and 4) insufficient controls to allow unauthorized parties to access sensitive data. The threat of data compromise is mainly due to the architectural or operational characteristics of the cloud environment [14-15].

6. RESEARCH DECISIONS

In order to implement the Cloud Computing in Bangladesh the following initiatives should be taken immediately by the government:

- Collaborate with other governments and reduce the complexity of compliance requirements
- Establish cloud security standards
- Provide free access to broadband Internet
- Subsidize cloud infrastructure build out
- Offer an accessible national cloud
- Certify cloud service providers
- Establish and enforce minimum requirements on uptime, recover time, etc.

For evaluating potential providers of cloud-based services, we should keep track on following security concerns in mind.

- Secure data transfer-Make sure your data is always travelling on a secure channel; data should always be encrypted and authenticated using industry standard protocols, such as IPsec (Internet Protocol Security), that have been developed specifically for protecting Internet traffic.
- Secure software interfaces-Reliance on a weak set of interfaces and APIs exposes organizations to a variety of security issues related to confidentiality, integrity, availability, and accountability.
- Secure stored data- Data should be securely encrypted when it's on the provider's servers and while it's in use by the cloud service.
- User access control- Data stored on a cloud provider's server can potentially be accessed by an employee of that company, and you have none of the usual personnel controls over those people. Consider carefully the sensitivity of the data you're allowing out into the cloud.
- Data separation-Every cloud-based service shares resources, namely space on the provider's servers and other parts of the provider's infrastructure.

7. CONCLUSION

Cloud Computing is the most popular notion in IT today. Developers would be wise to design their next generation of systems to be deployed into Cloud Computing. This is the time to define potential actions for universities, industry and governments to consider the acceleration of cloud adoption in Bangladesh with proper security countermeasures and generating benefits for all stakeholders – individuals, businesses, universities, governments, and society as a whole.

8. FUTURE SCOPE

With arrival of cloud computing the conventional way of computing has gone for a sea change. We will work on practical implementation phase of university cloud from this research paper.

References

[1] Mladen A. Vouk, "Cloud Computing – Issues, Research and Implementations", Journal of Computing and Information Technology - CIT 16, 2008, 4, pp. 235–246.

[2] Michael Armbrust, "Above the Clouds: A Berkeley View of Cloud Computing", UC Berkeley Reliable Adaptive Distributed Systems Laboratory http://radlab.cs.berkeley.edu/Feb 10, 2009.

[3] C.N. Hoefer, et al., "Taxonomy of cloud computing services", IEEE Globecom 2010 Workshop on Enabling the Future Service-Oriented Internet.

[4] Ben Kepes, "Understanding The Cloud Computing Stack SaaS, Paas, IaaS", 2011.

[5] Abu Sarwar Zamani, et al. , "Emerging Cloud Computing", International Journal of Enterprise Computing and Business Systems ISSN (Online) : 2230-8849, http://www.ijecbs.com, Vol. 1 Issue 2 July 2011.

[6] David chappell, "A short introduction to cloud platforms-an enterprise-oriented view", sponsored by Microsoft corporation, august 2008.

[7] Katarzyna Keahey, et al., "sky computing", Published by the IEEE Computer Society,1089-7801/09/$26.00 © 2009 IEEE, September/October 2009.

[8] D. Hamilton. 'Cloud computing' seen as next wave for technology investors. Financial Post, 04 June 2008. http://www.financialpost.com/money/story.html ?id=562877 [18 July 2008].

[9] Richard Chow, "Controlling Data in the Cloud: Outsourcing Computation without Outsourcing Control", 2009.

[10] Mehmet Fatih Erkoc, Serhat Bahadir Kert,"Cloud Computing For Distributed University Campus: A Prototype Suggession", International Conference The Future of Education.

[11] Md. Anwar Hossain Masud, Xiaodi Huang, "An E-learning System Architecture based on Cloud Computing", World Academy of Science, Engineering and Technology 62 2012.pp.74-78.

[12] European Network and Information Security Agency Cloud Computing Security Risk Assessment http://www.enisa.europa.eu/act/rm/files/deliverables/cloud-computing-risk-assessment Security and Resilience in Governmental Clouds http://www.enisa.europa.eu/act/rm/emerging-and-future-risk/deliverables/security-and-resilience-in-governmental-clouds.

[13] Mohamed Al Morsy, "An Analysis of The Cloud Computing Security Problem", In Proceedings of APSEC 2010 Cloud Workshop, Sydney, Australia, 30th Nov 2010.

[14] David Munoz Sanchez, "Comparison between security solutions in Cloud and Grid Computing", Aalto University, T-110.5290 Seminar on Network Security, 2010.

[15] Siani Pearson, "Taking Account of Privacy when Designing Cloud Computing Services", CLOUD '09: Proceedings of the 2009 ICSE Workshop on Software Engineering Challenges of Cloud Computing, pages 44-52, May 2009.

Proceeding of the
International Conference on Electrical, Computer and Telecommunication Engineering
01- 02 December 2012 (ICECTE2012), RUET, Rajshahi-6204, Bangladesh

ICECTE2012: PI-0146

Design and Fabrication of A Simple Cost Effective Spin Coater for Deposition of Thin film

Madhobilata, Mst. N.Tamanna, M. Fardousi, M. F. Hossain

Department of Electrical and Electronic Engineering, Rajshahi University of Engineering & Technology (RUET), Rajshahi-6204, Bangladesh.

*E-mail: faruk94_ruet@yahoo.com

ABSTRACT

This paper describe the design and fabrication of an inexpensive spin coating system to deposit thin films of materials dissolved in a volatile solvent. The system can be easily built with the knowledge of machine and electronics. The system is constructed by using a dc motor and electronics circuit, designed to control the spinning speed .the spinning speed is up to 3,000 rpm .in our design, the spinning speed is controlled manually step by step process. ZnO thin films are successfully prepared through this spin coater a mixture of zinc acetate dehydrate, ethanol and diethanolamine.The deposition of thin film by spin coating is a very simple and widely used technique to prepare films of uniform thickness.

KEY WORDS—Spin coating, zinc oxide, thin films, film deposition, substrate.

1. INTRODUCTION

Thin films science and technology plays an important role in the high-tech industries. Thin film technology has been developed primarily for the need of the integrated circuit industry. The demand for development of smaller and smaller devices with higher speed especially in new generation of integrated circuits requires advanced materials and new processing techniques suitable for integration technology. In this regard, physics and technology of thin films can play an important role to achieve this goal. The production of thin films for device purposes has been developed over the past 40 years. Thin films as a two dimensional system are of great importance to many real-world problems. Their material costs are very small as compared to the corresponding bulk material and they perform the same function when it comes to surface processes. Thus, knowledge and determination of the nature, functions and new properties of thin films can be used for the development of new technologies for future applications. Thin films are thin material layers ranging from fractions of a nanometre to several micrometers in thickness. An uniform thin film can be applied by different techniques like Chemical Vapour Deposition (CVD) and Physical Vapour Deposition (PVD). One other technique is spin coating.Spin coating is a fast and easy method to generate thin and homogeneous organic films. Spin coating is a procedure used to apply uniform thin films to a flat substrate. A machine used for spin coating is called a spin coater, or simply spinner. In short, an excess amount of a solution is placed on the substrate, which is then rotated at high speed in order to spread the fluid by centrifugal force.This method was first described by Emslie et al. (1958) and Meyerhofer et al.(1978) using several simplifications. Manufacturing techniques of these devices are relatively simple because equipments are available .One of the most important factors in spin coating is repeatability. Several methods to grow inorganic compound semiconductors are taking vital roles in the advancement of technologies. To obtain the performance of thin film based devices control over the film properties is necessary. Therefore many sophisticated techniques, namely laser assisted evaporation, molecular beam epitaxy, ion beam sputtering, thermal evaporation, vacuum deposition, chemical vapour deposition, sol-gel, chemical bath deposition etc are being used. These processes are energy intensive and involve high temperature, pressure and vaccum. But spin coating is one of the most suitable, cost effective, fast and simple method to deposit thin film and the way of preparing uniform and homogeneous thin films. Our proposed design is approximately 30% cost effective than the market available spin coating system.There is no time consuming delay and it is easy to clean after each operation.

2. METHODOLOGY

The complete set up of a simple spin coater system is shown in the following figure 2.1

Figure 2.1: Complete setup of a simple spin coater.

This contains a DC motor, regulator, spinning disk, substrate, LED. The internal circuit is kept inside a box. In our design 12V, 3000rpm motor is used, to control the spinning speed by varying the voltage supply from 0 to 12V using a regulator. A power supply can be built using a transformer connected to the ac supply to step the ac voltage to a desired amplitude, then rectifying that ac voltage, filtering with a capacitor. The connection of the complete voltage supply unit is shown on the figure .The ac voltage is step down to 12V rms across bridge transformer. A half-wave rectifier and capacitor filter then provides an unregulated dc voltage shown as a dc voltage, with ac ripple of a few volts. This voltage acts as an input to the voltage regulator. The circuit and the motor are mounted inside a box with the axis of the motor passing through one of the walls. The overall internal circuit diagram of the complete system is shown in the following figure 2.2

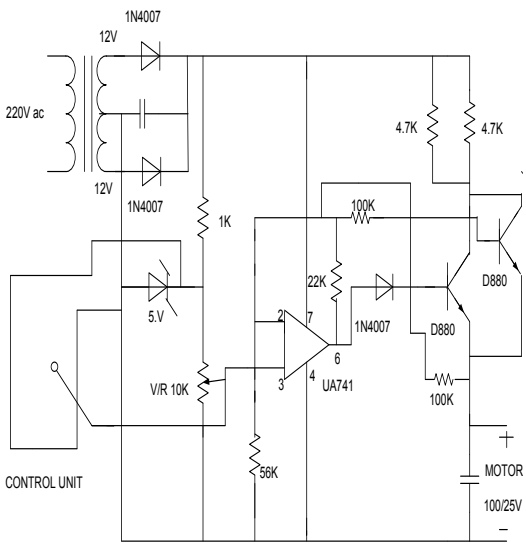

Figure 2.2: Internal circuit diagram of spin coater.

On the outside, a convenient arrangement of a push button, regulator knob and spinning circular disk is shown .The disk is connected to the motor shaft by pulley. The push button functions as the start button. LED is used to indicate the power supply; substrates are placed on the centre of the flat disk. The substrate is connected to the spinning disk using a small piece of double sided adhesive tape.

To avoid sprinkling of the solution and isolate film deposition from undesired air current, it is enclosed a by a plate made of glass. The plane of the disk that supports the substrates is perfectly levelled with the horizontal and the substrate must be clean and free of dust particles. Otherwise the film will not be uniform. These compatible, easy-to-use devices provide a convenient step-by-step method for precise and uniform deposition of thin films and coatings.

Spin Coating is a method to produce thin organic films that are uniform over large areas. The spin coating process can be broken down into the four stages .The deposition, spin up, and spin off stages occur sequentially while the evaporation stage occurs throughout the process, becoming the primary means of thinning near the end.

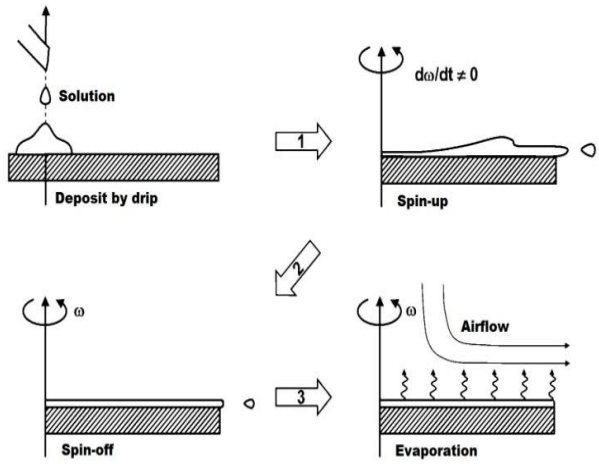

Figure2.3: Stages of thin film deposition by the spin coating method.

Four different stages of the spin coating process:

- Deposition of the coating fluid onto the wafer or a flat substrate
- The substrate is accelerated up to its final, desired, rotation speed
- The substrate is spinning at a constant rate and fluid viscous forces dominate the fluid thinning behavior.
- The substrate is spinning at a constant rate and solvent evaporation dominates the coating thinning behavior. After evaporation of the whole solvent, a solid film is generated.

Initial conditions that can be recommended for a good film deposition are the following:

• It must be assured that the plane of the disk that supports the substrates is perfectly leveled with the horizontal;

• The solution to be deposited should wet the substrate. If this does not happen, the solution will be thrown away from the substrate by centrifugal force without leaving any trace of material on the substrate. The flatness and/or roughness of the substrate are also a parameter that could affect the deposit;

• The solution that contains the material to be deposited should be uniform and homogeneous, free of lumps and air bubbles .The substrate must be clean and free of dust particles;

• There is an optimal relationship between spinning speed and concentration of the solution so that viscosity does not become an impediment to the flow of the solution on the substrate during spinning.

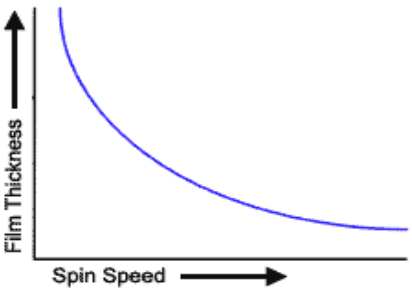

Figure2.4: Film thickness vs spin speed

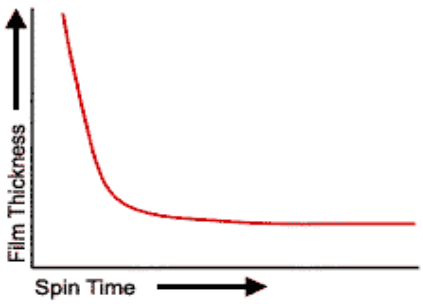

Figure 2.5: Film thickness vs spin time.

Rotation is continued while the fluid spins off the edges of the substrate, until the desired thickness of the film is achieved. The applied solvent is usually volatile, and simultaneously evaporates. So, the higher the angular speed of spinning, the thinner the film. The thickness of the film also depends on the concentration of the solution and the solvent.

Spin speed is one of the most important factors in spin coating. The speed of the substrate (rpm) affects the degree of radial (centrifugal) force applied to the liquid resin as well as the velocity and characteristic turbulence of the air immediately above it. The acceleration of the substrate towards the final spin speed can also affect the coated film properties. The thickness of films depends on different factors. To get homogeneous films, several different factors are important and have to be considered:

- Viscosity and concentration of the solution,
- The evaporation rate of the solvent,
- Rotational speed,
- Rotation time

There are several methods for deposition of thin film. Among different techniques for organic thin film deposition, spin-coating method has the merit of conveniences, use of low cost equipment and fast operating. Spin coating is general a convenient and reproducible method for applying highly uniform thin films to substrates of all kinds. It has applications in various industries, including the use of polymeric photo resist for photolithography, Sol – gel films for dielectric application, planner structure for various optical applications and microelectronic industries for fabrication of integrated circuits.

4. Results

In this work, ZnO films are prepared by using sol-gel spin coating method, and deposited on glass substrates by spin coating technique. The ZnO precursor solution are prepared by dissolving zinc acetate dehydrate (Zn (CH3COO)2·2H2O), in solution of ethanol and diethanolamine at room temperature. The solution is stirred to about half an hour till a clear and homogeneous solution is obtained. ZnO thin films are prepared by spin coating the stored solution on a glass substrate at different rotation speeds and spin time. The following ZnO films are obtained by using our designed spin coater-

Figure 3.1(a): For 20S

Figure 3.1(b): For 1 min

Figure7.1(c): 30S for varying speed and lower speed

The ZnO thin films a can be prepared using various methods: sputtering, spray pyrolysis, chemical vapor deposition, pulsed laser deposition, oxidation of metallic films etc. In respect of other methods, the sol-gel spin coating method has some merits such as easy control of used chemical components, deposition of thin films at low cost, less complicated deposition equipments.

In the recent years, ZnO have received considerable attention due to its applications in electrical, optical, mechanical and scientific research as well as industry. ZnO is a wide band gap n-type semiconductor with hexagonal wurtzite structure. It is a versatile material having potential use in many applications like solar cell, transparent conducting electrode, ultraviolet and blue light emitting diodes, laser diodes, thin film transistor, surface acoustic wave (SAW) devices and gas sensors. For transparent conducting application the film should have low resistivity, high transmittance in the visible range and good stability against corrosive environment.

4. CONCLUSION

The total system is very simple. Spin coaters are ideal tools for the preparation of thin films. In this work, ZnO thin films are successfully prepared by spin-coating method, using a simple and convenient chemical route. This spin coater can also be used for film deposition of different types of precursor solution.To tackle the problem of high instrumental costs; in this work we propose the development of apparatus of easy implementation in an undergraduate laboratory for the preparation of thin films using recycled electronic components.

5. FUTURE WORK

- To make microcontroller based digital spin coating system.
- To digitally control the motor speed step by step process.
- LCD display unit can be used which will show spin time, spin speed etc.
- To develop nanotechnologies in Bangladesh through spin coating system.
- Analysis of thin film(band gap, transparency,absorption,transmittance measurement)

6. ACKNOWLEDGMENT

The authors would like to thank the Department of Electrical and Electronic Engineering, Rajshahi University of Engineering & Technology (RUET) for giving the chance to use the different equipment of the photovoltaic and nanotechnology laboratory.

REFERENCES

[1]. R.G. Aguilar , J.O.López "*Low cost instrumentation for spin-coating deposition of thin films in an undergraduate laboratory*'' Received 8 April 2011, accepted 11 June 2011, *Lat. Am. J. Phys. Educ. Vol. 5, No. 2, June 2011.*

[2]. M. Smirnov, A .P. Rambu, C. Baban and G. I. Rusu "*Electronic Transport Properties in Polycrystalline ZnO Thin Films*" *M. Smirnov et al. / Journal of Advanced Research in Physics 1(2), 021011 (2010)*

[3]. H.F. Hussein, G. M.Shabeeb, S. Sh. Hashim[2] "*Preparation ZnO Thin Film by using Sol-gel-processed and determination of thickness and study optical properties*" Received in 27 May 2011, Revised 18 July 2011, Accepted 18 July 2011.

[4]. S.Panigrahi1,S. Waugh, S.K. Rout A. K. Hassan and A. K. Ray "*Study of Spin Coated Organic Thin Film Under Spectrophotometer*",Indian Journal of Physics, Vol 78, Iss 8, P 823-826, 2004

[5]. http://www.ece.gatech.edu/research/labs/vc/packaging/theory/spin_theory.html

Proceeding of the
International Conference on Electrical, Computer and Telecommunication Engineering
01- 02 December 2012 (ICECTE2012), RUET, Rajshahi-6204, Bangladesh

ICECTE2012: PI-0147

Automatic Speaker Recognition system using Mel Frequency Cepstral Coefficients (MFCC) and Vector Quantization (VQ) approach

MD. Abdullah-al-MAMUN[1], Firoz Mahmud[2] , Aminul Islam[3],Syed Tauhid Zuhori[4]
Department Computer Science & Engineering
Rajshahi University of Engineering & Technology

E-mail: mamun.ruet@yahoo.com, fmahmud.ruet,aminul35cse{gmail.com}, tauhid.ruet@yahoo.com

ABSTRACT
In this paper, automatic speaker recognition system is implemented by combining feature extraction and feature matching technique. Feature extraction method that is implemented by the Mel Frequency Cepstral Coefficients (MFCC). The Vector Quantization (VQ) is done using k-means algorithm that is used for the feature matching technique due to high accuracy but its simplicity. A speaker recognition experiments was performed using a 5-talkers (3 male and 2 female) with different conditions of Bangla sentence utterances. So, in this proposal achieved 96% efficiency for text dependent or independent speaker recognition system with 60 - 90 seconds duration test voice sample.

KEYWORDS: Speaker recognition, MFCC, Vector VQ, k-means clustering, Feature Extraction.

1. INTRODUCTION

Speech is one of the natural forms of human communication. Modern scientific technology has made it as a security systems based on speaker recognition system. So by the speaker recognition technology makes to control access to secret services, for example, for giving commands to computer, phone access to banking, database services, shopping or voice mail and access to secure equipment by a speaker's voice. Here we want to discuss a simplest model of speaker recognition system that could be applied to a speech of an unknown speaker but achieve more accuracy.

Figure 1: Speaker Recogniton application on the computer as an password sytem.

Speaker Recognition is the process of automatically recognizing who is speaking on the basis of individual information included in speech signals [1].
Speaker recognition can be classified into identification and verification.
Speaker Identification determines the caller is out of a set of known speaker, using utterance from a speaker. This is one-to-many comparison.

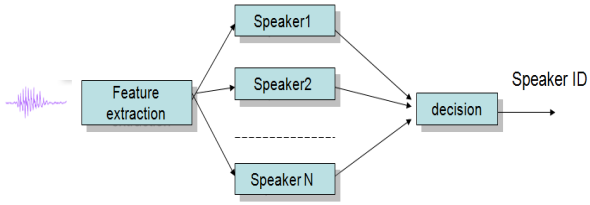

Figure 2: Speaker Identification system

Speaker Verification determines whether the caller is who he/she claims to be from the utterance of a speaker. This is one-to-one comparison.

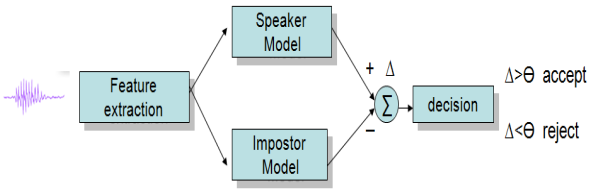

Figure 3: Speaker Verification system.

Speaker recognition methods can also be divided into text-independent and text-dependent methods.
Text-dependent recognition is the recognition system of the speaker's identity is based on knows text spoken by that person, like passwords, card numbers, PIN codes etc.
Text-independent recognition is the recognition system of the speaker models capture characteristics of somebody's speech which does not know text spoken by that person
So now we want to present efficient way to speaker recognition system by combining Mel Frequency Cepstral Coefficients (MFCC) and Vector Quantization (VQ) technique.

2. SPEAKER RECOGNIZER OVERVIEW

A speaker recognition system is mainly composed of the following four parts:

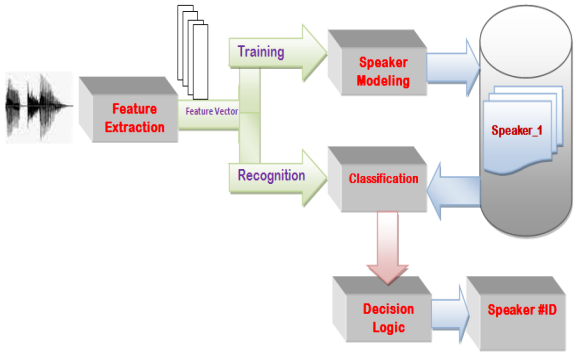

Figure 4: Block diagram of speaker recognition system.

2.1 Front-end processing: Input the speaker voice as audio files and produced the feature vector by the feature extraction method which is to strip unnecessary information from the input data and convert the properties of the signal that simplifies the distinction of the classes. The feature vector sequences are used to training and testing utterances are the inputs of the classification step of a speaker recognition system

2.2 Speaker training phase: In the training phase, each known or registered speaker has to provide speech samples so that database of the system can build or train a reference model for that speaker. It consists of two main parts. The first part consists of processing each person's input voice sample to compress and summarize the characteristics of their vocal tracts. The second part involves pulling each person's data together into a single, easily manipulated matrix [6]. A speaker-specific threshold is also computed in the training samples period, in order to speaker verification system.

2.3 Database Design: Each speaker training voice is stored as audio file and threshold also stored into the database list, i.e. each speaker models are stored here.

2.4 Speaker testing or Recognition: Speaker testing can be speaker identification or speaker verification. In the testing system, first the input signal (unknown) is converted to the feature vector, and then it is compared to the all model that is stored in the database. And compute the difference of that data set to selecting the best matching model which is the recognition decision.

3. FEATURE EXTRACTION

Feature extraction is a special form of dimensionality reduction process for an input signal. The feature extraction process cuts the digitized speech signal, that values are overlapping windows of equal length. The cut-out portions of that speech signal are called "frames", they are extracted out of the original signal every 10 or 20 ms. The length of each frame is about 30 ms. Each frame in the time domain is transformed to a MFCC vector, where each vector representing cepstral properties of the speech signal within the corresponding window. Especially the feature extraction process reduces the dimension of the data in order to avoid the "curse of dimensionality" property. The feature vector sequences of training and test utterances are the inputs of the classification step of a speaker recognition system [1]. There are several feature extraction methods are exists, such as Linear Prediction Coding (LPC), Mel-Frequency Cepstrum Coefficients (MFCC), Perceptual Linear Predictive Coefficients (PLP) and so on.

4. MEL FREQUENCY CEPSTRAL COEFFICIENTS (MFCC)

Mel-frequency cepstral coefficients (MFCCs) are coefficients that collectively make up an MFC where MFC (mel-frequency cepstrum) is a representation of the short-term power spectrum of a sound for audio processing. Here, cepstral means "spectrum-of-a-spectrum". The MFCCs are the amplitudes of the resulting spectrum.

5. CLASSIFICATION

Pattern recognition is a process of data classification. The process is usually based on statistical information extracted from data. Pattern Recognition aim is to detect relationships between variables [2].

The goal of pattern recognition is to classify objects of interest into one of a number of categories or classes. The objects of interest are generically called patterns and sequences of acoustic vectors that are extracted from an input speech. The classes here refer to individual speakers for this speaker recognition topics. Since the classification procedure is applied on extracted features, it can be also referred to as feature matching [1].

There are several feature matching techniques are used in speaker recognition system, such as, Dynamic Time Warping (DTW), Hidden Markov Modeling (HMM), Vector Quantization (VQ) and so on. The VQ approach has been used here for its ease of implementation and more accuracy.

6. VECTOR QUANTIZATION(VQ)

A vector quantizer maps k-dimensional vectors in the vector space R^k into a finite set of vectors $Y = \{y_i: i = 1, 2... N\}$ where each vector y_i is called a code vector or a codeword and the set of all the codewords is called a codebook. Associated with each codeword, y is a nearest neighbor region called

Voronoi region, and it is defined by: $\mathbf{V_i = \{x \in R^k : \| x - y_i \| \leq \| x - y_j \| \text{ for all } j \neq i\}}$. The set of Voronoi regions partition the entire space R^k such that: $\bigcup_{i=1}^{N} V_i = R^k$ and $\bigcap_{i=1}^{N} V_i = \emptyset$ for all $i \neq j$.

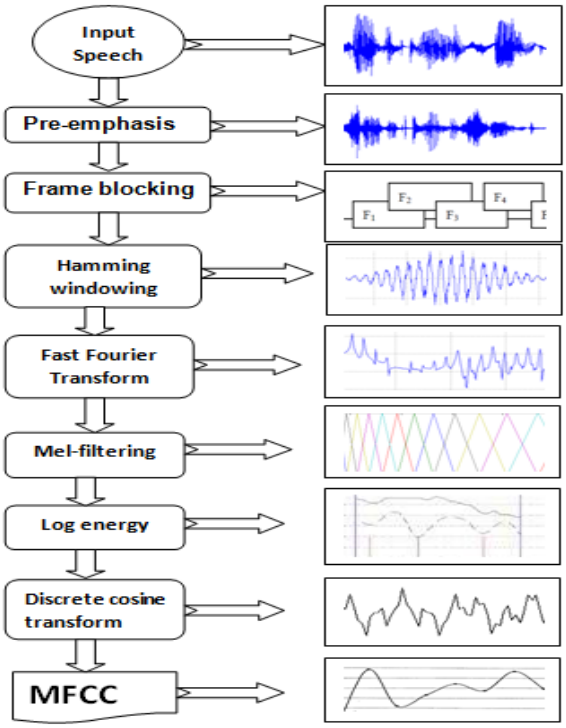

Figure 5: Steps for Mel Frequency Cepstral Coefficients (MFCC).

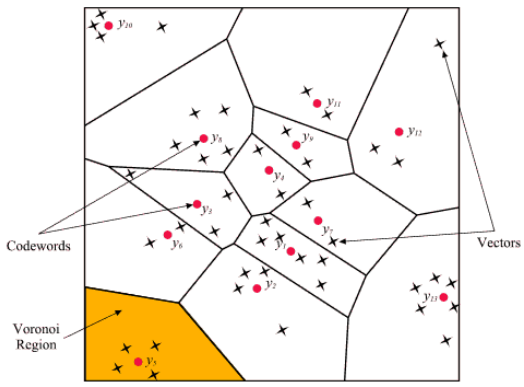

Figure 6: Codeword resides in its own Voronoi region for a given vector space.

7. WORKING STEPS OF VQ

Consider, The input speech signal is D={d1,d2,d3… di} where, i is the number of raw speech data.

The speech sample are converted number of speech feature vector $X=\{x_1, x_2 \ldots x_L\}$ by the feature extraction (i.e, MFCC).

And the feature vector X is partitioned into a set of mutually exclusive convex regions $S=\{s_1, s_2 \ldots s_N\}$, where $N \leq L$

For each region a centroid is assigned $C=\{c_1, c_2 \ldots c_N\}$ by the Euclidean distance. The collection of these centroids $C=\{c_1, c_2 \ldots c_N\}$ is known as a codebook.

7.1 Speaker Training:

In the training phase, using any clustering algorithm a speaker-specific VQ codebook is generated for each known speaker.

The clustering can be done by a clustering algorithm, such as, K-means clustering algorithm. K-means clustering is a method of classifying or grouping items into k groups (where k is the number of dimension). This grouping is compute by minimizing the sum of Euclidean distances between all samples and the corresponding centroid. The algorithm is composed of the following steps:

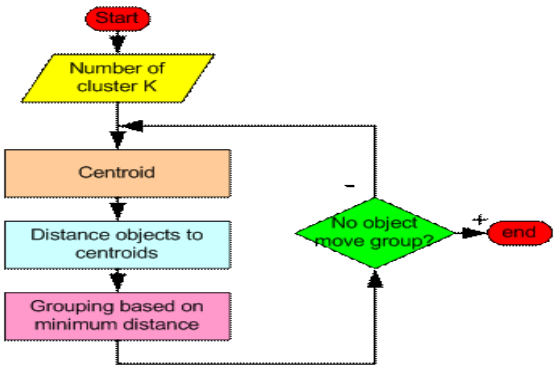

Figure 7: Steps for k-means clustring algorithm

The K-means algorithm partitions the *X* feature vectors into *N* centroids. The algorithm first chooses *N* cluster centroids among the *X* feature vectors [3]. Then each feature vector is assigned to the nearest centroid and the new centroids are calculated. This procedure is continued until a stopping criterion is met, that is the mean square error between the feature vectors and the cluster-centroids is below a certain threshold or there is no more change in the cluster-centre assignment [4].

7.2 Speaker Database

Database contains *N* codebooks $\{c_1, c_2 \ldots c_N\}$ for each speaker. These codebooks are collected from the speaker training period.

7.3 Speaker Matching

In the recognition phase an unknown speaker, represented by a sequence of feature vectors $\{x1 \ldots xT\}$, is compared with the codebooks in the database. For each codebook a distortion measure is computed, and the speaker with the lowest distortion is chosen [5]. For an unknown speaker, each feature vector *X* is compared with all the codebooks that stored into the

database and the codebook with the minimized average distance is chosen to be the best matching.

8. EXPERIMENTAL RESULT

The input speech signal description that is used to store audio file into the database and feature matching work is shown in the table 1.

Parameter	Characteristics
Language	Bangla
No. of speaker	5
Speech type	Sentence reading
Recording condition	A normal room condition
Audio Length	60-90 seconds
Audio type	Stereo
Sample Format	16-bit PCM
Sampling Frequency	8 KHz
Bit Rate	1411 kbps

Table 1: Database description.

According to the database description, there are number of samples are collection of database from different speakers are shown below.

Speaker	No. of input	Correct	Incorrect	Accuracy
Speaker_1	5	5	0	100%
Speaker_2	9	8	1	88.88%
Speaker_3	6	6	0	100%
Speaker_3	12	11	1	91.67%
Speaker_4	8	8	0	100%
Speaker_5	10	10	0	100%
Total Speaker	50	48	2	96%

Table 2: Test result for speaker recognition system.

9. CONCLUSIONS

We have proposed automatic speaker recognition system with the combine Mel Frequency Cepstral Coefficients (MFCC) that is used as feature extraction and k-mean cluster algorithm based Vector Quantization (VQ) approach with minimum distance classifier proposed for feature match or recognition purpose. According to this combining process a experiment was done for the text-dependent and text-independent recognition system with some male and female voice in different environment or conditions. So from the experimental result we had seen that 96% achievement for speaker recognition by the MFCC and VQ approach. According to the experimental result, speaker recognition result can be decreases some real life problem, such as, using poor microphone, noise of the environment, poor utterance of a speaker.

In a conclusion, the proposal approach achieve a better accuracy for text dependent or text-independent speaker recognition system by a simplest model using MFCC and VQ.

10. FUTURE WORK

This is the initial work about speaker recognition task for mine as this study is still ongoing. So I have a plane about this work, such as recognize the speaker if the speech is deal with crosstalk, laughter and uncharacteristic sounds. Next I try to develop it using Hidden Markov Model(HMM) to get achieve better accuracy.

REFERENCES

[1]. Prof. Ch.Srinivasa Kumar "Design of an Automatic Speaker Recognition System Using MFCC, Vector Quantization and LBG Algorithm" *in proc IJCSE ISSN : 0975-3397,* Vol. 3 No. 8 ,August 2011,pp. 2942-2954

[2]. Manjot Kaur Gill, Reetkamal Kaur, Jagdev Kaur "Vector Quantization based Speaker Identification" *in Proc International Journal of Computer Applications (0975 – 8887), Volume 4 – No.2, July 2010,* pp.(1-4)

[3]. Soong, F., A.E., A. R., Juang, B.-H., and Rabiner, L., "A vector quantization approach to speaker recognition" *in Proc AT & T Technical Journal* Volume 66, 1987, pp.(14–26).

[4]. Manjot Kaur Gill, Reetkamal Kaur, Jagdev Kaur ,"Vector Quantization based Speaker Identification" *in Proc International Journal of Computer Applications (0975 – 8887)*, Volume 4 – No.2, July 2010, pp.(1-4)

[5]. Manjot Kaur Gill, Reetkamal Kaur, Jagdev Kaur "Vector Quantization based Speaker Identification" *in proc International Journal of Computer Applications (0975 – 8887)*, Volume 4 – No.2, July 2010, pp.(1-4).

[6]. Dr. H. B. Kekre, Ms. Vaishali Kulkarni, "Speaker Identification by using Vector Quantization*" in Proc Dr. H. B. Kekre et al. / International Journal of Engineering Science and Technology,* Volume 2(5), 2010, pp.(1325-1331).

[7]. J. P. Cambell "Speaker Recognition A Tutorial" *in Proc. of the IEEE*, Volume 85(9), 1997, pp. 1437-1462.

[8]. Kyung Y.J., Lee H.S. Bootstrap and aggregating "VQ classifier for speaker recognition" *in proc Electronics Letters*, Volume 35(12), 1999, pp. 973-974.

[9]. Zheng F., Zhang, G. and Song "Comparison of different implementations of MFCC" *in proc J. Computer Science & Technology*, Volume 16(6),2001, pp.582-589.

[10]. He, J., Liu, L., Palm "A Discriminative Training Algorithm for VQ-based Speaker Identification" *in proc IEEE Transactions on Speech and Audio Processing*, Volume 7(3),1999, pp.353-356.

Proceeding of the
International Conference on Electrical, Computer and Telecommunication Engineering
01- 02 December 2012 (ICECTE2012), RUET, Rajshahi-6204, Bangladesh

ICECTE2012: PI-0148

Design a Microcontroller Based Automatic Switching System

Md. Asifur Rahman[1], Najmin Ara Sultana[2]
[1, 2] Department of EEE, Rajshahi University of Engineering & Technology, Rajshahi, Bangladesh
E-mail: ruetasif@gmail.com , najmineee@gmail.com

ABSTRACT
This paper represents the design of an automatic switching system which is an automation of conventional manual switching system. This is a microcontroller based system which does not require a human operator to operate the switching at accurate time. In this automatic system, one can easily set or change the various operating schedule for different load groups by using the keyboard and display. Then he can forget about it because it will operate the load groups automatically at the pre-set times. Automatic system is always more preferable than human operated switching as a man can forget but a machine cannot forget about proper time switching, beside this the additional costs of salary or wages of an operator also exists in manual system.

KEY WORDS: Automatic Control, Switching System, Microcontroller, Keyboard.

1. INTRODUCTION

Technology is the gateway of 21st century in which Bangladesh have not reached yet in a matured way. To fulfill this destination we have to embrace the concept of being a technologically developed nation. Technological development does not necessarily means only the development of IT sector but also the substantial development of practice of technology in every steps of our life. To reach the pinnacle of development we have to achieve development in every technological sector at a cost effective level and this project is a small attempt to the way of technological development.

2. SYSTEM CONFIGURATION

2.1 Display

Displays are used here for displaying the menu, showing the real time clock and active loads, in the menu shows the start and end time of each load group, controlling of the times and also setting the clock time in hours and minutes. Here the control push buttons activity and every change are directly shown in the display. For this purpose a LCD is used as display.

2.2 Keyboard

Keyboard is used to enter into the menu, set the clock time and input the load start time and end time. Here four push buttons are used as the keyboard input interfaced with Micro Controller.

2.3 Microcontroller

Microcontroller is the main unit of this project which stores the all information about start time and end time of loads, works as a real time clock, operates the loads according to the predetermined inputs via relay circuit and of course the display and keyboard are controlled with it.

3. HARDWARE DESIGN

3.1 Microcontroller

The microcontroller ATMega8L produced by AVR is used. ATMega8L is a 28 PIN DIP [1]. The program memory of ATMega8L is 8 Kbytes (highest) at which program is loaded. The used features of ATMega8L in this system are I/O Port, Interrupt, and Electrically Erasable Programmable Read Only Memory (EEPROM).

3.2 LCD

20*2 represents that this LCD contains 20 characters per line and total no. of line is 2. 20*2 LCD is used here for displaying the messages [2].

3.3 Keyboard

Four push buttons (two pins each) are used as a single column keyboard to input various data such as clock time, load start time and end time and menu entrance and exit.

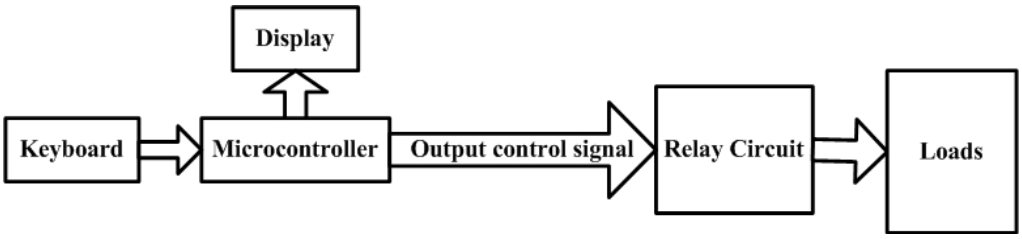

Fig 1: Basic Block Diagram.

4. SOFTWARE DESIGN

4.1 Flow Chart

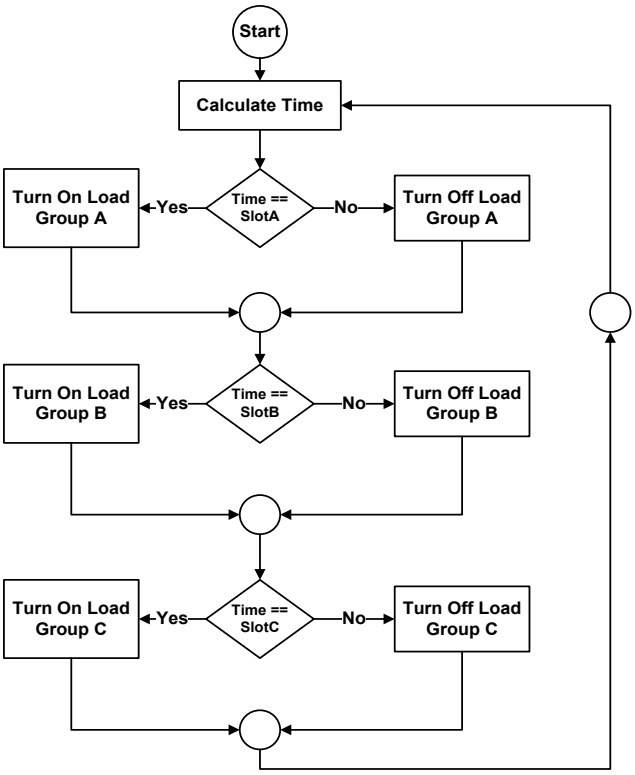

4.2Algorithm

Step 1: Start
Step 2: Calculate Time.
Step 3: Check time stamp.
Step 4: If Time Stamp is 1st Slot Turn On Load group A.
Step 5: If Time stamp is 2nd slot Turn On load group B.
Step 6: If time stamp is 3rd slot Turn On load group C.
Step 7: If time stamp is outside the time stamps Turn Off the loads.
Step 8: stop.

5. SIMULATION OF THE SYSTEM

The simulation studies are carried out in PROTEUS ISIS interactive circuit simulation environment. The program is written in C and then is compiled by a freeware version C compiler "WinAVR" [3], [4]. Implementation of the hardware for this automatic system is done using real time control. A microcontroller is used for implementing the real time control. A setup of simulation is shown in Fig. 3.

Fig. 2: Flow Chart

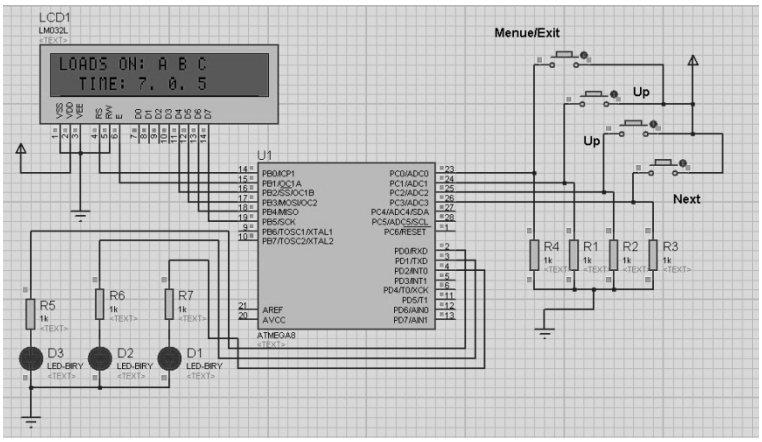

Fig. 3: Simulation set-up

6. COMPLETE CIRCUIT DIAGRAM

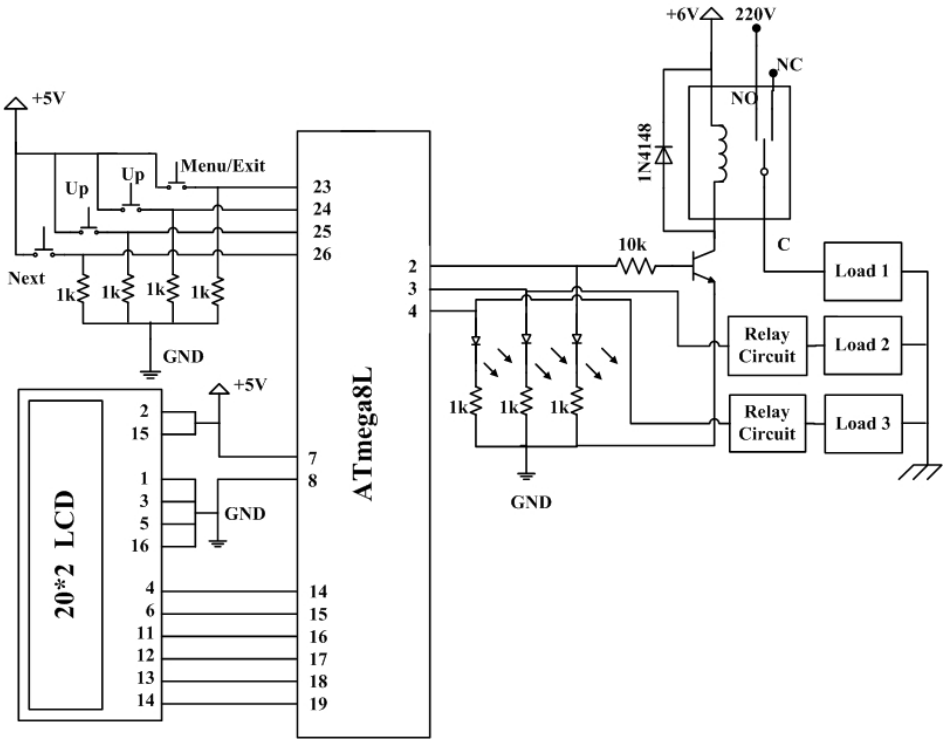

Fig 4: Complete Circuit Diagram.

6.1 Operation

At first, the default settings are displayed. The default settings are: time is 4:59:50, the start time and end time of load groups are A: 4 to 7, B:6 to 8 and C:7 to 9 o'clock. When push button 1 (Menu/Exit) is pressed, the display will show the start time and end time settings of Group A. The value of 1st line can be changed by pressing button 2 (upper "Up") and the value of 2nd line by pressing button 3 (lower "Up"). Then pressing the button 4 (Next) to go to the Group B and C or button 1 (Menu/Exit) to exit from menu. If anyone wants to change the clock time, this option is available in the clock setting menu which is placed after Group C menu, he/she can go by pressing next button. In the clock menu, hour can be set in the upper line and minute in the lower line by two 'Up' button (button 2, 3). When the new setting is complete, it will operate the load according to the setting and no other attention required at the switching time of load groups.

7. Results

7.1 Simulation Results

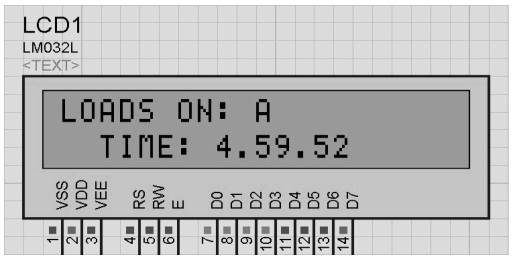

Fig. 5.1: At start up, Showing default time

Fig. 5.3: pressing Next Setting time for group B

Fig. 5.2: after pressing Menu, Setting time for group A

Fig. 5.5: pressing Next, Setting time of clock

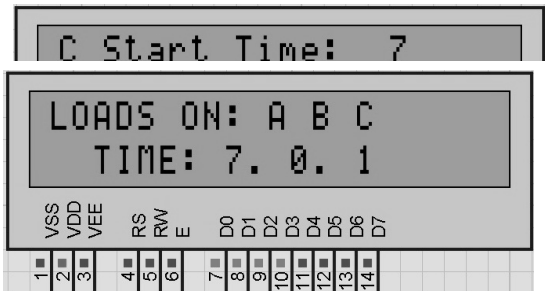

Fig. 5.6: pressing Exit Showing active load groups

8. CONCLUSION

This is a very simply operated, small and low cost automated switching system for general purpose use. In spite of having relatively higher installation cost than manual switching system, this project has a very low amount of power consumption and no running cost at all, which is very significant for the success of automation of a system. I hope "Microcontroller based automatic switching system" will open a new opportunity to run along the way to build a better Bangladesh.

REFERENCES

[1] Atmel AVR, datasheet of ATmega8L, website: http://www.atmel.com/avr

[2] All Datasheet, Datasheet of Display LM032L (20*2 LCD) from Alldatasheet.com. Website: http://www.alldatasheet.com

[3] MCS Electronics website, bascomAVR software, website: http://www.mcselec.com

[4] Atmel AVR RISC processor's software site, WinAVR software, website: http://www.winavr.sourceforge.net

Proceeding of the
International Conference on Electrical, Computer and Telecommunication Engineering
01- 02 December 2012 (ICECTE2012), RUET, Rajshahi-6204, Bangladesh

ICECTE2012: PI-0149

Developing a Framework for Generating Bilingual English-Bangla Dictionaries from Parallel Text Corpus

Mohammad Shamsul Arefin, Yasuhiko Morimoto, Chen Zhiming
Graduate School of Engineering
Hiroshima University, Kagamiyama 1-7-1, Higashi-Hiroshima 739-8521, Japan
Email: [d105660, morimo, m115395]@hiroshima-u.ac.jp

ABSTRACT
In this work, for the first time, we develop a framework for creating two bilingual English-Bangla dictionaries from parallel English and Bangla documents. One dictionary is for name entity and another one is for other entities. In our method, though it requires some level of dictionary editing, it decreases the workload of human correctors. Experimental evaluation shows that our system can build bilingual English-Bangla dictionaries at a satisfactory level.

KEY WORDS: Parallel corpus, keywords extraction, bilingual dictionary, name entity recognition.

1. INTRODUCTION

Bilingual dictionaries are vital resources for processing information in two different languages. However, the availability of such dictionaries among the language pairs is not large in number. The situation is even worse in case of less online resourceful language like Bangla. Though Bangla is the sixth largest speaking language in the world, the language is not yet an online resourceful language. Researchers are focusing in its development as a resourceful one in recent days. However, due to the lack of a proper bilingual English-Bangla online dictionary, they are facing difficulties in their research.

Considering these facts, we have developed a framework to build two bilingual English-Bangla dictionaries from parallel documents of Bangla and English. The developed framework can build bilingual dictionaries with a satisfactory level of accuracy. To correct inaccurate entries in the dictionary, we have provided dictionary editing facility.

The remainder of the paper is organized as follows. Section II provides a brief review of related works on dictionary creation. Section III describes the overall architecture and methods for bilingual dictionary creation. In Sections V, we present the experimental results. Finally, we conclude the paper in Section V.

2. LITERATURE REVIEW

In this section, we are providing a brief overview of the initiatives taken around the globe for building bilingual dictionaries. For the construction of such dictionaries, researchers mainly consider comparable corpora or an intermediary language known as pivot language.

Various corpus based, statistical methods were developed starting from the 1990's [1, 2, 3]. The biggest disadvantage these methods is the need for a large bilingual corpus. Considering this fact Tanaka et al. [4] proposed a new approach. As a resource, they used dictionaries to and from a pivot language to generate a new dictionary. These pivot language based methods rely on the idea that the lookup of a word in an uncommon language through a third, intermediated language can be automated. The work in [4] use bidirectional source-pivot and pivot-target dictionaries. Their method select correct translation pairs by means of inverse consultation. Inverse consultation is a method that relies on counting the number of pivot language definitions of the source word, through which the target language definitions can be identified. Sjobergh [5] also propsed an approach to pivot language based dictionary generation.

There are many improvements of the above methods, but for various reasons they failed to be implemented with any arbitrary language pair. Shirai et al. [6] used English to design a Korean-Japanese dictionary, but because the usage of language-specific information, they conclude that their method can be considered to be applicable to cases of generating among languages similar to Japanese or Korean through English. Paik et al. [7] proposed a method with multiple pivots to translate Sino-Korean entries. The authors in [8] describe a Japanese-Malay dictionary that uses a novel technique in its improved matching through normalization of the pivot language.

Our work in this paper is based on parallel corpus, where we considered parallel corpus in two different languages: English and Bangla.

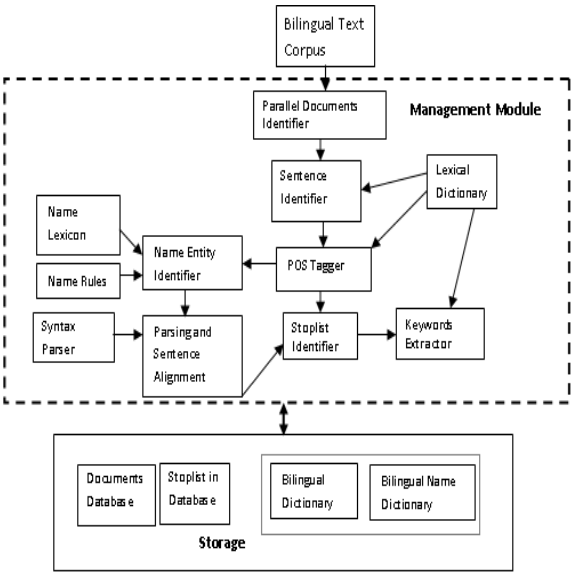

Fig. 1 System architecture of bilingual dictionary generation

3. SYSTEM ARCHITECTURE AND DESIGN

The system architecture for bilingual dictionary generation comprises two main modules: management module and storage module. The management module sets up the database from an initial set of documents against which we shall create our bilingual dictionaries. The storage module manages the storage of the parallel documents of two different languages using BFILE data type. It also stores other related information. The overall architecture is shown in **Fig. 1**. The single directional arrows represent the direction of next sub-module to be executed in a module and the double directional arrows represent the relationship of a sub-module with sub-modules from which the sub-module gets help for processing.

3.1 Management Module

Management module consists of the sub-modules: parallel documents identifier, sentence identifier, POS tagger, name entity identifier, keywords extractor, stoplist identifier, parsing and sentence alignment. The relationships among the sub-modules are shown in **Fig. 1**.

3.1.1 Parallel Documents Identifier

Parallel documents identifier sub-module identifies the pair of parallel documents. Let the input set of documents be D = $\{D_{b1}, D_{b2}, \ldots, D_{bn}, D_{e1}, D_{e2}, \ldots, D_{en}\}$. Here, D_{bi}, $1 \leq i \leq n$ is the list of documents in one language and D_{ej}, $1 \leq j \leq m$ is the list of their parallel documents in another language. The parallel documents identifier sub-module identifies the parallel document pairs (D_{bi}, D_{ej}) from D.

For identifying parallel documents, we used the concepts of [9], where the authors use vector space model [10]. At first, we select a document of a language as a query document and then perform relevancy check with the documents of another language. The document that shows highest relevancy is considered as the parallel document of the query document. Then, with this pair of documents, we proceed to the next sub-module.

3.1.2 Sentence Identifier

Sentence identifier sub-module takes a pair of parallel documents from parallel documents identifier sub-module and identifies individual sentences in each document with the help of lexical dictionary of the corresponding language. Identification of sentences is relatively easy as in most cases each sentence always ends with some special punctuation marks like - '.'. Therefore, scanning a document from the beginning for such punctuation marks can identify most of the sentences in a document. There are some possibilities of ambiguities. Therefore, we take proper mechanism for truckling ambiguities when identifying specific sentence. After finding out a sentence, we also identify the type of the sentence. We used the concept of [11] for identifying individual sentences and their type. We then pick two sentences: one sentence from one document and another sentence from another document having same sentence order in the documents.

3.1.3 POS Tagger

Part of Speech (POS) tagging is the task of labeling each word in a sentence with its appropriate syntactic category called part of speech. Part of speech tagging is a very important preprocessing task for language processing activities. We used the Stanford Tagger version 3.1.3 [12] for POS tagging in English and the concept of [13] for POS tagging in Bangla.

3.1.4 Stoplist Identifier

Stopwords are the words those are most frequently used in documents. We manually store such words as the entries in a table. When a new stopword is required to be added, we just manually add it in the table. Stop list identifier sub-module takes a tagged sentence as input and identifies whether a word is a stopword or not. If it finds that a word is a stop word, it just skips the word. Otherwise, it sends the word to the keyword extractor sup-module for identifying the keyword of that word.

3.1.5 Keyword Extractor

The keyword extractor sub-module receives the words from the stoplist identifier sub-module and extracts the roots of those words. For extraction of root the word, it checks the words against a list of predefined postfixes and prefixes. We used a simple variation of the algorithm presented in [9]. After we

find that there is at most one keyword of a specific part-of-speech in a sentence in one language and in its corresponding sentence in another language, then we add the words of the same part-of-speech in the dictionary with a one-to-one mapping between them.

3.1.6 Name Entity Identifier

Name entity identifier sub-module identifies the name from parallel sentences. We then store the name entries in bilingual name dictionary. For identifying name in a Bangla sentence, we use the name rules and n-gram models proposed in [14], while we use the concept of [15] for recognizing name in English. If there is more than one name in the parallel sentences, we perform transliteration of the name entry of one language to another language in use. Then, we perform mapping of a name in a language with the word of another language that has closest match after transliteration. For performing transliteration of words, we use the concept of work in [16].

3.1.7 Parsing and Alignment

In general, it is seen that a sentence in a document contains more than one words of same part-of-speech. In such a situation, we cannot select one-to-one correspondence between words of parallel sentences. Therefore, we need to perform parsing of the sentences. Our parsing approach is based on Context-Free Grammar (CFG) of each language. We used CFG presented in [17] for parsing Bangla sentences. After tagging the words of the sentence with appropriate information, we can construct the parse tree of it based of the language grammar. CFG is well known for the construction of parse trees. Then, we perform proper rotation of the parse tree corresponds to a sentence in a specific language so that two parallel sentences languages are aligned in the same order. Then, we perform one to one correspondence between the words those are in the same position at the leaf node in the corresponding parse tree. Then, again we send the pair of words to stoplist identifier sub-module to identify whether the words are stoplist words or not. Non-stoplist words are then sent to keywords extractor sub-module again to extract the keywords. We then keep the both keywords to the bilingual dictionary with one-to-one mapping between them.

3.2 Storage

Storage module stores information processed by management module. It stores the documents using BFILE data type, stoplist words in a table. We store the entries in the dictionaries in such a way that there is no redundancy in the dictionary entry. For ensuring non-redundancy in the dictionaries, we search the dictionary to check whether the entry is already in the dictionary or not. If we find that a word is already in the dictionary, we do not further add the word in the dictionary. Otherwise, we add the word in the dictionary.

4. EXPERIMENTS

We have implemented our system on a machine having an Intel(R) Core2 Duo, 2 GHz CPU, and 3 GB main memory, running on Microsoft Windows XP operating system. The system was implemented in Jbuilder-8 in the front and in Oracle 10g DBMS in the back-end for storing the text documents, dictionaries and other necessary information. We have used total 100 documents collected from the translation part of a Bangla Grammar book. Among these 100 documents, 50 documents contain information in Bangla and the remaining 50 documents contain information in English. Each of the 50 Bangla documents contains a paragraph of the book, while each of the 50 English documents contains same information of a paragraph in English. The documents are uniform in size and each document contains around 100 words. We first evaluate the processing time with varying documents pairs. **Fig. 3** shows the result.

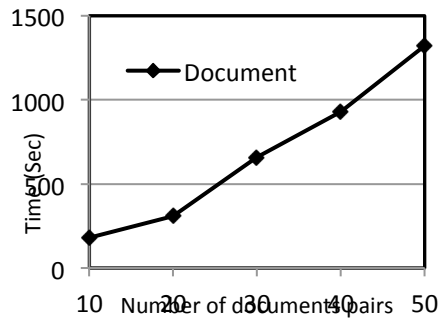

Fig. 3 Documents processing time varying the number of documents pairs

From **Fig. 3**, we can see that processing time increases with the increase in document pairs. Then, we evaluate the performance of our system based on recall and precision. In our experiment, recall is the ratio of word pairs those are correctly mapped in the dictionary and the number of words pairs actually present in the file, expressed in percent. Precision is the number of correctly mapped word pairs to the total number of words pairs mapped, expressed in percentage. **Fig. 4** shows the performance measure of

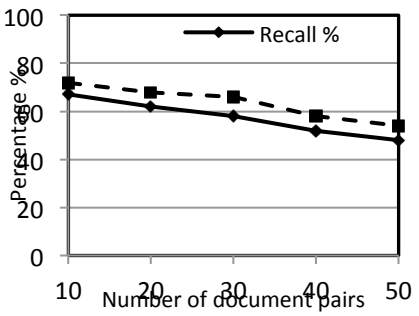

Fig. 4 Performance of the system

our system. Here, we consider 10, 20, 30, 40, and 50 documents pairs. From **Fig. 4**, we find that with the increase in the number of document pairs the performance of our system decreases. This is due to the fact that with the increase in the number of document pairs, there is also an increase in words pairs. Therefore, the possibility of making error increases.

5. CONCLUSION

Bilingual dictionaries can play a vital role in computerization of the contents of less resourceful languages. Considering this fact, in this paper, we have proposed a framework for building such a dictionary. We have implemented the systems for two languages: English and Bangla. Our experimental result demonstrates that our system can create bilingual English-Bangla dictionary up to a satisfactory level of accuracy. Though we have considered Bangla and English languages for the experimental purpose, the system can adapt other languages with slight modification in the dictionary and storage of documents structure.

In this work, we do not consider searching of parallel documents in the Internet. Instead, we consider an in-house respiratory of parallel documents and consider that there exists a parallel document pair in the respiratory. In future, we hope to develop a system that can efficiently identify parallel documents from the Internet and can use them for building bilingual dictionaries.

REFERENCES

[1] M. Kay, M. Roscheisen, "Text-translation alignment", *Computational Linguistics*, vol. 19, no. 1, 1993, pp. 121-142.

[2] R. D. Brown, "Automated dictionary extraction for knowledge-free example-based translation", *in Proc. of the 7th International Conference on Theoretical and Methodological Issues in Machine Translation*, 1997, pp. 111-118.

[3] P. Brown, J. Cocke, S. D. Pietra, V. D. Pietra, F. Jelinek, R. Mercer, P. Roossin, "A Statistical Approach to Language Translation", *in Proc. of COLING-88*, 1998, pp. 71-76.

[4] K. Tanaka, and K. Umemura, "Construction of a bilingual dictionary intermediated by a third language", *In Proc. of COLING-94*, 1994, pp. 297-303.

[5] J. Sjobergh, "Creating a free Japanese-English lexicon", *In Proc. of PACLING*, 2005, pp. 296-300.

[6] S. Shirai, K.Yamamoto, "Linking English words in two bilingual dictionaries to generate another pair dictionary", *ICCPOL-2001*, 2001. pp. 174-179.

[7] K. Paik, F. Bond, S. Shirai, "Using multiple pivots to align Korean and Japanese lexical resources", *NLPRS-2001*, 2001, pp. 63-70.

[8] F. Bond, K. Ogura, "Combining linguistic resources to create a machine-tractable Japanese-Malay dictionary", *Language Resources and Evaluation*, vol. 42, no. 2, 2007, pp. 127-136.

[9] M. S. Arefin, Y. Morimoto, M. A. Sharif, "Bilingual plagiarism detector", *In Proc. of 14th ICCIT*, 2011, pp. 451 - 456.

[10] G. Salton, A. Wong, and C. S. Yang, "A Vector space model for information retrieval", *Communications of ACM*, vol. 18, no. 11, 1975, pp 613–620.

[11] S. Azad, M. S. Arefin, "Bangla documents analyzer", *in Proc. of International Conference on Electronics, Computer and Communication*, 2008, pp 438-442.

[12] Stanford tagger version .1.3, Available at: http://nlp.stanford.edu/software/tagger.shtml#Download

[13] A. Ekbal, R. Haque, S. Bandyopadhyay, "Bengali Part of Speech Tagging using Conditional Random Field", *in Proc. of SNLP-2007*, 2007.

[14] B. B. Chaudhuri, S. Bhattacharya, "An experiment on automatic detection of Named Entity in Bangla", *in Proc. of the IJCNLP-08 Workshop on NER for South and South East Asian Languages*, 2008, pages 75–82.

[15] S. Cucerzan, "Large-scale named entity disambiguation based on Wikipedia data", *In Proc. of the 2007 Joint Conference on Empirical Methods in Natural Language Processing and Computational Natural Language Learning*, 2007, pp. 708–716.

[16] A. S. M. L. Hoque, M. S. Arefin., "Multilingual data management in database environment", *Malaysian Journal of Computer Science*, vol. 22, no. 1, 2009, pp. 44-63.

[17] K. M. A. Hasan, A. Mondal, A. Saha, "A context free grammar and its predictive parser for bangla grammar recognition", *in Proc. of 13th ICCIT*, 23-25 December, 2010, Dhaka, Bangladesh.

Proceeding of the
International Conference on Electrical, Computer and Telecommunication Engineering
01- 02 December 2012 (ICECTE2012), RUET, Rajshahi-6204, Bangladesh

ICECTE2012: PI-0150

Gender Independent Bangla ASR incorporating time and frequency parameters

Khaledun Nahar Babi, Bulbul Ahamed, B.K.M. Mizanur Rahman, M. R. A Kotwal and Mohammad Nurul Huda
Department of CSE, United International University, Dhaka, Bangladesh.
E-mail: khaledunnahar@yahoo.com, bulbul2767@gmail.com, bkm@eee.uiu.ac.bd, rokib39@gmail.com, mnh@cse.uiu.ac.bd

ABSTRACT
This paper describes an automatic speech recognition (ASR) for Bangla (widely used as Bengali) by reducing the gender effects based on local features extracted from an input speech. Speaker-specific properties play an important role on the performance of Bangla ASR. Gender factor shows adverse effect in the classifier while recognizing a speech by an opposite gender, such as, training a classifier by male but testing is done by female or vice-versa. To obtain a robust ASR system in practice it is necessary to invent a system that incorporates gender independent (GI) effect for particular gender. In this paper, we have proposed a GI technique for ASR that focused on a gender factor. For the experiments, we have designed a medium size Bangla speech corpus for both the male and female. The proposed system has showed a significant improvement of word correct rates, word accuracies and sentence correct rates in comparison with the method that suffers from gender effects using.

KEY WORDS: automatic speech recognition, Local features, gender factor, word correct rates, word accuracies, sentence correct rates, hidden Markov model.

I. INTRODUCTION

Various methods were proposed to obtain robust automatic speech recognition (ASR) system; however, the ASR system that shows enough performance at anytime and everywhere could not be realized now. One of the reasons is that the acoustic models (AMs) of an HMM-based classifier include many hidden factors such as speaker-specific characteristics that include gender types and speaking styles [1]-[3]. It is difficult to recognize speech affected by these factors, especially when an ASR system comprises only a classifier that made its training by a single type of gender. One solution is to employ an acoustic model for both types of gender. Though the robustness of this acoustic model by utilizing the both gender specific characteristic is limited, but it resolves the gender effects more precisely.

On the other hand, only a very few works [4]-[11] have been done in ASR for Bangla (can also be termed as Bengali) in spite of one of the largely spoken languages in the world. For example, Bangla vowel characterization is done in [4]; isolated and continuous Bangla speech recognition on a small dataset using hidden Markov models (HMMs) is described in [5]. Again, Bangla digit recognition was found in [12]. Before us, there was no Bangla ASR system that incorporates gender specific characteristics, but our method was based on Standard mel frequency cepstral coefficients (MFCCs) and consequently, it suffers from lower performance in the recognition stage [13].

In this paper, we have constructed a Gender-Independent (GI) ASR by utilizing the acoustic features [14], local features (LFs) for suppressing the gender-factor up to a particular level. Here, the proposed technique trains the classifier with the both types of gender, male and female, and evaluates the classifier for the male and female. For the experiments, we have designed a medium size Bangla speech corpus for both the male and female. The proposed system has showed a significant improvement of word correct rates, word accuracies and sentence correct rates in comparison with the method that suffers from gender effects. Since the local features incorporate frequency and time domain information, it shows significant improvement of recognition performance over the method based on MFCCs at fewer mixture components. Moreover, it requires a fewer mixture component in hidden Markov model (HMMs) and hence, computation time.

This paper is organized as follows. Sections II discusses Bangla phoneme schemes, Bangla speech corpus and triphone model. On the other hand, Section III outlines LFs extraction procedure, respectively and Section IV explains the proposed GI-based technique incorporating LFs. Section V describes an experimental setup, and section VI analyzes experimental results. Finally, section VII concludes the paper with some future remarks.

II. BANGLA PHONEME SCHEMES, TRIPHONE DESIGN AND BANGLA SPEECH CORPUS

Bangla phonetic scheme and IPA (International Phonetic Alphabet) for Bangla were described in [13]. The paper [13] also showed characteristics of some Bangla words by using the spectrogra and triphone model based on HMM were also analyzed for Bangla words.

At present, a real problem to do experiment on Bangla phoneme ASR is the lack of proper Bangla speech corpus. In fact, such a corpus is not available or at least not referenced in any of the existing literature. Therefore, we develop a medium size Bangla speech corpus, which is described below.

Hundred sentences from the Bengali newspaper "Prothom Alo" [15] are uttered by 30 male speakers of different regions of Bangladesh. These sentences (30x100) are used as male training corpus (D1). On the other hand, 3000 same sentences uttered by 30 female speakers are used as female training corpus (D2).

On the other hand, different 100 sentences from the same newspaper uttered by 10 different male speakers and by 10 different female speakers are used as male test corpus (D3) and female test corpus (D4), respectively. All of the speakers are Bangladeshi nationals and native speakers of Bangla. The age of the speakers ranges from 20 to 40 years. We have chosen the speakers from a wide area of Bangladesh: Dhaka (central region), Comilla – Noakhali (East region), Rajshahi (West region), Dinajpur – Rangpur (North-West region), Khulna (South-West region), Mymensingh and Sylhet (North-East region). Though all of them speak in standard Bangla, they are not free from their regional accent.

III. LOCAL FEATURE EXTRACTOR

At the acoustic feature extraction stage, the input speech is first converted into LFs that represent a variation in spectrum along the time and frequency axes. Two LFs, which are shown in Fig. 1, are then extracted by applying three-point linear regression (LR) along the time (t) and frequency (f) axes on a time spectrum pattern (TS), respectively. After compressing these two LFs with 24 dimensions into LFs with 12 dimensions using discrete cosine transform (DCT), a 25-dimensional (12 Δt, 12 Δf, and ΔP, where P stands for the log power of a raw speech signal) feature vector called LF is extracted.

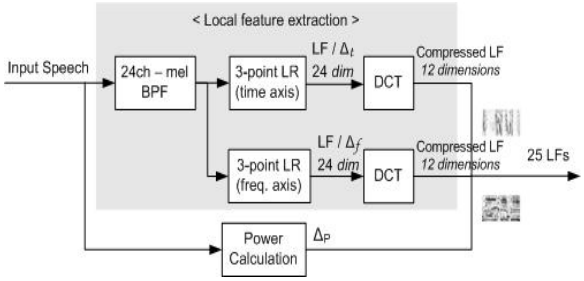

Fig. 1 LFs extraction procedure.

IV. PROPOSED LF-BASED GI ASR SYSTEM

Fig. 2 shows the proposed LF-based GI ASR system for Bangla Language. Here, an input speech is converted into LFs of 25 dimensions (12 Δt, 12 Δf, and ΔP, where P stands for the log power of a raw speech signal) at the acoustic feature extraction stage, which is described in Section III. Then, this extracted LFs (data set based on both male and female) of gender independent characteristics are used to train the GI classifier based on triphone HMM, while the Viterbi algorithm is used for evaluating the test data set for male and female.

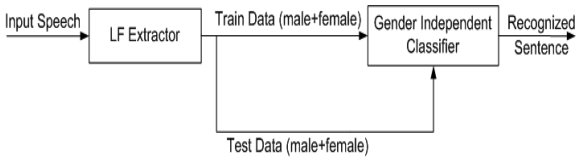

Fig. 2 The Proposed LF-based GI ASR System

V. EXPERIMENTAL SETUP

MFCCs and LFs comprised of 39 and 25 dimensional feature vectors, respectively. For designing an accurate continuous word recognizer, word correct rate (WCR), word accuracy (WA) and sentence correct rate (SCR) for (D3+D4) data set are evaluated using an HMM-based classifier. The D1 (male) and D2 (female) data sets are used to design Bangla triphones HMMs with five states, three loops, and left-to-right models. Input features for the classifier are 39 dimensional MFCCs and 25 dimensional LFs. In the HMMs, the output probabilities are represented in the form of Gaussian mixtures, and diagonal matrices are used. The mixture components are set to 1, 2, 4 and 8.

For evaluating the performance of different methods including the proposed method, we have designed the following experiments:

Experiment-I [Exp-I]

(a) MFCC (Train: 3000 male, Test: 1000 male + 1000 female).
(b) LF (Train: 3000 male, Test: 1000 male + 1000 female).

Experiment-II [Exp-II]

(c) MFCC (3000 female, Test: 1000 male + 1000 female).
(d) LF (3000 female, Test: 1000 male + 1000 female).

Experiment-III [Exp-III]

(e) MFCC (Train: 3000 male + 3000 female, Test: 1000 male + 1000 female).
(f) LF (Train: 3000 male + 3000 female, Test: 1000 male + 1000 female) [Proposed].

VI. Experimental Result and Analysis

Table 1 shows the speech recognition Performance for the Exp-I where MFCC and LF-based methods for the mixture components 1, 2, 4 and 8 are investigated. Here, training and testing are done by using the D1 (male) and D3+D4 (male and female) speech corpora, respectively. For all the mixture components in the Table 1, LF-based method shows higher word correct rate, word accuracy and sentence correct rate in comparison with the method that incorporated MFCCs as input feature. It may be mentioned that the mixture component one provides the highest level performance among the entire mixture component investigated.

Table I: Speech Recognition Performance for Exp-I using MFCC and LF-based methods using the mixture components 1, 2, 4 and 8. Training and testing are done by using the D1 and (D3+D4) speech corpora, respectively.

Mixture Components	Methods	Recognition Performance (%)		
		Word Correct Rate	Word Accuracy	Sentence Correct Rate
1	MFCC-based	83.20	81.71	81.45
	LF-based	88.32	84.85	86.10
2	MFCC-based	82.71	81.26	81.25
	LF-based	87.82	84.39	85.95
4	MFCC-based	78.02	77.26	77.20
	LF-based	86.79	83.24	84.65
8	MFCC-based	68.05	67.59	67.25
	LF-based	86.85	83.65	84.80

Table 2 generates the performance of similar pattern for the female dependent training in Exp-II. On the other hand, Table 3exhibits the gender independent performance where training and testing are done in the gender independent environment in Exp-III. It is claimed from the Tables 1, 2 and 3 that the LF-based method provides the higher recognition performance for all the mixture components. Besides, the proposed LF-based method in Exp-III provides the higher performance among the three experiments and outputs the highest recognition performance for all the investigated mixture components. Among the experimented mixture components, the best result is achieved in component one.

Table II: Speech Recognition Performance for Exp-II using MFCC and LF-based methods using the mixture components 1, 2, 4 and 8. Training and testing are done by using the D2 and (D3+D4) speech corpora, respectively.

Mixture Components	Methods	Recognition Performance (%)		
		Word Correct Rate	Word Accuracy	Sentence Correct Rate
1	MFCC-based	79.94	79.14	79.05
	LF-based	88.20	86.23	86.45
2	MFCC-based	83.45	82.62	82.35
	LF-based	85.48	83.38	83.65
4	MFCC-based	80.33	79.65	79.20
	LF-based	84.05	82.09	82.35
8	MFCC-based	71.11	70.70	70.30
	LF-based	80.20	77.91	78.50

Table III: Speech Recognition Performance for Exp-III using MFCC and LF-based methods using the mixture components 1, 2, 4 and 8. Training and testing are done by using the (D1+D2) and (D3+D4) speech corpora, respectively.

Mixture Components	Methods	Recognition Performance (%)		
		Word Correct Rate	Word Accuracy	Sentence Correct Rate
1	MFCC-based	90.36	89.67	88.90
	LF-based	92.27	90.30	90.65
2	MFCC-based	89.59	88.76	87.95
	LF-based	91.09	88.53	89.25
4	MFCC-based	91.23	90.53	89.85
	LF-based	91.50	89.18	89.50
8	MFCC-based	91.26	90.73	90.15
	LF-based	91.03	88.88	89.30

VII. Conclusion

This paper has proposed a gender independent automatic speech recognition technique for Bangla language by inputting local features. The following information concludes the paper.

i) The methods based on local features provide a higher speech recognition performance than the method that incorporates the standard MFCCs for all the experimented mixture components.

ii) For the LF-based methods, the mixture component one generates the highest level performance.

iii) The proposed LF-based gender independent method has showed the significant improvement of word correct rate, word accuracy and sentence correct

rate in comparison with the methods that are experimented in gender dependent environments.

In future, the authors would like to incorporate neural network based systems in gender independent for evaluating the performance.

REFERENCES

[1] S. Matsuda, T. Jitsuhiro, K. Markov and S. Nakamura, "Speech Recognition system Robust to Noise and Speaking Styles," Proc. ICSLP'04, Vol.IV, pp.2817-2820, Oct. 2004.

[2] M. A. Hasnat, J. Mowla, and Mumit Khan, "Isolated and Continuous Bangla Speech Recognition: Implementation Performance and application perspective, " in Proc. International Symposium on Natural Language Processing (SNLP), Hanoi, Vietnam, December 2007.

[3] R. Karim, M. S. Rahman, and M. Z Iqbal, "Recognition of spoken letters in Bangla," in Proc. 5th International Conference on Computer and Information Technology (ICCIT02), Dhaka, Bangladesh, 2002.

[4] A. K. M. M. Houque, "Bengali segmented speech recognition system," Undergraduate thesis, BRAC University, Bangladesh, May 2006.

[5] K. Roy, D. Das, and M. G. Ali, "Development of the speech recognition system using artificial neural network," in *Proc. 5th International Conference on Computer and Information Technology (ICCIT02)*, Dhaka, Bangladesh, 2003.

[6] M. R. Hassan, B. Nath, and M. A. Bhuiyan, "Bengali phoneme recognition: a new approach," in *Proc. 6th International Conference on Computer and Information Technology (ICCIT03)*, Dhaka, Bangladesh, 2003.

[7] K. J. Rahman, M. A. Hossain, D. Das, T. Islam, and M. G. Ali, "Continuous bangla speech recognition system," in *Proc. 6th International Conference on Computer and Information Technology (ICCIT03)*, Dhaka, Bangladesh, 2003.

[8] S. A. Hossain, M. L. Rahman, F. Ahmed, and M. Dewan, "Bangla speech synthesis, analysis, and recognition: an overview," in *Proc. NCCPB,* Dhaka, 2004.

[9] S. Young, et al, The HTK Book (for HTK Version. 3.3), Cambridge University Engineering Department, 2005. http:///htk.eng.cam.ac.uk/prot-doc/ktkbook.pdf.

[10] http://en.wikipedia.org/wiki/Bengali_script, Last accessed April 11, 2009.

[11] C. Masica, *The Indo-Aryan Languages*, Cambridge University Press, 1991.

[12] Ghulam Muhammad, Yousef A. Alotaibi, and Mohammad Nurul Huda, "Automatic Speech Recognition for Bangla Digits," ICCIT'09, Dhaka, Bangladesh, December 2009.

[13] Foyzul Hasan, Rokibul Alam Kotwal, Saiful Alam Khan and Mohammad Nurul Huda, "Gender Independent Bangla Automatic Speech Recognition," IEEE/IAPR Internationaol Conference on Informatics, Electronics and Vision (ICIEV) 2012, May 2012, Dhaka, Bangladesh .

[14] T. Nitta, "Feature extraction for speech recognition based on orthogonal acoustic-feature planes and LDA," Proc. ICASSP'99, pp.421-424, 1999.

[15] Daily Prothom Alo. Online: www.prothom-alo.com.

Proceeding of the
International Conference on Electrical, Computer and Telecommunication Engineering
01- 02 December 2012 (ICECTE2012), RUET, Rajshahi-6204, Bangladesh

ICECTE2012: PI-0151

A Neural Network Based Approach To Network Intrusion Detection And Analyzing Different Backpropagation Algorithm Training Approaches

Biprodip Pal[1], Md. Al Mehedi Hasan[1], Md. Mijanur Rahman Howlader[2]
[1]Dept. of CSE, Rajshahi University of Engineering & Technology, Motihar, Rajshahi, Bangladesh.
[2]Dept.of CSE,University of Information Technology & Sciences, Rajshahi, Bangladesh.
biprodip.cse@gmail.com, mehedi_ru@yahoo.com, mijan_cse_ruet@yahoo.com

ABSTRACT
To detect unwanted intrusions with more efficiency soft computing techniques are widely used. Yet the target is quiet elusive to provide much secured information system. In this paper artificial neural network is used for network intrusion detection. Different backpropagation algorithm training approaches are applied here to detect the attacks and non-attack connections. All the trained networks were allowed separately to find attacks from the test dataset that is different from the train dataset. The resilient backpropagation training mode is found to detect the attack connections with more efficiency compared to others.

KEY WORDS: *Backpropagation Algorithm*, Gradient Descent, Resilient Backpropagation, Intrusion Detection, Security.

1. INTRODUCTION

An intrusions detection (ID) system gathers and analyzes information from various areas within a computer or a network to identify possible security breaches, which include both intrusions (attacks from outside the organization) and misuse (attacks from within the organization)[1].Many intrusions detection systems used soft computing techniques. Expert Systems as well as Fuzzy rules are used in rule based intrusion detections[2][3]. Again *data mining* frameworks are also used for adaptively building intrusion detection models [4]. Multilayer perceptrons are also found to be very useful in ID systems[5][6] .We have used the Backpropagation learning algorithm to train the network and let it detect intrusions.

2. BACKPROPAGATION LEARNING ALGORITHM AND IDS

Application of soft computing techniques and particularly artificial neural networks (ANN) in implementing IDSs is to include an intelligent agent in the system that can disclose the latent patterns in abnormal and normal connection audit records, and to generalize the patterns to slightly different connection records of the same class. Backpropagation is a *supervised learning* algorithm that infer a function from *supervised* training data. The neural networks consists of three layers in general. Each neuron in the layers is basically a summing element and is followed by a function of activation. The learning process is an optimization process of the parameters of the best set of weights (that connects the neurons of different layers) to solve a problem and includes the following basic steps [7]:

- Present the neural network with a number of inputs (Vectors each representing a pattern)
- Check how closely the actual output generated for a specific input matches the desired output.
- Change the weights to better approximate the outputs.

3. BACKPROPAGATION TRAINING MODES

The input pattern is presented through activation of the input units. The pattern set consists of input activation vector x^p and a target vector t^p. Than feedforward computation is carried on to get the resulting output vector s^p. Distance between the vectors s^p and t^p are found from the function bellow:

$$E := \tfrac{1}{2} \cdot \sum_p \sum_n | t^p - s^p |^2 \qquad (1)$$

The weights and biases of the networks are adjusted to minimize the network performance function during training. In the batch mode weights and biases of the network are updated only after the entire training set has been applied to the network. The gradients $\frac{\partial E}{\partial w}(t)$ calculated at each training example are added together to determine the change in the weights and biases.

3.1 Batch Gradient Descent (BGD)

Here the weights and biases are updated in the direction of the negative gradient of the performance function. The weight updating depends on the equation (2).

$$\Delta w_{ij} = -\eta\, (\partial E / \partial w_{ij}) \qquad (2)$$

If the learning rate (η) is too large the algorithm becomes unstable. However, if the learning rate is too small, the algorithm takes a long time to converge.

Batch training is able to calculate the direction of the true gradient, but it does not know how far it can safely go in that direction before the gradient changes direction (or begins to go back "uphill").

3.2 Batch Gradient Descent with Momentum (BGDM)

It provides faster convergence than batch gradient descent by adding a momentum term in learning.

Standard back-propagation weight adjustment is calculated using the equation (3).

$$w(t+1) = w(t) + \eta(\delta w(t)) \qquad (3)$$

With a momentum term included, the update occurs according to the equation (4).

$$w(t+1) = w(t) + \eta(\delta w(t)) + \alpha(\delta w(t-1)) \qquad (4)$$

Where, α is the momentum constant. Momentum allows the network to respond not only to the local gradient, but also to recent trends in the error surface. It also allows the network to ignore small features in the error surface.

3.3 Resilient Backpropagation (RP)

Resilient Back-propagation (RP) method can be extremely fast in converging to a solution. It takes into account only the sign of the partial derivative over all patterns & not the magnitude, and acts independently on each weight. In intrusion detection systems this learning technique is used to increase the system intelligence to distinguish between intrusion and normal connections. The traditional Backpropagation algorithm modifies the weights of the partial derivatives ($\partial E/\partial w_{ij}$). But The size of this differential does not really represent the size of the necessary modification of the weight changes.

$$\triangle w_{ij}^{(t)} = \begin{cases} -\triangle_{ij}^{(t)} & , \text{ if } \frac{\partial E}{\partial w_{ij}}^{(t)} > 0 \\ +\triangle_{ij}^{(t)} & , \text{ if } \frac{\partial E}{\partial w_{ij}}^{(t)} < 0 \\ 0 & , \text{ else} \end{cases} \qquad (5)$$

$$w_{ij}^{(t+1)} = w_{ij}^{(t)} + \triangle w_{ij}^{(t)} \qquad (6)$$

Here Δ_{ij} is an ,update value, and The size of the weight change is exclusively determined by this weight-specific ,update value.

3.4 Batch Gradient Descent with Adaptive Learning Rate(BGDA)

As the size of the training set grows, the accumulated large weight changes leads batch training to use unreasonably large steps, which in turn leads to unstable learning and to the overshooting of curves and local minima in the error landscape. Therefore, a reduction in the size of the learning rate (or, equivalently, using the average weight change instead of the sum) is required for batch training to be stable as the size of the training set grows. The performance of the steepest descent algorithm can be improved if we allow the learning rate to change during the training process. An adaptive learning rate will attempt to keep the learning step size as large as possible while keeping learning stable (BGDA).It can be very faster than the traditional gradient descent approach. Again a combined approach of both batch gradient descents with adaptive learning rate with momentum (BGDMA) is expected to be much faster than others due to its capability of using momentum with the adaptation power.

4. BP APPROACH

4.1. Data Representation

Input patterns are bit equivalents of the selected features of the rules. Each of the hour, minute and second portion of the "Duration" feature consists of 6 bits each. The "Start time" feature is converted into some 15 minute slot and takes 7 bit to represent. So, time 09:04 belongs to slot (9*4) +1=37, (since minute 04 is in first 15 min slot, so minute is 1). "Source port" and "Destination port" (0 to 65535) number requires a total of 16 bits. For "Source IP" and "Destination IP" each octet is represented using 8 bit values. The value of the Attack field can be either 0 or 1. So, 1 bit is enough to represent the data. For attack classification the attack code is replaced by 4 nodes.

4.2 Network Structure

The set of features used are listed in Table 1. The network is a three layered network. The hidden layer is constructed using 40 nodes (figure1).

Table 1: Features used in different approaches.

List o Features
Duration, Start time, Source_port, Destination_port, Source_IP, Destination_IP, Attack

The neural network consists of 121 input nodes, and 4 output nodes(since the audit data consists of no more than 16 different types of attacks).

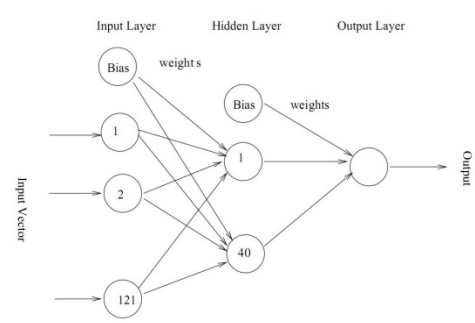

Fig. 1: Structure of the used network

5. EXPERIMENTAL SETUP

We have used the MATLAB neural network toolbox

Table 2 : The distributions of records in the datasets.

Record Type	Training Set	Testing Set
phf	1	1
guess	2	4
rcp	1	1
rlogin	1	1
rsh	1	2
port-scan	16	30
Normal	42	265

to implement the backpropagation approach. The DARPA 1998 intrusion detection dataset was used for training and testing purpose for the system. A subset of the dataset was used to train the system and then tested the system with the full set of data. The test dataset was the data in 'tcpdump.list' file provided with the DARPA1998 sample data and the training dataset was created by randomly selecting a subset of data from the data in the test dataset. The record distributions are given in Table 2.

6. EXPERIMENTAL RESULT

To determine the performance of intrusion detection systems two standard metrics are used. These are thedetection rate (DR) and the false positive rate(FPR) and can be calculated from equation (7) and (8). Generally, with the increase in detection rate, more false alarms are generated. Hence,accuracy (ACC), is used to evaluate the overall prediction accuracy of the system. It is "the ratio of correctly classified examples to the total number of classified examples"[8]. ACC can be calculated using equation (9).

$$DR = \frac{no.of\ detected\ attacks}{no.of\ total\ attacks} \quad (7)$$

$$FPR = \frac{no.of\ false\ alarms}{no.of\ total\ normal\ records} \quad (8)$$

$$ACC = \frac{no.of\ correct\ classification}{no.of\ total\ classification} \quad (9)$$

The learning algorithm for the network was executed with a learning rate of 0.30 until the calculated error value went bellow threshold limit 0.00001, or a number of 60000 epoch was reached. A log sigmoid function was used in the network architecture. The network was trained with the training dataset defined above. The trained networks were than allowed to classify connections as attack or non attack from the test dataset.All of the systems performances are summarized in Table 3. The detection rate of BGDM and BGDMA approaches are found to be less reliable than the adaptive learning rate approach BGDA. Though both of BGDA and RP approaches shows equal performance in attack detection rate(DR), but the RP

Table3:Detection Performance of the BP Approaches

Metrics	BGDM	BGDA	BGDMA	RP
FPR	0.083	0.086	0.056	0.075
DR	0.76	0.9	0.83	0.9

approach shows better performance considering the false positive rate of 0.075 to detect the normal connections compared to that of the BGDA approach. So, from both of the approach the RP approach of training the system with the rule sets are found to be much reliable compared to other approaches.

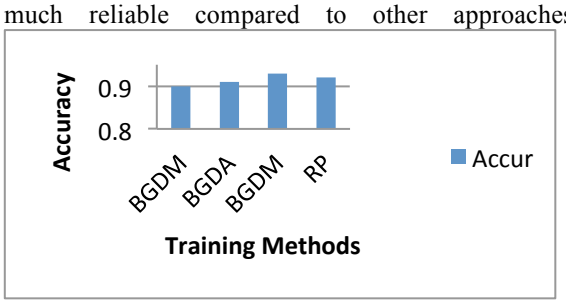

Fig. 2:Accuracy of different BP training approaches.

All the approach's performances in case of accuracy to attack and normal connection classification was than compared (figure 2) and the training performance

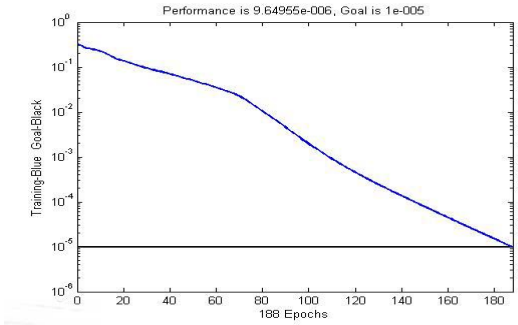

Fig. 3:BGDMA training performance.

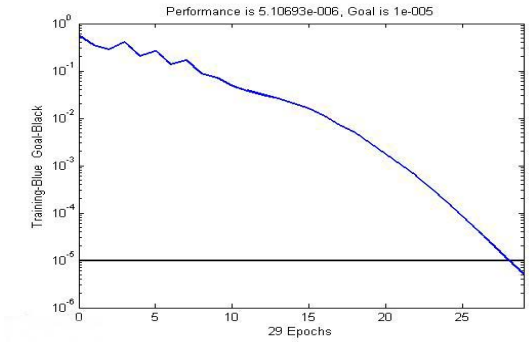

Fig. 4:RP training performance.

graph for RP and BGDMA method are given in figure 3 and figure 4. Since there is a combination of adaptive learning rate and momentum so the combined performance in case of both attack and the normal connection detection increases. But from the performance plot of the BGDMA and the RP training approaches it's noticeable that the RP training approach is very much better than BGDMA approach since it requires only 29 epochs to reach the goal compared to 188 of that of the BGDMA approach.

7. Conclusion

Our goal was to detect network intrusions efficiently and analyze the backpropagation algorithm's different training performances. The attack as well as normal connection classification performance of the BGDMA approach is well enough but total attack detection performance and the efficiency measure supports the RP method of training to be selected as the best one among them. Because of using heuristic techniques, developed from the analysis of the performance of the standard gradient descent algorithms RP approach is found here to be more efficient.

8. Future works

Depending on the achieved information future works on refining the RP training approach can be carried out by finding out the way of minimizing local minima problems, since this approach still suffers from it. Again to increase the performance of a system some integration of backpropagation and other evolutionary algorithm can be carried out. Since, neural network training converges slowly, so further change in the network architecture can be made to efficiently use the network with other approaches.

REFERENCES

[1] S.Janakiraman and Dr. V. Vasudevan,"FCM and GENETIC Coalesced Intelligent Agent for Intrusion Detection System.", *ISAST Transactions on Intelligent Systems No. 2 Vol. 2,2008.*

[2] Kumar, S. & Spafford, E. (1994) A Pattern Matching Model for Misuse Intrusion Detection. In Proceedings of the 17th National Computer Security Conference , pages 11-21.

[3] Jonatan Gomez and Dipankar Dasgupta, "Evolving Fuzzy Classifiers for Intrusion Detection",*Proceedings of the 2002 IEEE Workshop on Information Assurance.*

[4] Wenke Lee,Salvatore J. Stolfo Kui,W.Mok,"A Data Mining Framework for Building Intrusion Detection Models",*Department, Columbia University Computer Science,500 West 120th Street,New York,NY 10027.*

[5] A. K. Ghosh and A. Schwartzbard. A study in using neu-ral networks for anomaly and misuse detection. In In Pro-ceedings of USENIX Security Symposium, 1999.

[6] R. P. Lippmann and R. K. Cunningham. Improving intru-sion detection performance using keyword selection and neu-ral networks.Computer Networks (Amsterdam, Netherlands:1999), 34(4):597–603, 2000.

[7] Sergios Theodorios and Kons tantinos Koutroumbas, Pattern Recognition , Cambridge: Academic Press, 1999.

[8] L.Kuang, "DNIDS: A Dependable Network Intrusion Detection System Using the CSI-KNN Algorithm", *Master thesis, Queen's University, Canada, September 2007.*

Proceeding of the
International Conference on Electrical, Computer and Telecommunication Engineering
01- 02 December 2012 (ICECTE2012), RUET, Rajshahi-6204, Bangladesh

ICECTE2012: PI-0152

Normalization of Gender factor in Bangla ASR

Md. Asfak-Ur-Rahman, B.K.M Mizanur Rahman, Bulbul Ahamed, Foyzul Hassan and Mohammad Nurul Huda
Department of CSE, United International University, Dhaka, Bangladesh.
E-mail: asfak.ur.rahman@gmail.com, bkm@eee.uiu.ac.bd, bulbul2767@gmail.com, foyzul.hassan@gmail.com, mnh@cse.uiu.ac.bd

Abstract

This paper presents a Bangla (widely used as Bengali) automatic speech recognition system (ASR) by suppressing gender effects. Gender characteristic plays an important role on the performance of ASR. If there is a suppression process that represses the decrease of differences in acoustic-likelihood among categories resulted from gender factors, a robust ASR system can be realized. In the proposed method, we have designed a new ASR incorporating the Local Features (LFs) instead of standard mel frequency cepstral coefficients (MFCCs) as an acoustic feature for Bangla by suppressing the gender effects, which embeds three HMM-based classifiers for corresponding male, female and geneder-independent (GI) characteristics. In the experiments on Bangla speech database prepared by us, the proposed system has achieved a significant improvement of word correct rates (WCRs), word accuracies (WAs) and sentence correct rates (SCRs) in comparison with the method that incorporates Standard MFCCs.

Keywords: Acoustic Model, Automatic Speech Recognition, Gender Effects Suppression, Hidden Markov Model.

I. INTRODUCTION

The current automatic speech recognition (ASR) system had been investigated for achieving the adequate performance at anytime and everywhere; however, it could not be able for providing the highest level accuracies till to date. One of the reasons is that the acoustic models (AMs) of a hidden Markov model (HMM)-based classifier include many hidden factors such as speaker-specific characteristics that include gender types and speaking styles. It is difficult to recognize speech affected by these factors, especially when an ASR system contains only a single acoustic model. One solution is to employ multiple acoustic models, one model for each type of gender. By handling these gender effects appropriately the robustness of each acoustic model in an ASR can be extended to some limit.

A method of decoding in parallel with multiple HMMs corresponding to hidden factors has recently been proposed in [1], [2] for resolving these difficulties. Multi-path acoustic modeling, that represents hidden factors with several paths in the same AM instead of applying multiple HMMs, was also presented [3].

Unfortunately, only a very few works [4]-[11] have been done for ASR in Bangla (can also be termed as Bengali), which is one of the largely spoken languages in the world. Since no work in Bangla was found for suppressing the gender factor previously, we proposed a method [12] for that purpose by embedding multiple HMM-based classifiers. But this method of gender effect suppression did not incorporate any gender-independent (GI) classifier for resolving those male and female speakers whose voices have effect of opposite gender to some extent. To resolve this problem, we proposed another method for suppressing the gender factor more accurately by incorporating the GI classifier[13]; but this method could not be able to provide enough performance because of embedding standard mel frequency cepstral coefficients (MFCCs) as an input acoustic feature that did not include frequency domain information in its extraction process. Consequently, an exploitation of new feature is needed to obtain time and frequency domain information in its feature vector.

In this paper, we have designed a new ASR incorporating the Local Features (LFs) instead of standard mel frequency cepstral coefficients (MFCCs) as an acoustic feature for Bangla by suppressing the gender effects, which embeds three HMM-based classifiers for corresponding male, female and geneder-independent (GI) characteristics. In the experiments on Bangla speech database prepared by us, the proposed system has achieved a significant improvement of word correct rates (WCRs), word accuracies (WAs) and sentence correct rates (SCRs) in comparison with the method that incorporates Standard MFCCs.

This paper is organized as follows. Sections II discusses Bangla phoneme schemes, Bangla speech corpus and triphone model. On the other hand, Section III outlines LFs features extraction procedures and Section IV explains the proposed gender effect suppression method by incorporating LFs. Section V describes the experimental setup and Section VI shows experimental results and provides a discus-

sion. Finally, Section VII and VIII conclude the paper with some future remarks and references, respectively.

II. BANGLA PHONEME SCHEME, SPEECH CORPUS AND TRIPHONE MODEL

Bangla phonetic scheme and triphone models design were presented in our papers, [12] and [13]. These papers show ed how the left and right contexts are used to design the triphone models.

Hundred sentences from the Bengali newspaper "Prothom Alo" [14] are uttered by 30 male speakers of different regions of Bangladesh. These sentences (30x100) are used as male training corpus (D1). On the other hand, 3000 same sentences uttered by 30 female speakers are used as female training corpus (D2).

On the other hand, different 100 sentences from the same newspaper uttered by 10 different male speakers and by 10 different female speakers are used as male test corpus (D3) and female test corpus (D4), respectively. All of the speakers are Bangladeshi nationals and native speakers of Bangla. The age of the speakers ranges from 20 to 40 years.

III. LOCAL FEATURE EXTRACTOR

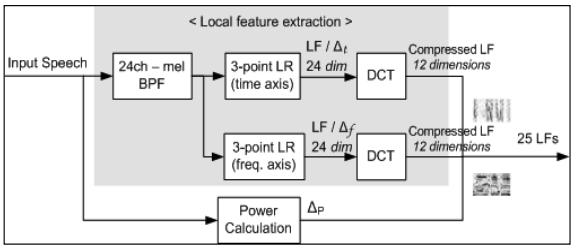

Fig. 1. Local feature extraction.

In Fig. 1 local feature extraction procedure is shown. At the acoustic feature extraction stage, the input speech is first converted into LFs that represent a variation in spectrum along the time and frequency axes. Two LFs are then extracted by applying three-point linear regression (LR) along the time (t) and frequency (f) axes on a time spectrum pattern (TS), respectively. After compressing these two LFs with 24 dimensions into LFs with 12 dimensions using discrete cosine transform (DCT), a 25-dimensional (12 Δt, 12 Δf, and ΔP, where P stands for the log power of a raw speech signal) feature vector called LF is extracted. It is the complete local feature extraction procedure.

IV. LF-BASED PROPOSED SUPPRESSION METHOD INCORPORATING GI CLASSIFIER

The diagram of the LF-based method is depicted in Fig. 2. Here, the extracted LFs [15] from the input speech signal are inserted into the male, female and GI HMM-based classifiers. The male, female and GI HMM-based classifiers are trained using the D1, D2 and (D1+D2) data sets. Here, output hypothesis is selected based on maximum output probabilities after comparing male, female and gender independent hypotheses, and passed the best matches hypothesis to the output.

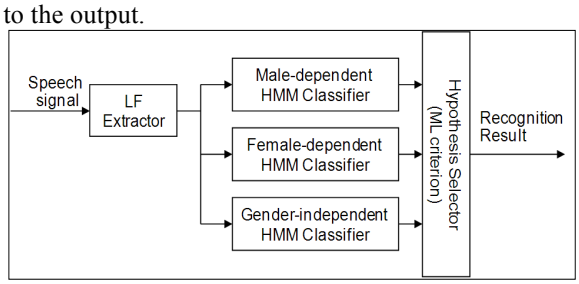

Fig.2 Proposed LF-based suppression method incorporating GI classifier.

V. EXPERIMENTAL SETUP

The frame length and frame rate are set to 25 ms and 10 ms (frame shift between two consecutive frames), respectively, to obtain acoustic features (MFCCs and LFs) from an input speech. MFCC and comprised of 39 (12-MFCC, 12-ΔMFCC, 12-ΔΔMFCC, P, ΔP and ΔΔP, where P stands for raw energy of the input speech signal) and 25 (12 delta coefficients along time axis, 12 delta coefficients along frequency axis, and delta coefficient of log power of a raw speech signal) dimensions, respectively.

For designing an accurate continuous word recognizer, word correct rate (WCR), word accuracy (WA) and sentence correct rate (SCR) for (D3+D4) data set are evaluated using an HMM-based classifier. The D1 and D2 data sets are used to design Bangla triphones HMMs with five states, three loops, and left-to-right models. Input features for the classifier are 39 dimensional MFCCs and 25 dimensional LFs. In the HMMs, the output probabilities are represented in the form of Gaussian mixtures, and diagonal matrices are used. The mixture components are set to 1, 2, 4 and 8.

For evaluating the performance of the methods, [12] and [13], we have designed the following experiments:

(a) MFCC (Train: 3000 male, Test: 1000 male+1000 female).
(b) MFCC (Train: 3000 female, Test: 1000 male+1000 female).
(c) MFCC (Train: 3000 male + 3000 female, Test:

1000 male +1000 female).

(d) MFCC (Train: 3000 male, Train: 3000 female, Test: 1000 male + 1000 female) [12].

(e) MFCC (Train: 3000 male, Train: 3000 female, Train: 3000 male + 3000 female, Test: 1000 male + 1000 female).

New experiments given below are designed for mixture component one using the LFs for evaluating the performance:

(a) LF (Train: 3000 male, Test: 1000 male+1000 female).

(b) LF (Train: 3000 female, Test: 1000 male+1000 female).

(c) LF (Train: 3000 male + 3000 female, Test: 1000 male +1000 female).

(d) **Proposed**, LF (Train: 3000 male, Train: 3000 female, Train: 3000 male + 3000 female, Test: 1000 male + 1000 female).

VI. EXPERIMENTAL RESULTS AND ANALYSIS

Table I. Word Correct Rates (WCRs), Word Accuracies (WA) and Sentence Correct Rates (SCRs) for LF and MFCC based methods, (a), (b), (c) and (d)/(e) using (D3+D4) data set for mixture component one. Here, methods (d) and (e) are LF-based and MFCC-based suppression methods with gender independent (GI) classifiers, respectively.

Experiments	Methods	WCR(%)	WA(%)	SCR(%)
#1	LF-based (a)	88.63	85.53	86.60
	MFCC-based (a)	76.38	75.41	75.30
#2	LF-based (b)	86.29	83.65	84.50
	MFCC-based (b)	76.16	75.50	75.45
#3	LF-based (c)	92.22	90.43	90.85
	MFCC-based (c)	88.39	87.83	87.15
#4	LF-based (d)	94.94	93.86	93.95
	MFCC-based (e)	91.00	90.43	90.05

Word Correct Rates (WCRs), Word Accuracies (WAs) and Sentence Correct Rates (SCRs) for LF and MFCC based methods, (a), (b), (c) and (d)/(e) using (D3+D4) data set are shown in Table I. Here, methods (d) and (e) represent LF-based and MFCC-based suppression methods with gender independent (GI) classifiers, respectively. From the experiment #1, where the HMM-based classifier is trained with D1 data set and evaluated with (D3+D4) data set, a tremendous improvement of WCRs, WAs and SCRs are exhibited by the LF-based ASR that incorporates gender effect Normalization module in the ASR process. Similarly, the same pattern of performance is also achieved in the experiment #2, where the HMM-based classifier is trained with D2 data set and evaluated with (D3+D4) data set. This trend explicates the LFs, which embeds time and frequency domain information in its extraction procedure, as excellent feature for the Bangla automatic speech recognition system. Again, the experiment #3, which shows the GI ASR for Bangla language based on LF and MFCC features, is trained with (D1+D2) and evaluated with (D3+D4) data sets and provides 3.83%, 2.60% and 3.70% improvements by the LF-based method in comparison with the MFCC-based counterpart. Finally, the methods in the experiment #4 imply two ASR systems for GI Bangla ASR by integrating gender factor Normalization process in its architecture and shows the highest level performance for WCRs, WAs and SCRs compare to the corresponding the methods in the experiments #1, #2 and #3. Since these methods of the experiment #4 always maximize the output probabilities obtained from the three classifiers: male, female and GI, it shows its maximum level of performance. Besides, the LF-based methods improves the WCRs, WAs and SCRs by 3.94%, 3.43% and 3.90%, respectively than the method that inputs MFCC features in the HMM-based classifier in the gender effect suppression process.

Moreover, word recognition performance for LF and MFCC based methods, (a), (b), (c) and (d)/(e) using (D3+D4) data set are summarized in the Table II. In the table, methods (d) and (e) represent LF-based and MFCC-based suppression methods with gender independent (GI) classifiers, respectively. The same speech corpora for training and evaluation are used for the experiments #1, #2, #3 and #4 which is already described in the earlier. It is observed from all the experiments that the LF-based method increases the number of correctly recognized words in comparison with its counterpart. The highest number of correctly recognized words shown by the experiment #4 with respect to their corresponding methods in the other experiments, #1, #2 and #3 are evident from the table. It can be mentioned as an example that the LF-based and MFCC-based methods of experiment #4 provide the highest numbers of correctly recognized words, which are 6247 and 5988, respectively, dictates the respective numerical figures obtained for the corresponding methods of all the other experiments. The reason for obtaining the best experimental results by the LF-based method of experiment #4 is also illustrated earlier.

Table II. Word recognition performance for LF and MFCC based methods, (a), (b), (c) and (d)/(e) using (D3+D4) data set for mixture component one. Here, methods (d) and (e) represent LF-based and MFCC-based suppression methods with gender independent (GI) classifiers, respectively.

Experiments	Methods	Word Recognition Performance (Total 6580 words)			
		Correctly Recognized Words, H	Deletion, D	Substitution, S	Insertion, I
#1	LF-based (a)	5832	58	690	204
	MFCC-based (a)	5026	438	1116	64
#2	LF-based (b)	5678	89	813	174
	MFCC-based (b)	5011	448	1121	43
#3	LF-based (c)	6068	55	457	118
	MFCC-based (c)	5816	152	612	37
#4	LF-based (d)	6247	33	300	71
	MFCC-based (e)	5988	140	452	38

VII. CONCLUSION

This paper has proposed an automatic speech recognition technique based on LFs for Bangla language by suppressing the gender effect incorporating HMM-based classifiers for male, female and Gender-Independent characteristics. The following information concludes the paper.

i) The MFCC-based method incorporating GI classifier provides the higher performance than the method that does not incorporate GI classifier. The MFCC-based method incorporating GI exhibits its superiority at all the mixture components investigated.

ii) The incorporation of GI HMM classifier improves the word correct rates, word accuracies and sentence correct rates significantly.

iii) The proposed LF-based method shows a significant improvement of word correct rates, word accuracies and sentence correct rates for mixture component one.

In future, the authors would like to evaluate performance by incorporating neural network based systems.

VIII. REFERENCES

[1] S. Matsuda, T. Jitsuhiro, K. Markov and S. Nakamura, “Speech Recognition system Robust to Noise and Speaking Styles,” Proc. ICSLP’04, Vol.IV, pp.2817-2820, Oct. 2004.

[2] T. Shinozaki and S. Furui, “Spontaneous Speech Recognition Using a Massively Parallel Decoder,” Proc. ICSLP’04, Vol.III, pp.2817-2820, Oct. 2004.

[3] A. Lee, Y. Mera, K. Shikano and H. Saruwatari, “Selective multi-path acoustic model based on database likelihoods,” Proc. ICSLP’02, Vol.IV, pp.2661-2664, Sep. 2002.

[4] A. K. M. M. Houque, "Bengali segmented speech recognition system," Undergraduate thesis, BRAC University, Bangladesh, May 2006.

[5] K. Roy, D. Das, and M. G. Ali, "Development of the speech recognition system using artificial neural network," in *Proc. 5th International Conference on Computer and Information Technology (ICCIT02)*, Dhaka, Bangladesh, 2003.

[6] M. R. Hassan, B. Nath, and M. A. Bhuiyan, "Bengali phoneme recognition: a new approach," in *Proc. 6th International Conference on Computer and Information Technology (ICCIT03)*, Dhaka, Bangladesh, 2003.

[7] K. J. Rahman, M. A. Hossain, D. Das, T. Islam, and M. G. Ali, "Continuous bangla speech recognition system," in *Proc. 6th International Conference on Computer and Information Technology (ICCIT03)*, Dhaka, Bangladesh, 2003.

[8] S. A. Hossain, M. L. Rahman, F. Ahmed, and M. Dewan, "Bangla speech synthesis, analysis, and recognition: an overview," in *Proc. NCCPB,* Dhaka, 2004.

[9] S. Young, et al, The HTK Book (for HTK Version. 3.3), Cambridge University Engineering Department, 2005. http:///htk.eng.cam.ac.uk/prot-doc/ktkbook.pdf.

[10] http://en.wikipedia.org/wiki/Bengali_script, Last accessed September 28, 2011.

[11] C. Masica, *The Indo-Aryan Languages*, Cambridge University Press, 1991.

[12] Mohammed Rokibul Alam Kotwal, Foyzul Hasan and Mohammad Nurul Huda, “Gender effects suppression in Bangla ASR by designing multiple HMM based classifiers,” CICN 2011, Gwalior, India.

[13] Foyzul Hasan, Mohammed Rokibul Alam Kotwal and Mohammad Nurul Huda, “Bangla ASR design by suppressing gender factor with gender-independent and gender-based HMM classifiers,” WICT 2011, December 2011, Mumbai, India.

[14] Prothom Alo. Online: www.prothom-alo.com.

[15] T. Nitta, "Feature extraction for speech recognition based on orthogonal acoustic-feature planes and LDA," Proc. ICASSP’99, pp.421-424, 1999.

Proceeding of the
International Conference on Electrical, Computer and Telecommunication Engineering
01- 02 December 2012 (ICECTE2012), RUET, Rajshahi-6204, Bangladesh

ICECTE2012: PI-0154

Design an Intelligent Robotic Head for Human Robot Interaction

Mohammed Moshiul Hoque[1], Dipankar Das[2], Yoshinori Kobayashi[2], Yoshinori Kuno[2], Kaushik Deb[1]
[1]Department of Computer Science and Engineering, CUET, Chittagong, Bangladesh
[2]Department of Information and Computer Sciences, Saitama University, Japan
E-mail: moshiul_240@cuet.ac.bd, dipankar@cv.ics.saitama-u.ac.jp

ABSTRACT
In order to works with humans, the robot should be able to perform a lot of social functions. This paper focuses on designing a robotic head to interact with humans in a natural and social ways. To evaluate the system, we conducted an experiment to perform an important social function such as making eye contact with human in three viewing situations (near peripheral field of view, far peripheral field of view, and out of field of view). Results show that the proposed robotic system is functioning effectively for making eye contact with human.

KEY WORDS: Human-robot interaction, attention, viewing situation, eye contact.

1. INTRODUCTION

Human-robot interaction (HRI) is an interdisciplinary research field aimed at improving the interaction between human beings and robots and to develop robots that are capable of functioning effectively in real-world domains, working, and collaborating with humans in their daily activities. In the future, the robots would be coexisting into the human world. To enter into the human's world, a social robot should perceive the world as humans do and learn from the interactions with environment and humans. In order to fully understand what humans do or intend to do, robots should be capable of detecting and understanding many of the communicative cues used by humans.

In order to make a successful interaction, both interacting partners need to read social cues from each other and display appropriate behaviors to each other. In this paper, we describe a robotic system that can be used for HRI experiments. We tested the robotic system in a scenario where the human is attending a task (i.e., watching painting) and the robot is trying to make eye contact with him/her. For making eye contact, robots should satisfy two important conditions: (i) gaze crossing (looking each other eyes or face), and (ii) gaze awareness (display an explicit behavior in response to the responding human). The robot can detect, and track the human head and body within a social distance (3meters). By using the information of head and body, the system can recognize the current attentional focus or viewing situation of the human. The robot applies an appropriate action based on these situations to gain his/her attention toward the robot. This will achieve the first condition. After meeting in face-to-face, the robot displays its eye blinking actions which satisfy the second condition.

For any social interaction to be initiated and maintained, parties need to establish eye contact. Eye contact behavior is the basis of and developmental precursor to more complex gaze behaviors such as joint visual attention [1]. Some robotic heads are designed for HRI such as Kismet [2], Andriod [3], and Robovie [4]. These heads are mechanically very complex and as such expensive to design, construct and maintain. Some robots used a flat screen monitor as the robot's head [5]. However, a flat screen monitor is unnatural as a face. Moreover, several robotic systems are performing the gaze crossing function as making eye contact [4, 7]. However, these works assumed that the human and the robot are facing each other initially and previous evidence showed that only gaze crossing function is not enough for making eye contact [8]. In this paper, we consider the cases where the human and robot are not facing each other and the robot is able to perform both gaze crossing and gaze awareness.

2. SYSTEM ARCHITECTURE

We have developed a robotic head for HRI experiments. **Fig. 1** shows an overview of the robotic head. The head consists of a 3D mask, an LED projector (3M pocket projector, MPro 150), a laser sensor (URG-40LX by Hokuyo Electric Machinery), two USB cameras (Qcam, and PTZ Logicool Inc.), and a pan-tilt unit (Direction Perception Inc., PTU-D46). In our current implementation, we put head tracking cameras and laser range sensor on a tripod and placed in front of the participants. The LED projector projects CG generated eyes on the transparent eyes of the face mask. The system has five main software modules: the head tracking module (HTM), the body tracking module (BTM), the situation recognition module (SRM), the eye contact module (ECM), and the robot control module (RCM). In the following sections, we discuss the functions of each module.

2.1 Head Tracking Module (HTM)

In order to track, and computes the direction of the human head in real time (30 frame/sec), we use FaceAPI [9]. It can measure 3D head position (x, y, z) and direction (yaw (α), pitch (β), and roll (γ)) within 3^0 errors. One USB camera is placed in front of the human to track his/her face up to $\pm 90^0$. The results of the HTM send to the SRM to determine the current viewing situation of the human.

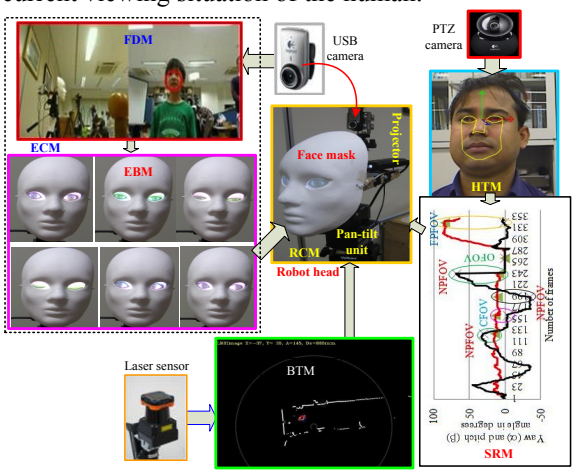

Fig. 1: Overview of the robotic head.

2.2 Body Tracking Module (BTM)

After detecting the human's current viewing situation, the robot should turn its head toward him/her for making eye contact. To turn its head toward the target person, the robot should know the location information of his/her head or body. Our robotic system continuously tracks the body direction of the target participant in real time using a laser range sensor. Therefore, the robot can turn its head toward the human by using the information of BTM.

A human body can be modeled as an ellipse (**Fig. 2 (a)**). We assume the coordinate system is represented with their X and Y axes aligned on the ground plane. Then, the human body model is consequently represented with center coordinates of ellipse [x, y] and rotation of ellipse (θ). These parameters are estimated in each frame by the particle filter framework [10]. When the distance data which captured by the laser range sensor is mapped on the 2D image plane, the contour of the participant's shoulder is partially observed shown in **Fig. 2 (b)**.

The likelihood of each sample is evaluated by the maximum distance between evaluation points and the nearest distance data using the **Eq. 1**.

$$\pi = e^{-\frac{d_{\max}^2}{\sigma_d}} \quad \textbf{(1)},$$

where π is the likelihood score based on the laser image, d_{max} is the maximum distance between evaluation points and the nearest distance data. At each time instance, once the distance image is generated from the laser image, each distance d_n is easily obtained. σ_d is the variance derived from d_n. Evaluation procedures are repeated for each sample. We employ several points on the observable contour as the evaluation points to evaluate hypotheses in the particle filter framework. Selection of evaluation points can be performed by calculating the inner product of normal vectors on the contour and its position vector from laser range sensor.

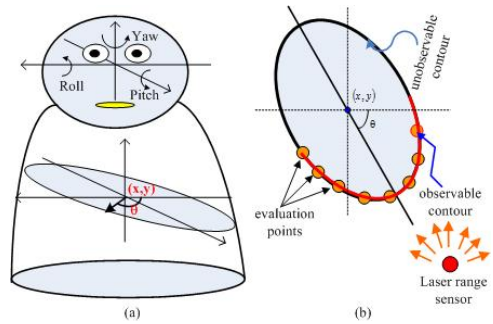

Fig. 2: (a) Human model, (b) Body contour model.

2.3 Situation Recognition Module (SRM)

To recognize the situation (where the human is currently looking), we observe the head direction and body orientation estimated by HDTM and BTM respectively. By extrapolating information from the person's head and body, SRM determines the existing situation. By examining these situations, we found that the human head and/or body orientations are varying from one situation to other. The HDTM tracks within $\pm 90^0$ (right/left) only, therefore, while the human attend to OFOV situation, the system losses head information, in that case, the robot recognize the current situation based on the body information (laser sensor can tracks up to 270^0). From the results of tracking modules, the system recognizes the four viewing situations of the human in terms of yaw (α), pitch (β) movements of head and body direction (θ) respectively using a set of predefined rules. In each rule, we set the values of α, β, θ, by observing several experimental trials.

- **Near peripheral field of view (NPFOV)**: recognized if the current head direction within $-10^0 > \alpha \geq +70^0$ or $+10^0 < \alpha \leq +75^0$ and $-10^0 \leq \beta \leq +10^0$ and remains 30 frames in the same direction.
- **Far peripheral field of view (FPFOV)**: recognized if current head direction within $-70^0 < \alpha \geq +90^0$ or $+70^0 \leq \alpha \leq +90^0$ and $-10^0 \leq \beta \leq +10^0$ and remains 30 frames in the same direction.
- **Out of field of view (OFOV)**: recognized if the human looking to the opposite direction with respect to robot. That means, the robot cannot capture the human face/head and current head direction within $\alpha = \beta = 0^0$ or body direction within $90^0 < \theta \leq +270^0$ or $-90^0 > \theta \geq -270^0$ and remains 30 frames in the same direction.

2.4 Eye Contact Module (ECM)

The ECM mainly consists of two sub modules: the face detection module (FDM), and the eye blinking module (EBM). The robot considers that the human has responded against the robot actions if s/he looks at the robot within expected time. In that case, FDM uses the image of the forehead camera to detect his/her frontal face [11]. After face detection, FDM sends the results to EBM for exhibiting eye blinks. Since the eyes are CG images, the robot can easily blink the eyes at the rate of 1 blink/second in response to the human's gazing at it.

2.6 Robot Control Module (RCM)

In order to capture the human attention toward the robot, it needs to perform several actions (such as, head turn, and head shaking. All of these physical actions are performed by the RCM with proper control signal coming from the several modules.

3. AN HRI EXPERIMENT

We conducted an HRI experiment to verify that our proposed system is functioning. We prepared a collaborative situation where the robot is performing the 'making eye contact' task. That means, the robot is trying to make eye contact with a human when s/he is attending a task (such as watching paintings).

3.1 Experimental Design and Procedures

We prepared two robots. Both were the same in appearance. We programmed each to show different behaviors. One was (i) *Moving robot (MR)*. Initially it is static and is looking in a direction not toward the human face. After recognizing the situation, it will produce three actions: (i) *head turning toward the human,* (ii) *head shaking (±20^0 from the current position, lasting about 3 seconds)*, and (iii) *uttering reference terms ('excuse me')* to attract the human attention. The second was (ii) *Static robot (SR)*. It is stationary all times and is looking toward the human. We placed SR to the right of the rightmost painting and MR to the left of the leftmost painting (for NPFOV and FPFOV situations). In OFOV situation, MR was placed back of the human. To assign a task for the human, we hung five paintings (P1-P5) on the wall at the same height (a bit above the eye level of participants sitting on the chair). Two video cameras were placed in appropriate positions to capture all interactions. **Fig. 3** illustrates the schematic settings of the experiment.

In the experiment, participants were asked to sit down on the chair one at a time. They were asked to look around the paintings. Since the robot's position was fixed, the participants felt the robot in their different fields of view while moving their head.

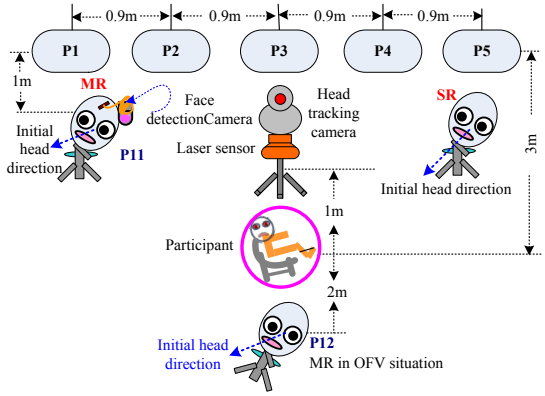

Fig. 3: Experimental set up.

In each condition, the robot tried interaction three times. In each trial, their looking directions were different. That means, they perceived the MR behaviors in their different viewing situations: near peripheral field of view (NPFOV: looking at picture P2 or P3), far peripheral field of view (FPFOV: looking at picture P5), and out of field of view (OFOV: looking at any painting but the MR is placed at behind of the participant). **Fig. 4** shows an experiment scene.

Fig. 4: A scene of the experiment.

3.2 Experimental Conditions

A total of 20 students of Saitama University, Japan participated in the experiment. The experiment had a within-subject design, and the order of all experimental trials was counterbalanced. To evaluate the effectiveness of our system, we prepared three conditions.

- **Method 1 (M1):** The robot turns its head alone toward the participant whatever the situation is. If s/he is looking (attracted) at the robot, it blinks its eyes about 3 seconds for making eye contact.
- **Method 2 (M2):** The robot turns its head first and then shaking head if fails in all situations. If the target person is looking at the robot, it waits about 3 seconds but does not display any eye blinking action.
- **Method 3 (M3):** This is our *proposed* robot. The robot turns its head toward the participant if it captures him/her its NPFOV. However, it shaking head, and uttering reference terms, if it captures the participant in its FPFOV and OFOV situations. The robot blinks its eyes about 3 seconds if it gains the participant's attention.

In all conditions, the robot tracks the participant during first half of the interaction. After 60 seconds, the robot recognizes the current situation (NPFOV, FPFOV, or OFOV). After recognizing the situation, the robot displays behavior according to each condition. When the participant's face direction became toward the robot, it adjust head orientation based on the body information. It waits for 4 seconds whether or not s/he gazed at it. If the participant gazed at the robot within this duration, the robot detects his/her face to ensure the attention capture and start blinks. However, in this experiment, if the participant did not gazed at the robot within 4 seconds, the robot considered the case as failure.

4. RESULTS

From the videos (total=3x20x3=180), we measured *success ratio* (the ratio between the numbers of cases where the robot detects the face (N_F) in response to the participant looked at it and the total number of cases (n)). **Table 1** shows the results of quantitative analysis. In overall, a substantial 92% of times the proposed method (M3) was successful while only 38% and 60% of times the robot was successful while employed methods 1 and 2 respectively for making the eye contact with human.

Table 1: Quantitative analysis

Situations	Cases (n=20/condition)			Success Ratio		
	M1	M2	M3	M1	M2	M3
	N_F/N_L	N_F/N_L	N_F/N_L	%	%	%
NPFOV	19/20	20/20	20/20	95	100	100
FPFOV	04/05	15/17	18/20	20	75	90
OFOV	0/0	01/02	17/19	0	5	85
Total	23/25	36/39	55/59	38	60	92

Fig. 5 shows the subjective evaluation based on the 1- to- 7 point Likert scales. Concerning Q1, repeated measures of analysis of variance (ANOVA) shows the significant differences between conditions ($F(2,38)=52.5$, $p<0.01$, $\eta^2=0.65$). We also conducted multiple comparisons with Benferroni method. They show that the proposed robot (M3) was preferred over M1 ($p<0.01$), and M2 ($p<0.01$). Concerning the Q2, ANOVA analysis shows a significant main effect between conditions ($F(2,38)=45.5$, $p<0.05$, $\eta^2=0.6$). Multiple comparisons with Benferroni method show that the proposed method (M3) was preferred over methods 1 ($p<0.001$), and 2 ($p<0.01$). Thus, the results reveal that the proposed system is functioning better than the alternative methods to make eye contact with the human.

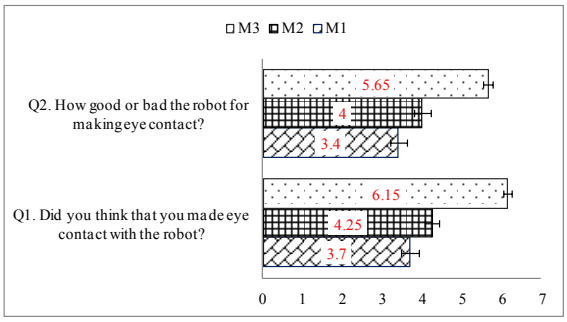

Fig. 5: Subjective evaluation results.

5. CONCLUSIONS

We would like to facilitate the increased introduction of robots into the human world to meet the potential applications in home, offices, or healthcare centers. For robots to be accepted in real world, they must be capable of behaving in ways analogous to those used by humans. To behave in a socially acceptable manner, the robots are capable of performing a lot of social and cognitive functions. In this paper, we showed that the robot is capable to perform an important social function such as making eye contact with humans. This system can be extended for performing other social functions such as attention control, and joint attention. Embodiment and other social cues can include for better performance.

REFERENCES

[1]. T. Farroni et al., "Infant perceiving and acting on the eyes: Tests of an evolutionary hypothesis", *Child Psy.*, vol. 85, no. 3, 2003, pp. 199-212.

[2]. C. Breazeal, Designing sociable robots. Cambridge, MA, USA: MIT Press, 2002.

[3]. D. Mastsui, T. Minato, K. Macdorman, H. Ishiguro, "Generating natural motion in an android by mapping human motion", *IROS* 2005, pp. 3301-3308.

[4]. T. Kanda et al., Development and Evaluation of an interactive robot Robovie, *ICRA*, 2002, pp.1848-1855.

[5]. D. Miyauchi et al., "Bidirectional eye contact for human-robot communication", *IEICE Trans. of Info. & Syst.*, vol. 88-D, no. 11, 2005, pp. 2509-2516.

[6]. B. Mutlu et al., "Footing in human robot conversations: How robots might shape participant roles using gaze cues", *Proc. HRI*, 2009, pp. 61-68.

[7]. M. V. Cranach, J. H. Ellgring, *The Perception of Looking Behavior,* Academic Press, London, 1973.

[8]. FaceAPI: Face Tracking for OEM Product Development, Seeing Machines Int., http://www.faceapi.com, 2010.

[9]. M. Isard, A. Blake, "Condensation-conditional density propagation for visual tracking", *Int. J. of Com. Vis.*, vol. 29, no. 1, 1998, pp. 5-28.

[10]. G. Bradsky et al., "Learning based computer vision with intel's open computer vision library", *J. of Intel Tech.*, vol. 9, no. 2, 2005, pp. 119-130.

Proceeding of the
International Conference on Electrical, Computer and Telecommunication Engineering
01- 02 December 2012 (ICECTE2012), RUET, Rajshahi-6204, Bangladesh

ICECTE2012: PI-0155

Lin-Kernighan Based Solution for Traveling Salesman Problem and Compare the Performance with Sequential Constructive Crossover Operator of Genetic Algorithm

Syed Tauhid Zuhori[1], Nasir Uddin Eisty[2] , Mahbubur Rahman Melon[3], Firoz Mahmud[4]
[1,4]Lecturer, Computer Science & Engineering, Rajshahi University of Engineering & Technology
[2,3]Undergraduate Student, Computer Science & Engineering, Rajshahi University of Engineering & Technology
E-mail: tauhid.ruet@yahoo.com, eisty_ruet@yahoo.com, melon_ruet@ymail.com, sabuzbd.ruet@gmail.com

ABSTRACT
This paper develops two different methods for solving the traveling salesman problem in an optimized time and in an optimized tour length. One is the Lin- Kernighan heuristic method and the other is Genetic Algorithm with sequential crossover operator. Lin-Kernighan is an O (n^2 log n) heuristic algorithm for solving the graph partitioning problem. And the sequential constructive crossover (SCX) for a genetic algorithm constructs an offspring from a pair of parents using better edges maintaining the sequence of nodes in the parent chromosomes. A competitive study on solving the traveling salesman problem with the two methods above and the comparison is shown in the paper.

KEY WORDS: Traveling Salesman Problem, Lin-Kernighan heuristic approach, Genetic Algorithm, Sequential Constructive Crossover Operator, NP-Hard Problem.

1. INTRODUCTION

The traveling salesman problem (TSP) is an NP-Hard problem in combinational optimization studied in operation research and theoretical computer science which has commanded much attention of mathematicians and computer scientists specifically. A TSP is to find the shortest path that visits each city exactly once and returns to the origin city where a list of cities and their pair wise distances are given.

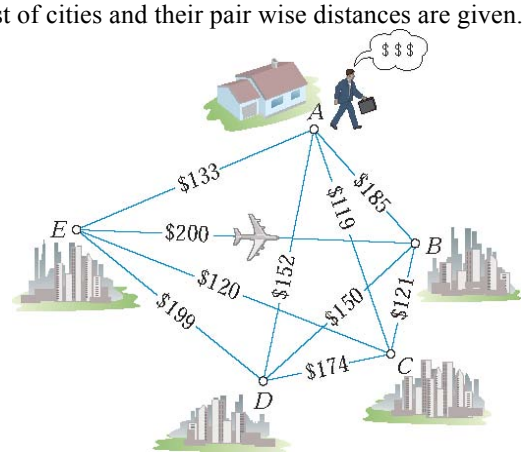

Fig. 1: Example of Traveling Salesman Problem [3]

As it is NP-hard, solving the TSP for n cities requires looking at (n-1)! feasible solutions. The Lin-Kernighan heuristic [1] is generally considered to be one of the most effective methods for generating optimal or near-optimal solutions or the symmetric traveling salesman problem. However, the design and implementation of an algorithm based on this heuristic is not trivial. There are many design and implementation decisions to be made, and most decisions have a great influence on performance [2]. Genetic algorithms have been used in two ways: as techniques for solving technological problems and as simplified scientific models that can answer questions about nature. The search of the solution space is done by creating new chromosomes from old ones. Sequential Constructive Crossover (SCX) is one of the best crossover operators of genetic algorithm. The SCX does not depend only on the parent's structure; it sometimes introduces new but good edges to the offspring, which are not even present in the present population. Hence, the changes of producing a better offspring are more than those other operator [3]. Our problem is to find the shortest path and minimum cost. We use two algorithms to solve this problem and then compare the performance of those two algorithms.

2. LITERATURE REVIEW

Mathematical problems related to the Traveling Salesman Problem were studied in the 1800's by the Irish mathematician Sir William Rowan Hamilton and by the British mathematician Thomas Pennington Kirkman. Hamilton created an Icosian game in 1857 that requires a player to complete a tour using only specified connectors through 20 points [6].TSP's were first studied in the 1930's by mathematician and economist Karl Menger in Vienna and Harvard. It was later investigated by Hassler Whitney and Merrill Flood at Princeton [6].

3. METHODOLOGY

3.1 Lin-Kernighan Approach:

Firstly generate a random starting tour T. Then set G*=0 [G* is the best improvement made so far]. Choose any node t_1 and let x_1 be one of the edges of

T adjacent to t_1. Let i=1. From other end point t_2 of x_1, choose y_1 to t_2 with $g_1>0$. If no such y_1 exists, we have to find alternative of x_1. Let i=i+1. Choose x_i and y_i [Where, $x_i= (t_{2i-1}, t_{2i})$ and $y_i= (t_{2i},t_{2i+1})$] as follows:

x_i is chosen such that t_{2i} is joined to t_1 and the resulting configuration is a tour.y_i is some available link at the endpoint t_{2i} shared with x_i, subject to

- ✓ To guarantee that the x's and y's aredisjoint, $x_i$cannot be a link previously joined and similarly y_i cannot be a link that is previously broken.
- ✓ $G_i=\sum g_j>0$. [j=1to i]
- ✓ In order to ensure that the feasibility criterion of can be satisfied at i+1, the chosen y_i must permit the breaking of x_{i+1}.

Before construction of y_i, we have to check by joining t_{2i} to $t_1$if the gain value is better than the previous best. Let y_i* be a link connecting t_{2i} to t_i and let g_i*=|y_i*|-|x_i|. If $G_{i-1}+g_i$*>G*, set G*=$G_{i-1}+g_i$* and k=i.

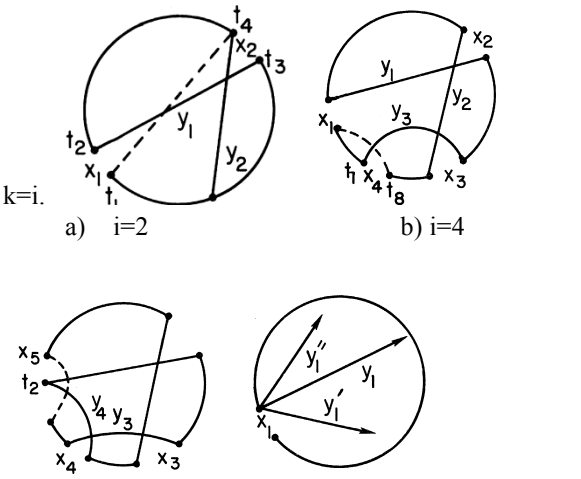

Fig. 2: Algorithm description[1]

Terminate the construction of x_i and y_i when either no further links of x_i and y_i satisfy the required condition or when G_i <=G*.If G*=0, a limited backtracking is invoked.

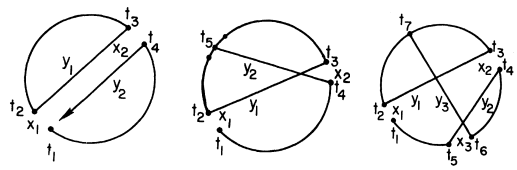

(a) cannot close choiceup at $x_2$for x_3 (b) two choices for x_3;limited Choice for y_3 (c)unique

Fig. 3: The effect of alternate x_2[1]

The procedure terminates when all n values of $t_1$have been examined without profit. At this time, we may consider further random tours and the procedure repeats.

3.1 Genetic Algorithm:

A genetic algorithm (GA) is one such versatile optimization method. Theoptimization process of a GA is shown in Figure 4. The two primary operations of GA are mating and mutation. The GA combines the best of the last generation through mating, in which parameter values are exchanged between parents to form offspring. Some of the parameters mutate [2]. At the same time, it exploits the best features of the last generation to converge increasingly better parameter sets.

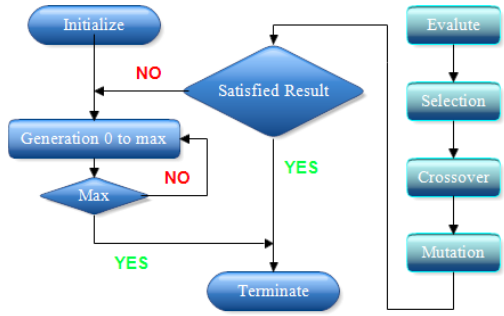

Fig. 4: Flowchart of optimization with a genetic algorithm

Some of the advantages of GAs include:

- They are able to optimize disparate variables, whether they are inputs to analytic functions, experimental data, or numerical model output.
- They can optimize either real valued, binary variables, or integer variables.
- They can process a large number of variables.
- They can produce a list of best variables as well as the single best solution.

Disadvantages are the lack of viable convergence proofs and the fact that they are not known for their speed.

3.2 Sequential Constructed Crossover Operator:

Sequential Constructive Crossover (SCX) is unconventional crossover operator which conserves good sequential structure of the parent's chromosomes during creation of new child chromosomes. Hence, the chances of producing a better offspring are more than those other operator [13].

Procedure:

Step1: Start from 'Node 1' (i.e., current node p =1).

Step2: Sequentially search both of the parent chromosomes and consider the firs 'legitimate node' (the node that is not yet visited) appeared after 'node p' in each parent. If no 'legitimate node' after 'node p' is present in any of the parent, search sequentially the nodes {2, 3, …, n} and consider the first 'legitimate' node, and go to Step 3.

Step 3: Suppose the 'Node α' and the 'Node β' are found in 1st and 2nd parent respectively, then for selecting the next node go to Step 4.

Step 4: If Cpα<Cpβ, then select 'Node α', otherwise, 'Node β' as the next node and concatenate it to the partially constructed offspring chromosome. If the offspring is a complete chromosome, then stop, otherwise, rename the present node as 'Node p' and go to Step 2.

Explanation:

Let a pair of selected chromosomes be P1: (1, 5, 7, 3, 6, 4, 2) and P2: (1, 6, 2, 4, 3, 5, 7) with values 312 and 331 respectively. Select 'node 1' as the 1st gene. The 'legitimate' nodes after 'node 1' in P1 and P2 are 'node 5' and 'node 6' respectively with c15=35 and c16=63. Since c15 < c16, we accept 'node 5'. So, the partially constructed chromosome will be (1, 5). The 'legitimate' node after 'node 5' in both P1 and P2 is 'node 7'. So, we accept the 'node 7', and the partially constructed chromosome will be (1, 5, 7). Again, the 'legitimate' node after 'node 2' in P1 is none, but in P2 is 'node 4'. So, for P1, we consider the first 'legitimate' node in the set {2, 3, 4, 5, 6, 7}, that is, 'node 3'. Since c24 = 46 < 86 = c23, we accept 'node 4'. So, the partially constructed chromosome will be (1, 5, 7, 2, 4). The 'legitimate' node after 'node 4' in P1 is none, but in P2 is 'node 3'Thus the complete offspring chromosome will be (1, 5, 7, 2, 4, 3, 6) with value 266 which is less than value of both the parent chromosomes. The crossover is shown in Figure 1. The parents are showing as (a) and (b), while (c) is a possible offspring. Parents' characteristics are inherited mainly by crossover operator. Also, the new edges (6, 2) and (7, 1) have lesser values. In addition, the SCX can generate a wide variety of offspring[18].

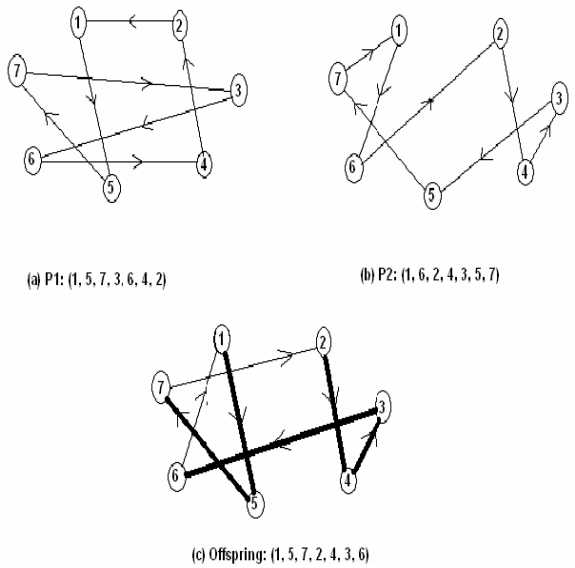

Fig. 5: Example of sequential crossover operator

4. EXPERIMENTAL RESULT

We solved the Traveling Salesman Problem by both algorithm (Lin-Kernighan and Sequential constructed Crossover operator). It is solved for different number of cities ranges from 50 to 500.

Number of Cities	Tour length	
	Lin-Kernighan Heuristic Algorithm	Sequential Constructive Crossover (SCX)Operator of GA
50	225	240
100	432	478
150	683	702
200	852	925
250	1026	1120
300	1350	1520
350	1502	1702
400	1712	1921
450	1908	2105
500	2026	2236

Table 1: Comparison between SCX and LK Heuristic in case of tour length

These values are obtained by taking the average value for several trials for each of the values are plotted in the following graphs to determine the comparison between the two techniques.

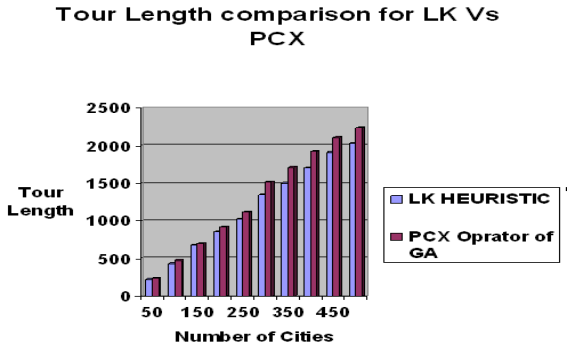

Fig. 6: Comparison between LK and PCX according to time

The time need to solve the TSP ranges from 50 to 500 cities is also found out. In the following table data are shown.

Number of Cities	Time(in Sec)	
	Lin-Kernighan Heuristic Algorithm	Sequential Constructive Crossover (SCX)Operator of GA
50	0.0121	0.0251
100	0.02811	0.0381
150	0.0389	0.0681
200	0.0521	0.0892

250	0.0681	0.1530
300	0.0825	0.3251
350	0.0982	0.5621
400	0.1224	0.8956
450	0.1258	0.9987
500	0.1356	1.2501

Table 2: Comparison between SCX and LK Heuristic in case of time.

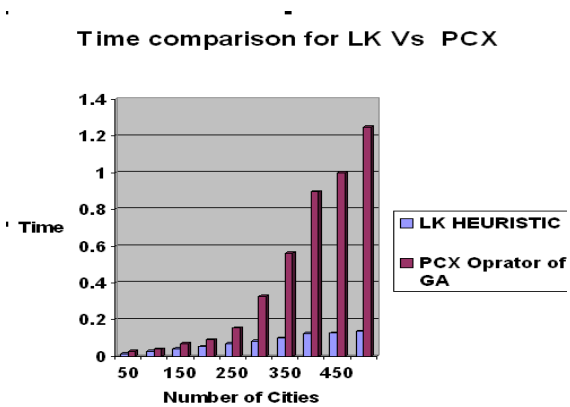

Fig. 7: Comparison between LK and PCX according to time

5. CONCLUSION and FUTURE WORK

The Traveling Salesman Problem (TSP) is very difficult in computational arithmetic and up till now no successful explanation process is known used for the common case. As the problem is to find the shortest path with minimum cost, we've used Lin-Kernighan algorithm and Genetic algorithm with Sequential Constructive Crossover Operator (SCX). Firstly, we performed the Lin-Kernighan algorithm for solving and then performed Genetic algorithm with SCX operator for comparing the performance. Finally, we compared the performance of these two algorithms. By studying all the above mentioned we found Good Lin-Kernighan implementations are the best performing local searches for TSP. We've also tried to solve the problem for the renowned problem set finding in the TSP library. In future work we'll take Lin-Kernighan approach which solves the TSP problem using appropriate fitness functions and finally finds the least complexity.

REFERENCES

[1]. S. Lin & B. W. Kernighan, "An Effective Heuristic Algorithm for the Traveling-Salesman Problem",*Oper.Res.*21, 498-516(1973).

[2]. KeldHelsgaun, "An Effective Implementation of the Lin-Kernighan Traveling Salesman Heuristic", Denmark.

[3].ZakirH. Ahmed, "Genetic Algorithm for the Traveling Salesman Problem using Sequential Constructive Crossover Operator",International Journal of Biometrics & Bioinformatics (IJBB), Volume (3): Issue (6).

[4]. Theofficial website of TSP library, "www.tsplib.org"

[5] D. Goldberg, "Genetic Algorithm in Search, Optimization and Machine Learning", Addison Wesley, 1989.

[6] Zakir H. Ahmed,"Genetic Algorithm for the Traveling Salesman Problem using Sequential Constructive Crossover Operator", International Journal of Biometrics & Bioinformatics (IJBB), Volume (3): Issue (6), 2010.

[7] V. A. Cicirello,"Non-wrapping order crossover: An order preserving crossover operator that respects absolute position", GECCO, pages 1125–1131, 2006.

[8] Milena Karova, Vassil Smarkov, Stoyan Penev,"Genetic operator's crossover and mutation in solving the TSP problem", pages 2-3, 2005.

[9] Syswerda, G.: Schedule Optimization using Genetic Algorithms. Handbook of Genetic Algorithms, L. Davis Eds,Van Nostrand Reinhold (1990) 332-349.

[10] Starkweather, T., McDaniel, S., Mathias, K., Whitley, D. and Whitley, C.: "A Comparison of Genetic Sequencing Operators". Proceedings of the Fourth International Conference on Genetic Algorithms, (1991) 69-76.

[11] Qi-yi,Zhang &Shu-chun, Chang (2009) "An Improved Crossover Operator of Genetic Algorithm", China: Transportation Command Department Automobile Management Institute of PLA.

[12] C. Moon, J. Kim, G. Choi and Y. Seo,"An efficient genetic algorithm for the traveling salesman problem with precedence constraints", European Journal of Operational Research 140, pp. 606-617, 2002.

[13]Zakir H. Ahmed,"Genetic Algorithm for the Traveling Salesman Problem using Sequential Constructive Crossover Operator",International Journal of Biometrics & Bioinformatics (IJBB) Volume (3): Issue (6).

Proceeding of the
International Conference on Electrical, Computer and Telecommunication Engineering
01- 02 December 2012 (ICECTE2012), RUET, Rajshahi-6204, Bangladesh

ICECTE2012: PI-0156

PC Based Incubator for Hatching Eggs Using Fuzzy Logic Controller

O. Farrok[1], R. R. Mahmud[2] and N. A. Shafi[3]
[1] Assistant Professor, Dept. of EEE, Ahsanullah University of Science and Technology (AUST)
[2]Assistant Professor, Dept. of EEE, Ahsanullah University of Science and Technology (AUST)
[3] Sr. NOC Engineer, Zamir Telecom Limitted
E-mail: [1]omarruet@gmail.com, [2]r.r.mahmud@gmail, [3]nahid_apee@yahoo.com

ABSTRACT
This paper presents incubator technique for controlling temperature and humidity for hatching eggs. It is a programmable PC based fuzzy logic control unit in which one PC can control some incubators at a time. Manual operating incubator is cheaper to purchase but maintenance cost is high. Again, automatic incubator is costly for purchasing but maintenance cost is cheaper. But our designed incubator is cheaper in both purchasing and maintaining. A temperature sensor which is very cheap and efficient is used in this incubator. The load factor is higher for other conventional incubators because of having ON-OFF control technique. But the proposed incubator is fuzzy logic based multistage control system which can maintain a reasonable load factor. A detail design procedure including circuit design, algorithm, flow chart and the practical outputs are presented in this paper.

KEY WORDS: Temperature sensor, Humidity sensor, Multiplexer, De-multiplexer, Analog to digital converter, Fuzzy logic controller.

1. INTRODUCTION

There are different types of incubators are invented by many researchers. Our proposed incubator is different from the other conventional incubators. In April 1996, the submarine Incubation system was first introduced by gabor Vajta, Paul Bartel et al [1]. It has been successfully both for routine embryo production and for experiments dealing with the different gas mixtures on embryo development. This system is a reliable and cost-efficient way to culture sensitive by using incubation system. Another Heraeus cytomat 6000 series incubator [2] was a robot accessible, automated co_2 incubator used for cell-based high throughput screening system. The system provides high speed, random access to all micro plate formats. In our proposed incubator for the hatching purpose is computer based incubator for hatching eggs using fuzzy logic controller which is very cheap from our practical observation.

2. DESIGN AND WORKING PRINCIPLES OF A PC BASED SYSTEM

The whole system works on seven steps. The flow diagram of the system is given below in the figure no 1.

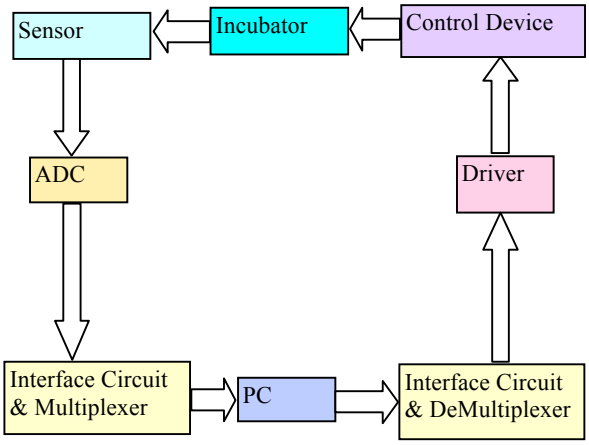

Fig. 1: Signal flow diagram of the total system

A single phase 220 V alternating current with 50 Hz frequency is the input of primary side of the step down transformer. A rectifier circuit is used to get dc output voltage which is fixed of 5 volt & 12 volt by regulator circuit. This regulator output is then used for VCC of ADC (analog to digital converter), Timer circuit that generates clock pulse and supplies to relay device. Temperature sensor is used here for sensing temperature and humidity respectively. When this temperature is high, the internal resistance of the temperature sensor is low and output voltage is low. This output voltage is applied to the input pin no 6 of the ADC. For single incubator pin no 11 to 14 of the same ADC are used for printer input port of pin no 10 to 13. Two ADC are used here. One is for temperature and another is for humidity. Pin no 11 to 14 are the output for both ADC. Printer port pin no 11 to 13 are for temperature and 14 to 17 are for humidity as the input signal. The parallel port of pin no 2 is used for the output of the programming signal that operates the relay circuit. A fan is used for circulating heat through surrounding area in the incubator. One multiplexer circuit is used here. For 1st clock pulse the sensing data of temperature and

humidity of the 1st incubator is input of the PC through multiplexer circuit. For next clock pulse the data of the second incubator is gone through the multiplexer circuit. In this way many incubators can be operated at the time with a single PC and thus the program creates the circuit run as necessity. The signal is converted from analog to digital by ADC. After getting high state pulse to the relay circuit that relay becomes energized and makes the heater turn on.

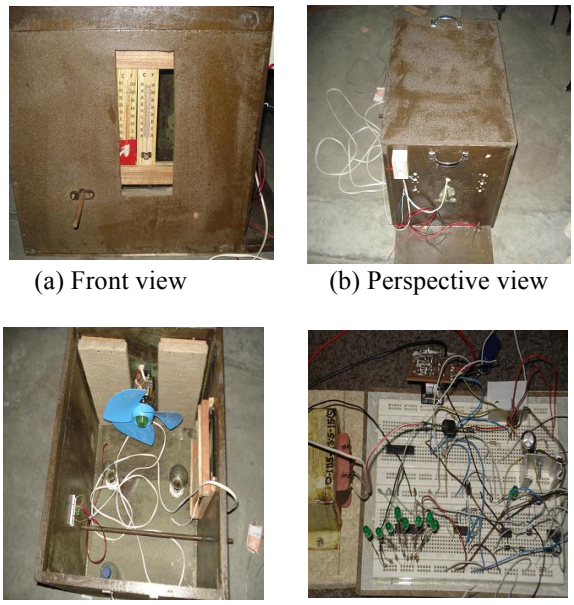

(a) Front view (b) Perspective view

(c) Inside view (d) Electronic Circuit

Fig. 2: Different views of our proposed system

3. FUZZY LOGIC BASED CONTROLLER

In this controller two inputs are applied, one is temperature and another is humidity. Minimum to maximum temperature and humidity range is 96°F to 102°F and 95°F to 101°F respectively. Triangle membership function is applied here. Heaters are used for controlling temperature and water inlet system for controlling humidity. For different range of temperature total 5 heaters are used. When humidity is low then water is dropping to the atmosphere through the water inlet. In this way temperature and humidity of the incubator are controlled.

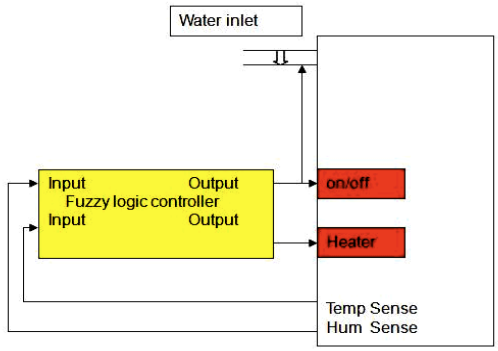

Fig. 3: Fuzzy control of temperature and humidity of the incubator box

The range of values that inputs and outputs may take is called the universe of discourse. The universe of discourse for all the inputs and outputs of the fuzzy logic controller have to be defined which all crisp values are following table shows the ranges.

Table 1
Universe of Discourse for Inputs and Outputs for Fuzzy Logic Controller

Name	Input/Output	Minimum value	Maximum value
Temp Sense	I	96	102
Heater	O	0	5
Hum Sense	I	95	101
Water Inlet Valve	O	0	1

From the above table when temperature sensor senses 96°F then 5 heaters are turn on and they are turn off for 102°F temperature. In the similar way when humidity sensor senses 95°F then water inlet valve is open, otherwise valve is turned off.

Table 2
Fuzzy Variable Ranges for Tem Sense

Crisp Input Range	Fuzzy Variable
96 – 97.8	**COLD**
97– 98.8	**COOL**
98.2–99.8	**NORMAL**
99.2–101	**WARM**
100.2–102	**HOT**

The incubator temperature is 99°F and humidity is 98 as the best choice for the hatching eggs. When the temperature is below 99°F then correspond one, two, three, four or five heaters are on. So it is controlled by five heaters in five stapes.

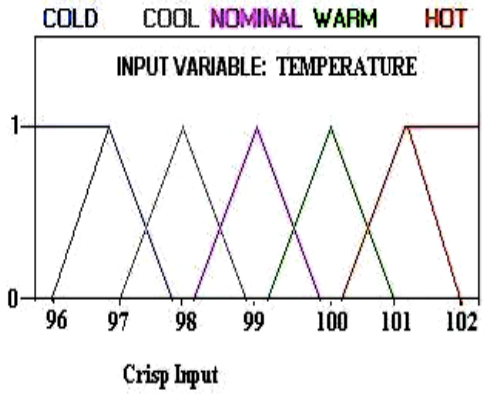

Fig. 4: Level and triangular membership function for the input variable for temperature

Table 3

Fuzzy Variable Ranges for Hum Sense

Crisp Input Range	Fuzzy Variable
95–96.8	WEAK
96–97.8	LOW
97.2–99.8	OK
98.2–100	STRONG
99.2–101	HIGH

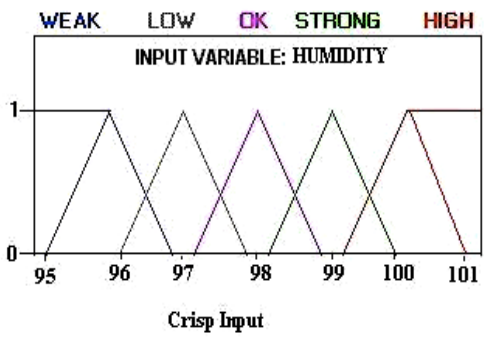

Fig. 5: Level and triangular membership function for the input variable for humidity

The table represents the condition of turn on the heaters and so on according to the response of the sensor. Humidity is controlled as same as temperature. Temperature is divided into five ranges –Cold, Cool, Normal, Warm, and Hot; and humidity is also divided into five ranges –Weak, Low, Ok, Strong and High. Temperature is controlled by turning on and off of the heaters and humidity is controlled by controlling the value of water inlet.

Temp Sense / Hum Sense	Cold	Cool	Normal	Warm	Hot
weak	five	four	three	x	x
low	three	two	one	x	x
ok	two	one	one	x	x
strong	two	one	one	x	x
high	one	one	x	x	x

From the rule base table some decision can be taken.

a) If temperature is cold & humidity is weak then five heaters are on.
b) If temperature is cold & humidity is low then three heaters are on.
c) If temperature is cold but humidity is ok or strong then two heaters are on.
d) If both temperature & humidity are cold then one heater is on.
e) If temperature is cool but humidity is weak then four heaters are on.
f) If temperature is normal but humidity is weak then three heaters are on.
g) One heater is on for the following cases
   temperature -cool & humidity -ok.
   temperature -cool & humidity -strong.
   temperature -cool & humidity -high.
   temperature -normal & humidity -low.
   temperature -normal & humidity -ok.
   temperature -normal & humidity -strong.

Besides these, for all other cases all the heaters are turned off. The input & output data are transmitting through the printer port. In order to control the heater, a crisp dial setting needs to obtain. So far, we have several of the IF–THEN rules of the fuzzy rule base firing at once, because the inputs have been fuzzy field. There are actually several different strategies for this; two of the most common are the center of area (COA) and the fuzzy or method. The easiest way to understand the process is the fuzzy or method. An example is given below.

crisp input temp sense = 99.4
crisp input hum sense = 97.5
warm = 0.25, normal = 0.60, all others = 0.0
ok = 0.3, low = 0.4, all others = 0.0
fuzzy outputs with membership values-
(0.25) or (0.3) or (0.4) = 0.4
output value = 2
heaters = two
water inlet valve = on

4. ALGORITHM OF THE FUZZY LOGIC CONTROLLER CONTROL PROGRAM

Step1: Initialize the LPT1 Port.

Step2: Read inputs of the humidity and temperature Sense through the LPT1 input port using pin no. 10 to 17.
Step3: If the range of humidity and temperature satisfy the inputs then go to the next process otherwise read inputs again.
Step4: By using fuzzy rule base and two inputs the response is detected.
Step5: Select the values for the incubator that is ON or OFF bulbs and ON or OFF the water inlet valve.
Step6: Send these selected data through LPT1 output port pin no 2 to 9.
Step7: End.

For programming, sensor data is converted into binary format. Each 0.2°F scale difference is applied for comparing the previous data of temperature and humidity. Sensor senses data and compares with the required value. If the value is greater then desired level then heaters are turned off. Otherwise heaters are turned on.

5. FLOW DIAGRAM FOR THE CONTROL OF THE FUZZY LOGIC CONTROLLER

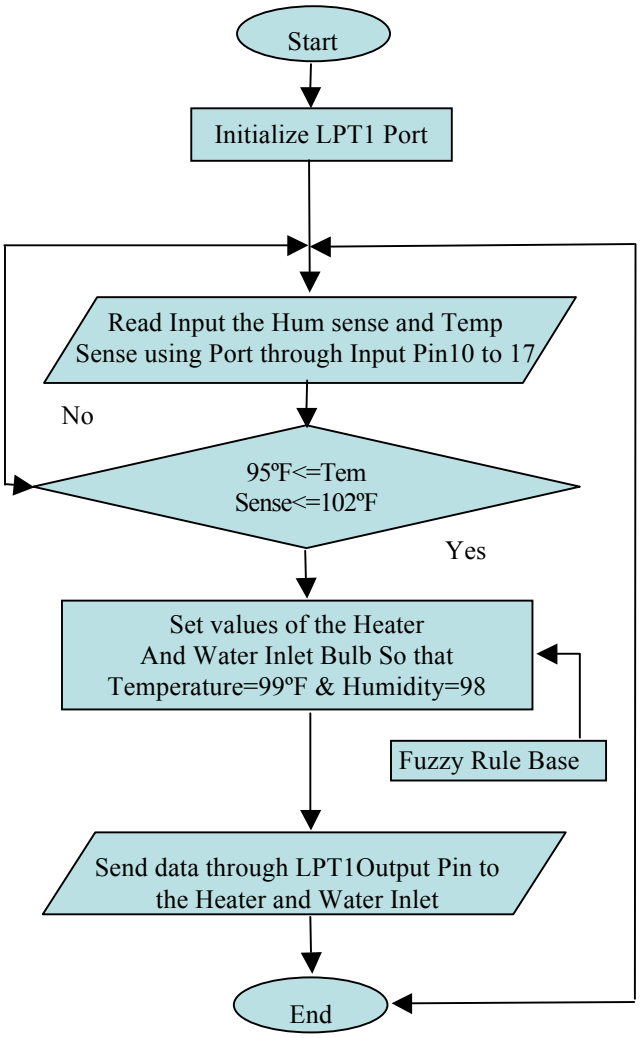

Fig. 6: Flow chart of the fuzzy logic program

6. CONCLUSIONS

The incubator for hatching purpose, by this way is so for the best and cheapest one as inferred from our practical observation by using the PC based incubator for hatching eggs using fuzzy logic controller. This incubator applies for usual load factor, costs less compared to the other incubator systems in the market. Therefore, if this present incubator can be applied in those countries whose normal temperature is less then 95°F in a large scale, it will help to develop those countries economy.

REFERENCES

1. G. Vajta, P. Bartel et al, "Production of a healthy calf by somatic cell nuclear transfer without micromanipulators and carbon dioxide incubators using the Handmade Cloning (HMC) and the Submarine Incubation System (SIS)", *An International Journal of Animal Reproduction,* 62(8), pp. 1465-1472, 2004.
2. M. R. Islam and M. W. H. Sadid, "Improvement of microprocessor based temperature monitoring and control system using fuzzy logic controller", *Accepted to the Asian Applied Computing Conference,* AACC 2005.
3. R. F. Coughlin and F. F. Driscoll, "Operational amplifier and linear integrated circuits", *Prentice Hall International,* Sixth Edition, pp. 20-23,363-371,463-465, 2003.
4. R. j. Tocci and N. S. Widmer, "Digital system principles and applications", *Prentice Hall International,* Ninth Edition, pp. 26, 27, 40, 62, 70, 593-630, 2005.
5. A. Engler, "Heraeus cytomat® 6000 series Incubators and storage systems from Kendro Laboratory Products", *An Official of the Society for Laboratory Automation and Screening,* pp. 38-41, May 2000.
6. S. Rajasekaran and G. A. Vijayalaksmi, "Neural Networks, Fuzzy Logic and Genetic Algorithm Synthesis and Applications," pp. 157-186
7. V. Rao and H. Rao, "*C++ Neural Network And Fuzzy Logic",* Second Edition, pp. 31-50 and 497-510.
8. Description of incubator at the web site: http://www.answers.com
9. About hatching technique at the web site: http://www.hatchtech.com
10. About poultry farming at the web site: http://www.the poultrysite.com
11. About Fuzzy Logic at the web site: http://www.seattlerobotics.org/encoder

12. Interfacing parallel port with VB6 language at the web site:
http://msdn2.microsoft.com/en-us/library/y7ae61bc(VS.80).aspx

Development of a Surveillance Robot for Controlling from Unlimited Distance

Shahajada Mahmudul Hasan[1], *M. Rokunuzzaman*[2]
[1,2]Department of Mechanical Engineering, Rajshahi University of Engineering and Technology
E-mail: smhme01@yahoo.com, rzaman_mctr@yahoo.com

ABSTRACT
Surveillance based robot are of huge interest in the recent development of Mobile Robotics. A Robot has been developed which is for that purpose. Its outstanding feature is that it can be controlled from unlimited distance. Four cameras are mounted over the robot for acquisition of images from the surroundings. Any user can now control the robot from long distance in condition of internet connection. The images from the four cameras and the control panel will be transmitted and displayed in the user's monitor and the user can control the robot from any distance where internet connections are available. Various experiments were carried out by controlling the robot from various distances and the robot always performed successfully. Data transmission rate were also evaluated for calculating the robot's performance.

KEY WORDS: Surveillance Robot, Long Distance Control, Internet connection, Image Transmission, Unlimited Distance.

1. INTRODUCTION

Tele-robotics is the area of robotics concerned with the control of robots from a distance, chiefly using wireless connections (like Wi-Fi, Bluetooth, the Deep Space Network, and similar), "tethered" connections, or the Internet. It is a combination of two major subfields, tele-operation and tele presence [16].

Tele-operated robots, or tele-robots are devices remotely operated from a distance by a human operator rather than following a predetermined sequence of movements. They are used when a human cannot be present on site to perform a job because it is dangerous, far away, or inaccessible. The robot may be in another room or another country, or may be on a very different scale to the operator. For instance, a laparoscopic surgery robot allows the surgeon to work inside a human patient on a relatively small scale compared to open surgery, significantly shortening recovery time.[4] They can also be used to avoid exposing workers to the hazardous and tight spaces such as in duct cleaning. When disabling a bomb, the operator sends a small robot to disable it. Several authors have been using a device called the Long pen to sign books remotely.[1] Tele-operated robot aircraft, like the Predator Unmanned Aerial Vehicle, are increasingly being used by the military. These pilotless drones can search terrain and fire on targets [8][9]. Hundreds of robots such as iRobot's Packbot and the Foster-Miller's TALON are being used in Iraq and Afghanistan by the U.S. military to defuse roadside bombs or improvised explosive devices (IEDs) in an activity known as explosive ordnance disposal (EOD) [6]

With the exception of the Apollo program most space exploration has been conducted with tele-robotic space probes. Most space-based astronomy has been conducted with tele-robotic telescopes. Recent noteworthy examples include the Mars exploration rovers (MER) and the Hubble Space Telescope. In the case of the MER mission, the spacecraft and the rover were each tele robotically operated. The International Space Station (ISS) uses a two armed tele manipulator called Dextre [3].

Marine remotely operated vehicles (ROVs) are widely used to work in water too deep or too dangerous for divers. They repair offshore oil platforms and attach cables to sunken ships to hoist them. They are usually attached by a tether to a control center on a surface ship. The wreck of the Titanic was explored by an ROV, as well as by a crew-operated vessel [3].
Additionally, a lot of tele-robotic research is being done in the field of medical devices, and minimally invasive surgical systems. With a robotic surgery system, a surgeon can work inside the body through tiny holes just big enough for the manipulator, with no need to open up the chest cavity to allow hands inside [3].
The UWA tele-robot is a historic landmark for the Internet and The University of Western Australia (UWA). It was the first tele-operable industrial robot made available for general use on the Internet in

1994. The UWA tele-robot was originally developed as part of a PhD thesis by Dr Kenneth Taylor [9] and was the subject of a later PhD by Dr Barney Dalton [5].

The first robot on the Internet, a plastic toy robot with only 2 degrees of freedom, was placed online by a team under Ken Goldberg at the University of Southern California[10] only three weeks before the UWA team released their website. The USC robot only lasted for seven months. The UWA robot is still online today, although the original robot was replaced in 1996[10] and the robot is no longer available for unrestricted public access, though interested parties can request permission.[8]
"An Improved Method for the Transmission of Large Image over Internet '' was developed by Kamrul Hasan Talukder and Koichi Harada, Graduate School of Engineering, Hiroshima University, Japan. They proposed a wavelet-based image transmission scheme in this paper which has used discrete wavelet transform to transform a digital image from spatial domain into frequency domain. Haar wavelet transformation has been chosen and used for wavelet transformation phase. Use of concurrent computing has significantly reduced computation time overhead as well as the transmission time up to a great extent as compared to the existing sequential discrete wavelet based transmission. The experimental result shows that the proposed scheme maintains the accuracy of reconstructed image.[7]

The Development of long distance controlled robot has a decade of research history. Recently this type of robot is serving in a diversified fields and areas. Akiyuki Minamide et al proposed a distant control robot [8] model where game robots are controlled from long distance through internet. They practically implemented the concept and arranged robot gaming competition between the children of a Japanese school and of a Singapore school.

Cyprian M. Wronka et al developed a concept of Internet remote control interface for a multipurpose robotic arm [9].In their work authors proposed a tele operated model for controlling a robotic arm. The subject of robotic tele-operation has been widely studied and a survey can be found in (Taylor and Dalton, 2000)[7,8], also describing an available public implementation of an Internet robot controller. Another interface enriched with force feedback data can be found in (Oboe, 2001).[10,9] One of the first industrial arms made available on the World Wide Web is presented in (Goldberg et al., 2000)[5,9]. Another system, presented in (Park et al., 2004),
[6,3] performs real-time control of an Internet robot. Raul Wirz et al developed a model for multi robot distant control system where they used internet for the purpose. [3,7]

Yongjin (James) Kwon et al proposed a model for Network-based Vision Guidance of Robot for Remote Quality Control which will be employed in e-manufacturing in industries [10] In Sanda Win et al's model authors proposed a remote controlled mobile robot which is designed using a microcontroller PIC16F873A. [10] Lots of works also found on multi-camera surveillance systems. Omar Javed and Mubarak Shah developed a multi-camera surveillance robot model. In their "*KNIGHT: A Multi-Camera Surveillance System"* project they developed a system where multiple camera will be employed at a time for surveillance based application. [10] SLAM is one of the most widely researched subfields of robotics. A solution to the SLAM problem would allow a robot to make maps without any human assistance whatsoever. Mapping by using Global Positioning Technology is also available in literatures. [9,5].

In this work authors integrated the following key points in a single robotic system. Distant control Robot, Surveillance Robot, Mobile Robot, Wireless Data Communication, Parallel Port Data Transfer, Using RF sensor and microcontroller, Capturing image via webcam, Combining Multi Camera Vision, Transmission of Images, A few software used in the research are being used practically for other purpose rather than this. The instruments are locally available and cheap. No significant research has been found utilizing these devices.

2. METHODOLOGY

For the development of the robot it was the first task for the authors to develop a base for the mobile robot. A car with rechargeable battery, chassis steering system and other necessary equipments has been chosen as the mobile robot. The controlling circuit is developed by removing the existing car circuit. The car can now be controlled by the computer taking inputs from the keyboard.

Fig 1: The complete arrangement of the Robot

For controlling the car with a desktop computer having a parallel port, a control circuit has been developed. For communication of data parallel port is used. Microcontroller TX-2B and radio frequency sensor has been used in both the transmitter and receiver circuits. The transmitter circuit with antenna should be kept within the radio frequency range of the robot's motion to be connected with it.

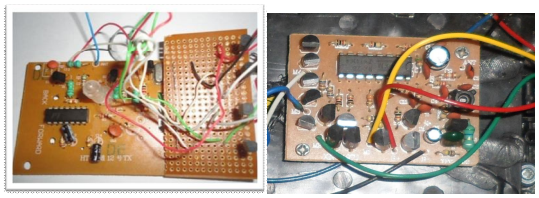

Fig 2: PCB layout of the transmitter (left) and reciever (right) circuit.

The existing steering system is now can be controlled by the computer keyboard and a robot computer interface circuit is developed. A control panel has been developed by using software Visual Basic and by the four arrows the direction of motion of the robot is controlled. By the four direction button as indicated in the window below, the direction of motion of the vehicle is maintained. The data transfer will be done through parallel port of the computer. The authors are currently replacing the parallel port data transfer to serial port. If so, the limitations of the existence of the desktop computer within the radio frequency range will overcome and then the robot mounted laptop can be used for the controlling of the robot when the robot will carry the both transmitter and receiver circuit resulting no radio frequency range limitations.

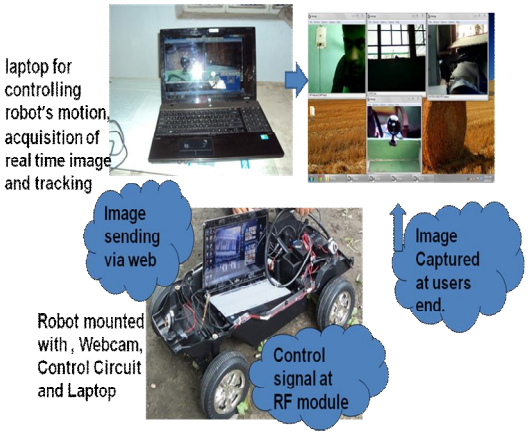

Fig 3: Schematic Diagram of the System

Four webcams are placed front, back, left and right of the robot to get the video images from the surroundings of the robot. The four different windows show the different views in the computer screen which is attached with the robot. The acquisition of images is done through Vmcap software. By using the Team viewer software we got the image by communicating between the two computers and transferring the 4 windows on the screen of the robot mounted computer to the distant one.

The two internet connected computer will now transfer images. For the transformation of images software Virtual Network Computing (VNC) has been used. For a user of the robot it is possible to control from unlimited distance in condition of internet connection. In the monitor of the user's computer the real time picture of the surroundings of the robot is seen.

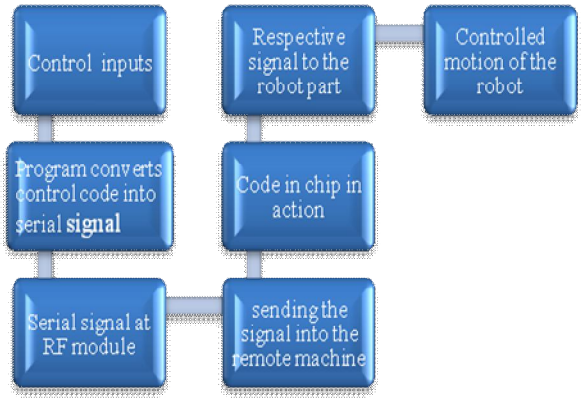

Fig 4: Data flow Diagram of the integrated system

PERFORMANCE EVALUATION:

From this work it is found that the image can be captured from 30 feet distance with A4tech camera. The accuracy of the system is high when the image is transferred with low frame rate but the quality of the images are poor and accuracy decreases with increase in frame rate when internet speed is constant. When internet speed is high image transferring rate is high and accuracy of the system is high.

Data of image transmission is taken by varying the distance and taking the internet speed as almost constant. Various data shows that the image transmission is independent of the distance between the user and the robot.

The plot of image transfer rate versus the distance shows that it is almost constant. From this it can be said that the robot is independent of the distance and can be controlled from unlimited distance.

No. of observation	Distance (Between the user and the robot)	Frame rate per sec	
		Actual capturing	After transferring
01	1m	50	39
02	3m	50	38
03	5 m	50	39
04	50 m	50	37
05	100m	50	38
06	500 m	50	39
07	1000m/1km	50	38
08	3 km	50	37
09	5km	50	38

Table 1: Data showing the variation of image transfer rate

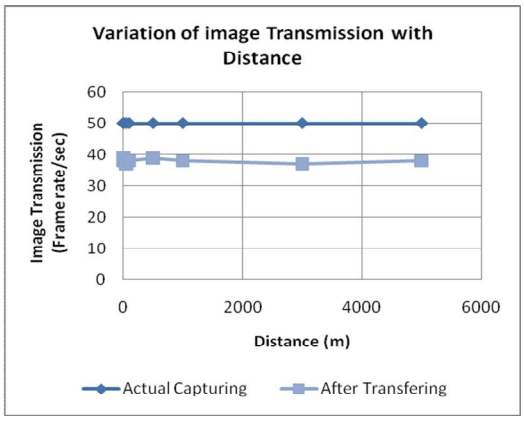

Fig 5 : Variation of image transmission with distance

FURTHER RESEARCH:

The research is going on to modify some of the features of the existing robot. The authors are working to change the parallel port data transmission system between the desktop computer and the computer over the robot with serial port. By this way the requirement of the desktop computer will be eliminated. Works are also going to use image processing for using the track map to make the robot intelligent one.

CONCLUSION

The authors tried to develop a distance controlled robot which has a wide applicable range as well as a wide control range. Authors successfully completed to develop the preliminary model and successfully controlled it from long distance.

REFERENCES

[1]. Akiyuki Minamide et al," *Engineering Education Using a Long-Distance-Controlled Robot System to Enhance Students Motivation ",* International Conference on Engineering Education – ICEE 2007 , Coimbra, Portugal

[2]. Cyprian M. Wronka et al, "Internet remote control interface for a m*ultipurpose robotic arm "*, International Journal of Advanced Robotic Systems, Vol. 3, No. 1 2006) ISSN 1729-8806, pp. 179-183 .

[3]. Raul Wirz et al, "*Remote programming over multiple heterogeneous robots: a case study on distributed multi-robot architecture",* Industrial Robot: An International Journal 33/6 (2006) 431– 442 Emerald Group Publishing Limited [ISSN 0143-991X]

[4]. Omar Javed a nd Mubarak Shah*," KNIGHT: A Multi-Camera Surveillance System "*, University of Central Florida, Orlando, Fl 32816(2002)

[5]. H. Irie, K. Imamura ," *DGPS for Outdoor Mobile Robots by o Wireless LAN",* WUJNS, Wuhan university journal of natural sciences , Vol. 8 No.2B 2003 581-586

[6]. Yongjin (James) Kwon et al, "Network-based Vision Guidance of Robot for Remote Quality Control ",book chapter, Robot Vision.

[7]. Sanda Win et al, "*Design and Construction of PIC-based IR Remote Control Moving Robot ",* World Academy of Science, Engineering and Technology 48 2008

[8]. Taylor, K. and Dalton, B. (2000). Internet robots: A new robotics niche. IEEE Robotics and Automation Magazine, 7(1):27–34.

[9]. Oboe, R. (2001). Web-interfaced, force reflecting tele-operation systems. IEEE Transactions on Industrial Electronics, 48(6):1257–1265.

[10]. Goldberg, K., Gentner, S., Sutter, C., and Wiegley, J. (2000). The mercury project: A feasibility study for internet robots. IEEE Robotics and Automation Magazine, 7(1):35–40.

Proceeding of the
International Conference on Electrical, Computer and Telecommunication Engineering
01- 02 December 2012 (ICECTE2012), RUET, Rajshahi-6204, Bangladesh

ICECTE2012: PI-0158

Estimation of Chromatic Dispersion Using the Variance of Equalized Signal in Digital Coherent Receivers

Md. MahmudurRahman, SaziaAnar and Md. SaifuddinFaruk
Department of Electrical and Electronic Engineering, Dhaka University of Engineering and Technology, Gazipur, Bangladesh
E-mail: m.rahman04@yahoo.com

ABSTRACT
Recent advancement of digital coherent receivers allows compensation of chromatic dispersion (CD) in digital domain. Since CD in a channel is almost static, we need to estimate it to design the fixed CD compensation filter. In this paper, we propose an effective chromatic dispersion (CD) estimation algorithm based on the calculation of variance of equalized signal. We validate the proposed algorithm with computer simulation of 100-Gbits/s polarization division multiplexed quadrature phase-shift keying (PDM-QPSK) transmission systems. Estimation with a good accuracy is confirmed from such simulation.

KEY WORDS: Optical fiber communication, digital coherent receivers, chromatic dispersion estimation, digital signal processing.

1. INTRODUCTION

To meet the ever increasing bandwidth demand, optical multilevel modulation format and polarization multiplexing are promising options for next generation optical communication systems. Digital coherent optical receivers allow demodulation of such multilevel modulation formats [1]. After converting the incoming optical signal into electrical signal using a phase and polarization diversity receiver, we use several digital signal processing (DSP) algorithms to recover the information. Generally two-fold oversampled digital signal is used for processing. The typical DSP core of the receivers includes clock recovery, fixed filter for chromatic dispersion (CD) compensation, adaptive filter for polarization demultiplexing and polarization-mode dispersion (PMD) compensation, carrier phase recovery to suppress phase noise of transmitting laser and local oscillator (LO) and decision circuit to decode the data [2]. The CD estimation is required for the CD compensator which is either a fixed time-domain finite-impulse-response (FIR) filter [3] or a frequency-domain equalizer (FDE) with overlap-save algorithm [4], [5]. Since any mismatch in the CD compensator will affect the subsequent DSP circuits, an accurate CD estimation is very important.

In [6] a CD estimation technique is demonstrated based on the constant modulus algorithm (CMA). However, since the CD estimation is done prior to timing frequency offset, the dispersion parameters for the CMA need to be estimated constantly and also two dispersion parameters are required for two fold oversampled sequence.

On the other hand, in this paper, we propose a new CD estimation algorithm which uses the interpolated received signal equalized with predefined test CD value and calculate the variance of equalized signal. We sweep the test CD values over the predicted CD range and decide the estimated CD value from the minimum variance of all the test sets. Such an approach has the benefit that its performance is invariant of timing frequency offset as it decides the optimal sampling-phase of analog-to-digital converters (ADCs). Such an approach is also tolerant to PMD.

To validate the proposed algorithm, we simulate 100-Gbits/s polarization division multiplexed quadrature phase shift keying (PDM-QPSK) transmission systems. We estimate the CD of the system using our proposed algorithm and the estimated value has a good accuracy. In our simulation, we used frequency domain approach for CD compensation; however, it is also easily extendable for time domain equalization case.

2. PROPOSED CD ESTIMATION SCHEME

Figure 1 shows the block diagram of the proposed algorithm. Consider the two-fold oversampled received signal from x- and y-polarization tributaries are $r^x(n)$ and $r^y(n)$, respectively, where n is the sampling index**.** In the DSP, first we interpolate $r^{x/y}(n)$to M samples/symbol which is denoted as $w^{x/y}(n)$. The interpolated signal is then demultiplexed into M blocks of data $S_m^{x/y}$, which contain one sample/symbol down-sampled signal with M different sampling phases. The subscript m corresponds to possible sampling phases (m=0, 1, 2,$\cdots M$-1). Each block of data is then converted to the

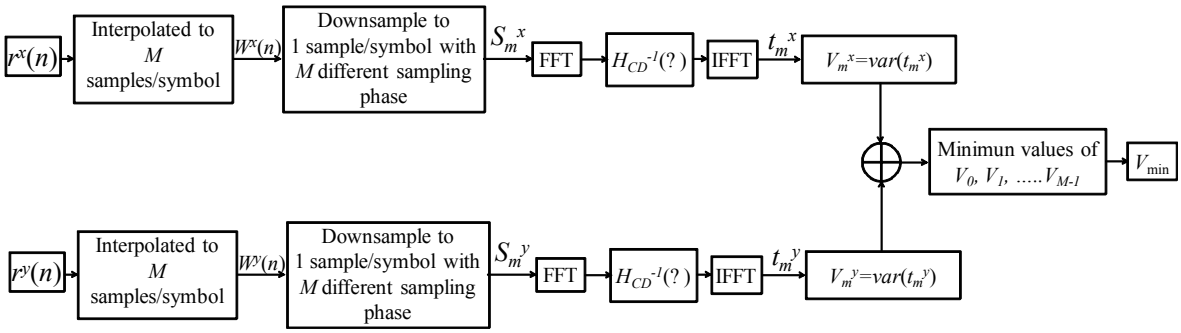

Fig.1: Block diagram of the proposed chromatic dispersion estimation scheme

frequency domain using fast Fourier transform (FFT) and multiplied by the inverse of the transfer function of the dispersive channel. The CD equalizer can be modeled in the frequency domain with an all pass filter having the transfer function given by

$$H_{CD}^{-1}(\omega) = \exp\left(\frac{-j\omega^2\beta_2 L}{2}\right), \qquad (1)$$

where ω is the angular frequency, β_2 is the dispersion parameter and L is the length of fiber. Then the time-domain equalized signal can be written as

$$t_m^{x/y} = IFFT\{FFT(s_m^{x/y}) \times H_{CD}^{-1}(\omega)\}, \qquad (2)$$

where, IFFT is the inverse FFT.

After that, the variances of $\left|t_m^{x/y}\right|$ are calculated as

$$V_m^{x/y} = E[\{|t_m^{x/y}| - \mu_m^{x/y}\}^2], \qquad (3)$$

where E is the statistical expectation operator and $\mu_m^{x/y}$ is the expected values of $|t_m^{x/y}|$. Among the M variances, the minimum variance is calculated as

$$V_{\min} = \min\{V_m\}, \qquad (4)$$

where, $V_m = V_m^x + V_m^y$. The variances from two polarization tributary is summed up to incorporate the effect from both polarization path. Such an approach makes the estimation PMD invariant.

Finally, for the CD estimation we sweep the test CD values in Eq. (1) over the predicted CD range and the estimated CD is obtained from the corresponding value of the V_{min} over the swept range.
For sweeping the CD values for the first iteration, we can use a large step size to roughly estimate the CD. Then, in the second iteration we use smaller step size around the CD value estimated in the first iteration.

3. SIMULATION RESULTS

We simulate 100-Gbits/s PDM-QPSK coherent transmission systems. In the transmitter, the signal is band-limited by a raised-cosine filter with a roll-off factor of 0.5. Then the signal is impaired by phase noise of the transmitter laser and passes through a fiber whose transfer function consists of a chromatic dispersion with D=17 ps/nm and a Jones matrix for fiber birefringence and first-order PMD. The phase noise from the local oscillator (LO) and the additive white Gaussian noise (AWGN) are then given to the signal. Both the transmitter laser and LO has the 3-dB linewidth of 100 kHz. After the signal is coherently detected and converted to digital domain with two samples/symbol and we fed it to the DSP unit.

In the DSP, CD value is estimated using the proposed algorithm. In the simulation, we use M=10. The block size is 1024 for the FFT operation and an overlapping factor is 50% to implement overlap-save operation.

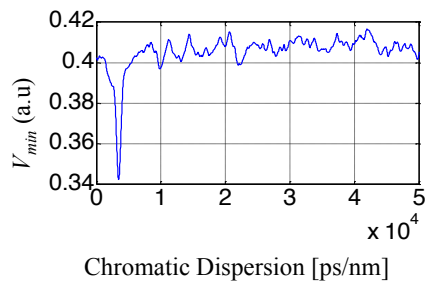

Fig. 2: Plot of $V_{\min}$ in the first iteration for a 3400-ps/nm CD value in the transmission link.

Figure 2 shows the measured V_{min} in the first iteration for a CD value of 3400 ps/nm in the transmission link. The test CD is swept over 0 to 34000 ps/nm with a step size of 170 ps/nm. We find that there is a minimum peak around 3400 ps/nm.

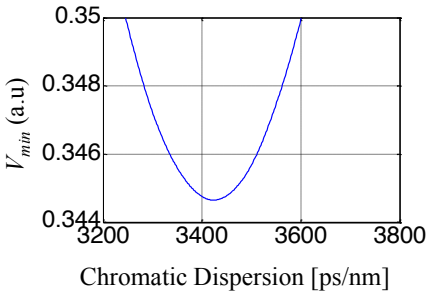

Fig. 3: Plot of $V_{\min}$ in the second iteration for a 3400-ps/nm CD in the transmission link.

In the next iteration, we vary the test CD from 3200 ps/nm to 3600 ps/nm with a step size of 2 ps/nm. From the plot of V_{min} in the second iteration, as shown in Fig.3, we get an estimation of CD value of 3420 ps/nm. That is, the estimation error is only 20 ps/nm.

Our proposed scheme is invariant of ADC sampling phase. We enable such functionality by digital interpolation in the first stage of our algorithm. To prove this statement, we measured variance for different sampling phases with the test CD equals the transmission line CD. In our simulation, the first sampling index (m=0) corresponds to the ideal sampling phase. As shown in Fig.4, the variance is also found minimum at first sampling index.

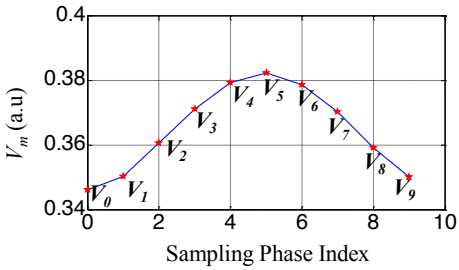

Fig. 4: Measured variances as a function of sampling phase index.

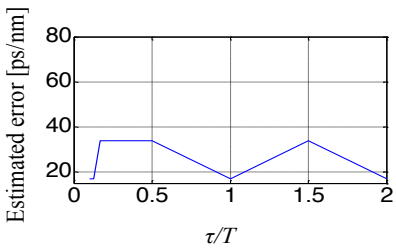

Fig. 5: Plot of estimation error as a function of τ/T.

Finally, we check the impact of first-order PMD on the proposed estimation technique. The first-order PMD, τ, is varied upto two symbol period $2T$. As shown in Fig.5, no significant estimation deviation is observed over that range.

4.CONCLUSIONS

We have proposed a novel method of CD estimation whose performance is invariant of timing frequency offset and PMD. The effectiveness of the proposed algorithm is verified with 100-Gbits/s PDM-QPSK transmission simulations.

5. FUTURE WORK

In this paper, we verified the proposed algorithm for QPSK modulation format. Further investigation is required for other modulation formats such as M-ary quadrature amplitude modulation (M-QAM).

REFERENCES

[1] K. Kikuchi, "Digital coherent optical communication systems: fundamentals and future prospects," *IEICE Elecron. Express,* vol.8, pp. 1642-1662, Oct. 2011.

[2] K. Kikuchi, "Coherent optical communications: Historical perspectives and future directions," in *High Spectral Density Optical Communication Technology,* edited by M. Nakazawa, K. Kikuchi, and T. Miyazaki (Springer, 2010), Chap. 2.

[3] Seb. J. Savory, "Digital filters for coherent optical receivers," *Opt. Express*, vol. 16, no. 2, pp. 804-817, Jan. 2008.

[4] R. Kudo, T. Kobayashi, K. Ishihara, Y. Takatori, A. Sano, and Y. Miyamoto, "Coherent optical single carrier transmission using overlap frequency domain equalization for long-haul optical systems," *J. Lightwave Technol.*, vol. 27, pp. 3721-3718, 2009.

[5] J. C. Geyer, C. R. S. Fludger, T. Duthel, C. Schulien, and B. Schmauss, "Efficient frequency domain chromatic dispersion compensation in a coherent polmux QPSK-receiver," in *Proc.OFC'10,*paper OWV5, 2010.

[6] M. Kuschnerov, F. N. Hauske, K. Piyawanno, B. Spinnler, A. Napoli, and B. Lankl, "Adaptive chromatic dispersion equalization for non-dispersion managed coherent systems," in *Proc. OFC'09,* paper OMT1, 2009.

Estimation of Potential and Electric Field for Sphere and Plane Electrodes by Charge Simulation Method.

Dr. Muhammad Abdul Goffar Khan[1] & Md. Khaled Hossain[2]
1.Professor,EEE 2. Ph.D. Student
Department of Electrical and Electronic Engineering
Rajshahi University of Engineering and Technology
Rajshahi, Bangladesh.
E-mail:khaledhossain0064@gmail.com
Mob: 01716-223829

Abstract

Knowledge of potential distribution in a dielectric between two electrodes subjected to high voltage is necessary for the investigation of the behavior of insulation. The economic utilization of insulator in high voltage equipment is determined by the stress developed due to the electric field. it is very difficult to investigate the distribution of equipotential lines in the dielectric for practical electrode systems having no regular geometrical shape. In this research, Charge Simulation Method have been used for the estimation of potential for sphere-sphere and sphere-plane electrode system. A computer program have been developed using CSM to determine the distribution of equipotential lines between electrodes subjected to high voltage which are commonly used in laboratory for practical experiment. This program is expected to be developed to give a generalized form so that any type of electrodes could be investigated. The developed computer program will be helpful for HV system designer to design high voltage equipment more effectively for better performance.

Keywords: Schwaiger factor, CSM, breakdown, Displacement ratio.

Introduction

The basic principle of Charge Simulation Method lies in the concept that the field under consideration is formed by superposition of many individual fields. For the calculation of electrostatic fields by this method, the distributed charge on the surface of a conductor is replaced by n discrete fictitious individual charges arranged suitably inside the conductor or in other words , outside the space in which the field is to be computed. The method implies that the potential function of the field at any point due to individual charges can be found by the summation of scalar potentials resulting from the individual charges. The potentials contributions made by individual fictitious charges are obtained by the solution of Laplace's and Poisson's equations [1]. The individual charges chosen here to be of point charges. These are placed suitably within an electrode system outside the space in which the field is to be computed. The field on the electrode surface is determined by the potential function of these individual charges. In order to determine the magnitude of these charges, n numbers of points are chosen on the surface of the conductor (contour points). The potential resulting from the superposition of field of the individual charges at any of these contour points must be equal to the known conductor potential $\boldsymbol{\varphi_c}$. The potential φ_i at the point P_i can be determined from the individual potential contributions made by different charges as following,

$$\boldsymbol{\varphi_i} = \sum_{j=1}^{n} \boldsymbol{Pij}.\boldsymbol{q_j} \qquad (1)$$

Where $\boldsymbol{P_{ij}}$ are known as Potential coefficients which are to be determined for different types of individual charges by a particular solution of Laplace's equation.

The magnitude of individual charges and their chosen positions are modified suitably in such a way that the equipotential surfaces must acquire the desired shape and the given potential. The potential φ_i resulting from the Superposition of the potentials due to individual charges is equal to the conductor potential $\boldsymbol{\varphi_c}$. The equation can be written as,

$$\sum_{j=1}^{n} \boldsymbol{P_{ij}}\, \boldsymbol{q_j} = \boldsymbol{\varphi_c} \qquad (2)$$

Where $\boldsymbol{q_j}$ is the discrete charge and $\boldsymbol{P_{ij}}$ the associated potential coefficient.

Application of this equation for n number of contour points leads to a system of n linear equations for unknown charges obtained in the following form:

$$[\boldsymbol{p}][\boldsymbol{q}] = [\boldsymbol{\varphi_c}] \qquad (3)$$

It is necessary to make a check whether the calculated set of charges fit the boundary conditions and the desired potential is acquired all over the electrode contour. This is done by using equation (1) once again to determine potentials at a number of checkpoints located on the electrode surface at known potentials. The difference between the computed and the given boundary potentials gives a measure of the accuracy of the simulation and hence the appropriateness of the number and location of simulation charges. In certain coordinate systems, the component of field in x-direction E_x is given by-

$$\boldsymbol{E_x} = \sum_{j=1}^{n} \frac{\partial \boldsymbol{P_{ij}}}{\partial \boldsymbol{x}}\, \boldsymbol{q_j} = \sum_{j=1}^{n} \left(\boldsymbol{f_{ij}}\right)_{\boldsymbol{x}}\, \boldsymbol{q_j} \qquad (4)$$

Where f_{ij} are known as field intensity coefficients in x-direction.

According to the general electrostatic field theory, the potential φ at a point P, distant 'd' from a single point charge is given by-

$$\varphi = \frac{\boldsymbol{q}}{\boldsymbol{4\pi\varepsilon d}} = pq \qquad (5)$$

From the analogy of (2) and (5), the general expression for the potential coefficient of a point charge at a distance'd' can be written as-

$$P = \frac{1}{4\pi\varepsilon d} \quad (6)$$

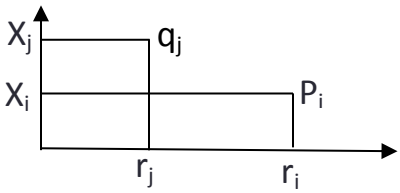

Fig 1: Individual simulation charge with notation

The potential coefficient of point charges for a point P_i is given by the equation-

$$P_{ij} = \frac{1}{4\pi\varepsilon\left[(r_i - r_j)^2 + (x_j - r_i)^2\right]^{1/2}} \quad (7)$$

The electric field intensity E has been calculated at a number of points along the shortest distance between the two electrodes, known as the electrode axis by using the following equation-

$$E_p = \sum_{i=1}^{n} \frac{q_i}{4\pi\varepsilon_0 R_{ip}2} \quad (8)$$

Where E_p is the value E at any point p in the dielectric, R_{ip} is the distance between point p and the position of ith charge q_i and n is the total number of point charges adopted to simulate both the electrodes.

2. Developmental Steps

2.1 Algorithm of computer programming

The algorithm [2] of computer programming of CSM involves the following steps:

1. Selection of the types and number of individual charges and their appropriate location within the electrode system.
2. Location of contour points on the surface of the electrodes.
3. Calculation of potential coefficients 'P_{ij}' of different types of individual charges for the contour points.
4. Inversion of potential coefficient matrix and multiplication with the potential vector of the contour points in order to calculate the charge vector.
5. Selection of checkpoints on the electrode surface. The checkpoints should be located so as to reflect the errors accurately.
6. On the basis of the magnitude of error calculated at the checkpoints collocation of discrete individual charges should be done within the electrode system.
7. Choice of suitable method for the calculation of equipotential lines is made considering the electrode contour to be equipotential surface.
8. The electric field at any point is then calculated analytically by superposition.

2.2 Flowchart for CSM

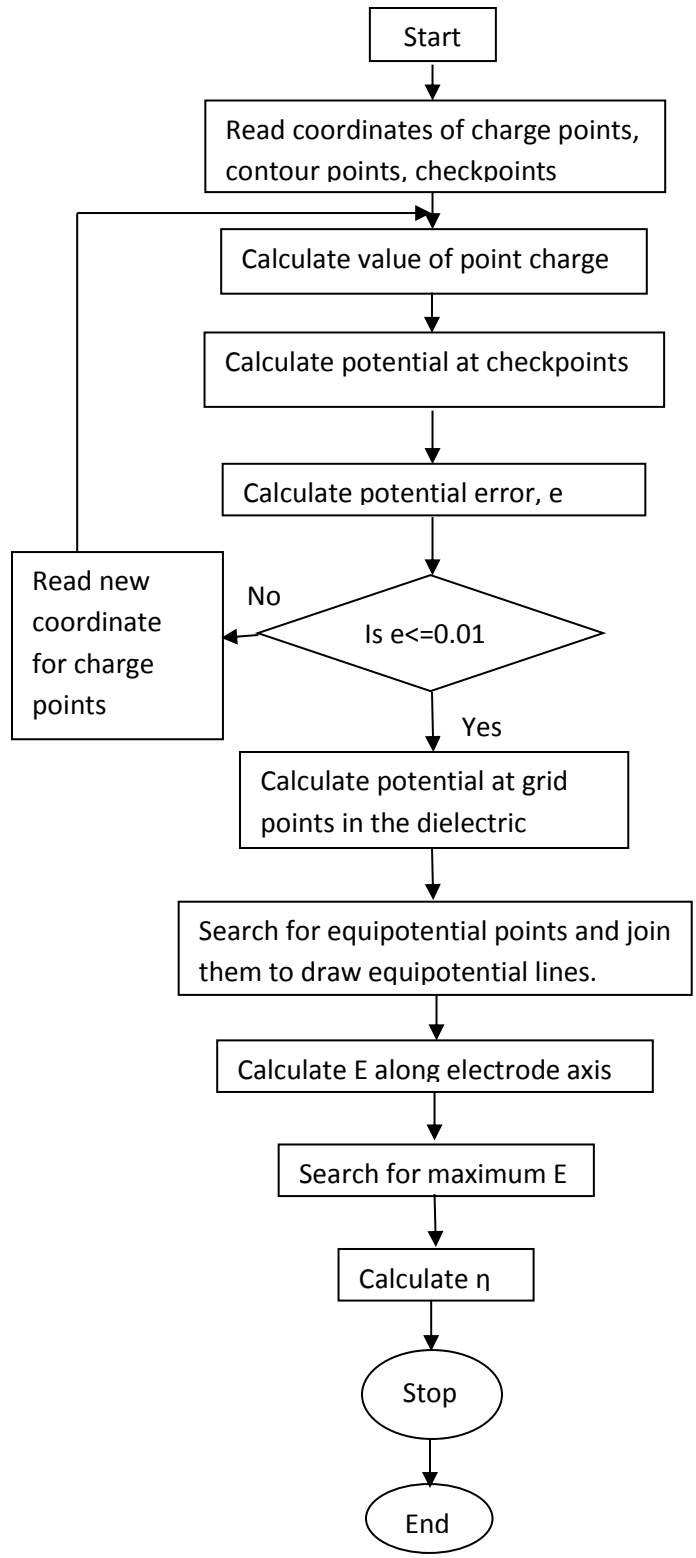

Fig: 2 Computer flowchart for charge simulation method

3. Estimation of equipotential lines

3.1 Electrode arrangement and applied voltage

A number of different electrode configurations were chosen to investigate the applicability configurations of CSM for the estimation of 'η'. Two different cases of the method of voltage applications were considered.

1. Symmetrically applied voltage of U/2 and –U/2.
2. Asymmetrically applied voltage of U and 0.

   The shape of different electrode combinations considered along with the mode of application of voltage and the number of point charges used to simulate the electrode surfaces are shown in Table below:

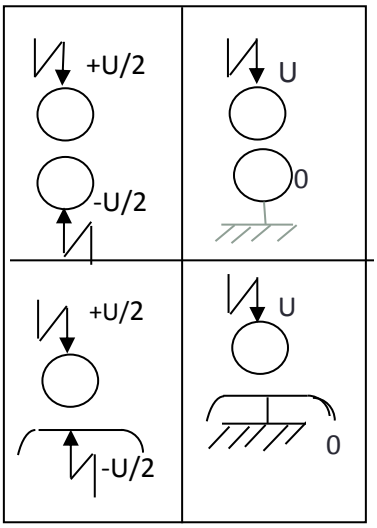

The Displacement ratio, β= df/ds is kept between 0.7 to 1.5 throughout the work [3]. The accuracy of the simulation is measured by the 'potential error', which is defined as the difference between the known potentials and the computed potentials at the electrode surface at various checkpoints.

The permissible error was less than 0.01% at the surfaces for both the symmetrically and asymmetrically applied voltages.

3.2 Simulation of equal Sphere-Sphere electrode system under symmetrical and asymmetrically applied voltage [4,5]:

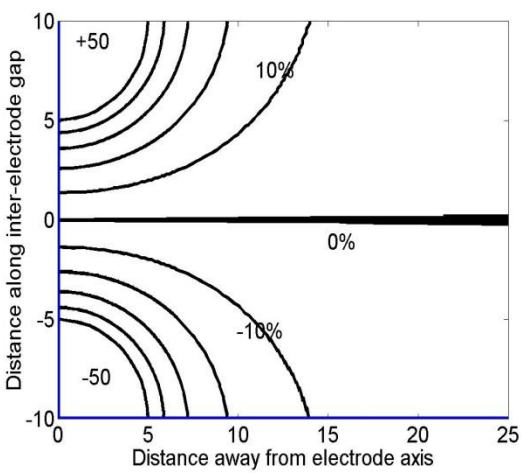

Fig.3: Equipotential lines for equal sphere – sphere electrode under symmetrical voltage.

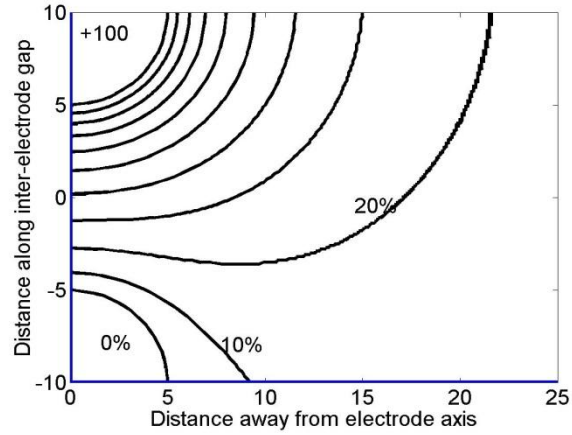

Fig.4: Equipotential lines for equal sphere - sphere electrode under asymmetrical voltage

Observations:

In case of symmetrically applied voltage, the 0% line passes through exactly the centre for the axis of the electrodes.

1. In case of symmetrically applied voltage, the equipotential lines of the equal sphere-sphere electrodes are not evenly placed which indicates that the dielectric in the gap is not stressed evenly everywhere.
2. The equipotential lines are close to each other near the upper and lower electrode indicating that the dielectric is stressed more at these points compared to other points.
3. In case of unsymmetrically applied voltage, all the lines show a tendency to follow the contour of the upper (HV) electrode except 10% line.
4. In case of unsymmetrically applied voltage, the equipotential lines are very close to each other near the surface of the HV electrode indicating that the dielectric to be stressed more unevenly compared to the case of symmetrically applied voltage.
5. The 50% line is not at the middle of the gap; rather it is slightly shifted towards the HV electrode.

3.3 Simulation of Sphere-Plane electrode system under symmetrically and asymmetrically applied voltage

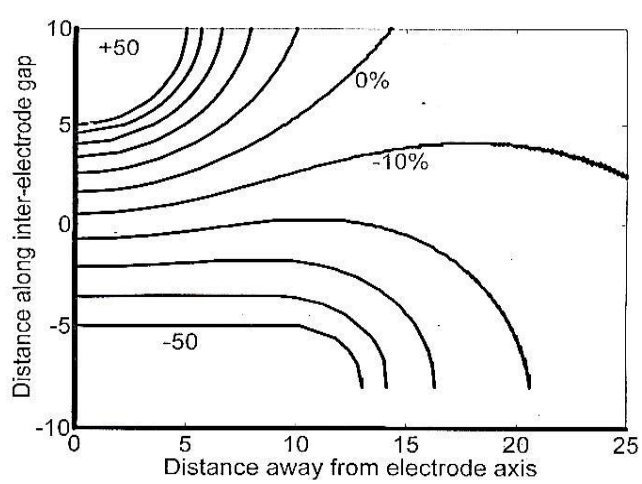

Fig.5: Equipotential lines for sphere – plane electrode under symmetrical voltage.

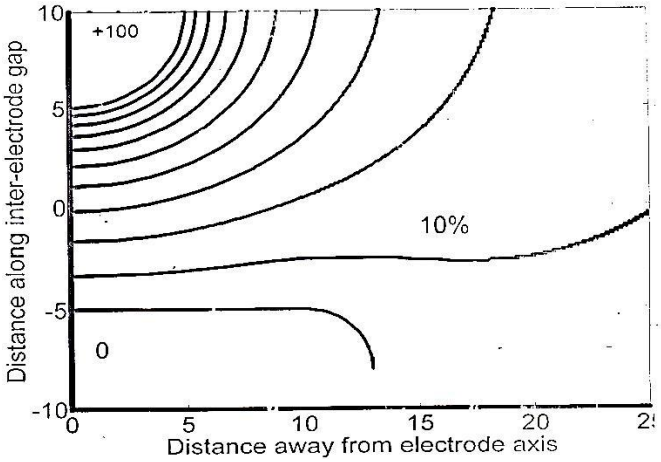

Fig.6: Equipotential lines for Sphere – plane electrode under asymmetrical voltage

Observations:

1. In case of symmetrically applied voltage, the equipotential lines are non-uniformly placed above and below the horizontal axis that shows the effect of changing the shape of the electrode.
2. The 0% line doesn't pass through the Centre of the gap distance rather it has been shifted upward.
3. The lines are close to each other near the upper sphere compared to the plane electrode.
4. In case of asymmetrically applied voltage, the equipotential lines are more unevenly distributed compared to the case of symmetrically applied voltage.
5. The equipotential lines are more crowded near the spherical electrode compared to the other points on the axis of the electrodes in case of unsymmetrically applied voltage. The effect is that the dielectric is stressed more compared to the case of symmetrically applied voltage.

3.4 Effect of changing the radius (upper sphere) of the HV electrode for Sphere-Sphere and Sphere-plane electrode system.

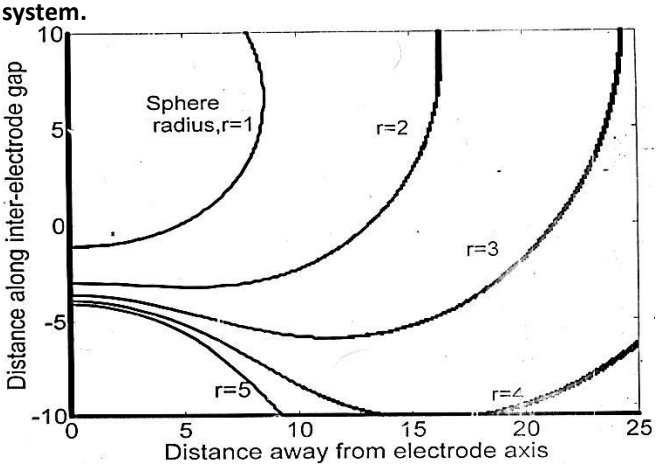

Fig.7: 10% Equipotential lines for sphere – sphere electrode under asymmetrical voltage for different radii of upper sphere.

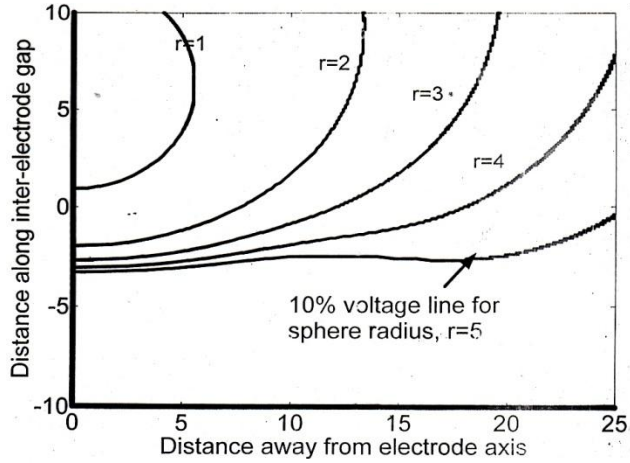

Fig.8: 10% Equipotential lines for sphere – plane electrode under asymmetrical voltage for different radii of upper sphere

Observations:

1. The distributions of equipotential lines have been seen to be changed.
2. The lines are more crowded near the high voltage electrode indicating that it causes more stress there.
3. The 0% voltage line is also shifted towards the electrodes having lower radius of curvature.
4. The lines near the grounded electrode are shifted towards the high voltage electrodes because of larger diameter of the grounded electrode.
5. The equipotential lines have a tendency to fall closer towards the HV electrodes of lower radius of curvature.

Conclusion

The estimation of equipotential lines in the inter-electrode gap of sphere-sphere and sphere-plane electrode system for symmetrically and asymmetrically applied voltage have been done successfully by Charge Simulation Method. The effect of varying the relative size of the grounded electrode has been estimated by changing the radius of the high voltage electrode for asymmetrically applied voltage. The observed effects are that the equipotential lines are unevenly distributed, close to the high voltage electrode and cause the dielectric to be stressed unevenly. This means that the dielectric at the vicinity of the HV electrode is much more stressed compared to that near the grounded electrode. Hence the possibility of PD as well as the initiation of breakdown process is more near the HV electrode.

References

1)J.M.Mattingley and H.M.Ryan," Potential and potential gradient distribution for standard and practical electrode system",Proc.IEEE, vol.118,No.5, 1971, pp. 720-733.
2)R.Arora and W.Mosch," High voltage insulation engineering", Wiley Eastern Ltd., New Delhi, 1995.
3)E.Kuffel and W.S.Zaengl, "High Voltage Engineering Fundamentals",Pergoman Press,New York, 1984.
4)A.S.Pillai and R.Hackam, "Electric field and potential distribution for unequal spheres using symmetric and unsymmetric applied voltages", IEEE trans. Vol. EI-18, 1983, pp. 477-484.
5) H.Singer, H.Steinbigler and P.Weiss, " A charge simulation method for the calculation of high voltage fields", IEEE trans., vol. PAS-93, 1974, pp.1660-1668.

Proceeding of the
International Conference on Electrical, Computer and Telecommunication Engineering
01- 02 December 2012 (ICECTE2012), RUET, Rajshahi-6204, Bangladesh

ICECTE2012: PI-0160

Design an Automatic Dipping and Withdrawing System for the Deposition of Thin Films

*Md. Feroz Ali, Utpal Saha and M.F.Hossain**
Department of Electrical and Electronic Engineering, Rajshahi University of Engineering and technology (RUET), Rajshahi-6204, Bangladesh.

*E-mail: faruk94_ruet@yahoo.com

ABSTRACT
Sol-gel is one of the paramount techniques to prepare microstructured thin films. The use of automatic control arrangement has been made it simpler and cost-effective. This controller unit consists of a stepper motor, keyboard, and a substrate holder. The whole arrangement is executed by the microcontroller unit. The greatest advantage of this automatic dipping and withdrawing system is that one needs not to be too adroit to deposit films by this method. Once the power supply has been on and the desired timing has been selected by pressing the specific button of the keyboard. The substrate will be dip into and withdraw from the solution automatically. Finally, prepared thin films has been annealed by rapid thermal annealing machine. This automatic dipping and withdrawing system can be used for large scale production of thin films.

KEY WORDS: thin film, sol-gel, deposition, automatic control, keyboard.

1. INTRODUCTION

Now-a-days the Thin Film has wide applications in many sectors such as the fabrication of electronic components, especially solid-state devices and microelectronic integrated circuits, have undoubtedly found the widest and most demanding applications for thin film depositions. These films typically consist of semiconductor materials, dielectric and insulating materials, and metal or refractory metal silicide conductors. Electronic displays are used for interfacing electronic equipment with human operators. Different components and device structures are required, such as Liquid-crystal displays, Light-emitting diodes (LEDs), Electroluminescent displays, Plasma and fluorescent displays, Electro chromic displays, The fabrication of these displays requires conductive films, transparent and conductive films, luminescent or fluorescent films as well as dielectric and insulating layers, optical coatings etc. The uses of thin films are microelectronic devices, telecommunication devices, wear resistant coatings, decorative coatings, optical coatings (windows, solar cells, etc.), sensors, catalysts etc. Here Thin means less than or equal to about 1 µm Film means layer of material on a substrate So A thin film is a layer of material ranging from fractions of a nanometer (monolayer) to several micrometers in thickness. There are many deposition techniques such as spray-pyrolysis, spin-coating, anode oxidation, hydrothermal method, chemical vapor deposition (CVD), physical vapor deposition (PVD), evaporation method, sputtering method etc. Most of them have many disadvantages such as High operating temperatures, toxic Gases, generally applicable to binary and elemental films, not suitable for production of metastable products. All of them, the Sol Gel dip-coating deposition technique is most effective to deposit specially Zinc Oxide (ZnO) thin film. These films typically consist of semiconductor materials, dielectric and insulating materials, and metal or refractory metal silicate conductors. In its simplest manifestation, sol-gel dip coating consists of the withdrawal of a substrate from a fluid sol: gravitational draining and solvent evaporation, accompanied by further condensation reactions, result in the deposition of a solid film[1]. Dip Coating Systems are very useful instruments for Fabricating & Characterizing Self-assembled Structures & Multi-layered Thin Films[4].Compared with conventional thin film forming processes such as chemical vapor deposition, evaporation, or sputtering, sol-gel dip coating requires considerably less equipment and is potentially less expensive[1]. We have prepared a sol gel dip coating system especially to deposit ZnO thin film on a glass substrate. ZnO thin films have interested as transparent conductor, because the n-type ZnO thin film has a wide band gap semiconductor (Eg=3.2 eV), and high transmission in the visible range, and ZnO thin films can take place of SnO2 and ITO because of their electrical and optical properties and its excellent stability which has been mentioned widely[2][3]. ZnO ®lms used in this study were crystalline with a hexagonal wurtzite structure, the lattice constants of which were calculated to be a .

3:254 A Ê and c . 5:213 A Ê from X-ray diffraction patterns of the ZnO ®lms [5].
The sol-gel process is a wet-chemical technique widely used in the fields of materials science and ceramic engineering. Such methods are used primarily for the fabrication of materials (typically metal oxides) starting from a colloidal solution (sol) that acts as the precursor for an integrated network (or gel) of either discrete particles or network polymers. Typical precursors are metal alkoxides and metal salts (such as chlorides, nitrates and acetates), which undergo various forms of hydrolysis and polycondensationreactions[6].

In this work, an automatic dipping and withdrawing system have been designed and prepared by using microcontroller, which is homemade, very simple and cost-effective, easy to control. The performance of this system has also been investigated and discussed.

2. EXPERIMENTAL SETUP

The schematic diagram of sol gel dip-coating system is shown in fig-1.

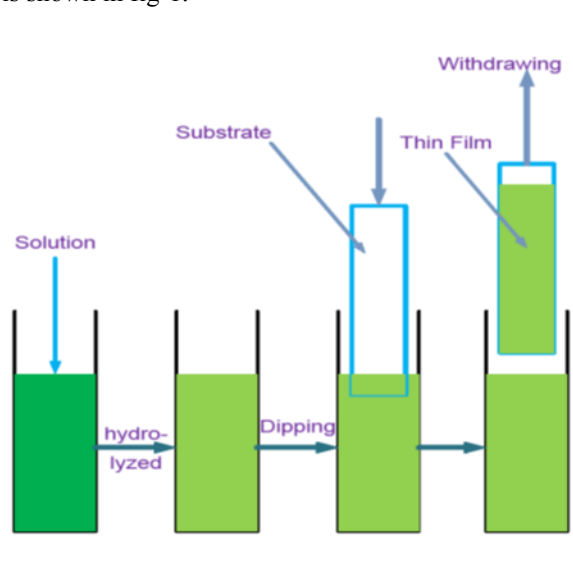

Figure 1. Dipping and withdrawing of sol-gel technique

The arrangements consists of control unit, stepper motor with dipping and withdrawing mechanism which is controlled by microcontroller based system, glass substrate on which film is deposited and beaker with precursor solution.
The sol-gel technique is based on hydrolysis of liquid precursors and formation of colloidal Sols. The sol-gel process is particularly attractive because of the following reasons: good homogeneity, ease of composition control, low processing temperature, large area coatings, low equipment cost, and good optical properties [7]. The Sol-Gel process allows the elaboration of porous matrices with tailored nano-holes. The process starts with the preparation of a Sol, a solution composed of various required ingredients. The resultant solution was stirred at room temperature for a certain time (1/2 h). To obtain a thin film, a substrate is dipped into the Sol and withdrawn at a certain speed (like 2 mm/sec). During the withdrawal process, the Sol becomes a Gel and the micelles are entrapped in the gel network. The substrates coated with gel films were dried at 600 C before calcined at crystalline temperature. After being dried, the film was washed with ethanol to remove the surfactant molecules. The thickness of the films is adjusted by repeating the cycle from dipping to heat treatment. Finally the films are calcined with its crystalline temperature [8].

At first the substrate on which the thin film was deposited must be cleaned with ethanol in ultrasonic cleaner for 5 or 10 minutes. Then the substrate were dried by air flow throw a nozzle and then in the sunlight so that all ethanol must be dried. After preparing solution it were hydrolyzed. Then it was ready for depositing thin film on the substrate. The substrate on which thin film is deposited at first placed on the clip of dip coating system which were home made by our self so that the substrate is hanged from the clip. The beaker with precursor solution was placed on the beaker base of the device. Then the beaker was so placed that the precursor solution must be touched on the lower part of the substrate which was accomplished with level adjusting screw on the bottom of the beaker base . Then the system was ready to deposit thin film. When we press the desired key then the stepper motor start to rotate and at the same time the ribbon from the motor shaft untight so that the substrate was dipped into the precursor solution at desired rate (1cm/min). When the substrate was totally dipped the motor wait for 10 seconds so that the substrate is immersed into the solution for 10 seconds. After that the motor was rotated in the reverse direction at the same speed (1cm/min) so that the substrate was withdrawn from the precursor solution. When the withdrawn was completed, the substrate was kept from the clip of the device. The substrate was dried for a while at atmospheric temperature and pressure and then annealed at 4500C for 2 hours to form thin film.

In an excellent review of dip coating, screven states that the thickness of the deposited film is related to the position of the streamline dividing the upward and downward moving layers. A competition between as many as six forces in the film deposition region governs the film thickness and position of the stream line [1]

3. BLOCK DIAGRAM OF PROPOSED SYSTEM

The block diagram of the proposed system is given in following Fig 2

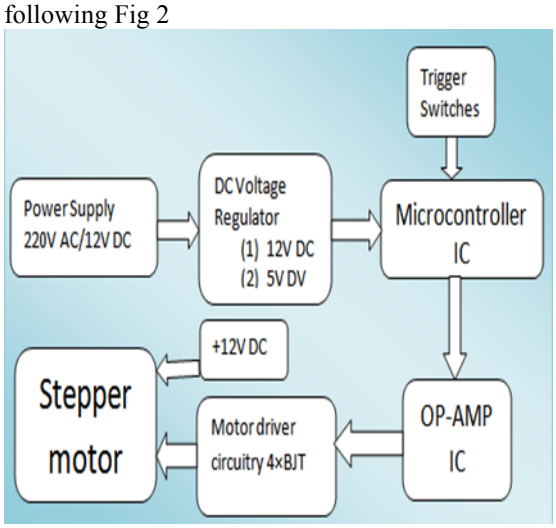

Figure 2. Block diagram of the proposed system

Fig 2 shows the different stages of the operating principles of the controlling unit. At first the system will ready for taking the input from the power supply which is a transformer in this case. Then for the desired speed of the stepper motor the switch associated with every definite speed has to be pressed. After pressing the specific switch the motor will rotate primarily in the forward direction and simultaneously the substrate will dip into the solution.

As the dipping and withdrawing time is the same owing to the microcontroller arrangement, so the solution is spread uniformly throughout the surface and the film characteristics bear resemblance to the actual characteristics. After rotating in the reverse direction the steeper motor stops automatically. This is another inherent advantage of this arrangement because the motor is not needed to be switched off manually. So time delay can be adjusted as per our requirement between the time of end of dipping and starting of another process. If the delay is higher, then some exceptional results can be obtained which will far more different from our desired outcome. To be very honest, the delay time must not be greater than 15 seconds. Another important criterion appears in the time of heating which (heat) needs to be uniform throughout the whole process of heating. The substrate containing the solution was kept into the pot and then it was placed in the heater. Then the heater was switched on and the temperature quickly reached the 450ºc mark. We used a specially designed heater which can produce this fixed temperature. the power was not interrupted during this very period; so the substrate was continuously exposed to hating without any interruption. So, there should be a very conscious effort to stabilize the power and if the power supply is not continuous then the expected film will diverge away from the desired characteristics.

The following Fig 2 shows the block diagram of the proposed system. At first the conventional 230V AC supply is step down by a transformer whose voltage of two outside wires is 18 V AC. This voltage is rectified by a bridge rectifier as shown in Fig 2 which is pulse setting DC. This pulse setting DC voltage is now filtered with 1000µF capacitor. Now we have 18V DC voltage. This 18V DC is fed to the 7805 regulator to produce 5V DC regulated voltage and also fed to 7812 regulator to produce 12V DC regulated voltage. For the proposed system ATmega8 microcontroller is used to control the stepper motor. The LM 324 op-amp IC also used to switch the transistors as shown in Fig 2. In this section four Bipolar Junction Transistors (BJTs) are connected as shown in above Fig 2. Each base is connected to 10KΩ resistor. Here each collector of each Bipolar Junction Transistor (BJT) is connected to the four wire of stepper motor. The Bipolar Junction Transistors (BJTs) are operated here as switching mode. The equivalent circuit of stepper motor is shown in Fig 2.

One of the most significant advantages of a stepper motor is its ability to be accurately controlled in an open loop system. The time between successive pulse is so designed that the motor shaft rotation such that the dipping and withdrawing rate into the solution is 1cm/min. In design section the target is that to rotate the stepper motor in specific direction and time so that the ribbon helps the substrate to dip and withdraw from the precursor solution to deposit thin film by this home made sol gel system effectively and efficiently.

4. DESIGNING SECTION

The proposed Automatic homemade sol gel system is shown in Fig 3. At first a wooden basement structure was designed so that the automatic control unit gets compatible with the structure. The stepper motor was placed upwards a rod of thin radius was attached to the motor shaft so that the ribbon and other accessories can be hanged. As the ribbon was too thin to be stable under any condition and the strip holding the substrate had a continuous swing in the natural wind, so a damper weight was connected with the strip to eliminate the swing and oscillation of it and thereby steadying the strip. The beaker containing the solution was placed right at the bottom & the up- down movement of the beaker was controlled by connecting screws with the wooden

structure to which the beaker was being upheld. the controlling screws were fitted beneath the basement which holds the beaker. In order to deposit films of various thickness six different switches was used to make the system capable of depositing different six sizes of film (2, 3, 4, 5, 6, and 7 cm). The desired time setting of each and every switch is being marked in the keyboard.

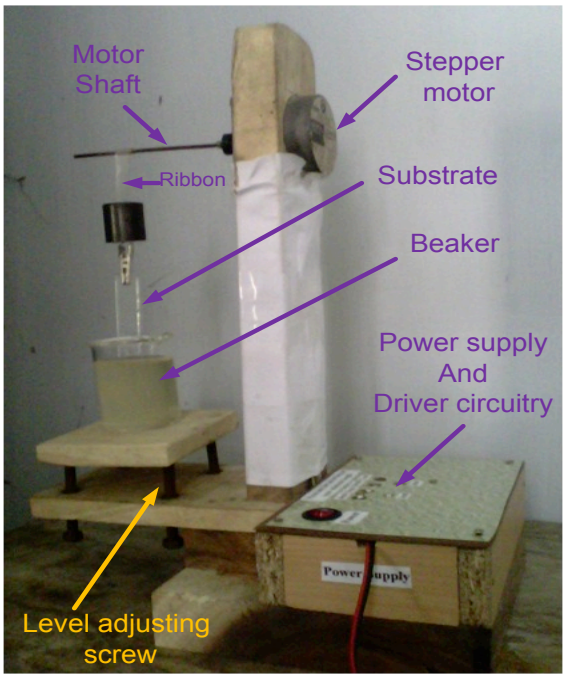

Figure 3. Proposed homemade automatic sol gel system

5. RESULTS AND DISCUSSIONS

For the desired application the prepared was heated at 450˚c for approximately two and half hours. After switching off the heater we dragged the substrate with a paper rather than the hand itself. Finally the substrate containing the deposited film was taken into the laboratory for investigating the properties. The deposition procedure came up with great results as the Optical properties (transmittance, reflectance, absorbance and Refractive index) were really impressive as experimented in the laboratory. The transmittance was approximately 80% which is more than acceptable at this point of time. The deposited film can be effectively used in the field of material science & ceramic engineering; composition control, microstructure control, photovoltaic solar cell, protective coating etc.

6. CONCLUSIONS

An Automatic dipping and withdrawing system for sol-gel method has been successfully designed and fabricated by using microcontroller, and stepper motor. This automatic system is homemade, very simple, and cost-effective. This system can be used for large scale thin films deposition.

7. ACKNOWLEDGEMENTS

The authors would like to thank of our university named Rajshahi University of Engineering & Technology (RUET) for giving the chance to use different equipments of our Nanotechnology and Photovoltaic's lab to complete our experiments successfully.

REFERENCES

[1]. C. J. Brinker, G. C. Frye, A. J. Hurd and C. S. Ashley Sandia National Laboratories, Albuquerque. NM 87185-5800 (U.S.A.) Received June 6, 1990; accepted January 7, 199l)

[2]. D. C. Look "Recent advances in ZnO materials and devices" Materials Science and Engineering B 80, 383-387 (2001)

[3]. F. K. Shan and Y. S. Yu "Band gap energy of pure and Al-doped ZnO thin films", Journal of the European Ceramic Society 24, 1869-1872 (2004).

[4]. http://www.apexicindia.com/en/products/dip-coating-unit

[5]. Powder Diffraction File, Data Card 5-644, 3c PDS International Centre for Diffraction Data, Swatmore, PA. of the European Ceramic Society 24, 1869-1872 (2004).

[6]. http://en.wikipedia.org/wiki/Sol-gel

[7]. Z.Liu, Z. Jin, W.Li,And J. Qiu, Mater. Lett. 3620 (2005) 59

[8]. M.F. Hossain, "Materials Used In DSCs Experimental Methodology, Characterization and Measurements" Chapter 3

Proceeding of the
International Conference on Electrical, Computer and Telecommunication Engineering
01- 02 December 2012 (ICECTE2012), RUET, Rajshahi-6204, Bangladesh

ICECTE2012: PI-0161

Design and Characterization of Square-Lattice Microstucture Optical Fiber for Dispersion Compensation

Md.Selim Habib[1], Md. Faisal Rashed[2], Md. Mizanur Rahman[3], Zunaid Ahmed[4]
Department of Electrical & Electronic Engineering, Rajshahi University of Engineering & Technology, Rajshahi-6204, Bangladesh.
E-mail: selim041073@yahoo.com[1], faisal_rashed_m@yahoo.com[2], mizan.eee07@gmail.com[3], zunaid365@gmail.com[4]

ABSTRACT
This paper presents a novel square-lattice microstructure optical fiber for dispersion compensation in a wide range of wavelengths. The finite element method with perfectly matched absorbing layers boundary condition is used to investigate the guiding properties. The designed novel dispersion compensating fiber shows that it is possible to obtain a larger negative dispersion coefficient of about –632 ps/(nm.km) at 1.55 µm and lower confinement losses over E to L wavelength bands by using a modest number of design parameters and very simple cladding design.

KEY WORDS: Microstructure optical fiber, Dispersion compensating fiber, Finite element method, Confinement loss.

1. INTRODUCTION

Microstructure optical fibers (MOFs) are optical fibers with a transversal array of air-holes that extends along all the fiber's length [1]. MOFs optical guiding is due to the multiple interference attributed to the periodical array of air-holes and also by the high index contrast between silica and air [2]. The rich geometry of the fiber's microstructure and its complex wave-guiding mechanism makes MOFs the suitable choice for a great deal of applications such as dispersion compensators, interferometers, super-continuum generators and polarization maintainers between others [3]. Up to now, the dispersive behavior on MOFs have been studied thoroughly for the core modes [4]. In comparison, little has been deepened in higher order modes propagating through the cladding of a MOF [5], despite of the geometrical richness and the dispersion control provided by their cladding structures. Microstructure optical fibers (MOFs) [6] consisting of a central defect region surrounded by air holes running parallel to the fiber length have been one of the most interesting recent developments in fiber optics. By varying the size of the holes and their number and position, the dispersive and modal properties can be controlled. MOFs are usually made from pure silica, and so the guided modes are inherently leaky because the core index is the same as the index of the outer cladding region without air holes.

In broadband communications systems, fiber dispersion and confinement loss play very important roles. Control of chromatic dispersion in MOFs is a very important problem for realistic applications in optical fiber communications [7], dispersion compensation [8], and so on. The dispersion value for a standard single mode fibers (SMFs) is of the order D = 10-20 ps/(nm.km). Dispersion causes pulses to spread and has to be compensated in the long distance optical data transmission systems. One way to realize this is to use dispersion compensating fibers (DCFs), which are designed to have large negative dispersion. The negative dispersion coefficient of conventional fiber is about $D = -100$ to -300 ps/(nm.km) at 1.55 µm wavelength with high losses [9]. To minimize losses and reduce costs, the DCFs should be as short as possible and, thus, the magnitude of negative dispersion should be as large as possible [10]. Various DCFs that were optimized to compensate for the dispersion in a single band, e.g., the S-band (1460-1530 nm), C-band (1530-1565 nm), and L-band (1565-1625nm), have been reported [13]. However, it is difficult for the DCF to compensate for dispersion over lower band, i.e. the E-band (1360-1460nm).

In this paper, we present novel pure silica square-lattice MOFs for optimizing the dispersion compensation of standard SMFs in the entire telecommunication band by using full-vector finite-element method (FEM) [11]. From the numerical simulation results, it is found that it is possible to obtain larger negative dispersion, and low confinement loss in the entire telecommunication band.

2. GEOMETRY OF THE PROPOSED DC-OHFS

Fig. 1 depicts the transverse cross-section of square-lattice MOFs. The material of the studied MOF is taken to be silica. The cladding is formed by a square-lattice of air-holes. The air-hole pitch is labeled Λ (the distance between the centers of neighboring air-holes). The air-hole diameter is

labeled d. First of all, it is reported the study of the dispersion properties of square-lattice MOFs with a high air-filling fraction, that is with small hole-to-hole spacing and large air-holes, which can be designed to compensate the anomalous dispersion and the dispersion slope of single-mode fibers [12]. In particular, the geometric parameters which characterize these square-lattice MOFs have been chosen to optimize the fiber length and the dispersion compensation over a wide wavelength range.

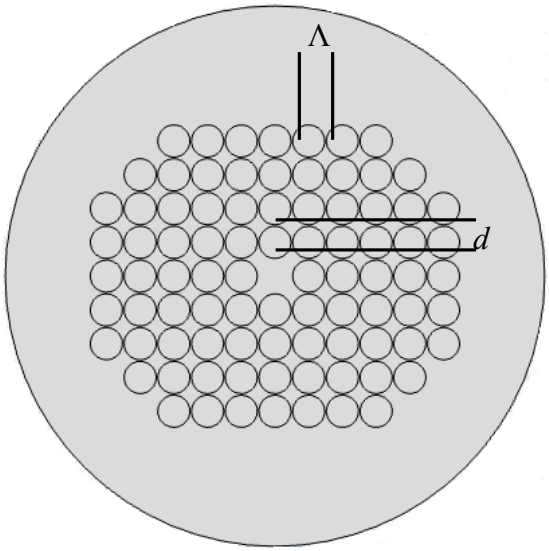

Fig. 1 Transverse cross-section of the square-lattice MOFs with pitch and air-hole ring diameter**.**

3. NUMERICAL METHODS

The finite element method (FEM) [11] with perfectly matched boundary layers (PML) is used to calculate the chromatic dispersion, confinement loss, and effective area of MOFs. Using the FEM, the MOF cross-section, with the finite number of air-holes is divided into homogeneous subspaces where Maxwell's equations are solved by accounting for the adjacent subspaces. These subspaces are triangles that allow a good approximation of the circular structures. Using the PML, from Maxwell's curl equations the following vectorial equation is obtained [14]

$$\nabla \times ([s]^{-1} \nabla \times E) - k_0^2 n_{eff}^2 [s] E = 0 \qquad (1)$$

where E is the electric field vector, k_0 is the wave number in the vacuum, n_{eff} is the refractive index of the domain, [s] is the PML matrix, $[s]^{-1}$ is the inverse matrix of [s]. Once the modal effective indices n_{eff} is obtained by solving an eigen value problem using FEM, the chromatic dispersion $D(\lambda)$, confinement loss L_c, and effective area A_{eff} can be calculated given by [11].

3.1 Chromatic dispersion

The chromatic dispersion $D(\lambda)$ of MOFs is easily calculated from the n_{eff} values vs. Wavelength using the following [11, 15]

$$D = -\frac{\lambda}{c} \frac{d^2 \mathrm{Re}[n_{eff}]}{d\lambda^2} \qquad (2)$$

in ps/(nm.km),where Re[n_{eff}] is the real part of effective refractive index n_{eff}, λ is the wavelength, c is the velocity of light in vacuum. The material dispersion can be obtained from the three-term Sellmeier formula and is directly included in the calculation.

3.2 Confinement loss

Confinement loss is the light confinement ability within the core region. The increase of air hole rings help the confinement of light in the core region, which results in smaller losses than those with less air hole rings. The confinement loss L_c is obtained from the imaginary part of n_{eff} as follows

$$L_c = 8.686 \times k_0 \mathrm{Im}[n_{eff}] \qquad (3)$$

with the unit dB/m, where Im[n_{eff}] is the imaginary part of the refractive index, $k_0 = 2\pi/\lambda$ is the wave number in the free space.

3.3 Effective area

The effective area A_{eff} is calculated as follows [11]

$$A_{eff} = \left(\iint |E|^2 dxdy\right)^2 / \iint |E|^4 dxdy \qquad (4)$$

in (μm^2), where E is the electric field in the medium.

4. NUMERICAL RESULTS AND DISCUSSION

The first fibers considered have d/Λ = 0.95 and Λ which varies between 0.81 and 0.85 μm. A high value of air-hole diameter to pitch is chosen for better field confinement. Fig. 2 shows the effective index profile over E to L wavelength bands. It is found that the effective refractive index decreases with the increase in wavelength and increases with increase of pitch, Λ. Fig. 3 shows the mode field distribution of the MOF at wavelength of 1.55 μm. The positions of air-holes are evident in it. The mode field distribution has its maximum amplitude at the center core region. Since the mode field of the MOF is largely inside the inner core, the dispersion characteristic of the MOF is more sensitive to the inner core structure. Fig. 4 shows wavelength dependence of chromatic dispersion of the proposed square-lattice MOF for optimum design parameters. Optimizing the parameters d, and Λ, high negative dispersion of –632 ps/(nm.km) is obtained at the wavelength 1.55 μm for Λ = 0.81 μm and , d/Λ = 0.95, while for conventional DCFs it is typically –100 ps/(nm.km) at this wavelength. As it can be seen for the optimum design parameters Λ = 0.81 μm, d/Λ = 0.95, the designed square-lattice MOF has negative dispersion of –365~ –498 ps/(nm.km) over E-band. In addition, the MOF shows negative

dispersion of −498 ~ −585 ps/(nm.km), −585 ~ −650 ps/(nm.km), −650 ~ −700 ps/(nm.km) over S, C and L bands respectively.

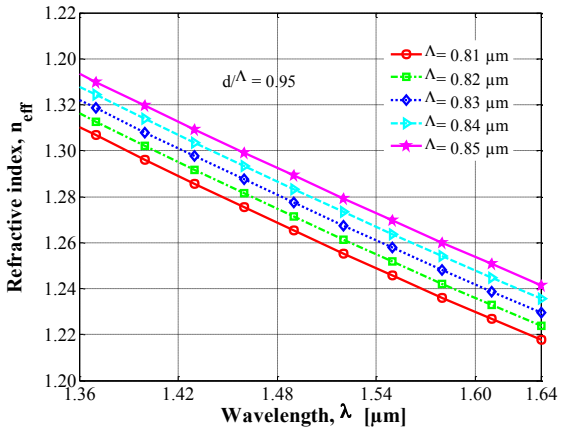

Fig. 2 Effective refractive index vs wavelength.

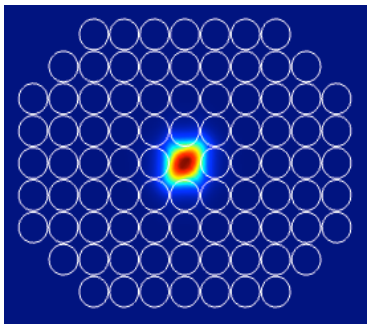

Fig. 3 Fundamental mode field distribution of the MOF at 1.55 μm wavelength.

Fig. 5 shows the variation of the chromatic dispersion of the optimized MOF and SMF as a function of the wavelength. It can be clearly seen that for the optimized set of parameters and air-hole ring configurations, a large negative dispersion coefficient of −90 ps/(nm.km) to −220 ps/(nm.km) can be obtained which is monotonically decreasing over S to L-band for Λ = 1.01 μm, d/Λ = 0.95 and possesses negative dispersion slope, providing fine dispersion compensation. Fig. 6 corresponds to the residual dispersion obtained after the dispersion compensation by 1.09-km long MOF for the dispersion accumulated in one span (40 km) of SMF. It can be observed that the residual dispersion is ±700 ps/nm, which is within the range of ±1000 ps/nm, enabling the proposed MOF structure to be suitable for 10 Gb/s transmission system.

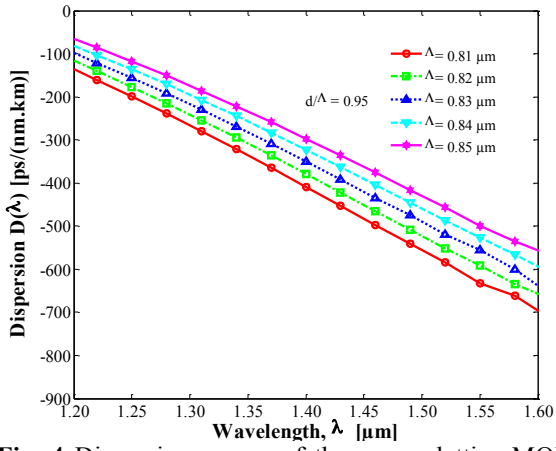

Fig. 4 Dispersion curves of the square-lattice MOF with d/Λ = 0.95 and different Λ values.

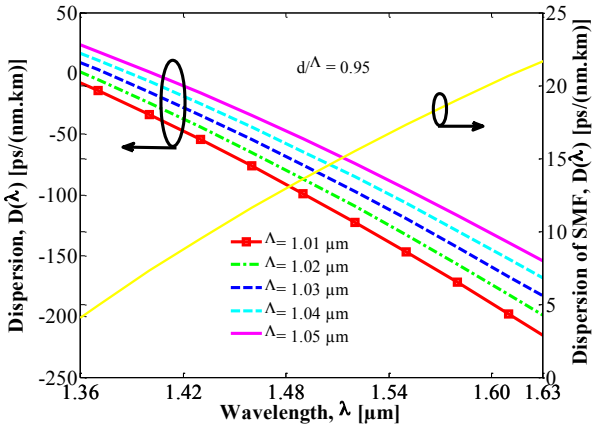

Fig. 5 Chromatic dispersion of the optimized MOF structure and SMF.

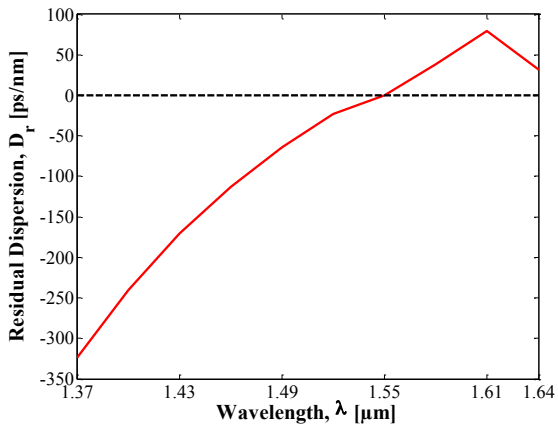

Fig. 6 Residual dispersion after compensation of dispersion in one span (40-km) of SMF link by 1.09-km long optimized MOF.

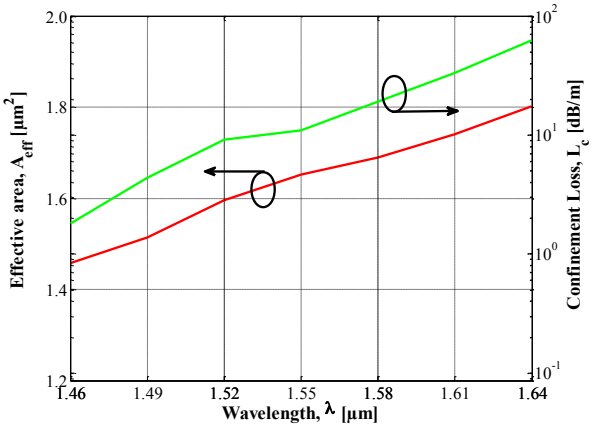

Fig. 7 Wavelength dependence of effective area and confinement loss of the proposed MOF.

Fig. 7 shows the confinement loss and effective area for the optimum design parameters: Λ = 0.81 μm and d/ Λ = 0.95. The effective area of the proposed DC-MOFs for the optimum design parameter is 1.65 μm^2 at 1.55 μm. The confinement loss below remains 10 dB/m at 1.55 μm.

5. CONCLUSION

In this paper, we have investigated the negative chromatic dispersion coefficient of square-lattice MOF for broadband dispersion compensation by using FEM. It was found that by adjusting structural parameters of the fiber, broadband square-lattice MOF with large negative dispersion over E to L bands, and low confinement loss is obtained. Another main advantage is that compared with previously presented MOFs, the design procedure for this proposed MOFs structure could be more efficient, easier because relatively lesser geometrical parameters and simple cladding design are needed to be optimized.

REFERENCES

[1]. J. C. Knight, T. A. Birks, P. S. J. Russell, and D. M. Atkin,"All-silica single-mode optical fiber with photonic crystal cladding," Opt. Lett. **21**(19), 1547–1549 (1996).

[2]. A. Ferrando, E. Silvestre, J. J. Miret, P. Andr´es, and M. V.Andr´es,"Donor and acceptor guided modes in photonic crystal fibers," Opt. Lett. **25**(18), 1328–1330 (2000).

[3]. A. Ortigosa-Blanch, J. C. Knight, W. J. Wadsworth, J. Arriaga, B. J. Mangan, T. A. Birks, and P. S. J. Russell, et al.,"Highly birefringent photonic crystal fibers," Opt. Lett. **25**(18), 1325–1327 (2000).

[4]. A. Ferrando, E. Silvestre, J. J. Miret, and P. Andr´es, "Nearly zero ultraflattened dispersion in photonic crystal fibers," Opt. Lett. **25**(11), 790–792 (2000).

[5]. B. Eggleton, P. Westbrook, C. White, et al., "Cladding-mode-resonances in air-silica microstructure optical fibers," J. Lightwave Technol. **18**(8), 1084–1100 (2000).

[6]. T. A. Birks, J. C. Knight, B. J. Mangan, P. St. J. Russell, "Photonic crystal fibers: an endless variety", IEICE Trans Electron 2001:585.

[7]. M. D. Nielsen, C. Jacobsen, N. A. Mortensen, J. R. Folkenberg, H. R. Simonsen, "Low-loss photonic crystal fibers for transmission systems and their dispersion properties", Opt Exp 2004:1372.

[8]. L. P. Shen, W. P. Huang, S. S. Jian, "Design and optimization of photonic crystal fibers for broadband dispersion compensation", IEEE Photon Technol Lett 2003:540.

[9]. J. Laegsgaard, S. E. BarkouLibori, K. Hougaard, et al., "Dispersion properties of photonic crystal fibers-issues and opportunities", Mater Res Soc Symp Proc 2004:797.

[10]. L. Gruner-Nielsen, S. N. Knudsen, B. Edvold, T. Veng, D. Magnussen, C. C. Larsen, et al. "Dispersion compensating fibers", Opt Fiber Technol 2000:164.

[11]. H. Ademgil and S. Haxha, "Highly birefringent photonic crystal fibers with ultra-low chromatic dispersion and low confinement losses," J. Lightw. Technol., vol. 26, no. 4, pp. 441–448, Feb.15 2008.

[12]. F. Poli, A. Cucinotta, M. Fuochi, S. Selleri, L.Vincetti,"Characterization of microstructured optical fibers for wideband dispersion compensation", J Opt Soc Am A 2003:1958.

[13]. L. Gruner-Nielsen, S. Knudsen, T. Veng, B. Edvold, and C. Larsen, "Design and manufacture of dispersion compensating fiber for simultaneous compensation of dispersion and dispersion slope," *Proceeding of .OFC*, San Diego, CA, pp.232-234, Mar.1999.

[14]. K. Saitoh and M. Koshiba, "Full-vectorial imaginary-distance beam propagation method based on a finite element scheme: Application to photonic crystal fibers," *IEEE J. Quantum Electron.*, vol. 38, no. 7, pp. 927–933, Jul. 2002.

[15]. K. Saitoh and M. Koshiba, "Leakage loss and group velocity dispersion in air-core photonic bandgap fibers", Opt Exp 2003:3100.

Proceeding of the
International Conference on Electrical, Computer and Telecommunication Engineering
01- 02 December 2012 (ICECTE2012), RUET, Rajshahi-6204, Bangladesh

ICECTE2012: PI-0162

Reducing Net Total Cost of Ownership (TCO) for a Cloud network

Firoz Mahmud[1], Md. Arafat Hossain[2], Syed Tauhid Zuhori[3]
Department of Computer Science and Engineering
Rajshahi University of Engineering & Technology
Rajshahi-6204, Bangladesh
fmahmud.ruet@gmail.com[1], arafat07ruet@yahoo.com[2], tauhid.ruet@yahoo.com[3].

ABSTRACT
Cloud computing is one of the common terms in utility providing sector. One can easily access some utility through internet with spending penny. Cloud network is mostly based on the "pay per use". Now-a-days many of the cloud networks are building for business purpose. Many services are available in a cloud network. However, cloud network are much more attractive when the Total Cost of Ownership (TCO) become smaller. In that case, owner and user are both get benefited. The processes and methods are discussed in this paper include the effective way to reduce the Total Cost of Ownership (TCO) for a cloud network. It brings the cloud services much more cheaply than previous.

KEY WORDS: Cloud Computing, Regression Analysis, Standard Deviation, Total Cost of Ownership (TCO).

1. INTRODUCTION

The cloud itself is a set of hardware, networks, storage, services, and interfaces that enables the delivery of computing as a service [1]. Cloud Computing as Fig. 1 makes a virtual pool of resources such as storage, CPU, networks and memory to fulfill the user's resource requirement and provides on demand (pay per use) hardware and software without barriers [6].

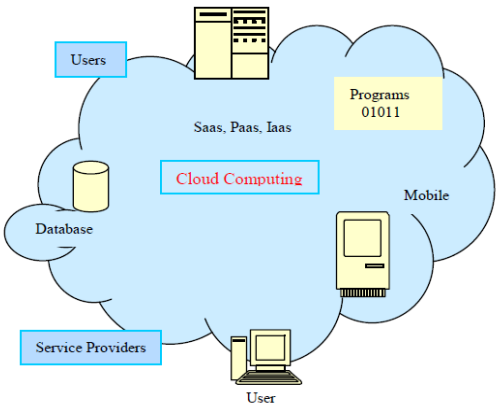

Fig. 1: Cloud computing architecture [6].

Cloud computing is three-layer model of computing as a pyramid with infrastructure at the bottom, the platform in the middle and software at the top [9]. Services are available in three basic utility.

Total Cost of Ownership (TCO) is the all cost that occurs in a life cycle at a workstation and Net TCO is the summation of all workstation and other cost of the network. Lower the TCO tends to the better and better cloud network. TCO costs include both tangible and intangible costs, and often the intangible costs can contribute significantly to the total expense of operating a platform [7]. Lower cost computers for users, lower IT infrastructure costs, fewer maintenance issues, universal access to documents etc. are the main features for a cloud network [2]. Cloud computing encompasses any subscription-based or pay-per-use service that, in real time over the Internet [3]. In the future an organization's IT will be viewed as a utility expense not dissimilar to that of a water or electricity bill. It might seem farfetched, but it is quickly becoming a reality. That means use based payment method is applied in cloud network. The most important thing is that in the sense of cost effectiveness is the calculation of total cost of ownership. There have two types of costs: fixed cost and variable cost. Fixed costs are fixed for all time and may not be changed. Variable costs are varies time to time. Software purchased cost is one kind of variable cost.

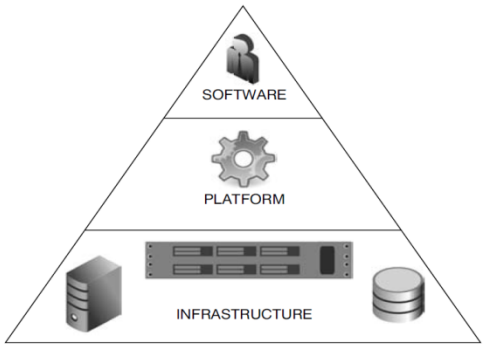

Fig. 2: A simple three-layer pyramid model of cloud computing [9].

2. TCO FACTORS

There are many factors that need to be considered during the course of a TCO study, involved in purchasing, deploying, maintaining, and upgrading the hardware and software required for a server platform should encompass these factors [7]:

- Purchase price of the hardware and software
- Maintenance and service contract costs
- Network infrastructure costs

- Fixed operating costs
- Deployment costs, including database conversions and application migration
- Integration expenses to existing systems
- Ongoing operating costs, as affected by reliability, availability, serviceability, and manageability of the platform

In this paper, we want to reduce the variable cost of purchasing of hardware, software and network maintenance cost.

3. METHODS

In the cloud network, uses want to access services (i.e. software, platform or infrastructure) time to time. Users don't want to wait for services. That is, concurrent accessibility is needed. Those services are available from any of the cloud server. In general case, we don't know that how much availability is needed for each of these service utility. If we know the future uses for these servicing utility, then we can produce the availability of these utility not the fixed amount as previous manner. So, now I have the data for all servicing utility including its no of uses, concurrent access requests. We use two methods to maintain "add or remove services, rearranging the utility of services".

A. Standard Deviation
B. Regression analysis

A. Standard Deviation:

The Standard Deviation is a measure of how spreads out numbers are and how close individual data points are to the mean or average value of the sample. Its symbol is σ. The formula is

$$\sigma = \sqrt{\frac{\sum_{i=1}^{N}(x_i-\mu)^2}{N}} \quad (1)$$

Where, μ is population mean and N is the total number of population. In this paper we use it to rearranging service utility, the first step is to make standardize/usable data. Standard Deviation indicates the popularity of any of the servicing utility.

B. Regression analysis:

Regression analysis is a very common and popular technique for prediction or forecasting. If we apply regression technique in a data sample then we can get an idea what will be happened in near future that means we can predict our future state from the present state or what to do in next? Regression analysis is used for explaining or modeling the relationship between a single variable Y, called the response, output or dependent variable, and one or more predictor, input, independent or explanatory variables, X_1, X_2…, X_n [10]. In this paper, we use this for predict the future uses of the servicing utility from some previous data.

4. APPROACH

Suppose, we have highest no concurrent access request (day by day) about 100 days of a servicing utility. From the input at first we have to standardize the data. Fig 3 is a flow chart which is used to standardize the data.

Where DS is the Standard Data, SD is the Standard Deviation. These data contains the highest concurrent request with day by day basis.

After completed standardize of our data, this data is used for regression analysis.

Let,

$$z = ax + be^y + c \quad (2)$$

Where, z = No of highest concurrent req. in a day
x = time (day)
y = rating of performance
a, b, c = coefficients

Calculating the coefficients by the equations

$$\sum z = a\sum x + b\sum e^y + nc \quad (3)$$

$$\sum zx = a\sum x^2 + b\sum xe^y + c\sum x \quad (4)$$

$$\sum ze^y = a\sum xe^y + b\sum e^{2y} + c\sum e^y \quad (5)$$

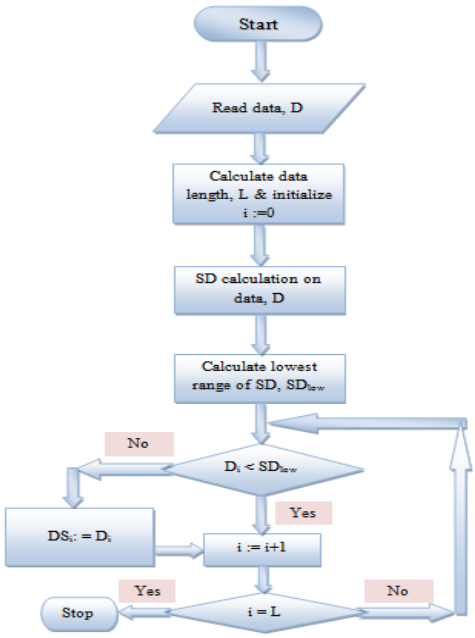

Fig. 3: Flowchart for data standardization

After calculating these coefficients, we can calculate the future highest no of concurrent request by varying times. Performance rating remains same. This performance rating is calculated by failure rate, waiting time for the servicing utility, the efficiency and user response.

5. EXPERIMENTAL RESULT

For our experimental result at first we assumed 100 days of data randomly for one utility or resource. Our initial data look like the following table (Table 1). This table represents total 100 days concurrent number request or servicing for one utility or resource.

Day count	No of request	performance
1	210	0.8
2	220	0.9
3	198	0.5
4	175	0.6
5	70	0.61
6	110	0.78
7	120	0.7
8	97	0.4
……	……..	……
99	201	0.95
100	204	0.86

Table 1: Data for access request

After applying standard deviation which is described in flowchart (fig 3) we got the following data look like the Table 2.

Day count	No of request	Performance
1	210	0.8
2	220	0.9
3	198	0.5
4	175	0.6
6	110	0.78
7	120	0.7
9	221	0.5
12	141	0.45
……	…….	……..
99	201	0.95
100	204	0.86

Table 2: Data after standardization

Now, analyze the data with regression analysis. Future value of highest concurrent access request is calculated by varying the day number only.

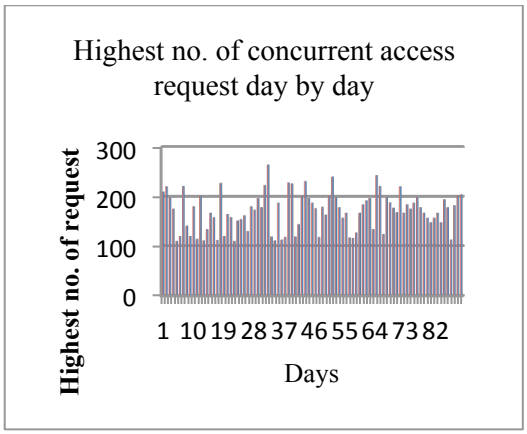

Fig. 4: Graph before regression analysis

After analyzing the regression method we gain the result of these coefficients (i.e. a, b or c) by solving equation 3, 4 and 5. Then varying the day count (i.e. next day's such as 101,102,….) to put in equation (2) and get the next day's highest no of request. The result is then modified by 25% (because of accuracy purpose), which is shown at the Table 3 and Corresponding graph are looks like the Fig 5.

Next days	Performance	Predicted values	Modified values
101	0.8	180.3504	225.438
102	0.9	182.7477	228.4347
103	0.5	175.2181	219.0226
104	0.6	177.0391	221.2989
……	……	……	……..
196	0.67	194.2793	242.8491
197	0.9	199.254	249.0675
198	0.89	199.1952	248.994
199	0.95	200.7995	250.9994
200	0.86	198.859	248.5738

Table 3: Data after regression analysis

After getting the predicted values of concurrent request, the administrator then give the concurrently accessibility with the days or a period of time. From the graph we can see that 1 to 30 days the highest no of concurrent request is around 232 (Fig 6).

So, in this period the accessibility may become around 232 (may be 235). Next 30 days can have around 240 and so on. In that case, the constant accessibility is removed then. If at first gives the accessibility is for 500 (totally highest concurrent request), then the cost for it 500×40$ = 20000$ (40$ per day), now it reduces to (235×40$ = 9400$ and 240×40$ = 9600$) 9500$.

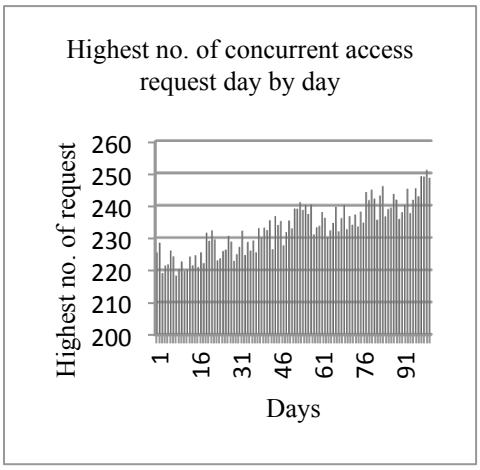

Fig. 5: Graph after regression analysis

This approach is used for all of the servicing utility in the network. This utility installation/arranging are then made by the following approach.

If a cloud administrator controls the network from a central point or location, then the administrator needs to check the popularity of any servicing utility (software, application etc.). It is also gained by the standard deviation calculation. All the servicing utility uses data is now essential. Decision of servicing utility installation is made by the following steps.

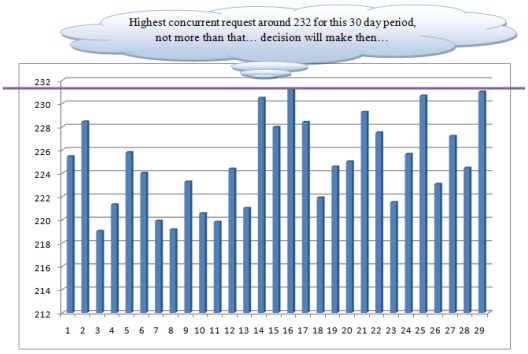

Fig. 6: Making decision from the predicted value

Step 1.Taking all of the data uses from all location on the basis of utility servicing.
Step 2.Calculate average and standard deviation (SD).
Step 3.Check if the standard deviation (SD) is greater than 50% of its mean then the service utility installation is made at the central server. Then go to Step 6.
Step 4.Probability calculation with the formula, $P(L) = \frac{\text{Average uses for that location}}{\text{Total average uses for all locatiion}}$, where P(L) is probability of uses at any location.
Step 5.Calculate the no of accessibility for that location, $A_L = concurrent\ accessibility \times P(L)$.
Step 6.If all utility is finished then end the process otherwise continue step 1 for the next utility.
Step 7.Stop.

6. CONCLUSIONS

In this paper, we discuss two methods to reduce the net Total Cost of Ownership (TCO). All data may not standard, so firstly doing the data usable with standard deviation. In the regression analysis, the equation has the performance rating e^y because of the rating can exponential growth of the uses. Some steps we introduce to rearranging the utility of services.
Cloud computing mostly depends on the cost computing and security purpose. Less you have the TCO more you benefited as owner and of course as user. We believe that those methods are being used later in near future.

REFERENCES

[1] "Cloud Computing For Dummies", Judith Hurwitz, Robin Bloor, Marcia Kaufman, and Dr. Fern Halper.
[2] "Cloud computing", Shivaji P. Mirashe, Dr. N.V. Kalyankar, "Journal of Computing" , Volume-2, Issue-3, March 2010, Page 78-82
[3] "What cloud computing really means", Eric Knorr, Galen Gruman, Published on "InfoWorld", 12th June 2010.
[4] "TCO reduction", Aziz, M.H., "Communications, 2003. APCC 2003. The 9th Asia-Pacific Conference on 21-24 Sept. 2003", page: 1147 - 1151 Vol.3
[5] "Virtualization Techniques and Cloud Computing", Ahmed Mekkawy.
[6] "Cloud Computing: The Fifth generation of Computing", Sameer Rajan, Apurva Jairath, "2011 International Conference on Communication Systems and Network Technologies", page 665-667
[7] The official website of Intel, http://software.intel.com/en-us/articles/total-cost-of-ownership-factors-to-consider
[8] Velte A. T, Velte T.J. and Elsenpeter R, "Cloud Computing – A Practical Approach", Tata McGraw-Hill Edition 2010, ISBN: 978-0-07-162695-8, pp. 214-215.
[9] "A quick start guide to cloud computing", Dr Mark I Williams, © Mark Ian Williams 2010, ISBN 978 0 7494 6130 0
[10] "A short introduction to cloud platforms: An enterprise-oriented view", Chappell, D, ITPro, pp. 23–27, August 2008.
[11] "Cloud Computing and Development Trend", Zhang Shuai, zhang Shufen, Chen Xuebin & Huo Xiuzhen, Proc. of IEEE Second International Conference on Future Networks, pp 70-75, 2010.
[12] "Introduction to cloud computing architecture", Sun Microsystems, White Paper, Sun Microsystems, June 2009.
[13] "Cloud Computing – A Practical Approach", Velte A. T, Velte T.J. and Elsenpeter R, Tata McGraw-Hill Edition 2010, ISBN-13: 978-0-07-068351-8, pp. 69-87.
[14] "Cloud Computing Identity Management", Gopalakrishnan A, SETLabs Briefings Vol. 7, No.7, pp. 45-54, 2009
[15] "Cloud Economics", Duncan Rutland, White paper, © 2012 Rackspace US, Inc.

Proceeding of the
International Conference on Electrical, Computer and Telecommunication Engineering
01- 02 December 2012 (ICECTE2012), RUET, Rajshahi-6204, Bangladesh

ICECTE2012: PI-0163

A Genetic Algorithm Approach for Solving a Definite Constrained-Based Large Scale Bidline Generation Problem by Optimized Railway Crew Scheduling

Syed Tauhid Zuhori[1], Mamun-Ur-Rashid[2], Firoz Mahmud[3]
[1,3]Lecturer, Computer Science & Engineering, Rajshahi University of Engineering & Technology
[2]Undergraduate student, Computer Science & Engineering, Rajshahi University of Engineering & Technology
E-mail: tauhid.ruet@yahoo.com, diehard.ruet@gmail.com, sabuzbd.ruet@gmail.com

ABSTRACT
Railway Crew scheduling is an important part of Railway Organization. This paper is concerned with the crew scheduling by creating the work schedules for the crew member to cover a planned timetable. This is a well-known problem in operation research and associated with railway and mass transit companies. The complexities of the problem are such that a human scheduler has difficulty in producing a near optimal schedule so that the total cost of the crew is minimized. Several methods are available which regularly solve scheduling problem. Genetic Algorithm can be used for solving larger problem more robustly, more speedily and more cost effectively than existing methods. This paper shows a Genetic Algorithm approach by which the cost of the railway is minimized by scheduling the crew members' duty.

KEY WORDS: Large scale problem, Bidline generation problem, Crew scheduling, Genetic Algorithm, Optimization.

.

1. INTRODUCTION

Railway Crew Scheduling is a Bidline generation problem based on the cost of crew for the railway organization. The Bidline generation problem is the problem of assigning *K* crews to N trip with fixed Start and finish times such that each crew does not exceed a limit on the total time it can spend working [2]. In this paper, we consider a specific set of operational constraints and implement these constraints for reducing the total cost of the crew. The objectives of this paper are to maximize the quality of the schedules produced and to minimize the total cost of the crew.

2. LITERATURE SURVEY

The more works are done for solving the bidline generation problem. Here some evaluations are given in the following table.

Type of the works	Year
Integrated Airline Crew Pairing and Crew Assignment by Dynamic Constraint Aggregation By Mohammed Saddoune.	2012
A three phase approach to solving the Bidline problem by Weir	2004
Large Scale Model in the Airline Industry by Diego Klabjan	2003
A Two-Phase Genetic Algorithm for Large Scale Bidline Generation Problems at Delta Air Lines by Ioannis T. Christo	1999
Algorithm for Railway Crew Management By Alberto Caprara	1997

Table 1: Evaluation of bidline generating problem [4].

3. METHODOLOGY

Crew scheduling is a problem which has been historically associated with mass transit companies, especially in Europe, where deregulation and privatization issues are forcing a re-organization of the rail industry and better productivity and e-client services are strongly required by the market and the public ownership [1,3].Therefore, this sector is showing an increasing interest in Operations Research and Management Science. Railway crew planning represents hard problem due to both the dimensions and the operational/regulation constraints involved.

3.1 The Bidline Generation Process

The complete Bidline generation processes are given below:

Step1: Define some constraints.

Step 2: Initialize Crew Member with specific member id & cost per hour.

Step3: Take Railway Train Schedule for some station.

Step4: Develop a Fitness Function based on cost of Crew.

Step5: Generate the initial crew set (Population) with corresponding string.

Step6: Calculate the fitness value (cost) of all the crew set by using appropriate Fitness Function.

Step7: Select some of the best crew set by applying selection method.

Step8: Generate the next generation by Crossover or Mutation.

Step9: Repeat step5 to step7 until optimal solution is found.

Step10: Draw the Bidline.

3.2 Genetic Algorithm

Here Genetic Algorithm is used for solving the bidline generation problem. On a quick glance we say that it is very useful as it is

- ⇨ A good mechanism for generating the solution.
- ⇨ Testing how good it is?
- ⇨ Improving solution generation by generation.
- ⇨ Easy to find appropriate solution if optimization [6].

  Here the flow chart of Genetic Algorithm is given:

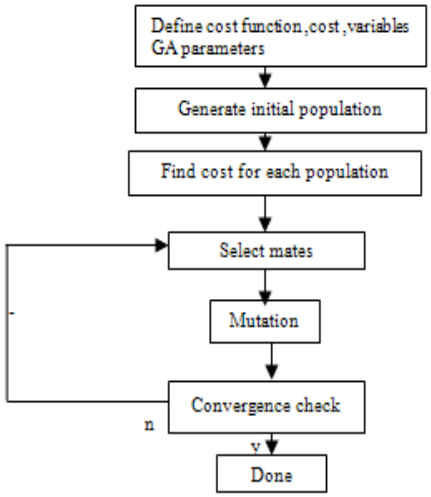

Fig. 1: Flow Chart of Genetic Algorithm

3.3 Crew Member Information

In this paper, we consider three different types of crew such as Senior Crew, Medium Crew & Junior Crew. The members of each crew type have a different pay scale. The cost of the senior crew is greater than the cost of the junior crew (Senior Crew>Medium Crew>Junior Crew). The cost of each crew is measured by the level of the crew and the time of the duty.

Crew Type	Crew id	Cost/hr.
Senior	SC1,SC2	100
Senior	SC3,SC4	95
Senior	SC5,SC6	90
Senior	SC7,SC8	85
Medium	MC1,MC2,MC3	80
Medium	MC4,MC5,MC6	75
Medium	MC7,MC8,MC9	70
Medium	MC10,MC11,MC12	65
Medium	MC13,MC14	60
Medium	MC15, MC16	55
Junior	JC1,JC2,JC3	45
Junior	JC4,JC5,JC6	40
Junior	JC7,JC8,JC9	35
Junior	JC10,JC11,JC12	30
Junior	JC13,JC13,JC15	25
Junior	JC16,JC17,JC18	20
Junior	JC19,JC20,JC21	15
Junior	JC22,JC23,JC24	10

Table 2: Crew Member with Individual Cost / hour

3.4 Map of external member information

We consider 5 big Station and 10 small Station. The map of the railway Station is Given Below:

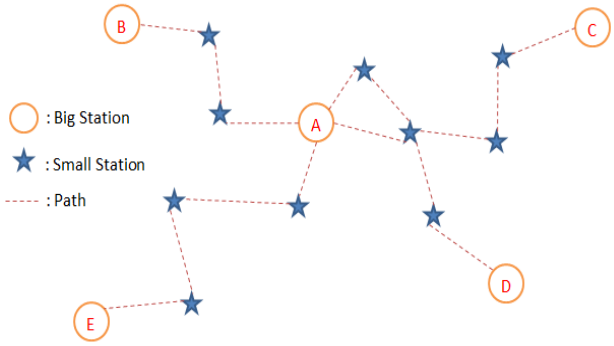

Fig. 2: Railway station

3.5 Train schedule

Train Schedule consists of 5 important fields for a trip such as Train number, departure city, Destination city, Departure time, approximate arrival time. Different Station has different train Schedule. All train schedules are given below.

Train Number	Dep. City	Des. City	Dep. Time	Arr. Time

01	A	B	00.00	06.00
02	A	C	00.30	05.30
03	A	D	01.00	07.00
04	A	E	01.30	8.00
05	A	C	05.00	10.00
06	A	E	06.00	12.30
07	A	B	07.00	13.00
08	A	D	08.00	14.00
09	A	B	12.00	18.00
10	A	C	12.30	17.30
11	A	D	13.00	20.00
12	A	E	13.30	21.00
13	A	C	14.00	19.00
14	A	E	14.30	21.00
15	A	B	15.00	21.00
16	A	D	15.30	23.30

Table 3: Train Schedule for Station A

Train Number	Dep. City	Des. City	Dep. Time	Arr. Time
01	B	A	06.30	12.30
07	B	A	13.30	19.30
09	B	A	18.30	N-00.30
15	B	A	21.30	N-03.30

Table 3.3: Train Schedule for Station B

3.6 Crew string generation

The general Structure for the Crew string:

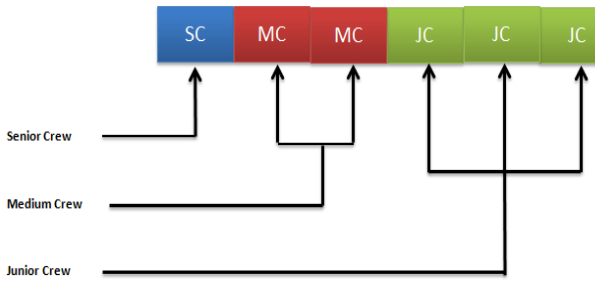

Fig. 3: Crew String Structure

A crew set consists 6 crew for a trip. We can change the structure of the crew string if it is urgent. In this implementation, we consider 16 crew set. We randomly generate 16 crew strings according to the general structure of the crew String.

3.7 Fitness function

$$F=\sum_{i=1}^{n} cost_senior_i \ x \ time \ x \ duty+\sum_{j=1}^{m} cost_medium_j \ x \ time \ x \ duty+\sum_{k=1}^{p} cost_junior_k \ x \ time \ x duty \qquad (1)$$

Where

n= number of senior crew

m= number of medium crew

p=number of junior crew

cost_senior, cost_medium, cost_junior represent the cost of the senior, medium and junior crew for per hours duty respectively.

Time represents the total time of the trip.

duty= 0 if a crew member not assigns for a trip

duty=1 if a crew member assigns for a trip

Crew Set No.	Crew String	Fitness Value(Cost)
01	1,1,2,13,14,15	4020
02	2,3,4,16,17,18	3780
03	3,5,6,19,20,21	3480
04	4,7,8,1,2,3	4440
05	5,9,10,4,5,6	4140
06	6,11,12,7,8,9	3900
07	7,14,13,10,11,12	3540
08	8,15,16,22,23,24	2700
09	2,1,16,19,20,21	3360
10	3,2,15,16,17,18	3645
11	5,3,14,13,14,15	3660
12	7,8,12,22,23,24	3000
13	4,7,11,10,11,12	3840
14	1,6,10,7,8,9	4140
15	8,5,12,4,5,6	4140
16	6,4,13,1,2,3	4320

Table 4: Crew String with corresponding Fitness value

3.8 Mutation

If we need to change a crew member of the crew set for a trip, then we perform the mutation operation. There is several reasons for Perform mutation operation, such as…

- Senior member bid for this trip.
- Overlap maximum number of duty.

Example:If (a) is generated for trip t1, but SC1 bid this trip then SC3 replaced by SC1. Because SC1>SC3 (Priority).

(a)

(b)

Figure 4: Mutation Operation (a) Before mutation (b) After Mutation.

4. EXPERIMENTAL RESULT

We schedule the crew members duty and then calculate the cost of the train management. The crew members duty select by the genetic operators.

Train No.	Before Optimize		After Optimize	
	Crew ID	Cost	Crew ID	Cost
01	SC1, SC2, MC1, MC2, JC1, JC2	5400	SC6, MC4, MC12, JC9, JC11, JC16	3780
02	SC3, SC4, MC3, MC4, JC3, JC4	2150	SC8, MC13, MC15, JC7, JC10, JC13	1450
03	SC5, SC6, MC5, MC6, JC5, JC6	2460	SC4, MC7, MC16, JC3, JC21, JC24	1740
04	SC7, SC8, MC7, MC8, JC7, JC8	2470	SC1, MC2, MC14, JC6, JC5, JC23	2145

Table 5: Compares between before & after optimization

Now we draw a graph which shows the optimization result:

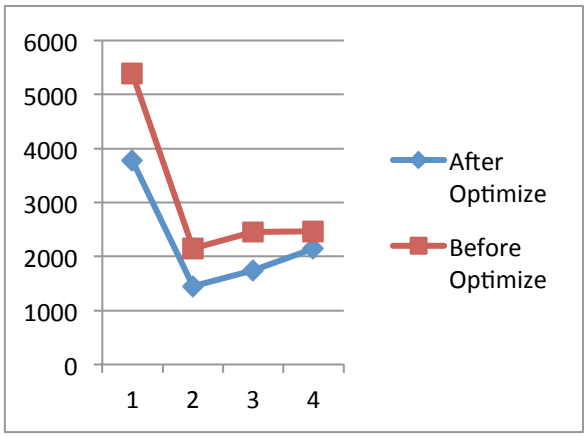

Fig. 5: Train Number vs. Cost graph

5. CONCLUSION

Large scale bidline generation problem is a real life problem and this is very important issue to schedule a crew member duty list. In this work we try to optimize the cost of the railway administration. In this paper we solve the problem for a small part. We continue the genetic algorithm for only a certain generation. The cost will be more smaller than the original if this algorithm works for a large generation.

REFERENCES

[1]. Michael Affenzeller, "Genetic Algorithm and Genetic Programming Modern Concepts and practical Applications.Gabriel Luque, Parallel Genetic Algorithms theory and real world applications"

[2]. Mohammed Saddoune, *Weir* , "Integrated Airline Crew Pairing and Crew Assignment by Dynamic Constraint Aggregation By *A three phase approach to solving the Bidline problem (2004)."*

[3]. Diego Klabjan, "Large Scale Model in the Airline Industry (2003)."

[4]. Ioannis T. Christou, "A Two-Phase Genetic Algorithm for Large Scale Bidline Generation Problems at Delta Air Lines(1999)"

[5]. Alberto Caprara, "Algorithm for Railway Crew Management (1997)."

[6]. Gabriel Luque, "Parallel Genetic Algorithms theory and real world applications."

[7]. Weir, "A three phase approach to solving the Bidline problem (2004) ".

Proceeding of the
International Conference on Electrical, Computer and Telecommunication Engineering
01- 02 December 2012 (ICECTE2012), RUET, Rajshahi-6204, Bangladesh

ICECTE2012: PI-0164

An Improvement of the Performance of Multi Depot Vehicle Routing Problem Comparing with Clarke and Wrights Conventional Method

Syed Tauhid Zuhori[1], Firoz Mahmud[2], Zahrul Jannat Peya[3]
[1,2]Lecturer, Computer Science & Engineering, Rajshahi University of Engineering & Technology
[3]Undergraduate Student, Computer Science & Engineering, Rajshahi University of Engineering & Technology
E-mail: tauhid.ruet@yahoo.com, sabuzbd.ruet@gmail.com, peya_cse07@yahoo.com

ABSTRACT
Typical Vehicle Routing Problem means determining routes for several vehicles from a depot to a number of customers and then returning to the depot. Since the problem is related with single depot, the VRP is also named Single-depot VRP. Single-depot VRPs are not suitable for practical situations. The Multi-Depot Vehicle Routing Problem (MDVRP), an extension of classical VRP, is a NP-hard problem for simultaneously determining the routes for several vehicles from multiple depots to a set of customers with demand and then return to the same depot. Main goal of this thesis is to solve MDVRPSD in three phases. Firstly we've used nearest neighbor classification method for grouping the customers then Sum of Subset method have been used for routing. Finally the routes are optimized using greedy method. The routes obtained using these methods are better for the vehicles considering demands of the customers. The performance of our work is better than conventional method by Clarke and Wrights.

KEY WORDS: Multi Depot, Vehicle routing problem, Greedy method, Sum of subset problem, nearest neighbor grouping method.

1. INTRODUCTION

Typical Vehicle Routing Problem means determining routes for several vehicles from a depot to a number of customers and then returning to the depot.

Since the problem is related with single depot, the VRP is also named Single-depot VRP. Single-depot VRPs are not suitable for practical situations.

VRPs with more than one depot are known as Multi-depot Vehicle Routing Problem [1]. Our topics are Multi-depot Vehicle Routing Problem with Stochastic Demand. Here the customers are characterized by their own demand. The customers' demands are stochastic variables, on which only the probability distribution for each customer is assumed known at the time of planning, so that it is the expected total travel cost which is subjected to minimization [2].

Nearest-neighbour classifiers are very simple to design, and often equal or exceed in accuracy much more complicated classification methods [3]. For this reason we have used this classifier for grouping. Sum of Subset method first combines the demands of the customers for satisfying fixed constraints. This method finds routes at a faster rate thus providing computationally efficient solutions. Finally routes are scheduled using greedy method.

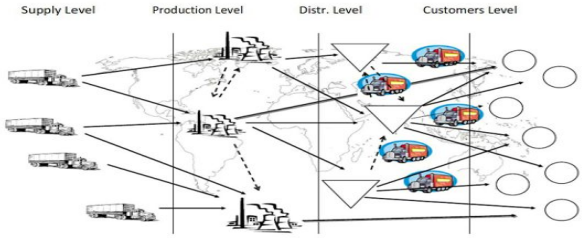

Fig. 1: Typical vehicle routing problem with different level.[2]

2. LITERATURE SURVEY

In 1959, Dantzig and Ramser first introduced vehicle routing problem [6]. Wu et Al., reports a simulated annealing (SA) heuristic for solving the multi-depot location routing problem (MDLRP) [7]. Giosa et Al.[8], developed a "cluster first, route second" strategy for the MDVRP with Time Windows (MDVRPTW), an extension of the MDVRP. This can be shown by a table:

1964	Clarke and Wright developed a heuristic solution method named savings method and was the first algorithm that became widely used[2]
1969	Tillman first addresses the VRPSD as a modification of the savings method
1986	Reviews of work on the VRPSD are provided by Dror and Trudeau
1989 1996	Dror et al. and Gendreau et al. Stewart and Golden presented three models for the VRPSD[2]
1992	Laporte et al. introduced the VRP with stochastic travel and service times[2].

Table 1: Related work of Multi depot vehicle routing problem with stochastic demand.

3. METHODOLOGY

We've used three independent methods to solve MDVRPSD.

3.1 Inputs

Figure2.1 indicates the initial customers and depot Locations. The circles indicate the customers (20 customers) and the rectangles indicate the depot locations (4 depots). The numbers associated with each customer denote the demands of the customers.

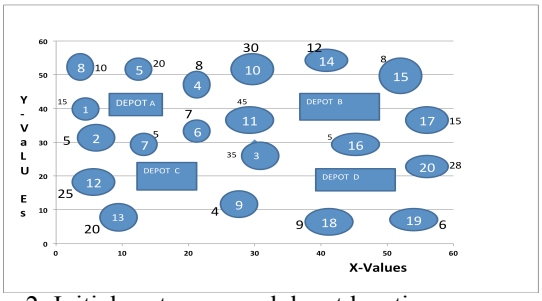

Fig. 2: Initial customers and depot locations.

We can represent the figure in the following table where every customers are included with their stochastic demand.

Customer Number	Demand	Customer Number	Demand
1	15	11	45
2	5	12	25
3	35	13	20
4	8	14	12
5	20	15	8
6	7	16	5
7	5	17	15
8	10	18	9
9	4	19	6
10	30	20	28

Table 2: Customers with corresponding demands.

3.2 Nearest neighbour method

Nearest Neighbours technique makes a decision based on the shortest distance to the neighbouring class samples. We have used this technique to assign the customers to their nearest depot. This process of assigning is called grouping.

For measuring distance in Nearest Neighbor method we have used the following formula:

$$D(c_i, k) = \sqrt{(x_{c_i} - x_k)^2 + (y_{c_i} - y_k)^2}$$

Here, c_i = ith customer, k=depot

After measuring distance the customers are assigned according to the following formula:

-If $D(c_i, A) < D(c_i, B)$, then customer c_i is assigned to depot A

- If $D(c_i, A) > D(c_i, B)$, then customer c_i is assigned to depot B

-If $D(c_i, A) = D(c_i, B)$, then customer c_i is assigned to a depot chosen arbitrarily between A and B.

The input of our main problem is given in figure. The circles indicate the customers (20 customers) and the rectangles indicate the depot locations (4 depots). The numbers associated with each customer denote the demands of the customers.

These customers are assigned to individual depots using nearest neighbor method. Here for example in the input figure1 the distance from customer 6 to depot A is 16.12 and the distance to depot D is 15.62.As distance to D is minimum,6 is assigned to depot D(Figure 3.2). In this way all other customers are assigned.

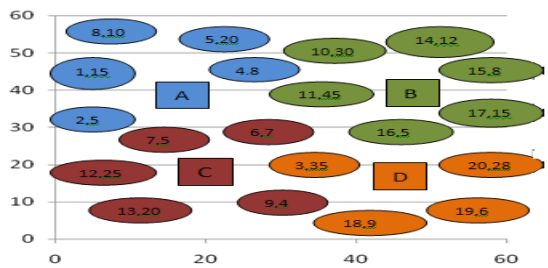

Fig. 3: After grouping using nearest neighbour method

Here customers 1,2,4,5,8 are assigned to depot A, customers 10,11,14,15,16,17 are assigned to depot B, customers 6,7,9,12,13 are assigned to depot C, customers 3,18,19,20 are assigned to depot D.

3.3 Sum of subset method

Sum of subset is a special case of the knapsack problem and is defined as follows: given a set of positive integers $\{a_1, \ldots, a_n\}$, n ≥ 1, and a positive integer B (the bound), find a subset of the a_i's such that their sum is as close as possible to B, without exceeding B.

This problem is NP-hard (see e.g. (Garey & Johnson 1979)), therefore it is very unlikely that there exists a polynomial time algorithm for finding optimal solutions for arbitrary instances. In practice however one is often satisfied with an approximate, sub-optimal solution, which can be found quite efficiently (i.e. in polynomial time).

So the mathematical definition can be given as: given a set of n items and a knapsack, with

w_j = weight of item j

C = capacity of the knapsack,

Select a subset of the items whose total weight is closest to, without exceeding , C, i.e.

$$\text{Maximize} \quad z = \sum_{j=1}^{n} w_j x_j$$

Subject to $\sum_{j=1}^{n} w_j x_j \le C,$

$x_j = 0$ or 1 $\quad j \in N = \{1,\ldots\ldots\ldots,n\}$

Where $x_j = 1$ if item j is selected, otherwise $x_j = 0$.

Here $1 \le i \le n$.And denotes the demands of the customers. The value of m is given 50. After grouping we've used sum of subsets for determining the routes. In this case following flowchart is used.

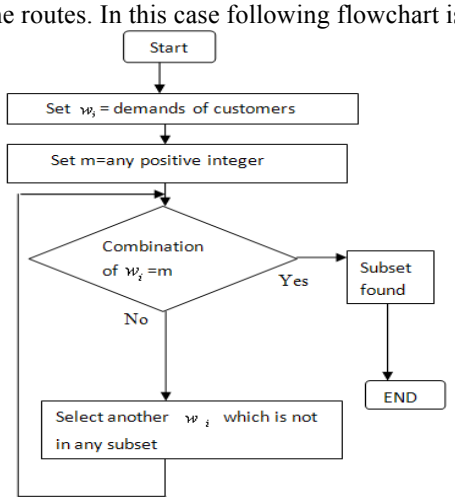

Fig. 4: Flow chart of Sum of subset approach.

Here when combinations of w_i i.e. demands of customers sum to 50 then we get a subset and it is the route. So the customers whose demands sum to 50 are linked to one route. Otherwise we try to make another subset with the rest customer's demands. If no other subset is found then the rest customers are linked to an individual route.

The result of applying Sum of Subset is shown in figure 4.

Here in depot A (figure 5) the sum of the demands of the customers 1, 2, 8 and 5 is 50.The value of m is also 50.So we get a subset here. For this reason these customers are linked to one route. In depot A there is another customer i.e. customer 4.Demand of customer 4 is 8. It is not possible to get another subset here. A new vehicle is used to service customer 4.In this way other routes are determined.

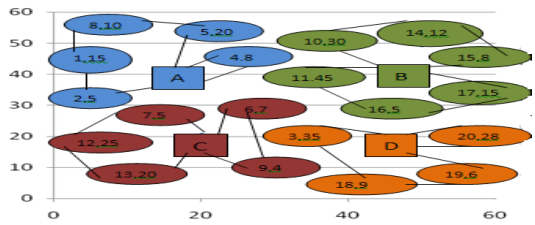

Fig. 5: Route obtain using Sum of subset approach

In this way all other routes are determined.

Depot	Routes	Vehicles
A(11,40)	A-2-1-8-5-A	2
	A-4-A	
B(45,40)	B-10-14-15-B	3
	B-11-16-B	
	B-17-B	
C(15,20)	C-13-12-7-C	2
	C-6-9-C	
D(45,20)	D-3-18-19-D	2

Table 3: Assignment of customers to depot using sum of subset.

3.4 Greedy Method

Greedy method is the most straightforward design technique. This method suggests that one can devise an algorithm that works in stages, considering one input at a time. At each stage, a decision is made that appears to be the best (under some constraints) at the time [4]. In this case we have used the following flowchart:

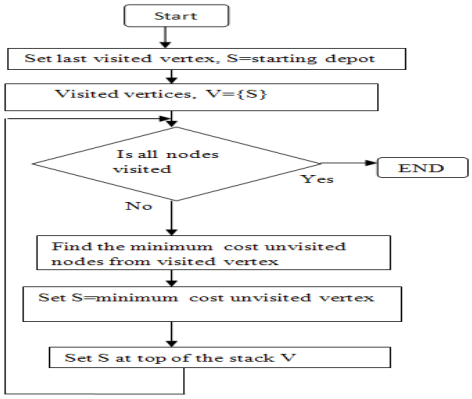

Fig. 5: Flow chart of Greedy method

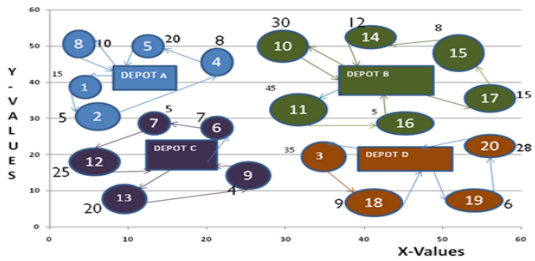

Fig. 6: Route obtained using Greedy method

4. RESULT ANALYSIS

For comparing the performance we solve the problem for 10 depots and 50 customers. For an example here the toughest input in our system the 7 Depot and 35 customers result re shown. Here we see that according to savings method 15 routes are needed and according to sum of subset approach 17 routes are needed.

Number	Numbers of vehicle needed		Time for finding routes	
	Proposed Method	Conventional	Proposed Method	Conventional

of routes		method		Method
2	4	4	3.1241	1.5652
3	5	7	3.2236	1.5854
4	8	10	3.4568	1.5925
5	11	12	3.6894	1.6256
6	13	15	3.9845	1.7365
7	15	17	4.1453	1.9521

Table 4: Performance comparison table between our proposed method and conventional method.

We can put the values in a graph and then compare the performance of two methods easily.

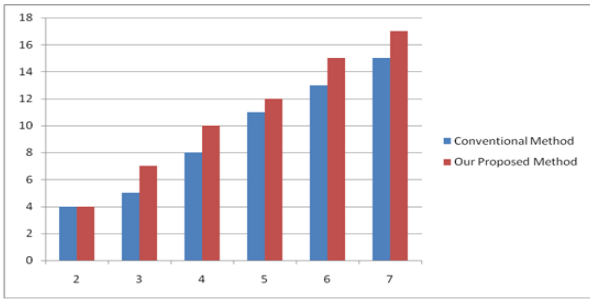

Fig. 7: Performance comparison between our proposed method and conventional method in case of numbers of vehicle needed.

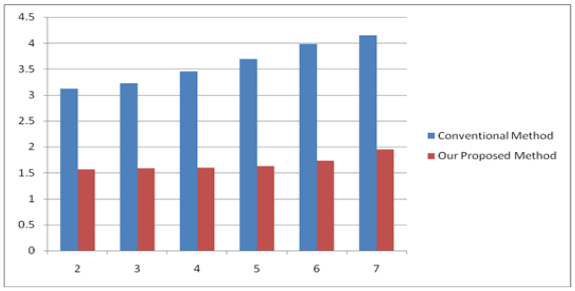

Fig. 8: Performance comparison between our proposed method and conventional method in case time.

5. CONCLUSION

The main problem was to find routes of Multiple Depot Vehicle Routing Problem with Stochastic Demand. We first grouped the customers using nearest neighbor classification method. We analyze the Clark and Wright savings method for finding routes as conventional approach uses it. It takes too much time. Our approach determines routes using sum of subset. The process of this method is simple and takes less time. We compare performance of the two methods. But there was no indication for which customer will be serviced first. For this reason greedy method was applied for optimizing routes. In this case conventional approach uses genetic algorithm for scheduling the routes. We also compare their performance here. Finally some optimized routes were obtained using minimum cost and less number of vehicles.

REFERENCES

[1] Surekha P. and Dr. S .Sumathi , “Solution To Multi-Depot Vehicle Routing Problem Using Genetic Algorithms”, Journal of Algorithm Optimization-August,2011, Pages 118-131.

[2] Graham K Rand, “The life and times of the Savings Method for Vehicle Routing Problems”, International Journal of Operational Research,October-2009, Pages 132-135.

[3] Neural Networks, Fuzzy Logic and Genetic Algorithms by S. Rajasekaran and C. A. Vijayalakshmi Pal, Chapter 2, Pages 29-30.

[4] Fundamentals of Computer Algorithms by Ellis Horowitz,Sartaj Sahni and Sanguthevar Rajasekaran, Chapter 7, Pages 341-357.

[5] Neural Computing; An Introduction by R Beale and T Jackson, Chapter 2, Page 20.

[6] Aslaug Soley Bjarnadottir, “Solving the Vehicle Routing Problem with Genetic Algorithms”, International Journal of Electrical and Computer Engineering-April 2004, pages 23-27.

[7] T. H. Wu, C. Low, and J. W. Bai, "Heuristic solutions to multi-depot location-routing problem," *Computers & Operations Research,* vol. 29, pp. 1393–1415, 2002.

[8] I. D. Giosa, I. L. Tansini, and I. O. Viera, "New assignment algorithms for the multi-depot vehicle routing problem," *Journal of the Operational Research Society,* vol. 53, pp. 977-984, 2002.

Proceeding of the
International Conference on Electrical, Computer and Telecommunication Engineering
01- 02 December 2012 (ICECTE2012), RUET, Rajshahi-6204, Bangladesh

ICECTE2012: PI-0165

A Job Shop Scheduling Problem using Genetic Algorithm and Round Robin Algorithm and Their Performance Comparison

Arifa Sultana Rumpa[1], Md. Arafat Hossain[2]
Department of Computer Science and Engineering
E-mail: rumpa_07ruet@yahoo.com, arafat.ruet03@gmail.com

ABSTRUCT
The job shop scheduling problem (jssp) is one of the most important issues in the planning and operation of manufacturing system, but the generation of consistently good schedules has proven to be extremely difficult. The difficulty is due mainly to the higher number of constraints. The problem is that optimal scheduling solutions involve costly. The goal of this research is to develop an efficient scheduling method based on genetic algorithm to address jssp. This paper shows how the gas can be used to optimize the job shop problem with many tasks, many machines and the precedence constraints. The results are compared with other proposed approaches. The superior results indicate the successful incorporation of a method to generate initial population into the genetic operators. We demonstrate the performance of the algorithm with examples of real-world size. We terminate with a discussion and suggestions for further research.

KEY WORDS: Job shop, burst time, makespan, tardiness, preemptive job, fitness function, time quantum

1. INTRODUCTION

In a job shop-scheduling problem, a set of jobs, where each job consists of a chain of operations, has to be processed on a set of machines [1]. Each machine can process one operation at a time. Operations need to be processed during an uninterrupted period of a given length on a given machine. There is a good deal of research that considers different issues of theoretical or practical nature that appears in scheduling.

Scheduling is broadly defined as the process of assigning a set of task to resources over a period of time[2] or it may be defined as ‘‘the allocation of resources over time to perform a collection of tasks[3]’’. Scheduling problems are difficult to solve because they involve complex combinatorial optimization. For example, if n jobs are to be performed on m machines, there are potentially $(n!)^m$ sequences, although many of these may be infeasible due to various constraints.

The Job Shop Scheduling problem is formalized as a set J of n jobs, and a set M of m machines. Each job J_j has ni subtasks (called operations), and each operation J_{ij} must be scheduled on a predetermined machine $\mu_{ij} \in M$ a fixed amount of time, d_{ij} , without interruption. No machine may process more than one operation at a time, and each operation J_{ij} € J_j must complete before the next operation in that job ($J_{i(i+1)}$) begins. Every operation x has a release (start) time denoted r_x, and tail time denoted t_x which is the longest path from the time x is completed to the end.

2. WHAT IS JOB SHOP

The usual job shop, from a research standpoint, is one in which there are m machines and n jobs to be processed. Each job requires m operations, one on each different for each job[4]. Real job-shops are more complicated. Jobs may not require all in machines; and yet they may have to visit some machines more than once. Clearly, workflow is not unidirectional in a job-shop. Any given machine may observe new jobs arriving from outside the shop (as new inputs), and from other machines within the shop (as WIP), the same machine may be the last machine for a particular job, or it may be an intermediate processing step. Thus, the workflow can be illustrated as in Figure 2.1

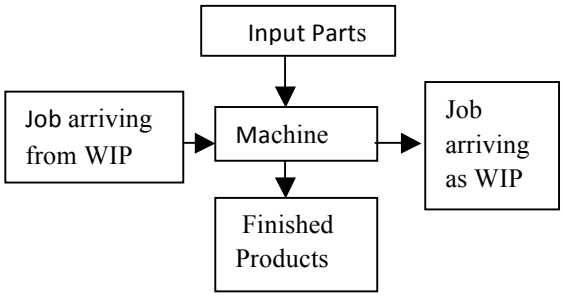

Fig. 1: One machine in job shop

Flow time (F_j): It is the amount of time job j spends in system.
Makespan: It is the total amount of time for all jobs to finish processing
Lateness (L_j): It is the amount of time by which the completion time differs from the due date. [5].

Tardiness (T_j): It is the lateness of the job j if it fails to meet its due date, or zero. i.e. $T_j = \max\{0, L_j\}$[6].

Mean flow time: $\overline{F} = \frac{1}{n}\sum_{j=1}^{n} F_j$ (Eq.1)

It is the time that the total jobs spend in the system.

Mean tardiness: $\overline{T} = \frac{1}{n}\sum_{j=1}^{n} T_j$ (Eq.2)

The lateness of the total jobs from j=1 to j=n.

Maximum flowtime: $F_{\max} = \max_{1 \le j \le n} \{F_j\}$ (Eq.3)

It represents the maximun spent time of all jobs.

Maximum tardiness: $T_{\max} = \max_{1 \le j \le n} \{T_j\}$ (Eq.4)

It represents the maximun lateness of all jobs.

Number of tardy job: $N_T = \sum_{j=1}^{n} \int(T_j)$ (Eq.5)

Where $\int(T_j) = 1$ If $T_j > 0$

and $\int(T_j) = 0$, otherwise

It represents total number of jobs that fail to meet their due date

3. METHODOLOGY

There are several solution approaches given below:

1. Simulated Annealing algorithm
2. Ant colony optimization algorithm
3. Optimization algorithm
4. Shifting Bottleneck Algorithm
5. Neural network approach
6. Round Robin Algorithm
7. FCFS Algorithm

Among those several algorithms we have used two approaches those are given below:

1. Round Robin Algorithm
2. Genetic Algorithm.

In short term we have to meet the criteria's:

1. Minimize total tardiness.
2. Minimize the number of late jobs.
3. Maximize system/resource utilization.
4. Balance resource usage.
5. Maximize production rate.

Depending on the above criteria scheduling algorithm is selected for implementation. GA and RR algorithm can meet the above criteria comparatively better.

3.1 ROUND ROBIN ALGORITHM

The round-robin (RR) scheduling algorithm is designed especially for timesharing systems. It is similar to FCFS scheduling, but preemption is added to switch between processes. A small unit of time, from 10 to 100 milliseconds, is called a time quantum or time slice. The CPU scheduler goes around the ready queue, allocating the CPU to each process for a time interval of up to 1 time quantum.

To implement RR scheduling, we keep the ready queue as a FIFO queue of processes. New processes are added to the tail of the ready queue. The CPU scheduler picks the first process from the ready queue, sets a timer to interrupt after 1 time quantum, and dispatches the process.

The CPU scheduler will then select the next process in the ready queue.

Table 1: Schedule table

Process	Burst Time
P1	24
P2	3
P3	3

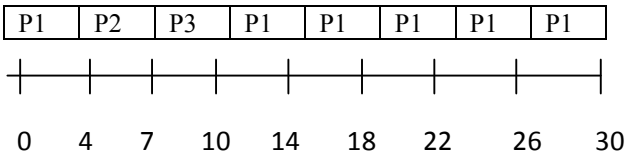

Fig 2: Schedule sequence

If we use a time quantum of 4 milliseconds, then process Pi gets the first 4 milliseconds. Since it requires another 20 milliseconds, it is preempted after the first time quantum, and the CPU is given to the next process in the queue, process P2. Since process Pi does not need 4 milliseconds, it quits before its time quantum expires. The CPU is then given to the next process, process P3. Once each process has received 1 time quantum, the CPU is returned to process Pi for an additional time quantum. The resulting RR schedule is

P1 P2 P3 P1 P1 P1 P1 P1

The average waiting time is 17/3 = 5.66 milliseconds.

3.1.1 IMPLEMENTATION of RR

As I have implemented Round robin algorithm this portion shows its experimental result and performance.

Experimental Result:

The total no of process = 9.

The sequence of process=1, 2, 3, 4, 5, 6, 7, 8, 9.

The time quantum=9

Table 2: Schedule chart of RR

Process sequence	Burst time(ms)	Waiting Time(ms)	Turnaround Time(ms)
1	9	0	9

2	4	9	13
3	7	13	20
4	3	20	23
5	8	23	31
6	5	31	36
7	2	36	38
8	1	38	39
9	6	39	45

Table 3: Schedule chart RR

Average Waiting Time (ms)	Average Turnaround Time (ms)
23.222221	28.222221

3.2 GENETIC ALGORITHM

There are mainly three genetic operators. They are

1. Reproduction or Selection
2. Crossover
3. Mutation

To perform the crossover operation we have used the 2- point crossover. That is like that…

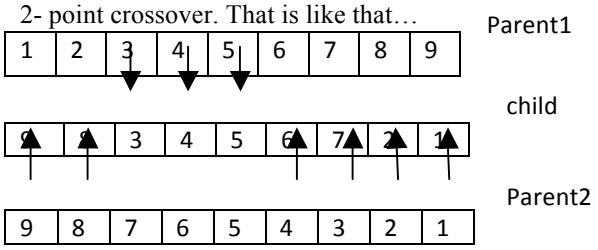

3.2.1 Flow chart of GA:

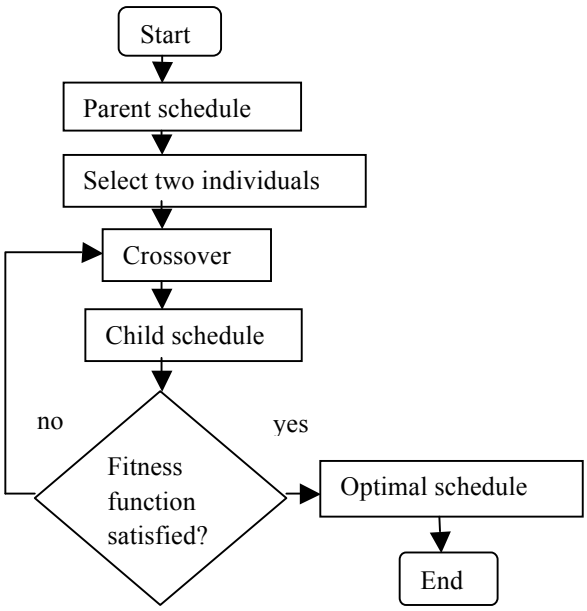

3.2.1

Fig 3. Flow chart of GA

IMPLEMENTATION of GA

Following tables shows the result of Genetic Algorithm for the same no. of process & same time quantum as in Round Robin.

Table 4: Schedule chart of GA

Process sequence	Burst time(ms)	Waiting Time(ms)	Turnaround Time(ms)
1	9	0	6
2	4	6	7
3	7	7	9
4	3	9	12
5	8	12	20
6	5	20	25
7	2	25	32
8	1	32	36
9	6	36	45

Table 5: Average Schedule chart GA

Average Waiting Time(ms)	Average Turnaround Time(ms)
16.333334	21.333334

The optimal schedule is =9, 8, 7, 4, 5, 6, 3, 2, 1

As we have applied Genetic Algorithm so the more we perform crossover operation the more we get the optimal solution of schedule.

The above optimal schedule is found after 100 crossover operation.

3. PERFORMANCE COMPARISON

Table 6: Performance comparison table of RR and GA

No. of pro-cess	Genetic Algorithm		Round Robin Algorithm	
	Average Waiting Time(ms)	Average Turnaround Time(ms)	Average Waiting Time(ms)	Average Turnaround Time (ms)
10	28.900000	34.500000	41.299999	42.900002
15	46.400002	51.799999	59.066666	60.466667
20	70.750000	71.800003	81.650002	88.699997
25	91.440002	98.160004	99.000000	111.720001
30	144.199997	156.63333	154.39999	167.833328
35	189.8285	203.171432	202.988888	223.271432

4.1 Graphical Representation of process versus waiting time

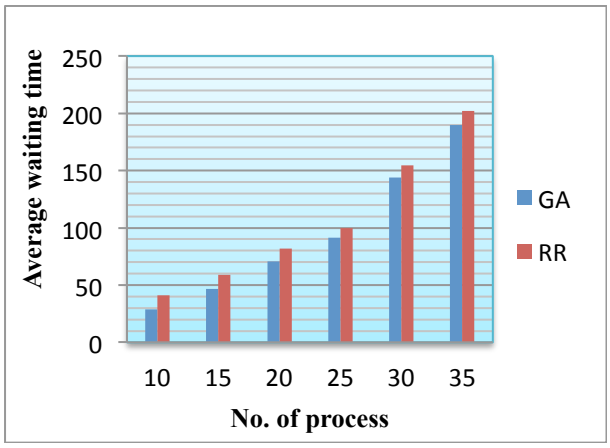

Fig. 4: Performance comparison of waiting time between RR and GA

In the above figure the red pillar represents the waiting time of Round Robin algorithm and the blue pillar represents the waiting time of Genetic algorithm. From the figure we can easily see that the Round Robin algorithm takes large time to schedule and allow to get services a same amount of process in a machine than Genetic algorithm. So the waiting time of each process has increased in Round Robin algorithm than the Genetic algorithm. If it takes less time to complete a task then it will be better for scheduling jobs because the next process will have to wait for a little time. So due to having less waiting time, we can understand the Genetic algorithm is better than Round Robin algorithm in case of job shop scheduling.

4.2 Graphical Representation of process versus turnaround time

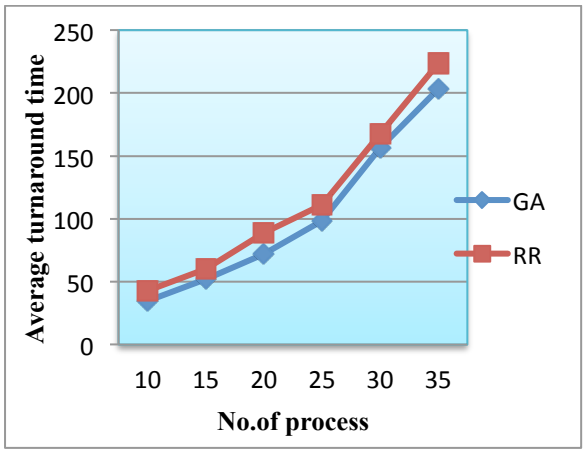

Fig. 5: performance comparison of turnaround time between RR and GA

In the above figure the red curve represents the turnaround time of Round Robin algorithm and the blue curve represents the turnaround time of Genetic algorithm. From the figure we can easily see that the Round Robin algorithm takes large time to schedule than Genetic algorithm for the same set of processes. So in case of turnaround time for each process set Round Robin algorithm uses large time to schedule than the Genetic algorithm. If it takes less time to complete a task then it will be better for scheduling jobs because good scheduling depends on the small size of the turnaround time. So for the less turnaround time, we can understand the Genetic algorithm is better than Round Robin algorithm in case of job shop scheduling.

5. SUMMERY AND CONCLUSION:

In this thesis paper we have used two algorithms, Round Robin algorithm and Genetic algorithm, in order to schedule job shop. We have also analyzed the performance of those two algorithms in case of turnaround time and waiting time. Our experimental result shows that the Genetic algorithm is better than Round Robin algorithm for both waiting time and turnaround time. Because Genetic algorithm can find out result through its operators from a huge search space comparing the result with the fitness function. The fitness value for this thesis is the summation of turnaround time and waiting time.

The GA may be very useful for real world scheduling problems because of simplification based on hybridization of GA and existing algorithm and creative evolution procedure.

REFERENCES:

[1]. Pinedo, M., "Scheduling Theory, Algorithms, and Systems", Prentice Hall, Second Edition, 2002.

[2]. Pinedo, M., "Scheduling: Theory,Algorithms, and Systems", Prentice-Hall, New York, 2001.

[3]. Baker, K.R., "Introduction to Sequencing and Scheduling", Wiley and Sons, New York, 1974.

[4]. Silver, E. A., Pyke, D. F., Peterson, R., "Inventory Management and Production Planning and Scheduling Management", John Wiley & sons, USA, 1998.

[5]. Hopp, W. J., Spareman, M. L., "Factory Physics Foundation of Manufacturing Management", McGraw-Hill, Singapore. Vol. lll, pp. 30-33, 2001.

[6]. Panneerselvam, R., Production and Operation Management, Prentice Hall, New Delhi, India, 2006.

Proceeding of the
International Conference on Electrical, Computer and Telecommunication Engineering
01- 02 December 2012 (ICECTE2012), RUET, Rajshahi-6204, Bangladesh

ICECTE2012: PI-0166

Fuzzy based Risk Identifier for Electronic Procurement Process

Md. Ashek-Al-Aziz, Abdullahil Azeem
Department of Industrial and Production Engineering
Bangladesh University of Engineering and Technology (BUET), Dhaka, Bangladesh
E-mail: md_ashek@yahoo.com, azeem@ipe.buet.ac.bd

ABSTRACT

RISK IDENTIFIER IS A VITAL FUNCTION FOR ELECTRONIC PROCUREMENT SYSTEM. TO AVOID RISK POTENTIALITIES, A FUZZY BASED KNOWLEDGE BASE IS DEVELOPED WHICH PROVIDES RISK MESSAGES TO USERS TO MITIGATE THE RISK IN THE CORRESPONDING AREA OF RISK ATTRIBUTES DEFINED AND AN ACCEPTABLE VULNARABLITY IS PROVIDED TO USERS THROGUH ALGORITHM EXECUTION. FUZZY MULTIPLE CRITERIA DECISION MAKING AND RISK MITIGATION ALGORITHM IS THE KEY STRENGTH FOR THE NEWLY DEVELOPED SYSTEM MODEL OF RISK REMOVAL.

KEY WORDS: Fuzzy Pair wise decision matrix, Risk Identifier, Risk Mitigation Algorithm.

1. INTRODUCTION

All procurement processes go through an uncertainty until it reaches at the final success of receiving procuring item or services and after that post procurement functions end. The aim of this research was to develop a fuzzy based model that allows evaluators to assess any particular case of procurement and risk level is identified with the help of a risk scale and also to mitigate the risk providing messages to users of this system from a knowledge base. The objective is to formulate the mathematical foundation and algorithm to incorporate proposed model of risk identifier and to illustrate the newly designed model with mathematical illustration to demonstrate the implementation.

2. BACKGROUD

In the practice of procurement, an unbiased consensus decision is a mandetory requirement for efficient procurement reducing unexceptability and uncertainity. A software based risk mitigation system has been presented by Raymond J. Madachy(1995) that generates decision from a knowledge base getting weightage factors and ratings given by Dicision Makers using the software. The model was developed based on COCOMO which is known as software cost estimation model[1]. Though the technique is quite preferable for automated procurement decisions and its risk mitigation, its determinants are needed to be revised for application in all general procurement cases and build mathematical model with fuzzy logic.

3. e-PROCUREMENT RISK IDENTIFIER MODEL

Risk assessor and cost estimator, the primary tool to predict the chance of success and failure of any project, to minimize the failure chance mitigating the problem factors to maximize success potentiality, a new approach of fuzzy based risk derivation through proper quantification and mathematical foundation is introduced in this section. The generalized procurement Risk attributes are identified in Table 1.

Category	Description of Attributes
Product or Service Attributes	Required product or service reliability (RELY)
	Required product volume or service duration (DURN)
	Product complexity or service (CPLX)
Customer Attributes	Product complementary infrastructure (CPIS)
	Customer skills, knowhow and adaptability (CADP)
Personnel Attributes	Service Providers or consultants or bidders capability (SCAP)
	Workforce size (WSZE)
	Workforce skills (WSKL)
	Service experience (SEXP)
Project Attributes	Use of modern technologies (UMTG)
	Required supply or service schedule (SCED)
Process Attributes	Process experience (PMEX)
	Process documentation thoroughness (PDTH)
	Risk eliminated by rules and regulations (RISK)
	Requirements volatility (RVOL)

Table 1: Generalized e-Procurement Risk Attributes

The above 15 Risk attributes are rated by grading scale mentioned in Table 2 by the Decision Makers. The calculated risk is described by Risk Value (*Rv*) of Table 3 and calculated by using eq (1), eq (2) and eq (3).

$f(x_i, x_j)$	Risk/Maturity weight of x_i with respect to x_j
1	Low Risk
3	Moderate Risk
5	High Risk
7	Very High Risk
9	Extra High Risk
2,4,6,8	Intermediate values between above levels

Table 2: Suggested numbers for risk rating

Risk Value *(Rv)*	**Risk Description**
00.000~03.000	Very Low Risk
03.001~06.000	Low Risk
06.001~09.000	Moderate Risk
09.001~12.000	High Risk
12.001~15.000	Very High Risk

Table 3: Risk Scale

At the time of rating by the Decision Makers, their assessments are quantified in two dimensional fuzzy matrixes which form 210 knowledge predictors which are to be used for messaging the risk location and purpose to mitigate the respective area going towards risk free condition for procurement execution according to Algorithm 1. Following formula mentioned in George J. Klir[2] will do first normalization of fuzzy variable input as weight values for generalized risk attributes of procurement.

$$f(x_i, x_j) = \frac{f(x_i, x_j)}{\max[f(x_i, x_j), f(x_j, x_i)]} \ldots \textbf{eq (1)}$$

$$f^{/}(x_k) = \min(X_i) \ldots\ldots\ldots\ldots\ldots\ldots\ldots \textbf{eq (2)}$$

where k = 1 to 15 and X=generalized risk/maturity attributes

The total risk value of risk indicator will be calculated using following formula,

$$Rv = \sum_{k=1}^{15} f^{/}(X_k) \ldots\ldots\ldots\ldots\ldots\ldots\ldots\ldots \textbf{eq (3)}$$

4. ILLUSTRATIVE EXAMPLE

15 generalized risk attributes in 5 categories are defined in Table 1. These risk attributes have been rated in fuzzy pair wise comparison matrix in Table 5 which is further normalized in Table 6 by using eq (1) and later values of 15 different risk attributes have been determined with their respective risk levels by using eq (2) which are then added together to determine the value of *Rv*. The values of risk levels are summarized in Table 4 for fuzzy rating in Table 5.

Category	**Attributes**	**Risk Level**
Product or Service	RELY	0.33
	DURN	0.429
	CPLX	0.33
Customer	CPIS	0.33
	CADP	0.11
Personnel	SCAP	0.11
	WSZE	0.11
	WSKL	0.11
	SEXP	0.2
Project	UMTG	0.6
	SCED	0.33
Process	PMEX	0.143
	PDTH	0.2
	RISK	0.429
	RVOL	0.11
		Rv = 3.87 (Low Risk)

Table 4: Calculation of Risk Value

Step 1: if $f^{/}(X_k)$ has more than zero rows then Select: Attribute (max[$f^{/}(X_k)$]) else goto Step5

Step 2: if (max[$f^{/}(X_k)$]) > 0.1 then goto Step 3 else goto Step 5

Step 3: Risk Message ← Description (Knowledge Base): Attribute - X_j Where X_j= All other attributes except the selected attribute

Step 4: Resolve the discrepancies, remove row from $f^{/}(X_k)$, goto Step 1

Step 5: Risk mitigated/Insufficient Risk

Algorithm 1: Algorithm for e-Procurement risk mitigation

$f(x_i, x_j)$	RELY	DURN	CPLX	CPIS	CADP	SCAP	WSZE	WSKL
RELY	1	3	7	9	7	9	3	5
DURN	5	1	3	5	5	3	7	5
CPLX	9	5	1	9	9	9	7	9
CPIS	3	3	5	1	1	3	3	5
CADP	9	1	1	1	1	1	3	3
SCAP	5	7	5	3	1	1	7	7

Through the implementation of fuzzy pair wise comparison matrix, a fuzzy based knowledge base is generated by nomenclature of risk attributes pair e.g. RELY-DURN (Reliability with limited duration of supply or service), CPLX-SCED (Optimization of product or job complexity for delivering product or service within tight schedule), UMTG-RVOL (Bidder's usage of modern technology is required to be cope able with any kind of requirement volatility) etc. 210 knowledge atoms have been identified all of which are to be used as risk messages focusing the location where risk exist which is subject to be mitigated. In the execution of risk mitigation algorithm mentioned in Algorithm 1, 16 times of iterations has been found to remove all major risks in this case. In the first iteration, the algorithm generated risk messages are UMTG-RELY, UMTG-DURN, UMTG–CPLX, UMTG–CPIS, UMTG–CADP, UMTG–SCAP, UMTG–WSZE, UMTG–WSKL, UMTG –SEXP**,** UMTG– SCED, UMTG–PMEX, UMTG–PDTH, UMTG–RISK, UMTG–RVOL as highest risk level existence has been noticed for UMTG (Use of modern technologies) is 0.6. After execution of Step 1, Step 2, Step 3 and Step 4 in first iteration, the algorithm is again iterated to loop back at Step 1. Meeting the criteria at Step 1, second iteration goes to Step 2, Step 3 and Step 4 again. The risk messages generated in this iteration are DURN-RELY, DURN-CPLX, DURN-CPIS, DURN-CADP, DURN-SCAP, DURN-WSZE,

DURN-WSKL, DURN-SEXP, DURN-UMTG, DURN-SCED, DURN-PMEX, DURN-PDTH, DURN RISK, DURN-RVOL concentrating on Project Duration main attribute with risk value 0.429. After resolution of risk showed, the algorithm is iterated further for third loop back and so on. The process is iterated for 15 times and then at the sixteenth iteration, the loop is terminated meeting the condition at Step 1. Thus, the procurement risk is mitigated completely and procuring agency can proceed toward bidder selection and other procuring process.

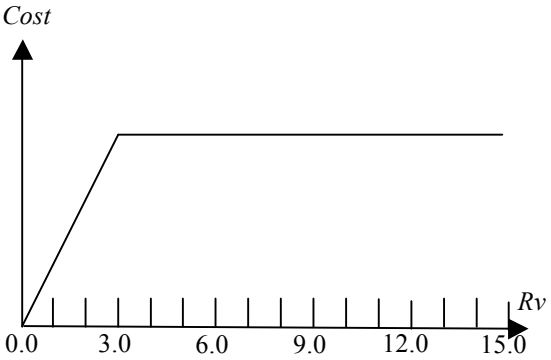

Figure 1: Efficiency of Risk mitigation algorithm

5. CONCLUSIONS

The major disadvantage of Algorithm 1, algorithmic approach for procurement risk mitigation is to remove all risk issues completely from procurement process is given mandatory which may become problematic in a real case where procurement process is needed to be executed with some sort of risk. In such case this model will stuck the whole process until risk is totally removed as it is in the loop of the algorithm. The remedy to this problem is nothing but it is to insert another conditional statement whether to leave the risk value to exist in the procurement process or it is really needed to remove risks and make the process totally risk free before the selection process starts. Moreover, we have devised 210 rules for knowledge base or rule base where all the rules have been used as message for risk definition and its risk potentiality. There could be more accurate knowledge base if attribute pairs are paired further and new knowledge description is determined. Raymond J. Madachy[1] also derived about 210 rules and he separated some of them as suggestions, some as rules and few as useless but we have considered all 210 rules as message to users and risk factor to be mitigated.

6. FUTURE WORK

Reliability measure of proposed e-Procurement risk identifier model is badly necessary before implementation of the proposed model. We encourage assessing the decisions taken in many tendering and procurement cases, samples collected from public and private sectors and feed into this new model, to analyze the deviations including the thorough studies of the risk attributes. Moreover, in the illustrative example, fuzzy rating is shown by one decision maker whereas many decision makers' rating will make the decision result more appropriate. To achieve this fuzzy MCDM with fuzzy TOPSIS with the help of some mathematical techniques could be applied obtaining more sophisticated model. Development of neuro-fuzzy and fuzzy-genetic approach will be an effective way of implication of such a model for better efficiency.

7. ACKNOWLEDGEMENTS

We wish to acknowledge Raymond Madacy that he did a valuable work for software procurement process on which we could have tried to implicate and fit it into general e-Procurement process. We wish some of our friends who have encouraged we to solve the problem. We would also like to thank George J. Klir, Bo Yuan for beautiful illustrations of fuzzy formulations in their book which were very helpful for this work

REFERENCES

[1]. Raymond J. Madachy, "Knowledge-Based Risk Assessment and Cost Estimation", *Automated Software Engineering* Vol 2,No 3, P 219-230, Kluwer Academic Publishers, Boston (1995).

[2]. George J. Klir, Bo Yuan, "Fuzzy Sets and Fuzzy Logic: Theory and Applications", *Prentice-Hall of India Private Limited* (2003)

[3]. S. Rajasekaran, G.A. Vijayalakshmi Pai, "Neural Networks, Fuzzy Logic, and Genetic Algorithms: Synthesis and Applications", *Prentice-Hall of India Private Limited* (2007)

Proceeding of the
International Conference on Electrical, Computer and Telecommunication Engineering
01- 02 December 2012 (ICECTE2012), RUET, Rajshahi-6204, Bangladesh

ICECTE2012: PI-0167

Electrical Energy Harvesting Technique from Speed Breaker

M. E. Hoque[1], M. B. Hossain[2], M. A. Kader[1]
[1]Department of Mechanical Engineering, Rajshahi University of Engineering & Technology, Bangladesh
[2]Department of Power Engineering, Dinajpur Polytechnic Institute, Dinajpur, Bangladesh
E-mail: emdadulhoque@gmail.com, belayet9328@gmail.com

ABSTRACT
The regular activities of the people of developing countries are seriously disrupted by the shortage of power supply. This paper presents the energy harvesting technique from the waste energy of vehicles going up on a speed breaker. The alternative energy will be harvested from the speed breakers that will be very helpful to meet the rising demand. Developing countries like Bangladesh has a serious crisis of power generation where oil and gas supply is very limited to produce electricity, and nuclear power is also uncertain.Therefore harvesting energy from unconventional sources will be a reliable source of energy and can provide the necessary amount of clean energy for climate stabilization and reduce the consumption of fossil fuel.

KEY WORDS: Energy harvesting, energy from speed breaker, unconventional energy sources, electro-mechanical system.

1. INTRODUCTION

In today's world with the increasing population, the world's energy needs are growing steadily and the crisis for power is also increasing. Conventional energy resources are not good enough to meet up the energy demand of vast population and there is incessant depletion of fossil fuel. Most of the people depend on traditional energy sources, which are very confined and have environmental imperilment. The superior alternative for meet up the challenge of energy crisis is renewable energy and some unconventional sources of energy which can be replenished again and again.

The hunger for energy of the world is growing year by year. The energy consumption of recent and future years is shown in Fig. 1 [1].

Energy produced from the conventional sources like coal, natural gas, furnace oil, high speed diesel, etc. are responsible for producing gases like CO_2, NOX, SOX, etc. that causes global warming. Moreover, its sources are consumed much faster than nature can create them. Beside conventional sources of energy, there exist many alternative sources. Alternative energy refers to energy sources which are not based on the

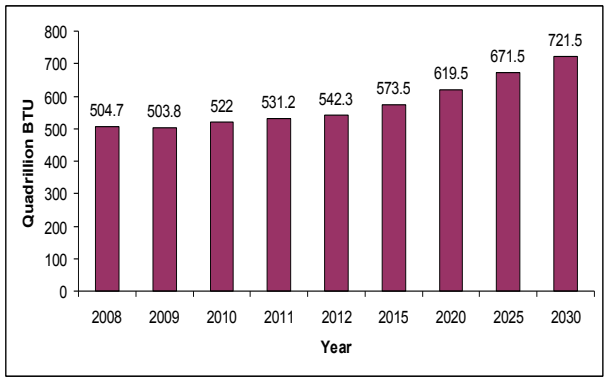

Fig. 1 World energy consumption growth

burning of fossil fuels or the splitting of atoms. The renewed interest in this field of study comes from the undesirable effects of pollution both from burning fossil fuels and from nuclear waste byproducts. Fortunately, there are many means of harnessing energy which have less damaging impacts on our environment. The possible alternatives may be solar, wind power, geothermal, tidal, hydroelectric, etc. The living standard and prosperity of a nation vary with increase in use of power. As technology is advancing, the consumption of power is steadily rising. The energy consumption mix was estimated as: indigenous biomass 60%, indigenous natural gas 27.45%, and imported oil 11.89%, imported coal 0.44% and hydro 0.23% [2]. Bangladesh has one of the lowest per capita energy consumption in the region and about 51% of its 155 million populations have no access to power. The government of Bangladesh has undertaken a master plan under the Vision-2021 to reach electricity facilities to every village of the country. Approximately 48,754 villages out of 87,372 villages have been brought under electricity facilities till April 2011 [3]. Even then, the national power generation capacity is only 4500-4750 MW against a peak demand of 6500 MW. The current rate of increase in consumption is 10% annually [4]. Moreover, per capita power generation is only 236 kWh. The cumulative efforts of exploration for oil and gas resources in Bangladesh has resulted in the discovery of 23 gas fields of various sizes producing 2000 mncft of natural gas . Currently, from our 5 discovered mines, only

Barapukuria coal mine is in operation at this stage. The estimated reserves of coal are close to 3300 million tons, while the proven reserve is about 884 million tones [5]. The scope of hydropower generation is very limited in Bangladesh because of its plain lands, except in some hilly region in the northeast and southeast parts of the country. At present, only 230MW of hydropower is utilized in Karnafuli hydro station through 5 units of Kaplan turbine [6].

In this work, an idea endeavors to show how energy can be trapped from a commonly used system, the road speed breakers. The number of vehicles passing over the speed breaker in roads is increasing day by day. There is possibility of tapping the energy and generating power by making the speed breaker as a power generation unit. Moreover, the useful purpose for these types of generators is as a remote source of small power generation (MW to W range) where access to a fixed grid supply is not available and other options of remote power are less viable (such as solar, batteries, diesel generator, etc.). They could actually light up small villages off the highway. An amateur innovator in Guwahati has developed a simple contraption that can generate power when a vehicle passes over a speed breaker. The innovation has caught the eye of the Indian Institute of Technology (IIT), Guwahati, which will fund a pilot project to generate electricity from speed-breakers. IIT Guwahati has evaluated the machine and recommended it to the Assam ministry of power for large scale funding. A K Das, a professor at IIT's design department says it is a 'very viable proposition' to harness thousands of mega watts of electricity untapped across the country every day [7]. A survey has been conducted about electricity consumption from Tamil Nadu electricity board website. It says that the amount of electricity consumed in one night by all the street lights around Chennai city is equal to consumption of electricity in a remote village for one month and 14 days. This survey inspired us a lot and made us to think about saving this wasted power, which made us introduce this new technique [8].

In this work , a small- scale speed breaker model is developed using mild steel plate. Experiments are carried out to measure the power generated from the speed breaker.

2. EXPERIMENTAL SET UP

In this project, a prototype is shown in Fig. 2 and Fig. 3 have been prepared comprising flexible speed breaker, flexible sheet, compression spring, wooden block, rack and pinion gear, spur gear, generator and battery to store power. When the vehicle moves over the speed breaker, it comes down resulting the compression of spring and the rack moves downwards. A small pinion coupled with a big gear is meshed with the rack.

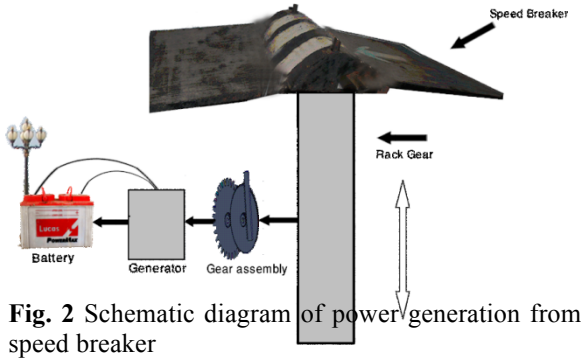

Fig. 2 Schematic diagram of power generation from speed breaker

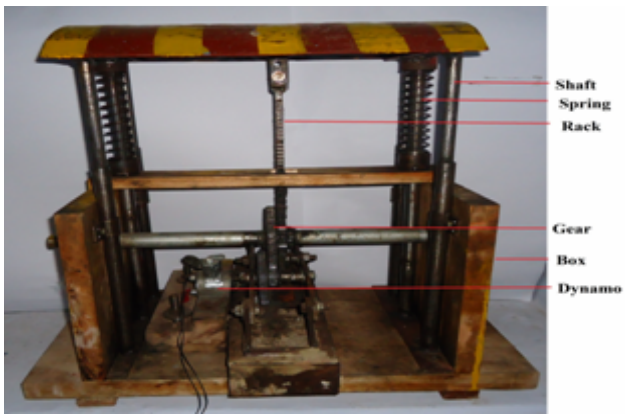

Fig. 3 A typical energy harvester from speed breaker

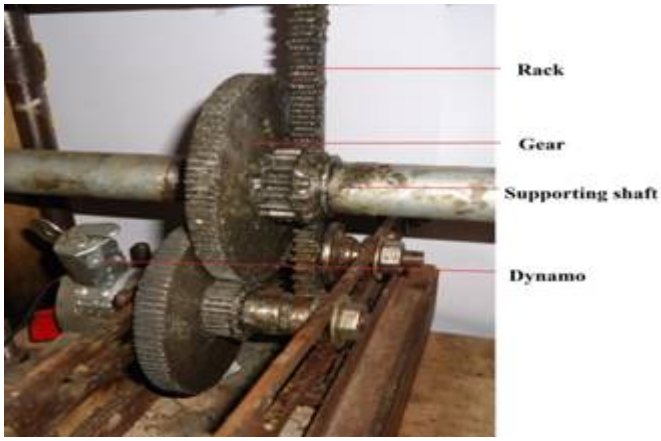

Fig. 4 Different Gear Assembly of Fig. 3

The downward motion of the rack causes the rotation of the pinion, which is transmitted to the big gear. A small pinion is attached to the dynamo shaft which is mashed with the big gear. The rotation of the big gear is now transferred to the dynamo shaft and the

kinetic energy is converted into electricity. Due to the use of different gear ratio, the linear movement of the rack is increased step by step and finally, the speed of the dynamo shaft becomes about 30 times to the rack speed. This electricity is stored in a rechargeable battery. Then the output of the battery is used to lighten the street lamps on the road. As during daytime, electricity is not required for lightening the street lamps, so a control switch is incorporated in order to automatic control of electricity output. The control switch is connected by wire to the output of the battery. The control switch has ON/OFF mechanism, which allows the current to flow when considered necessary.

3. WORKING PRINCIPLE

A vehicle has certain weight. The speed breaker arrangement is made in such a way that the speed breaker can move up and down. There is spring arrangement which makes this up and downward movement possible. When vehicles pass over this speed breaker, a linear motion is obtained to the speed breaker from the pressure load of vehicle. A picture of the speed breaker arrangement of this type shown in Fig. 2. A rack gear is attached under the speed breaker. Since the rack has teeth connected to gears, there exists conversion of reciprocating motion of rack into rotary motion of gears which is transferred to another gear. The downward motion of the rack helps to rotate the gear. The motion of the shaft is normally of lower speed. So it is needed to make it higher speed. Gear box is used to get higher speed of the shaft. This rotational speed is used to rotate the rotor of generator. Thus, power is generated in the generator. The generator used an A.C. bridge rectifiers to convert the A.C. current into D.C. to store in the battery. Speed breaker comes back its initial position with the aid of spring as soon as it has been liberated from the exerted pressure of vehicle weight.

4. EXPERIMENTAL PROCEDURE

Performance test of the models have been done by making hole in the ground and implant the speed breaker in the ground. Then motor cycle was passing over the speed breaker (Fig. 3). Minimum weight passing over the speed breaker was 170 kg and maximum was 260 kg. Now the reciprocating motion of the rack gear converted into rotational speed by pinion and the motion goes to generator through the gear box. Generator is connected to the multimeter. Voltage, current, RPM and deflection was measured against weight. Power was also measured. Next, a battery was charged by the speed breaker by passing motor cycle.

5. SELECTION OF DYNAMO

Gear box contain two gears and two pinions. $Gear_1$, $pinion_1$, $gear_2$ and $pinion_2$ has 110, 28, 92 and 15 teeth respectively. $Pinion_1$ is meshed with $gear_1$ and coupled with $gear_2$. $Pinion_2$ is meshed with $gear_2$.

We know, $Ng_1 / Np_1 = Tp_1 / Tg_1$ (1)

Where, N = speed of respective gear or pinion

T = number of teeth of respective gear or pinion

If Ng_1 = 1 rpm, then from **Eq. (1),** $Np_1 = 3.92$

Again, $Ng_2 / Np_2 = Tp_2 / Tg_2$ (2)

$Np_1 = Ng_2 = 3.92$

From **Eq. (2),** $Np_2 = 24$

Thus the speed ratio between $gear_1$ and $pinion_2$ is 1: 24

For maximum mass, m = 200kg

rpm of dynamo = 150

Then, rpm of gear mesh with rack = 16.67

Height of deflection, r = 0.04m

Torque (T) = Force (F) × Radius (r)

$= m \times g \times r$

$= 200 \times 9.8 \times 0.04$

$= 78.4$ Nm

Input power = torque × angular velocity

$= 78.4 \times (2 \times 3.14 \times 16.67/60)$

$= 136.79$W

Considering various loss such as friction loss

Let, efficiency = 50%

Output power = 68.39W

For this, a dynamo can be chosen of maximum power output 68.4 W. But due to unavailability in the market we used 24V and 25W A.C dynamo.

6. RESULT AND DISCUSSION

The maximum input power was 16.75 watt and output power was 16.75 watt for 10 cm height. The power, Voltage, current, deflection, RPM depends upon weight of the vehicle passing over the speed breaker. Figure 5 shows the load versus voltage characteristics of the speed breaker model. It shows the increase of voltage with the increase of load. It was almost linearly increasing with change of load. Load was given by running a motorcycle and variation of man and some additional loads.

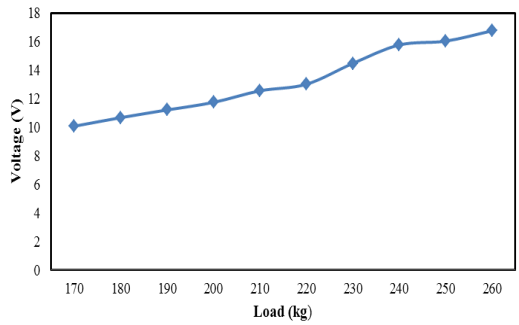

Fig. 5 Load vs. voltage characteristics

Figure 6 shows the load versus current characteristics of the speed breaker model. It shows the increase of current with the increase of load. It was also almost linearly increasing with change of load.

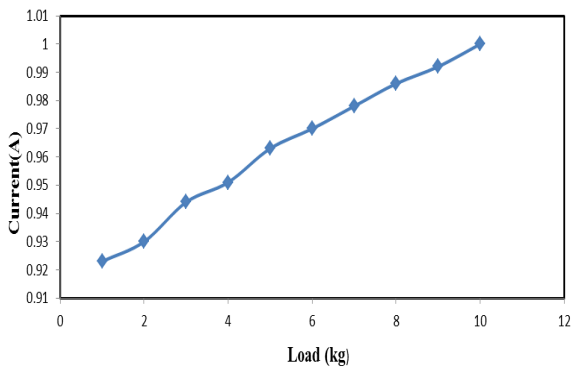

Fig. 6 Load vs. current characteristics

Fig. 7 shows the variation of voltage when a motor cycle passing over the speed breaker. Here is three consecutive passing of motor cycle with same load.

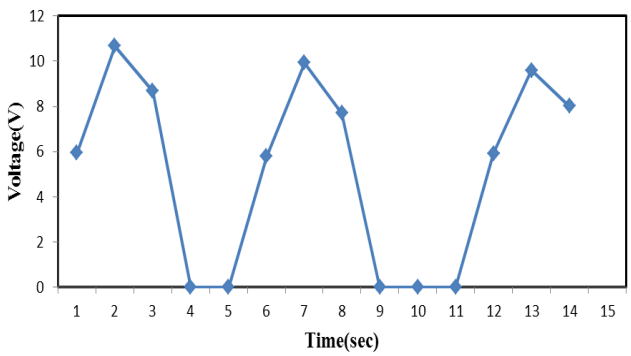

Fig. 7 Time vs. voltage characteristics

7. CONCLUSIONS

In this world where there is shortage of electrical power supply, this project will be helpful to solve the power crisis to some extent. This project has some advantages such as; it is economical and easy to install, free from all types of pollutions as well as low maintenance cost. A speed breaker power generator prototype has been designed, built and experimentally tested. The generator relies on the use of different gear combination to harness power from the speed breaker. This concept is quite promising due to its good efficiency as well as energy recovery criteria.

8. FUTURE WORK

For professional use of the system, some electronics improvement is needed such as voltage control. For smooth charging a battery is needed a constant voltage output. To ensure constant voltage output a voltage stabilizer can be applied before the battery or load.

9. ACKNOWLEDGEMENTS

Authors express cordial thanks to Dr. Mohd. Rafiqul Alam Beg, Dr. Md. Nurun Nabi, Dr. Mohammad Rofiqul Islam, Dr. Nirendra Nath Mustafi, Department of Mechanical Engineering, for their constructive advice and NOVARA Technical School, Dinajpur for their kind co-operation for fabricating and developing the physical models.

REFERENCES

[1]. http://www.eia.gov/forecasts/ieo_table.cfm, Energy Information Administration, 19 September 2012, “International Energy Outlook 2011: World total energy consumption by region and fuel”.

[2]. M. R. Islam, M.R. Islam, M. R. A. Beg, "A Renewable Energy Resources and Techniques Practice in Bangladesh", Renewable and Sustainable Energy reviews, 12, 299-343, 2008.

[3]. Rural Electrification Board (REB) www.bangladeshgov.org (accessed on 12.6.07)

[4]. A. Hossain, O. Badr, "Prospect of Renewable Energy Utilization for Electricity Generation in Bangladesh", Renewable and Sustainable Energy Reviews 11, 1617-1649, 2007.

[5]. Petrobangla, 2010, Bangladesh

[6]. M. Rahman, "Executive Board Report at the 15th Council of ICC", B, 2010.

[7]. http://wiki.answers.com/(accessed on 20.6.2011)

[8]. www.tneb.gov.in (accessed on 20.06.2011)

[9]. Road and Highway Department, www.rhd.gov.bd (accessed on 25.04.2012)

[10]. www.brta.gov.bd (accessed on 02.05.2012)

Proceeding of the
International Conference on Electrical, Computer and Telecommunication Engineering
01- 02 December 2012 (ICECTE2012), RUET, Rajshahi-6204, Bangladesh

ICECTE2012: PI-0168

Generation of Electric Energy from Municipal Solid Wastes in the area of Rajshahi City Corporation

Mohammad Iqbal Hossain[1], M. R. I. Sheikh[2]
[1]EEE Department, Rajshahi University of Engineering and Technology
[2]Professor of EEE Department, Rajshahi University of Engineerig and Technology
iqbal_liku@yahoo.com, ris_ruet@yahoo.com

ABSTRACT
The global electrical power demand is steadily increasing. The absolute dependence of conventional energy resources such as oil, coal or natural gas to meet this demand is problematic for many reasons. The rising and unstable prices for fossil fuels and for some nations energy security is considered as indispensable part of the national security. Therefore, renewable energy technologies have been playing a key role in the worldwide electrical power production. Among renewable municipal solid wastes energy is the fastest growing, however world has abundant amount of usable municipal solid wastes energy which has not been utilized. This paper discuss about municipal solid wastes energy and then it covers essential topics about generation of electric energy from municipal solid wastes systems such as steam generation system, wastes energy power output, mechanical power extracted from municipal solid wastes. Finally it was design municipal solid wastes to power system and show how amount of power is outputted.

KEY WORDS: Municipal solid waste, alternative source of electricity, waste and energy, Matlab, pyrolysis.

1. INTRODUCTION

Bangladesh is one of the densely populated country, Now about 15.5 crore people lives in this country. And the population will be about 17 crore by 2020. Municipal solid waste is a serious environmental hazard and social problem in Bangladesh. A massive volume of solid waste is generated every day in the city areas and unfortunately solid waste management is being deteriorated day by day. Here in Bangladesh, in most cases wastes are disposed of only by land filling. While, there is a great opportunity of producing energy like as well as electricity. In many parts of the world, solid waste is used to produce electric power via incineration or gasification of the fuel, or through landfill methane capture, and much research has focused on waste-to energy solutions. Now one of the best technology is pyrolysis, where there reduce generate green house gas. Thermal treatment may reduce the waste volume up to 90%, this simultaneously could address two problems: disposal of solid waste and generation of electricity. Bangladesh's installed electric generation capacity was 4.7 GW in 2009; only three-fourth of which is considered to be 'available' (Energy Bangla, 2010; The New Nation, 2010). Only 30 percent people of the population of Bangladesh has access to electricity and frequent load shedding disrupts the whole economy of the country. There are some mega-cities in Bangladesh namely Dhaka, Chittagong, Rajshahi, Khulna, Barisal, Rangpur, Sylhet etc. produce a huge amount of solid waste every day which are only disposed by land filling. The technologies for recovery of energy from wastes can play a vital role in mitigating the problems. At present there are 522 urban centers in the country including 254 pourashavas and 6 City Corporations, generate about 13,332 tonnes of solid wastes per day and it will be about 47000 tons/day by 2025. Rajshahi City Corporation is one of the second biggest densely populated cities in Bangladesh.

2. A BRIEF ON RAJSHAHI CITY CORPORATION (RCC)

Rajshahi City is located in the north west of Bangladesh bordering India to the south. Rajshahi City Corporation (RCC), which was formed in 1987, covers an area of approximately of 96.69 square km (37.33 sq mi) being. There are a number of schools, colleges, universities etc. having a population of 1 million. The city generates approximately 400 tones of solid waste/day. Of the total, only 70% are collected and dumped into the open dumping ground, the remaining 30-40% of waste are dumped straight into drains, water bodies and open spaces. There are 30 wards in RCC, only 13 wards are covered by 'door to door waste collection' facilities. RCC has only one dumping site (3.5 feet deep in 15.98 acre

area) and 35 secondary collection points. The waste is only used as a land filling material which is now being a burden for RCC and will create a great problem for the next generation. Still, there is no electricity generation unit has been set up in Rajshahi as a result the city dwellers are often facing acute load-shedding and erratic power supply. Due to frequent load shedding, mills and factories are experiencing setback (The Daily Independent, 2010). Power Development Board can supply only 25 megawatts of electricity against the demand of 65MW and the sales of instant power supply appliances have sharply increased on its outskirts against the backdrop of severe load-shedding Now, the alternative source of power generation has become a crucial demand.

3. OBJECTIVE OF THE STUDY

1. To identify how much waste is produced per capita per day and determining how suitable it is for energy production.
2. To determine the amount of energy produced by the incineration process.
3. How much energy can be produced to convert it into electricity and the total possible electric energy is calculated here.

3.1. Field Protocol

The preliminary survey was conducted to 5 representative wards of RCC which has different waste generation sources such as domestic, commercial, street sweeping, industrial, clinical etc. The commercial establishments were categorized as wet market, shopping complex, hotel, restaurant, educational institutions and others. In industrial and clinical areas husking mill, saw mill, garments factory, pharmaceuticals, hospitals, diagnostic centre were selected. The daily average generation rate per capita in each source was evaluated. A total 150 MSW sample from different source were collected to determine the waste composition in RCC.

3.2. Laboratory Protocol

The weight of the collected waste samples were measured in the laboratory of Local Government Engineering Department (LGED), Bangladesh and then transported to the designated shed for sorting. Firstly the waste generated per capita per day in RCC is calculated . Secondly the MSW was categorized in to six typical categories Domestic waste Street sweeping Commercial including market waste Industrial waste Clinical waste Others. Then the composition was categorized into ten major categories as Organic material; Food / vegetable waste, Paper product, Garden waste, Polyethylene, Plastic / Rubber, Wood, Textiles, Leather, Glass and Inorganic material.

4. ANALYSIS OF ELECTRICITY GENERATION

For the analysis of electricity generation Dulong`s formula is used. The principal products of anaerobic decomposition are methane and carbon dioxide; ammonia, hydrogen sulfide and mercaptans (sulfonated hydrocarbons) are also generated (Themelis & Kim, 2002). The percentages of carbon hydrogen oxygen and nitrogen or sulfur in different constituents of the waste are shown in Table 1.

Table 1: Ultimate analysis of "Dry Stream" component of MSW

Component of waste stream	% weight				
	C	H	O	N	S
Food/Vegetable waste	46.5	43	42.8	2.4	0.1
Paper product	43.5	6.0	44.0	0.3	0.2
Garden waste	44.2	5.4	45.6	2.6	0.2
Polyethylene	80.5	14.3	3.2	2.0	-
Plastic/Rubber	60.0	7.2	22.8	-	-
Wood	49.0	6.0	42.7	0.2	0.1
Textile	55.0	6.6	31.2	4.6	0.2
Leather	69.0	9.0	5.8	6.0	0.2
Others	26.3	3.0	2.0	0.5	0.2

Source: Adapted from Themelis & Kim, 2002.

The above values may not be so accurate for RCC except vegetable and garden waste these values will not change a large. Therefore the components of MSW from the analysis of Themelis and Kim could be used in case of analyzing the MSW of RCC.

Table 2: Weight of organic component of MSW per day with respect to moisture content

Organic waste component	% of total	Moisture content (%)	Moist mass (ton)	Dry mass (ton)
Food/vegetable waste	88.68	64	266.04	95.77
Paper product	3.27	07	9081	9.12
Garden waste	1.83	48	5.49	2.86
Polyethylene	1.95	04	5.85	5.65
Plastic/rubber	0.85	02	2.55	2.50
Wood	0.02	12	0.06	0.05
Textiles	1.11	14	3.33	2.86
Leather	0.04	07	0.12	0.11

Again, for determining the approximate chemical formula for dry combustibles and percentage

composition of carbon, hydrogen, nitrogen and sulfur, table 1 is reviewed.

Table 3: Chemical composition of waste fraction in RCC

Organic waste component	Dry mass (ton)	% weight				
		C	H	O	N	S
Food/vegetable waste	95.77	46.5	7.3	39.8	2.4	0.1
Paper product	9.123	43.5	6.0	44.0	0.3	0.2
Garden waste	2.86	44.2	5.4	45.6	2.6	0.2
Polyethylene	5.65	80.5	14.3	3.2	2.0	-
Plastic/rubber	2.50	60.0	7.2	22.8	-	-
Wood	0.053	49.0	6.0	42.7	0.2	0.1
Textiles	2.86	55.0	6.6	31.2	4.6	0.2
Leather	0.11	69.0	9.0	5.8	6.0	0.2
Others	3.69	26.3	3.0	2.0	0.5	0.2
Tons per day	113.49	58.45	8.99	46.046	2.67	.1329
% composition		51.50	7.92	40.57	2.35	.1171
Atomic Weight (kg/kmol):		12.01	1.01	16.00	14.01	32.07
No. of Mmol/day:		4.86	8.90	2.87	0.19	~0.0
Number of atoms		6	10.98	3.54	0.23	~0.0
Source: Author, 2010						
Approximate chemical formula of "dry" combustibles: $C_6H_{10.98}O_{3.54}$						

(1ton=1000Kg
C=Carbon, **H**=Hydrogen, **O**=Oxygen, **N**=Nitrogen, **S**=Sulfur)

The heat released from combustion of solid wastes is partly stored in the combustion products (gases and ash) and partly transferred by convection, conduction, and radiation to the incinerator walls and to incoming waste. The energy content of the waste can be estimated using the modified **Dulong Equation** or the heating value of individual waste components.

Modified Dulong's Equation:

Heat (KJ/kg) = 337C + 1428 (H – O/8) + 9S

Where,
C = Carbon (%)
H = Hydrogen (%)
O = Oxygen (%)
S = Sulfur (%)

∴ **Heat (KJ/kg)** = 337 * 0.515 + 1428 (0.0792 – 0.4057/8) + 9* 0.1171
= **215.29 KJ/kg**

∴ **Steam energy available** = 70 % of heat energy
= (0.70 * 215.29) KJ/kg
= 150.703 KJ/kg

∴ **Electric power generation** = Steam energy /11395 KJ/KWh
= (150.703/11395) KWh/kg
= 0.013225 KWh/kg

(Waste generation of RCC=1x0.4x1000000=400000kg/day)

∴ **Total electric power generation =** (0.013225 * 400000) KWh/day
= 5290 KWh/day
= **5.290 MWh/day**

Now,

∴ **Station service allowance** = 6% of electric power generation
= 0.3174 MWh/day

∴ **Unaccounted heat loss** = 5% of electric power generation
= 0.2645 MWh/day

∴ **Net electric power generation** = Electric power generation – (Station service allowance +Unaccounted heat loss)
= 5.290 – (0.3174 + 0.2645)
= 4.7 MWh/day

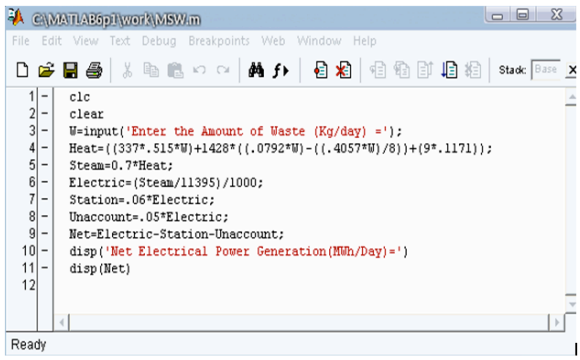

Figure 1: Matlab program

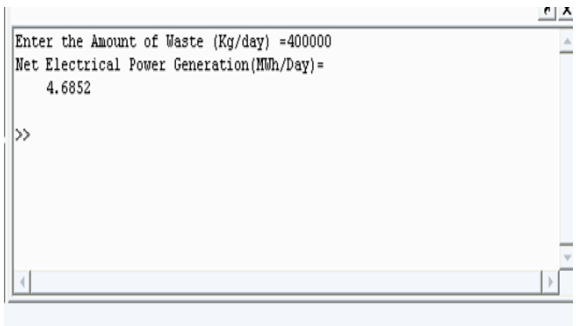

Figure 2: Matlab output file

5. TECHNOLOGY PREFERRED

In contrast to combustion, pyrolysis is the thermal degradation of a substance in the absence of oxygen. This process requires an external heat source to maintain the temperature required. Typically, relatively low temperatures of between 400ºC to 900ºC are used during pyrolysis of materials such as MSW. The products produced from pyrolysing materials are a solid residue and a synthetic gas (syngas). The solid residue (sometimes described as a char) is a combination of non-combustible materials and carbon. The syngas is a mixture of gases (combustible constituents include carbon monoxide, hydrogen, methane and a broad range of other volatile organic compounds). A proportion of these can be condensed to produce oils, waxes and tars. The syngas typically has a net calorific value (NCV) of between 10 and 20 MJ/Nm3. If required, the condensable fraction can be collected by cooling the syngas, potentially for use as a liquid fuel.

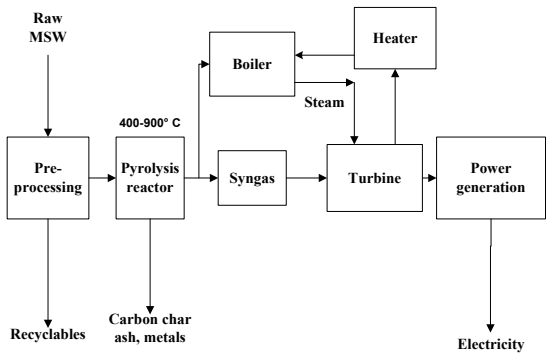

Figure 3: Typical pyrolysis system of electricity generation from MSW

6. FUTURE WORK

Elaborately research on pyrolysis technique to improve electricity about 5 MWh/day. Also we can use solar water heating system for water heating to the boiler.

7. CONCLUSIONS

Waste to energy solves the problem of MSW disposal while recovering the energy from the waste materials with the significant benefits of environmental quality, increasingly accepted as a clean source of energy. Research and technology development focusing on corrosion phenomena, flue gas control, fly ash management and beneficial reuse of residues will further drive the growth of WTE (waste to energy) industry. WTE incineration needs to be implemented to make greater contribution in supplying renewable energy in Bangladesh, while helping solving the country's MSW management problem in the coming decade. The challenge of MSW disposal and the demand for alternative energy resources are common in many developing countries. Experimentally a 5-10 MW power plant may be installed based on the quality and current generation of solid wastes in RCC. It can also be considered as a Waste Management Plan rather than as an Electricity Generation Project as the technology can lead to a substantial reduction in the overall waste quantities requiring final disposal, which can be better managed for safe disposal in a controlled manner while meeting the pollution control standards. In addition, power produced from the WTE activity can reduce the costly natural resources "fossil fuel" utilization in power generation. It is expected that the, experience on the development of WTE in Bangladesh can offer some helpful lessons to other developing counties.

ACKNOWLEDGEMENTS

At last, all the praise is paid to the Almighty, the most kind Allah for keeping us alive, giving us the knowledge to successfully finish our work.
It is pleasure to express our profound gratitude and esteemed regards to Professor Dr. Md. Rafiqul Islam Sheikh, Proffesor and Head of the Department of Electrical and Electronic Engineering, Rajshahi University of Engineering and Technology, who inspired us to undertake the work. His continuous assistance, encouragement, meditative and incentive guidance and valuable suggestions throughout the work period made this work in reality. We are also grateful to our EEE department for supporting to finish the work.

REFERENCES

[1]. Md. Abdur Rouf, *2nd International Conference on Environmental Engineering and Applications 2011,* IPCBEE vol.17 (2011) © (2011) IACSIT Press, Singapore
[2].RCC (Rajshahi City Corporation). (2010). *Rajshahi City Corporation Report-2010*. Rajshahi: RCC.
[3]. http://en.wikipedia.org/wiki/Rajshahi
[4] Clemett, A. Amin, M. M., Ara, S. & Akan, M. M. R. (2006). *Background information for Rajshahi City,Bangladesh.*Stockholm:Stockholm Environment Institute.

[5].Themelis, N. J. & Kim, Y. H. (2002). Material and energy balances in large-scale aerobic bioconversion cell. *Waste Management and Research, 20*, 234-242.
[6].http/www.eastriding.gov.uk/environment/pdf/waste_treatment_technologies.pdf

Proceeding of the
International Conference on Electrical, Computer and Telecommunication Engineering
01- 02 December 2012 (ICECTE2012), RUET, Rajshahi-6204, Bangladesh

ICECTE2012: PI-0169

An Approach to Evaluate Classifiers for Automatic Disease Detection and Classification of Plant Leaf

Md. Nazrul Islam[1], M.A. Kashem[1], Mahmuda Akter[2] and Md. Jamilur Rahman[2]
[1]Department of Computer Science and Engineering, Dhaka University of Engineering and Technology
Gazipur-1700, Bangladesh
[2]Department of Information and Communication Technology, Mawlana Bhasani Science and Technology
University Tangail, Bangladesh
E-mail: nazrul_ruet@yahoo.com, drkashemll@yahoo.com, badhan_mbstu@yahoo.com, zamiljitu@gmail.com

ABSTRACT
This paper is aimed to build an automatic disease detection and classification approach of plant leaf for computer vision based recognition system by evaluating the performance of Genetic Algorithm (GA) and Probabilistic Neural Network (PNN). The leaf disease is classified based on the extracted parameters like threshold, mean, standard deviation, entropy, contrast, correlation, energy and homogeneity which are then used for training of Neural Network. The proposed solution is an improvement to the future extension proposed in [1] with an extra phase named Genetic Algorithm which is based on principles like selection, crossover and mutation. The experimental results demonstrate that the proposed approach is a robust technique to suggest remedial measures for the detection of plant leaves diseases with less computational time than human naked eye. The Genetic Algorithm proposed here showed a more precise classification rate like 97% than Neural Network classification rate like 94.75%.

KEY WORDS: Genetic Algorithm, Leaf Disease Recognition, Texture Features Analysis, Neural Networks.

1. INTRODUCTION

Plant carries significant information for the development of the countries that primarily depend on agriculture in its economy. Successful cultivation of crops depends on identifying plants, leaves, stems and finding out the pest or diseases, percentage of the pest or disease incidence, symptoms of the pest or disease attack [2]. Plant diseases have turned into a dilemma as it can cause significant reduction in both quality and quantity of agricultural products as well as increasing value of total damage. The University of Georgia, College of Agricultural and Environmental Sciences, estimated 2009 plant disease losses in Georgia (USA) is approximately $653.06 million[3]. Of this amount, around $225 million USD was spent on controlling the diseases and the rest is the values of damage caused by the diseases.

Crop productivity can be increased by advising the farmers regarding the treatment of incidence of pest and diseases to their crops and suggestions for control from experts. Sometimes seeking the expert advice is very expensive and time consuming. The proposed approach is aimed to establish an automatic system by evaluating the performance of GA with PNN for vision based disease detection and classification system for some tomato leaf diseases.

The rest of this paper is organized as follows. Sec. 2 discusses background analysis of our present work. Sec. 3 introduces Genetic algorithm. Proposed approach and methodology is discussed in Sec. 4. Sec. 5 briefly describes each individual stages of proposed system. Sec. 6 focuses on implementation procedures. Experimental results and comparison between two approaches are given in Sec. 7. Sec. 8 concludes this paper.

2. BACKGROUND ANALYSIS

In [7], a fast and accurate new method is developed based on computer image processing for grading of plant diseases. For that, leaf region was segmented by using Otsu method. After that the disease spot regions were segmented by using Sobel operator to detect the disease spot edges. Finally, plant diseases are graded by calculating the quotient of disease spot and leaf areas.

The morphological features of leaves are used for plant classification and in the early diagnosis of certain plant diseases. Paper [4] presents design and implementation of an artificial vision system which extracts specific geometric and morphological features from plant leaves. In [5] the performance of conventional multiple regression, artificial neural network (back propagation neural network, generalized regression neural network) and support vector machine (SVM) was compared.

The above Studies showed that Machine learning methods can successfully be applied as an effectual disease detection mechanism. Although a study [2] was done to fit a hybrid methods i.e., multiple classifier with Genetic Algorithm for leaf disease detection, they did not implement it. In [8] better performance in texture-based segmentation can be attained by using Genetic Algorithm but they did not consider statistical texture characteristics of a leaf image. So now we are going to propose an approach which include evolutionary algorithm like Genetic Algorithm to compare the performance with Neural Network classifier by considering all texture features of a leaf image

3. GENETIC ALGORITHM

The genetic algorithm is an optimization technique that mimics biological evolution as a problem-solving strategy. Once an initial population of elements (chromosomes) has been created, the techniques used by this algorithm to converge to a solution of the problem

3.1 Selection

Some chromosomes of the current population are selected to breed a new generation.

3.2 Genetic operations

Once the first chromosomes have been defined by those that fit better the fitness function, the rest of the population is going to be created using genetic operations.

3.3 Mutation

Modifying one or more bits (gens) of some chromosomes of the population.

3.4 Crossover

Crossing two or more chromosomes of the population between them.

3.5 GA Cycle of Reproduction

The cyclic process of Genetic algorithm for reproduction of children is shown in figure 1[6].

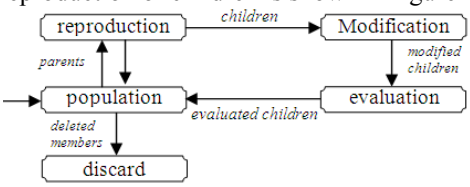

Fig. 1 Cyclic Process of Genetic Algorithm.

3.5.1 Population: Population is represented as Chromosomes such as Bit strings; real numbers;

3.5.2 Reproduction: Parents are selected at random.

3.5.3 Modification: Chromosome modification is stochastically triggered; Operator types are: Mutation, Crossover.

3.5.4 Evaluation: The evaluator decodes a chromosome and assigns it a fitness measure.

4. PROPOSED APPROACH STRUCTURE AND METHODOLOGY

Stage-by-stage activity of our proposed approach structure is shown in Figure 2 is described as below:

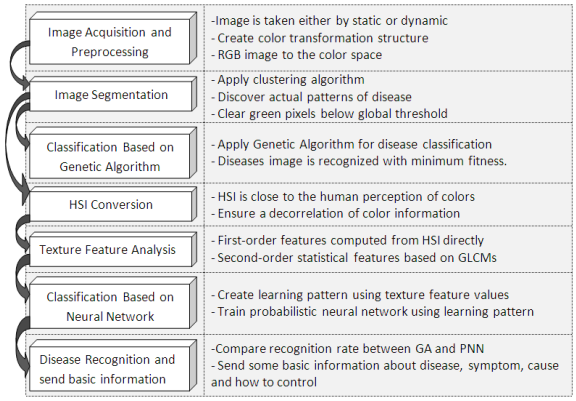

Fig. 2 Proposed approach activity stage-by-stage.

4.1 Stage 1&2: Image Acquisition, Preprocessing and Segmentation

The RGB leaf image can be taken either by static or dynamic are segmented using K-Means clustering technique. Finally, the mostly green pixels have no valuable weight to the disease identification and represent healthy areas in the leave. So we have to cleared them using Otsu's method.

4.2 Stage 3: Classification based on GA

Creation i.e. loads all the learning images.
while (!solution)
(a)Evaluate the fitness of all the chromosomes.
(b) The best chromosomes will be selected to reproduce, using mutation and crossover.
(c) Substitute the worst chromosomes.

This stage is recognized and classified diseased leaf according to minimum fitness primarily.

4.3 Stage 4: HSI Conversion

Infected RGB images of Stage 3 are converted into Hue Saturation Intensity (HSI) color space by Eqs. 1~3 as it close to the human perception of colors.

$$H = \cos^{-1}\left\{\frac{\frac{1}{2}[(R-G)+(R-B)]}{[(R-B)^2+(R-B)(G-B)]^{1/2}}\right\} \quad (1)$$

$$S = 1 - \frac{3}{(R+G+B)}[\min(R,G,B)] \quad (2)$$

$$I = \frac{(R+G+B)}{3} \quad (3)$$

4.4 Stage 5 and onward: Texture Feature Analysis

After completing stage 4, The First-order features computed directly from HSI images as follows:

4.4.1 Mean: It is a measure of brightness,

$$\mu_P = \frac{1}{n^2}\sum_{r=0}^{n-1}\sum_{s=0}^{n-1} P_{r,s}$$

, where $p_{r,s}$ is pixel at location (r,s).

4.4.2 Standard deviation: It is a measure of contrast,

$$\sigma_P = \left[\frac{1}{n^2}\sum_{r=0}^{n-1}\sum_{s=0}^{n-1}\left[P_{r,s}-\mu_P\right]^2\right]^{1/2}$$

4.4.3 Entropy: It is a measure of randomness

$$e = -\sum_{b}^{L-1} P(b)\log_2 P(b)$$

, where $p(b) \approx N(b)/n^2$ for $\{0 \le b \le L-1\}$,

Second-order statistical features based on gray-level co-occurrence matrices (GLCMs) computed for primitive texture cell from HSI image where the size of GLCM is set by the number of gray levels is 8,

and graylimits is set to [ ] to count the minimum and maximum grayscale values in the image as limits, and finally, offset is set to [0 1] to consider neighbors. The features are calculated by follows:

4.4.4 Contrast: sharpness of the structural variations

$$Contrast = \sum_{n=0}^{Ng} n^2 \quad \text{, where} \quad n = \sum_{i=1}^{Ng}\sum_{j=1}^{Ng} P_{i,j}|i-j|$$

Ng = number of gray levels.

4.4.5 Angular second moment measure of uniformity

$$Angular\ Second\ Moment = \sum_i \sum_j P^2 i, j$$

4.4.6 Inverse difference moment: local homogeneity

$$Inverse\ Difference\ Moment = \sum_i \sum_j \frac{1}{1+(i-j)^2} P_{i,j}$$

4.4.7 Correlation: gray-level linear dependency

$$Correlation = \frac{\sum_i \sum_j (i,j) P_{i,j} - \mu^2}{\sigma^2}$$

4.4.8 Homogeneity and Variance

$$Homogeneity = \sum_i \sum_j \frac{P_{i,j}}{1+|i-j|} \qquad Variance = \sum_i \sum_j (i,j) P_{i,j} - \mu^2$$

All texture features with target output class is trained in PNN. After that we evaluate the accuracy of two classification techniques. If both returns the same disease type of unknown disease image, then basic information about disease like name, cause, symptom and how to control is displayed in matlab GUI.

5. IMPLEMENTATION OF OUR PROPOSED APPROACH

5.1 *Samples Leaf Database & Image Segmentation*

The leaf samples used in this paper were collected from camera, mobile, some from Bangladesh Agricultural Research Institute (BARI) database, and

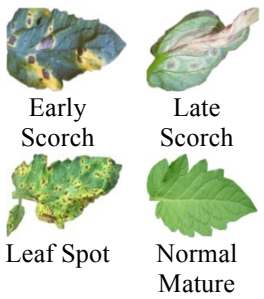

Fig. 3 Sample tomato leaf database.

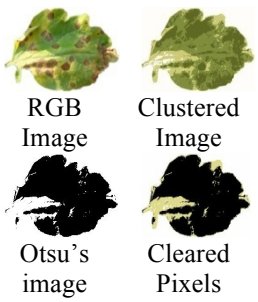

Fig. 4 Image result at stages 1&2.

a few from different websites. Leaves were graded manually into classes by an expert extension agent. Images of leaf samples are shown in Fig. 3. And after implementing stage 1&2 mentioned the previous section we get the images as shown in Fig. 4.

5.2 Classification based on GA

This stage inputs cleared green pixel image of the unknown image from previous stage and return output as any of the learned image on basis of minimum fitness value is shown in figure 5.

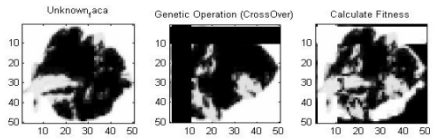

Fig. 5 GA operations on previous stage image.

5.3 Classification based on PNN

The cleared green pixel image is further converted into HSI image as shown in figure 6 for texture feature collection which then will be trained by PNN to recognize an unknown leaf disease image and returns a disease class close to the training classes.

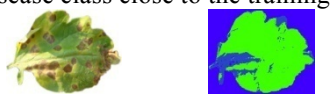

RGB Image HSI Image

Fig. 6 Image result at stage 4.

6. EXPERIMENTAL SETUP AND RESULTS

6.1 User Interface

This work is implemented with MATLAB GUIDE tool and creates a user interface given in figure 7.

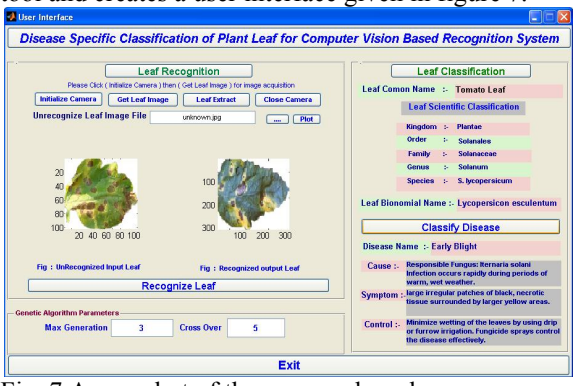

Fig. 7 A snapshot of the proposed work.

6.2 Input Data Preparation

The sample database contains 83 samples of the original RGB leaf images, Cleared green pixel image for GA processing. For Neural Network learning the train file contains 9 rows and 83 columns. Each column had a unique number (1, 2, 3 or 4) which represented the disease class of the particular pattern (or leaf image) of data. "1" for normal matured leaf, "2" for early scorch disease, "3" for late scorch disease and "4" for leaf spot/ tiny whiteness disease. Table 1 showed a sample learned features for PNN.

6.2.1 Data for PNN in this paper

Table 1 Sample learned feature set of leaf diseases

Features	P1	P2	P3	P4
Threshold	0.74902	0.66667	0.74706	0.65882
Mean	0.42797	0.40601	0.30817	0.39406
S.D.	0.07459	0.06012	0.06293	0.06908
Entropy	0.73716	0.98806	0.96914	1.0573
Contrast	0.33204	0.50215	1.9809	0.51035
Correlation	0.97671	0.96432	0.83258	0.96243
Energy	0.36622	0.24339	0.26519	0.31634
Homogeneity	0.98877	0.96981	0.94081	0.97471
Disease Class	1	2	3	4

6.2.2 Data for GA in this paper

A sample of three different leaf diseases with their corresponding disease class is as follows:

tomato1.jpg 2 tomato2.jpg 3 tomato3.jpg 4

When an unknown disease class of a leaf entered as an input, Genetic Operations is performed by setting Maximum Generation and Crossover factor value to 3 and 5 respectively with the learned images. After that the Generation matrix and Fitness function formed as follows for the unknown leaf sample:

Generation =

296304	292786	267370	28406
382375	342909	277426	159769
380117	335472	271722	192958

Min_Fit =

1 884866 2 1162479 3 1180269

Finally, the disease class for the minimum fitness value will be returned as the disease class for the unknown leaf disease.

6.3 Experimental Results

The results for GA classification and PNN classification for testing samples is given in Table 2 and in figure 8. This result is obtained using a GA and NN classifier for different three classes of diseases. In particular, model Genetic Algorithm achieved the highest overall classification accuracy, in which it achieved an overall accuracy of 97% compared to the 94.75% accuracy achieved in PNN.

Table 2 Classification rates of plant leaf diseases

Disease / Model	Early Scorch	Late Scorch	Leaf Spot	Normal	Overall Average
GA	98	94	96	100	97
PNN	94	92	93	100	94.75
GA+PNN	90	92	88	96	91.5

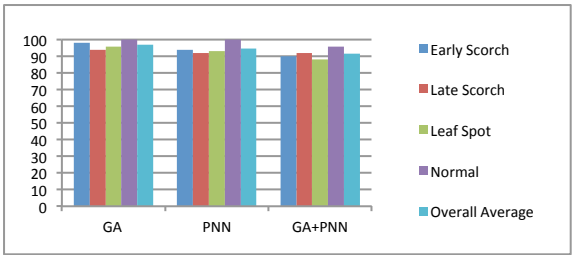

Fig. 8 Percentage of classification of diseases

7. CONCLUSIONS

7.1 Conclusion

The experimental result indicates that the proposed approach is valuable, can significantly evaluate two classifiers GA and PNN to support an accurate detection of leaf diseases in a little computational effort where successful classification rate of GA is more than PNN.

7.2 Limitation

For dynamic image acquisition the recognition rate varies due to background, light and camera position. The learning time for all leaf disease images for GA shows much more than that of PNN. Moreover we need to maintain huge leaf disease database for top level accuracy.

8. FUTURE WORK

This work can be implemented in robotics, AI, HCI and for end farmers. We are working on wavelet based multiple classifier for observing highly optimized algorithm which will reduce learning time as well as increasing classification rate.

REFERENCES

[1]. H. Al-Hiary, S. Bani-Ahmad, M. Reyalat, M. Braik and Z. ALRahamneh. "Fast and Accurate Detection and Classification of Plant Diseases". IJCA Volume 17– No.1, March 2011.

[2]. Jayamala K. Patil , Raj Kumar, "Advanced in Image Processing for Detection of Plant Diseases". Journal of Advanced Bioinformatics Applications and Research. Vol 2, Issue 2, 2011

[3]. Martinez, A., (2009). 2009 Georgia Plant Disease Loss Estimates. http://www.caes.uga.edu/ Publications/pubDetail.cfm?pk_id=7762. Viewed on Saturday, 15, January, 2011.

[4]. Rakesh Kaundal, Amar S Kapoor and Gajendra PS Raghava. "Machine learning techniques in disease forecasting: a case study on rice blast prediction", BMC Bioinformatics 2006.

[5]. Yuan Tian, Chunjiang Zhao, Shenlian Lu, Xinyu Guo, "Multiple Classifier Combination for Recognition of Wheat Leaf Diseases". Intelligent Automation and Soft Computing, Vol. 15, No. X, pp. 1-10, 2009.

[6]. Wendy Williams, "Metaheuristic Algorithms". Genetic Algorithm: A tutorial.

[7]. Weizheng, S., Yachun, W., Zhanliang, C., and Hongda, W. (2008). Grading Method of Leaf Spot Disease Based on Image Processing. In Proceedings of the 2008 international Conference on CSSE. IEEE Computer Society, Washington, DC, 491-494.

[8]. Adrian Doloca "" Feature Selection for Texture Analysis using Genetic Algorithms" Intern. J. Computer Math., Vol. 74, pp. 279-292, 2000.